AUBURN

SAMUEL GINN
COLLEGE OF ENGINEERING

Research Report No. 2F for ALDOT Project 930-601

REPAIR OF CRACKED PRESTRESSED CONCRETE GIRDERS, I-565, HUNTSVILLE, ALABAMA

Submitted to

The Alabama Department of Transportation

Prepared by

Wesley O. Bullock

Robert W. Barnes

Anton K. Schindler

JULY 2011

Highway Research Center

Harbert Engineering Center
Auburn, Alabama 36849

www.eng.auburn.edu/research/centers/hrc.html

1. Report No.	2. Government Accession No.	3. Recipient Catalog No.
FHWA/ALDOT 930-601-2F		

4 Title and Subtitle	5 Report Date
Repair of Cracked Prestressed Concrete Girders, I-565, Huntsville, Alabama	July 2011
	6 Performing Organization Code
7. Author(s)	**8 Performing Organization Report No.**
Wesley O. Bullock, Robert W. Barnes, and Anton K. Schindler	FHWA/ALDOT 930-601-2F
9 Performing Organization Name and Address	**10 Work Unit No. (TRAIS)**
Highway Research Center Department of Civil Engineering 238 Harbert Engineering Center Auburn, AL 36849	**11 Contract or Grant No.**
12 Sponsoring Agency Name and Address	**13 Type of Report and Period Covered**
Alabama Department of Transportation 1409 Coliseum Boulevard Montgomery, Alabama 36130-3050	Technical Report
	14 Sponsoring Agency Code

15 Supplementary Notes

Research performed in cooperation with the Alabama Department of Transportation

16 Abstract

Wide cracks were discovered in prestressed concrete bridge girders shortly after their construction in Huntsville, Alabama. Previous investigations of these continuous-for-live-load girders revealed that the cracking resulted from restrained thermal deformations and inadequate reinforcement details, and that the cracking compromised the strength of the girder end regions. A wet-layup fiber-reinforced polymer (FRP) repair system was installed. To assess the efficacy of the FRP repair solution, load testing and finite-element analyses were conducted for pre- and post-repair conditions of two repaired spans.

Post-repair testing included controlled truck loading as well as the monitoring of structural response to diurnal thermal conditions. Results indicate that the girders should be considered simply supported for conservative strength-limit-state design of the FRP repair system. FRP response to thermal conditions was accurately estimated using simplified analysis of restrained temperature gradient effects.

A design procedure was developed for FRP repair of similar structures in accordance with AASHTO LRFD Bridge Design Specifications and the recommendations of ACI 440.2R-08. The reported procedure was formulated to provide the girder end regions with adequate strength for the combined effects of shear and flexure, as well as to provide adequate performance under daily truck loads and temperature variations.

17 Key Words	18 Distribution Statement
Bridges, continuity, cracking, damage, fiber-reinforced polymer reinforcement, repair, restraint stresses, strengthening, thermal effects	No restrictions. This document is available to the public through the National Technical Information Service, Springfield, Virginia 22161

19 Security Classification (of this report)	20 Security Classification (of this report)	21 No. of pages	22 Price
Unclassified	Unclassified	621	

Research Report FHWA/ALDOT 930-601-2F

REPAIR OF CRACKED PRESTRESSED CONCRETE GIRDERS, I-565, HUNTSVILLE, ALABAMA

Submitted to

The Alabama Department of Transportation

Prepared by

Wesley O. Bullock
Robert W. Barnes
Anton K. Schindler

JULY 2011

DISCLAIMERS

The contents of this report reflect the views of the authors, who are responsible for the facts and the accuracy of the data presented herein. The contents do not necessarily reflect the official views or policies of Auburn University or the Federal Highway Administration. This report does not constitute a standard, specification, or regulation.

NOT INTENDED FOR CONSTRUCTION, BIDDING, OR PERMIT PURPOSES

Robert W. Barnes, Ph.D., P.E.
Anton K. Schindler, Ph.D., P.E.
Research Supervisors

ACKNOWLEDGEMENTS

Material contained herein was obtained in connection with a research project ALDOT 930-601, conducted by the Auburn University Highway Research Center. Funding for the project was provided by the Federal Highway Administration (FHWA) and the Alabama Department of Transportation (ALDOT). The funding, cooperation, and assistance of many individuals from each of these organizations are gratefully acknowledged. The authors would like to acknowledge the various contributions of the following individuals:

George H. Conner, State Maintenance Engineer, ALDOT
Robert King, Structural Engineer, FHWA
Eric Christie, Bridge Maintenance Engineer, ALDOT
W. Sean Butler, First Division, ALDOT
Randall Mullins, Section Supervisor, Bridge Bureau, ALDOT
James F. Boyer, Bridge Rating Engineer, ALDOT
Robert A. Fulton, formerly of Maintenance Bureau, ALDOT
Mark Strickland, Specifications Engineer, ALDOT
Lyndi Blackburn, Assistant Materials and Tests Engineer, ALDOT

ABSTRACT

After the construction of elevated portions of I-565 in Huntsville, Alabama, cracks were discovered in numerous prestressed concrete bulb-tee bridge girders that were constructed to exhibit continuous behavior in response to post-construction loads. Previous investigations conducted by Alabama Department of Transportation (ALDOT) and Auburn University Highway Research Center (AUHRC) personnel resulted in determinations that the cracking was a result of restrained thermal deformations and inadequate reinforcement details, and that the cracking compromised the strength of the girder end regions. A wet-layup fiber-reinforced polymer (FRP) repair scheme was proposed to address the deficiency. To assess the efficacy of the FRP repair solution, load testing and finite element model (FEM) analyses were conducted for pre- and post-repair conditions of Northbound Spans 10 and 11. Pre-repair testing was conducted on June 1 and 2, 2005. The FRP reinforcement system was installed in December 2007. Post-repair testing was conducted on May 25 and 26, 2010.

Post-repair testing included controlled truck loading as well as the monitoring of structural response to diurnal thermal conditions. Analysis of pre- and post-repair results indicated that the efficacy of the repair solution could not be assessed with direct comparisons between pre- and post-repair measurements due to unforeseen unintentional support conditions that were in effect during the pre-repair testing. Direct analysis of post-repair behavior indicated that the structure exhibits continuity degradation in response to heavy truck loads and should be considered simply supported for conservative strength-limit-state design. Analysis of responses to thermal conditions indicated the FRP reinforcement exhibits behavior that can be accurately estimated with simplified analysis of linear temperature gradient effects on restrained girders. Based on conditions observed after more than 2 years in service, the installed FRP reinforcement system was determined to be performing appropriately.

Based on the experimental observations, a design procedure was developed for FRP repair of similar structures with damaged regions near continuous ends of prestressed concrete bridge girders in accordance with AASHTO LRFD Bridge Design Specifications and the recommendations of ACI 440.2R-08. The design procedure was formulated to provide the girder end regions with adequate strength-limit-state resistance for the combined effects of shear and flexure, as well as to provide adequate performance under service loads—including the effects of daily temperature variations. A design example is presented.

TABLE OF CONTENTS

LIST OF TABLES xvi
LIST OF FIGURES xx

CHAPTER 1
INTRODUCTION 1
1.1 Project Overview 1
1.2 Need for Research 3
1.3 Project Objectives 5
1.4 Project Tasks 5
1.4.1 Task 1: Preliminary Engineering for FRP Repair 6
1.4.2 Task 2: Literature Review on Current State of the Art 6
1.4.3 Task 3: Preliminary Load Testing 6
1.4.4 Task 4: Construction Monitoring 6
1.4.5 Task 5: Post-Repair Load Testing 6
1.4.6 Task 6: Performance Monitoring under Traffic Loads 7
1.4.7 Task 7: Evaluation of Bridge Performance 7
1.4.8 Task 8: Evaluation of Acoustic Emission Monitoring 7
1.4.9 Task 9: Preparation of Final Project Reports 7
1.5 Report Organization 7

CHAPTER 2
HISTORY OF THE BRIDGE STRUCTURE AND ASSOCIATED RESEARCH 9
2.1 Introduction 9
2.2 Bridge Construction 9
2.3 Structural Geometry and Material Properties 9
2.3.1 Spans Investigated 10
2.3.2 Girder Types 13
2.3.3 Prestressing Strands 14
2.3.4 Shear Reinforcement 19
2.3.5 Continuity Reinforcement 23
2.3.6 Bridge Deck 25
2.4 Unexpected Cracking 28
2.4.1 Crack Locations 28
2.4.2 Previous Repairs and Safety Measures 32
2.4.3 Causes for Cracking 34

2.4.3.1 Construction Sequence 34
2.4.3.2 Time-Dependent Effects 35
2.4.3.3 Temperature Effects 35
2.4.3.4 Internal Reinforcement Details 36
2.4.4 Ramifications of Cracking 37
2.5 Bridge Behavior Analysis 38
2.5.1 Behavior Types Considered 38
2.5.2 Analysis Methods 38
2.5.2.1 Elastic Structural Analysis—Unfactored Demands 39
2.5.2.2 Sectional Model Analysis—Strength Capacities 39
2.5.2.3 Strut-and-Tie Analysis—Flow of Forces 40
2.6 Design of External Fiber-Reinforced Polymer Strengthening System 43
2.7 Load Tests Prior to FRP Reinforcement Installation 46
2.7.1 Instrumentation for Pre-Repair Load Testing 46
2.7.2 Procedures for Pre-Repair Load Testing 47
2.7.3 Results of Pre-Repair Load Testing 47
2.8 Finite-Element Analysis of Bridge Behavior 48
2.8.1 Uncracked Model 48
2.8.2 Cracked Model 48
2.8.3 Cracked-with-Reinforcement Model 49
2.8.4 Pre-Repair Model 49
2.8.5 Post-Repair Model 49
2.9 Installation of External FRP Reinforcement 49
2.9.1 Surface Preparation 50
2.9.2 Adhesion Testing 53
2.9.3 Tensile Testing 54
2.9.4 FRP Fabric Installation Procedures 56
2.9.5 FRP Fabric Installation—First Layer 59
2.9.6 FRP Fabric Installation—Second Layer 59
2.9.7 FRP Fabric Installation—Third Layer 60
2.9.8 FRP Fabric Installation—Fourth Layer 60
2.9.9 Painting of Installed FRP Reinforcement 61
2.9.10 FRP Reinforcement Installation Timeline 62
2.9.10.1 December 11, 2007 63
2.9.10.2 December 12, 2007 63
2.9.10.3 December 13, 2007 63
2.9.10.4 December 14, 2007 64

2.9.10.5 December 15, 2007 64
2.9.10.6 December 16, 2007 64
2.9.10.7 December 17, 2007 64
2.9.10.8 December 18, 2007 64
2.9.10.9 December 19, 2007 64
2.9.10.10 After December 19, 2007 64
2.10 Installation and Testing Concerns 65
2.10.1 FRP Orientation 65
2.10.2 FRP Samples for Tensile Testing 65
2.10.3 FRP Tensile Testing Observation 65
2.10.4 FRP Tensile Test Results 66
2.11 Current Research 67

CHAPTER 3
BRIDGE INSTRUMENTATION 68
3.1 Introduction 68
3.2 Instrumentation Overview 68
3.3 Crack-Opening Displacement Gages 70
3.3.1 COD Gage Locations 72
3.3.2 COD Gage Installation 72
3.4 Deflectometers 74
3.4.1 Deflectometer Locations 75
3.4.2 Deflectometer Installation 78
3.5 Strain Gages 81
3.5.1 Strain Gage Locations 82
3.5.1.1 Cross Section Locations 91
3.5.1.2 Gage Locations within A Typical Cross Section 92
3.5.1.3 Discontinued, Additional, and Replacement Gages 92
3.5.2 Concrete Strain Gages 93
3.5.3 FRP Strain Gages 94
3.5.4 Strain Gage Installation 95
3.6 Data Acquisition System 101
3.7 Sensor Notation 102

CHAPTER 4
BRIDGE TESTING PROCEDURES 104
4.1 Introduction 104
4.2 Traffic Control 104
4.3 Load Testing Trucks 105
4.3.1 Load Truck Block Configurations 109
4.3.2 Resultant Force Comparisons—Pre- and Post-Repair 113
4.3.3 Night 1—AE Preloading—LC-6.5 114
4.3.4 Night 2—AE Loading and Multiposition Load Test—LC-6 115
4.3.5 Truck Weight Limits 115
4.4 Load Testing Traverse Lanes and Stop Positions 115
4.4.1 Traverse Lanes 116
4.4.2 Stop Positions 118
4.5 Acoustic Emissions Load Testing 120
4.6 Bridge Monitoring 122
4.6.1 Weather Conditions during Pre-Repair Testing 123
4.6.2 Weather Conditions during Post-Repair Testing 123
4.7 Multiposition Load Testing 125
4.8 Superposition Testing 126
4.9 Data Reduction and Analysis 129

CHAPTER 5
RESULTS AND DISCUSSION 130
5.1 Introduction 130
5.2 Bearing Pad Effects 130
5.3 Bridge Response to Truck Loads—Post-Repair 136
5.3.1 Response to Different Horizontal Truck Alignments 136
5.3.2 Indications of Damage to Instrumented Girders 141
5.3.2.1 Crack-Opening Displacements 141
5.3.2.2 Crack-Opening Displacement Observations 144
5.3.2.3 Bottom-Fiber Strains 145
5.3.2.4 Bottom-Fiber Strain Observations 150
5.3.2.5 COD and Bottom-Fiber Strain Comparisons 150
5.3.2.6 Damage Indication Conclusions 154
5.3.3 Post-Repair Continuity Behavior Assessment 154
5.3.3.1 Deflections 154
5.3.3.2 Bottom-Fiber Strains 159

5.3.3.3 Crack Behavior 170
5.3.3.4 Continuity Behavior Conclusions 177
5.3.4 Linear-Elastic Behavior 178
5.3.4.1 Linear-Elastic Behavior Assessment—Two-Span Structure 178
5.3.4.2 Linear-Elastic Behavior Assessment—Damaged Regions 180
5.3.4.3 Linear-Elastic Behavior Conclusions 185
5.3.5 Relationship between Truck Position and FRP Tensile Demand 185
5.4 Bridge Response to Ambient Thermal Conditions 193
5.4.1 Theoretical Response to Ambient Thermal Conditions 193
5.4.1.1 Structural Analysis 194
5.4.1.2 Expected Behavior 198
5.4.2 Measured Responses to Ambient Thermal Conditions 206
5.4.2.1 Deflections 207
5.4.2.2 Bottom-Fiber Strains 213
5.4.2.3 Crack-Opening Displacements 231
5.5 Performance of FRP Reinforcement 238
5.6 Conclusions 239

CHAPTER 6
FRP REINFORCEMENT DESIGN 241
6.1 Introduction 241
6.2 Necessity of FRP Reinforcement 241
6.3 FRP Reinforcement Product Selection 242
6.4 Strength-Limit-State Design 243
6.4.1 Critical Cross-Section Locations 244
6.4.2 Critical Load Conditions 244
6.4.3 Strength-Limit-State Temperature Demands 245
6.4.4 Material Properties 245
6.4.4.1 Concrete 245
6.4.4.2 Steel Reinforcement 246
6.4.4.3 FRP Reinforcement 246
6.4.5 Dimensional Properties 247
6.4.5.1 Cross-Section Dimensions 248
6.4.5.2 Reinforcement Dimensions 248
6.4.6 Initial Estimate of Required FRP Layers 250
6.4.7 Vertical Shear Strength Resistance 251
6.4.7.1 Nominal Strength for Bending Moment Resistance 252

6.4.7.2 Effective Shear Depth 252
6.4.7.3 Net Tension Strain 253
6.4.7.4 Diagonal Shear Crack Parameters 254
6.4.7.5 Components of Vertical Shear Strength 255
6.4.7.6 Nominal Vertical Shear Strength 256
6.4.7.7 Factored Strength for Resisting Shear Demand 256
6.4.8 Tensile Strength 257
6.4.8.1 Nominal Strength for Resisting Tension 257
6.4.8.2 Factored Tension Demand 257
6.4.9 Check Strengths of Each Location with Equal Layers of FRP 258
6.5 Length of FRP Reinforcement Installation 258
6.6 Anchorage 259
6.7 Service Limit State 261
6.8 Design Summary 262
6.9 Installation Recommendations 262
6.9.1 Preparing for Installation 262
6.9.1.1 Adhesion Testing 262
6.9.1.2 Crack Injection 263
6.9.1.3 Surface Preparation and Profiling 263
6.9.2 FRP Reinforcement Installation 264
6.9.2.1 Epoxy Saturation 264
6.9.2.2 Application of FRP Reinforcement 265
6.9.2.3 Protective Coating 265
6.9.2.4 Quality Control Testing and Inspection 265

CHAPTER 7
SUMMARY AND CONCLUSIONS 267
7.1 Project Summary 267
7.2 Conclusions 268
7.2.1 FRP Reinforcement Installation 269
7.2.2 Observed Responses to Truck Loads 269
7.2.3 Theoretical Responses to Ambient Thermal Conditions 270
7.2.4 Observed Responses to Ambient Thermal Conditions 270
7.2.5 Performance of FRP Reinforcement 271
7.2.6 FRP Design Recommendations 271
7.2.7 FRP Reinforcement Installation Recommendations 272

CHAPTER 8
RECOMMENDATIONS 274
8.1 Design of FRP Reinforcement Repair Solutions 274
8.2 Installation of FRP Reinforcement Systems 274
8.3 Northbound Spans 10 and 11 of I-565 275
8.4 Recommendations for Further Research 276
8.4.1 In-Service Load Testing 276
8.4.2 In-Service Bridge Monitoring 276
8.4.3 Laboratory Testing 277

REFERENCES 278

APPENDIX A
ABBREVIATIONS AND NOTATION 281

APPENDIX B
MULTIPOSITION LOAD TEST—GRAPHICAL RESULTS 285
B.1 Lane A 286
B.1.1 Crack-Opening Displacements 286
B.1.2 Deflections 291
B.1.3 Cross-Section Strains 296
B.1.3.1 Cross-Section Strains—Girder 7 296
B.1.3.2 Cross-Section Strains—Girder 8 316
B.1.4 Bottom-Fiber Strains—Both Girders 336
B.1.4.1 Bottom-Fiber Strains—Girder 7 341
B.1.4.2 Bottom-Fiber Strains—Girder 8 346
B.2 Lane C 351
B.2.1 Crack-Opening Displacements 351
B.2.2 Deflections 356
B.2.3 Cross-Section Strains 361
B.2.3.1 Cross-Section Strains—Girder 7 361
B.2.3.2 Cross-Section Strains—Girder 8 381
B.2.4 Bottom-Fiber Strains—Both Girders 401
B.2.4.1 Bottom-Fiber Strains—Girder 7 406
B.2.4.2 Bottom-Fiber Strains—Girder 8 411

APPENDIX C
MULTIPOSITION LOAD TEST—MEASUREMENTS 416
C.1 Lane A 417
C.2 Lane C 427

APPENDIX D
BRIDGE MONITORING—GRAPHICAL RESULTS 437
D.1 Crack-Opening Displacements 438
D.2 Deflections 439
D.3 Bottom-Fiber Strains 440
D.4 Bottom-Fiber Strains and Crack-Opening Displacements 442

APPENDIX E
BRIDGE MONITORING MEASUREMENTS 445
E.1 Crack-Opening Displacements 446
E.2 Deflections 447
E.3 Cross-Section Strains 449
E.4 Bottom-Fiber Strains 457
E.5 FRP Strains 461

APPENDIX F
BRIDGE MONITORING—MEASUREMENT ADJUSTMENTS 464
F.1 Inconsistent Measurements 465
F.2 Deflectometer Behavior 465
F.3 Deflection Adjustments 465
F.4 Graphical Presentations of Deflection Adjustments 466
F.4.1 Original Deflections—Girders 7 and 8 466
F.4.2 Adjusted Deflections of Girder 7 in Span 10 467
F.4.3 Adjusted Deflections of Girder 7 in Span 11 470
F.4.4 Adjusted Deflections of Girder 8 in Span 10 473
F.4.5 Adjusted Deflections of Girder 8 in Span 11 476
F.4.6 Final Adjusted Deflections—Girders 7 and 8 479
F.5 Strain Measurement Adjustments 480

APPENDIX G
SUPERPOSITION—GRAPHICAL RESULTS 482
G.1 Crack-Opening Displacements 483
G.2 Deflections 487
G.3 Bottom-Fiber Strains 491

APPENDIX H
SUPERPOSITION—MEASUREMENTS 495

APPENDIX I
AE STATIC POSITIONS—GRAPHICAL RESULTS 500
I.1 Crack-Opening Displacements 501
I.2 Deflections 506
I.3 Bottom-Fiber Strains 511
I.3.1 Bottom-Fiber Strains—Girder 7 516
I.3.2 Bottom-Fiber Strains—Girder 8 521

APPENDIX J
AE STATIC POSITIONS—MEASUREMENTS 526

APPENDIX K
FALSE SUPPORT BEARING PAD EFFECTS DURING LOAD TESTING 539
K.1 Installation of False Supports with Bearing Pads 539
K.2 Pre-Repair Bearing Pad Conditions 542
K.3 Bearing Pad Removal during FRP Installation 543
K.4 Post-Repair Bearing Pad Conditions 546
K.5 Analysis of Numerical Results 546
K.5.1 Deflections—Multiposition Load Testing 546
K.5.2 Crack-Opening Displacements—Multiposition Load Testing 551
K.5.3 Surface Strains 554
K.5.4 Superposition Deflections 563
K.6 Bearing Pad Effects 565

APPENDIX L
DATA ACQUISITION CHANNEL LAYOUT 566

APPENDIX M

STRAIN GAGE INSTALLATION PROCEDURE—FRP REINFORCEMENT 570

APPENDIX N

FRP REINFORCEMENT DESIGN EXAMPLE 578

N.1 Introduction 578

N.2 Product Selection 578

N.3 Strength-Limit-State Design 578

N.3.1 Critical Cross-Section Locations 579

N.3.2 Critical Load Conditions 584

N.3.3 Material Properties 587

N.3.4 Dimensional Properties 588

N.3.5 Initial Estimate of Required FRP Layers 596

N.3.6 Shear Strength Check—Three Layers 598

N.3.6.1 Limiting Effective FRP Debonding Strain—Three Layers 598

N.3.6.2 Effective Shear Depth—Three Layers 600

N.3.6.3 Net Longitudinal Tensile Strain—Initial Estimate 601

N.3.6.4 Layers Required to Satisfy Tensile Strain Demand 603

N.3.7 Shear Strength—Five Layers 604

N.3.7.1 Effective FRP Strain—Five Layers 605

N.3.7.2 Effective Shear Depth—Five Layers 606

N.3.7.3 Net Longitudinal Tensile Strain—Five Layers 606

N.3.7.4 Vertical Shear Strength—Five Layers 608

N.3.7.5 Longitudinal Tension Strength Provided—Five Layers 612

N.3.7.6 Longitudinal Tension Strength Required—Five Layers 613

N.3.7.7 Longitudinal Tension Strength Verification—Five Layers 614

N.3.7.8 Strength and Demand Comparisons—Five Layers 614

N.4 Extent of FRP Installation 615

N.5 Anchorage 618

N.6 Service-Limit-State Verification 618

N.7 Design Summary 619

N.8 Installation Recommendations 619

N.9 Comparison of Design Recommendation and Previously Installed FRP 619

N.10 Varying Modulus of Elasticity for FRP Reinforcement 621

LIST OF TABLES

Table 2.1: Stirrup mild steel bar details (ALDOT 1988; Swenson 2003) 21
Table 2.2: Summary of cracking in prestressed concrete girders made continuous for live loads (ALDOT 1994) 31
Table 2.3: Weather during FRP reinforcement installation (NOAA 2008) 63
Table 2.4: Summary of Reported ASTM D 3039 Tensile Test Results 66
Table 3.1: COD gage locations 72
Table 3.2: Deflectometer locations 78
Table 3.3: Strain-gaged cross sections 84
Table 3.4: Strain gage locations within cross section 90
Table 4.1: Load truck weight distributions—pre-repair 109
Table 4.2: Load truck weight distributions—post-repair 110
Table 4.3: Comparison of unconventional load truck weight distributions 110
Table 4.4: Resultant force comparisons—ST-6400—LC-6 113
Table 4.5: Resultant force comparisons—ST-6400—LC-6.5 113
Table 4.6: Resultant force comparisons—ST-6902 and ST-6538—LC-6 114
Table 4.7: Resultant force comparisons—ST-6902 and ST-6538—LC-6.5 114
Table 4.8: Stop position locations 118
Table 4.9: Weather during pre-repair bridge testing (NOAA 2005) 123
Table 4.10: Weather during post-repair bridge testing (NOAA 2010) 124
Table 4.11: Temperatures measured during bridge monitoring (NOAA 2010) 124
Table 5.1: Bearing pad effects—crack-opening displacements 135
Table 5.2: Midspan truck positions—deflections 140
Table 5.3: AE truck positions—crack-opening displacements 144
Table 5.4: AE truck positions—bottom-fiber strains—Girder 7 148
Table 5.5: AE truck positions—bottom-fiber strains—Girder 8 149
Table 5.6: Midspan truck positions—deflections 157
Table 5.7: Midspan truck positions—bottom-fiber strains—Girder 7 162
Table 5.8: Midspan truck positions—bottom-fiber strains—Girder 8 163
Table 5.9: Damaged region truck positions—bottom-fiber strains—Girder 7 166
Table 5.10: Damaged region truck positions—bottom-fiber strains—Girder 8 167
Table 5.11: Midspan truck positions—maximum crack closures 173
Table 5.12: Damaged region truck positions—maximum crack openings 176
Table 5.13: Superposition—deflections 179
Table 5.14: Superposition—maximum crack closures 181
Table 5.15: Superposition—bottom-fiber strains—Girder 7 183

Table 5.16: Superposition—bottom-fiber strains—Girder 8 184
Table 5.17: FRP tensile demand—bottom-fiber strains—Span 11 truck positions 192
Table 5.18: Crack openings—Span 11 truck positions 192
Table 5.19: Temperatures measured during bridge monitoring (NOAA 2010) 207
Table 5.20: Maximum upward deflections—thermal conditions 209
Table 5.21: Maximum upward deflections—post-repair 210
Table 5.22: Deflections—ambient thermal conditions 213
Table 5.23: Maximum bottom-fiber tensile strains—Girder 7—thermal conditions 216
Table 5.24: Maximum bottom-fiber tensile strains—Girder 8—thermal conditions 217
Table 5.25: Maximum bottom-fiber tensile strains—Girder 7 217
Table 5.26: Maximum bottom-fiber tensile strains—Girder 8 218
Table 5.27: Bottom-fiber strains—Girder 7—ambient thermal conditions 221
Table 5.28: Bottom-fiber strains—Girder 8—ambient thermal conditions 222
Table 5.29: Maximum crack openings—thermal conditions 233
Table 5.30: Maximum crack openings—thermal and load truck conditions 233
Table 5.31: Crack-opening displacements—ambient thermal conditions 234
Table 5.32: Crack openings and bottom-fiber strains—thermal conditions 237
Table C.1: Lane A—crack-opening displacements 417
Table C.2: Lane A—deflections 418
Table C.3: Lane A—cross-section strains—Girder 7—Span 10 419
Table C.4: Lane A—cross-section strains—Girder 7—Span 11 420
Table C.5: Lane A—cross-section strains—Girder 8—Span 10 421
Table C.6: Lane A—cross-section strains—Girder 8—Span 11 422
Table C.7: Lane A—bottom-fiber strains—Girder 7 423
Table C.8: Lane A—bottom-fiber strains—Girder 8 424
Table C.9: Lane A—FRP strains—Girder 7 425
Table C.10: Lane A—FRP strains—Girder 8 426
Table C.11: Lane C—crack-opening displacements 427
Table C.12: Lane C—deflections 428
Table C.13: Lane C—cross-section strains—Girder 7—Span 10 429
Table C.14: Lane C—cross-section strains—Girder 7—Span 11 430
Table C.15: Lane C—cross-section strains—Girder 8—Span 10 431
Table C.16: Lane C—cross-section strains—Girder 8—Span 11 432
Table C.17: Lane C—bottom-fiber strains—Girder 7 433
Table C.18: Lane C—bottom-fiber strains—Girder 8 434
Table C.19: Lane C—FRP strains—Girder 7 435
Table C.20: Lane C—FRP strains—Girder 8 436

Table E.1: Bridge monitoring—crack-opening displacements 446
Table E.2: Bridge monitoring—deflections—Girder 7 447
Table E.3: Bridge monitoring—deflections—Girder 8 448
Table E.4: Bridge monitoring—strains—Girder 7—Section 1 449
Table E.5: Bridge monitoring—strains—Girder 7—Section 2 450
Table E.6: Bridge monitoring—strains—Girder 7—Section 3 451
Table E.7: Bridge monitoring—strains—Girder 7—Section 4 452
Table E.8: Bridge monitoring—strains—Girder 8—Section 1 453
Table E.9: Bridge monitoring—strains—Girder 8—Section 2 454
Table E.10: Bridge monitoring—strains—Girder 8—Section 3 455
Table E.11: Bridge monitoring—strains—Girder 8—Section 4 456
Table E.12: Bridge monitoring—bottom-fiber strains—Girder 7 457
Table E.13: Bridge monitoring—bottom-fiber strains—Girder 8 459
Table E.14: Bridge monitoring—FRP strains—Girder 7 461
Table E.15: Bridge monitoring—FRP strains—Girder 8 462
Table H.1: Superposition—crack-opening displacements 496
Table H.2: Superposition—deflections 497
Table H.3: Superposition—bottom-fiber strains—Girder 7 498
Table H.4: Superposition—bottom-fiber strains—Girder 8 499
Table J.1: AE static positions—crack-opening displacements 529
Table J.2: AE static positions—deflections 530
Table J.3: AE static positions—cross-section strains—Girder 7—Span 10 531
Table J.4: AE static positions—cross-section strains—Girder 7—Span 11 532
Table J.5: AE static positions—cross-section strains—Girder 8—Span 10 533
Table J.6: AE static positions—cross-section strains—Girder 8—Span 11 534
Table J.7: AE static positions—bottom-fiber strains—Girder 7 535
Table J.8: AE static positions—bottom-fiber strains—Girder 8 536
Table J.9: AE static positions—FRP strains—Girder 7 537
Table J.10: AE static positions—FRP strains—Girder 8 538
Table K.1: Deflections—A1 547
Table K.2: Deflections—A9 548
Table K.3: Deflections—C1 549
Table K.4: Deflections—C9 550
Table K.5: Bearing pad effects—crack-opening displacements 554
Table K.6: Deflections—superposition—A1 and A9 564
Table K.7: Deflections—superposition—A1 + A9 565
Table L.1: Data acquisition channels—crack-opening displacement gages 567

Table L.2: Data acquisition channels—deflectometers 567
Table L.3: Data acquisition channels—strain gages—Span 10 568
Table L.4: Data acquisition channels—strain gages—Span 11 569
Table N.1: Critical cross-section locations 579
Table N.2: Critical load conditions 584
Table N.3: Material properties 588
Table N.4: Cross section dimensional properties 589
Table N.5: Reinforcement dimensional properties 591
Table N.6: Initial estimate for minimum area of FRP required 596
Table N.7: Initial estimate for minimum layers of FRP required 597
Table N.8: Effective FRP debonding strain—three layers 599
Table N.9: Effective shear depth—three layers 600
Table N.10: Net longitudinal tensile strain—three layers 602
Table N.11: Layers required satisfying net longitudinal tensile strain 604
Table N.12: Effective FRP debonding strain—five layers 605
Table N.13: Effective shear depth—five layers 606
Table N.14: Net longitudinal tensile strain—five layers 607
Table N.15: Vertical shear strength—concrete—five layers 608
Table N.16: Vertical shear strength—vertical reinforcement—five layers 609
Table N.17: Nominal shear strength—five layers 610
Table N.18: Vertical shear strength verification—five layers 611
Table N.19: Longitudinal tension strength—five layers 612
Table N.20: Longitudinal tension demand—five layers 613
Table N.21: Longitudinal tension strength verification—five layers 614
Table N.22: Comparisons of strength and demand—five layers 615

LIST OF FIGURES

Figure 1.1: Elevated spans of I-565 in Huntsville, Alabama 1
Figure 1.2: Northbound Bent 11 of I-565 in Huntsville, Alabama 2
Figure 1.3: Cracked pre-tensioned bulb-tee girders of I-565 (Barnes et al. 2006) 2
Figure 1.4: Girder 9 of Northbound Spans 10 and 11—repaired 4
Figure 1.5: Girders 7, 8, and 9 of Northbound Span 10—repaired 5
Figure 2.1: Plan view of the two-span continuous unit (ALDOT 1988) 10
Figure 2.2: Elevation view of the two-span continuous unit (ALDOT 1988) 11
Figure 2.3: Detailed plan view of the two-span continuous unit (ALDOT 1988) 12
Figure 2.4: Cross section of a typical BT-54 girder (ALDOT 1988; Swenson 2003) 14
Figure 2.5: Prestressed strand pattern near girder end (ALDOT 1988; Swenson 2003) 15
Figure 2.6: Prestressed strand pattern near girder midpoint (ALDOT 1988; Swenson 2003) 16
Figure 2.7: Prestressed strand profile (Swenson 2003) 18
Figure 2.8: Vertical shear reinforcement near girder end (ALDOT 1988; Swenson 2003) 19
Figure 2.9: Vertical shear reinforcement near girder midpoint (ALDOT 1988; Swenson 2003) 20
Figure 2.10: Location and spacing of vertical shear reinforcement (ALDOT 1988; Swenson 2003) 22
Figure 2.11: Continuity reinforcement—continuity diaphragm detail (ALDOT 1988; Swenson 2003) 23
Figure 2.12: Continuity reinforcement of a typical BT-54 cross section (ALDOT 1988; Swenson 2003) 24
Figure 2.13: Cross section view of deck slab reinforcement over an exterior girder (ALDOT 1988; Swenson 2003) 26
Figure 2.14: Cross section view of deck slab reinforcement over an interior girder (ALDOT 1988; Swenson 2003) 27
Figure 2.15: Portion of I-565 containing cracked bridge girders (Swenson 2003) 29
Figure 2.16: Cracking pattern in end region of precast girder (Barnes et al. 2006) 29
Figure 2.17: Cracked pre-tensioned bulb-tee girders (Barnes et al. 2006) 30
Figure 2.18: Typical diaphragm face crack (Swenson 2003) 30
Figure 2.19: Typical diaphragm end crack (Swenson 2003) 31
Figure 2.20: Cracks injected with epoxy (Fason 2009) 32
Figure 2.21: Steel frame false supports (Fason 2009) 33
Figure 2.22: False support bearing pad with gap between pad and girder (Fason 2009) 33

Figure 2.23: False support bearing pad in contact with girder (Fason 2009) 34
Figure 2.24: Cracked girder with continuity reinforcement details (Barnes et al. 2006) 36
Figure 2.25: Typical strut-and-tie model (Swenson 2003) 41
Figure 2.26: Longitudinal configuration profile for FRP (Barnes et al. 2006) 44
Figure 2.27: Cross-sectional configuration of FRP near diaphragm (Swenson 2003) 45
Figure 2.28: Cross-sectional configuration of FRP beyond bearing pad (Swenson 2003) 45
Figure 2.29: Surface cleaning—final removal of dust and debris 50
Figure 2.30: Use of saw for bearing pad removal 51
Figure 2.31: Use of torch for bearing pad removal 52
Figure 2.32: Successful removal of bearing pad 52
Figure 2.33: Bearing pad after forceful removal 53
Figure 2.34: Adhesion test equipment (Swenson 2007) 54
Figure 2.35: Performance of on-site adhesion test 54
Figure 2.36: Preparation of sample for tension testing 55
Figure 2.37: Representative sample for tension testing 56
Figure 2.38: Cutting strips of FRP fabric 57
Figure 2.39: Epoxy saturation of FRP fabric 57
Figure 2.40: Applying epoxy to girder surface before FRP fabric installation 58
Figure 2.41: Installation of first layer of FRP fabric 58
Figure 2.42: Four layers of installed FRP fabric 59
Figure 2.43: FRP installation sequence–first layer 59
Figure 2.44: FRP installation sequence—second layer 60
Figure 2.45: FRP installation sequence—third layer 60
Figure 2.46: FRP installation sequence—fourth layer 61
Figure 2.47: Painting of FRP reinforcement 61
Figure 2.48: Painted FRP reinforcement of Span 10 62
Figure 3.1: Instrumentation overview 69
Figure 3.2: Crack-opening displacement gage (TML 2011) 71
Figure 3.3: Anchor blocks for COD gage installation (Fason 2009) 73
Figure 3.4: COD gage attached to anchor blocks 74
Figure 3.5: Typical deflectometer 75
Figure 3.6: Deflectometer locations—Girder Line 7 77
Figure 3.7: Deflectometer locations—Girder Line 8 77
Figure 3.8: Girder attachment point for deflectometer wire 79
Figure 3.9: Deflectometer aluminum bar—pre-bent with adjusted turnbuckle 80
Figure 3.10: Deflectometer area—Span 11 81
Figure 3.11: Strain gage cross section locations 83

Figure 3.12: Strain gage locations—Girder 7—Section 1 85
Figure 3.13: Strain gage locations—Girder 7—Section 2 85
Figure 3.14: Strain gage locations—Girder 7—Section 3 86
Figure 3.15: Strain gage locations—Girder 7—Section 4 86
Figure 3.16: Strain gage locations—Girder 8—Section 1 87
Figure 3.17: Strain gage locations—Girder 8—Section 2 87
Figure 3.18: Strain gage locations—Girder 8—Section 3 88
Figure 3.19: Strain gage locations—Girder 8—Section 4 88
Figure 3.20: Strain gage locations—Girders 7 and 8—Section 5 89
Figure 3.21: Strain gage locations—Girders 7 and 8—Sections 6, 7, and 8 89
Figure 3.22: Strain gage locations—CRACK 90
Figure 3.23: Surface-mounted strain gage—concrete (Fason 2009) 94
Figure 3.24: Surface-mounted strain gage—FRP reinforcement 95
Figure 3.25: Strain gage installation—applying degreaser to gage location 96
Figure 3.26: Strain gage installation—removal of surface irregularities 96
Figure 3.27: Strain gage installation—initial surface cleaning 97
Figure 3.28: Strain gage installation—clean surface prepared for solid epoxy 97
Figure 3.29: Strain gage installation—application of solid epoxy 98
Figure 3.30: Strain gage installation—epoxy surface 98
Figure 3.31: Strain gage installation—gage application with thin epoxy 99
Figure 3.32: Strain gage installation—gage applied to FRP reinforcement 100
Figure 3.33: Strain gage installation—rubber coating for moisture protection 101
Figure 3.34: Strain gage installation—mastic tape for mechanical protection 101
Figure 3.35: Data acquisition hardware 102
Figure 4.1: ST-6400 (standard load truck) 105
Figure 4.2: ST-6902 (pre-repair unconventional truck) 106
Figure 4.3: ST-6538 (post-repair replacement for pre-repair unconventional truck) 106
Figure 4.4: Footprint of ALDOT load testing trucks (ST-6400 and ST-6538) 107
Figure 4.5: Footprint of ALDOT tool trailer truck (ST-6902) 108
Figure 4.6: LC-6.5 block configuration—post-repair ST-6400 111
Figure 4.7: LC-6 block configuration—post-repair ST-6400 111
Figure 4.8: LC-6.5 block configuration—post-repair ST-6538 112
Figure 4.9: LC-6 block configuration—post-repair ST-6538 112
Figure 4.10: Traverse lanes and stop positions—overhead photo 116
Figure 4.11: Lane A—Horizontal truck positioning (multiposition test) 117
Figure 4.12: Lane C—Horizontal truck positioning (multiposition and AE tests) 117
Figure 4.13: Stop position locations 119

Figure 4.14: Acoustic emissions test—stop position locations 121
Figure 4.15: Superposition test—horizontal lane positioning 127
Figure 4.16: Superposition test—stop position locations 128
Figure 5.1: Crack-opening displacements—pre- and post-repair—A4 132
Figure 5.2: Crack-opening displacements—pre- and post-repair—A7 133
Figure 5.3: Crack-opening displacements—pre- and post-repair—C4 133
Figure 5.4: Crack-opening displacements—pre- and post-repair—C7 134
Figure 5.5: Lane A—horizontal truck positioning 136
Figure 5.6: Lane C—horizontal truck positioning 137
Figure 5.7: Deflections—A1 137
Figure 5.8: Deflections—A9 138
Figure 5.9: Deflections—C1 138
Figure 5.10: Deflections—C9 139
Figure 5.11: AE Span 10 truck position—crack-opening displacements—LC-6.5 142
Figure 5.12: AE Span 11 truck position—crack-opening displacements—LC-6.5 142
Figure 5.13: AE Span 10 truck position—crack-opening displacements—LC-6 143
Figure 5.14: AE Span 11 truck position—crack-opening displacements—LC-6 143
Figure 5.15: AE Span 10 truck position—bottom-fiber strains—LC-6.5 146
Figure 5.16: AE Span 11 truck position—bottom-fiber strains—LC-6.5 146
Figure 5.17: AE Span 10 truck position—bottom-fiber strains—LC-6 147
Figure 5.18: AE Span 11 truck position—bottom-fiber strains—LC-6 147
Figure 5.19: COD and bottom-fiber strain comparisons—LC-6.5—AE Span 10 151
Figure 5.20: COD and bottom-fiber strain comparisons—LC-6.5—AE Span 11 151
Figure 5.21: COD and bottom-fiber strain comparisons—LC-6—AE Span 10 152
Figure 5.22: COD and bottom-fiber strain comparisons—LC-6—AE Span 11 152
Figure 5.23: Deflections—A1 155
Figure 5.24: Deflections—A9 155
Figure 5.25: Deflections—C1 156
Figure 5.26: Deflections—C9 156
Figure 5.27: Deflections—post-repair—measurements and predictions—A9 158
Figure 5.28: Deflections—post-repair—measurements and predictions—C9 158
Figure 5.29: Bottom-fiber strain—A1 160
Figure 5.30: Bottom-fiber strain—A9 160
Figure 5.31: Bottom-fiber strain—C1 161
Figure 5.32: Bottom-fiber strain—C9 161
Figure 5.33: Bottom-fiber strain—A4 164
Figure 5.34: Bottom-fiber strain—A7 165

Figure 5.35: Bottom-fiber strain—C4 165
Figure 5.36: Bottom-fiber strain—C7 166
Figure 5.37: Bottom-fiber strain—post-repair—measurements and predictions—A7 168
Figure 5.38: Bottom-fiber strain—post-repair—measurements and predictions—A9 169
Figure 5.39: Bottom-fiber strain—post-repair—measurements and predictions—C7 169
Figure 5.40: Bottom-fiber strain—post-repair—measurements and predictions—C9 170
Figure 5.41: Midspan truck positions—crack-opening displacements—A1 171
Figure 5.42: Midspan truck positions—crack-opening displacements—A9 172
Figure 5.43: Midspan truck positions—crack-opening displacements—C1 172
Figure 5.44: Midspan truck positions—crack-opening displacements—C9 173
Figure 5.45: Damaged region truck positions—crack-opening displacements—A4 174
Figure 5.46: Damaged region truck positions—crack-opening displacements—A7 175
Figure 5.47: Damaged section truck positions—crack-opening displacements—C4 175
Figure 5.48: Damaged region truck positions—crack-opening displacements—C7 176
Figure 5.49: Superposition—deflections—predicted and measured 179
Figure 5.50: Superposition—crack-opening displacements—predicted and measured 181
Figure 5.51: Superposition—bottom-fiber strains—predicted and measured 183
Figure 5.52: Longitudinal truck positions—C6 186
Figure 5.53: Longitudinal truck positions—AE LC-6 Span 11 *and* C7 187
Figure 5.54: Longitudinal truck positions—C8 188
Figure 5.55: Bottom-fiber strains—C6 190
Figure 5.56: Bottom-fiber strains—AE LC-6 Span 11 190
Figure 5.57: Bottom-fiber strains—C7 191
Figure 5.58: Bottom-fiber strains—C8 191
Figure 5.59: Linear temperature gradient 194
Figure 5.60: Two-span continuous structure subjected to linear thermal gradient 194
Figure 5.61: Expected deformations—two theoretical load conditions 195
Figure 5.62: Moment diagrams—two theoretical load conditions 196
Figure 5.63: Curvature diagrams—two theoretical load conditions 197
Figure 5.64: Curvature due to temperature gradient with restraint 200
Figure 5.65: Moment due to temperature gradient with restraint 201
Figure 5.66: Shear due to temperature gradient with restraint 202
Figure 5.67: Bottom-fiber strain due to temperature gradient with restraint 203
Figure 5.68: Bottom-fiber stress due to temperature gradient with restraint 204
Figure 5.69: Deflections due to temperature gradient with restraint 206
Figure 5.70: Deflections—normal traffic—twenty-four hours—Girder 7 208
Figure 5.71: Deflections—normal traffic—twenty-four hours—Girder 8 208

Figure 5.72: Deflections—8:30 a.m. 211
Figure 5.73: Deflections—4:30 p.m. 211
Figure 5.74: Deflections—8:30 p.m. 212
Figure 5.75: Deflections—2:30 a.m. 212
Figure 5.76: Bottom-fiber strains—Girder 7—within 80 in. from diaphragm 214
Figure 5.77: Bottom-fiber strains—Girder 7—beyond 80 in. from diaphragm 214
Figure 5.78: Bottom-fiber strains—Girder 8—within 80 in. from diaphragm 215
Figure 5.79: Bottom-fiber strains—Girder 8—beyond 80 in. from diaphragm 215
Figure 5.80: Bottom-fiber strains—8:30 a.m. 219
Figure 5.81: Bottom-fiber strains—4:30 p.m. 220
Figure 5.82: Bottom-fiber strains—8:30 p.m. 220
Figure 5.83: Bottom-fiber strains—2:30 a.m. 221
Figure 5.84: Bottom-fiber strains—concrete—Girder 7—6:30 a.m. 223
Figure 5.85: Bottom-fiber strains—concrete—Girder 7—4:30 p.m. 223
Figure 5.86: Bottom-fiber strains—concrete—Girder 7—8:30 p.m. 224
Figure 5.87: Bottom-fiber strains—concrete—Girder 7—2:30 a.m. 224
Figure 5.88: Bottom-fiber strains—concrete—Girder 8—6:30 a.m. 225
Figure 5.89: Bottom-fiber strains—concrete—Girder 8—4:30 p.m. 225
Figure 5.90: Bottom-fiber strains—concrete—Girder 8—8:30 p.m. 226
Figure 5.91: Bottom-fiber strains—concrete—Girder 8—2:30 a.m. 226
Figure 5.92: Bottom-fiber strains—damaged region—8:30 a.m. 228
Figure 5.93: Bottom-fiber strains—damaged region—4:30 p.m. 229
Figure 5.94: Bottom-fiber strains—damaged region—8:30 p.m. 229
Figure 5.95: Bottom-fiber strains—damaged region—2:30 a.m. 230
Figure 5.96: Crack-opening displacements—normal traffic—twenty-four hours 232
Figure 5.97: Bottom-fiber strain and COD—thermal conditions—Girder 7—Span 10 235
Figure 5.98: Bottom-fiber strain and COD—thermal conditions—Girder 7—Span 11 235
Figure 5.99: Bottom-fiber strain and COD—thermal conditions—Girder 8—Span 10 236
Figure 5.100: Bottom-fiber strain and COD—thermal conditions—Girder 8—Span 11 236
Figure 6.1: Cross-sectional configuration of FRP—near diaphragm (Swenson 2003) 249
Figure 6.2: Cross-sectional configuration of FRP—typical (Swenson 2003) 249
Figure 6.3: Simplified model for initial estimate of FRP requirement 250
Figure 6.4: FRP fan anchorage system (Niemitz et al. 2010) 260
Figure B.1: Crack-opening displacements—A1 286
Figure B.2: Crack-opening displacements—A2 287
Figure B.3: Crack-opening displacements—A3 287
Figure B.4: Crack-opening displacements—A4 288

Figure B.5: Crack-opening displacements—A5 288
Figure B.6: Crack-opening displacements—A6 289
Figure B.7: Crack-opening displacements—A7 289
Figure B.8: Crack-opening displacements—A8 290
Figure B.9: Crack-opening displacements—A9 290
Figure B.10: Deflections—A1 291
Figure B.11: Deflections—A2 292
Figure B.12: Deflections—A3 292
Figure B.13: Deflections—A4 293
Figure B.14: Deflections—A5 293
Figure B.15: Deflections—A6 294
Figure B.16: Deflections—A7 294
Figure B.17: Deflections—A8 295
Figure B.18: Deflections—A9 295
Figure B.19: Strains—Girder 7—Section 1—A1 296
Figure B.20: Strains—Girder 7—Section 1—A2 297
Figure B.21: Strains—Girder 7—Section 1—A3 297
Figure B.22: Strains—Girder 7—Section 1—A4 298
Figure B.23: Strains—Girder 7—Section 1—A5 298
Figure B.24: Strains—Girder 7—Section 1—A6 299
Figure B.25: Strains—Girder 7—Section 1—A7 299
Figure B.26: Strains—Girder 7—Section 1—A8 300
Figure B.27: Strains—Girder 7—Section 1—A9 300
Figure B.28: Strains—Girder 7—Section 2—A1 301
Figure B.29: Strains—Girder 7—Section 2—A2 302
Figure B.30: Strains—Girder 7—Section 2—A3 302
Figure B.31: Strains—Girder 7—Section 2—A4 303
Figure B.32: Strains—Girder 7—Section 2—A5 303
Figure B.33: Strains—Girder 7—Section 2—A6 304
Figure B.34: Strains—Girder 7—Section 2—A7 304
Figure B.35: Strains—Girder 7—Section 2—A8 305
Figure B.36: Strains—Girder 7—Section 2—A9 305
Figure B.37: Strains—Girder 7—Section 3—A1 306
Figure B.38: Strains—Girder 7—Section 3—A2 307
Figure B.39: Strains—Girder 7—Section 3—A3 307
Figure B.40: Strains—Girder 7—Section 3—A4 308
Figure B.41: Strains—Girder 7—Section 3—A5 308

Figure B.42: Strains—Girder 7—Section 3—A6 309
Figure B.43: Strains—Girder 7—Section 3—A7 309
Figure B.44: Strains—Girder 7—Section 3—A8 310
Figure B.45: Strains—Girder 7—Section 3—A9 310
Figure B.46: Strains—Girder 7—Section 4—A1 311
Figure B.47: Strains—Girder 7—Section 4—A2 312
Figure B.48: Strains—Girder 7—Section 4—A3 312
Figure B.49: Strains—Girder 7—Section 4—A4 313
Figure B.50: Strains—Girder 7—Section 4—A5 313
Figure B.51: Strains—Girder 7—Section 4—A6 314
Figure B.52: Strains—Girder 7—Section 4—A7 314
Figure B.53: Strains—Girder 7—Section 4—A8 315
Figure B.54: Strains—Girder 7—Section 4—A9 315
Figure B.55: Strains—Girder 8—Section 1—A1 316
Figure B.56: Strains—Girder 8—Section 1—A2 317
Figure B.57: Strains—Girder 8—Section 1—A3 317
Figure B.58: Strains—Girder 8—Section 1—A4 318
Figure B.59: Strains—Girder 8—Section 1—A5 318
Figure B.60: Strains—Girder 8—Section 1—A6 319
Figure B.61: Strains—Girder 8—Section 1—A7 319
Figure B.62: Strains—Girder 8—Section 1—A8 320
Figure B.63: Strains—Girder 8—Section 1—A9 320
Figure B.64: Strains—Girder 8—Section 2—A1 321
Figure B.65: Strains—Girder 8—Section 2—A2 322
Figure B.66: Strains—Girder 8—Section 2—A3 322
Figure B.67: Strains—Girder 8—Section 2—A4 323
Figure B.68: Strains—Girder 8—Section 2—A5 323
Figure B.69: Strains—Girder 8—Section 2—A6 324
Figure B.70: Strains—Girder 8—Section 2—A7 324
Figure B.71: Strains—Girder 8—Section 2—A8 325
Figure B.72: Strains—Girder 8—Section 2—A9 325
Figure B.73: Strains—Girder 8—Section 3—A1 326
Figure B.74: Strains—Girder 8—Section 3—A2 327
Figure B.75: Strains—Girder 8—Section 3—A3 327
Figure B.76: Strains—Girder 8—Section 3—A4 328
Figure B.77: Strains—Girder 8—Section 3—A5 328
Figure B.78: Strains—Girder 8—Section 3—A6 329

Figure B.79: Strains—Girder 8—Section 3—A7 329
Figure B.80: Strains—Girder 8—Section 3—A8 330
Figure B.81: Strains—Girder 8—Section 3—A9 330
Figure B.82: Strains—Girder 8—Section 4—A1 331
Figure B.83: Strains—Girder 8—Section 4—A2 332
Figure B.84: Strains—Girder 8—Section 4—A3 332
Figure B.85: Strains—Girder 8—Section 4—A4 333
Figure B.86: Strains—Girder 8—Section 4—A5 333
Figure B.87: Strains—Girder 8—Section 4—A6 334
Figure B.88: Strains—Girder 8—Section 4—A7 334
Figure B.89: Strains—Girder 8—Section 4—A8 335
Figure B.90: Strains—Girder 8—Section 4—A9 335
Figure B.91: Bottom-fiber strains—A1 336
Figure B.92: Bottom-fiber strains—A2 337
Figure B.93: Bottom-fiber strains—A3 337
Figure B.94: Bottom-fiber strains—A4 338
Figure B.95: Bottom-fiber strains—A5 338
Figure B.96: Bottom-fiber strains—A6 339
Figure B.97: Bottom-fiber strains—A7 339
Figure B.98: Bottom-fiber strains—A8 340
Figure B.99: Bottom-fiber strains—A9 340
Figure B.100: Bottom-fiber strains—Girder 7—A1 341
Figure B.101: Bottom-fiber strains—Girder 7—A2 342
Figure B.102: Bottom-fiber strains—Girder 7—A3 342
Figure B.103: Bottom-fiber strains—Girder 7—A4 343
Figure B.104: Bottom-fiber strains—Girder 7—A5 343
Figure B.105: Bottom-fiber strains—Girder 7—A6 344
Figure B.106: Bottom-fiber strains—Girder 7—A7 344
Figure B.107: Bottom-fiber strains—Girder 7—A8 345
Figure B.108: Bottom-fiber strains—Girder 7—A9 345
Figure B.109: Bottom-fiber strains—Girder 8—A1 346
Figure B.110: Bottom-fiber strains—Girder 8—A2 347
Figure B.111: Bottom-fiber strains—Girder 8—A3 347
Figure B.112: Bottom-fiber strains—Girder 8—A4 348
Figure B.113: Bottom-fiber strains—Girder 8—A5 348
Figure B.114: Bottom-fiber strains—Girder 8—A6 349
Figure B.115: Bottom-fiber strains—Girder 8—A7 349

Figure B.116: Bottom-fiber strains—Girder 8—A8 350
Figure B.117: Bottom-fiber strains—Girder 8—A9 350
Figure B.118: Crack-opening displacements—C1 351
Figure B.119: Crack-opening displacements—C2 352
Figure B.120: Crack-opening displacements—C3 352
Figure B.121: Crack-opening displacements—C4 353
Figure B.122: Crack-opening displacements—C5 353
Figure B.123: Crack-opening displacements—C6 354
Figure B.124: Crack-opening displacements—C7 354
Figure B.125: Crack-opening displacements—C8 355
Figure B.126: Crack-opening displacements—C9 355
Figure B.127: Deflections—C1 356
Figure B.128: Deflections—C2 357
Figure B.129: Deflections—C3 357
Figure B.130: Deflections—C4 358
Figure B.131: Deflections—C5 358
Figure B.132: Deflections—C6 359
Figure B.133: Deflections—C7 359
Figure B.134: Deflections—C8 360
Figure B.135: Deflections—C9 360
Figure B.136: Strains—Girder 7—Section 1—C1 361
Figure B.137: Strains—Girder 7—Section 1—C2 362
Figure B.138: Strains—Girder 7—Section 1—C3 362
Figure B.139: Strains—Girder 7—Section 1—C4 363
Figure B.140: Strains—Girder 7—Section 1—C5 363
Figure B.141: Strains—Girder 7—Section 1—C6 364
Figure B.142: Strains—Girder 7—Section 1—C7 364
Figure B.143: Strains—Girder 7—Section 1—C8 365
Figure B.144: Strains—Girder 7—Section 1—C9 365
Figure B.145: Strains—Girder 7—Section 2—C1 366
Figure B.146: Strains—Girder 7—Section 2—C2 367
Figure B.147: Strains—Girder 7—Section 2—C3 367
Figure B.148: Strains—Girder 7—Section 2—C4 368
Figure B.149: Strains—Girder 7—Section 2—C5 368
Figure B.150: Strains—Girder 7—Section 2—C6 369
Figure B.151: Strains—Girder 7—Section 2—C7 369
Figure B.152: Strains—Girder 7—Section 2—C8 370

Figure B.153: Strains—Girder 7—Section 2—C9 370
Figure B.154: Strains—Girder 7—Section 3—C1 371
Figure B.155: Strains—Girder 7—Section 3—C2 372
Figure B.156: Strains—Girder 7—Section 3—C3 372
Figure B.157: Strains—Girder 7—Section 3—C4 373
Figure B.158: Strains—Girder 7—Section 3—C5 373
Figure B.159: Strains—Girder 7—Section 3—C6 374
Figure B.160: Strains—Girder 7—Section 3—C7 374
Figure B.161: Strains—Girder 7—Section 3—C8 375
Figure B.162: Strains—Girder 7—Section 3—C9 375
Figure B.163: Strains—Girder 7—Section 4—C1 376
Figure B.164: Strains—Girder 7—Section 4—C2 377
Figure B.165: Strains—Girder 7—Section 4—C3 377
Figure B.166: Strains—Girder 7—Section 4—C4 378
Figure B.167: Strains—Girder 7—Section 4—C5 378
Figure B.168: Strains—Girder 7—Section 4—C6 379
Figure B.169: Strains—Girder 7—Section 4—C7 379
Figure B.170: Strains—Girder 7—Section 4—C8 380
Figure B.171: Strains—Girder 7—Section 4—C9 380
Figure B.172: Strains—Girder 8—Section 1—C1 381
Figure B.173: Strains—Girder 8—Section 1—C2 382
Figure B.174: Strains—Girder 8—Section 1—C3 382
Figure B.175: Strains—Girder 8—Section 1—C4 383
Figure B.176: Strains—Girder8—Section 1—C5 383
Figure B.177: Strains—Girder 8—Section 1—C6 384
Figure B.178: Strains—Girder 8—Section 1—C7 384
Figure B.179: Strains—Girder 8—Section 1—C8 385
Figure B.180: Strains—Girder 8—Section 1—C9 385
Figure B.181: Strains—Girder 8—Section 2—C1 386
Figure B.182: Strains—Girder 8—Section 2—C2 387
Figure B.183: Strains—Girder 8—Section 2—C3 387
Figure B.184: Strains—Girder 8—Section 2—C4 388
Figure B.185: Strains—Girder 8—Section 2—C5 388
Figure B.186: Strains—Girder 8—Section 2—C6 389
Figure B.187: Strains—Girder 8—Section 2—C7 389
Figure B.188: Strains—Girder 8—Section 2—C8 390
Figure B.189: Strains—Girder 8—Section 2—C9 390

Figure B.190: Strains—Girder 8—Section 3—C1 391
Figure B.191: Strains—Girder 8—Section 3—C2 392
Figure B.192: Strains—Girder 8—Section 3—C3 392
Figure B.193: Strains—Girder 8—Section 3—C4 393
Figure B.194: Strains—Girder 8—Section 3—C5 393
Figure B.195: Strains—Girder 8—Section 3—C6 394
Figure B.196: Strains—Girder 8—Section 3—C7 394
Figure B.197: Strains—Girder 8—Section 3—C8 395
Figure B.198: Strains—Girder 8—Section 3—C9 395
Figure B.199: Strains—Girder 8—Section 4—C1 396
Figure B.200: Strains—Girder 8—Section 4—C2 397
Figure B.201: Strains—Girder 8—Section 4—C3 397
Figure B.202: Strains—Girder 8—Section 4—C4 398
Figure B.203: Strains—Girder 8—Section 4—C5 398
Figure B.204: Strains—Girder 8—Section 4—C6 399
Figure B.205: Strains—Girder 8—Section 4—C7 399
Figure B.206: Strains—Girder 8—Section 4—C8 400
Figure B.207: Strains—Girder 8—Section 4—C9 400
Figure B.208: Bottom-fiber strains—C1 401
Figure B.209: Bottom-fiber strains—C2 402
Figure B.210: Bottom-fiber strains—C3 402
Figure B.211: Bottom-fiber strains—C4 403
Figure B.212: Bottom-fiber strains—C5 403
Figure B.213: Bottom-fiber strains—C6 404
Figure B.214: Bottom-fiber strains—C7 404
Figure B.215: Bottom-fiber strains—C8 405
Figure B.216: Bottom-fiber strains—C9 405
Figure B.217: Bottom-fiber strains—Girder 7—C1 406
Figure B.218: Bottom-fiber strains—Girder 7—C2 407
Figure B.219: Bottom-fiber strains—Girder 7—C3 407
Figure B.220: Bottom-fiber strains—Girder 7—C4 408
Figure B.221: Bottom-fiber strains—Girder 7—C5 408
Figure B.222: Bottom-fiber strains—Girder 7—C6 409
Figure B.223: Bottom-fiber strains—Girder 7—C7 409
Figure B.224: Bottom-fiber strains—Girder 7—C8 410
Figure B.225: Bottom-fiber strains—Girder 7—C9 410
Figure B.226: Bottom-fiber strains—Girder 8—C1 411

Figure B.227: Bottom-fiber strains—Girder 8—C2 412
Figure B.228: Bottom-fiber strains—Girder 8—C3 412
Figure B.229: Bottom-fiber strains—Girder 8—C4 413
Figure B.230: Bottom-fiber strains—Girder 8—C5 413
Figure B.231: Bottom-fiber strains—Girder 8—C6 414
Figure B.232: Bottom-fiber strains—Girder 8—C7 414
Figure B.233: Bottom-fiber strains—Girder 8—C8 415
Figure B.234: Bottom-fiber strains—Girder 8—C9 415
Figure D.1: Crack-opening displacements—24 hrs 438
Figure D.2: Deflections—24 hrs—Girder 7 439
Figure D.3: Deflections—24 hrs—Girder 8 439
Figure D.4: Bottom-fiber strains—24 hrs—Girder 7—within 80 in. from diaphragm 440
Figure D.5: Bottom-fiber strains—24 hrs—Girder 7—beyond 80 in. from diaphragm 440
Figure D.6: Bottom-fiber strains—24 hrs—Girder 8—within 80 in. from diaphragm 441
Figure D.7: Bottom-fiber strains—24 hrs—Girder 8—beyond 80 in. from diaphragm 441
Figure D.8: Bottom-fiber strains—24 hrs—FRP near crack locations 442
Figure D.9: Bottom-fiber strain and COD—24 hrs—Girder 7—Span 10 442
Figure D.10: Bottom-fiber strain and COD—24 hrs—Girder 7—Span 11 443
Figure D.11: Bottom-fiber strain and COD—24 hrs—Girder 8—Span 10 443
Figure D.12: Bottom-fiber strain and COD—24 hrs—Girder 8—Span 11 444
Figure F.1: Original deflection results—Girder 7 466
Figure F.2: Original deflection results—Girder 8 467
Figure F.3: Original deflection results—Girder 7—Span 10 467
Figure F.4: Adjusted deflection results—D7_10_A 468
Figure F.5: Adjusted deflection results—D7_10_B 468
Figure F.6: Adjusted deflection results—Girder 7—Span 10 469
Figure F.7: Final deflection results—Girder 7—Span 10 469
Figure F.8: Original deflection results—Girder 7—Span 11 470
Figure F.9: Adjusted deflection results—D7_11_C 470
Figure F.10: Adjusted deflection results—D7_11_D 471
Figure F.11: Adjusted deflection results—D7_11_E 471
Figure F.12: Adjusted deflection results—D7_11_F 472
Figure F.13: Adjusted deflection results—Girder 7—Span 11 472
Figure F.14: Final deflection results—Girder 7—Span 11 473
Figure F.15: Original deflection results—Girder 8—Span 10 473
Figure F.16: Adjusted deflection results—D8_10_A 474
Figure F.17: Adjusted deflection results—D8_10_B 474

Figure F.18: Adjusted deflection results—Girder 8—Span 10 475
Figure F.19: Final deflection results—Girder 8—Span 10 475
Figure F.20: Original deflection results—Girder 8—Span 11 476
Figure F.21: Adjusted deflection results—D8_11_C 476
Figure F.22: Adjusted deflection results—D8_11_D 477
Figure F.23: Adjusted deflection results—D8_11_E 477
Figure F.24: Adjusted deflection results—D8_11_F 478
Figure F.25: Adjusted deflection results—Girder 8—Span 11 478
Figure F.26: Final deflection results—Girder 8—Span 11 479
Figure F.27: Final deflection results—Girder 7 479
Figure F.28: Final deflection results—Girder 8 480
Figure F.29: Crack location FRP strain measurements—original F8_10_CK 481
Figure F.30: Crack location FRP strain measurements—adjusted F8_10_CK 481
Figure G.1: Crack-opening displacements—A1 (east) 483
Figure G.2: Crack-opening displacements—A9 (east) 484
Figure G.3: Crack-opening displacements—A1 (east) + A9 (east) 484
Figure G.4: Crack-opening displacements—superposition—actual and predicted 485
Figure G.5: COD—superposition—actual and predicted—Girder 7 485
Figure G.6: COD—superposition—actual and predicted—Girder 8 486
Figure G.7: Deflections—A1 (east) 487
Figure G.8: Deflections—A9 (east) 488
Figure G.9: Deflections—A1 (east) + A9 (east) 488
Figure G.10: Deflections—superposition—actual and predicted 489
Figure G.11: Deflections—superposition—actual and predicted—Girder 7 489
Figure G.12: Deflections—superposition—actual and predicted—Girder 8 490
Figure G.13: Bottom-fiber strains—A1 (east) 491
Figure G.14: Bottom-fiber strains—A9 (east) 492
Figure G.15: Bottom-fiber strains—A1 (east) + A9 (east) 492
Figure G.16: Bottom-fiber strains—superposition—actual and predicted 493
Figure G.17: Bottom-fiber strains—superposition—actual and predicted—Girder 7 493
Figure G.18: Bottom-fiber strains—superposition—actual and predicted—Girder 8 494
Figure I.1: Crack-opening displacements—LC 6.5—AE Span 10 (east) 501
Figure I.2: Crack-opening displacements—LC 6.5—AE Span 10 (both) 502
Figure I.3: Crack-opening displacements—LC 6.5—AE Span 11 (east) 502
Figure I.4: Crack-opening displacements—LC 6.5—AE Span 11 (both) 503
Figure I.5: Crack-opening displacements—LC 6—AE Span 10 (east) 503
Figure I.6: Crack-opening displacements—LC 6—AE Span 10 (both) 504

Figure I.7: Crack-opening displacements—LC 6—AE Span 11 (east) 504
Figure I.8: Crack-opening displacements—LC 6—AE Span 11 (both) 505
Figure I.9: Deflections—LC 6.5—AE Span 10 (east) 506
Figure I.10: Deflections—LC 6.5—AE Span 10 (both) 507
Figure I.11: Deflections—LC 6.5—AE Span 11 (east) 507
Figure I.12: Deflections—LC 6.5—AE Span 11 (both) 508
Figure I.13: Deflections—LC 6—AE Span 10 (east) 508
Figure I.14: Deflections—LC 6—AE Span 10 (both) 509
Figure I.15: Deflections—LC 6—AE Span 11 (east) 509
Figure I.16: Deflections—LC 6—AE Span 11 (both) 510
Figure I.17: Bottom-fiber strains—LC 6.5—AE Span 10 (east) 511
Figure I.18: Bottom-fiber strains—LC 6.5—AE Span 10 (both) 512
Figure I.19: Bottom-fiber strains—LC 6.5—AE Span 11 (east) 512
Figure I.20: Bottom-fiber strains—LC 6.5—AE Span 11 (both) 513
Figure I.21: Bottom-fiber strains—LC 6—AE Span 10 (east) 513
Figure I.22: Bottom-fiber strains—LC 6—AE Span 10 (both) 514
Figure I.23: Bottom-fiber strains—LC 6—AE Span 11 (east) 514
Figure I.24: Bottom-fiber strains—LC 6—AE Span 11 (both) 515
Figure I.25: Bottom-fiber strains—Girder 7—LC 6.5—AE Span 10 (east) 516
Figure I.26: Bottom-fiber strains—Girder 7—LC 6.5—AE Span 10 (both) 517
Figure I.27: Bottom-fiber strains—Girder 7—LC 6.5—AE Span 11 (east) 517
Figure I.28: Bottom-fiber strains—Girder 7—LC 6.5—AE Span 11 (both) 518
Figure I.29: Bottom-fiber strains—Girder 7—LC 6—AE Span 10 (east) 518
Figure I.30: Bottom-fiber strains—Girder 7—LC 6—AE Span 10 (both) 519
Figure I.31: Bottom-fiber strains—Girder 7—LC 6—AE Span 11 (east) 519
Figure I.32: Bottom-fiber strains—Girder 7—LC 6—AE Span 11 (both) 520
Figure I.33: Bottom-fiber strains—Girder 8—LC 6.5—AE Span 10 (east) 521
Figure I.34: Bottom-fiber strains—Girder 8—LC 6.5—AE Span 10 (both) 522
Figure I.35: Bottom-fiber strains—Girder 8—LC 6.5—AE Span 11 (east) 522
Figure I.36: Bottom-fiber strains—Girder 8—LC 6.5—AE Span 11 (both) 523
Figure I.37: Bottom-fiber strains—Girder 8—LC 6—AE Span 10 (east) 523
Figure I.38: Bottom-fiber strains—Girder 8—LC 6—AE Span 10 (both) 524
Figure I.39: Bottom-fiber strains—Girder 8—LC 6—AE Span 11 (east) 524
Figure I.40: Bottom-fiber strains—Girder 8—LC 6—AE Span 11 (both) 525
Figure J.1: Transverse load position—AE testing—Lane C—east truck 527
Figure J.2: Transverse load position—AE testing—Lane C—both trucks 527
Figure J.3: Longitudinal stop positions—AE testing—Spans 10 and 11 528

Figure K.1: Steel frame false supports 539
Figure K.2: Bearing pad between false support and exterior girder 540
Figure K.3: Bearing pad location *with* space between the bearing pad and girder 541
Figure K.4: Bearing pad location *without* space between the bearing pad and girder 541
Figure K.5: Bearing pad in contact with girder during pre-repair testing 542
Figure K.6: Use of reciprocating saw during bearing pad removal 543
Figure K.7: Use of propane torch during bearing pad removal 544
Figure K.8: Successful removal of bearing pad 545
Figure K.9: Bearing pad after forceful removal 545
Figure K.10: Deflections—A1 547
Figure K.11: Deflections—A9 548
Figure K.12: Deflections—C1 549
Figure K.13: Deflections—C9 550
Figure K.14: Crack-opening displacements—pre- and post-repair—A4 552
Figure K.15: Crack-opening displacements—pre- and post-repair—A7 552
Figure K.16: Crack-opening displacements—pre- and post-repair—C4 553
Figure K.17: Crack-opening displacements—pre- and post-repair—C7 553
Figure K.18: Bottom-fiber strain—A4 555
Figure K.19: Strain profile—Girder 7—Section 1—A4 556
Figure K.20: Strain profile—Girder 8—Section 1—A4 556
Figure K.21: Bottom-fiber strain—C4 557
Figure K.22: Strain profile—Girder 7—Section 1—C4 558
Figure K.23: Strain profile—Girder 8—Section 1—C4 558
Figure K.24: Bottom-fiber strain—A7 559
Figure K.25: Strain profile—Girder 7—Section 4—A7 560
Figure K.26: Strain profile—Girder 8—Section 4—A7 560
Figure K.27: Bottom-fiber strain—C7 561
Figure K.28: Strain profile—Girder 7—Section 4—C7 562
Figure K.29: Strain profile—Girder 8—Section 4—C7 562
Figure K.30: Deflections—superposition—A1 and A9 563
Figure K.31: Deflections—superposition—A1 + A9 564
Figure M.1: Strain gage installation—applying degreaser to gage location 572
Figure M.2: Strain gage installation—removal of surface irregularities 572
Figure M.3: Strain gage installation—initial surface cleaning 573
Figure M.4: Strain gage installation—clean surface prepared for solid epoxy 573
Figure M.5: Strain gage installation—application of solid epoxy 574
Figure M.6: Strain gage installation—epoxy surface 574

Figure M.7: Strain gage installation—rubber coating for moisture protection 575
Figure M.8: Strain gage installation—mastic tape for mechanical protection 575
Figure M.9: Strain gage installation—gage application with thin epoxy 576
Figure M.10: Strain gage installation—gage applied to FRP reinforcement 576
Figure M.11: Strain gage installation—rubber coating for moisture protection 577
Figure M.12: Strain gage installation—mastic tape for mechanical protection 577
Figure N.1: Cracked girder with continuity reinforcement details (Barnes et al. 2006)..... 580
Figure N.2: Longitudinal configuration profile for FRP (adapted from Barnes et al. 2006).... 581
Figure N.3: Cross-sectional configuration of FRP—near diaphragm (Swenson 2003) 582
Figure N.4: Cross-sectional configuration of FRP—typical (Swenson 2003) 583
Figure N.5: Factored shear demand—simply supported (Swenson 2003)..... 585
Figure N.6: Factored moment demand—simply supported (Swenson 2003)..... 586
Figure N.7: Typical girder-deck composite cross section 590
Figure N.8: Continuity reinforcement—typical BT-54 cross section (ALDOT 1988; Swenson 2003) 592
Figure N.9: Cross-sectional configuration of FRP—near diaphragm (Swenson 2003) 593
Figure N.10: Cross-sectional configuration of FRP—typical (Swenson 2003) 593
Figure N.11: Vertical shear reinforcement—location and spacing (ALDOT 1988; Swenson 2003) 595
Figure N.12: Longitudinal configuration profile for five-layer FRP reinforcement system..... 617

Chapter 1

INTRODUCTION

1.1 PROJECT OVERVIEW

Spans of the elevated portion of interstate highway I-565 in Huntsville, Alabama were constructed to be multi-span continuous structures for post-construction loads. Elevated portions of the interstate are shown in Figures 1.1 and 1.2. In 1992, shortly after construction was completed, large and unexpected cracks were discovered at the continuous end of many prestressed concrete bulb-tee girders within these spans. Cracking of two adjacent prestressed concrete girders of I-565 is shown in Figure 1.3.

Figure 1.1: Elevated spans of I-565 in Huntsville, Alabama

Figure 1.2: Northbound Bent 11 of I-565 in Huntsville, Alabama

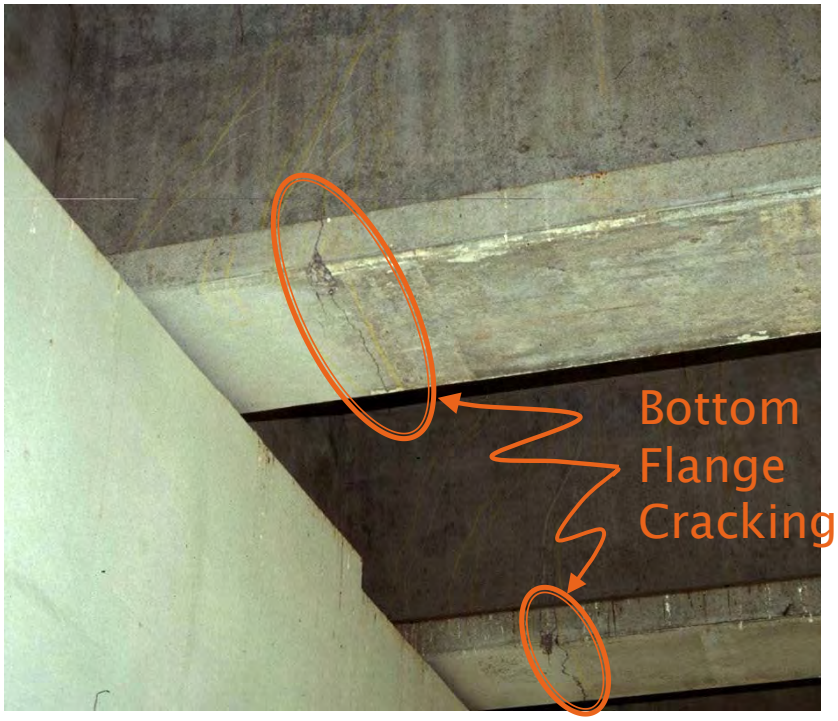

Figure 1.3: Cracked pre-tensioned bulb-tee girders of I-565 (Barnes et al. 2006)

The Alabama Department of Transportation (ALDOT) installed false supports under damaged girders to safely allow for the investigation of the cause of damage and to determine potential repair solutions, while preventing catastrophic collapse in case of further deterioration of bridge girders.

Previous investigations conducted by Alabama Department of Transportation (ALDOT) and Auburn University Highway Research Center (AUHRC) personnel resulted in determinations that the cracking was a result of restrained thermal deformations and inadequate reinforcement details, and that the cracking compromised the strength of the girder end regions (ALDOT 1994; Gao 2003; Swenson 2003). An externally bonded wet lay-up fiber-reinforced polymer (FRP) repair scheme was proposed to repair damaged regions and address the perceived strength deficiency (Swenson 2003). Analysis of pre- and post-repair structural responses to service-level truck loads was recommended to assess the efficacy of this repair system.

Post-repair bridge testing and resulting conclusions are documented in this report. Conclusions supported by post-repair bridge testing have been used to evaluate in-service performance of the FRP reinforcement system and to propose design recommendations for repair of conditions similar to those of the damaged spans of I-565 using FRP.

1.2 NEED FOR RESEARCH

Many states have bridge structures that contain spans that were constructed to be multi-span continuous structures for post-construction loads. The National Cooperative Highway Research Program (NCHRP) published a report titled *Connection of Simple-Span Precast Concrete Girders for Continuity* (NCHRP Report 519) that investigated some of the different continuous-for-live-load connections used in various states (Miller et al. 2004). The damaged girders of I-565 in Huntsville, Alabama are reviewed within NCHRP Report 519, which states that very few multi-span continuous bridge structures exhibit significant cracking similar to what was observed on the Alabama bridge structures. However, NCHRP Report 519 does state that various respondents to their survey indicated difficulties associated with the positive bending moment continuity reinforcement during girder fabrication and bridge construction.

Although NCHRP Report 519 suggests that the damage observed in the Alabama bridge girders is unique, Auburn University researchers have had several conversations with transportation officials and consulting engineers from around the United States that indicate otherwise. NCHRP Report 519 also stated that Alabama bridge structures continued to perform as designed (Miller et al. 2004). However, this continued performance is with respect to service conditions and not with respect to the strength-limit-state.

Bridge structures exhibiting damage conditions similar to those observed in the damaged spans of I-565 in Huntsville may adequately resist service loads, but repairs may be necessary to ensure safety for a design overload event, without requiring complete reconstruction. It is

desirable to develop a repair solution for these conditions that would require minimal traffic disruption or delay during repair. The proposed FRP reinforcement system, which was installed on Northbound Spans 10 and 11 of I-565 in Huntsville in December of 2007, provides an unobtrusive repair solution, but this solution required verification through testing before further implementation could confidently be recommended. Girders repaired with FRP reinforcement are shown in Figures 1.4 and 1.5.

Figure 1.4: Girder 9 of Northbound Spans 10 and 11—repaired

Figure 1.5: Girders 7, 8, and 9 of Northbound Span 10—repaired

1.3 PROJECT OBJECTIVES

The main objective of the research presented in this report is to verify that an FRP reinforcement system is a viable solution for the repair of multi-span continuous structures that exhibit damage at the continuous end of prestressed concrete bridge girders. The specific objectives of this research are as follows:

1. Evaluate the practicality and effectiveness of an externally bonded FRP repair system for the I-565 bridges in Huntsville and for other similarly damaged structures;
2. Develop recommendations for the implementation of externally bonded FRP repair systems;
3. Assess the effectiveness of acoustic emission monitoring for FRP repairs and develop recommendations for its efficient implementation.

1.4 PROJECT TASKS

In order to achieve the project objectives, the following nine tasks were completed.

1.4.1 Task 1: Preliminary Engineering for FRP Repair

Auburn University investigators cooperated with ALDOT Bridge Bureau personnel to develop design drawings and specifications for the FRP repair of the I-565 structure. The design drawings and specifications were translated from an FRP strengthening system proposed during a previous study conducted by the Auburn University Highway Research Center (AUHRC). ALDOT and AUHRC personnel cooperated to develop a special provision for the contracting and construction process of the FRP repair system.

1.4.2 Task 2: Literature Review on Current State of the Art

Literature was reviewed to identify the most effective measurement techniques for assessing the performance of the I-565 structure before and after the installation of the FRP repair system. Methods for monitoring deformations that were investigated included the measurement of crack-opening displacements, girder deflections, and surface strains of concrete and FRP. Methods for monitoring acoustic emissions (AE) to quantify girder damage were also investigated.

1.4.3 Task 3: Preliminary Load Testing

Preliminary load testing was conducted on June 1 and 2, 2005 to establish benchmark data for comparison to post-repair structural behavior. Crack-opening displacements, girder deflections, concrete surface strains, and acoustic emissions were monitored in response to specified positioning of load-test trucks provided by ALDOT.

1.4.4 Task 4: Construction Monitoring

The FRP reinforcement system was installed on the investigated spans during December, 2007. An Auburn University researcher documented the installation process.

1.4.5 Task 5: Post-Repair Load Testing

Post-repair load testing was conducted on May 25 and 26, 2010. Additional strain gages were installed on the FRP surface prior to testing. Structural behavior was monitored in response to the same truck positions and testing procedures of the preliminary load testing. The post-repair load testing represented long-term testing of the structure after two years of service. During those two years, the repaired structure was subjected to thermal variations similar to those that were the cause of initial cracking.

1.4.6 Task 6: Performance Monitoring under Traffic Loads

The bridge structure was also monitored under normal traffic loads during post-repair testing. Sensors that monitored the structural behavior in response to post-repair load testing were monitored at fifteen minute intervals for the twenty-four hours between the two nights of load testing.

1.4.7 Task 7: Evaluation of Bridge Performance

Structural responses measured during preliminary load testing, post-repair load testing, and post-repair bridge monitoring under normal traffic loads were analyzed by Auburn University researcher personnel. This task included the determination of pre-repair structural behavior and an assessment of the post-repair performance of the FRP reinforcement system.

1.4.8 Task 8: Evaluation of Acoustic Emission Monitoring

The overall effectiveness and practicality of using AE monitoring as a tool for the nondestructive evaluation of concrete bridges was evaluated by Auburn University research personnel.

1.4.9 Task 9: Preparation of Final Project Reports

This report addresses performance of the FRP repair of the I-565 structure. The report includes further discussion of tasks 1, 3, 4, 5, 6, and 7. Further discussion of tasks 2 and 8, which pertain to AE testing, has been presented by Hadzor et al. (2011).

1.5 REPORT ORGANIZATION

A summary of the project background and previous research is presented in Chapter 2 of this report. The project background includes construction details and the cause and location of damage that was observed soon after the completion of construction. Previous research includes analyses that assisted with the design of an FRP reinforcement system, analysis of load testing measurements before the installation of the repair system, and the development of a finite-element model that was used to analyze modeled bridge behavior before and after the installation of FRP reinforcement. The chapter concludes with a summary of the FRP reinforcement installation process.

Chapter 3 contains a discussion of the bridge instrumentation details. This discussion includes the locations and installation procedures for bridge testing sensors. The sensors installed include deflectometers, crack-opening displacement gages, and surface-mounted strain gages.

Chapter 4 contains a detailed explanation of bridge testing procedures. The load testing procedures include truck weights and stop positions. The procedures for monitoring bridge behavior for a twenty-four hour period are also discussed.

Chapter 5 contains a presentation of the results of analysis following the post-repair bridge testing. This analysis includes comparisons of pre- and post-repair support conditions and post-repair behavior. Theoretical analysis of the behavior of a two-span continuous bridge structure in response to ambient thermal conditions is presented. The measured behavior in response to thermal conditions observed during bridge monitoring is also presented.

Chapter 6 includes a recommended design procedure for implementation of this repair solution on similar bridge structures that exhibit similar damage. An example of the design procedure is presented in Appendix N. The example is a redesign of an FRP reinforcement system for the investigated bridge structure using the same FRP material that has already been installed.

Chapter 7 includes a summary of conclusions supported within this report, and Chapter 8 is a discussion of recommendations for further research and the installation of similar repair systems for similar conditions.

Chapter 2

HISTORY OF THE BRIDGE STRUCTURE AND ASSOCIATED RESEARCH

2.1 INTRODUCTION

An elevated portion of Interstate Highway 565 in Huntsville, Alabama, consists of bridge structures with spans that were constructed to be continuous for live loads. Shortly after construction, inspectors discovered unexpected cracks in concrete girders near the interior supports of several continuous spans. These cracks have been further investigated, and varying repair techniques have been proposed and implemented. This chapter summarizes the history of the bridge structure, previous mitigation techniques and bridge-response analysis methods, and the currently implemented fiber-reinforced polymer strengthening system.

2.2 BRIDGE CONSTRUCTION

The elevated I-565 bridge structures were erected during a five-part construction project. Construction of the bridge structures began in January of 1988 and was completed in March of 1991 (ALDOT 1994). The elevated spans consist of either steel or prestressed concrete bulb-tee girders supporting a cast-in-place composite reinforced concrete (RC) deck. The deck and cast-in-place continuity diaphragms result in simply supported precast girders acting as two-, three-, or four-span units made continuous for live load to preclude durability problems associated with open joints (Swenson 2003).

2.3 STRUCTURAL GEOMETRY AND MATERIAL PROPERTIES

Specific bridge structures of I-565 in Huntsville were selected to be the main focus of research efforts. The selected structures are two-span structures that were constructed to be fully continuous for live loads. These spans consist of similar girder types, reinforcement details, and continuous bridge decks. Structural geometry and material property details discussed in this section are presented by ALDOT (1988).

2.3.1 Spans Investigated

Northbound Spans 4 and 5 were the focus of research efforts that have been reported by Swenson (2003) and Gao (2003) of the Auburn University Highway Research Center (AUHRC). These spans each contain nine prestressed concrete bulb-tee girders, and form a two-span continuous structure with span lengths of 98.29 ft and a radius of horizontal curvature of about 1950 ft. The length of each span is measured along the curved centerline of the bridge deck from the centerline of the interior bent to the joint at the simply supported end of the span.

Northbound Spans 10 and 11 were selected for further research. These spans are more ideal than Spans 4 and 5 for testing bridge response to service-level truck loads and thermal conditions because they have zero horizontal curvature. Spans 10 and 11 have span lengths of 100 ft. Plan and elevation views of Northbound Spans 10 and 11 are shown in Figures 2.1–2.3.

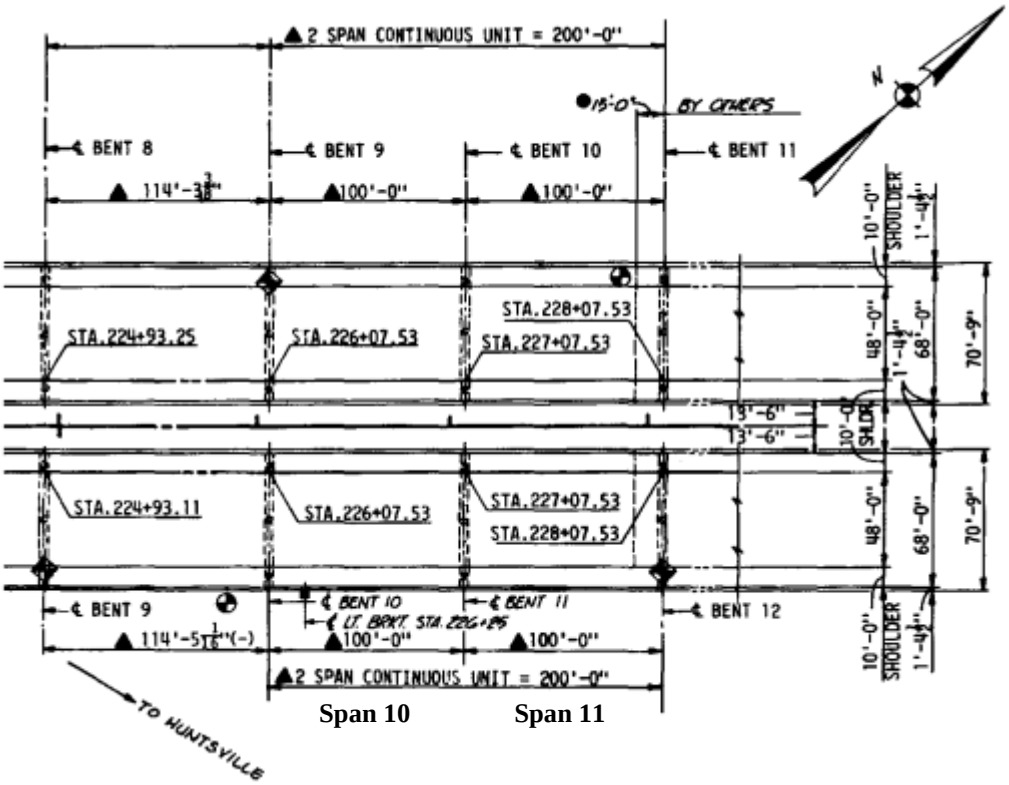

Figure 2.1: Plan view of the two-span continuous unit (ALDOT 1988)

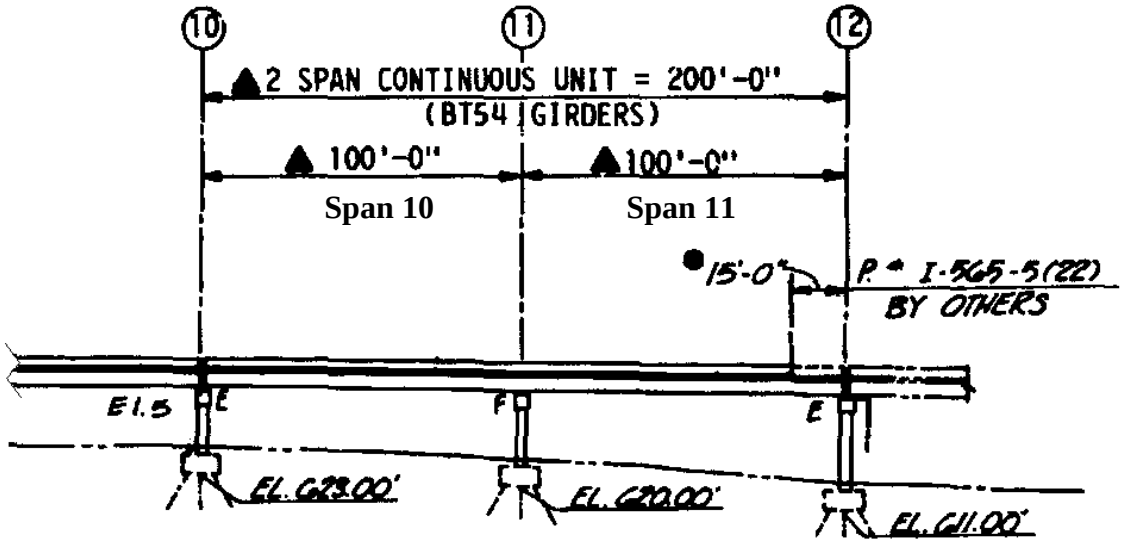

Figure 2.2: Elevation view of the two-span continuous unit (ALDOT 1988)

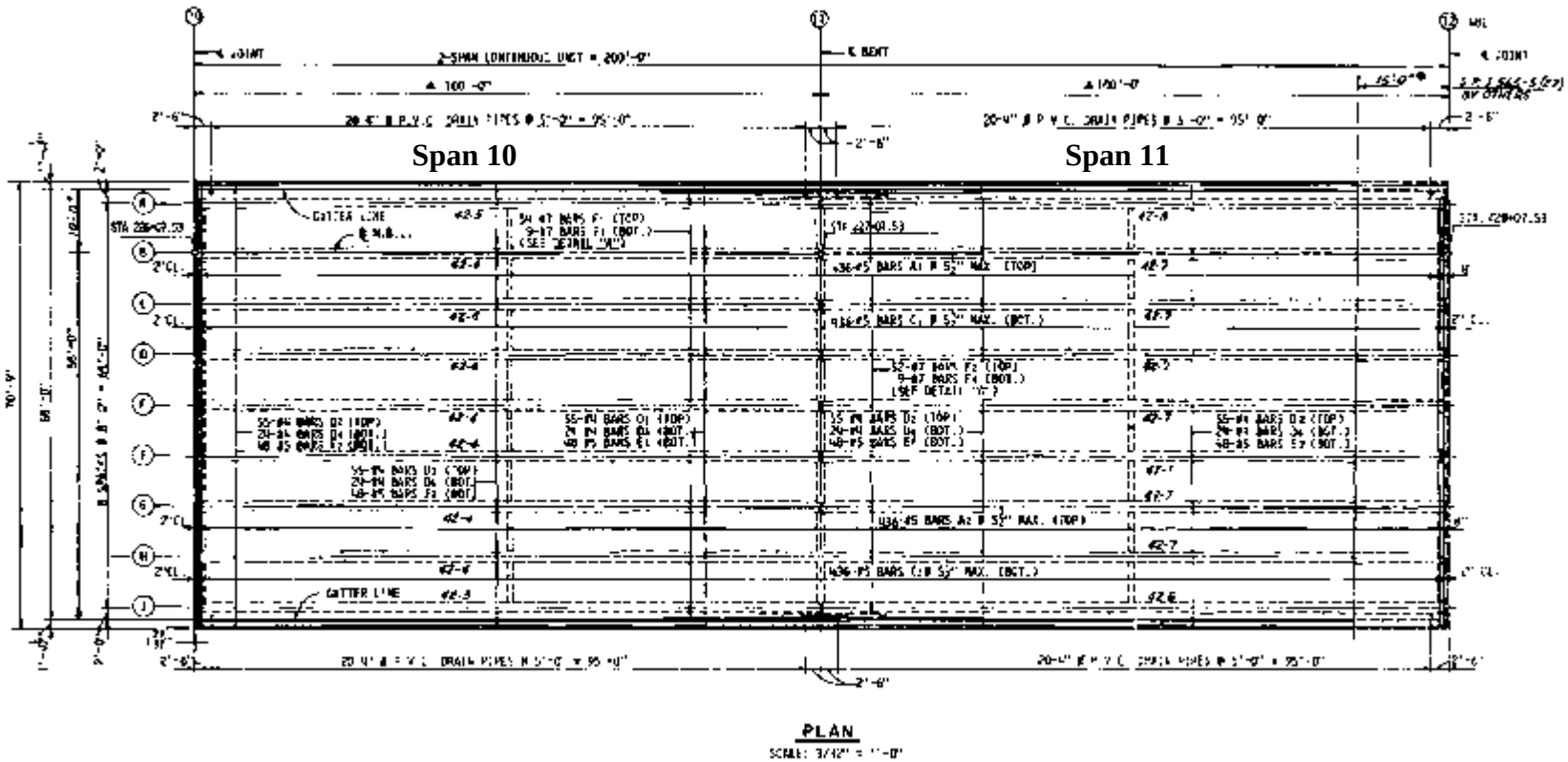

Figure 2.3: Detailed plan view of the two-span continuous unit (ALDOT 1988)

2.3.2 Girder Types

Over the length of the elevated portion of I-565, different prestressed concrete girder types were used within different spans. These girder types include AASHTO girders (Types I, III, and IV) and bulb-tee girders (BT-54 and BT-63). The AASHTO girders were prevalent in the original design, but bulb-tee girders were suggested for a majority of spans during a value engineering redesign of the bridge structures. The final design consisted of 246 AASHTO girders, 796 BT-63 girders, and 1292 BT-54 girders (ALDOT 1994). The two-span continuous structure selected for bridge response testing (Spans 10 and 11) was constructed with BT-54 girders that, over time, exhibited cracking near their continuous ends. The dimensions of a typical BT-54 girder are shown in Figure 2.4.

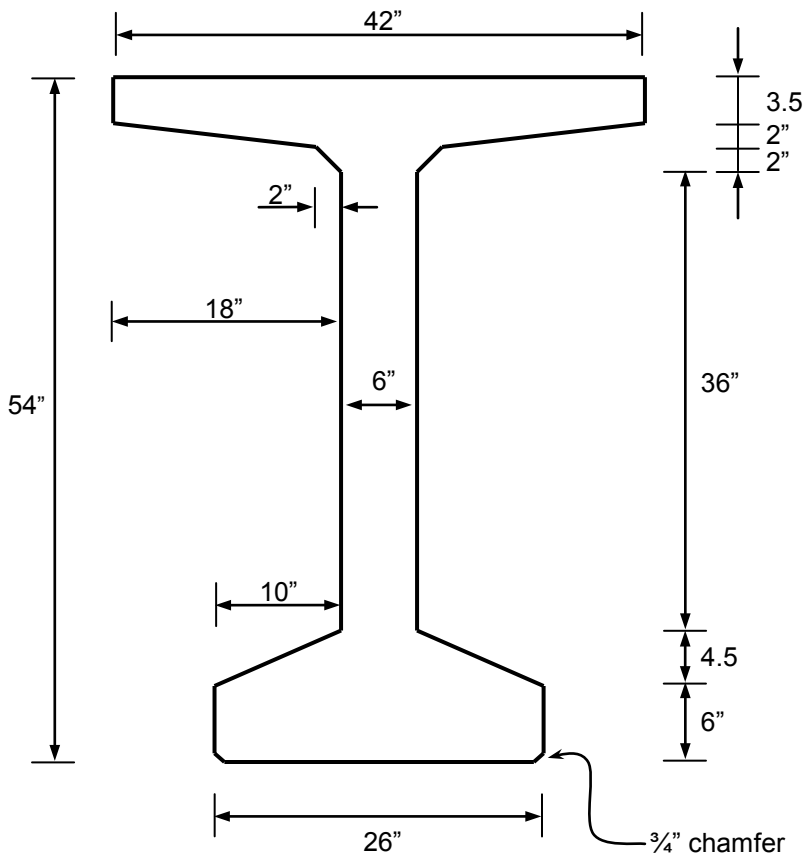

Cross-Section Properties

A = 659 in.^{2}
I = 268080 in.^{4}
h = 54 in.
y_t = 26.37 in.

Figure 2.4: Cross section of a typical BT-54 girder (ALDOT 1988; Swenson 2003)

2.3.3 Prestressing Strands

Each BT-54 girder in the studied spans was reinforced with a total of thirty-eight prestressing strands during girder fabrication. The strand pattern at each girder end and midpoint can be seen in Figures 2.5 and 2.6 respectively.

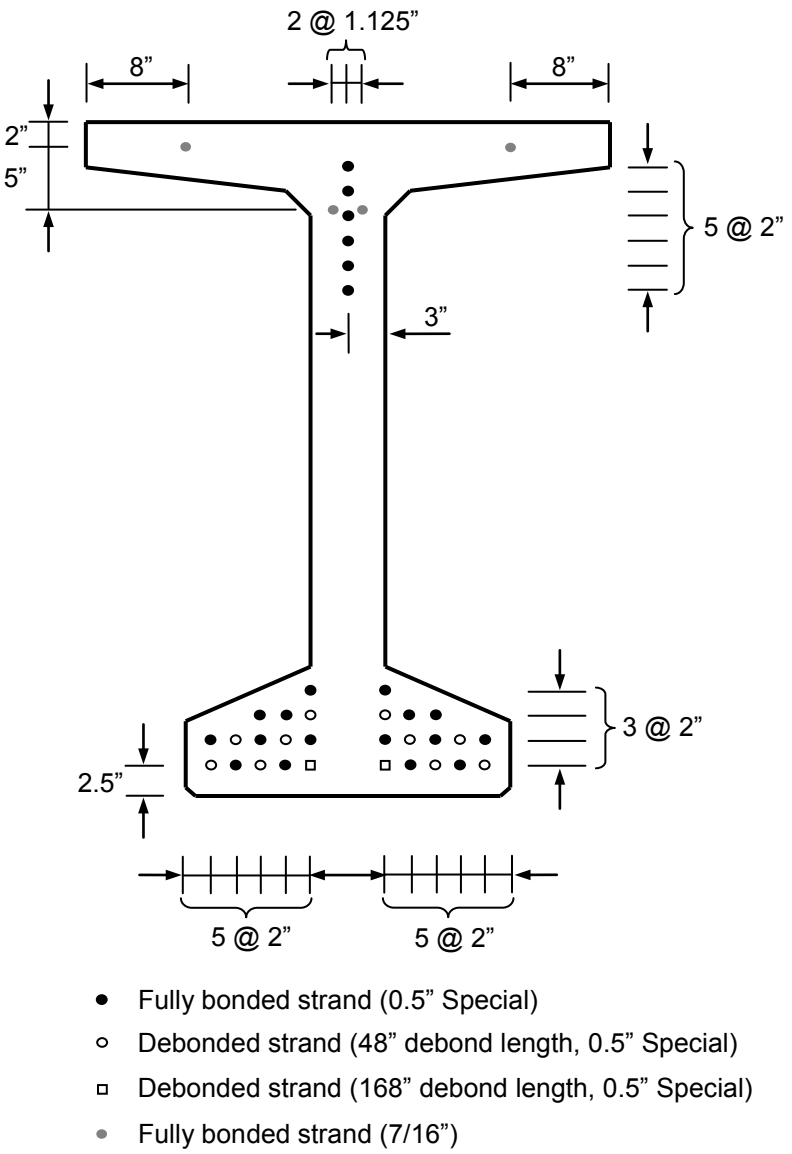

Figure 2.5: Prestressed strand pattern near girder end (ALDOT 1988; Swenson 2003)

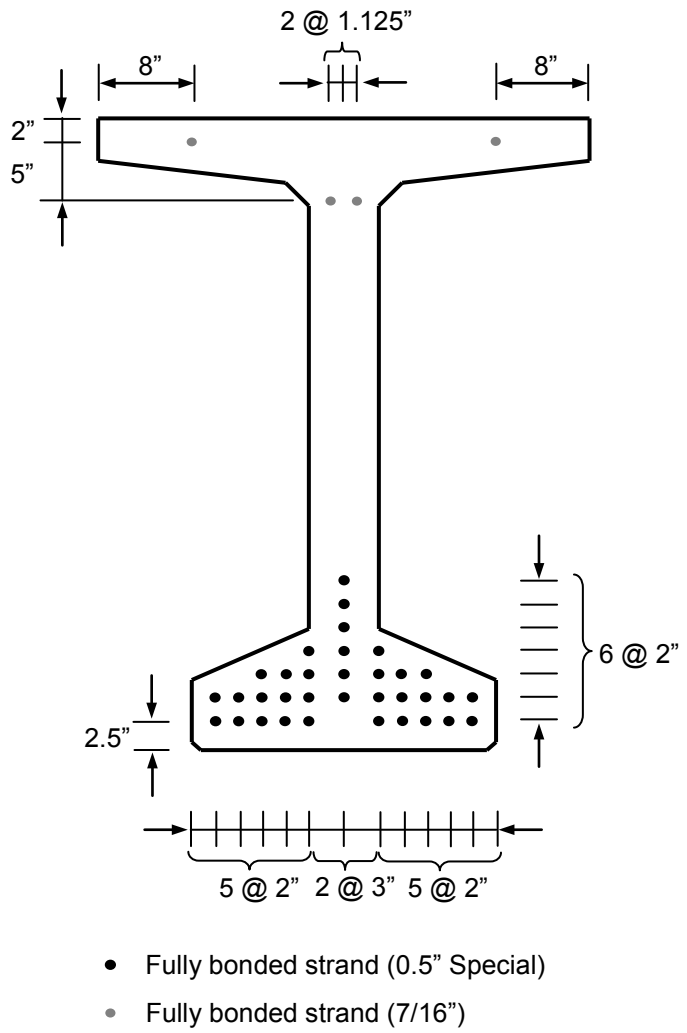

Figure 2.6: Prestressed strand pattern near girder midpoint (ALDOT 1988; Swenson 2003)

Thirty-four of the thirty-eight strands are 0.5 in. special, low-relaxation, prestressing strands that were jacked to a stress of 202.5 ksi during girder fabrication. The remaining four strands are 7/16 in. diameter, low-relaxation, prestressing strands that were jacked to a stress of 69.6 ksi during girder fabrication. Due to the low prestressing force, the 7/16 in. strands are assumed to not contribute to the shear or flexural capacity of the structure (Swenson 2003).

Six of the thirty-four 0.5 in. special strands were harped during girder fabrication. The hold-down points for harped strands are 120 in. from the girder midpoint. The harped strands have a constant eccentricity between hold-down points. The strand profile typical of the investigated BT-54 girders can be seen in Figure 2.7.

The other twenty-eight 0.5 in. special strands have a constant eccentricity along the entire length of each girder. Twelve of the strands with constant eccentricity are partially debonded. Ten of these strands are partially debonded for a length of 48 in. from the girder end,

and the remaining two strands are partially debonded for a length of 168 in. from the girder end (ALDOT 1988).

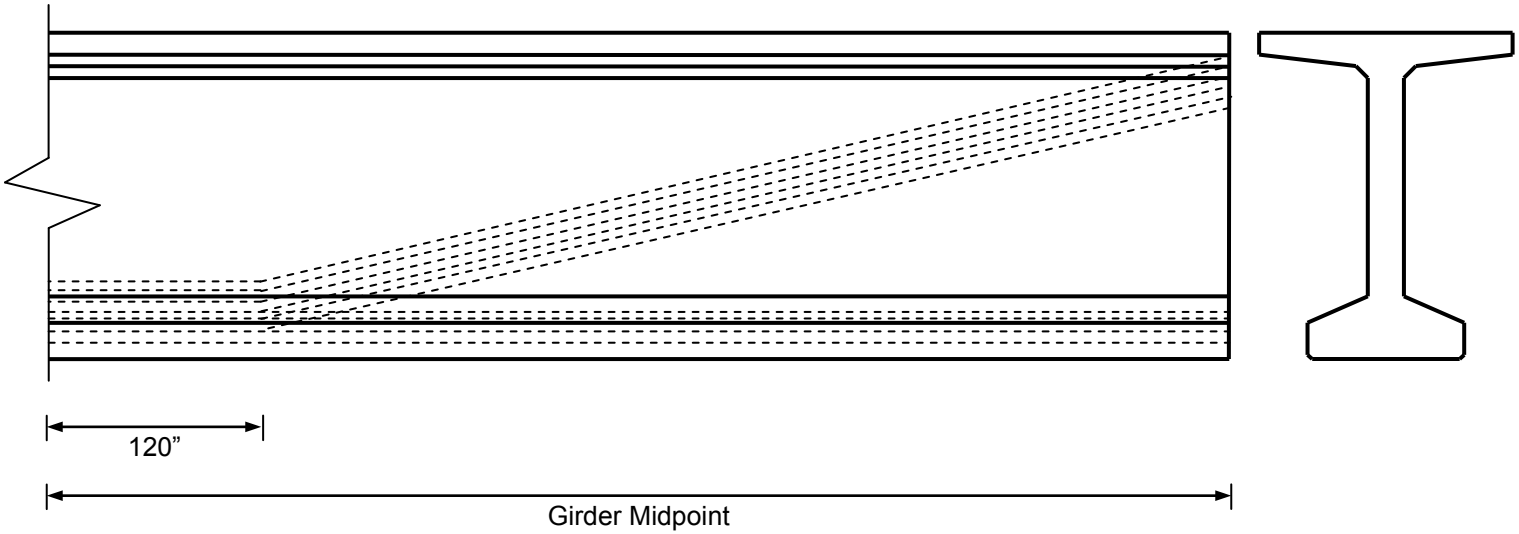

Figure 2.7: Prestressed strand profile (Swenson 2003)

2.3.4 Shear Reinforcement

The vertical shear reinforcement for each girder consists of stirrups cast into each girder during fabrication. These stirrups are composed of multiple pieces of mild steel reinforcement. The stirrups near the girder ends have a different steel bar arrangement compared to the stirrups near midspan as shown in Figures 2.8 and 2.9 respectively. The details of the different mild steel bars used to make the stirrups can be seen in Table 2.1.

The spacing of vertical shear reinforcement varies from 3.5 in. near the girder ends to 12 in. near the girder midpoint. The size of stirrup bars also varies. Vertical legs of stirrups within 24 ft of the girder midpoint are size #4 rebar. The remaining stirrups outside of this middle region have vertical legs that are size #5 rebar. The location and spacing of the vertical shear reinforcement along a typical BT-54 girder can be seen in Figure 2.10 (ALDOT 1988).

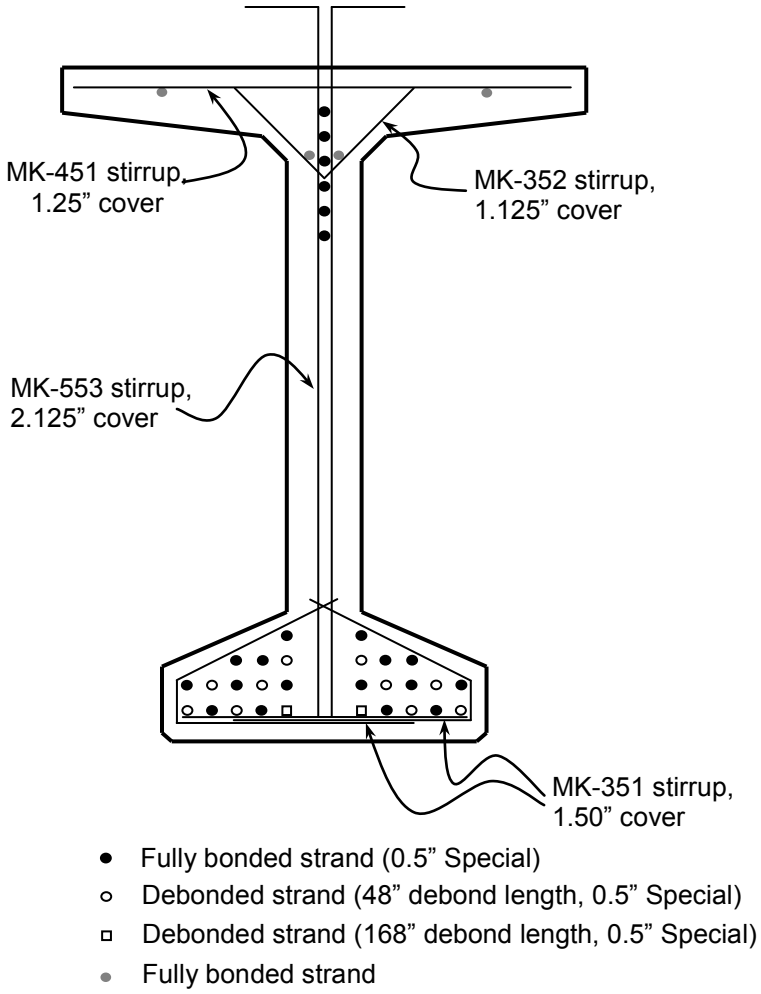

Figure 2.8: Vertical shear reinforcement near girder end (ALDOT 1988; Swenson 2003)

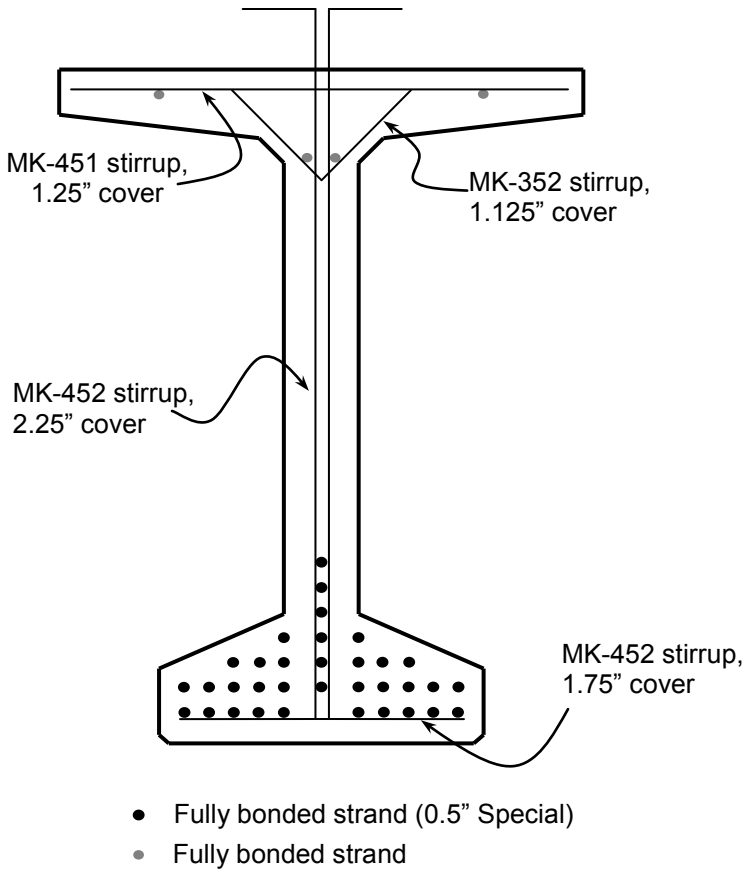

Figure 2.9: Vertical shear reinforcement near girder midpoint (ALDOT 1988; Swenson 2003)

Table 2.1: Stirrup mild steel bar details (ALDOT 1988; Swenson 2003)

Designation	Bar Size	Location	Shape
MK-351	#3	Lower Flange	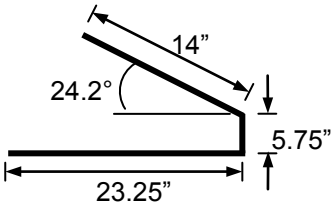
MK-352	#3	Upper Flange/ Web	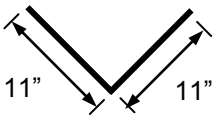
MK-451	#4	Upper Flange	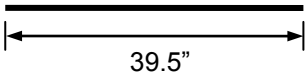
MK-452	#4	Web	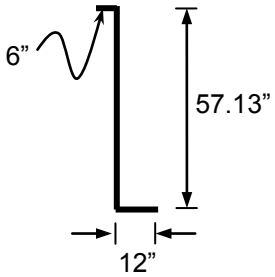
MK-553	#5	Web	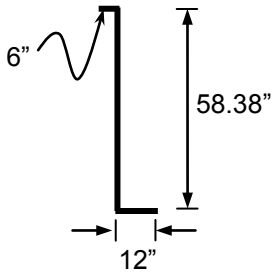

1 in. = 25.4 mm

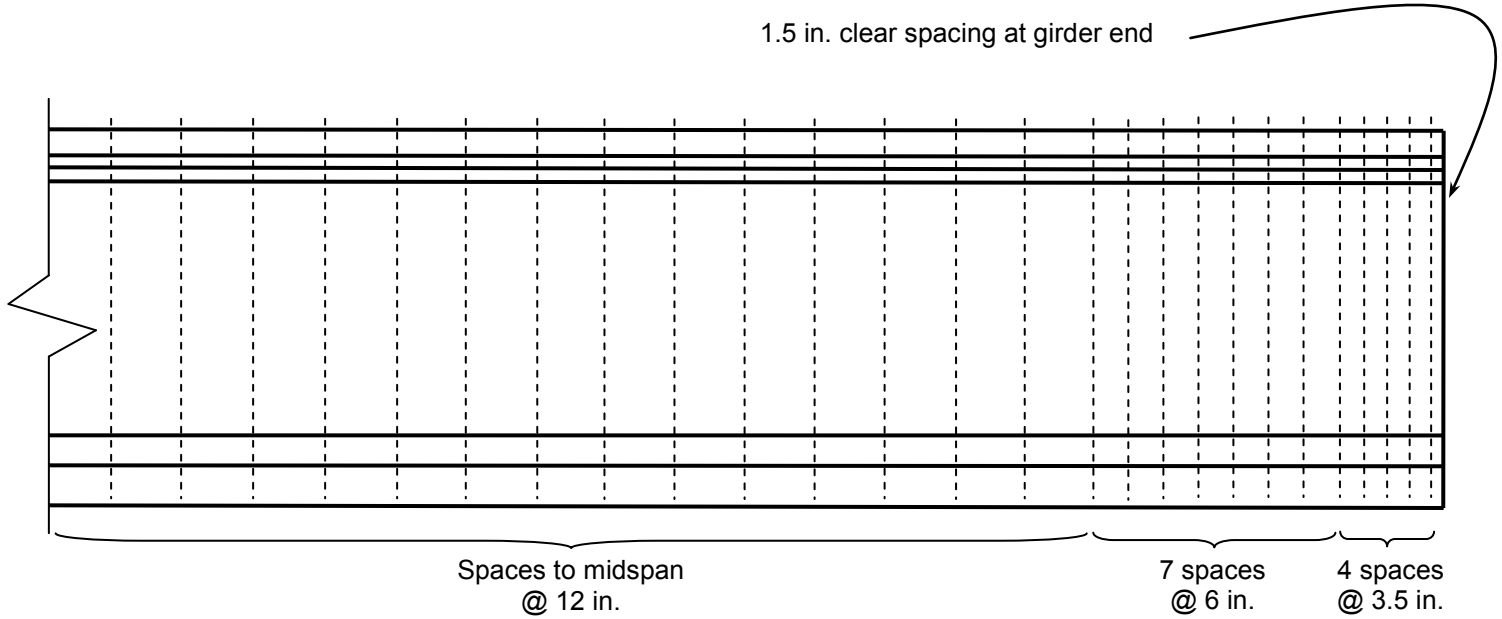

-- All stirrups within 24 ft of midspan are #4 bars (MK-452) @ 12 in. spacing.
All other stirrups are #5 bars (MK-553), spaced as shown above.

Figure 2.10: Location and spacing of vertical shear reinforcement (ALDOT 1988; Swenson 2003)

2.3.5 Continuity Reinforcement

During girder fabrication, eight mild steel bent bars were cast into each girder end that would be made continuous for live loads. These mild steel bars act as positive bending moment reinforcement. The bent bars are size #6 rebar with dimensions as shown in Figure 2.11. The locations of the bars within a typical BT-54 cross section are shown in Figure 2.12.

Each steel bar has a total length of 61 in. Each bar is bent to form a 90-degree hook with leg lengths of 12 in. and 49 in. During girder fabrication, the longer leg of each bar was embedded 41 in. within the girder end. During bridge construction, the remaining 20 in. of each bar were cast into the cast-in-place continuity diaphragm. Each bar extended 8 in. into the continuity diaphragm, and then extended 12 in. vertically within the continuity diaphragm.

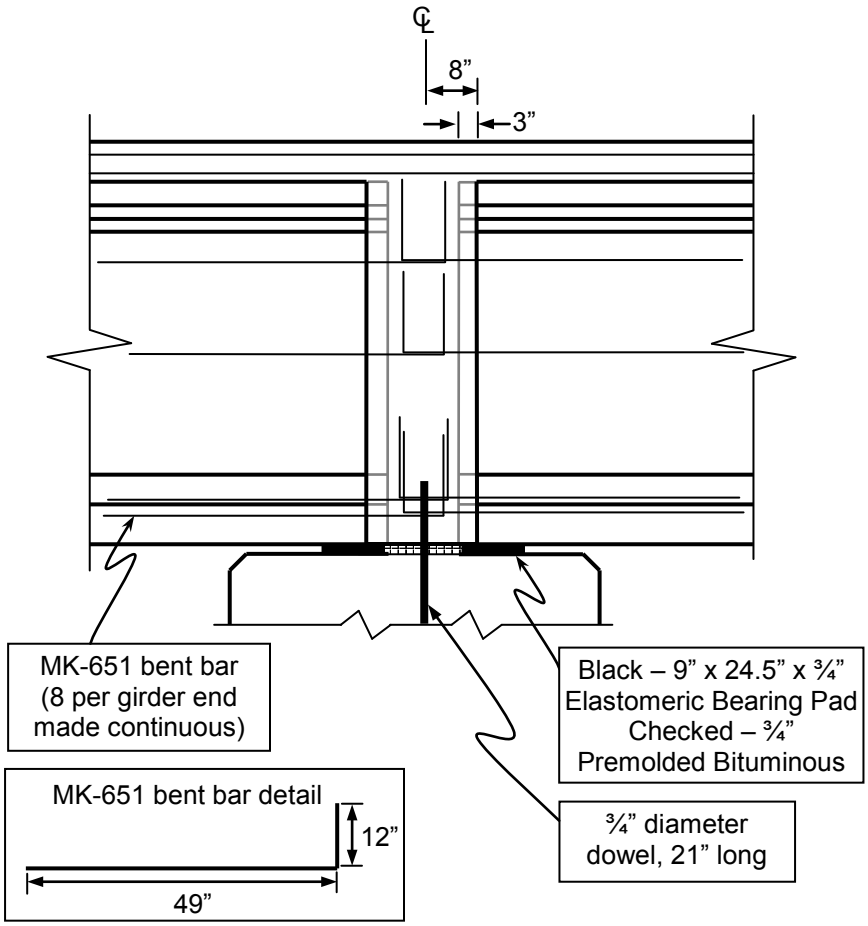

Figure 2.11: Continuity reinforcement—continuity diaphragm detail (ALDOT 1988; Swenson 2003)

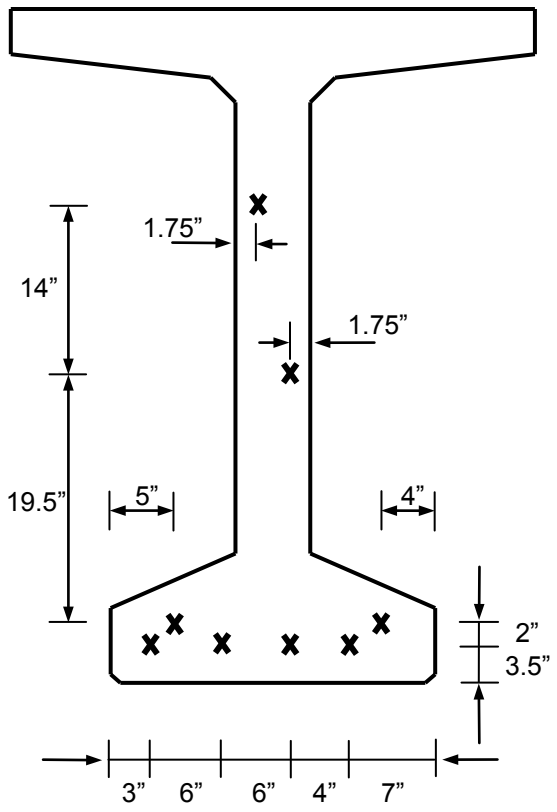

✘ Mild Steel Bent Bar (3/4” diameter)

Figure 2.12: Continuity reinforcement of a typical BT-54 cross section (ALDOT 1988; Swenson 2003)

2.3.6 Bridge Deck

The bridge deck for Spans 10 and 11 was constructed to be one continuous slab of cast-in-place reinforced concrete. The bridge deck has a consistent thickness of 6.5 in. and an additional "build up depth" over each girder that varies from 3 in. near the support to 1 in. near midspan. Mild steel reinforcing bars were cast into the slab during construction to provide reinforcement in the longitudinal and transverse directions. The longitudinal reinforcement resists tension forces in the deck slab induced by shear and acts as negative bending moment reinforcement for the bridge structure. The transverse deck reinforcement does not contribute to the calculated shear or flexural capacity of the structure (Swenson 2003).

The longitudinal reinforcement within a typical deck slab cross section over an exterior girder can be seen in Figure 2.13, and the reinforcement within a deck slab cross section over an interior girder is shown in Figure 2.14. The size #7 bars are only continuous over the interior support, and not continuous throughout the entire two-span structure. The size #7 bars extend a minimum of 15 ft from the centerline of the continuity diaphragm, and some of the size #7 bars extend an additional 10 ft. All other longitudinal reinforcement is continuous throughout both spans.

The slab was also designed to act compositely with the prestressed bridge girders. During girder fabrication, the stirrups that were cast into each girder were long enough to protrude from the top surface of the girder. The top surface of each girder was also roughened during girder fabrication. During construction, the protruding stirrups were cast into the cast-in-place deck slab. The stirrups and roughened girder surfaces promote composite behavior between the deck slab and bridge girders.

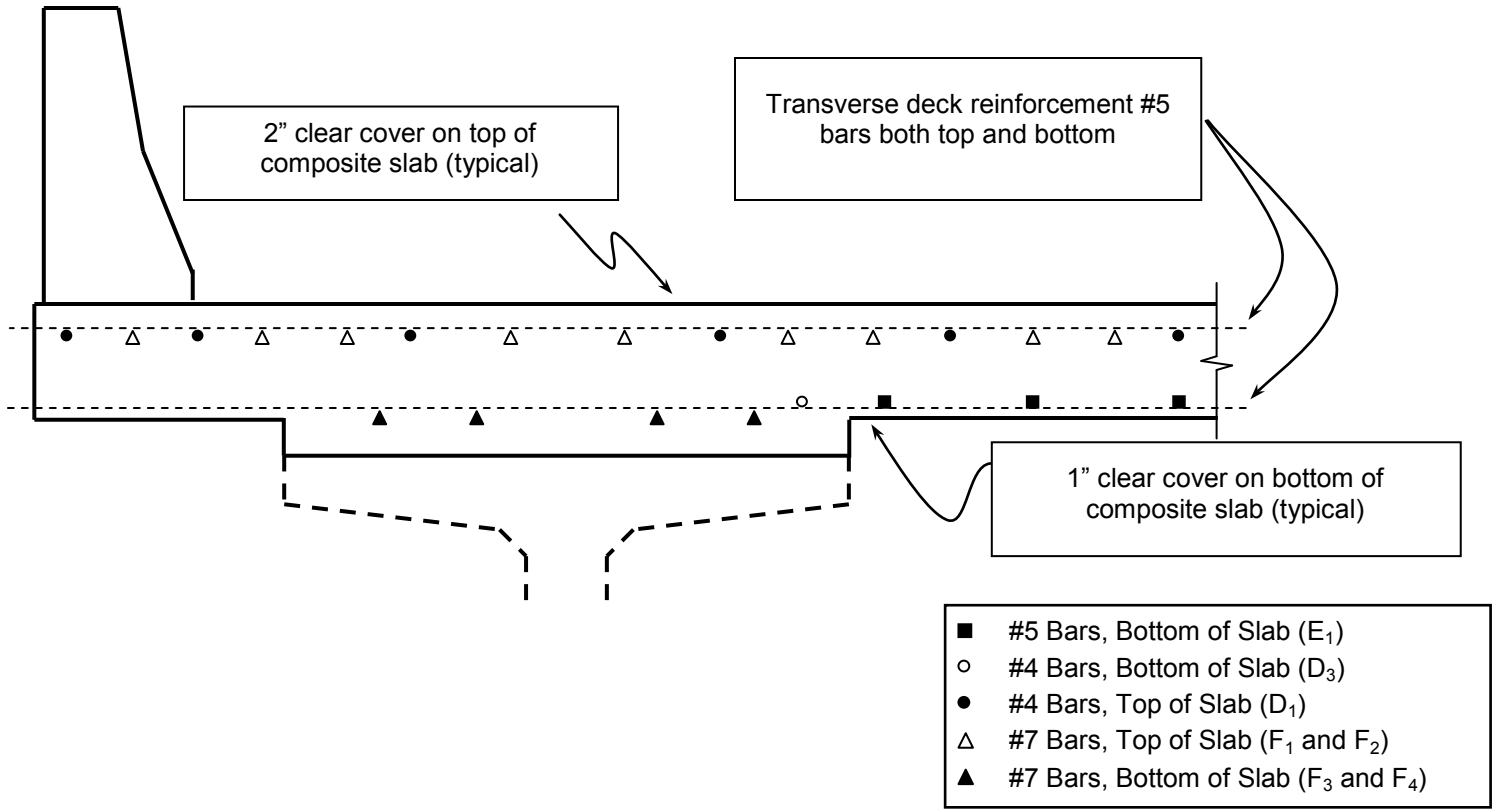

Figure 2.13: Cross section view of deck slab reinforcement over an exterior girder (ALDOT 1988; Swenson 2003)

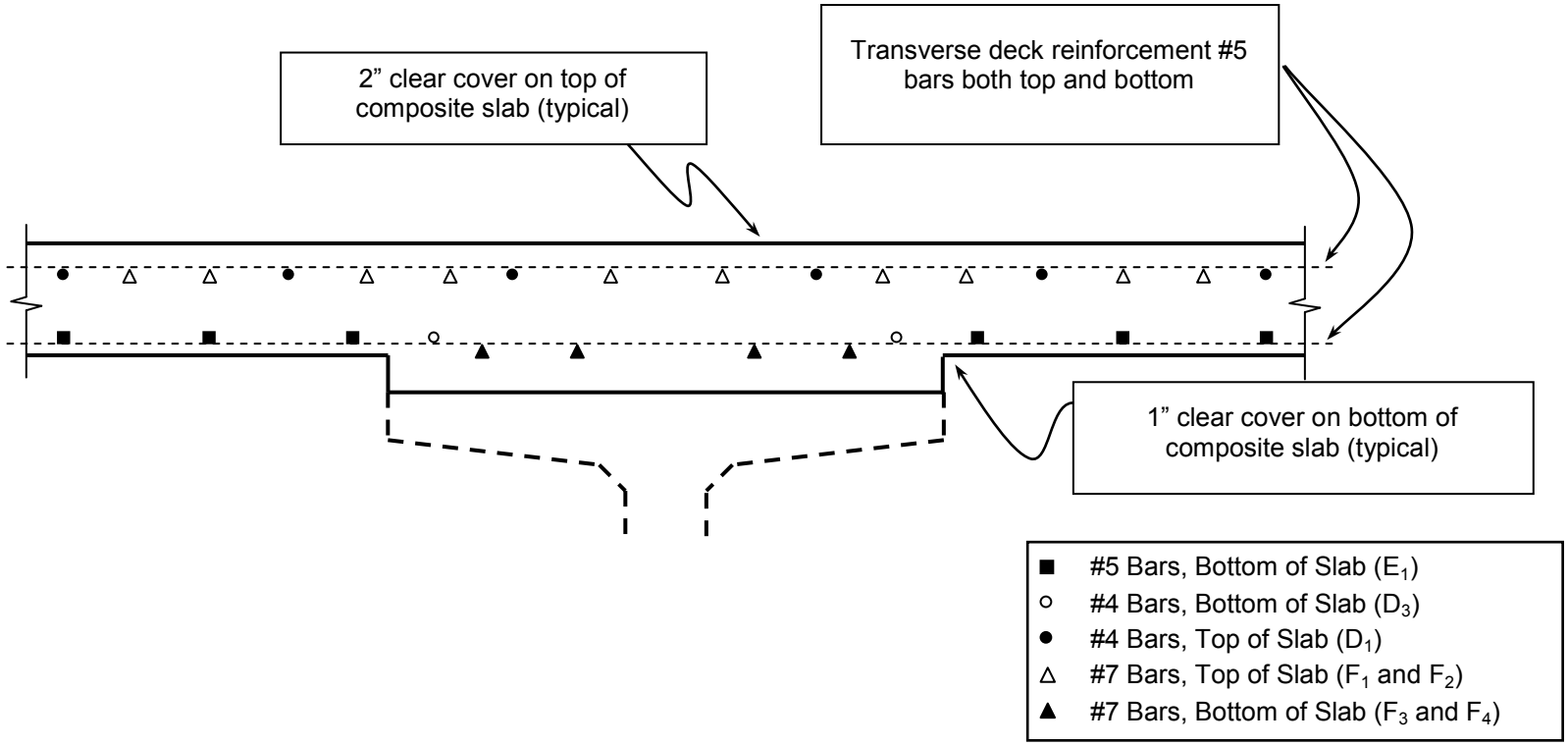

Figure 2.14: Cross section view of deck slab reinforcement over an interior girder (ALDOT 1988; Swenson 2003)

2.4 UNEXPECTED CRACKING

Hairline cracks in many of the prestressed bulb-tee girder ends made continuous for live loads were discovered during a routine inspection in 1992. The occurrence of hairline cracks is not uncommon in prestressed concrete girders at an early age, and is not necessarily a cause for serious concern, but the presence of early-age cracking did justify further evaluation. In 1994, a second inspection revealed that many of the hairline cracks had propagated and widened (ALDOT 1994). Some cracks had extended through the bottom flange, into the web, and as far as the intersection of the web and upper flange. Typical crack widths ranged from 0.002 in. (0.05mm) to 0.25 in. (6 mm) (Swenson 2003).

2.4.1 Crack Locations

Cracked girders were found at ten different sites between Eighth Street and Oakwood Avenue (ALDOT 1994). The portion of I-565 containing cracked bridge girders is illustrated in Figure 2.15. The pattern of cracking found in one BT-54 girder of Span 5 is illustrated in Figure 2.16. The inclined web cracks were limited to approximately 0.06 in. (1.5 mm) due to the transverse reinforcement that the cracks intersected. The vertical bottom-flange cracks only crossed the longitudinal prestressed strands and crack widths were not controlled by transverse reinforcement. Some of the larger bottom-flange cracks with widths up to 0.25 in. (6 mm) were visible from the ground in 1994, as shown in Figure 1.3.

The 1994 investigation also resulted in the discovery of continuity diaphragm cracking. The two types of cracks present in some of the continuity diaphragms were face cracks and end cracks. An example of a typical continuity diaphragm face crack can be seen in Figure 2.18, and an example of a typical diaphragm end crack can be seen in Figure 2.19. Approximately 57 percent of bents supporting bulb-tee girders contain diaphragm face cracks, and roughly 85 percent of bent contain diaphragm end cracks. All interior bents in two-span continuous structures constructed with BT-54 girders exhibit diaphragm end cracks (ALDOT 1994).

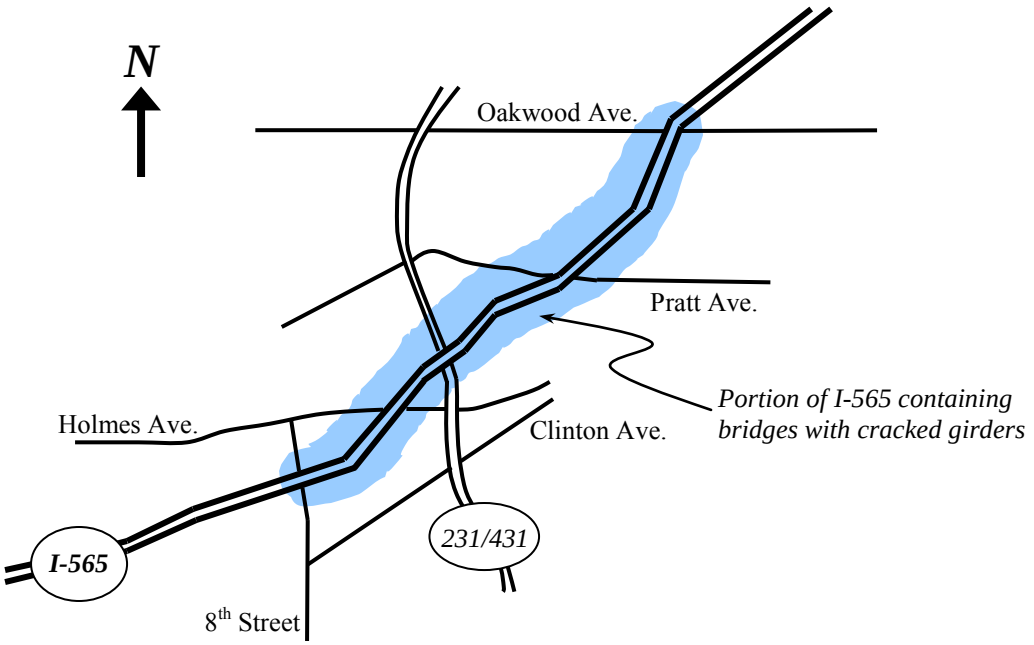

Figure 2.15: Portion of I-565 containing cracked bridge girders (Swenson 2003)

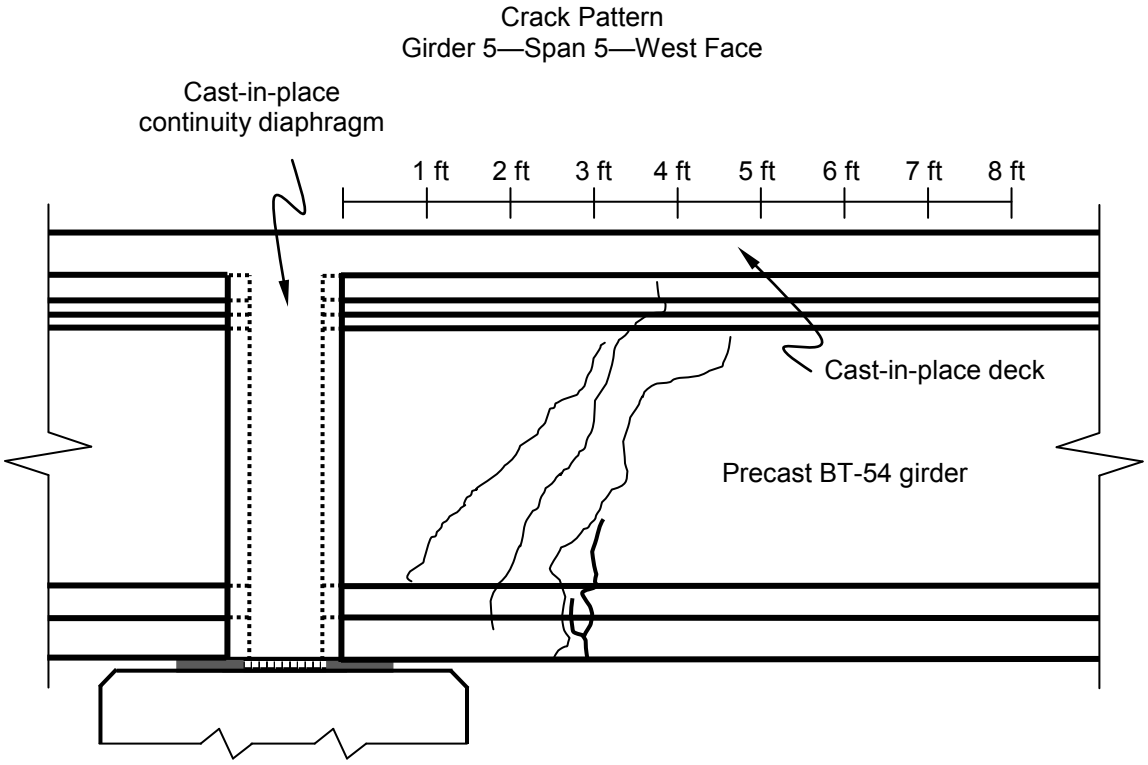

Figure 2.16: Cracking pattern in end region of precast girder (Barnes et al. 2006)

Figure 2.17: Cracked pre-tensioned bulb-tee girders (Barnes et al. 2006)

Figure 2.18: Typical diaphragm face crack (Swenson 2003)

Figure 2.19: Typical diaphragm end crack (Swenson 2003)

Due to the 1994 discovery that cracks were widening over time, a survey encompassing all of the Huntsville I-565 prestressed concrete bridge girders was conducted to locate cracks and document their size. For each girder type, the total number of girders was recorded as well as the number of girders associated with girder or diaphragm cracking. It was determined that typical AASHTO I-shaped girders exhibited no cracking, and that damaged regions were only found where bulb-tee girders were made continuous for live loads. It was also concluded that eighty-five percent of the bents supporting continuous ends of bulb-tee girders exhibited continuity-diaphragm end cracks (ALDOT 1994). The results of the girder survey performed by ALDOT personnel are shown in Table 2.2.

Table 2.2: Summary of cracking in prestressed concrete girders made continuous for live loads (ALDOT 1994)

	BT-54 Girders		BT-63 Girders		AASHTO Types I, III, IV Girders	
	No. of Girders	No. of Cracked Girders	No. of Girders	No. of Cracked Girders	No. of Girders	No. of Cracked Girders
Mainline	732	33	656	9	72	0
Ramp	560	24	140	8	174	0
Total	1292	57	796	17	246	0

2.4.2 Previous Repairs and Safety Measures

The severity of the cracks required immediate attention, and ALDOT personnel responded to the situation accordingly. The initial repair technique involved injecting the cracks with a structural epoxy, as shown in Figure 2.20, in an attempt to seal existing cracks and prevent future crack growth. However, new cracks often formed near the epoxy-injected cracks, and many epoxy-injected cracks reopened, indicating that this repair technique was ineffective. Other safety measures had to be implemented before a more effective repair method could be determined.

Steel frame false supports, as shown in Figure 2.21, were installed near all bents that were associated with girders containing cracked end regions. The false supports were positioned slightly beyond the cracked regions. The false supports were also installed with clearance of roughly 1 in. between the top of the false support and the bottom of the girder. Elastomeric bearing pads were installed between the false supports and each girder bottom to allow the false supports to carry loads, if necessary, while limiting impact forces that could result in damage to the girders or false supports. Although the bearing pads were installed to limit impact-related damage, it was undesirable for bearing pads to remain in contact with bridge girders. An installed bearing pad with proper space between the pad and girder is shown in Figure 2.22. A bearing pad that is in contact with a girder and transferring loads through the false support is shown in Figure 2.23.

Figure 2.20: Cracks injected with epoxy (Fason 2009)

Figure 2.21: Steel frame false supports (Fason 2009)

Figure 2.22: False support bearing pad with gap between pad and girder (Fason 2009)

Figure 2.23: False support bearing pad in contact with girder (Fason 2009)

2.4.3 Causes for Cracking

After conducting initial repairs and safety measures, the affected bridges were monitored to determine what caused the severe cracking. Ningyu Gao (2003) of Auburn University analyzed an interior BT-54 girder line of a typical two-span continuous portion of the elevated I-565 bridge structure in search of a cause for the extensive cracking. Gao calculated stresses in the girder, deck slab, and continuity diaphragm while considering construction sequence, time-dependent effects, and temperature distribution. The primary focus of the analysis was identifying the cause of positive bending moments near the continuous ends of the girders.

2.4.3.1 Construction Sequence

The construction sequence is related to the age of the girder when the deck and the diaphragm are cast. It was concluded with further investigation of the Huntsville I-565 bridge structure that the staged casting of the bridge deck and diaphragms was not performed in the order originally specified in the contract documents (ALDOT 1988). Previous research (Ma et al. 1998) has shown that the amount of time between diaphragm and deck casting can significantly affect the behavior of this type of bridge system. Gao (2003) concluded from a step-by-step analysis that the actual construction sequence did result in slightly smaller bottom-flange compressive stresses near the continuity diaphragm when compared to the stresses expected following the specified construction sequence. However, the difference between the two stresses was not large enough to be a likely cause of the observed tensile cracking.

2.4.3.2 Time-Dependent Effects

Time-dependent effects that could potentially cause cracking in the restrained girder ends include creep due to prestress forces and concrete shrinkage. The creep and shrinkage could cause enough of a member length change to induce a positive moment at the restrained girder end. However, Gao (2003) concluded that time-dependent effects are not large enough to be the primary cause of cracking—especially considering the early age at which the cracking occurred.

2.4.3.3 Temperature Effects

Ambient thermal conditions can result in temperature variations between the top of the bridge deck and the bottom of the girders. This temperature distribution can result in an upward deflection known as “sun cambering” in spans constructed to be continuous for live loads. This upward deflection due to temperature has the potential to induce bottom-flange tensile stresses associated with positive bending moments near the continuity diaphragm. It has been concluded that the relevant design standards used to design the I-565 bridge structures did not supply sufficient information regarding stresses due to temperature gradients (Barnes et al. 2006).

ALDOT personnel recorded temperature data at several different times during the investigation. The worst-case temperature gradient recorded occurred at 14:15 CST on May 19, 1994. An ambient temperature of 64.8° F (18.2° C) was reported. The deck surface reportedly had a temperature of 95.7° F (35.4° C), while the temperature at the bottom of a girder was 52.0° F (11.1° C), which resulted in a temperature difference of 43.7° F (24.3° C) (ALDOT 1994).

Ambient, deck, and girder temperatures were only monitored for a few days, and it is unlikely that these temperatures represent the worst load scenario related to temperature distributions that the bridge has experienced in its lifetime. The temperature difference of 43.7° F (24.3° C) measured for the bridge structure in Huntsville, Alabama is less than the maximum temperature difference of 48.6° F (27.0° C) calculated by Potgieter and Gamble (1989) for a bridge structure in Nashville, Tennessee (the city nearest to Huntsville, Alabama within the scope of their report). It is feasible for the ambient temperature in Huntsville to exceed 100° F (38° C) during an extreme event on a sunny summer day, which would likely result in a greater temperature difference than the difference that resulted from the ambient temperature of 64.8° F (18.2° C) measured on May 19, 1994. Due to direct sun exposure, an increased ambient temperature will likely have a greater effect on a deck surface than a girder bottom, resulting in an increased temperature difference that induces tensile stresses of greater magnitude near the continuity diaphragm (Gao 2003).

2.4.3.4 Internal Reinforcement Details

The bottom-flange flexural cracking near the continuous ends of these girders is reported to be associated with positive bending moments related to restrained forces of thermal load conditions. The maximum positive bending moment due to thermal load conditions would occur at the continuity diaphragm, which explains the diaphragm face and end cracks, but in some cases the cracks do not correspond with the point of maximum moment. Along multiple concrete girders, cracking has been observed to originate at distances from the continuity diaphragm that are similar to other origins of cracking on other girders. The internal reinforcement details for the BT-54 girders of I-565 were investigated to determine if localized stress concentrations could explain the similar crack locations (Barnes et al. 2006).

Prestressing strand debonding and continuity reinforcement details discussed in Sections 2.3.3 and 2.3.5 have an effect on the positive bending moment capacity near the continuity diaphragm. The continuity reinforcement length of 41 in. and the debonded length of 48 in. for more than one-third of the strands have been superimposed with the crack pattern observed at Girder 5 of Span 5, as shown in Figure 2.24.

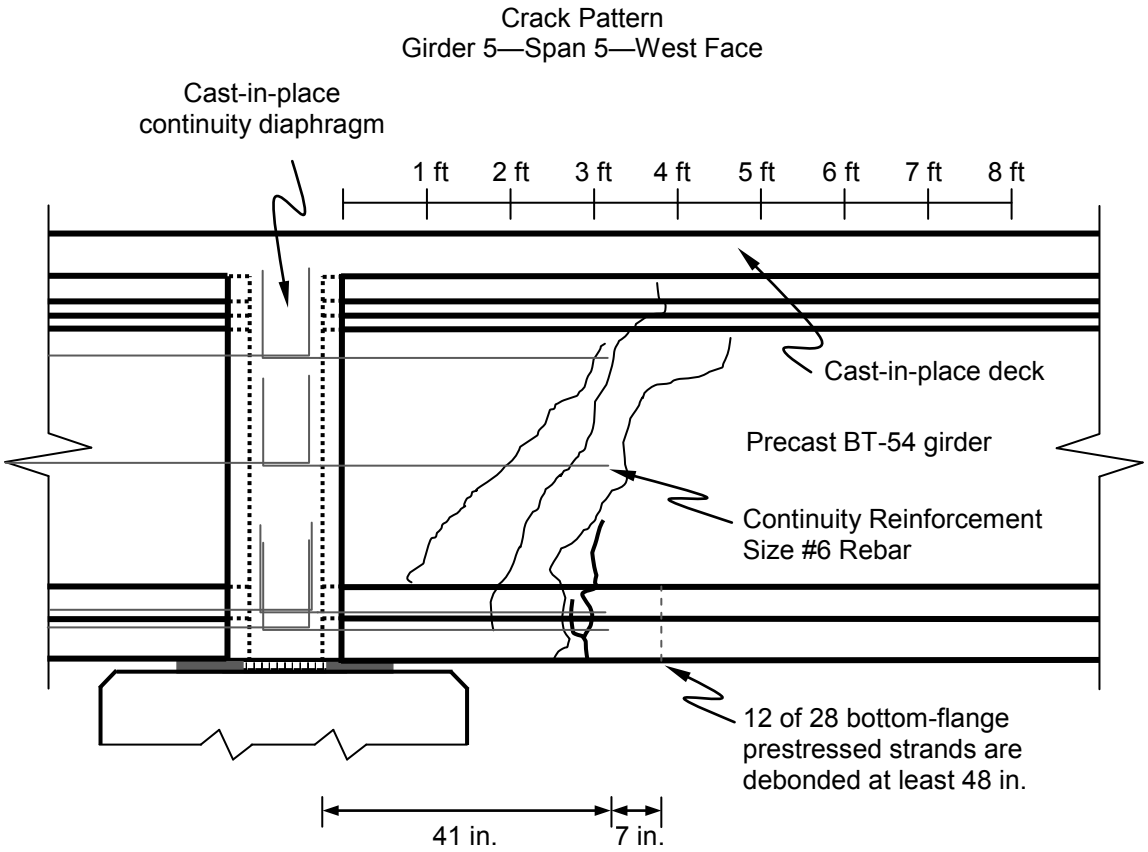

Figure 2.24: Cracked girder with continuity reinforcement details (Barnes et al. 2006)

During a critical thermal event, bottom-flange tensile stresses could be induced near the continuity diaphragm along the girder. The debonded strands result in cross sections with a relatively weak positive moment bending capacity compared to the midspan cross sections. Due to relatively weak cross sections for a distance of 48 in. and local stress concentrations that can occur near the continuity reinforcement termination point at 41 in., cross sections near the continuity reinforcement termination location are likely points of origin for flexural cracking in response to positive moment bending.

2.4.4 Ramifications of Cracking

Cracking within the anchorage zone of prestressed strands has the potential to reduce the effective prestress force, which consequently reduces the shear and flexural capacities of the girder. Cracks that remain open after the initiating event are an indication of inelastic behavior at the cracked cross section. This inelastic behavior could be caused by strands either yielding or slipping at the crack locations.

Yielding of prestressed strands at a crack location is one type of failure that results in a reduction of effective prestress force. Inelastic behavior caused by strand yielding results in permanent elongation of the strand, allowing crack widths to remain open after crack inducing loads are removed. A portion of the strain in the prestressing strand would be lost, which would result in a reduction of the effective prestressing force transferred to the end region of the girder.

In order for yielding to occur, yield level stresses must be developed in the prestressed strand at the crack location. This requires that the strands be adequately anchored on both sides of the crack. Swenson (2003) calculated the development length of a 0.5 in. special prestressing strand to be 80 in. in accordance with Article 5.11.4.2 of the AASHTO LRFD Bridge Design Specifications (2002). Swenson also noted that the typical cracking in the I-565 girders occurs within 41 in. of the continuous girder end. Since the strands are only anchored a distance roughly half of the full development length before the crack location, development of yielding stresses in the prestressing strands is not likely.

Slipping of prestressed strands at the crack location also results in the reduction of the effective prestress force transferred to the end region of a girder. Adequately developed prestressed strands result in concrete compressive stresses which increase shear capacity. Strand slip due to a lack of effective anchorage reduces pre-compression effects and may also result in girders with insufficient resistance to shear forces in the girder end region.

Swenson (2003) determined that the theoretical total slip resulting if all prestressing force was lost corresponded to the range of crack widths present in the I-565 girders. Swenson concluded that the prestressing strands slipped as a result of the cracks and that it is appropriate and conservative to assume that the prestressing force in the strands has been completely lost between each crack location and girder end. Visual inspection of the girders in 2010 indicated

that the girder end regions have experienced much less camber curvature over time than the rest of the span. This agrees with Swenson's contention that much of the effective prestress in the end regions has been lost.

2.5 BRIDGE BEHAVIOR ANALYSIS

Swenson (2003) used analytical methods to determine if the prestressed bulb-tee girders have strength deficiencies. Different girder behaviors and analysis methods were considered. The results of this analysis were taken into consideration during the design of an externally bonded fiber-reinforced polymer (FRP) reinforcement repair method. Bridge behavior analysis from Swenson (2003) is summarized in this section.

2.5.1 Behavior Types Considered

The two-span structures of I-565 were designed to behave as fully continuous structures for live loads. However, three possible girder behavior types were considered during analysis. The two-span structures have been analyzed as behaving as either

- Two simply-supported spans with no continuity at the interior support,
- One fully continuous structure, as originally constructed, or
- A two-span continuous structure with internal hinge behavior at crack locations.

2.5.2 Analysis Methods

The three possible bridge behaviors were evaluated with three analysis methods. The three analysis methods include

- Elastic structural analysis,
- Sectional model analysis, and
- Strut-and-tie model analysis.

Factored ultimate shear and moment envelopes for both interior and exterior girders were determined with elastic structural analysis. Shear and moment capacities of a typical cracked BT-54 girder were determined with sectional model analysis. The calculated capacities were then compared to the factored ultimate shear and moment envelopes to determine the location and magnitude of strength deficiencies. The forces transferred through the prestressed strands and future externally bonded fiber-reinforced polymer (FRP) reinforcement were determined with strut-and-tie model analysis. An adequate FRP reinforcement design was formulated based on the resistance force required of the FRP at the crack location.

2.5.2.1 Elastic Structural Analysis—Unfactored Demands

Elastic structural analysis of the two-span structure was conducted using structural analysis software. Shear and bending moment reactions in response to unfactored live loads were determined for each of the three behavior type models. Analysis of the simply supported model resulted in

- A maximum positive bending moment of around 26,000 kip-in. at midspan,
- A maximum shear force of roughly 96 kips at the supports, and
- No negative moments.

Analysis of the two-span fully continuous model resulted in

- A maximum shear force of roughly 87 kips at the non-continuous support,
- A maximum shear force of roughly 105 kips at the interior support,
- A maximum positive bending moment of roughly 19,200 kip-in. nearly 500 in. from the non-continuous end, and
- A maximum negative moment of roughly 22,000 kip-in. at the interior support.

Analysis of the two-span continuous model with an internal hinge resulted in reactions that were bounded in magnitude by the other two models. These reactions include
a less severe maximum shear force at the interior support compared to both the simply supported and fully continuous model, less severe maximum positive moment compared to the simply supported model, and a less severe maximum negative moment at the interior support compared to the continuous model. Due to distribution factors calculated for the two-span continuous bridge structure, the live load effects for ultimate shear demand are more severe for interior girders than exterior, and the live load effects for ultimate moment demand are more severe for exterior girders.

2.5.2.2 Sectional Model Analysis—Strength Capacities

Strength capacities for a typical cracked BT-54 girder were determined with sectional model analysis. The strength capacities were compared to the factored ultimate load demands determined for each type of behavior. The actual behavior may be more similar to the behavior expected of the continuous model with an internal hinge at the crack location, but the factored load demands of both the simply-supported and continuous bridge behavior were satisfied when designing a repair method for the strength deficiencies.

Simply supported behavior was determined to control the factored ultimate shear demand, exceeding the shear capacity of a typical cracked BT-54 girder by as much as 49 kips for an interior girder and 4 kips for an exterior girder.

Simply supported behavior was determined to control the factored ultimate positive moment demand, exceeding the positive moment capacity of a typical cracked BT-54 girder for cross sections located between the cracked cross section and the interior support. Due to the assumption that the prestressed strands have slipped and the prestress force has been lost, a strength reduction factor of 0.90 for flexure in non-prestressed concrete members was applied in accordance with Article 5.5.4.2.1 of the AASHTO LRFD.

Continuous behavior was determined to control the factored ultimate negative moment demand, exceeding the negative moment capacity of a typical cracked BT-54 girder. The negative moment capacity at the continuous end of a typical exterior girder was determined to be deficient for a length of 48 in. from the interior support.

Simply supported behavior was determined to control the longitudinal reinforcement capacity calculated in accordance with Article 5.8.3.5 of AASHTO LRFD (2002). The longitudinal reinforcement capacity provided was determined to be unsatisfactory over a length of 14 in. from the exterior support and over a length of 64 in. from the interior support. The longitudinal reinforcement at the cracked end was determined to be insufficient for a length of roughly 20 in. beyond the typical crack location within the two-span bridge structure.

2.5.2.3 Strut-and-Tie Analysis—Flow of Forces

Forces within a BT-54 girder with external reinforcement added to the bottom flange were determined with strut-and-tie model analysis. A typical strut-and-tie model is presented in Figure 2.25.

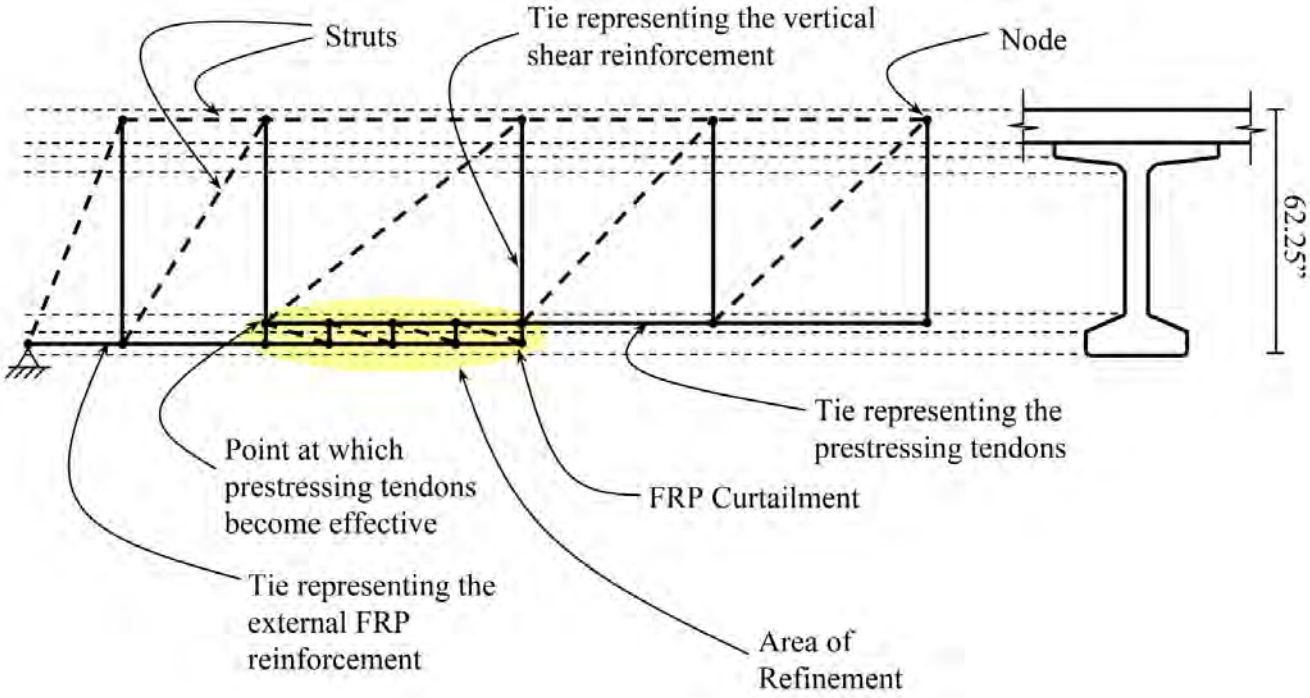

Figure 2.25: Typical strut-and-tie model (Swenson 2003)

Three separate models (A, B, and C) were produced to analyze the flow of forces within one girder for each of the three prospective bridge behavior conditions. Specific ties within the strut-and-tie models represent forces required to be carried by the longitudinal reinforcement. During the design of an external reinforcement repair method, the tensile capacity of the longitudinal reinforcement should satisfy the factored ultimate tensile force demand along the entire length of each tie.

Model A represents a simply supported girder with FRP reinforcement. Load configurations were examined to produce maximum shear and positive moment effects at the assumed cracked cross section. The maximum factored ultimate tensile force expected in the FRP reinforcement was 255 kips and the tensile force expected in prestressing strands at the same distance from the interior support was 300 kips. As the distance from the interior support increased, the tensile force expected in the FRP reinforcement decreased and the force expected in the prestressing strands increased. The element representing the FRP reinforcement furthest from the interior support expected a factored ultimate tensile force of 62 kips and the element representing the prestressing strands at that same distance from the interior support expected a tensile force of 491 kips. The expected factored ultimate tensile force in the element representing the prestressing strands following the curtailment of the FRP reinforcement was 631 kips.

Model B represents a girder that is part of a two-span structure made fully continuous for live loads. Load configurations were examined to produce maximum shear effects at the assumed cracked cross section. The ties representing the longitudinal tensile reinforcement were primarily in compression near the cracked cross section. None of the ties representing the FRP reinforcement were expected to be in tension. The element representing the FRP reinforcement furthest from the interior support expected a factored ultimate compressive force of 9 kips and the element representing the prestressing strands at that same distance from the interior support expected a tensile force of 150 kips. The expected factored ultimate tensile force in the element representing the prestressing strands following the curtailment of the FRP reinforcement was 344 kips.

Model C represents a girder that is part of a two-span structure made continuous for live loads, but contains an internal hinge representing a cracked cross section. Load configurations were examined to produce maximum shear effects at the assumed cracked cross section. The flow of forces in Model C were similar to the simply supported model (Model A), but the tensile forces expected in the longitudinal reinforcement decreased in magnitude. The maximum factored ultimate tensile force expected in the FRP reinforcement was 140 kips and the tensile force expected in prestressing strands at the same distance from the interior support was 189 kips. As the distance from the interior support increased, the tensile force expected in the FRP reinforcement decreased and the force expected in the prestressing strands increased. The element representing the FRP reinforcement furthest from the interior support expected a

factored ultimate tensile force of 35 kips and the element representing the prestressing strands at that same distance from the interior support expected a tensile force of 294 kips. The expected factored ultimate tensile force in the element representing the prestressing strands following the curtailment of the FRP reinforcement was 552 kips.

It was determined that the simply supported model (Model A) should control the required tensile capacity of the longitudinal reinforcement including the prestressing strands and external FRP reinforcement. Although the structure may not be purely simply supported, the girders should be strengthened to dependably resist factored ultimate loads for all three potential behavior types.

Longitudinal reinforcement tensile forces must be fully developed at the end of the tie closest to the support. For the tie extending from the nodal zone at the interior support (Member 1), the tensile force must be developed at the point where the centroid of the reinforcement extends beyond the extended nodal zone (ACI Committee 318 2002). During the design of an FRP reinforcement repair method, the FRP reinforcement forces were considered fully developed at the inside face of the bearing pad.

2.6 DESIGN OF EXTERNAL FIBER-REINFORCED POLYMER STRENGTHENING SYSTEM

Four FRP-reinforcement repair designs were presented by Swenson (2003). The FRP reinforcement systems were designed to either correct strength deficiencies that have resulted from cracking, or prevent strength deficiencies from occurring. Three complementary objectives were considered during the design of potential strengthening systems. Two objectives were to provide adequate positive bending resistance, as well as adequate shear resistance, regardless of continuity conditions. The other objective was to shift future cracking, associated with the restrained deformations of time- and temperature-dependent effects, to a more acceptable location at the face of, or within, the continuity diaphragm.

The FRP reinforcement selected for the design of potential repair systems was the Tyfo SCH-41 composite manufactured by Fyfe Co. This product is a wet lay-up system comprised of Tyfo SCH-41 reinforcing fabric and Tyfo S epoxy. Tyfo SCH-41 reinforcing fabric is comprised of unidirectional carbon fibers backed with a glass veil to increase and support fabric stability during installation. Tyfo S epoxy is a two-part adhesive used to both saturate the composite fabric and bond the fabric to the concrete.

The repair solution recommended by Swenson (2003) was a 4-ply FRP system applied near the continuity diaphragm along the bottom flange of every girder, even those which are uncracked. The longitudinal and cross sectional configurations of the recommended 4-ply FRP system are shown in Figures 2.26–2.28.

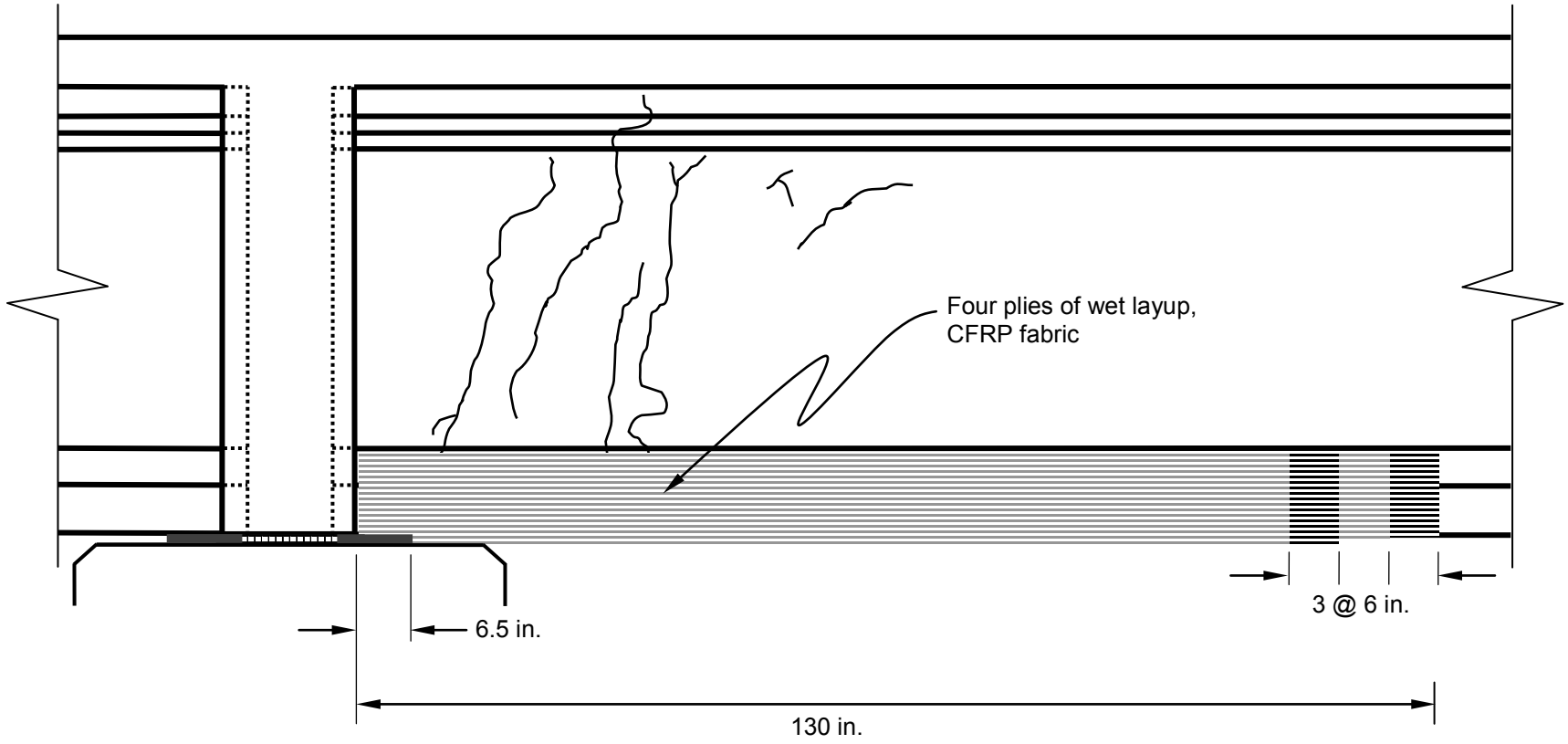

Figure 2.26: Longitudinal configuration profile for FRP (Barnes et al. 2006)

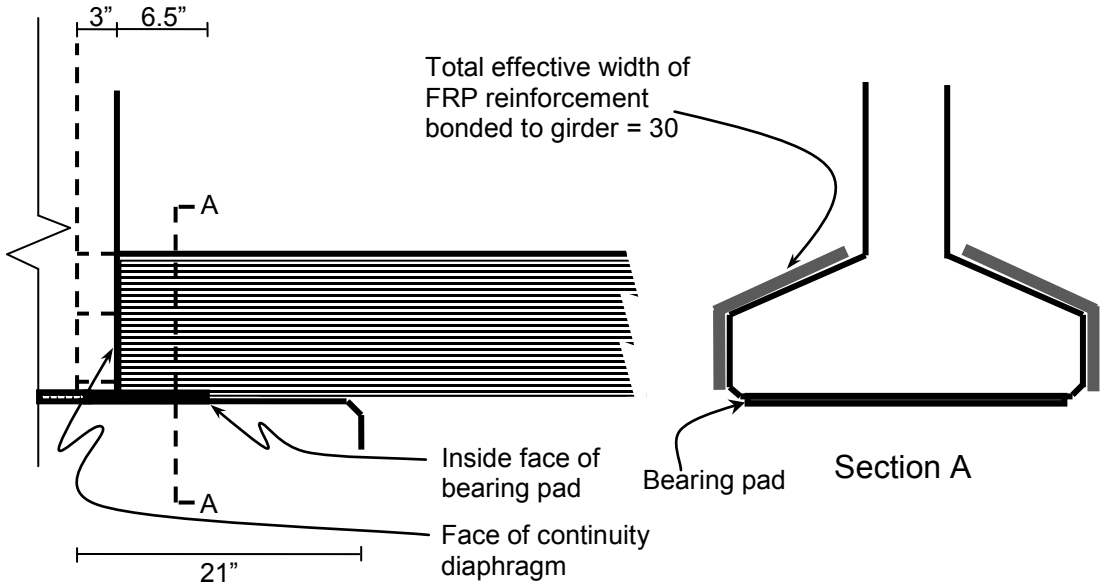

Figure 2.27: Cross-sectional configuration of FRP near diaphragm (Swenson 2003)

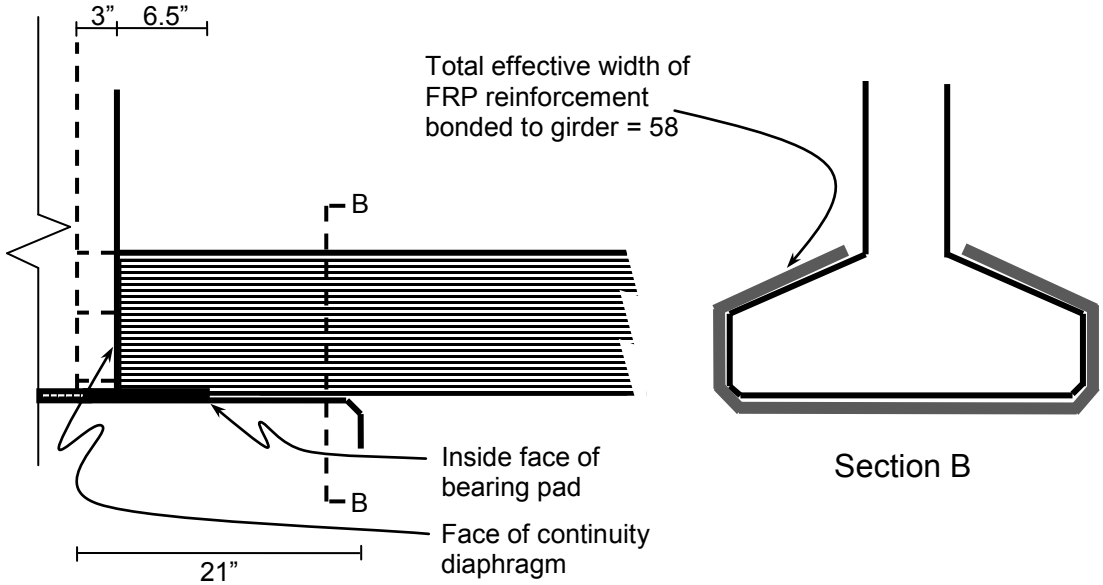

Figure 2.28: Cross-sectional configuration of FRP beyond bearing pad (Swenson 2003)

The FRP system terminates at a distance of 130 in. from the face of the continuity diaphragm. Only the first installed layer of FRP extends the full 130 in. from the diaphragm. Each subsequently installed layer terminates 6 in. earlier than the previous layer to allow for the gradual transfer of forces into the FRP and to minimize stress concentrations at the termination

points. FRP applied to the bottom surface of the flange cannot extend to the continuity diaphragm because of the girder bearing; instead it extends to roughly 10 in. from the face of the diaphragm, and terminates within 1 in. of the bearing pad.

2.7 LOAD TESTS PRIOR TO FRP REINFORCEMENT INSTALLATION

Load tests scheduled to be performed before and after installation of the FRP system were planned to quantify the effectiveness of the FRP reinforcement. The pre-repair load tests were conducted on the nights of May 31, and June 1, 2005. Specific girders were instrumented to document responses to various load conditions. Two ALDOT load trucks were positioned to apply loads to the bridge structure at designated locations. General behavior of the damaged bridge structure was analyzed with measured responses to the pre-repair load tests. Detailed documentation of the instrumentation, procedures, and results of pre-repair testing has been reported by Fason (2009) and is summarized in this section.

The instrumentation and procedure of the pre-repair testing were similar to those of the post-repair testing documented in this report. Specific details regarding the setup and execution of post-repair testing can be found in Chapters 3 and 4 of this report.

2.7.1 Instrumentation for Pre-Repair Load Testing

Prior to pre-repair testing, Girders 7 and 8 of Northbound Spans 10 and 11were instrumented with sensors designated to measure girder responses to varying load conditions. The installed sensors include

- Crack opening displacement (COD) gages,
- Deflectometers, and
- Surface-mounted strain gages.

A total of four COD gages, one per instrumented girder, were installed. Each COD gage was installed near the continuity diaphragm to span a single crack that extends into the web on each instrumented girder. A total of twelve deflectometers were positioned underneath the instrumented girders. A total of fifty-six surface-mounted strain gages were installed on the concrete surface of the instrumented girders. Eight cross sections contain gages at varying heights within the cross section, while eight other cross sections have only one concrete gage on the bottom surface of the bottom flange.

Sensor installation procedures prior to pre-repair testing have been described by Fason (2009). The majority of these sensors were maintained for post-repair testing, and specific post-repair sensor instrumentation details from can be found in Chapter 3 of this report.

2.7.2 Procedures for Pre-Repair Load Testing

Three distinct horizontal truck alignments represented load truck traverse lanes. Each traverse lane contained nine stop positions. Load trucks were held at stop positions long enough for sensors to measure girder response.

The first night of testing was dedicated to acoustic emissions testing. Analysis of the measurements from the acoustic emissions sensors do not fall within the scope of this report, but the sensors installed for static load testing did measure girder responses to the static truck positions of the acoustic emissions test.

The second night of testing included a repeat of the acoustic emissions test followed by static load testing at all stop positions. Each stop position was recorded three times to allow for averaging and elimination of outliers. Static load testing concluded with a superposition test.

Pre-repair testing procedures have been reported by Fason (2009). The majority of these load tests were repeated during post-repair testing, and specific details of post-repair load testing procedures can be found in Chapter 4 of this report.

2.7.3 Results of Pre-Repair Load Testing

The overall bridge behavior was analyzed following the pre-repair tests. Fason (2009) determined that the girders were not acting as simply supported girders, which was the worst-case behavior selected by Swenson for design of the FRP system. It was also determined that, at the time of the pre-repair load tests, the girders were not behaving as though they were hinged at the crack locations. It was noted by Fason that crack sizes observed during testing were visibly not as large as the crack sizes observed during sensor installation.

The superposition test was conducted to assess if the damaged bridge structure exhibited linear elastic behavior. It was determined that the deflections measured during superposition testing indicated that the bridge was exhibiting responses similar to linear-elastic behavior. Although the overall bridge behavior was considered to be linear-elastic, there were some discrepancies with the localized measurements of the crack-opening devices and strain gages. The cracks within the girders were observed to be behaving similar to a nonlinear spring, with the stiffness factor increasing as the deflection increased and crack openings decreased.

The influence of the false supports on bridge behavior during the pre-repair tests was also reported. A strain gage installed on one column of the false supports measured a small compressive strain during normal traffic conditions, which indicated that the false supports were providing some actual support during normal traffic conditions. Strains measured near the bent during superposition testing were also reportedly affected by the presence of the false supports. When only one span was loaded, the false supports under that span seemed to carry significant load, reducing the strain measured at the bent. When both spans were loaded simultaneously,

the continuity effects that promote an upward deflection of the opposite span allowed for the false supports under each span to carry fewer loads individually.

It was concluded by Fason (2009) that direct comparisons between pre- and post-repair measured responses would not be independently indicative of the effectiveness of the FRP repair. This was based on the assumption that the weather conditions during post-repair testing could be more conducive to wider crack openings immediately prior to load testing, and the fact that the false support bearing pads would be removed during the installation of the FRP reinforcement.

2.8 FINITE-ELEMENT ANALYSIS OF BRIDGE BEHAVIOR

Shapiro (2007) used ABAQUS/CAE to develop a finite element model (FEM) to represent the elevated two-span section of I-565 being investigated. Information regarding FEM development including: element selection, member geometry, material properties, support conditions, member connections, and load application has been detailed by Shapiro (2007). Once the fundamental model was created, the model was refined in three stages. Load test results were used to verify and refine the model as necessary. The final stage of the refinement process became the pre-repair condition model. Once a pre-repair model was established, the FRP reinforcement was then added to provide expected results for the post-repair load tests. The unintended support prvided by the false supports was not considered in the model development. A summary of the finite-element model analysis presented by Shapiro (2007) is discussed in this section.

2.8.1 Uncracked Model

The first stage of model refinement assumes an ideal scenario of uncracked girders. When compared to the pre-repair load test results, the *Uncracked* model results generally exhibit more compression (or less tension) strain on the bottom surface of the bottom flange than observed during testing. This discrepancy was even more evident at the cross sections near the cracked region, especially comparing results associated with midspan loadings. The *Uncracked* model overestimates the continuity of the cracked girder-system.

2.8.2 Cracked Model

The second stage of model refinement incorporated ABAQUS *seams* within the model to represent existing cracks. The resulting *Cracked* model represents a worst-case scenario of no reinforcement contribution at crack locations. The seams cut through the concrete and steel as if the steel has fractured at the crack locations or the bond between the steel and the concrete has deteriorated to the extent that no stresses can be transferred from the concrete to the steel. As a result, the model suggests that no bending moment is developed near the crack locations. The

load test results are more complicated and do not reflect the zero strain behavior suggested by the *Cracked* model results.

2.8.3 Cracked-with-Reinforcement Model

The *Cracked* model was refined by accounting for the presence of steel at the cracked cross sections. A *Cracked-with-Reinforcement* model was developed by adding two groups of reinforcing steel to represent the draped and undraped prestressing strands. Although this reinforcement was added, no attempt was made to apply a prestressing force to the model since it was considered unlikely that the prestress force would be effective at the cracked sections. The *Cracked-with-Reinforcement* model results fell between those of the *Uncracked* and *Cracked* models, better resembling the pre-repair load test results.

2.8.4 Pre-Repair Model

Through further analysis it was suggested that the *Cracked-with-Reinforcement* model could be refined by adding seams in the model to represents cracks at the face of the continuity diaphragm. The addition of seams at the face of the continuity diaphragm yielded results that best resembled the pre-repair load test results. This refined model became the *Pre-Repair* model to officially compare analytical results to experimental load test results. This model was also refined by modeling the addition of the FRP reinforcement to estimate the post-repair behavior of the bridge structure.

2.8.5 Post-Repair Model

The wet lay-up FRP reinforcement was modeled to behave as a laminate, or thin plate. The FRP reinforcement material properties were modeled as both isotropic and laminar. The isotropic material exhibits the same properties in all directions. The laminar material acts as a simplified form of an orthotropic material, which differentiates material properties in principal or perpendicular directions to each other. Shapiro (2007) concluded that the laminar representation of the FRP material more accurately modeled the orthotropic properties of the FRP reinforcement selected to be installed. The laminate FRP reinforcement was added to the *Pre-Repair* model to create a *Post-Repair* model for comparison with the results of the post-repair load tests.

2.9 INSTALLATION OF EXTERNAL FRP REINFORCEMENT

FRP reinforcement installation, which took place during December of 2007, was performed in accordance with the ALDOT Special Provision regarding the use of fiber reinforced polymer for girder repair. The on-site activities taking place from December 11, through December 19, 2007

were documented by Jiangong Xu for the AUHRC. Xu, an Auburn Univeristy research assistant at the time of the installation process, documented activities including

- Surface preparation,
- Adhesion testing of Tyfo S epoxy on concrete surface,
- Preparation of FRP-composite samples for tensile testing
- Procedures of FRP reinforcement installation process, and
- Painting of the FRP reinforcement that concluded installation.

2.9.1 Surface Preparation

Prior to FRP fabric installation, the contractor was required to prepare the surface to ensure adequate contact between the FRP and concrete. Surface preparation procedures were conducted in accordance with the ALDOT Special Provision regarding the use of fiber-reinforced polymer reinforcement for girder repair. Surface preparation techniques included surface grinding of irregularities such as excess crack-injected epoxy, surface patching of unacceptable voids and depressions, light surface roughening for improved bond quality, and final surface cleaning to remove dust and all other bond-inhibiting material. The use of compressed air for final cleaning is shown in Figure 2.29.

Figure 2.29: Surface cleaning—final removal of dust and debris

Girder preparation also involved the removal of the false support bearing pads. These bearing pads inhibited FRP installation to the bottom of the girder at false-support locations. The

bearing pads under Span 11 were, in general, more difficult to remove than the bearing pads under Span 10. Initially, the contractor attempted to remove each bearing pad by punching it out of place using a chisel and hammer. When a bearing pad was under enough pressure to prevent removal, the contractor then used a reciprocating saw on the pad to alleviate some of that pressure, as shown in Figure 2.30. In some cases, saw cutting alone was not effective at alleviating enough pressure for successful bearing pad removal. In these cases, a propane torch was used to soften the rubber and allow for a more effective sawing process, which is shown in Figure 2.31. After successful pressure alleviation, the bearing pad was removed using the initial chisel-and-hammer removal method, as shown in Figure 2.32. An example of a bearing pad that required extensive removal efforts is shown in Figure 2.33.

Figure 2.30: Use of saw for bearing pad removal

Figure 2.31: Use of torch for bearing pad removal

Figure 2.32: Successful removal of bearing pad

Figure 2.33: Bearing pad after forceful removal

2.9.2 Adhesion Testing

Tyfo S saturant epoxy manufactured by Fyfe Co. was used throughout the FRP installation. Adhesion testing of the Tyfo S epoxy on the concrete surface was required to ensure that the bond strength of the epoxy exceeded the tensile strength of the concrete. The adhesion tests were conducted in accordance with the requirements given in ASTM D4541. Detailed description of the ASTM D4541 adhesion testing procedure has been reported by Swenson (2007).
A minimum of three tests were required for each day in which FRP reinforcement was installed, and a minimum of one test was required per 500 square feet of installed FRP reinforcement. Adhesion testing equipment is shown in a laboratory setting in Figure 2.34. On-site adhesion testing is shown in Figure 2.35.

Figure 2.34: Adhesion test equipment (Swenson 2007)

Figure 2.35: Performance of on-site adhesion test

2.9.3 Tensile Testing

Tensile testing of FRP reinforcement samples was required to ensure the quality of the FRP reinforcement installed. A minimum of two testing samples were required for each day that FRP

reinforcement was installed. A testing sample, prepared as shown in Figures 2.36 and 2.37, was to consist of two 12 in. by 12 in. panels representative of the four-layer FRP and epoxy composite. However, the contractor fabricated each panel with only two plies of fabric, interpreting this as “representative” of the four-ply system. The samples were sent to a testing laboratory accredited in accordance with ISO/IEC 17025. The required testing procedures are presented in ASTM D3039. The tensile strength, ultimate tensile strain, and tensile modulus of elasticity were tested in a minimum of five sample batches.

Figure 2.36: Preparation of sample for tension testing

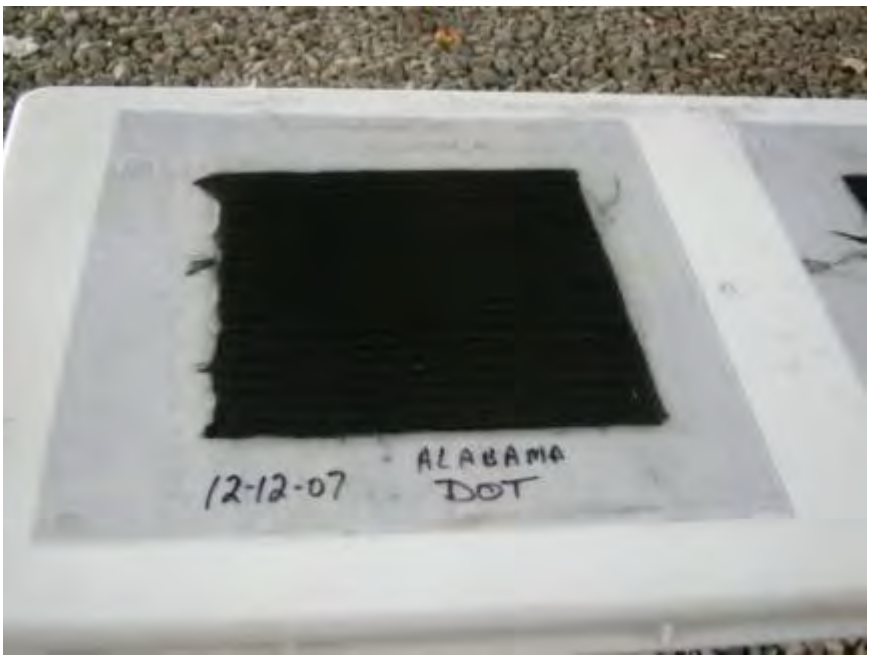

Figure 2.37: Representative sample for tension testing

2.9.4 FRP Fabric Installation Procedures

The FRP reinforcement repair consisted of four layers of FRP fabric. Due to the width of FRP fabric required to wrap around a typical bottom flange, three FRP fabric sheets were necessary per layer of installation. Two of the fabric sheets were of equal width and the third fabric sheet was narrower.

Each sheet of FRP fabric was cut to size and then saturated with epoxy. The typical fabric cutting and epoxy saturation procedures are shown in Figures 2.38 and 2.39. Epoxy was also applied to the surface of the girders prior to application of the first layer of FRP fabric, as shown in Figure 2.40. The first layer of FRP fabric was then installed as shown in Figure 2.41. Successive layers of FRP and epoxy were then applied, and an example of a typical four-layer installation is shown in Figure 2.42.

Figure 2.38: Cutting strips of FRP fabric

Figure 2.39: Epoxy saturation of FRP fabric

Figure 2.40: Applying epoxy to girder surface before FRP fabric installation

Figure 2.41: Installation of first layer of FRP fabric

Figure 2.42: Four layers of installed FRP fabric

2.9.5 FRP Fabric Installation—First Layer

The installation sequence for the first layer of FRP fabric is illustrated in Figure 2.43. The two wider strips were installed beginning at the joint of the web and top of bottom flange on their respective faces of the girder and wrapped around to extend partially along the bottom of the bottom flange. The narrower strip was applied along the centerline of the bottom of the bottom flange of the girder to fill the gap between the termination points of the two wider FRP fabric sheets.

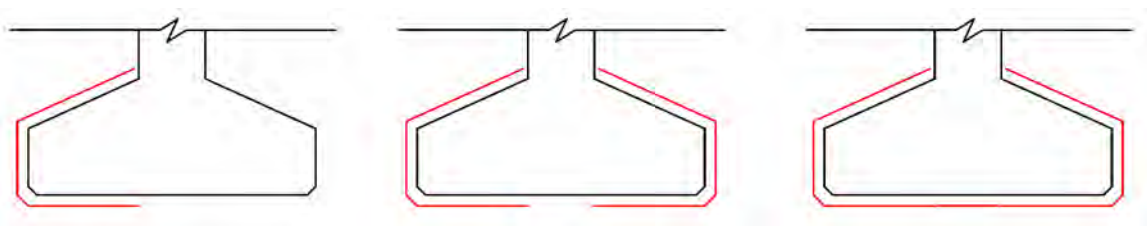

Figure 2.43: FRP installation sequence–first layer

2.9.6 FRP Fabric Installation—Second Layer

The installation sequence for the second layer of FRP fabric is illustrated in Figure 2.44. The narrow sheet was applied at the joint of the web and top of bottom flange on one face of the girder. One of the wide sheets was applied beginning at the edge of the narrow sheet and

overlapped the centerline of the girder on the bottom flange. The remaining wide sheet began at the termination of the first wide sheet and wrapped around the bottom flange to terminate at the joint of the web and top of the bottom flange.

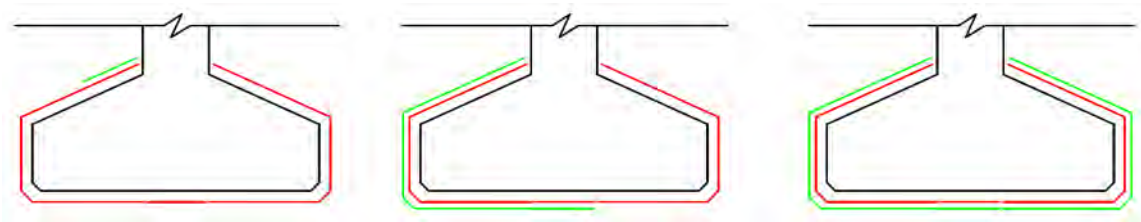

Figure 2.44: FRP installation sequence—second layer

2.9.7 FRP Fabric Installation—Third Layer

The third layer was similar to the second layer, but the installation began with the narrow sheet being applied to the face of the girder opposite of the narrow sheet in the second layer. The sheets were arranged in this opposing pattern so that fabric of the third layer overlapped the seams in the second layer. The installation sequence for the third layer of FRP fabric is presented in Figure 2.45.

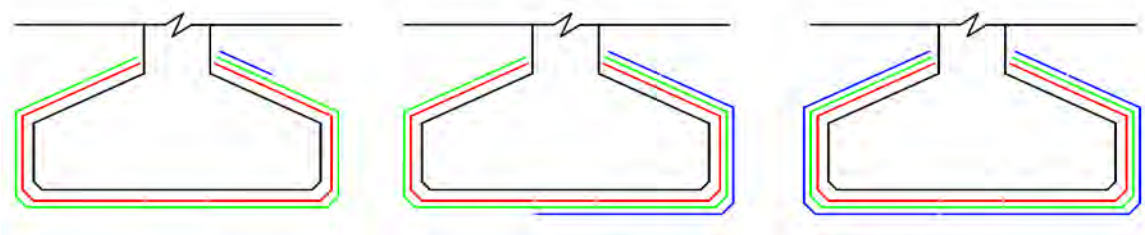

Figure 2.45: FRP installation sequence—third layer

2.9.8 FRP Fabric Installation—Fourth Layer

The fourth layer pattern was identical to the symmetric first layer pattern. The installation sequence for the fourth layer of FRP fabric is presented in Figure 2.46.

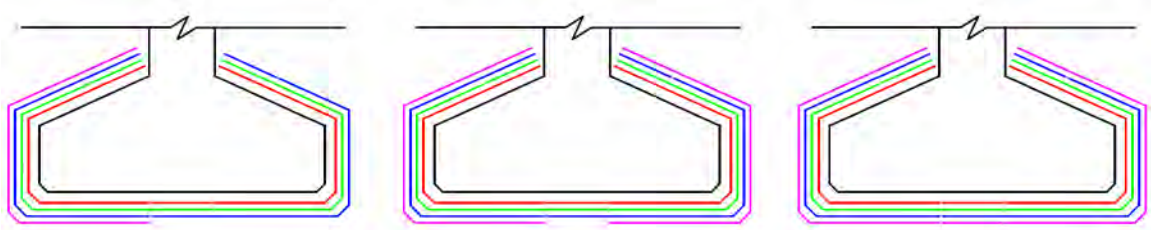

Figure 2.46: FRP installation sequence—fourth layer

2.9.9 Painting of Installed FRP Reinforcement

After the epoxy of the FRP reinforcement sufficiently cured, the FRP surface was painted using Masonry, Stucco, and Brick Paint manufactured by Behr. This white acrylic latex paint was used to further protect the reinforcement from ultraviolet rays and weather-related distress over time. The paint was sprayed onto the FRP surface as shown in Figure 2.47, and the finished girders of Span 10 are shown in Figure 2.48.

Figure 2.47: Painting of FRP reinforcement

Figure 2.48: Painted FRP reinforcement of Span 10

2.9.10 FRP Reinforcement Installation Timeline

FRP installation activities occurred between Tuesday, December 11, and Wednesday, December 19, 2007. The weather conditions reported at the Huntsville International Airport for these dates are presented in Table 2.3. A summary of the FRP reinforcement installation activities that were conducted each day is presented in this section based on documentation provided by an Auburn University researcher.

Table 2.3: Weather during FRP reinforcement installation (NOAA 2008)

Date	Minimum Temperature (°F)	Maximum Temperature (°F)	Mean Temperature (°F)	Precipitation (in.)
Dec. 11, 2007	56	77	67	0.00
Dec. 12, 2007	56	71	64	0.00
Dec. 13, 2007	47	69	58	0.05
Dec. 14, 2007	39	51	45	0.00
Dec. 15, 2007	40	69	55	0.08
Dec. 16, 2007	28	43	36	T
Dec. 17, 2007	23	48	36	0.00
Dec. 18, 2007	27	54	41	T
Dec. 19, 2007	44	54	49	T

Note: T = Trace precipitation amount (between 0.00 and 0.01 in.)

2.9.10.1 December 11, 2007

FRP reinforcement was installed on Girder 9 of Span 10 on Tuesday, December 11, 2007, which was the first day of installation. The first layer of FRP took close to 1 hour to install. Installation of all four FRP layers was completed in roughly 2.5 hours. A tensile testing sample was prepared before beginning the installation process.

2.9.10.2 December 12, 2007

FRP reinforcement was installed on Girders 8, 7, and 6 of Span 10 on Wednesday, December 12, 2007. FRP installation was completed in roughly 1.5 hours for Girder 8, 1.25 hours for Girder 7, and 2hours for Girder 6. It was also documented that, before beginning installation, an adhesion test was performed and a tensile testing sample was prepared.

2.9.10.3 December 13, 2007

The 0.05 in. of precipitation noted for Thursday, December 13, 2007 in Table 2.3 reportedly accumulated between the hours of 5:00 a.m and 2:00 p.m. CST (NOAA 2008). This weather and resulting moisture conditions were not conducive to proper FRP installation, and the contractor decided to focus efforts on surface preparation.

2.9.10.4 December 14, 2007

FRP reinforcement was installed on Girders 5, 4, 3, and 2 of Span 10 on Friday, December 14, 2007. FRP installation was completed in roughly 1 hour for Girder 5, 1 hour for Girder 4, 1.5 hours for Girder 3, and 1 hour for Girder 2. It was again documented that, before beginning installation, an adhesion test was performed and a tensile testing sample was prepared.

2.9.10.5 December 15, 2007

The forceful removal of Span 11 bearing pads began on Saturday, December 15, 2007. Complete removal of all Span 11 bearing pads was unsuccessful.

2.9.10.6 December 16, 2007

No work was documented by the AUHRC for Sunday, December 16, 2007

2.9.10.7 December 17, 2007

Span 11 bearing pad removal continued on Monday, December 17, 2007.

2.9.10.8 December 18, 2007

FRP reinforcement was installed on Girders 9, 8, 7, 6, and 5 of Span 11 on Tuesday, December 18, 2007. FRP installation was completed in roughly 1 hour for Girder 9, 1 hour for Girder 8, and 2 hours for Girder 7, 1 hour for Girder 6, and 1hour for Girder 5. It was documented that another tensile testing sample was prepared before beginning installation.

2.9.10.9 December 19, 2007

The contractor began painting installed FRP fabric on Wednesday, December 19, 2007. Girders 9–2 of Span 10 were painted before beginning other FRP installation. FRP reinforcement was installed on Girder 1 of Span 10 and Girder 1 of Span 11. FRP installation was completed in roughly 2 hours for Girder 1 of Span 10 and 1 hour for Girder 1 of Span 11. These girders were painted immediately following FRP installation. It was also documented that a tensile testing sample was prepared, before beginning installation.

2.9.10.10 After December 19, 2007

FRP installation activities performed after Wednesday, December 19, 2007 were not documented by AUHRC personnel. The remaining activities included FRP installation on Girders 4, 3, and 2 of Span 11 and the painting of installed FRP fabric on Girders 9–2 of Span 11.

2.10 INSTALLATION AND TESTING CONCERNS

Several issues related to FRP installation and testing were identified during and after the installation process. These concerns are discussed in this section.

2.10.1 FRP Orientation

AUHRC personnel visited the site on the first day of planned FRP installation and discovered that the contractor was cutting FRP fabric segments in preparation to install this fabric with the primary carbon fibers oriented perpendicular to the specified direction. This mistake occurred despite the primary fiber direction being correctly and explicitly indicated on the FRP installation plans. The on-site ALDOT inspector—who had no previous experience with FRP installation—exhibited no comprehension of the importance of the correct FRP orientation. Had the FRP been installed with the incorrect orientation, none of the required strengthening would have been achieved. The error was pointed out to the installation contractor and ALDOT personnel prior to actual installation, and all of the FRP was installed with the correct orientation. It is critical that design documents clearly show the correct fiber orientation, *and* that ALDOT inspectors and FRP installers understand the proper orientation prior to FRP installation.

2.10.2 FRP Samples for Tensile Testing

Panels of cured FRP composite were prepared for ASTM D 3039 tensile testing. The AUHRC/ALDOT special provision (No. 06-0302, Section 595) for FRP specified that the sample panels consist of "cured composite that is representative of the installed system." The original intention of this specification was that a sample composite panel would consist of four cured layers of fabric because the installation involved a four-layer FRP system for the I-565 girders. However, the samples prepared by the contractor and submitted for tensile testing only consisted of two layers bonded together. Thus, the true mechanical properties of the actual four-layer system installed are not known, but rather must be inferred from the two-layer tensile test results. It is not certain that the unit stiffness and ultimate tensile strength remain constant as the number of layers in the composite increases. The "tensile testing" subsection of the ALDOT special provision for FRP needs to be modified to clearly state that "all tensile test samples shall consist of the same number of fabric layers as are installed on the actual concrete structure."

2.10.3 FRP Tensile Testing Observation

The AUHRC/ALDOT special provision for FRP specified that the contractor notify ALDOT and AUHRC at least two weeks prior to tensile testing, and that the testing laboratory allow ALDOT and AUHRC personnel to witness the testing. The contractor did not notify AUHRC researchers

of this testing until two weeks after it was completed. Therefore testing procedures could not be documented for this research and implementation study.

2.10.4 FRP Tensile Test Results

The specified minimum (five) of sample tensile test batches were tested for the contractor by OCM Test Laboratories of Anaheim, California, and the results were submitted to ALDOT First Division. As mentioned in the previous section, these tests were not witnessed by AUHRC or ALDOT personnel. The tests were performed January 22–23, 2008 when the samples were approximately six weeks old. Reported test results are summarized in Table 2.4, along with the specified design values and "typical test values" reported by the FRP manufacturer. Two of the sample dates listed by the contractor (December 10 and 13) correspond to days on which no FRP was installed. It is therefore uncertain whether any of the five dates listed accurately describe the actual date that a sample was fabricated.

Table 2.4: Summary of Reported ASTM D 3039 Tensile Test Results

	Ultimate Strength (ksi)		Modulus of Elasticity (ksi)		Elongation (%)	
Test Results from Testing Laboratory (each sample consists of five tested coupons)						
FRP Sample Date	Mean	S.D.	Mean	S.D	Mean	S.D.
Dec. 10	165	10	*16,400*	*1,300*	1.06	0.05
Dec. 11	**106**	14	13,300	4,100	0.91	0.14
Dec. 12	**101**	11	12,500	1,900	0.87	0.14
Dec. 13	144	14	14,000	1,100	1.05	0.11
Dec. 14	126	10	*13,900*	*5,500*	1.05	0.12
AUHRC/ALDOT-Specified Design Values for I-565 Installation						
	121		11,900		0.85	
"Typical Test Values" Published by Manufacturer						
	143		13,900		1.00	

Note: Mean and S.D. are mean and standard deviation, respectively, of five-coupon sample

The modulus of elasticity (E_f) values displayed in italics (Dec. 10 and 14) are questionable because one coupon in that batch of five coupons has a reported E_f result that appears erroneously high (two or more standard deviations above the mean of the five-coupon sample). It is impossible to evaluate the accuracy of these suspicious results because stress versus strain data plots were not provided. The modulus of elasticity plays a critical role in the design procedure for this type of FRP repair. Unlike ultimate strength values, FRP modulus values that are *too high* relative to design assumptions can result in strength deficiencies. This is true in regions where only a short bonded length is available for anchorage—like around the bearings in the I-565 girders. Therefore, it can be more conservative to perform FRP anchorage and development computations using a typical *average* test value for E_f rather than a lower-bound "design value". There is further discussion of this issue in Appendix N.

The ultimate strength values displayed in bold indicate tensile strengths less than the specified design strength. These values are not absolutely critical because the FRP design for the I-565 installation was based on an assumed debonding failure mode at tensile stresses well below 100 ksi (Swenson 2003). However, the inter-batch variability of the ultimate tensile strength results is somewhat disconcerting and indicates the importance of good quality procedures during installation. Again, it is unknown how well these two-layer FRP test coupons represent the behavior of the four-layer composite FRP that was applied to the concrete bridge girders.

2.11 CURRENT RESEARCH

Post-repair testing was required to gauge the effectiveness of the FRP reinforcement repair. The FRP material installed on the instrumented girders was inspected for signs of delamination prior to testing, and no significant signs of bond failure were observed for the repair that had been in service for more than 2 years at the time of post-repair testing. Also, additional strain gages were installed to measure the response of the FRP material during testing. The bridge structure was then subjected to load tests similar to those conducted prior to the repair. The instrumentation, procedure, and results of post-repair testing are presented in subsequent chapters of this report.

Chapter 3

BRIDGE INSTRUMENTATION

3.1 INTRODUCTION

Northbound Spans 10 and 11 were instrumented with sensors to quantify bridge behavior and the response of selected girders during specific loading scenarios. The desired quantifiable responses included the opening or closing of cracks within a girder web, girder deflections, and girder surface strains of concrete and FRP reinforcement. Sensor locations and installation procedures are discussed in this chapter.

3.2 INSTRUMENTATION OVERVIEW

Girders 7 and 8 in Spans 10 and 11 exhibited significant cracking at their continuous ends and were selected for instrumentation. Two girders per span were heavily instrumented rather than installing fewer sensors per girder for all nine girders per span. Another factor leading to the selection of Girders 7 and 8 was the need to keep one lane open to vehicular traffic during load testing. These girders are the second and third interior girders from the east edge of the bridge, which allowed the west lane to remain open without significant effect on test results. The exterior girder (Girder 9) was not chosen because of anticipated analytical complications related to the proximity of the west barrier rail (Fason 2009).

The instruments installed on each girder included crack-opening displacement (COD) gages, deflectometers, and surface-mounted strain gages installed on concrete and FRP reinforcement. A total of seventy-two sensors were installed. Four sensors were COD gages: each straddled one crack per instrumented girder. Twelve sensors were deflectometers placed along the ground directly underneath the instrumented girders to measure deflections at incremental distances from the continuity diaphragm. The remaining fifty-six sensors were surface-mounted strain gages installed along the instrumented girders. Eight cross sections, four on each girder line, were instrumented with surface-mounted strain gages at different girder heights to allow for strain profile analysis. Bottom-fiber strain gages were installed at eight different locations along each girder line. An overview of the instrumentation locations per girder line is illustrated in Figure 3.1.

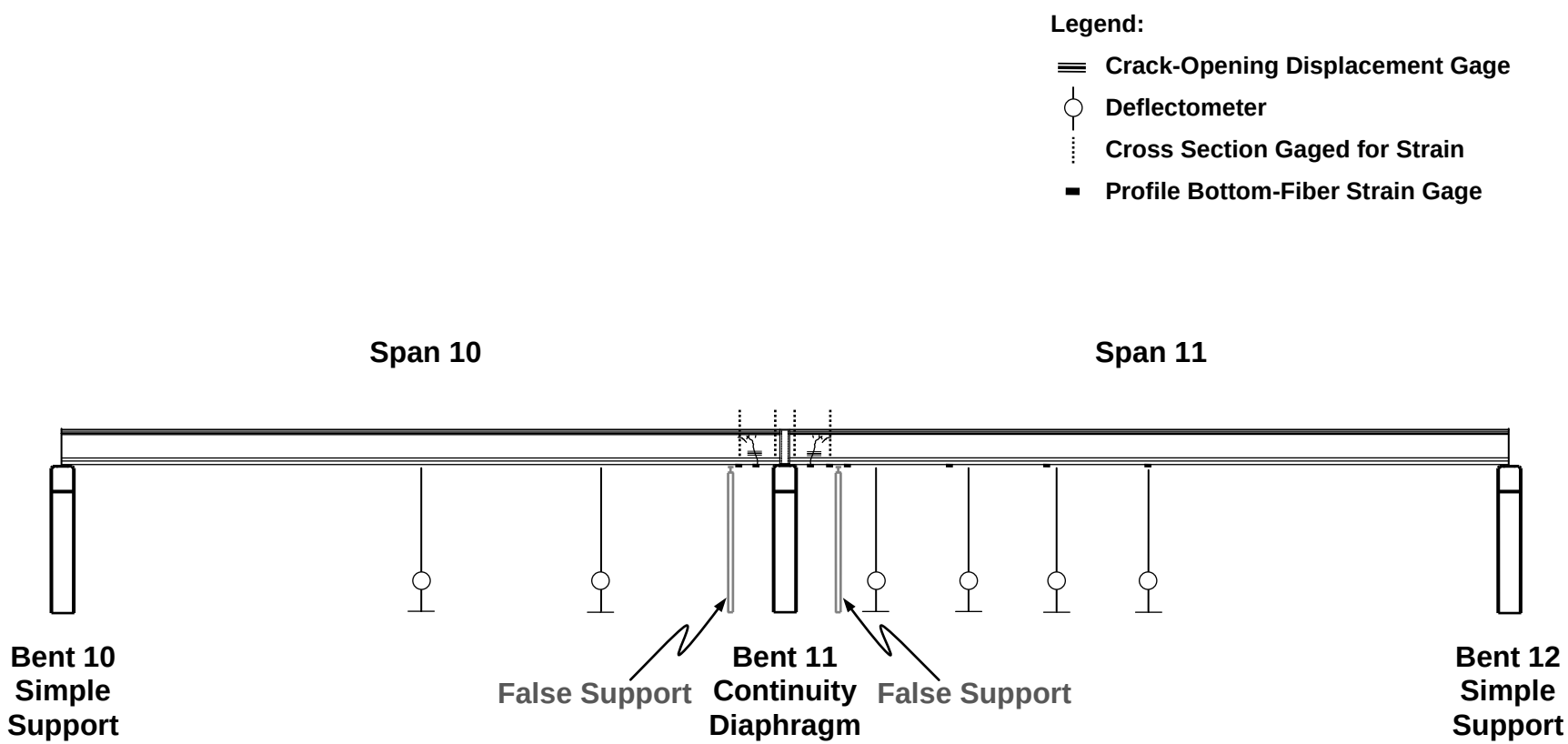

Figure 3.1: Instrumentation overview

A data acquisition system was used to collect sensor measurements during testing. The data acquisition system had seventy-two 350-ohm channels available. The COD gages were full-bridge sensors, and the deflectometers and strain gages were quarter-bridge sensors. Four-wire configurations were used for the full-bridge sensors. Three-wire configurations were used with the quarter-bridge sensors to reduce lead-wire temperature effects (Fason 2009).

3.3 CRACK-OPENING DISPLACEMENT GAGES

Crack-opening displacement (COD) gages were installed to measure the opening or closing deformations of one crack per instrumented girder. Each COD gage was attached to anchor blocks that were installed on either side of the crack using an epoxy. The type of COD gage selected for testing is capable of measuring crack openings or closures of up to 2 mm (0.08 in.). The COD gages are full-bridge instruments that were calibrated prior to testing. A diagram of the specific model of COD gage used for the pre- and post-repair tests can be seen in Figure 3.2.

PI-2-50

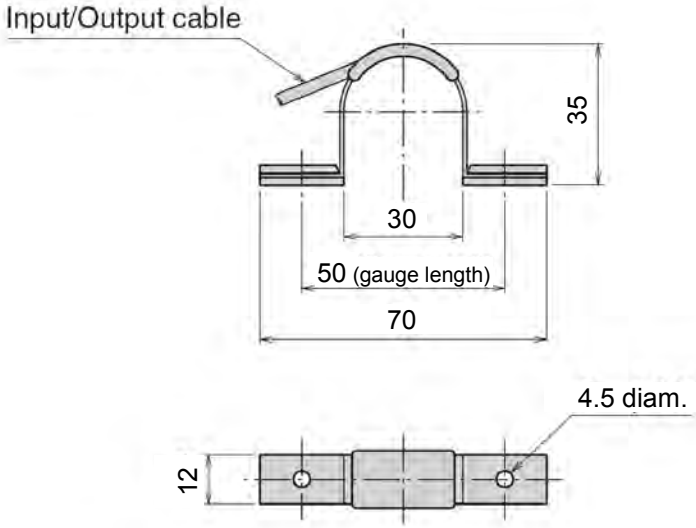

Note: dimensions are shown as mm

Figure 3.2: Crack-opening displacement gage (TML 2011)

3.3.1 COD Gage Locations

Four crack-opening displacement gages (A–D) were installed prior to the pre-repair load tests. The specific COD gage locations can be seen in Table 3.1. Each COD gage was installed to span a significant crack in a girder web near the girder's continuous end. The anchor blocks for each COD gage location were installed three inches above the joint of the bottom-flange and the web. The COD gage installed on Girder 8 of Span 10 was located on the west face of the girder. The other COD gages were located on the east face of their respective girders.

Each COD gage was installed in the same respective location for pre- and post-repair testing. During analysis each gage was referenced according to installed location rather than COD ID.

Table 3.1: COD gage locations

Span	Girder	Distance from Continuity Diaphragm Centerline (in.)	Girder Face (east/west)	COD ID (A–D)
10	7	50	east	C
	8	40	west	A
11	7	48	east	D
	8	56	east	B

3.3.2 COD Gage Installation

Prior to pre-repair testing, two anchor blocks were attached to the surface of each instrumented girder using a 5-minute epoxy. A photo of installed anchor blocks can be seen in Figure 3.3.

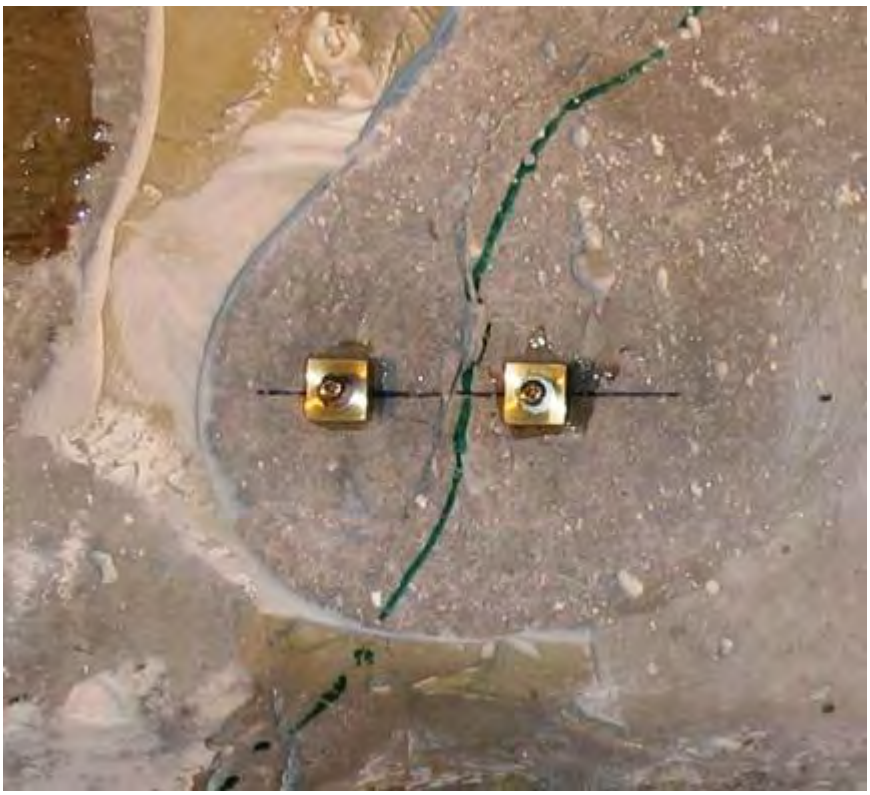

Figure 3.3: Anchor blocks for COD gage installation (Fason 2009)

To provide consistent initial distances between anchor blocks, a reference bar was mechanically attached with screws to the anchor blocks prior to installation. The reference bar had a distance of 50.0 mm (1.97 in.) between mechanical attachment points. The anchor blocks were then attached to the concrete girder surface using the 5-minute epoxy. After the epoxy set, the reference bar was removed and a COD gage was mechanically attached to the anchor blocks (Fason 2009).

Following the conclusion of pre-repair testing, the COD gages were detached from their respective anchor blocks and safely stored until reinstalled for post-repair testing. The only COD gage installation required prior to the post-repair tests was the mechanical attachment of the COD gages to their respective anchor blocks that remained installed after pre-repair testing. Each COD gage was located in the same respective location and was connected to the data acquisition system using the same respective 4-wire cable from the pre-repair tests. A photo of a COD gage attached to anchor blocks can be seen in Figure 3.4.

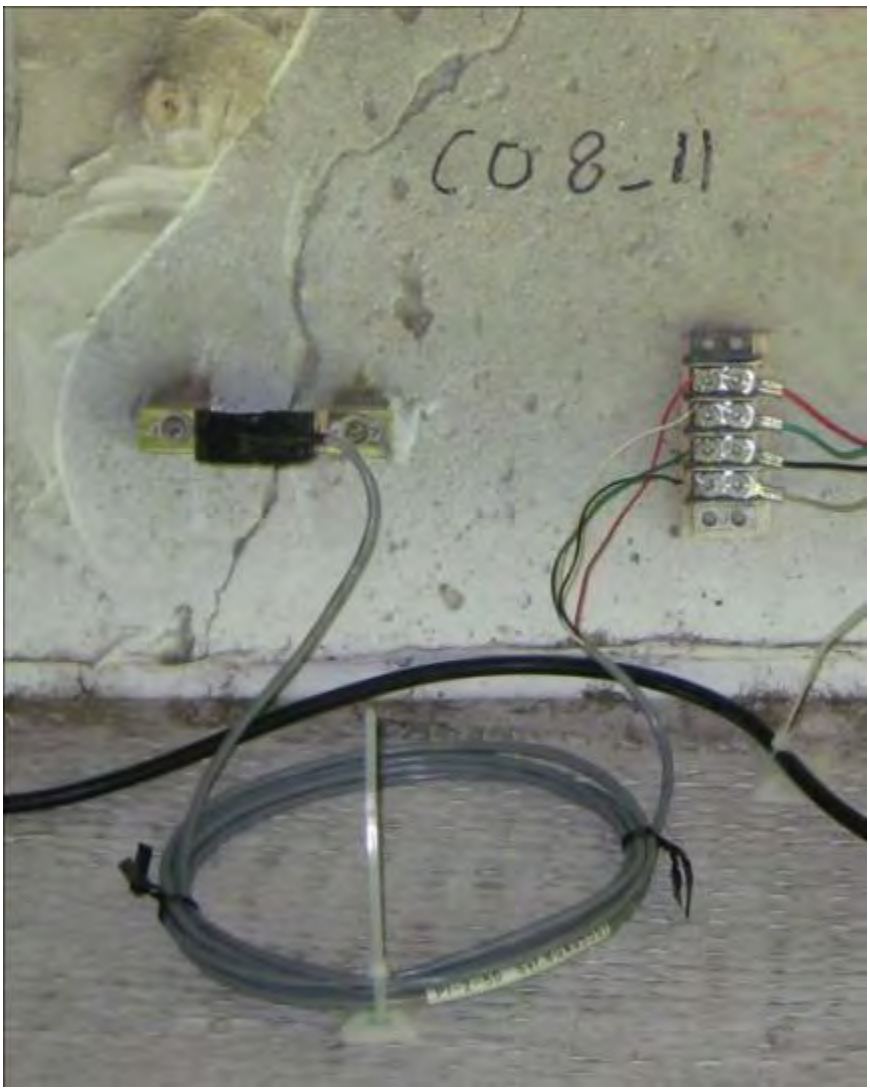

Figure 3.4: COD gage attached to anchor blocks

3.4 DEFLECTOMETERS

Deflectometers were used to measure bottom-fiber girder deflections, due to different load conditions, at specific points along each instrumented girder. A picture of a typical deflectometer used during bridge testing can be seen in Figure 3.5.

Figure 3.5: Typical deflectometer

Each deflectometer was positioned under the bridge girder at the ground level and connected to the underside of the bridge girder using a wire. The wire length was adjusted to ensure the aluminum bar of the deflectometer remains bent with the bottom of the bar in tension throughout the bridge testing. As the bridge girder deflected downward or upward at the deflectometer location, the flexural tension in the cantilevered aluminum bar was relieved or amplified respectively. A single quarter-bridge surface-mounted strain gage on the underside of the aluminum bar was used to measure the flexural strain. A decrease in tension resulted in a negative strain that represents a downward deflection in the bridge and an increase in tension resulted in a positive strain that represents an upward deflection. As long as the aluminum bar is not bent past its proportional limit, there is a linear relationship between the strain and deflection. The strain-to-deflection conversion factors for all deflectometers were calibrated before and after testing.

3.4.1 Deflectometer Locations

Twelve deflectometers were installed at the same respective locations for pre- and post-repair testing. The deflectometer positions along each girder line are illustrated in Figures 3.6 and 3.7. The specific deflectometer locations for the bridge testing are presented in Table 3.2.

Six deflectometers were assigned to each girder line. Along each girder line, two deflectometers were installed under Span 10, and four deflectometers were installed under Span 11 at the locations shown in Figures 3.6 and 3.7.

The individual deflectometers have identification labels A–L. However, the notation used to distinguish between deflectometer locations during analysis and reporting consists of the girder (7 or 8), span (10 or 11), and girder line location (A–F).

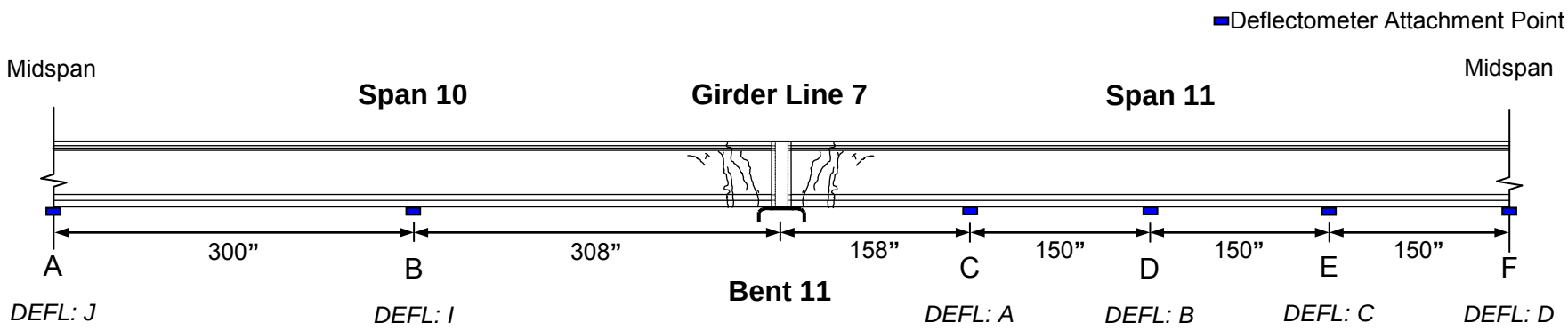

Figure 3.6: Deflectometer locations—Girder Line 7

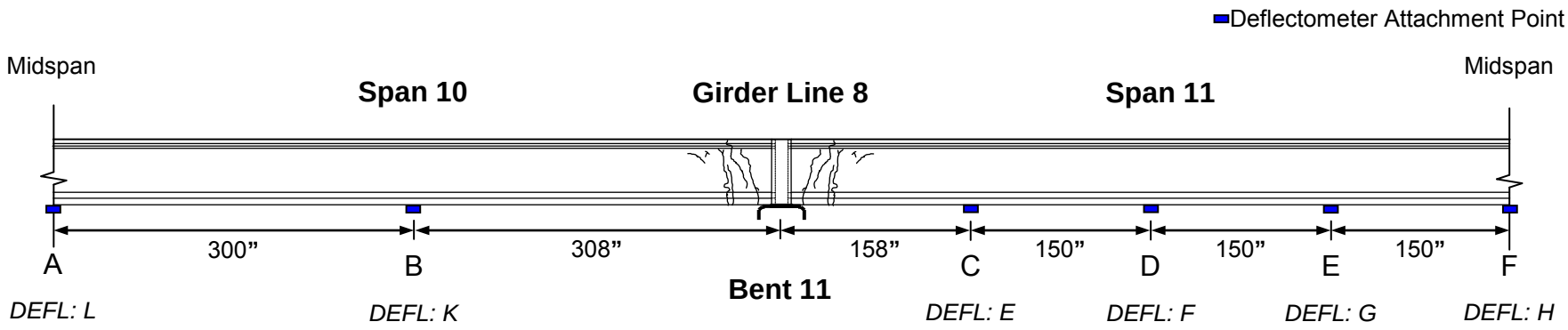

Figure 3.7: Deflectometer locations—Girder Line 8

Table 3.2: Deflectometer locations

Span	Girder	Distance from Continuity Diaphragm Centerline (in.)	Girder Line Location (A–F)	DEFL ID (A–L)
10	7	608	A	J
		308	B	I
	8	608	A	L
		308	B	K
11	7	158	C	A
		308	D	B
		458	E	C
		608	F	D
	8	158	C	E
		308	D	F
		458	E	G
		608	F	H

3.4.2 Deflectometer Installation

Deflectometers were constructed and installed prior to the pre-repair tests in 2005. Information regarding the construction and installation of deflectometers prior to the pre-repair tests has been reported by Fason (2009). Each deflectometer was installed in the same location for both pre- and post-repair testing. Each deflectometer used the same 4-wire cable to connect to the data acquisition system for both pre- and post-repair testing.

Prior to the pre-repair tests, deflectometer attachment points were installed to the underside of the bottom-flange at the desired locations along each instrumented girder. A picture of a typical attachment point is shown in Figure 3.8.

Figure 3.8: Girder attachment point for deflectometer wire

The attachment points consist of an epoxy-mounted bracket of two metal plates connected with two metal bars. Metal wire was used to connect each attachment point to its respective deflectometer on the ground directly beneath the attachment point. For the pre-repair tests, the metal wires were tied directly to the attachment points. For the post-repair tests, metal S-hooks were used to connect the metal wires to their respective attachment points, allowing for easier wire installation and detachment.

A turnbuckle was attached to each wire at the ground level to allow for wire length adjustment while pre-bending each deflectometer aluminum bar. Each turnbuckle was attached to an eye-hook at the end of the corresponding deflectometer aluminum bar. Some of the turnbuckles used during the post-repair tests required an additional s-hook to connect to the of the aluminum bar. Each turnbuckle was adjusted until the vertical distance between the tip of the pre-bent aluminum bar and the base of the deflectometer was roughly 4 inches. A picture of an adjusted turnbuckle and pre-bent aluminum bar can be seen in Figure 3.9.

Figure 3.9: Deflectometer aluminum bar—pre-bent with adjusted turnbuckle

Plywood boards were used to level and stabilize each deflectometer as much as possible. Each deflectometer was then connected to the data acquisition system using the same 4-wire cable from the pre-repair tests. Since the deflectometers were at the ground level throughout the testing, it was important to deter accidental human interference. All deflectometer wires were marked with flagging at eye level, and the deflectometer areas under Spans 10 and 11 were marked with a perimeter of flagging. Movement through the deflectometer areas was avoided as much as possible. A photo of the deflectometer area under Span 11 is shown in Figure 3.10.

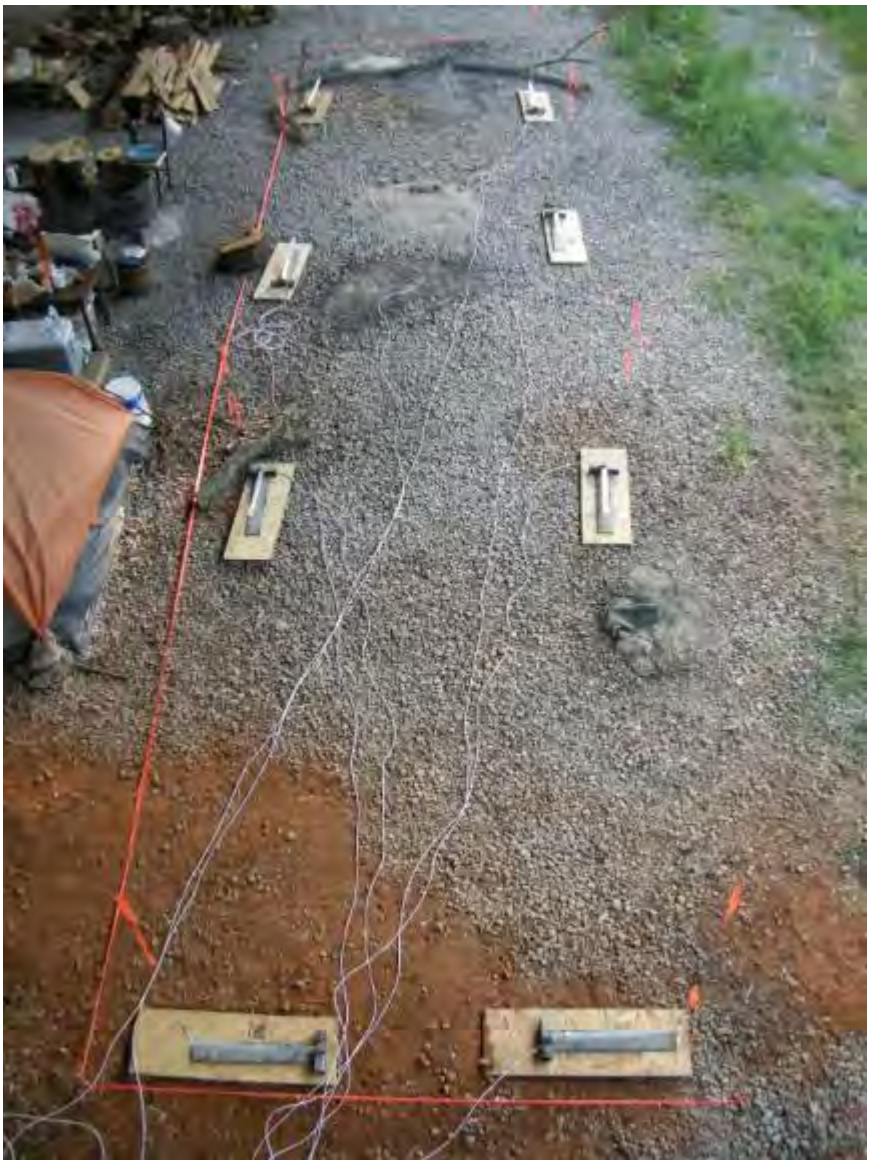

Figure 3.10: Deflectometer area—Span 11

3.5 STRAIN GAGES

Surface-mounted strain gages were installed to monitor material strains in response to different loading conditions. Electrical-resistance strain gages were mounted directly to structural material including concrete and FRP reinforcement at different locations along each instrumented girder. The majority of the strain gages were installed near the continuity diaphragm to allow for better analysis of the bridge behavior near the support. Prior to the pre-repair tests, strain gages were installed on the concrete at specified locations. Prior to the post-repair tests, strain gages were installed on the FRP reinforcement at specified locations. The FRP reinforcement strain gages allowed for analysis of the forces carried by the FRP reinforcement due to specific loading

conditions, and the analysis of the transfer of stresses from the concrete to the FRP reinforcement. The gage locations, gage types, and installation procedures for the surface-mounted strain gages are discussed in Sections 3.5.1–3.5.4.

3.5.1 Strain Gage Locations

Fifty-six surface-mounted strain gages were installed for bridge testing. An illustration of the strain gage cross section locations along one girder line can be seen in Figure 3.11. The specific locations of the strain gage cross sections and the amount of gages in each cross section are provided in Table 3.3. Illustrations of the post-repair strain gage locations within each cross section can be seen in Figures 3.12–3.22. The potential gage locations within a cross section are detailed in Table 3.4.

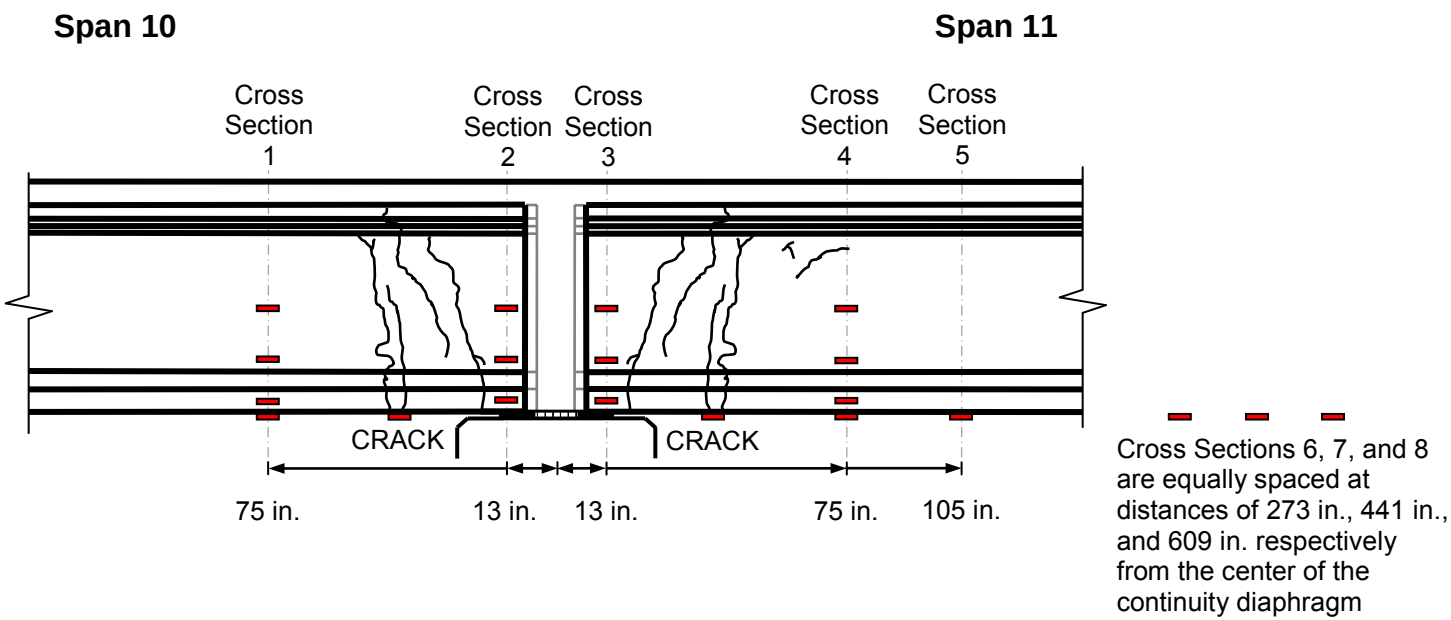

Notes: Dimensions shown are from the centerline of the continuity diaphragm. Cracks shown are meant only to illustrate the typical crack zone and do not represent actual crack locations.

Figure 3.11: Strain gage cross section locations

Table 3.3: Strain-gaged cross sections

Span	Girder	Cross Section	Distance from Continuity Diaphragm Centerline (in.)	No. of Concrete Strain Gages	No. of FRP Strain Gages	Total Gages
10	7	1	75	4	1	5
		CRACK	47	–	1	1
		2	13	4	1	5
	8	1	75	4	2	6
		CRACK	41	–	1	1
		2	13	3	2	5
11	7	3	13	5	0	5
		CRACK	47	–	1	1
		4	75	4	1	5
		5	105	1	1	2
		6	273	1	–	1
		7	441	1	–	1
		8	609	1	–	1
	8	3	13	3	2	5
		CRACK	52	–	1	1
		4	75	4	2	6
		5	105	1	1	2
		6	273	1	–	1
		7	441	1	–	1
		8	609	1	–	1
			Total Gages	**39**	**17**	**56**

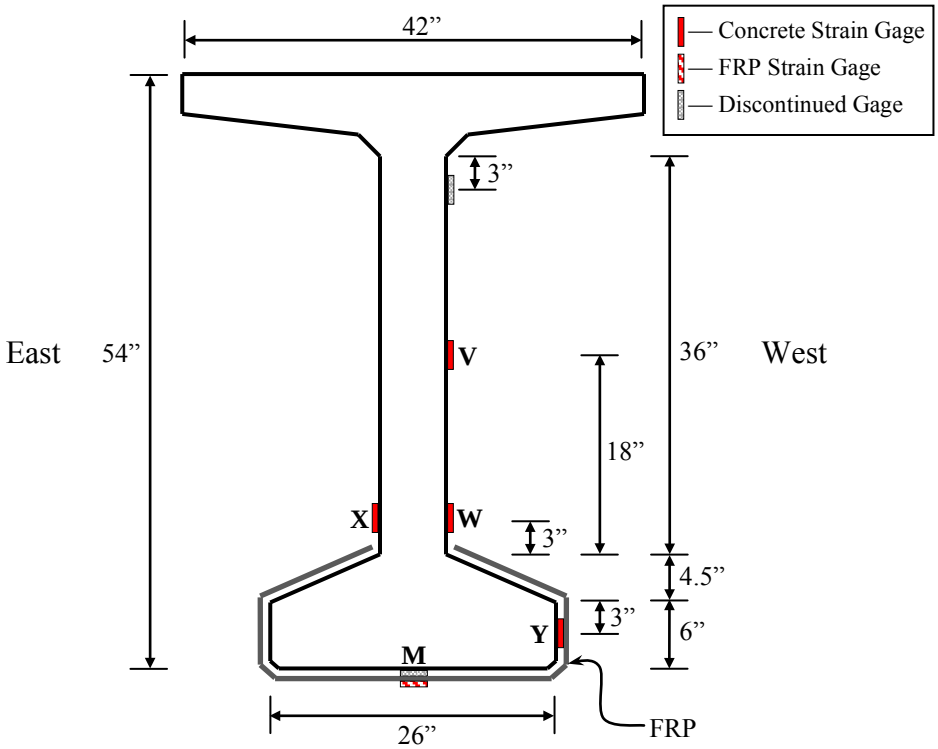

Figure 3.12: Strain gage locations—Girder 7—Section 1

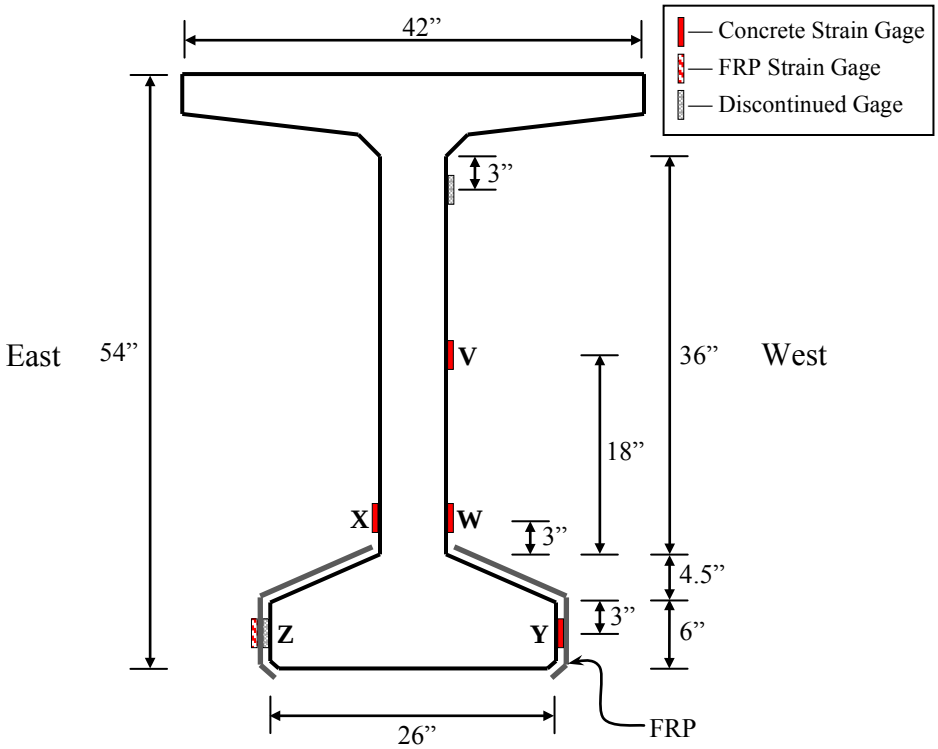

Figure 3.13: Strain gage locations—Girder 7—Section 2

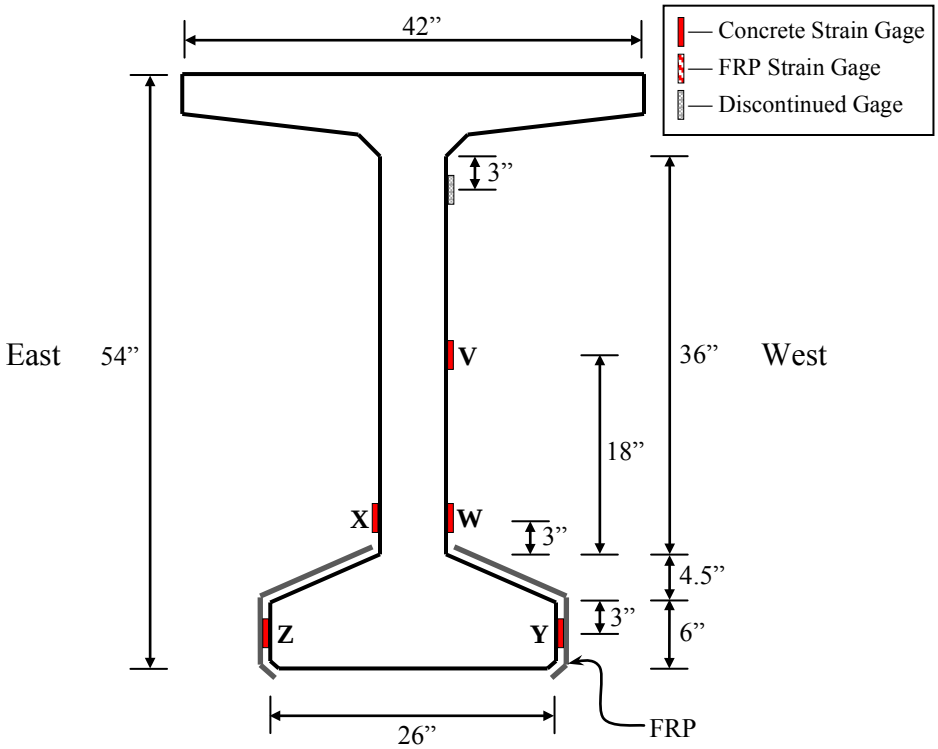

Figure 3.14: Strain gage locations—Girder 7—Section 3

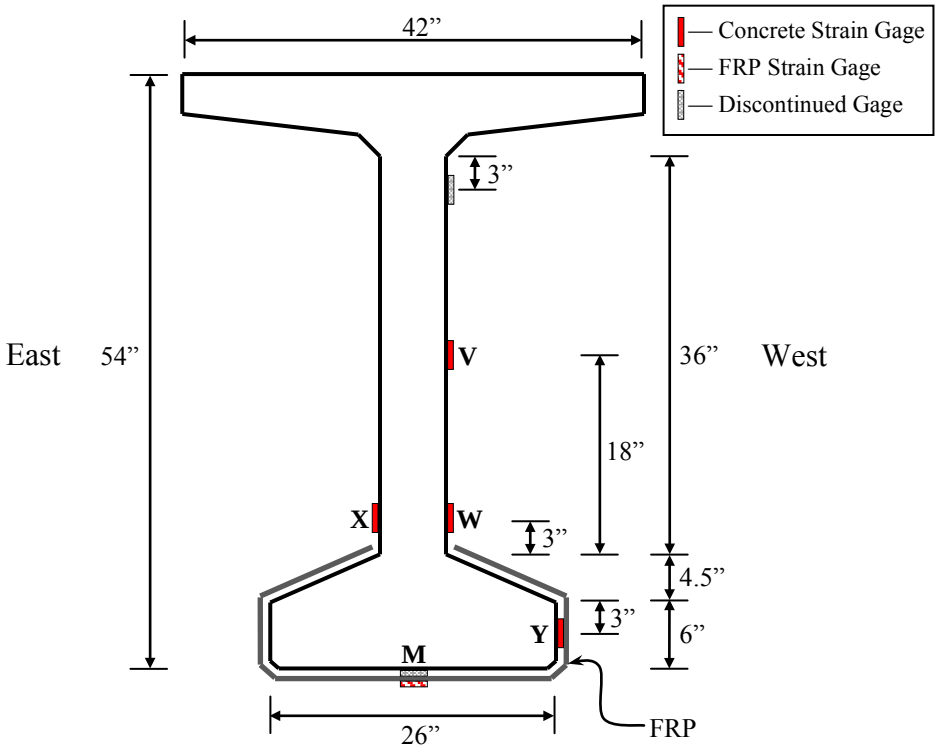

Figure 3.15: Strain gage locations—Girder 7—Section 4

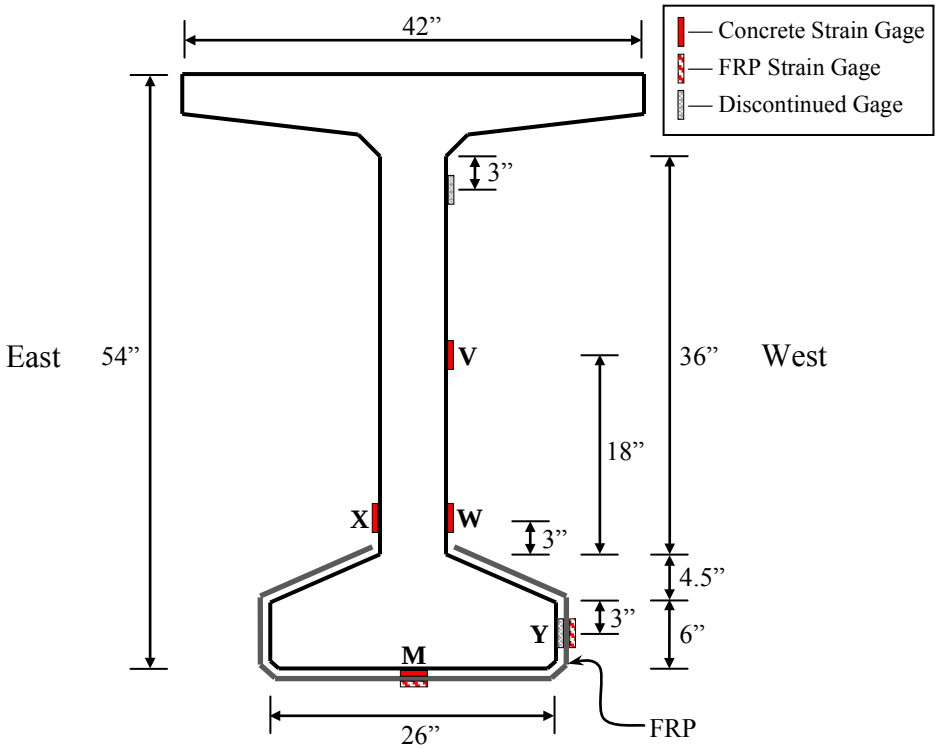

Figure 3.16: Strain gage locations—Girder 8—Section 1

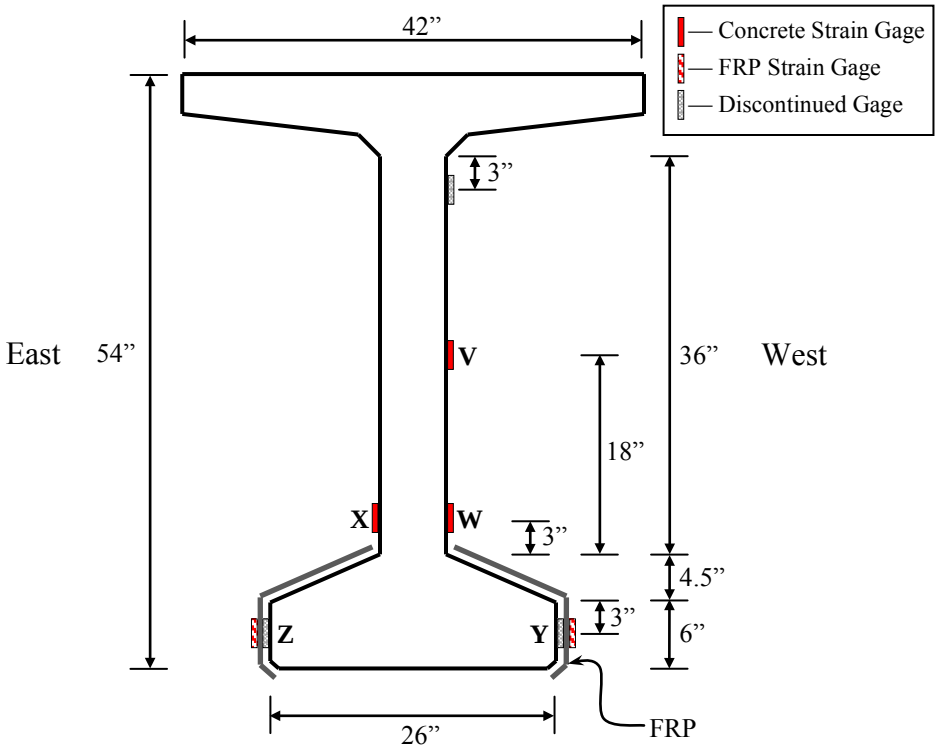

Figure 3.17: Strain gage locations—Girder 8—Section 2

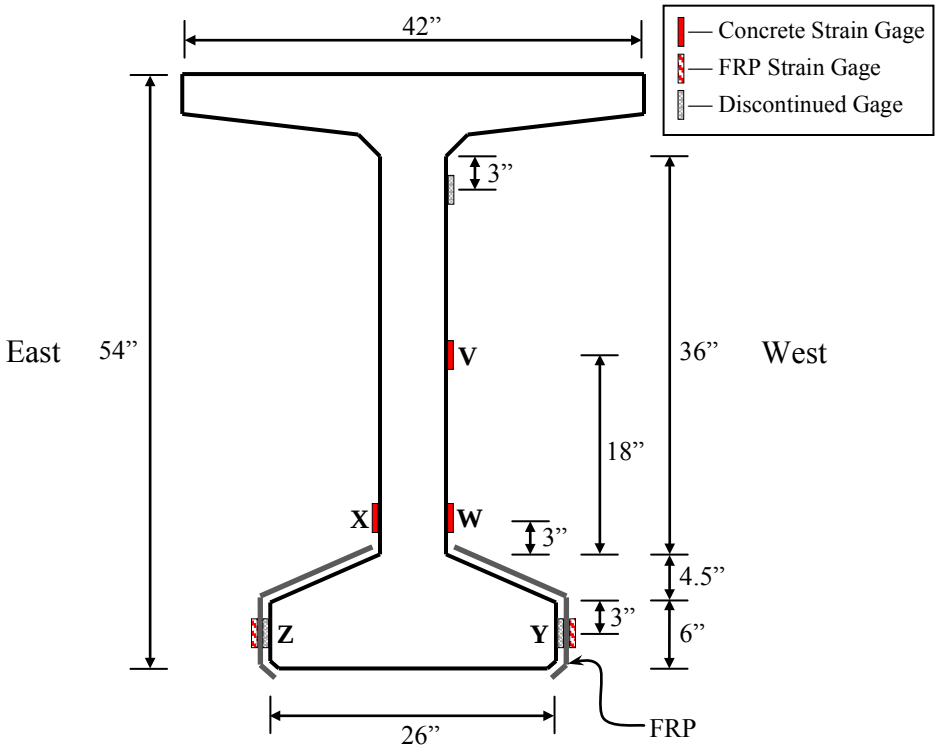

Figure 3.18: Strain gage locations—Girder 8—Section 3

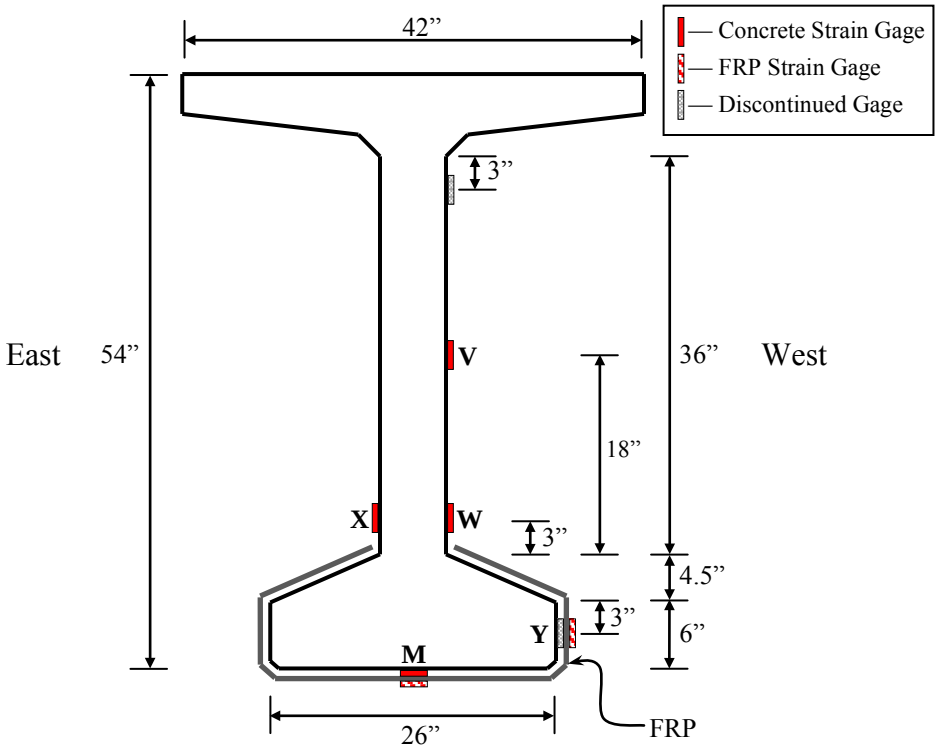

Figure 3.19: Strain gage locations—Girder 8—Section 4

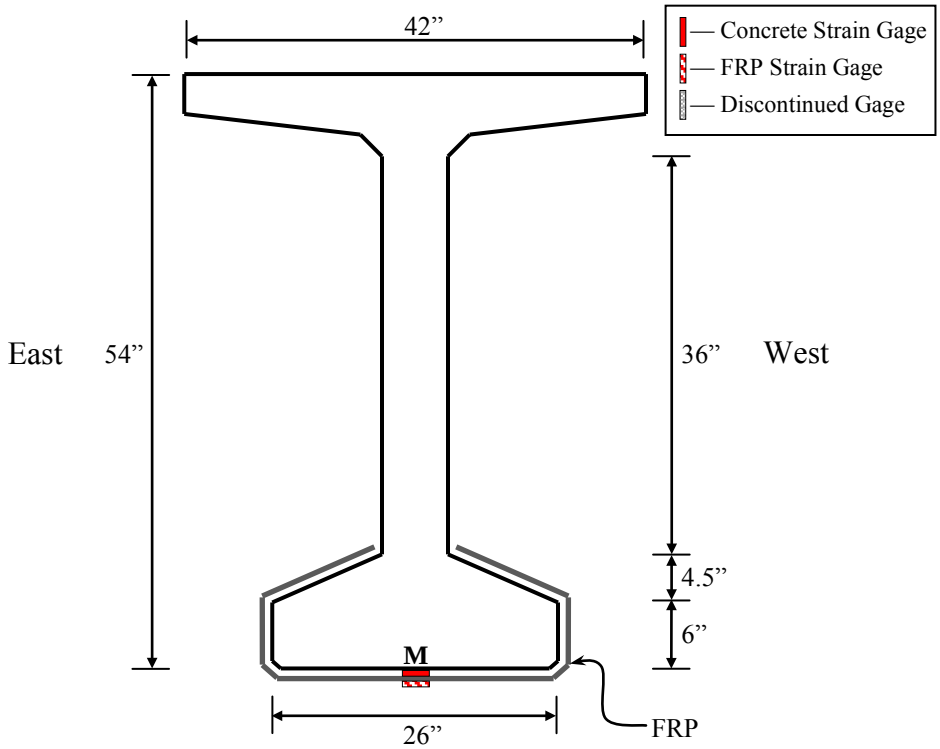

Figure 3.20: Strain gage locations—Girders 7 and 8—Section 5

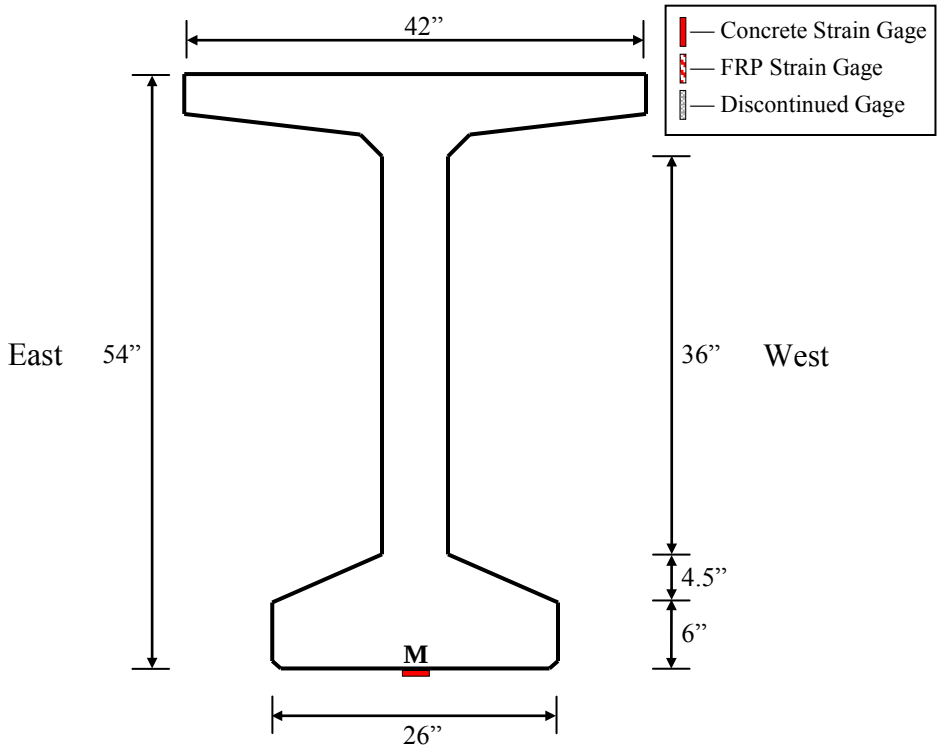

Figure 3.21: Strain gage locations—Girders 7 and 8—Sections 6, 7, and 8

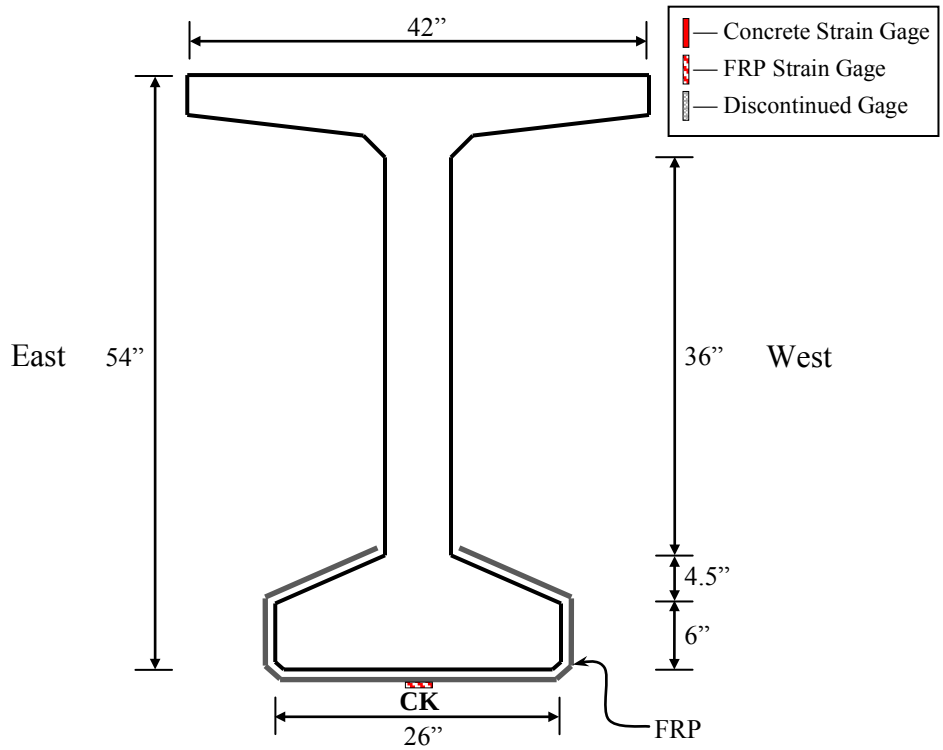

Figure 3.22: Strain gage locations—CRACK

Table 3.4: Strain gage locations within cross section

Location Notation	Distance from Bottom of Bottom-Flange (in.)	Location Description	Girder Face
F	43.5	Top of Web	West
V	28.5	Middle of Web	West
W	13.5	Bottom of Web	West
X	13.5	Bottom of Web	East
Y	3	Side of Bottom Flange	West
Z	3	Side of Bottom Flange	East
M	0	Bottom of Bottom Flange	Bottom
CK	0	Bottom of Bottom Flange	Bottom

Note: The gage location at the top of the web (Location F) was discontinued for post-repair testing

Strain gage instrumentation was concentrated in the end regions of Girders 7 and 8 near the continuity diaphragm between Spans 10 and 11. Strain gages were installed at various girder heights at two main cross sections on each instrumented girder. One cross section in each girder is located near the face of the continuity diaphragm, while the other cross section is located just beyond the cracked region. The two girders in Span 11 also contain strain gages along the bottom of the girders at different locations out to midspan. The strain gages at the end region cross sections allow for the analysis of localized behaviors around the cracked regions of each girder. The strain gages along the bottom of each girder allow for analysis of overall girder behavior.

3.5.1.1 Cross Section Locations

There are a total of ten cross sections on each girder line that contain strain gages. Span 10 girders contain three strain-gaged cross sections. Two cross sections in Span 10 are instrumented for strain profile analysis, and one cross section consists of an FRP strain gage on the bottom of the girder at the primary crack location. The two Span 10 cross sections instrumented for strain profile analysis are located at distances of 75 in. (Cross Section 1) and 13 in. (Cross Section 2) from the center of the continuity diaphragm. The gages at these cross sections are installed at different heights on both faces of the girder. The cross section containing an FRP strain gage at the primary crack location is located between Cross Section 1 and Cross Section 2 for both girders. The crack section FRP strain gages are located at distances of 47 in. and 41 in. from the continuity diaphragm on Girders 7 and 8 respectively.

The Span 11 girders contain seven strain-gaged cross sections. Two cross sections in Span 11 are instrumented for strain profile analysis, and five cross sections contain strain gages located on the bottom of the girder. One of the cross sections with a bottom-fiber strain gage is located at the primary crack location on each girder. The other four cross sections with bottom-fiber strain gages are equally spaced out to midspan from just beyond the false support. The two Span 11 cross sections instrumented for strain profile analysis are located at distances of 13 in. (Cross Section 3) and 75 in. (Cross Section 4) from the center of the continuity diaphragm. The gages at these cross sections are installed at different heights on both faces of the girder. The cross section containing an FRP strain gage at the primary crack location is located between Cross Section 3 and Cross Section 4 for both girders. The crack section FRP strain gages are located at distances of 47 in. and 52 in. from the continuity diaphragm on Girders 7 and 8 respectively. The first of the four equally spaced bottom-fiber strain gages is located at a distance of 105 in. (Cross Section 5) from the center of the continuity diaphragm. The other three locations are then equally spaced out to midspan at distances of 273 in. (Cross Section 6), 441 in. (Cross Section 7), and 609 in. (Cross Section 7) from the center of the continuity diaphragm. Cross Section 5 contains two strain gages, a concrete strain gage and an FRP strain

gage at the same overlaying location. Cross Sections 6, 7, and 8 only contain one concrete strain gage each on the bottom of the girder.

There were some inconsistencies concerning the pre-repair strain gage cross section locations that resulted in a slightly different installation location for the post-repair FRP strain gages considered to be a companion with a previously installed concrete strain gage. The concrete strain gages average the surface strain measured over their entire length (2.4 in. [60 mm]), but were installed placing one edge of the gage at the reported cross section location from the face of the continuity diaphragm. The FRP strain gages (1/4 in. [6 mm]) were installed with the center of the gage at the previously reported cross section location. This resulted in the location of the average measured strain for concrete gages to be roughly 1 in. (25 mm) different compared to the location of the average measured strain of FRP strain gages at the same cross section. For the purpose of gage notation, concrete strain gages and FRP strain gages are still considered to be in the same cross sections, but the locations of the average strain for each gage are reported when tabulating and graphically illustrating results.

3.5.1.2 Gage Locations within A Typical Cross Section

For each gaged cross section, there are seven different potential gage locations. The gage locations are as follows: top of the web at 3 in. below the joint of the top flange and web on the west face (discontinued for post-repair tests), middle of the web at 18 in. above the joint of the bottom-flange and web on the west face (Location V), bottom of web at 3 in. above the joint of the bottom-flange and web on the west face (W) and east face (X), side of bottom flange at 3 in. below the top edge of the side of the bottom flange on the west face (Y) and east face (Z), and center of the underside of the bottom flange at 13 in. from the side of the bottom flange (M or CK). Concrete surface strain gages were installed at the following locations: V, W, X, Y, Z, and M. After applying the FRP reinforcement, FRP surface strain gages were installed at the following locations: Y, Z, M, and CK.

3.5.1.3 Discontinued, Additional, and Replacement Gages

Every available channel of the data acquisition system was employed during the pre-repair tests. In order to install and record strain gages at desired locations on the FRP, it was necessary to discontinue some concrete strain gages from the pre-repair tests. For the pre-repair tests, there was a concrete strain gage installed 3 in. below the joint of the web and top flange at Cross Sections 1–4 on both girder lines. After analysis of the pre-repair results, it was recommended to discontinue the eight concrete strain gages located near the top of the web of Cross Sections 1–4 on both girder lines, and to replace them with FRP strain gages at bottom-fiber locations of Cross Sections 4 and 5 on both girder lines and at the main crack location of each instrumented girder (Shapiro 2007).

Some of the concrete strain gages from the pre-repair tests that were at desirable girder height locations were unfortunately no longer functioning at the time of the post-repair tests. Concrete strain gages were installed at the same girder height location to replace nonfunctioning concrete strain gages that were accessible, but other nonfunctioning concrete strain gages had been covered by the FRP reinforcement and had to be discontinued for the post-repair tests. Where nonfunctioning concrete strain gages covered by the FRP reinforcement were discontinued, FRP strain gages were installed at the same location for the post-repair tests and assigned the same channel and 3-wire cable assigned to the respective pre-repair concrete strain gage. Two nonfunctioning concrete strain gages were accessible and replaced with another concrete strain gage. Nine nonfunctioning concrete strain gages were inaccessible and replaced with FRP strain gages.

3.5.2 Concrete Strain Gages

Prior to pre-repair testing, strain gages were installed on the concrete surface of girders. Prior to post-repair testing, strain gages were only installed on the concrete surface to replace a previously installed strain gage that was no longer functioning properly. Strain gages installed on a concrete surface must have a greater gage length than strain gages on other material surfaces due to the heterogeneous properties of concrete. Longer gage lengths allow for an averaging effect that includes strains in the aggregate and the surrounding mortar. It is suggested that strain gages installed on concrete surfaces should be several times longer than the largest coarse aggregate material used during production of the concrete (Vishay 2010). The strain gages installed on the concrete surfaces prior to the pre-repair tests were 60 mm (2.4 in.) quarter-bridge gages with a resistance of 350 Ω (MFLA-60•350-1L). A photo of an installed concrete surface strain gage before the application of weather protection can be seen in Figure 3.23.

Figure 3.23: Surface-mounted strain gage—concrete (Fason 2009)

3.5.3 FRP Strain Gages

Strain gages were installed on the FRP reinforcement to correspond with previously installed concrete gages or previously noted concrete crack locations. The gages located on the FRP reinforcement did not require as long of a gage length as the concrete surface strain gages, because the FRP strain gages average strains along fibers of similar material composition. The strain gages installed on the FRP reinforcement were 6 mm (1/4 in.) quarter-bridge gages with a resistance of 350 Ω (FLA-6-350-11-1LT). A photo of an installed FRP reinforcement strain gage before the application of weather protection can be seen in Figure 3.24.

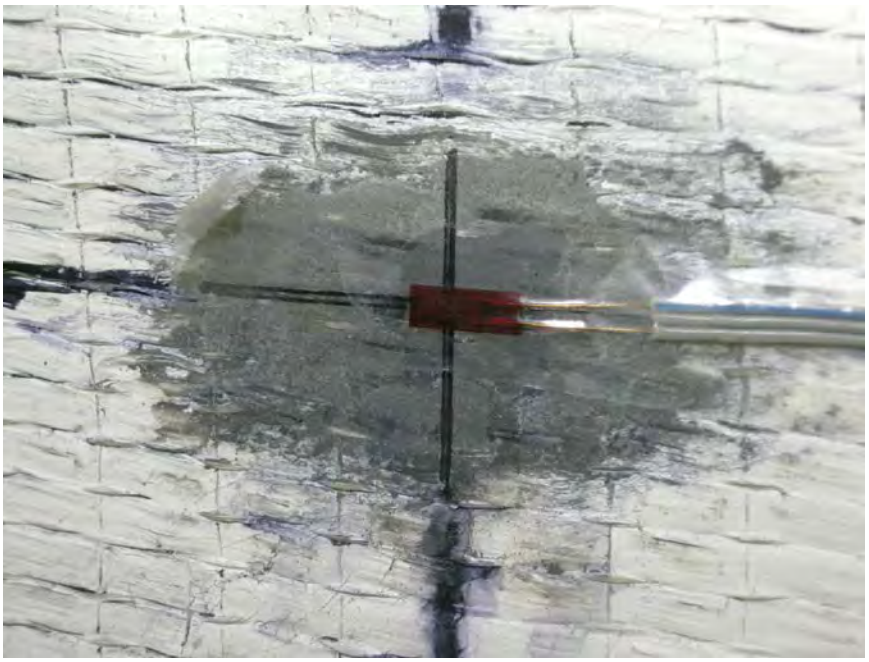

Figure 3.24: Surface-mounted strain gage—FRP reinforcement

3.5.4 Strain Gage Installation

The concrete strain gages were installed prior to the pre-repair tests using the installation procedure noted by Fason (2009). Any nonfunctioning concrete gages were replaced with new concrete gages prior to the post-repair tests in accordance with the same procedure.

FRP reinforcement strain gages were installed using a modified procedure suited for the composite material. The strain gage installation procedure for the FRP reinforcement consisted of five main processes: initial surface preparation, smoothing the gaging surface with solids-epoxy, surface preparation for gage application, gage installation, and gage protection. The main difference between the strain gage installation procedures for concrete and FRP reinforcement is the surface preparation required for each material. Also, due to the fact that an FRP strain gage was one-tenth the length of a concrete strain gage, it was possible to use a quick-setting gaging epoxy. A step-by-step strain gage installation procedure for the FRP composite material is presented in Appendix M. Pictures illustrating portions of the FRP strain gage installation procedure can be seen in Figures 3.25–3.34.

Initial surface preparation required the removal of paint, excess epoxy remaining from the FRP installation, and other irregularities on the FRP surface. After initial location of the gaging area, degreaser was applied to the area to initiate the surface preparation. A wire brush, an electric grinder, sand-paper, and compressed air were used to assist with initial surface

preparation. Photographs of initial surface preparation procedures are shown in Figures 3.25–3.28.

Figure 3.25: Strain gage installation—applying degreaser to gage location

Figure 3.26: Strain gage installation—removal of surface irregularities

Figure 3.27: Strain gage installation—initial surface cleaning

Figure 3.28: Strain gage installation—clean surface prepared for solid epoxy

The FRP reinforcement is composed of woven fibers, creating an uneven surface which is not ideal for strain gage application. The exposed FRP fibers were further cleaned using isopropyl alcohol and gauze. After cleaning the FRP surface, a solids-epoxy mixture (PC-7) was applied to level the surface. The epoxy was not meant to completely cover the FRP and was only

applied to fill small voids near the final gage location. Photographs of surface leveling are shown in Figures 3.29 and 3.30.

Figure 3.29: Strain gage installation—application of solid epoxy

Figure 3.30: Strain gage installation—epoxy surface

The gage location was cleaned again after the solids-epoxy mixture was allowed to cure. Sand-paper and isopropyl alcohol were used to clean the gage location with added solids-epoxy. Following another surface cleaning, the gage location was treated with a cleaning agent (Vishay M-Prep A–Conditioner) and neutralizer (Vishay M-Prep 5A–Neutralizer). After thoroughly cleaning the surface, a heat gun was used to dry the gage location. Once the surface was clean and dry, it was prepared for gage installation.

The gage application procedures are very similar for the FRP and concrete strain gages. Due to their shorter gage length, the FRP strain gages were easier to install than concrete strain gages. A clean acrylic plate was used to apply a strip of tape to the back of each gage. The tape was smoothly applied to the gage without creating any air bubbles. The gage and tape were then carefully removed from the acrylic plate and taped in position at the gage location. Once in position, the gage and tape were carefully peeled back from the gaging surface to reveal the underside of the strain gage. A catalyst (Vishay 200 Catalyst-C) was then applied to the underside of the strain gage in one stroke, and allowed to dry. A small amount of gaging epoxy (Vishay M-Bond 200) was then applied just behind the gage location towards the peeled-back gage and tape. The peeled-back gage and tape were then applied to the gage location. While applying the gage and tape, a thin layer of gaging epoxy was spread under the gage and tape for the entire length of the gage location. Pressure was applied to the gage and tape for at least one minute, allowing the gaging epoxy to set. After removing pressure and waiting a few more minutes, the tape was very carefully removed from the back of the gage. Photographs of an installed FRP strain gage are shown in Figures 3.31 and 3.32.

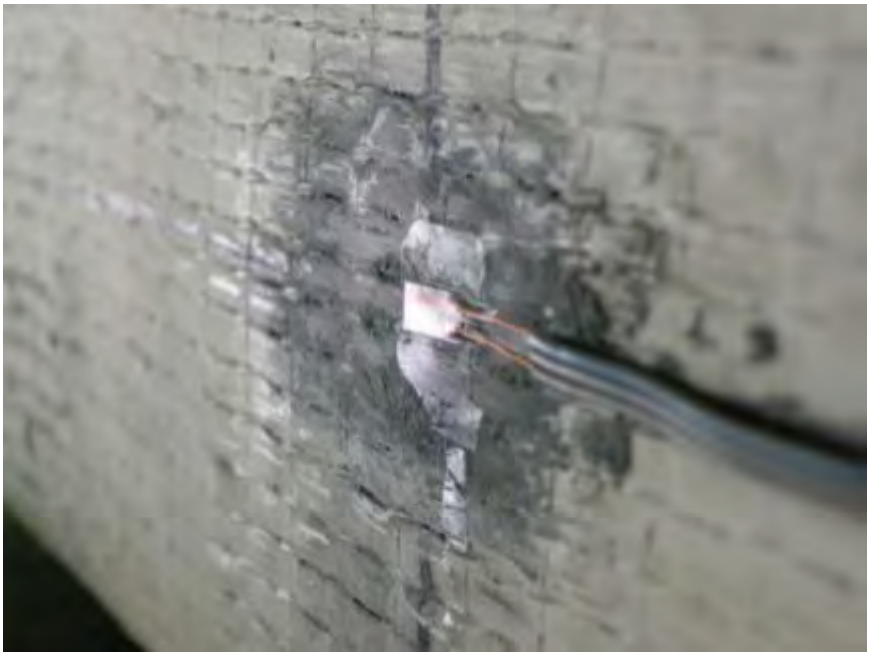

Figure 3.31: Strain gage installation—gage application with thin epoxy

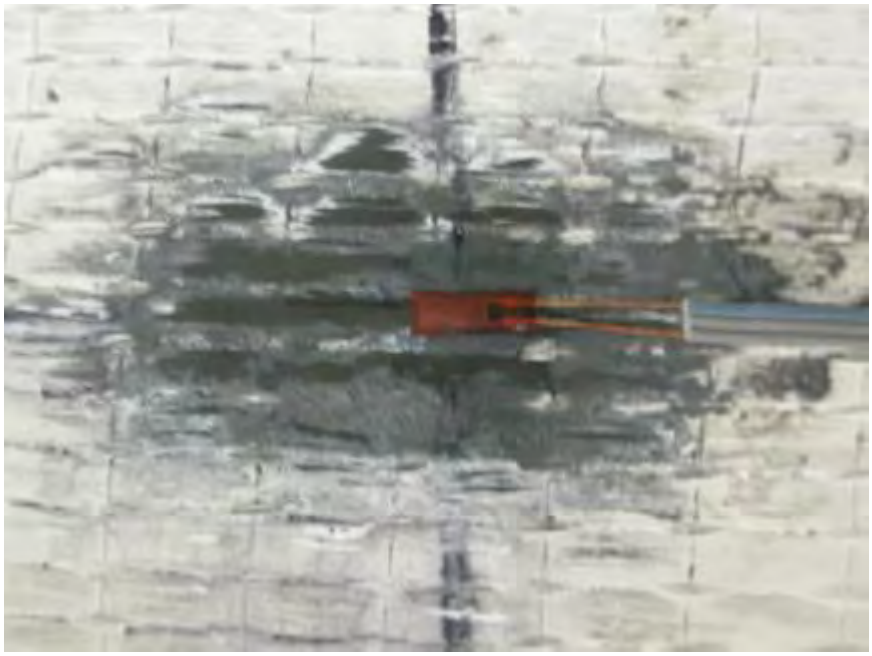

Figure 3.32: Strain gage installation—gage applied to FRP reinforcement

Following the application of each gage, moisture and mechanical protection was applied in order to increase the durability of the gage. A liquid rubber coating was applied to the gage and surrounding surface to act as moisture protection. After the rubber coating dried, a strip of mastic tape was applied to provide mechanical protection. The mastic tape strip was long enough to provide some support for the pre-attached lead wires extending from the gage to a terminal strip mounted on the girder, adding protection against the wires detaching from the gage due to unexpected tension. Photographs of an FRP strain gage with installed protection are shown in Figures 3.33 and 3.34.

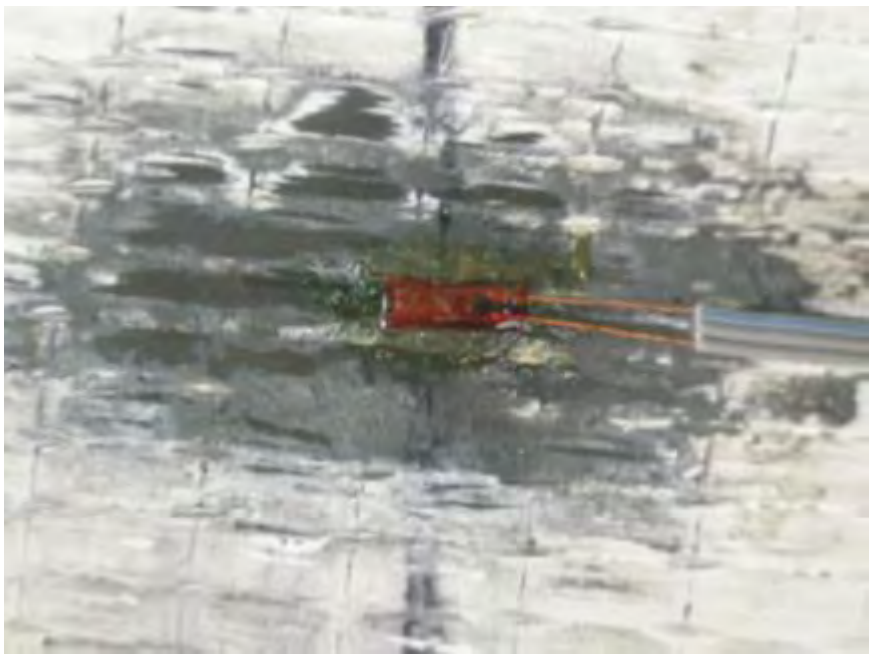

Figure 3.33: Strain gage installation—rubber coating for moisture protection

Figure 3.34: Strain gage installation—mastic tape for mechanical protection

3.6 DATA ACQUISITION SYSTEM

A total of seventy-two sensors were attached to a data acquisition system, and each sensor was assigned a specific channel. An Optim Megadac® data acquisition system recorded

measurements corresponding with each sensor at a rate of either 60 or 120 scans per second. A picture of the data acquisition system used during bridge testing can be seen in Figure 3.35.

Figure 3.35: Data acquisition hardware

3.7 SENSOR NOTATION

For data acquisition and analysis purposes, each sensor was assigned unique identification. The notation for sensor identification incorporated the instrument type, girder number, span number, and instrument location. The instrument type was assigned the following notation: CO for crack-opening displacement gage, D for deflectometer, S for concrete surface strain gage, and F for FRP reinforcement surface strain gage. Immediately following the instrument type, a number is used to represent the girder line (7 or 8) for the instrument. Following the girder line notation and an underscore, another number is used to represent the span (10 or 11) containing the instrument. Following the span notation and another underscore, the instrument location notation concludes the sensor identification.

The different sensor types require different instrument location notation. The COD gage locations are only indicated by the girder number and span number and do not require additional gage location notation. The twelve deflectometers require six location designations per girder line. The notation selected for these six deflectometer locations range from A through F, with A located at the midspan of Span 10 and F located at the midspan of Span 11. Figures and tables detailing these deflectometer locations can be seen in Section 3.4.1. Strain gage location notation is derived by cross section and then the location on the girder within that specific cross

section. The cross section notation is indicated by a number (1–8). The potential concrete surface strain gage locations within a cross section are indicated by letters (V, W, X, Y, Z, and M). Similarly, the potential FRP reinforcement surface strain gage locations within a cross section are indicated by letters (Y, Z, M, and CK). Figures and tables detailing these strain gage locations can be seen in Section 3.5.1. The data acquisition channel layout assigned to the seventy-two sensors can be seen in Appendix L. The following are examples of the data acquisition sensor identification for each instrument type:

CO8_10 - Crack Opening Displacement Gage
Girder Line 8, Span 10

D8_11_F - Deflectometer
Girder Line 8, Span 11, Location F

S7_10_1V - Concrete Surface Strain Gage
Girder Line 7, Span 10, Cross Section 1, Gage Location V

F7_10_1M - FRP Reinforcement Strain Gage
Girder Line 7, Span 10, Cross Section 1, Gage Location M

Chapter 4

BRIDGE TESTING PROCEDURES

4.1 INTRODUCTION

Bridge testing was conducted to analyze the behavior of the damaged bridge after installed FRP reinforcement had been in service for more than 2 years. This testing took place over two nights. The first night of load testing included the designation of truck traverse lanes and stop positions, and the completion of the first phase of acoustic emissions (AE) testing. Immediately following the first night of load testing, sensor measurements were monitored at fifteen-minute intervals between the two nights of testing to investigate the bridge response to diurnal thermal conditions. The second night of load testing included the second phase of acoustic emissions testing, multiposition load testing, and a superposition load test. Details and procedures of the post-repair bridge testing are discussed within this chapter. Full details of the post-repair acoustic emissions testing have been reported by Hadzor et al. (2011).

4.2 TRAFFIC CONTROL

The instrumented spans of I-565 in Huntsville support four lanes of northbound traffic. During pre-repair load testing, it was determined that traffic traveling in the far west lane of the northbound bridge had a minimal influence on readings taken from the east side of the bridge (Fason 2009). Girders 7 and 8, the instrumented girders, are located on the east side of the northbound bridge. It was decided that leaving the west lane of traffic open during testing would be acceptable as long as measurements were collected during times of minimal traffic interference. In order to provide a safe working environment during the overnight testing hours, ALDOT officially closed the three east lanes with standard lane closure procedures including placement of safety cones and adequate warning signs. The lanes were closed for a distance long enough to provide the load trucks space with which to maneuver once clear of the spans being tested, Northbound Spans 10 and 11.

The effect of traffic control on normal traffic flow demands was also considered. Previously collected traffic volume data was analyzed to determine that the best period for lane closures was between 11 p.m. and 4 a.m. daily. This time frame also coincides with optimal load testing circumstances due to relatively steady-state atmospheric conditions. ALDOT began

closing the three east lanes at 11 p.m. and the lanes were re-opened to normal traffic before 4 a.m. each night of load testing.

4.3 LOAD TESTING TRUCKS

Two trucks were used to load the bridge for testing purposes. For the pre-repair tests, one of the standard load test trucks was out of service and replaced immediately prior to testing with a nonstandard truck. The replacement truck used during pre-repair testing was an ALDOT tool trailer truck (ST-6902). The other truck used during the pre-repair tests was a standard ALDOT load test truck (ST-6400).

To maintain consistent test conditions for the post-repair testing, it was suggested that both trucks used during pre-repair testing continue their roles as load test trucks for the post-repair tests. The standard truck (ST-6400) did continue its role as a load test truck, but the replacement truck (ST-6902) was no longer available at the time of post-repair testing. Another standard ALDOT load test truck (ST-6538) was chosen to replace the tool trailer truck (ST-6902) for post-repair testing. The ST-6538 truck has the same footprint as the ST-6400 truck. Photos of the three different ALDOT trucks can be seen in Figures 4.1, 4.2, and 4.3. The footprints of the different ALDOT trucks can be seen in Figures 4.4 and 4.5.

Figure 4.1: ST-6400 (standard load truck)

Figure 4.2: ST-6902 (pre-repair unconventional truck)

Figure 4.3: ST-6538 (post-repair replacement for pre-repair unconventional truck)

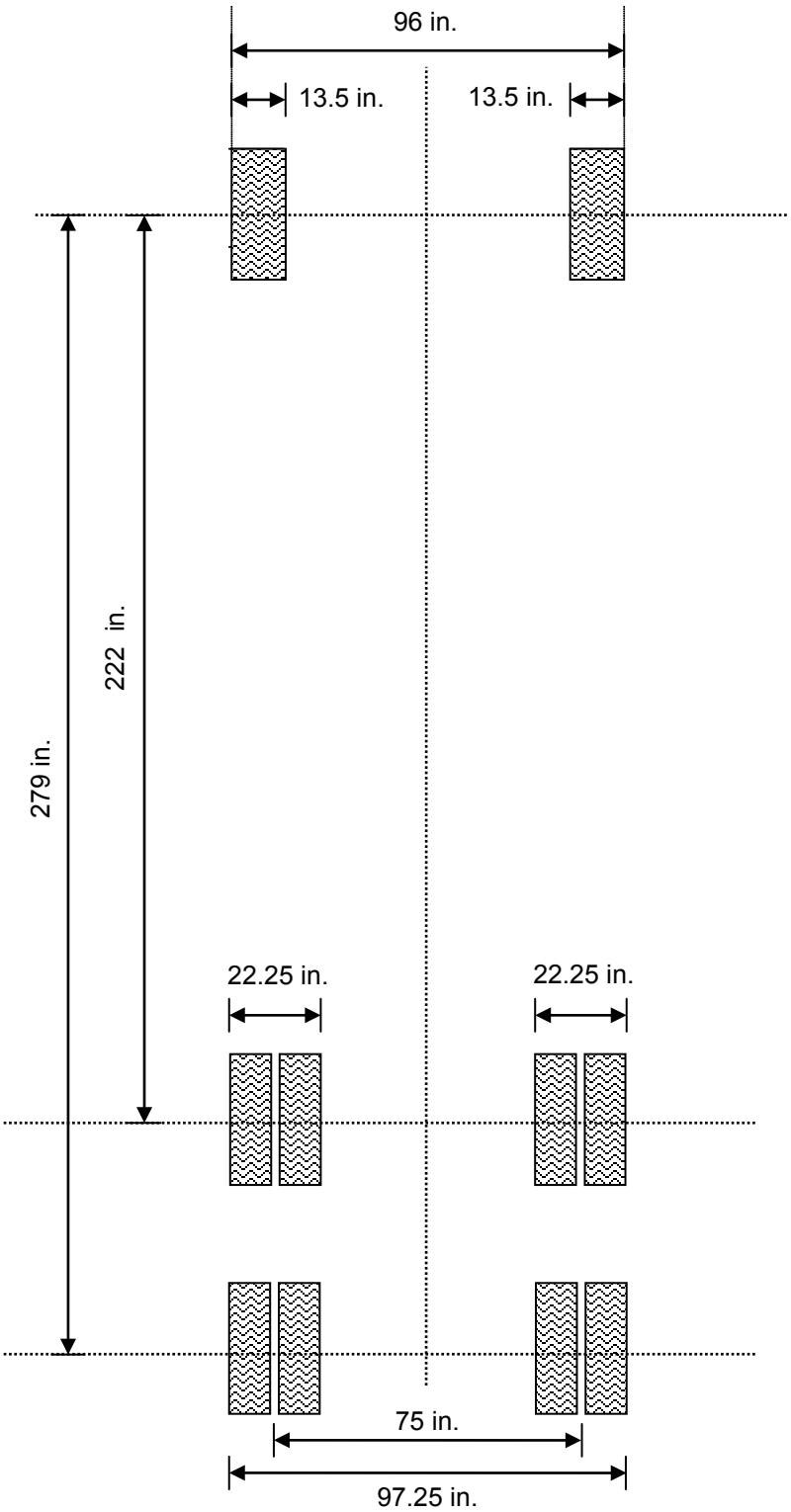

Figure 4.4: Footprint of ALDOT load testing trucks (ST-6400 and ST-6538)

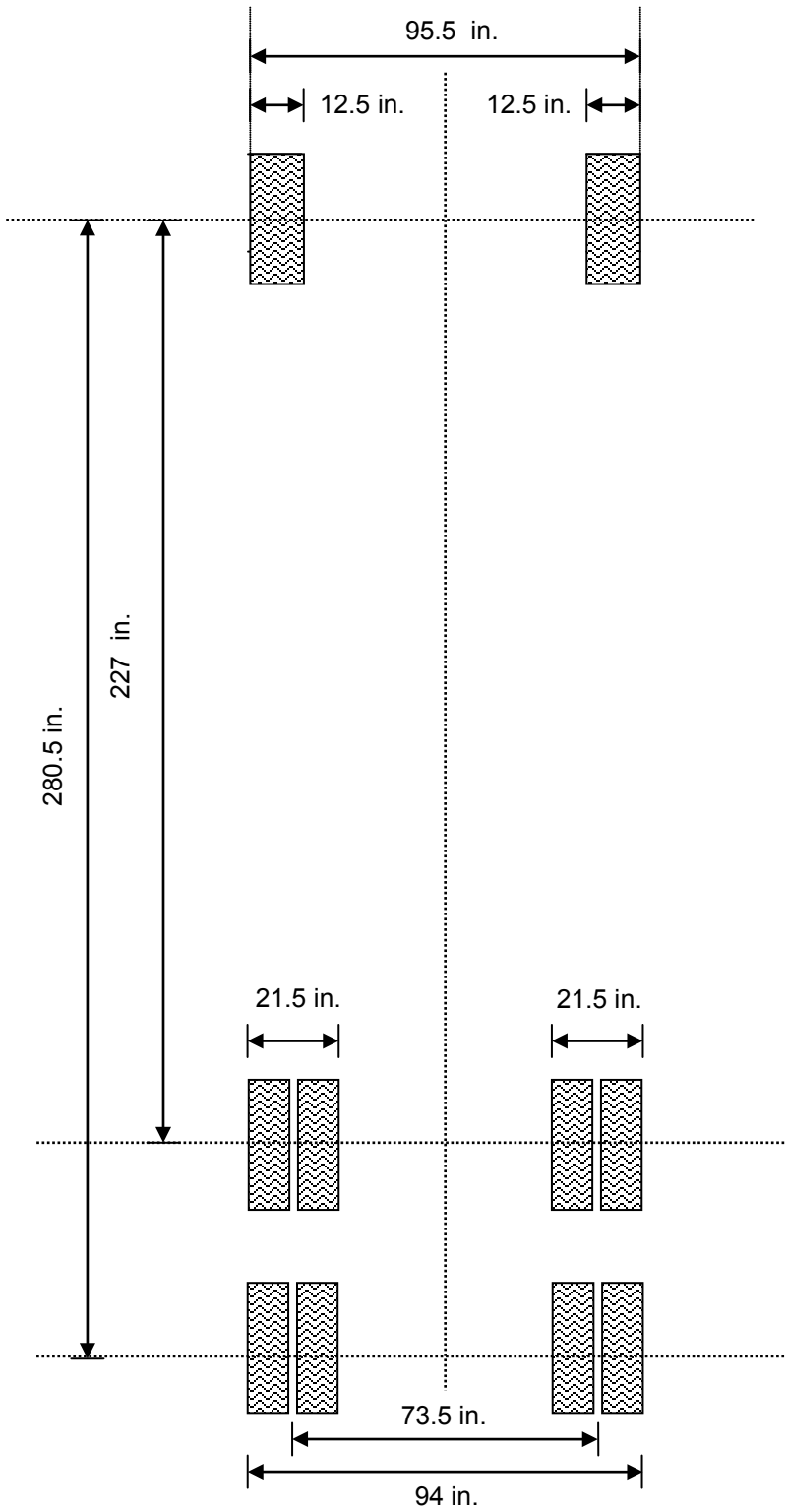

Figure 4.5: Footprint of ALDOT tool trailer truck (ST-6902)

4.3.1 Load Truck Block Configurations

The first night of testing consisted of a nonstandard ALDOT load test block configuration for the acoustic emissions pre-load tests. This AE pre-load block configuration was titled LC-6.5. The weights of the load trucks were decreased for the second night of testing by loading the trucks with a standard ALDOT load truck block configuration titled LC-6.

Load trucks were originally intended to be loaded with identical block configurations during testing, but the bed of the pre-repair replacement truck (ST-6902) extended further beyond the back axle in comparison to the bed of the standard truck (ST-6400), which resulted in slightly different weight distributions. Prior to pre-repair testing, an attempt was made to rearrange the blocks on the replacement truck to compensate for the different truck dimensions. However, the resulting weight distributions were not accurately determined until after the completion of the pre-repair testing, when the truck weights for the pre-repair block configurations were measured at ALDOT headquarters in Montgomery, Alabama. The measured weight distributions of each truck for the LC-6.5 and LC-6 pre-repair load conditions can be seen in Table 4.1.

Table 4.1: Load truck weight distributions—pre-repair

Axle	Group	Tires	ST-6400		ST-6902	
			LC-6.5 (lbs)	LC-6 (lbs)	LC-6.5 (lbs)	LC-6 (lbs)
Front	Left	Single	11500	10750	7575	7850
	Right	Single	11500	10900	7200	7450
Rear 1	Left	Double	19450	18900	20300	19350
	Right	Double	19150	18350	19500	18750
Rear 2	Left	Double	18000	17200	19450	18600
	Right	Double	17850	17500	20150	19250
	Total Weight (lbs)		**97450**	**93600**	**94175**	**91250**

The load truck block configurations for the post-repair load tests were designed to replicate the measured weight distributions from the pre-repair load tests. The block configurations for the standard load truck (ST-6400) remained the same, but the block configurations for the standard load truck (ST-6538) that replaced the unconventional truck (ST-6902) had to be modified. Blocks were moved appropriately to best match the magnitude and location of the resultant loads measured after the conclusion of pre-repair testing. The weight distributions for the post-repair tests were measured before conducting any post-repair testing. The recorded weight distributions of each truck for the LC-6 and LC-6.5 post-repair load conditions can be seen in Table 4.2.

Table 4.2: Load truck weight distributions—post-repair

Axle	Group	Tires	ST-6400		ST-6538	
			LC-6.5 (lbs)	LC-6 (lbs)	LC-6.5 (lbs)	LC-6 (lbs)
Front	Left	Single	10950	10800	8150	7750
	Right	Single	11600	11000	7950	8100
Rear 1	Left	Double	18050	17500	20200	19200
	Right	Double	19300	18600	19300	18400
Rear 2	Left	Double	18000	17250	20450	19850
	Right	Double	19100	18750	18650	17700
	Total Weight (lbs)		**97000**	**93900**	**94700**	**91000**

A comparison of the weight distributions for the unconventional pre-repair truck (ST-6902) and its post-repair standard load truck replacement (ST-6538) with modified block configurations can be seen in Table 4.3. The post-repair block configurations are shown in Figures 4.6–4.9. For all block configurations, each axle load is illustrated with a solid line, and the net resultant truck load is illustrated with a dashed line.

Table 4.3: Comparison of unconventional load truck weight distributions

Axle	Group	Tires	ST-6902 (pre-repair)		ST-6538 (post-repair)	
			LC-6.5 (lbs)	LC-6 (lbs)	LC-6.5 (lbs)	LC-6 (lbs)
Front	Left	Single	7575	7850	8150	7750
	Right	Single	7200	7450	7950	8100
Rear 1	Left	Double	20300	19350	20200	19200
	Right	Double	19500	18750	19300	18400
Rear 2	Left	Double	19450	18600	20450	19850
	Right	Double	20150	19250	18650	17700
	Total Weight (lbs)		**94175**	**91250**	**94700**	**91000**

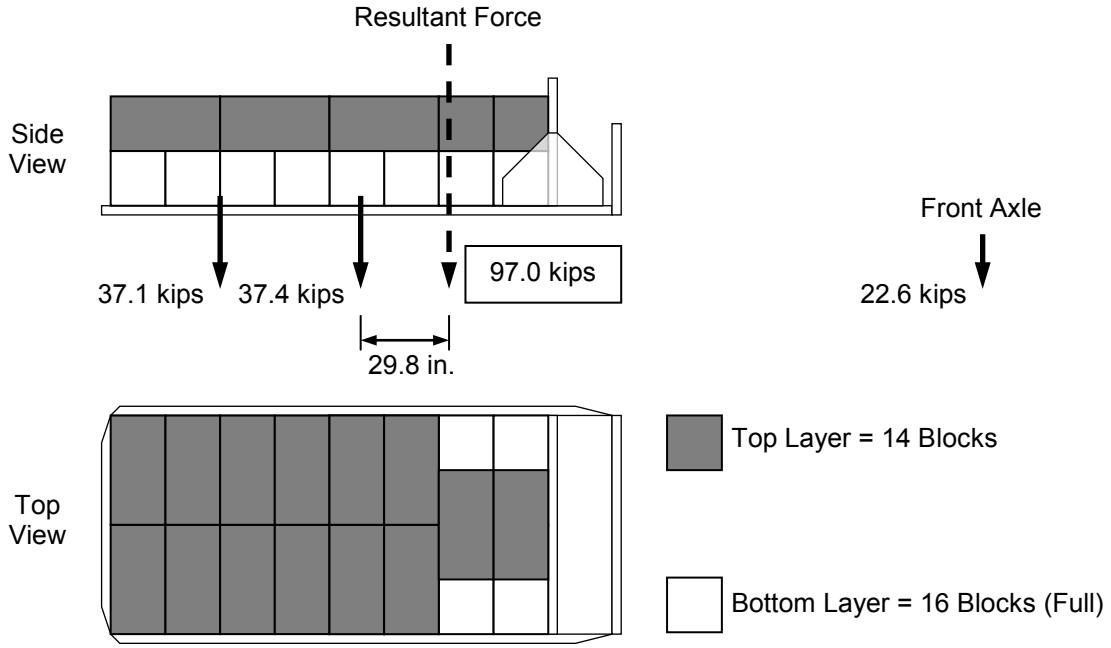

Figure 4.6: LC-6.5 block configuration—post-repair ST-6400

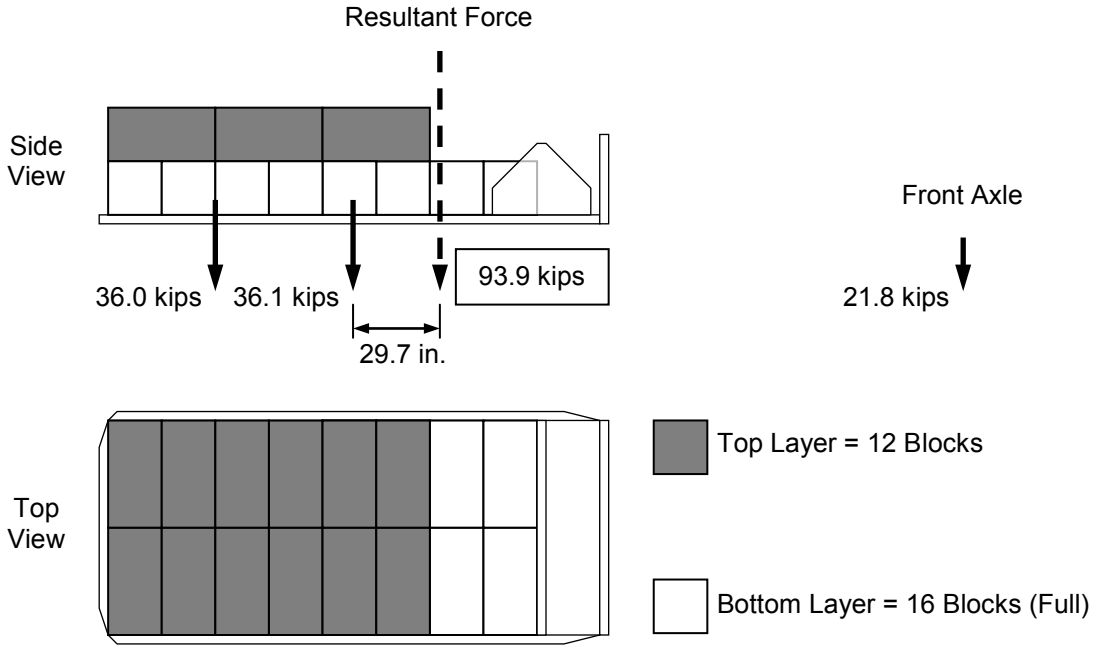

Figure 4.7: LC-6 block configuration—post-repair ST-6400

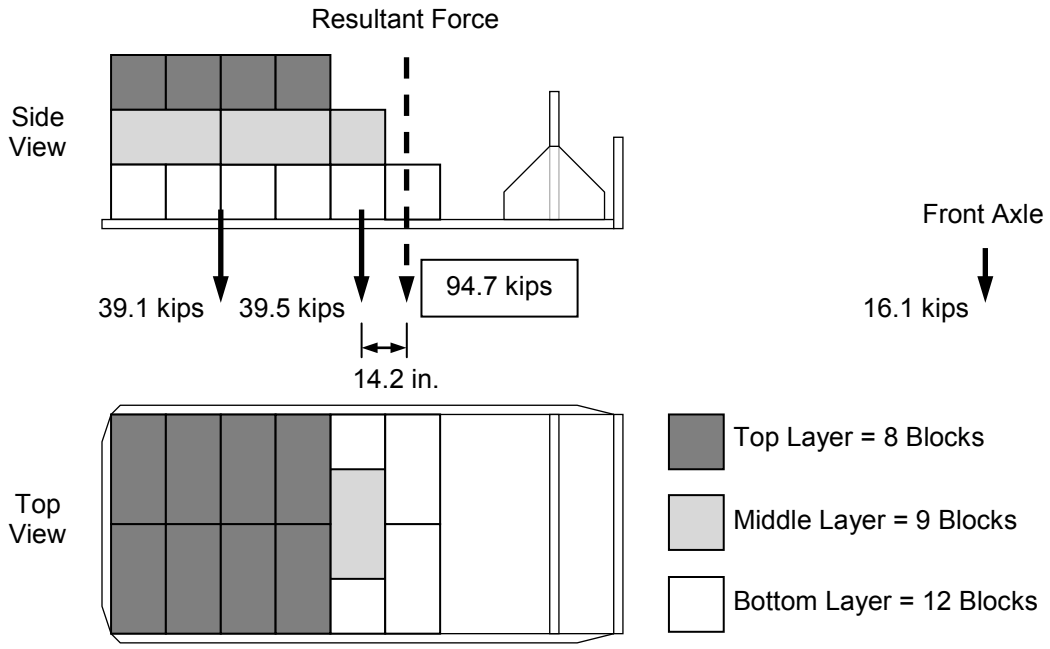

Figure 4.8: LC-6.5 block configuration—post-repair ST-6538

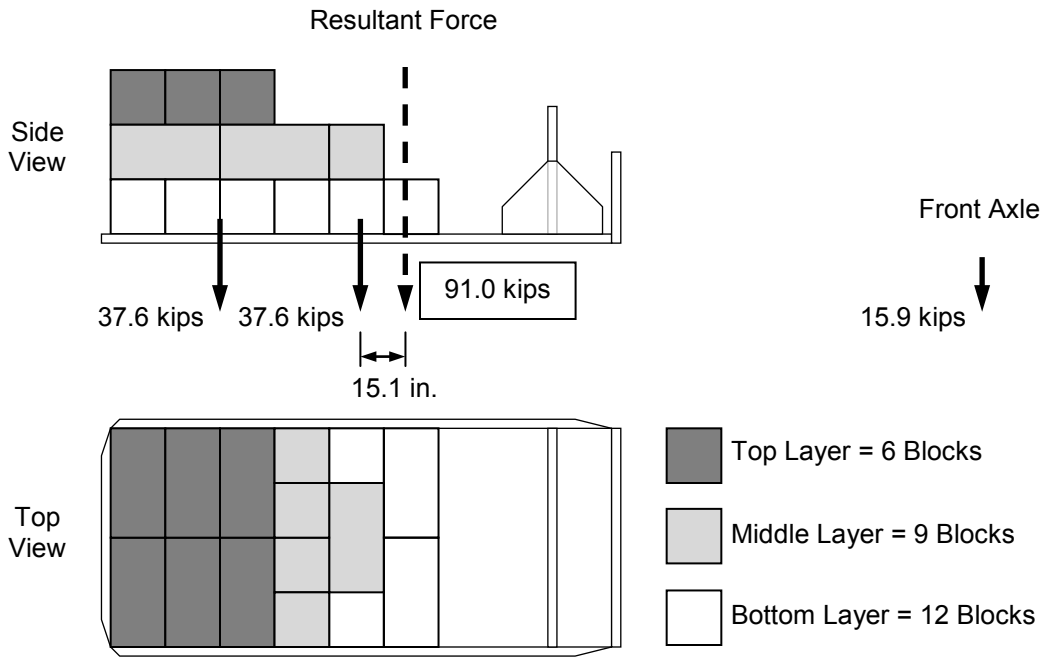

Figure 4.9: LC-6 block configuration—post-repair ST-6538

4.3.2 Resultant Force Comparisons—Pre- and Post-Repair

As previously mentioned, the resultant force for each load truck was monitored when modifying the post-repair block configurations. The magnitude and location of the resultant forces varied for the consistent load truck (ST-6400) with consistent block configurations, as shown in Tables 4.4 and 4.5.

Table 4.4: Resultant force comparisons—ST-6400—LC-6

Load Configuration LC-6	Total Weight (kips)	Resultant Location	
		from *middle* axle (in.)	from *rear* axle (in.)
Pre-Repair (ST-6400)	93.6	30.2	87.2
Post-Repair (ST-6400)	93.9	29.7	86.7
Difference	**0.3**	**-0.5**	**-0.5**

Table 4.5: Resultant force comparisons—ST-6400—LC-6.5

Load Configuration LC-6.5	Total Weight (kips)	Resultant Location	
		from *middle* axle (in.)	from *rear* axle (in.)
Pre-Repair (ST-6400)	97.4	31.4	88.4
Post-Repair (ST-6400)	97.0	29.8	86.8
Difference	**-0.4**	**-1.6**	**-1.6**

The change in the location and magnitude of the resultant force for the two inconsistent load trucks are shown in Tables 4.6 and 4.7.

Table 4.6: Resultant force comparisons—ST-6902 and ST-6538—LC-6

Load Configuration LC-6	Total Weight (kips)	Resultant Location	
		from *middle* axle (in.)	from *rear* axle (in.)
Pre-Repair (ST-6902)	91.2	15.9	69.4
Post-Repair (ST-6538)	91.0	15.1	72.1
Difference	**-0.2**	**-0.8**	**2.7**

Table 4.7: Resultant force comparisons—ST-6902 and ST-6538—LC-6.5

Load Configuration LC-6.5	Total Weight (kips)	Resultant Location	
		from *middle* axle (in.)	from *rear* axle (in.)
Pre-Repair (ST-6902)	94.2	13.1	66.6
Post-Repair (ST-6538)	94.7	14.2	71.2
Difference	**0.5**	**1.1**	**4.6**

After modifying the block configurations for the replacement truck (ST-6538), the magnitude of the resultant force exhibited similar magnitudes of variation compared to those of the consistent load truck (ST-6400). The location of the resultant force exhibited similar variation when measured from the middle axle, but, due to the change in truck dimensions, the location of the resultant exhibited larger variations when measured from the rear axle. Each truck was positioned based on its middle axle for all tests except the acoustic emissions tests, in which each truck was positioned based on its rear axle. These slight variations of magnitude and location of resultant forces were considered negligible based on the scale of the load testing.

4.3.3 Night 1—AE Preloading—LC-6.5

The acoustic emissions pre-load test was designed to apply a heavier load than the bridge had ever experienced in service. The load combination LC-6.5 was designed to be slightly heavier

than the standard ALDOT load test combination LC-6 and to induce load effects approximately 10–15 percent larger than those corresponding to service limit state design. The purpose of this heavier load scenario was to activate any existing cracks. More information regarding the acoustic emissions test procedure can be found in Section 4.5. The post-repair LC-6.5 block configurations for load test trucks ST-6400 and ST-6538 can be seen in Figures 4.6 and 4.8 respectively.

4.3.4 Night 2—AE Loading and Multiposition Load Test—LC-6

The second night of load testing included a repeat of the acoustic emissions tests using the lighter load combination, LC-6. Due to the decreased truck weights relative to the first night, no new crack initiation was expected, but existing cracks were expected to open and close. Following the completion of the acoustic emissions testing, multiposition load tests were conducted with the same LC-6 block configurations. More information regarding the multiposition load test procedure can be found in Section 4.7. The post-repair LC-6 block configurations for load test trucks ST-6400 and ST-6538 can be seen in Figures 4.7 and 4.9 respectively.

4.3.5 Truck Weight Limits

The load combinations used during the load tests were heavier than any truck legally allowed on Alabama highways. Fason (2009) stated that the maximum total weight of any legal truck is 84 kips for a six-axle truck (3S3_AL). The maximum total weight of a legal truck with a similar footprint to ALDOT load test trucks is 75 kips for a tri-axle dump truck. The total weight of a single ALDOT load test truck used during post-repair and pre-repair testing ranged from 91to 97 kips.

4.4 LOAD TESTING TRAVERSE LANES AND STOP POSITIONS

Specific load testing lanes and stop positions were required to consistently provide known truck positions during testing. Information regarding the detailed locations of these lines can be found in Sections 4.4.1 and 4.4.2. The load truck traverse lanes and stop positions were painted on the driving surface of the bridge after traffic control allowed for a safe work environment. An overhead photo of the painted lines representing traverse lanes and stop positions can be seen in Figure 4.10.

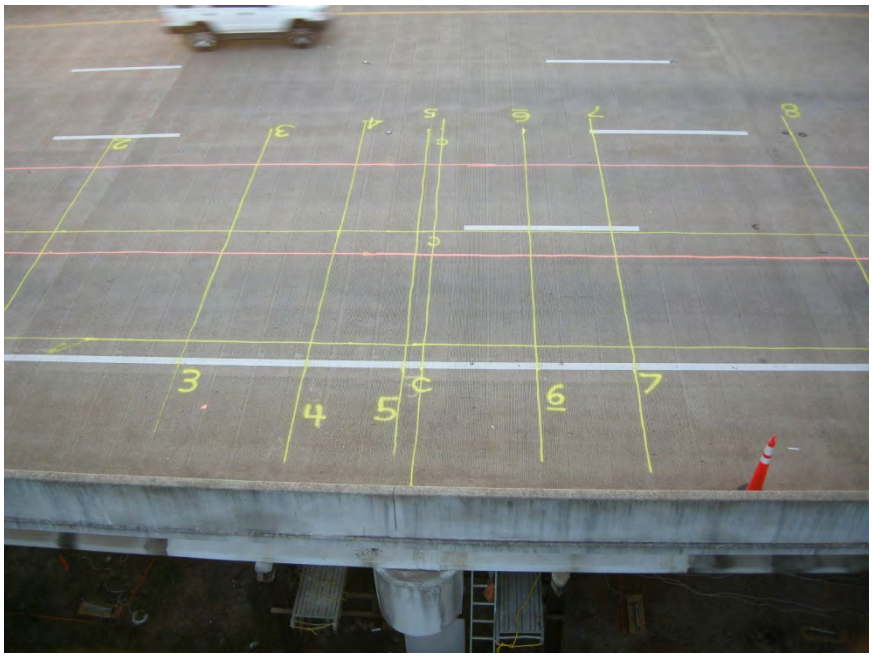

Figure 4.10: Traverse lanes and stop positions—overhead photo

4.4.1 Traverse Lanes

During pre-repair testing, three load lane configurations were designed to apply specific load scenarios to each girder of interest. Each load lane required two traverse lines, one for the east truck and one for the west truck. For the pre-repair multiposition load testing, the conventional load test truck (ST-6400) was always the east truck, while the unconventional load test truck (ST-6902) was always the west truck. The three load truck traverse lanes were titled Lanes A, B, and C. Lane A centered the west wheel group of the east truck directly over Girder 7. Lane B centered the east wheel group of the west truck directly over Girder 7. Lane C centered the west wheel group of the east truck directly over Girder 8. After analysis of the pre-repair load test results, it was determined that Lanes A and C yielded the most useful results for determining bridge response (Fason 2009). Thus, only these two lane configurations were utilized during post-repair load testing. The truck wheel positions of Lanes A and C are shown in Figures 4.11 and 4.12 respectively.

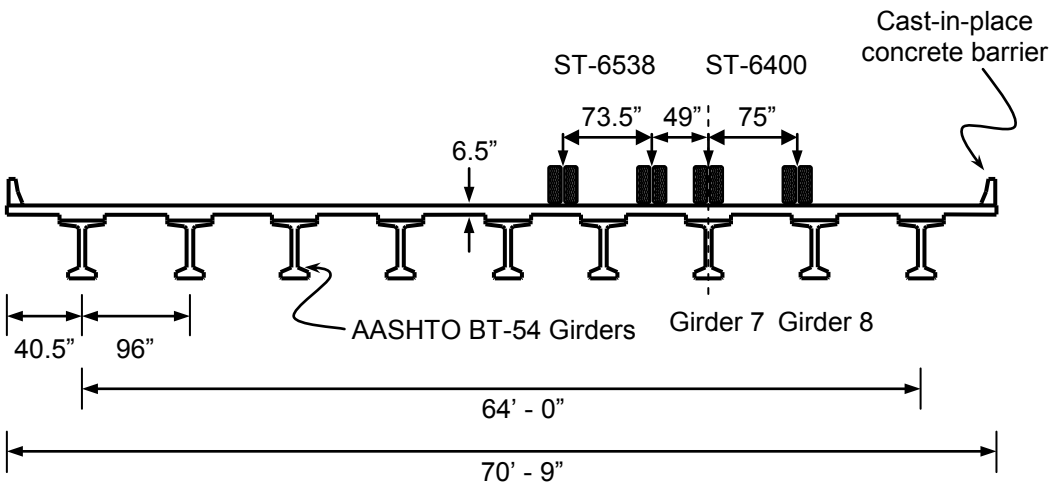

Figure 4.11: Lane A—Horizontal truck positioning (multiposition test)

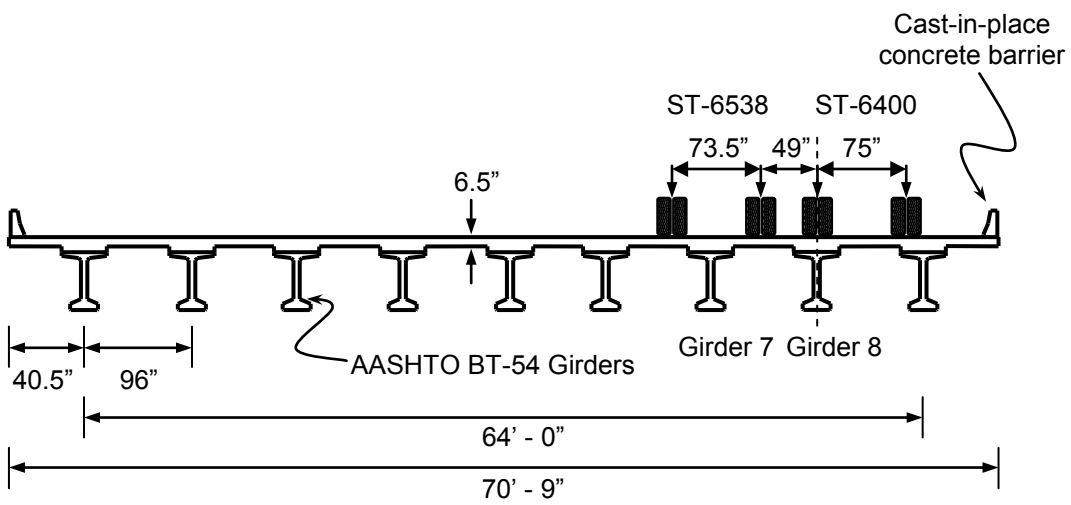

Figure 4.12: Lane C—Horizontal truck positioning (multiposition and AE tests)

For the post-repair load testing, Lane C was traversed for the acoustic emissions and multiposition load tests, and Lane A was only traversed during the multiposition load test. ST-6400 retained its role as the east load truck, while ST-6538 replaced ST-6902 as the west load truck during the post-repair static load tests. To better distinguish between the two lanes, different colored paint was used to indicate the north-south traverse lanes. Orange paint indicated Lane A, and yellow paint indicated Lane C.

4.4.2 Stop Positions

Prior to pre-repair testing, nine stop positions along each traverse lane were designated to provide consistent stationary truck positions for repeated data collection. The nine stop positions range from the midspan of Span 10 to the midspan of Span 11. These longitudinal stop positions are illustrated in Figure 4.13. Five stop positions are located on Span 10, while four stop positions are located on Span 11. Descriptions of the nine stop position locations relative to the centerline of the continuity diaphragm can be seen in Table 4.8. Yellow lines were painted in the east-west direction across all north-south traverse lines to indicate the nine stop positions. For acoustic emissions tests, the load trucks were stopped when their back axle was aligned with the desired east-west stop position line. For the multiposition load tests, the load trucks were stopped when their middle axle was aligned with the desired stop position line.

Table 4.8: Stop position locations

Stop Position	Position Description	Distance from Center of Continuity Diaphragm [middle axle] (in.)
1	middle axle—midspan of span 10	-600
2	front axle—cross section 1	-291
3	front axle—cross section 4	-151
4	middle axle—cross section 1	-70
5	rear axle—cross section 1	-12
6	middle axle—cross section 4	70
7	rear axle—cross section 4	128
8	middle axle—quarter-span of span 11	300
9	middle axle—midspan of span 11	600

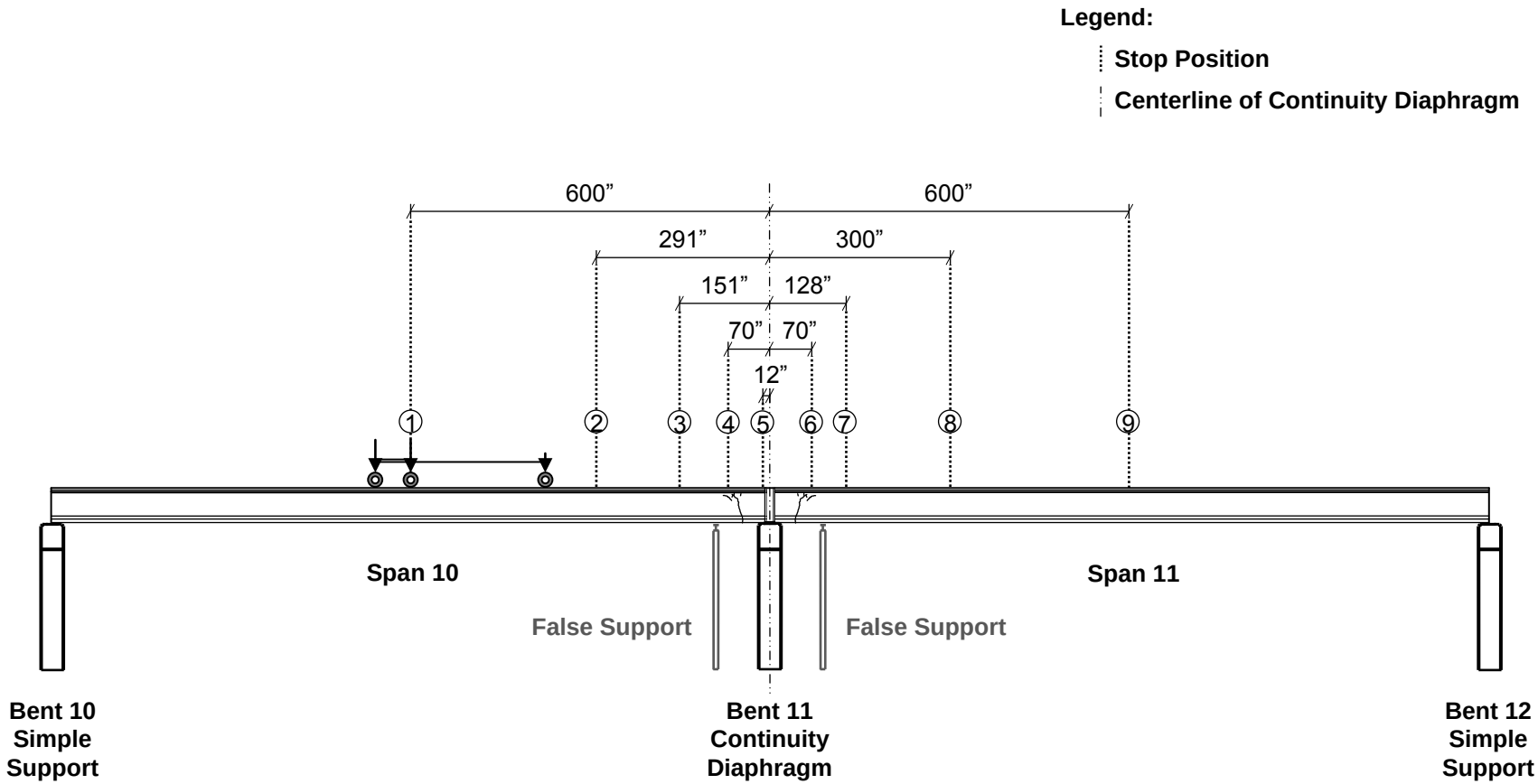

Figure 4.13: Stop position locations

4.5 ACOUSTIC EMISSIONS LOAD TESTING

The acoustic emissions testing and analysis do not fall within the scope of this report. Hadzor et al. (2011) have reported the details and results of this testing. Although the AE results are not presented in this report, data were collected from the static load test instruments to assist with the AE testing analysis. Measurements from all of the static load test sensors (strain gages, deflectometers, and COD gages) were recorded during the AE testing.

AE testing took place both nights. The first night of AE testing began later in the night due to the time allotted for painting the lines designating load truck lanes and stop position. With no load trucks and minimal traffic on Spans 10 and 11, all of the static load test instrument channels were balanced (zeroed) before beginning the first night of AE testing. The channels were not rebalanced for the remainder of the post-repair load tests.

The acoustic emission test procedures were consistent for the pre- and post-repair tests. The AE testing began when baseline data were collected to represent the zero-load condition. Both load trucks then backed down traverse Lane C until their back axles reached the desired stop positions. The two AE stop positions are illustrated in Figure 4.14. The back axles aligned with Stop Position C4 for Span 10 testing, and aligned with Stop Position C6 for Span 11 testing.

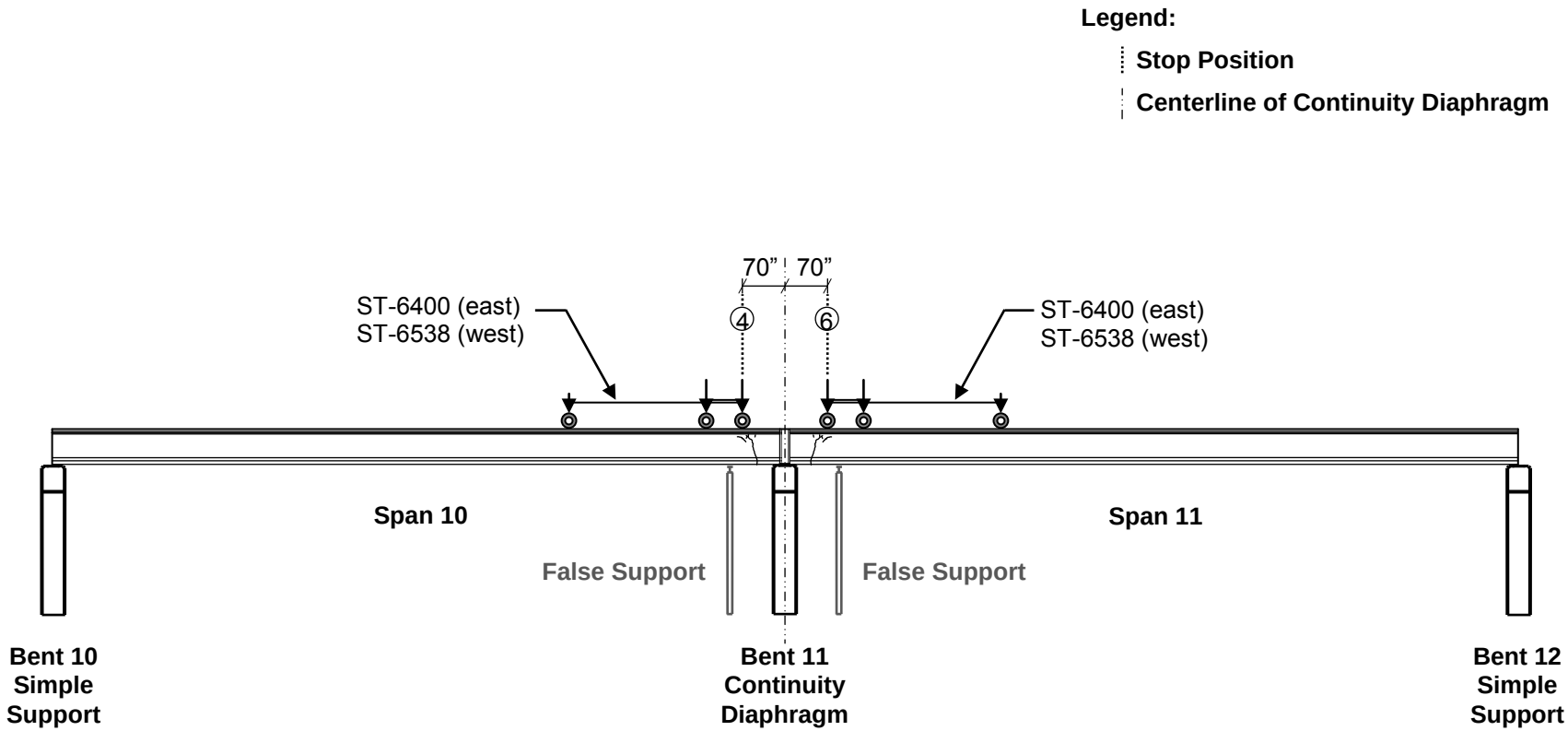

Figure 4.14: Acoustic emissions test—stop position locations

Span 10 was the first span tested during both nights of AE testing. Span 10 AE testing began once both trucks were aligned with their respective Lane C traverse lines on Span 9. The east truck (ST-6400) was slowly driven backward along Lane C in Span 10 until the back axle reached Stop Position C4. Once the east truck was in position, it was held in position for six minutes. While the truck was held in position, a short time interval of measurements from the static load test sensors was recorded. The west truck (ST-6538) was then slowly backed along Span 10 until its back axle also reached Stop Position C4. Both trucks were then held in position for another six minutes, and static load test measurements were recorded. The trucks were then simultaneously driven forward off of Span 10 and onto Span 9. The west lane that was open to normal traffic was used to transport the trucks from Span 9 to Span 12 for the second round of AE testing.

Span 11 AE testing began once both trucks were in position on Span 12, and another baseline reading was recorded to represent the current zero-load condition. The east truck (ST-6400) was backed onto Span 11 until its back axle reach Stop Position C6, and held in position for six minutes. Static load test measurements were recorded while ST-6400 was held in position. The west truck (ST-6538) was then backed into position, and both trucks were held in position for six minutes. Static load test measurements were recorded with both trucks held in position. Both trucks then simultaneously drove forward off of Span 11 and onto Span 12 to conclude the AE testing.

The acoustic emissions test procedure was completed twice during both the pre- and post-repair tests. The first night of acoustic emissions testing was conducted with the heavier LC-6.5 block configurations, and the second night of testing was conducted with the LC-6 block configurations.

4.6 BRIDGE MONITORING

The instrumented girders were monitored over the course of one twenty-four hour time period to allow for analysis of bridge behavior due to temperature change during a typical late-spring day/night cycle. After the completion of the first night of acoustic emissions testing, sensor measurements were recorded every fifteen minutes. Due to increased traffic volume and no lane closures during the day, at least ten seconds of measurements were recorded at a rate of sixty scans per second to provide more data for analysis at each fifteen-minute interval. The raw data was then reduced by selecting the most time-frames that yielded the most consistent measurements with minimal electrical noise and as close to a zero traffic loading condition as possible. These fifteen-minute recording intervals were continued until the beginning of the second night of load testing. The baseline set of measurements for the first night of AE testing is considered to exhibit the baseline conditions for all of the bridge monitoring measurements.

4.6.1 Weather Conditions during Pre-Repair Testing

Bridge monitoring was not conducted during the pre-repair load tests of 2005, but it is still pertinent to compare the weather conditions during both the pre- and post-repair load tests. Fason (2009) stated that the weather conditions during the pre-repair tests included significant cloud cover and rain. These pre-repair conditions were not conducive to temperature variations throughout the day. It was noted that cracks in the girders were visibly smaller on the days surrounding the pre-repair tests than on earlier days when sensors were installed (Fason 2009).

Weather data collected at the Huntsville International Airport for the days encompassing pre-repair testing is presented in Table 4.9.

Table 4.9: Weather during pre-repair bridge testing (NOAA 2005)

Date	Minimum Temperature (°F)	Maximum Temperature (°F)	Mean Temperature (°F)	Precipitation (in.)
May 31, 2005	61	77	69	0.02
June 1, 2005	63	70	67	0.93
June 2, 2005	63	81	72	0.04

4.6.2 Weather Conditions during Post-Repair Testing

The weather conditions for the days surrounding the post-repair load tests in 2010 were conducive to temperature variations throughout the day. On these days, there was little to no cloud cover and no rain, which resulted in significantly higher maximum temperatures for the days surrounding the post-repair tests when compared to the maximum temperatures for the days surrounding the pre-repair tests. Even though the maximum post-repair temperatures were greater than the maximum pre-repair temperatures, the minimum post-repair temperatures at night, which is when load testing was conducted, were similar to the minimum pre-repair temperatures. Weather data collected at the Huntsville International Airport for the days encompassing post-repair testing are presented in Table 4.10.

Table 4.10: Weather during post-repair bridge testing (NOAA 2010)

Date	Minimum Temperature (°F)	Maximum Temperature (°F)	Mean Temperature (°F)	Precipitation (in.)
May 24, 2010	67	94	81	0.00
May 25, 2010	68	85	77	0.00
May 26, 2010	66	90	78	0.26

Note: Precipitation on May 26 accumulated after the conclusion of post-repair testing

The post-repair weather conditions were favorable for the desired analysis of structural behavior in response to large temperature variations experienced during a daily cycle. Temperatures measured at the Huntsville International Airport every three hours during post-repair bridge monitoring are presented in Table 4.11. Sunrise reportedly occurred at 4:38 a.m., and sunset reportedly occurred at 6:50 p.m. on May 25, 2010. (NOAA 2010)

Table 4.11: Temperatures measured during bridge monitoring (NOAA 2010)

Date	Time (CST)	Temperature (°F)
May 25, 2010	12:00 a.m.	72
	3:00 a.m.	71
	6:00 a.m.	71
	9:00 a.m.	78
	12:00 p.m.	80
	3:00 p.m.	84
	6:00 p.m.	82
	9:00 p.m.	75
May 26, 2010	12:00 a.m.	70
	3:00 a.m.	66

4.7 MULTIPOSITION LOAD TESTING

Multiposition load tests were conducted for the pre-repair condition on June 2, 2005, and were repeated for the post-repair condition on May 25, 2010. Lanes A, B, and C were sequentially traversed during the pre-repair tests, but only Lanes A and C were traversed during the post-repair tests. Load trucks simultaneously traversed northbound, keeping the driver-side tires aligned with their respective lane line, and stopped at designated stop positions for a time interval long enough for steady measurements to be recorded.

A baseline representing the zero-load condition was established by collecting measurements while no trucks were on the instrumented spans. The trucks stopped at each of the nine stop positions along each traverse lane long enough to allow for measurements to be recorded at a rate of 120 scans per second for a minimum of three seconds without traffic interference. Lane C was traversed three times consecutively, and the trucks stopped at all nine stop positions during each traverse. This process was then repeated for Lane A.

Every sensor was measured and recorded three times for each stop position. The data collected were organized according to the traverse lane, stop position, and round of testing, for example C3—Round 2. The measurements for each sensor from each of the three traverse rounds were averaged, with the option of eliminating an outlier, to establish one reported measurement for each sensor with respect to each stop position load condition.

The following list describes the step-by-step procedure for the multiposition load testing:

1. While on Span 9, align both trucks with the lines necessary to traverse Lane C
2. Record data for three seconds to establish a baseline for the current conditions
3. Drive both trucks to Position 1 and record data for three seconds
4. Repeat Step 3 for Positions 2–9.
5. Drive trucks back to their starting positions on Span 9 and record another baseline
6. Repeat Steps 3 and 4 to complete a second round of testing
7. Drive trucks back to their starting positions on Span 9 and record a third baseline
8. Repeat Steps 3 and 4 to complete a third round of testing
9. Drive trucks back to Span 9 and realign with traverse Lane A
10. Repeat Steps 2–8 to complete all testing for Lane A

4.8 SUPERPOSITION TESTING

After the last round of static load testing, a supplemental static load test was conducted to analyze the bridge behavior with respect to the superposition of load effects. Load trucks were aligned along the east line of Lane A as shown in Figure 4.15. Measurements were collected while both trucks were off of the instrumented spans to establish a baseline for the current zero-load condition. ST-6400 was driven to Stop Position A9 and held in position long enough for sensor measurements to be collected without traffic interference. With ST-6400 still holding at Stop Position A9, ST-6538 was driven to Stop Position A1. Both trucks were held in position for measurements representing the effects of the combined loading. ST-6400 was then driven off of Span 11 and onto Span 12 while ST-6538 was held in position for measurements representing a single-truck loading at Stop Position A1. The stop position locations for the superposition test are illustrated in Figure 4.16. Only one round of superposition testing was completed.

During analysis, the results of the two single-truck load scenarios can be added together and compared to the results of the load scenario with both trucks simultaneously at their respective stop positions. Theoretically, if the overall bridge behavior is linear-elastic throughout the loading range, for each sensor the sum of the results from the two single-truck loadings should equal the result from the dual-truck loading.

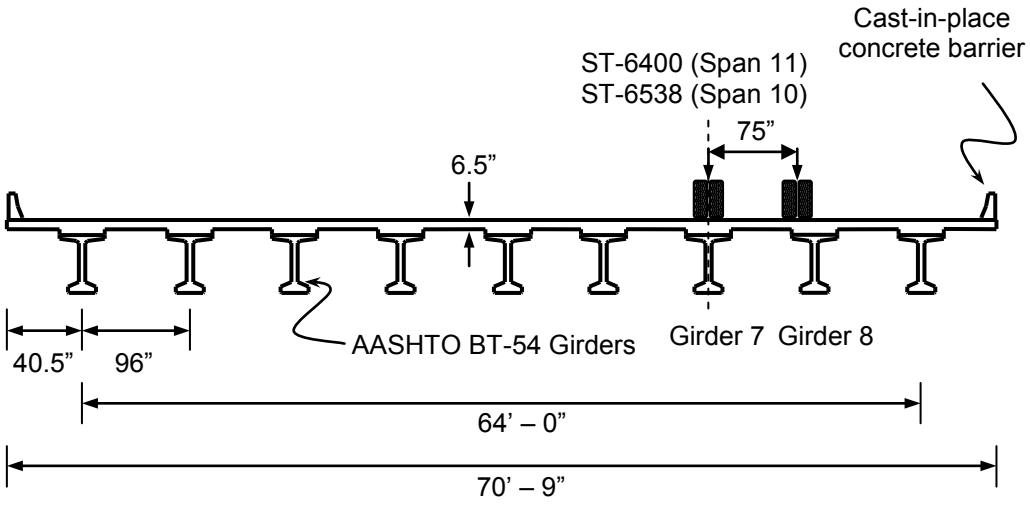

Figure 4.15: Superposition test—horizontal lane positioning

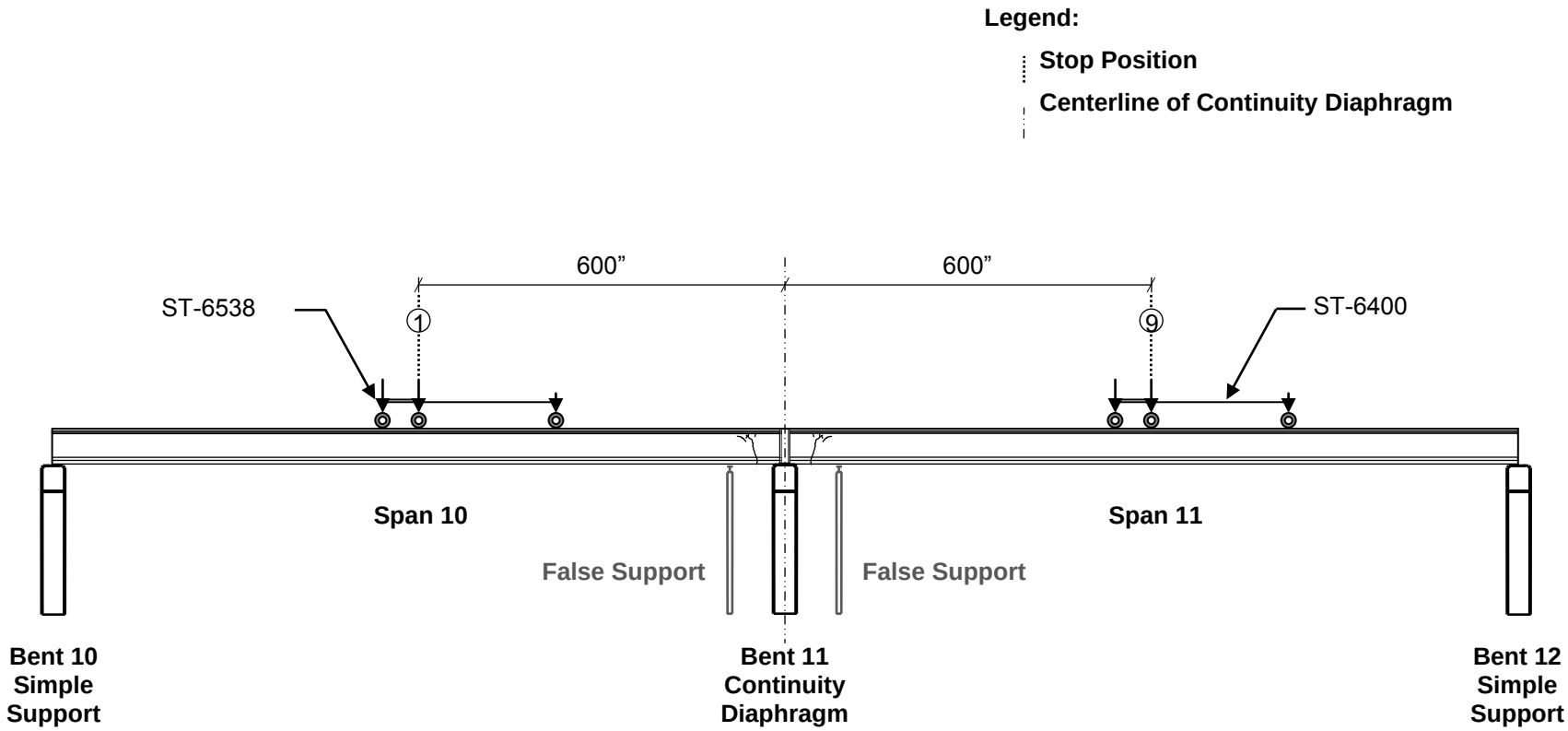

Figure 4.16: Superposition test—stop position locations

4.9 DATA REDUCTION AND ANALYSIS

For analysis purposes, a single numerical result for each sensor was desired for each recorded event. Even though data collection occurred during static loading conditions, every sensor experienced some variance during each recording interval. This variance seems to be mainly related to electrical noise, but could also be associated with physical effects related to normal traffic loads or lingering dynamic loads resulting from moving load trucks into position. For the static load tests, only one lane was open to normal traffic and recorded events were only affected by electrical noise and potentially the dissipation of dynamic loads associated with moving the load trucks into position. During bridge monitoring, all lanes were open to normal traffic and some recorded events correlated with traffic events. Due to increased variable traffic loading, bridge monitoring data collection required an increased recording window to allow for the identification of a suitable traffic-free time interval. Selective data reduction was implemented to reduce effects the inconsistencies might have on the final reported results for all post-repair tests.

During data collection, a separate raw data file was created for each recording interval. Raw data files were organized according to their respective tests and load conditions. Initial data analysis included plotting the raw data measurements over time. These raw data plots were inspected, and reduced time intervals exhibiting relatively consistent behavior were selected for further data analysis. Each reduced time interval was then plotted for each sensor, and a slightly more reduced time interval was then selected to represent even more consistent data. The average numerical result for each sensor over this more consistent time interval was recorded for further analysis. For each recorded event, average values for up to three consistent time intervals were recorded for each sensor. These average values were then averaged together to represent a single numerical result for each sensor relative to each recorded event.

During initial data analysis it was determined that certain sensors were more likely than others to exhibit inconsistent raw data. Sensors judged to be more vulnerable to inconsistencies included the following:

- D7_11_F(Deflectometer—Girder 7—Span 11—Location F [Midspan])
- S8_11_3W(Concrete Strain Gage—Girder 8—Span 11—Section 3—Location W)
- F8_11_4M(FRP Strain Gage—Girder 8—Span 11—Section 4—Location M)

For each recorded event, the least consistent sensors were used to efficiently identify the reduced time intervals to be analyzed for *all* sensors. The majority of the sensors were consistent enough that results rounded to an appropriate precision remained constant regardless of the time intervals selected during data reduction.

Chapter 5

RESULTS AND DISCUSSION

5.1 INTRODUCTION

During post-repair testing of Northbound Spans 10 and 11 of I-565 in Huntsville, Alabama, structural behaviors were measured in response to varying load-truck positions as well as varying ambient thermal effects during normal traffic conditions. Pre- and post-repair measured responses to truck loads were analyzed to address the suspicion that contact between girders and false support bearing pads—which were present during pre-repair testing but removed prior to FRP installation—had an effect on pre-repair structural behavior, thus making direct comparison between pre- and post-repair behavior inappropriate for assessing the effectiveness of the FRP repair (Fason 2009). Post-repair behavioral responses were analyzed independent of pre-repair measured responses to specifically assess structural behavior observed during post-repair testing. Post-repair measured responses to service-level truck loads were also compared to post-repair structural behavior predicted using finite-element modeling (FEM) techniques (Shapiro 2007). In addition to analyzing behavioral responses to truck loads, theoretical and measured responses to varying ambient thermal conditions were analyzed to assess the effects of temperature-induced loading on the instrumented girders.

Measurements from pre-repair testing have been reported by Fason (2009). Predicted responses to post-repair testing have been reported by Shapiro (2007). Reported post-repair measurements are presented within the appendices of this report. The analysis of specific measurements and theoretical behavior predictions is discussed within this chapter.

5.2 BEARING PAD EFFECTS

Inconsistent structural conditions during pre- and post-repair testing could impact the ability to assess the effectiveness of an installed repair solution using direct comparisons of pre- and post-repair measured behavior. Variable conditions that could affect the ability to directly relate behavioral changes measured between pre- and post-repair testing to the performance of a repair solution include

- Different temperature gradients during pre- and post-repair testing,

- Different temperature gradients during pre-repair testing and installation of the repair,
- Additional damage occurring between pre-repair testing and installation of the repair, and
- Addition or removal of load-bearing support conditions between pre- and post-repair testing.

Of these variable conditions, adding or subtracting support conditions would have the most apparent effect on bridge behavior measured in response to load testing. For this reason, it is important to determine if the steel false supports installed slightly beyond the damaged regions of Spans 10 and 11 were acting as load-bearing supports during testing.

Elastomeric bearing pads were located on top of the false supports prior to pre-repair testing of the bridge structure. These bearing pads were supposed to be removed prior to the first day of pre-repair testing, but complete removal of all pads was unsuccessful because some of the girders were in contact with the bearing pads. The bearing pads under Span 10 were easier to remove than the bearing pads under Span 11. Under Span 10, the bearing pad corresponding to Girder 8 was completely removed, and the bearing pad corresponding to Girder 7 was partially removed. The bearing pads corresponding to Girders 7 and 8 of Span 11 could not be removed prior to the pre-repair tests. All of the false-support bearing pads were finally removed during the FRP installation process, so they were not present during post-repair testing.

Following pre-repair testing, it was noted by Fason (2009) that the remaining bearing pads likely allowed some of the load to be transmitted through the false supports rather than spanning to the bents. Fason also reported that, due to the pre-repair bearing pad effects, direct comparisons between pre- and post-repair measurements may not be indicative of the effectiveness of the FRP repair. For this reason, post-repair measurements were analyzed to check whether these bearing pads had enough of an impact on the pre-repair measurements that the effectiveness of the repair could not be accurately assessed by direct comparison of measurements from pre- and post-repair testing.

Multiple comparisons were made to assess the pre-repair bearing pad effects. These comparisons include deflections, crack-opening displacements, and strains measured in response to different load-truck positions. A summary of bearing pad conditions and comparisons of pre-and post-repair measurements are presented in 0 of this report.

The comparison of crack-opening displacements from the pre- and post-repair tests in response to the same truck positions is one behavior that indicates that the bearing pads had a significant effect on the pre-repair measurements. Stop positions that resulted in crack openings were analyzed. Stop position locations are described in Section 4.4 of this report. During both the pre- and post-repair tests, Stop Position 4 had the greatest effect on the Span 10 crack

openings, and Stop Position 7 had the greatest effect on the Span 11 crack openings. The pre- and post-repair crack-opening displacement measurements for Stop Positions A4, A7, C4, and C7 are presented in Figures 5.1–5.4 and Table 5.1. The arrows in the figures represent the position of the wheel loads on the bridge.

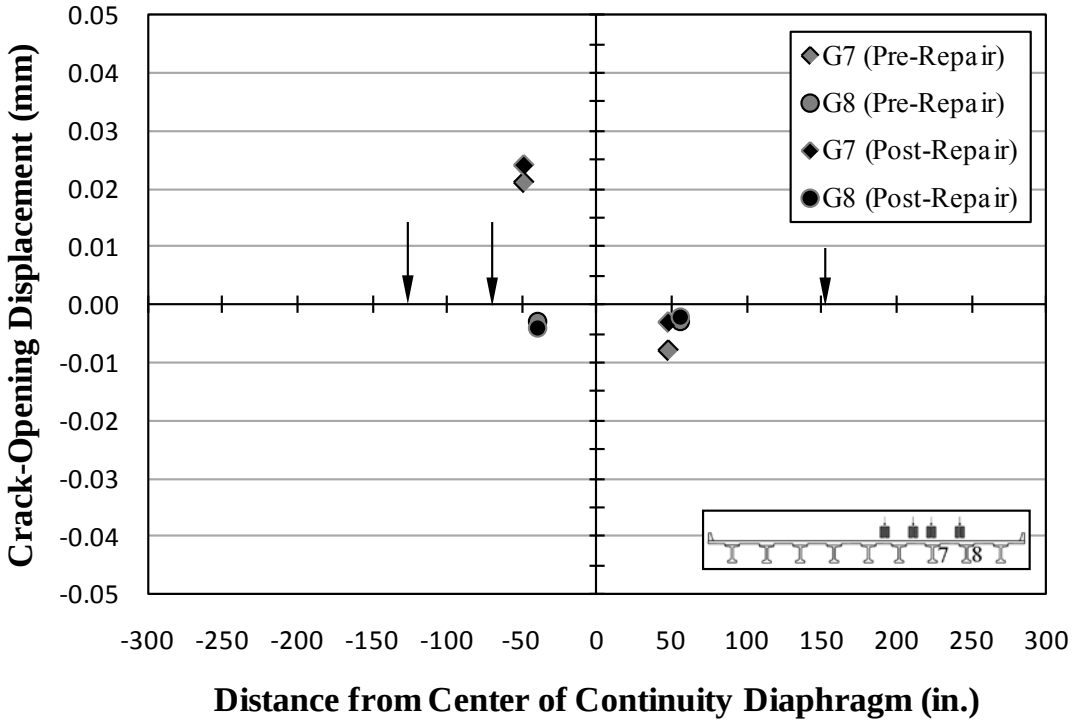

Figure 5.1: Crack-opening displacements—pre- and post-repair—A4

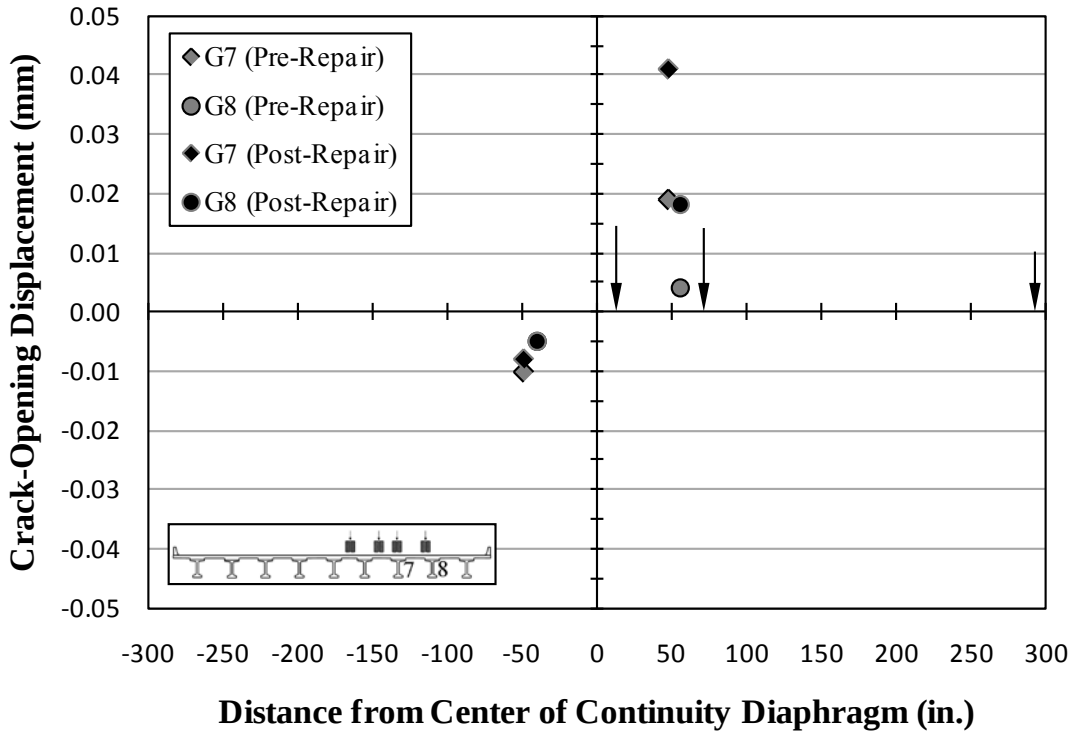

Figure 5.2: Crack-opening displacements—pre- and post-repair—A7

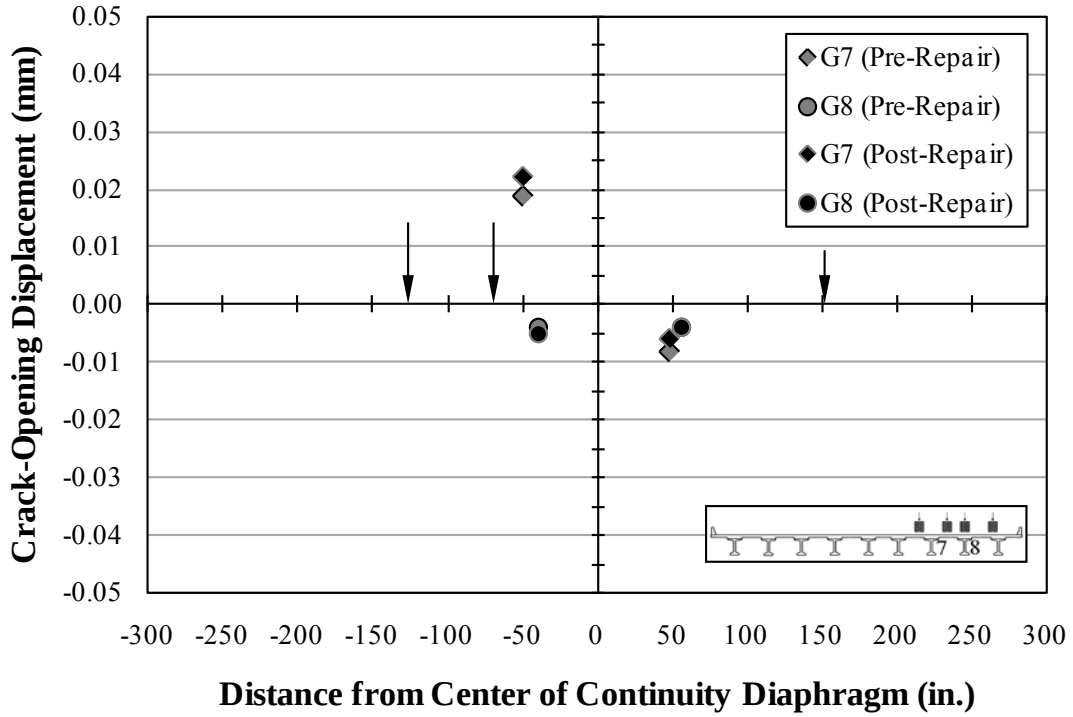

Figure 5.3: Crack-opening displacements—pre- and post-repair—C4

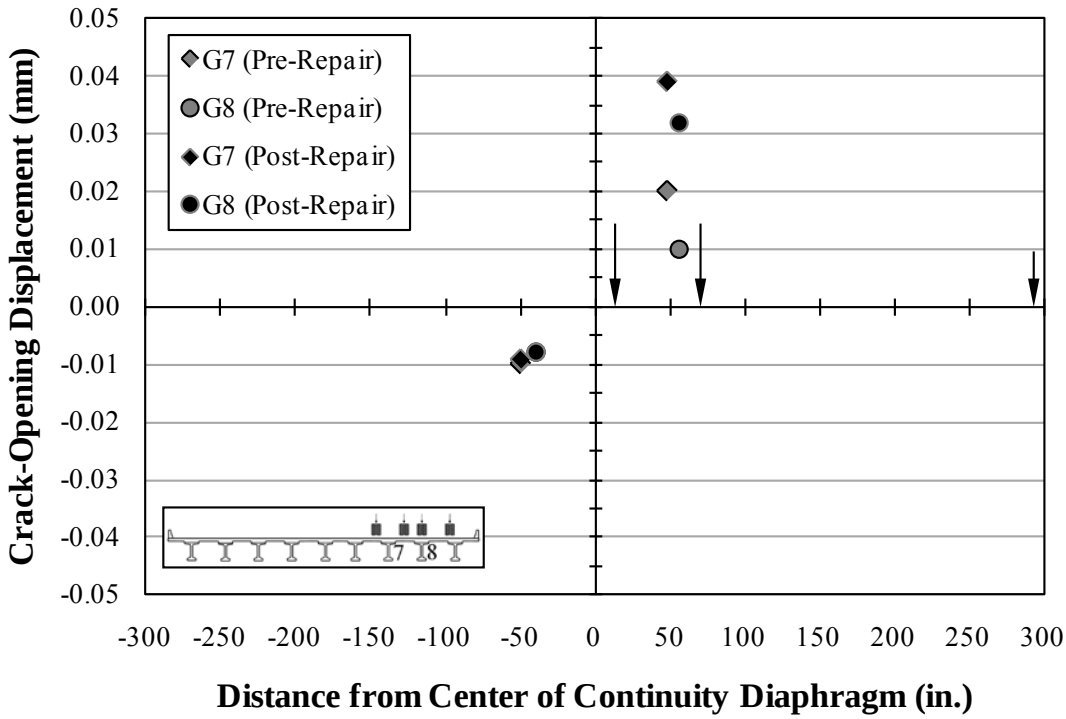

Figure 5.4: Crack-opening displacements—pre- and post-repair—C7

Table 5.1: Bearing pad effects—crack-opening displacements

Girder	Span	*Pre-* or Post-Repair	Crack-Opening Displacement (mm) – closing + opening			
			A4	A7	C4	C7
7	10	*Pre-*	0.021	-0.010	0.019	-0.010
		Post-	0.024	-0.008	0.022	-0.009
	11	*Pre-*	-0.008	**0.019**	-0.008	**0.020**
		Post-	-0.003	**0.041**	-0.006	**0.039**
8	10	*Pre-*	-0.003	-0.005	-0.004	-0.008
		Post-	-0.004	-0.005	-0.005	-0.008
	11	*Pre-*	-0.003	**0.004**	-0.004	**0.010**
		Post-	-0.002	**0.018**	-0.004	**0.032**

Notes: Measurements presented in **bold** represent the crack openings with the greatest difference between pre- and post-repair testing
1 in. = 25.4 mm

The crack-opening displacements measured in Span 10 were similar for both pre- and post-repair testing, but the crack-opening displacements measured in Span 11 in response to the Stop Position 7 load condition of the post-repair test increased in comparison to the crack-opening displacements measured in response to the same load condition during pre-repair testing. This behavior corresponds with the Span 10 bearing pads being partially removed prior to pre-repair testing, and the Span 11 bearing pads being under enough pressure to prevent any removal prior to pre-repair testing. It is apparent that girder contact with the false support bearing pads under Span 11 resulted in additional support conditions that affected pre-repair measurements. This conclusion is further supported by the other comparisons that are located in Appendix K.

Due to the apparent effects that the bearing pads had on the pre-repair tests, direct comparisons of the pre- and post-repair measured behavior cannot be used to accurately gauge the effectiveness of the FRP repair. Analysis of the post-repair measurements, independent of the pre-repair measurements, is required to assess the post-repair behavior of the overall structure and the FRP reinforcement.

5.3 BRIDGE RESPONSE TO TRUCK LOADS—POST-REPAIR

Sensor measurements in response to different load-truck static positions were analyzed to assess bridge behavior in response to applied gravity loads. These assessments include: girder-line responses to different horizontal truck alignments, signs of damage exhibited by sensor measurements, continuity behavior, and linear-elastic behavior of both the overall structure and the damaged sections.

5.3.1 Response to Different Horizontal Truck Alignments

The horizontal truck alignments for the two traverse lanes had an effect on the measured responses. Lane A aligns the west wheels of the east truck with Girder 7 and the east wheels of the east truck nearly align with Girder 8, while the west truck straddles Girder 6. Lane C aligns the west wheels of the east truck with Girder 8 while the west truck straddles Girder 7. These horizontal truck alignments are illustrated in Figures 5.5 and 5.6.

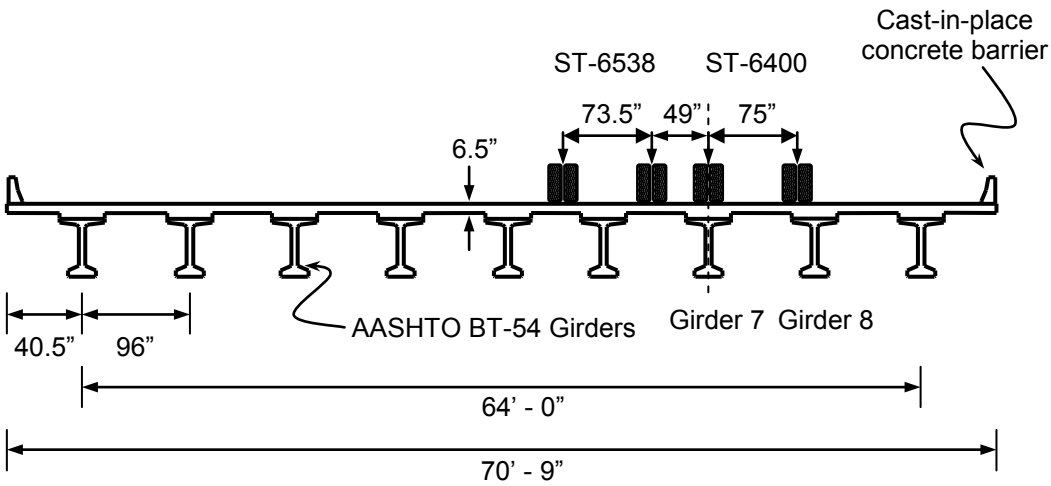

Figure 5.5: Lane A—horizontal truck positioning

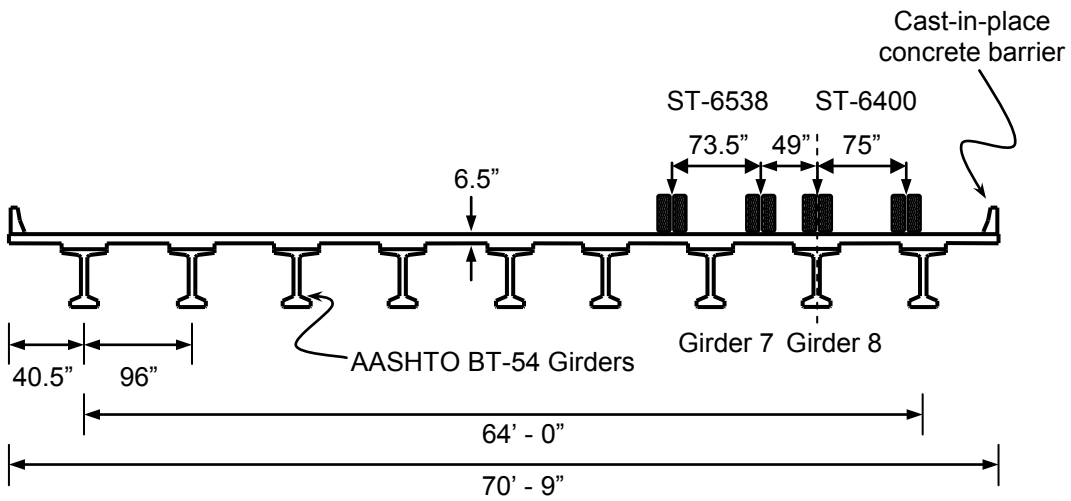

Figure 5.6: Lane C—horizontal truck positioning

Girder deflections measured in response to trucks positioned at midspan were analyzed to assess the effects that the two horizontal truck alignments had on the two instrumented girder lines during load testing. Deflection measurements from midspan truck positions of post-repair testing are presented in Figures 5.7–5.10 and Table 5.2.

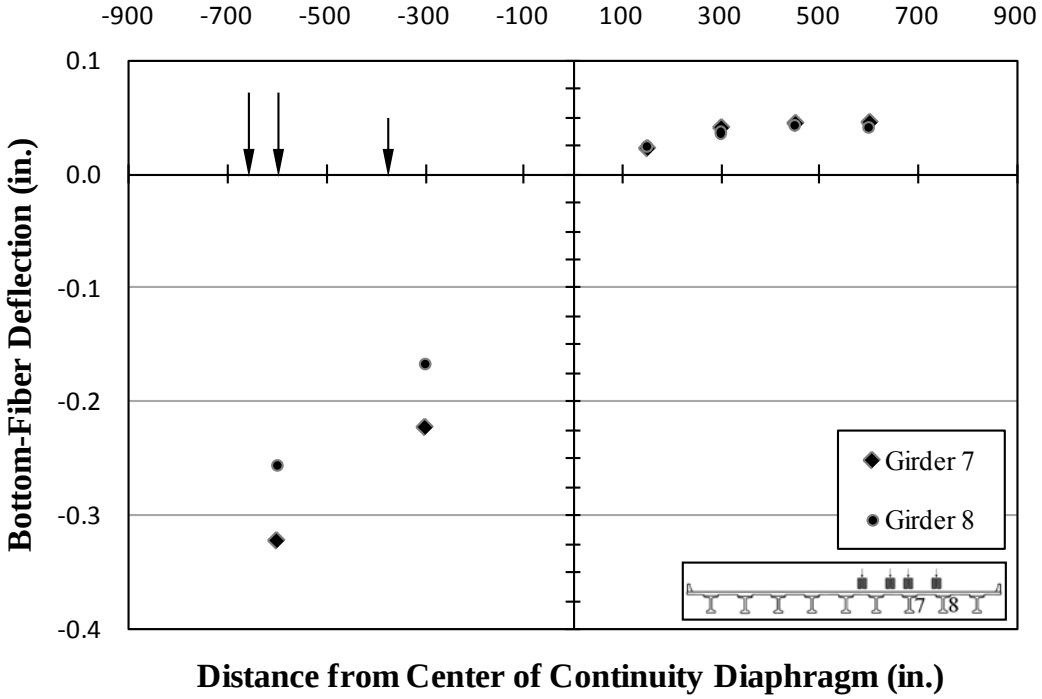

Figure 5.7: Deflections—A1

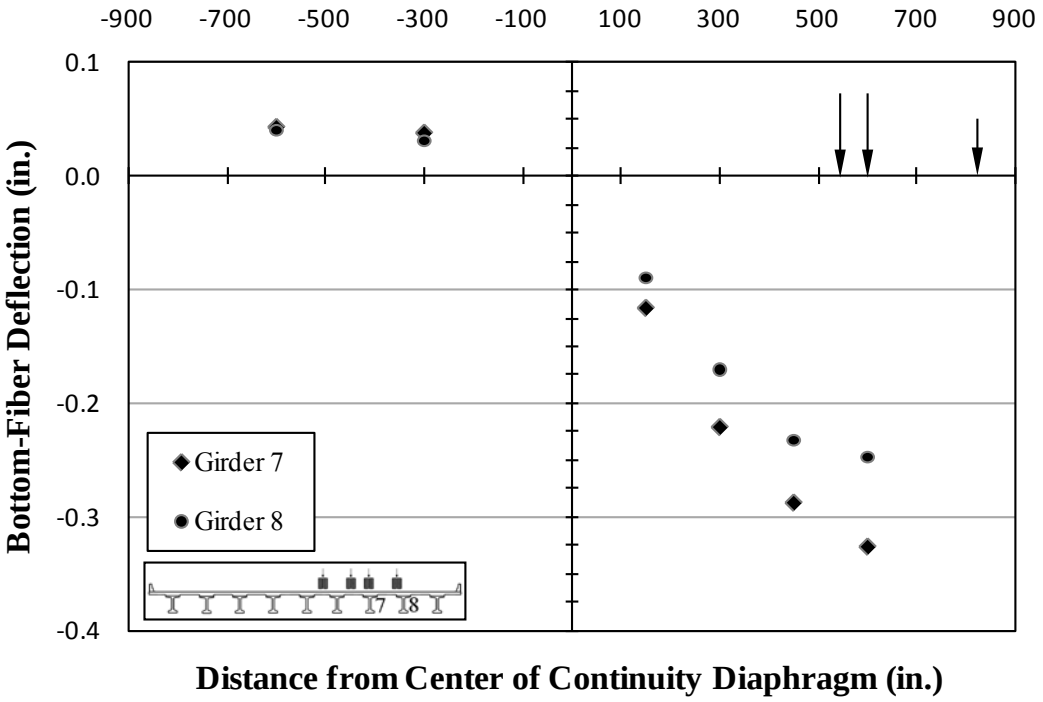

Figure 5.8: Deflections—A9

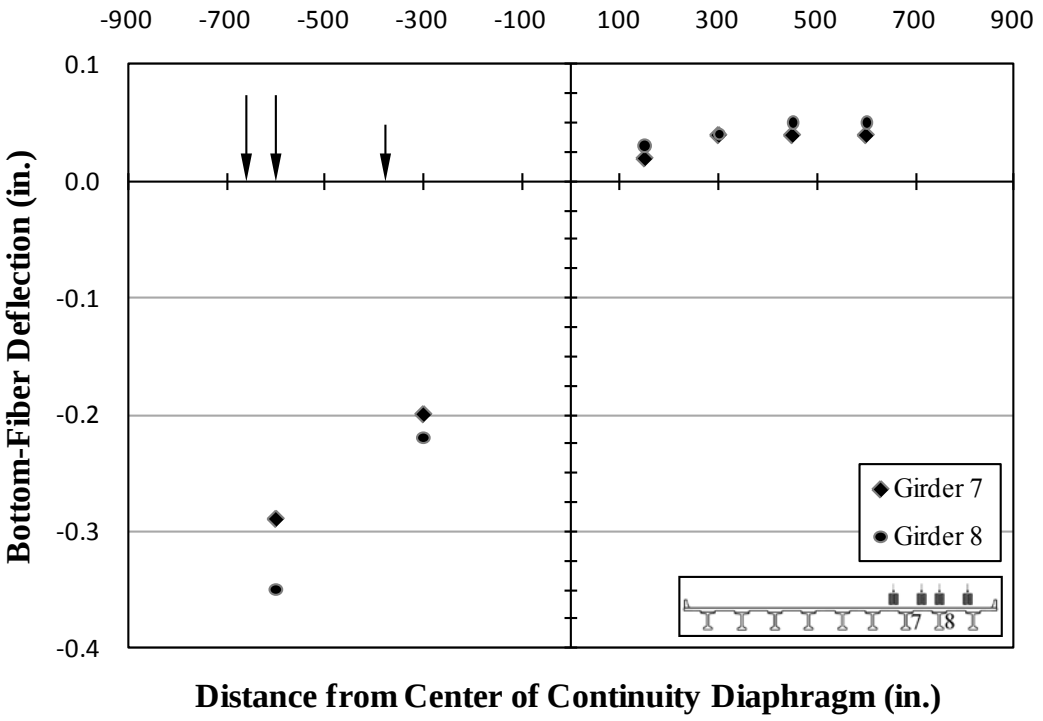

Figure 5.9: Deflections—C1

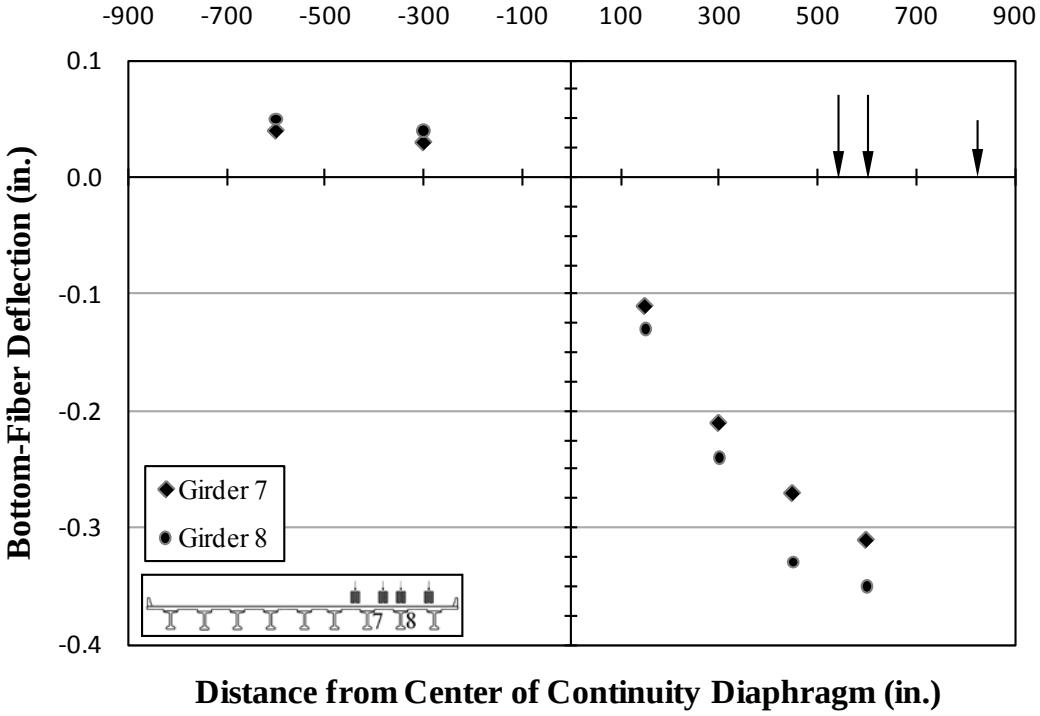

Figure 5.10: Deflections—C9

Table 5.2: Midspan truck positions—deflections

Girder	Span	Location *from continuity diaphragm at Bent 11*	Deflections (in.) – downward + upward			
			A1	A9	C1	C9
7	10	midspan	**-0.32**	0.04	-0.29	0.04
		quarterspan	**-0.22**	0.04	-0.20	0.03
	11	quarterspan	0.04	**-0.22**	0.04	-0.21
		midspan	0.05	**-0.33**	0.04	-0.31
8	10	midspan	-0.26	0.04	**-0.35**	0.05
		quarterspan	-0.17	0.03	**-0.22**	0.04
	11	quarterspan	0.04	-0.17	0.04	**-0.24**
		midspan	0.04	-0.25	0.05	**-0.35**

Note: Measurements presented in **bold** represent the maximum downward deflection per sensor location during all post-repair static load tests

The deflections measured while traversing Lane A resulted in greater deflections, upward and downward, for Girder 7 than for Girder 8. The deflections measured while traversing Lane C resulted in greater deflections, upward and downward, for Girder 8 than for Girder 7. The difference between deflection measurements for both traverse lanes was more significant for Girder 8 deflections than for Girder 7 deflections.

The Girder 8 downward deflections at quarterspan and midspan increased by approximately 30–40 percent when comparing the deflections due to the midspan truck positions aligned with Lane C to the deflections resulting from the midspan truck positions aligned with Lane A. Conversely, the Girder 7 downward deflections at quarterspan and midspan increased by only 5–10 percent when comparing the deflections due to the midspan truck positions aligned with Lane A to the deflections resulting from the midspan truck positions aligned with Lane C.

Load trucks aligned with Lane A have the greatest effect on Girder 7. Load trucks aligned with Lane C have the greatest effect on Girder 8. The Girder 8 deflections due to the Lane C midspan alignments were greater than the Girder 7 deflections due to the Lane A midspan alignments. Due to producing absolute maximum deflections in response to truck loads,

the Lane C horizontal truck alignment resulted in better *overall* results for the analysis of the behavior of the instrumented girders.

5.3.2 Indications of Damage to Instrumented Girders

Crack-opening displacements and bottom-fiber strains measured during acoustic emissions (AE) testing were analyzed to assess damage indicated by the two spans when subjected to identical load conditions mirrored about the centerline of the continuity diaphragm. Information regarding the procedures and truck positions of the post-repair AE tests is presented in Section 4.5 of this report.

Analysis of the post-repair acoustic emissions measurements obtained using the AE sensors is not within the scope of this report. The post-repair AE analysis of the AE sensor measurements is reported by Hadzor et al. (2011). Crack-opening displacements and surface strains measured in response to the post-repair AE static positions are presented graphically in Appendix G and in tabular format in Appendix H of this report.

5.3.2.1 Crack-Opening Displacements

Crack-opening displacement magnitude in response to a specific load can be considered a measured indication of the relative degree of damage to a specific cross section. Crack-opening displacement measurements in response to the AE static positions were analyzed to compare the current amount of damage exhibited by the instrumented girders in response to the identical AE load conditions applied to both spans. The crack-opening displacement measurements from the post-repair AE static positions with both trucks in position can be seen in Figures 5.11–5.14 and Table 5.3.

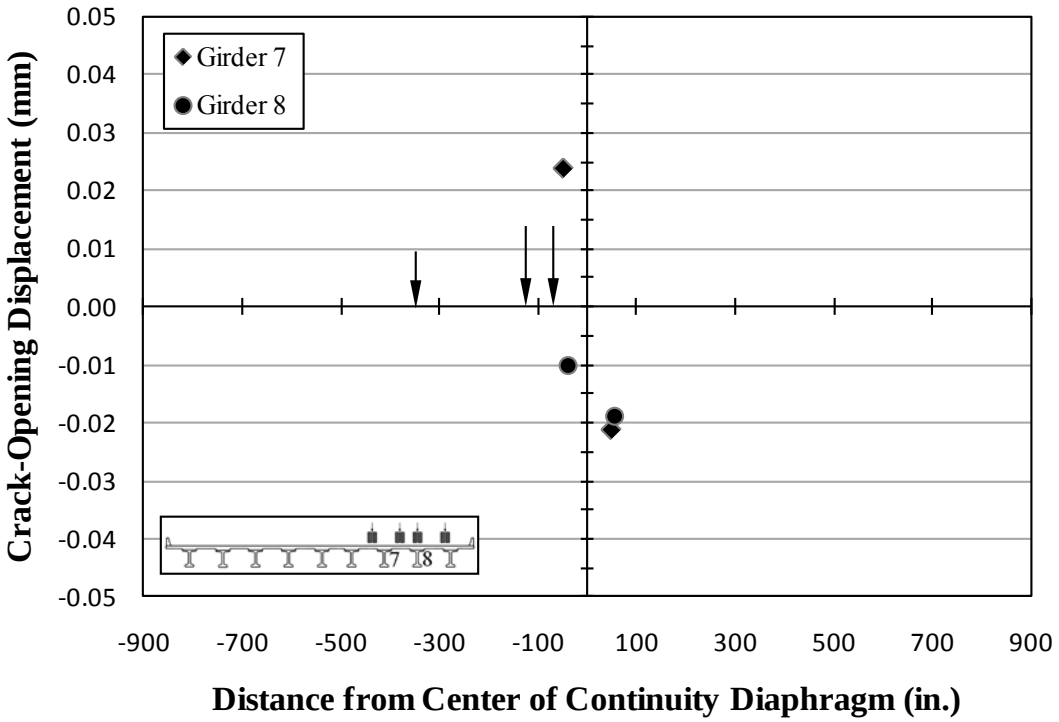

Figure 5.11: AE Span 10 truck position—crack-opening displacements—LC-6.5

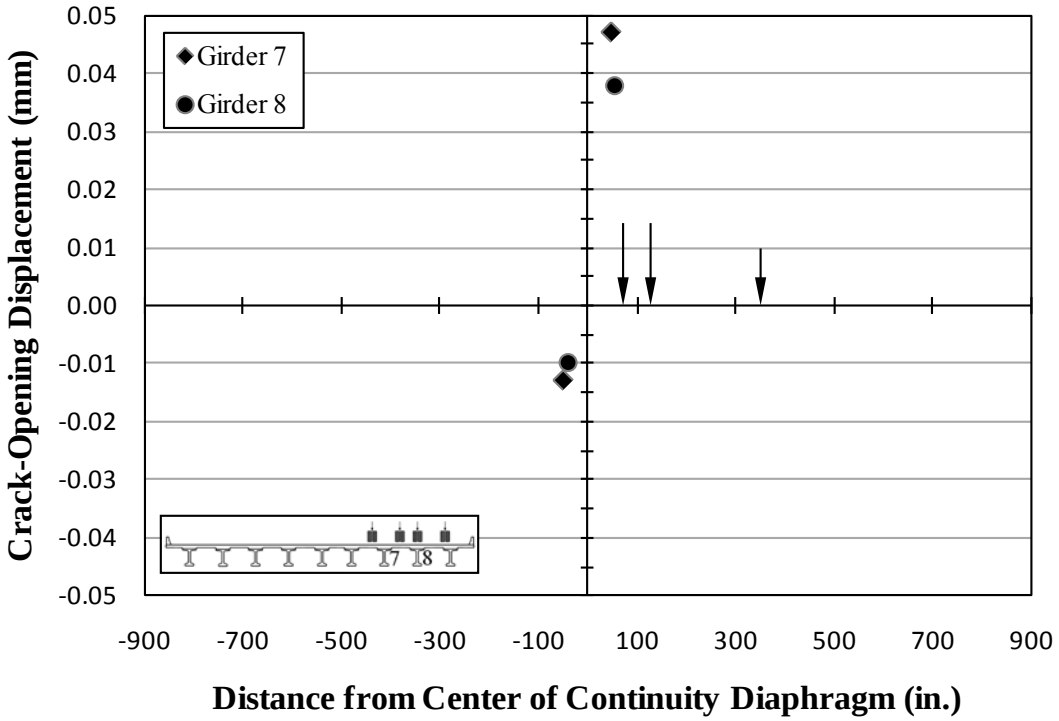

Figure 5.12: AE Span 11 truck position—crack-opening displacements—LC-6.5

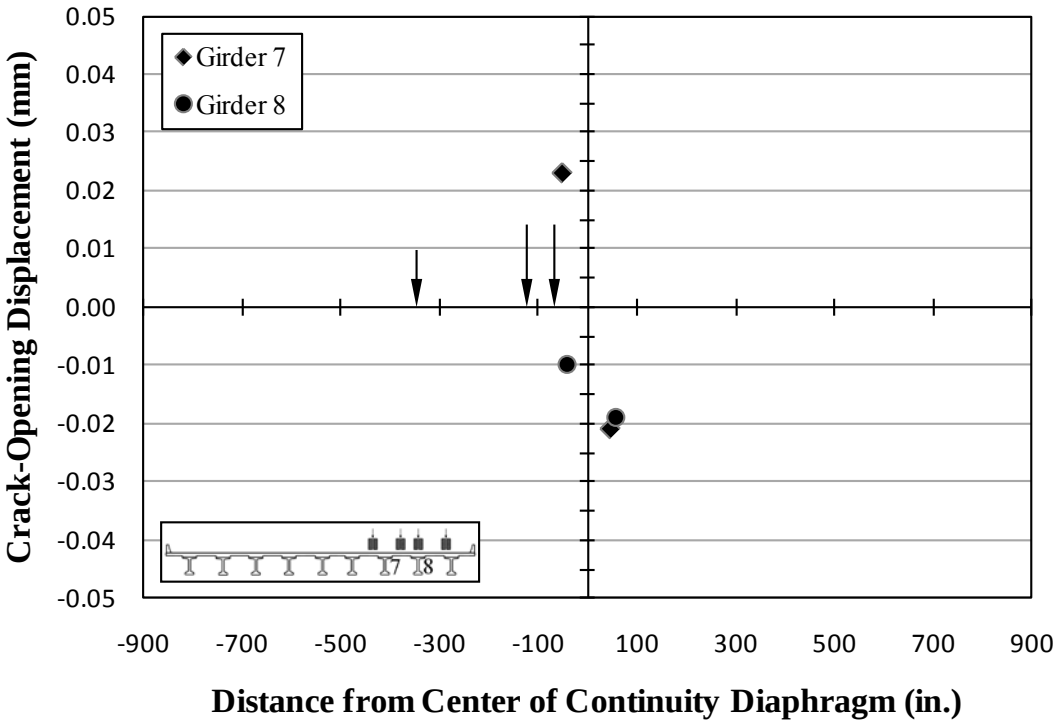

Figure 5.13: AE Span 10 truck position—crack-opening displacements—LC-6

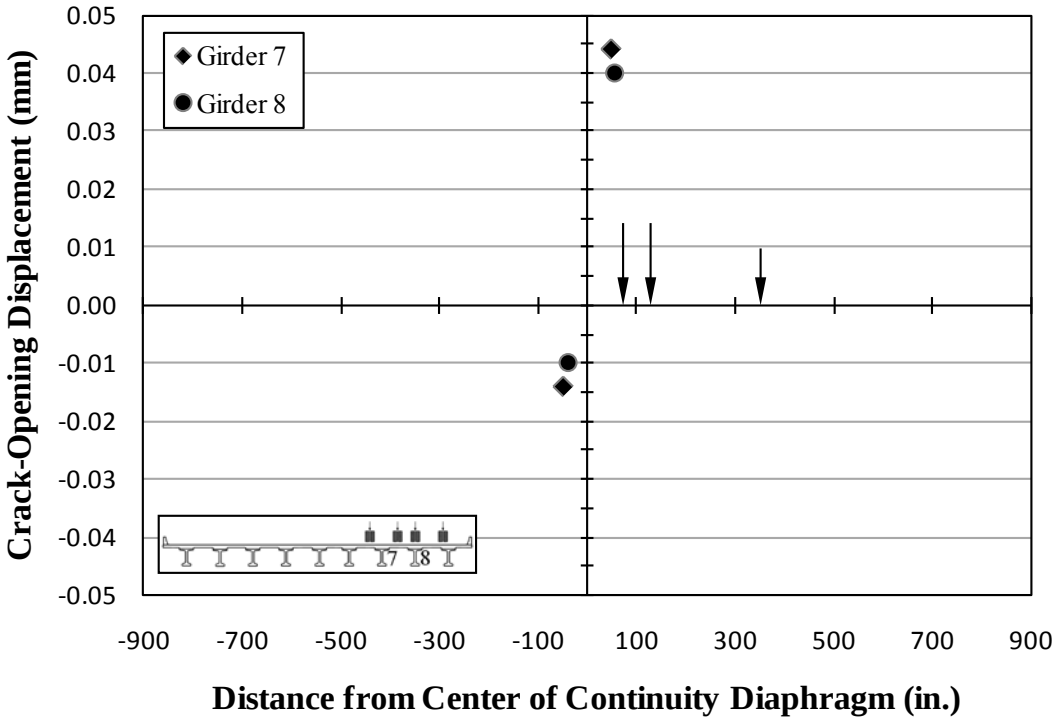

Figure 5.14: AE Span 11 truck position—crack-opening displacements—LC-6

Table 5.3: AE truck positions—crack-opening displacements

Girder	Span	Crack Opening Displacement (mm) – closing + opening			
		LC-6.5		LC-6	
		Span		Span	
		10	11	10	11
7	10	**0.024**	-0.013	0.023	-0.014
	11	-0.021	**0.047**	-0.021	0.044
8	10	-0.010	-0.010	-0.010	-0.010
	11	-0.019	0.038	-0.019	**0.040**

Notes: Measurements presented in **bold** represent the maximum crack opening per gage for the AE truck positions
1 in. = 25.4 mm

A maximum crack opening of 0.047 mm (1.83 x 10^{-3} in.) was measured by the COD gage on the east face of Girder 7 in Span 11 in response to the AE Span 11 static position.
A maximum crack closure of 0.021 mm (0.84 x 10^{-3} in.) was measured by the same COD gage on the east face of Girder 7 in Span 11 but in response to the Span 10 static position. The COD gage on the west face of Girder 8 in Span 10 did not measure a crack opening due to any of the AE static positions.

5.3.2.2 Crack-Opening Displacement Observations

The crack openings measured on the instrumented girders of Span 11 due to the Span 11 static position were of greater magnitude than the Span 10 crack openings due to the Span 10 static position. Similarly, the crack closures measured on the instrumented girders of Span 11 due to the Span 10 static position were of greater magnitude than the Span 10 crack closures due to the Span 11 static position. In response to trucks with consistent load-block configurations, the maximum range of crack-opening displacements on an instrumented Span 11 crack was 0.068 mm (2.67 x 10^{-3} in.) measured by the COD gage on Girder 7 of Span 11. The maximum range of crack-opening displacements on an instrumented Span 10 crack was 0.037 mm (1.47 x 10^{-3} in.) measured by the COD gage on Girder 7 of Span 10.

The crack-opening displacements measured for the instrumented crack on Girder 8 of Span 10 exhibited behavior that was inconsistent with the other three instrumented cracks.

Fason (2009) also noted that, during the pre-repair AE static position measurements, the COD gage installed on the west face of Girder 8 in Span 10 exhibited different behavior when compared to the other COD gages installed on the east face of the other instrumented girders. During the pre-repair AE tests, the COD gage on Girder 8 of Span 10 did not exhibit crack openings due to the Span 10 static position, and all other COD gages did exhibit crack opening due to the static position of their respective span. Fason reported that the possible reasons for this difference were either due to the failure to remove all false support bearing pads prior to pre-repair testing or out-of-plane bending that resulted in different behavior on the west face of the girder than on the east face.

Even after the successful removal of all bearing pads, the post-repair AE static position crack-opening displacements for the COD gage of Girder 8 in Span 10 exhibited behavior similar to the behavior indicated by the pre-repair AE static position measurements. The COD gage on Girder 8 of Span 10 still did not exhibit a crack opening due to any of the AE static positions, but in response to the Span 11 static position the COD gage on Girder 8 of Span 10 did exhibit closures similar to those observed by the COD gage on Girder 7 of Span 10.

Similar behavior measured at the COD gage location on Girder 8 of Span 10 during both pre- and post-repair AE testing is an indication that the pre-repair crack-opening displacement behavior measured at this location was related to something other than the bearing pad under Girder 8 of Span 10 being the only bearing pad completely removed prior to pre-repair testing. If the complete removal of only one bearing pad is not the reason for the COD gage on Girder 8 of Span 10 to behave differently, then the gage may be measuring a response to out-of-plane bending as suggested by Fason (2009).

As stated previously, a lack of significant cracking on the east face of Girder 8 in Span 10 influenced the decision to install the COD gage on the west face of Girder 8, which is the opposite girder face compared to the installation of the other three COD gages. The instrumented crack also did not extend completely through the thickness of the web, which could influence out-of-plane bending behavior being measured at the COD gage location. In addition to the potential response to out-of-plane bending, it is possible that the girder is behaving uniquely simply because it is less damaged than the other instrumented girders.

5.3.2.3 Bottom-Fiber Strains

The bottom-fiber strains measured within 105 in. of the centerline of the continuity diaphragm in response to the post-repair AE static positions were also analyzed to compare the signs of damage exhibited by each instrumented girder. The bottom-fiber strain measurements from the AE static positions are presented in Figures 5.15–5.18 and Tables 5.4 and 5.5.

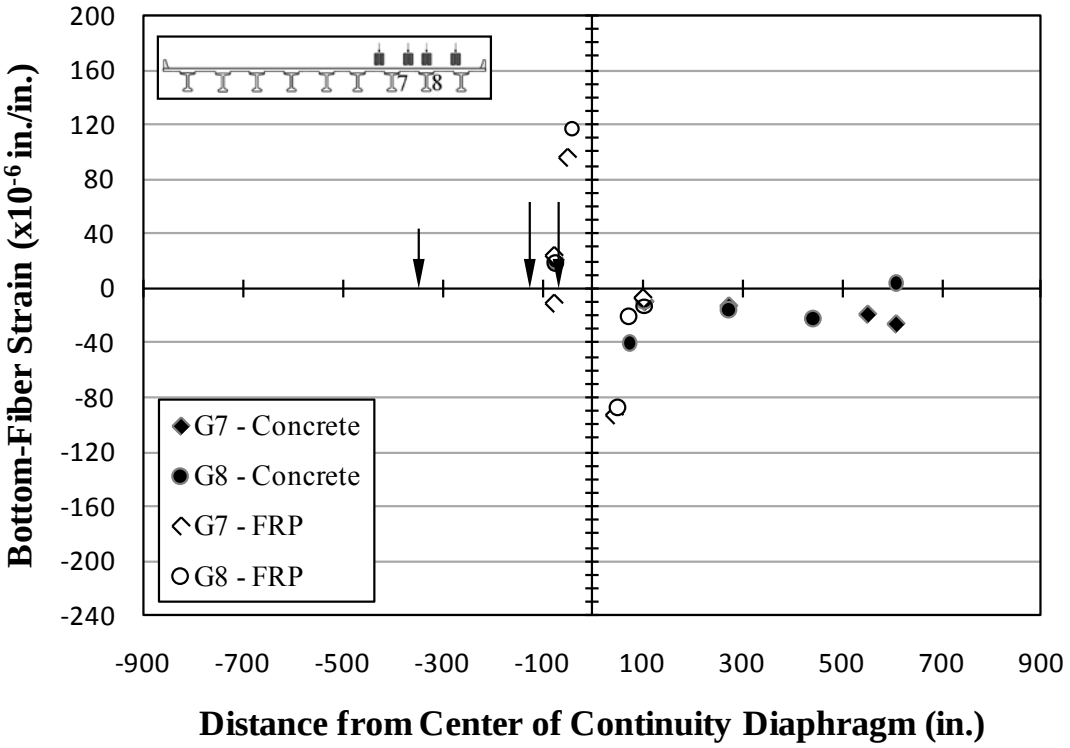

Figure 5.15: AE Span 10 truck position—bottom-fiber strains—LC-6.5

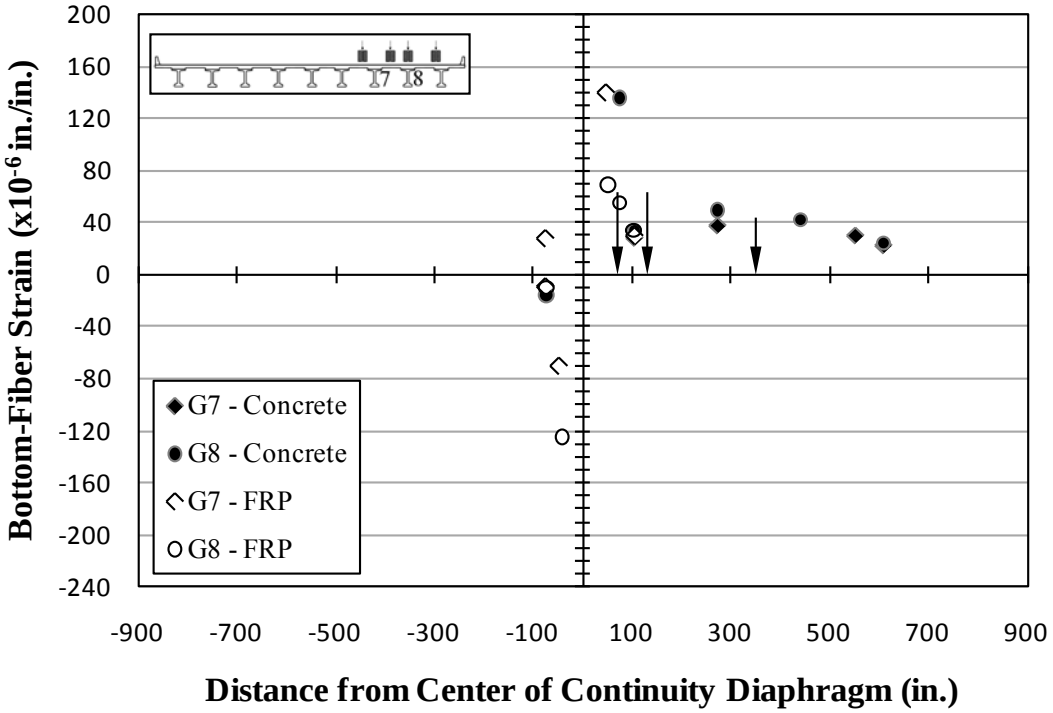

Figure 5.16: AE Span 11 truck position—bottom-fiber strains—LC-6.5

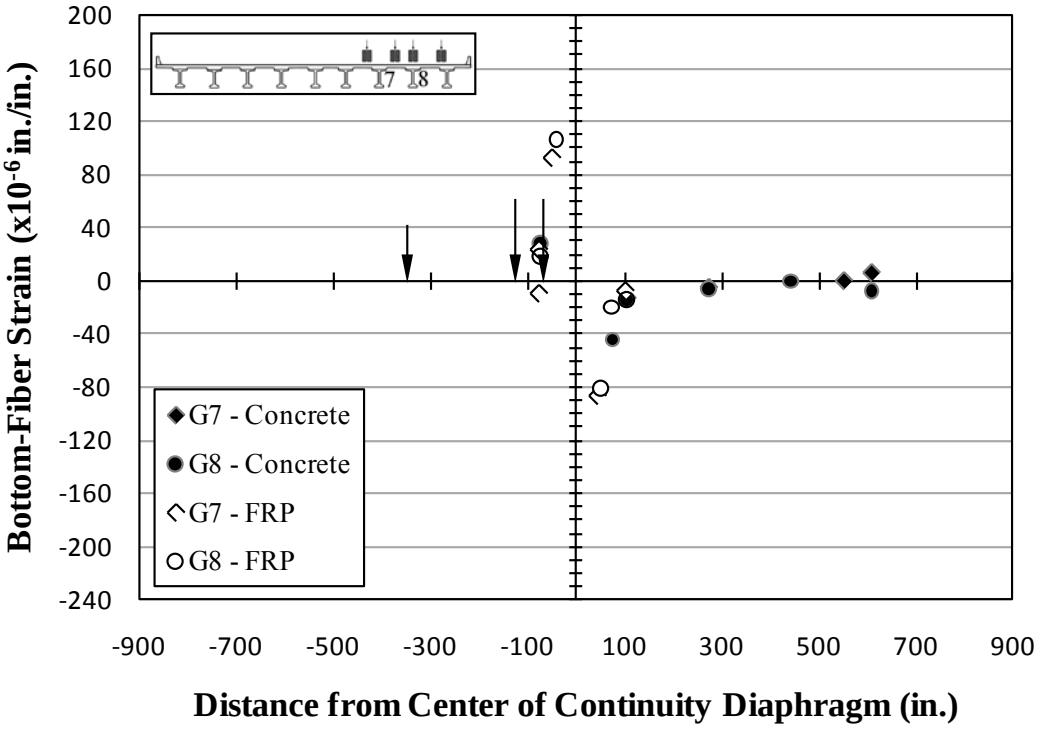

Figure 5.17: AE Span 10 truck position—bottom-fiber strains—LC-6

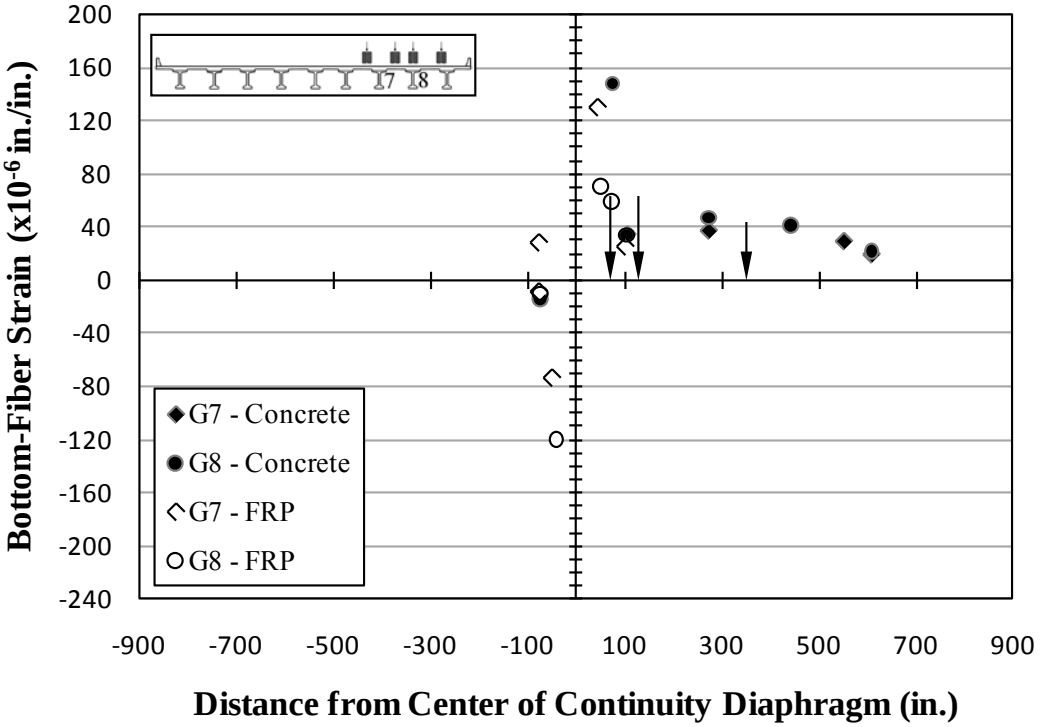

Figure 5.18: AE Span 11 truck position—bottom-fiber strains—LC-6

Table 5.4: AE truck positions—bottom-fiber strains—Girder 7

Span	Distance from center of continuity diaphragm (in.) – Span 10 + Span 11	Location Description	Bottom-Fiber Strain ($x10^{-6}$ in./in.) – compressive + tensile			
			LC-6.5		LC-6	
			Span		Span	
			10	11	10	11
10	-74	FRP	**24**	-9	23	-9
	-47	FRP-Crack	**96**	-70	92	-74
11	47	FRP-Crack	-93	**140**	-87	130
	74	FRP	-11	**28**	-10	**28**
	104	FRP	-7	**30**	-8	25
	105	Concrete	-10	28	-13	**35**
	273	Concrete	-13	**38**	-5	**38**
	441	Concrete	-19	**30**	0	**30**
	609	Concrete	-26	**22**	6	20

Note: Measurements presented in **bold** represent the maximum tensile strains per gage for the AE truck positions

Table 5.5: AE truck positions—bottom-fiber strains—Girder 8

Span	Distance from center of continuity diaphragm (in.) – Span 10 + Span 11	Location Description	Bottom-Fiber Strain ($x10^{-6}$ in./in.) – compressive + tensile			
			LC-6.5		LC-6	
			Span		Span	
			10	**11**	**10**	**11**
10	-75	Concrete	20	-16	**28**	-14
	-74	FRP	**19**	-10	**19**	-10
	-41	FRP-Crack	**117**	-125	106	-120
11	52	FRP-Crack	-87	69	-81	**71**
	74	FRP	-21	55	-20	**59**
	75	Concrete	-40	136	-44	**148**
	104	FRP	-13	**34**	-14	**34**
	105	Concrete	-10	**34**	-14	**34**
	273	Concrete	-16	**49**	-6	47
	441	Concrete	-22	**42**	0	41
	609	Concrete	4	**24**	-7	22

Note: Measurements presented in **bold** represent the maximum tensile strains per gage for the AE truck positions

5.3.2.3.1 Concrete Beyond Primary Crack Locations

A maximum bottom-fiber concrete tensile strain of 148 x 10^{-6} in./in. was measured 75 in. from the center of the continuity diaphragm on Girder 8 of Span 11 due to the Span 11 static truck position. A maximum bottom-fiber concrete compressive strain of 44 x 10^{-6} in./in. was measured 75 in. from the center of the continuity diaphragm on Girder 8 of Span 11 in response to the Span 10 static position.

5.3.2.3.2 FRP Reinforcement Beyond Primary Crack Locations

Disregarding the FRP reinforcement strain gages assigned to crack locations, a maximum bottom-fiber FRP reinforcement tensile strain of 59 x 10^{-6} in./in. was measured 74 in. from the

center of the continuity diaphragm on Girder 8 of Span 11 in response to the Span 11 static position. A maximum bottom-fiber FRP reinforcement compressive strain of 21 x 10^{-6} in./in. was measured 74 in. from the center of the continuity diaphragm on Girder 8 of Span 11 in response to the Span 10 static position.

5.3.2.3.3 FRP Reinforcement Near Primary Crack Locations

A maximum bottom-fiber near-crack FRP reinforcement tensile strain of 140 x 10^{-6} in./in. was measured 47 in. from the center of the continuity diaphragm at the crack on Girder 7 of Span 11 in response to the Span 11 static position. A maximum bottom-fiber near-crack FRP reinforcement compressive strain of 125 x 10^{-6} in./in. was measured 41 in. from the center of the continuity diaphragm at the crack on Girder 8 of Span 10 in response to the Span 11 static position.

5.3.2.4 Bottom-Fiber Strain Observations

In response to the AE static positions, the FRP strain gage installed at the crack location of Girder 7 in Span 11 measured tensile and compressive strains of greater magnitude than the strains measured at the gage installed at the crack location of Girder 7 in Span 10. The FRP strain gage installed at the crack location of Girder 8 in Span 10 measured strains of greater magnitude than the strains measured at the gage installed at the crack location of Girder 8 in Span 11. The magnitudes of strain measured at the FRP gage corresponding with the crack location on Girder 8 of Span 11 were not consistent with the magnitudes of strain measured at the crack locations of the other girders. Also, the concrete strain gage on Girder 8 of Span 11 located 75 in. from the continuity diaphragm measured tensile strains similar to the tensile strains measured at the FRP corresponding with the crack locations of the other girders.

When considering the FRP strain measurements representing strains measured at the crack location, it is possible that the FRP strain gages may have been installed at varying proximities to the actual cracks. This variation is due to the inability to accurately locate each crack through the FRP reinforcement during strain gage installation. Based on the difference between the FRP strain measurements at the crack location on Girder 8 of Span 11 and the measurements at the other crack locations, it is possible that the FRP strain gage at the crack location on Girder 8 of Span 11 was installed the least accurately with respect to the actual crack location.

5.3.2.5 COD and Bottom-Fiber Strain Comparisons

Theoretically, the bottom-fiber strain measured at the crack location of a girder should be related to the crack-opening displacement measured at the instrumented crack of that same girder. The

crack-opening displacements and near-crack bottom-fiber strains measured during the AE static positions are presented for graphical comparison in Figures 5.19–5.22.

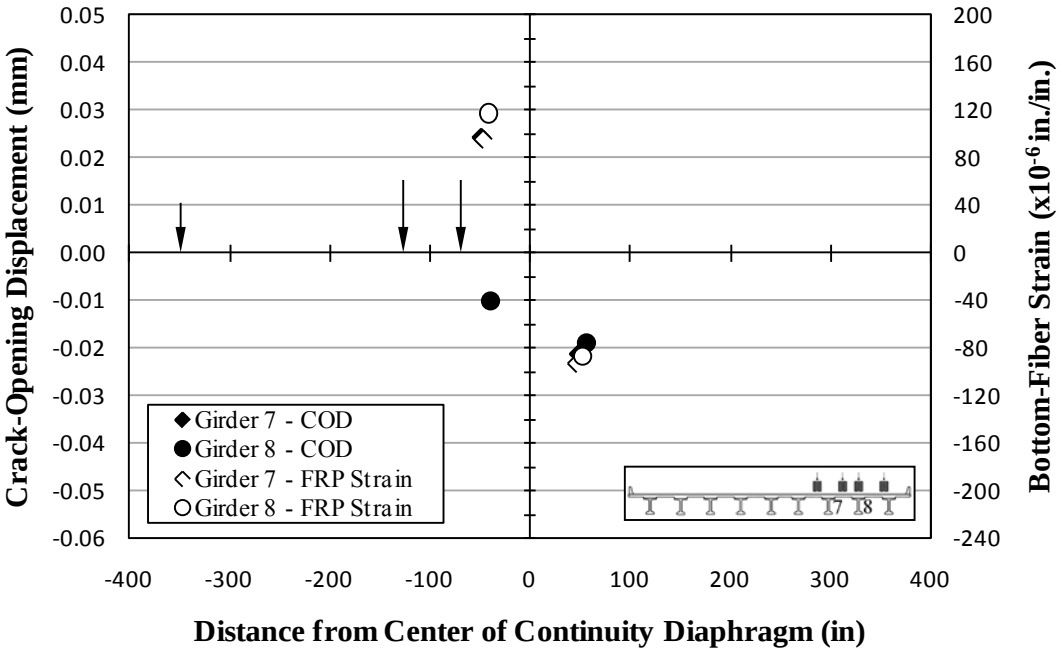

Figure 5.19: COD and bottom-fiber strain comparisons—LC-6.5—AE Span 10

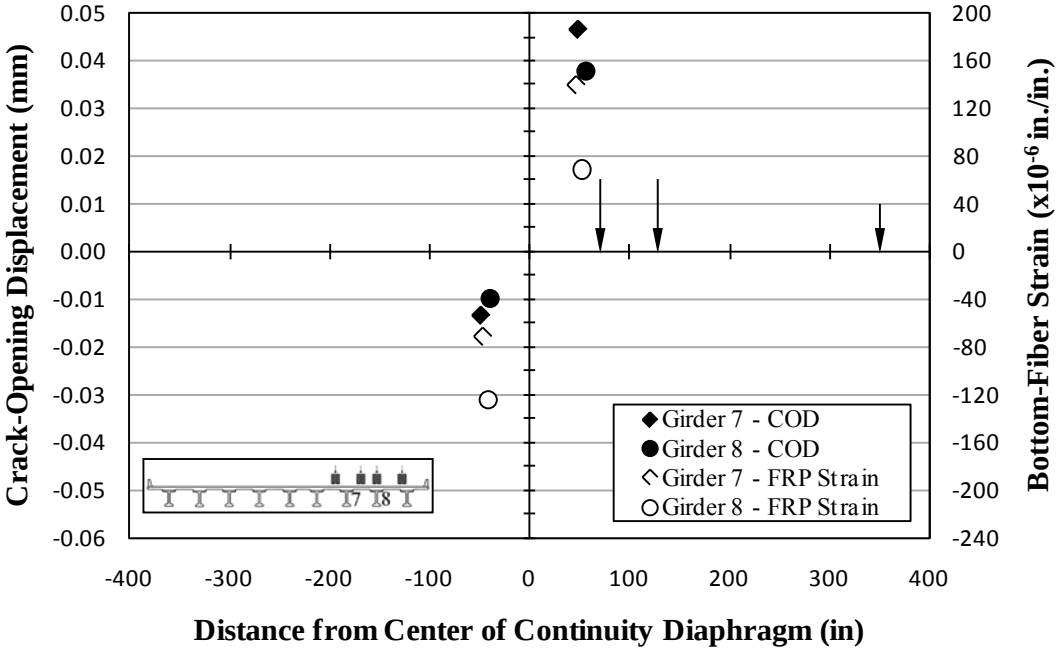

Figure 5.20: COD and bottom-fiber strain comparisons—LC-6.5—AE Span 11

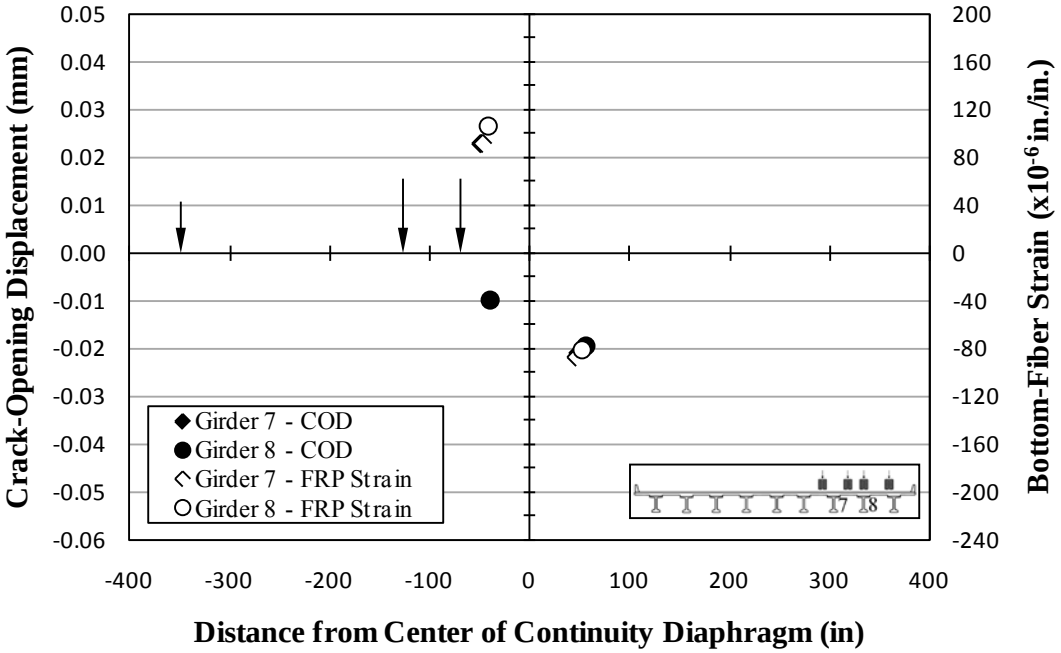

Figure 5.21: COD and bottom-fiber strain comparisons—LC-6—AE Span 10

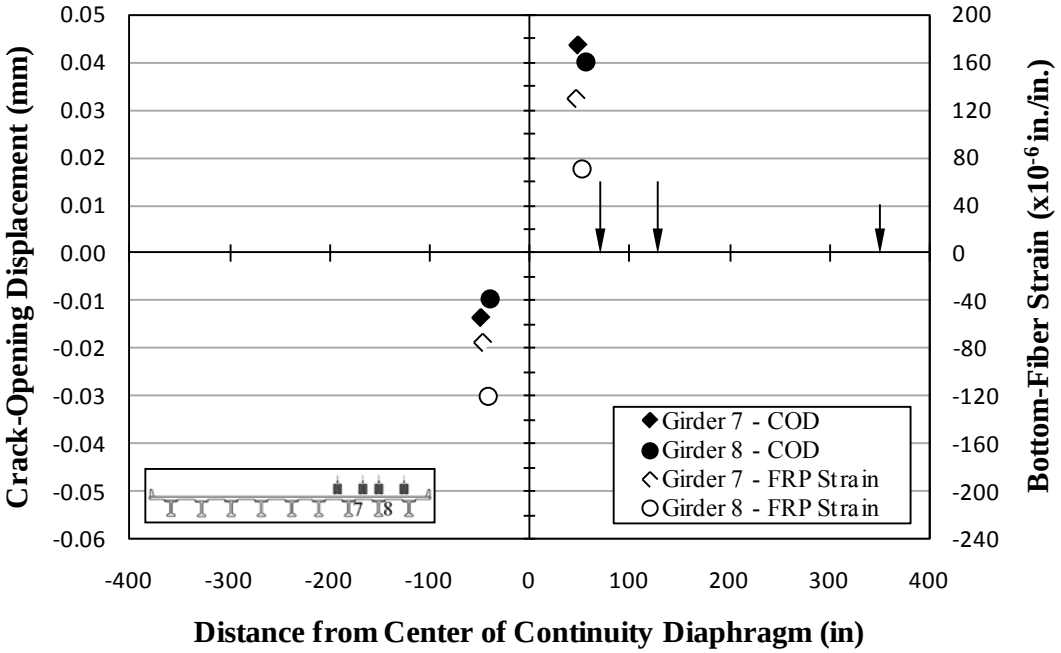

Figure 5.22: COD and bottom-fiber strain comparisons—LC-6—AE Span 11

The COD and near-crack bottom-fiber strain measurements of Girder 8 in Span 10 exhibited contradicting behavior. Crack closure was measured in response to the Span 10 load condition while a near-crack bottom-fiber tensile strain was measured. The tensile strain measured at the Girder 8-Span 10 near-crack strain gage location was similar to the tensile strain

measured at the Girder 7-Span 10 near-crack strain gage location in response to the same Span 10 load condition. The difference between the Girder 8-Span 10 COD gage and the Girder 7-Span 10 COD gage is that the COD gages are installed on opposite girder faces. The combination of similar bottom-fiber strain behavior and conflicting crack-opening displacement behavior for the Girder 8-Span 10 COD gage supports the conclusion that out-of-plane bending behavior has an effect on crack-opening displacements measured during live-load testing—particularly when a wheel load is placed very close to the girder cross section under investigation.

The crack-opening displacement behavior of Girder 8 in Span 11 was similar to the bottom-fiber strain behavior at the crack location of the same girder. Tensile strains were measured when crack-openings were observed, and compressive strains were measured when crack closures were observed. However, the relationship between the bottom-fiber strain and crack-opening displacement for Girder 8-Span 11 was not similar to the relationships observed in Girder 7-Span 11 and Girder 7-Span 10. The bottom-fiber strain gage on Girder 8 of Span 11 measured less tensile strain relative to a respective crack opening when compared to the other two girders. In response to the load conditions resulting in the maximum crack openings for each COD gage, the ratio of crack opening to the near-crack bottom-fiber FRP strain was 250 mm (10 in.) for Girder 7-Span 10, 330 mm (13 in.) for Girder 7-Span 11, and 570 mm (22 in.) for Girder 8-Span 11. These three ratios are an indication that the relationship between crack opening and bottom-fiber tensile strain varies for each damaged region.

One constant for each damaged section is the location of the COD gage within the height of the girder. The distances from the continuity diaphragm are also similar for the damaged section COD and bottom-fiber strain gages. Due to the strain gage application process, one potential difference between each damaged section is the proximity of the bottom-fiber FRP strain gage to the actual crack location. Ideally the FRP strain gage would be installed to straddle the underlying crack in the structural concrete, but the inability to accurately locate cracks underneath the installed FRP reinforcement may have resulted in strain gages being applied near cracks rather than directly at the crack location.

Theoretically, the further a strain gage varies from the actual crack location, the more the tensile strain measured by that strain gage will decrease relative to the measured crack opening. This is because the gage is in a region where the tension is shared between the concrete and FRP, rather than carried solely by the FRP. This theoretical behavior supports the earlier conclusion that the Girder 8-Span 11 near-crack bottom-fiber strain gage was not installed at the desired crack location as accurately as the bottom-fiber strain gages installed at the crack locations of Girder 7 in both Spans 10 and 11.

5.3.2.6 Damage Indication Conclusions

Crack-openings and bottom-fiber tension strains measured in response to AE static positions are indications of damage exhibited by the instrumented girders. The relationships between crack-opening displacement and near-crack bottom-fiber strain supports the conclusion that the installation of the Girder 8-Span 10 COD gage on the opposite face of the girder compared to the other COD gages has an effect on the COD measurements, which is likely attributable to out-of-plane bending as suggested by Fason (2009). These relationships also support the conclusion that the near-crack bottom-fiber strain gage of Girder 8-Span 11 was not accurately installed at the location of the underlying crack.

5.3.3 Post-Repair Continuity Behavior Assessment

Deflections, bottom-fiber strains, and crack-opening displacements were analyzed in response to multiposition load testing to assess the post-repair continuity behavior of the bridge structure. During this continuity assessment, sensor measurements were analyzed in response to live-load static positions at different specified distances from the continuity diaphragm. Details regarding the different truck position locations are given in Section 4.4. Post-repair deflections, bottom-fiber strains, and crack-opening displacements measured in response to the eighteen multiposition load test truck positions (A1–A9 and C1–C9) are presented graphically in Appendix B and in tabular format in Appendix C of this report.

Sensor measurements were also compared to responses predicted using an FEM model of the bridge structure, which was modeled as a continuous structure with an internal hinge representing a primary crack location. Structural responses to four load truck positions (A7, A9, C7, and C9) were predicted using an FEM model of the post-repair bridge structure. Graphical presentations of the predicted responses are presented by Shapiro (2007).

5.3.3.1 Deflections

Deflections measured during post-repair multiposition load testing exhibit continuous behavior for the bridge structure. This behavior is evident due to the upward deflections measured within the non-loaded span. The maximum deflections were measured in response to the midspan load conditions. The deflections measured in response to load trucks traversing Lanes A and C and stopping at the midspan stop positions (Stop Positions 1 and 9) are presented graphically in Figures 5.23–5.26. The summary of deflection measurements due to the midspan static positions is presented in Table 5.6.

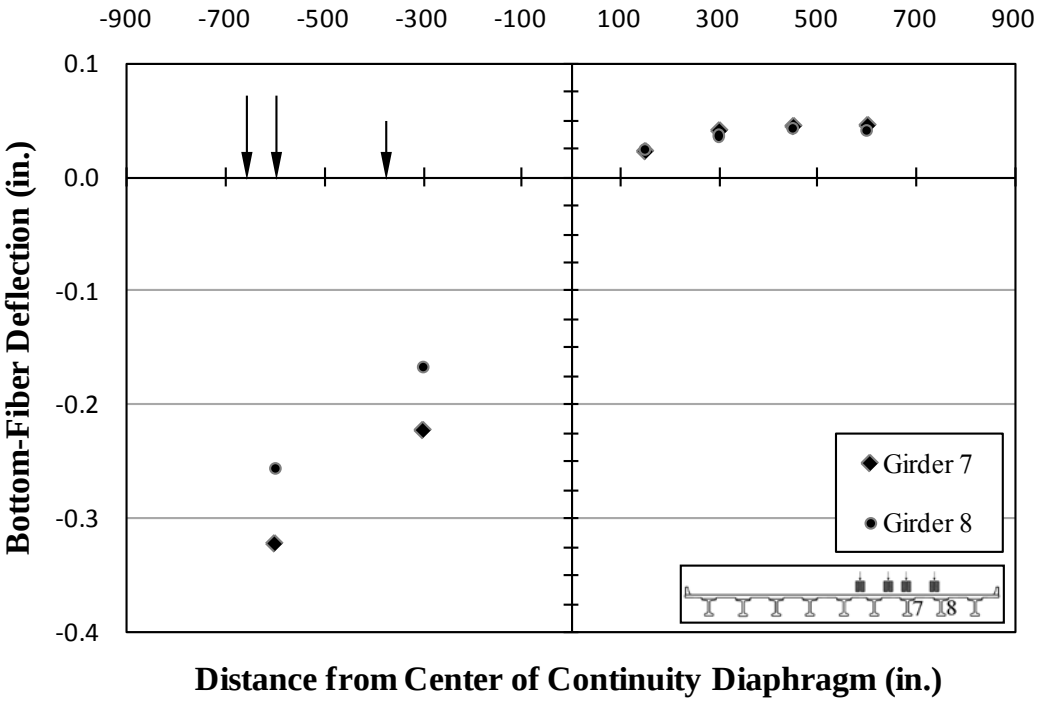

Figure 5.23: Deflections—A1

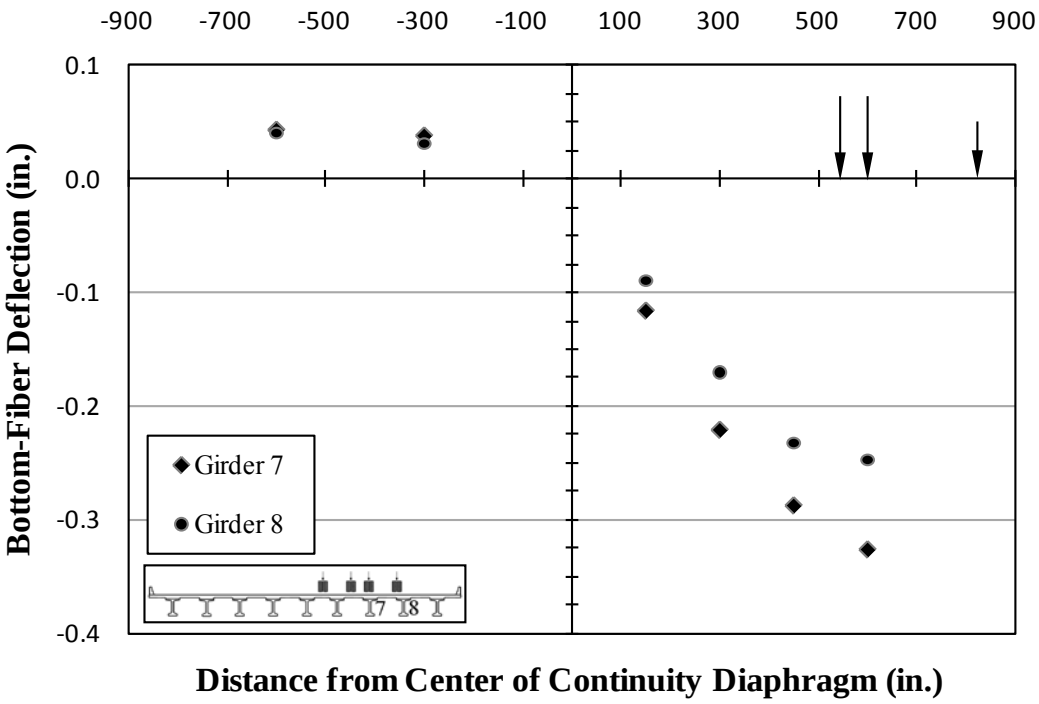

Figure 5.24: Deflections—A9

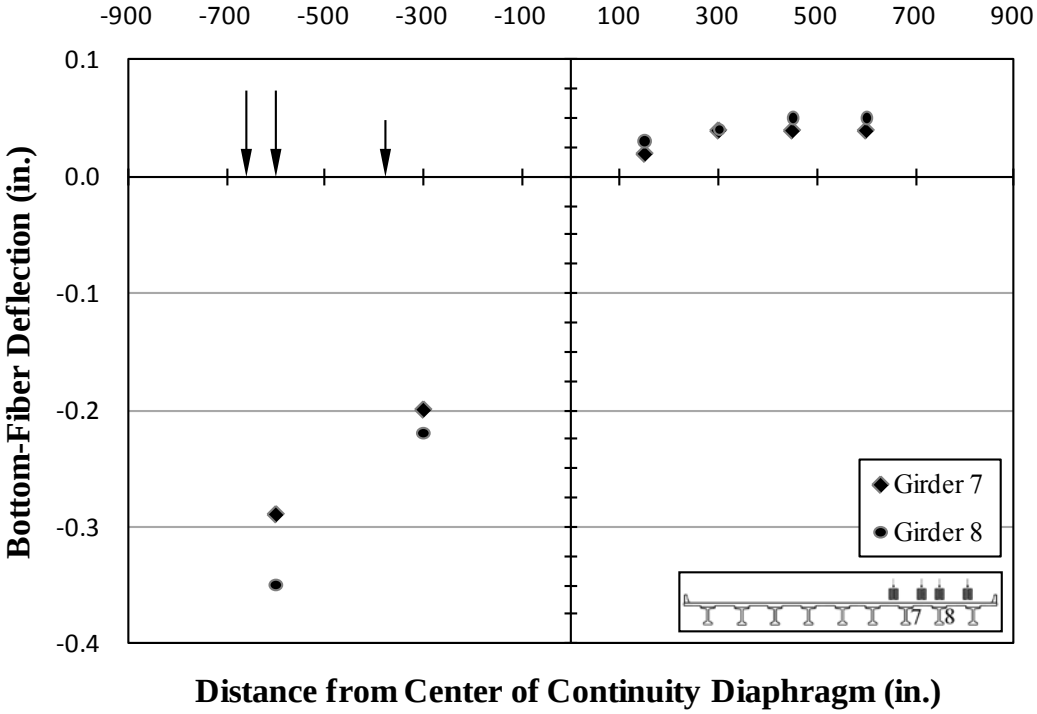

Figure 5.25: Deflections—C1

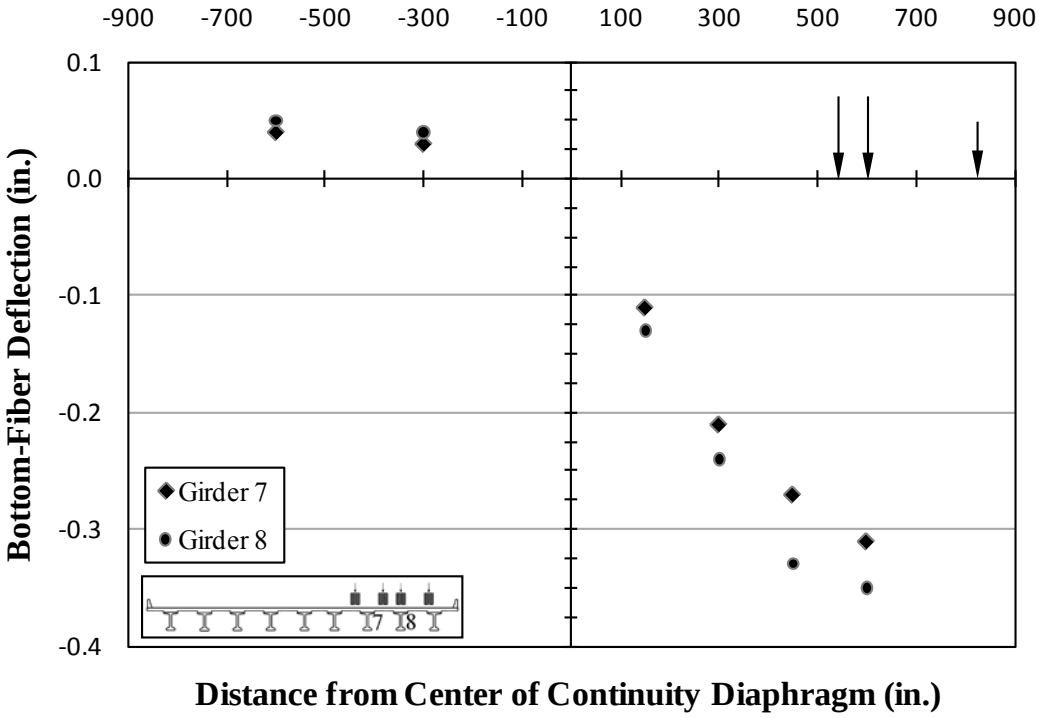

Figure 5.26: Deflections—C9

Table 5.6: Midspan truck positions—deflections

Girder	Span	Location *from continuity diaphragm at Bent 11*	Deflections (in.) – downward + upward			
			A1	A9	C1	C9
7	10	midspan	**-0.32**	0.04	-0.29	0.04
		quarterspan	**-0.22**	0.04	-0.20	0.03
	11	quarterspan	0.04	**-0.22**	0.04	-0.21
		midspan	0.05	**-0.33**	0.04	-0.31
8	10	midspan	-0.26	0.04	**-0.35**	0.05
		quarterspan	-0.17	0.03	**-0.22**	0.04
	11	quarterspan	0.04	-0.17	0.04	**-0.24**
		midspan	0.04	-0.25	0.05	**-0.35**

Note: Measurements presented in **bold** represent the maximum downward deflection per sensor location during the post-repair multiposition load tests

The Span 10 midspan load condition (Stop Position 1) caused downward deflections at Span 10 (loaded span) deflectometer locations, and upward deflections at Span 11 (non-loaded span) deflectometer locations. Similarly, the Span 11 midspan load condition (Stop Position 9) caused downward deflections in Span 11 and upward deflections in Span 10.

A maximum downward deflection of 0.35 in. was measured at the midspan location of Span 11 due to the Span 11 midspan load condition. A maximum upward deflection of 0.05 in. was measured at three different locations due to separate load conditions. The upward deflections due to live loads are an indicator that partial continuity has been preserved.

The continuous behavior indicated by the post-repair deflection measurements was compared to the predicted behavior of the FEM model provided by Shapiro (2007). The post-repair model was constructed to be a continuous structure with an internal hinge representing the typical crack location observed on damaged BT-54 girders of I-565. Comparisons between the measured and predicted behavior are illustrated in Figures 5.27 and 5.28.

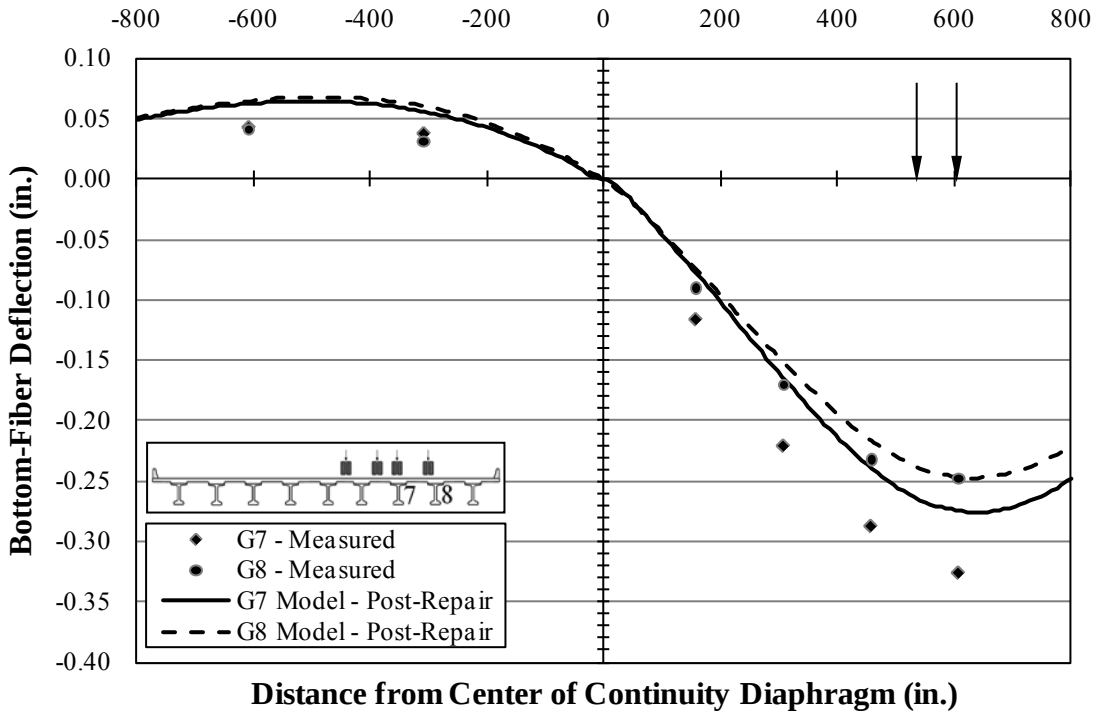

Figure 5.27: Deflections—post-repair—measurements and predictions—A9

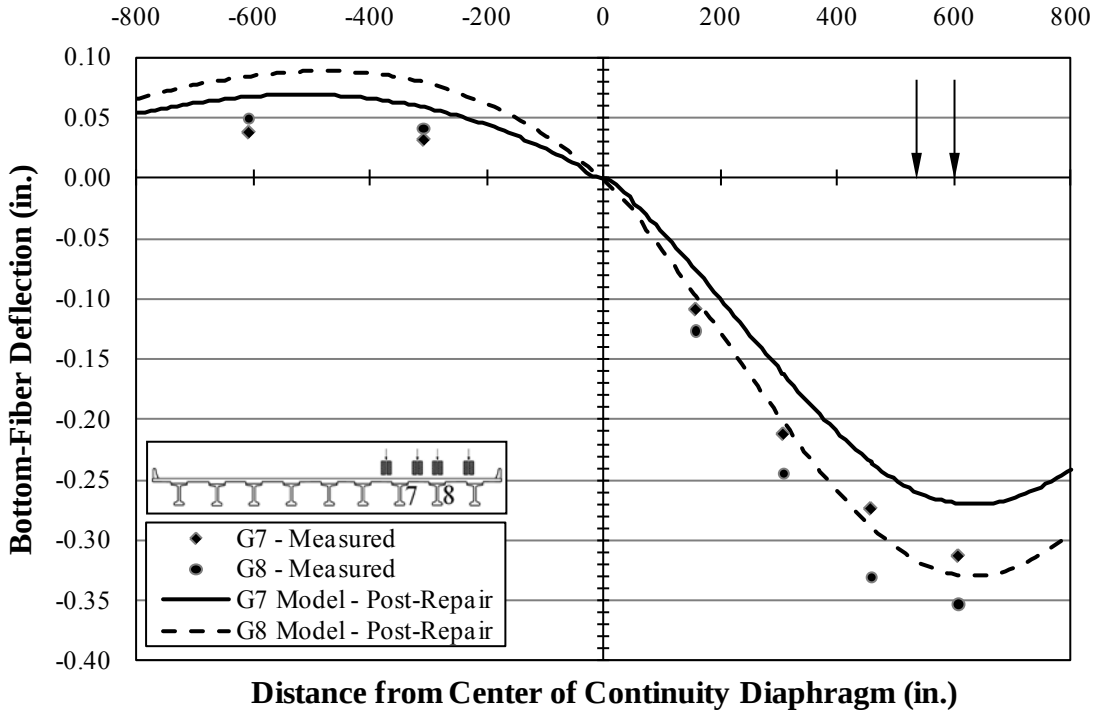

Figure 5.28: Deflections—post-repair—measurements and predictions—C9

Post-repair deflection measurements are an indication that the *modeled* post-repair structure exhibits more apparent stiffness and continuity than the *actual* post-repair structure. The downward deflections measured in the loaded span were greater than the downward deflections predicted. The upward deflections measured in the non-loaded span were less than the upward deflections predicted.

Although the upward deflections measured during the post-repair static load test are signs of continuity, it is evident that the structure is no longer behaving fully continuous under live loads. The damaged sections have an effect on the bridge behavior that, when modeling the structure, could not be accurately accounted for with a seam acting as an internal hinge. The post-repair structure exhibits less continuity behavior in response to live loads than indicated by the post-repair FEM model, which was already modeled to be less continuous than originally constructed.

5.3.3.2 Bottom-Fiber Strains

Bottom-fiber compressive strains measured near the continuity diaphragm in response to live loads are an indicator of continuous behavior. Maximum measured compressive strains were located at the FRP reinforcement near crack locations in response to midspan load conditions. Bottom-fiber strains measured in response to midspan load conditions of Lanes A and C are presented graphically in Figures 5.29–5.32. The summary of bottom-fiber strains measured in response to midspan load conditions is presented in Tables 5.7 and 5.8.

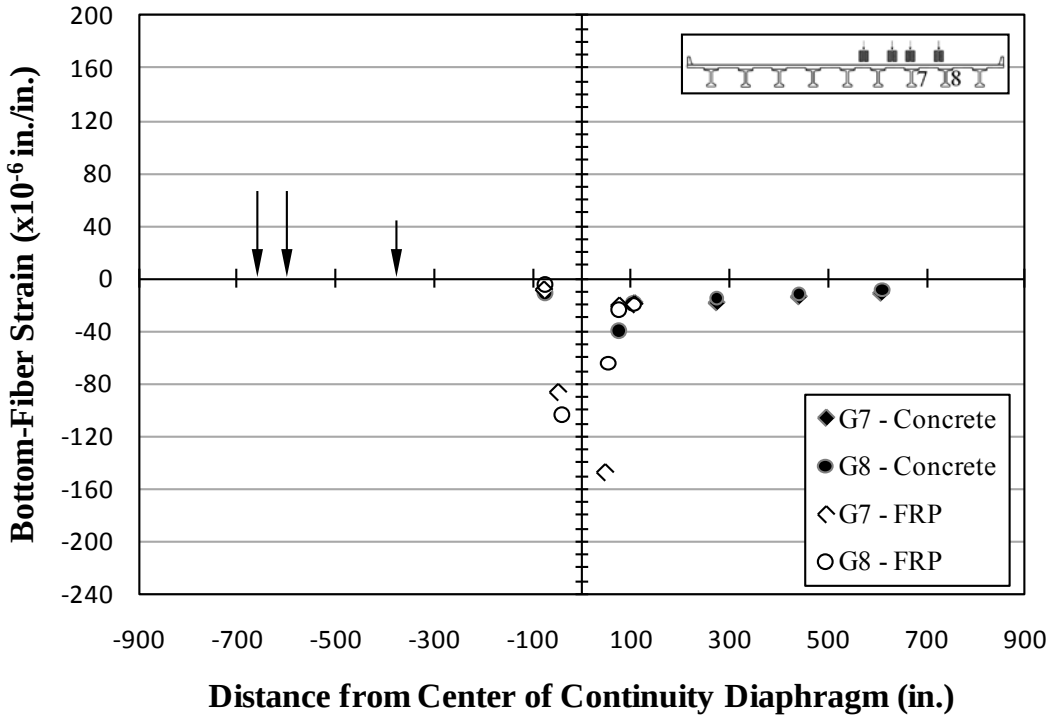

Figure 5.29: Bottom-fiber strain—A1

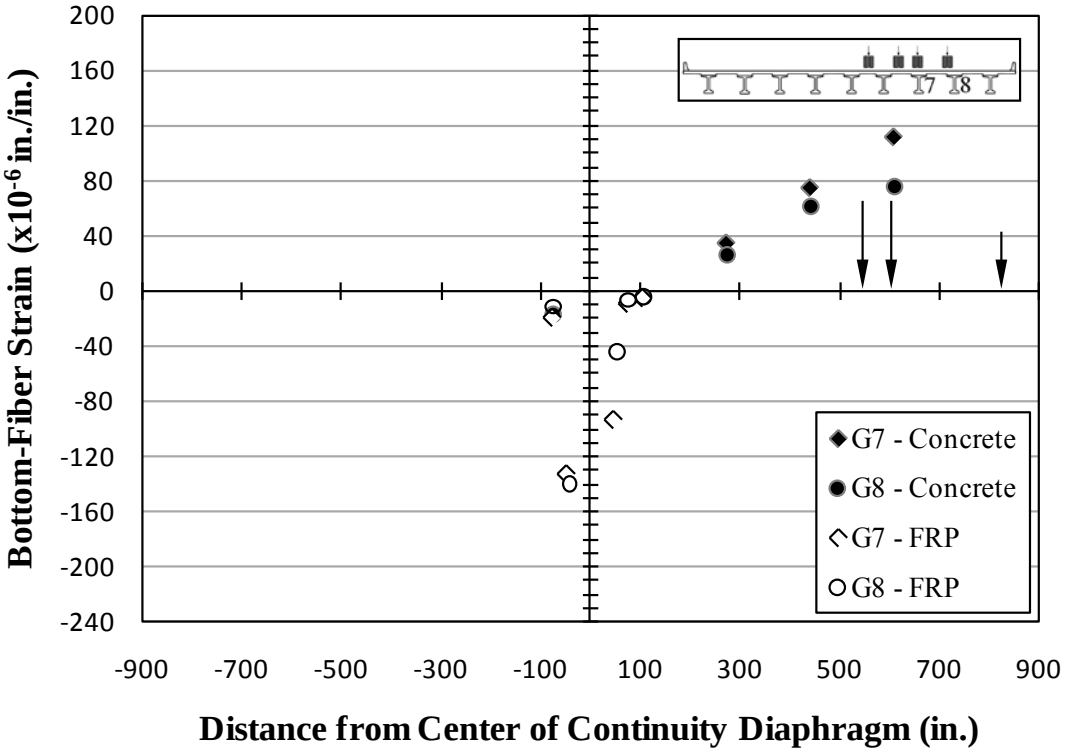

Figure 5.30: Bottom-fiber strain—A9

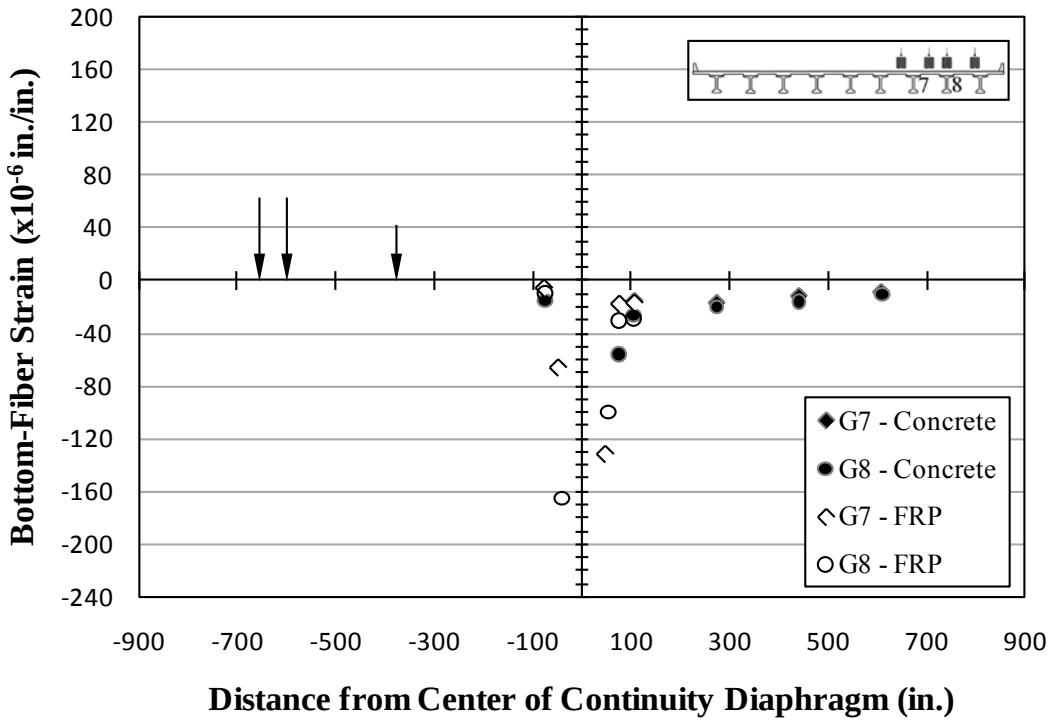

Figure 5.31: Bottom-fiber strain—C1

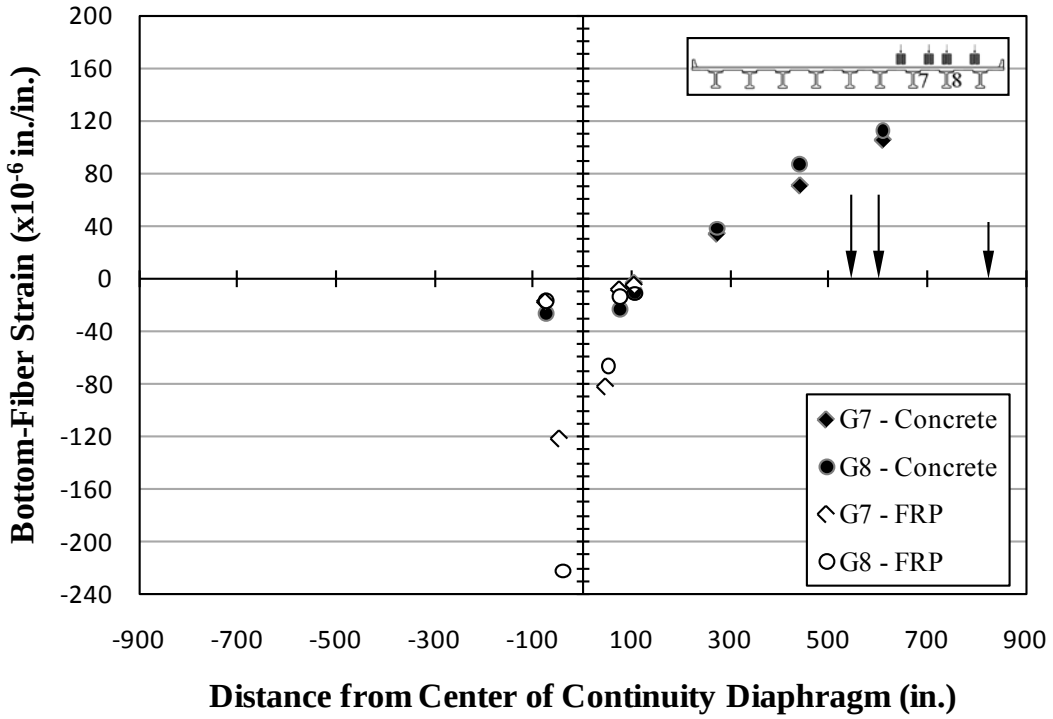

Figure 5.32: Bottom-fiber strain—C9

Table 5.7: Midspan truck positions—bottom-fiber strains—Girder 7

Span	Distance from center of continuity diaphragm (in.) – Span 10 + Span 11	Location Description	Bottom-Fiber Strain ($x10^{-6}$ in./in.) – compressive + tensile			
			A1	A9	C1	C9
10	-74	FRP	-9	**-19**	-6	-17
	-47	FRP-Crack	-87	**-132**	-67	-122
11	47	FRP-Crack	**-148**	-93	-132	-82
	74	FRP	**-21**	-9	-18	-8
	104	FRP	**-18**	-5	-16	-4
	105	Concrete	**-20**	-5	-17	-4
	273	Concrete	**-19**	35	-18	34
	441	Concrete	**-14**	75	-12	71
	609	Concrete	-8	75	**-9**	105

Note: Measurements presented in **bold** represent the maximum compressive strains per gage for the multiposition load test truck positions

Table 5.8: Midspan truck positions—bottom-fiber strains—Girder 8

Span	Distance from center of continuity diaphragm (in.) – Span 10 + Span 11	Location Description	Bottom-Fiber Strain ($x10^{-6}$ in./in.) – compressive + tensile			
			A1	A9	C1	C9
10	-75	Concrete	-11	-17	-15	**-27**
	-74	FRP	-4	-11	-10	**-17**
	-41	FRP-Crack	-104	-139	-165	**-222**
11	52	FRP-Crack	-65	-44	**-100**	-67
	74	FRP	-23	-6	**-31**	-13
	75	Concrete	-39	-7	**-56**	-23
	104	FRP	-20	-4	**-29**	-12
	105	Concrete	-18	-5	**-26**	-11
	273	Concrete	-15	26	**-20**	38
	441	Concrete	-11	61	**-16**	87
	609	Concrete	-8	75	**-10**	113

Note: Measurements presented in **bold** represent the maximum compressive strains per gage for the post-repair multiposition load test truck positions

The maximum bottom-fiber compressive strain measured during the post-repair static load test was 222 x 10^{-6} in./in. at the FRP reinforcement near the crack location of Girder 8 in Span 10 due to the Lane C midspan static position of Span 11. This bottom-fiber compressive response in the non-loaded span is a sign of continuous behavior.

Bottom-fiber tensile strains measured near the continuity diaphragm that are of greater magnitude than tensile strains measured further from the continuity diaphragm are an indicator that the structure is not behaving as a fully continuous structure for live loads as originally constructed. The local behaviors of the damaged sections have an effect on the continuity of the bridge structure. The maximum bottom-fiber tensile strains were measured near the crack-locations in response to the positioning of loads near the damaged regions, which resulted in significant shear demand within the damaged region and positive bending moment at respective bottom-fiber crack locations. Bottom-fiber strains measured in response to four load conditions (A4, A7, C4, and C7) positioning trucks near the damaged regions are presented in Figures 5.33–5.36. The summary of bottom-fiber strains measured in response to these load conditions with trucks near the damaged sections is presented in Tables 5.9 and 5.10

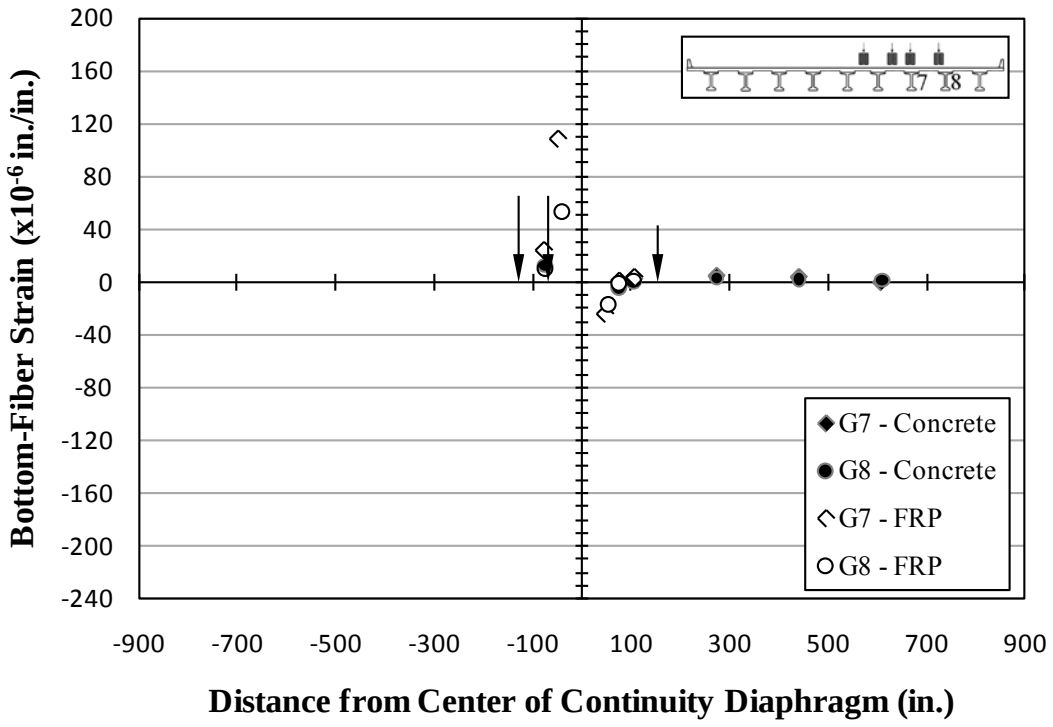

Figure 5.33: Bottom-fiber strain—A4

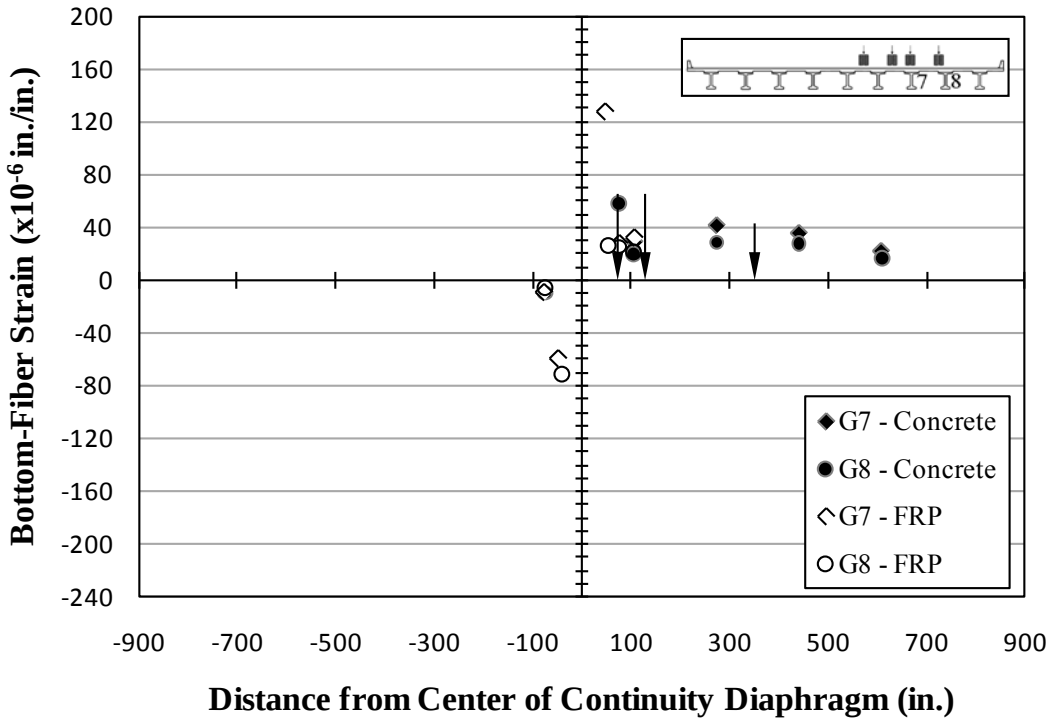

Figure 5.34: Bottom-fiber strain—A7

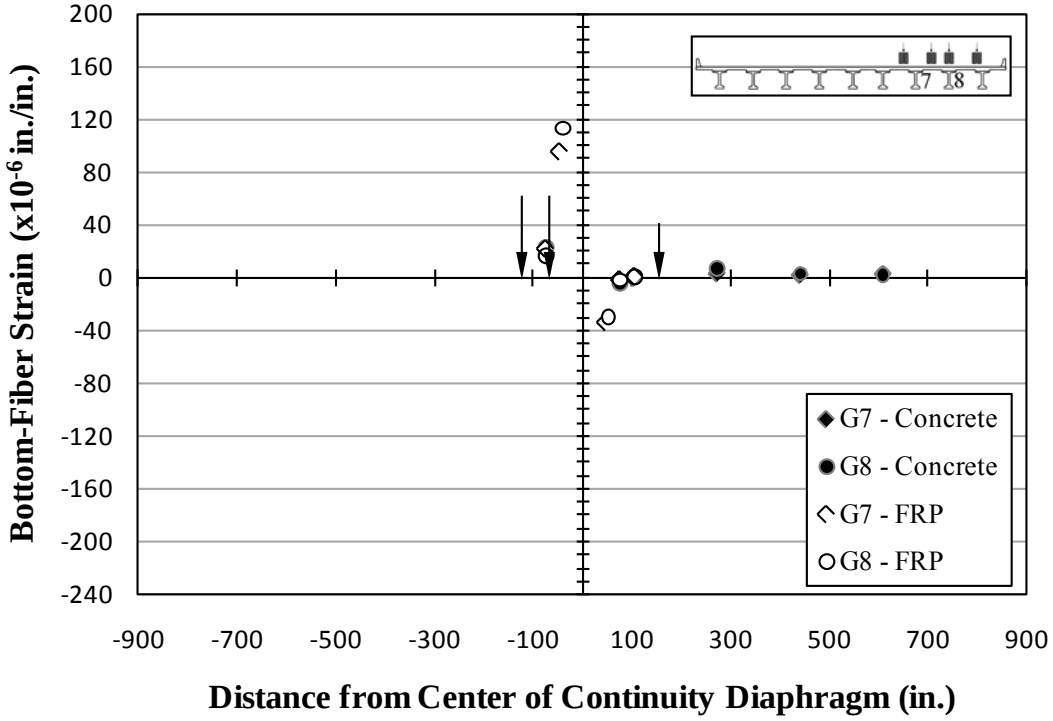

Figure 5.35: Bottom-fiber strain—C4

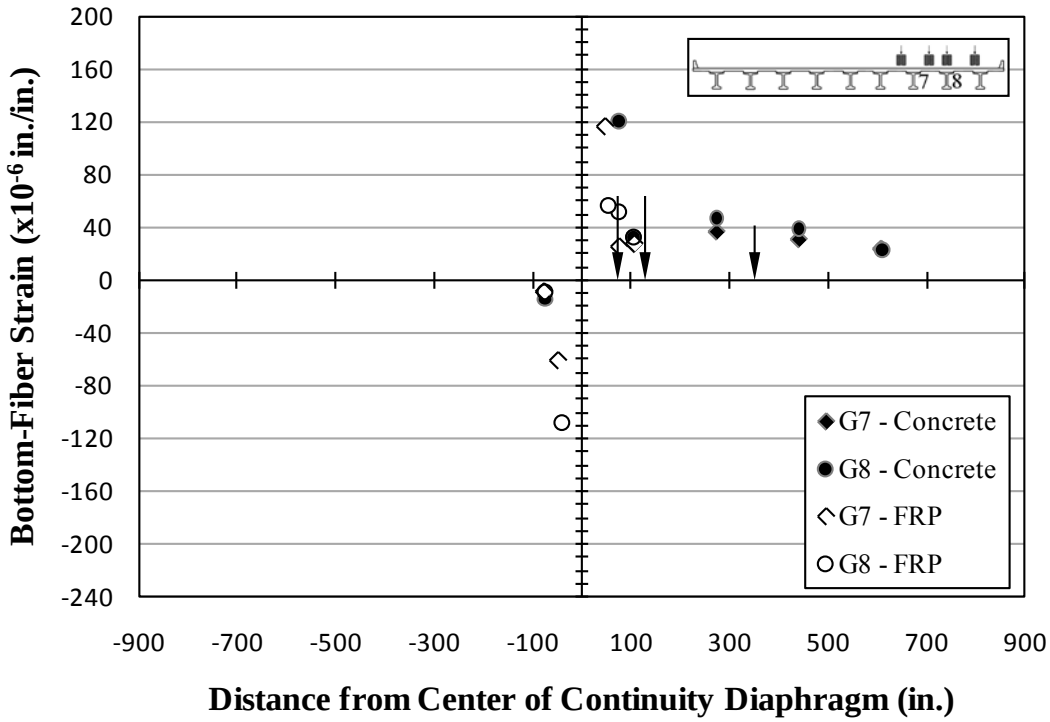

Figure 5.36: Bottom-fiber strain—C7

Table 5.9: Damaged region truck positions—bottom-fiber strains—Girder 7

Span	Distance from center of continuity diaphragm (in.) – Span 10 + Span 11	Location Description	Bottom-Fiber Strain ($x10^{-6}$ in./in.) – compressive + tensile			
			A4	A7	C4	C7
10	-74	FRP	**23**	-9	22	-8
	-47	FRP-Crack	**108**	-60	95	-60
11	47	FRP-Crack	-25	**128**	-34	116
	74	FRP	0	**28**	-2	25
	104	FRP	2	**29**	0	27
	105	Concrete	3	**32**	1	28
	273	Concrete	4	**42**	3	37
	441	Concrete	4	**36**	2	31
	609	Concrete	1	16	3	**24**

Note: Measurements presented in **bold** represent the maximum tensile strains per gage for the post-repair multiposition load test truck positions

Table 5.10: Damaged region truck positions—bottom-fiber strains—Girder 8

Span	Distance from center of continuity diaphragm (in.) – Span 10 + Span 11	Location Description	Bottom-Fiber Strain ($x10^{-6}$ in./in.) – compressive + tensile			
			A4	A7	C4	C7
10	-75	Concrete	13	-9	**23**	-14
	-74	FRP	10	-6	**16**	-9
	-41	FRP-Crack	53	-71	**113**	-108
11	52	FRP-Crack	-17	27	-30	**56**
	74	FRP	-4	58	-4	**121**
	75	Concrete	-1	25	-2	**52**
	104	FRP	1	20	1	**32**
	105	Concrete	1	22	1	**32**
	273	Concrete	3	28	7	**46**
	441	Concrete	2	27	3	**39**
	609	Concrete	1	16	2	**24**

Note: Measurements presented in **bold** represent the maximum tensile strains per gage for the post-repair multiposition load test truck positions

The maximum bottom-fiber tensile strain measured in response to the eighteen post-repair traversing-load-test truck positions was 128 x 10^{-6} in./in. near the crack location 47 in. from the continuity diaphragm along Girder 7 of Span 11 in response to trucks aligned with Lane A and positioned near the damaged section (A7). A bottom-fiber tensile strain of 28 x 10^{-6} in./in. was measured 74 in. from the continuity diaphragm along the same girder and in response to the same load condition. This bottom-fiber tensile response near the continuity diaphragm is a sign of local behavior that decreases the overall continuity of the bridge structure.

Measured bottom-fiber strains have also been compared to strains predicted by the post-repair model provided by Shapiro. The comparisons between measured and predicted bottom-fiber strains are illustrated in Figures 5.37–5.40.

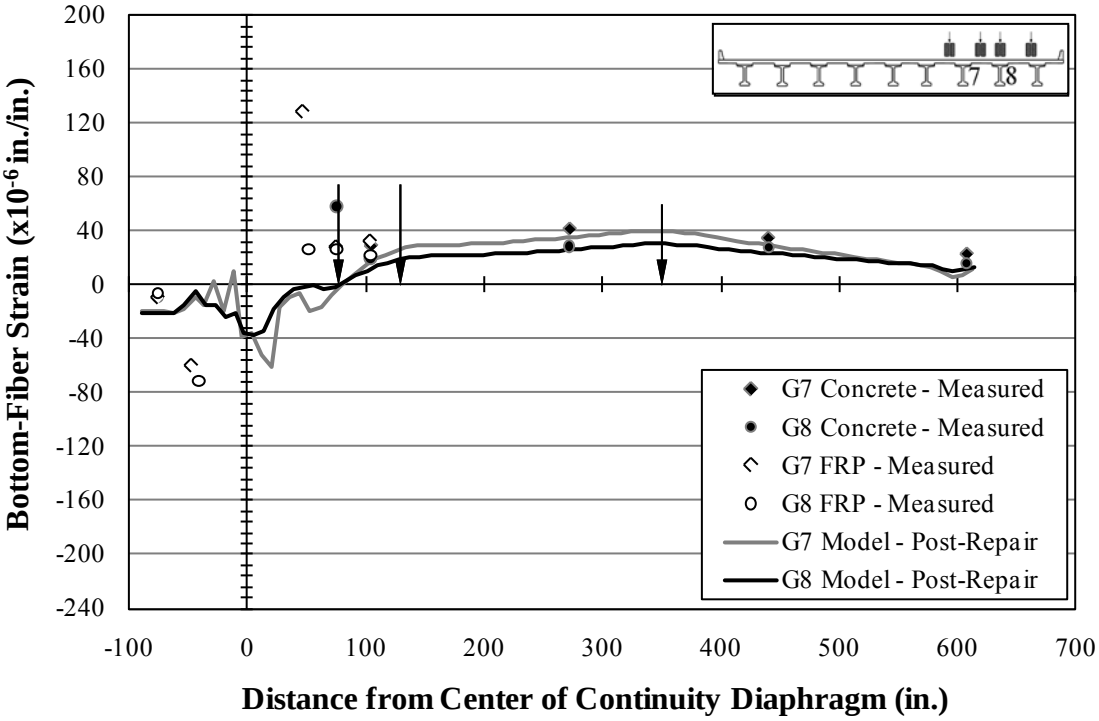

Figure 5.37: Bottom-fiber strain—post-repair—measurements and predictions—A7

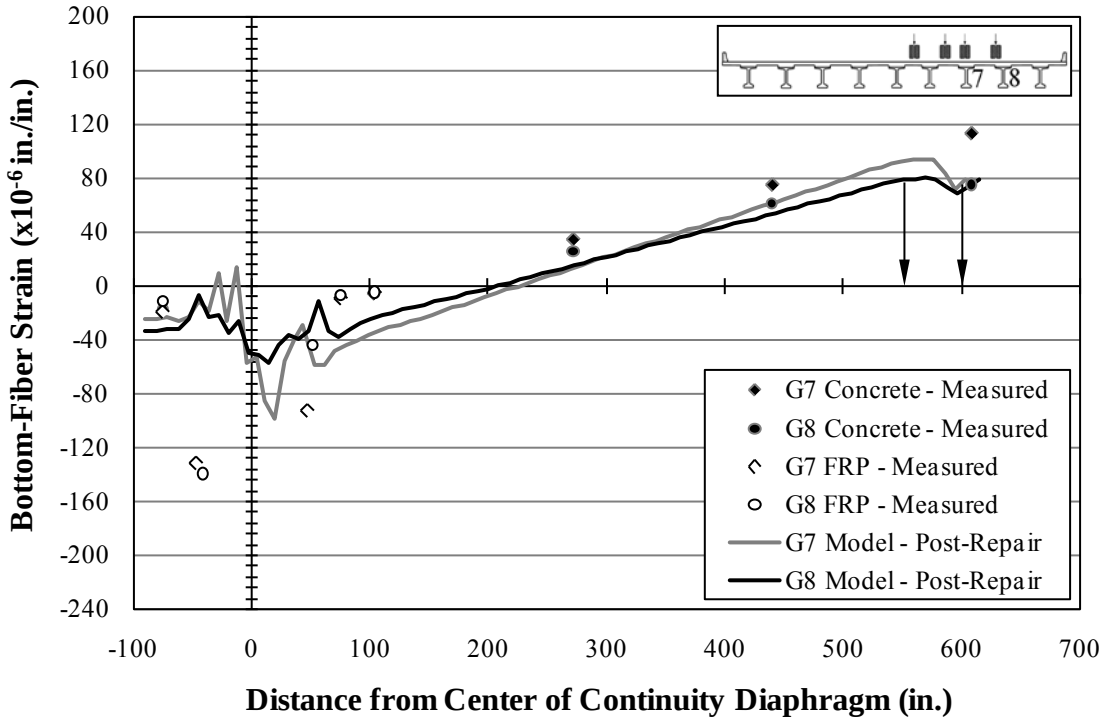

Figure 5.38: Bottom-fiber strain—post-repair—measurements and predictions—A9

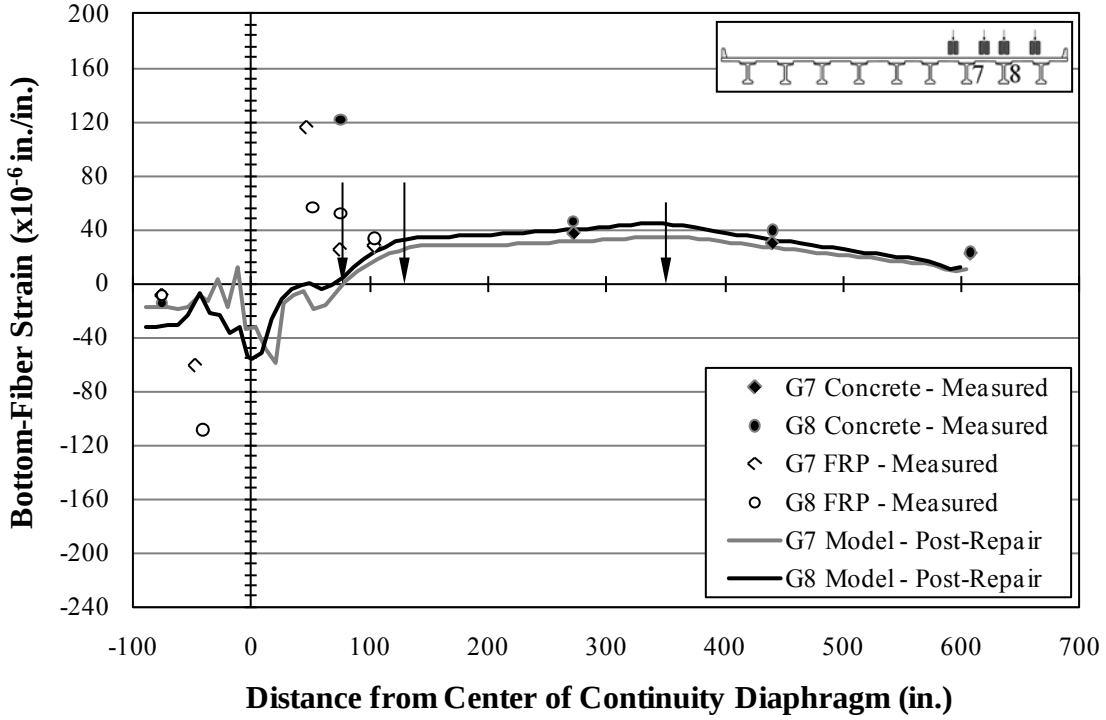

Figure 5.39: Bottom-fiber strain—post-repair—measurements and predictions—C7

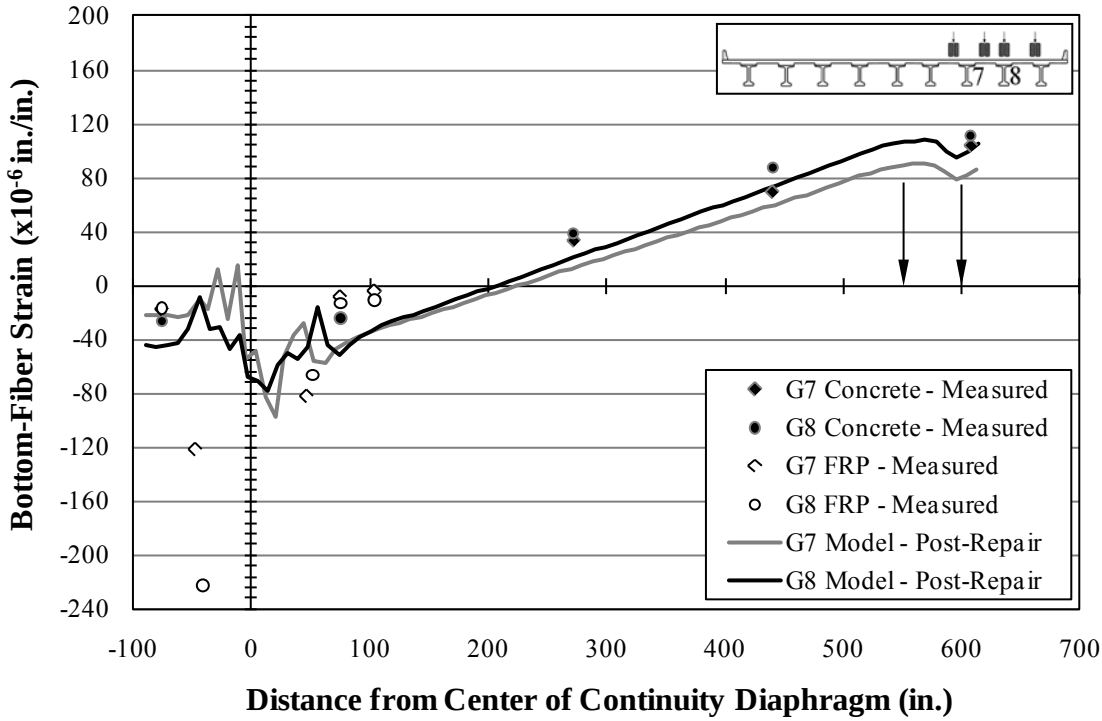

Figure 5.40: Bottom-fiber strain—post-repair—measurements and predictions—C9

Bottom-fiber strains measured beyond the damaged regions were similar to the predicted strains, but they were slightly more tensile. This is an indicator that the bridge structure is behaving continuously, but with slightly less apparent stiffness than modeled. The measured bottom-fiber strains near the damaged region were not similar to the predicted strains. When the trucks were positioned near the damaged regions of Span 11, the bottom-fiber strains measured near the crack locations of Span 11 were more tensile than predicted. When the trucks were positioned near midspan of Span 11, the bottom-fiber strains measured near the crack locations of Span 10 were more compressive than predicted.

Although bottom-fiber strains measured during the post-repair static load test exhibit some continuity, it is evident that the structure is no longer behaving as if fully continuous for post-construction loads. The damaged sections have an effect on the bridge behavior that could not be accurately modeled. This damaged section behavior results in the instrumented girders exhibiting less apparent stiffness than assumed by the post-repair FEM model developed by Shapiro (2007).

5.3.3.3 Crack Behavior

Crack closures measured near the continuity diaphragm, particularly within a non-loaded span, are an indicator of continuous behavior. The maximum post-repair crack closures were

measured in response to the midspan load conditions. Crack-opening displacements measured in response to four midspan load conditions (A1, C1, A9 and C9) are presented graphically in Figures 5.41–5.44. The summary of crack-opening displacements measured in response to the four midspan load conditions is presented in Table 5.11.

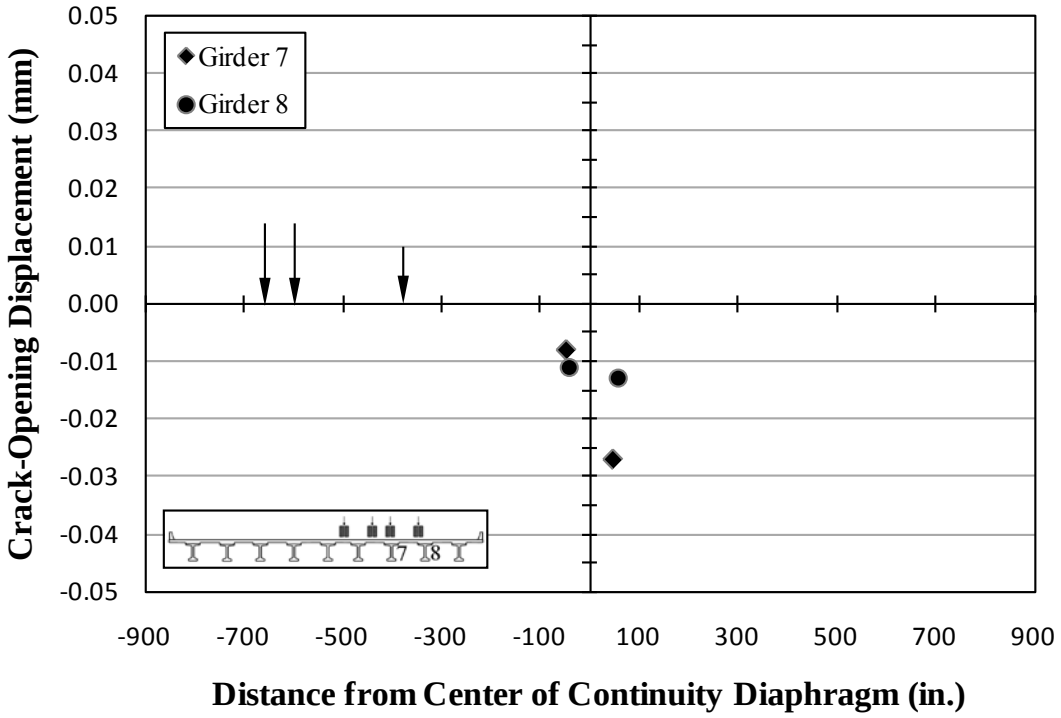

Figure 5.41: Midspan truck positions—crack-opening displacements—A1

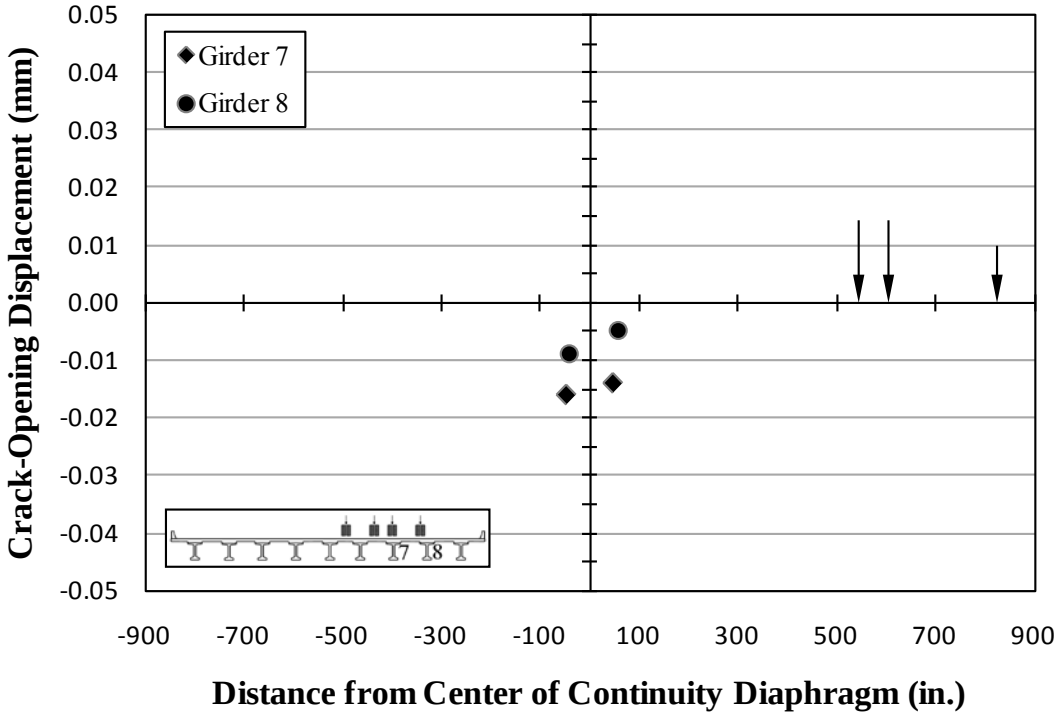

Figure 5.42: Midspan truck positions—crack-opening displacements—A9

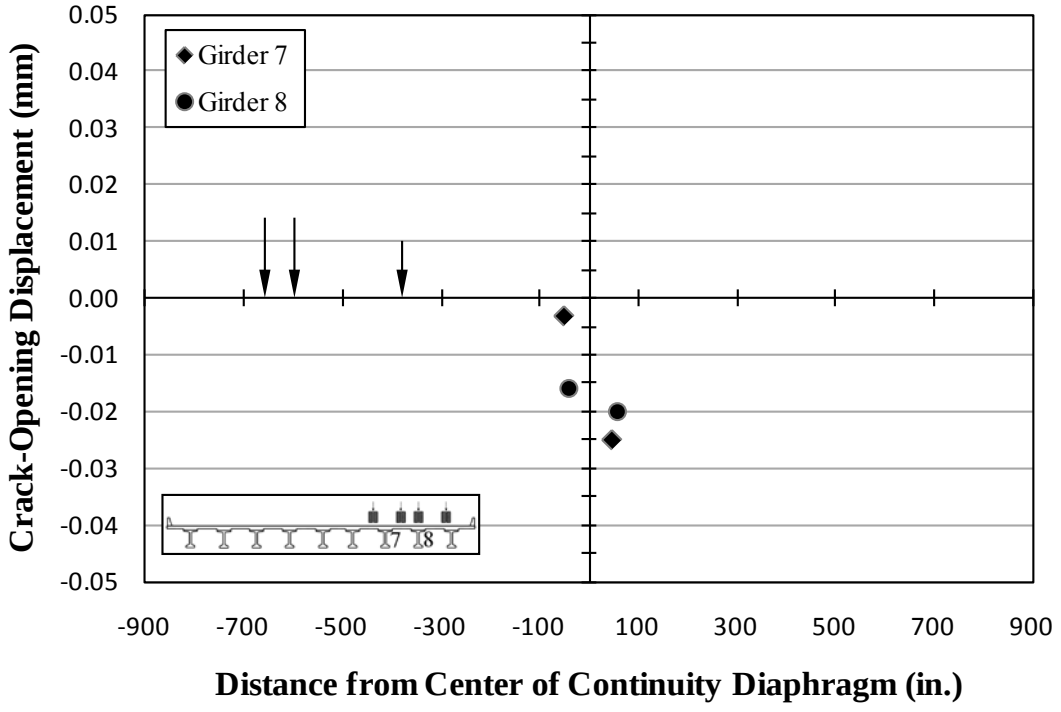

Figure 5.43: Midspan truck positions—crack-opening displacements—C1

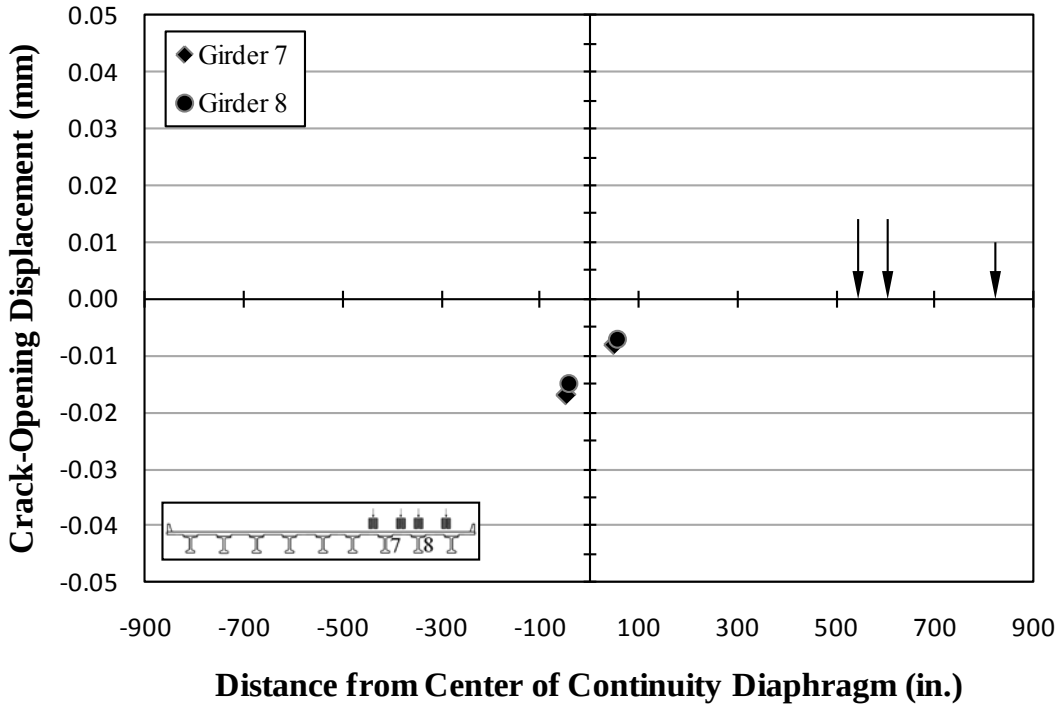

Figure 5.44: Midspan truck positions—crack-opening displacements—C9

Table 5.11: Midspan truck positions—maximum crack closures

Girder	Span	Crack-Opening Displacement (mm) – closing + opening			
		A1	A9	C1	C9
7	10	-0.008	-0.016	-0.003	**-0.017**
	11	**-0.027**	-0.014	-0.025	-0.008
8	10	-0.011	-0.009	**-0.016**	-0.015
	11	-0.013	-0.005	**-0.020**	-0.007

Notes: Measurements presented in **bold** represent the maximum crack closure per gage measured during the post-repair multiposition load tests
1 in. = 25.4 mm

Crack closures were measured at all of the COD gage locations in response to all four midspan truck positions of the post-repair traversing load test. The maximum crack closure measured during the post-repair traversing load test was 0.027 mm (1.08 x 10^{-3} in.) at the crack location of Girder 7 in Span 11 in response to the Lane A midspan load condition of Span 10 (A1). The maximum crack closure of Span 10 was 0.017 mm (0.65 x 10^{-3} in.) at the crack

location of Girder 7 in response to the Lane C midspan load condition of Span 11 (C9). Crack closures measured at damaged regions of both spans in response to midspan truck positions are signs of continuous behavior being partially preserved as well as decreased local apparent stiffness.

Midspan load conditions were the only load conditions of the post-repair static load test that did not result in the measurement of at least one crack opening. Maximum crack openings were measured in response to truck positions near gaged crack locations, which are the truck positions that cause the greatest shear demand within the damaged region. Crack-opening displacements measured in response to load trucks positioned near gaged damaged regions are presented graphically in Figures 5.45–5.48. The summary of crack-opening displacements measured in response to load trucks positioned near gaged damaged regions is presented in Table 5.12.

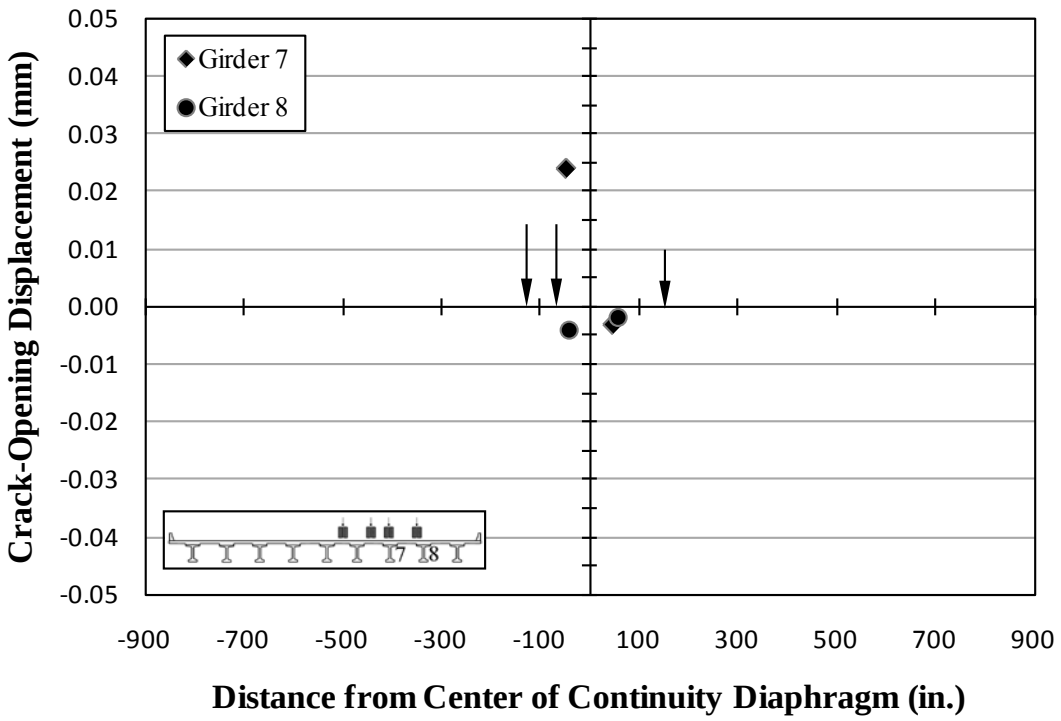

Figure 5.45: Damaged region truck positions—crack-opening displacements—A4

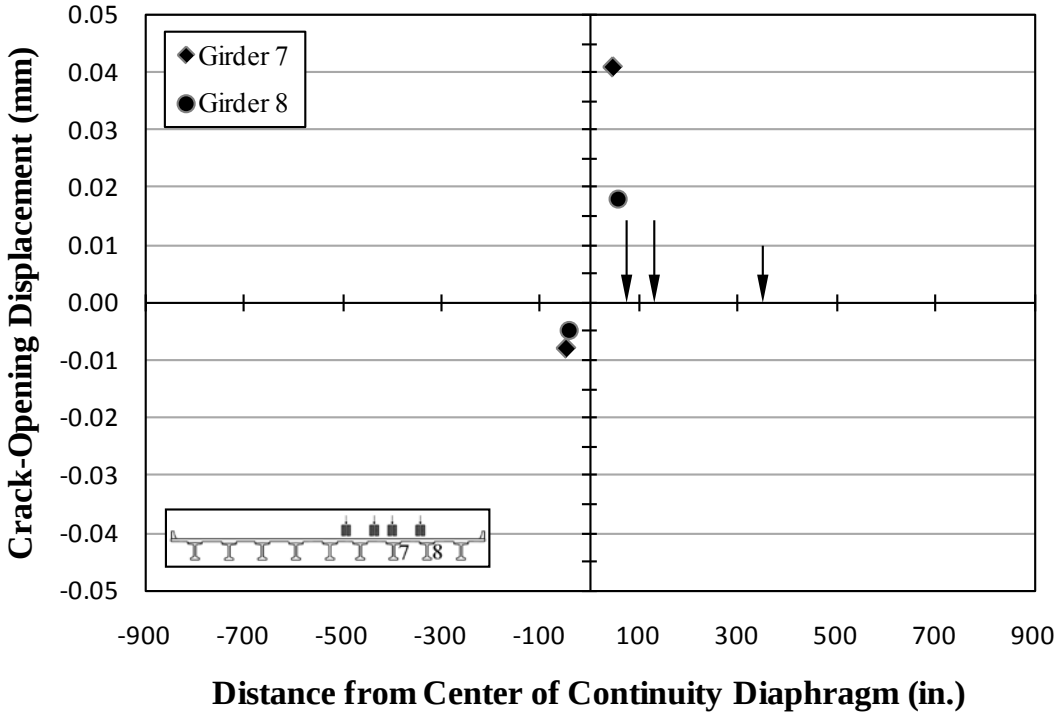

Figure 5.46: Damaged region truck positions—crack-opening displacements—A7

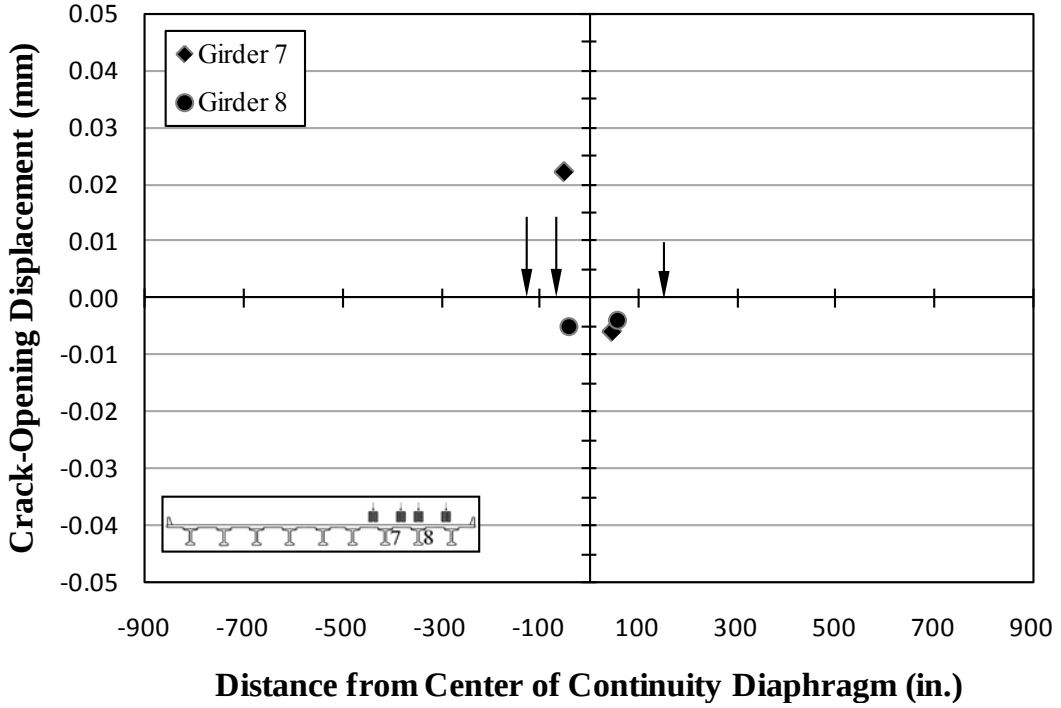

Figure 5.47: Damaged section truck positions—crack-opening displacements—C4

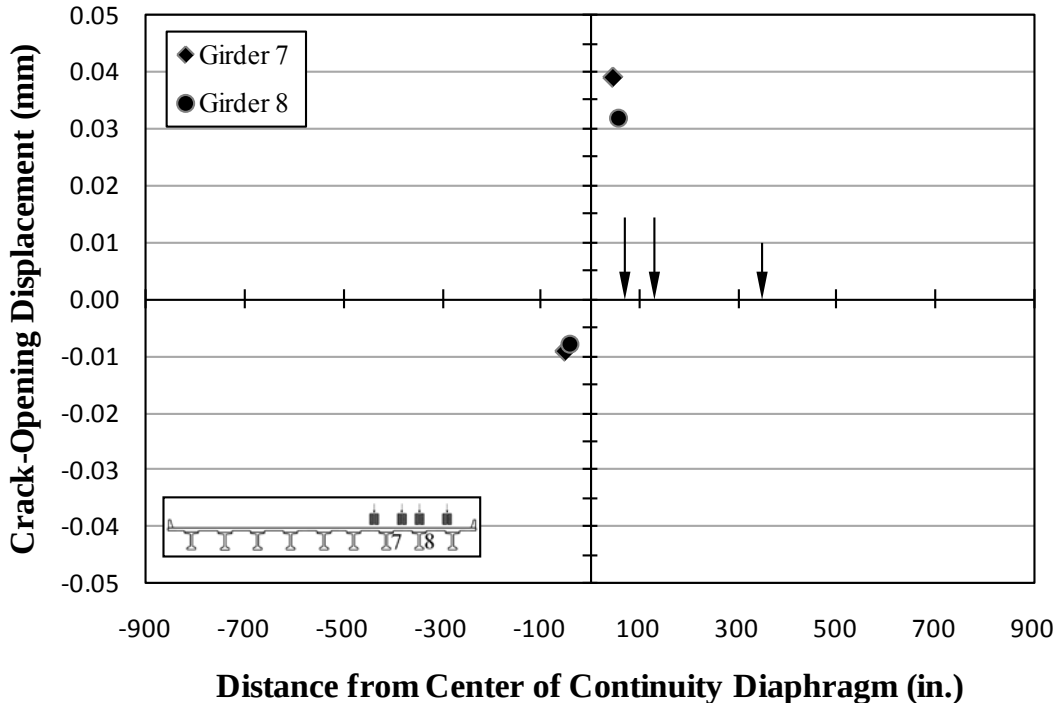

Figure 5.48: Damaged region truck positions—crack-opening displacements—C7

Table 5.12: Damaged region truck positions—maximum crack openings

Girder	Span	Crack-Opening Displacement (mm) – closing + opening			
		A4	A7	C4	C7
7	10	**0.024**	-0.008	0.022	-0.009
	11	-0.003	**0.041**	-0.006	0.039
8	10	-0.004	-0.005	-0.005	-0.008
	11	-0.002	0.018	-0.004	**0.032**

Notes: Measurements presented in **bold** represent the maximum crack opening measured per gage during the post-repair multiposition load tests
1 in. = 25.4 mm

The maximum crack opening measured during the post-repair traversing load test was 0.041 mm (1.62 x 10^{-3} in.) at the crack location of Girder 7 in Span 11 in response to the Lane A load condition with trucks near the Span 11 damaged sections (A7). The maximum Span 10 crack opening measured was 0.024 mm (0.95 x 10^{-3} in.) at the crack location of Girder 7 in Span 10 in response to the Lane A load condition with trucks near the Span 10 damaged sections

(A4). Crack openings measured within a loaded span are also signs of decreased apparent stiffness within damaged regions.

The COD gage installed on the west face of Girder 8 in Span 10 did not measure a crack opening in response to any of the traversing-load-test stop positions. For the COD gage of Girder 8 in Span 10, the maximum crack opening (least crack closure) measured during the traversing load test was a closure of 0.002 mm (0.07 x 10^{-3} in.) in response to trucks being aligned with Lane C and positioned near the continuity diaphragm (C5).

As stated previously, the COD gage on Girder 8 in Span 10 was installed on the opposite face of the girder compared to the other COD gages and likely does not accurately represent behavior similar to what is being measured by the other COD gages. This different behavior for the crack-opening displacement measurements of Girder 8 in Span 10 is likely due to out-of-plane bending as noted by Fason (2009).

Regardless of the cause of behavior for the COD gage on Girder 8 of Span 10, the crack-opening displacements measured at the other three crack locations are indications that the bridge structure is exhibiting overall continuous behavior that cannot be considered fully continuous for post-construction loads due to the local behavior of damaged regions.

5.3.3.4 Continuity Behavior Conclusions

Upward deflections of non-loaded spans during post-repair testing are indications that continuity in response to post-construction loads has been partially preserved for the bridge structure. However, further analysis of post-repair deflection measurements and model predictions has provided evidence that the structure is behaving less continuously in response to post-construction loads than assumed by the post-repair FEM model, which was already modeled to be less continuous than originally constructed.

Compressive strains measured within non-loaded spans during post-repair testing are additional indications that continuity is partially preserved for the bridge structure. However, tensile strains measured near the continuity diaphragm in loaded spans are additional indications that the structure is not behaving as a fully continuous structure in response to live loads as originally constructed.

Crack closures measured within non-loaded spans during post-repair testing are additional indications that continuity has been partially preserved for the bridge structure. However, crack openings measured within loaded spans are additional indications that the structure is not behaving as a fully continuous structure in response to live loads as originally constructed.

Based on the behaviors observed within damaged regions as well as the decrease in apparent stiffness and continuity compared to the post-repair FEM model, it is appropriate to assume that increased damage may further reduce the apparent stiffness and continuity behavior

of the bridge structure. It is recommended to assume complete degradation of continuity in response to strength-limit-state demands. Thus, an assumption of simply supported girder behavior is recommended for the design of repair solutions for bridge structures containing girders with damage at continuous ends. Decreased continuity behavior will decrease the shear demand, but will also decrease the shear resistance provided by negative bending moments.

5.3.4 Linear-Elastic Behavior

Superposition test measurements were analyzed to assess if the bridge structure is exhibiting linear-elastic behavior. During analysis, general behavior of the bridge structure and local behavior of the damaged sections were considered. Bridge responses were measured while two load-test trucks were independently positioned at midspan locations of both spans. Bridge responses were also measured while the load-test trucks were simultaneously positioned at those same respective locations. More details regarding superposition test procedures are given in Section 4.8 of this report.

Theoretically, a structure exhibits linear-elastic behavior if the sum of the measured responses representing both trucks at their respective positions independently is equal to the actual measured response representing both trucks at their respective positions simultaneously. The measurements for the post-repair superposition test can be found presented graphically in Appendix G and in a tabular format in Appendix H of this report.

5.3.4.1 Linear-Elastic Behavior Assessment—Two-Span Structure

Deflections measured during the post-repair superposition test were analyzed to assess the general behavior of the bridge structure. The predicted and measured superposition deflections are illustrated in Figure 5.49. The differences between the predicted and measured superposition deflections are presented in Table 5.13.

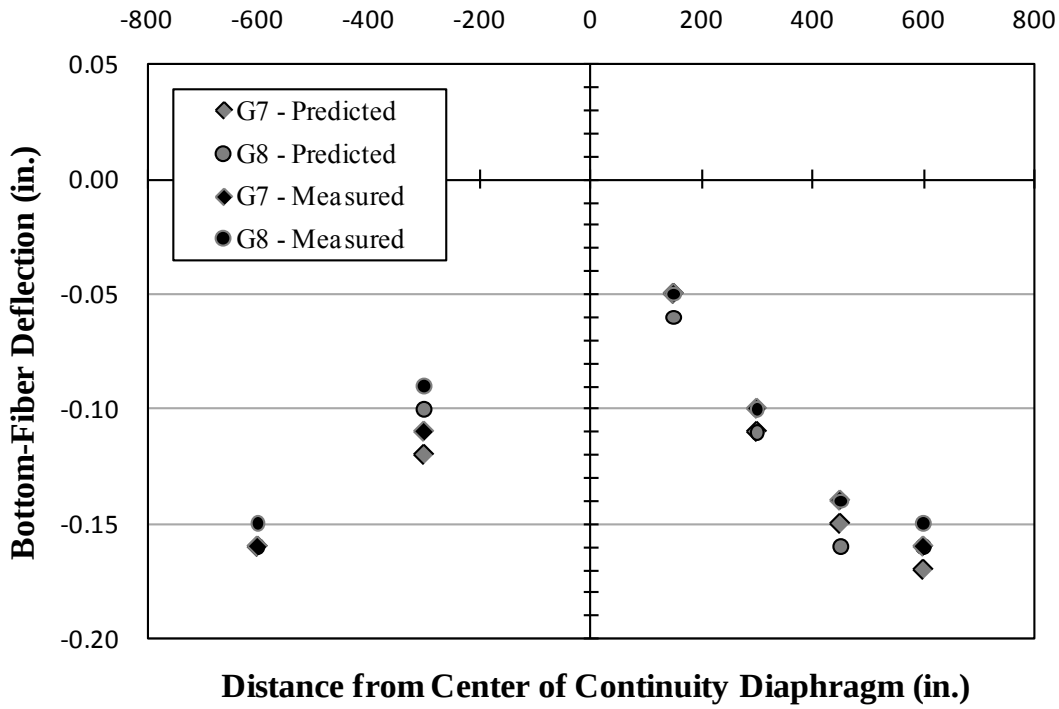

Figure 5.49: Superposition—deflections—predicted and measured

Table 5.13: Superposition—deflections

Girder	Span	Location *from Bent 11*	Superposition Deflections (in.) – downward + upward		Difference (Pred.–Meas.)	
			Predicted (A1 + A9)	Measured (A1 & A9)	in.	%
7	10	midspan	-0.16	-0.16	0.00	0
		quarterspan	-0.12	-0.11	-0.01	-9
	11	quarterspan	-0.11	-0.10	-0.01	-10
		midspan	-0.17	-0.16	-0.01	-6
8	10	midspan	-0.16	-0.15	-0.01	-7
		quarterspan	-0.10	-0.09	-0.01	-10
	11	quarterspan	-0.11	-0.10	-0.01	-10
		midspan	-0.16	-0.15	-0.01	-7

Note: Percent difference is reported as a percentage of the measured superposition

The superposition deflection measurements from the post-repair test were consistent for all sensor locations. The actual simultaneously positioned load condition resulted in downward deflections for all sensors that were of less magnitude than the summation of the deflections measured in response to the trucks positioned independently. The average difference was approximately 0.01 in. and the average percentage difference from the measured superposition was less than 10 percent. These relatively small differences between measured and predicted deflections are an indication that overall the bridge structure exhibited nearly linear-elastic behavior during the post-repair superposition test.

5.3.4.2 Linear-Elastic Behavior Assessment—Damaged Regions

Crack-opening displacements and bottom-fiber strains measured during the post-repair superposition test were analyzed to assess the local behavior of the damaged regions. Damaged region behavior can be assessed by analyzing the crack-opening displacement behavior in response to the superposition test. Cracked region behavior can be also be assessed by comparing near-crack bottom-fiber strain behavior to bottom-fiber strain behavior observed further from the primary crack location. The relationship between near-crack bottom-fiber strain behavior and crack-opening displacement behavior can also be analyzed to further support conclusions regarding the behavior of the damaged regions and previously stated conclusions regarding damage comparisons and continuity behavior.

5.3.4.2.1 Crack-Opening Displacements

The predicted and measured superposition crack-opening displacements are illustrated in Figure 5.50. The differences between the predicted and measured superposition crack-opening displacements are presented in Table 5.14.

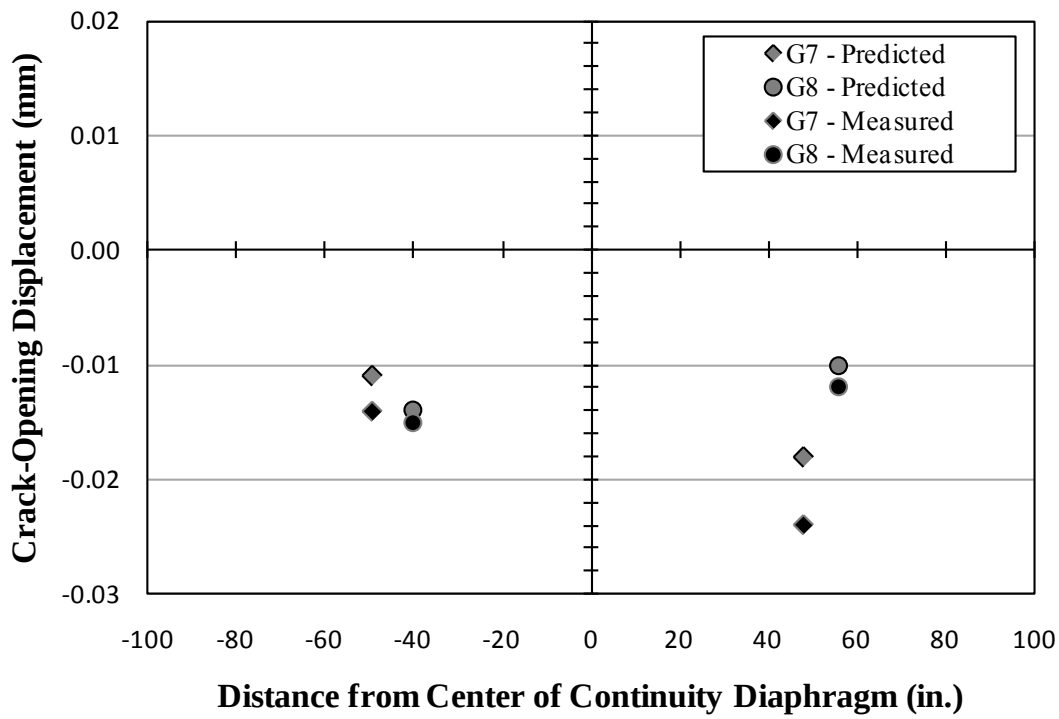

Figure 5.50: Superposition—crack-opening displacements—predicted and measured

Table 5.14: Superposition—maximum crack closures

Girder	Span	Superposition Crack-Opening Displacement (mm) – closing + opening		Difference (Pred.–Meas.)	
		Predicted (A1 + A9)	Measured (A1 & A9)	mm	%
7	10	-0.011	-0.014	0.003	21
	11	-0.018	-0.024	0.006	25
8	10	-0.014	-0.015	0.001	7
	11	-0.010	-0.012	0.002	17

Notes: Percent difference is reported as a percentage of the measured superposition
1 in. = 25.4 mm

Each instrumented crack experienced closure due to all of the superposition-test load conditions. The crack closures measured in response to the combined load condition (A1 and A9) were greater in magnitude than the crack closures predicted by superposition (A1 + A9). The maximum difference between the measured and predicted superposition crack closures was 0.006 mm (0.27 x 10^{-3} in.) at the crack on the east face of Girder 7 in Span 11. This difference

resulted in a percentage difference from the measured superposition of 25 percent. The average difference between the measured and predicted crack closures for all four crack locations was 0.003 mm (0.14 x 10^{-3} in.), and the average percentage difference was 18 percent of the measured result.

The magnitudes of the differences and percentage differences between measured and predicted crack closures during the post-repair superposition test indicate that the principle of superposition is not valid in the cracked regions. Therfore, crack locations are exhibiting nonlinear behavior. As previously noted, the location of the COD gage on Girder 8-Span 10 likely had an effect on the crack-opening displacement measurements making this gage less reliable for comparison. The damaged region of Girder 7 in Span 11 exhibited the apparent least linear behavior. The damaged region of Girder 8 in Span 10 exhibited the most apparent linear behavior. These varying degrees of linear behavior can be related to varying degrees of damage within each girder.

Nonlinear behavior exhibited by measured crack closures is possibly associated with the presence of multiple cracks surrounding the instrumented crack locations. Load conditions that result in closure of a gaged crack will likely also result in closure of smaller neighboring cracks. As smaller neighboring cracks close, the local cross-sectional area of the concrete effectively transmitting compression is increased. Due to the increased local effective compression zone, the application of additional loads that would result in closure of a gaged crack, if applied independently, will result in additional crack closure of greater magnitude than the closure in response to the independent load condition. This neighboring crack closure explanation, as the possible cause of nonlinear behavior, is supported by the observation that the trucks positioned simultaneously produced crack closures that were measured to be of greater magnitude than the summation of the measured crack closures in response to the trucks positioned independently.

5.3.4.2.2 Bottom-Fiber Strains

The predicted and measured superposition bottom-fiber strain measurements are presented in Figure 5.51. The differences between the predicted and measured superposition bottom-fiber strain measurements are presented in Tables 5.15 and 5.16.

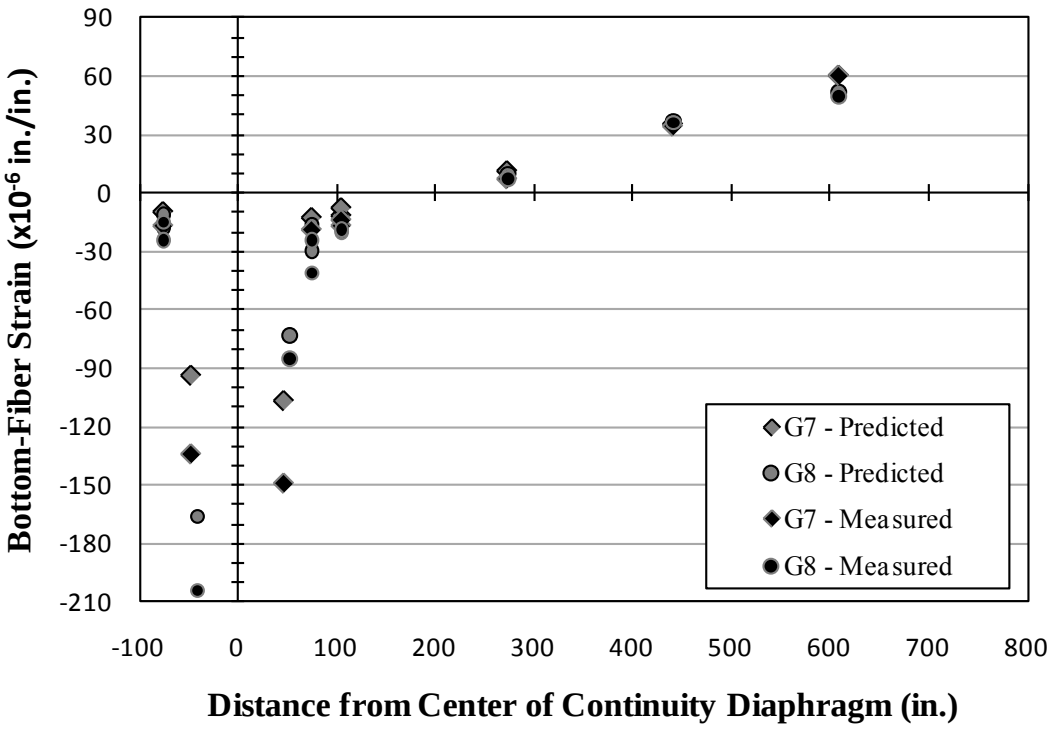

Figure 5.51: Superposition—bottom-fiber strains—predicted and measured

Table 5.15: Superposition—bottom-fiber strains—Girder 7

Span	Distance from center of continuity diaphragm (in.) – Span 10 + Span 11	Location Description	Superposition Bottom-Fiber Strain ($x10^{-6}$ in./in.) – compressive + tensile		Difference (Pred.–Meas.)	
			Predicted (A1 + A9)	Measured (A1 & A9)	$x10^{-6}$ in./in.	%
10	-74	FRP	-10	-17	7	41
	-47	FRP-Crack	-94	-134	40	30
11	47	FRP-Crack	-107	-149	42	28
	74	FRP	-13	-19	6	32
	104	FRP	-8	-14	6	40
	105	Concrete	-12	-17	5	29
	273	Concrete	11	7	4	60
	441	Concrete	35	34	1	3
	609	Concrete	60	60	0	0

Note: Percent difference is reported as a percentage of the measured superposition

Table 5.16: Superposition—bottom-fiber strains—Girder 8

Span	Distance from center of continuity diaphragm (in.) – Span 10 + Span 11	Location Description	Superposition Bottom-Fiber Strain ($x10^{-6}$ in./in.) – compressive + tensile		Difference (Pred.–Meas.)	
			Predicted (A1 + A9)	Measured (A1 & A9)	$x10^{-6}$ in./in.	%
10	-75	Concrete	-18	-24	6	25
	-74	FRP	-11	-15	4	27
	-41	FRP-Crack	-166	-204	38	19
11	52	FRP-Crack	-73	-85	12	14
	74	FRP	-16	-24	8	33
	75	Concrete	-30	-41	11	27
	104	FRP	-13	-19	6	32
	105	Concrete	-15	-20	5	25
	273	Concrete	10	7	3	40
	441	Concrete	37	36	1	3
	609	Concrete	52	50	2	4

Note: Percent difference is reported as a percentage of the measured superposition

All of the bottom-fiber strain gages measured compressive strains in response to the individual Span 10 load condition (A1 east). In response to the individual Span 11 load condition (A9 east), the bottom-fiber gages within 8 ft from the face of the continuity diaphragm measured compressive strains, and the remaining strain gages out to midspan measured tensile strains. The maximum compressive strains were measured by the bottom-fiber strain gages installed on the FRP at the assumed underlying crack location on each girder.

The maximum compressive strain measured in response to the superposition-test Span 10 truck position (A1) was 73 x 10^{-6} in./in. at the strain gage installed on the FRP corresponding with the primary crack location of Girder 8 in Span 10. The maximum compressive strain measured in response to the Span 11 truck position (A9) was 93 x 10^{-6} in./in. at the same crack location strain gage of Girder 8 in Span 10.

The differences between predicted and measured superposition strains were observed to be of greater magnitude at the FRP near the primary crack locations. A maximum difference of 42 x 10^{-6} in./in. was observed at the FRP strain gage installed near the crack location on Girder 7 of Span 11. From this difference, it is evident that the damaged region of Girder 7 in Span 11 exhibits the least apparent linear behavior of the four instrumented damaged regions.

5.3.4.3 Linear-Elastic Behavior Conclusions

Deflections measured during the superposition test provide evidence that the *overall* bridge structure exhibits behavior that is nearly linear elastic under truck loads. However, the bottom-fiber strain and crack-opening displacement measurements from the superposition test indicate that the damaged regions exhibit a localized nonlinear response to truck loads.

5.3.5 Relationship between Truck Position and FRP Tensile Demand

The FRP tensile demand was analyzed in response to each truck position of post-repair testing. Analysis of bottom-fiber strains measured in response to four of the Span 11 truck positions provides evidence for determining critical truck positions. The four truck positions selected for further analysis include C6, C7, C8, and the Span 11 static position of AE testing, which are illustrated in Figures 5.52–5.54.

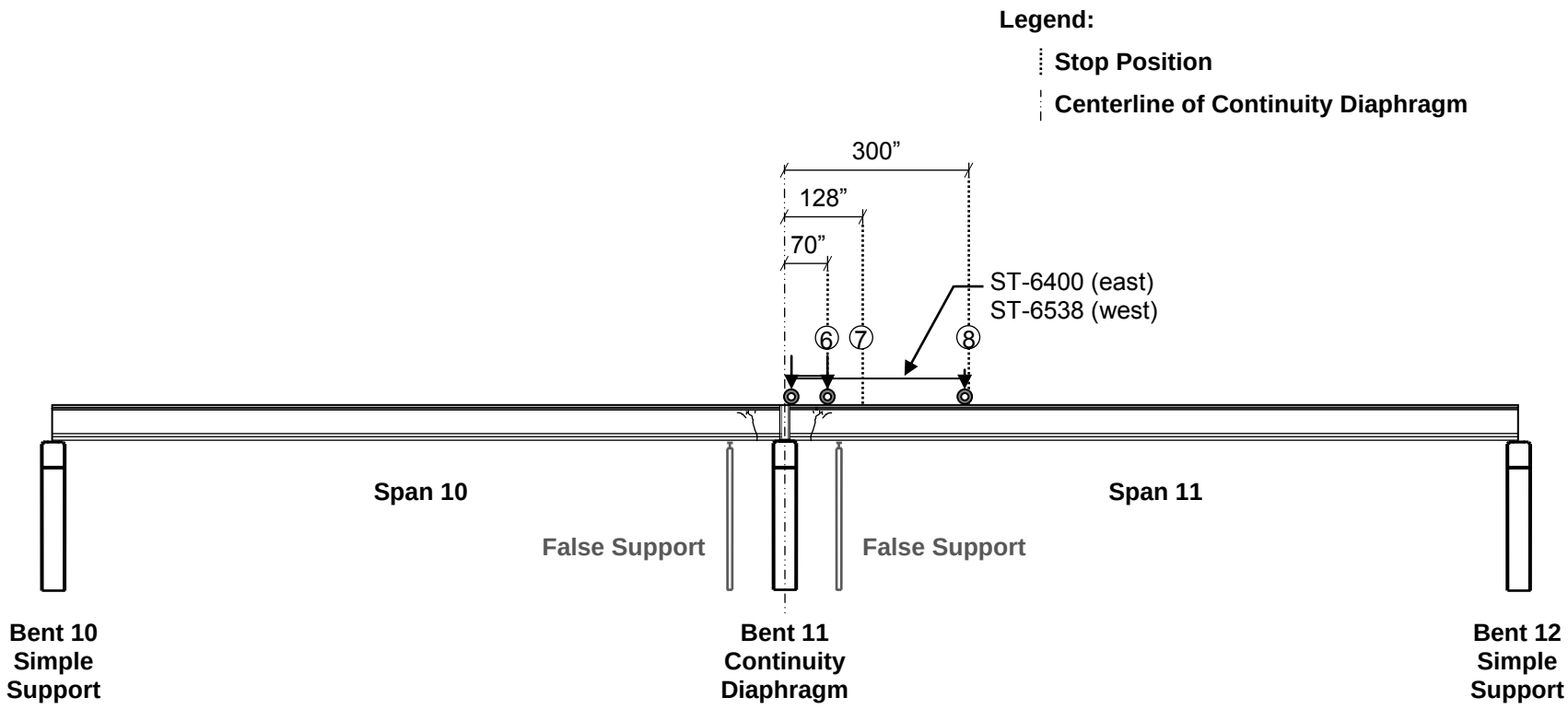

Figure 5.52: Longitudinal truck positions—C6

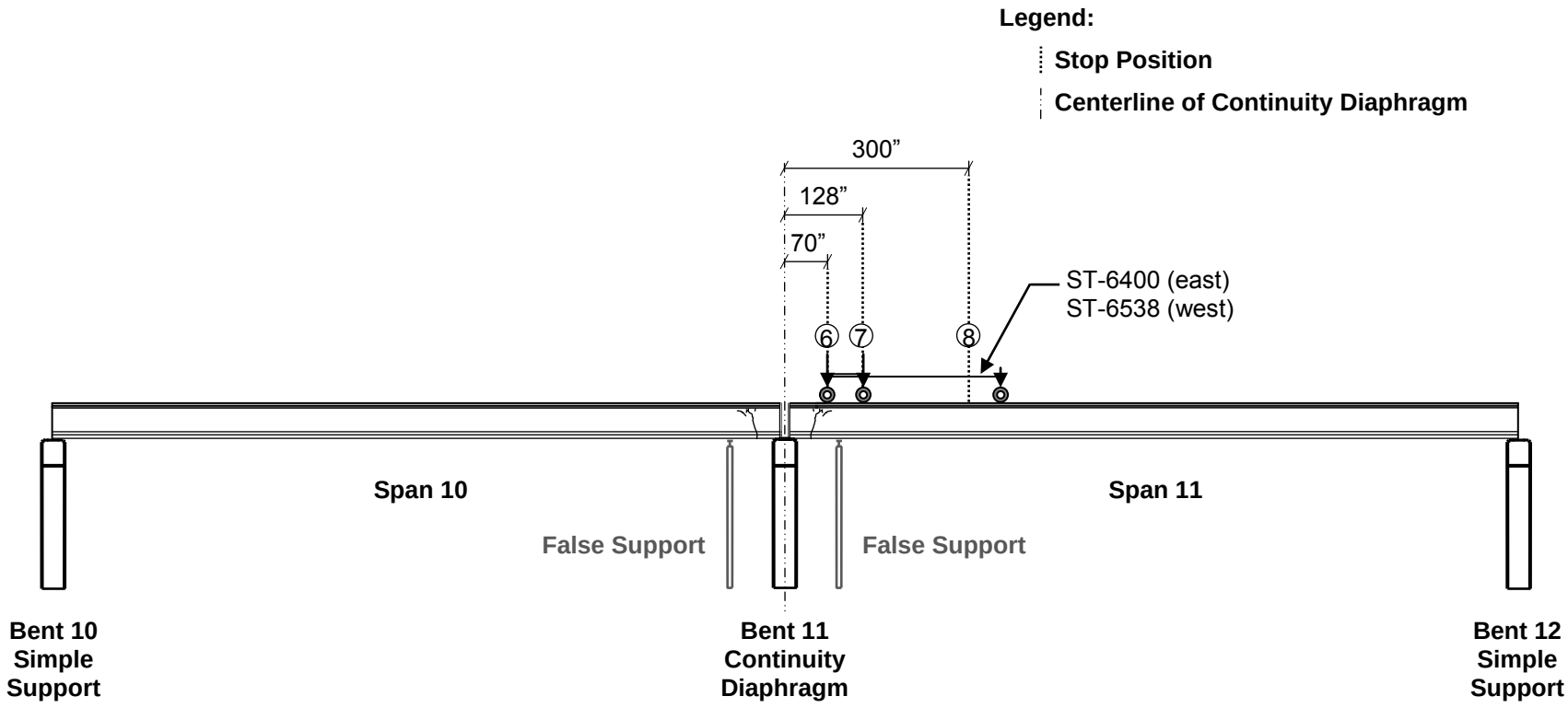

Figure 5.53: Longitudinal truck positions—AE LC-6 Span 11 *and* C7

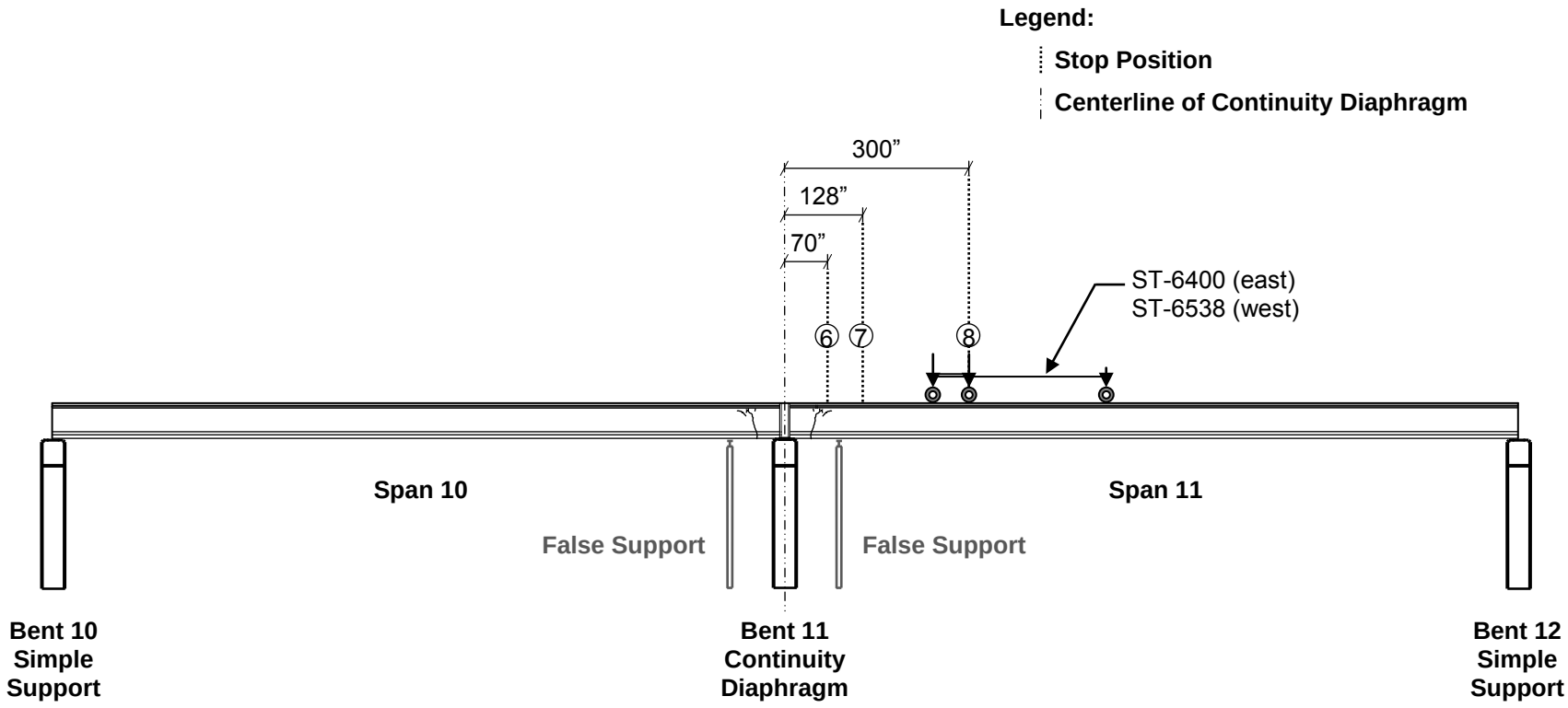

Figure 5.54: Longitudinal truck positions—C8

When the trucks are at Static Position C6, the back axles of each truck straddle the damaged region. The middle axle is positioned 70 in. from the center of the continuity diaphragm, and the rear axle is approximately 13 in. from the center of the diaphragm, as shown in Figure 5.52. The distance between the rear axle and middle axle is 57 in. for the standard ALDOT load truck.

The Span 11 static position of the AE tests is similar to Static Position C7 of the multiposition load-tests. These stop positions are similar enough to be presented as one stop position, as shown in Figure 5.53, however, there is a slight difference between the two truck positions. Truck positioning for AE testing was based on aligning the rear axle, and truck positioning for the multiposition tests was based on aligning the middle axle. For the AE Span 11 static position, the rear axle is positioned 70 in. from the center of the continuity diaphragm, and the middle axle is approximately 127 in. from the center of the diaphragm. When the trucks are at Static Position C7, the middle axle is positioned 128 in. from the center of the continuity diaphragm, and the rear axle is approximately 71 in. from the center of the diaphragm.

When the trucks are at Static Position C8, all truck axles are beyond the damaged region. The middle axle is positioned 300 in. from the center of the continuity diaphragm, and the rear axle is approximately 243 in. from the center of the diaphragm, as shown in Figure 5.54.

These four static positions were tested with the LC-6 load truck block configurations of the second night of bridge testing. The bottom-fiber strains measured in response to these four truck position are presented in Figures 5.55–5.58. To indicate the FRP tensile demand, the Span 11 bottom-fiber FRP strains have been presented in Table 5.17. To further support FRP tensile demand conclusions, crack openings measured in response to the same four truck positions have been presented in Table 5.18.

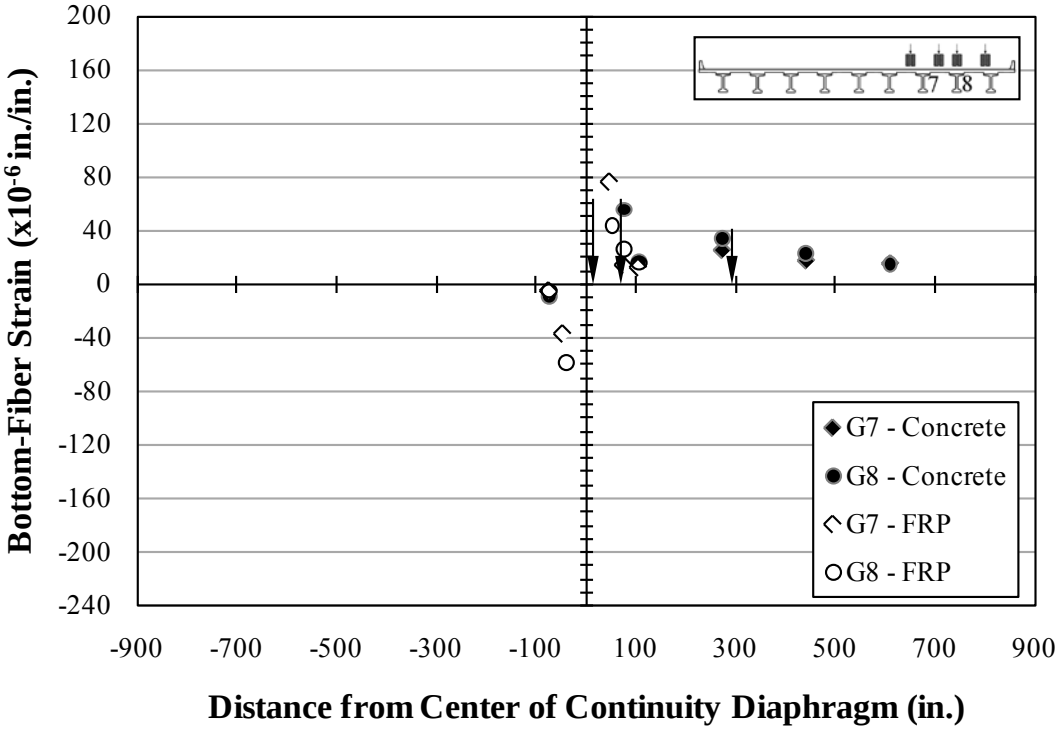

Figure 5.55: Bottom-fiber strains—C6

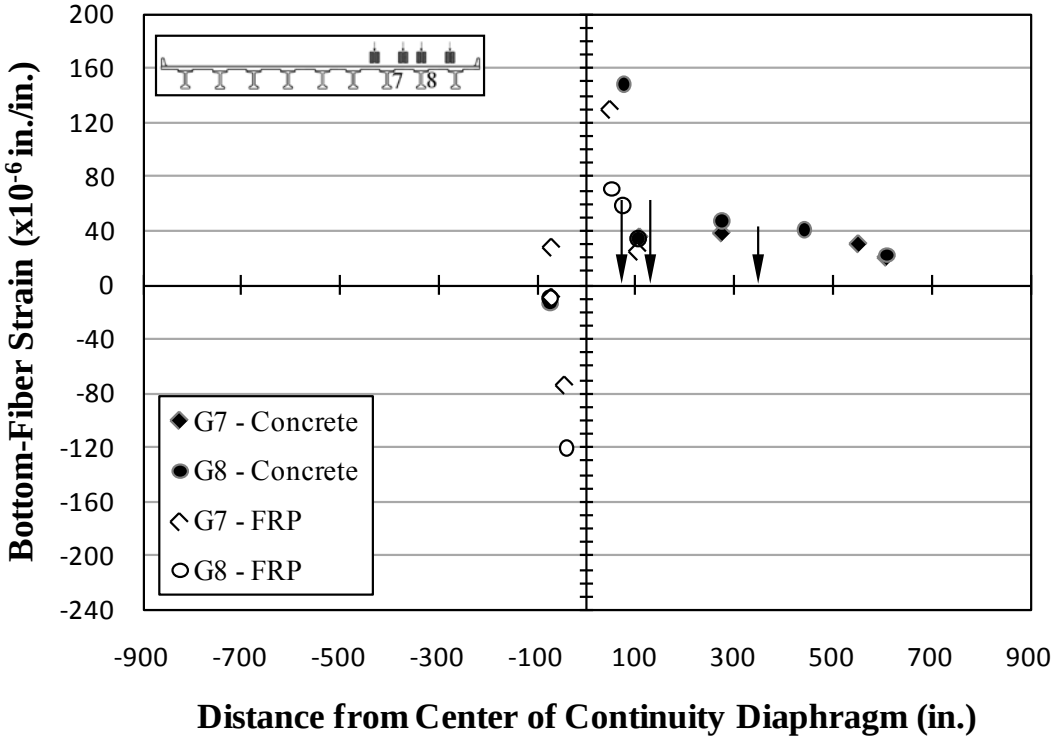

Figure 5.56: Bottom-fiber strains—AE LC-6 Span 11

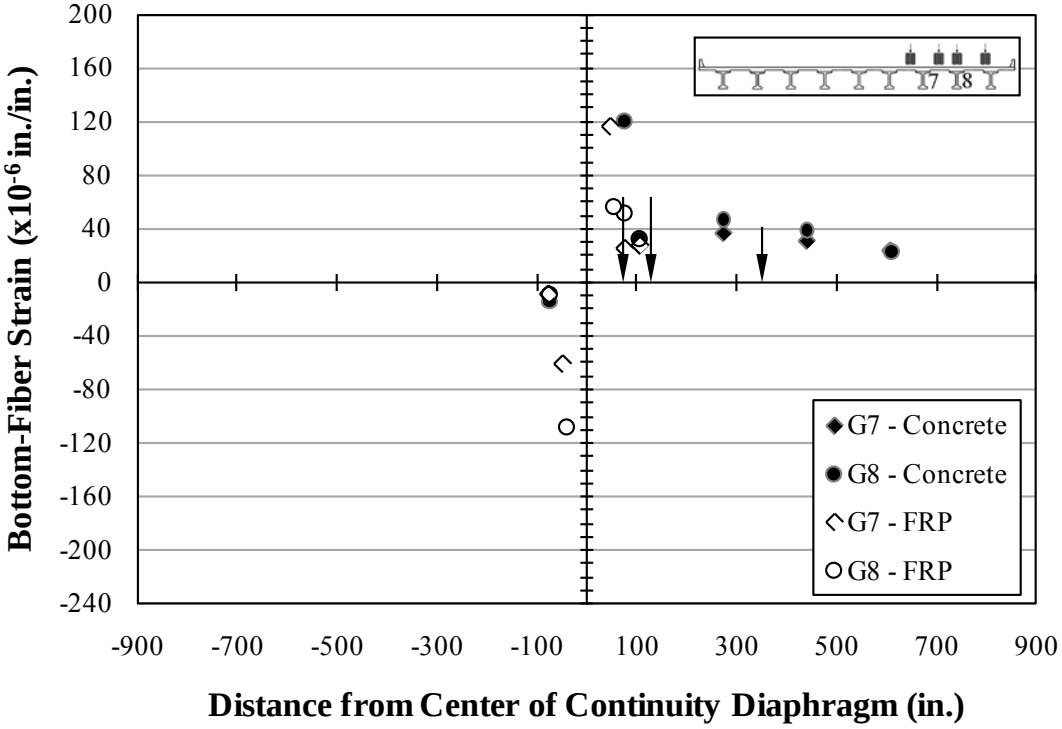

Figure 5.57: Bottom-fiber strains—C7

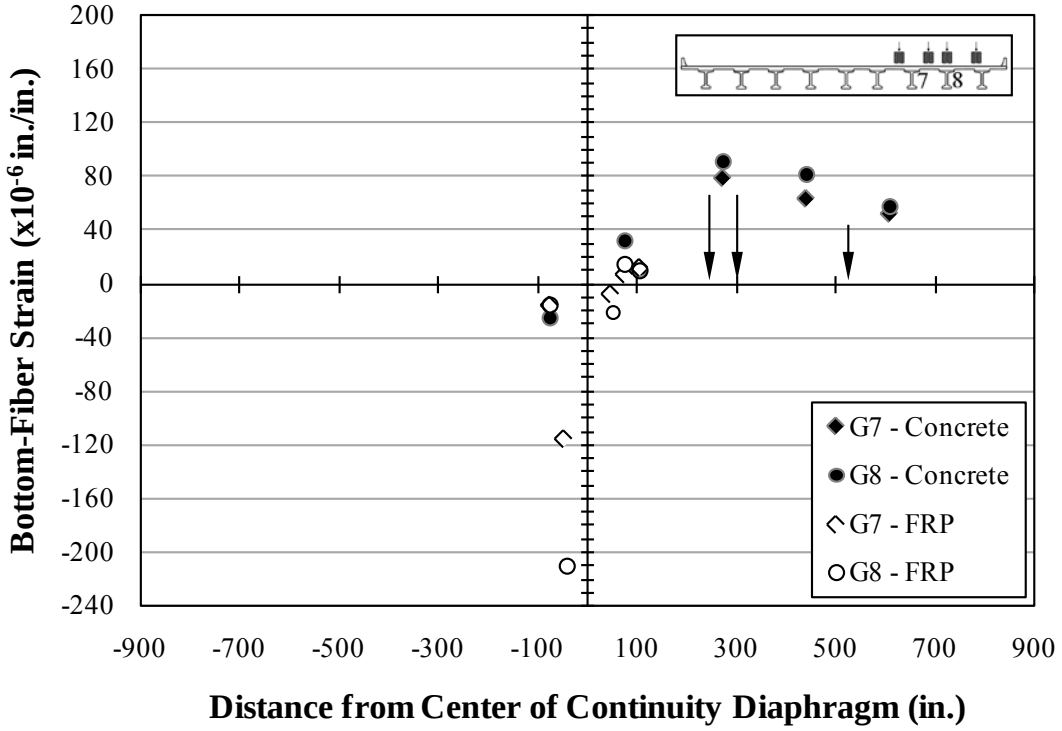

Figure 5.58: Bottom-fiber strains—C8

Table 5.17: FRP tensile demand—bottom-fiber strains—Span 11 truck positions

Girder	Distance from center of continuity diaphragm (in.) – Span 10 + Span 11	Location Description	Bottom-Fiber Strain ($x10^{-6}$ in./in.) – compressive + tensile			
			C6	AE LC-6 Span 11	C7	C8
7	47	FRP-Crack	76	**130**	116	-8
	74	FRP	14	**28**	25	7
	104	FRP	12	25	**28**	12
8	52	FRP-Crack	44	**71**	56	-21
	74	FRP	26	**59**	52	14
	104	FRP	26	**34**	32	10

Note: Measurements presented in **bold** represent the maximum tensile strains per gage for all truck positions

Table 5.18: Crack openings—Span 11 truck positions

Girder	Distance from center of continuity diaphragm (in.) – Span 10 + Span 11	Crack-Opening Displacement (mm) – closing + opening			
		C6	AE LC-6 Span 11	C7	C8
7	48	0.020	**0.044**	0.039	0.015
8	56	0.017	**0.040**	0.032	0.011

Notes: Measurements presented in **bold** represent the maximum crack opening per gage for all truck positions
1 in. = 25.4 mm

The Span 11 static position of the AE test and the C7 static position of the multiposition test resulted in similar FRP tensile strains of greater magnitude than the other truck positions. When comparing all static truck positions, the positioning of axles near the primary crack location, but without straddling the crack location, resulted in the larger measured FRP tensile demand in response to truck loads. This corresponds to the truck position that generates the largest shear demand on the damaged cross section. The Span 11 static position of the AE test also resulted

in crack openings of greater magnitude compared to the other truck positions, which further supports the conclusion that these stop positions were the most critical truck positions observed during post-repair bridge testing.

Truck positions resulting in the greatest FRP tensile demand correspond with truck positions resulting in the greatest shear demand at damaged regions. Analysis procedures for determining maximum shear force demand for a girder should be used to determine the load effects and design forces for FRP repair of damaged continuous girder ends.

5.4 BRIDGE RESPONSE TO AMBIENT THERMAL CONDITIONS

It has been previously reported (Gao 2003) that initial cracking of I-565 concrete bulb-tee girders was more likely due to thermal gradients than traffic loads. During post-repair testing, sensor measurements were monitored for twenty-four hours of normal traffic conditions to assess structural behavior in response to ambient thermal conditions. These assessments include continuity behavior of the bridge structure, confirmation that thermal gradient loading is responsible for initial cracking, and confirmation of other conclusions supported by static live load analysis. Before the presentation of bridge monitoring measurements, theoretical bridge behavior is discussed for a two-span continuous structure subjected to a linear thermal gradient. The measured responses to ambient temperature will then be compared to theoretical responses to ambient temperature and previously discussed measured responses to truck loads.

5.4.1 Theoretical Response to Ambient Thermal Conditions

The theoretical temperature gradient along a typical cross-section height (h) is assumed to be linearly decreasing from the top-fiber of the bridge deck to the bottom-fiber of a typical girder. This linear temperature gradient results in a positive temperature difference (ΔT_h) when subtracting the temperature at the top of the bridge deck from the temperature at the bottom of a typical girder. The formula for the temperature difference is presented as Equation 5.1. The formula for the change in temperature difference ($\delta(\Delta T_h)$) between two points in time is presented as Equation 5.2. A linear temperature gradient example is illustrated in Figure 5.59.

$$\Delta T_h = T_{top} - T_{bottom} \qquad \textbf{Eq. 5.1}$$

$$\delta(\Delta T_h) = (\Delta T_h)_2 - (\Delta T_h)_1 \qquad \textbf{Eq. 5.2}$$

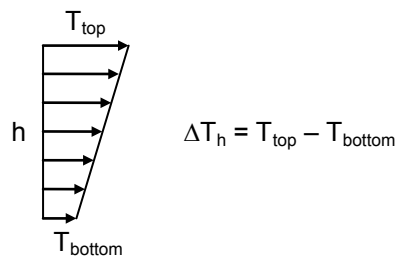

Figure 5.59: Linear temperature gradient

The bridge structure was also considered to be acting as originally constructed, fully continuous for post-construction loads. A theoretical two-span continuous structure subjected to a thermal load effects is illustrated in Figure 5.60. The structure consists of two identical span lengths (L). The exterior supports (A and C) represent simple supports, and the interior support (B) represents the continuity achieved by a typical continuity diaphragm.

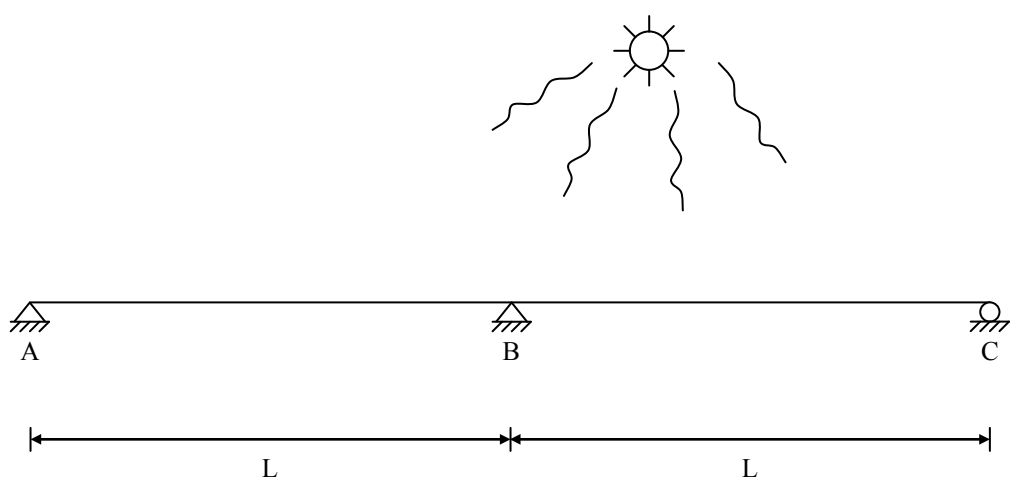

Figure 5.60: Two-span continuous structure subjected to linear thermal gradient

After initial cracking, it is likely that the bridge structure does not exhibit fully continuous behavior, but theoretical analysis as a fully continuous structure will allow for conservative estimations of bottom-fiber strains that may lead to initial cracking of uncracked girders. Theoretical bottom-fiber FRP strains expected within a damaged region should be considered during the design of an FRP reinforcement repair.

5.4.1.1 Structural Analysis

During analysis, the vertical restraint of the interior support was treated as a redundant support condition to determine the theoretical behavior of the two-span indeterminate structure. The

resulting simply-supported structure was subjected to two separate load conditions as shown in Figure 5.61.

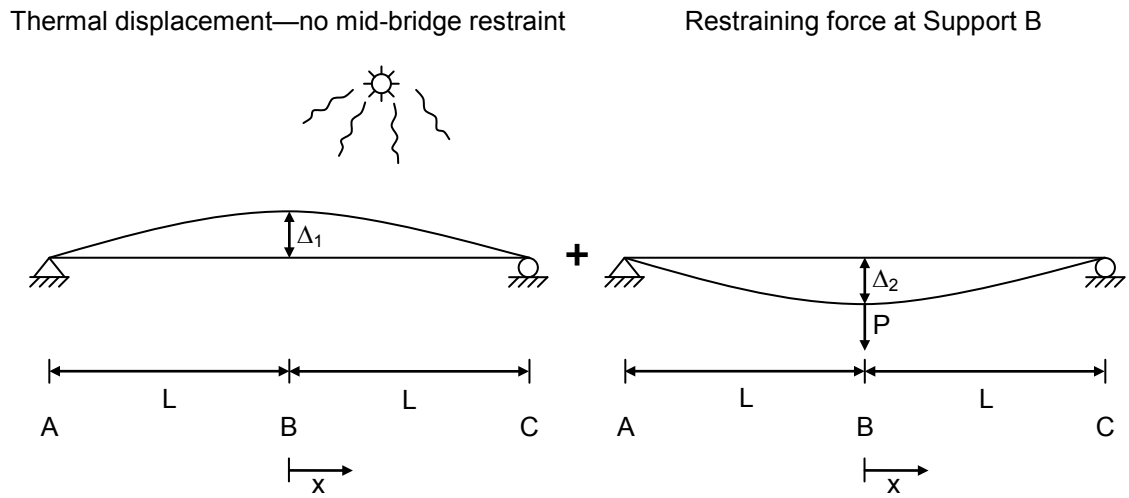

Figure 5.61: Expected deformations—two theoretical load conditions

The first load condition consists of a linear thermal gradient without restraint from the interior support. The second load condition consists of a vertical force (P) representing the restraining force that had been removed from the first load condition. The theoretical deformations, moments, and curvatures were determined for both of the two simply supported load conditions. These theoretical behaviors are mirrored about the interior support (B). For the purpose of defining behavior with respect to location within a span, behavior functions will originate at the interior support. Location within the span (x) will be defined as equal to zero at Support B and equal to L at Support C.

5.4.1.1.1 Deformations

The expected deformations (Δ) of the two load conditions are also illustrated in Figure 5.61. The mid-bridge deformation Δ_1 results from thermal conditions without restraint at the interior support. The mid-bridge deformation Δ_2 results from application of a theoretical restraining force at the location of the theoretically removed interior support. As indicated in Equation 5.3, the summation of the two resulting deflections at the interior support must be equal to zero to match the support conditions of the actual bridge.

$$\Delta_1 + \Delta_2 = 0 \qquad \textbf{Eq. 5.3}$$

5.4.1.1.2 Bending Moments

Bending moment (M) diagrams for the two load conditions of the simply supported structure are presented in Figure 5.62. Although the thermal gradient load condition results in deformation, the simply supported structure does not develop bending moments along the length of the structure due to unrestrained linear thermal gradient alone. The restraining force load condition does result in a linear function of bending moment. The yet-to-be-determined restraining force (P) and span length have an effect on the bending moment function with a maximum moment of PL/2 at the mid-bridge location and zero moment at the simple supports. The bending moment function for Span BC in response to the restraining force applied at Support B is presented as Equation 5.4.

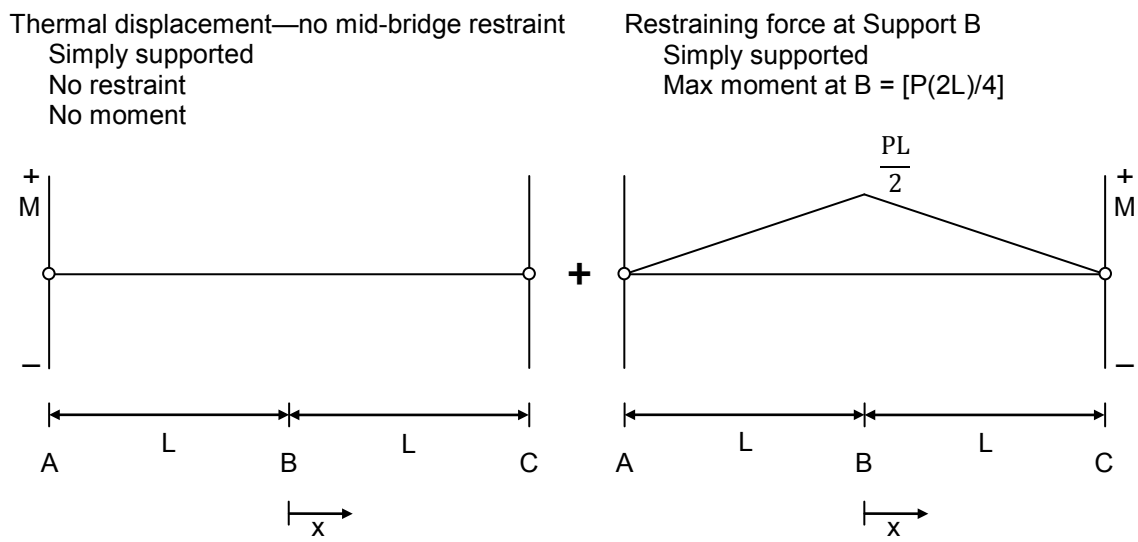

Figure 5.62: Moment diagrams—two theoretical load conditions

$$M_2(x) = \left[\frac{PL}{2}\right]\left(1 - \frac{x}{L}\right) \qquad \textbf{Eq. 5.4}$$

5.4.1.1.3 Curvatures

Curvature ($\emptyset$) diagrams for the two theoretical load conditions of the simply supported structure are presented in Figure 5.63.

The curvature ($\emptyset_1$) due to a linear temperature gradient with no restraint is consistent along the length of the structure. This curvature is also referred to as the temperature-gradient curvature ($\emptyset_T$). The temperature-gradient curvature is a function of the coefficient of thermal expansion (α_T), temperature difference (ΔT_h) from the top of the deck to the bottom of a typical

girder, and the typical cross-section height (h) including the height of the deck. The relationship used to calculate $\emptyset_T$ is presented as Equation 5.5. The curvature function due to an unrestrained response to thermal conditions is presented as Equation 5.6.

Thermal displacement—no mid-bridge restraint
$\emptyset_1 = \emptyset_T$

Restraining force at Support B
$\emptyset_2 = \frac{M}{EI}$

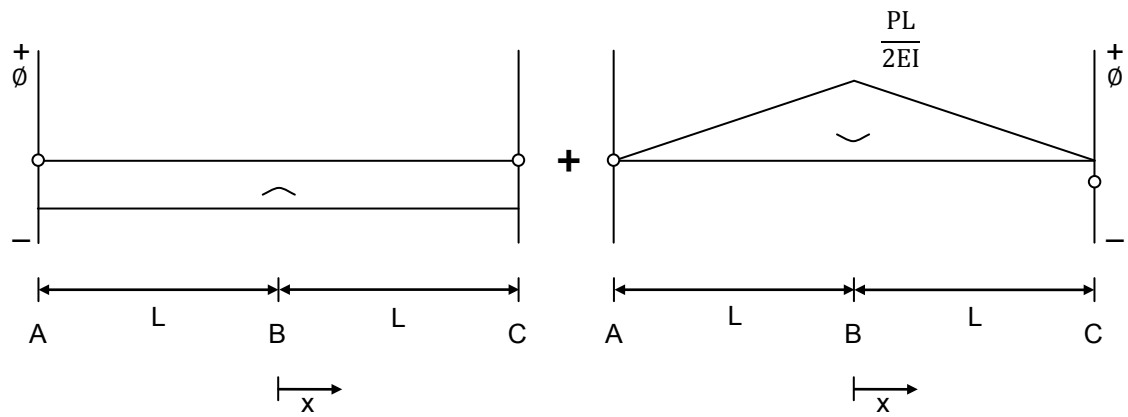

Figure 5.63: Curvature diagrams—two theoretical load conditions

$$\emptyset_T = -\left[\frac{\alpha_T \delta(\Delta T_h)}{h}\right] \qquad \textbf{Eq. 5.5}$$

$$\emptyset_1(x) = \emptyset_T \qquad \textbf{Eq. 5.6}$$

The curvature ($\emptyset_2$) due to the restraining force is presented in terms of the moment due to the restraining force and cross-section properties. It is assumed that the modulus of elasticity (E) and the moment of inertia (I) are constant along the length of the bridge. The basic function for the curvature due to the restraining force is presented as Equation 5.7. This curvature function has also been presented in terms of the moment function variables including the restraint force (P) as shown in Equation 5.8

$$\emptyset_2(x) = \frac{M_2(x)}{EI} \qquad \textbf{Eq. 5.7}$$

$$\emptyset_2(x) = \frac{PL}{2EI}\left[1 - \frac{x}{L}\right] \qquad \textbf{Eq. 5.8}$$

5.4.1.1.4 Restraint Force at Interior Support

The theory of consistent deformations was used to determine the theoretical restraint force at B. The theoretical mid-bridge deformations were determined in terms of variables within the curvature and moment functions. The formulas for the theoretical mid-bridge deflections Δ_1 and Δ_2 are shown as Equations 5.9 and 5.10 respectively.

$$\Delta_1 = \frac{\alpha_T \delta(\Delta T_h) L^2}{2h} \qquad \textbf{Eq. 5.9}$$

$$\Delta_2 = \frac{-PL^3}{6EI} \qquad \textbf{Eq. 5.10}$$

The restraint force is a function of the same properties used to define the moments and curvatures resulting from the two theoretical load conditions. The deflections Δ_1 and Δ_2 were substituted into the consistent deformations relationship presented as Equation 5.3, and the resulting formula is shown as Equation 5.11. This formula was then manipulated to solve for the restraint force P in terms of the other variables as shown in Equation 5.12.

$$\frac{\alpha_T \delta(\Delta T_h) L^2}{2h} - \frac{PL^3}{6EI} = 0 \qquad \textbf{Eq. 5.11}$$

$$P = \frac{3\alpha_T \delta(\Delta T_h) EI}{hL} \qquad \textbf{Eq. 5.12}$$

5.4.1.2 Expected Behavior

The expected behavior of the two-span continuous structure can be determined by superimposing the behaviors of the simply supported structure resulting from the temperature gradient and restraint force load conditions. The expected response characteristics are presented as functions of the distance (x) from the interior support. The behaviors presented

include the net curvature (∅), bending moment (M), shear force (V), bottom-fiber strain (ε), and bottom-fiber stress (f). The bottom-fiber strains are computed from the curvatures, and the shear forces and bottom-fiber stresses are derived from the bending moments. The bottom-fiber strains and stresses are also a function of the distance (y_{bot}) from the cross section centroid to the bottom fiber.

5.4.1.2.1 Curvature

The formula for the expected net curvature presented as Equation 5.13 is derived by superimposing the previously defined curvature functions of the two theoretical load conditions. The curvature ($\emptyset_1$) due to a temperature gradient without restraint is presented as Equation 5.14. The restraint force variable (P) within the curvature function presented as Equation 5.8, which represents the curvature due to the restraint force associated with temperature effects that restrained at the interior support, can be substituted with the restraint force formula defined as Equation 5.12. The resulting curvature ($\emptyset_2$) due to the restraint force is presented as Equation 5.15.

$$\emptyset(x) = \emptyset_1(x) + \emptyset_2(x) \qquad \textbf{Eq. 5.13}$$

$$\emptyset_1(x) = -\left[\frac{\alpha_T \delta(\Delta T_h)}{h}\right] \qquad \textbf{Eq. 5.14}$$

$$\emptyset_2(x) = \frac{PL}{2EI}\left[1 - \frac{x}{L}\right]$$

$$P = \frac{3\alpha_T \delta(\Delta T_h) EI}{hL}$$

$$\emptyset_2(x) = \frac{3}{2}\left[\frac{\alpha_T \delta(\Delta T_h)}{h}\right]\left[1 - \frac{x}{L}\right] \qquad \textbf{Eq. 5.15}$$

The curvature functions defined in Equations 5.14 and 5.15 can be superimposed to determine the expected net curvature function due to a linear temperature gradient with restraint at the interior support, which is presented as Equation 5.16.

$$\emptyset(x) = \frac{1}{2}\left[\frac{\alpha_T \Delta T}{h}\right]\left[1 - 3\left(\frac{x}{L}\right)\right] \qquad \textbf{Eq. 5.16}$$

The expected net curvature function can then be simplified by condensing the temperature gradient curvature variables into one term as shown in Equation 5.17, where $\emptyset_T$ is the curvature due to *unrestrained* temperature gradient defined in Equation 5.5.

$$\emptyset(x) = -\frac{1}{2}\emptyset_T\left[1 - 3\left(\frac{x}{L}\right)\right] \qquad \textbf{Eq. 5.17}$$

The curvature function can then be solved to determine that the expected point of zero curvature is located a distance of one third the span length from the interior support as shown in Equation 5.18.

$$\emptyset = 0 \text{ @ } x = \frac{L}{3} \qquad \textbf{Eq. 5.18}$$

An illustration of the expected curvature as a function of the distance from the interior support is presented in Figure 5.64. The curvatures expected at the interior and exterior supports are also provided within this figure.

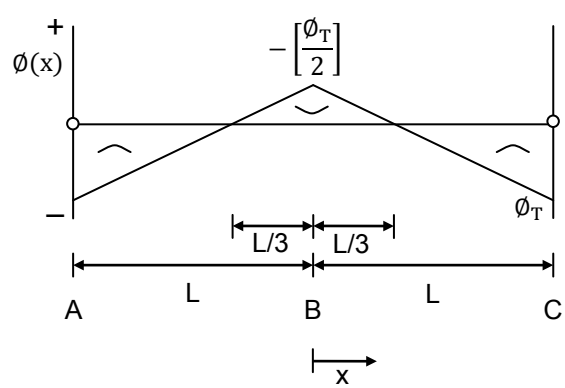

Figure 5.64: Curvature due to temperature gradient with restraint

5.4.1.2.2 Bending Moment

The bending moment is a function of the restraint force developed. The restraint force (P) within the bending moment function presented as Equation 5.4 can be substituted with the restraint force defined as Equation 5.12. The resulting function for bending moment that results from the restraint force is presented as Equation 5.19, and represents the expected moment due to a linear temperature gradient with restraint at the interior support in a two-span continuous beam. The expected moment function can then be simplified by condensing the temperature gradient

curvature variables into one term as shown in Equation 5.20. An illustration of the expected moment as a function of the distance from the interior support is presented in Figure 5.65. The moment expected at the interior support is also provided within this figure.

$$M(x) = M_2(x) = \left[\frac{PL}{2}\right]\left(1 - \frac{x}{L}\right)$$

$$P = \frac{3\alpha_T \delta(\Delta T_h) EI}{hL}$$

$$M(x) = \frac{3}{2}\left[\frac{\alpha_T \delta(\Delta T_h)}{h}\right]\left[1 - \frac{x}{L}\right] EI \qquad \textbf{Eq. 5.19}$$

$$M(x) = -\frac{3}{2}\emptyset_T \left[1 - \frac{x}{L}\right] EI \qquad \textbf{Eq. 5.20}$$

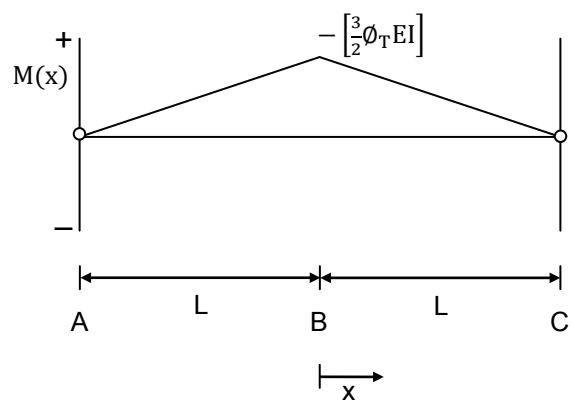

Figure 5.65: Moment due to temperature gradient with restraint

5.4.1.2.3 Shear Force

The shear force function is a constant value with opposing direction of action on either side of the interior support. The shear force is computed from the slope of the moment function as shown in Equation 5.21. The formula for the maximum bending moment, which is expected at the interior support as shown in Figure 5.65, is defined as Equation 5.22. Substituting the formula for the maximum expected moment into the shear force function shown in Equation 5.21 provides the expanded shear force formula presented as Equation 5.23. The expected shear force function can then be simplified by condensing the temperature gradient curvature variables into one term

as shown in Equation 5.24. An illustration of the expected shear force as a function of the distance from the interior support is presented in Figure 5.66.

$$V(x) = \pm \frac{M_{max}}{L} \qquad \textbf{Eq. 5.21}$$

$$M_{max} = \frac{3}{2}\left[\frac{\alpha_T \delta(\Delta T_h)}{h}\right] EI \qquad \textbf{Eq. 5.22}$$

$$V(x) = \pm \frac{3}{2}\left[\frac{\alpha_T \delta(\Delta T_h)}{h}\right] \frac{EI}{L} \qquad \textbf{Eq. 5.23}$$

$$V(x) = \pm \frac{3}{2} \emptyset_T \frac{EI}{L} \qquad \textbf{Eq. 5.24}$$

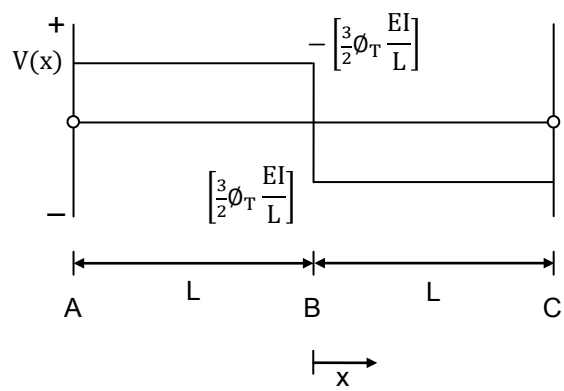

Figure 5.66: Shear due to temperature gradient with restraint

5.4.1.2.4 Bottom-Fiber Strain—Uncracked Cross Sections

The bottom-fiber strain function of the theoretically uncracked structure is derived from the curvature function using the distance from the centroid of a typical uncracked cross section to the bottom of the girder. The basic bottom-fiber strain function formula is shown as Equation 5.25. The expected curvature function of Equation 5.16 can be substituted into the basic bottom-fiber strain function to provide the expanded bottom-fiber strain function presented as Equation 5.26. The expected bottom-fiber strain function can then be simplified by condensing the temperature gradient curvature variables into one term as shown in Equation 5.27. An illustration of the expected bottom-fiber strain as a function of the distance from the interior support is presented in Figure 5.67.

$$\varepsilon_{bot}(x) = \emptyset(x) y_{bot} \qquad \textbf{Eq. 5.25}$$

$$\varepsilon_{bot}(x) = \frac{1}{2}\left[\frac{\alpha_T \delta(\Delta T_h)}{h}\right]\left[1 - 3\left(\frac{x}{L}\right)\right] y_{bot} \qquad \textbf{Eq. 5.26}$$

$$\varepsilon_{bot}(x) = \frac{1}{2}\emptyset_T\left[1 - 3\left(\frac{x}{L}\right)\right] y_{bot} \qquad \textbf{Eq. 5.27}$$

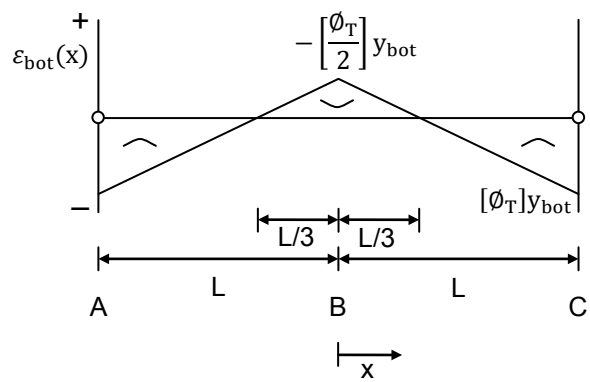

Figure 5.67: Bottom-fiber strain due to temperature gradient with restraint

5.4.1.2.5 Bottom-Fiber Stress—Uncracked Cross Section

The bottom-fiber stress function of the theoretically uncracked structure is derived from the moment function, the distance from the centroid of a typical uncracked cross section to the bottom of the girder, and the moment of inertia. The basic bottom-fiber stress function formula is shown as Equation 5.28. The expected moment function of Equation 5.19 can be substituted into the basic bottom-fiber stress function to provide the expanded bottom-fiber stress function presented as Equation 5.29. The expected bottom-fiber stress function can then be simplified by condensing the temperature gradient curvature variables into one term as shown in Equation 5.30. An illustration of the expected shear force as a function of the distance from the interior support is presented in Figure 5.68. The bottom-fiber stress is *not* proportional to the bottom-fiber strain because a portion of the total strain is due to stress-independent thermal changes.

$$f_{bot}(x) = \frac{M(x)y_{bot}}{I} \qquad \textbf{Eq. 5.28}$$

$$f_{bot}(x) = \frac{3}{2}\left[\frac{\alpha_T \delta(\Delta T_h)}{h}\right]\left[1 - \frac{x}{L}\right] E y_{bot} \qquad \textbf{Eq. 5.29}$$

$$f_{bot}(x) = -\frac{3}{2}\emptyset_T \left[1 - \frac{x}{L}\right] E y_{bot} \qquad \textbf{Eq. 5.30}$$

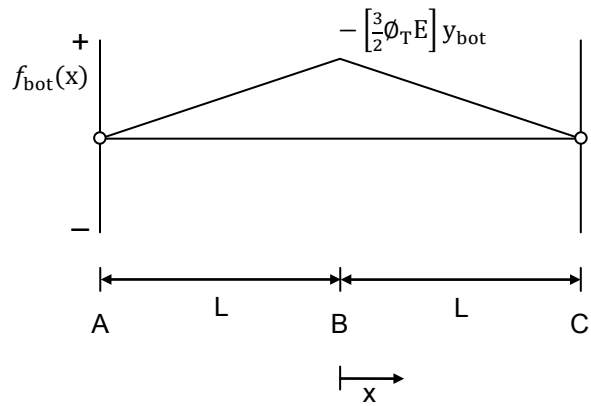

Figure 5.68: Bottom-fiber stress due to temperature gradient with restraint

5.4.1.2.6 Bottom-Fiber Strain—Cracked Cross Section—FRP

The theoretical uncracked concrete behavior presented is not applicable for the local behavior at damaged sections selected for potential FRP repair. The damaged cross section must be considered cracked during analysis to determine the bottom-fiber FRP strain expected in response to temperature effects.

Assuming the cross section to be cracked eliminates the theoretical bottom-fiber strain due to a temperature gradient without restraint at the interior support. However, there is still an FRP strain expected due to an unrestrained temperature change. This FRP strain is associated with the ambient temperature at the FRP location at two different times. The difference between these two temperatures results in a temperature change (ΔT_{FRP}) that can be multiplied by the longitudinal coefficient of thermal expansion ($\alpha_{T,FRP}$) specified for the repair material. The formula for the FRP strain expected in response to unrestrained temperature change in the FRP material is presented as Equation 5.31. This strain component is stress-independent.

$$\varepsilon_{FRP,1}(x) = \alpha_{T,FRP}\Delta T_{FRP} \qquad \textbf{Eq. 5.31}$$

The FRP must also undergo the stress-dependent bottom-fiber strain due to the restraint force associated with a linear temperature gradient applied to the entire two-span continuous structure. This strain is based on the theoretical curvature due to the restraint force load condition, which corresponds to the bending moment that results from this restraint. This theoretical curvature has been previously defined as Equation 5.15. The basic formula for the strain expected due to curvature has been previously defined as Equation 5.25, and is associated with the distance (y_{bot}) from the centroid of the cross section to the bottom of the girder. The distance ($y_{cr,bot}$) from the centroid of a cracked section to the bottom of the girder of a cracked section is of greater magnitude than the distance from centroid of an uncracked section to the bottom of the girder, which results in an increase of expected strain due to the cracked nature of the cross section. The formula for the FRP strain expected due to the restraint force is presented as Equation 5.32. This formula can also be presented with the distance from the centroid to the bottom fiber and the girder height considered a ratio as presented in Equation 5.33.

$$\varepsilon_{FRP,2}(x) = \frac{3}{2}\left[\frac{\alpha_T\delta(\Delta T_h)}{h}\right]\left[1-\frac{x}{L}\right]y_{cr,bot} \qquad \textbf{Eq. 5.32}$$

$$\varepsilon_{FRP,2}(x) = \frac{3}{2}\left[\alpha_T\delta(\Delta T_h)\right]\left[1-\frac{x}{L}\right]\frac{y_{cr,bot}}{h} \qquad \textbf{Eq. 5.33}$$

The bottom-fiber strain functions defined in Equations 5.31 and 5.33 can be superimposed to determine the expected FRP strain due to ambient temperature effects with restraint at the interior support, which is presented as Equation 5.34.

$$\varepsilon_{FRP}(x) = \alpha_{T,FRP}\Delta T_{FRP} + \frac{3}{2}\left[\alpha_T\delta(\Delta T_h)\right]\left[1-\frac{x}{L}\right]\frac{y_{cr,bot}}{h} \qquad \textbf{Eq. 5.34}$$

5.4.1.2.7 Deflection

The expected displacement of a two-span continuous structure due to a linear temperature gradient is illustrated in Figure 5.69. Inflection points are expected at the previously

defined points of zero curvature located a distance of one third of the span length from the interior support.

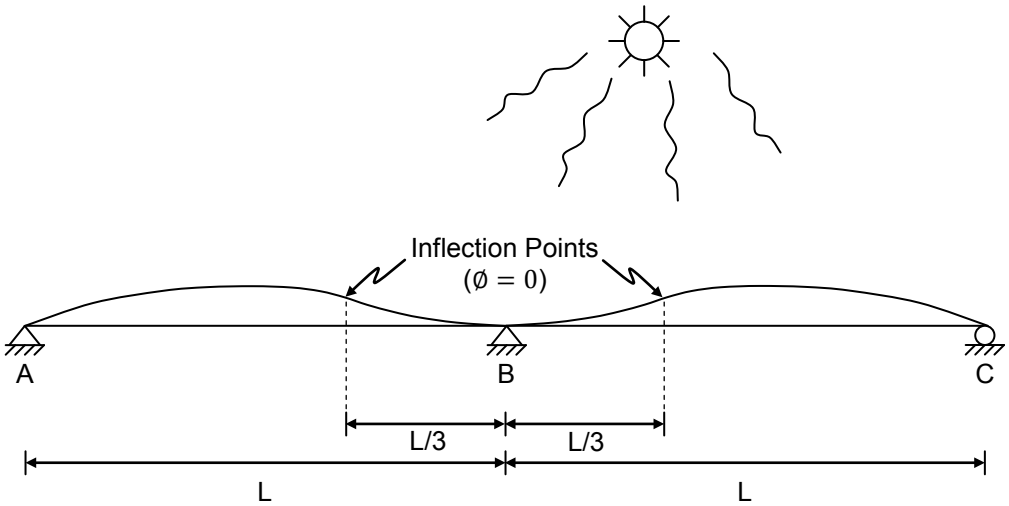

Figure 5.69: Deflections due to temperature gradient with restraint

5.4.2 Measured Responses to Ambient Thermal Conditions

Bridge monitoring measurements were analyzed to assess the post-repair behavior of the instrumented girders for twenty-four hours. The temperature and weather conditions during bridge monitoring were ideal for observing the bridge behavior in response to a near worst-case thermal gradient load condition for the geographic bridge location. The bridge monitoring measurements can be compared to the measured responses to truck placement and can also be related to the theoretical behavior of a continuous structure subjected to a linear thermal gradient.

All bridge monitoring measurements are relative to initial conditions measured at 2:30 a.m. on the first night of bridge testing. These initial conditions are not necessarily equal to the initial conditions observed during the static load tests on the second night of testing, but are similar enough to allow for approximate comparisons of magnitude for measured responses to load truck placement and ambient thermal conditions. The bridge monitoring measurements are presented graphically in Appendix D and in tabular format in Appendix E of this report.

For the purpose of analyzing the change in deflection and bottom-fiber strain profiles, four specific times were selected based on the observation of measured responses for all sensor types. The times selected were 6:30 a.m., 4:30 p.m., 8:30 p.m., and 2:30 a.m. Measurements at 6:30 a.m. represent responses measured just before the thermal conditions begin to rapidly change at dawn. Measurements at 4:30 p.m. represent a near-maximum response to thermal conditions. Measurements at 8:30 p.m. represent responses measured while the bridge deck

was cooling down after sunset. Measurements at 2:30 a.m. represent responses measured at the conclusion of the twenty-four hour period.

The post-repair weather conditions were favorable for the desired analysis of structural behavior in response to large temperature variations experienced during a daily cycle. Temperatures measured at the Huntsville International Airport every three hours during post-repair bridge monitoring are presented in Table 5.19. Sunrise reportedly occurred at 4:38 a.m., and sunset reportedly occurred at 6:50 p.m. on May 25, 2010. (NOAA 2010)

Table 5.19: Temperatures measured during bridge monitoring (NOAA 2010)

Date	Time (CST)	Temperature (°F)
May 25, 2010	12:00 a.m.	72
	3:00 a.m.	71
	6:00 a.m.	71
	9:00 a.m.	78
	12:00 p.m.	80
	3:00 p.m.	84
	6:00 p.m.	82
	9:00 p.m.	75
May 26, 2010	12:00 a.m.	70
	3:00 a.m.	66

5.4.2.1 Deflections

Deflection measurements in response to ambient thermal conditions are relative to initial conditions at 2:30 a.m. on the first night of bridge testing. Positive deflection measurements indicate upward deflections compared to initial conditions, and negative deflection measurements indicate downward deflections compared to initial conditions. The deflections measured in response to thermal conditions are presented in Tables E.2 and E.3. Graphical presentations of the midspan and quarterspan deflections measured during the twenty-four hour period are shown in Figures 5.70 and 5.71.

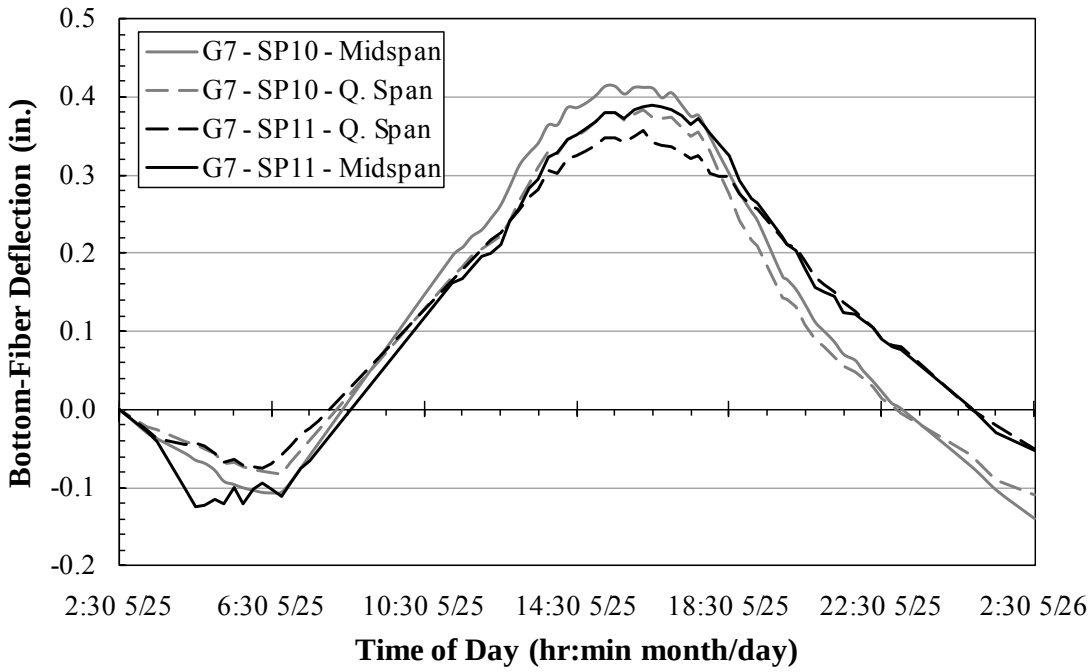

Figure 5.70: Deflections—normal traffic—twenty-four hours—Girder 7

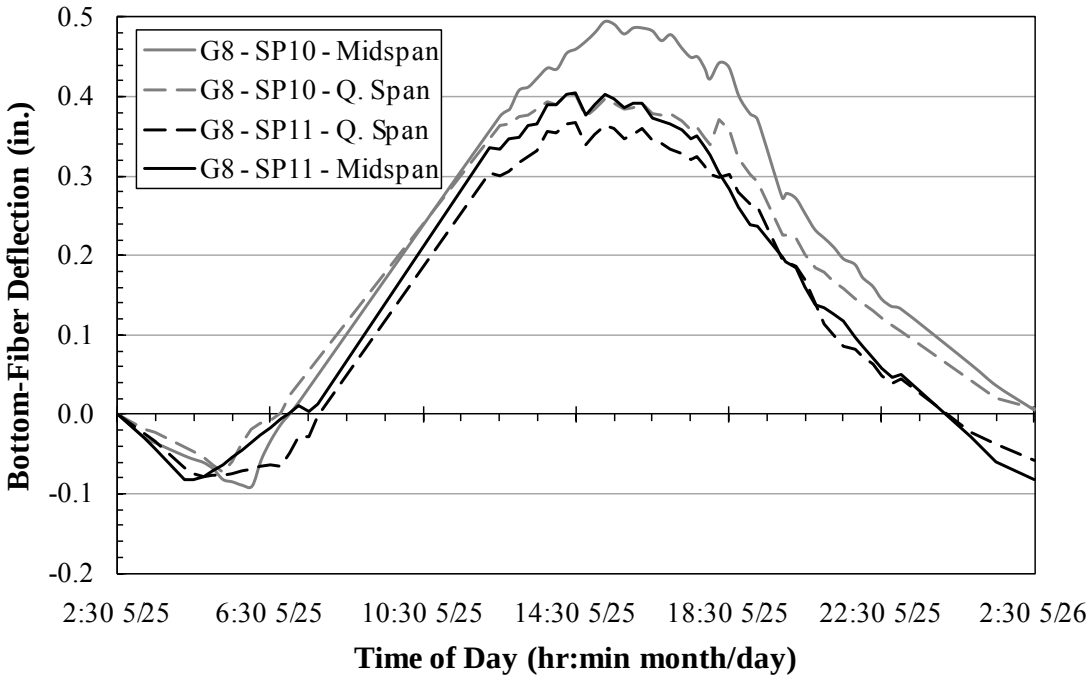

Figure 5.71: Deflections—normal traffic—twenty-four hours—Girder 8

5.4.2.1.1 Maximum Upward Deflections

The upward deflections measured in response to ambient thermal conditions were compared to the upward deflections measured in response to truck loads. The maximum upward deflections at midspan and quarterspan due to thermal conditions are presented in Table 5.20. These maximum upward deflections due to thermal conditions are compared to the maximum upward deflections due to truck loads as shown in Table 5.21.

Table 5.20: Maximum upward deflections—thermal conditions

Girder	Span	Location *from continuity diaphragm at Bent 11*	Deflection (in.)	Time Measured (hr:min a.m./p.m.)
7	10	midspan	0.41	3:30 p.m.
		quarterspan	0.38	4:30 p.m.
	11	quarterspan	0.36	4:30 p.m.
		midspan	0.39	4:30 p.m.
8	10	midspan	0.49	3:30 p.m.
		quarterspan	0.40	2:30 p.m.
	11	quarterspan	0.37	2:30 p.m.
		midspan	0.40	2:30 p.m.

Table 5.21: Maximum upward deflections—post-repair

Girder	Span	Location *from continuity diaphragm at Bent 11*	Maximum Upward Deflection (in.)	
			Thermal Conditions	Load Truck Conditions
7	10	midspan	0.41	0.04
		quarterspan	0.38	0.04
	11	quarterspan	0.36	0.04
		midspan	0.39	0.05
8	10	midspan	0.49	0.05
		quarterspan	0.40	0.04
	11	quarterspan	0.37	0.04
		midspan	0.40	0.05

NCHRP Report 519 (Miller et al. 2004) indicates that a maximum camber of 0.41 in. at midspan was observed in response to solar effects during ALDOT bridge testing (ALDOT 1994). The maximum upward deflections were observed at the time of day when the thermal gradient would be reaching its peak. A maximum upward deflection of 0.49 in. was measured at roughly 3:30 p.m. by the midspan deflectometer of Girder 8 in Span 10, and the other three midspan sensors measured maximum upward deflections of 0.39 in., 0.40 in., and 0.41 in. The magnitudes of the maximum midspan upward deflections for each instrumented girder—disregarding Girder 8-Span 10—were very similar to the maximum upward deflection measured by ALDOT in 1994.

The maximum upward deflection measured due to any load truck position during post-repair bridge testing was 0.05 in. at the midspan locations of three of the four girders. These maximum upward deflections measured during bridge testing were all in response to the midspan truck position in the opposite span. The maximum midspan and quarterspan upward deflections measured in response to thermal condition are approximately ten times greater than the maximum upward deflections measured in response to service-level truck loads.

5.4.2.1.2 Deflected Shape—Measured and Theoretical

Measured deflections were illustrated to observe the change in deflected shape due to ambient thermal conditions. The deflections measured at 6:30 a.m., 4:30 p.m., 8:30 p.m. and 2:30 a.m.

are presented graphically in Figures 5.72–5.75. A summary of the midspan and quarterspan deflections measured at these times is presented in Table 5.22.

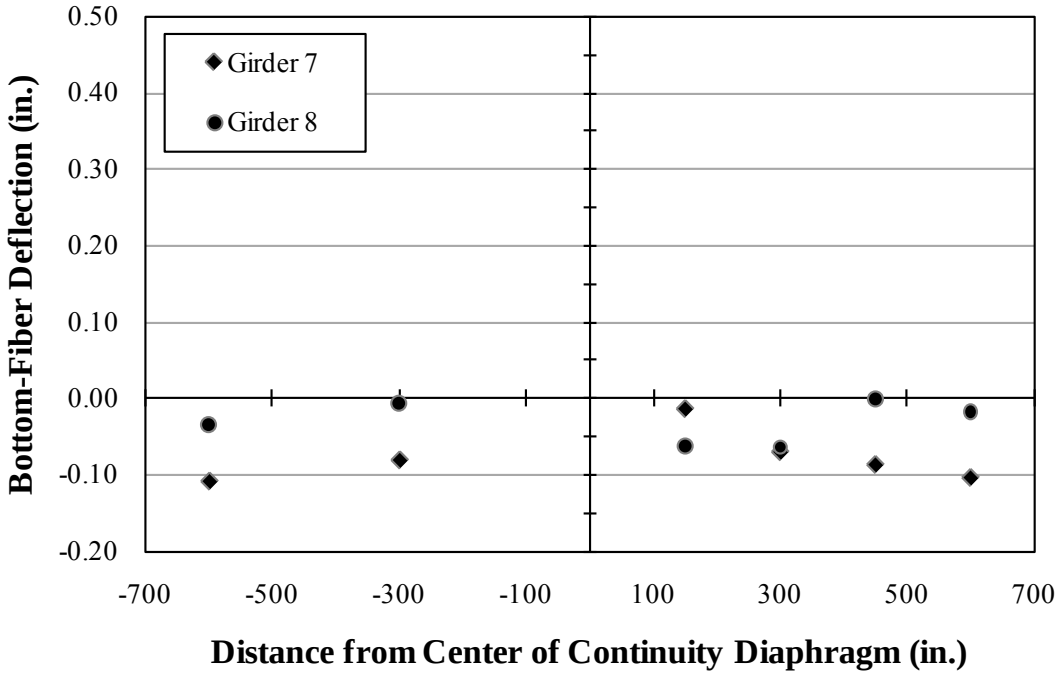

Figure 5.72: Deflections—8:30 a.m.

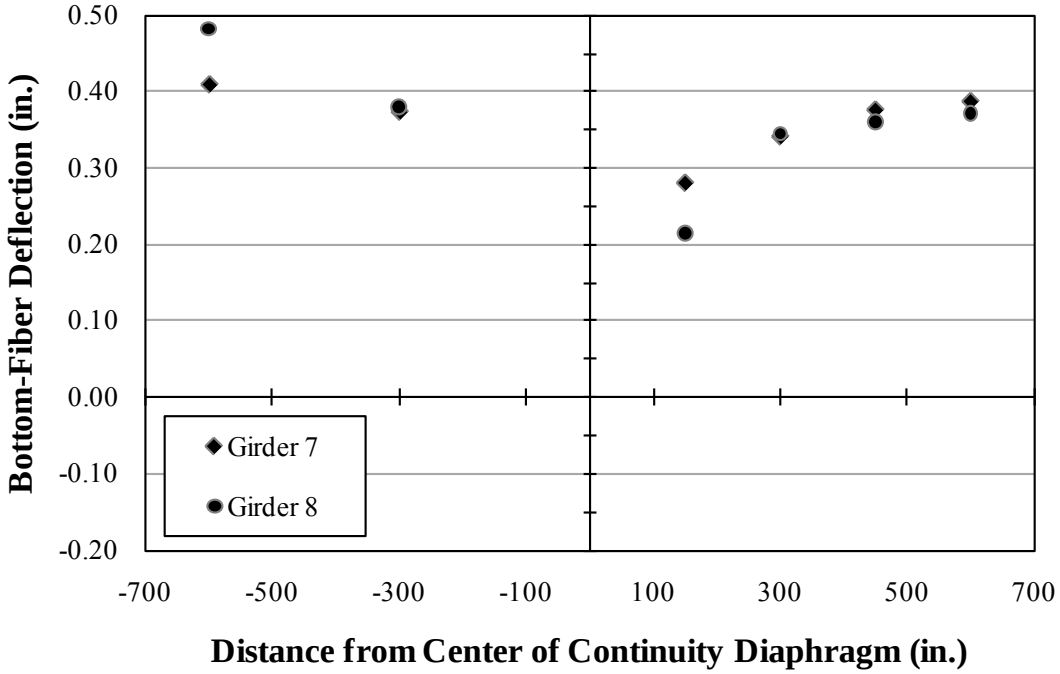

Figure 5.73: Deflections—4:30 p.m.

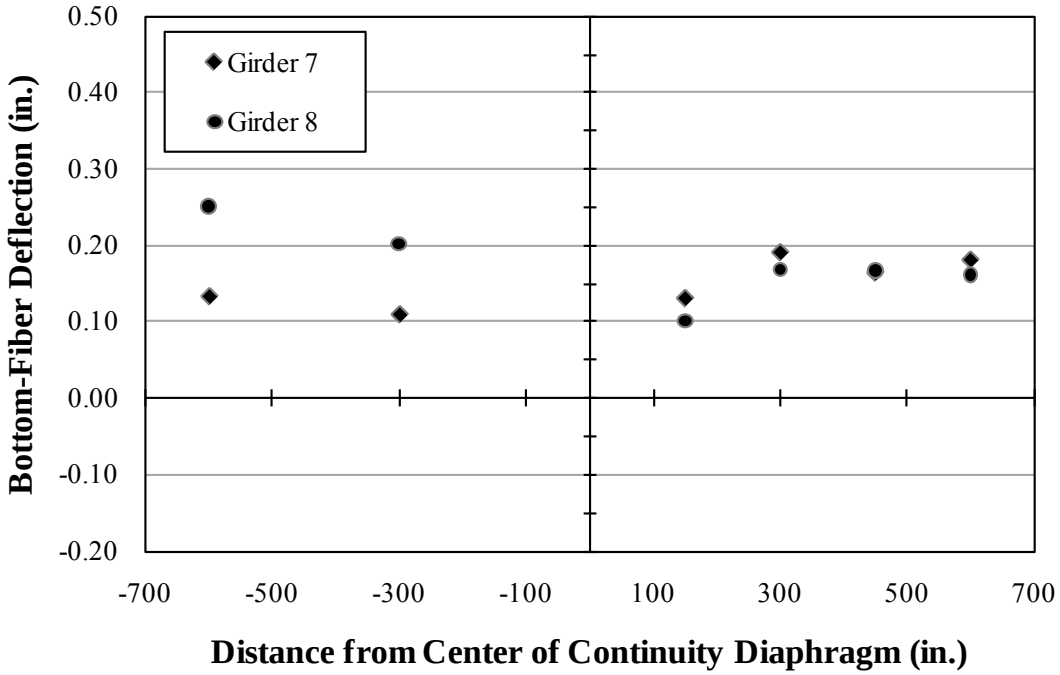

Figure 5.74: Deflections—8:30 p.m.

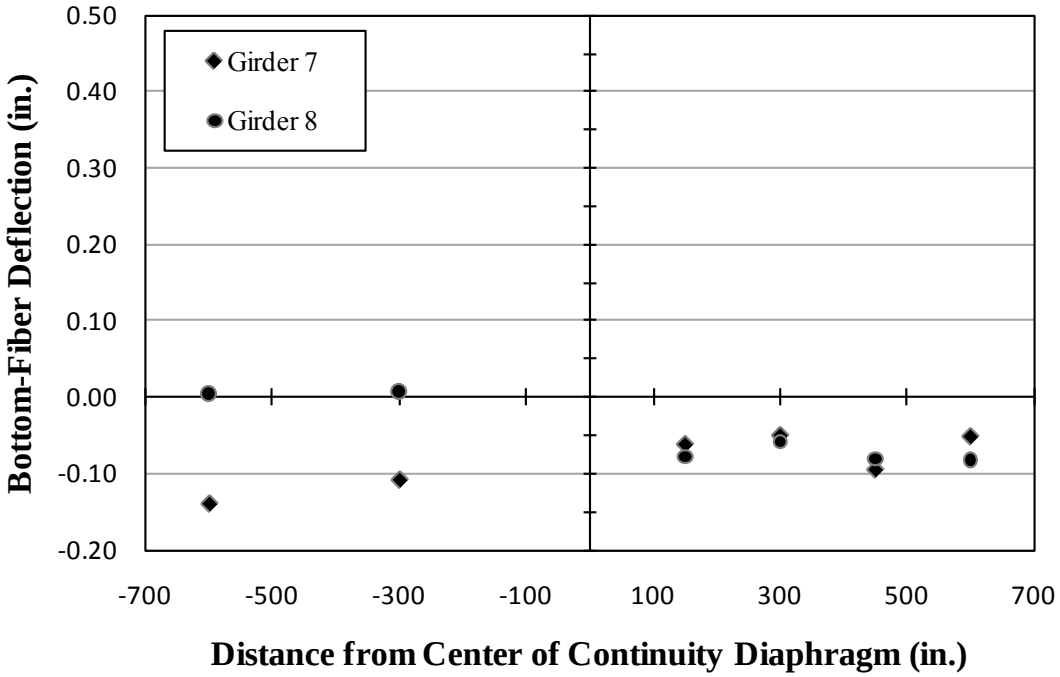

Figure 5.75: Deflections—2:30 a.m.

Table 5.22: Deflections—ambient thermal conditions

Girder	Span	Location *from continuity diaphragm at Bent 11*	Deflections (in.) – downward + upward			
			6:30 a.m.	4:30 p.m.	8:30 p.m.	2:30 a.m.
7	10	midspan	-0.11	0.41	0.13	-0.14
		quarterspan	-0.08	0.37	0.11	-0.11
	11	quarterspan	-0.07	0.34	0.34	-0.05
		midspan	-0.10	0.39	0.39	-0.05
8	10	midspan	-0.03	0.48	0.25	0.01
		quarterspan	-0.01	0.38	0.20	0.01
	11	quarterspan	-0.06	0.34	0.17	-0.06
		midspan	-0.02	0.37	0.16	-0.08

The deflections measured at 4:30 p.m. and 8:30 p.m. result in deflected shapes that are similar to the deflected shape expected of a continuous structure subjected to a thermal gradient as shown in Figure 5.69. However, additional measured deflections would be useful for providing clearer evidence of an inflection point in response to restrained thermal effects.

5.4.2.2 Bottom-Fiber Strains

Strain measurements in response to ambient thermal conditions are relative to initial conditions at 2:30 a.m. on the first night of bridge testing. Positive strains measurements indicate elongation relative to the initial conditions, and negative strain measurements indicate relative contraction. The bottom-fiber strains measured due to thermal conditions are presented in Tables E.12 and E.13. Graphical presentations of the bottom-fiber strains measured during the twenty-four hour period are shown in Figures 5.76–5.79.

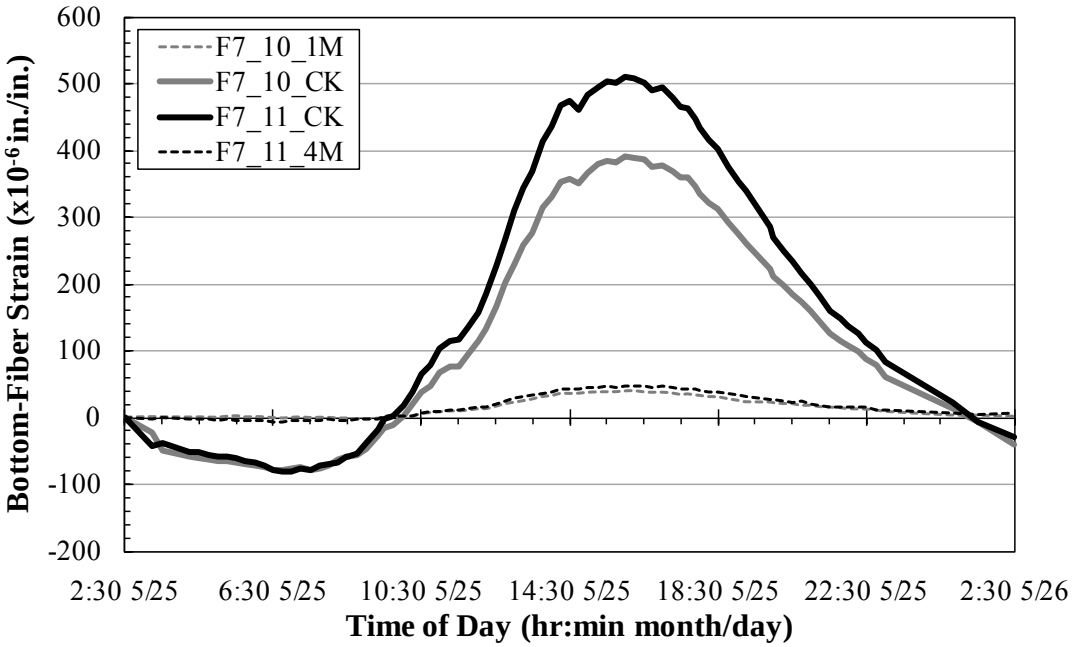

Figure 5.76: Bottom-fiber strains—Girder 7—within 80 in. from diaphragm

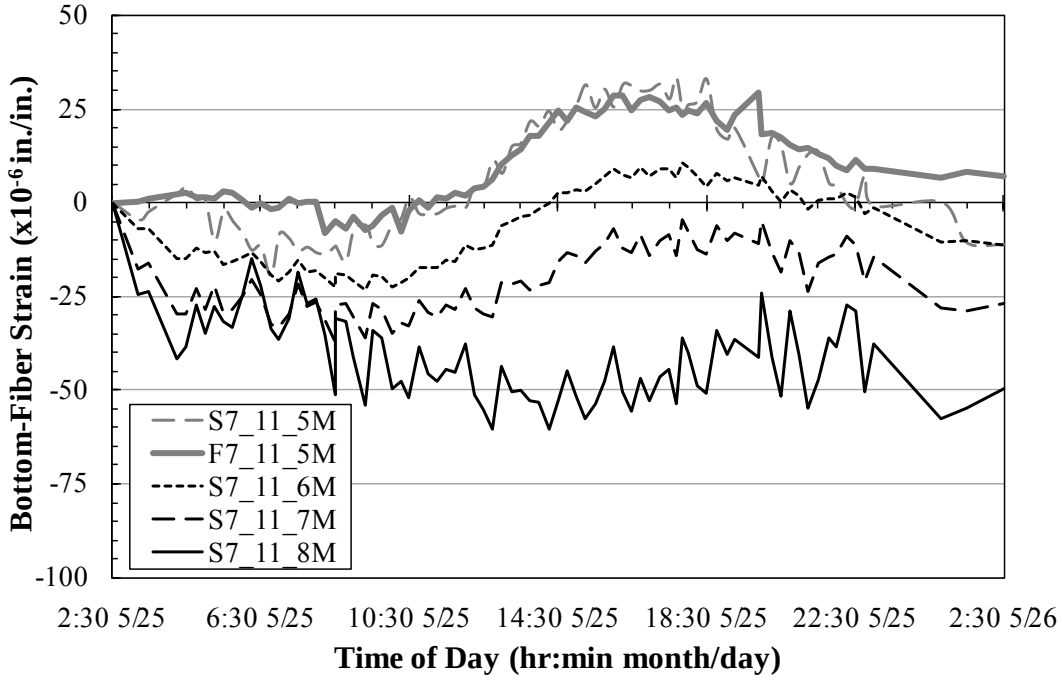

Figure 5.77: Bottom-fiber strains—Girder 7—beyond 80 in. from diaphragm

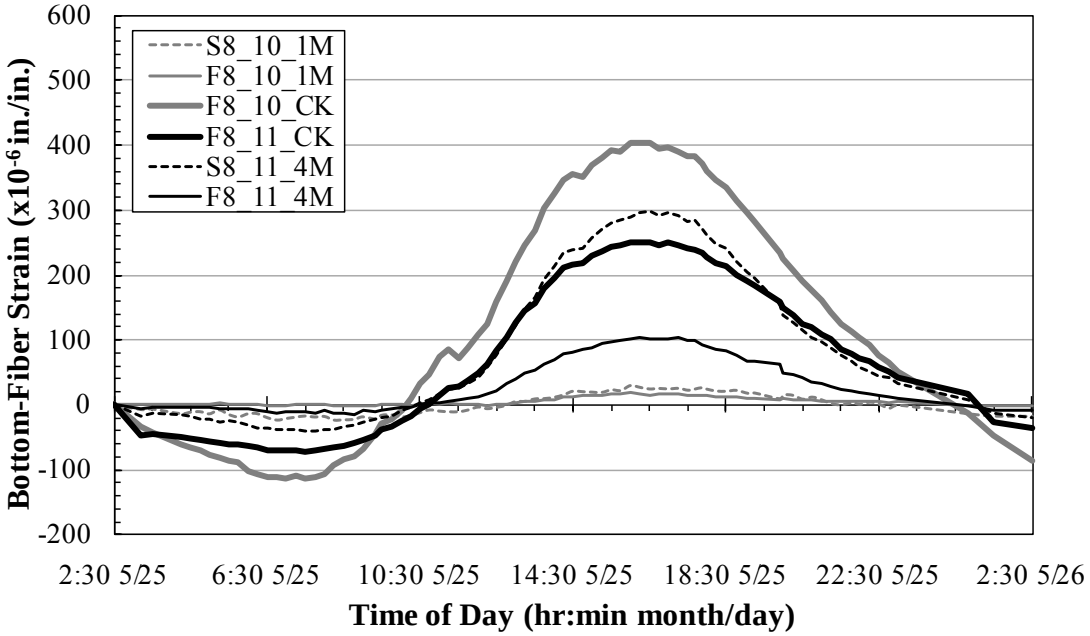

Figure 5.78: Bottom-fiber strains—Girder 8—within 80 in. from diaphragm

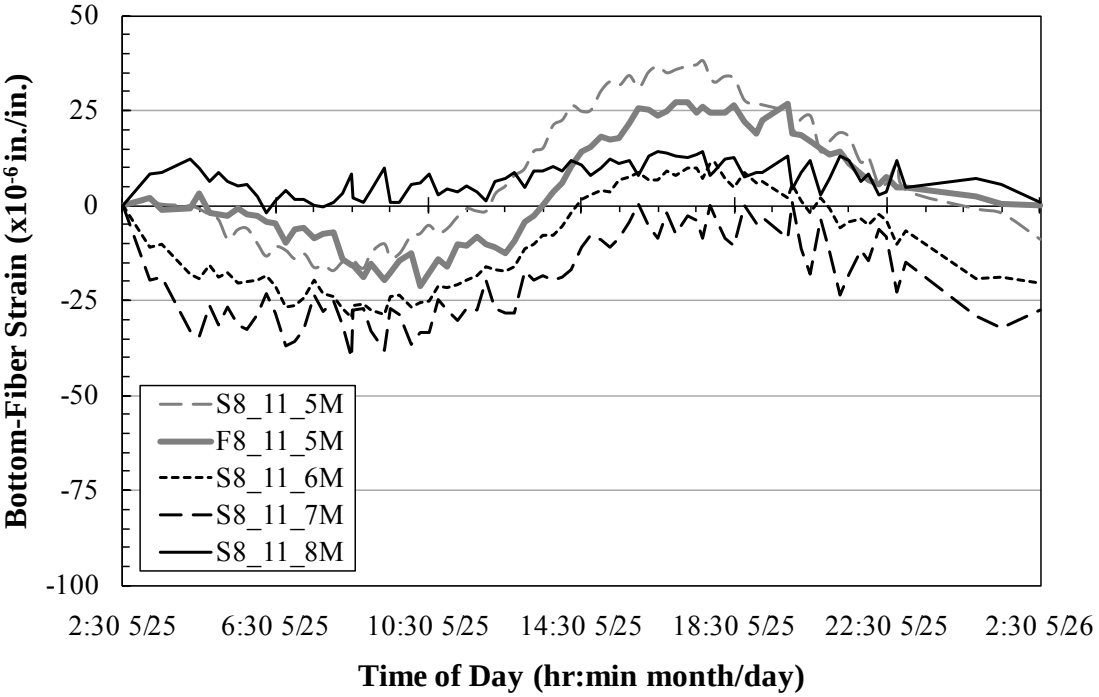

Figure 5.79: Bottom-fiber strains—Girder 8—beyond 80 in. from diaphragm

5.4.2.2.1 Maximum Bottom-Fiber Tensile Strains

The maximum bottom-fiber tensile strains measured in response to ambient thermal conditions were compared to the maximum bottom-fiber tensile strains measured in response to truck loads. The bottom-fiber strain gages in Span 11 beyond 105 in. from the center of the continuity diaphragm did not measure significant tensile strains due to ambient thermal conditions compared to the other bottom-fiber strain gages. The maximum bottom-fiber tensile strains measured by gages located 105 in. from the continuity diaphragm or closer in response to ambient thermal conditions are presented in Tables 5.23 and 5.24. These maximum tensile strains measured in response to thermal conditions are compared to the maximum bottom-fiber tensile strains measured in response to truck loads as shown in Tables 5.25 and 5.26.

Table 5.23: Maximum bottom-fiber tensile strains—Girder 7—thermal conditions

Span	Distance from center of continuity diaphragm (in.) – Span 10 + Span 11	Location Description	Bottom-Fiber Strain ($x10^{-6}$ in./in.) – compressive + tensile	Time Measured (hr:min a.m./p.m.)
10	-74	FRP	38	4:30 p.m.
	-47	FRP-Crack	387	4:30 p.m.
11	47	FRP-Crack	504	3:30 p.m.
	74	FRP	46	4:30 p.m.
	104	FRP	27	6:30 p.m.
	105	Concrete	33	6:30 p.m.

Table 5.24: Maximum bottom-fiber tensile strains—Girder 8—thermal conditions

Span	Distance from center of continuity diaphragm (in.) – Span 10 + Span 11	Location Description	Bottom-Fiber Strain ($x10^{-6}$ in./in.) – compressive + tensile	Time Measured (hr:min a.m./p.m.)
10	-75	Concrete	25	4:30 p.m.
	-74	FRP	16	3:30 p.m.
	-41	FRP-Crack	404	4:30 p.m.
11	52	FRP-Crack	251	4:30 p.m.
	74	FRP	101	4:30 p.m.
	75	Concrete	297	4:30 p.m.
	104	FRP	27	6:30 p.m.
	105	Concrete	37	5:30 p.m.

Table 5.25: Maximum bottom-fiber tensile strains—Girder 7

Span	Distance from center of continuity diaphragm (in.) – Span 10 + Span 11	Location Description	Maximum Bottom-Fiber Tensile Strain ($x10^{-6}$ in./in.)	
			Thermal Conditions	Load Truck Conditions
10	-74	FRP	38	24
	-47	FRP-Crack	387	108
11	47	FRP-Crack	504	140
	74	FRP	46	28
	104	FRP	27	32
	105	Concrete	33	35

Table 5.26: Maximum bottom-fiber tensile strains—Girder 8

Span	Distance from center of continuity diaphragm (in.) – Span 10 + Span 11	Location Description	Maximum Bottom-Fiber Tensile Strain ($x10^{-6}$ in./in.)	
			Thermal Conditions	Load Truck Conditions
10	-75	Concrete	25	28
	-74	FRP	16	19
	-41	FRP-Crack	404	117
11	52	FRP-Crack	251	71
	74	FRP	101	59
	75	Concrete	297	148
	104	FRP	27	34
	105	Concrete	37	34

The maximum bottom-fiber tensile strains were observed at the time of day when the thermal gradient would be reaching its peak. A maximum bottom-fiber tensile strain of 504 x 10^{-6} in./in. was measured at roughly 3:30 p.m. by the near-crack bottom-fiber FRP strain gage on Girder 7 in Span 11.

The maximum bottom-fiber tensile strain measured in response to any load truck position during post-repair bridge testing was 148 x 10^{-6} in./in. at the bottom-fiber concrete strain gage located 75 in. from the center of the continuity diaphragm along Girder 8 in Span 11. The majority of the maximum bottom-fiber tensile strains in response to truck loads were associated with the AE static positions. Compared to the maximum bottom-fiber strains in response to truck loads, the maximum bottom-fiber tensile strains due to thermal conditions are more significantly increased for the gages installed on the FRP near the crack locations than at any other gage location. Overall comparisons of maximum bottom-fiber tensile strains due to thermal loads versus truck loads clearly indicate that the ambient thermal conditions at the time of the post-repair bridge testing resulted in greater tension demand on the damaged regions than any of the load truck conditions. These measured bottom-fiber strains support the conclusion that restraint of ambient thermal conditions was the cause of initial cracking.

5.4.2.2.2 Strain Profile—Measured and Theoretical

The bottom-fiber strain measurements were illustrated to observe the bottom-fiber strain profile along the length of the bridge structure due to ambient thermal conditions at different times throughout the twenty-four hour period. The bottom-fiber strains measured at 6:30 a.m., 4:30 p.m., 8:30 p.m. and 2:30 a.m. are presented graphically in Figures 5.80–5.83. A summary of these bottom-fiber strain measurements are presented in Tables 5.27 and 5.28.

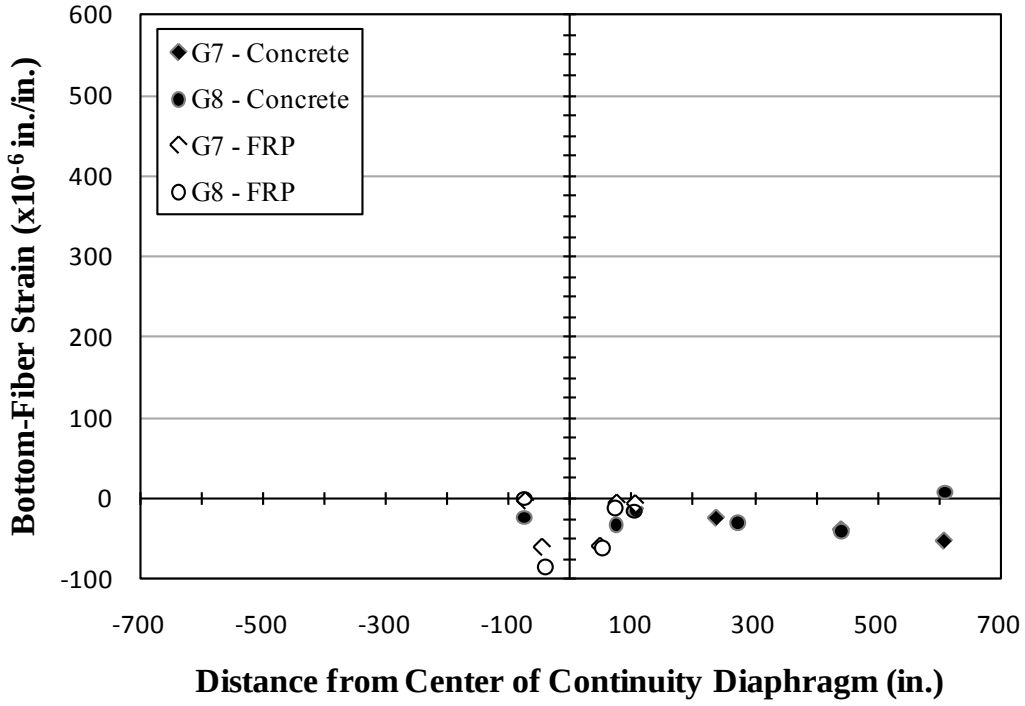

Figure 5.80: Bottom-fiber strains—8:30 a.m.

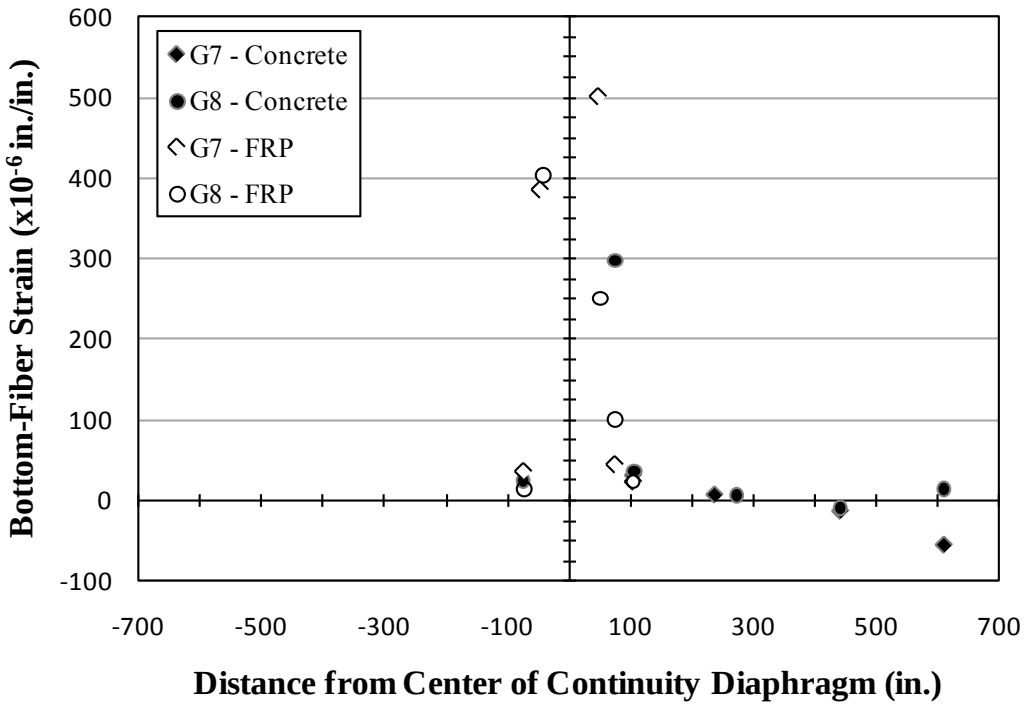

Figure 5.81: Bottom-fiber strains—4:30 p.m.

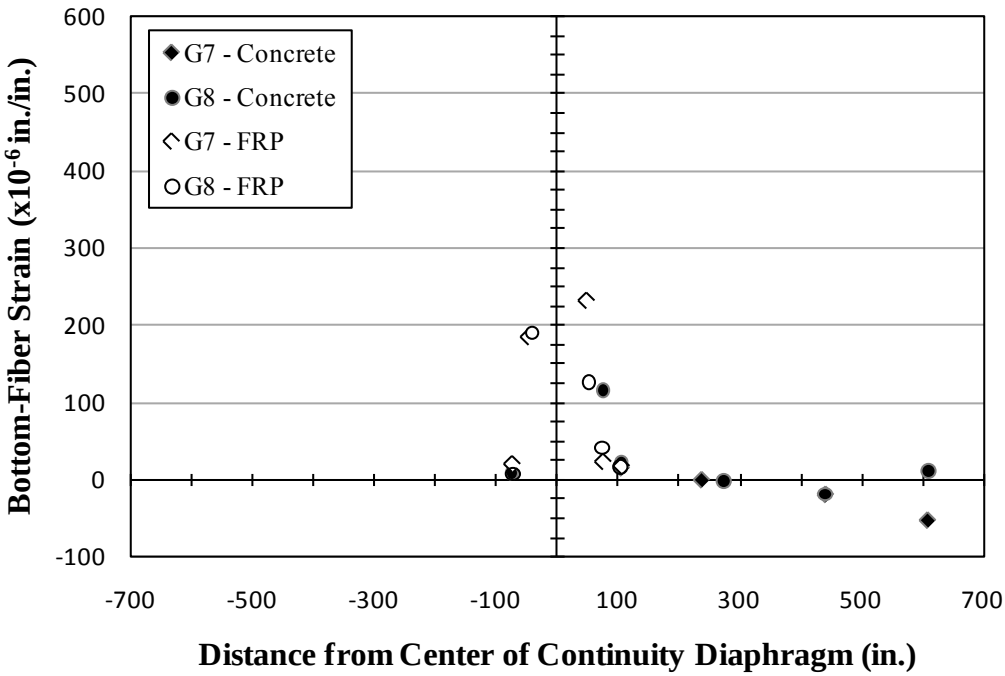

Figure 5.82: Bottom-fiber strains—8:30 p.m.

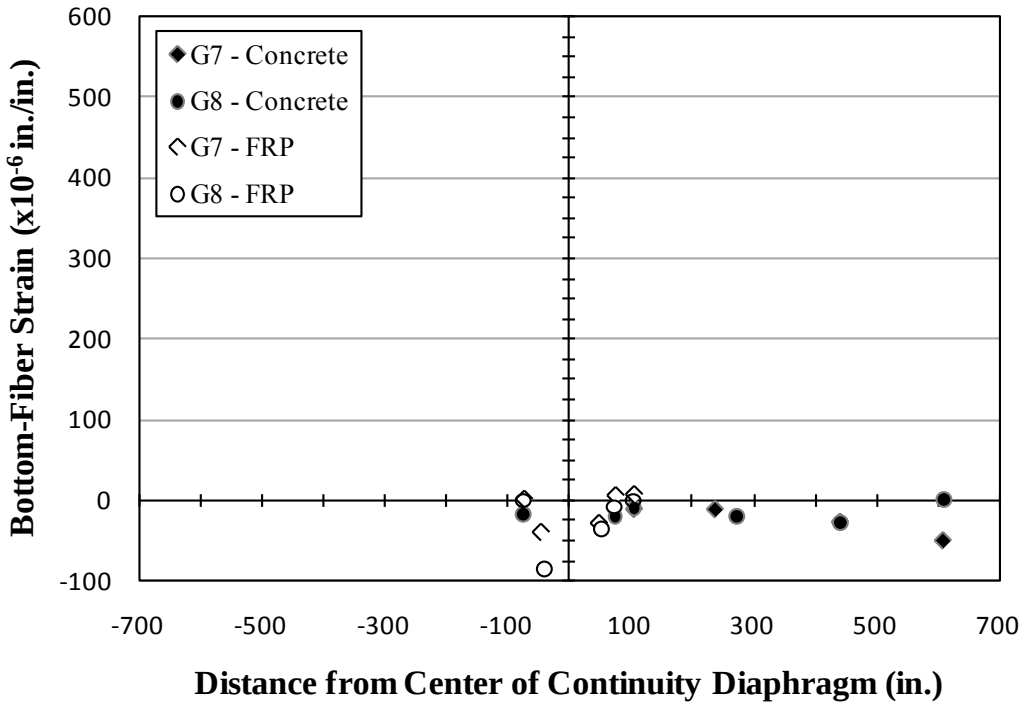

Figure 5.83: Bottom-fiber strains—2:30 a.m.

Table 5.27: Bottom-fiber strains—Girder 7—ambient thermal conditions

Span	Distance from center of continuity diaphragm (in.) – Span 10 + Span 11	Location Description	Bottom-Fiber Strain ($x10^{-6}$ in./in.) – compressive + tensile			
			6:30 a.m.	4:30 p.m.	8:30 p.m.	2:30 a.m.
10	-74	FRP	-1	38	20	1
	-47	FRP-Crack	-78	387	185	-39
11	47	FRP-Crack	-79	502	233	-28
	74	FRP	-6	46	23	6
	104	FRP	0	25	17	7
	105	Concrete	-12	31	15	-11
	273	Concrete	-16	7	0	-11
	441	Concrete	-24	-14	-19	-27
	609	Concrete	-22	-56	-52	-50

Table 5.28: Bottom-fiber strains—Girder 8—ambient thermal conditions

Span	Distance from center of continuity diaphragm (in.) – Span 10 + Span 11	Location Description	Bottom-Fiber Strain ($x10^{-6}$ in./in.) – compressive + tensile			
			6:30 a.m.	4:30 p.m.	8:30 p.m.	2:30 a.m.
10	-75	Concrete	-20	25	9	-18
	-74	FRP	-1	15	8	-1
	-41	FRP-Crack	-111	404	190	-86
11	52	FRP-Crack	-69	251	126	-36
	74	FRP	-9	101	41	-8
	75	Concrete	-36	297	116	-20
	104	FRP	-5	24	17	0
	105	Concrete	-11	37	23	-9
	273	Concrete	-21	7	-2	-21
	441	Concrete	-28	-9	-18	-28
	609	Concrete	1	14	12	1

To allow for better comparison between measured bottom-fiber strains and theoretical bottom-fiber strains of a continuous uncracked structure, the bottom-fiber concrete strains for each girder line are also presented at the same previously mentioned times, but independent of the other bottom-fiber strain measurements. The bottom-fiber concrete strains for Girder Line 7 are presented in Figures 5.84–5.87, and the bottom-fiber concrete strains for Girder Line 8 are presented in Figures 5.88–5.91. The slopes of linear trend lines for the more reliable concrete strain gages in Span 11 beyond the damaged zone have been noted in each figure. These slopes indicate that during service conditions the structure experiences larger differences of bottom-fiber strain along a girder line during times associated with larger temperature gradients. This behavior is another indication that the bridge structure is exhibiting continuous behavior.

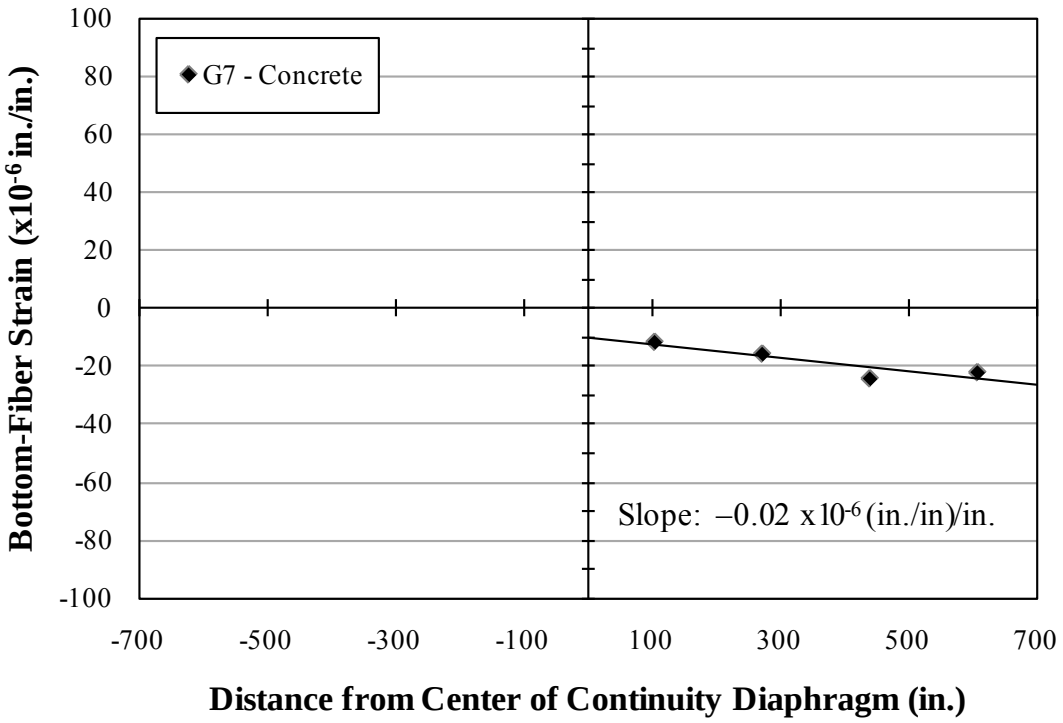

Figure 5.84: Bottom-fiber strains—concrete—Girder 7—6:30 a.m.

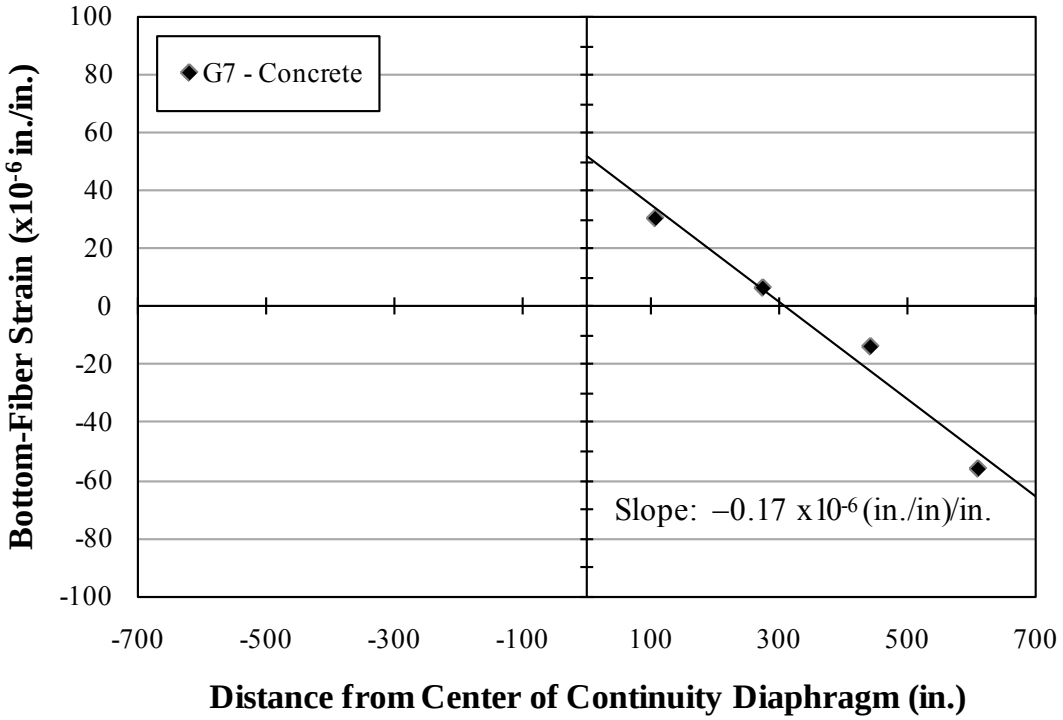

Figure 5.85: Bottom-fiber strains—concrete—Girder 7—4:30 p.m.

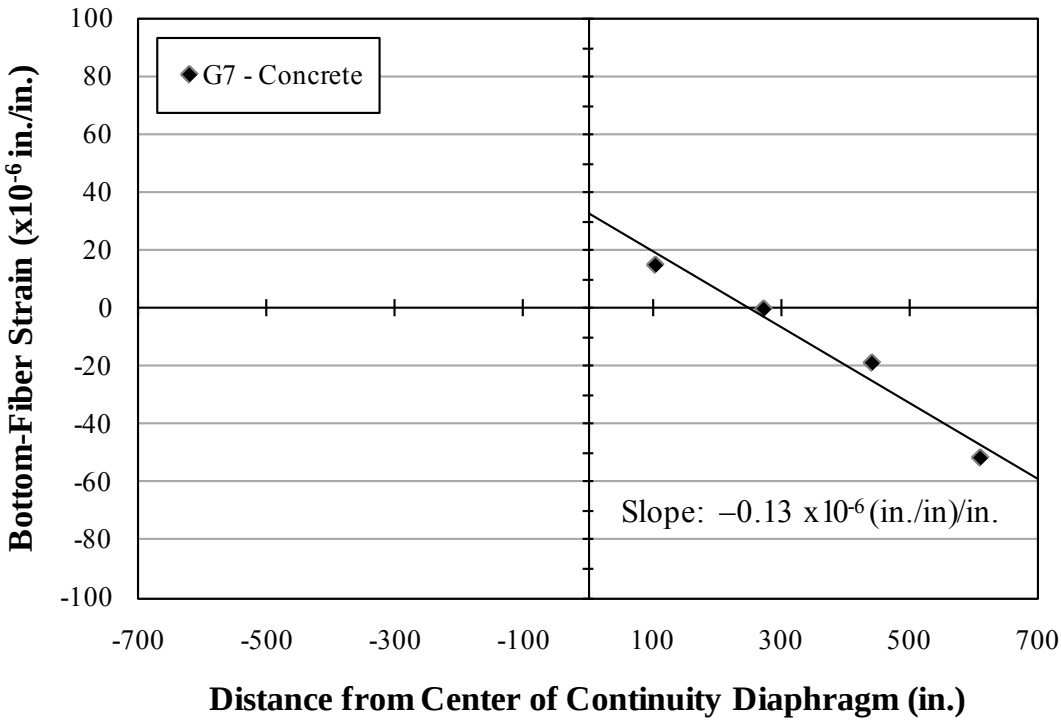

Figure 5.86: Bottom-fiber strains—concrete—Girder 7—8:30 p.m.

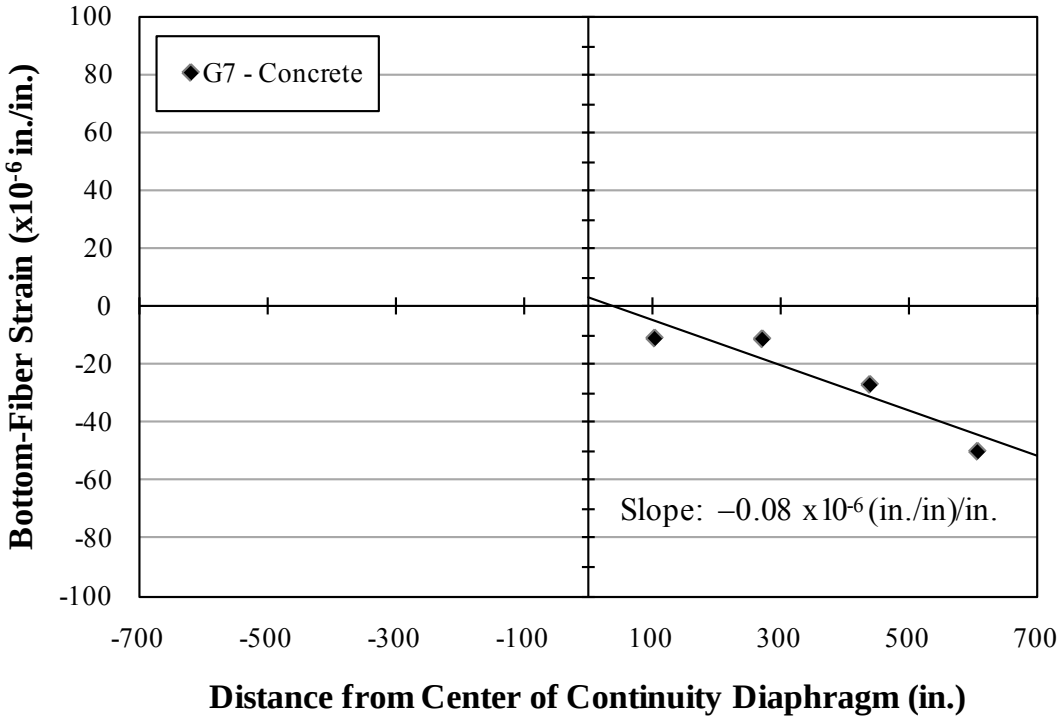

Figure 5.87: Bottom-fiber strains—concrete—Girder 7—2:30 a.m.

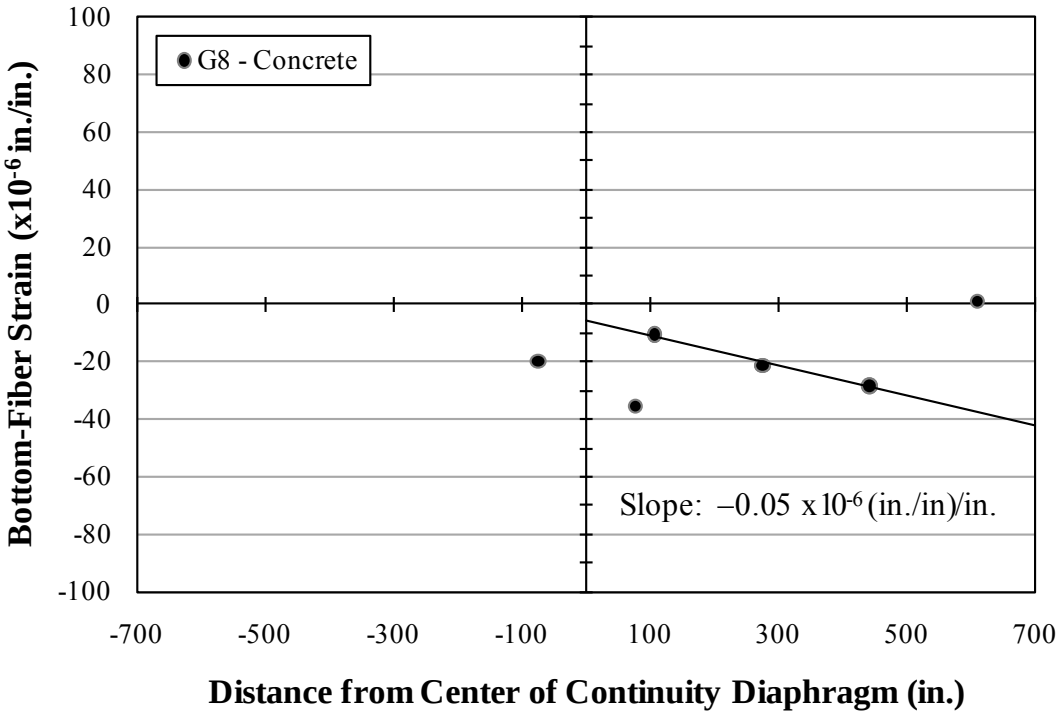

Figure 5.88: Bottom-fiber strains—concrete—Girder 8—6:30 a.m.

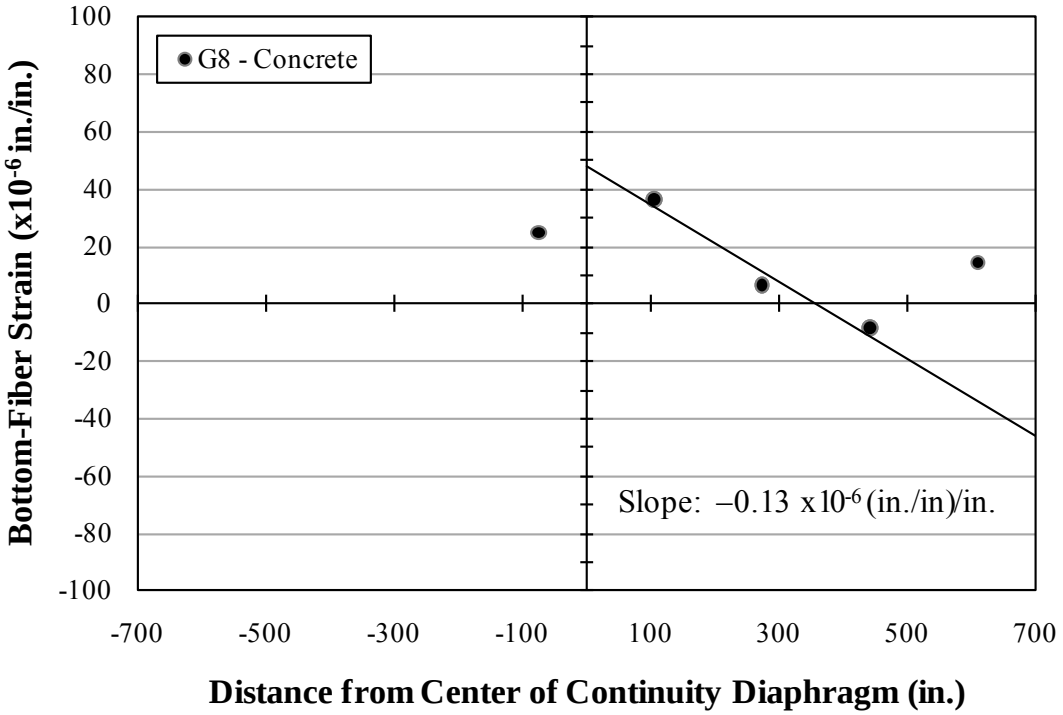

Figure 5.89: Bottom-fiber strains—concrete—Girder 8—4:30 p.m.

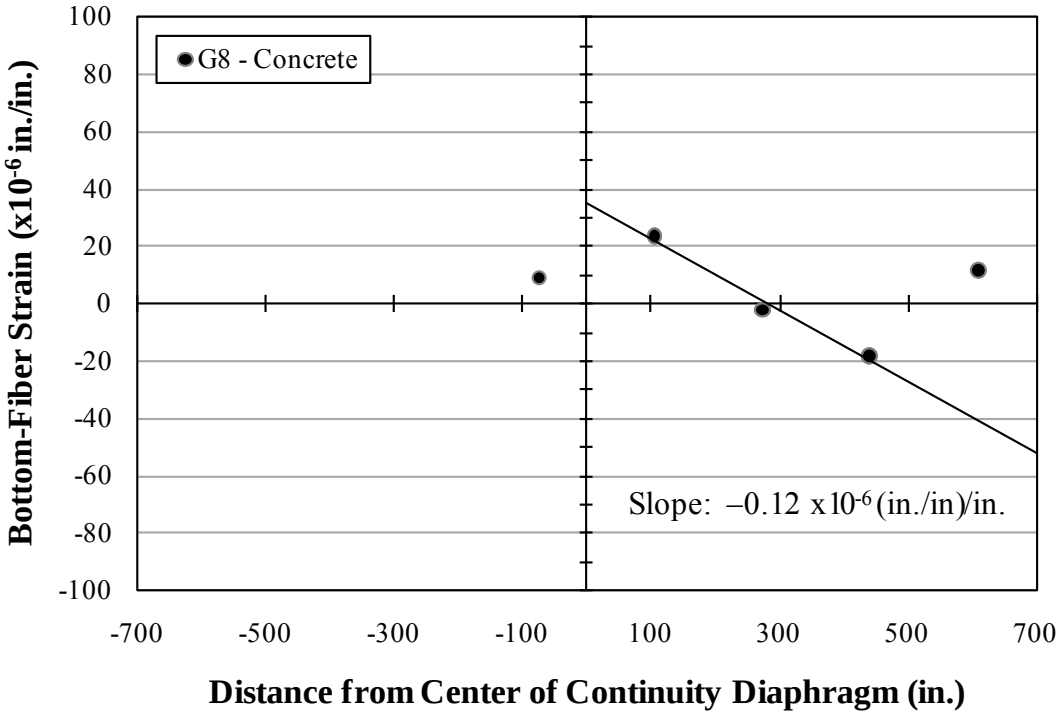

Figure 5.90: Bottom-fiber strains—concrete—Girder 8—8:30 p.m.

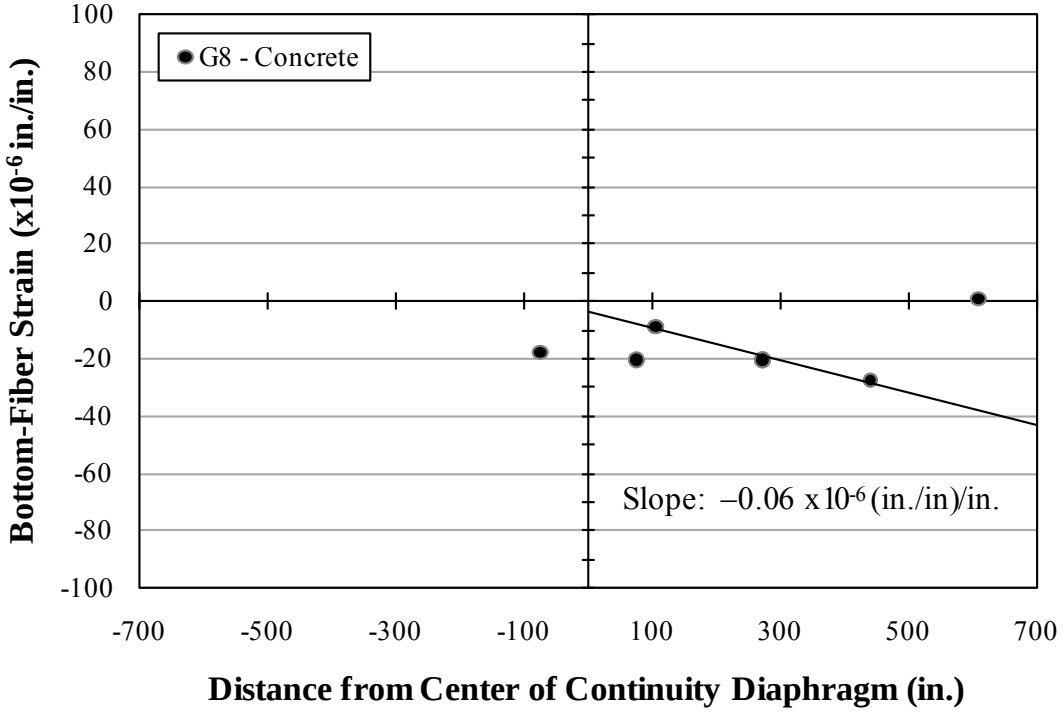

Figure 5.91: Bottom-fiber strains—concrete—Girder 8—2:30 a.m.

The trend line slopes can also be compared to the slope of the theoretical bottom-fiber strain profile presented in Figure 5.67. The formula for this theoretical slope is presented as Equation 5.35. Values for the formula variables, and the slope of the bottom-fiber strain profile expected due to these conditions, are presented following the equation. The temperature variation ($\delta(\Delta T_h)$) from the top of the deck to the bottom of a typical girder is assumed to be 44 °F, which was reported for ALDOT bridge testing (ALDOT 1994) with a maximum measured upward deflection similar to the maximum upward deflections measured during post-repair bridge monitoring. Also, the ALDOT bridge testing (May 19, 1994) and post-repair bridge monitoring (May 25, 2010) were conducted at a similar time of the year.

$$\frac{d}{dx}\varepsilon_{bot}(x) = \frac{-\frac{3}{2}\left[\frac{\alpha_T \delta(\Delta T_h)}{h}\right] y_{bot}}{L} \qquad \textbf{Eq. 5.35}$$

$$\alpha_T = 6 \text{ x } 10^{-6} (\text{in./in.})/°\text{F}$$

$$\delta(\Delta T_h) = 44 \text{ °F}$$

$$h = 61.5 \text{ in.}$$

$$y_{bot} = 42.5 \text{ in.}$$

$$L = 1156 \text{ in.}$$

$$\frac{d}{dx}\varepsilon_{bot}(x) = -0.24 \text{ x } 10^{-6} \text{ (in./in.)/in.}$$

The slope of the bottom-fiber strain profile expected due to these conditions is -0.24 x 10^{-6} (in./in.)/in., which is similar to the -0.17 x 10^{-6} (in./in.)/in. slope of the measured strain profile for Girder 7 in Span 11 at 4:30 p.m. as presented in Figure 5.85. The slope of the measured strain profile is less steep than the slope of the theoretical strain profile, which could be an indication that the girder is not exhibiting fully continuous behavior as theoretically assumed, or that the actual temperature gradient was less than the estimated value. This decrease in continuity exhibited by the slope of the measured strain profile is likely due to the local behavior of the damaged region.

The bottom-fiber strains near the damaged region are shown to be greater than the strains projected by trend lines associated with concrete strains beyond the damaged region. These near damage zone bottom-fiber strains are presented in Figures 5.92–5.95. The

magnitudes of the bottom-fiber tensile strains measured within the damaged region at 4:30 p.m. as shown in Figure 5.93 are an indication that the ambient thermal conditions have a significant effect on the damaged regions.

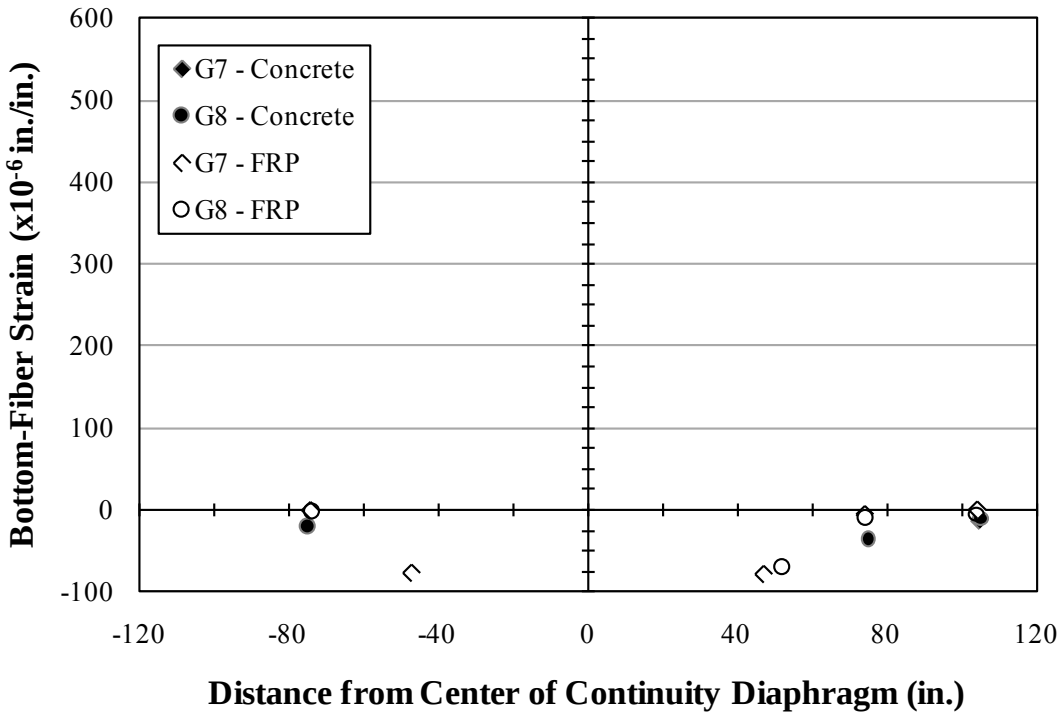

Figure 5.92: Bottom-fiber strains—damaged region—8:30 a.m.

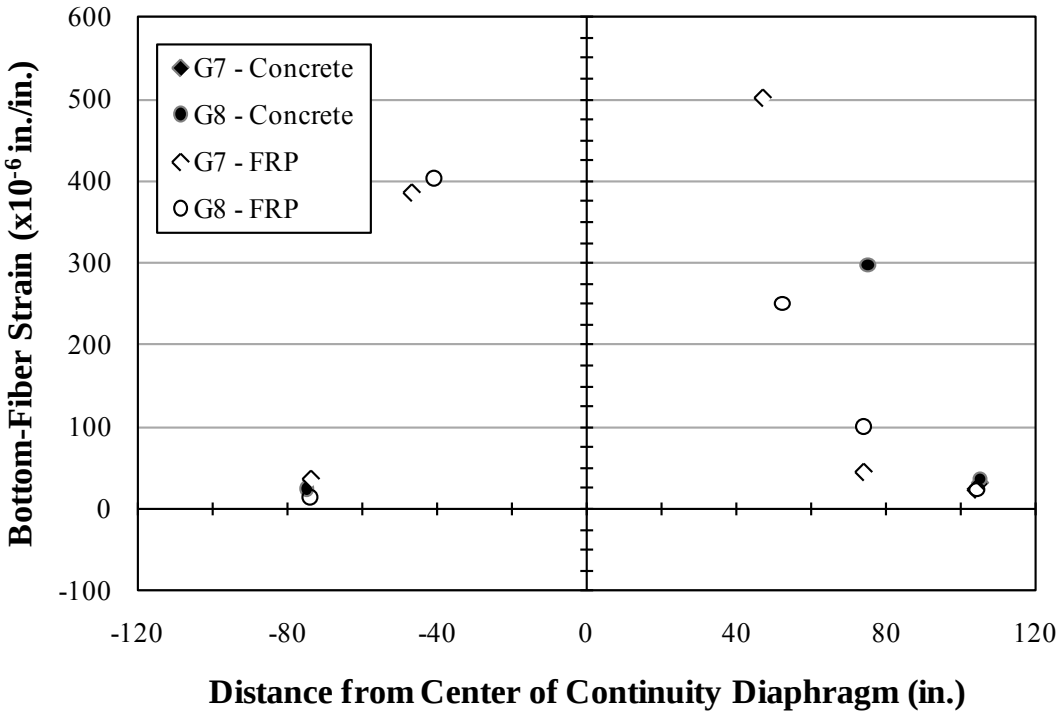

Figure 5.93: Bottom-fiber strains—damaged region—4:30 p.m.

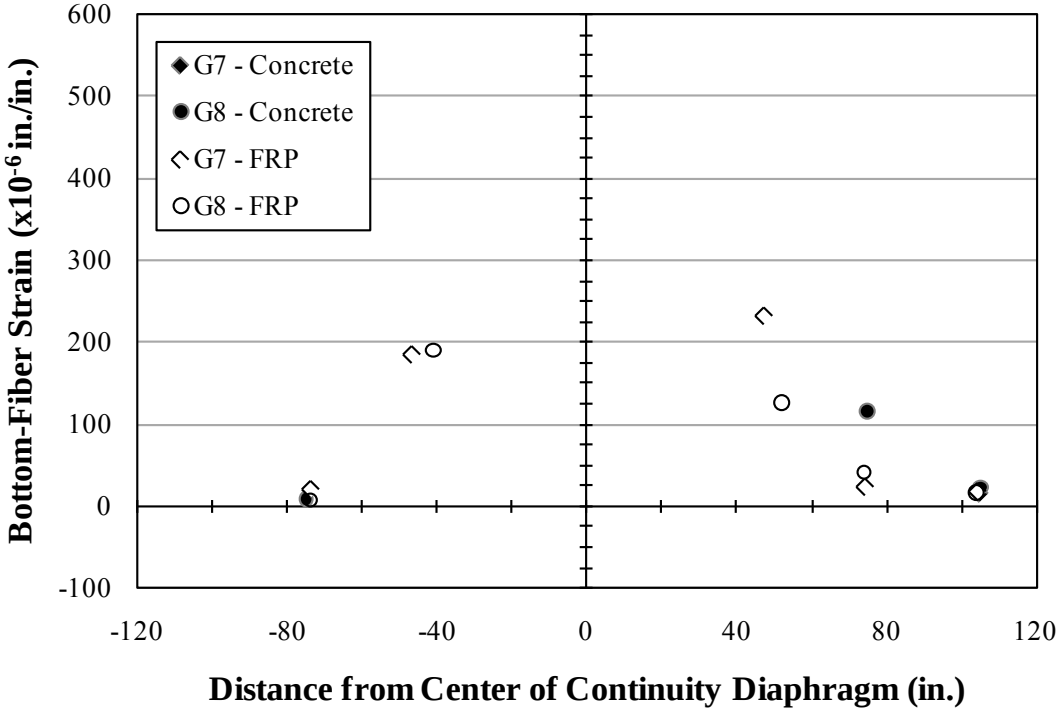

Figure 5.94: Bottom-fiber strains—damaged region—8:30 p.m.

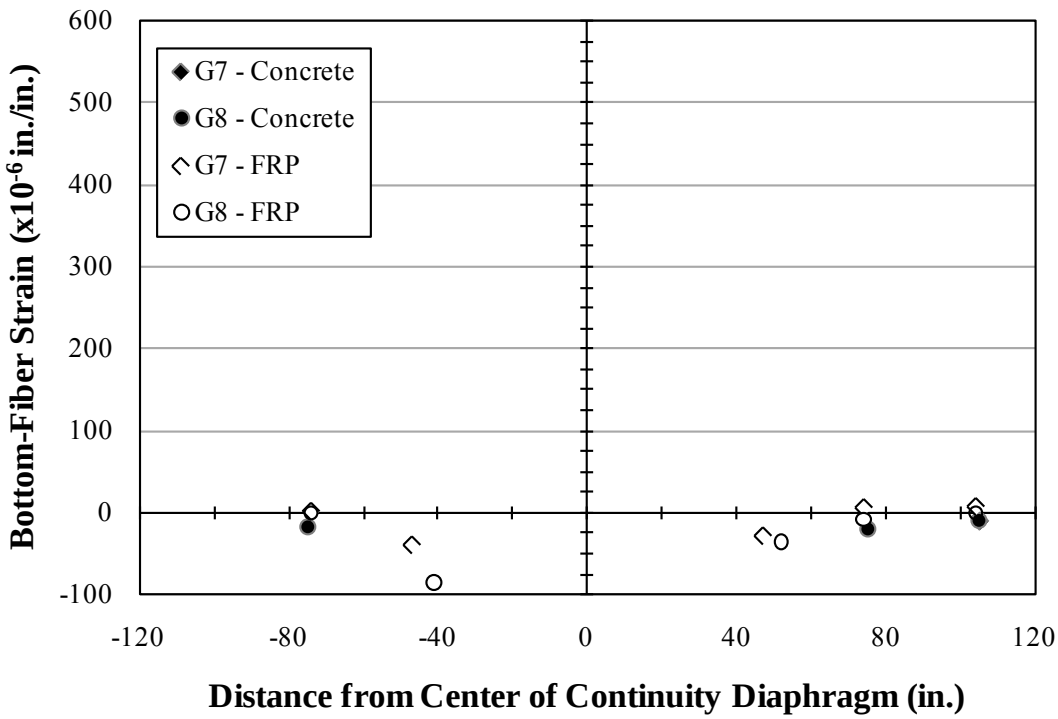

Figure 5.95: Bottom-fiber strains—damaged region—2:30 a.m.

The force resisted by the FRP at a cracked cross section must make up for the decreased flexural stiffness of the cracked section. The formula for the theoretical bottom-fiber FRP strain expected due to thermal conditions is presented as Equation 5.34.

The typical crack location observed at the continuous ends of the investigated girders is less than 4 percent of the respective span length. Due to the variation of crack location from the continuous end of the girder, it is conservative to assume that the ratio between the crack location and span length is nearly equal to zero. Also, due to the previously reported assumption that prestressing strands are considered to have slipped at a typical crack location, it is conservative to assume that the ratio between the distance from the cracked section neutral axis to the bottom of the girder and the overall height of the cross section is only slightly less than one—as would be expected in a cross section that is lightly reinforced with a wide compression flange. Based on these assumptions, the formula for the theoretical bottom-fiber FRP strain expected due to thermal conditions can be simplified as presented in Equation 5.36.

$$\varepsilon_{FRP}(x) = \alpha_{T,FRP}\Delta T_{FRP} + \frac{3}{2}[\alpha_T \delta(\Delta T_h)]\left[1 - \frac{x}{L}\right]\frac{y_{cr,bot}}{h}$$

$$\frac{x}{L} \approx 0$$

$$\frac{y_{cr,bot}}{h} \approx 1$$

$$\varepsilon_{FRP}(x) \approx \alpha_{T,FRP}\Delta T_{FRP} + \frac{3}{2}[\alpha_T \delta(\Delta T_h)] \qquad \textbf{Eq. 5.36}$$

Values for the formula variables, and the bottom-fiber strain expected due to these conditions, are presented following this paragraph. The concrete thermal properties remain the same as previously presented. The longitudinal coefficient of thermal expansion of the FRP (α_{FRP}) is approximately 3.6 x 10^{-6} (in./in.)/°F according to the manufacturer (Fyfe 2010). An FRP temperature variation (ΔT_{FRP}) of 30 °F is assumed based on the range of maximum and minimum ambient temperatures reported for the days encompassing post-repair testing (NOAA 2010).

$$\varepsilon_{FRP}(x) \approx \alpha_{T,FRP}\Delta T_{FRP} + \frac{3}{2}[\alpha_T \delta(\Delta T_h)]$$

$$\alpha_{T,FRP} = 3.6 \text{ x } 10^{-6} \text{ (in./in.)/in.}$$

$$\Delta T_{FRP} = 30 \text{ °F}$$

$$\alpha_T = 6 \text{ x } 10^{-6} \text{ (in./in.)/°F}$$

$$\delta(\Delta T_h) = 44 \text{ °F}$$

$$\varepsilon_{FRP}(x) \approx 110 \text{ x } 10^{-6} \text{ in./in.} + 400 \text{ x } 10^{-6} \text{ in./in.}$$

$$\varepsilon_{FRP}(x) \approx 510 \text{ x } 10^{-6} \text{ in./in.}$$

The bottom-fiber FRP strain expected due to these conditions is a tensile strain of 510 x 10^{-6} in./in., which is similar to the maximum tensile strains measured at the crack locations as presented in Tables 5.23 and 5.24. These similar tensile strains support the conclusion that this simplified analysis of structural response to a linear temperature gradient can be used to establish the tensile strain that must be resisted on a regular basis by an FRP repair system.

5.4.2.3 Crack-Opening Displacements

Crack-opening displacements in response to ambient thermal conditions are relative to initial conditions at 2:30 a.m. on the first night of bridge testing. Positive crack-opening displacement measurements indicate crack openings compared to the initial conditions, and negative crack-opening displacement measurements indicate crack closures compared to the initial conditions. The crack-opening displacements measured in response to ambient thermal conditions are

presented in Table E.1. Graphical presentations of these crack-opening displacements are shown in Figure 5.96.

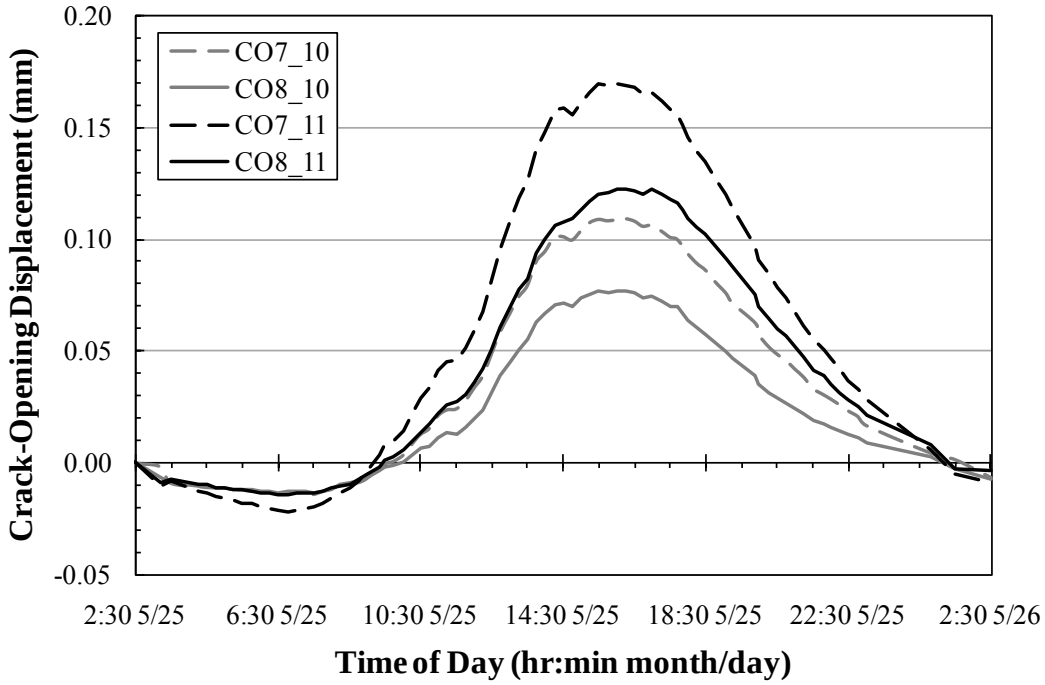

Figure 5.96: Crack-opening displacements—normal traffic—twenty-four hours

5.4.2.3.1 Maximum Crack Openings

The maximum crack openings measured in response to ambient thermal conditions have been compared to the maximum crack openings measured in response to truck loads. The maximum crack openings in response to ambient thermal conditions are presented in Table 5.29. These maximum crack openings measured in response to thermal conditions are compared to the maximum crack openings measured in response to truck loads as shown in Table 5.30.

Table 5.29: Maximum crack openings—thermal conditions

Girder	Span	Crack-Opening Displacement (mm) – closing + opening	Time Measured (hr:min a.m./p.m.)
7	**10**	0.109	3:30 p.m.
	11	0.169	3:30 p.m.
8	**10**	0.077	3:30 p.m.
	11	0.122	4:30 p.m.

Note: 1 in. = 25.4 mm

Table 5.30: Maximum crack openings—thermal and load truck conditions

Girder	Span	Maximum Crack Opening (mm) – closing + opening	
		Thermal Conditions	Load Truck Conditions
7	10	0.109	0.024
	11	0.169	0.047
8	10	0.077	-0.002
	11	0.122	0.040

Note: 1 in. = 25.4 mm

Table 5.31: Crack-opening displacements—ambient thermal conditions

Girder	Span	Crack-Opening Displacement (mm) – closing + opening			
		6:30 a.m.	4:30 p.m.	8:30 p.m.	2:30 a.m.
7	10	-0.014	0.108	0.049	-0.006
	11	-0.022	0.168	0.078	-0.009
8	10	-0.014	0.076	0.029	-0.007
	11	-0.014	0.122	0.060	-0.004

Note: 1 in. = 25.4 mm

The maximum crack openings measured in response to thermal conditions were observed around the time of day when the thermal gradient would be expected to peak. A maximum crack opening of 0.169 mm (6.66 x 10^{-3} in.) was measured at roughly 3:30 p.m. by the COD gage on the east face of Girder 7 in Span 11. The maximum crack opening measured in response to any load truck position during post-repair bridge testing was 0.047 mm (1.83 x 10^{-3} in.) at the same COD gage location on Girder 7 of Span 11 in response to the AE Span 11 static position. All of the COD gages measured crack openings of greater magnitude in response to thermal conditions compared to crack openings due to truck loads.

The COD gage on Girder 8 of Span 10 did not measure a crack opening in response to any of the static truck positions, but this same gage measured a crack opening of 0.077 mm (3.02 x 10^{-3} in.) due to ambient thermal conditions at roughly 3:30 p.m. The crack openings measured due to thermal conditions by the COD gage on Girder 8 of Span 10 are another indication that crack initiation or propagation is more likely due to extreme thermal conditions than oversized truck loads. These crack openings also support the static load test conclusion that out-of-plane bending had an effect on the COD measurements of this COD gage in response to truck loads. This is due to the fact that thermal conditions are less likely to produce out-of-plane bending in an interior girder than a wheel load placed on the bridge deck.

5.4.2.3.2 Crack Openings and Near-Crack FRP Tensile Strains

The crack-opening displacement measurements and near-crack bottom-fiber FRP strain measurements in response to ambient thermal conditions allow for analysis of gage performance. The crack-opening displacement and FRP strain relationship for the crack location of each instrumented girder has been presented in Figures 5.97–5.100. The measurements for each sensor at 4:30 p.m. have been presented in Table 5.32.

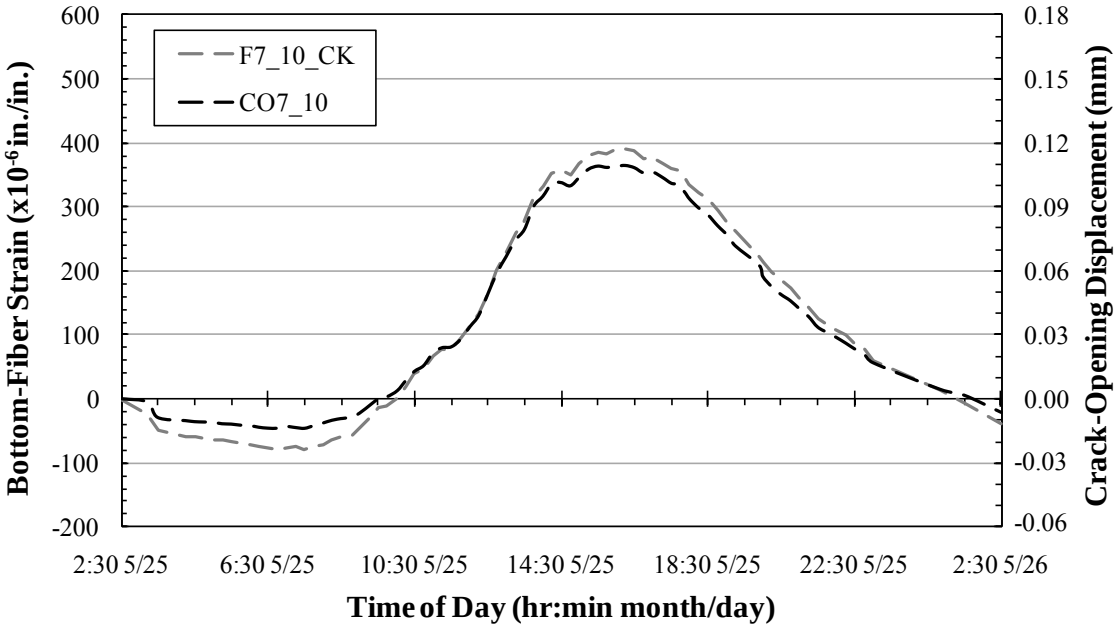

Figure 5.97: Bottom-fiber strain and COD—thermal conditions—Girder 7—Span 10

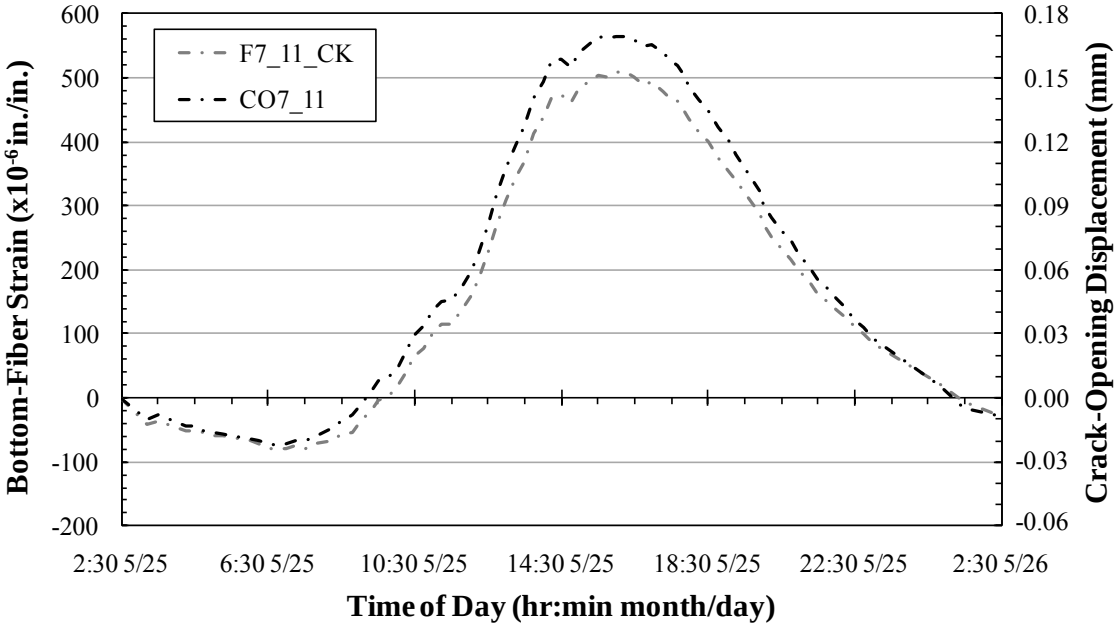

Figure 5.98: Bottom-fiber strain and COD—thermal conditions—Girder 7—Span 11

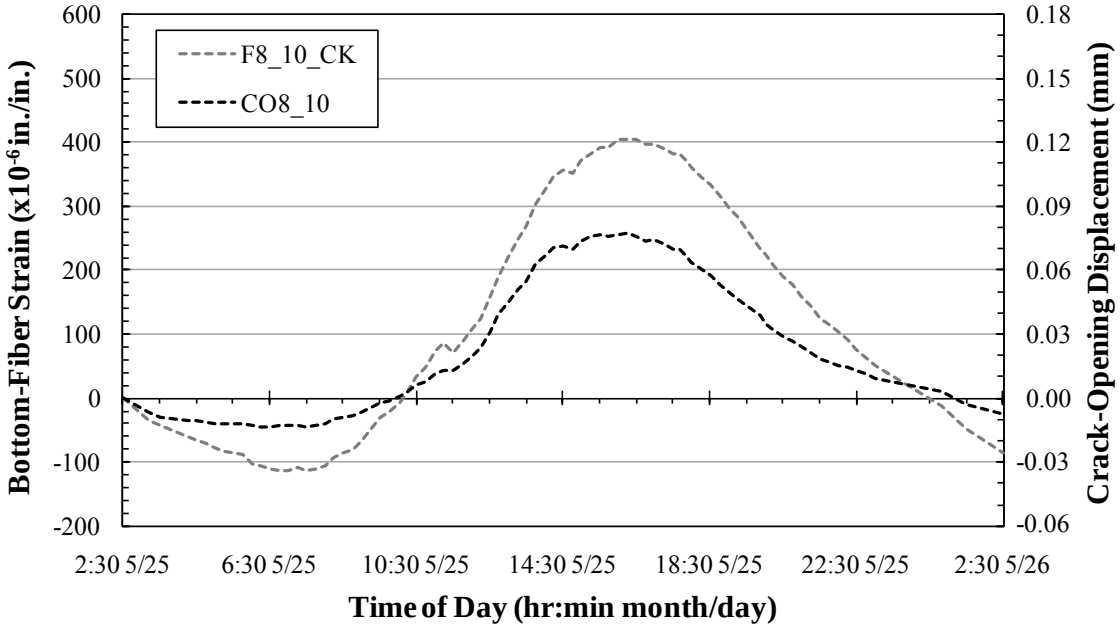

Figure 5.99: Bottom-fiber strain and COD—thermal conditions—Girder 8—Span 10

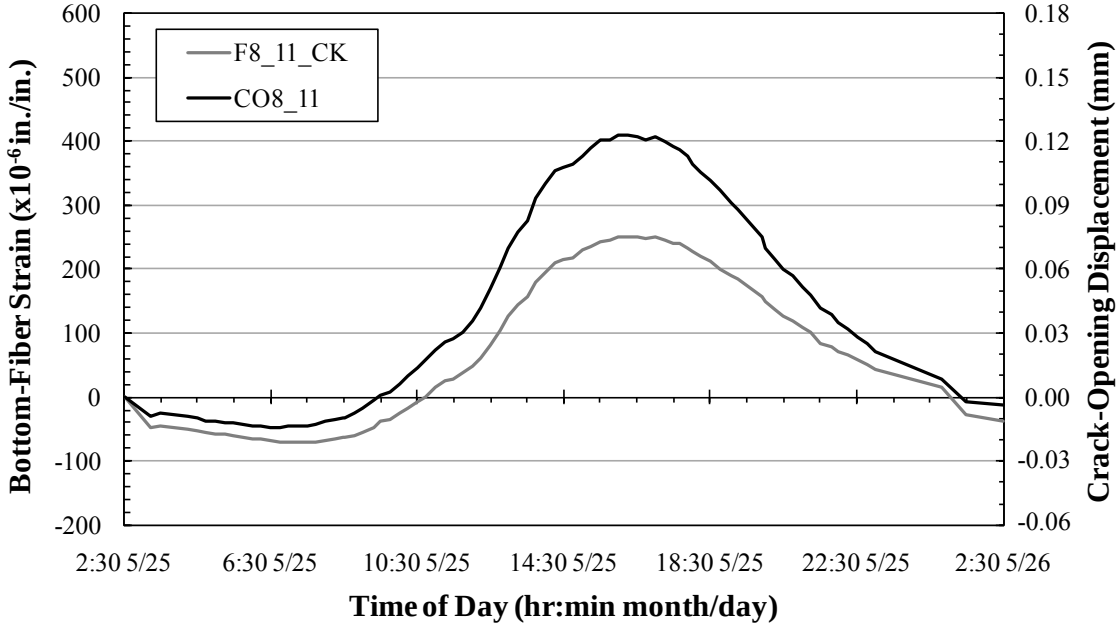

Figure 5.100: Bottom-fiber strain and COD—thermal conditions—Girder 8—Span 11

Table 5.32: Crack openings and bottom-fiber strains—thermal conditions

Girder	Span	Thermal Conditions 4:30 p.m.	
		Crack Opening (mm)	Bottom-Fiber Strain ($x10^{-6}$ in./in.)
7	10	0.108	387
	11	0.168	502
8	10	0.076	404
	11	0.122	251

Note: 1 in. = 25.4 mm

Due to the previous conclusion that Girder 7 sensors provide the most reliable measurements, the crack-opening displacements and FRP strains have been presented using scales that provided the best graphical comparisons between the Girder 7 sensors.

As previously discussed, the Girder 8-Span 10 COD gage measured crack openings in response to ambient thermal conditions but not in response to truck loads. Although the measured behavior at this gage location is more similar to the other gages in response to ambient temperature than it was in response to truck loads, the COD and FRP strain relationship is not similar to the relationships observed at the Girder 7 crack locations of both instrumented spans. The FRP strain measurements for Girder 8 of Span 10 were similar to the FRP strain measurements for Girder 7 of Span 10, but the COD measurements for the two girders were not similar under the same conditions. The smaller magnitude of the Girder 8-Span 10 COD measurements can be associated with the fact that cracks within the girder web are only present on the west face. The relationship observed in Figure 5.99 supports the previous conclusions that the performance of the COD gage on Girder 8 of Span 10 has been affected by the presence of cracks only on the west face of the girder web resulting in different cross sectional behavior compared to the other instrumented damaged regions and also requiring that the COD gage be installed on an opposite girder face compared to the other COD gages.

The FRP strains measured at the crack location of Girder 8 in Span 11 were consistently the least tensile of the four instrumented girders. This behavior is not consistent with the crack-opening displacements measured by the COD gage on the same girder. The relationship shown in Figure 5.100 between the COD measurements and the bottom-fiber FRP strain measurements at the crack location of Girder 8-Span 11 supports the previous conclusion that the bottom-fiber FRP strain gage assigned to that crack location was not accurately installed as close to the actual underlying crack location as the other FRP strain gages assigned to their respective crack locations.

5.5 PERFORMANCE OF FRP REINFORCEMENT

At the time of post-repair testing in May 2010, the FRP reinforcement installed in December 2007 had been in service for more than 2 years. Most importantly, the FRP reinforcement system had been subjected to two summer cycles and likely experienced varying temperature gradients similar to the thermal conditions that reportedly caused initial cracking. At the time of post-repair testing, the bridge structure did not exhibit additional severe cracking of structural concrete or debonding/deterioration of FRP reinforcement bonded to the concrete surface. During post-repair testing, stress-induced tensile strains were measured on the surface of the FRP reinforcement in response to truck loads and daily temperature variations. The FRP reinforcement was installed to provide tension resistance to limit additional damage without debonding and becoming ineffective. It is apparent that the FRP installed on Northbound Spans 10 and 11 of I-565 is

providing tension resistance without debonding, and that it would be appropriate to recommend a design procedure for the repair of prestressed bridge girders that exhibit damage near continuous ends using FRP reinforcement.

5.6 CONCLUSIONS

Analysis of the post-repair measurements in response to truck loads confirmed that contact between false support bearing pads and bridge girders during pre-repair testing resulted in additional load-bearing support conditions that affected behavior observed during pre-repair testing. It is evident that comparisons between pre- and post-repair structural behavior measured during testing are not useful for assessing the efficacy of the FRP reinforcement repair.

Post-repair measurements in response to truck loads confirmed that, although extensive cracking near the continuous ends of girders has occurred, the bridge structure exhibits continuous behavior. However, it is also evident that damaged regions exhibit local nonlinear behavior preventing the bridge structure from behaving as a fully continuous two-span structure under live loads as originally constructed. When designing similar FRP repair systems, the bridge should be considered to consist of simply-supported girders with complete loss of continuity at the interior support in response to strength-limit-state demands.

Post-repair measurements in response to various truck positions confirmed that the most critical load conditions for crack openings and FRP tensile demand were those that correspond with the greatest shear demand within the damaged region. Design-critical loading configurations for the damaged regions coincide with truck positions that result in the maximum shear force at the most damaged regions. Analysis procedures for determining the maximum shear force demand for a simply girder should be used to determine the load effects and design forces for FRP repair of girders with damaged continuous ends.

Analysis of the post-repair measurements in response to ambient thermal conditions supports the previously documented conclusion that restraint of temperature-induced deformations was the cause of initial cracking near the continuous ends of the I-565 bridge girders. Upward deflections measured in response to ambient thermal conditions during post-repair bridge monitoring were similar to upward deflections measured in response to solar effects during an ALDOT investigation of the same spans in 1994.

Linear profiles of bottom-fiber concrete strains measured beyond the primary crack location of damaged regions were similar to the theoretical linear profiles expected of a fully continuous structure in response to the restraint of thermal deformations. The slope of the bottom-fiber strain profiles were less than theoretically expected of a fully continuous structure subjected to a linear temperature gradient similar to the gradient measured by ALDOT in 1994, which is an indication that either the structure is not exhibiting fully continuous behavior or the temperature gradient was less than theoretically assumed.

Post-repair measurements in response to thermal conditions also provide evidence that the typical daily strain range experienced by the FRP reinforcement at a primary crack location is similar to the theoretical behavior expected in response to a linear temperature gradient similar to the gradient measured by ALDOT in 1994.

Simplified linear temperature gradient analysis can be used to effectively estimate the tensile strain that an FRP repair system must resist due to daily temperature variations. This theoretical strain behavior in response to thermal conditions should be considered when selecting a specific FRP reinforcement system for repair.

After more than 2 years of service, the repaired bridge structure did not exhibit additional severe cracking of structural concrete or debonding/deterioration of FRP reinforcement bonded to the concrete surface. It is apparent that the FRP installed on Northbound Spans 10 and 11 of I-565 is providing tension resistance without debonding, and that it would be appropriate to recommend a design procedure for the repair of prestressed bridge girders that exhibit damage near continuous ends using FRP reinforcement.

Chapter 6

FRP REINFORCEMENT DESIGN

6.1 INTRODUCTION

Behavioral observations from bridge testing were used to formulate FRP reinforcement design recommendations for repairing damaged regions similar to the continuous ends of girders in Northbound Spans 10 and 11 of I-565 in Huntsville, Alabama. These recommendations include parameters for selecting appropriate FRP reinforcement products, determining critical cross-section locations and critical load conditions, determining an amount of reinforcement required to satisfy strength-limit-state demands, and, if necessary, selecting appropriate solutions for providing supplementary anchorage. Design recommendations for an FRP reinforcement solution (similar to the repair system discussed in this report) intended for the repair of damaged multi-span bridge structures constructed to be continuous for post-construction loads (similar to the bridge structure discussed in this report) are presented in this chapter. An example of the design procedure, considering the investigated I-565 bridge structure and FRP reinforcement product selected by the Auburn University Highway Research Center (AUHRC), is presented in Appendix N of this report.

6.2 NECESSITY OF FRP REINFORCEMENT

The conditions investigated within the scope of this report include girder cracking at the continuous ends of bridge structures that were constructed to be continuous for post-construction loads. As discussed in Chapter 2 of this report, this cracking is attributable to inadequate detailing of reinforcement to account for positive bending moment demands associated with ambient temperature conditions (Gao 2003). The primary inadequate detail is the premature termination of positive bending moment continuity reinforcement within the girder. If large cracks have been observed to intersect prestressed strands, it has been determined that it is no longer appropriate to assume that these strands provide significant precompression stresses or act as effective longitudinal reinforcement for positive bending moment resistance between the crack location and the face of the continuity diaphragm—particularly under strength-limit-state demands. Thus, additional longitudinal reinforcement is required to satisfy shear- and flexure-

dependent ultimate strength demands that were previously dependent upon the performance of these prestressed strands.

6.3 FRP REINFORCEMENT PRODUCT SELECTION

A manufacturer of FRP reinforcement must be able to confidently recommend the selected FRP product for bridge girder reinforcement. Recommendations for determining qualifying FRP reinforcement products are presented by the American Concrete Institute (ACI) Committee 440.2R-08 *Guide for the Design and Construction of Externally Bonded FRP Systems for Strengthening Concrete Structures* (ACI Committee 440 2008), referred to as ACI 440.2R-08 from this point forward. Product selection recommendations are also presented by the National Cooperative Highway Research Program (NCHRP) Report 655 *Recommended Guide Specification for the Design of Externally Bonded FRP Systems for the Repair and Strengthening of Concrete Bridge Elements* (Zureick et al. 2010), referred to as NCHRP Report 655 from this point forward.

Material properties should be reported for the cured composite material of FRP fibers and adhesive. The tension failure strain (ε_{fu}) and Young's modulus of elasticity (E_f) should be reported by the manufacturer as determined in accordance with ASTM D3039. The glass transition temperature (T_g) should be reported in accordance with ASTM D4065.

For design purposes, these properties should take into account material degradation due to prolonged environmental exposure. It is recommended that the durability of an FRP product be tested for conditions that are consistent with the environment of the installation location. Conditions that could have an effect on durability include

- Freeze-thaw cycling,
- Hot-wet cycling,
- Alkaline immersion,
- Ultraviolet exposure,
- Dry heat, and
- Salt water exposure.

If the material properties documented by the manufacturer do not account for durability effects, then an environmental reduction factor (C_E) must be applied in accordance with ACI 440.2R-08.

To account for fatigue associated with service life environmental exposure, tensile properties reported by the manufacturer should be adjusted in accordance with provisions presented in Section 9.4 of ACI 440.2R-08. Young's modulus of elasticity is typically unaffected by environmental conditions, because the design tensile strength and design rupture strain are both modified by the same reduction coefficient for environmental exposure (ACI Committee 440 2008).

According to ACI 440.2R-08, of all types of FRP composites for infrastructure applications, carbon FRP (CFRP) is the least prone to fatigue failure. The fatigue strength at ultimate strength is relatively unaffected by environmental conditions, unless the resin or fiber/resin interface is substantially degraded by environmental exposure.

According to NCHRP Report 655, the tension failure strain should be documented at greater than 0.85 percent after environmental effects. NCHRP Report 655 also recommends that the glass transition temperature should represent a temperature more than 40 °F warmer than the maximum design temperature ($T_{max,design}$) expected at the geographic location of the bridge structure. This maximum design temperature is defined in Article 3.12.2.2 of the American Association of State Highway and Transportation Officials *LRFD Bridge Design Specification* (AASHTO 2010), referred to as AASHTO LRFD from this point forward.

To assess the feasibility of an FRP repair system, it is recommended to assume FRP material properties similar to those of the FRP material installed on the girders of Northbound Spans 10 and 11 of I-565. However, it is permissible to design a repair system with other FRP products that are recommended by the manufacturer for the reinforcement of bridge girders. Potential FRP reinforcement products must have documented material properties obtained through testing. Additional testing may be required to verify these documented properties if the designer or bridge owner is unfamiliar with the product.

6.4 STRENGTH-LIMIT-STATE DESIGN

After selecting an FRP reinforcement product with confirmed acceptable material properties, the amount of reinforcement required to satisfy strength-limit-state demands can be determined. For the purpose of this discussion, strength-limit-state capacities and demands are determined in accordance with AASHTO LRFD; however, another framework of consistent analysis and design procedures could be utilized at the discretion of the bridge owner—as long as each of the relevant failure modes are adequately addressed.

Strength-limit-state capacities must be modified to include the effects of longitudinal FRP reinforcement. Limiting behavior expected of FRP reinforcement is determined in accordance with provisions presented by ACI 440.2R-08.

FRP reinforcement design requirements are determined according to the minimum tensile capacity required of the net flexural reinforcement in response to strength-limit-state demands. Strength-limit-state design includes the determination of

- Critical cross-section locations,
- Critical load conditions for those locations,
- Material properties of the existing structure and FRP reinforcement,
- Cross-section dimensions,

- Reinforcement dimensions at each critical location,
- Shear strength after reinforcement,
- Tension strength of longitudinal reinforcement,
- Length of FRP installation, and
- Supplemental anchorage solution necessity.

The subsequent sections of this chapter detail this strength design process. An example of the FRP reinforcement design process is presented in 0 of this report. This example refers to the conditions of the investigated bridge structures of Northbound Spans 10 and 11 of I-565 in Huntsville, Alabama.

6.4.1 Critical Cross-Section Locations

Critical cross-section locations are those that are associated with support conditions or reinforcement transition points within a damaged or potentially damaged region. Reinforcement transitions occur where the cross-sectional area of longitudinal reinforcement area changes due to the addition or termination of reinforcement. Reinforcement details that result in these changes in reinforcement area include the termination of mild steel reinforcement, partial debonding of strands during girder fabrication, and changes in FRP widths that can be installed due to obstructions. Reinforcement transitions also occur where the spacing of vertical reinforcement changes.

6.4.2 Critical Load Conditions

Load testing has provided evidence that damaged end regions of bridge structures constructed to be fully continuous for post-construction loads exhibit partially continuous behavior, but not fully continuous behavior, in response to service-level truck loads. When determining strength-limit-state demands, it is conservative and appropriate to assume that a multi-span structure constructed to be continuous for post-construction loads will consist of independent simply supported spans near failure. This assumption results in a safe estimate of tensile demand in the bottom flange. As a bridge structure becomes less continuous there is a decrease in tensile demand associated with shear, but there is also a reduction of tensile resistance provided by negative bending moments near the interior support.

Load testing has also provided evidence that the most critical load conditions controlling FRP reinforcement performance are those that correspond to maximum shear demand within the damaged end regions. The strength limit state for maximum shear demand, along with the corresponding bending moment demand, at a critical location will control the tension requirements of an FRP reinforcement repair solution.

Strength-limit-state tension demand is determined by assuming the bridge structure exhibits simply supported behavior near failure and applying a combination of dead- and live-load effects to the structure. Impact force effects that are normally associated with behavior near open bridge joints may be appropriately reduced or neglected at the discretion of the bridge owner when assessing damaged regions located near continuous support conditions (where there is no open joint). Strength-limit-state demands at critical cross-section locations of the *assumed* simply supported bridge structure can be determined in accordance with AASHTO LRFD or another framework of consistent analysis and design procedures at the discretion of the bridge owner. All demands associated with simply supported behavior assumption should be satisfied along the *entire length* of the girder. This includes shear and bending moment demands at midspan.

6.4.3 Strength-Limit-State Temperature Demands

Temperature demands do not need to be considered in conjunction with other strength-limit-state demands. The FRP reinforcement repair has been conservatively designed to strengthen girders that have experienced complete continuity degradation and exhibit simply supported behavior in response to live loads. After the degradation of continuity behavior, thermal effects are no longer restrained and do not result in stress-induced strains. If the continuity remains partially effective, temperature effects will be restrained and result in stress-induced strain, but the tension demands on the FRP in response to truck loads will be decreased by a greater magnitude than the additional tension demands related to these stress-induced thermal strains. It is thus appropriate to disregard thermal effects during strength-limit-state design.

6.4.4 Material Properties

During the design process it is important to know specific material properties. The materials that will have an effect on the repair system design include the girder concrete, deck concrete, longitudinal steel continuity reinforcement, vertical steel shear reinforcement (stirrups), and the selected FRP reinforcement.

6.4.4.1 Concrete

The 28-day design compressive strength (f'_c) of the concrete placed during girder fabrication and deck placement is required to determine post-repair strength capacities. Due to the thickness and effective width (b) of the bridge deck, the compression zone for providing nominal bending moment resistance will be located within the bridge deck. For this reason, the concrete strength of the bridge deck affects the strength for bending moment resistance—although only slightly for typical bridge girders. When determining the nominal strength for shear resistance (V_n), the

effective concrete is located in the girder web between the compression and tension zones. For this reason, the concrete strength of the girder controls nominal strength for shear resistance.

For design purposes, the typical concrete strengths are considered to range from 3 ksi to 8 ksi. Although higher strength concretes may be utilized for prestressed girders, it is recommended that these higher concrete strengths be taken no higher than 8 ksi during the design of an FRP reinforcement system (Zureick et al. 2010).

6.4.4.2 Steel Reinforcement

The material properties of steel reinforcement installed during girder fabrication are also required for strength design. It is undesirable for an FRP failure to occur before the steel reinforcement yields. For this reason, the design yield strength (f_y) of both the longitudinal and vertical steel reinforcement should be known.

6.4.4.3 FRP Reinforcement

The material properties of the FRP composite material (fabric and cured epoxy) also have an effect on strength design. The tensile modulus of elasticity (E_f) and nominal one-layer laminate thickness ($t_{f,n}$) of the composite material are required to be presented in product specifications provided by the manufacturer.

FRP reinforcement does not exhibit yielding behavior similar to steel, but rather exhibits brittle failure modes, typically associated with debonding from the concrete. The FRP strain must be conservatively limited to prevent this failure mode because FRP debonding represents an undesirable failure of reinforcement instantaneously becoming ineffective at the debonded location. Thus, the effective debonding strain (ε_{fe}) of laminate FRP reinforcement must be limited during strength design based on the debonding strain (ε_{fd}), development length (L_{df}), bonded length provided (L_b), and an appropriate upper limit debonding strain.

The debonding strain (ε_{fd}) is contingent upon other material properties including concrete strength, FRP modulus of elasticity, the thickness of one layer of laminate, and the total number of layers (n) installed at a specific location. A formula for the strain level at which an FRP laminate may debond from a concrete substrate—even if ample bonded length is provided on either side of the critical section—is presented as Equation 6.1, as proposed by ACI 440.2R-08.

$$\varepsilon_{fd} = 0.083\sqrt{\frac{f'_c}{nE_f t_f}} \text{ in.} \quad \text{(in.–lb units)} \qquad \textbf{Eq. 6.1}$$

The bond capacity of FRP reinforcement is developed over a critical length (L_{df}) from termination points. This development length of the reinforcement has an effect on the expected debonding strain, and is based on the same material properties of the concrete and FRP

reinforcement. A formula for the development length of FRP reinforcement is presented as Equation 6.2, as proposed by ACI 440.2R-08 (in.–lb units) based on the formula proposed by Teng et al. (2003) (SI units).

$$L_{df} = 0.057\sqrt{\frac{nE_f t_f}{\sqrt{f_c'}}} \text{ in.} \quad \text{(in.–lb units)} \qquad \textbf{Eq. 6.2}$$

If the bonded length (L_b) between a termination point and a critical location is less than the required development length, the expected debonding strain at the critical location must be reduced. Although a reduction factor for inadequate development length is not presented by ACI 440.2R-08, a reduction factor is presented by the source of the development length formula (Teng et al. 2003). A strain reduction factor (β_L) for locations where the available bonded length is less than the required development length is presented as Equation 6.3.

$$\beta_L = \sin\left(\frac{\pi L_b}{2L_{df}}\right) \qquad \textbf{Eq. 6.3}$$

β_L is equal to 1 for locations where the bonded length exceeds the required development length. Equation 6.3 describes the development of FRP bond capacity as a half sine curve that reaches full development at L_{df}. Past published literature suggests that supplemental anchorage can be provided to decrease the required development length at locations of inadequate bonded length; however, the effectiveness of proposed anchorage methods should be experimentally tested prior to installation.

Debonding of FRP reinforcement can occur at intermediate crack locations along the length of the reinforced region. Thus, the effective FRP strain at *all* locations should be limited regardless of expected bond capacities or known effectiveness of supplemental anchorage. A maximum effective debonding strain of 0.004 in./in. (0.4%) is proposed by ACI 440.2R-08.

The formula for determining the limiting effective debonding strain (ε_{fe}) of laminate FRP reinforcement during strength design is based on the debonding strain (ε_{fd}), bonded length reduction factor (β_L), and an upper limit debonding strain (0.004 in./in.), as shown in Equation 6.4.

$$\varepsilon_{fe} = \varepsilon_{fd}\beta_L \leq 0.004 \text{ in./in.} \quad \text{(in.–lb units)} \qquad \textbf{Eq. 6.4}$$

6.4.5 Dimensional Properties

Details of the cross-section dimensions and reinforcement dimensions at critical cross-section locations are required for strength design of an FRP reinforced system.

6.4.5.1 Cross-Section Dimensions

Cross-section dimensions are dependent upon the girder type and construction methods. If the structure is constructed for composite behavior between the girders and the bridge deck, then an effective width and total height of the bridge deck is included in the cross- section dimensions. The required cross-section dimensions include total height (h), web width (b_v), and compression zone width (b).

6.4.5.2 Reinforcement Dimensions

Reinforcement dimensions are dependent upon the reinforcement type, size, amount, and location. The types of reinforcement include longitudinal steel, FRP reinforcement, and vertical steel.

6.4.5.2.1 Longitudinal Steel Reinforcement

Longitudinal steel reinforcement includes any mild steel reinforcement or prestressed steel strands installed during girder fabrication. The area of reinforcement (A_s and A_{ps}) and the location of the centroid (y_s and y_{ps}) of each reinforcement type should be known for ultimate-strength design.

Prestressed strands are conservatively and appropriately considered to be ineffective for tension and shear resistance between the face of the diaphragm and damaged regions. Thus, prestressed strand dimensions are only applicable beyond the damaged region.

Mild steel installed as continuity reinforcement remains effective for tension resistance between the face of the diaphragm and damaged regions. Although continuity reinforcement is typically installed throughout the girder height, it is conservative to simply consider only the reinforcement located in the tension flange during ultimate-strength design. Consideration of the continuity reinforcement in the flange is complicated by uncertainty about whether or not this reinforcement yields prior to failure of the FRP reinforcement.

6.4.5.2.2 FRP Reinforcement

The dimensions of the tension flange control the dimensions of the FRP reinforcement. The width of FRP reinforcement (b_f) and the location of the centroid (y_f) are required for ultimate-strength design.

Sheets of FRP fabric are applied as continuous sheets of reinforcement along the entire length of the repair system. The end regions of continuous sheets of reinforcement are shaped appropriately to account for interference of supports. At support locations where the bottom of the girder rests on a bearing pad, FRP reinforcement cannot be installed along the bottom of the girder, as shown in Figure 6.1. Wherever possible, FRP reinforcement should be installed to

wrap around the entire perimeter of the tension flange, as shown in Figure 6.2. The FRP should be installed so that the primary fibers are parallel to the girder axis and can provide effective tension reinforcement to the bottom flange.

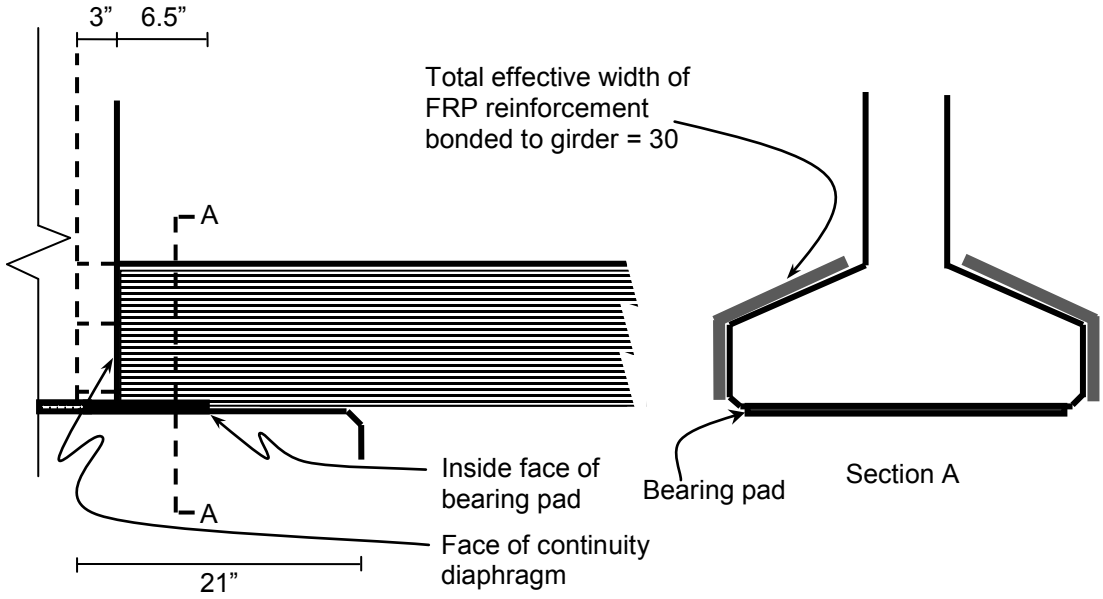

Figure 6.1: Cross-sectional configuration of FRP—near diaphragm (Swenson 2003)

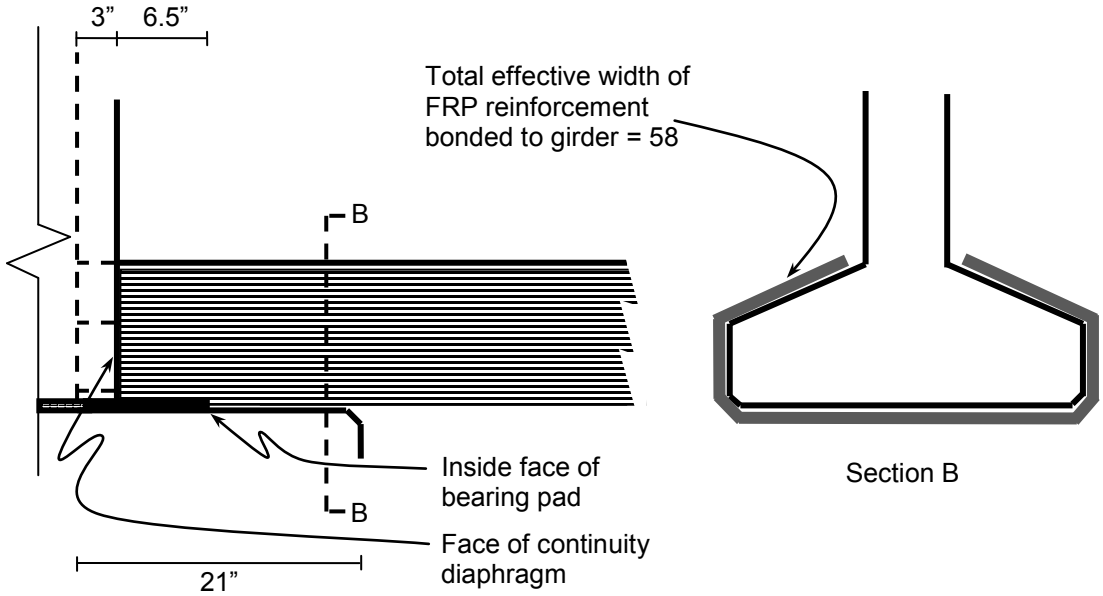

Figure 6.2: Cross-sectional configuration of FRP—typical (Swenson 2003)

6.4.5.2.3 Vertical Steel Reinforcement

Vertical steel reinforcement includes any steel stirrups installed during girder fabrication. The area of reinforcement (A_v) and the reinforcement spacing (s) for the region surrounding a critical cross-section location are required for ultimate-strength design.

6.4.6 Initial Estimate of Required FRP Layers

To begin designing an FRP reinforcement solution that satisfies ultimate-strength demand, an initial estimate of the FRP thickness is required. This initial thickness can be estimated with a simplified assumption that the longitudinal tension demand (T) is equal to the maximum factored shear demand (V_u). A simplified model for the transfer of forces is shown in Figure 6.3.

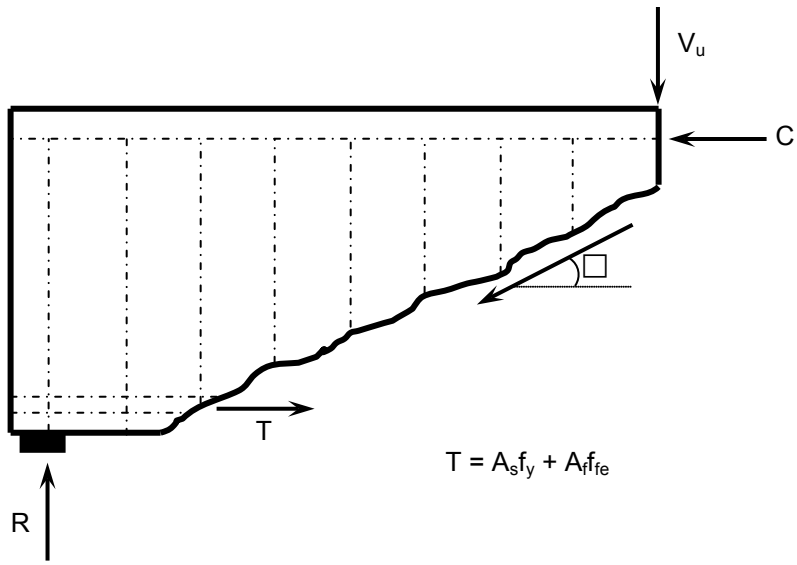

Figure 6.3: Simplified model for initial estimate of FRP requirement

During ultimate-strength design of an FRP reinforcement repair, it is desirable for steel reinforcement to yield before the FRP reinforcement reaches an effective debonding stress (f_{fe}) associated with FRP failure. Typical steel with a yield stress of 60 ksi yields at a strain of roughly 0.002 in./in., thus, an initial estimate of an FRP effective debonding strain ($\varepsilon_{fe,min}$) of 0.003 in./in. at failure is appropriate for the initial estimation of FRP required.

The simplified formula for tension resistance required is presented as Equation 6.5.

$$T_{n,req} = \frac{V_u \cot(\theta)}{\phi} \qquad \textbf{Eq. 6.5}$$

The tension capacity that should satisfy the simplified tension demand is shown as Equation 6.6.

$$T_{n,prov} = A_s f_y + A_f f_{fe,min} \quad \textbf{Eq. 6.6}$$

If there is no steel reinforcement, the FRP thickness must satisfy the entire tension demand for that cross section. The tension capacity, reduced by an appropriate resistance factor (ϕ) of 0.9, must be greater than the tension demand, as shown in Equation 6.7.

$$T_{n,prov} > T_{n,req} \quad \textbf{Eq. 6.7}$$

The formula for the estimated minimum FRP thickness required ($t_{f,req}$) can then be derived from Equations 6.5–6.7, which is presented as Equation 6.8.

$$t_{f,req} = \frac{\left(\frac{V_u \cot(\theta)}{\phi} - A_s f_y\right)}{b_f f_{fe,min}} \quad \textbf{Eq. 6.8}$$

The angle θ is not yet known at this stage of the design process. However, values of cot(θ) will typically range from 1.0 to 1.5. The designer should begin the process by selecting a trial value in this range.

The minimum thickness required should be determined for critical cross-section locations. The greatest required thickness of these locations will control the initial FRP thickness estimated for the entire reinforcement system. The number of layers (n) of FRP required is determined based on the manufacturer specified nominal thickness ($t_{f,n}$) per layer of FRP laminate, as shown in Equation 6.9.

$$n = \frac{t_{f,req}}{t_{f,n}} \quad \textbf{Eq. 6.9}$$

FRP reinforcement is applied as long continuous sheets of fabric. The number of layers required to satisfy the maximum thickness requirement of critical locations will control the initially estimated thickness of reinforcement.

6.4.7 Vertical Shear Strength Resistance

Although longitudinal FRP reinforcement does not directly provide additional vertical strength resistance, the additional reinforcement does allow for an increase of the vertical shear strength resistance provided by the concrete and vertical steel reinforcement. The additional reinforcement results in an increase of the nominal strength for bending moment resistance (M_n),

an increase of the effective shear depth (d_v) of the cross section, a decrease of the net longitudinal tensile strain (ε_s) expected in response to design load conditions, and a decrease of the expected angle of inclination for shear cracking (θ), which leads to an increase in the nominal vertical shear strength (V_n) provided by the concrete and vertical steel reinforcement.

6.4.7.1 Nominal Strength for Bending Moment Resistance

The nominal strength for bending moment resistance can be determining in accordance with typical design provisions. Additional terms may be appropriately included to account for the effects of the FRP reinforcement. When determining the nominal strength for bending moment resistance, the standard Whitney uniform compression block theory may not accurately represent the compression block behavior of the repaired structure. This is due to the failure mode of the structure being controlled by an FRP debonding failure instead of a concrete crushing failure. Although the Whitney compression block theory may not accurately represent the actual cross-section compressive stress distribution, this simplified theory can reasonably be applied for cross sections with relatively low positive bending moment demands, such as the end regions of bridge girders. Formulas used to calculate nominal bending moment resistance are presented in Equations 6.10–6.13.

$$M_n = A_s f_y \left(d_s - \frac{a}{2}\right) + A_f \varepsilon_{fe} E_f d_f - \frac{a}{2} + 0.85 f'_c \qquad \textbf{Eq. 6.10}$$

$$a = \frac{A_s f_y + A_f \varepsilon_{fe} E_f}{0.85 f'_c b} \qquad \textbf{Eq. 6.11}$$

$$d_s = h - y_s \qquad \textbf{Eq. 6.12}$$

$$d_f = h - y_f \qquad \textbf{Eq. 6.13}$$

Because the deck provides a very wide compression flange for positive-moment resistance in bridge girders, the flexural strength is relatively insensitive to the assumed compressive stress distribution.

6.4.7.2 Effective Shear Depth

The effective shear depth (d_v) for each critical cross-section location is the greatest of three values calculated in accordance with Article 5.8.2.9 of AASHTO LRFD.

One effective shear depth value is dependent upon the nominal bending moment resistance and the tensile forces at failure. It is appropriate to assume that FRP reinforcement failure occurs due to reaching the FRP effective debonding strain after the steel yields but before the compression-zone concrete crushes. This effective shear depth is calculated as the distance between the centroid of the compression zone and the location of the net tensile force, as shown in Equation 6.14.

$$d_{v,1} \geq \frac{M_n}{A_s f_y + A_f f_{fe}} \qquad \textbf{Eq. 6.14}$$

The second effective shear depth value is ninety percent of the depth (d_e) from the top of the cross section to the location of the net tensile stress, as shown in Equations 6.15 and 6.16.

$$d_e = \frac{A_s f_y d_s + A_f f_{fe} d_f}{A_s f_y + A_f f_{fe}} \qquad \textbf{Eq. 6.15}$$

$$d_{v,2} \geq 0.9 d_e \qquad \textbf{Eq. 6.16}$$

The third effective shear depth value is seventy-two-percent of the total height (h) of the cross section, as shown in Equation 6.17.

$$d_{v,3} \geq 0.72h \qquad \textbf{Eq. 6.17}$$

The maximum of these three effective shear depths controls design in accordance with AASHTO LRFD provisions. However, the larger of the two values that do not require the calculation of the nominal bending moment capacity can be used for simplicity if desired.

6.4.7.3 Net Tension Strain

In order to prevent FRP debonding failure under the combined influence of flexure and shear, the net longitudinal tension strain (ε_s) corresponding to the nominal strength for shear resistance must not exceed the effective debonding strain limit for the FRP reinforcement. The net longitudinal tension strain can be calculated in accordance with Article 5.8.3.4 of AASHTO LRFD, modified to include FRP effects, as shown in Equation 6.18.

$$\varepsilon_s = \frac{\frac{M_u}{d_v} + V_u}{E_s A_s + E_f A_f} \leq \varepsilon_{fe} \qquad \textbf{Eq. 6.18}$$

Terms associated with strength provided by prestressed strands (V_p, $A_p f_{po}$, and $A_{ps} E_p$) have been disregarded from the AASHTO formula based on the unknown effectiveness of prestressed strands within damaged regions.

When determining the net longitudinal tension strain, the factored bending moment demand corresponding to the maximum factored shear demand must not be taken less than the theoretical bending moment resulting from the factored shear demand being applied a distance equal to the effective shear depth from the critical location. The factored bending moment demand of the net tension strain equation is considered to be the greater of these two bending moment demands, as shown in Equation 6.19.

$$M_u \geq V_u d_v \qquad \textbf{Eq. 6.19}$$

If the net tension strain calculated in response to the factored demands for shear strength exceeds the effective debonding strain of the FRP reinforcement, more layers of FRP may be required to satisfy demand. The effective FRP strain can be substituted into the net tension strain equation, which can then be rearranged to solve for the number of layers of FRP required to satisfy the net tension strain demands in response to factored demands for shear strength, as shown in Equation 6.20.

$$n = \frac{\frac{M_u}{d_v} + V_u - E_s A_s \varepsilon_{fe}}{E_f w_f t_{f,n} \varepsilon_{fe}} \qquad \textbf{Eq. 6.20}$$

If additional layers are required to satisfy the net tension demand, the net tension strain must be recalculated with the appropriate number of layers before continuing to check vertical shear strength.

6.4.7.4 Diagonal Shear Crack Parameters

After determining an appropriate net tension strain in response to factored shear strength demands, the vertical shear strength can be determined. The net tension strain dictates parameters associated with diagonal shear cracking, which have an effect on vertical shear strength provided by concrete and vertical steel reinforcement. These parameters are calculated in accordance with Article 5.8.3.4 of AASHTO LRFD.

The ability of diagonally cracked concrete to transmit tension and shear is related to the net tension strain. The AASHTO LRFD formula for the factor (β) applied to the concrete shear strength is presented as Equation 6.21.

$$\beta = \frac{4.8}{1 + 750\varepsilon_s} \qquad \textbf{Eq. 6.21}$$

The angle of inclination (θ) of diagonal shear cracking has an effect on the amount of vertical shear resistance provided by transverse steel reinforcement (stirrups) within a region of shear cracking. The AASHTO LRFD formula for this angle of inclination is presented as Equation 6.22.

$$\theta = 29 + 3500\varepsilon_s \qquad \textbf{Eq. 6.22}$$

6.4.7.5 Components of Vertical Shear Strength

The nominal vertical shear strength consists of both concrete and steel components of shear resistance. These concrete and steel components of vertical shear strength are calculated in accordance with Article 5.8.3.3 of AASHTO LRFD.

The shear strength (V_c) provided by the concrete is dependent upon the design strength of the girder concrete (f'_c), the effective shear depth (d_v), the width of girder web (b_v), and the net tension strain shear strength factor (β). The formula for the shear strength provided by the concrete, calculated in accordance with the *general procedure* of Article 5.8.3.4.2 of AASHTO LRFD, is presented as Equation 6.23.

$$V_c = 0.0316\beta\sqrt{f'_c}b_v d_v \quad \text{(in.–kip units)} \qquad \textbf{Eq. 6.23}$$

The shear strength (V_s) provided by the vertical steel reinforcement is dependent upon the amount of vertical steel reinforcement intersecting a diagonal shear crack. The factors affecting the shear strength include the effective shear depth (d_v), the angle of inclination (θ), the spacing of reinforcement (s), the area of intersecting reinforcement (A_v) within one typical cross section containing vertical reinforcement, and the assumption that the vertical reinforcement reaches a yield stress (f_y) in response to ultimate strength demands. The formula for the shear strength provided by vertical steel reinforcement, calculated in accordance with the *general procedure* of Article 5.8.3.4.2 of AASHTO LRFD, is presented as Equation 6.24.

$$V_s = \frac{A_v f_y d_v \cot(\theta)}{s}$$ **Eq. 6.24**

6.4.7.6 Nominal Vertical Shear Strength

The combined shear strengths provided by the concrete and vertical steel reinforcement represents the nominal vertical shear strength, as shown in Equation 6.25.

$$V_n = V_c + V_s$$ **Eq. 6.25**

An upper limit is applied to the nominal vertical shear strength, in accordance with Article 5.8.3.3 of AASHTO LRFD, to ensure that the vertical steel reinforcement yields prior to concrete crushing. This upper limit nominal shear strength formula is presented as Equation 6.26.

$$V_{n,max} = 0.25 f'_c b_v d_v$$ **Eq. 6.26**

6.4.7.7 Factored Strength for Resisting Shear Demand

The resistance factor for the shear strength of normal weight reinforced concrete, presented in Article 5.5.4.2 of AASHTO LRFD, reduces the nominal vertical shear strength to be compared to the factored shear demand. To satisfy ultimate strength design, the factored shear strength (ϕV_n) must be greater than the factored shear demand (V_u), as shown in Equation 6.27.

$$\phi V_n > V_u$$ **Eq. 6.27**

Additional longitudinal FRP reinforcement may increase the net tension strength in response to shear demands, but will not greatly improve the nominal vertical shear strength of critical cross-section locations. Thus, if the vertical shear strength does not satisfy the vertical shear demand, an additional repair solution is necessary to provide additional vertical shear strength. FRP reinforcement solutions for providing additional vertical shear strength have been proposed by ACI Committee 440 and the NCHRP; however, an additional repair solution for vertical shear reinforcement is not within the scope of this report.

6.4.8 Tensile Strength

The combined demands of flexure and shear induce tension forces that must be resisted by the flexural tension region of the cross section. It is conservative and appropriate to assume that the concrete does not provide any tensile strength after cracking, and that all tension demand must be satisfied with tension capacity provided by longitudinal reinforcement. To determine the tension strength provided, Article 5.8.3.5 of AASHTO LRFD may be modified with additional terms that account for resistance capacity provided by externally bonded FRP reinforcement.

6.4.8.1 Nominal Strength for Resisting Tension

The nominal strength for resisting tension is provided by longitudinal reinforcement at the flexural tension region of the cross section. Based on the typical difference in modulus of elasticity for steel and laminate FRP, it is appropriate to assume that the steel will yield before the FRP reaches an effective debonding strain limit. It is also appropriate to assume that the effective debonding strain limit for the FRP will be reached before concrete crushes. Thus, the nominal strength for resisting tension ($T_{n,prov}$) is limited by the area of longitudinal steel that yields and the area of FRP that is appropriately assumed to provide tension resistance until reaching the effective stress limit, as shown in Equation 6.28.

$$T_{n,prov} = A_s f_y + A_f f_{fe} \qquad \textbf{Eq. 6.28}$$

6.4.8.2 Factored Tension Demand

The factored tension demand ($T_{n,req}$) in response to ultimate-strength demand is based on the maximum factored shear and corresponding bending moment demands at the critical location. The formula for required tension capacity, presented in Article 5.8.3.5 of AASHTO LRFD, applies the individual resistance factors for flexure (ϕ_f) and shear (ϕ_v), respectively, to compute the increased demand that corresponds to simultaneous attainment of the nominal strengths in flexure *and* shear on the cross section rather than applying a single tension resistance factor to reduce the computed tensile capacity, as shown in Equation 6.29.

$$T_{n,req} = \left[\frac{M_u}{d_v \phi_f}\right] + \left[\frac{V_u}{\phi_v} - 0.5V_s\right]\cot(\theta) \qquad \textbf{Eq. 6.29}$$

Vertical shear resistance provided by vertical reinforcement reduces the demand on longitudinal reinforcement due to the diagonal nature of the critical flexure-shear crack. However,

AASHTO LRFD limits the contribution of the vertical shear resistance (V_s) to no more than the factored vertical shear demand, as shown in Equation 6.30.

$$V_s \leq \frac{V_u}{\phi_v} \qquad \textbf{Eq. 6.30}$$

Because the shear and flexure resistance factors have already been applied to determine the required nominal tension capacity, it is appropriate to not apply a reduction factor to the nominal strength for tension resistance when checking for satisfaction of the nominal tension capacity, as shown in Equation 6.31.

$$T_{n,prov} > T_{n,req} \qquad \textbf{Eq. 6.31}$$

6.4.9 Check Strengths of Each Location with Equal Layers of FRP

FRP reinforcement systems are installed with continuous sheets of FRP fabric. As the number of FRP layers increases, the required development length increases and the limiting effective strain (to prevent debonding) decreases. For this reason, the performance at critical locations must be checked with the maximum number of layers required of any other location, particularly with respect to net tension strain in response to shear demands.

6.5 LENGTH OF FRP REINFORCEMENT INSTALLATION

As previously mentioned, the FRP reinforcement is installed as continuous sheets of fabric that originate at the face of the continuity diaphragm and terminate beyond the damaged region. When determining the length of reinforcement required, the original reinforcement details of girder fabrication should be considered. The FRP reinforcement should extend far enough along the girder so that forces can be transferred through the concrete into the fully developed prestressing reinforcement beyond the damaged region. For this reason, it is recommended that the FRP reinforcement extend (a) beyond the debonded length of strands by a minimum distance equal to the development length of the prestressed strands and (b) beyond any existing bottom flange cracks by the same minimum distance.

According to AASHTO LRFD design provisions, the development length (ℓ_d) for the prestressed strands is dependent upon the stress required to provide the nominal flexural or tension strength and the effective stress in the strands after accounting for time-dependent losses. Considering typical values for these parameters, a conservative approximation of the

development length being equal to 180 strand diameters is appropriate for determining the length of FRP reinforcement required. This approximation is presented as Equation 6.32.

$$\ell_d = 180 d_b \qquad \textbf{Eq. 6.32}$$

It is also recommended that the termination of the FRP reinforcement layers be stepped down to prevent stress concentrations at the reinforcement termination location. ACI 440.2R-08 recommends that each layer be terminated 6 in. earlier than the underlying layer. When determining the recommended lengths of each layer of FRP reinforcement, the initial (longest) layer of reinforcement should be designed to extend the recommended distance mentioned previously.

6.6 ANCHORAGE

The length of adequately bonded reinforcement between a termination location and critical cross-section location directly affects performance of the reinforcement system. Adequate stress transfer is required to limit stress concentrations that could result in bond failure of the reinforcement system. Wherever possible, the FRP reinforcement should (a) extend beyond the point where it is no longer required for strength and (b) have a bonded length adequate to develop the effective FRP strain required at each critical section.

Additional anchorage should be considered for regions that do not allow for desired bonded lengths. There are various methods for providing additional anchorage to increase the stress capacity at end regions with short bonded lengths; however, more research of anchorage performance is recommended before selecting a specific anchorage method to be implemented.

Recent research indicates that carbon fiber anchors may be useful for providing supplemental anchorage at end regions (Ceroni and Pecce 2010; Niemitz et al. 2010; Orton et al. 2008). These anchors, which are depicted in Figure 6.4, include FRP strips that are bundles at one end and free at the other.

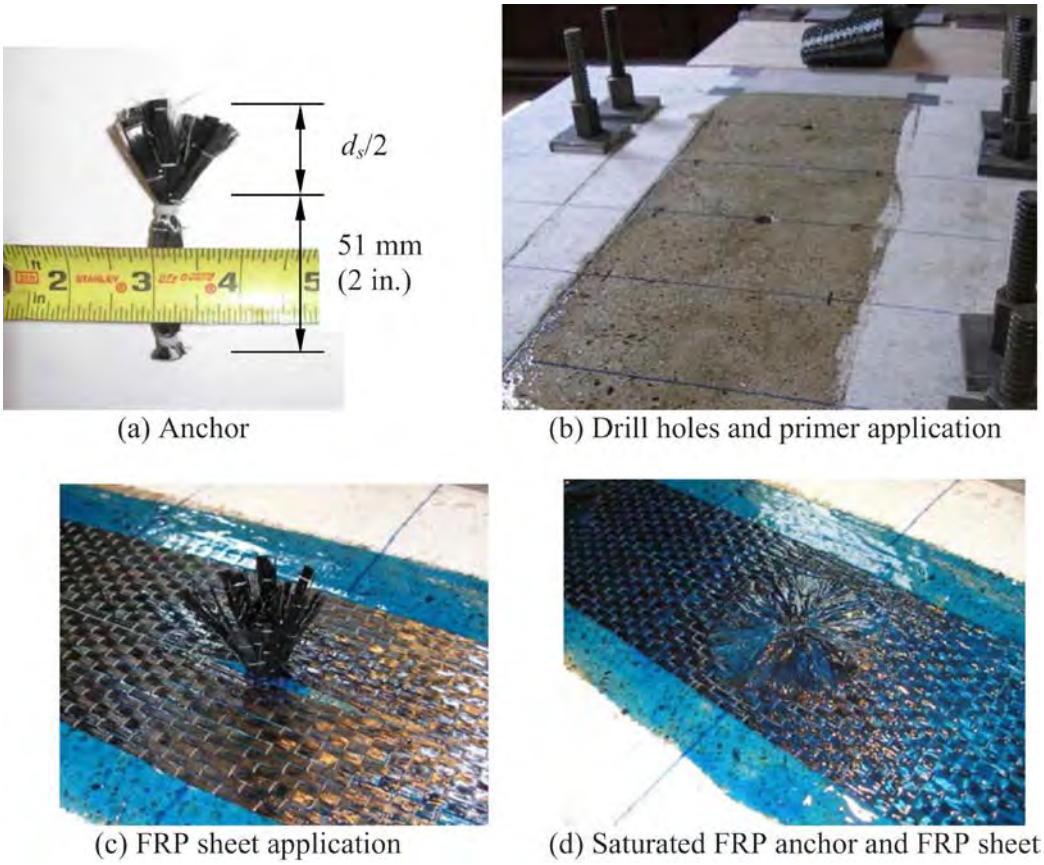

Figure 6.4: FRP fan anchorage system (Niemitz et al. 2010)

The bundled ends of the FRP strips are installed into a hole drilled into the structural concrete. The free ends of the FRP strips are fanned out onto the first installed layer of *uncured* FRP reinforcement. Epoxy is applied inside the drilled hole as well as on the fanned FRP strips. Subsequent layers of reinforcement can then be installed on top of the fanned FRP strips. The use of multiple smaller anchors to cover a large area is suggested (Orton et al. 2008).

Research indicates that it is safe to estimate a debonding strength increase of about 25 percent for FRP reinforcement solutions that utilize this fanned FRP anchorage system (Ceroni and Pecce 2010). However, until further research can be conducted to verify anchorage performance in conjunction with wrapped FRP systems installed on in-service bridge girders, it is recommended that the maximum FRP strain at all locations be limited to be conservative and appropriate for regions of relatively short bonded lengths. It is uncertain whether the depth of concrete cover available in these girders is adequate to fully develop this type of anchor.

The amount of damage exhibited at the time of the repair is another factor that must be considered during the determination of an acceptable strain capacity. FRP reinforcement has the potential to debond due to behavior exhibited at existing crack locations. These debonding conditions due to crack behavior include failure at one specific crack location and failure of a

shortened bonded region between two crack locations. Additional anchorage provided by transverse wrapping of FRP reinforcement around the bottom flange may be beneficial at locations of excessive cracking that has extended through the bottom chord of the tension flange prior to repair. Additional testing is required to verify this supplemental anchorage method.

6.7 SERVICE LIMIT STATE

Bridge testing has provided evidence that supports the conclusion that the structure maintains some continuous behavior for service load conditions. Before any repair methods had been implemented, a review of the I-565 bridge structures presented in NCHRP Report 519 stated that the damaged bridge structures continued to perform as designed (Miller et al. 2004). The strength-limit-state design assumption of simply supported bridge behavior at failure is an even more conservative assumption for the service limit state. After a bridge structure has been repaired to satisfy the strength-limit-state demands, assuming simply supported behavior, the service-limit-state demands should be appropriately satisfied with the same reinforcement, assuming any partial continuity exists.

During post-repair testing, FRP tensile strains measured in response to ambient thermal conditions were observed to be of greater magnitude than FRP tensile strains measured in response to truck loads. The strains measured in response to ambient temperature conditions were greater than the strains in response to truck loads because of the non-stress-induced strain exhibited by the FRP material in response to ambient temperature. Only the stress-induced strain associated with thermal conditions will have an effect on service conditions of the structure.

To determine a critical diurnal strain range, it is conservative and appropriate to assume that the two-span structure exhibits fully continuous behavior in response to ambient thermal conditions. The formula for the tension-flange FRP strain expected in response to ambient thermal conditions is presented as Equation 5.36 in Section 5.4.2.2.2. The strain associated with the unrestrained expansion of FRP material due to thermal conditions is not considered a stress-induced strain; however, the strain associated with restraint of the temperature differential between the top of the deck and bottom of the girder does induce stress-related strain in the FRP reinforcement. This stress-induced strain, based on a change in temperature differential ($\delta[\Delta T_h]$) and the appropriate concrete coefficient of thermal expansion (α_T), represents the FRP strain that must be accounted for in response to diurnal ambient thermal conditions. The limiting effective debonding strain (ε_{fe}) of the FRP reinforcement shall exceed the stress-induced FRP strain demand in response to thermal conditions, as shown in Equation 6.33.

$$\varepsilon_{fe} > \frac{3}{2}[\alpha_T \delta(\Delta T_h)] \qquad \textbf{Eq. 6.33}$$

6.8 DESIGN SUMMARY

An FRP reinforcement system that appropriately satisfies all design requirements may be summarized after completing the design procedure. The design summary should include the

- Name of the FRP reinforcement product,
- Assumed FRP material properties,
- Fiber orientation in the installed FRP,
- Number of layers required to satisfy ultimate strength demands,
- Distance that each layer must extend,
- Verification that service demands are satisfied, and
- Assessment of supplemental anchorage requirements.

6.9 INSTALLATION RECOMMENDATIONS

An FRP reinforcement system that satisfies design requirements must be appropriately installed to ensure that the assumed FRP reinforcement conditions remain valid. Installation must be performed by skilled professionals that have experience following the installation guidelines of the manufacturer for the selected FRP reinforcement product. Before the FRP reinforcement can be installed, the structural substrate and surface must be prepared for the installation process. After the substrate and surface are prepared, the FRP reinforcement can then be appropriately installed. Specific installation recommendations are presented in this section.

6.9.1 Preparing for Installation

Prior to installation, preparation procedures must be performed in accordance with manufacturer specifications. In addition to manufacturer guidelines, there are some standard procedures that must be performed that may not be specifically recommended by the manufacturer. These procedures include specific details with regard to crack injection and surface preparation.

6.9.1.1 Adhesion Testing

Prior to beginning surface preparation for installation, it is important to test the strength of the structural concrete that the FRP reinforcement will be bonded to during installation. Adhesion testing of the FRP reinforcement epoxy on the concrete surface is required to ensure that the bond strength of the epoxy exceeds the tensile strength of the concrete. Adhesion testing should be conducted in accordance with the requirements given in ASTM D4541 (2009).

6.9.1.2 Crack Injection

Existing cracks should be injected with structural epoxy shortly prior to the installation of FRP reinforcement. To minimize the possibility of new cracks forming prior to installation, it is important to schedule the FRP installation for a time of day or year with minimal temperature-induced stresses that could result in crack re-formation.

Cracks that are 0.01 in. (0.3 mm) and wider can adversely affect FRP reinforcement performance, as stated by ACI 440.2R-08. The specific concern for this project is the actual attainment of the computed concrete contribution (V_c) to the vertical shear strength. The computation of V_c is based on an assumption that shear can be resisted along the diagonal crack face due to aggregate interlock. This may not be true for overly large crack widths. Thus, it is recommended that wide cracks be pressure injected with structural epoxy prior to FRP installation. It is also recommended that smaller cracks be resin injected or sealed to prevent corrosion of existing steel, especially on exterior girders which are more exposed to aggressive environmental conditions. All crack injection procedures are recommended to be performed in accordance with the general procedures for epoxy injection presented by ACI Committee 224.1R-07 *Causes, Evaluation, and Repair of Cracks in Concrete Structures*, referred to as ACI 224.1R-07 (ACI Committee 224 2007). The procedures presented by ACI 224.1R-07 include

- Cleaning the crack,
- Sealing the crack to prevent epoxy contained during injection,
- Installation of entry and venting ports,
- Mixing structural epoxy,
- Pressure injecting the epoxy, and
- Removing the surface seals after the epoxy has cured.

6.9.1.3 Surface Preparation and Profiling

After the structural epoxy that has been injected into wide cracks has cured, the surface must be prepared for installation. FRP installation recommendations of ACI 440.2R-08 state that surfaces must be prepared for adequate bonding conditions in accordance with the recommendations of ACI Committee 546 *Concrete Repair Guide*, referred to as ACI 546R-04 (ACI Committee 546 2004), and International Concrete Repair Institute (ICRI) Committee 310 *Guide for Surface Preparation for the Repair of Deteriorated Concrete Resulting from Reinforcing Steel Corrosion*, referred to as ICRI 310.1R-2008, formerly ICRI 03730 (ICRI Committee 310 2008). Surface preparation specifications of the NCHRP Report 609 *Recommended Construction Specifications and Process Control Manual for Repair and Retrofit of Concrete Structures Using Bonded FRP Composites*, referred to as NCHRP Report 609, also recommend consulting with ACI 546R-04 and ICRI 310.1R-2008 for assuring proper surface preparation (Mirmiran et al. 2008).

General guidelines for surface preparation include the clearing of all irregularities, unevenness, and sharp protrusions in the surface profile. It is recommended by NCHRP Report 609 that these obstructions be grinded away to a smooth surface with less than 1/32 in. deviation. Any excess epoxy or sealer from the crack injection process should also be removed to provide a smooth surface.

It is recommended by ACI 440.2R-08 that all corners be rounded or chamfered to a minimum radius of 0.5 in. during surface preparation. The rounding of corners helps to prevent stress concentrations in the FRP system and voids from forming between the FRP system and the concrete. This stipulation is not critical for applications such as the damage girders in this study in which the primary fiber orientation is parallel to the girder corners. It is also recommended that corners that have been roughened during the rounding process be smoothed with putty prior to installation.

After the removal of obstructions, the surface must be profiled to remove any remaining unevenness in the surface. Surface profiling guidelines are presented by ACI 546R-04 and ICRI 310.1R-2008. It is recommended by NCHRP Report 609 to smooth any remaining bug holes, depressions, protrusions, and roughened corners using putty made of epoxy resin mortar, or polymer cement mortar, with a cured strength greater than the strength of the original concrete. It is also recommended that the patching material be cured for a minimum of 7 days prior to installation of the FRP reinforcement system.

To complete surface preparation, the bonding surface should be appropriately cleaned. NCHRP Report 609 states that surface cleaning includes the removal of all bond-inhibiting material such as dust, curing compounds, or paint coatings.

After completing surface cleaning, the moisture content of the surfaces must be checked. ACI 440.2R-08 states that the clean bonding surfaces must be as dry as recommended by the FRP system manufacturer to ensure appropriate resin penetration. The moisture content can be evaluated in accordance with the requirements of ACI Committee 503 *Standard Specifications for Repairing Concrete with Epoxy Mortars*, referred to as ACI 503.4-92 (ACI Committee 503 1992).

6.9.2 FRP Reinforcement Installation

Installation of the FRP reinforcement system should be conducted in accordance with manufacturer specifications. General guidelines for the installation of FRP reinforcement systems are also presented by ACI 440.2R-08 and NCHRP Report 609.

6.9.2.1 Epoxy Saturation

Due to the large surface area available for bonding around the perimeter of the girder bottom flange, a wet-layup FRP reinforcement system is recommended for this application. Wet-layup systems consist of dry FRP fabrics that are saturated with epoxy during installation. The epoxy of

the FRP reinforcement system should be mixed in accordance with manufacturer specifications, which should include recommended batch sizes, mixture ratios, mixing methods, mixing times, and pot-life limits (ACI Committee 440 2008). The epoxy should be applied uniformly on the concrete surface where the FRP is to be installed. The sheets of FRP fabric may also be saturated prior to installation. Immediately following surface saturation, the first layer of FRP reinforcement should be installed. Successive layers of epoxy and FRP should be installed before the previously installed layers have cured (ACI Committee 440 2008).

6.9.2.2 Application of FRP Reinforcement

Prior to epoxy saturation, the sheets of dry FRP fabric should be cut to size, which includes cutting different lengths for different layers, and modifying one end to appropriately account for support conditions. FRP fabric materials should be handled in accordance with manufacturer recommendations. Installers should ensure that the fabric is cut and installed so that the primary fiber orientation matches the direction stipulated on the contract drawings. Any signs of kinks, folds, or other forms of severe waviness should be reported appropriately (ACI Committee 440 2008). The sequence of installation should be documented prior to installation. If multiple sheets are required within each layer, then fabric installation sequences should be designed to prevent the alignment of seams in successive layers. FRP reinforcement should be applied without entrapping air between the fabric and concrete surface or successive layers of fabric. Any entrapped air should be released along the reinforcement in the direction parallel to the fibers, and should never be rolled perpendicular to the fiber direction (Mirmiran et al. 2008)

6.9.2.3 Protective Coating

Protective coatings should be applied to cured FRP reinforcement systems for improved durability from environmental conditions, impact, fire, or vandalism. The protective coating must be approved by the manufacturer and may be a polymer-modified portland cement coating, or a polymer-based latex coating, with a final appearance that matches, within reason, the color and texture of the adjacent concrete (Mirmiran et al. 2008).

6.9.2.4 Quality Control Testing and Inspection

The FRP reinforcement system and protective coating should be tested and inspected during and after FRP installation according to ACI 440.2R-08, NCHRP Report 609, and manufacturer recommendations. Topics of concern during inspections include

- Representative tensile strength of FRP reinforcement samples,
- Weather conditions such as temperature and humidity,
- Surface temperature of the concrete,

- Widths of cracks not injected with epoxy, and the
- Location and size of any delaminations or air voids.

The tensile strength of a representative sample of the installed FRP reinforcement system should be tested in accordance with the procedures of ASTM D3039 (2008). The definition of a representative sample of FRP reinforcement for tensile testing should be discussed and agreed upon prior to installation. The tension modulus of elasticity of the FRP reinforcement affects the effective debonding strength of the installed repair system. Supplemental anchorage may be recommended for FRP reinforcement materials that are determined to have a tension modulus of elasticity greater than assumed during design.

FRP systems should finally be evaluated and accepted based on conformance or nonconformance with the design drawings and specifications of the designer and manufacturer. It is recommended that the selected installation contractor be qualified by the FRP and epoxy manufacturer.

Chapter 7

SUMMARY AND CONCLUSIONS

7.1 PROJECT SUMMARY

Construction of the elevated portion of I-565 in Huntsville, Alabama began in January of 1988. The elevated highway is composed of simply supported steel or prestressed concrete girders that were constructed to act as two-, three-, and four-span continuous structures in response to post-construction loads. The elevated highway was completed on March 27, 1991. In 1992, Alabama Department of Transportation (ALDOT) bridge inspectors discovered large and unexpected cracks at the continuous end of many prestressed concrete bulb-tee girders.

Analysis conducted by Gao (2003) of Auburn University confirmed ALDOT's suspicion that the damage was a result of the daily variation in temperature gradient between the top of the bridge deck and the bottom of the concrete bridge girders. Warmer temperatures of the bridge deck in relation to the bottom of bridge girders results in upward deflections of the bridge spans, a behavior known as "sun cambering." Due to restraint of these temperature-induced deformations at the continuous ends of girders, substantial positive bending moments formed near these girder ends. Gao (2003) also identified the contribution of the positive bending moment continuity reinforcement details to the severity of the cracking.

Swenson (2003) of Auburn University examined how the cracks could affect bridge performance. It was determined that the prestressed strands at the cracked girder ends are likely inadequately developed as a result of cracking and may not provide dependable shear and flexural resistance in these regions. Swenson designed a fiber-reinforced polymer (FRP) reinforcement system to provide additional longitudinal reinforcement at the damaged regions that would supply additional tension resistance and strengthen the damaged girders.

In late spring of 2005, prior to installation of the recommended FRP reinforcement system, Auburn University researchers measured behavioral bridge responses to service-level truck loads. Four girders (Girders 7 and 8 of Northbound Spans 10 and 11) were instrumented to measure deflections, crack-opening displacements, and surface strains of the concrete during load testing (Fason 2009).

Following the pre-repair load testing, a finite-element model (FEM) of the instrumented bridge structure was created for further analysis of the structural behavior of the bridge in

response to modeled load conditions. Measurements from the pre-repair load tests were used to refine the pre-repair model. After the pre-repair model was finalized, the recommended FRP reinforcement system was added to the model to allow for analysis of the predicted post-repair behavior of the structure (Shapiro 2007).

In December of 2007, the recommended FRP reinforcement system was installed on the eighteen girders of Northbound Spans 10 and 11. The project plans and specifications were developed through the collaborative efforts of the Auburn University Highway Research Center (AUHRC) and ALDOT.

This report includes the details of the post-repair performance monitoring and load testing of the bridge conducted in the late spring of 2010. The majority of the sensors used during the pre-repair load tests were maintained for post-repair testing, and additional strain gages were installed on the surface of the FRP reinforcement. In addition to repeating the pre-repair load testing procedures, the sensors measuring bridge behavior were also monitored for roughly 24 hours to allow for analysis of the post-repair structure's behavioral response to a daily cycle in ambient thermal conditions.

Initially, the post-repair bridge behavior was compared to the behavior observed during pre-repair testing. It was determined that, due to inconsistent support conditions between pre- and post-repair testing, comparisons between the pre- and post-repair measurements in response to truck loads are not appropriate for assessing the efficacy of the repair system. Thus, the post-repair bridge test results were analyzed independently to gain insight into the post-repair structural performance.

It was determined that an FRP reinforcement system is an effective repair solution for damage conditions similar to those observed for the girders of I-565. An updated and simplified FRP-strengthening design procedure that synthesizes the AASHTO LRFD bridge design specifications and the FRP-strengthening recommendations of ACI Committee 440 was developed. This procedure is explained to facilitate application to FRP repair solutions for bridge structures that exhibit damage at the continuous end of concrete girders. A design example was developed for the FRP strengthening of girders in Northbound Spans 10 and 11 using the material properties of the FRP reinforcement used for this project. Recommendations are also provided for appropriate installation of an FRP reinforcement repair solution.

7.2 CONCLUSIONS

Conclusions stated within this report include AUHRC findings related to:

- The FRP reinforcement installation process that occurred in December 2007,
- Measured responses to service-level truck loads,
- Theoretical responses to ambient thermal conditions,
- Measured responses to ambient thermal conditions,

- Performance of FRP reinforcement installed in December 2007, and
- Design recommendations for the repair of other bridge structures exhibiting damaged regions at the continuous ends of prestressed concrete girders.

7.2.1 FRP Reinforcement Installation

- The installation process in December 2007 indicated that plans and procedures should be explicitly discussed with the contractor on site before beginning the reinforcement installation process.
- Proper quality control testing procedures should be discussed and monitored.
- The contractor became noticeably more efficient with the installation process, consistently installing four layers of FRP reinforcement in roughly one hour during the repair of the second of the two spans.

7.2.2 Observed Responses to Truck Loads

- Contact between false support bearing pads and bridge girders during pre-repair testing resulted in additional load-bearing support conditions that affected structural behavior observed during pre-repair testing.
- Because of differences in support conditions, comparisons between pre- and post-repair structural behavior measured during testing are not useful for assessing the efficacy of the FRP reinforcement repair.
- The crack closures measured at the COD gage on Girder 8 of Span 10 during both pre- and post-repair load testing are an indication of potential out-of-plane bending behavior in response to truck loads.
- The post-repair structure exhibited an even greater loss of continuity in response to live loads than indicated by the post-repair FEM model, which was modeled to be less continuous than the original undamaged structure.
- The *overall* bridge structure exhibited a nearly linear elastic response to midspan truck positions during superposition testing.
- The *damaged regions* of the bridge structure exhibited a localized nonlinear response to midspan truck positions during superposition testing.
- The magnitude of damage exhibited at a cracked region near the continuous end of a concrete girder was observed to relate to the degree of continuity degradation indicated for that girder line in response to live loads.

- It is appropriate to assume that the bridge structure would exhibit simply supported girder behavior in response to strength-limit-state design loads that control the design of repair solutions.
- Truck positions that induced the greatest shear demand on damaged regions resulted in greatest measured FRP tensile demands.
- Strength-limit-state demands for damaged regions should be determined in accordance with AASHTO LRFD or another framework of consistent analysis and design procedures at the discretion of the bridge owner.

7.2.3 Theoretical Responses to Ambient Thermal Conditions

- For design purposes, it is appropriate to assume that a bridge structure with damaged continuous girder ends repaired with FRP reinforcement exhibits fully continuous behavior in response to ambient thermal conditions.
- The stress-induced strain expected in FRP reinforcement installed to repair damaged continuous ends of multi-span continuous girder systems is primarily a function of the structural concrete coefficient of thermal expansion, height of the girder-deck composite cross section, variation of temperature gradient conditions, and distance from the continuity diaphragm to the damaged region.
- For design purposes, it is conservative and simple to assume that the girder stresses in the damaged region are approximately the same as the stresses at the adjacent continuous support.

7.2.4 Observed Responses to Ambient Thermal Conditions

- Upward deflections measured in response to ambient thermal conditions during post-repair bridge monitoring were similar to upward deflections measured in response to solar effects during an ALDOT investigation of the same spans in 1994.
- Linear profiles of bottom-fiber concrete strains measured beyond damaged regions indicate the bridge structure exhibited some preservation of continuous behavior in response to thermal effects.
- The slope of bottom-fiber concrete strain profiles were less than theoretically expected of a fully continuous structure subjected to a linear temperature gradient similar to the gradient measured by ALDOT in 1994, which indicates that either the structure is not exhibiting fully continuous behavior or the actual temperature gradient was less than theoretically assumed.

- Maximum bottom-fiber FRP strains measured at crack locations in response to thermal conditions were similar to the bottom-fiber FRP strain estimated in response to the linear temperature gradient measured by ALDOT in 1994.
- Simplified linear temperature gradient analysis can be used to effectively estimate the tensile strain that an FRP repair system must resist due to daily temperature fluctuations.
- Ambient thermal conditions resulted in damaged region crack-opening displacements and FRP surface strains roughly 3–4.5 times greater than maximum respective measurements in response to service-level truck loads.
- Comparisons of structural responses to thermal gradient effects and truck loads support the conclusion that temperature effects caused initial cracking.

7.2.5 Performance of FRP Reinforcement

- The FRP reinforcement was observed to carry tension forces and effectively serve as additional longitudinal reinforcement to service-level truck loads and ambient thermal conditions.
- During post-repair testing, the repair system had been in service for more than 2 years without exhibiting signs of debonding or other deterioration.
- No additional signs of severe cracking were observed at the repaired region since the installation of the FRP reinforcement.
- The installed FRP reinforcement does not satisfy the design procedure presented in Chapter 6 of this report, but the strength deficiency is less than 5 percent (on the basis of AASHTO LRFD strength-limit-state design loads).
- The FRP reinforcement that has already been installed is acceptable, but future design and installation should conform to guidelines and procedures discussed in Chapter 6 of this report.

7.2.6 FRP Design Recommendations

- FRP reinforcement product can be selected for bridge girder repair using guidelines presented by ACI 440.2R-08 and NCHRP Report 655.
- FRP reinforcement systems can be designed to resist strength-limit-state demands determined in accordance with AASHTO LRFD bridge design specifications—or other strength-limit-state demands at the discretion of the bridge owner.

- Designed repair solutions should satisfy strength-limit-state demands at all locations of (FRP or internal) reinforcement transitions assuming simply supported girder behavior.
- Debonding failure of FRP reinforcement systems due to tension strains expected in response to combined shear and bending moment demands has been observed to control the design of FRP reinforcement repair solutions.
- A simplified formula ($\ell_d = 180d_b$) for approximating prestressed strand development lengths that begin at or beyond damaged regions has been proposed as a guideline for determining the extent of FRP reinforcement.
- FRP anchorage and development computations performed using a typical *average* test value for E_f are more conservative than when performed using a lower-bound "design value."
- Solutions for providing supplemental anchorage at locations of short available bonded length require further research before they can be recommended.
- Temperature demands do not need to be considered in conjunction with strength-limit-state demands because temperature-induced deformations are no longer restrained once the structure transitions to the simply supported behavior recommended for strength-limit-state design.

7.2.7 FRP Reinforcement Installation Recommendations

- The contractor should have experience following the guidelines of the manufacturer for the selected FRP and epoxy reinforcement product.
- Design documents should clearly show the correct fiber orientation, *and* contractors and inspectors should demonstrate comprehension of the proper orientation prior to FRP installation.
- Existing cracks should be injected with structural epoxy prior to installation of FRP reinforcement.
- Structural substrates should be appropriately prepared for adequate bonding of the FRP reinforcement to the concrete surface for the entire length installed.
- Protective coatings should be applied to cured FRP reinforcement systems for improved durability.
- Quality control testing and inspections should be conducted during and following the installation process to ensure proper installation.

- Tensile test samples should consist of the same number of fabric layers as are installed on the actual structure, *and* the ALDOT special provision for FRP should be modified to clearly state this requirement.

Chapter 8

RECOMMENDATIONS

8.1 DESIGN OF FRP REINFORCEMENT REPAIR SOLUTIONS

FRP reinforcement can be utilized for the repair of prestressed concrete bridge girders with damage conditions near continuous ends, similar to the damage observed near the continuous ends of girders within Northbound Spans 10 and 11 of I-565 in Huntsville, Alabama. The design procedure presented in Chapter 6 of this report has been formulated in accordance with specifications of AASHTO LRFD, NCHRP Report 655 (Zureick et al. 2010), and ACI 440.2R-08.

An FRP reinforcement system designed in accordance with the guidelines presented in this report provides adequate tension reinforcement for the resistance of strength-limit-state demands of combined shear and flexure. The FRP repair solution also provides resistance to the tension stresses induced by daily temperature variations on the continuous structure. The design procedure detailed in this report includes guidelines for the determination of

- An appropriate FRP reinforcement product,
- Critical cross-section locations,
- Critical load conditions for those locations,
- Material and dimensional properties at those locations,
- Layers of FRP reinforcement required to satisfy strength demands, and
- Length of FRP reinforcement required for appropriate development of prestressed strands.

8.2 INSTALLATION OF FRP REINFORCEMENT SYSTEMS

FRP reinforcement installation procedures should be performed in accordance with the specifications of the manufacturer. Guidelines presented in Chapter 6 of this report for ensuring proper FRP reinforcement installation include guidelines that are also presented in NCHRP Report 609 (Miller et al. 2008) and ACI 440.2R-08. These guidelines include recommended procedures for:

- Crack injection,
- Surface preparation,

- FRP reinforcement installation, and
- Quality control inspection and testing.

8.3 NORTHBOUND SPANS 10 AND 11 OF I-565

The FRP reinforcement system installed on Northbound Spans 10 and 11 of I-565 in December 2007 was designed by Auburn University researchers (Swenson 2003). The FRP reinforcement was designed to resist tension forces that were predicted with strut-and-tie models. The reinforcement system was also designed in accordance with the effective debonding strain (ε_{fe}) specifications presented by ACI 440.2R-02, which have since been updated to reflect the findings of more recent research as presented by ACI 440.2R-08.

The design procedure presented in Chapter 6 of this report has been formulated in accordance with AASHTO LRFD specifications (AASHTO 2010) and the updated effective debonding strain specifications of ACI 440.2R-08. An updated FRP reinforcement system design example is presented in Appendix N of this report.

The FRP reinforcement systems that were installed on Spans 10 and 11 in December 2007 do not satisfy the updated design recommendation, but installation of an additional layer of reinforcement may not be absolutely necessary. The limiting effective debonding strain ($\varepsilon_{fe} \leq 0.004$ in./in.) controls the recommendation of 5 layers of reinforcement instead of 4 layers. The current installation of 4 layers satisfies strength requirements at the interior face of the bearing pad, but results in a strength deficiency of less than 5 percent at the termination of the continuity reinforcement in response to factored shear demand.

The installed 4 layers of reinforcement nearly satisfy the requirements of the updated design recommendations of this report. The small computed strength deficiency is based on full strength-limit-state AASHTO LRFD design loads for new construction in conjunction with the conservative limiting effective debonding strain of the FRP reinforcement. The length of FRP reinforcement currently installed allows for adequate development of prestressed strands beyond the primary crack locations in these particular spans. It is unknown if an additionally installed fifth layer of reinforcement would perform as expected when bonded to previously installed FRP reinforcement that has been fully cured. Surface preparation procedures required for proper installation of additional FRP reinforcement may also be detrimental to the integrity of the existing FRP reinforcement. Whether or not the computed strength discrepancy justifies the cost, effort, and uncertainty associated with installation of an additional layer of FRP in Spans 10 and 11 is a decision best left to the discretion of ALDOT after consideration of these factors in light of the department's established maintenance philosophy. On the other hand, FRP reinforcement configurations for new repairs should be designed to satisfy the design recommendations proposed within this report.

8.4 RECOMMENDATIONS FOR FURTHER RESEARCH

Further research would be beneficial to provide a better understanding of the behavioral responses observed during the testing of Northbound Spans 10 and 11. Further testing is also recommended to gain a better understanding of the performance of FRP composite material as a reinforcement solution.

8.4.1 In-Service Load Testing

Truck positions that resulted in large shear demand at the damaged region resulted in significant reinforcement tension demand. Future load testing of structures that exhibit damage regions similar to those of Spans 10 and 11 should focus on these high shear demand truck positions. Superposition testing should also be conducted with truck positions that result in significant damaged-region tension demand.

For future pre- and post-repair testing of in-service bridge structures, it is recommended that variables which may have an effect on bridge behavior during testing be limited to allow for more appropriate comparisons of pre- and post-repair measured bridge behavior. Variables observed during the research discussed within this report that had an effect on the ability to assess the efficacy of the installed FRP reinforcement repair system by directly comparing pre- and post-repair measurements include

- False supports that were unintentionally load-bearing supports during pre-repair testing but were not load-bearing supports during post-repair testing,
- Weather conditions that resulted in significantly cooler ambient temperatures during pre-repair testing compared to the temperatures of post-repair testing,
- Vehicles with different dimensions that required modifications to load block configurations during both pre- and post-repair testing,
- Time elapsed between pre-repair testing and reinforcement installation, and
- Time elapsed between reinforcement installation and post-repair testing.

8.4.2 In-Service Bridge Monitoring

Bridge monitoring provided information that supports the conclusion that temperature effects are the primary cause of cracking observed in damaged regions near continuous ends of prestressed concrete bridge girders. For future in-service load testing of pre- and post-repair conditions of bridge structures, it is recommended that bridge monitoring be conducted during the days encompassing both the pre- and post-repair in-service load testing. It is also recommended that bridge monitoring be conducted for more than one daily cycle during both pre- and post-repair

testing. Additionally, it is recommended to measure ambient, deck, and girder temperatures during future bridge monitoring tests.

8.4.3 Laboratory Testing

The limiting effective debonding strain ($\varepsilon_{fe} \leq 0.004$ in./in.) specified by ACI 440.2R-08 is a conservative assumption that has been observed to frequently control the amount of FRP required when executing the design procedure recommended in Chapter 6 of this report. This conservative assumption is recommended until further testing can validate that higher effective debonding strains can be achieved consistently and concervatively. Controlled laboratory testing of longitudinal FRP reinforcement system that wraps around the tension flange at one end of a simply supported girder could provide insight into the actual performance of this repair system near failure (strength limit state) conditions. This testing would require that a girder sustain "controlled" damage near one end of the girder before installing the FRP reinforcement.

Laboratory-controlled testing of solutions for providing additional FRP reinforcement anchorage for locations of short bonded length between critical cross-section locations and FRP reinforcement termination is recommended before permitting the installation of FRP reinforcement systems that require supplemental anchorage.

The design effective debonding strain in areas of short bonded lengths is a function of the design modulus of elascticity of the composite FRP reinforcement. For design purposes, it is recommended to assume the design modulus of elasticity of the composite FRP reinforcement reported by the manufacturer; however, testing of representative samples may indicate that the installed product exhibits more stiffness than originally assumed during design. To better understand the ramifications of this issue, laboratory testing is recommended to assess the effective debonding strain for FRP reinforcement products with varying stiffnesses determined in accordance with the procedures (ASTM D3039 2008) recommended for testing representative samples of installed FRP reinforcement systems.

Further testing of FRP reinforcement is recommended to better understand the performance of this composite material; however, the design procedure recommended in this report provides appropriately conservative specifications for the design of repair solutions similar to the reinforcement systems installed to repair the damaged girders of Northbound Spans 10 and 11 of I-565 in Huntsville, Alabama.

REFERENCES

AASHTO. 2002. *AASHTO LRFD Bridge design specifications: Customary U.S. Units.* Second Edition. Washington, D.C.: American Association of State Highway and Transportation Officials (AASHTO).

AASHTO. 2010. *AASHTO LRFD Bridge design specifications: Customary U.S. Units.* Fifth Edition. Washington, D.C.: American Association of State Highway and Transportation Officials (AASHTO).

ACI Committee 224. 2007. *Causes, evaluation, and repair of cracks in concrete structures (ACI 224.1R-07)*. Farmington Hills, MI: American Concrete Institute (ACI).

ACI Committee 318. 2002. *Building code requirements for structural concrete and commentary (ACI 318R-02)*. Farmington Hills, MI: American Concrete Institute (ACI).

ACI Committee 318. 2008. *Building code requirements for structural concrete and commentary (ACI 318-08)*. Farmington Hills, MI: American Concrete Institute (ACI).

ACI Committee 440. 2008. *Guide for the design and construction of externally bonded FRP systems for strengthening concrete structures (ACI 440.2R-08)*. Farmington Hills, MI: American Concrete Institute (ACI).

ACI Committee 503. 1992. *Standard specifications for repairing concrete with epoxy mortars (ACI 503.4-92)*. Farmington Hills, MI: American Concrete Institute (ACI).

ACI Committee 546. 2004. *Concrete repair guide (ACI 546R-04)*. Farmington Hills, MI: American Concrete Institute (ACI).

Alabama Department of Transportation (ALDOT). 1988. Construction plans for Project ID-565-5(21)358. Montgomery, AL: Alabama Department of Transportation (ALDOT).

Alabama Department of Transportation (ALDOT). 1994. *Cracks in precast prestressed bulb tee girders on Structure No.'s I-565-45-11.5 A. and B. on I-565 in Huntsville, Alabama*. Report and attachments (A–L). Montgomery, AL: Alabama Department of Transportation (ALDOT).

ASTM Standard D3039. 2008. Test method for tensile properties of polymer matrix composite materials (ASTM D3039-08). West Conshohocken, PA: ASTM International.

ASTM Standard D4065. 2006. Practice for plastics: dynamic mechanical properties: determination and report of procedures (ASTM D4065-06). West Conshohocken, PA: ASTM International.

ASTM Standard D4541. 2009. Standard test method for pull-off strength of coatings using portable adhesion testers (ASTM D4541-09). West Conshohocken, PA: ASTM International.

Barnes, R. W., K. S. Swenson, N. Gao, A. K. Schindler, and W. E. Fason. 2006. Cracking and repair of prestressed concrete bridge girders made continuous for live loads. In the *Proceedings of Structural Faults and Repair, Eleventh International Conference: Edinburgh, Scotland. 13–15 June 2006*.

Ceroni, F. and M. Pecce. 2010. Evaluation of bond strength in concrete elements externally reinforced with CFRP sheets and anchoring devices. *ASCE Journal of Composites for Construction* 14 (5): 521–530.

Fason, W. E. 2009. Static load testing of a damaged, continuous prestressed concrete bridge. M.S. thesis. Auburn, AL: Auburn University.

Fyfe Co. Tyfo Fiberwrap Systems. 2010. Tyfo SCH-41 Composite using Tyfo S Epoxy data sheet. San Diego, CA: Fyfe Co. LLC.

Gao, N. 2003. Investigation of cracking in prestressed girders made continuous for live load. M.S. thesis. Auburn, AL: Auburn University.

Hadzor, T. J., R. W. Barnes, P. H. Ziehl, J. Xu, and A. K. Schindler. 2011. *Development of acoustic emission evaluation method for repaired prestressed concrete bridge girders*. Research Report FHWA/ALDOT 930-601-1. Auburn, Alabama: Auburn University Highway Research Center.

ICRI Committee 310. 2008. *Guide for surface preparation for the repair of deteriorated concrete resulting from reinforcing steel corrosion (ICRI 310.1R-2008)*. Farmington Hills, MI: International Concrete Repair Institute (ICRI).

ISO/IEC Technical Committee. 2005. *General requirements for the competence of testing and calibration laboratories (ISO/IEC 17025)*. Geneva, Switzerland: International Organization for Standardization (ISO) and International Electrotechnical Commission (IEC).

Ma, Z., X. Huo, M. K. Tadros, and M. Baishya. 1998. Restraint moments in precast/prestressed concrete continuous bridges. *PCI Journal* 43 (6): 40–57.

Miller, R. A., R. Castrodale, A. Mirmiran, and M. Hastak. 2004. *Connection of simple-span precast concrete girders for continuity.* NCHRP Report 519. Washington, D.C.: Transportation Research Board (TRB).

Mirmiran, A., M. Shahawy, A. Nanni, V. Karbhari, and B. Yalim, and A. S. Kalayci. 2008. *Recommended construction specifications and process control manual for repair and retrofit of concrete structures using bonded FRP composites.* NCHRP Report 609. Washington, D.C.: Transportation Research Board (TRB).

National Oceanic and Atmospheric Administration (NOAA). 2005a. *Local Climatological Data: Huntsville, AL: May 2005*. Rocket Center, WV: National Climatic Data Center (NCDC).

National Oceanic and Atmospheric Administration (NOAA). 2005b. *Local Climatological Data: Huntsville, AL: June 2005*. Rocket Center, WV: National Climatic Data Center (NCDC).

National Oceanic and Atmospheric Administration (NOAA). 2008. *Local Climatological Data: Huntsville, AL: December 2007*. Rocket Center, WV: National Climatic Data Center (NCDC).

National Oceanic and Atmospheric Administration (NOAA). 2010. *Local Climatological Data: Huntsville, AL: May 2010*. Rocket Center, WV: National Climatic Data Center (NCDC).

Niemitz, C. W., R. James, and S. F. Breña. 2010. Experimental behavior of carbon fiber-reinforced polymer (CFRP) sheets attached to concrete surfaces using CRFP anchors. *ASCE Journal of Composites for Construction* 14 (2): 185–194.

Orton, S. L., J. O. Jirsa, and O. Bayrak. 2008. Design considerations of carbon fiber anchors. *ASCE Journal of Composites for Construction* 12 (6): 608–616.

Potgieter, I. C. and W. L. Gamble. 1989. Nonlinear temperature distributions in bridges at different locations in the United States. *PCI Journal* 34 (4): 80–103.

Shapiro, K. A. 2007. Finite-element modeling of a damaged prestressed concrete bridge. M.S. thesis. Auburn, AL: Auburn University.

Swenson, K. S. 2003. Feasibility of externally bonded FRP reinforcement for repair of cracked prestressed concrete girders. M.S. thesis. Auburn, AL: Auburn University.

Swenson, K. S. and R. W. Barnes. 2007. *Feasibility of externally bonded FRP reinforcement for repair of cracked prestressed concrete girders, I-565, Huntsville Alabama*. Report IR-07-02. Auburn, AL: Auburn University Highway Research Center (AUHRC).

Teng, J. G., J. F. Chen, S. T. Smith, and L. Lam. 2002. *FRP-strengthened RC structures*. Chichester, West Sussex, UK: John Wiley and Sons.

Teng, J. G., S. T. Smith, J. Yao, and J.F. Chen. 2003. Intermediate crack induced debonding in RC beams and slabs. *Construction and Building Materials* 17 (6-7): 447–462.

TML. 2011. PI displacement transducer data sheet. *TML manual: strain gauge-type transducers.* TML Pam E-701B. Tokyo, Japan: TML Tokyo Sokki Kenkyujo Co., Ltd.

Vishay Precision Group. 2010. *Strain gage selection: criteria, procedures, and recommendations.* Tech Note TN-505-4. Raleigh, NC. Vishay Precision Group.

Zureick, A.-H., B. R. Ellingwood, A. S. Nowak, D. R. Mertz, and T. C. Triantafillou. 2010. *Recommended guide specification for the design of externally bonded FRP systems for repair and strengthening of concrete bridge elements.* NCHRP Report 655. Washington, D.C.: Transportation Research Board (TRB).

Appendix A

ABBREVIATIONS AND NOTATION

AASHTO	American Association of State Highway and Transportation Officials
ACI	American Concrete Institute
AE	acoustic emissions
ALDOT	Alabama Department of Transportation
ASTM	American Society for Testing and Materials
AUHRC	Auburn University Highway Research Center
BT	bulb-tee
CFRP	carbon fiber-reinforced polymer
ERSG	electrical-resistance strain gauge
FEM	finite-element modeling
FRP	fiber-reinforced polymer
I-565	Interstate Highway 565
ICRI	International Concrete Repair Institute
IEC	International Electrotechnical Commission
ISO	International Organization for Standardization
LRFD	load and resistance factor design
NCDC	National Climatic Data Center
NCHRP	National Cooperative Highway Research Program
NOAA	National Oceanic and Atmospheric Administration
PCI	Precast/Prestressed Concrete Institute
RC	reinforced concrete
TRB	Transportation Research Board

a	depth of compression zone
A	area
A_f	area of FRP reinforcement
A_{ps}	area of prestressed strand reinforcement
A_s	area of steel reinforcement
A_v	area of vertical steel reinforcement
b	width of compression zone
b_f	width (perimeter) of FRP reinforcement
b_v	width of girder web
C_E	environmental reduction factor for composites
d_e	effective depth from top of cross section
d_f	depth to centroid of FRP reinforcement
d_s	depth to centroid of longitudinal steel reinforcement
d_v	effective shear depth
E	modulus of elasticity
E_f	modulus of elasticity—FRP reinforcement
E_p	modulus of elasticity—prestressed strand
E_s	modulus of elasticity—steel reinforcement
f'_c	design compressive strength of concrete
f_{bot}	stress at the bottom of the cross section
f_{fe}	effective debonding stress of FRP reinforcement system
f_{po}	modulus of elasticity of prestressing strands multiplied by the locked-in difference in strain between the prestressing strands and the surrounding concrete
f_y	tension yield strength
h	height of the cross section
I	moment of inertia of the cross section
L	span length
L_b	bonded length of FRP reinforcement
ℓ_d	development length of prestressed strand
L_{fd}	development length of FRP reinforcement
M	bending moment demand
M_n	nominal bending moment capacity
M_u	factored bending moment demand
n	layers of FRP-epoxy composite
P	restraint force due to thermal gradient
s	spacing of reinforcement

T	temperature; tension demand
T_{bot}	temperature of girder bottom flange
t_f	thickness of one layer of FRP fabric
$t_{f,n}$	nominal thickness of one layer of FRP-epoxy composite
T_g	glass transition temperature
$T_{max,design}$	maximum design temperature based on geographic location
$T_{n,prov}$	nominal longitudinal tension capacity provided
$T_{n,req}$	nominal longitudinal tension capacity required
T_{top}	temperature of bridge deck
ΔT_h	temperature gradient—difference between T_{top} and T_{bot}
$\delta(\Delta T_h)$	change in temperature gradient with respect to time
V	shear demand
V_c	shear capacity provided by concrete
V_n	nominal shear capacity
V_p	shear capacity provided by prestressed reinforcement
V_s	shear capacity provided by steel reinforcement
V_u	factored shear demand
x	distance along girder from continuous support
y_t	distance from neutral axis to the top of the cross section
y_{bot}	distance from neutral axis to the bottom of the cross section
$y_{cr,bot}$	distance from cracked section neutral axis to the bottom of the cross section
y_f	location of centroid of FRP reinforcement
y_{ps}	location of centroid of prestressed strand reinforcement
y_s	location of centroid of steel reinforcement

α_T	coefficient of thermal expansion—concrete
$\alpha_{T\square FRP}$	coefficient of thermal expansion—FRP
β	factor relating effect of longitudinal strain on the shear capacity, as indicated by the ability of diagonally cracked concrete to transmit tension
β_L	effective debonding strain reduction factor for locations of short bonded length
Δ	deflection
ε_{fd}	debonding strain of FRP reinforcement system
ε_{fe}	effective debonding strain of FRP reinforcement system
ε_{fu}	tension failure strain of FRP
ε_s	strain in FRP due to thermal expansion
$\varepsilon_{T,FRP}$	strain in FRP due to thermal expansion
Ø	curvature
$Ø_T$	curvature in response to unrestrained temperature gradient effects
ϕ	resistance factor
ϕ_f	resistance factor for flexure
ϕ_v	resistance factor for shear
θ	angle of inclination for shear cracking

Appendix B

MULTIPOSITION LOAD TEST—GRAPHICAL RESULTS

B.1 LANE A

B.1.1 Crack-Opening Displacements

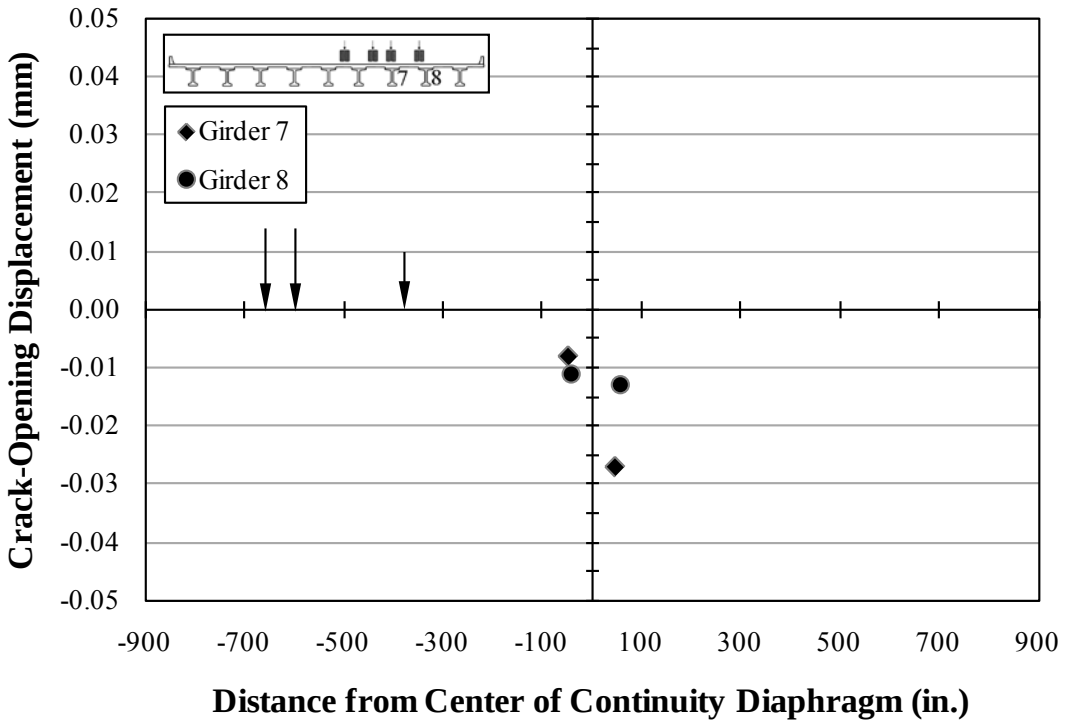

Figure B.1: Crack-opening displacements—A1

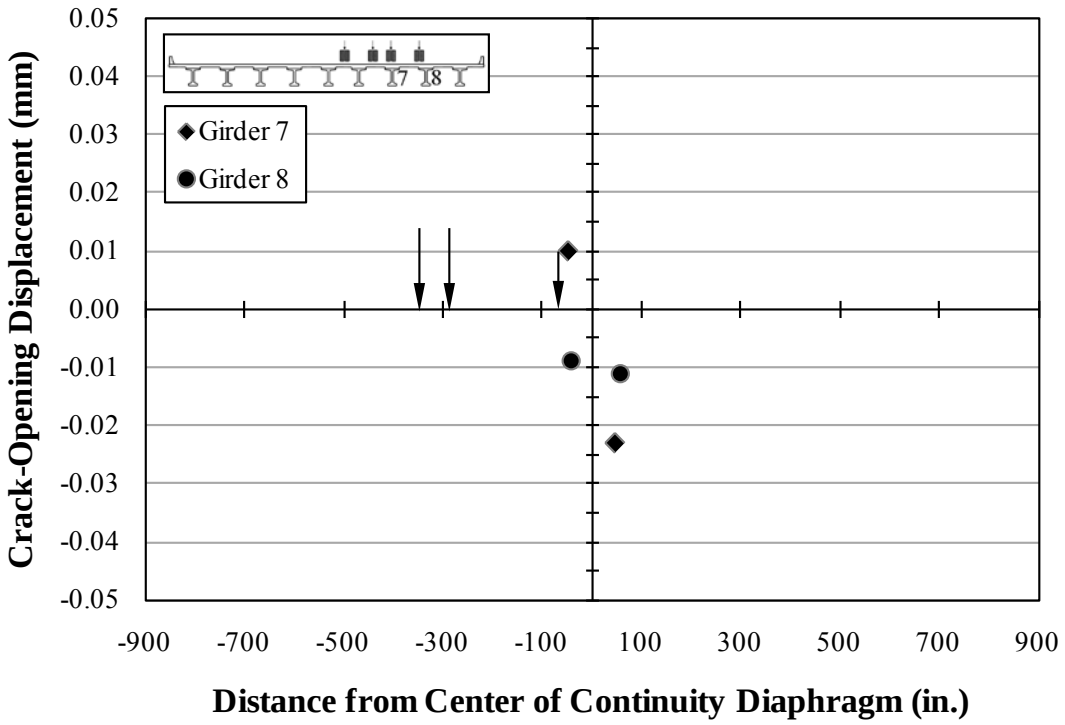

Figure B.2: Crack-opening displacements—A2

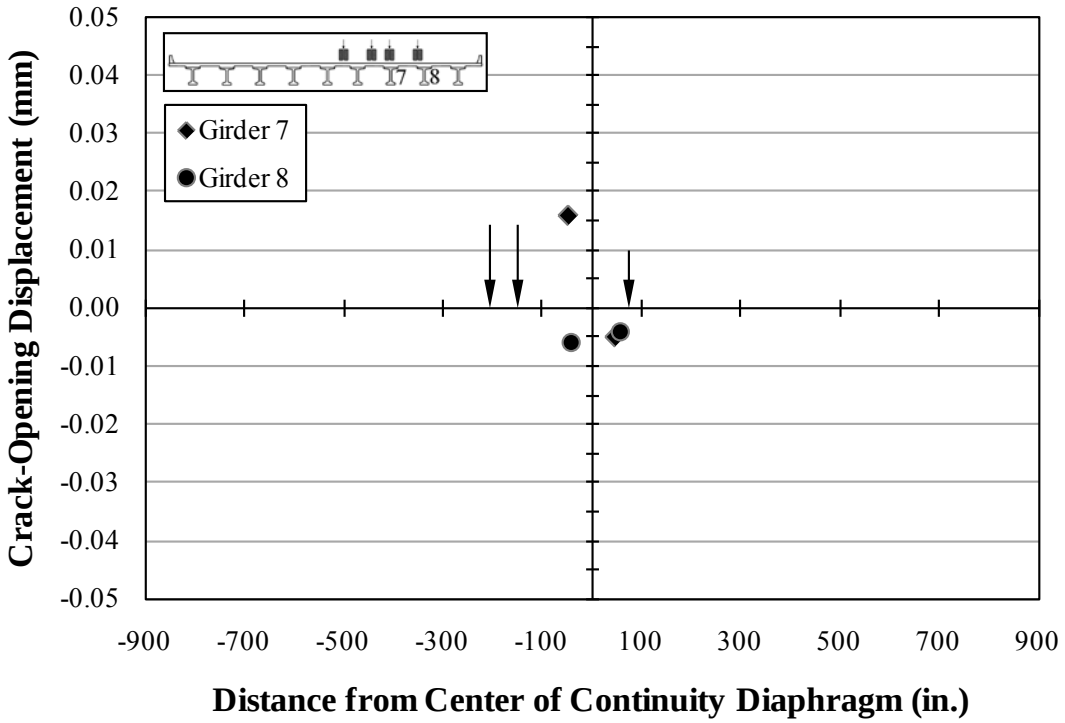

Figure B.3: Crack-opening displacements—A3

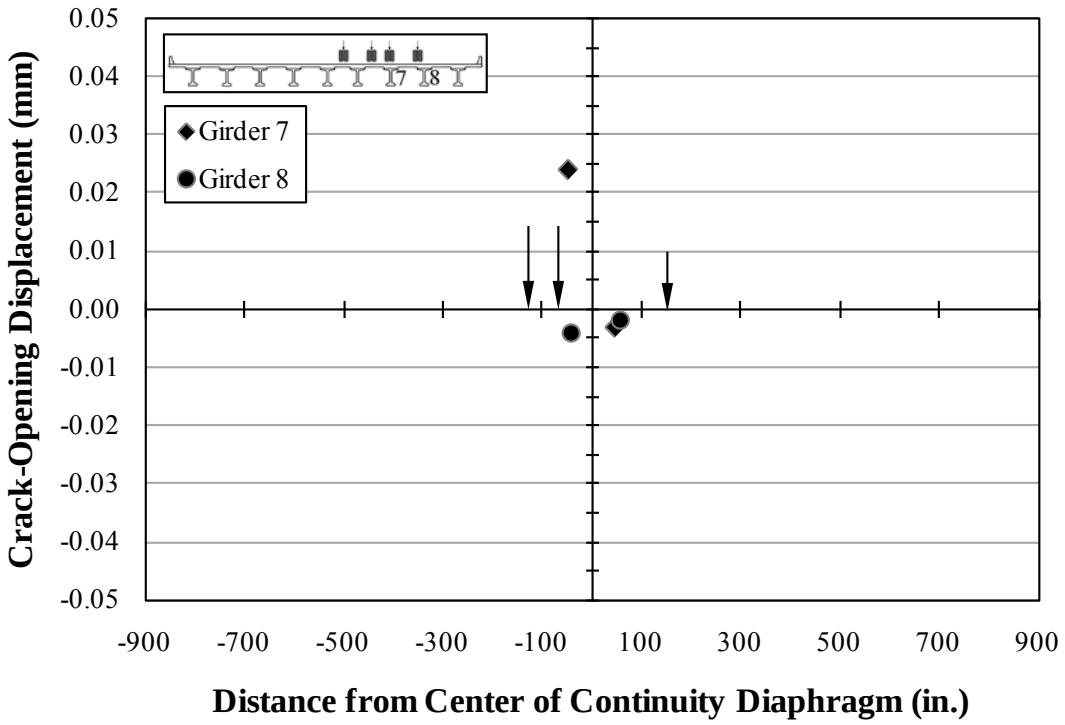

Figure B.4: Crack-opening displacements—A4

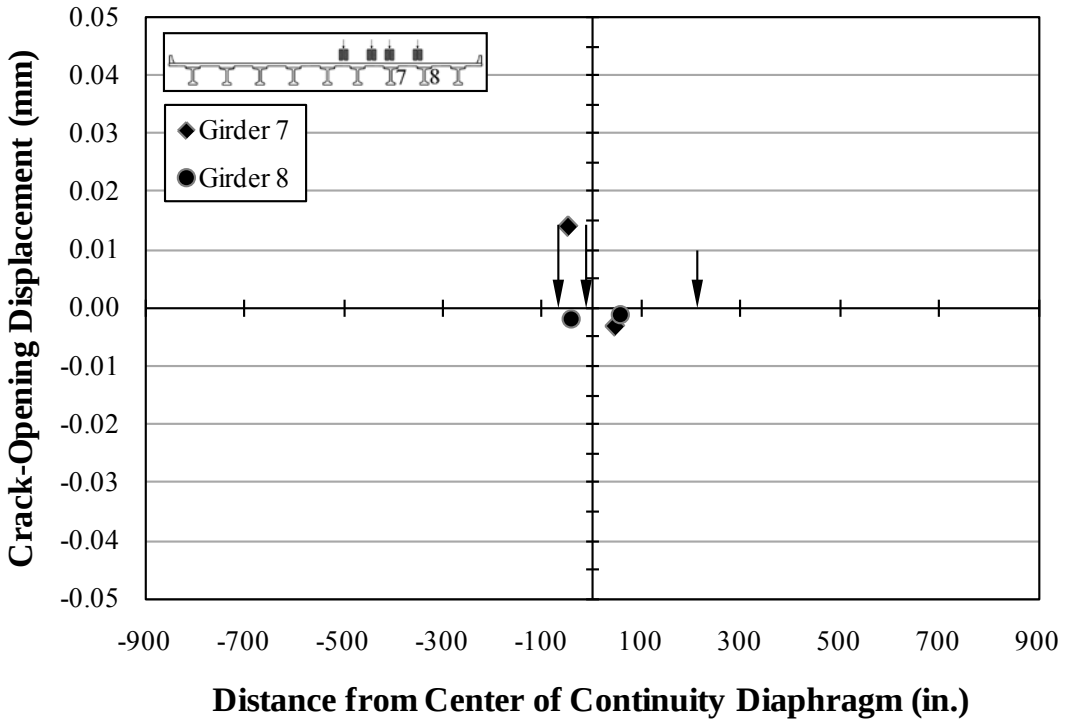

Figure B.5: Crack-opening displacements—A5

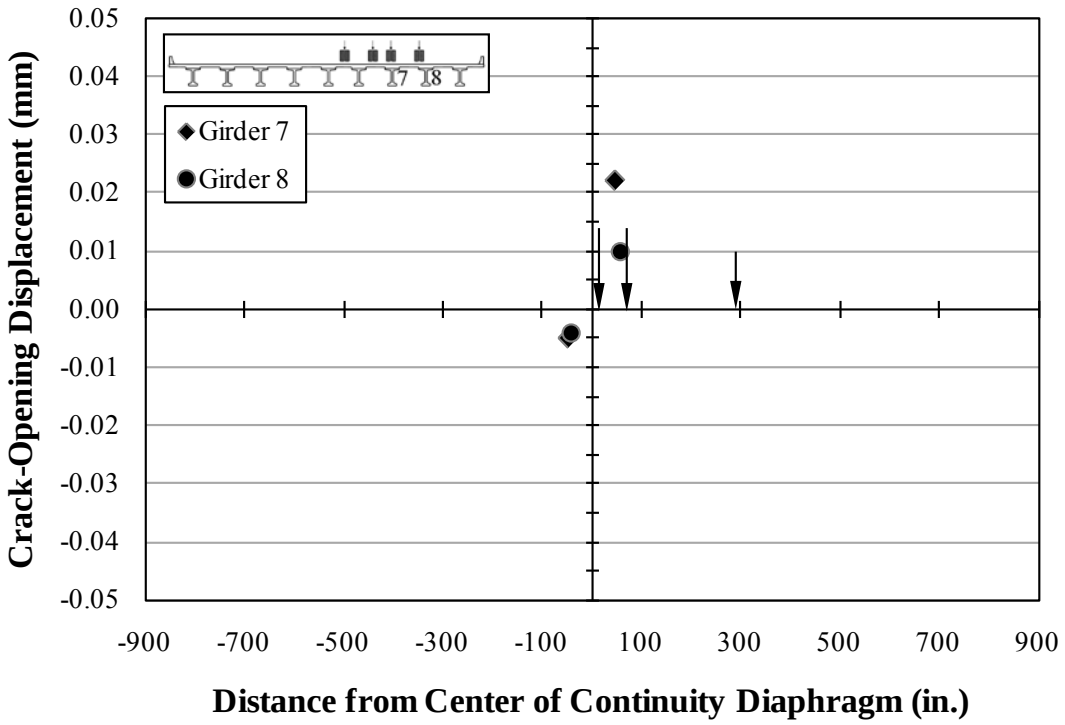

Figure B.6: Crack-opening displacements—A6

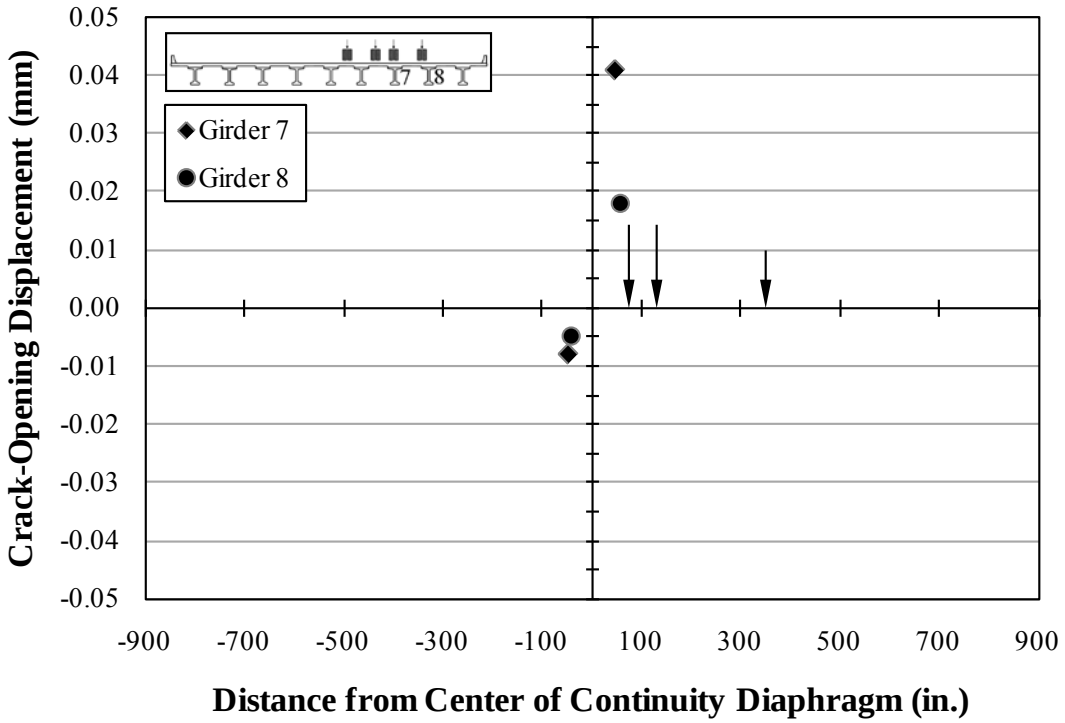

Figure B.7: Crack-opening displacements—A7

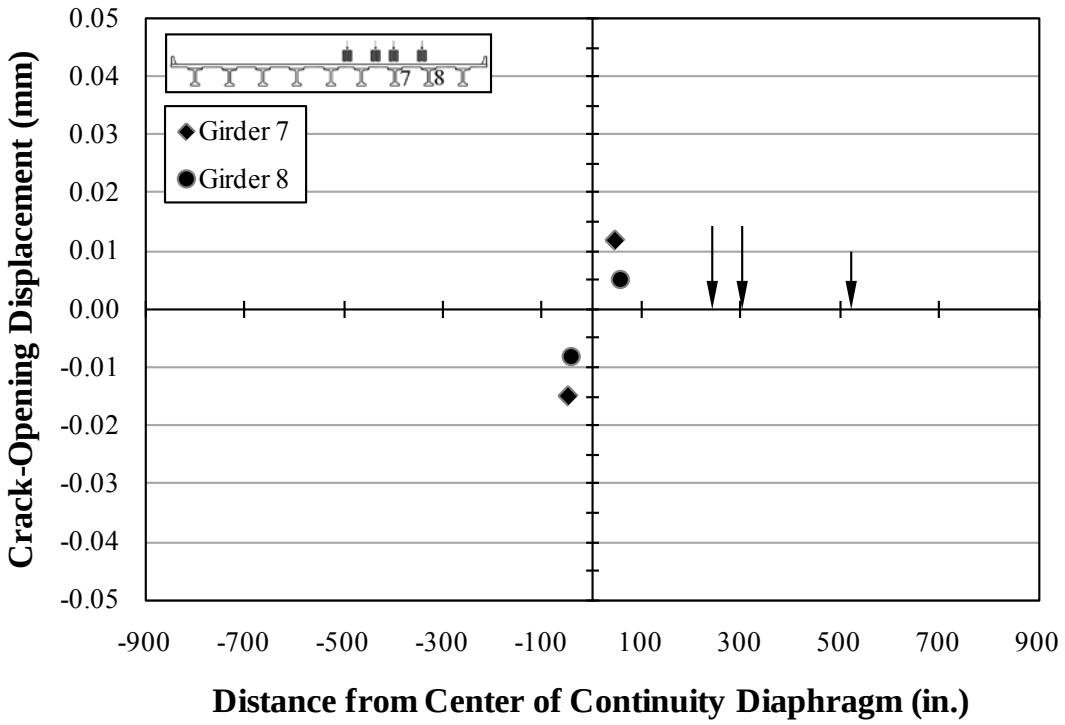

Figure B.8: Crack-opening displacements—A8

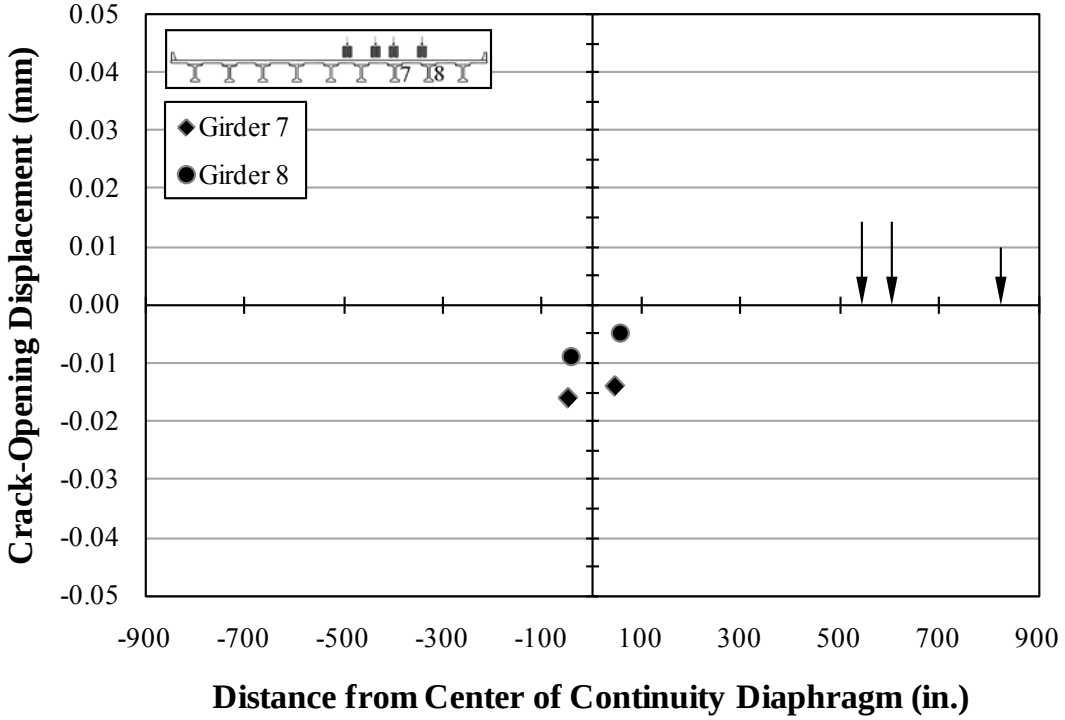

Figure B.9: Crack-opening displacements—A9

B.1.2 Deflections

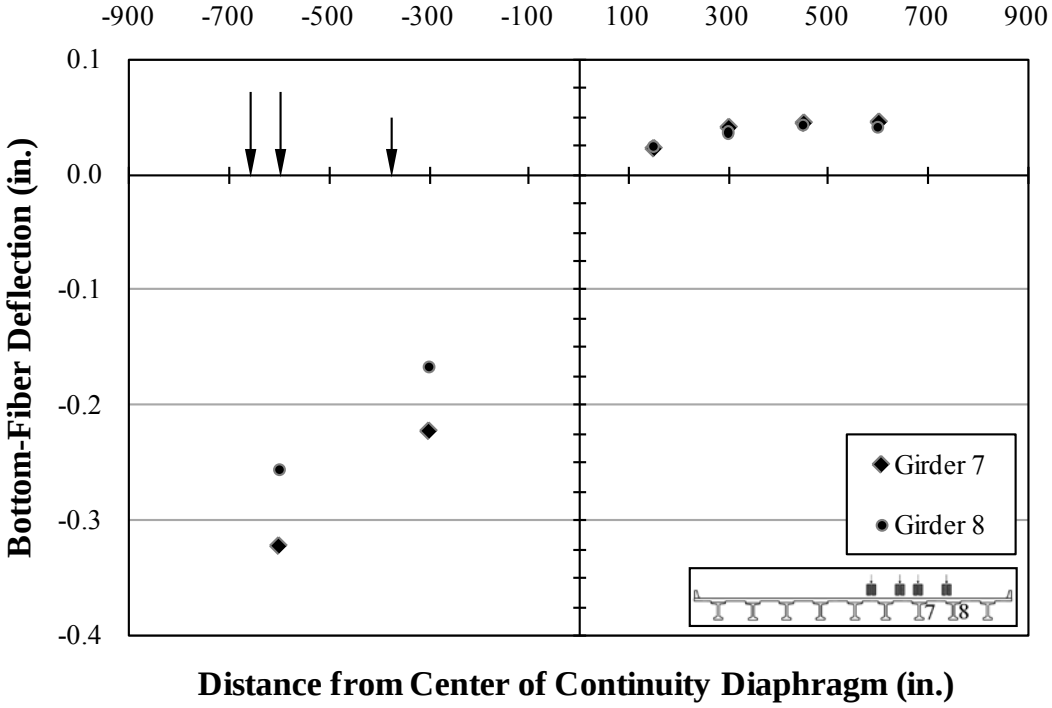

Figure B.10: Deflections—A1

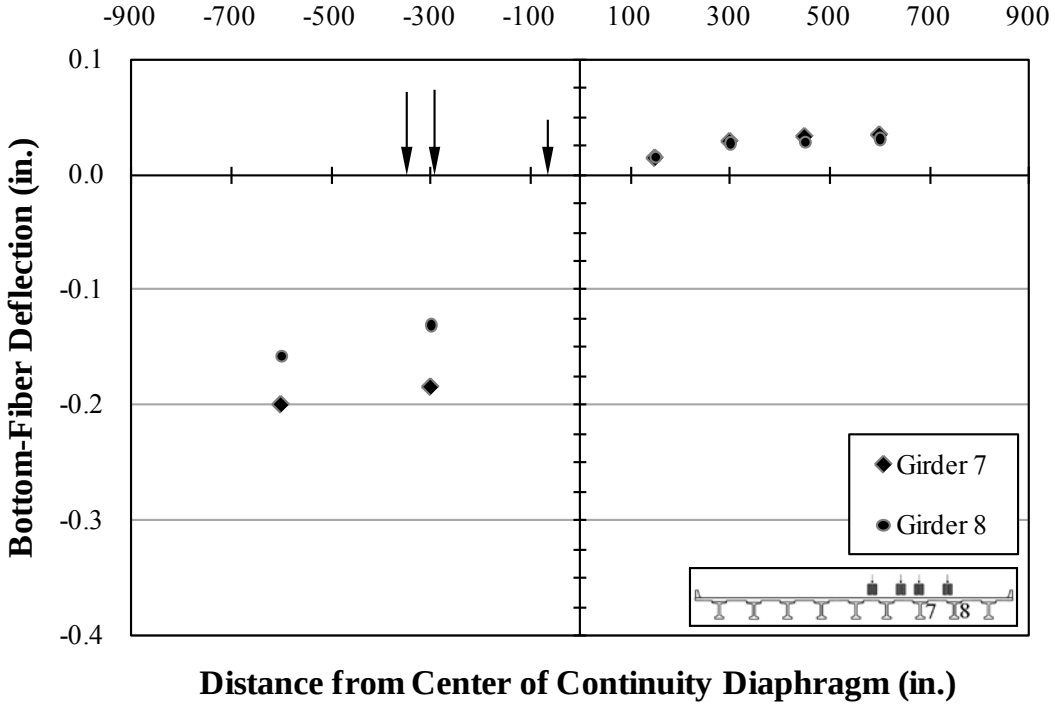

Figure B.11: Deflections—A2

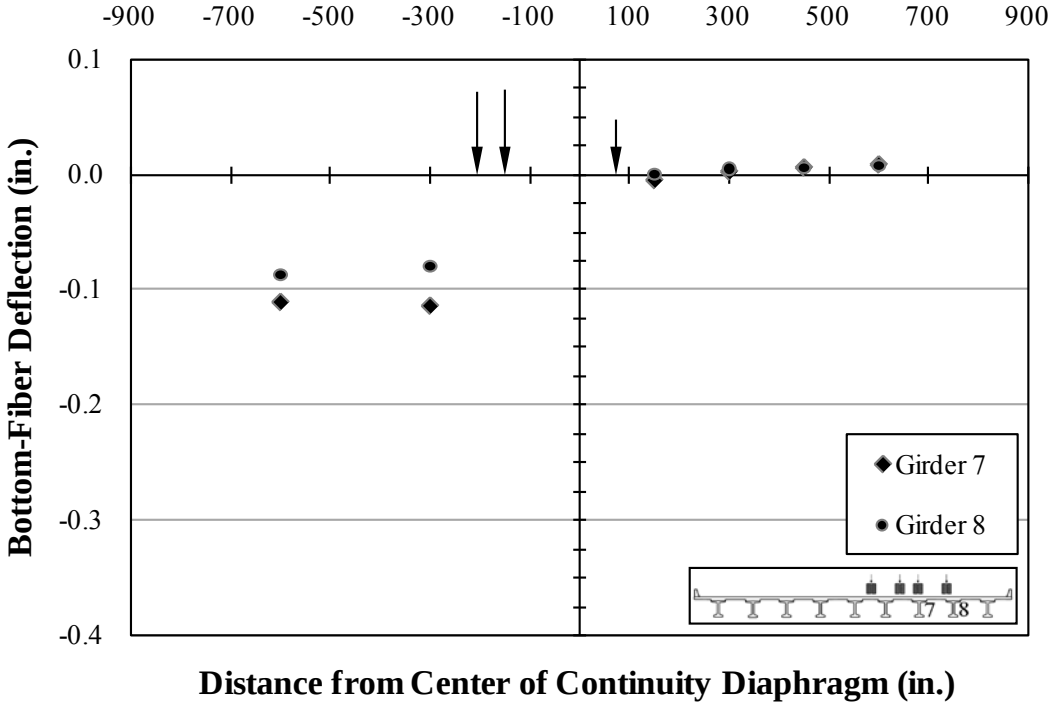

Figure B.12: Deflections—A3

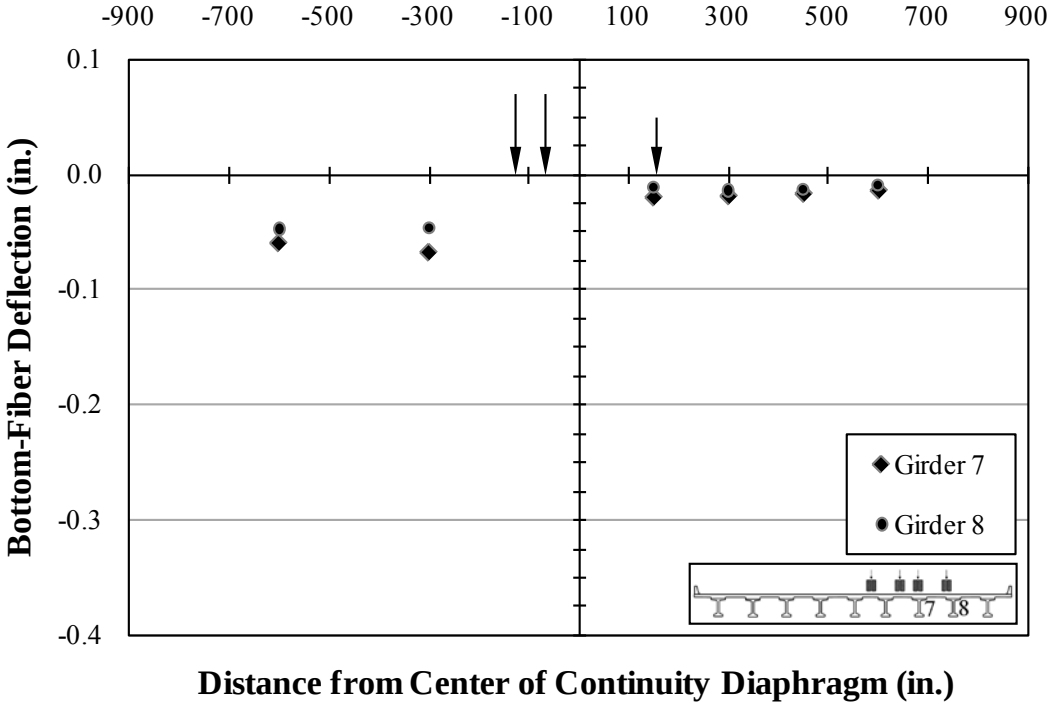

Figure B.13: Deflections—A4

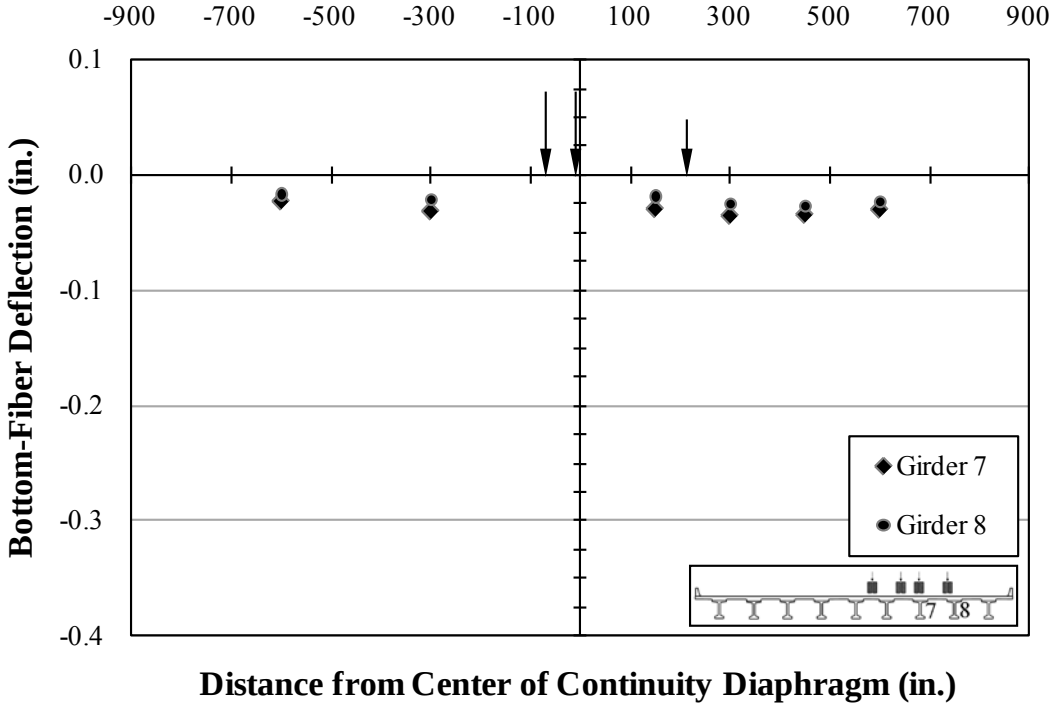

Figure B.14: Deflections—A5

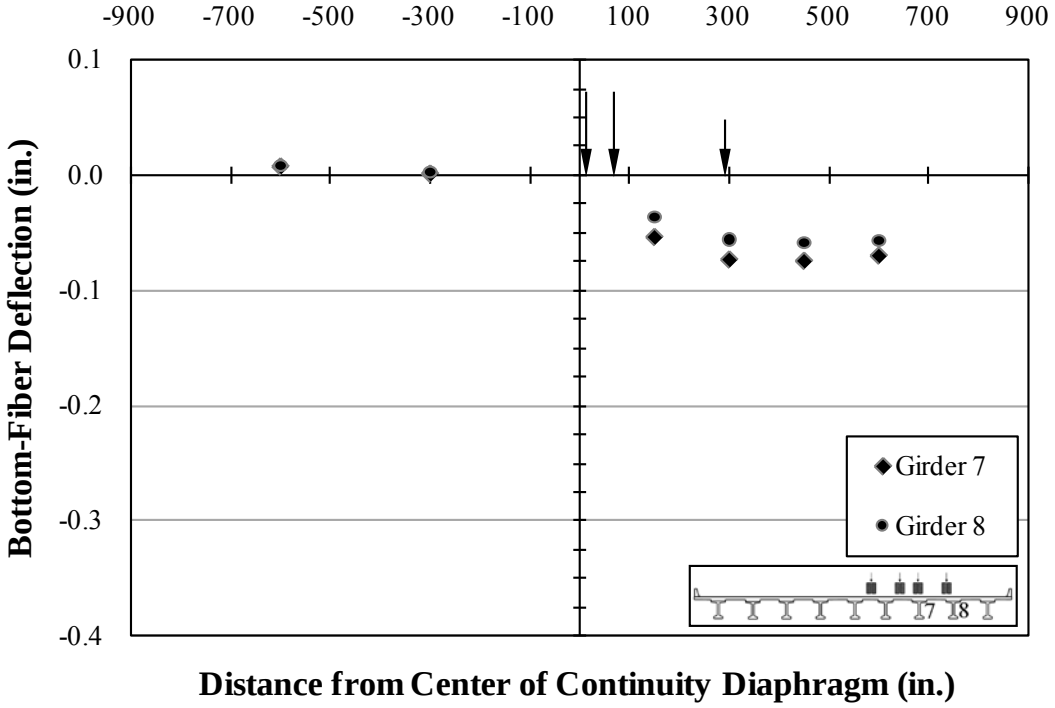

Figure B.15: Deflections—A6

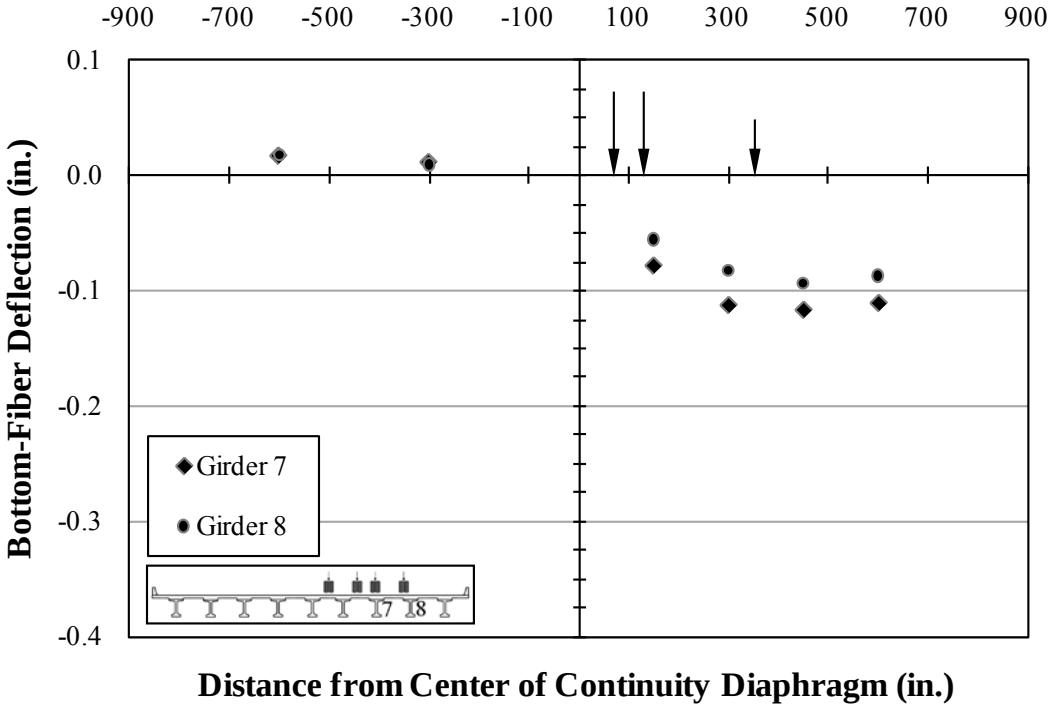

Figure B.16: Deflections—A7

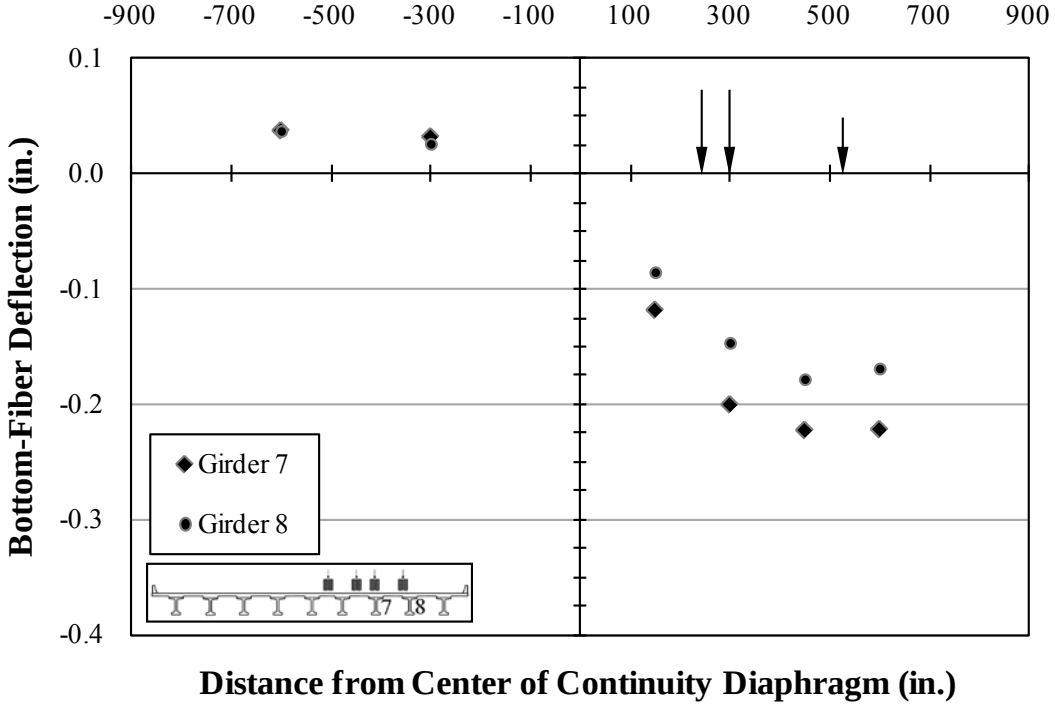

Figure B.17: Deflections—A8

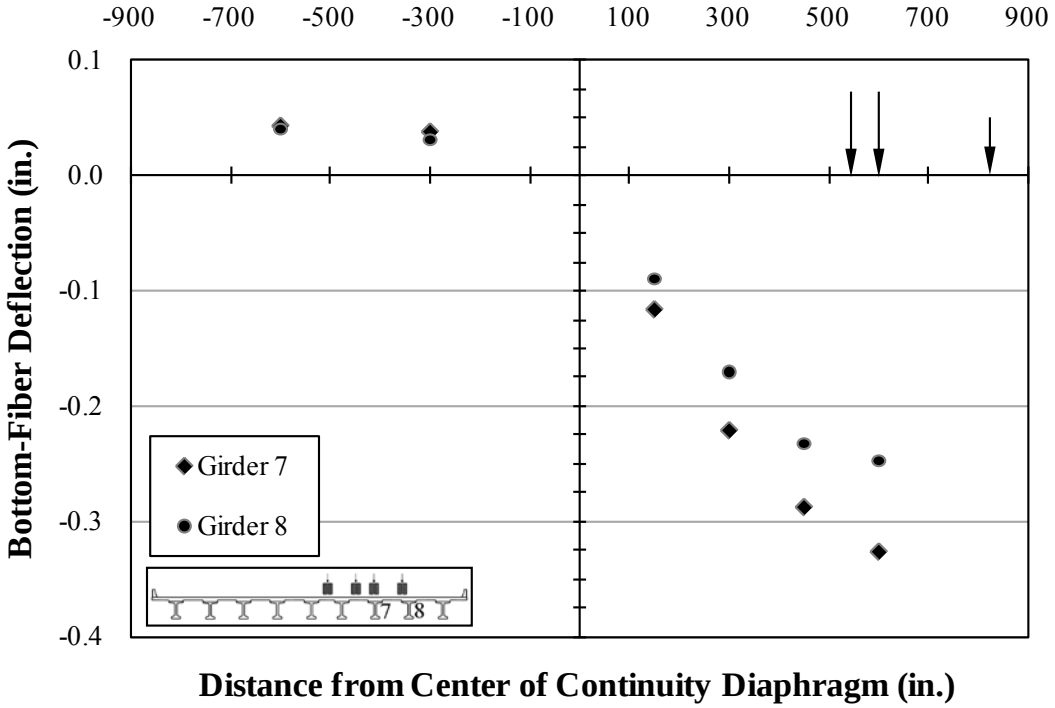

Figure B.18: Deflections—A9

B.1.3 Cross-Section Strains

B.1.3.1 Cross-Section Strains—Girder 7

B.1.3.1.1 Strains—Girder 7—Cross Section 1

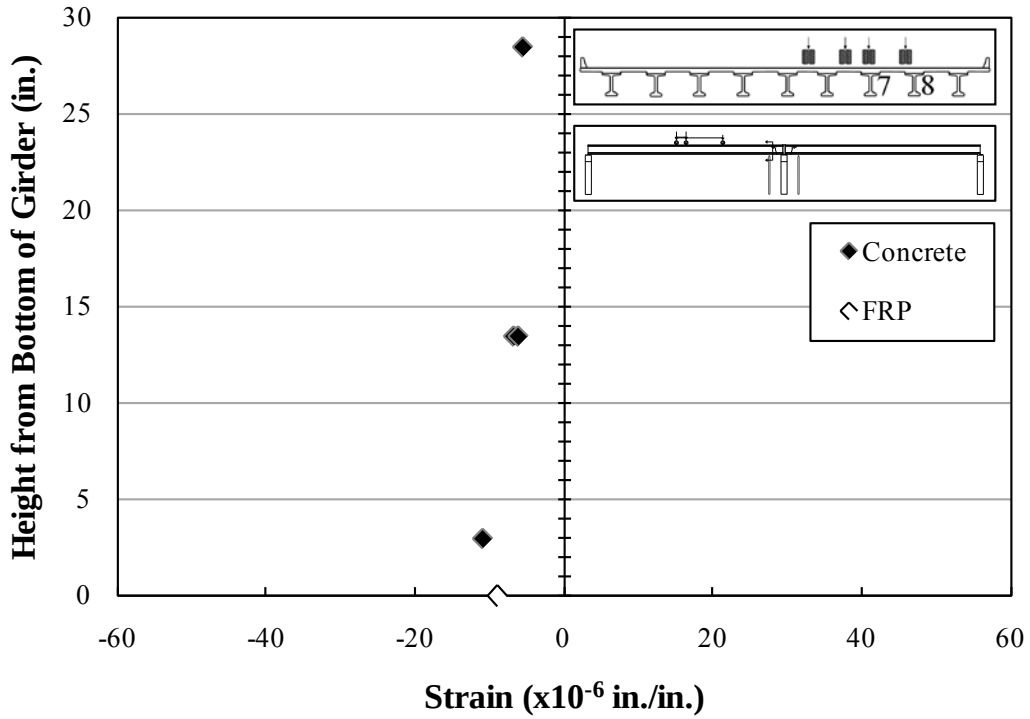

Figure B.19: Strains—Girder 7—Section 1—A1

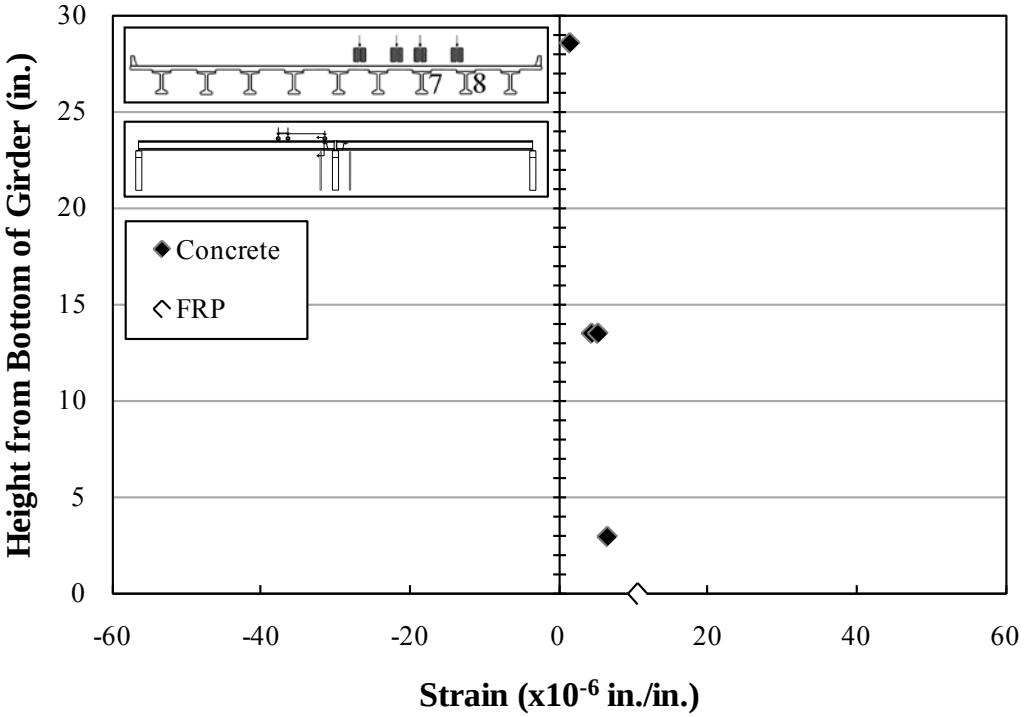

Figure B.20: Strains—Girder 7—Section 1—A2

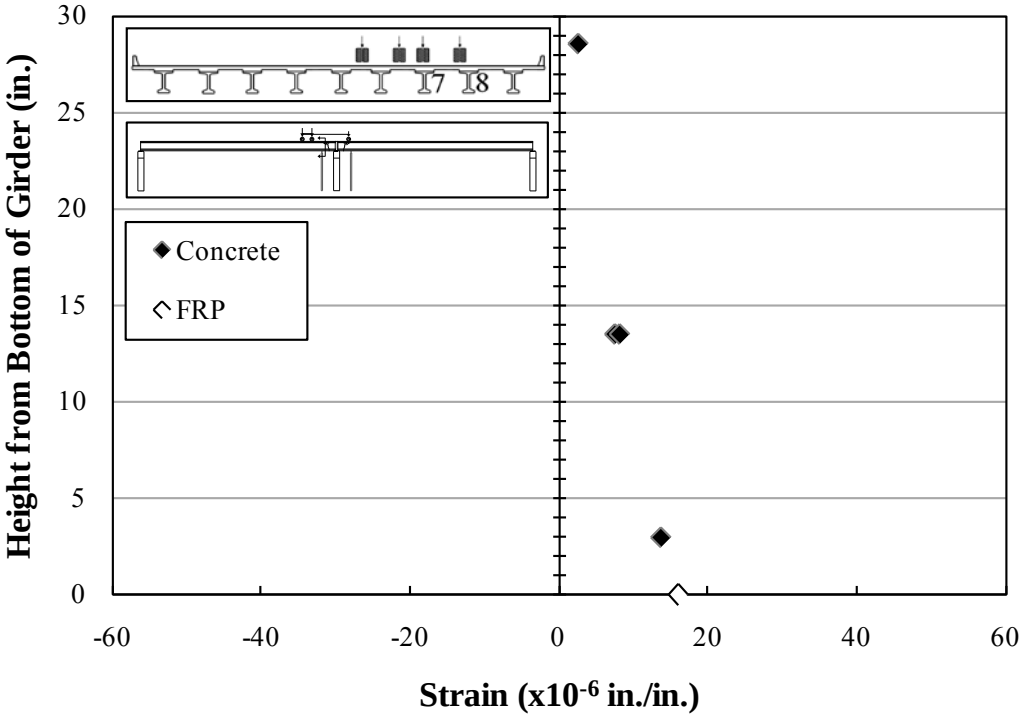

Figure B.21: Strains—Girder 7—Section 1—A3

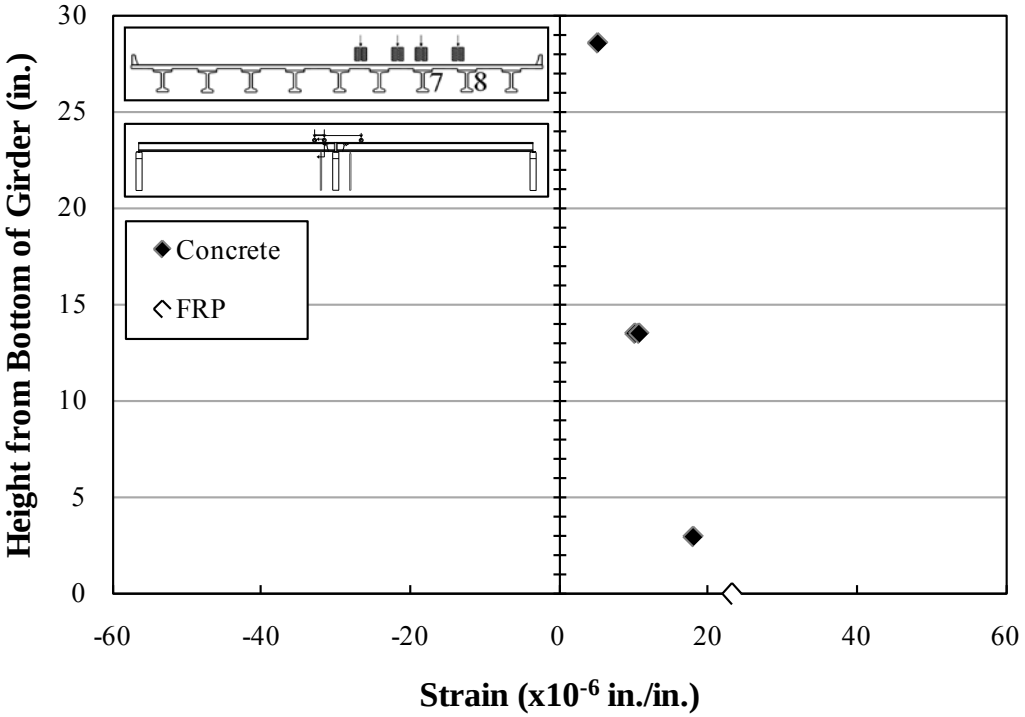

Figure B.22: Strains—Girder 7—Section 1—A4

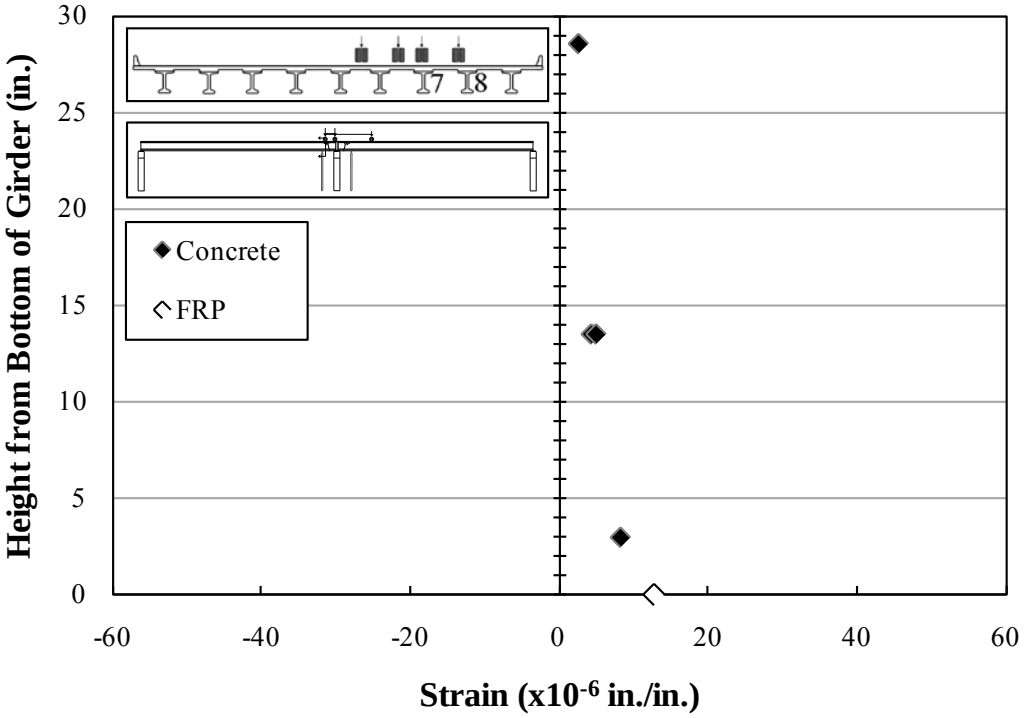

Figure B.23: Strains—Girder 7—Section 1—A5

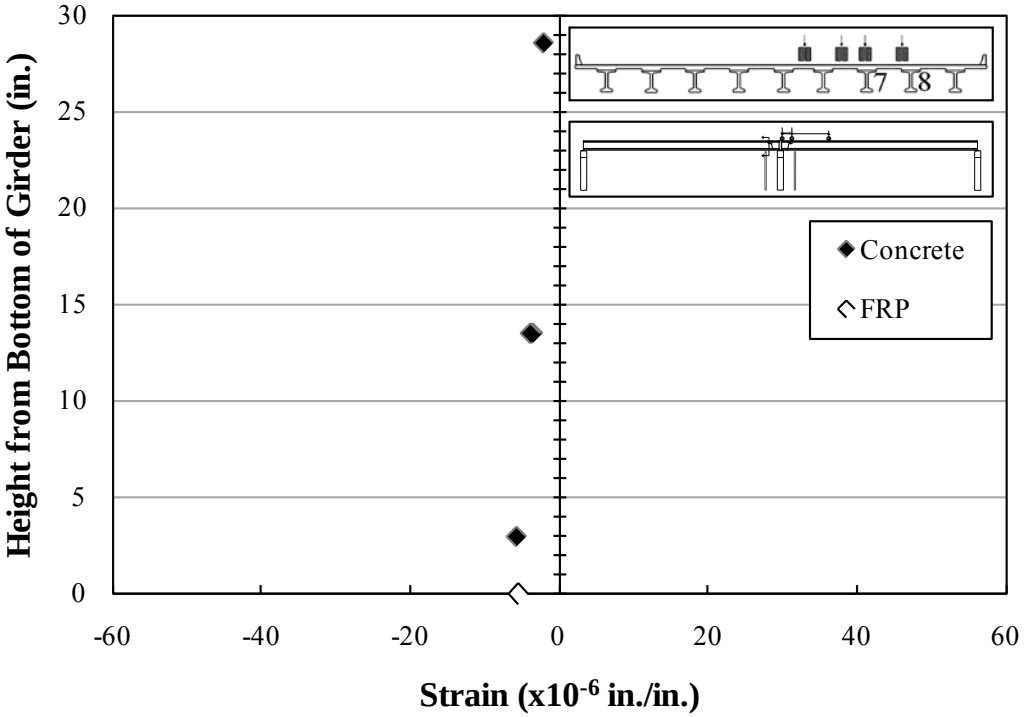

Figure B.24: Strains—Girder 7—Section 1—A6

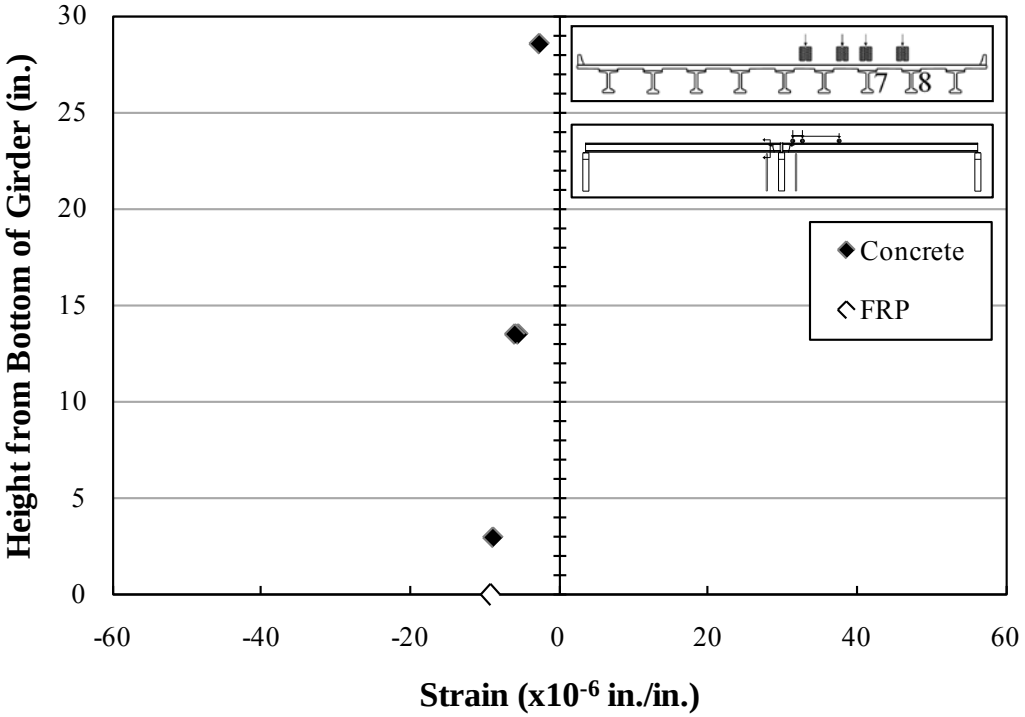

Figure B.25: Strains—Girder 7—Section 1—A7

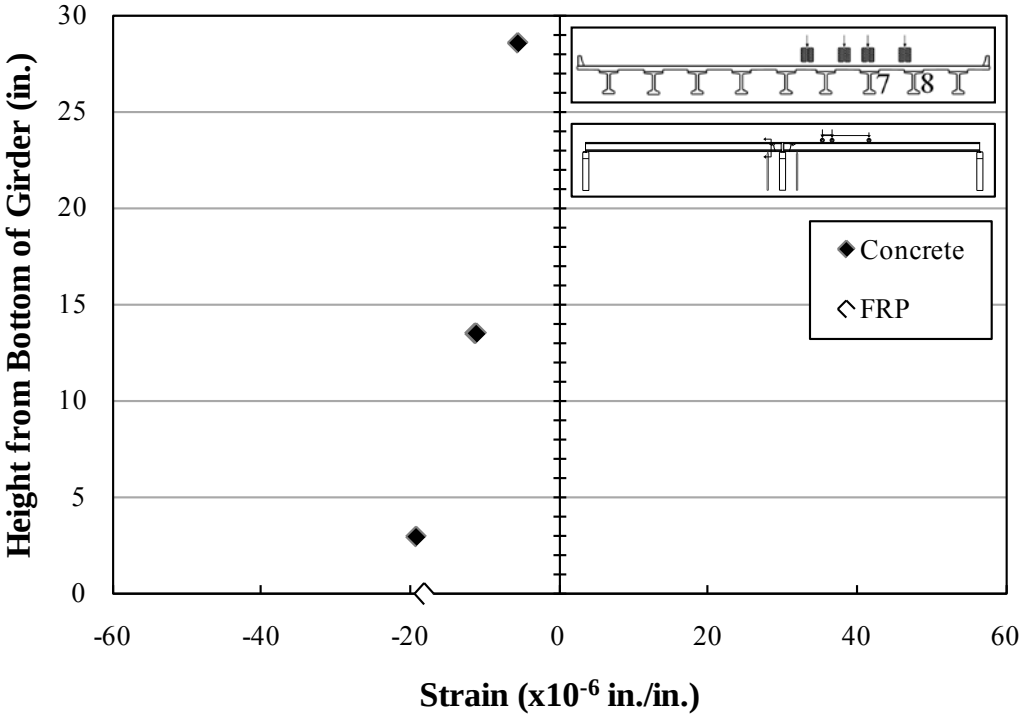

Figure B.26: Strains—Girder 7—Section 1—A8

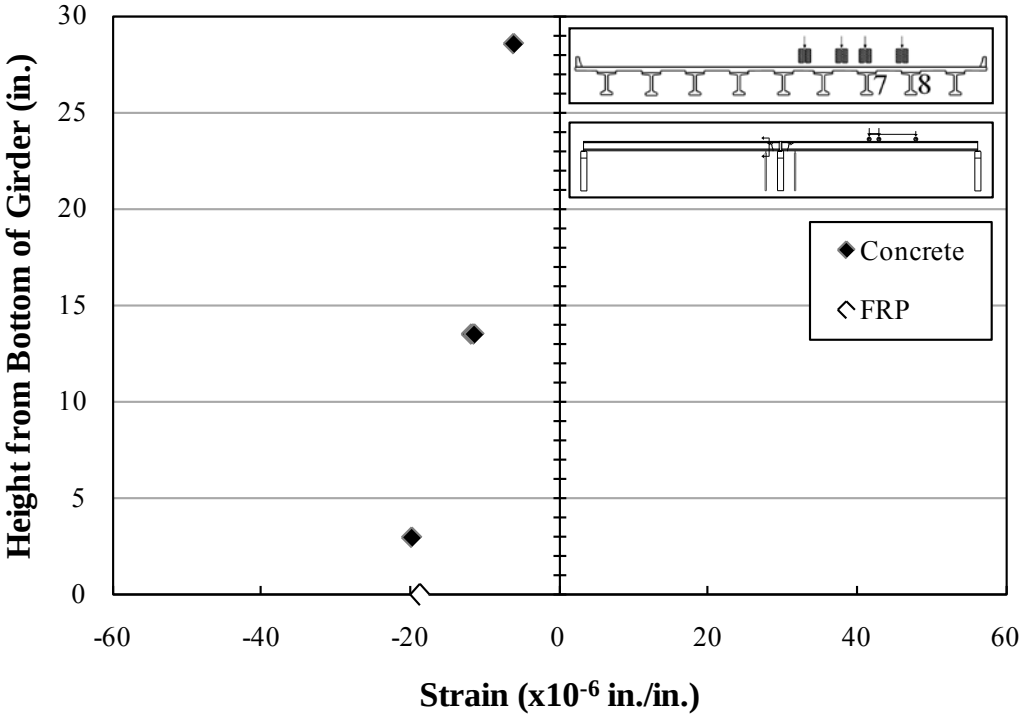

Figure B.27: Strains—Girder 7—Section 1—A9

B.1.3.1.2 Strains—Girder 7—Cross Section 2

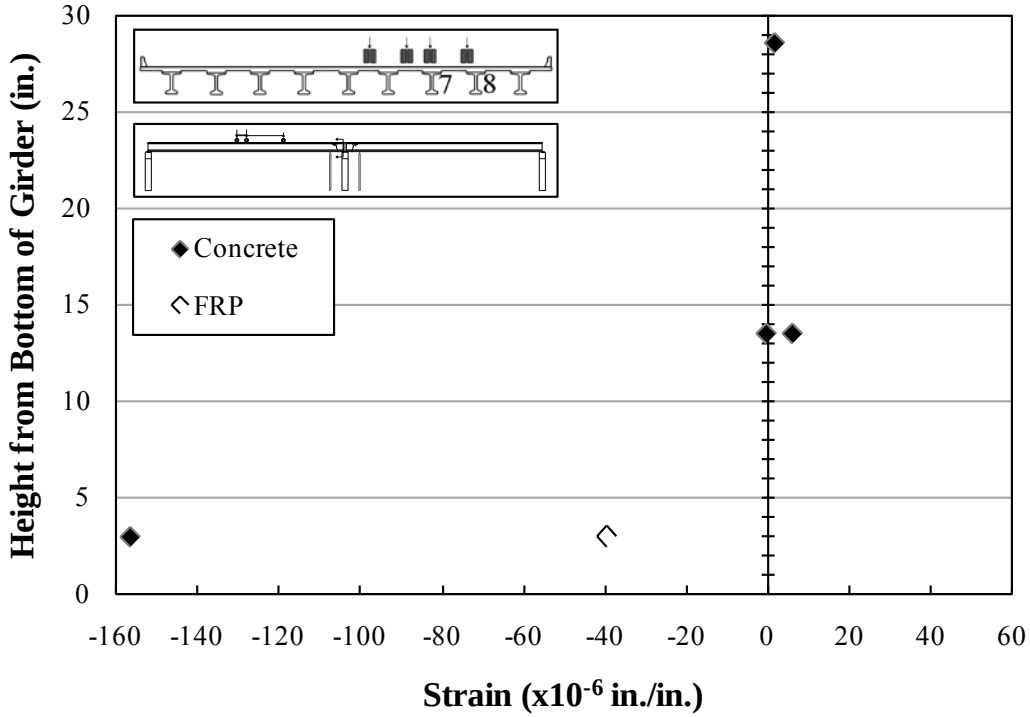

Figure B.28: Strains—Girder 7—Section 2—A1

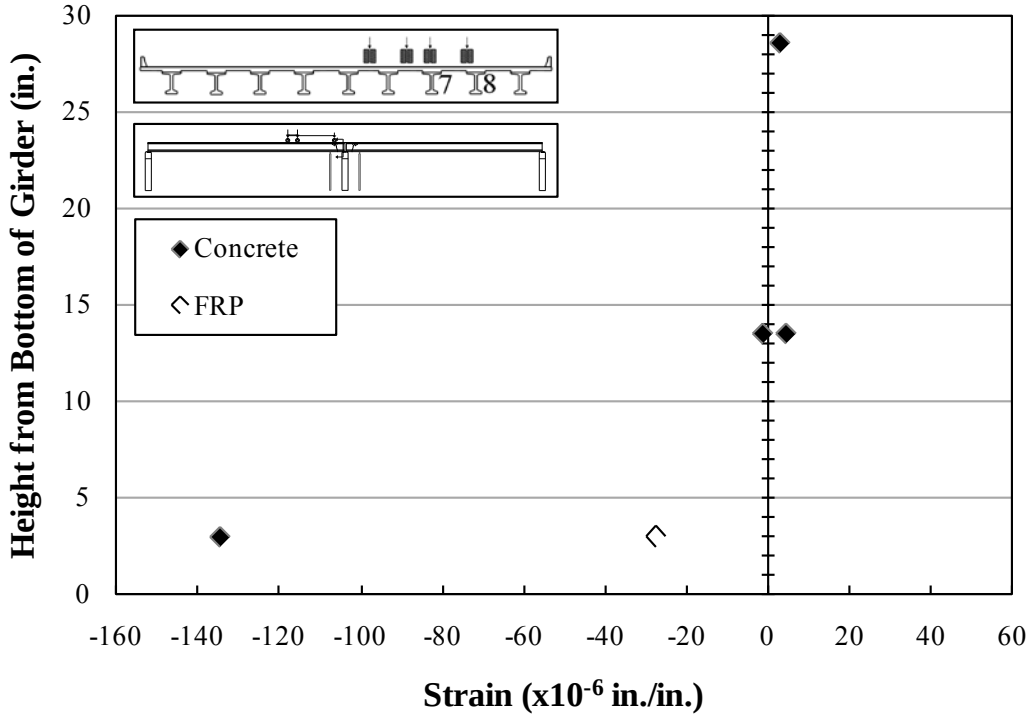

Figure B.29: Strains—Girder 7—Section 2—A2

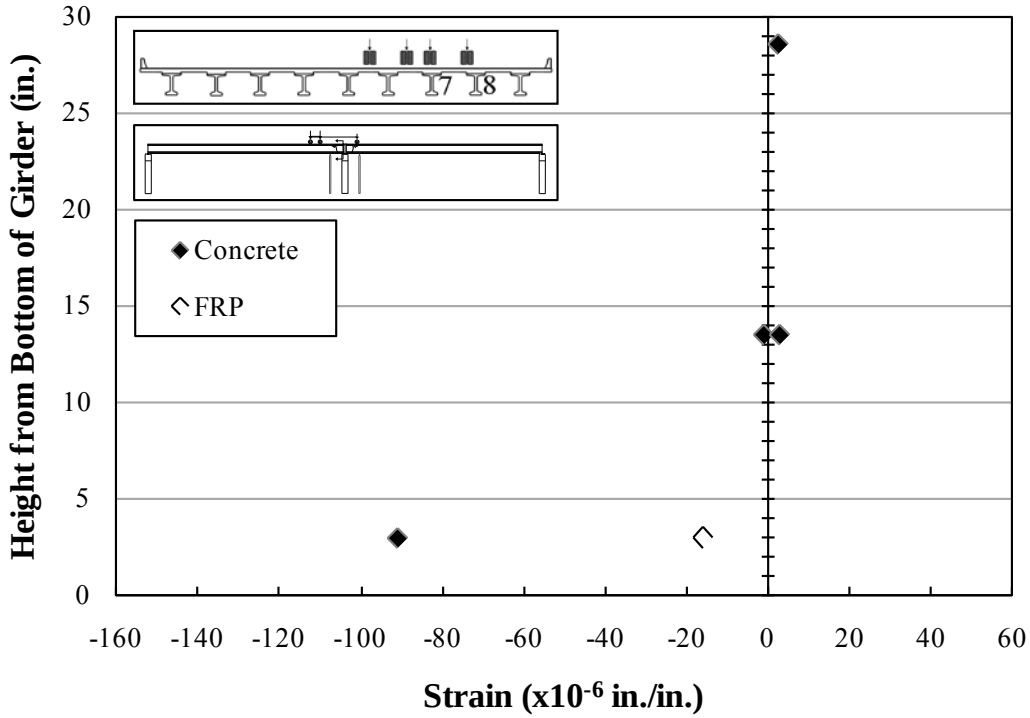

Figure B.30: Strains—Girder 7—Section 2—A3

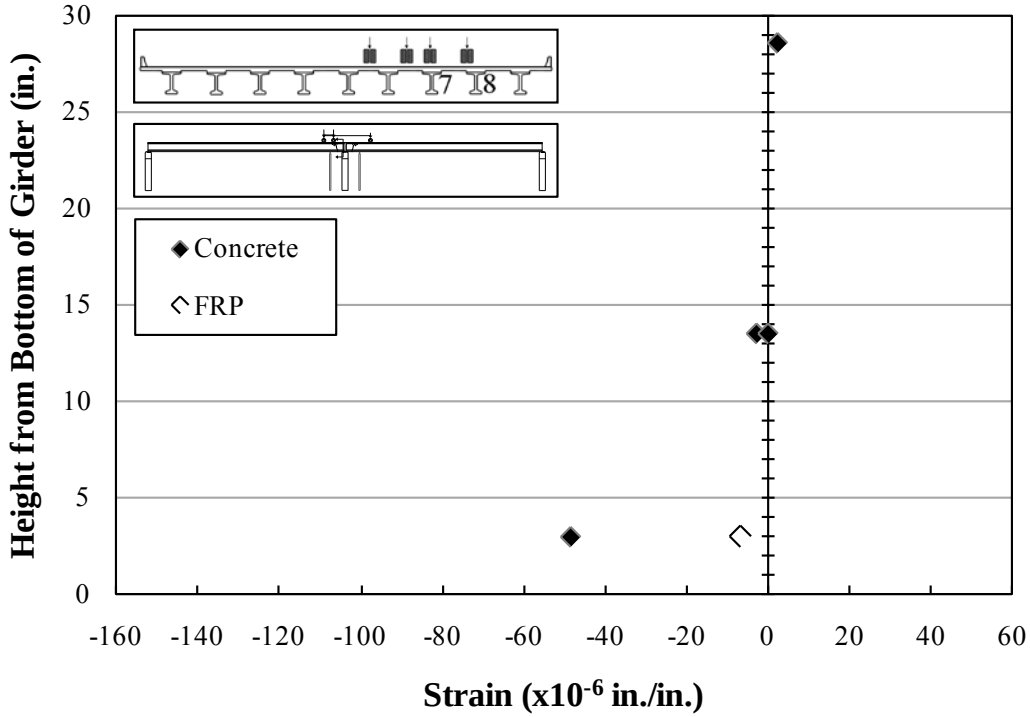

Figure B.31: Strains—Girder 7—Section 2—A4

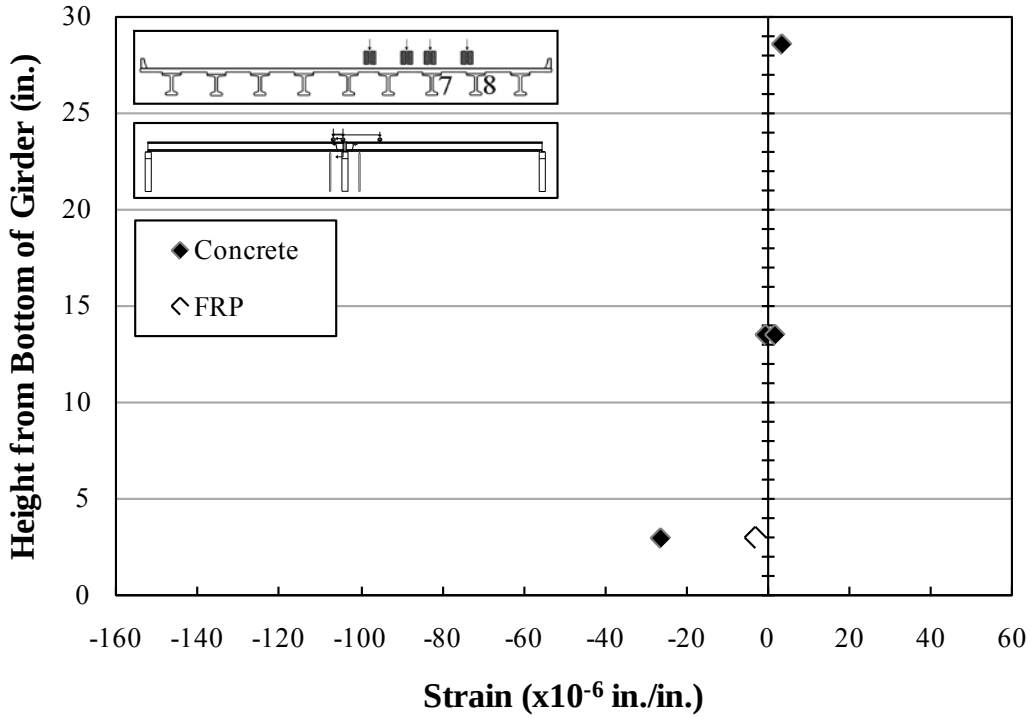

Figure B.32: Strains—Girder 7—Section 2—A5

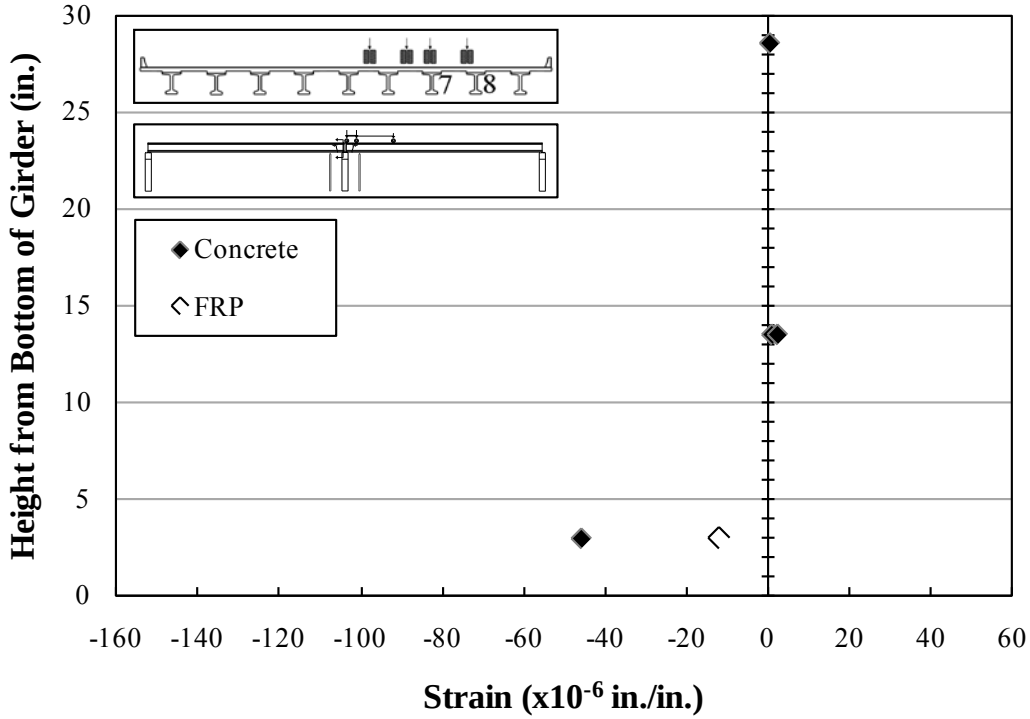

Figure B.33: Strains—Girder 7—Section 2—A6

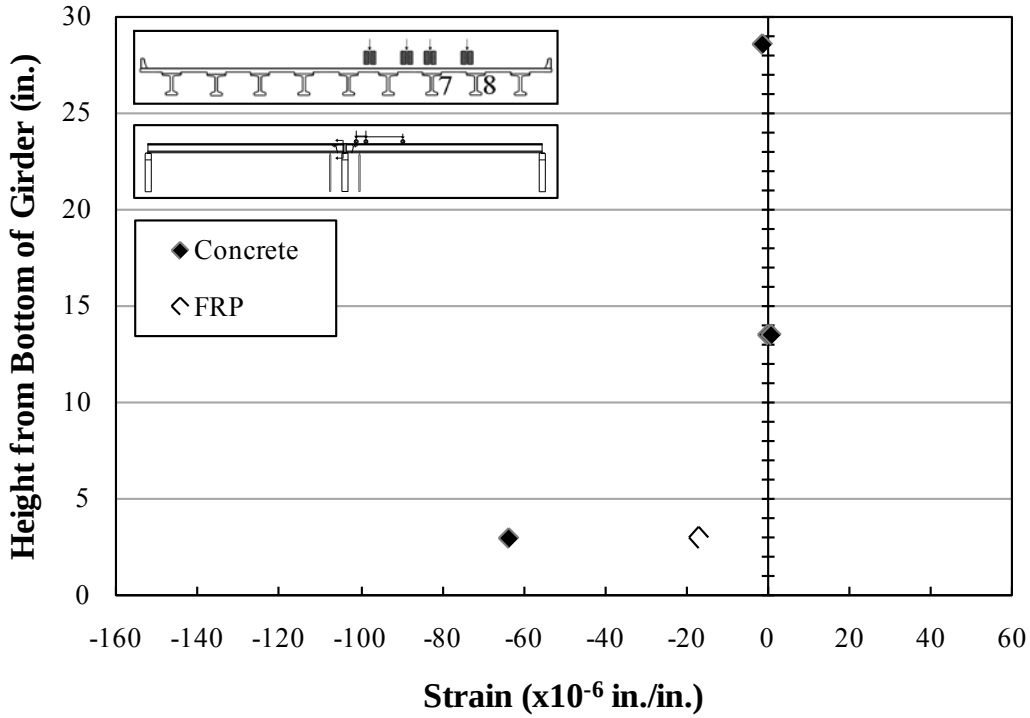

Figure B.34: Strains—Girder 7—Section 2—A7

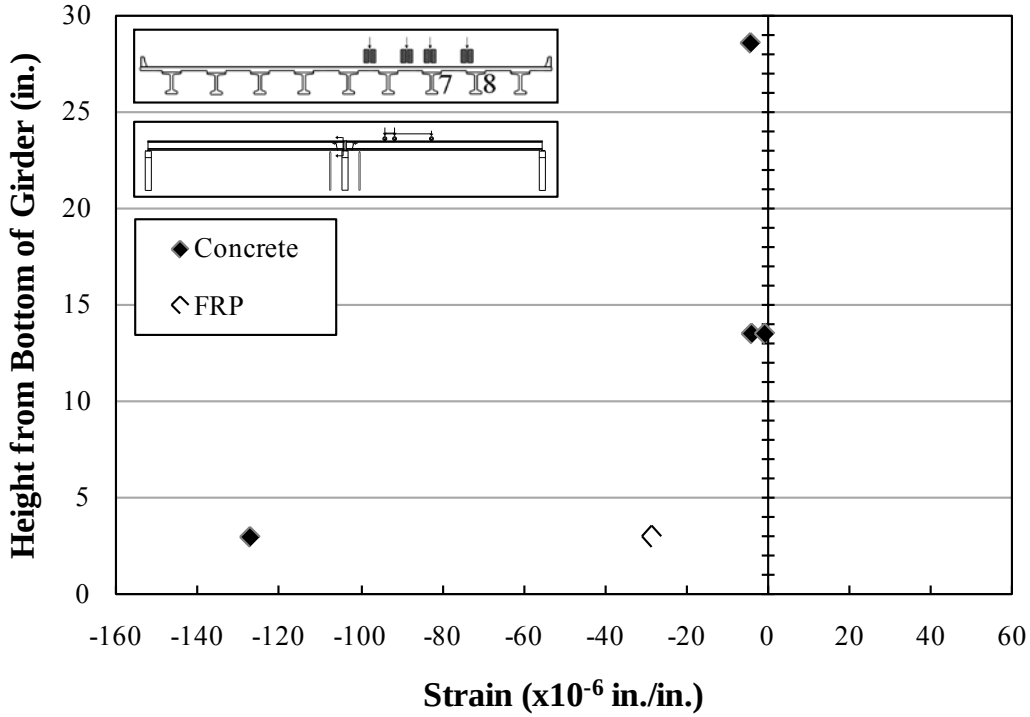

Figure B.35: Strains—Girder 7—Section 2—A8

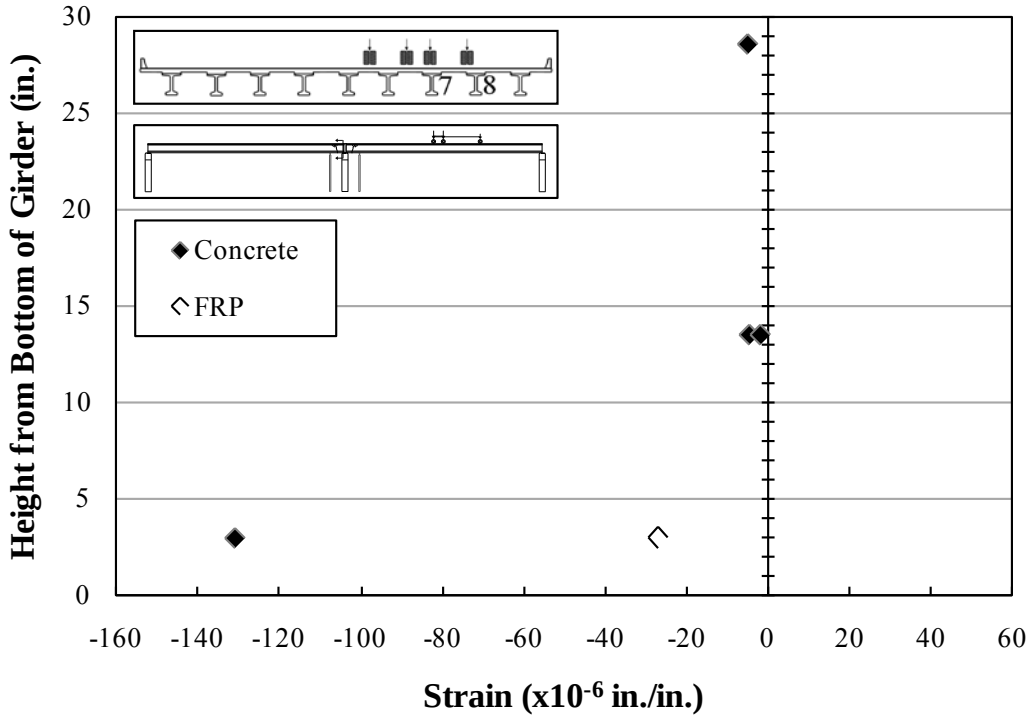

Figure B.36: Strains—Girder 7—Section 2—A9

B.1.3.1.3 Strains—Girder 7—Cross Section 3

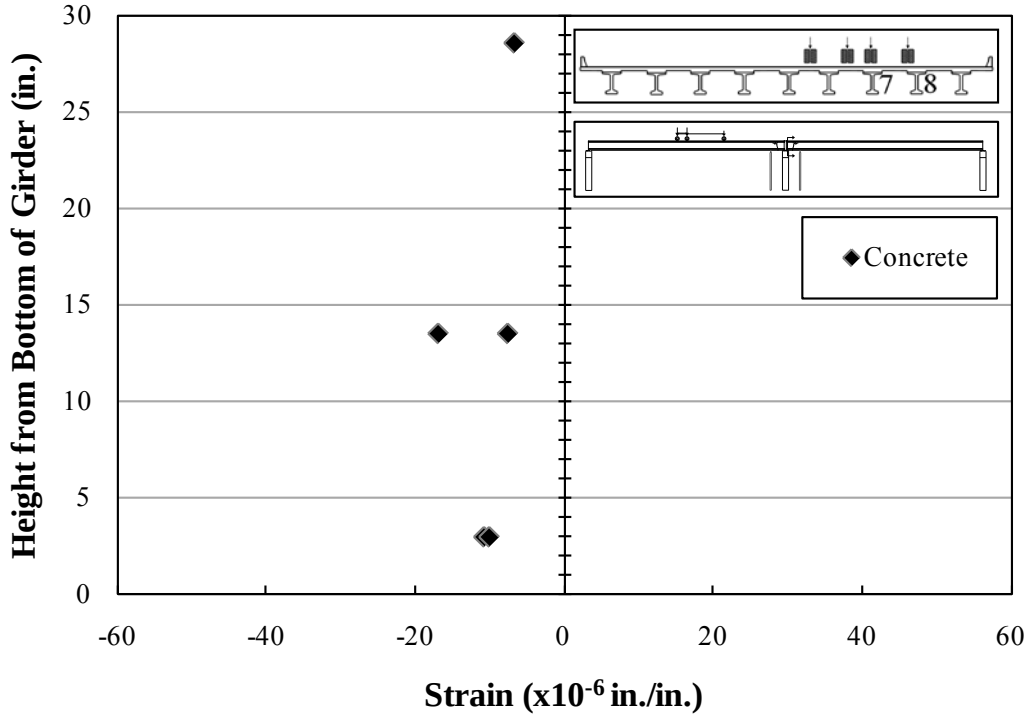

Figure B.37: Strains—Girder 7—Section 3—A1

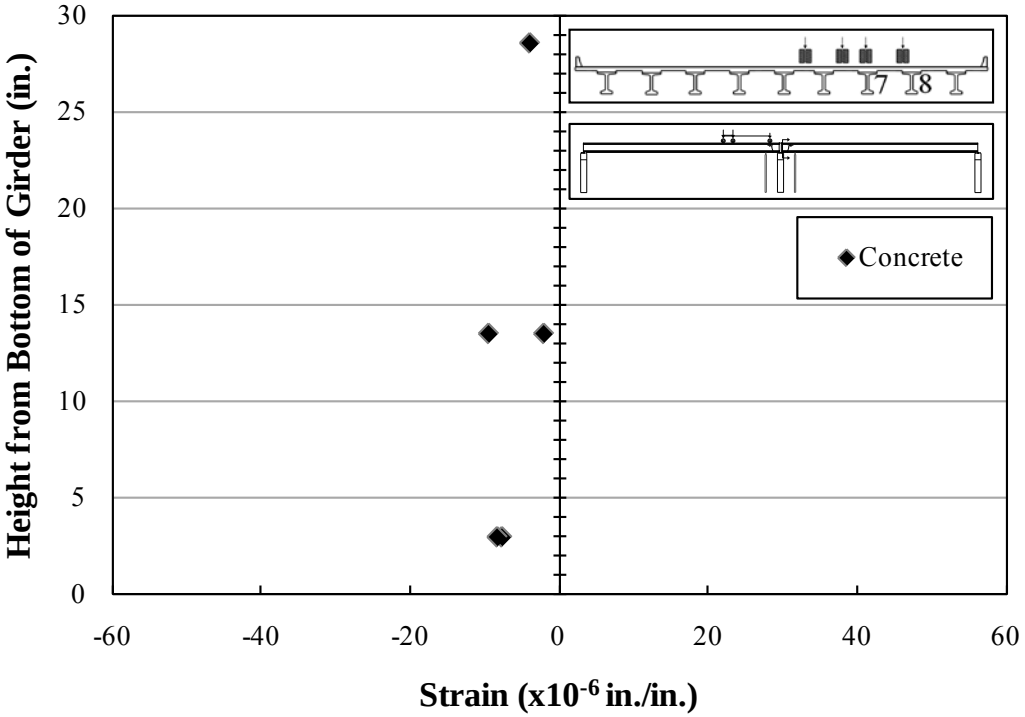

Figure B.38: Strains—Girder 7—Section 3—A2

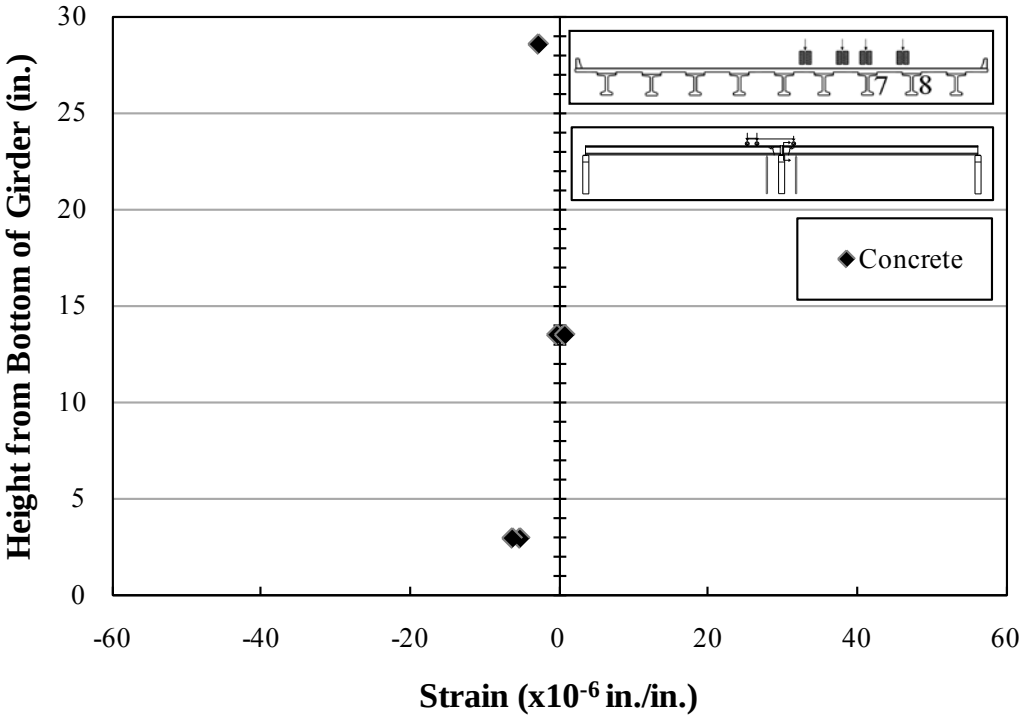

Figure B.39: Strains—Girder 7—Section 3—A3

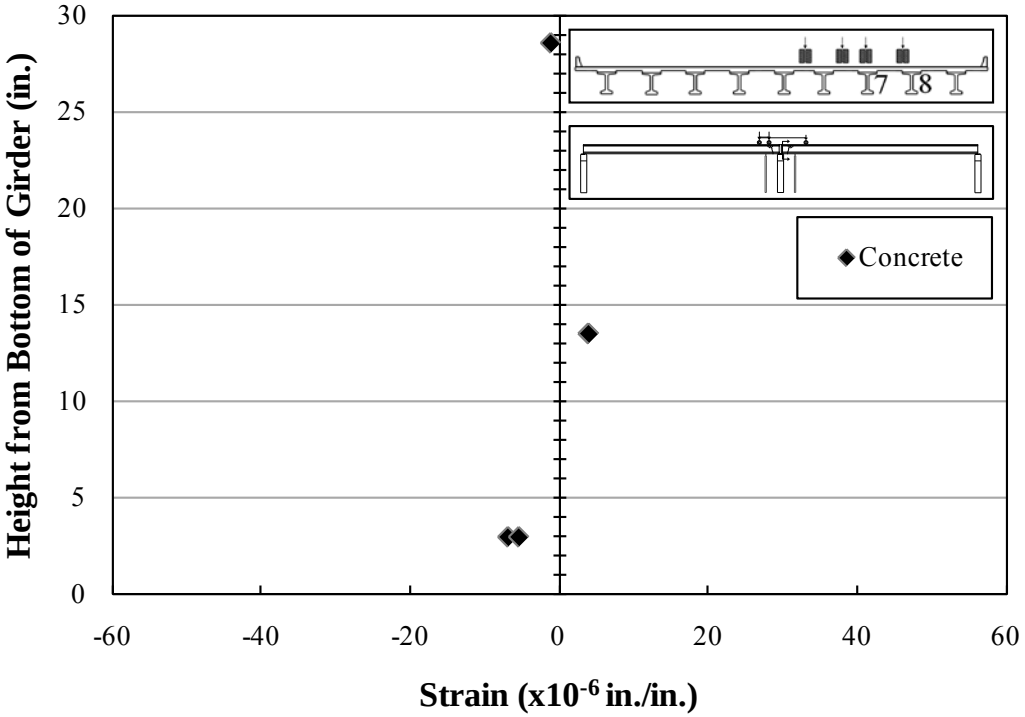

Figure B.40: Strains—Girder 7—Section 3—A4

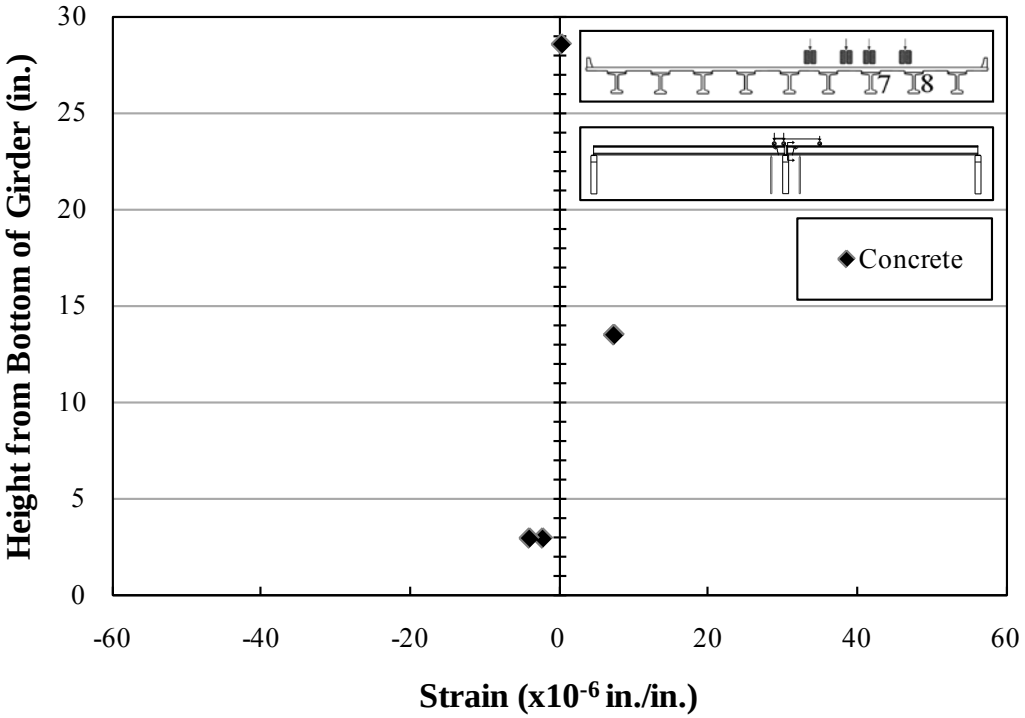

Figure B.41: Strains—Girder 7—Section 3—A5

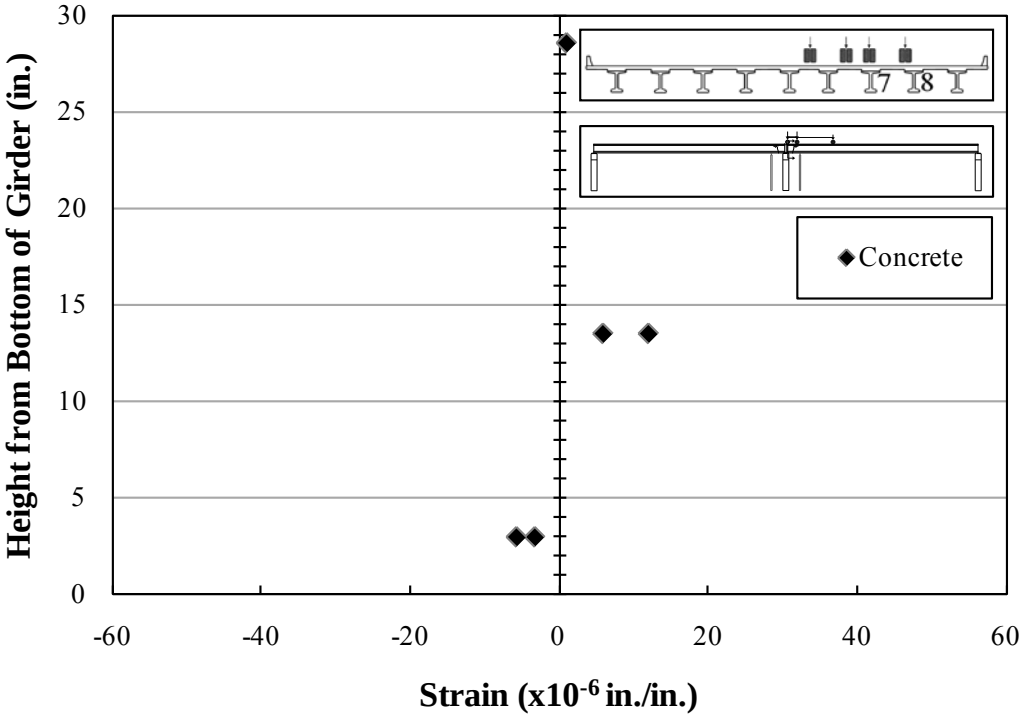

Figure B.42: Strains—Girder 7—Section 3—A6

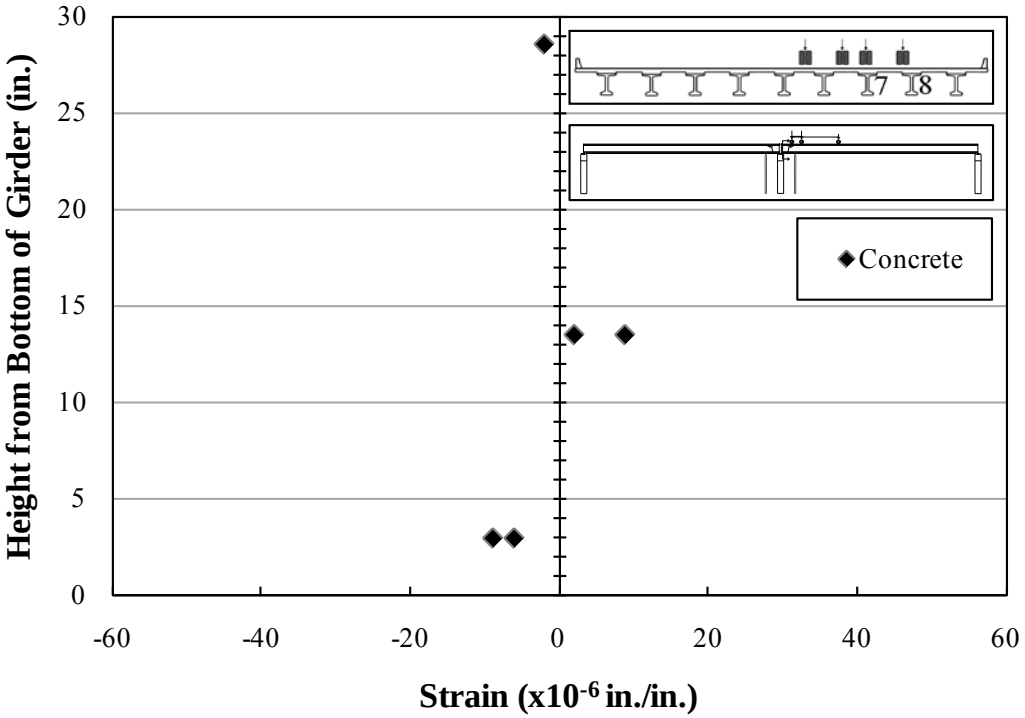

Figure B.43: Strains—Girder 7—Section 3—A7

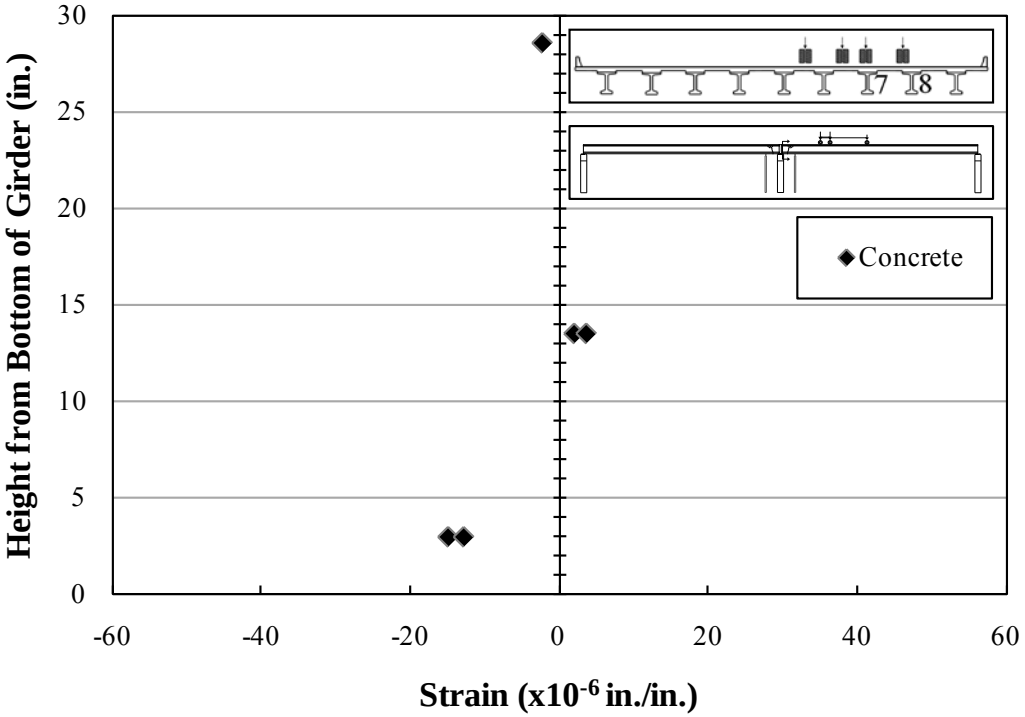

Figure B.44: Strains—Girder 7—Section 3—A8

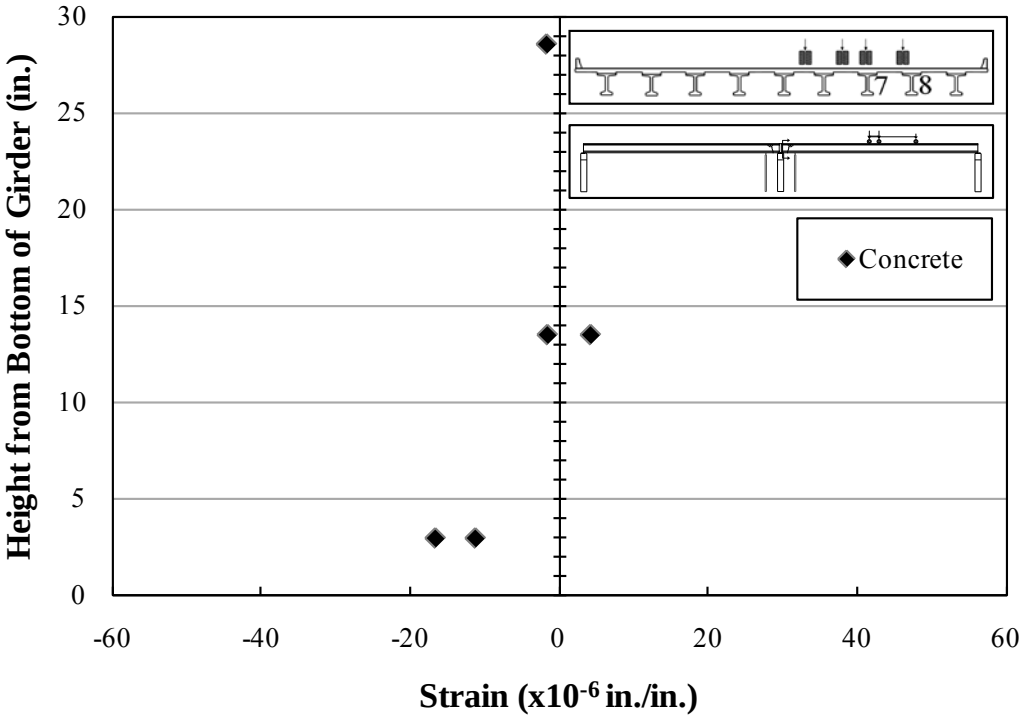

Figure B.45: Strains—Girder 7—Section 3—A9

B.1.3.1.4 Strains—Girder 7—Cross Section 4

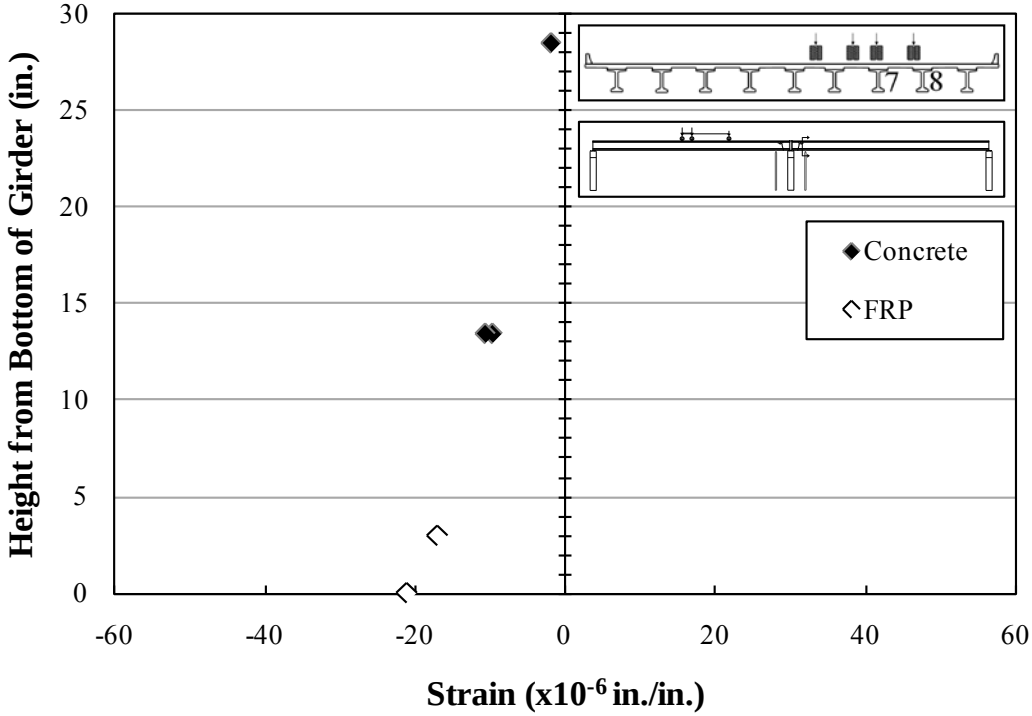

Figure B.46: Strains—Girder 7—Section 4—A1

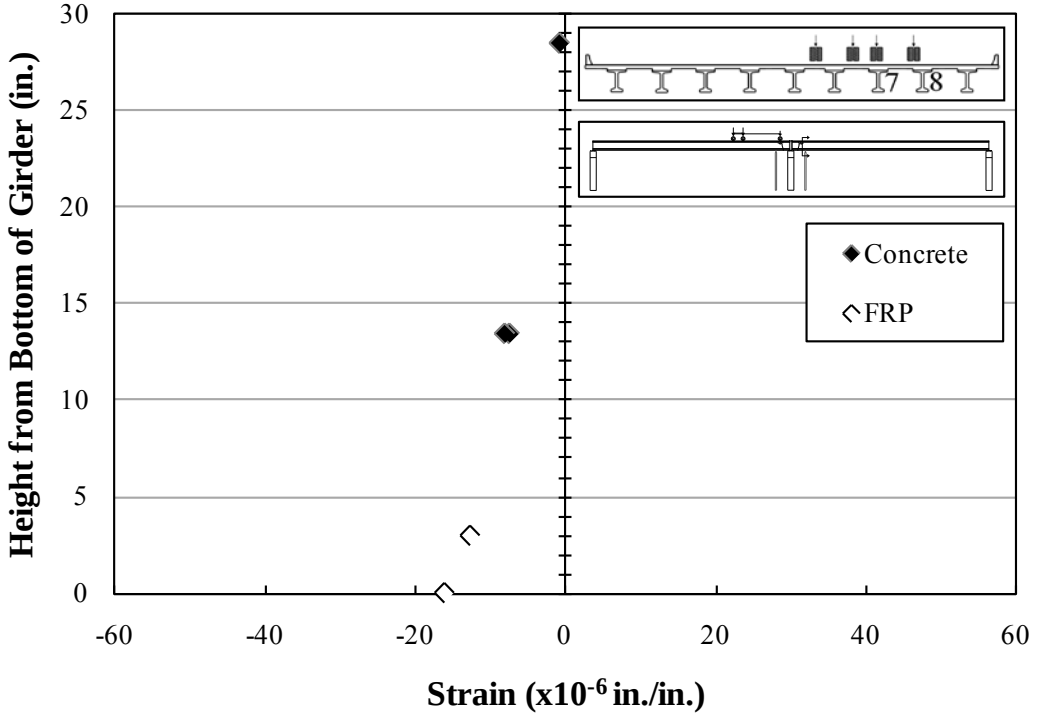

Figure B.47: Strains—Girder 7—Section 4—A2

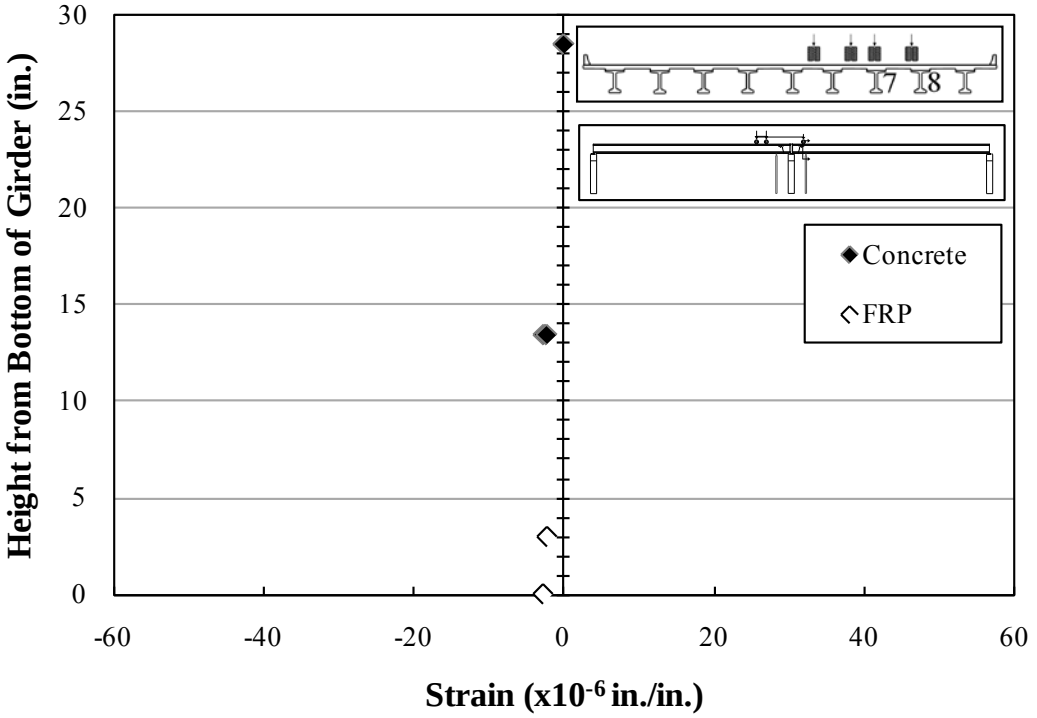

Figure B.48: Strains—Girder 7—Section 4—A3

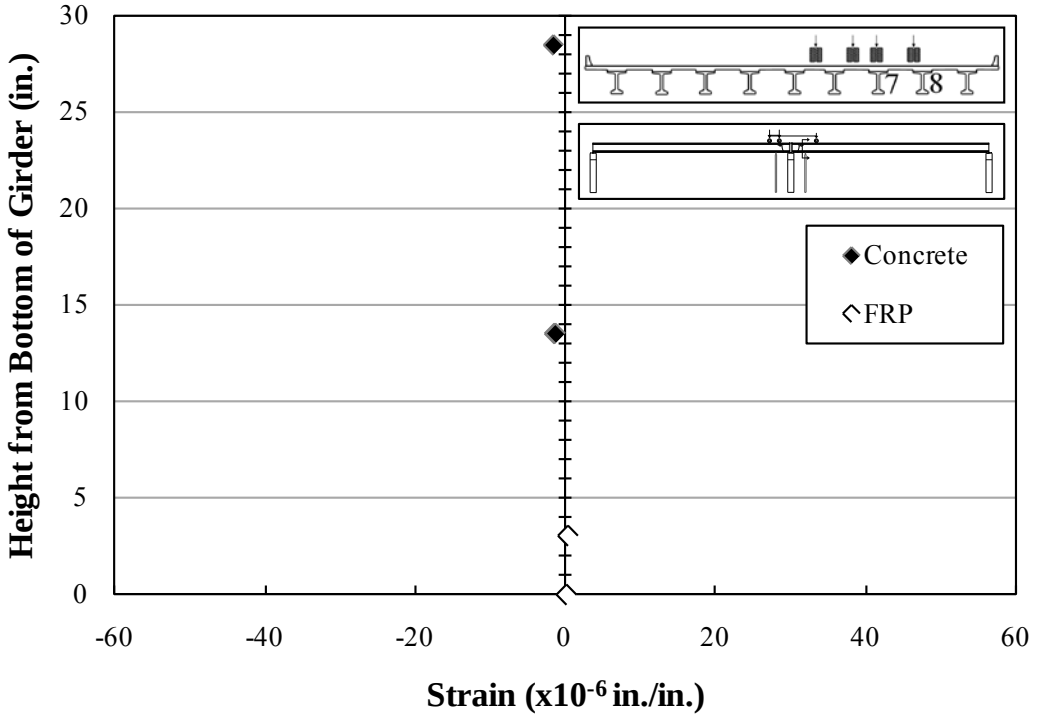

Figure B.49: Strains—Girder 7—Section 4—A4

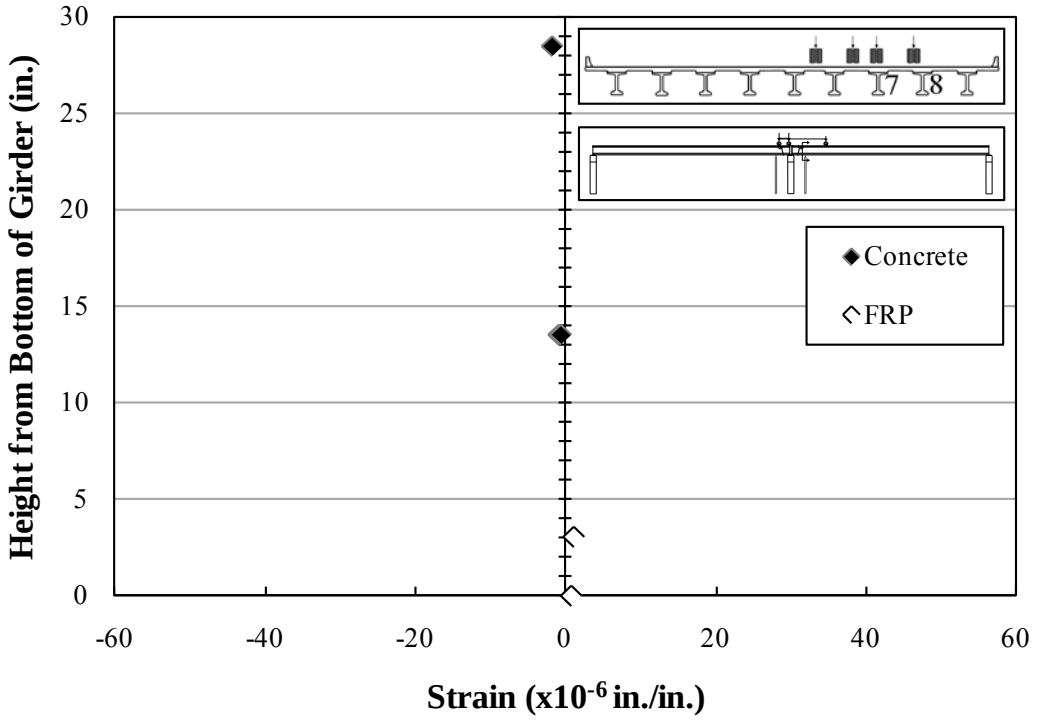

Figure B.50: Strains—Girder 7—Section 4—A5

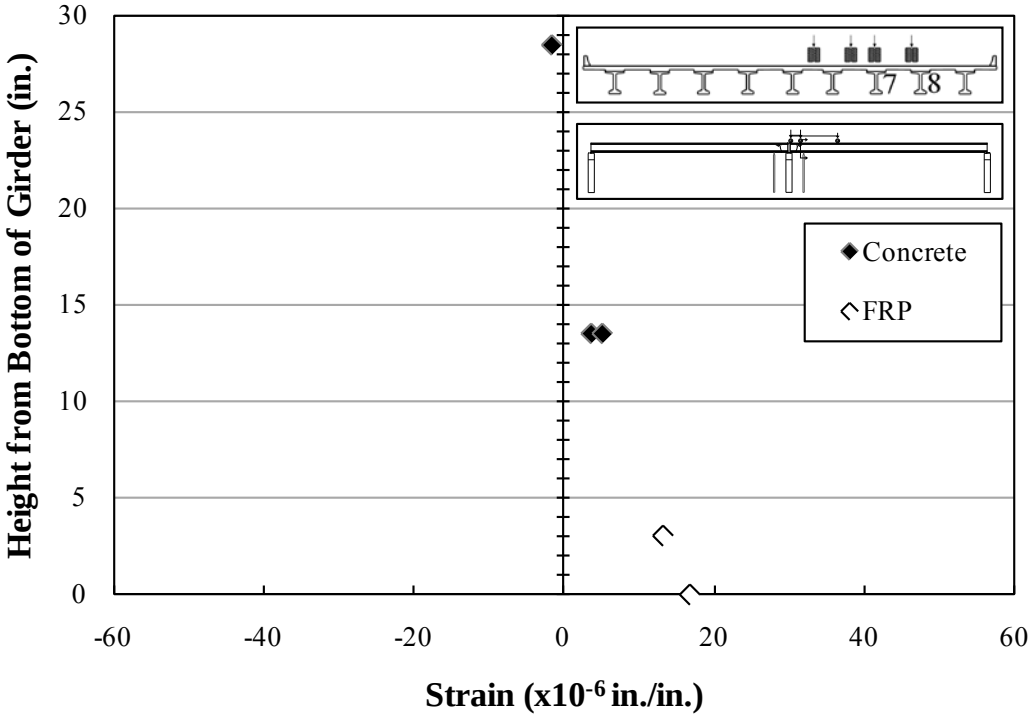

Figure B.51: Strains—Girder 7—Section 4—A6

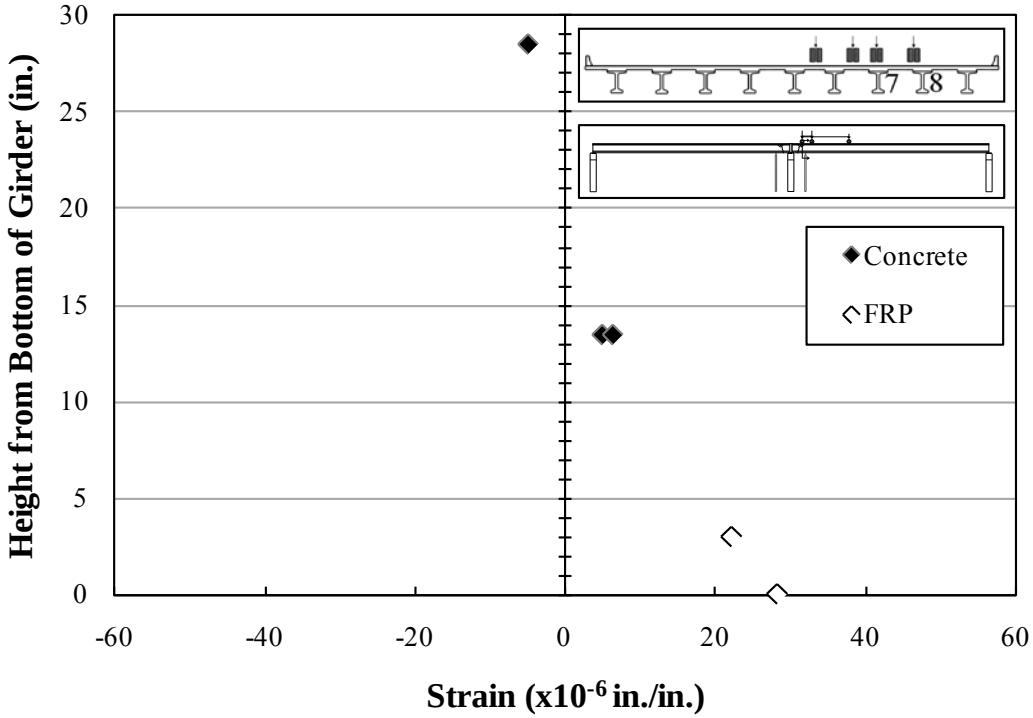

Figure B.52: Strains—Girder 7—Section 4—A7

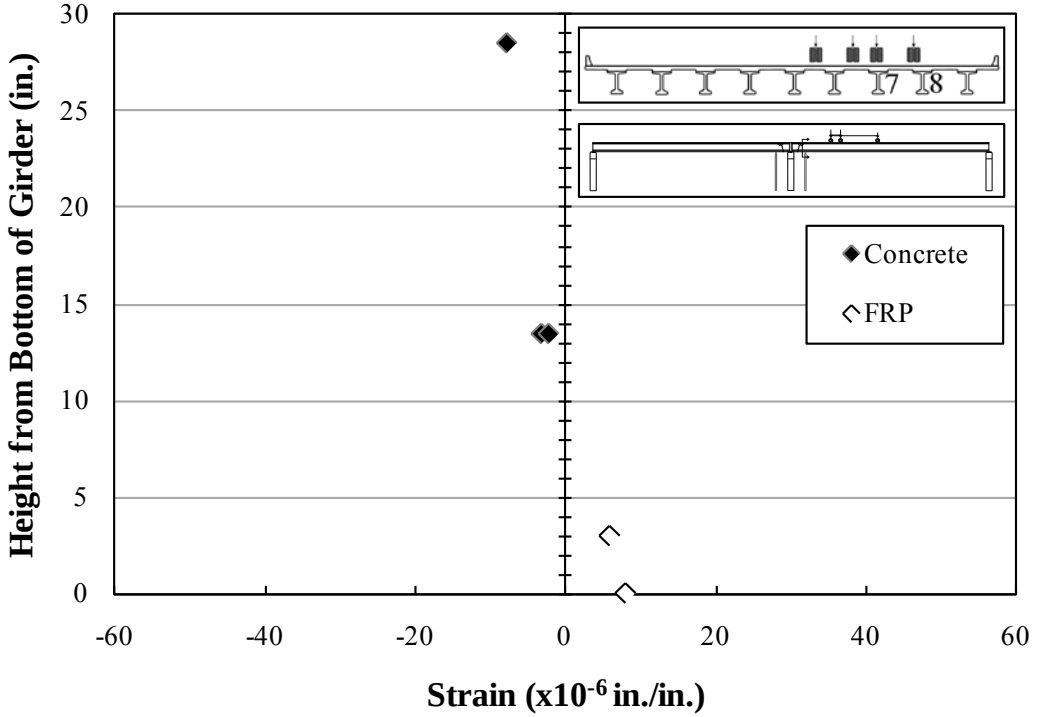

Figure B.53: Strains—Girder 7—Section 4—A8

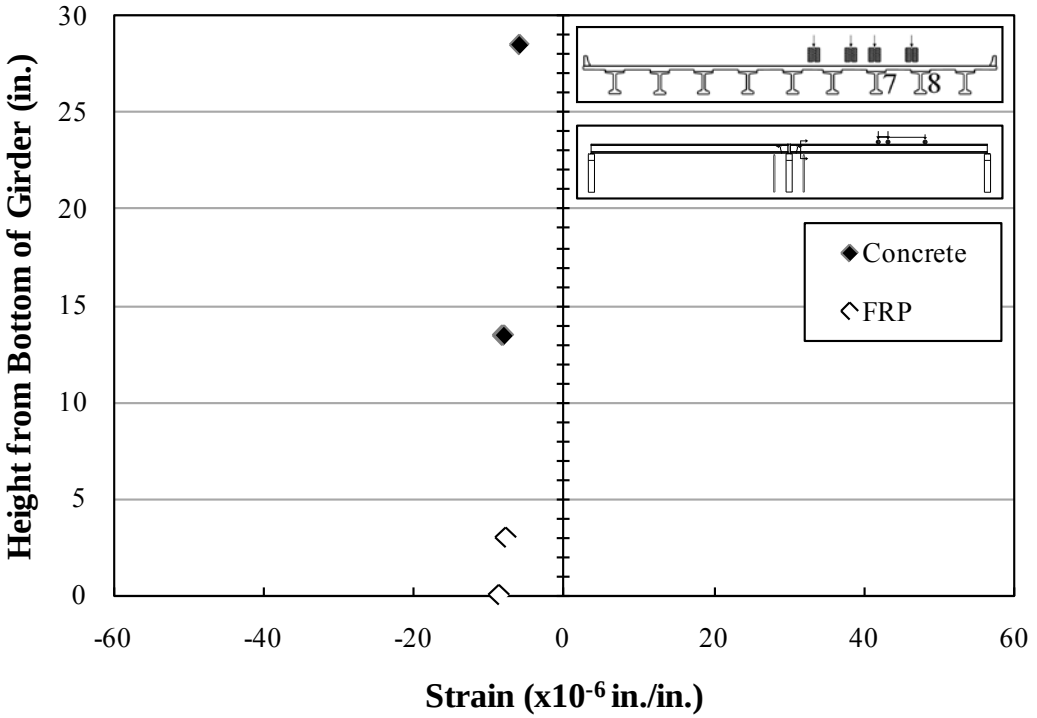

Figure B.54: Strains—Girder 7—Section 4—A9

B.1.3.2 Cross-Section Strains—Girder 8

B.1.3.2.1 Strains—Girder 8—Cross Section 1

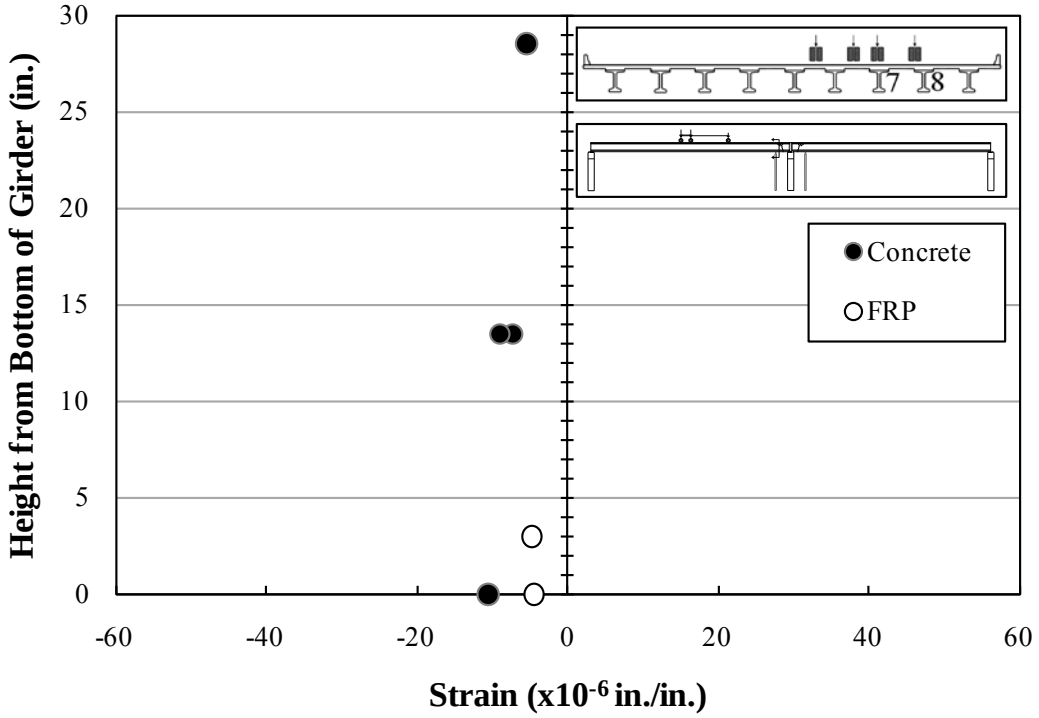

Figure B.55: Strains—Girder 8—Section 1—A1

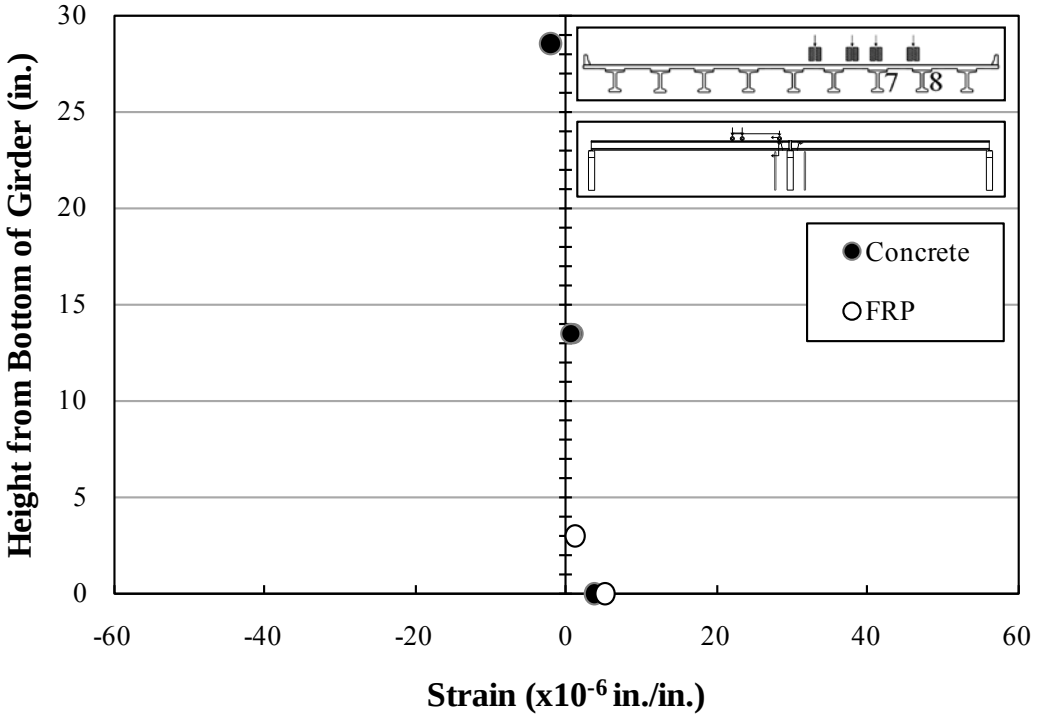

Figure B.56: Strains—Girder 8—Section 1—A2

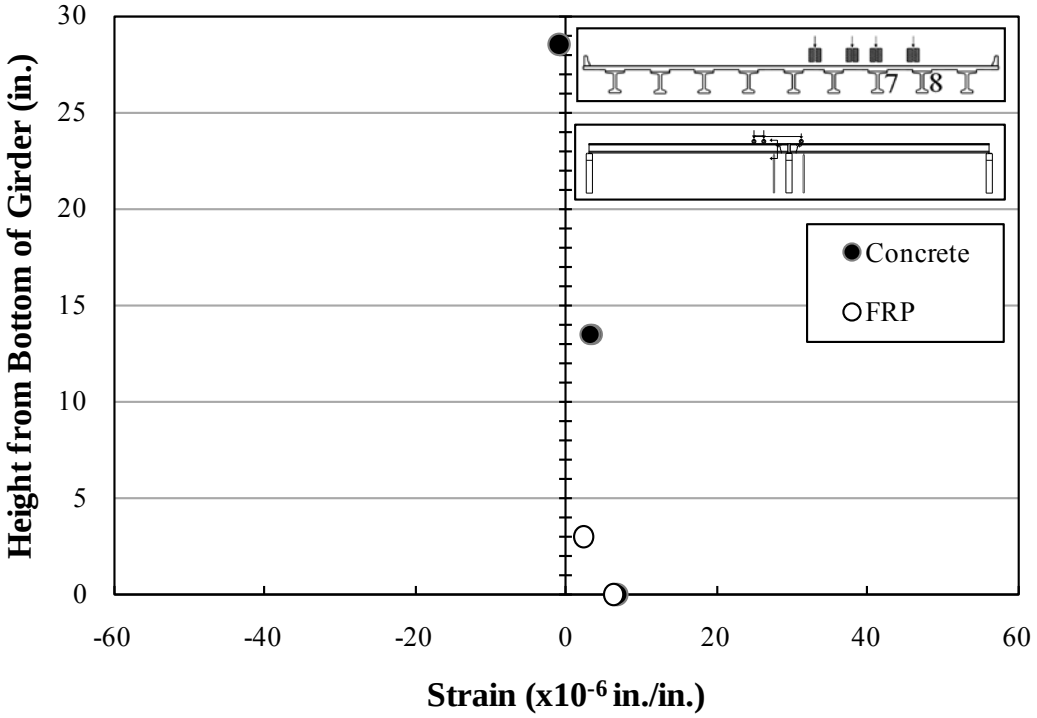

Figure B.57: Strains—Girder 8—Section 1—A3

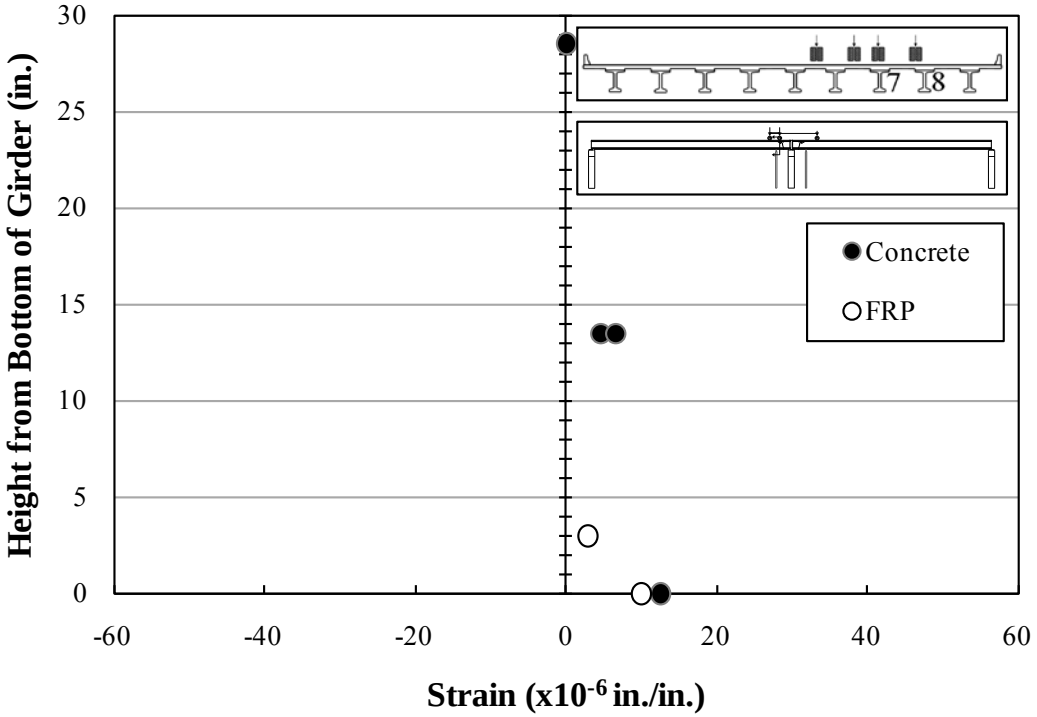

Figure B.58: Strains—Girder 8—Section 1—A4

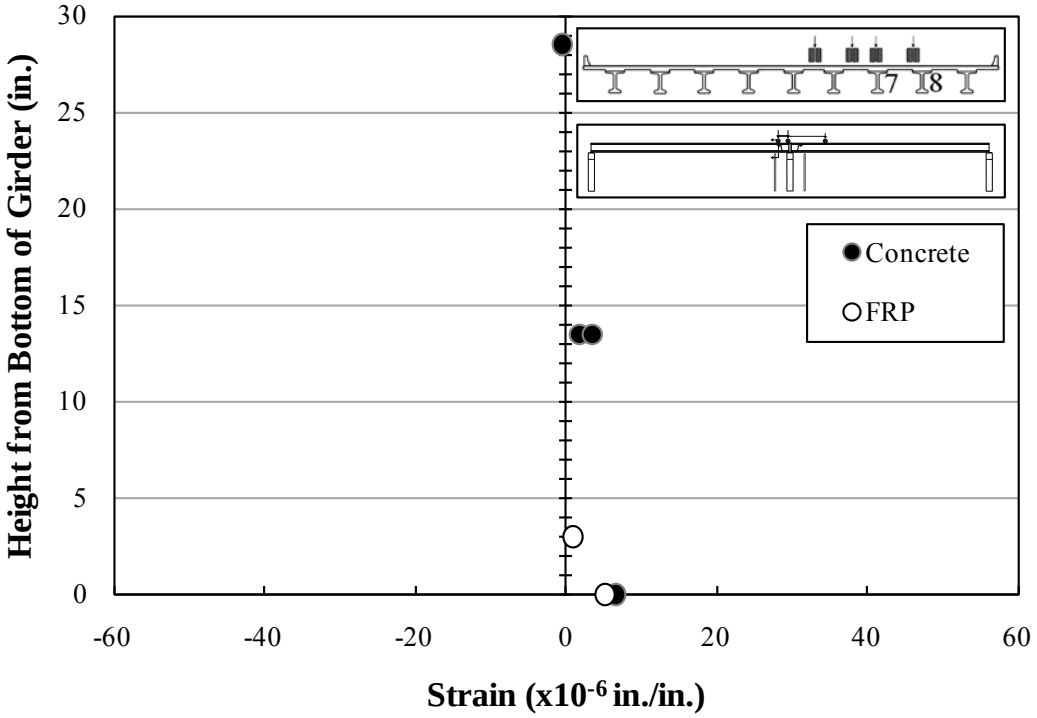

Figure B.59: Strains—Girder 8—Section 1—A5

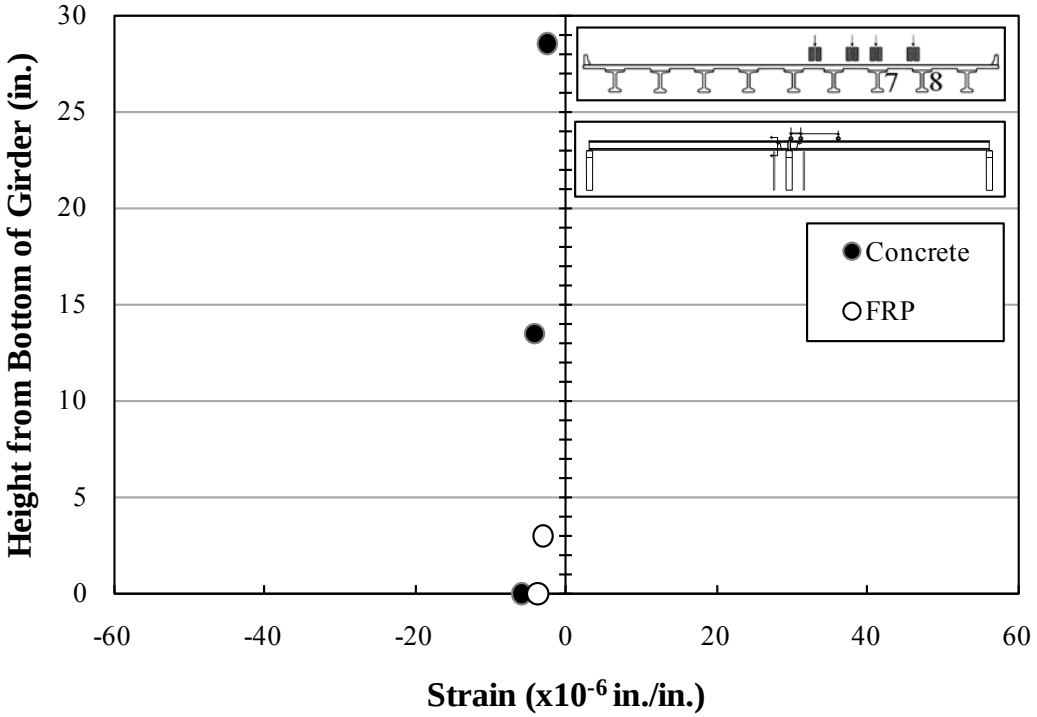

Figure B.60: Strains—Girder 8—Section 1—A6

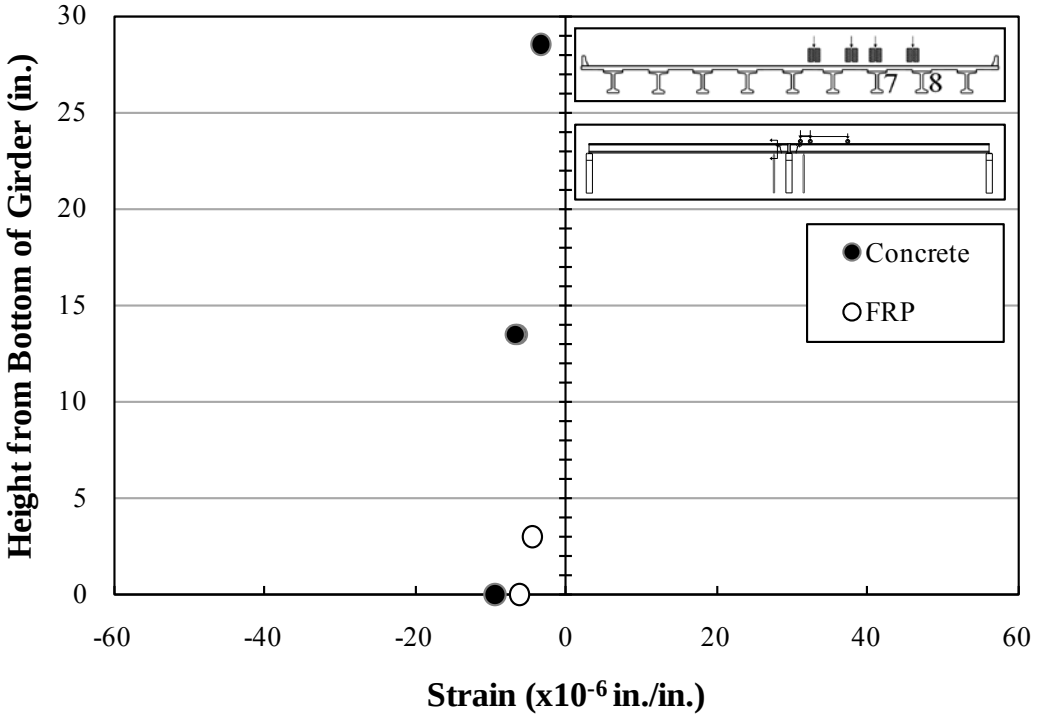

Figure B.61: Strains—Girder 8—Section 1—A7

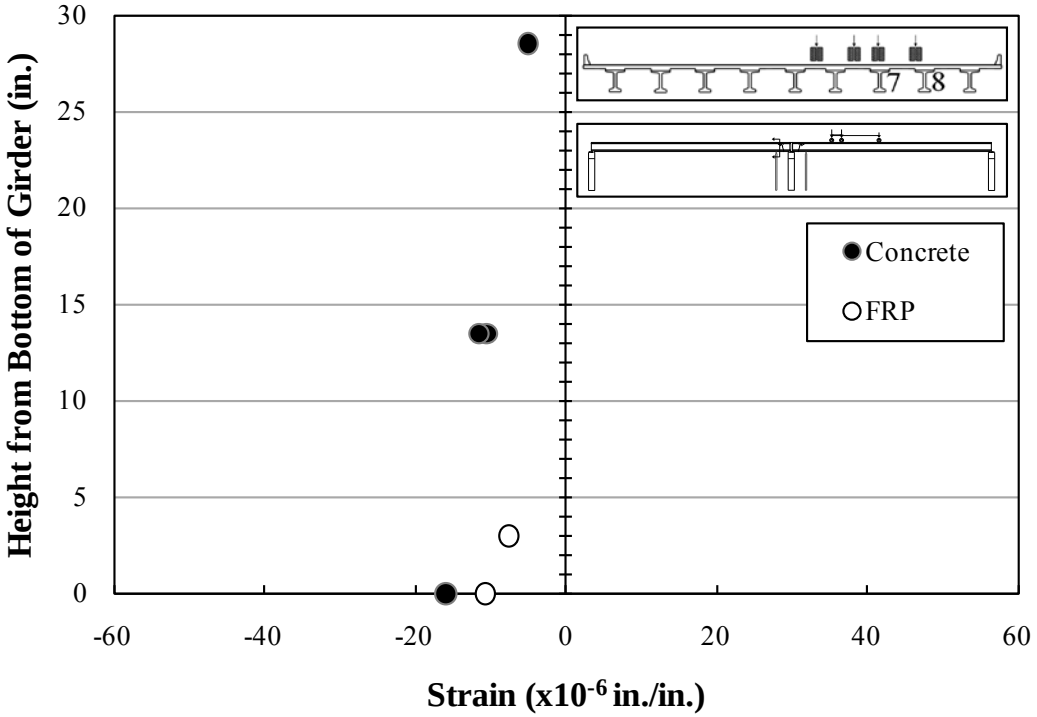

Figure B.62: Strains—Girder 8—Section 1—A8

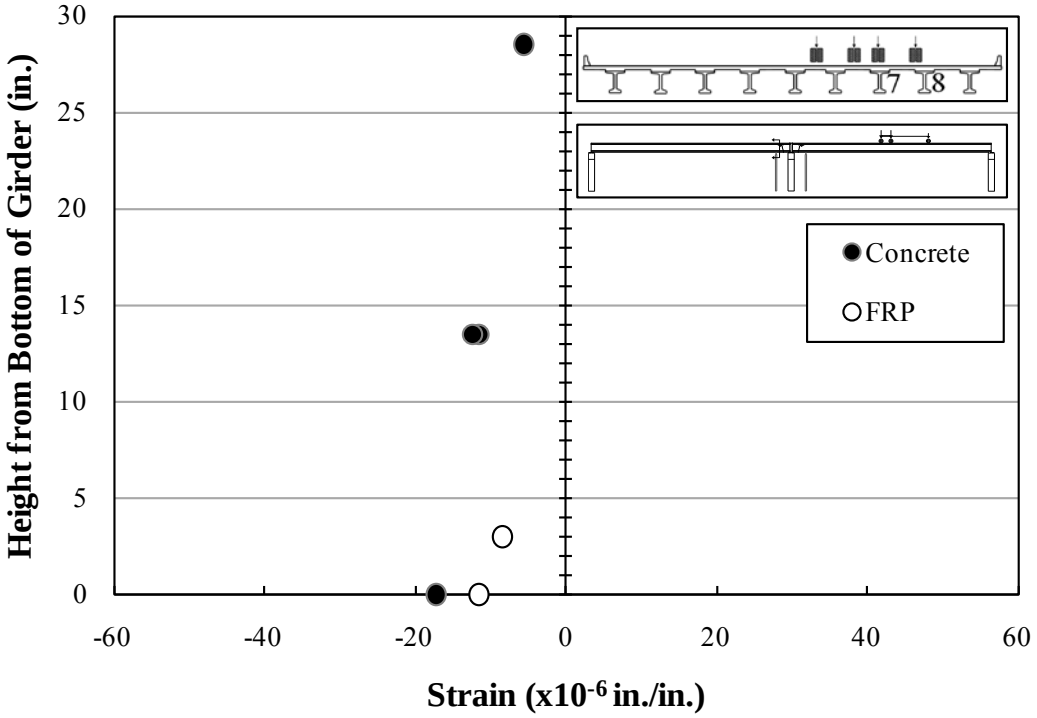

Figure B.63: Strains—Girder 8—Section 1—A9

B.1.3.2.2 Strains—Girder 8—Cross Section 2

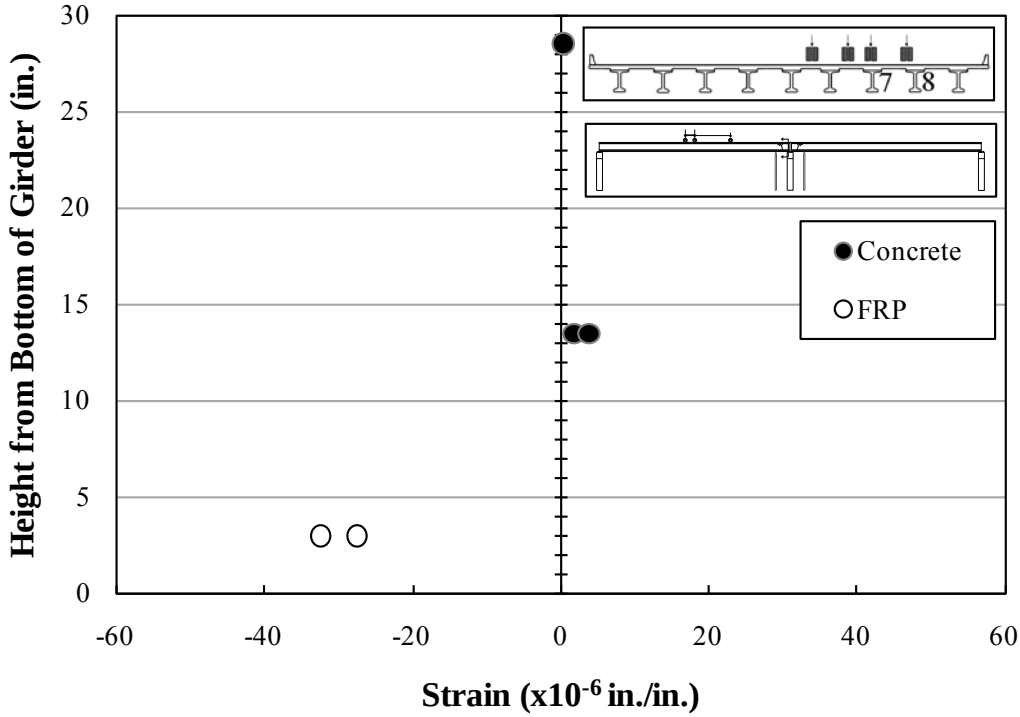

Figure B.64: Strains—Girder 8—Section 2—A1

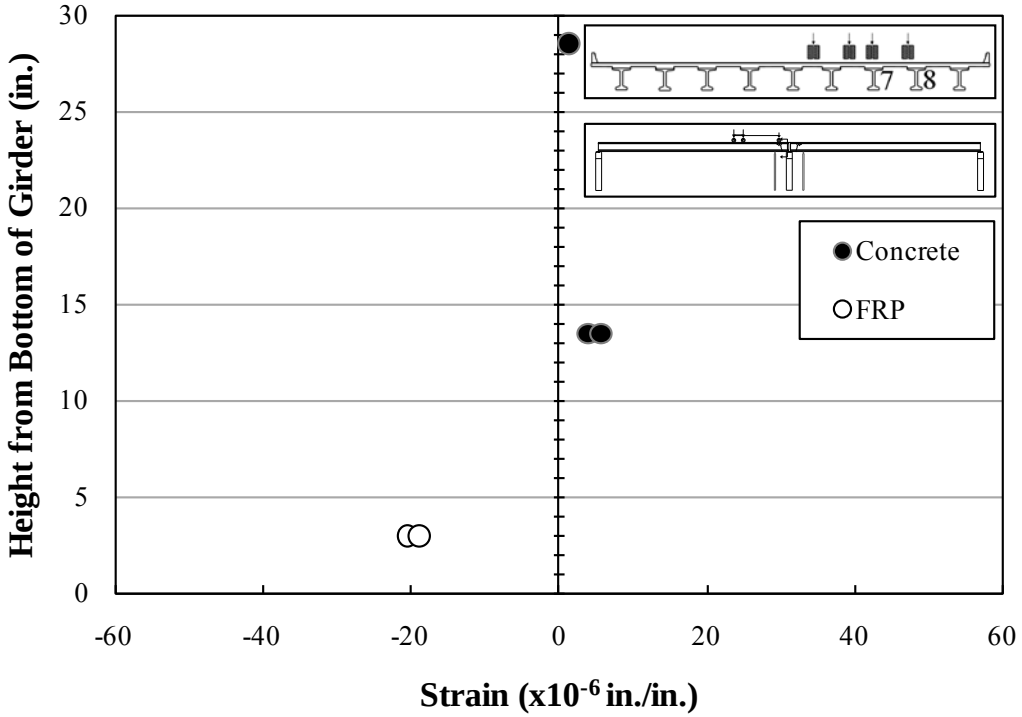

Figure B.65: Strains—Girder 8—Section 2—A2

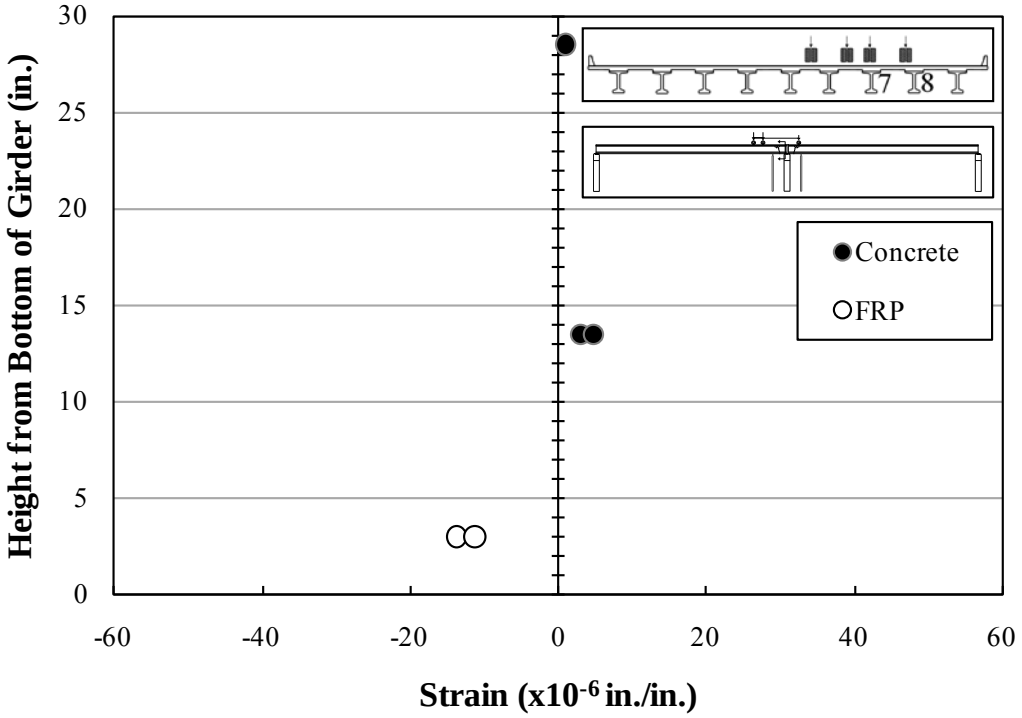

Figure B.66: Strains—Girder 8—Section 2—A3

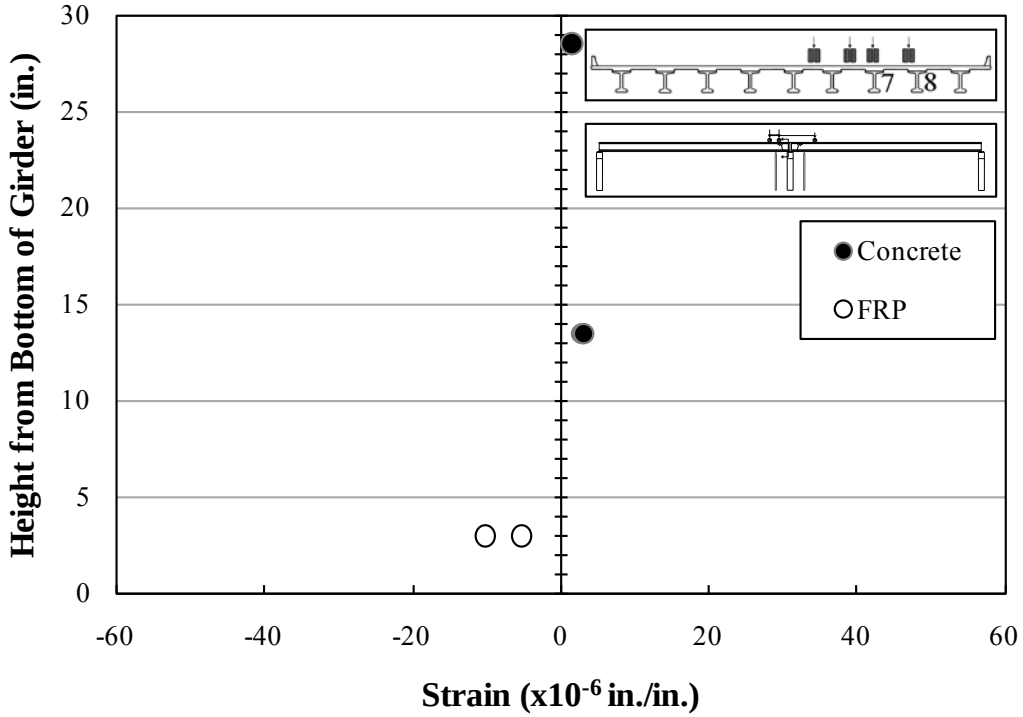

Figure B.67: Strains—Girder 8—Section 2—A4

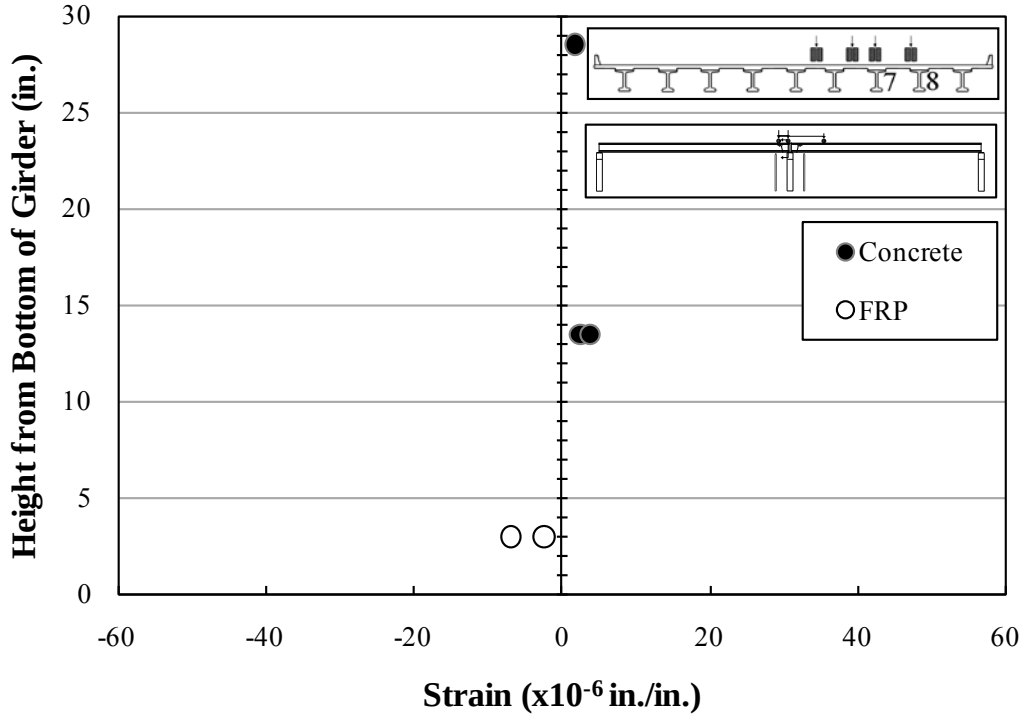

Figure B.68: Strains—Girder 8—Section 2—A5

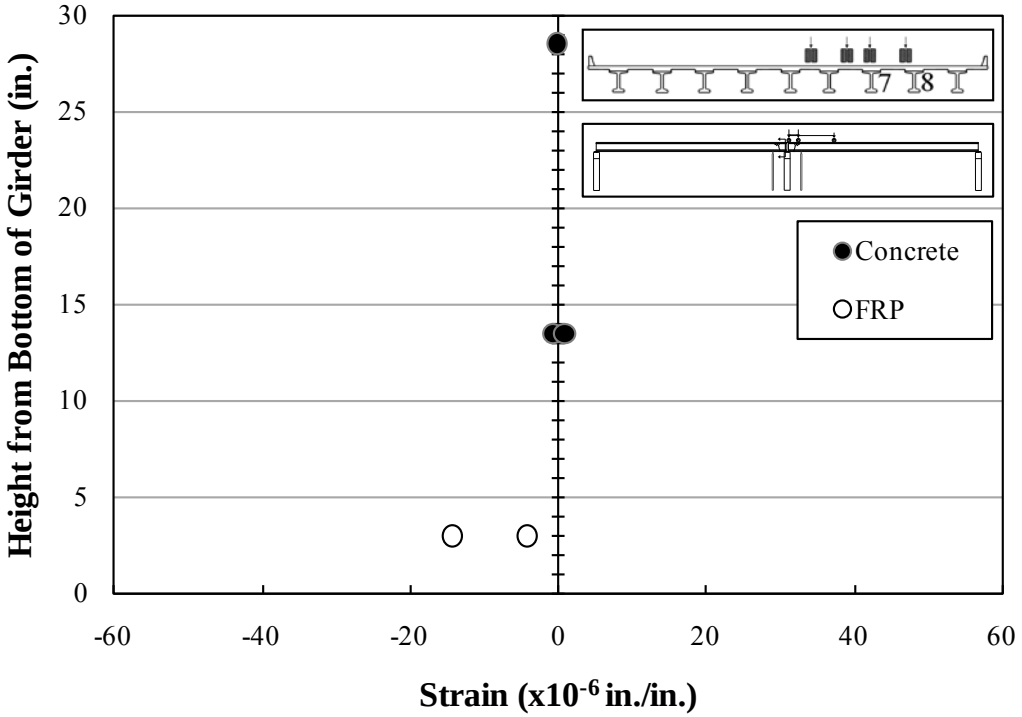

Figure B.69: Strains—Girder 8—Section 2—A6

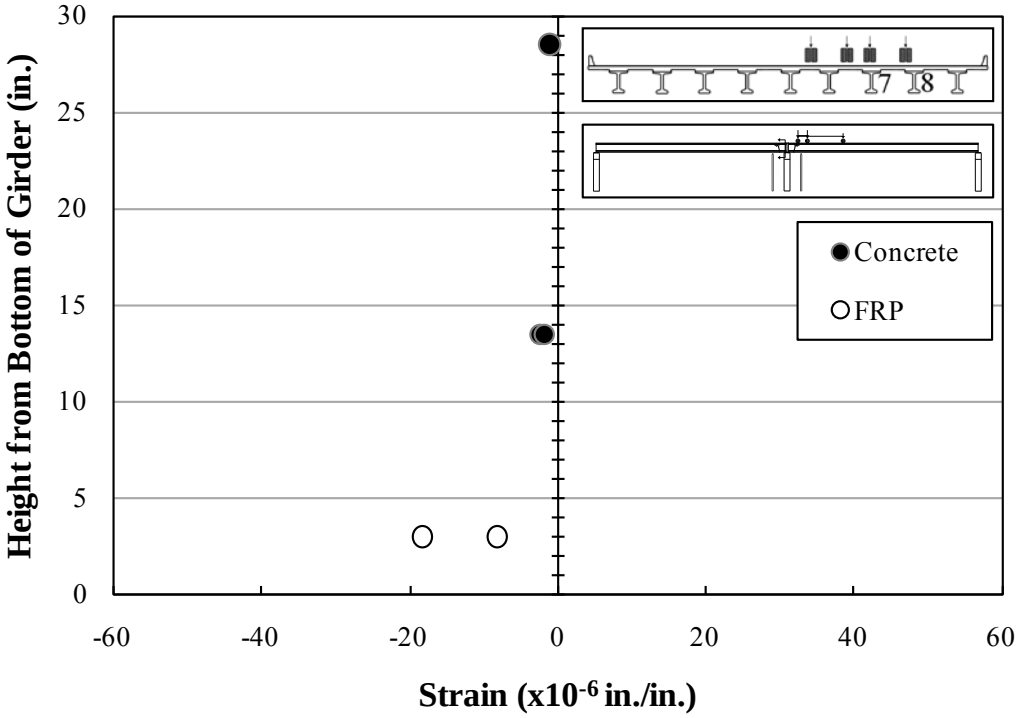

Figure B.70: Strains—Girder 8—Section 2—A7

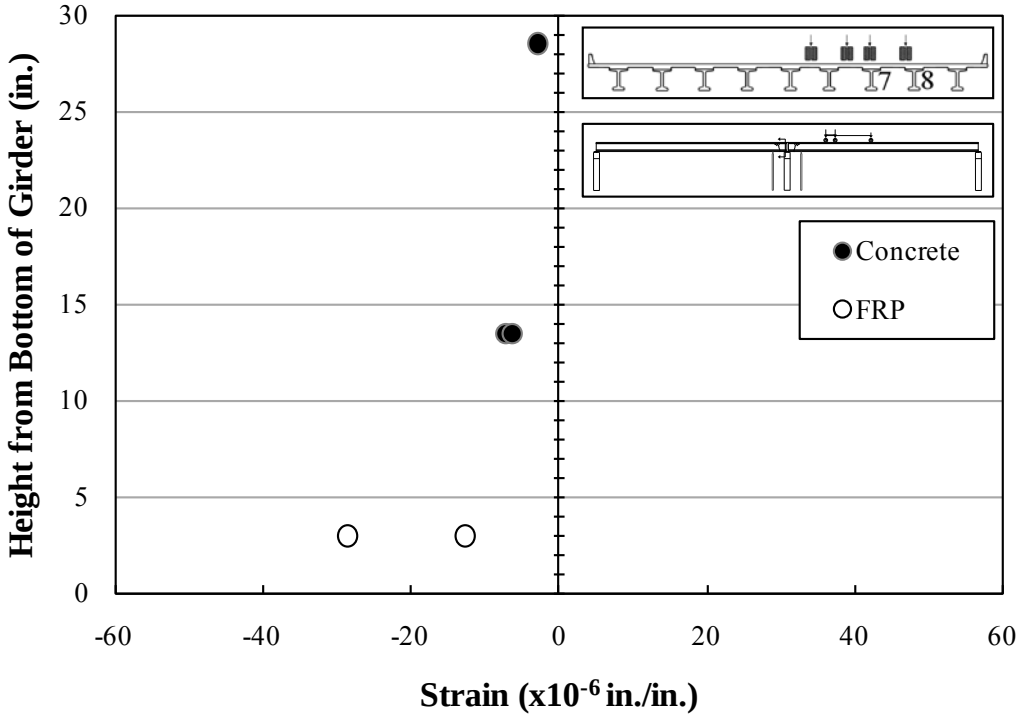

Figure B.71: Strains—Girder 8—Section 2—A8

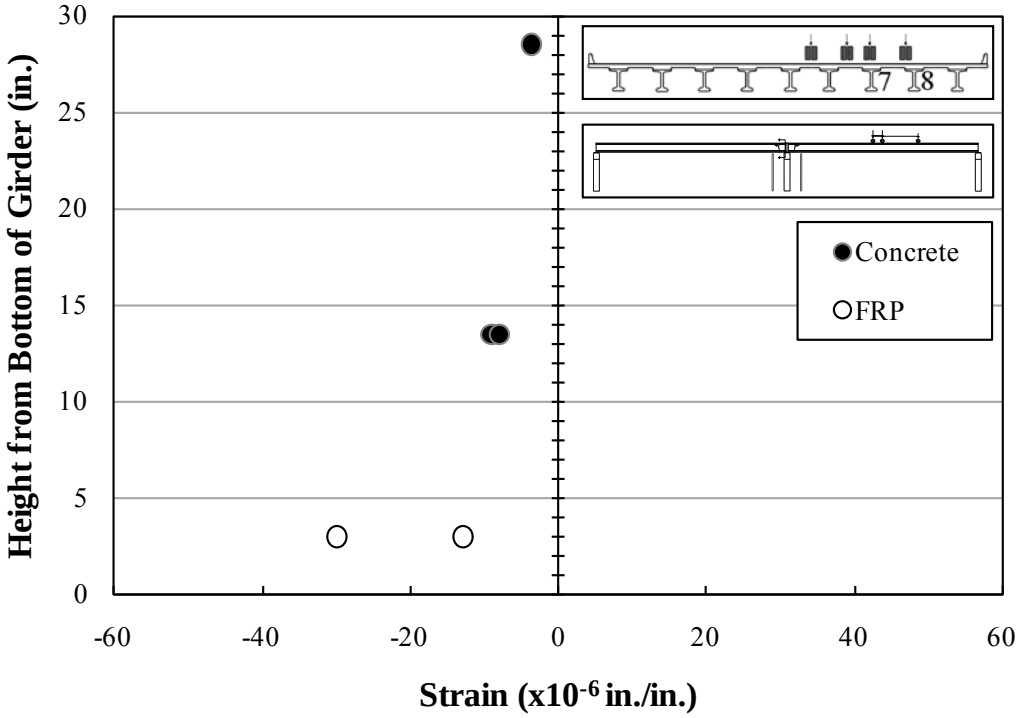

Figure B.72: Strains—Girder 8—Section 2—A9

B.1.3.2.3 Strains—Girder 8—Cross Section 3

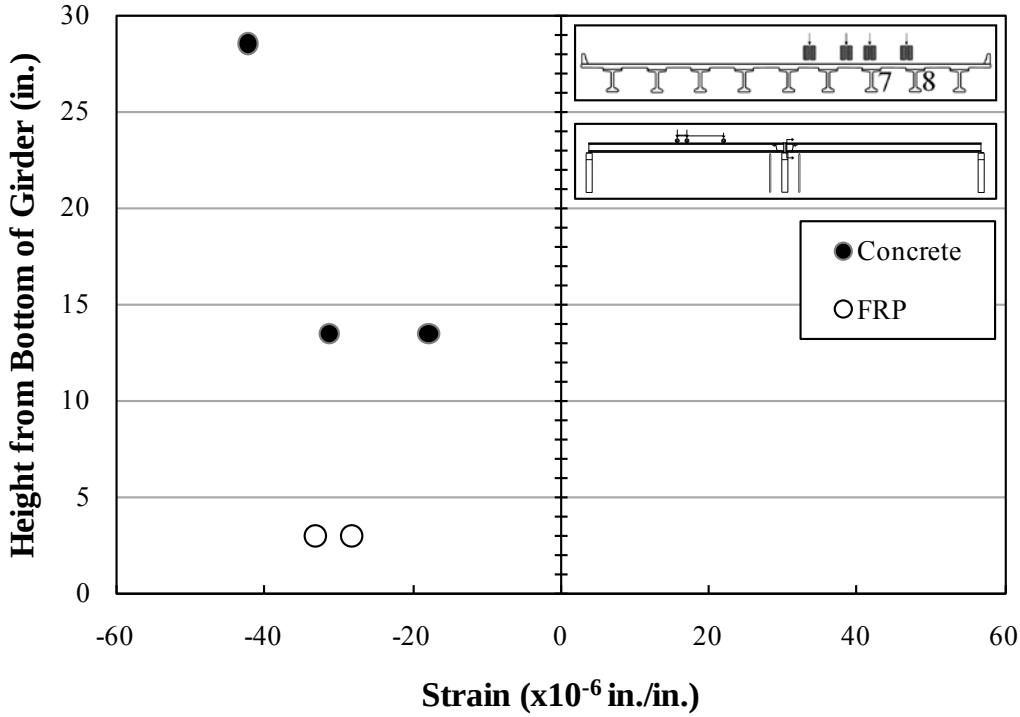

Figure B.73: Strains—Girder 8—Section 3—A1

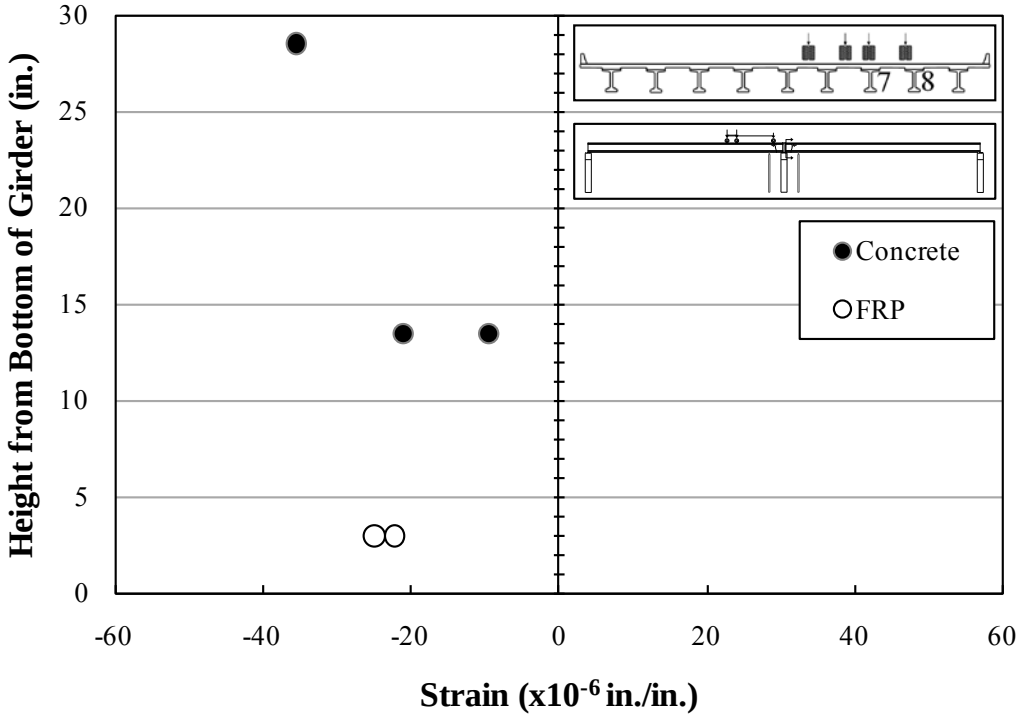

Figure B.74: Strains—Girder 8—Section 3—A2

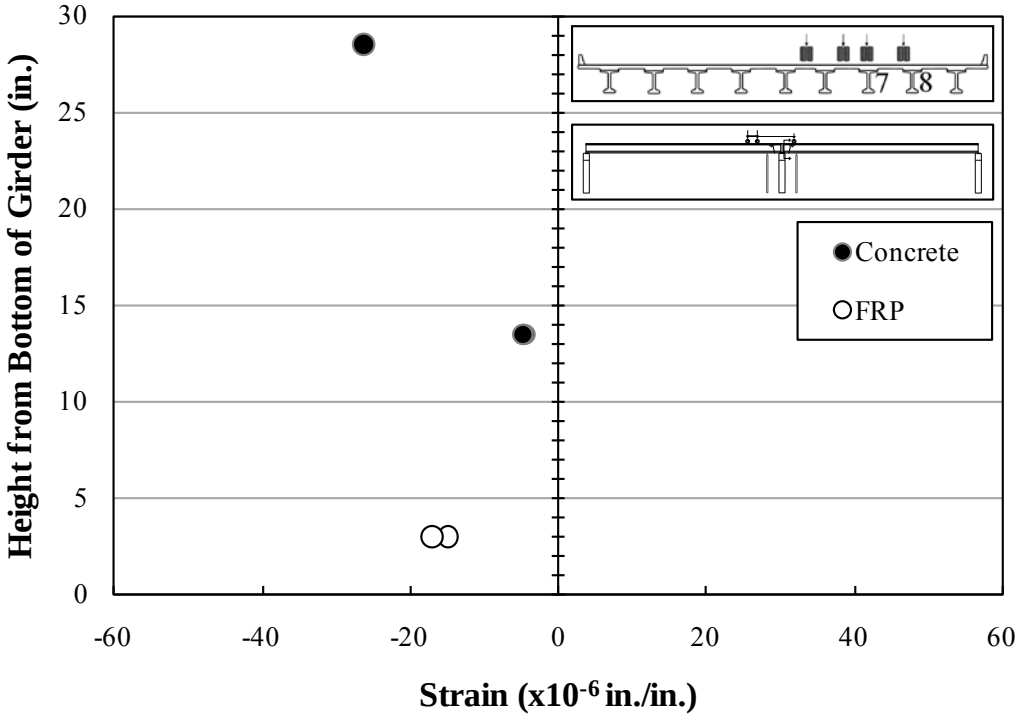

Figure B.75: Strains—Girder 8—Section 3—A3

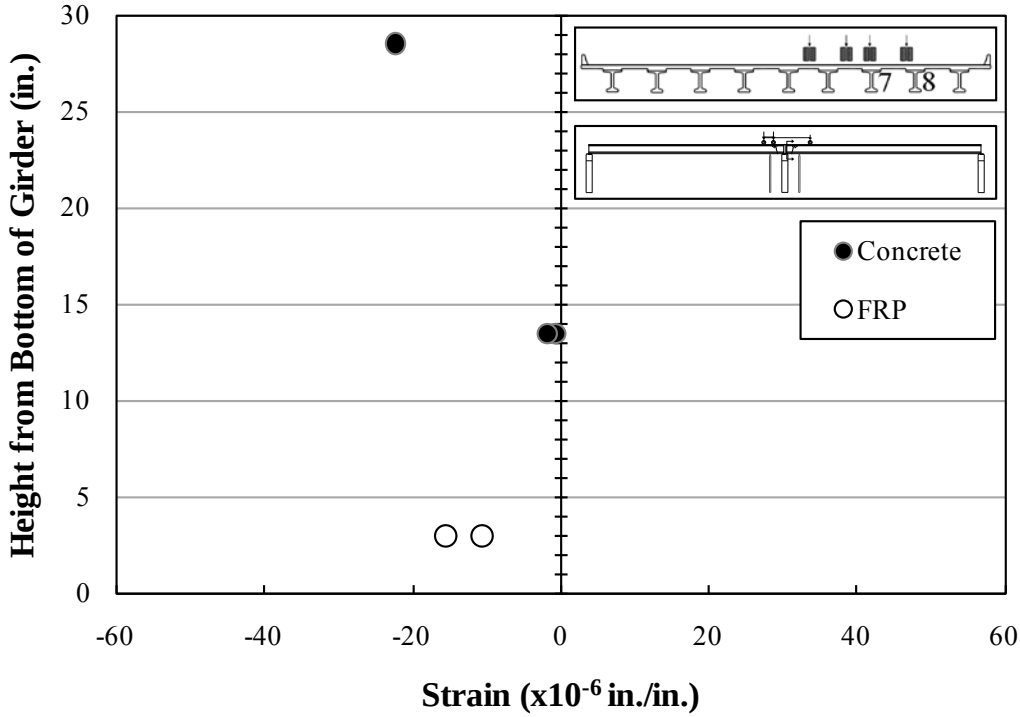

Figure B.76: Strains—Girder 8—Section 3—A4

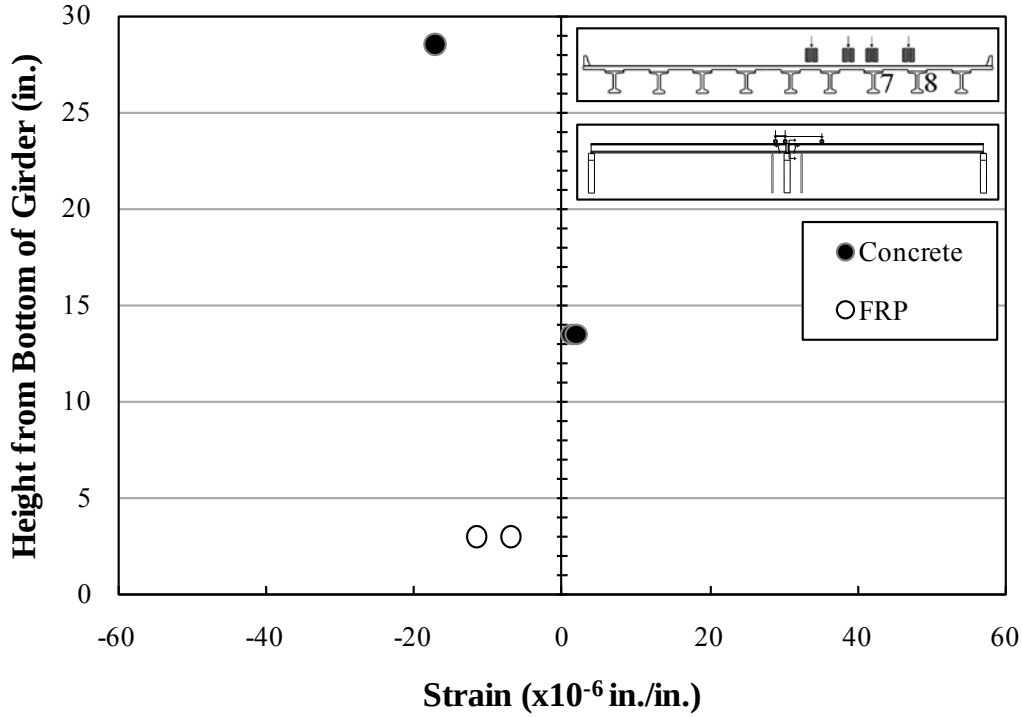

Figure B.77: Strains—Girder 8—Section 3—A5

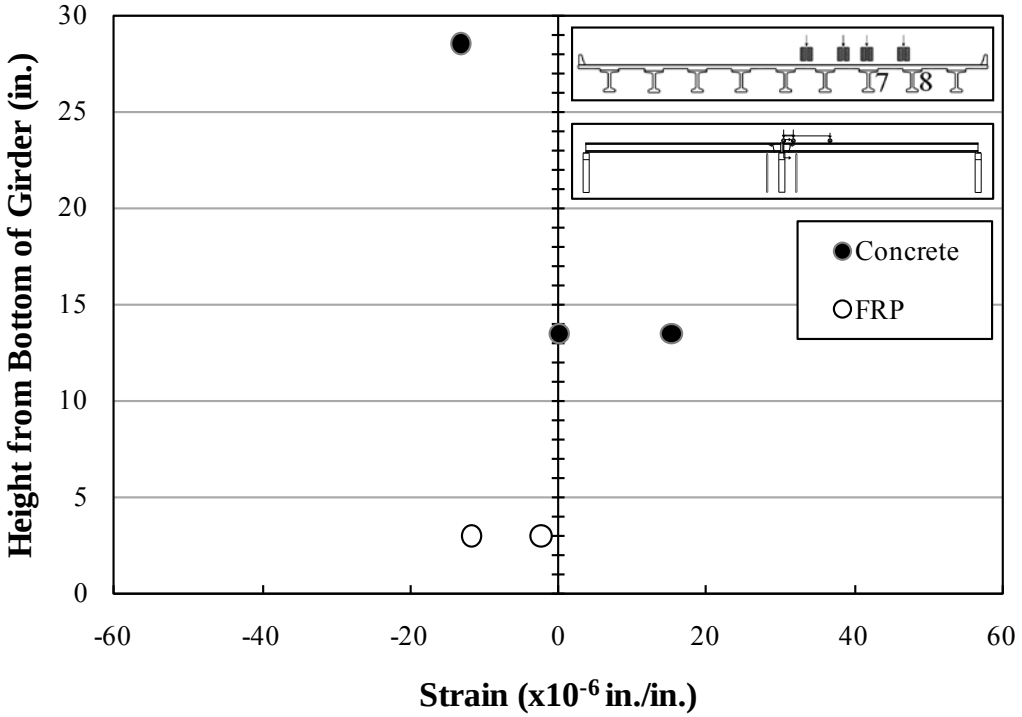

Figure B.78: Strains—Girder 8—Section 3—A6

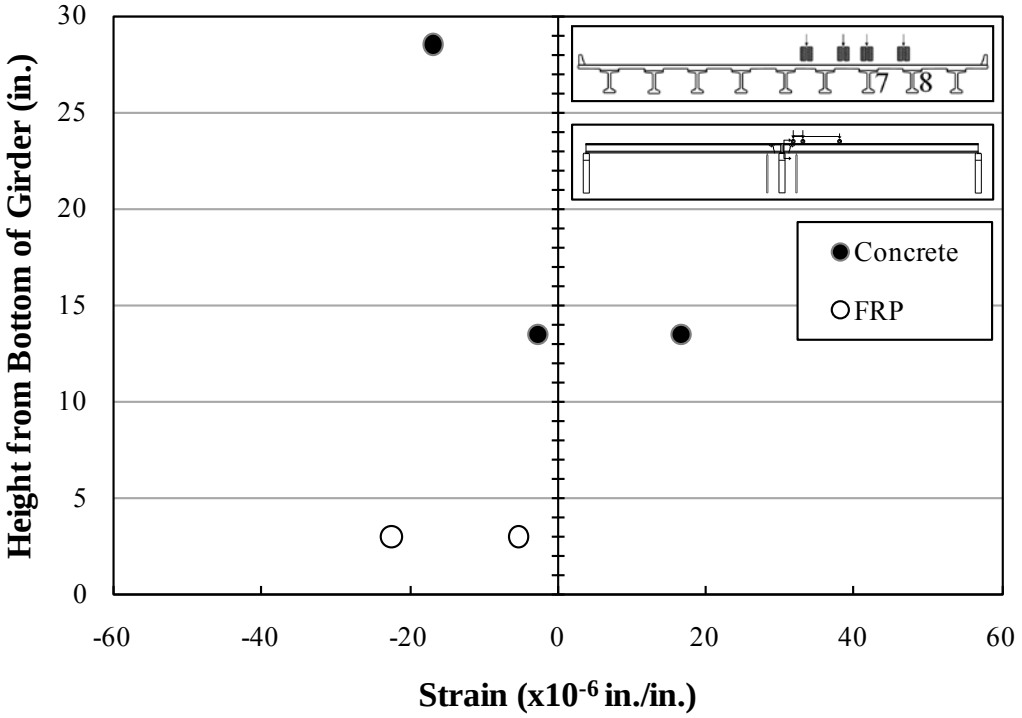

Figure B.79: Strains—Girder 8—Section 3—A7

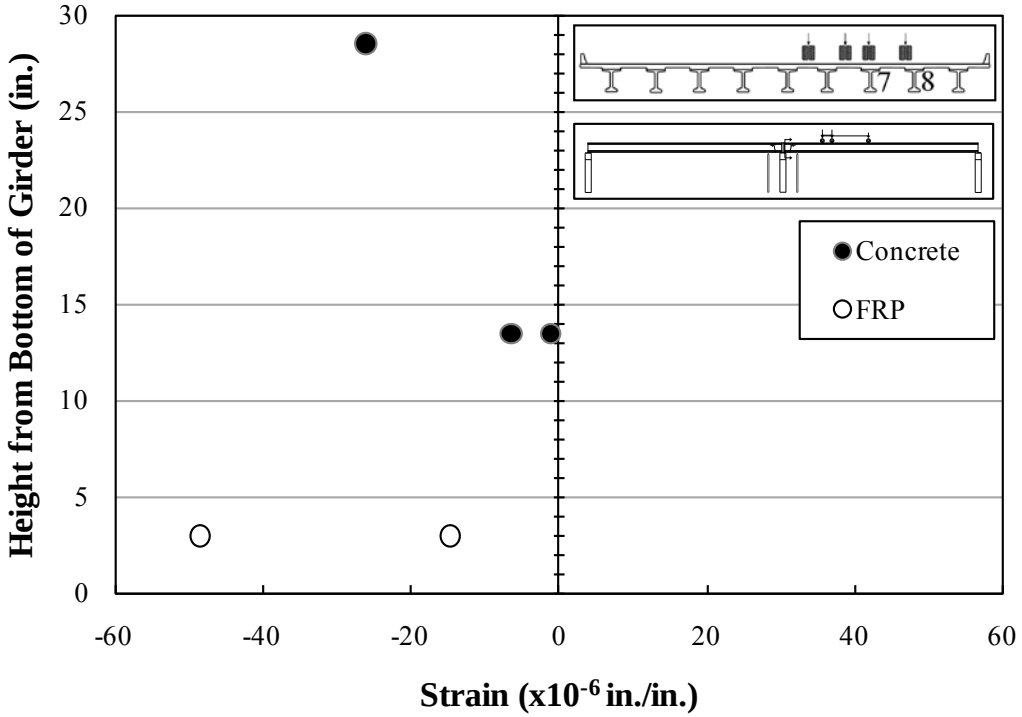

Figure B.80: Strains—Girder 8—Section 3—A8

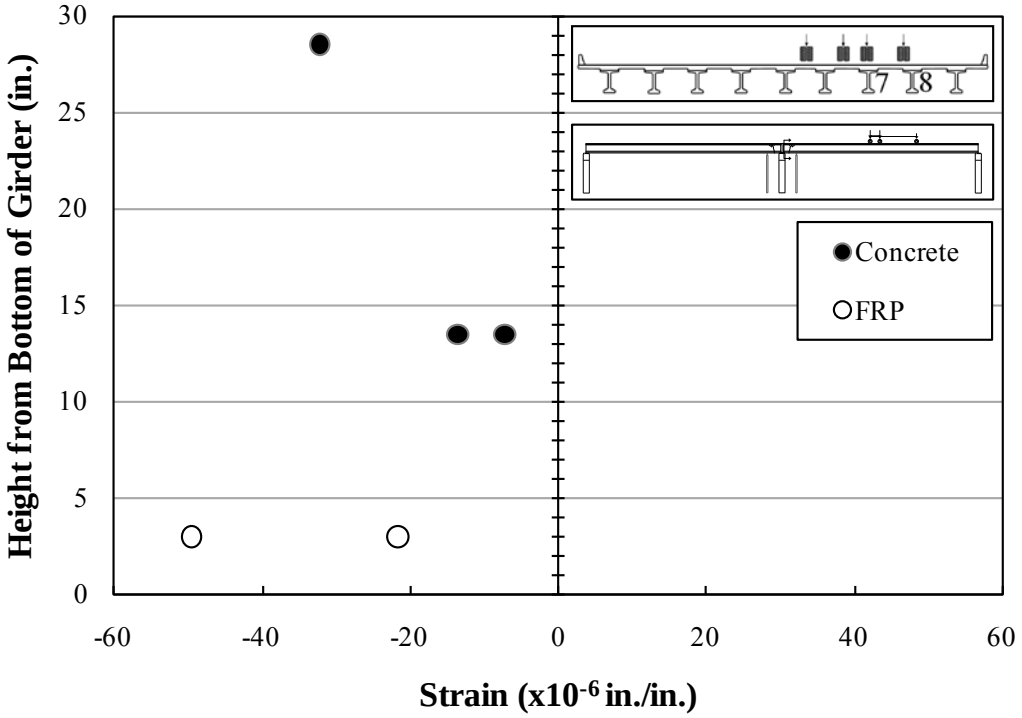

Figure B.81: Strains—Girder 8—Section 3—A9

B.1.3.2.4 Strains—Girder 8—Cross Section 4

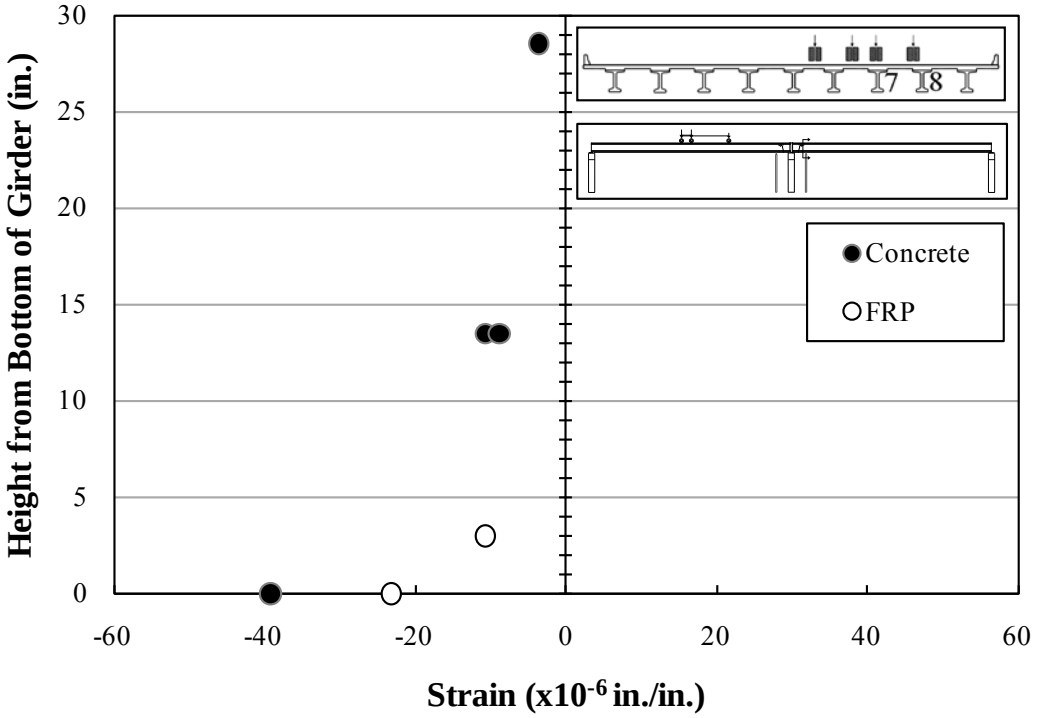

Figure B.82: Strains—Girder 8—Section 4—A1

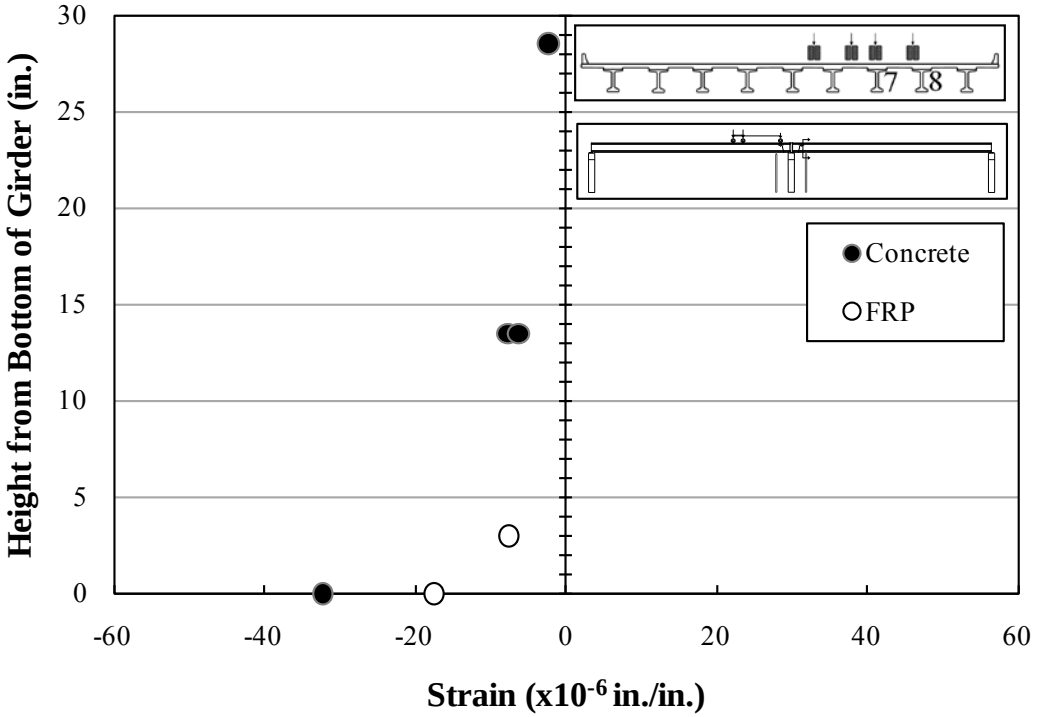

Figure B.83: Strains—Girder 8—Section 4—A2

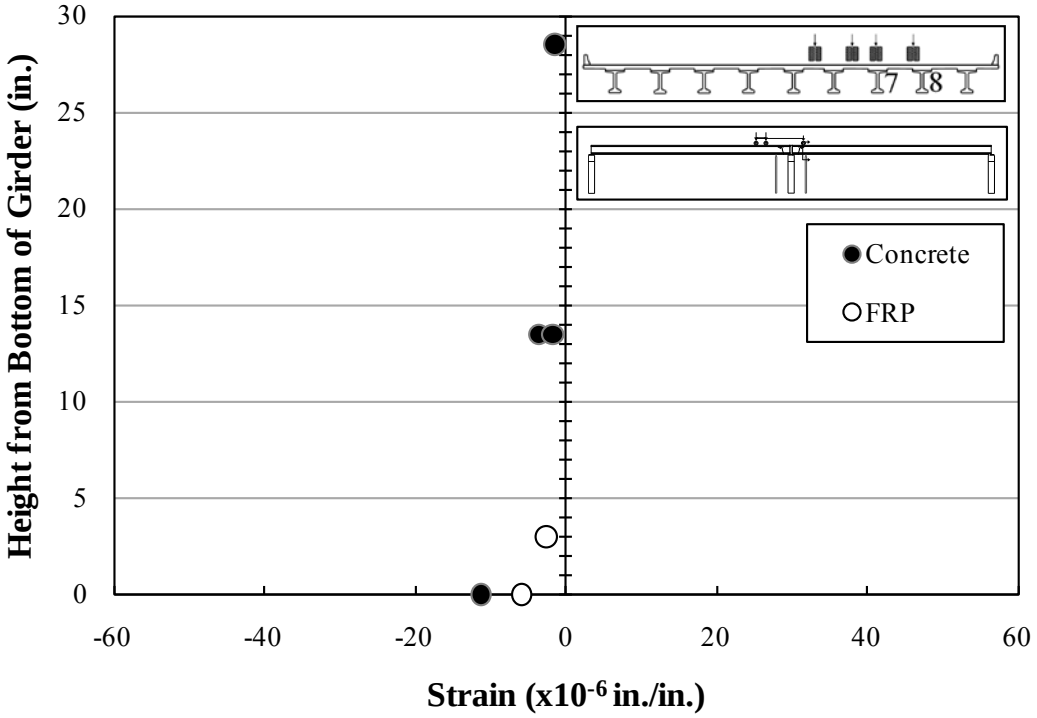

Figure B.84: Strains—Girder 8—Section 4—A3

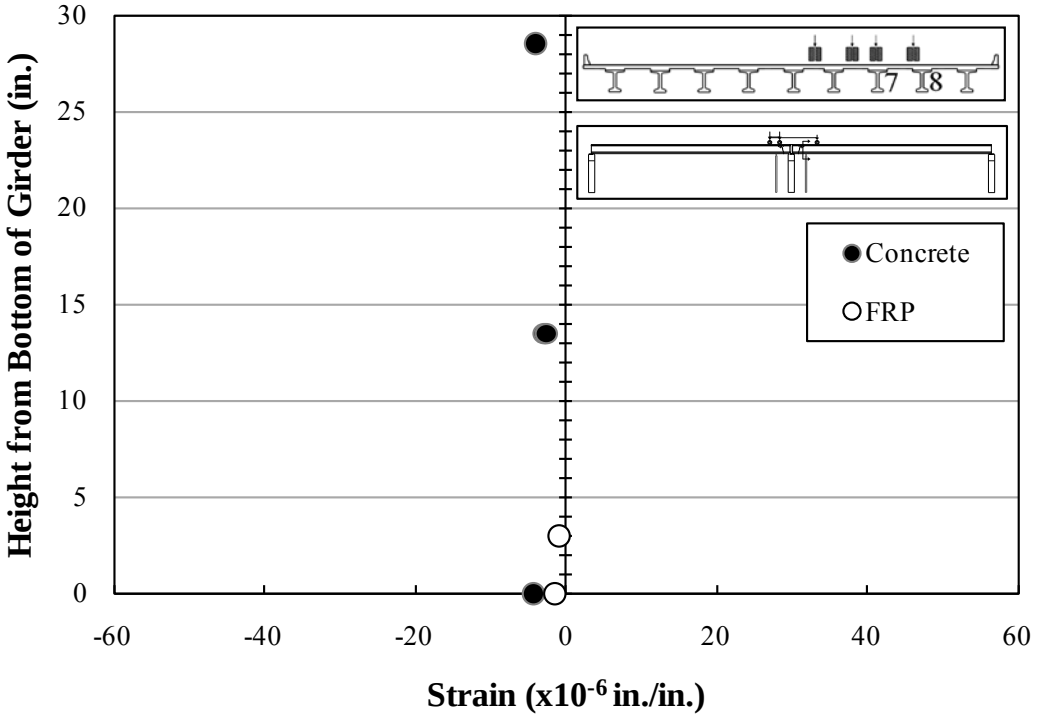

Figure B.85: Strains—Girder 8—Section 4—A4

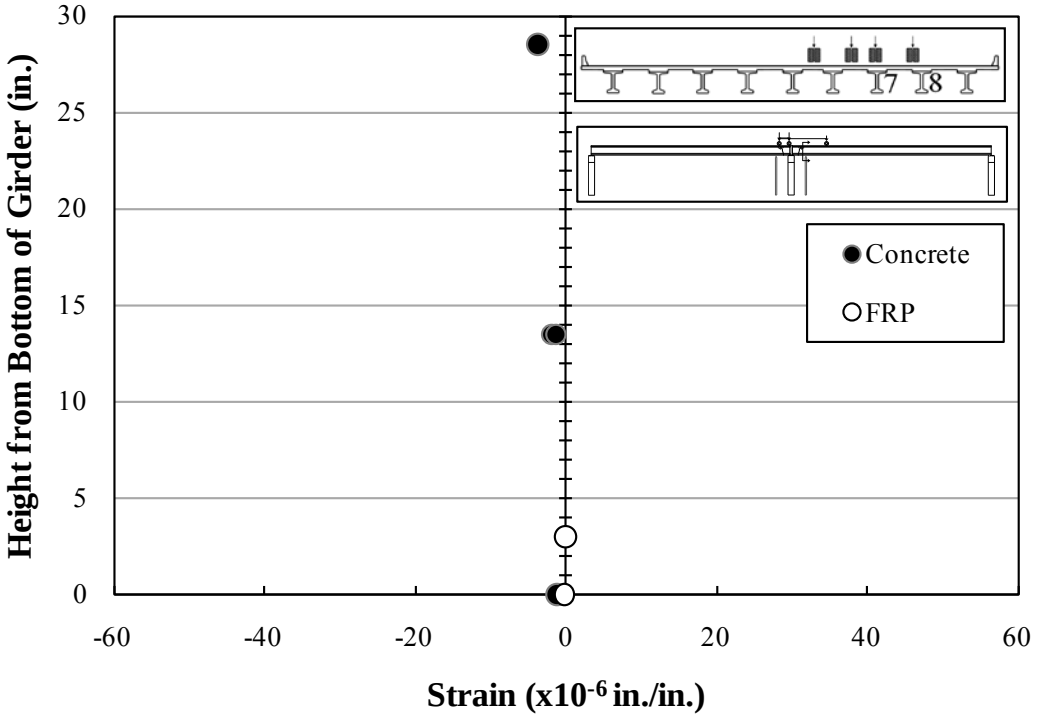

Figure B.86: Strains—Girder 8—Section 4—A5

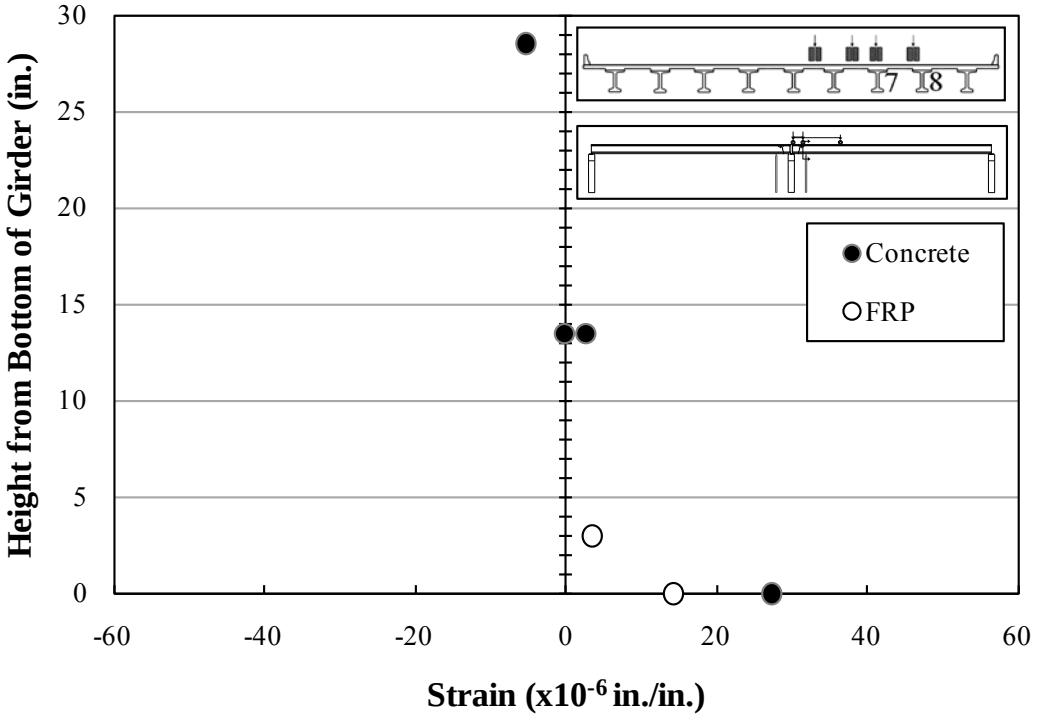

Figure B.87: Strains—Girder 8—Section 4—A6

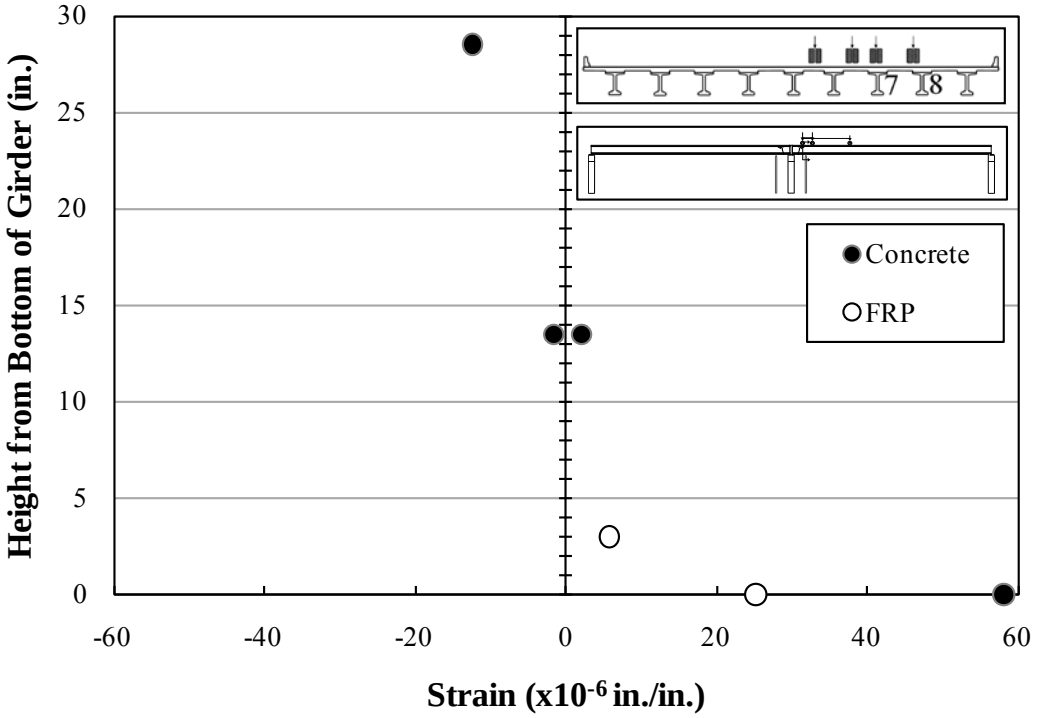

Figure B.88: Strains—Girder 8—Section 4—A7

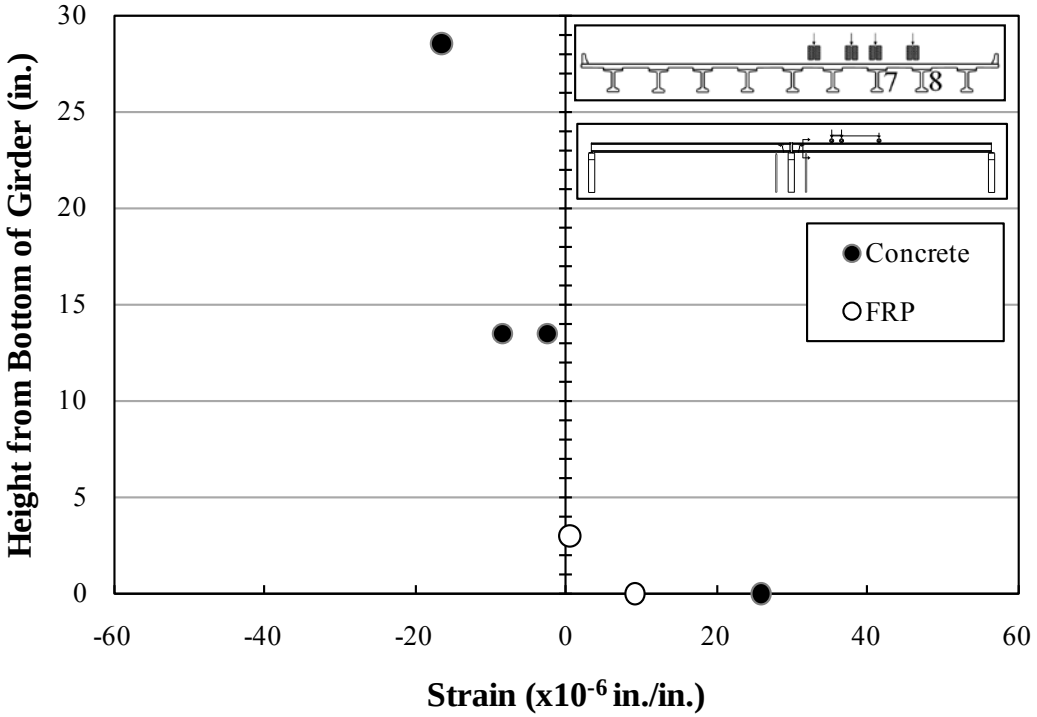

Figure B.89: Strains—Girder 8—Section 4—A8

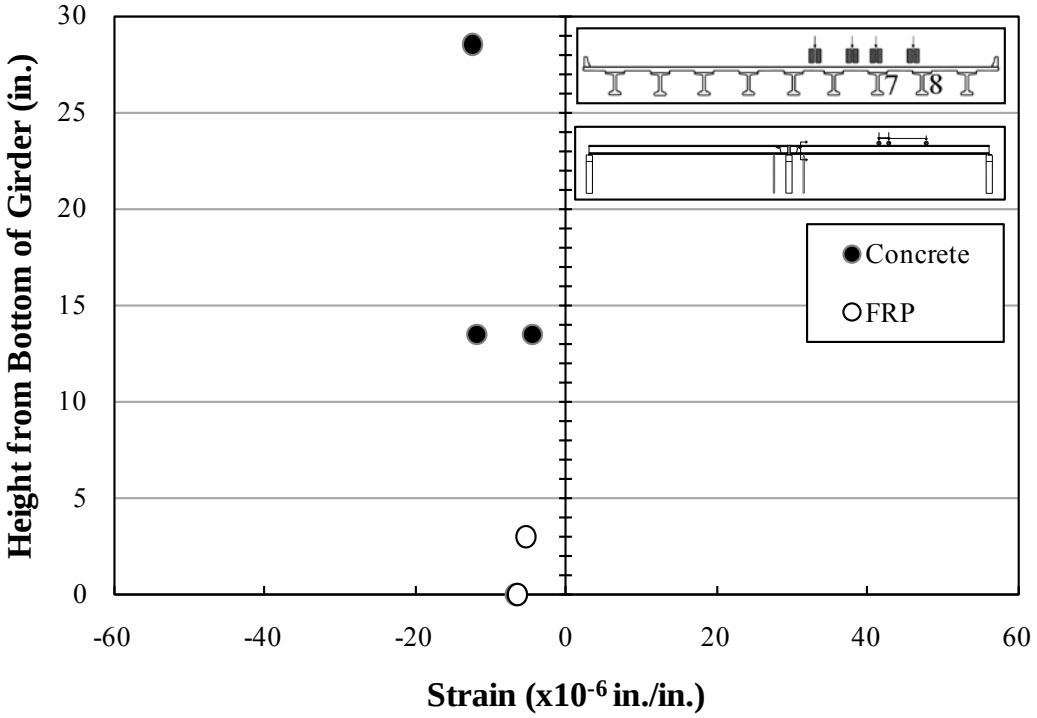

Figure B.90: Strains—Girder 8—Section 4—A9

B.1.4 Bottom-Fiber Strains—Both Girders

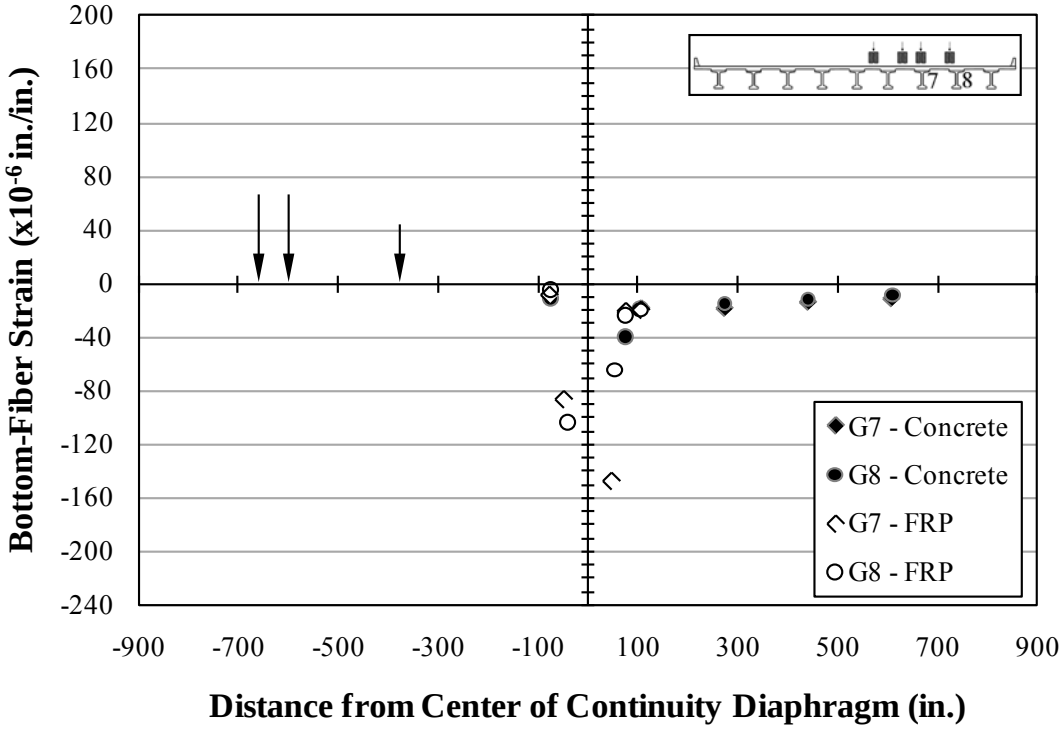

Figure B.91: Bottom-fiber strains—A1

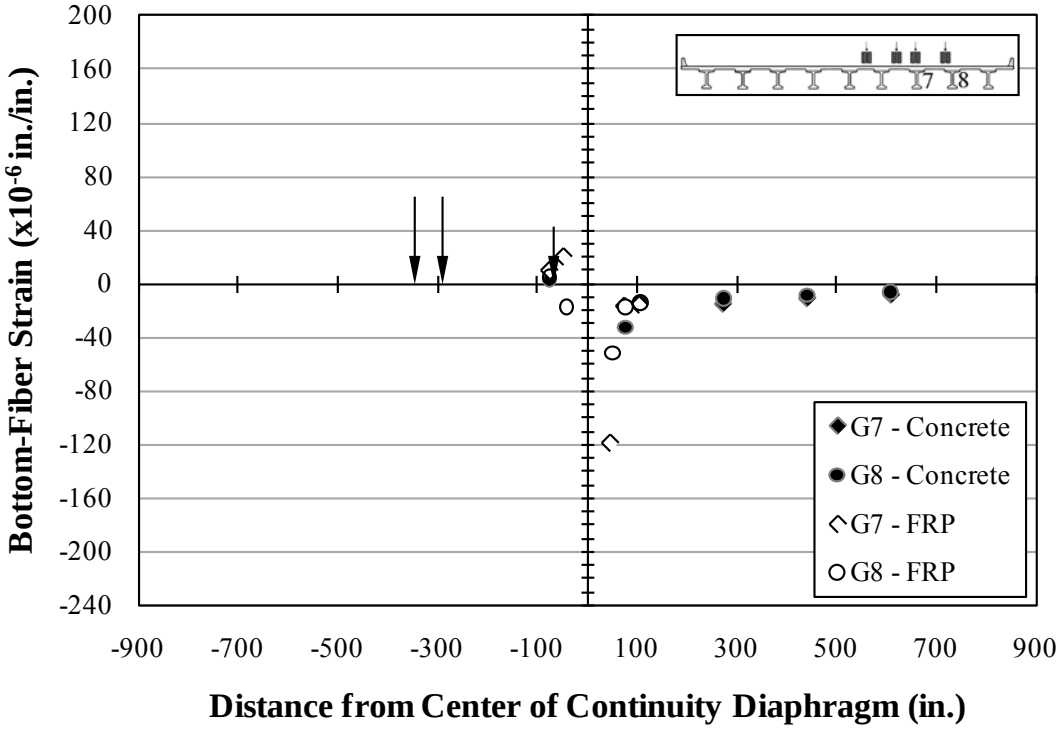

Figure B.92: Bottom-fiber strains—A2

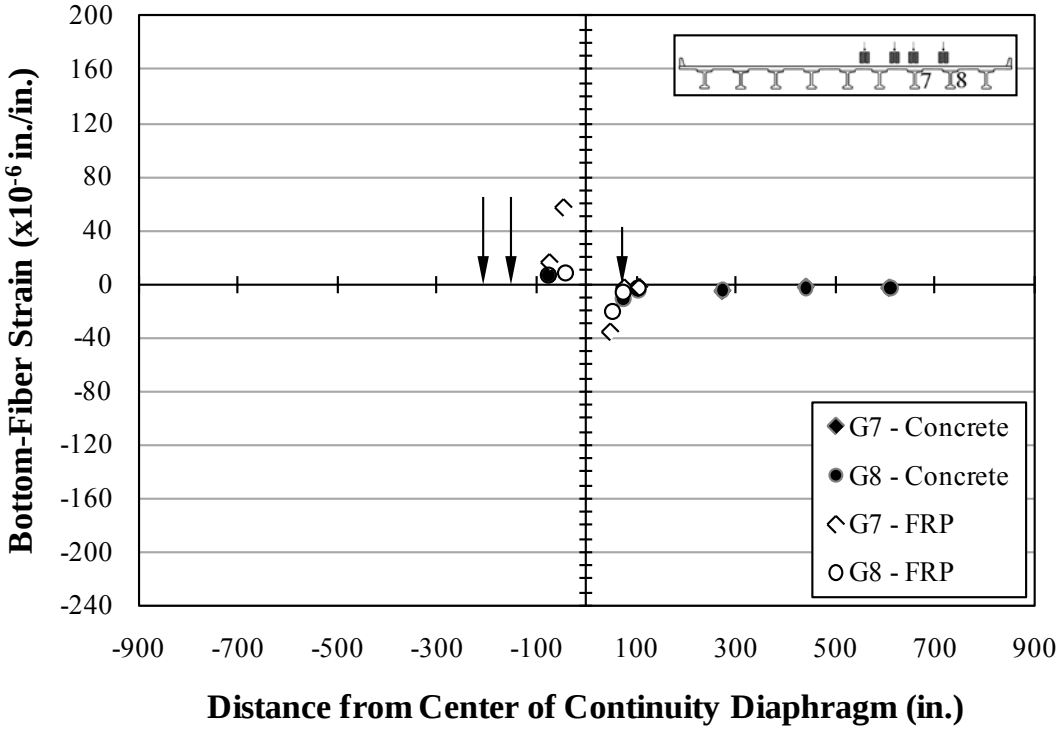

Figure B.93: Bottom-fiber strains—A3

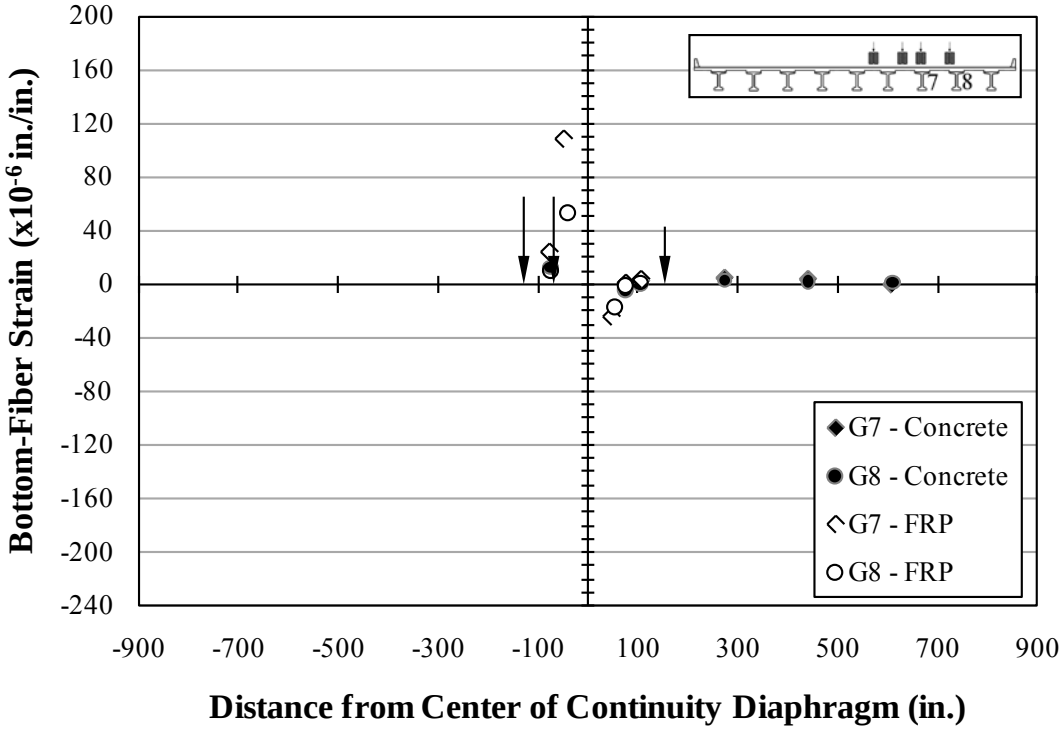

Figure B.94: Bottom-fiber strains—A4

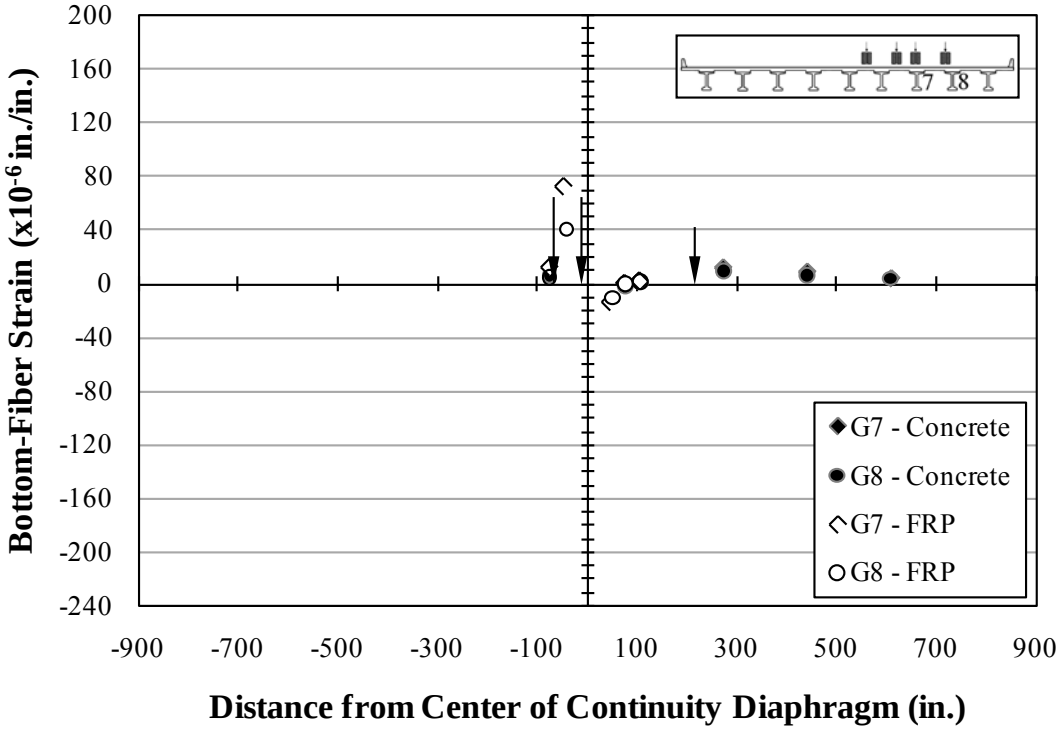

Figure B.95: Bottom-fiber strains—A5

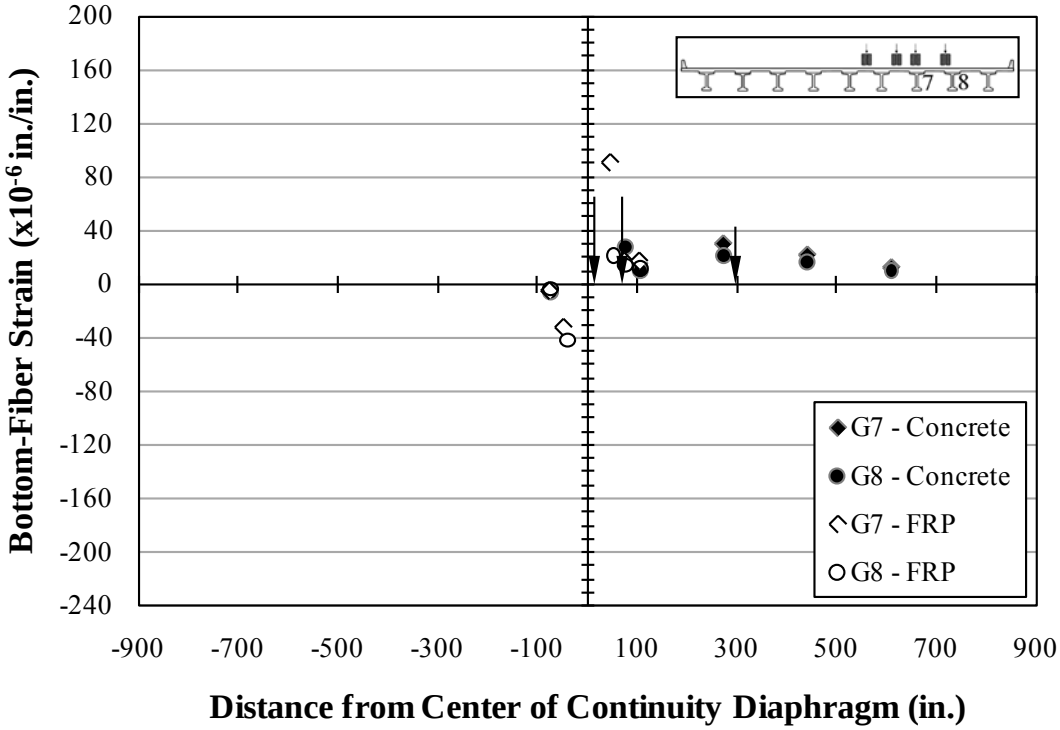

Figure B.96: Bottom-fiber strains—A6

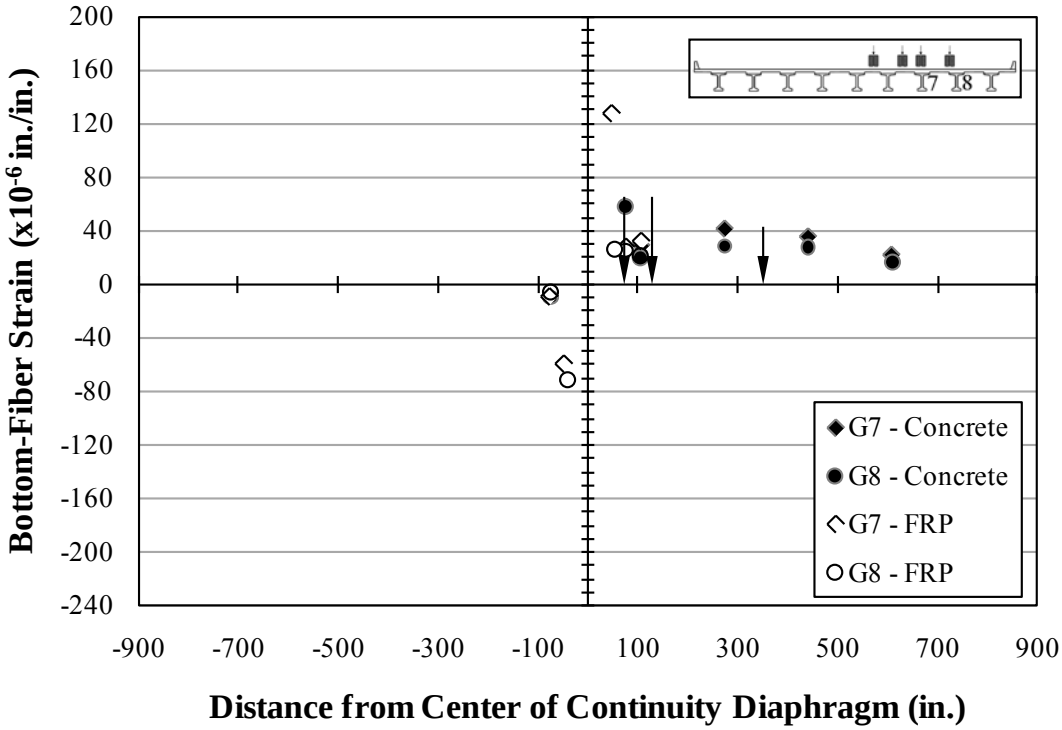

Figure B.97: Bottom-fiber strains—A7

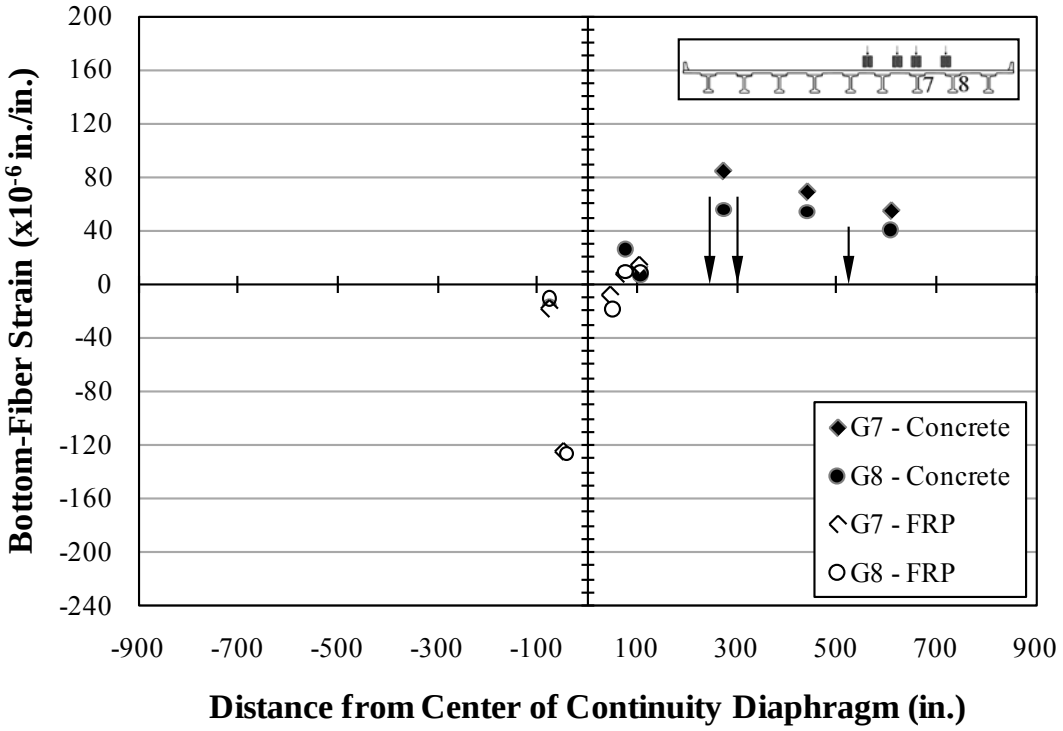

Figure B.98: Bottom-fiber strains—A8

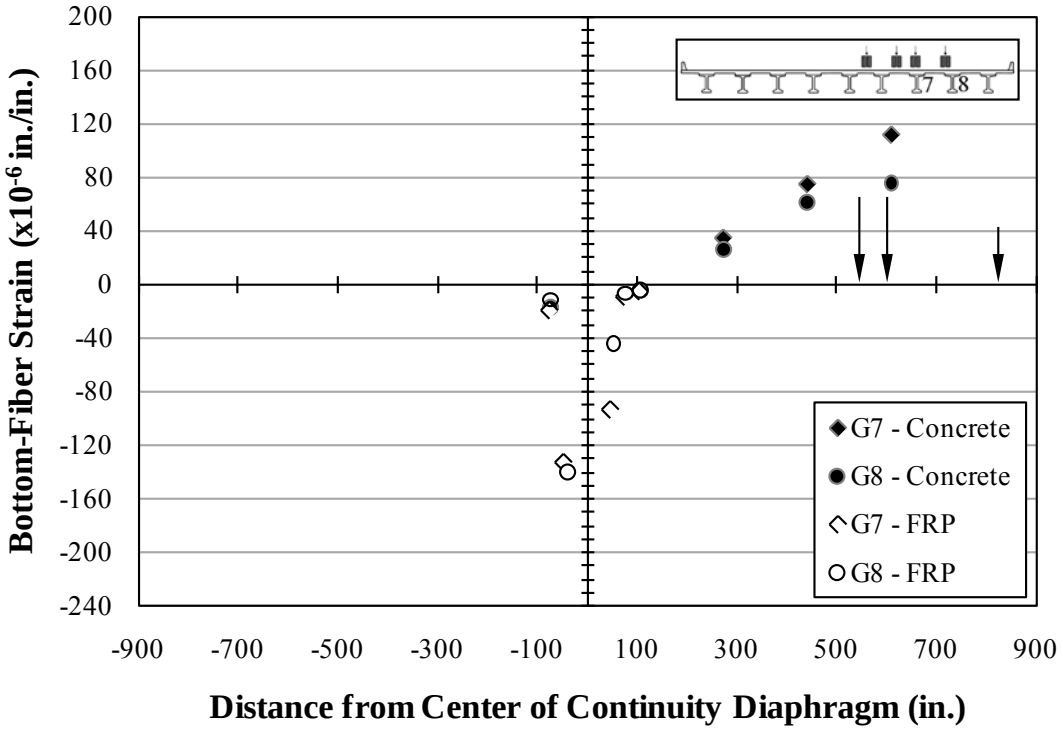

Figure B.99: Bottom-fiber strains—A9

B.1.4.1 Bottom-Fiber Strains—Girder 7

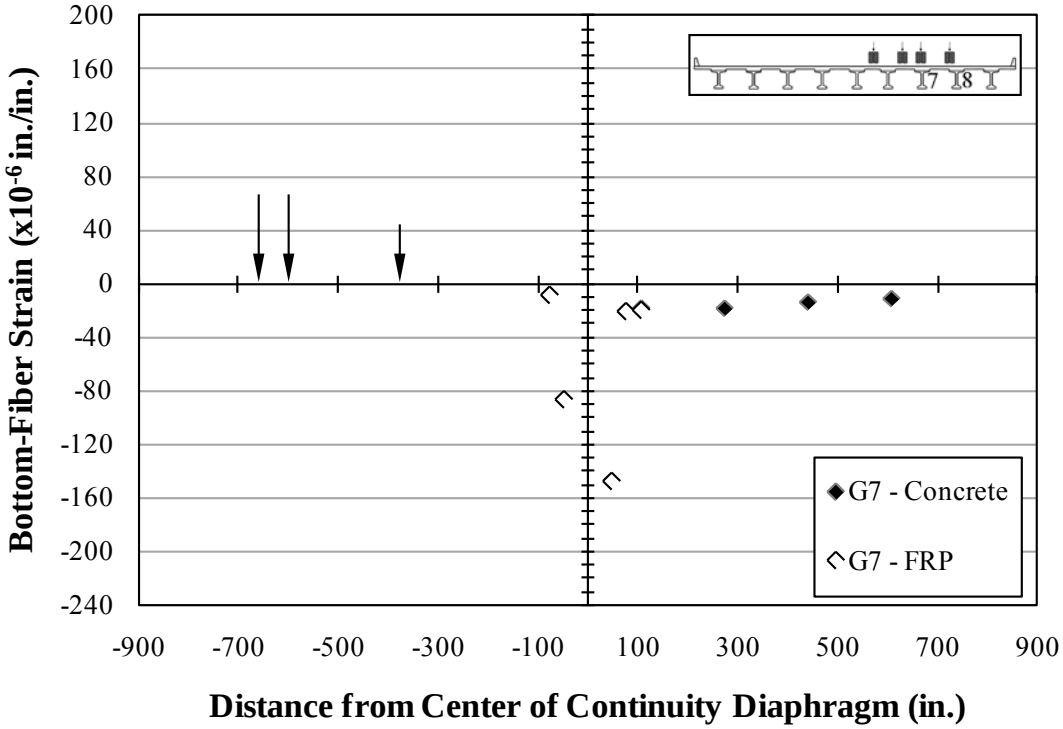

Figure B.100: Bottom-fiber strains—Girder 7—A1

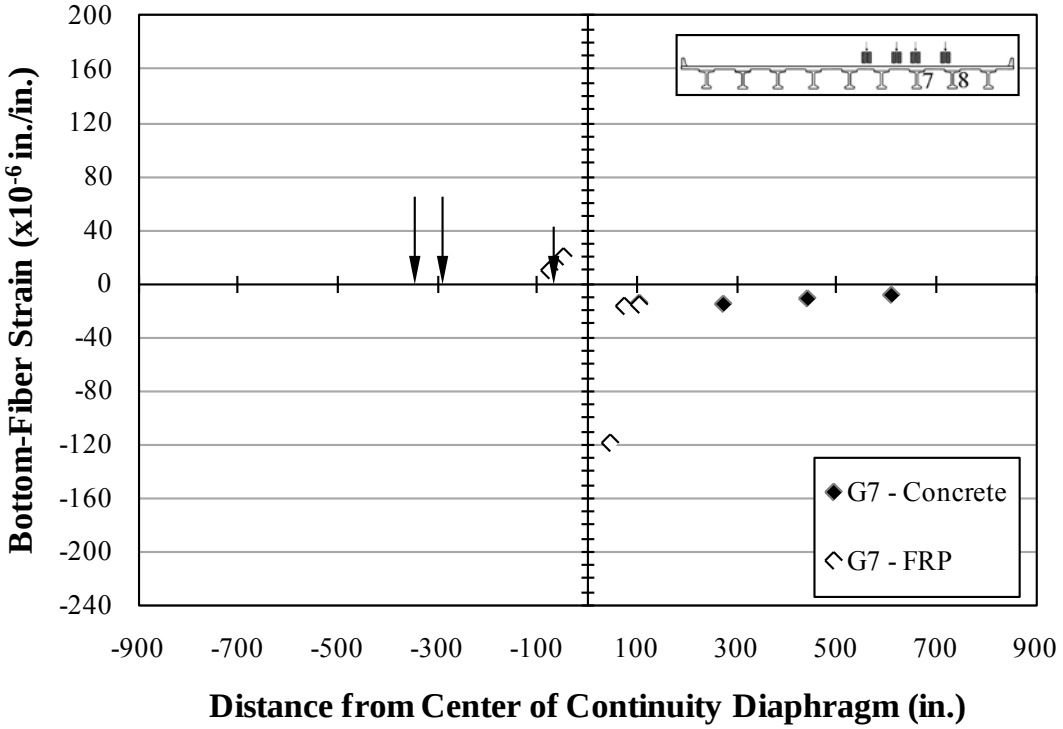

Figure B.101: Bottom-fiber strains—Girder 7—A2

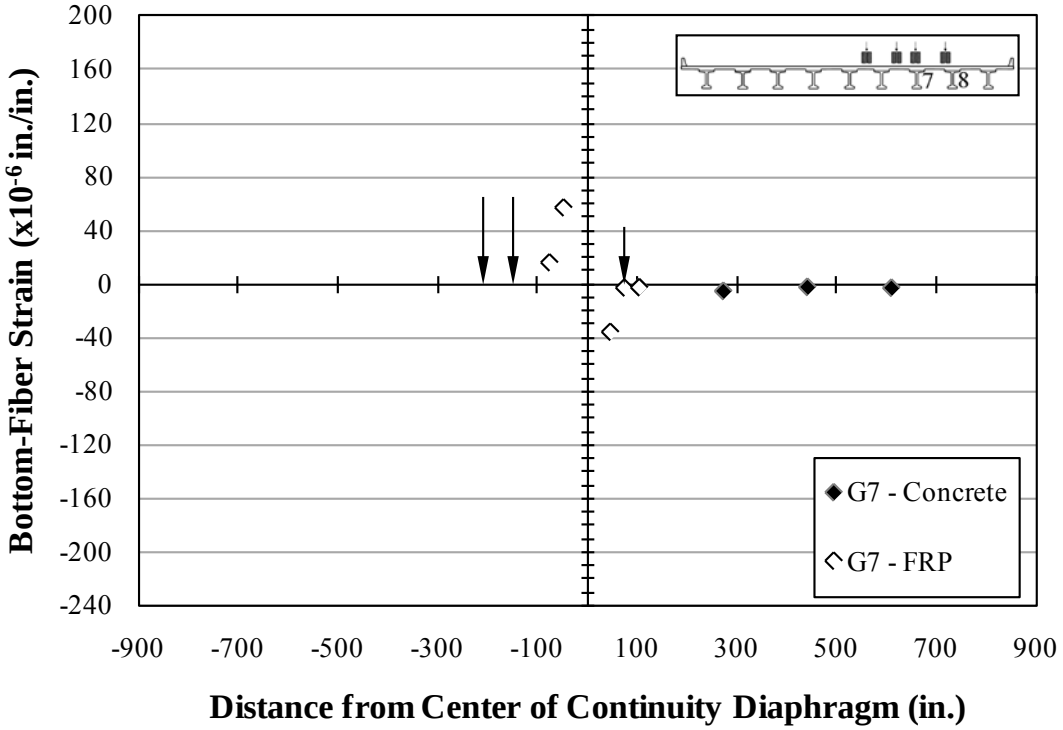

Figure B.102: Bottom-fiber strains—Girder 7—A3

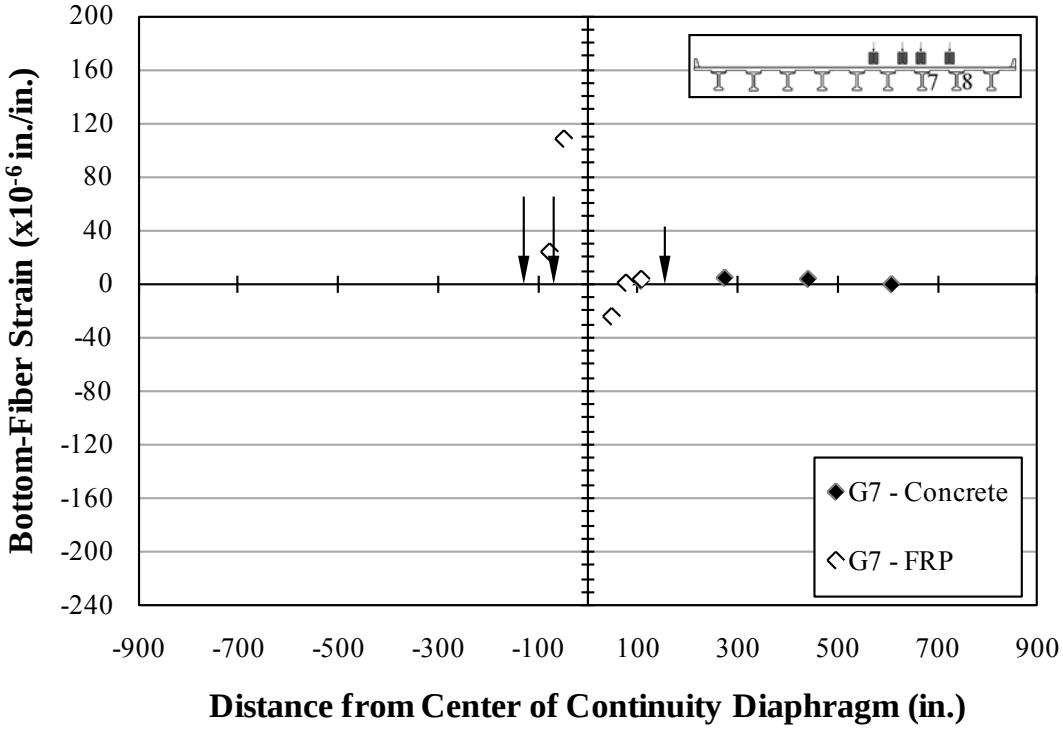

Figure B.103: Bottom-fiber strains—Girder 7—A4

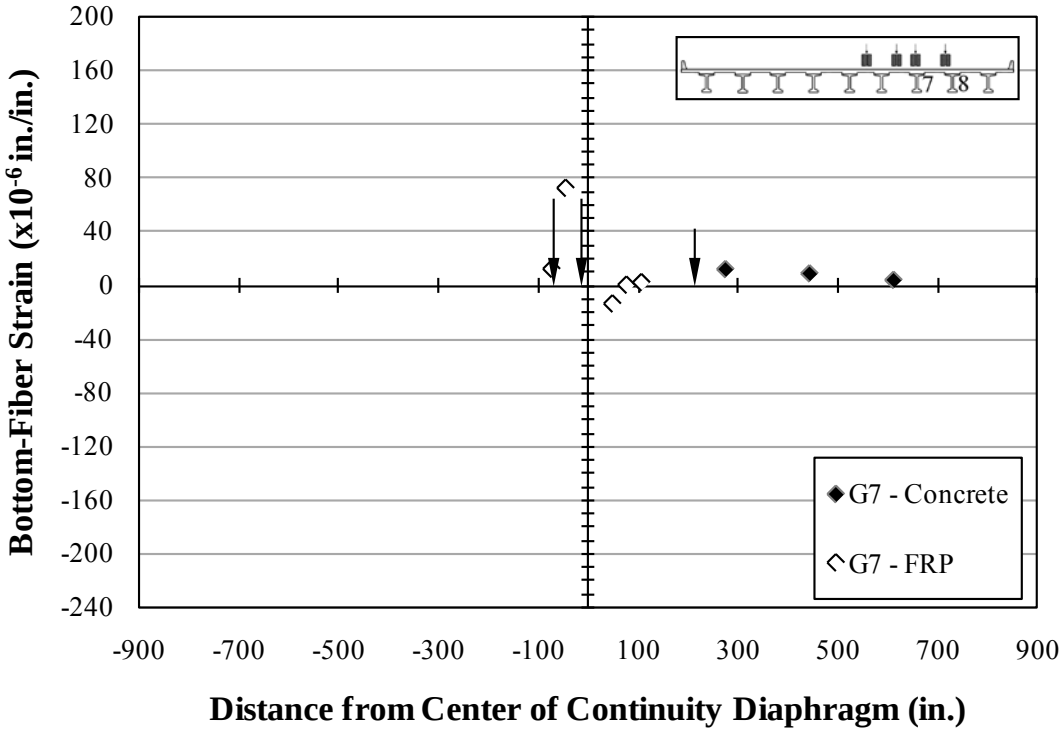

Figure B.104: Bottom-fiber strains—Girder 7—A5

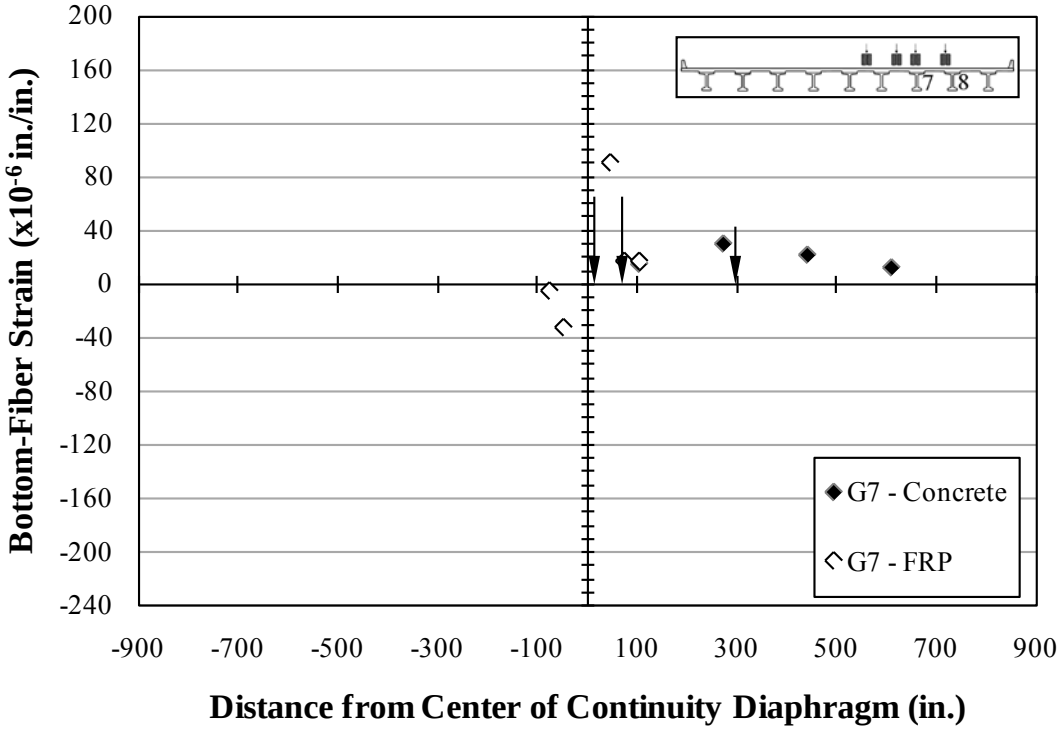

Figure B.105: Bottom-fiber strains—Girder 7—A6

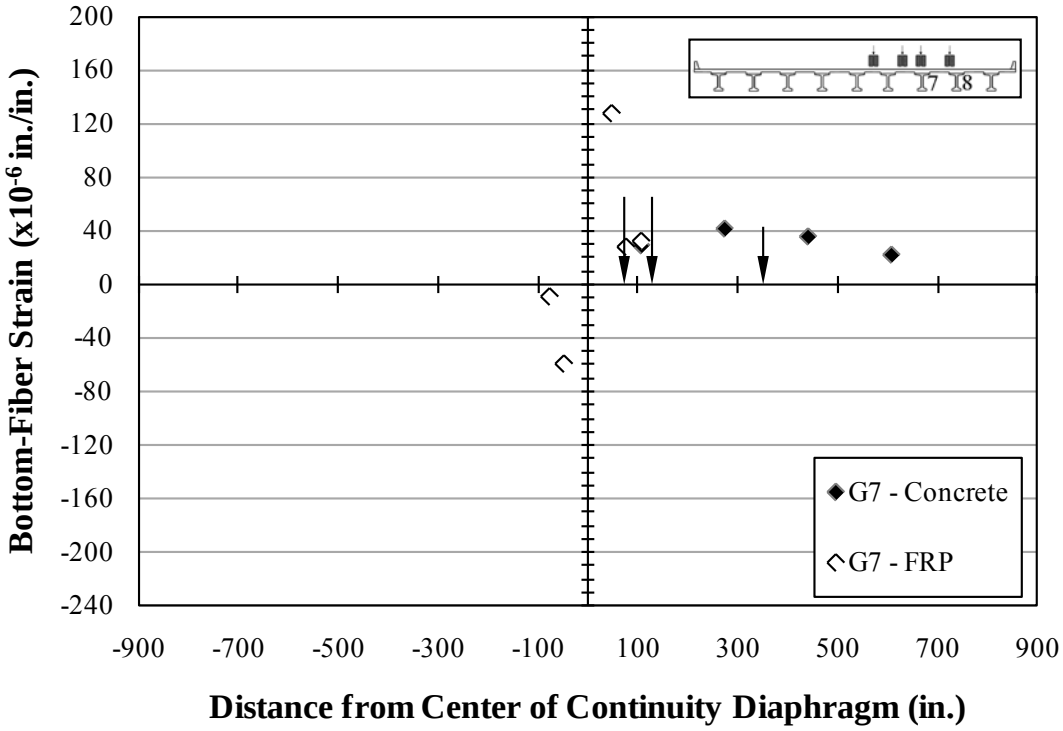

Figure B.106: Bottom-fiber strains—Girder 7—A7

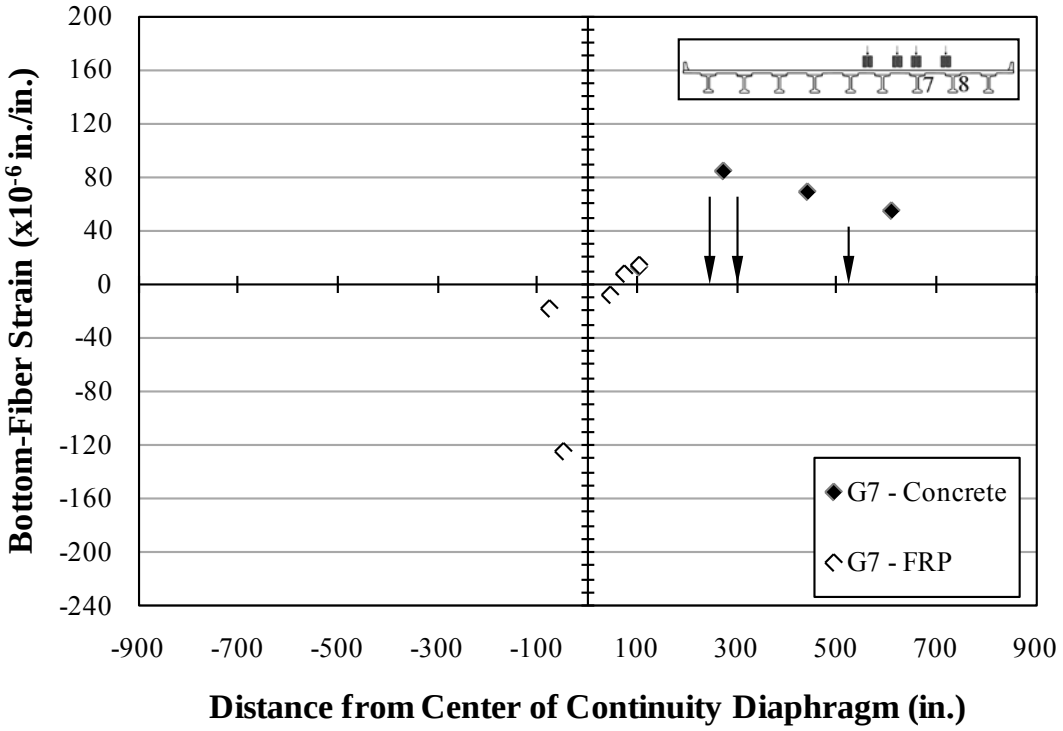

Figure B.107: Bottom-fiber strains—Girder 7—A8

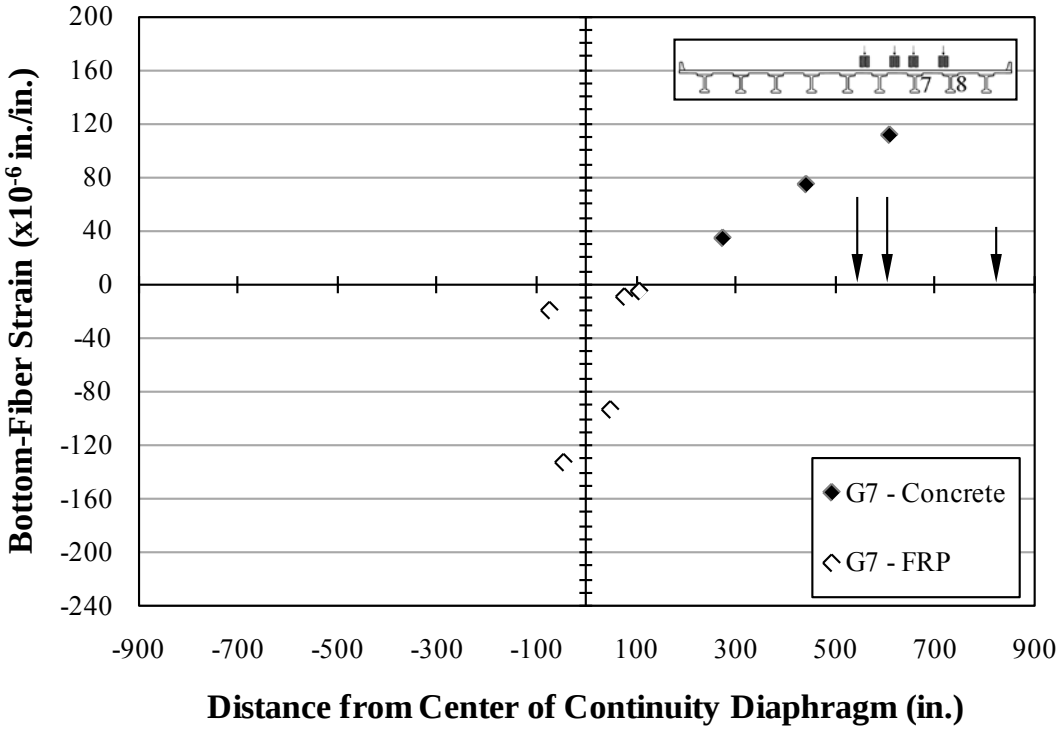

Figure B.108: Bottom-fiber strains—Girder 7—A9

B.1.4.2 Bottom-Fiber Strains—Girder 8

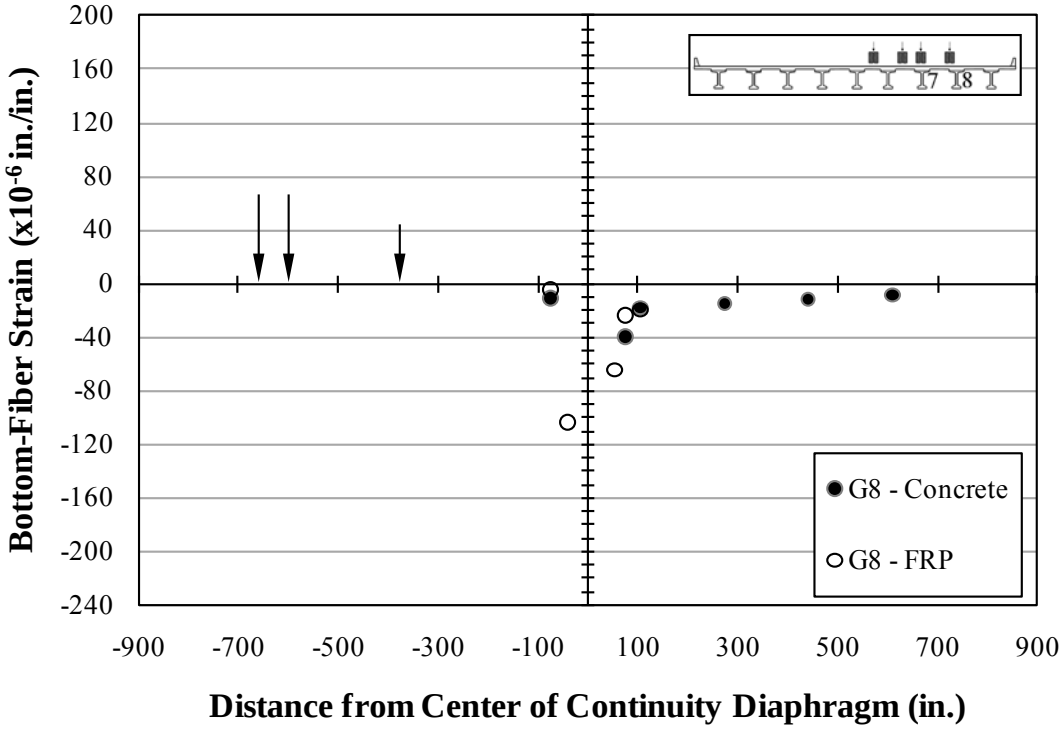

Figure B.109: Bottom-fiber strains—Girder 8—A1

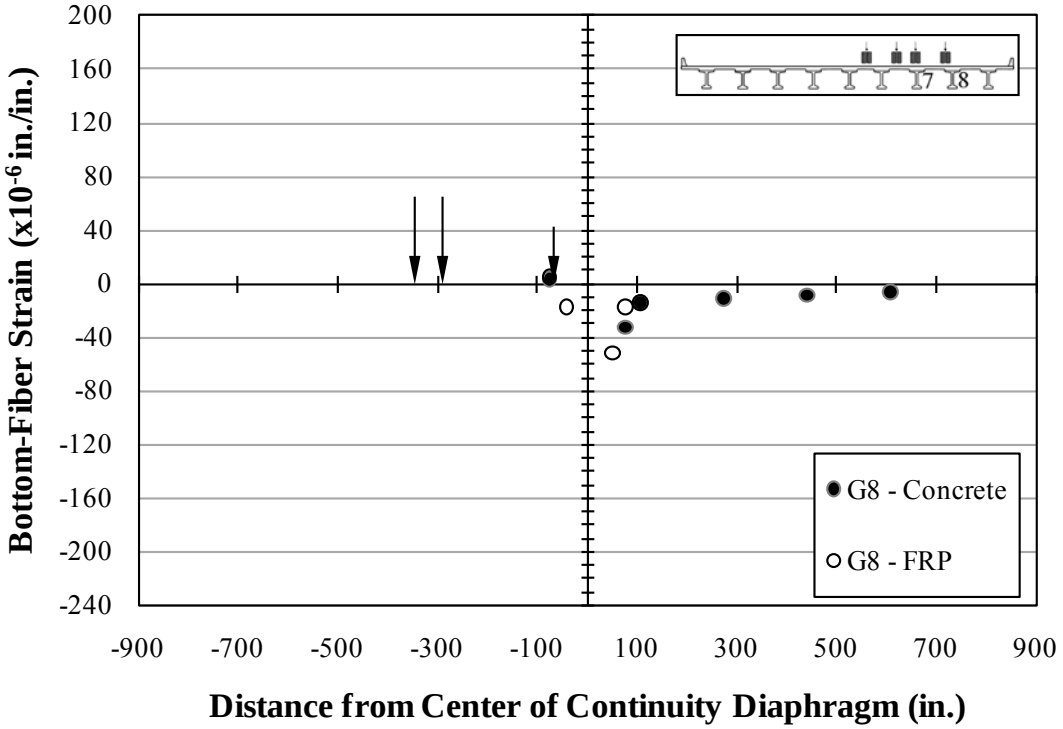

Figure B.110: Bottom-fiber strains—Girder 8—A2

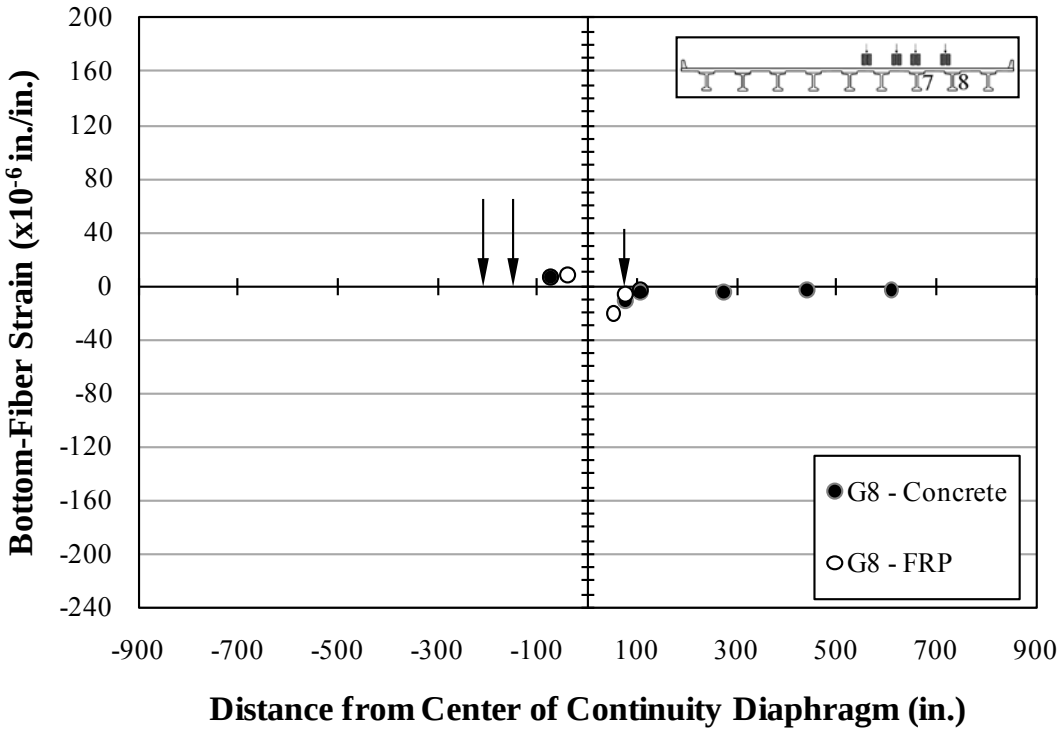

Figure B.111: Bottom-fiber strains—Girder 8—A3

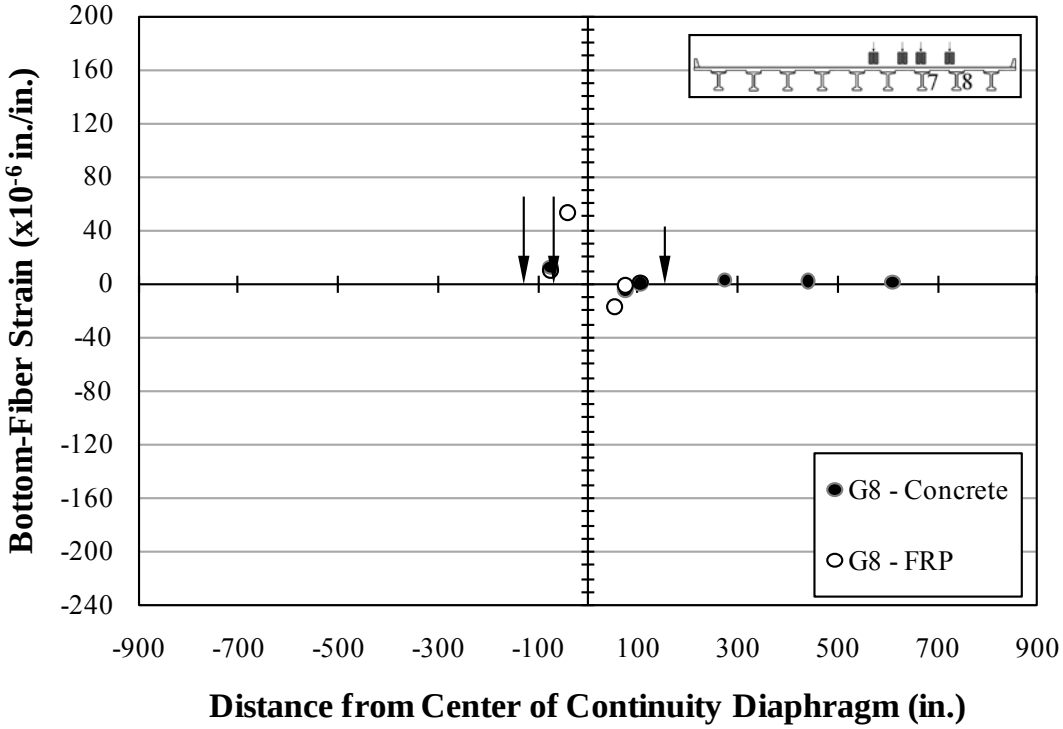

Figure B.112: Bottom-fiber strains—Girder 8—A4

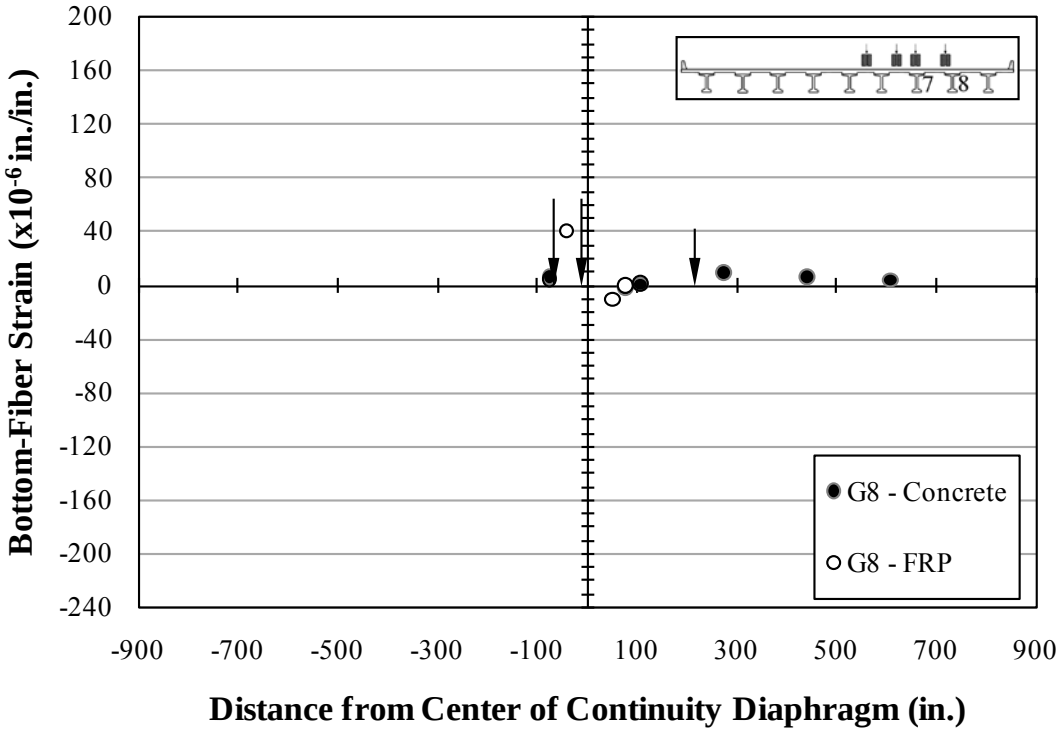

Figure B.113: Bottom-fiber strains—Girder 8—A5

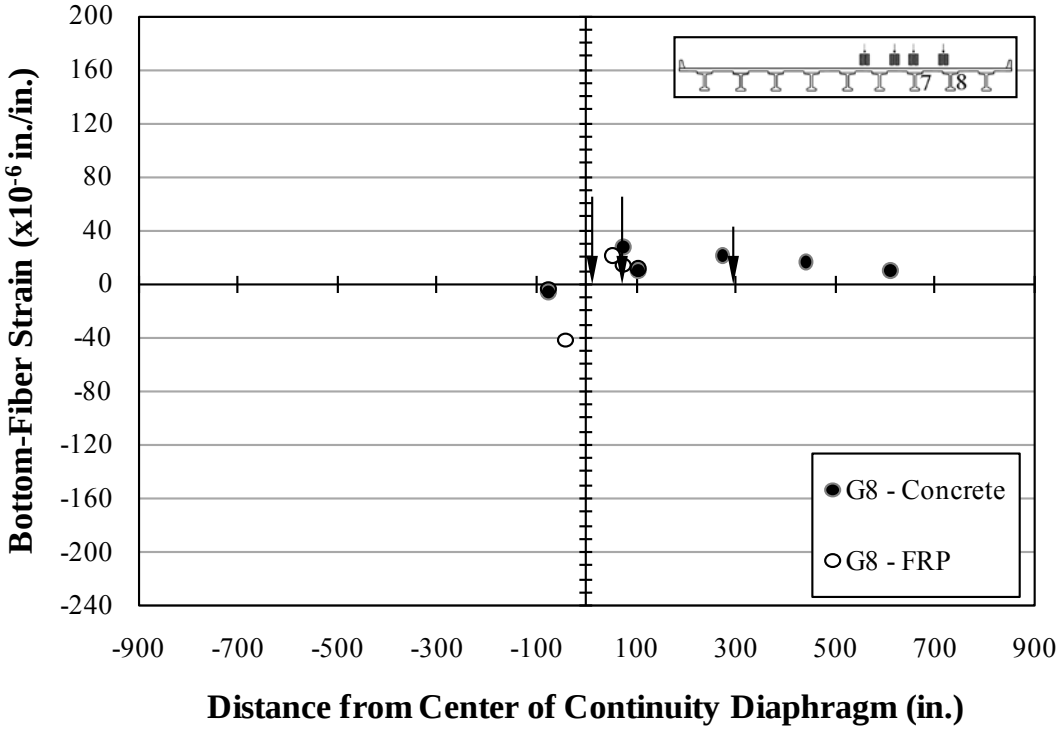

Figure B.114: Bottom-fiber strains—Girder 8—A6

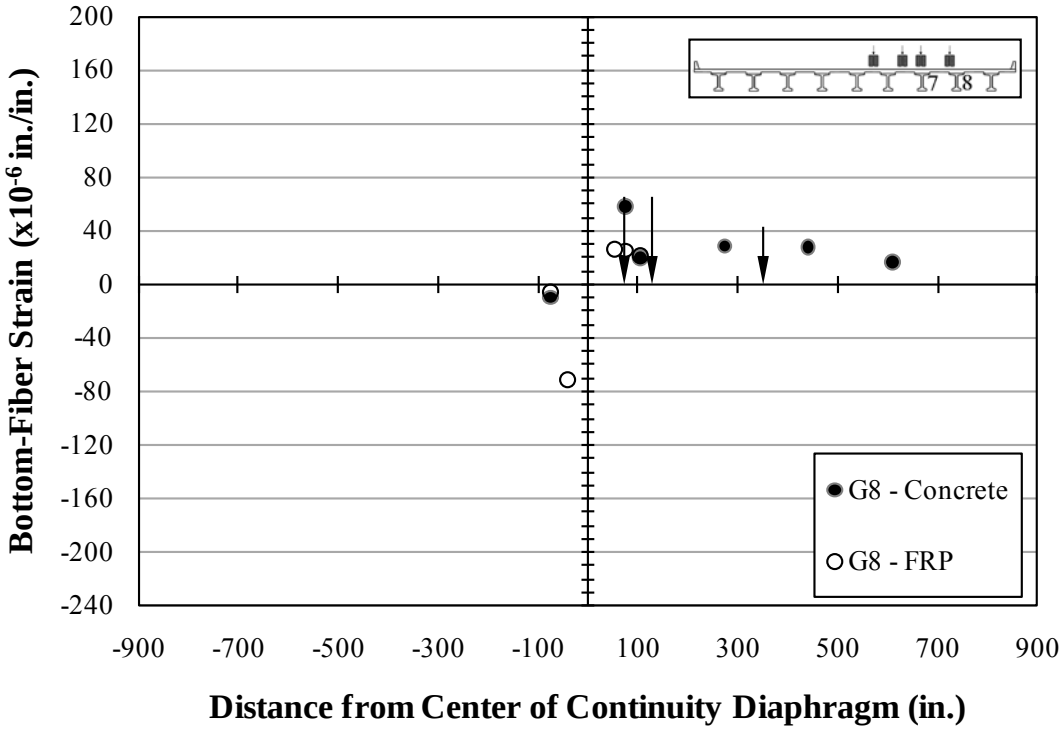

Figure B.115: Bottom-fiber strains—Girder 8—A7

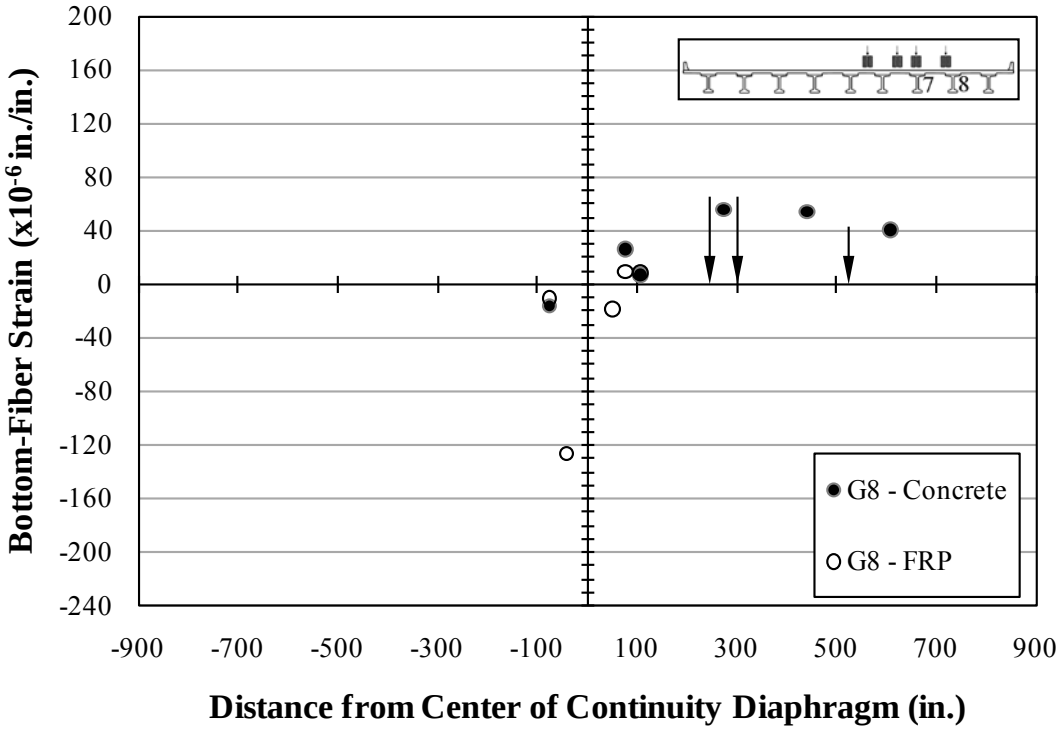

Figure B.116: Bottom-fiber strains—Girder 8—A8

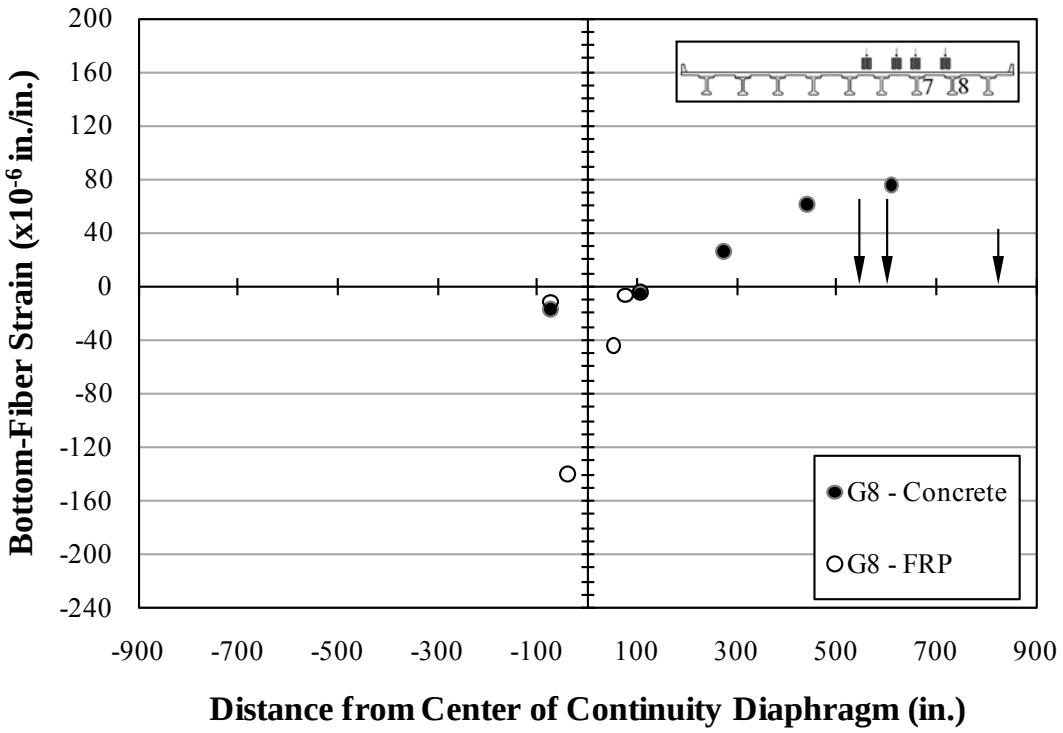

Figure B.117: Bottom-fiber strains—Girder 8—A9

B.2 LANE C

B.2.1 Crack-Opening Displacements

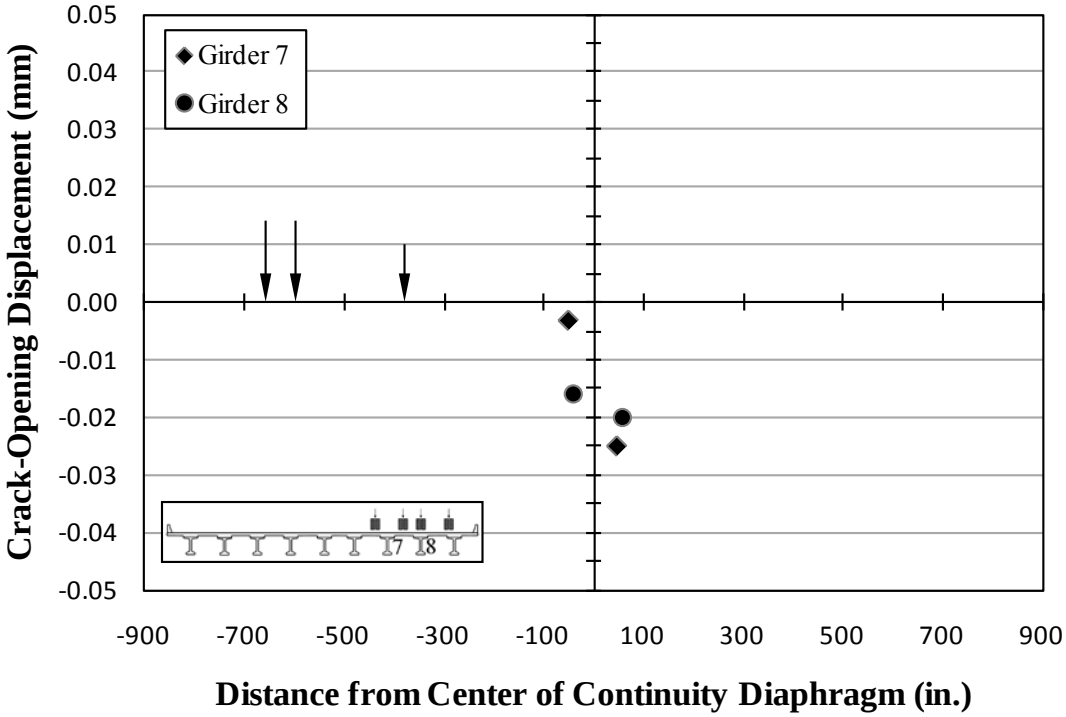

Figure B.118: Crack-opening displacements—C1

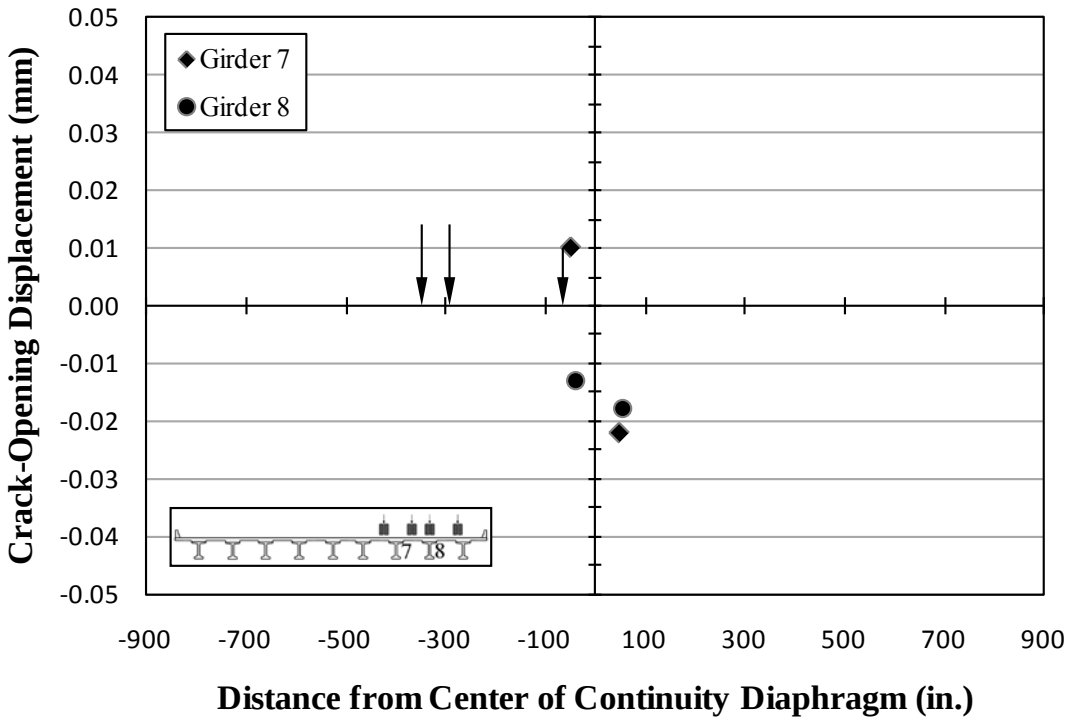

Figure B.119: Crack-opening displacements—C2

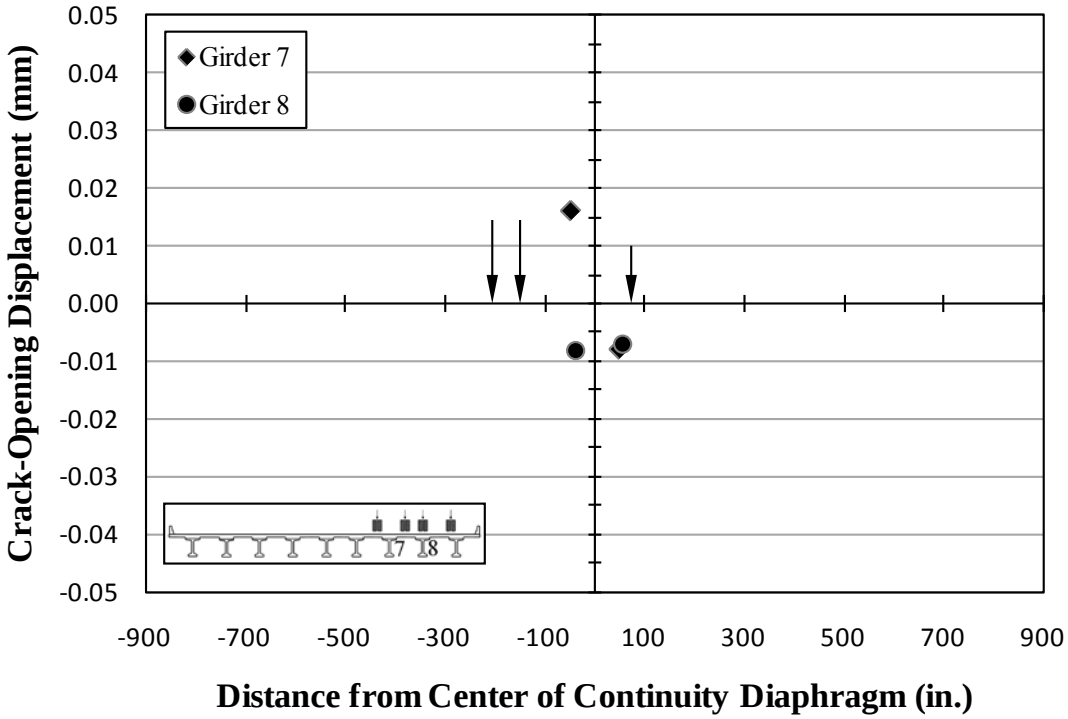

Figure B.120: Crack-opening displacements—C3

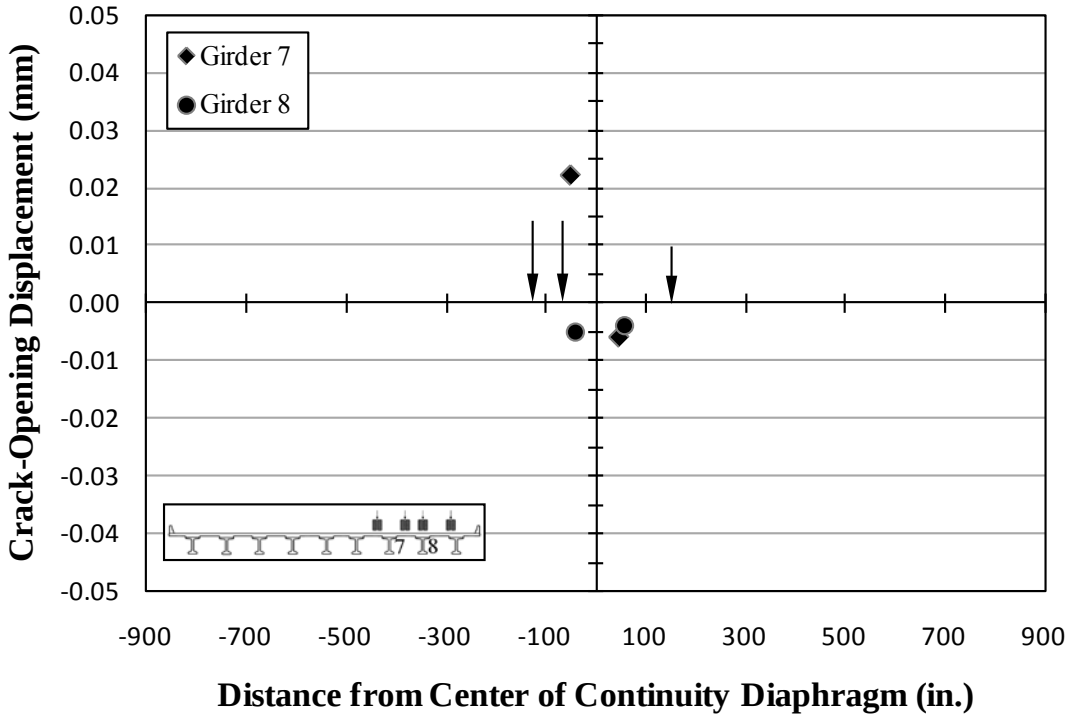

Figure B.121: Crack-opening displacements—C4

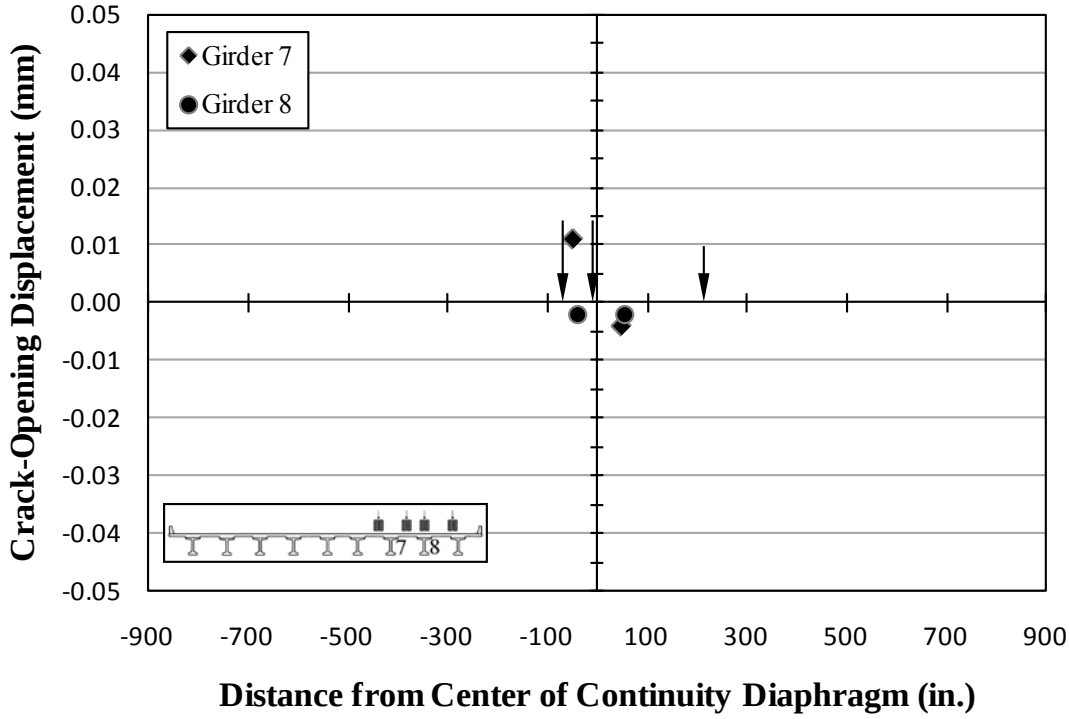

Figure B.122: Crack-opening displacements—C5

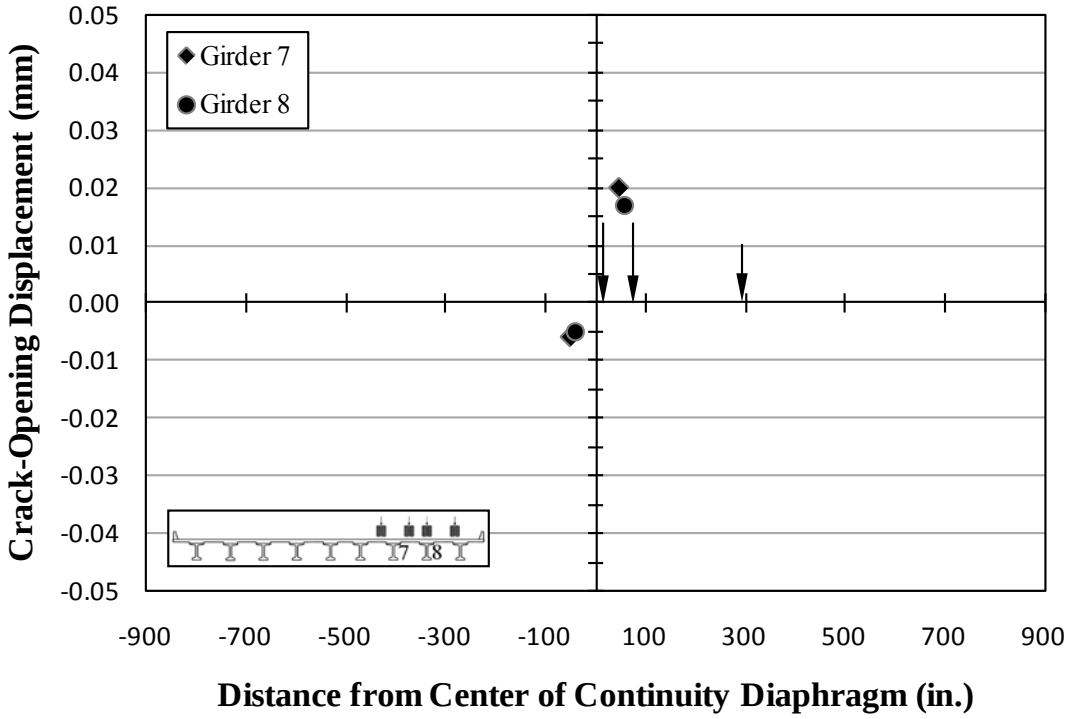

Figure B.123: Crack-opening displacements—C6

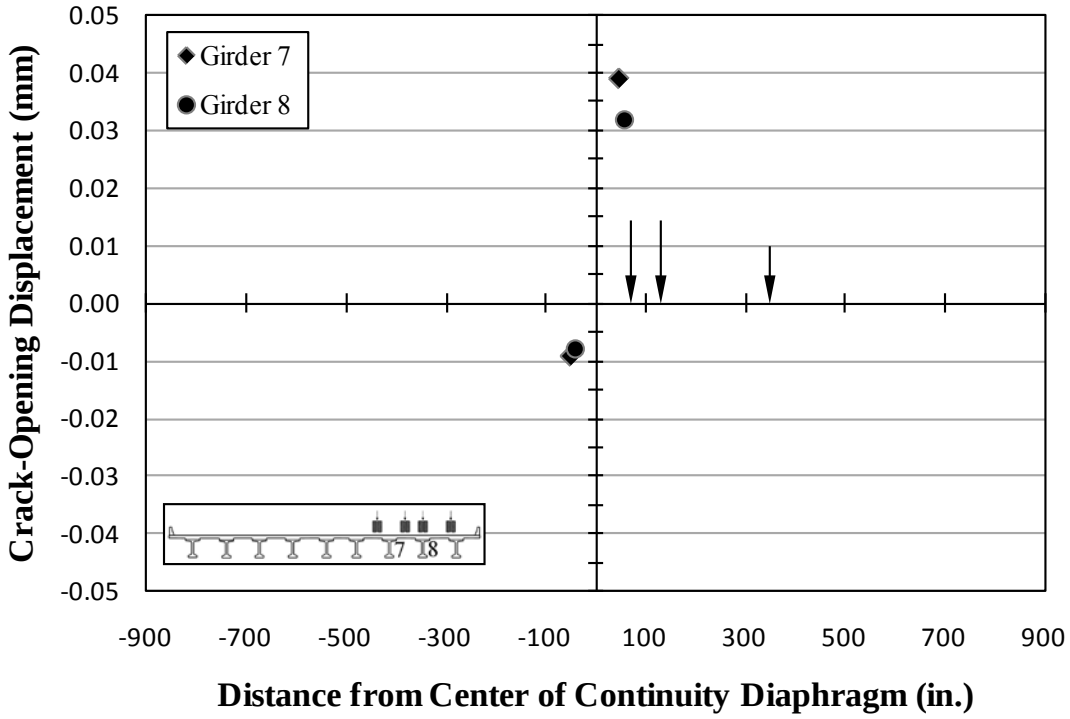

Figure B.124: Crack-opening displacements—C7

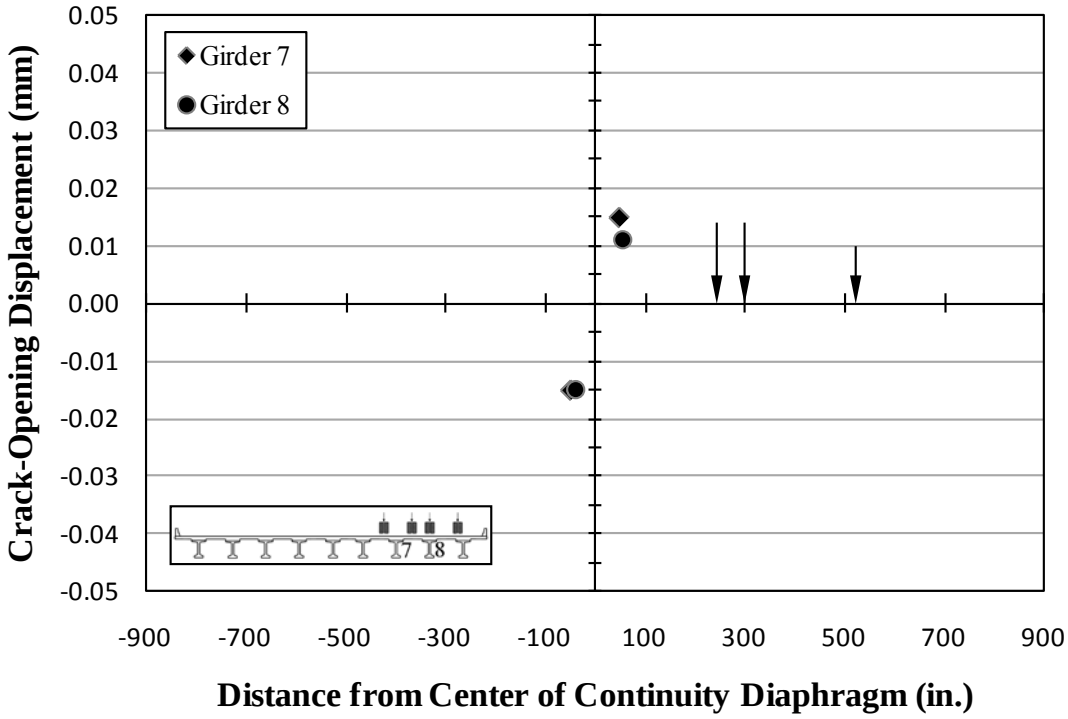

Figure B.125: Crack-opening displacements—C8

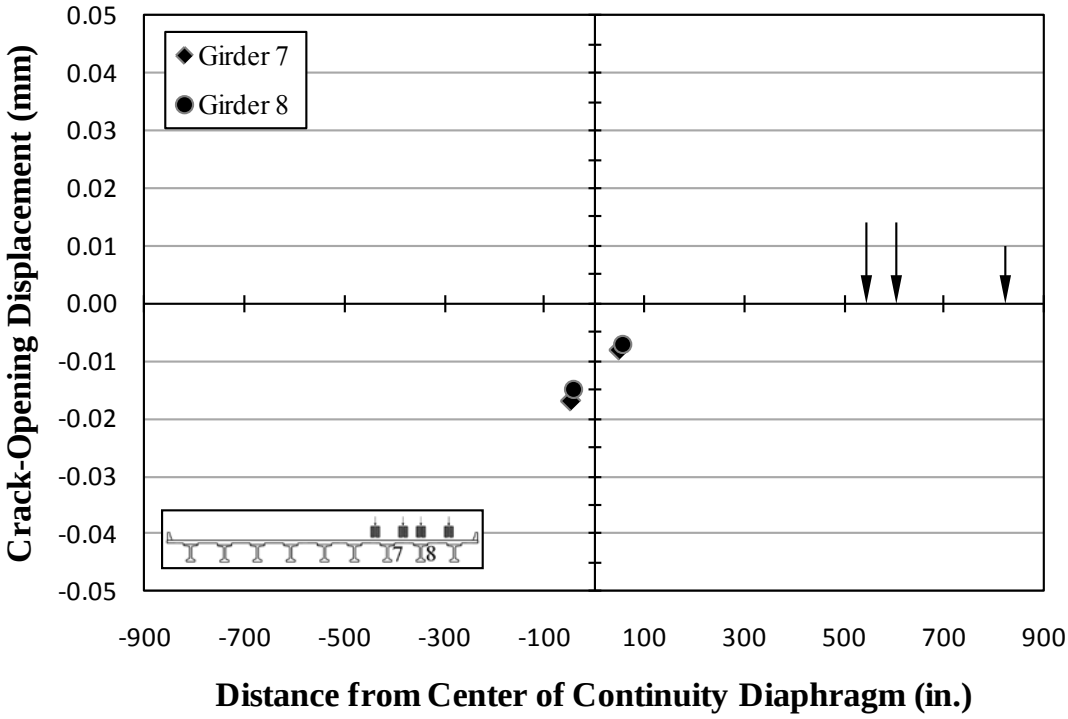

Figure B.126: Crack-opening displacements—C9

B.2.2 Deflections

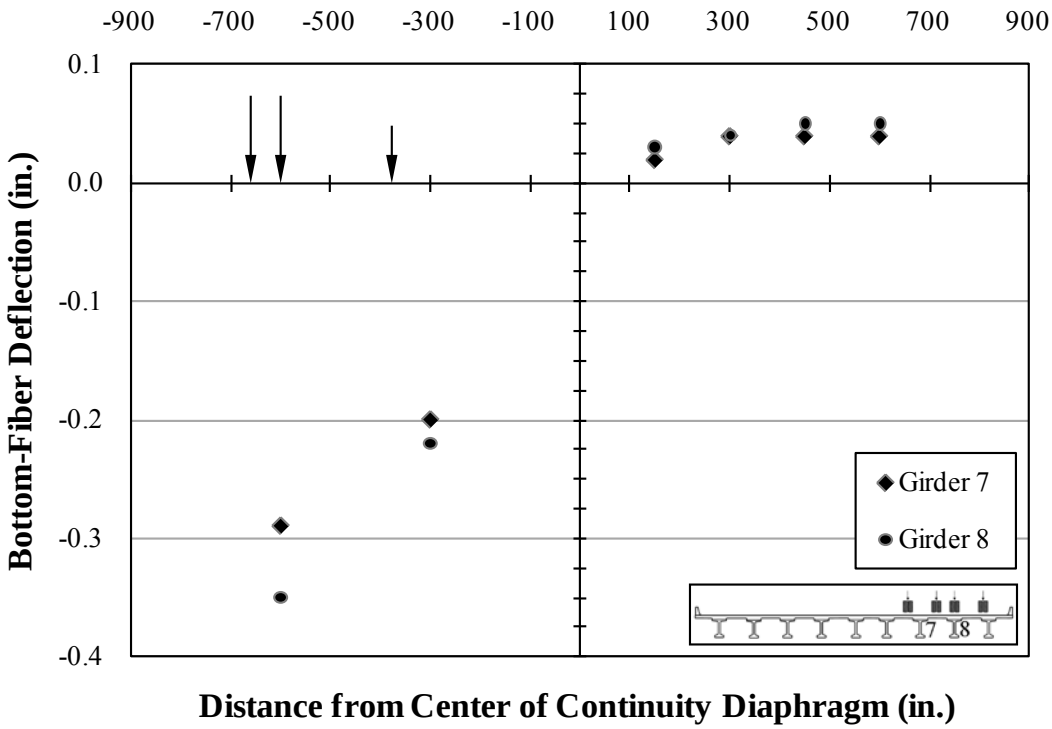

Figure B.127: Deflections—C1

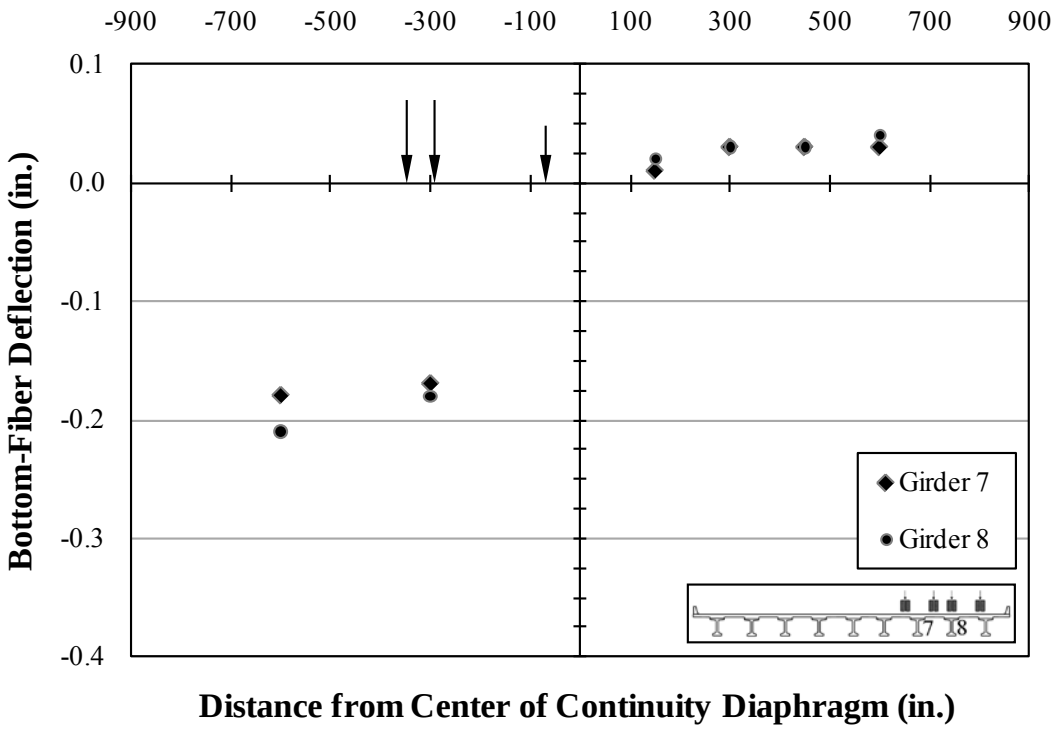

Figure B.128: Deflections—C2

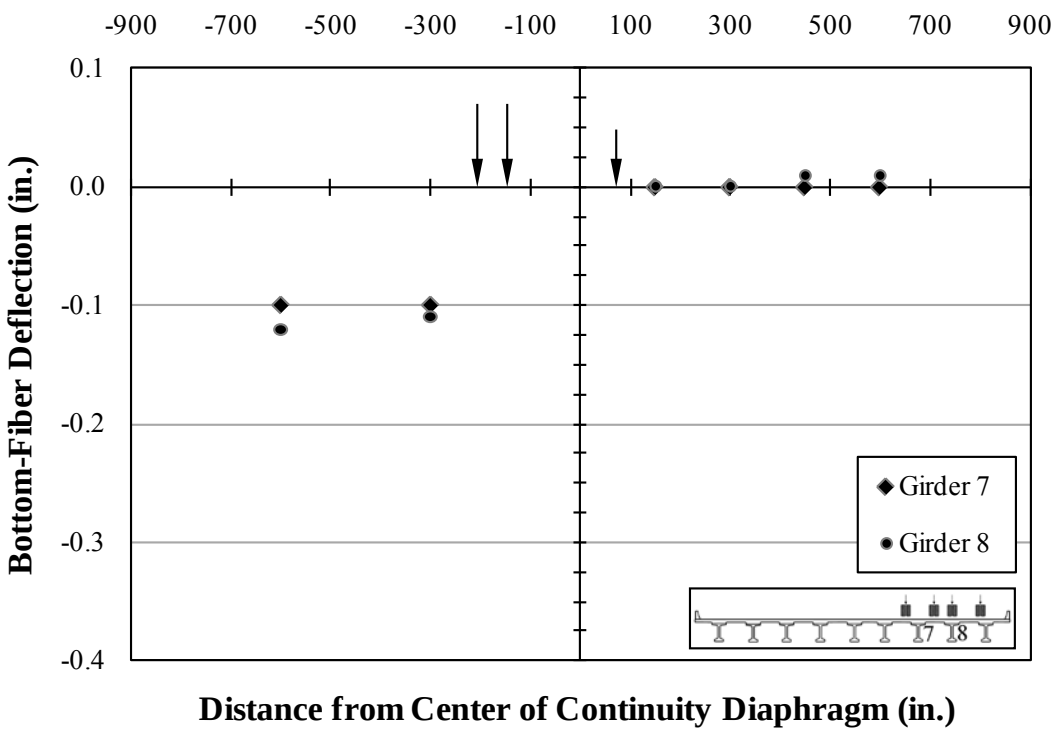

Figure B.129: Deflections—C3

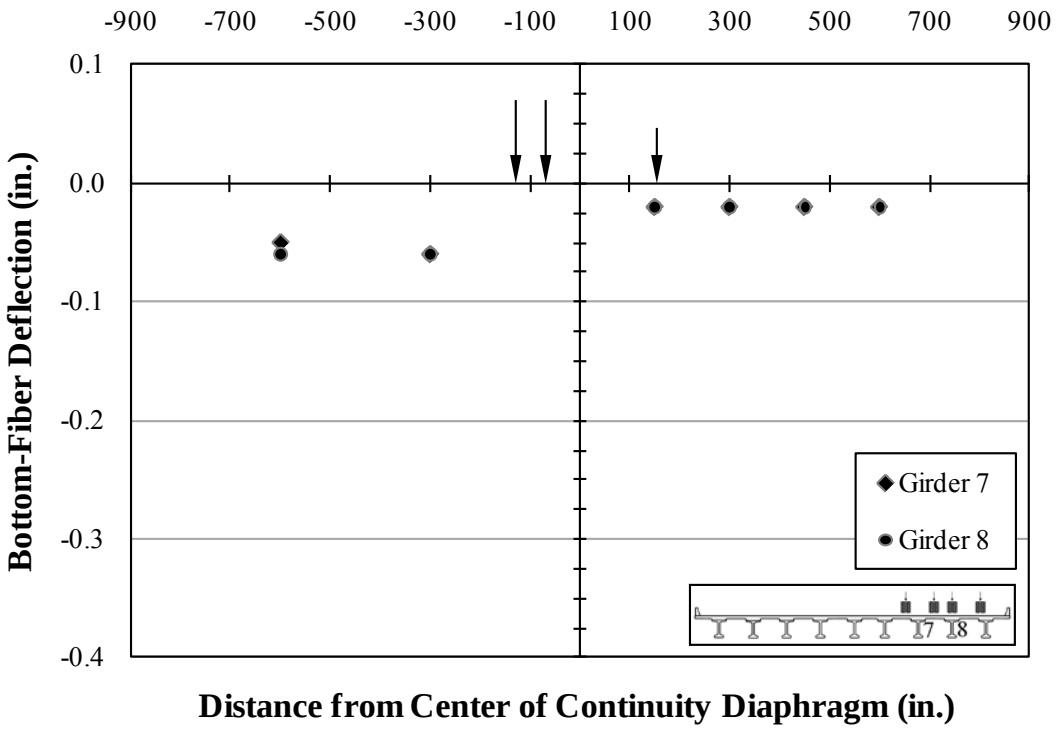

Figure B.130: Deflections—C4

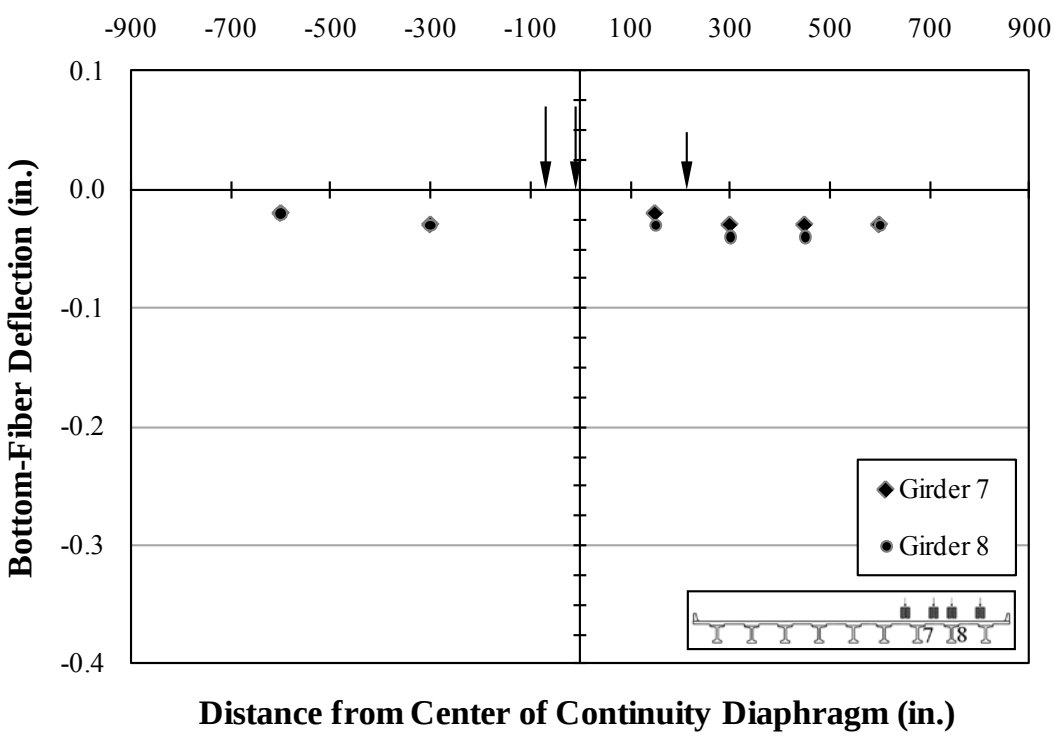

Figure B.131: Deflections—C5

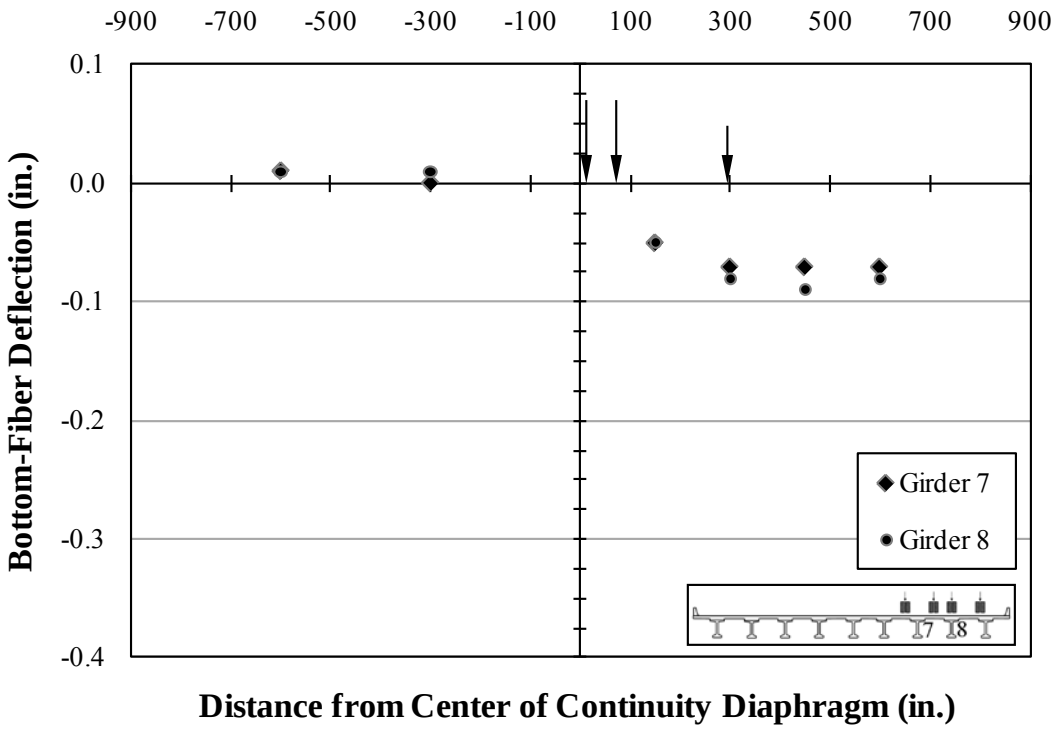

Figure B.132: Deflections—C6

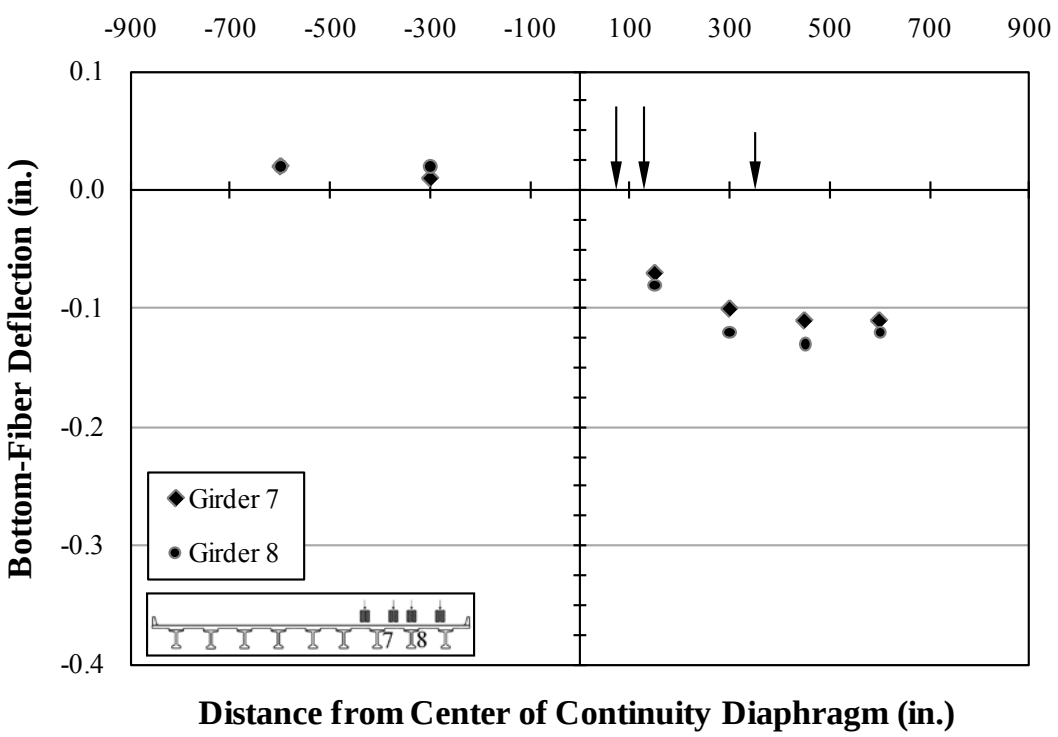

Figure B.133: Deflections—C7

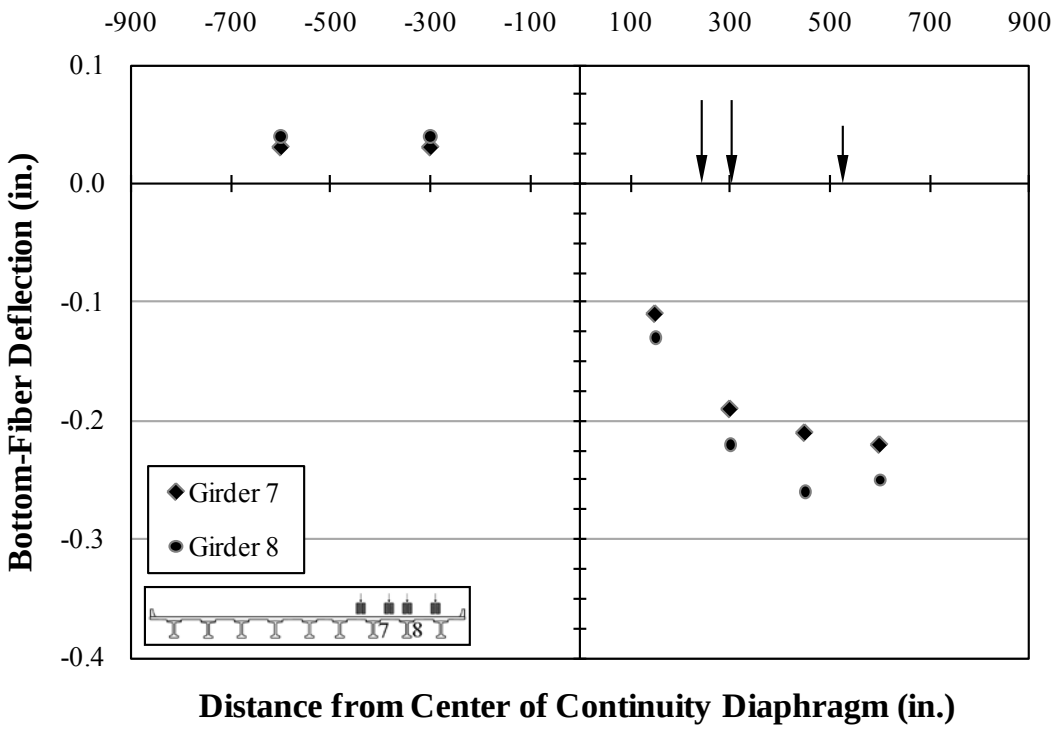

Figure B.134: Deflections—C8

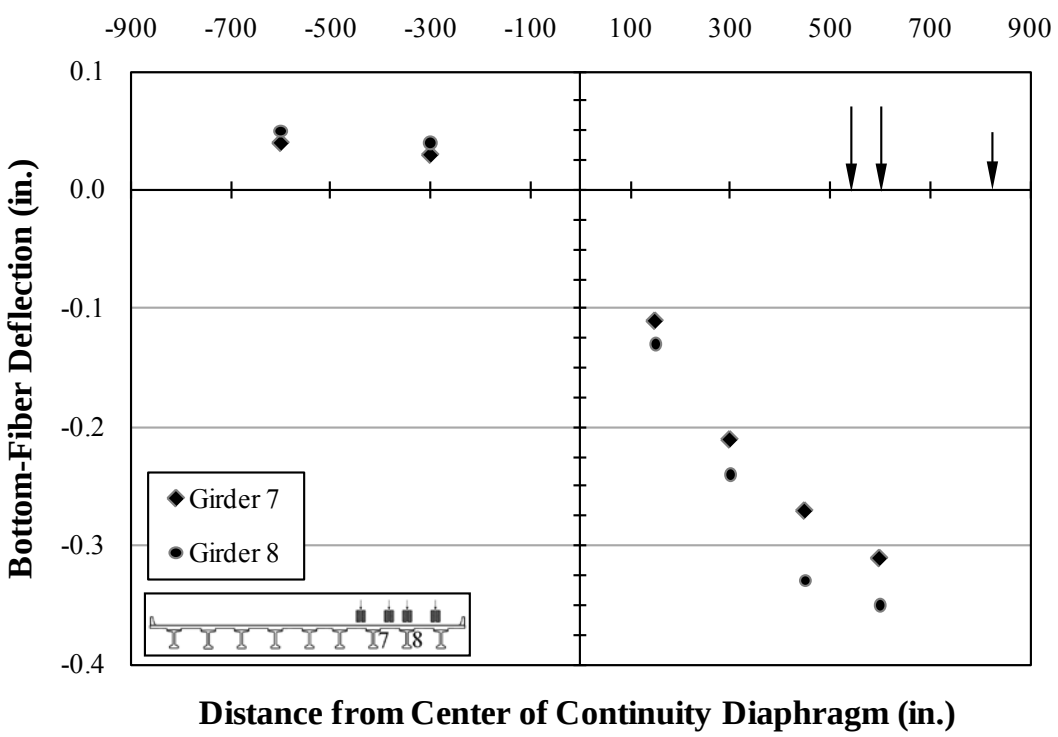

Figure B.135: Deflections—C9

B.2.3 Cross-Section Strains

B.2.3.1 Cross-Section Strains—Girder 7

B.2.3.1.1 Strains—Girder 7—Cross Section 1

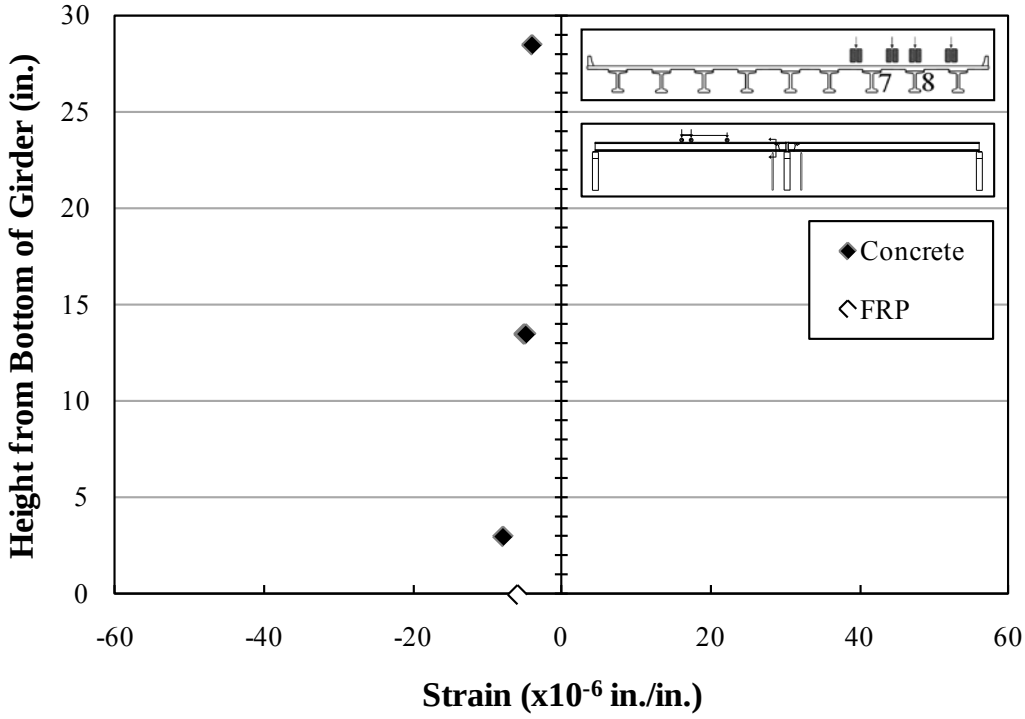

Figure B.136: Strains—Girder 7—Section 1—C1

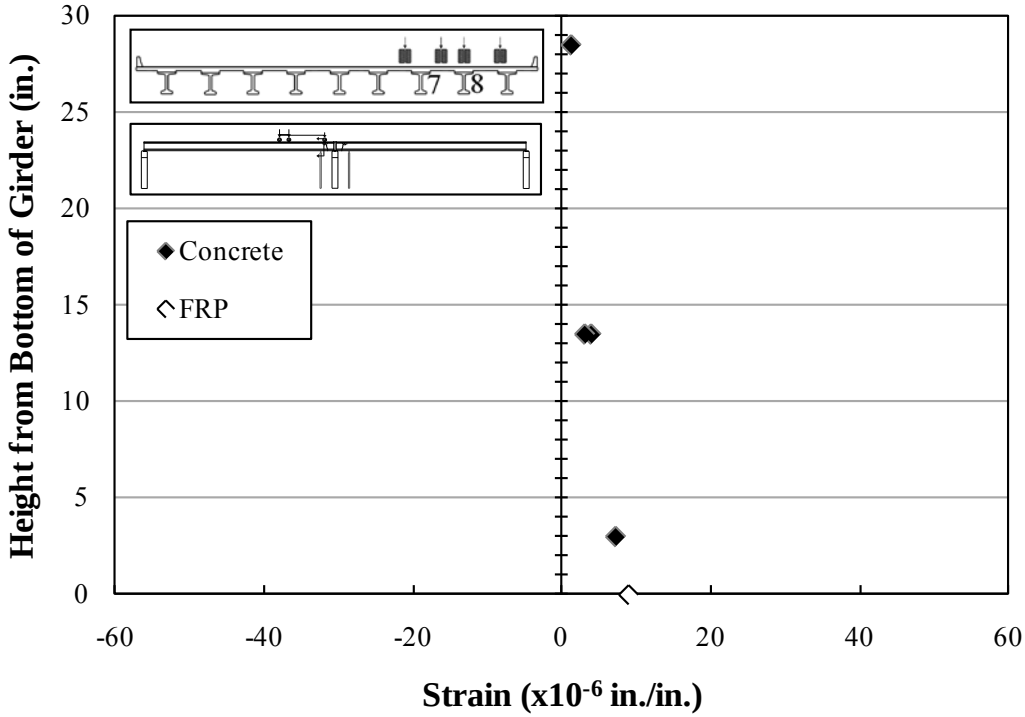

Figure B.137: Strains—Girder 7—Section 1—C2

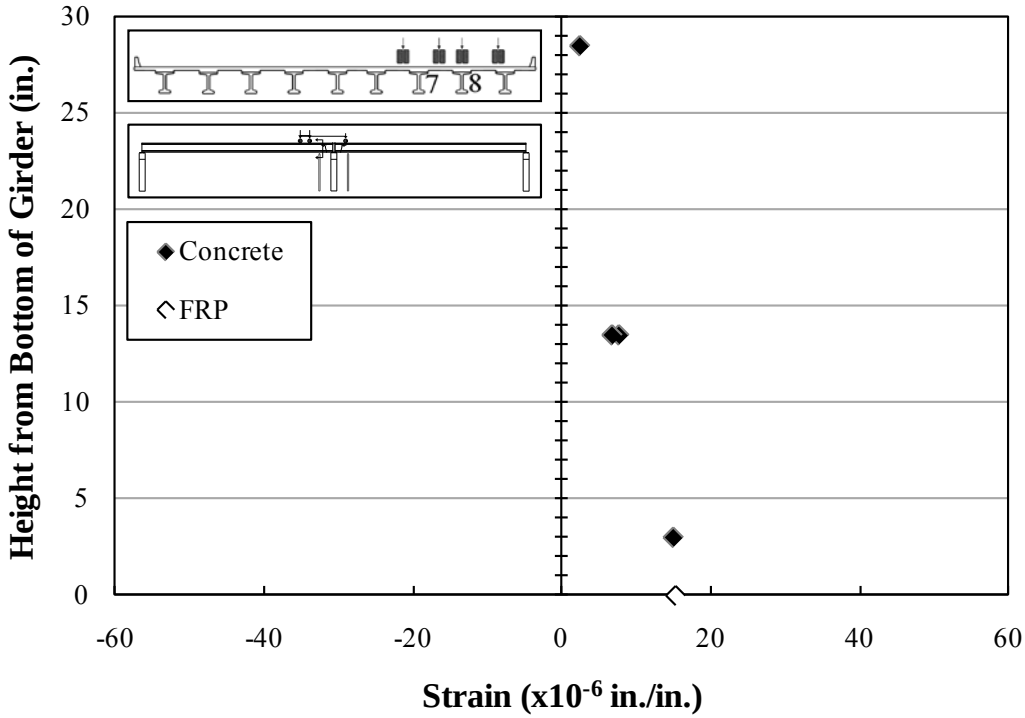

Figure B.138: Strains—Girder 7—Section 1—C3

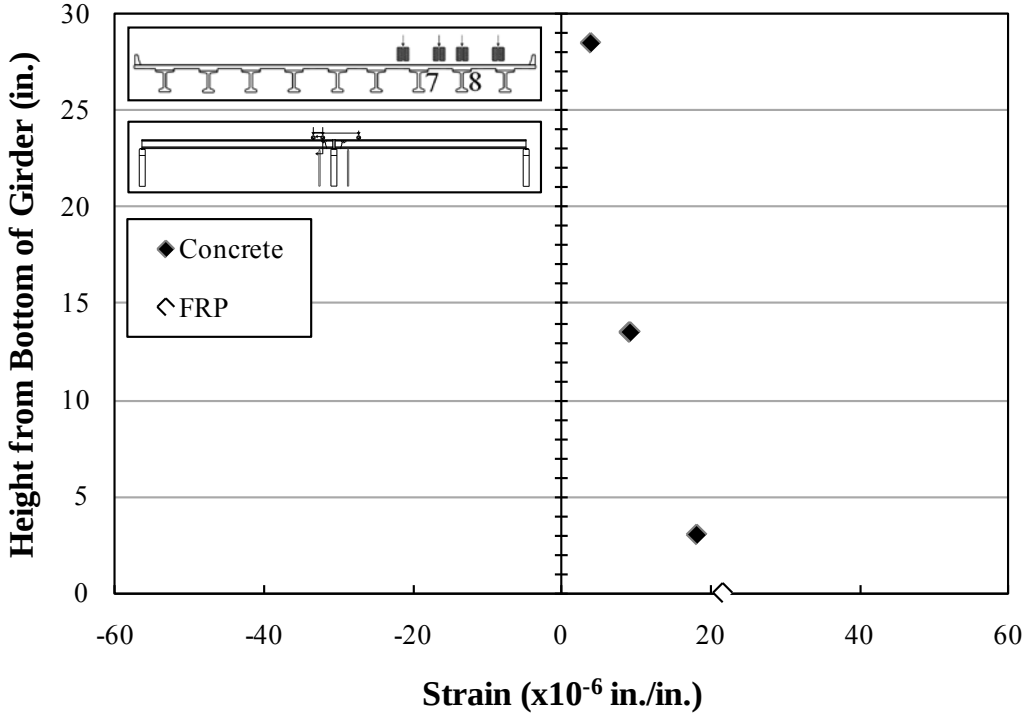

Figure B.139: Strains—Girder 7—Section 1—C4

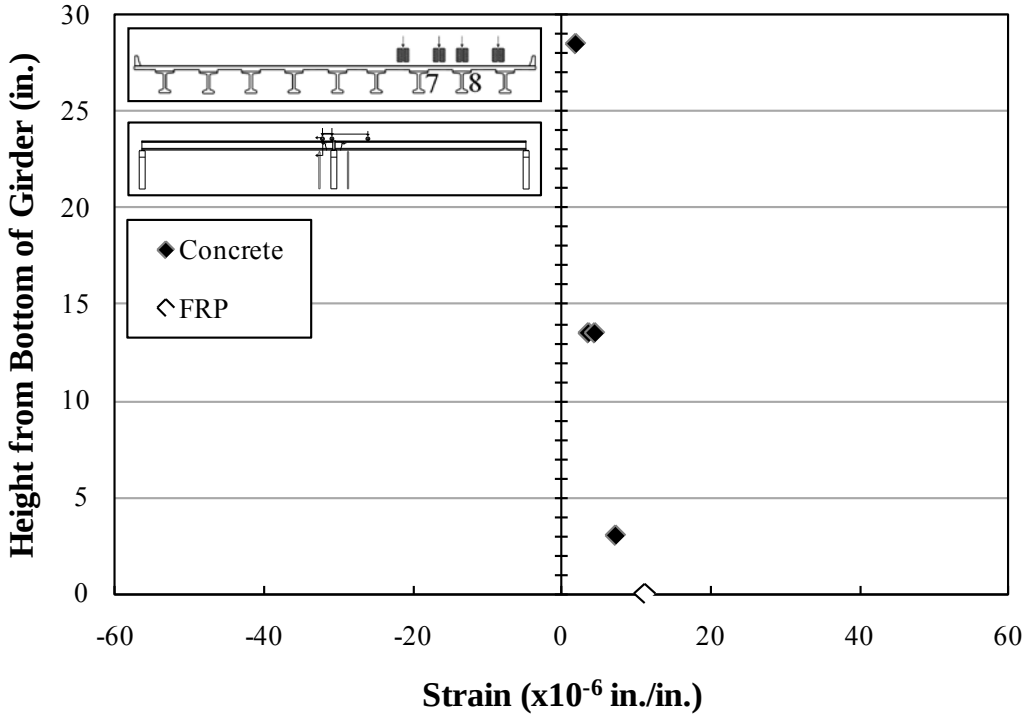

Figure B.140: Strains—Girder 7—Section 1—C5

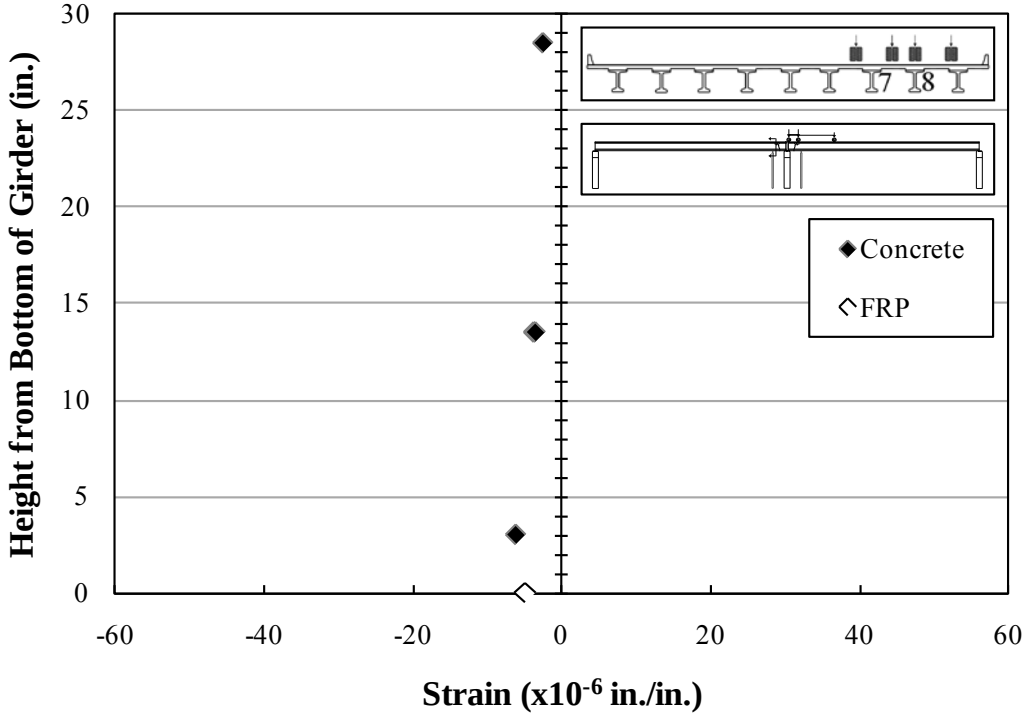

Figure B.141: Strains—Girder 7—Section 1—C6

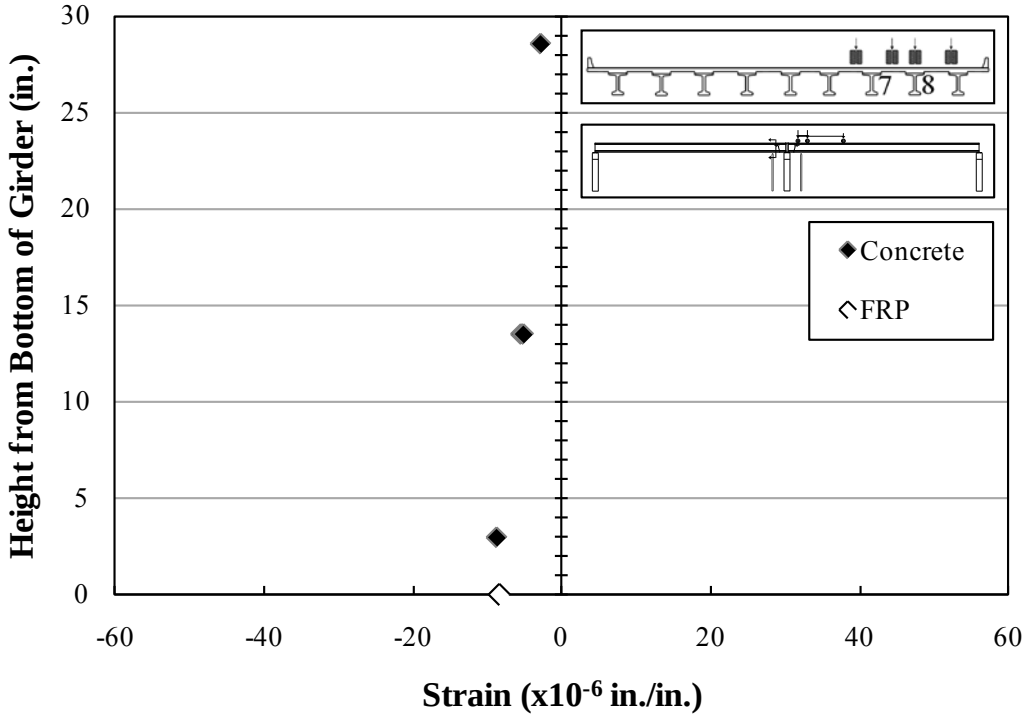

Figure B.142: Strains—Girder 7—Section 1—C7

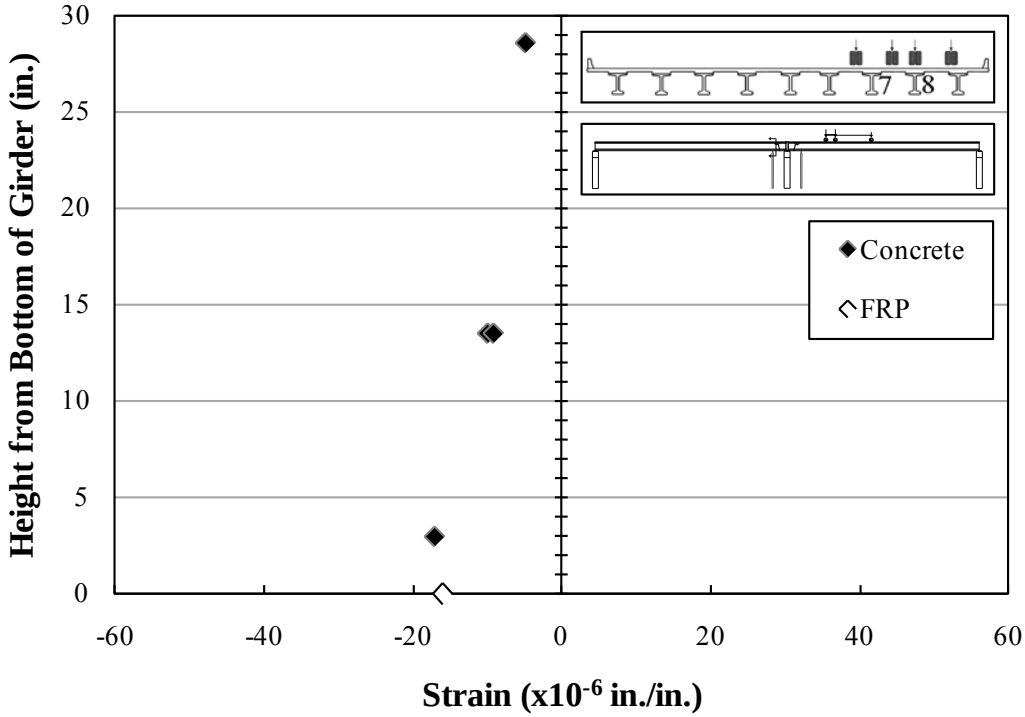

Figure B.143: Strains—Girder 7—Section 1—C8

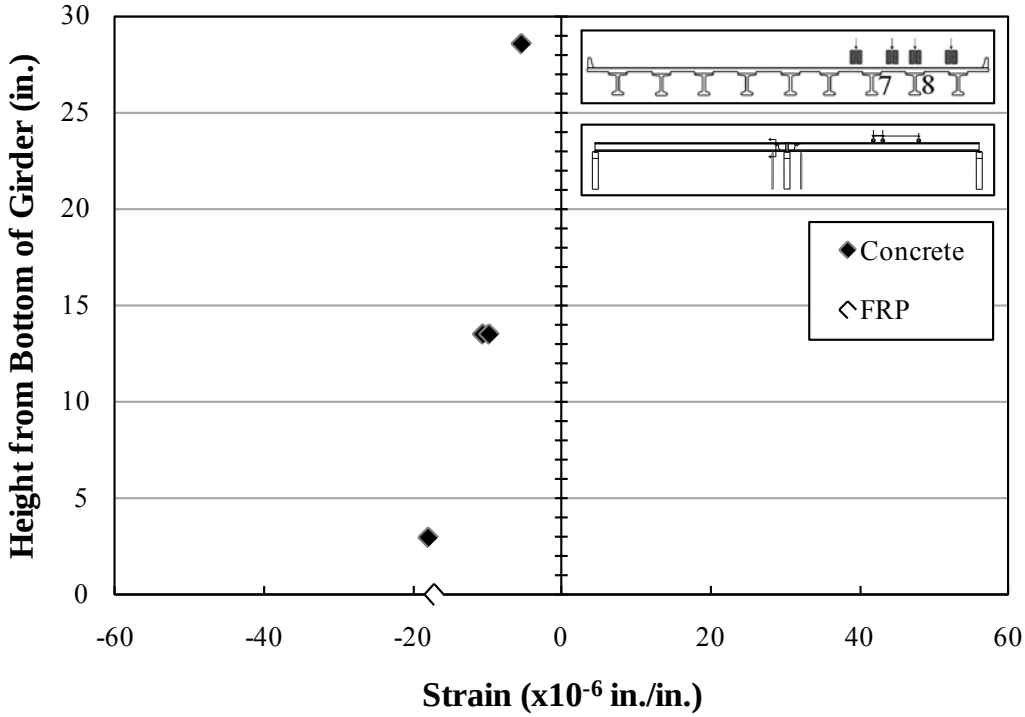

Figure B.144: Strains—Girder 7—Section 1—C9

B.2.3.1.2 Strains—Girder 7—Cross Section 2

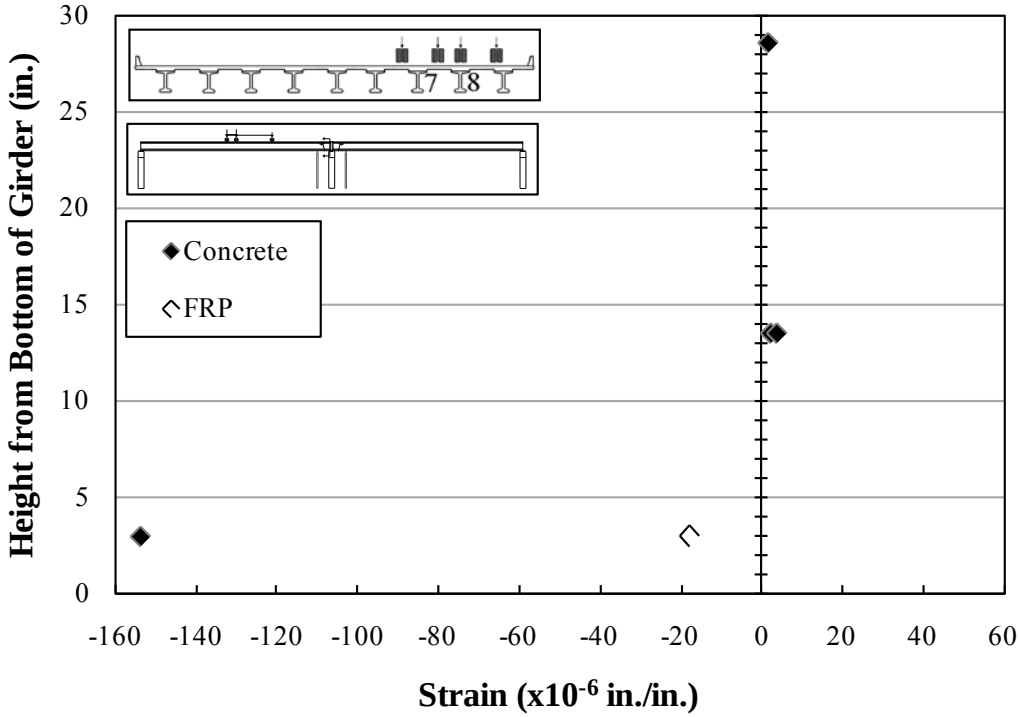

Figure B.145: Strains—Girder 7—Section 2—C1

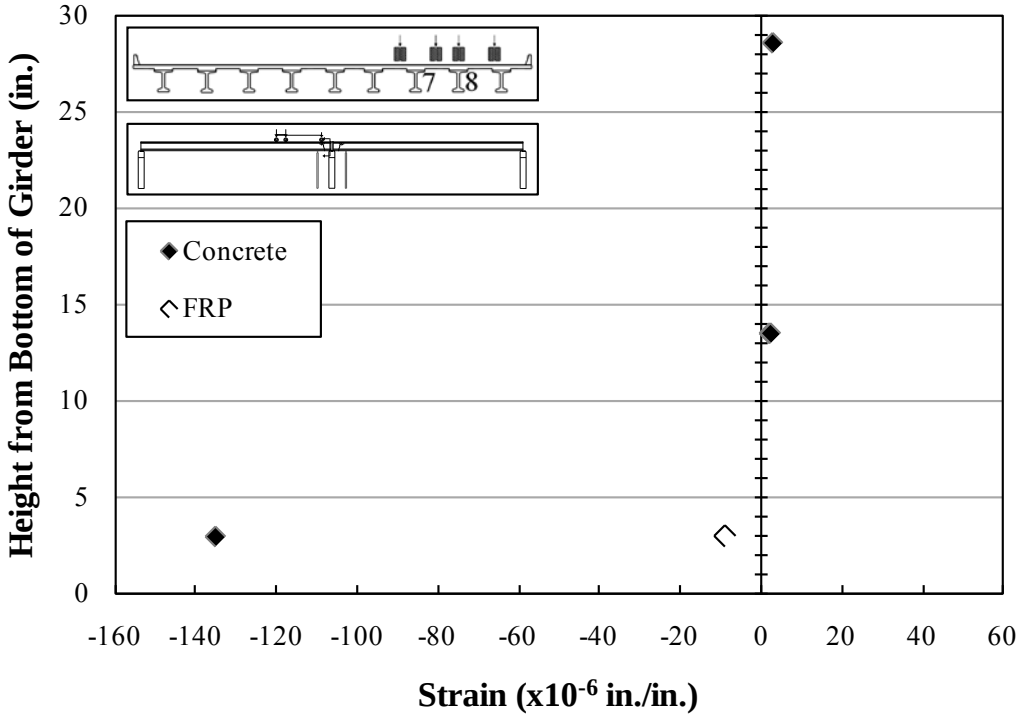

Figure B.146: Strains—Girder 7—Section 2—C2

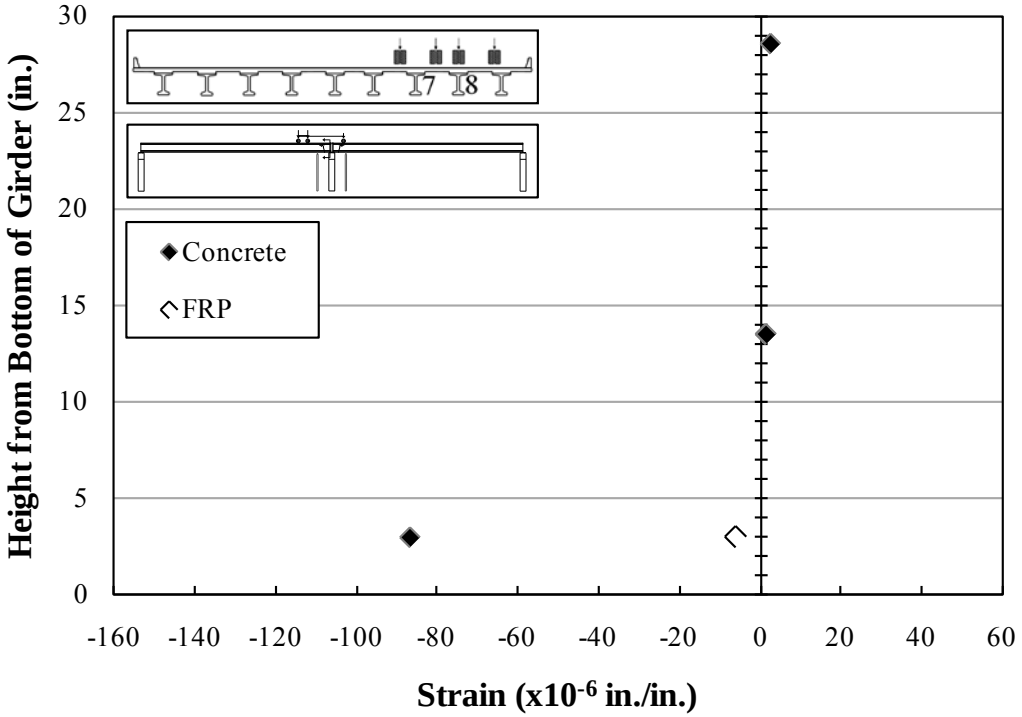

Figure B.147: Strains—Girder 7—Section 2—C3

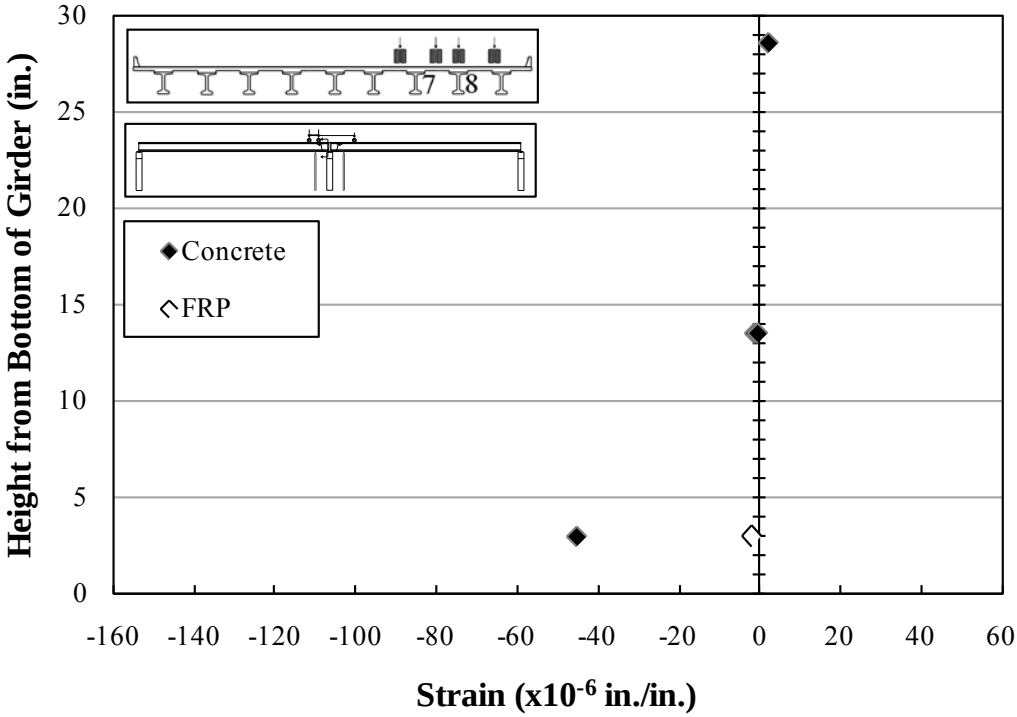

Figure B.148: Strains—Girder 7—Section 2—C4

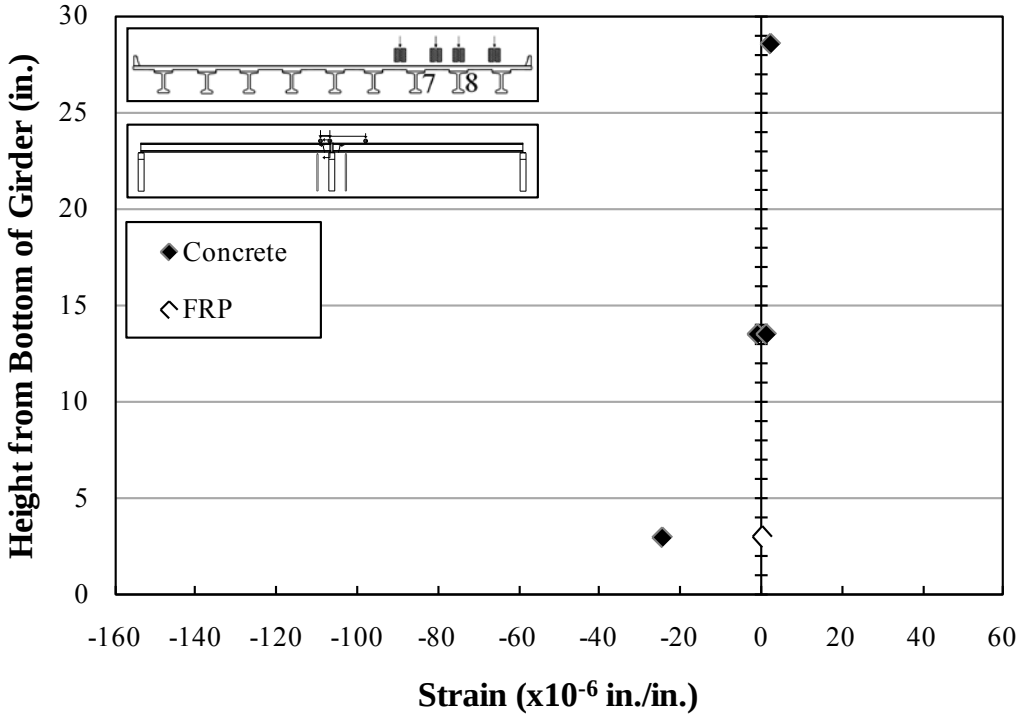

Figure B.149: Strains—Girder 7—Section 2—C5

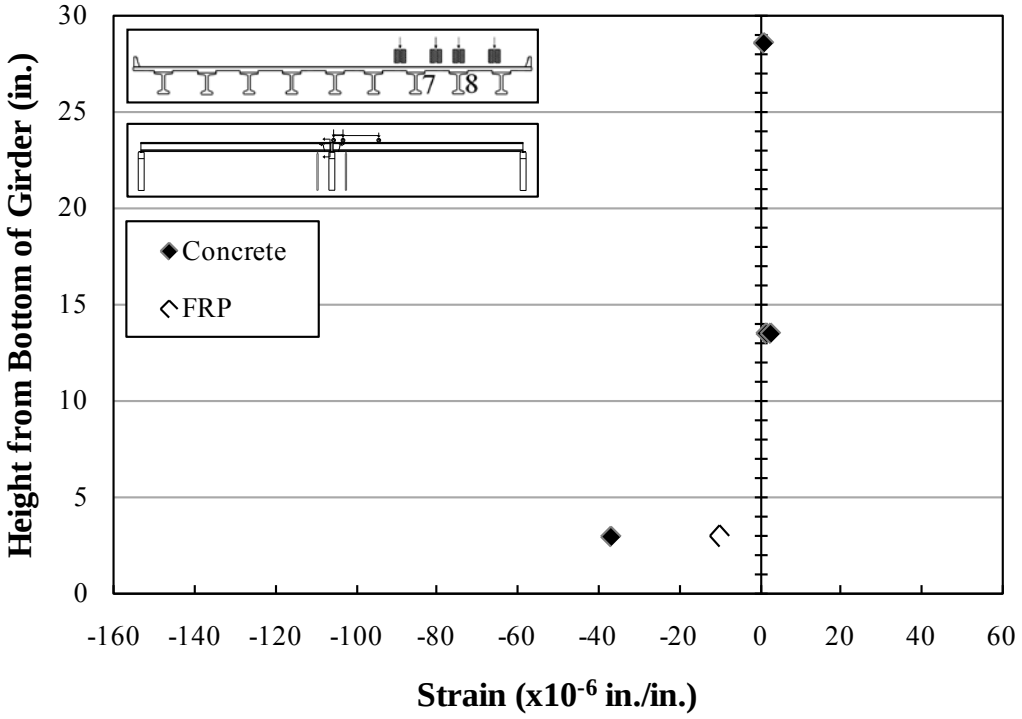

Figure B.150: Strains—Girder 7—Section 2—C6

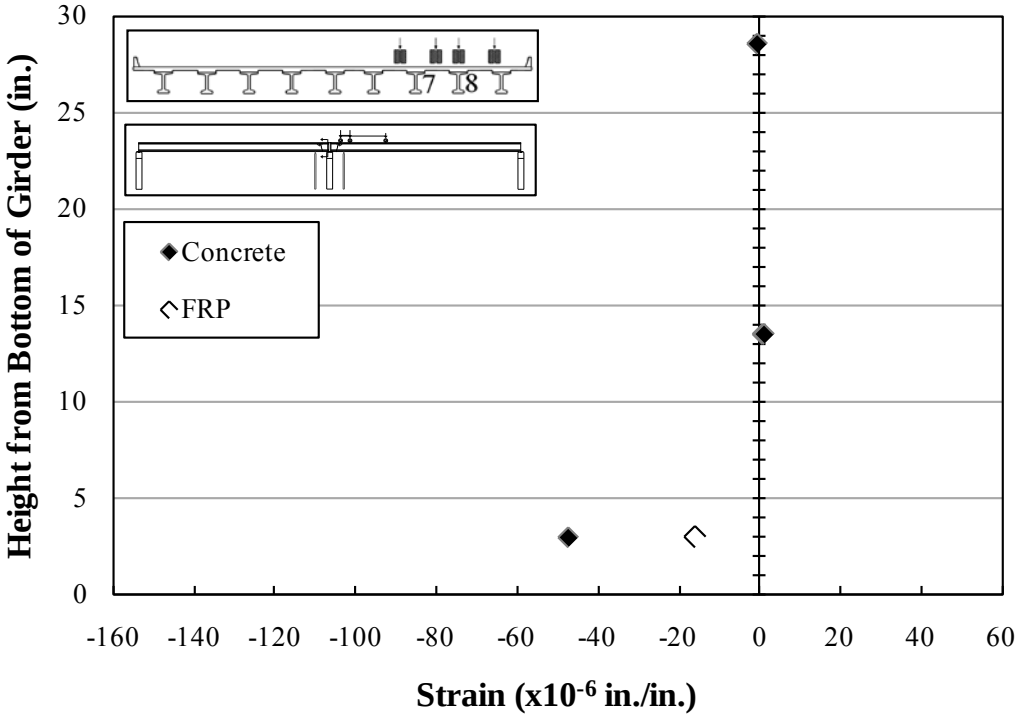

Figure B.151: Strains—Girder 7—Section 2—C7

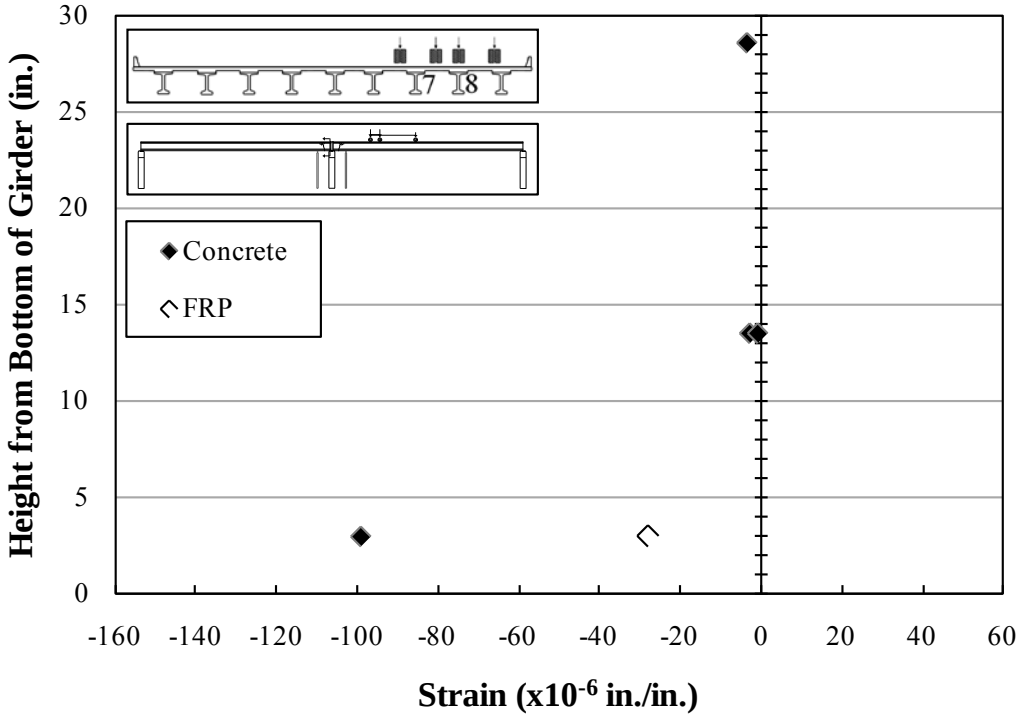

Figure B.152: Strains—Girder 7—Section 2—C8

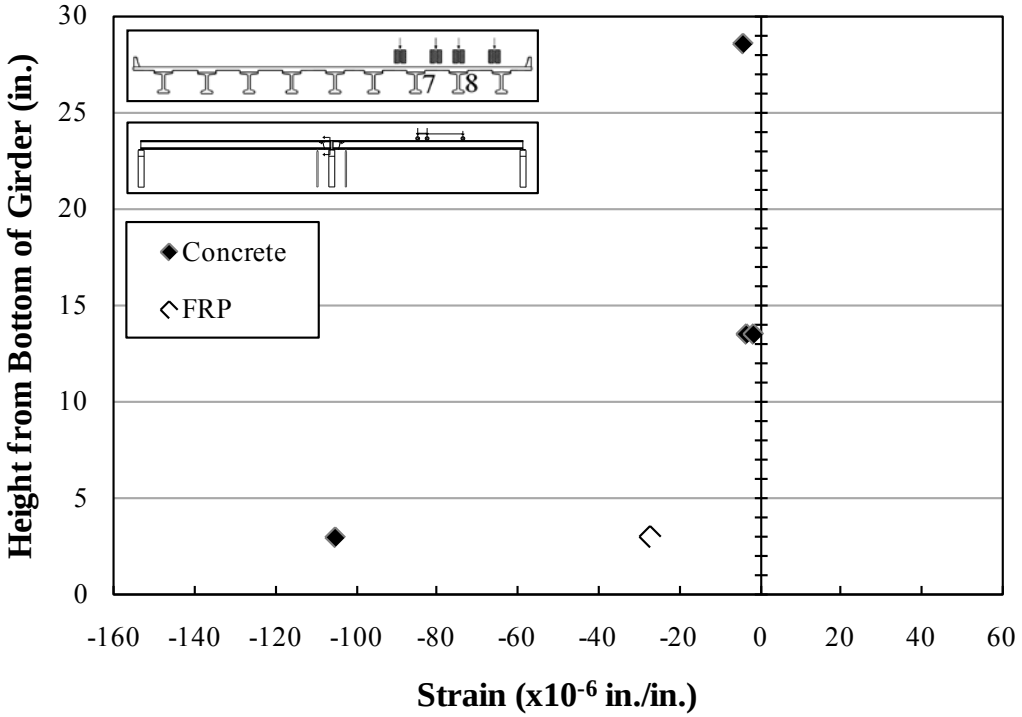

Figure B.153: Strains—Girder 7—Section 2—C9

B.2.3.1.3 Strains—Girder 7—Cross Section 3

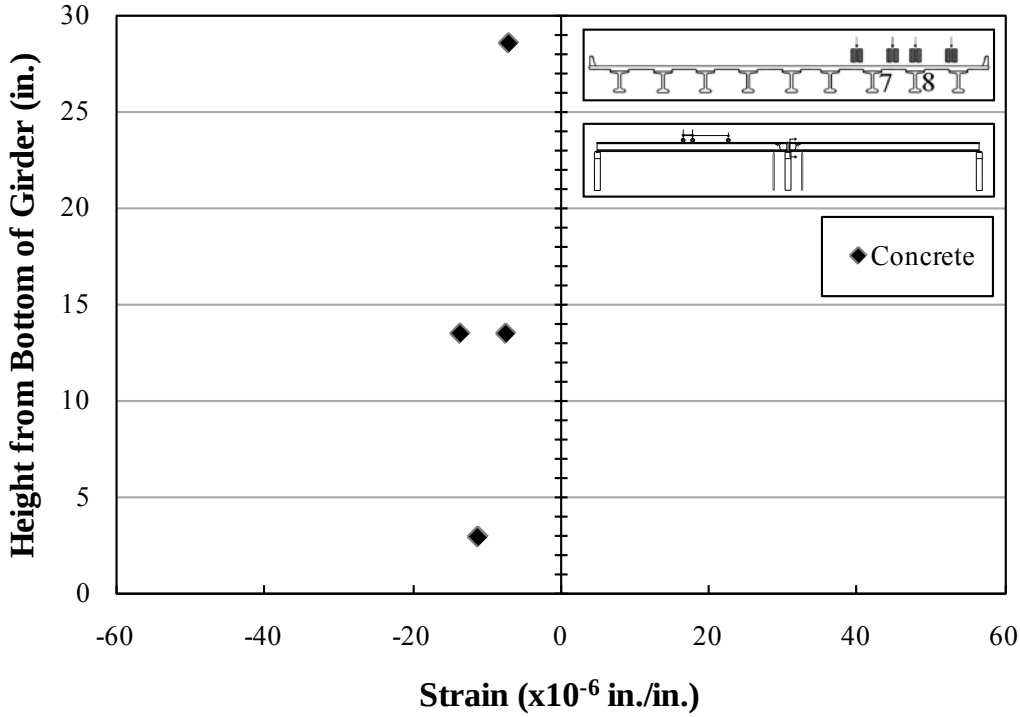

Figure B.154: Strains—Girder 7—Section 3—C1

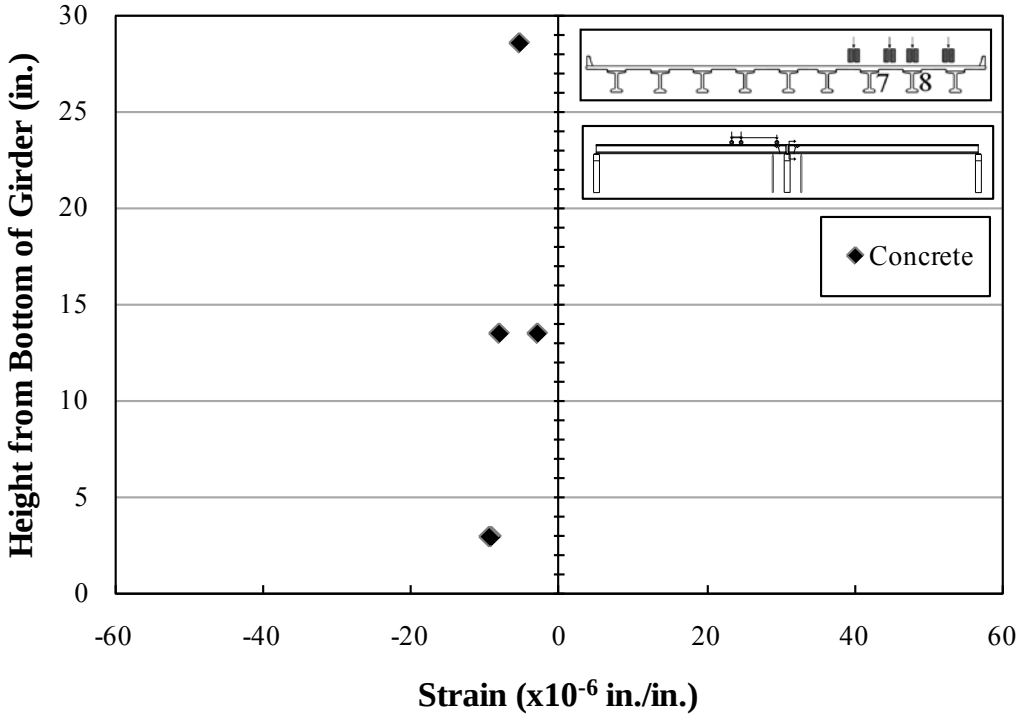

Figure B.155: Strains—Girder 7—Section 3—C2

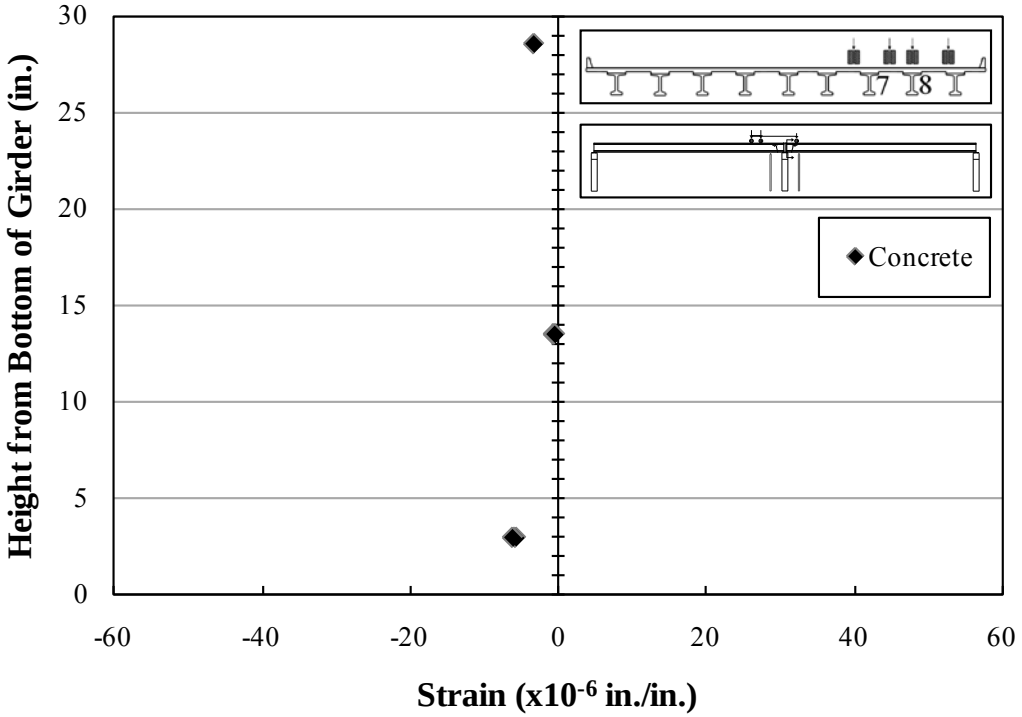

Figure B.156: Strains—Girder 7—Section 3—C3

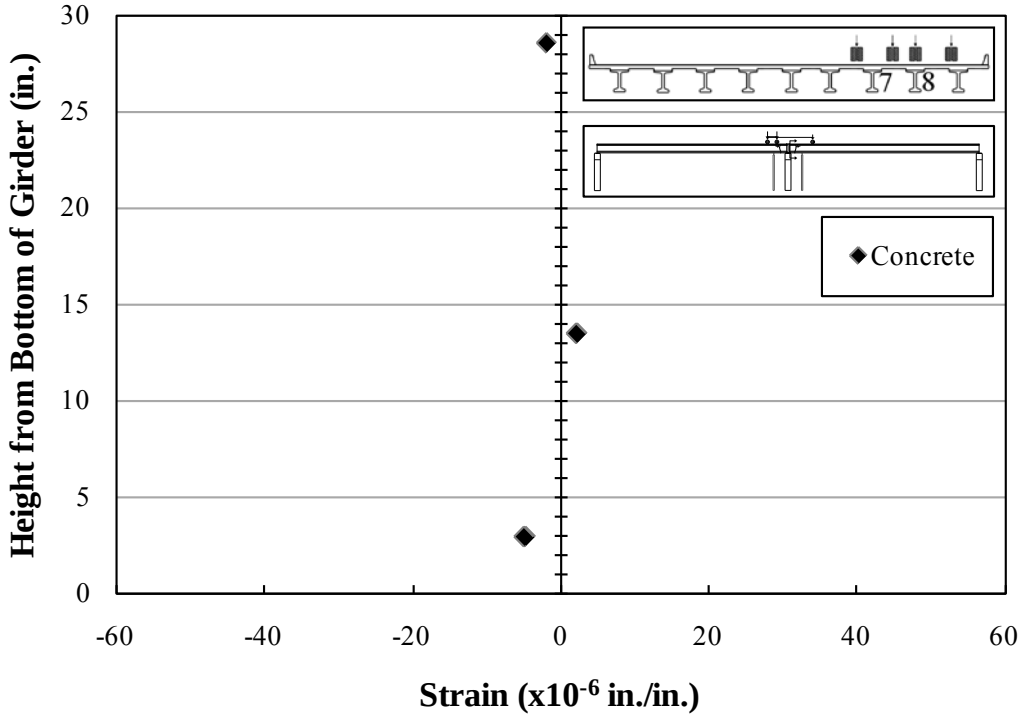

Figure B.157: Strains—Girder 7—Section 3—C4

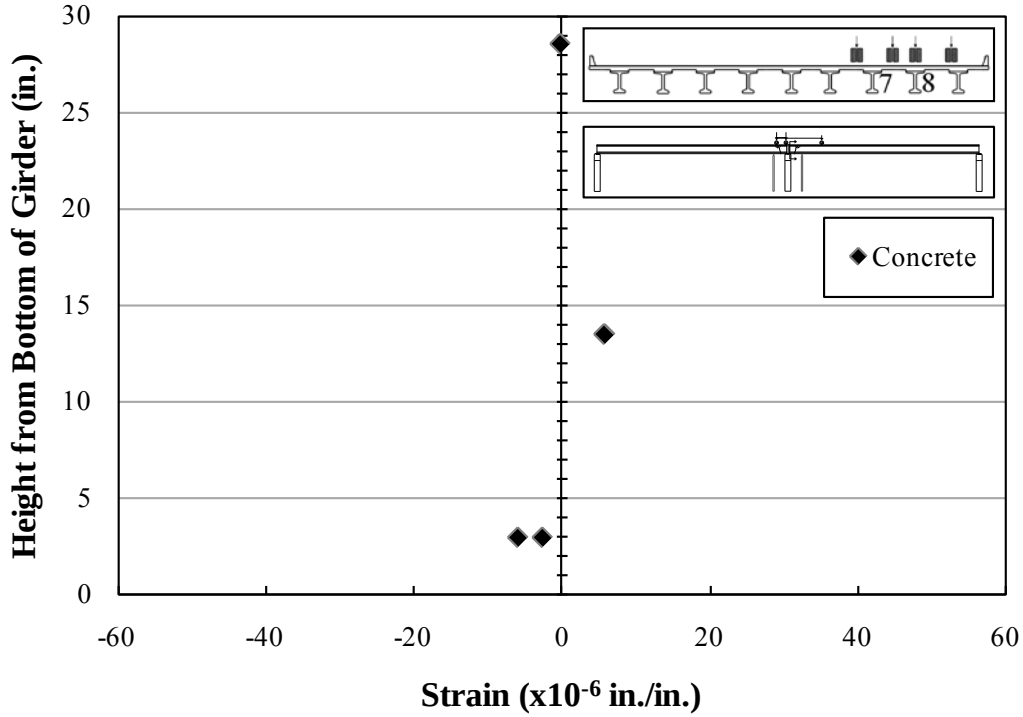

Figure B.158: Strains—Girder 7—Section 3—C5

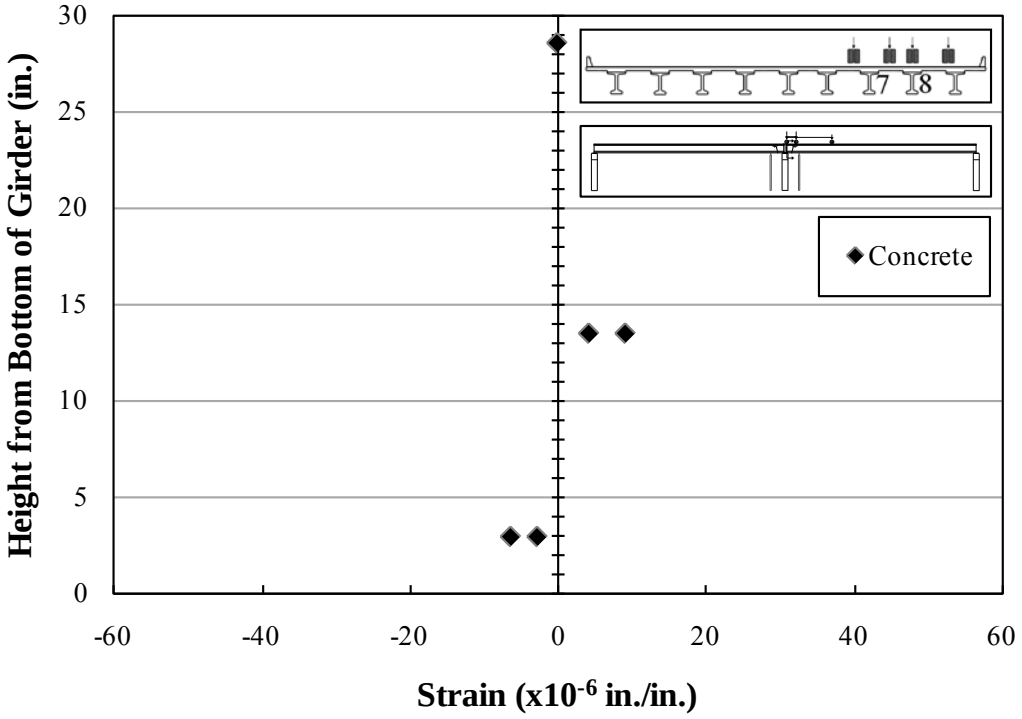

Figure B.159: Strains—Girder 7—Section 3—C6

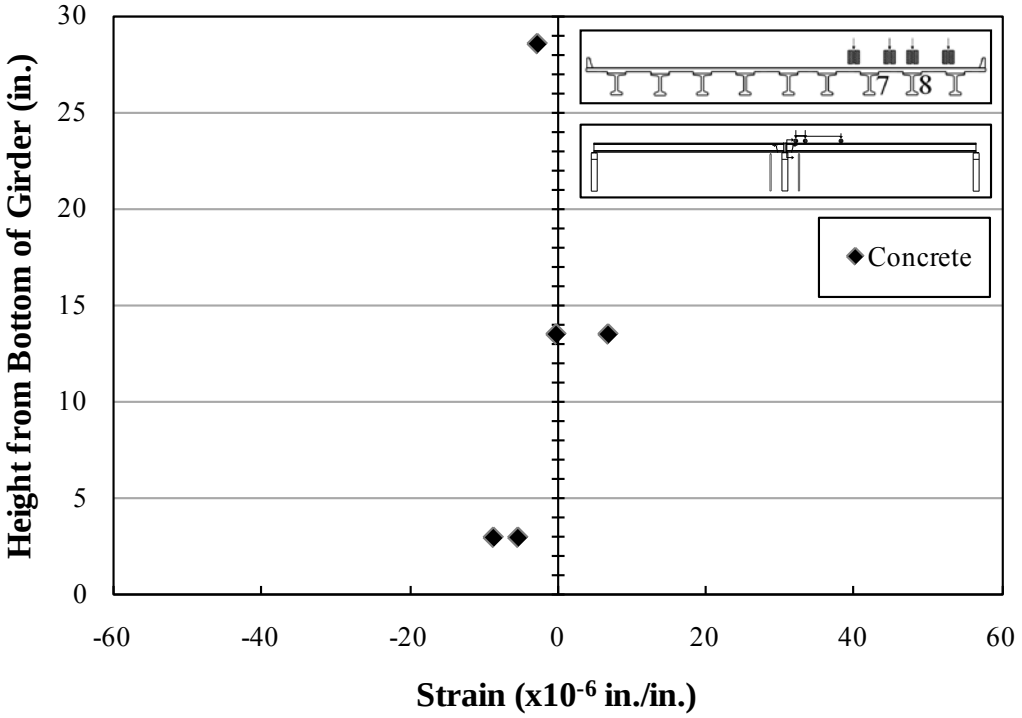

Figure B.160: Strains—Girder 7—Section 3—C7

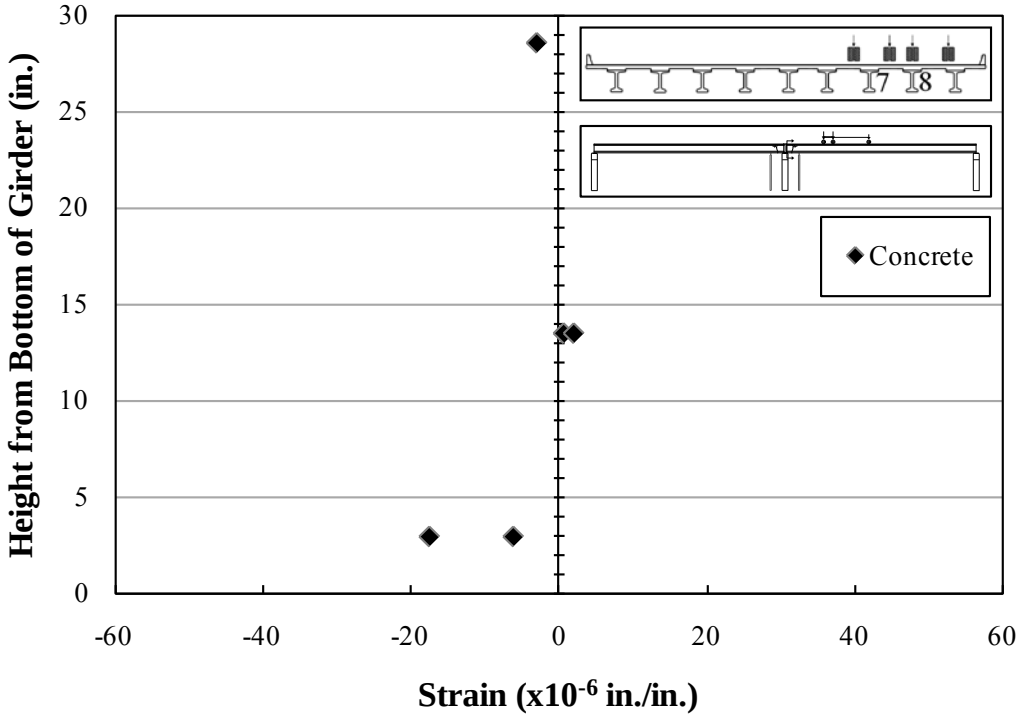

Figure B.161: Strains—Girder 7—Section 3—C8

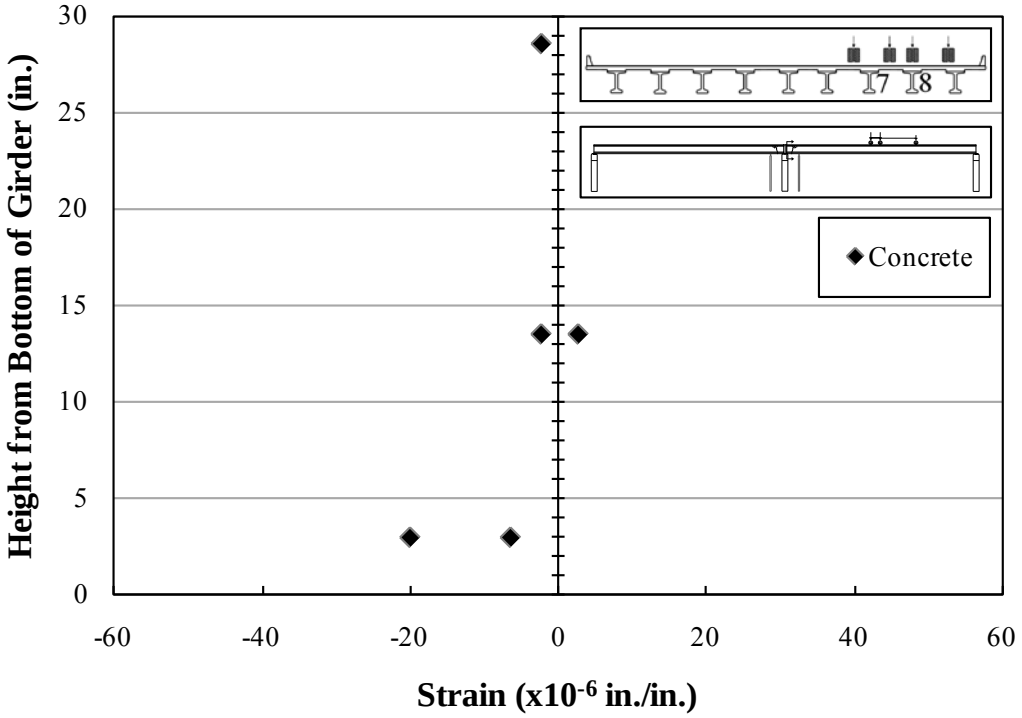

Figure B.162: Strains—Girder 7—Section 3—C9

B.2.3.1.4 Strains—Girder 7—Cross Section 4

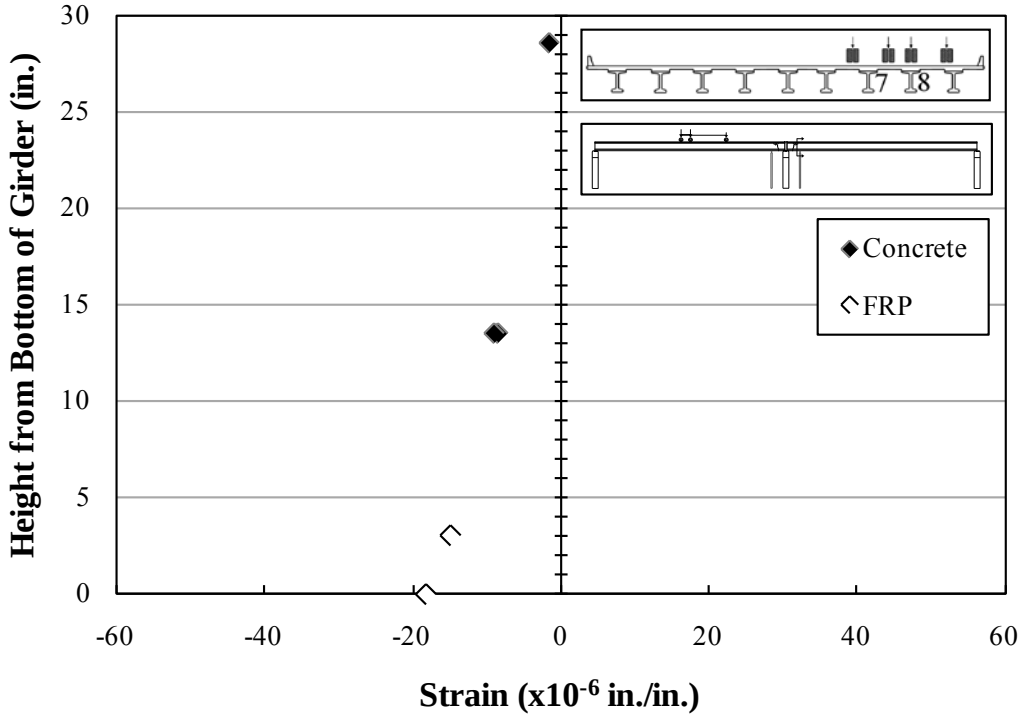

Figure B.163: Strains—Girder 7—Section 4—C1

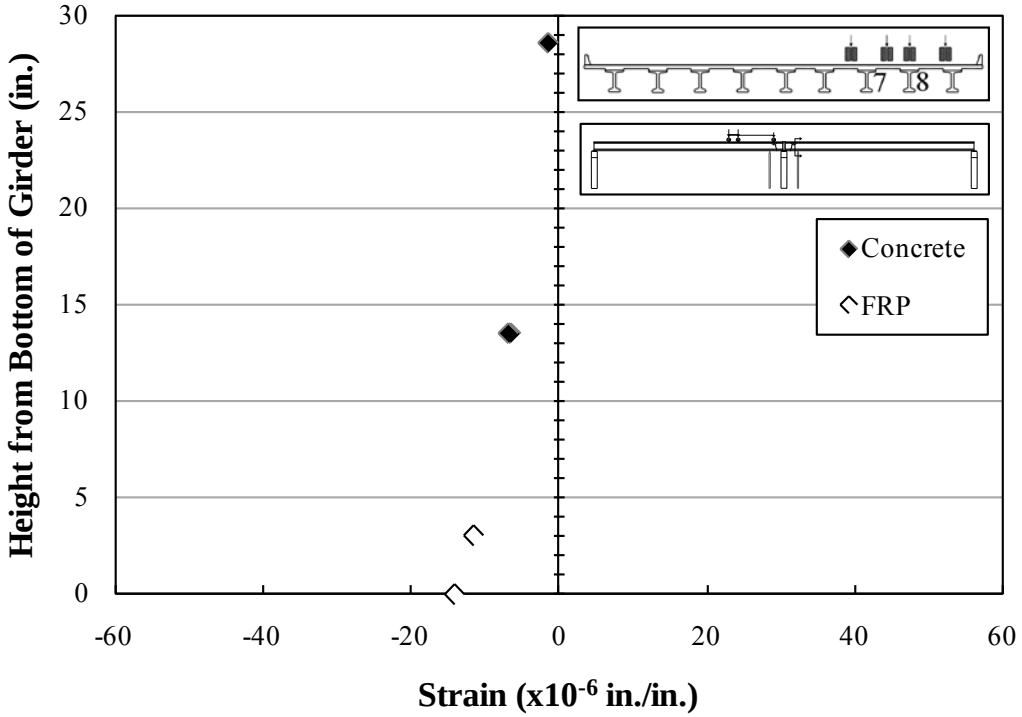

Figure B.164: Strains—Girder 7—Section 4—C2

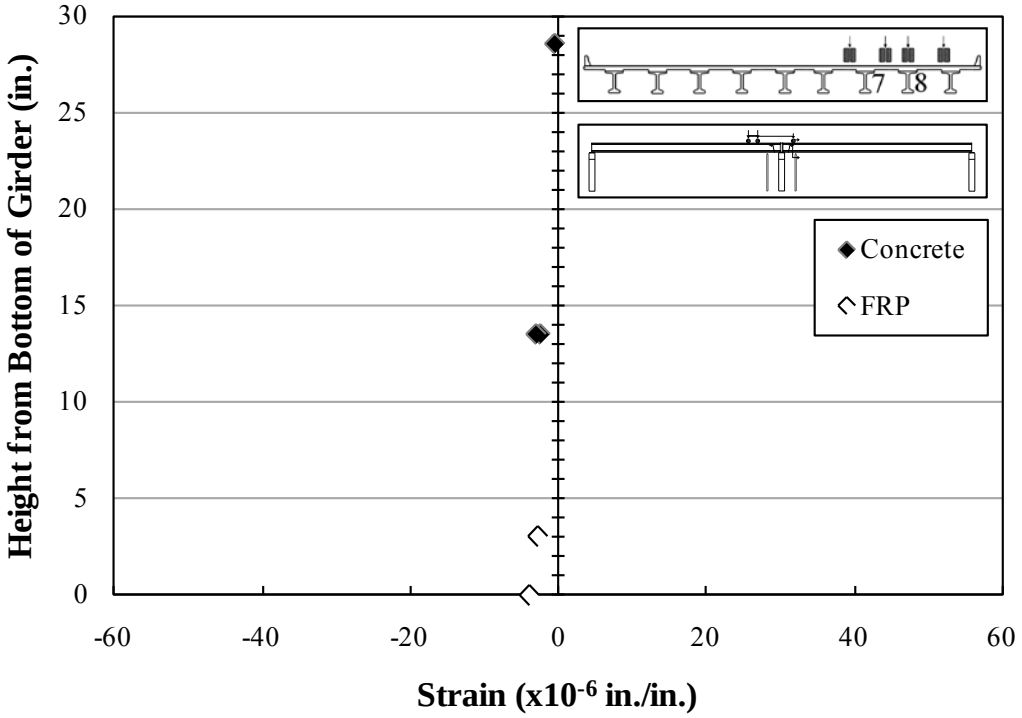

Figure B.165: Strains—Girder 7—Section 4—C3

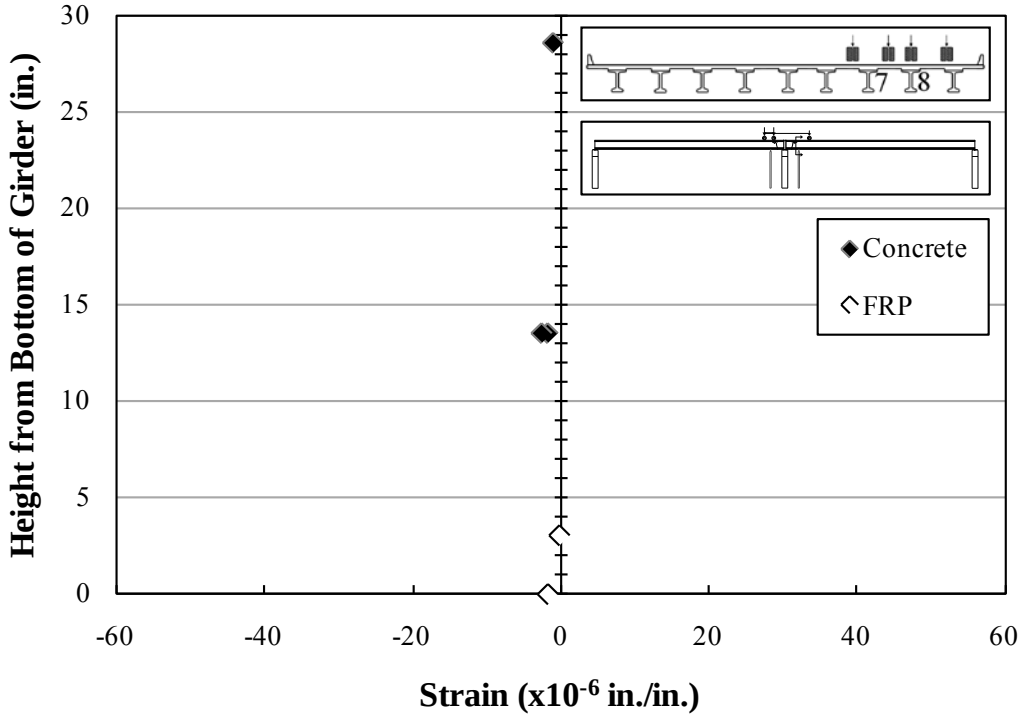

Figure B.166: Strains—Girder 7—Section 4—C4

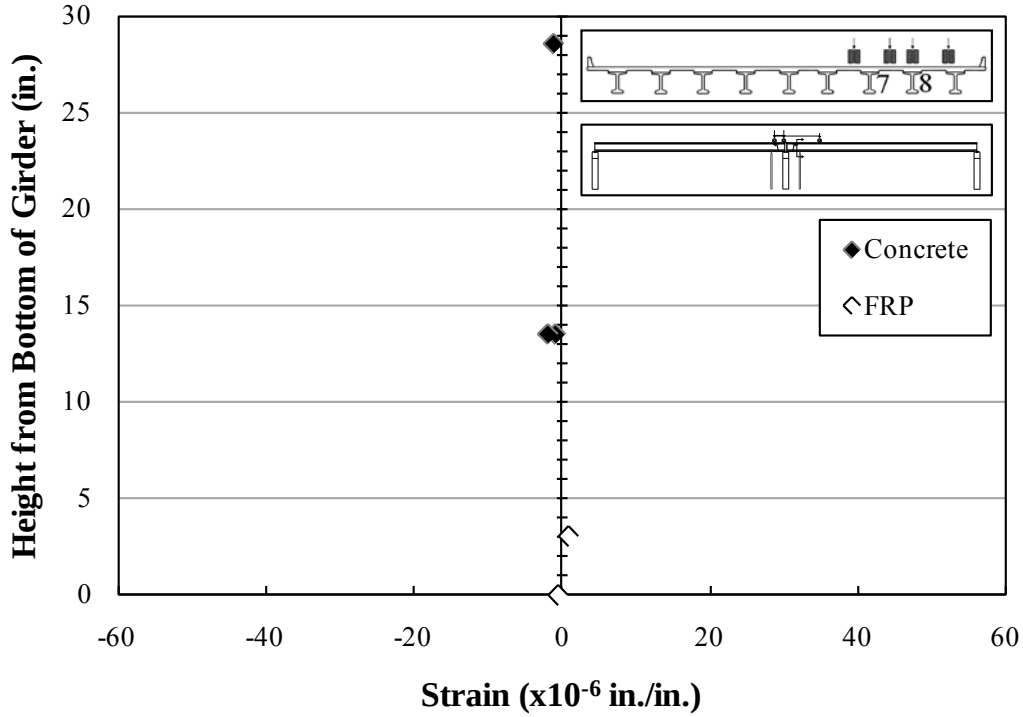

Figure B.167: Strains—Girder 7—Section 4—C5

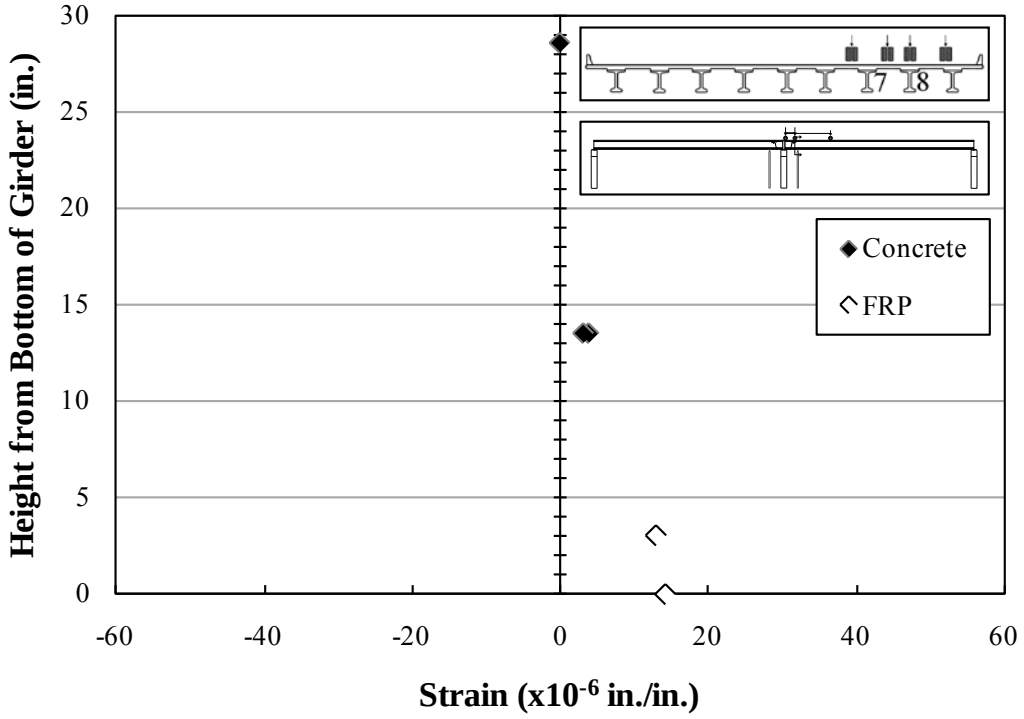

Figure B.168: Strains—Girder 7—Section 4—C6

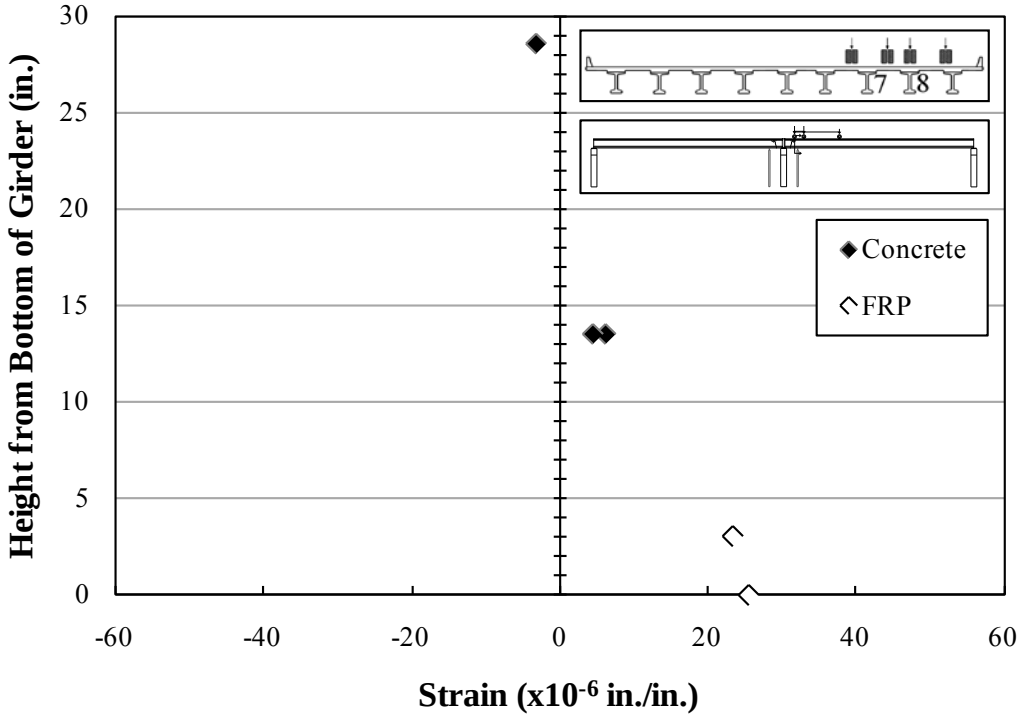

Figure B.169: Strains—Girder 7—Section 4—C7

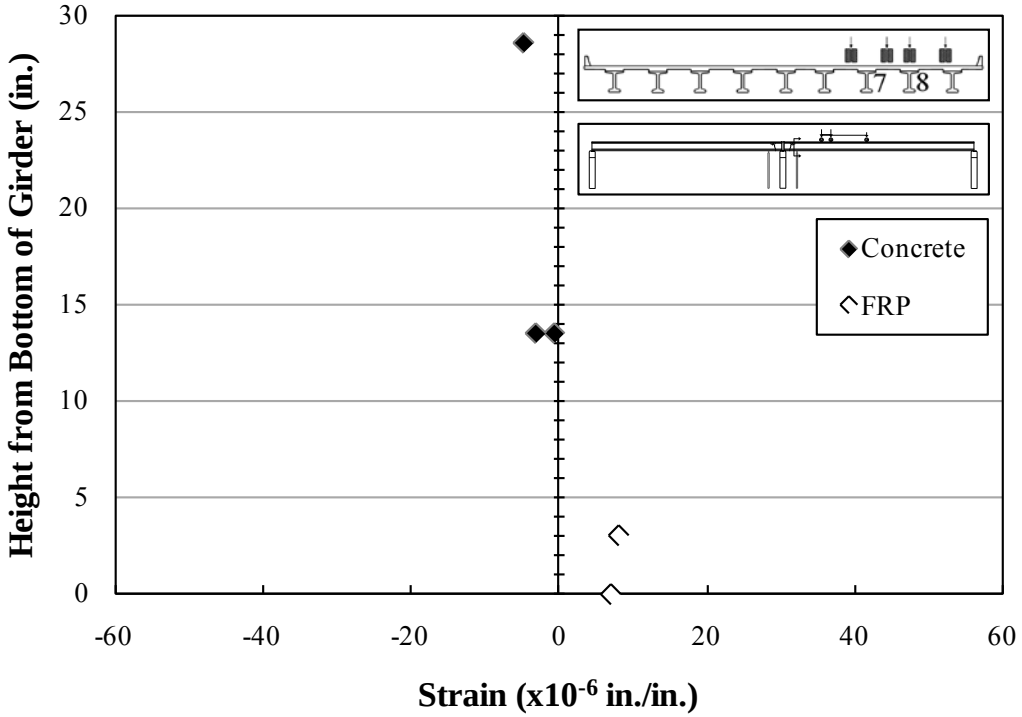

Figure B.170: Strains—Girder 7—Section 4—C8

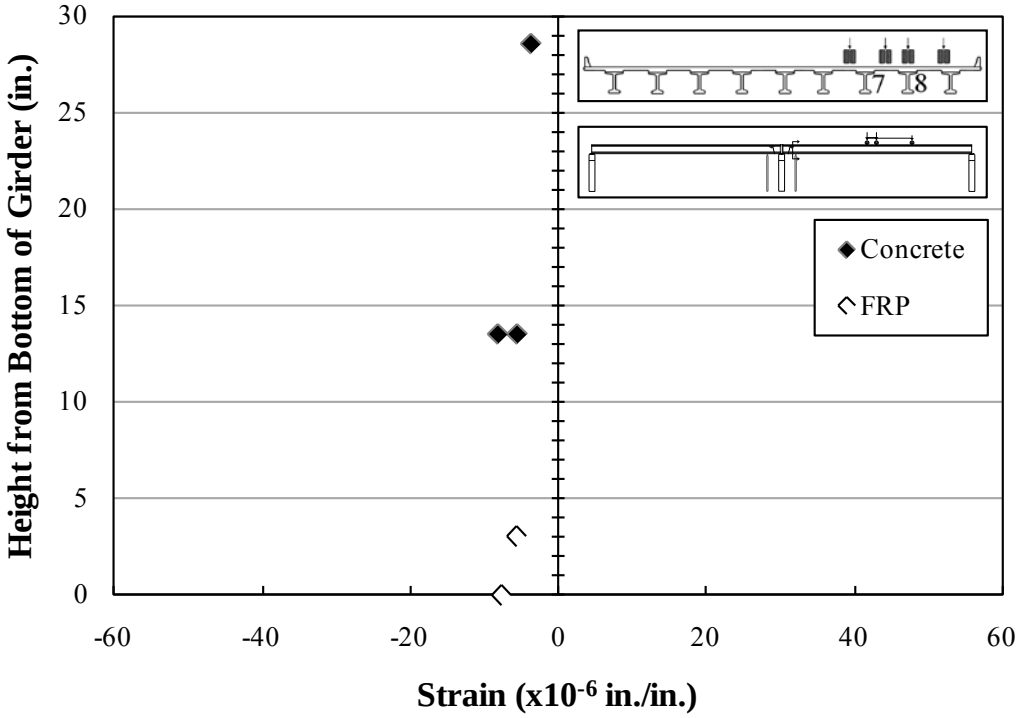

Figure B.171: Strains—Girder 7—Section 4—C9

B.2.3.2 Cross-Section Strains—Girder 8

B.2.3.2.1 Strains—Girder 8—Cross Section 1

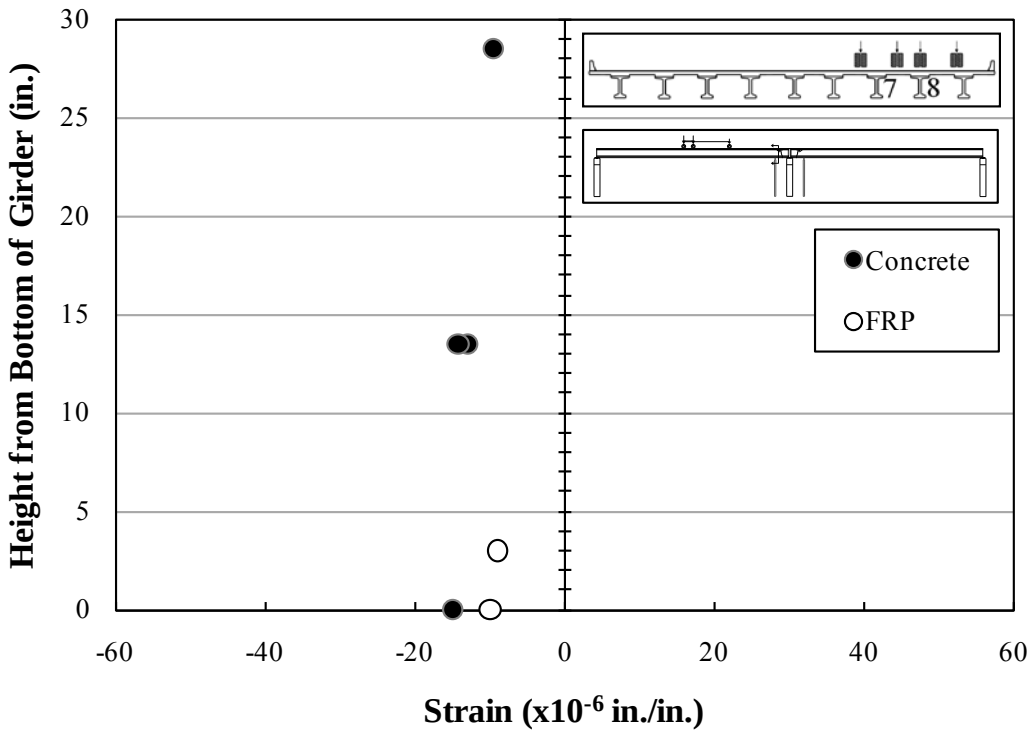

Figure B.172: Strains—Girder 8—Section 1—C1

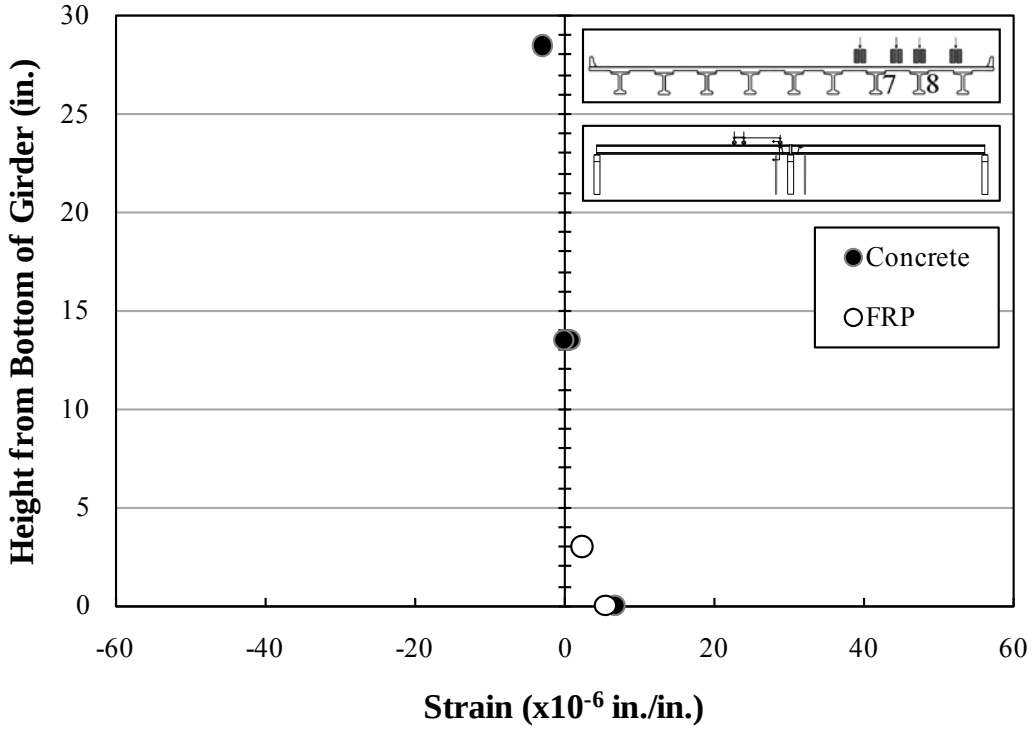

Figure B.173: Strains—Girder 8—Section 1—C2

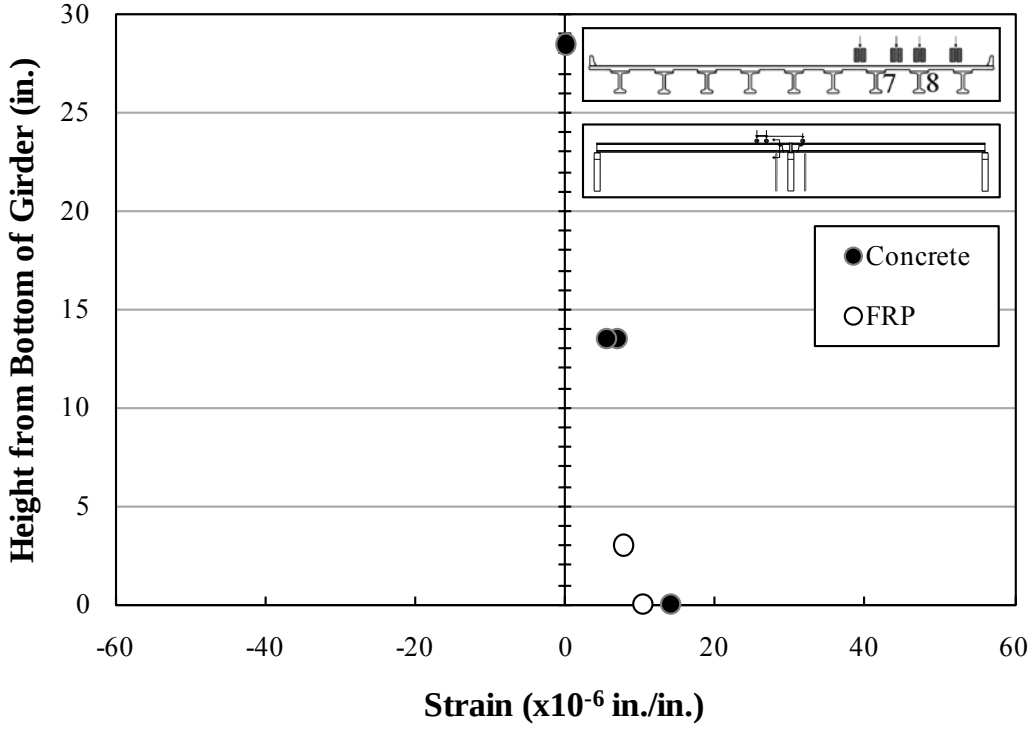

Figure B.174: Strains—Girder 8—Section 1—C3

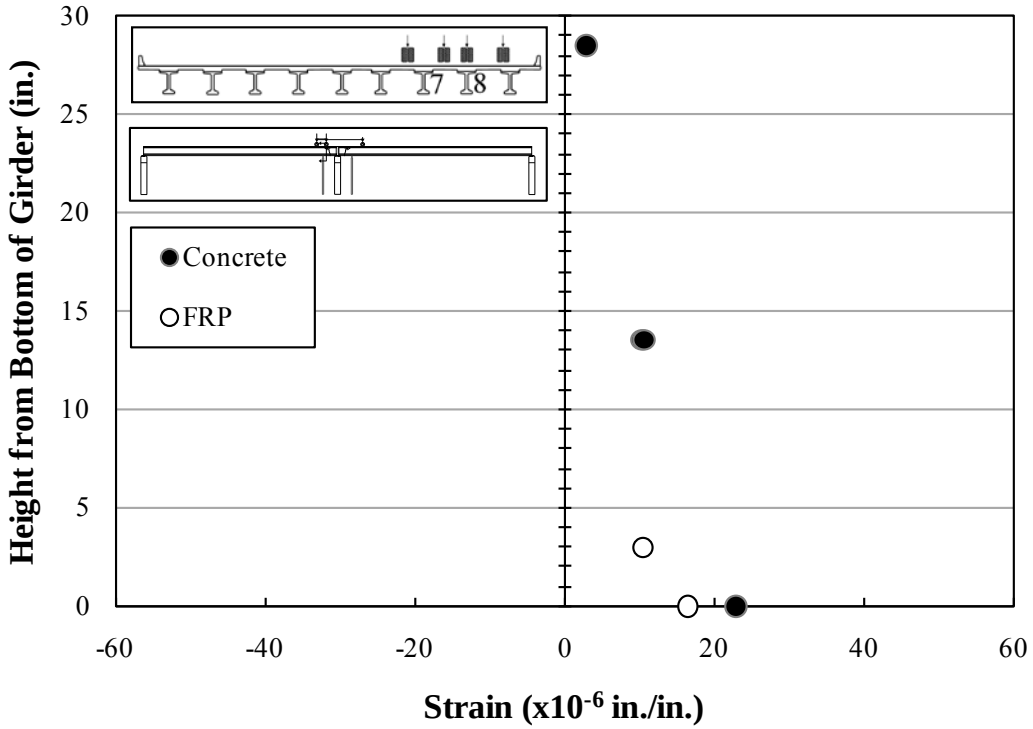

Figure B.175: Strains—Girder 8—Section 1—C4

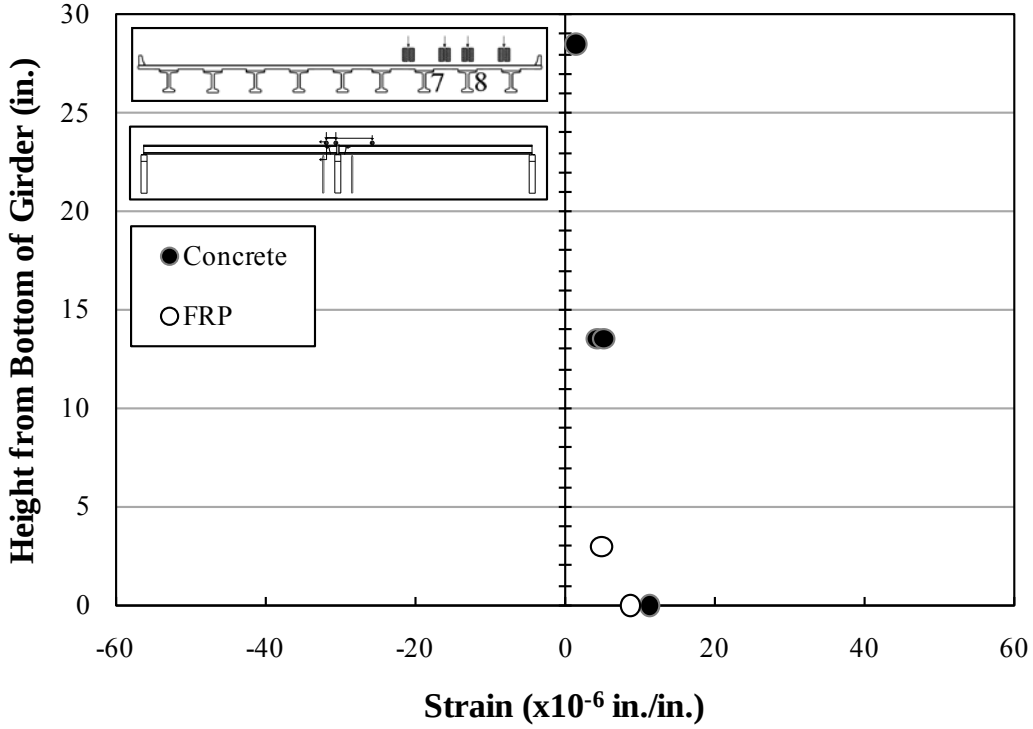

Figure B.176: Strains—Girder8—Section 1—C5

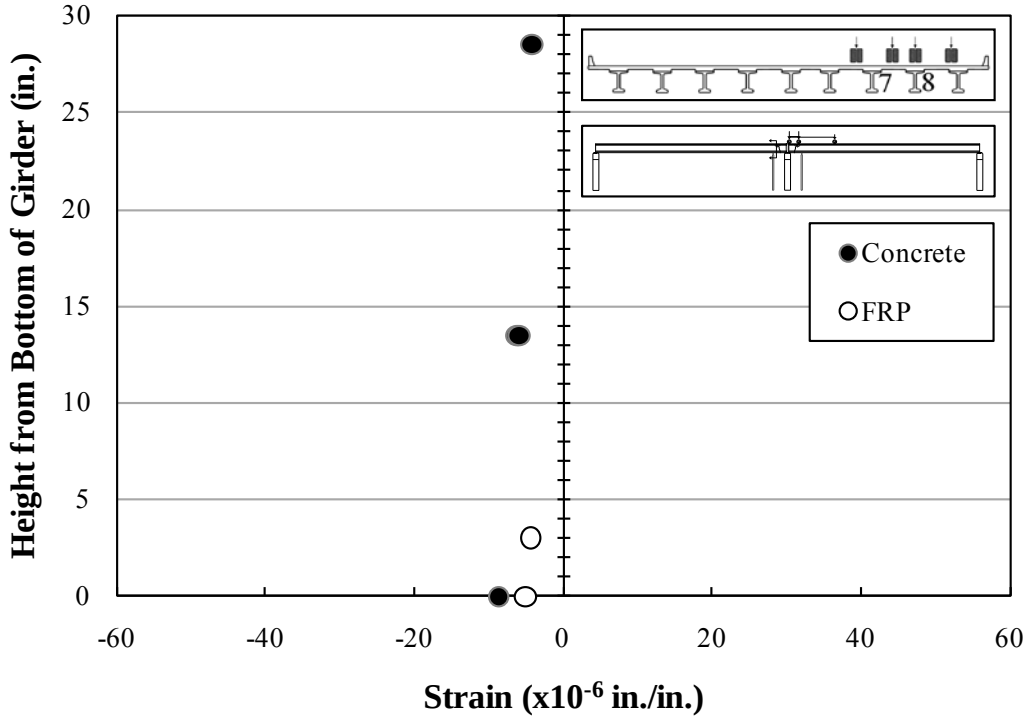

Figure B.177: Strains—Girder 8—Section 1—C6

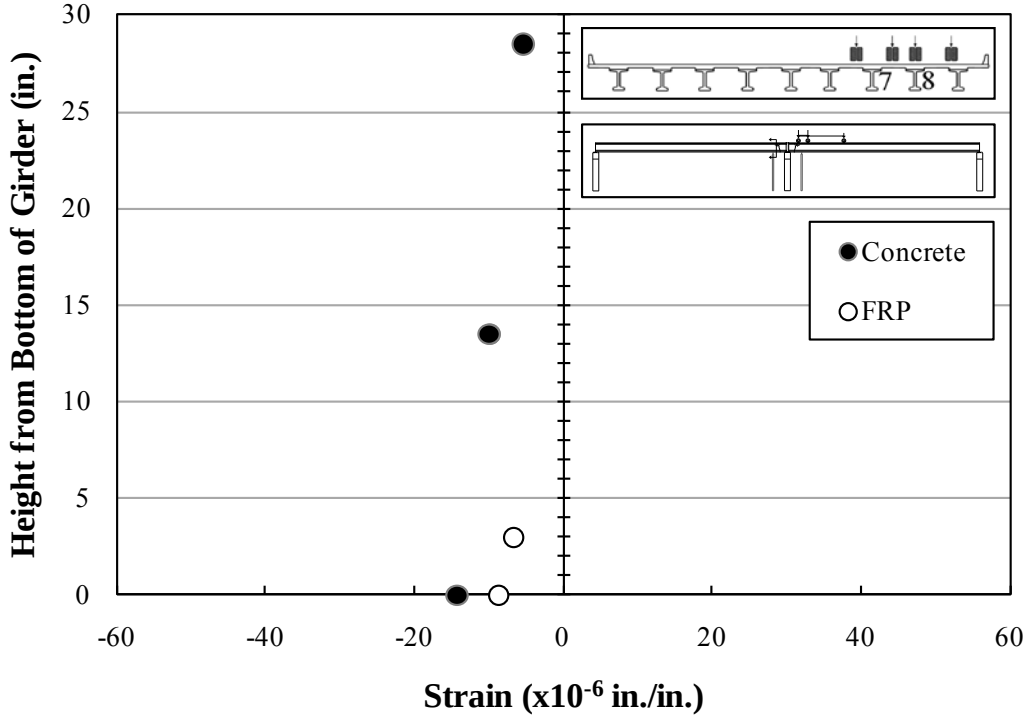

Figure B.178: Strains—Girder 8—Section 1—C7

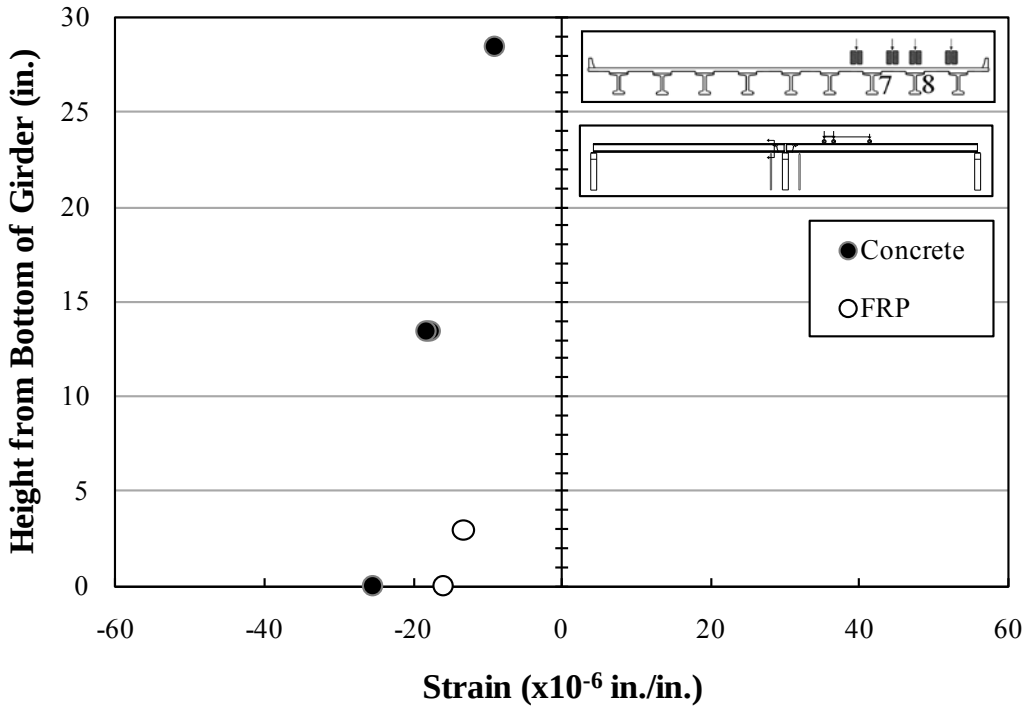

Figure B.179: Strains—Girder 8—Section 1—C8

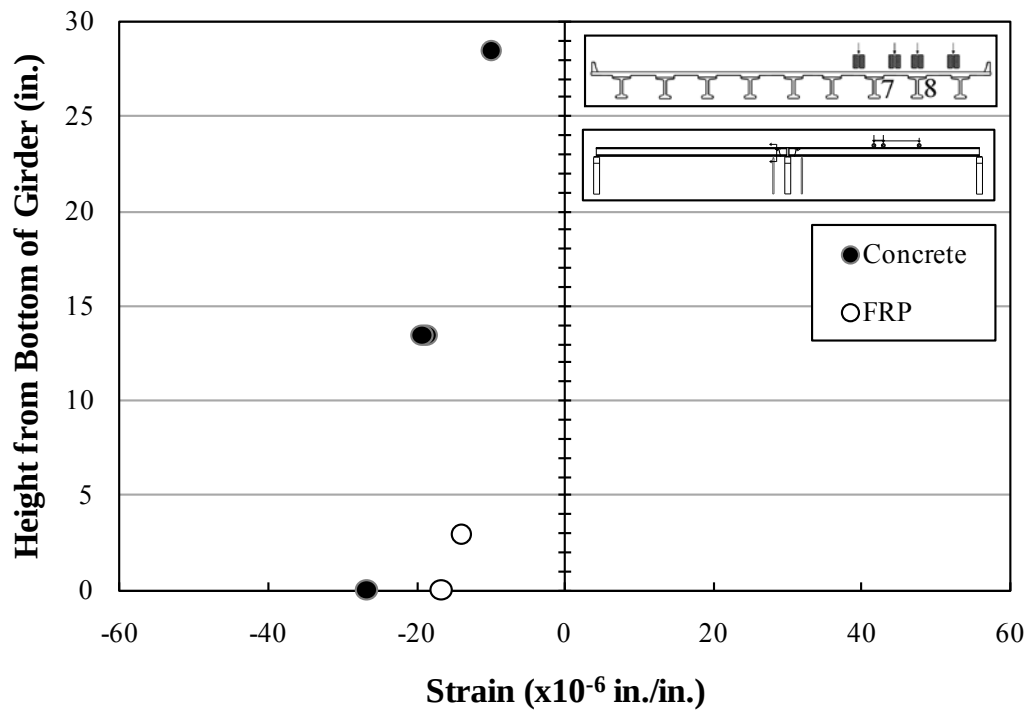

Figure B.180: Strains—Girder 8—Section 1—C9

B.2.3.2.2 Strains—Girder 8—Cross Section 2

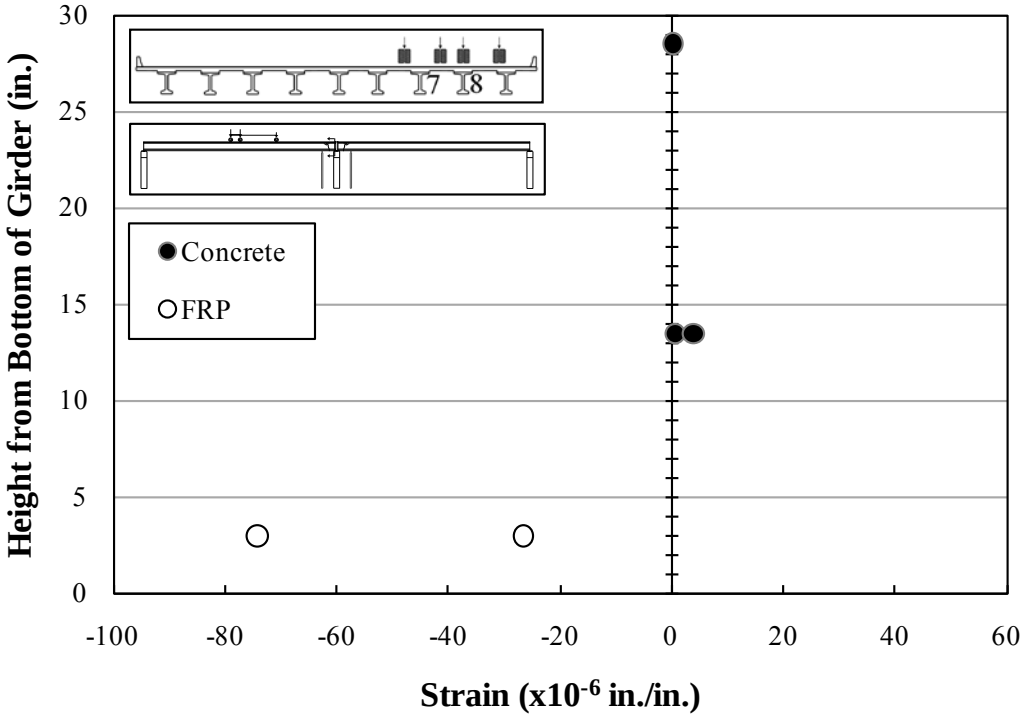

Figure B.181: Strains—Girder 8—Section 2—C1

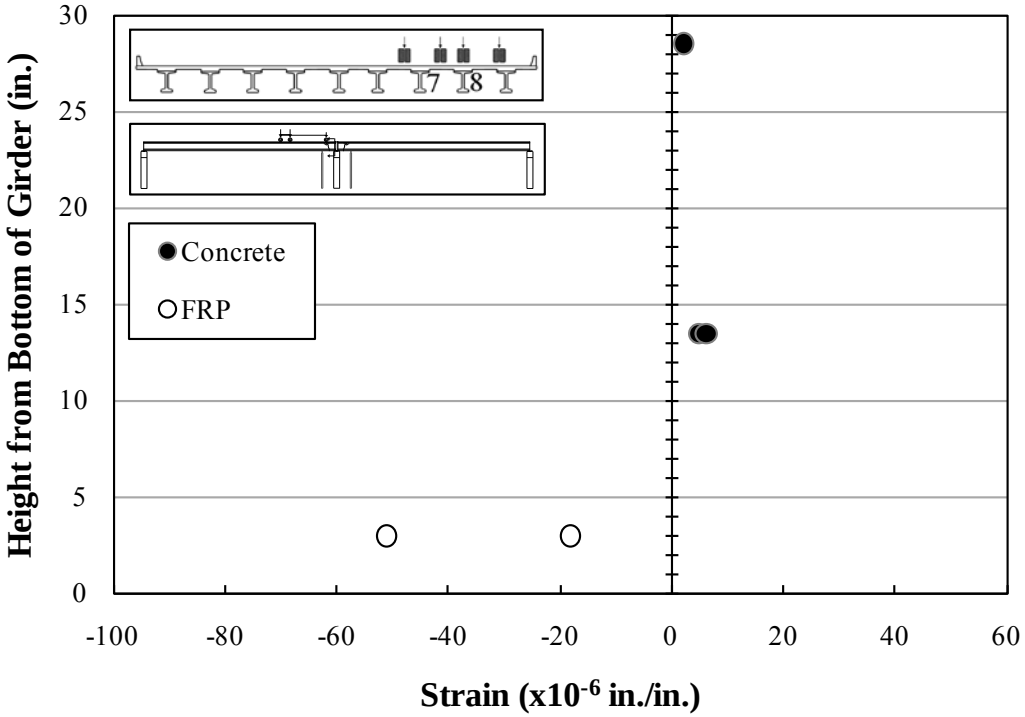

Figure B.182: Strains—Girder 8—Section 2—C2

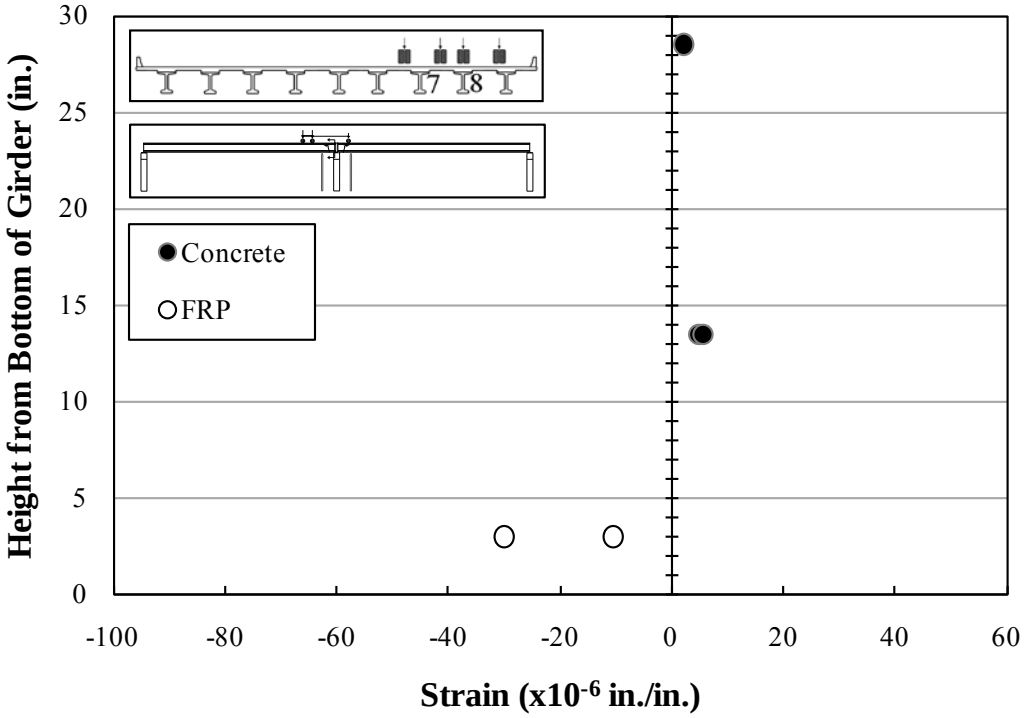

Figure B.183: Strains—Girder 8—Section 2—C3

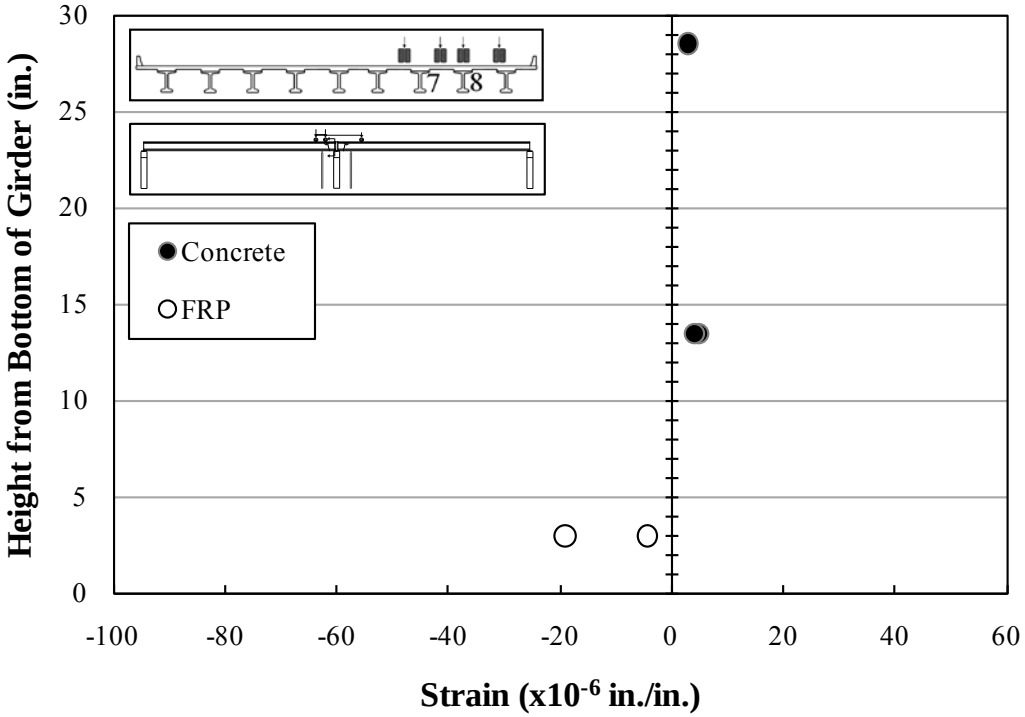

Figure B.184: Strains—Girder 8—Section 2—C4

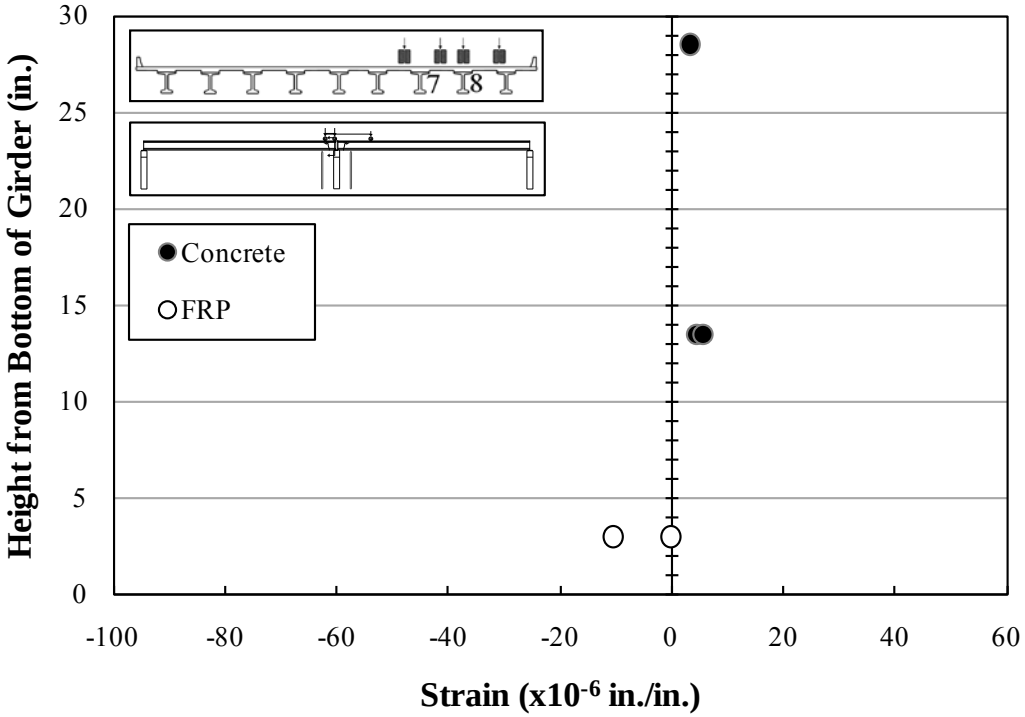

Figure B.185: Strains—Girder 8—Section 2—C5

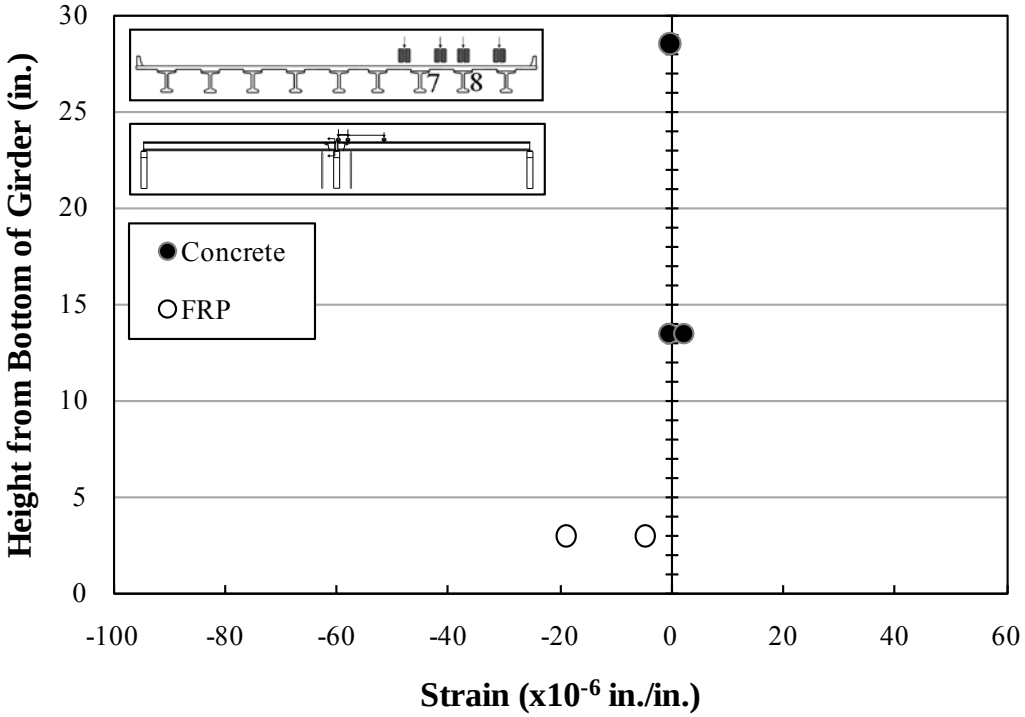

Figure B.186: Strains—Girder 8—Section 2—C6

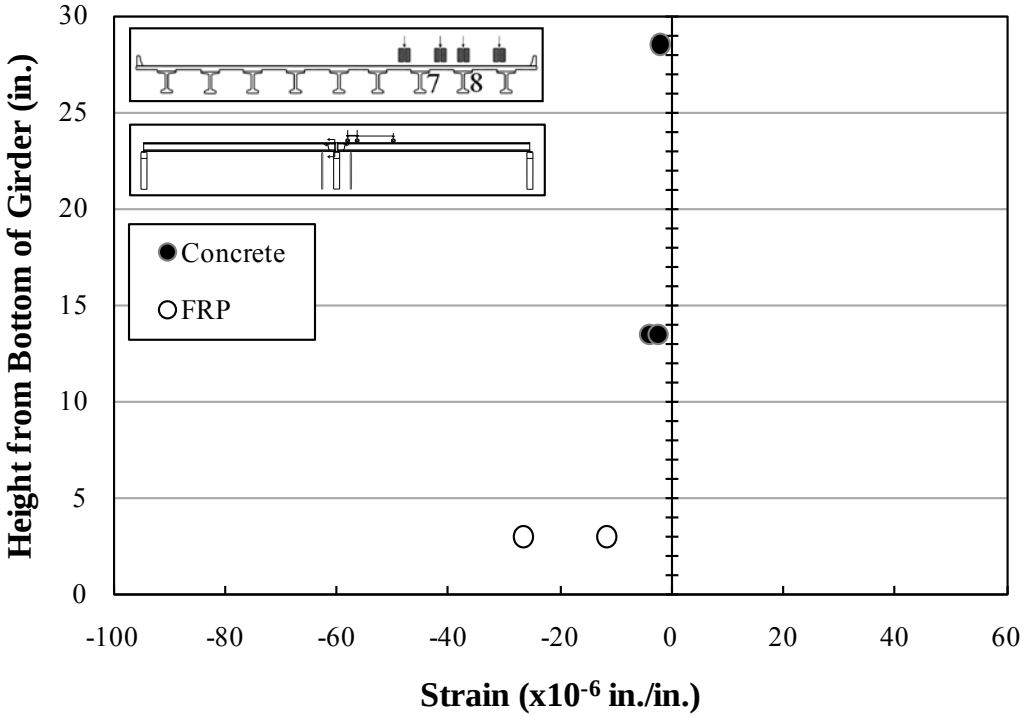

Figure B.187: Strains—Girder 8—Section 2—C7

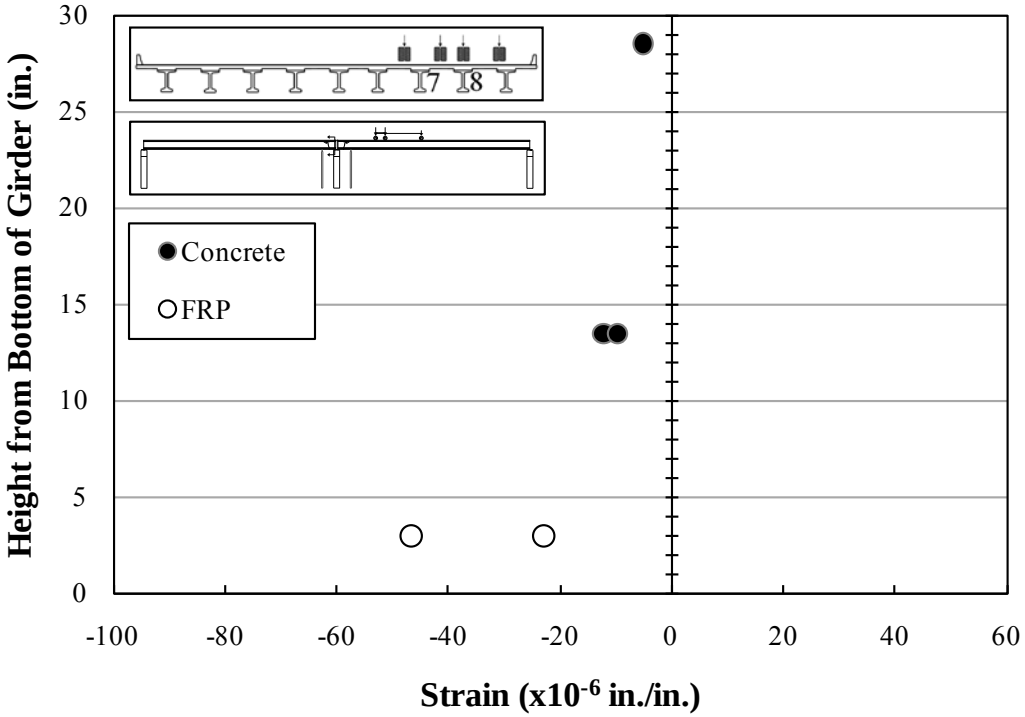

Figure B.188: Strains—Girder 8—Section 2—C8

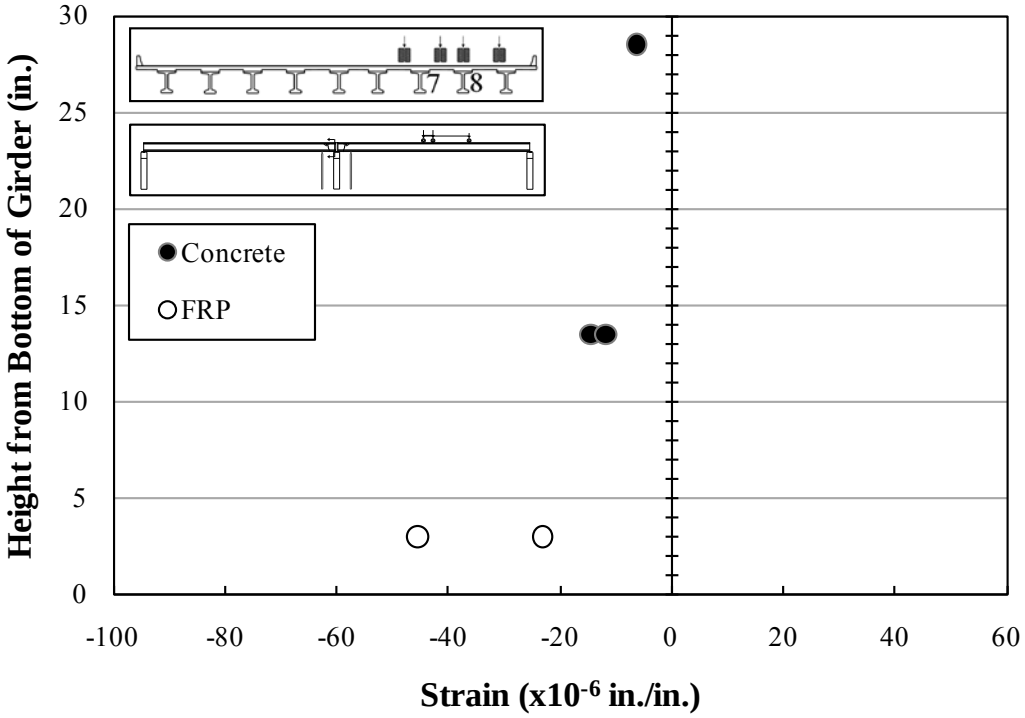

Figure B.189: Strains—Girder 8—Section 2—C9

B.2.3.2.3 Strains—Girder 8—Cross Section 3

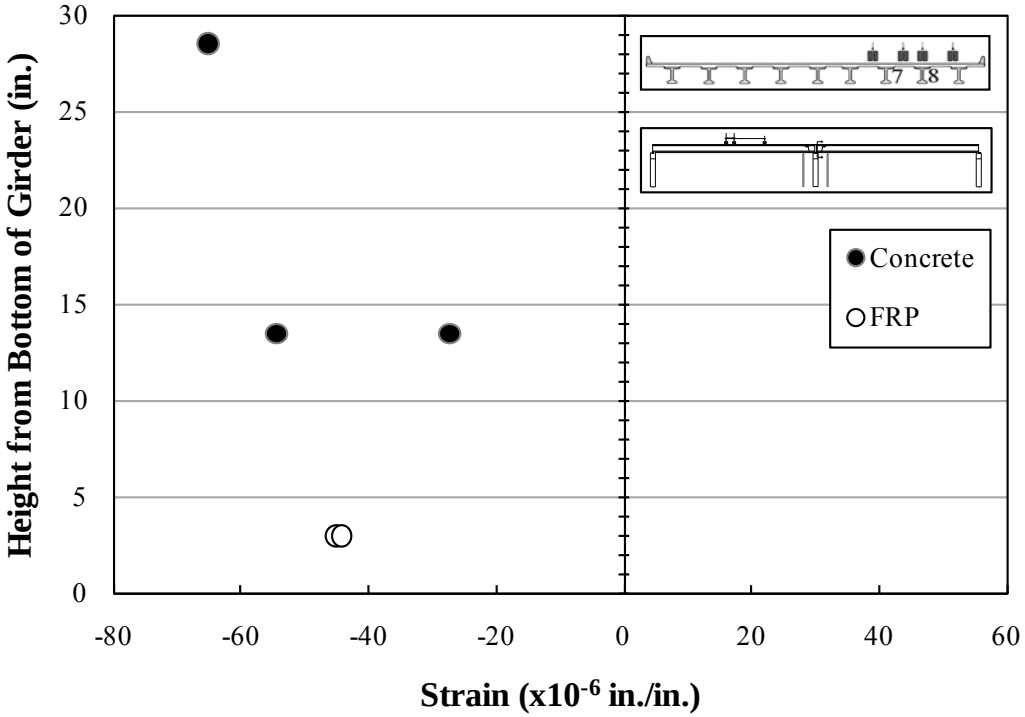

Figure B.190: Strains—Girder 8—Section 3—C1

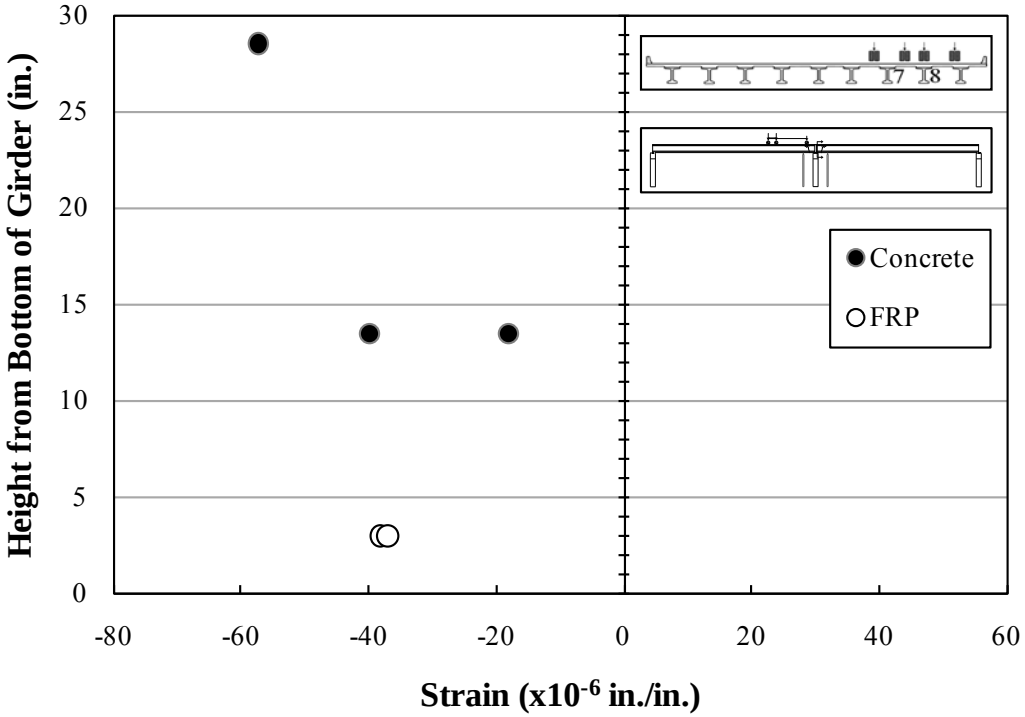

Figure B.191: Strains—Girder 8—Section 3—C2

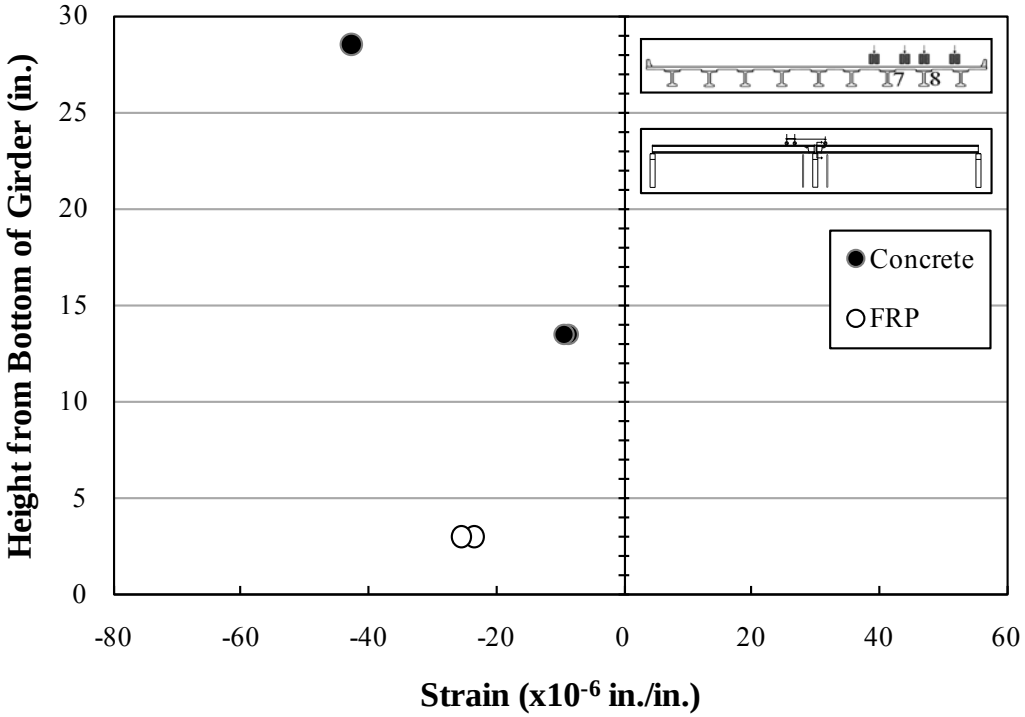

Figure B.192: Strains—Girder 8—Section 3—C3

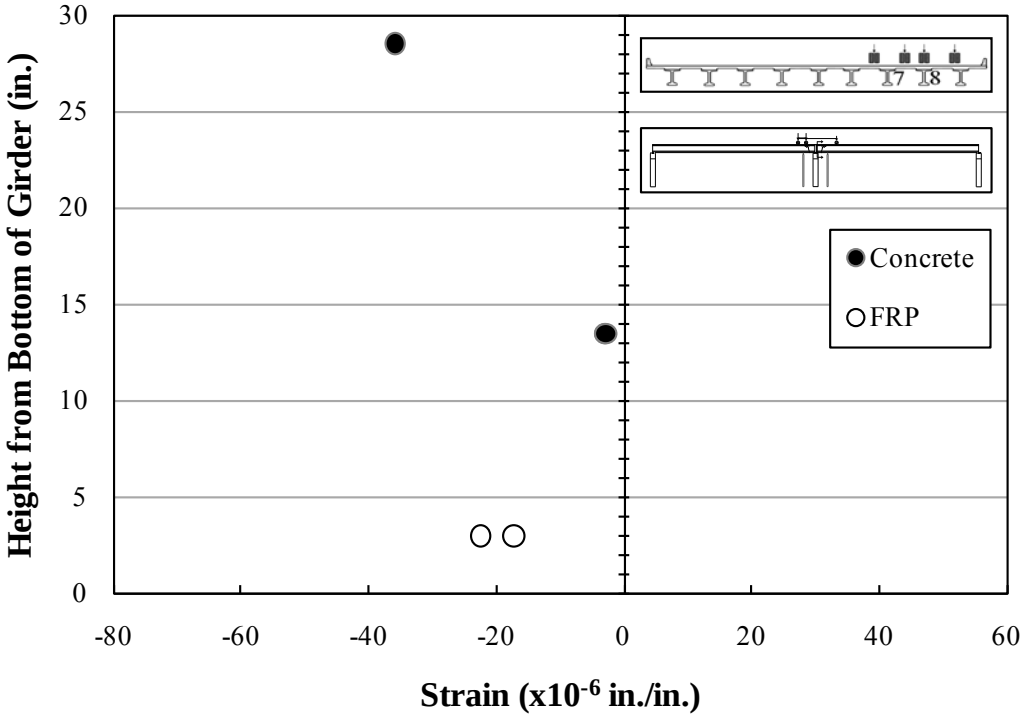

Figure B.193: Strains—Girder 8—Section 3—C4

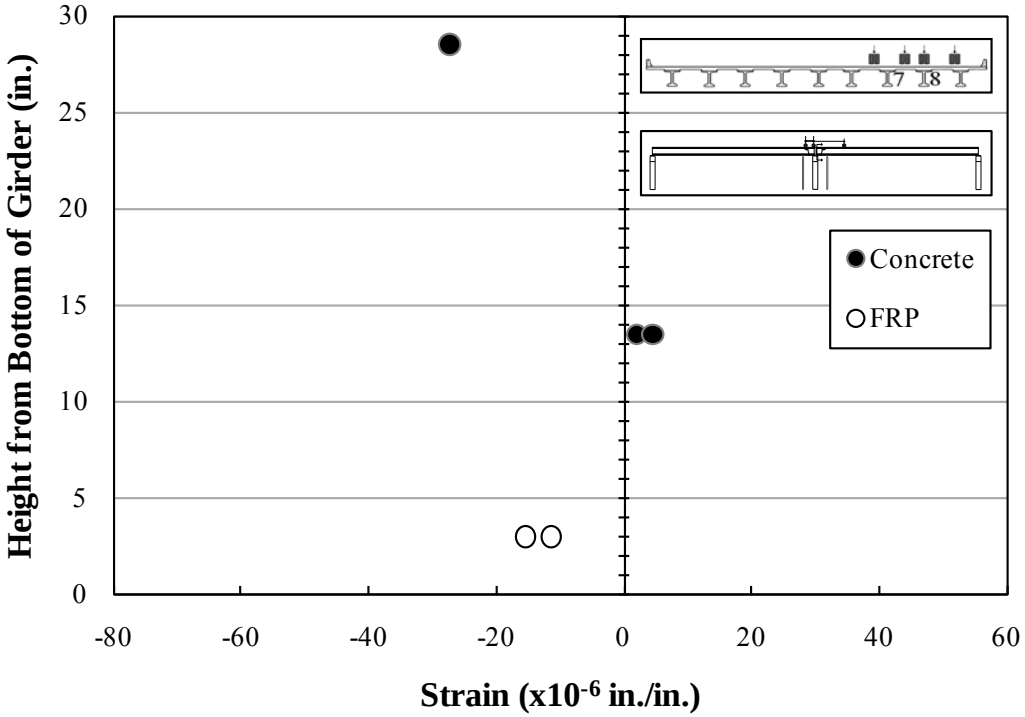

Figure B.194: Strains—Girder 8—Section 3—C5

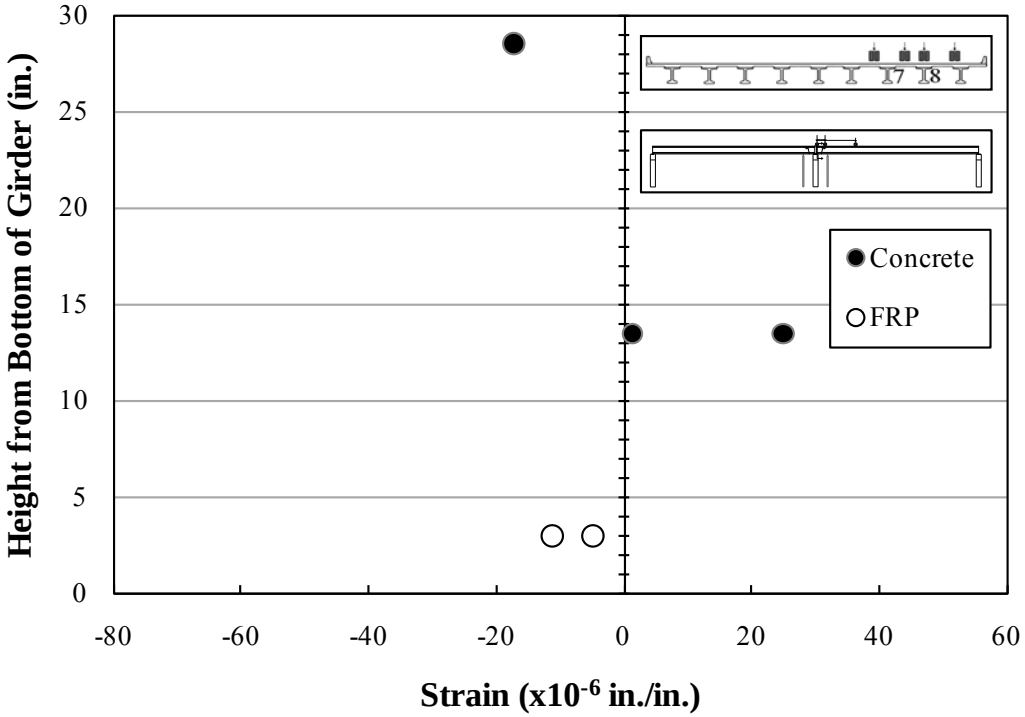

Figure B.195: Strains—Girder 8—Section 3—C6

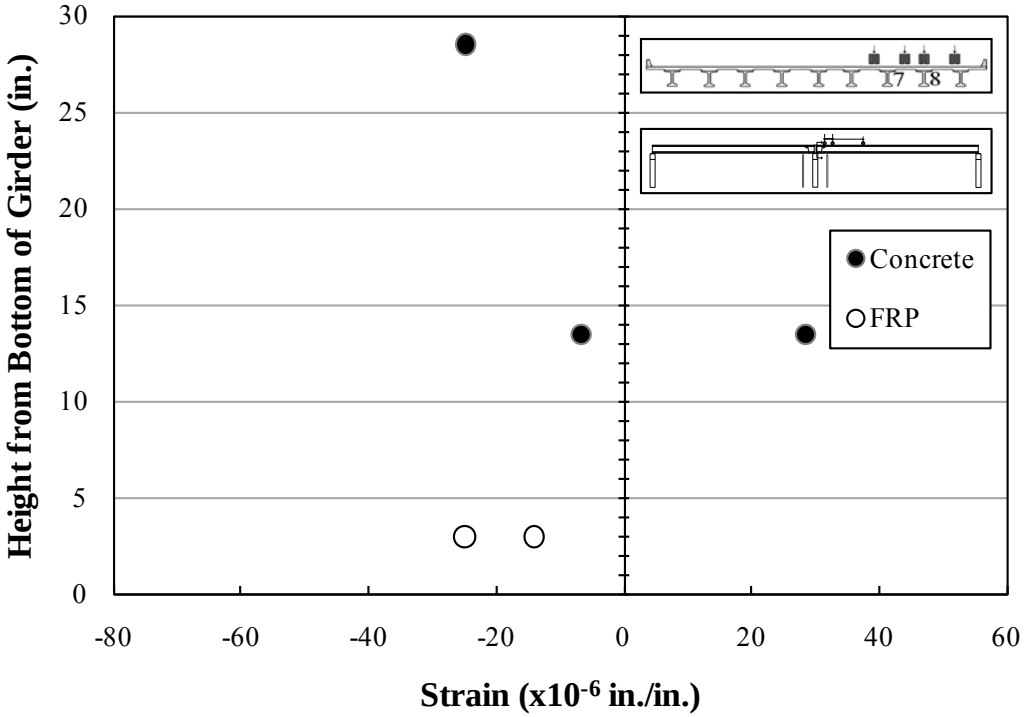

Figure B.196: Strains—Girder 8—Section 3—C7

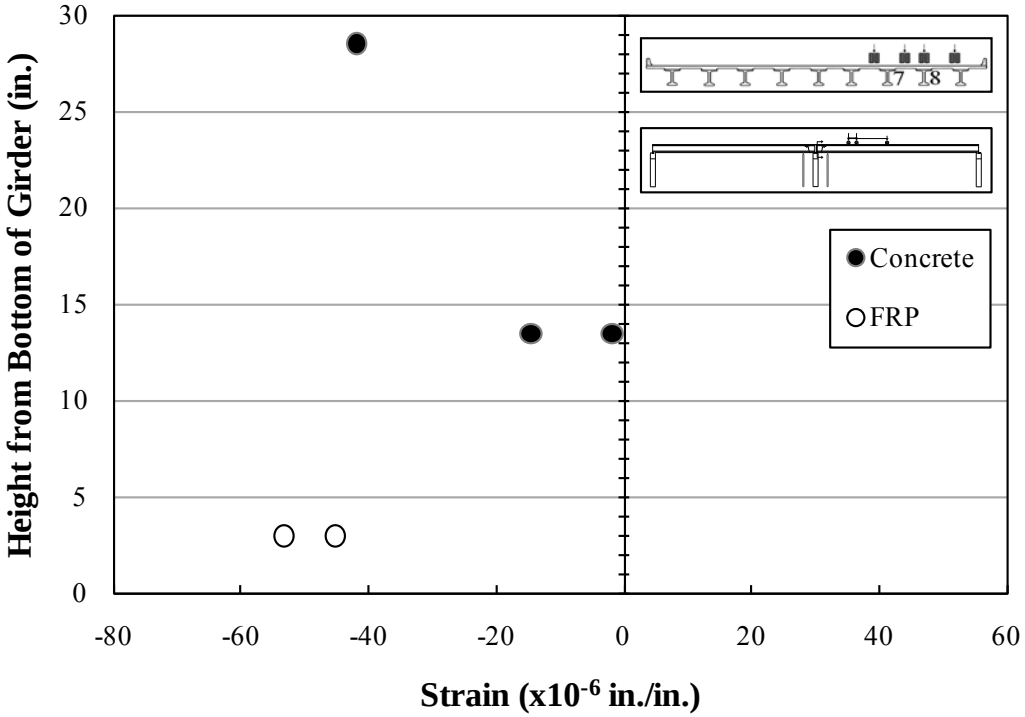

Figure B.197: Strains—Girder 8—Section 3—C8

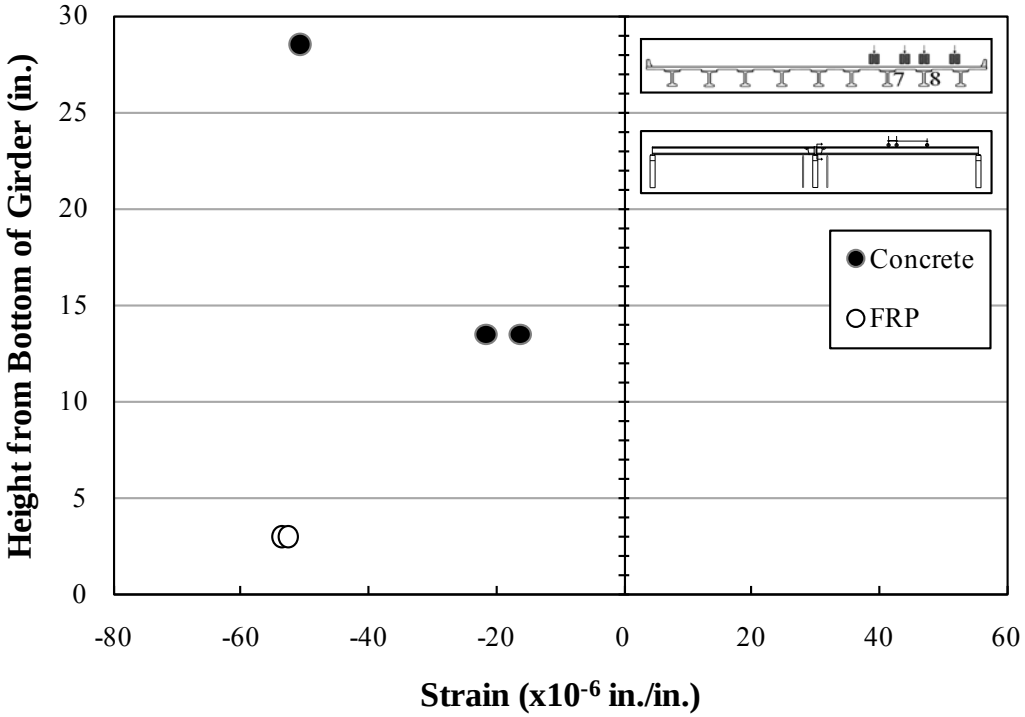

Figure B.198: Strains—Girder 8—Section 3—C9

B.2.3.2.4 Strains—Girder 8—Cross Section 4

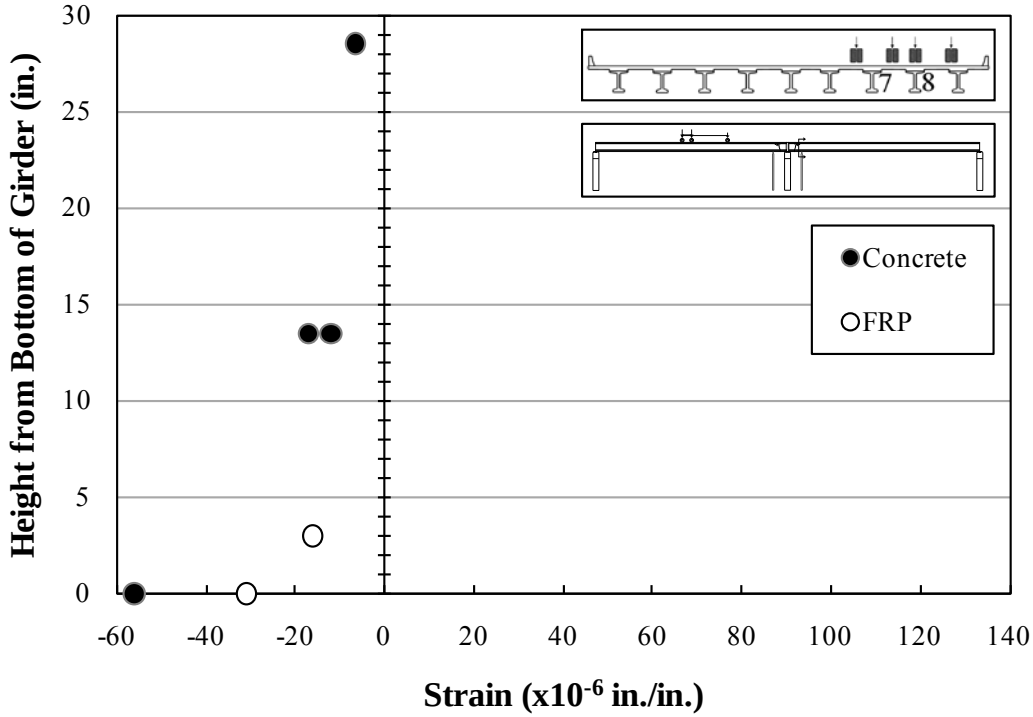

Figure B.199: Strains—Girder 8—Section 4—C1

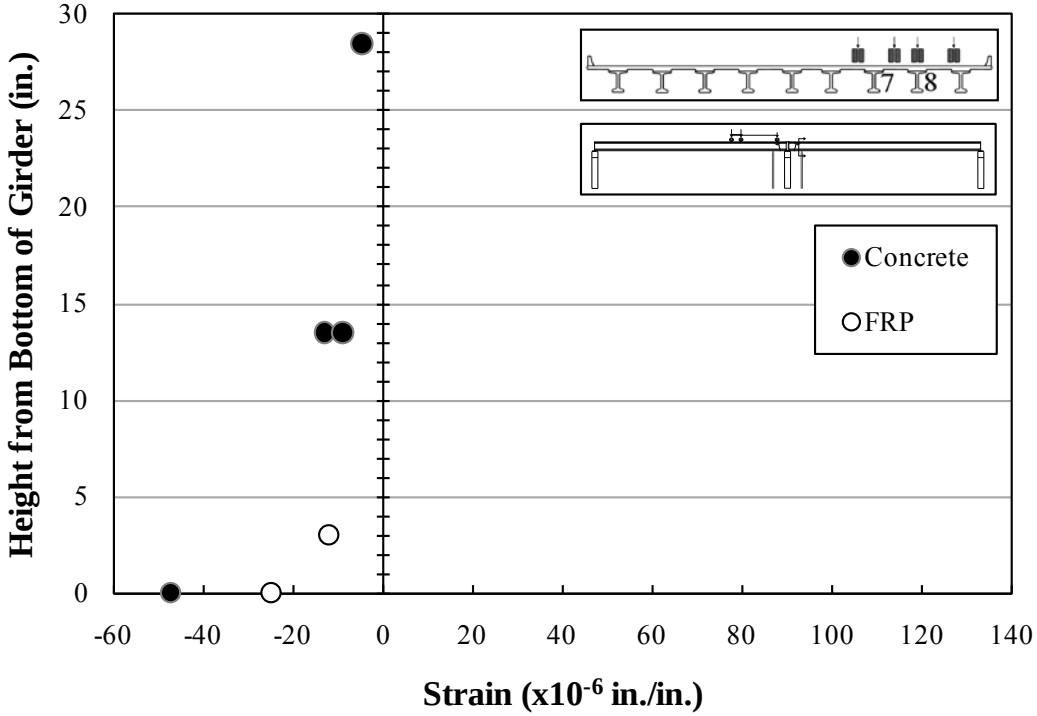

Figure B.200: Strains—Girder 8—Section 4—C2

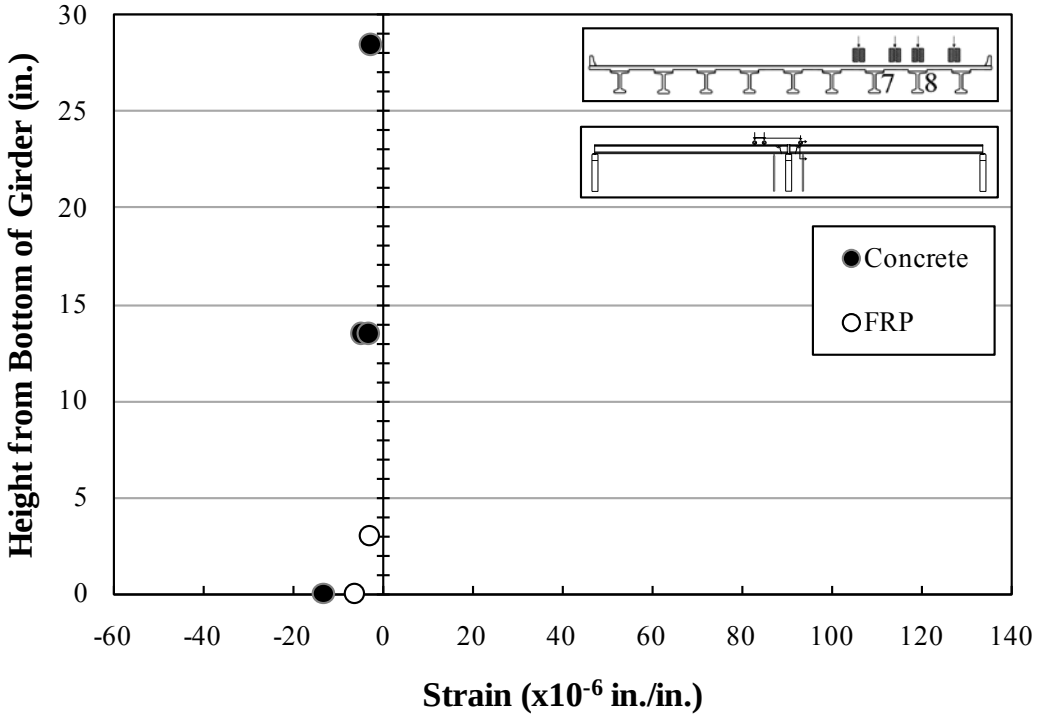

Figure B.201: Strains—Girder 8—Section 4—C3

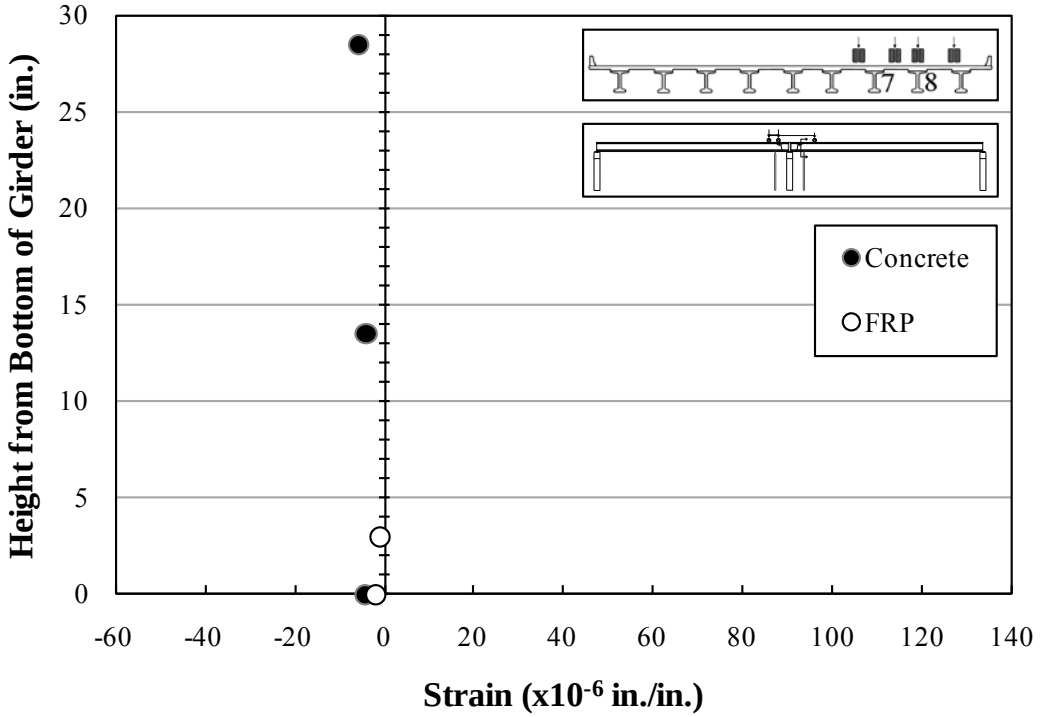

Figure B.202: Strains—Girder 8—Section 4—C4

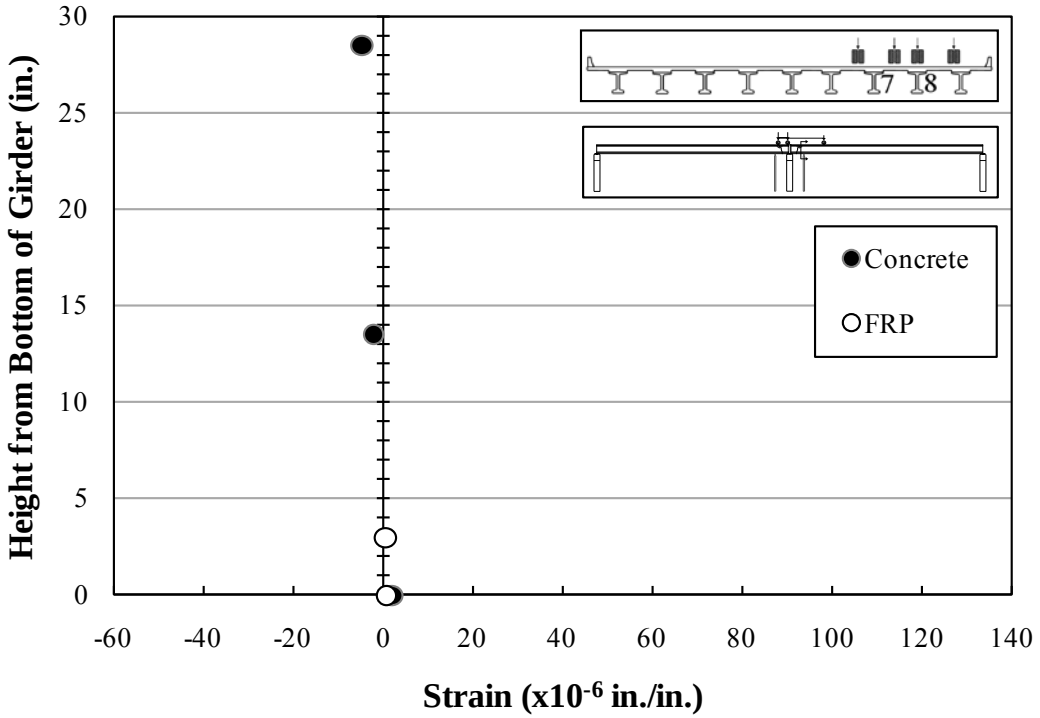

Figure B.203: Strains—Girder 8—Section 4—C5

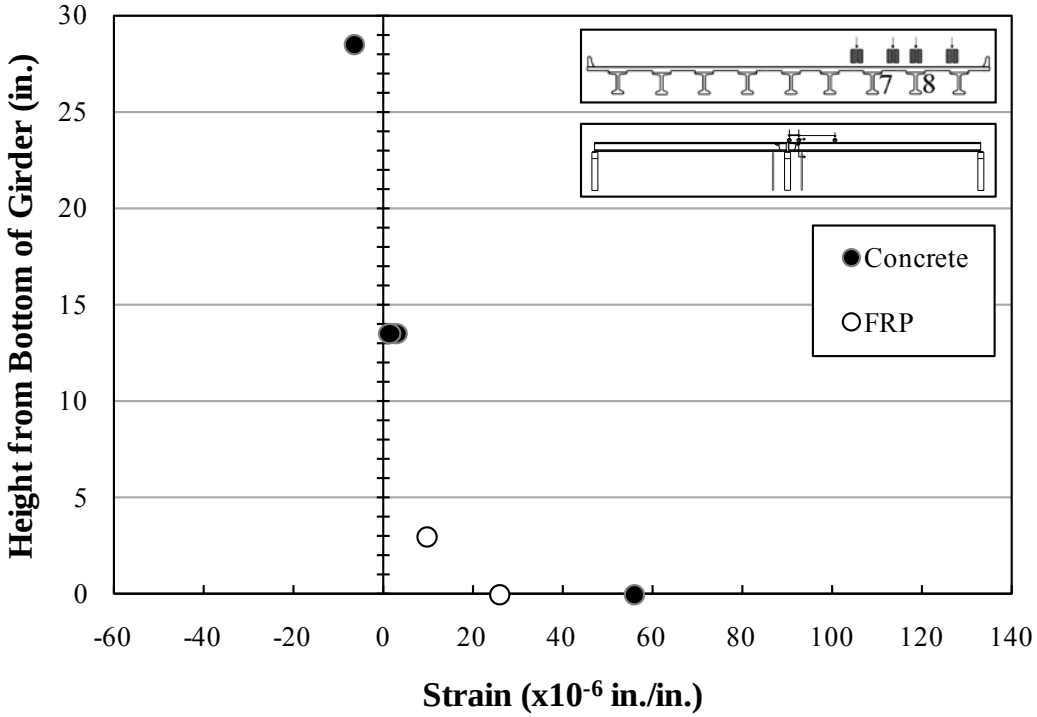

Figure B.204: Strains—Girder 8—Section 4—C6

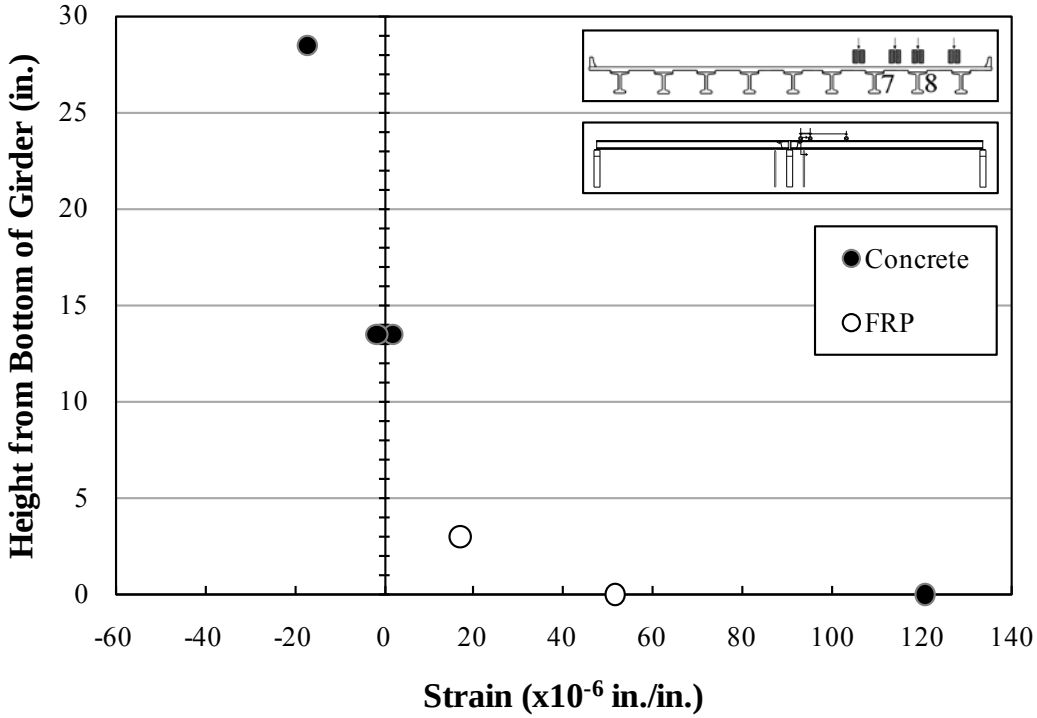

Figure B.205: Strains—Girder 8—Section 4—C7

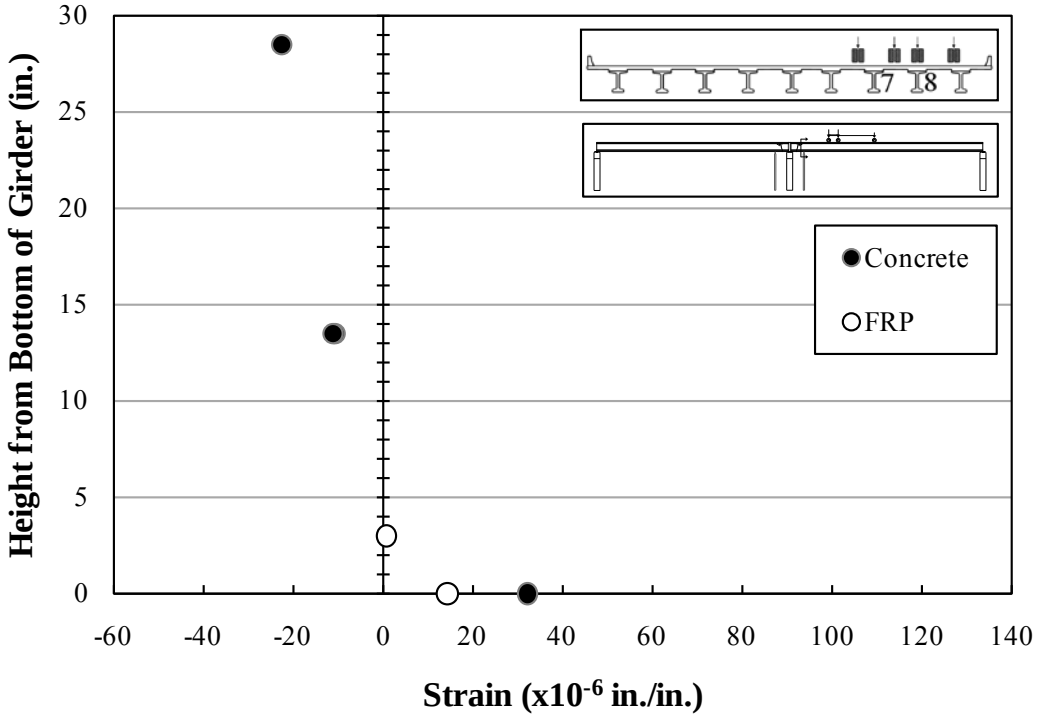

Figure B.206: Strains—Girder 8—Section 4—C8

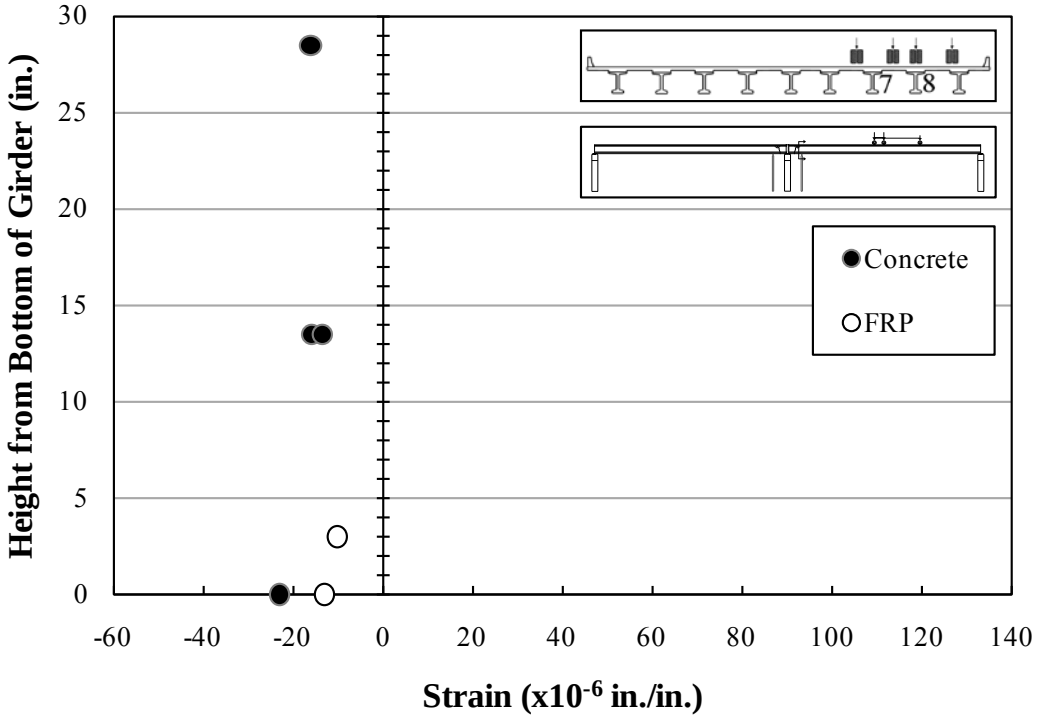

Figure B.207: Strains—Girder 8—Section 4—C9

B.2.4 Bottom-Fiber Strains—Both Girders

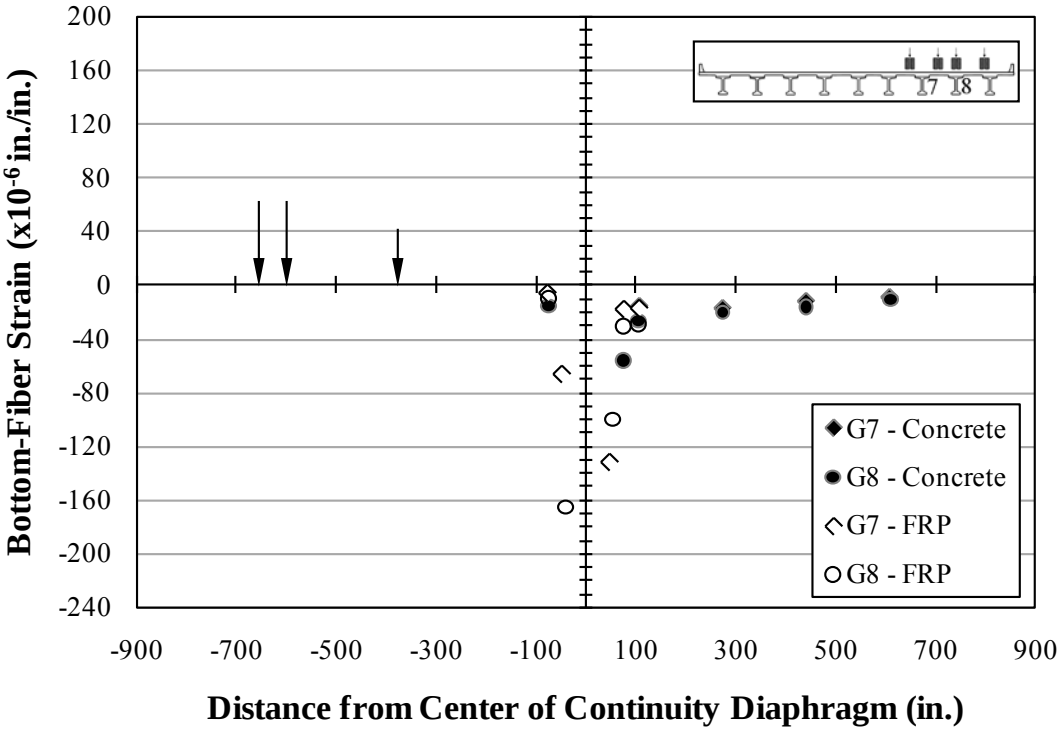

Figure B.208: Bottom-fiber strains—C1

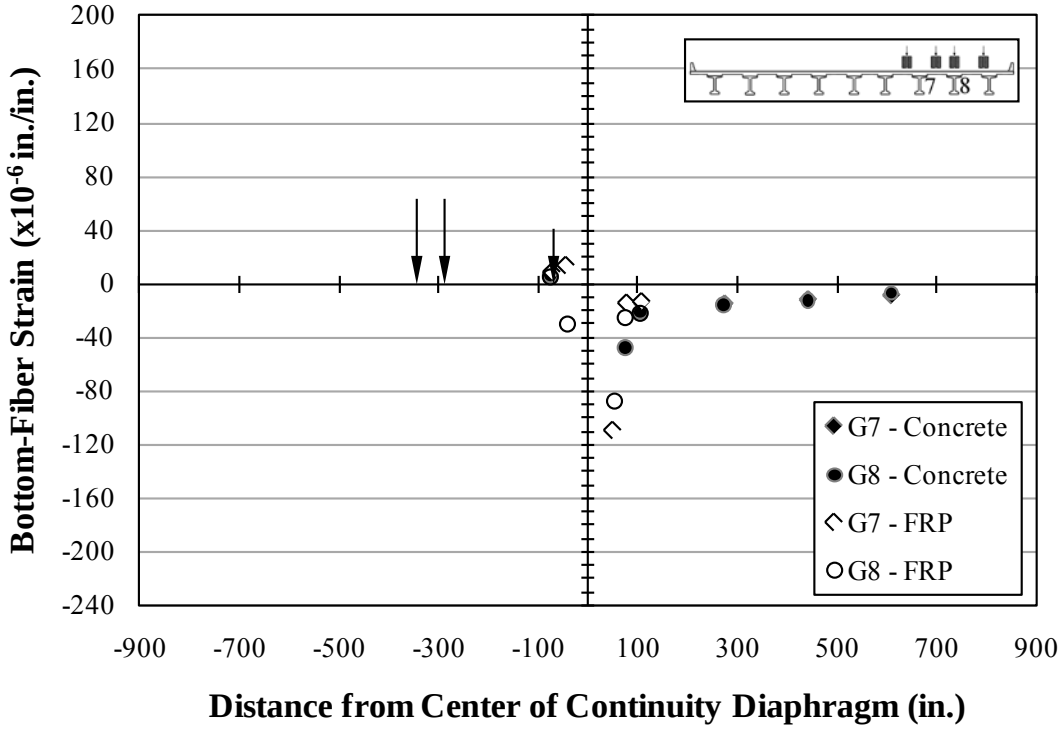

Figure B.209: Bottom-fiber strains—C2

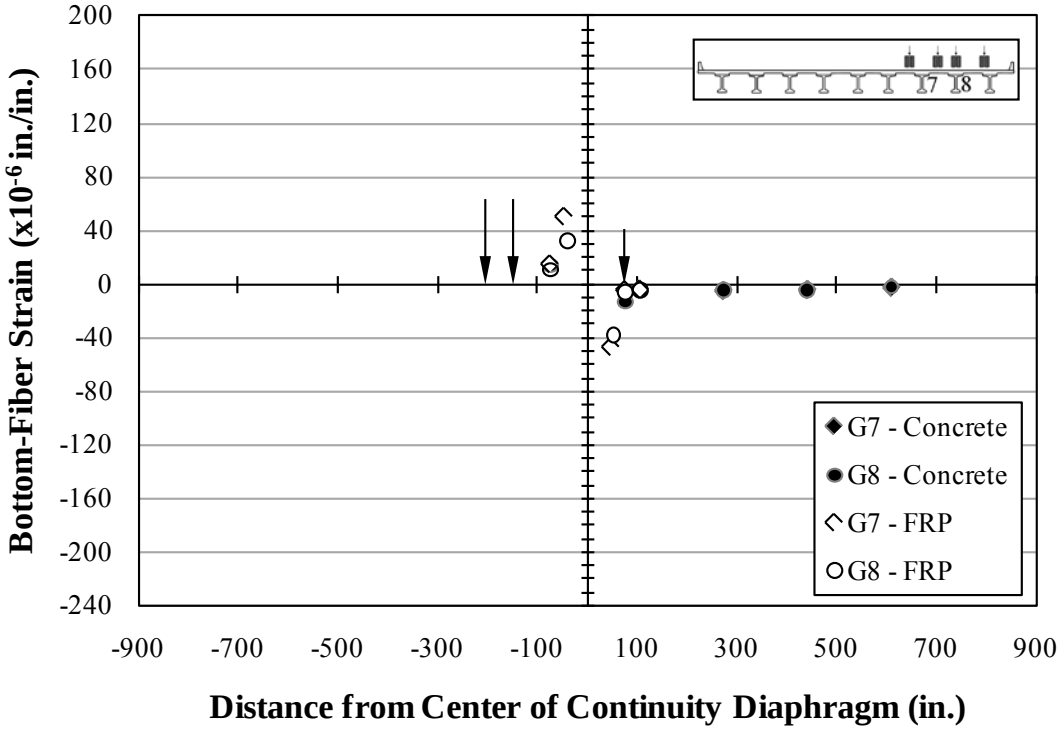

Figure B.210: Bottom-fiber strains—C3

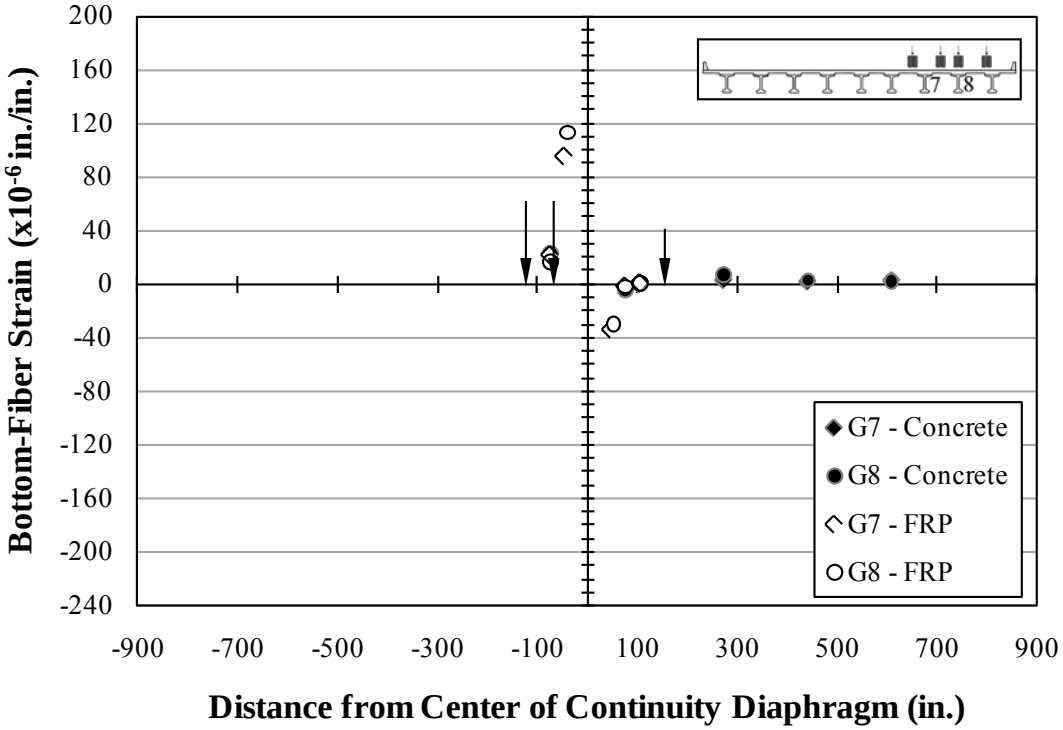

Figure B.211: Bottom-fiber strains—C4

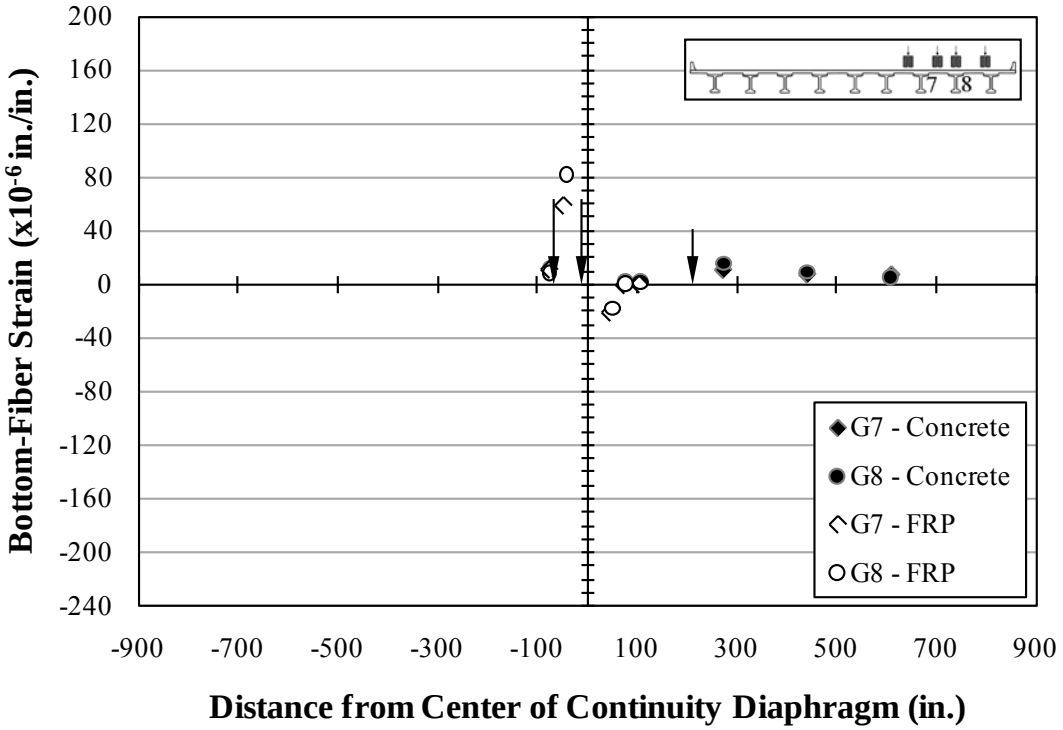

Figure B.212: Bottom-fiber strains—C5

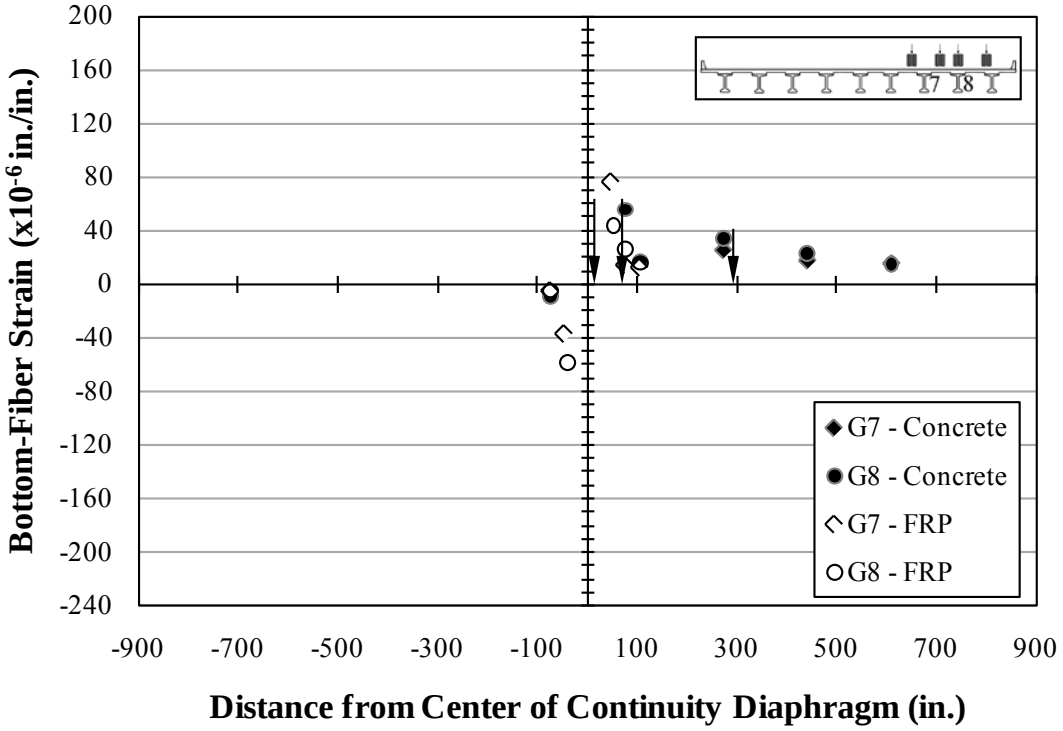

Figure B.213: Bottom-fiber strains—C6

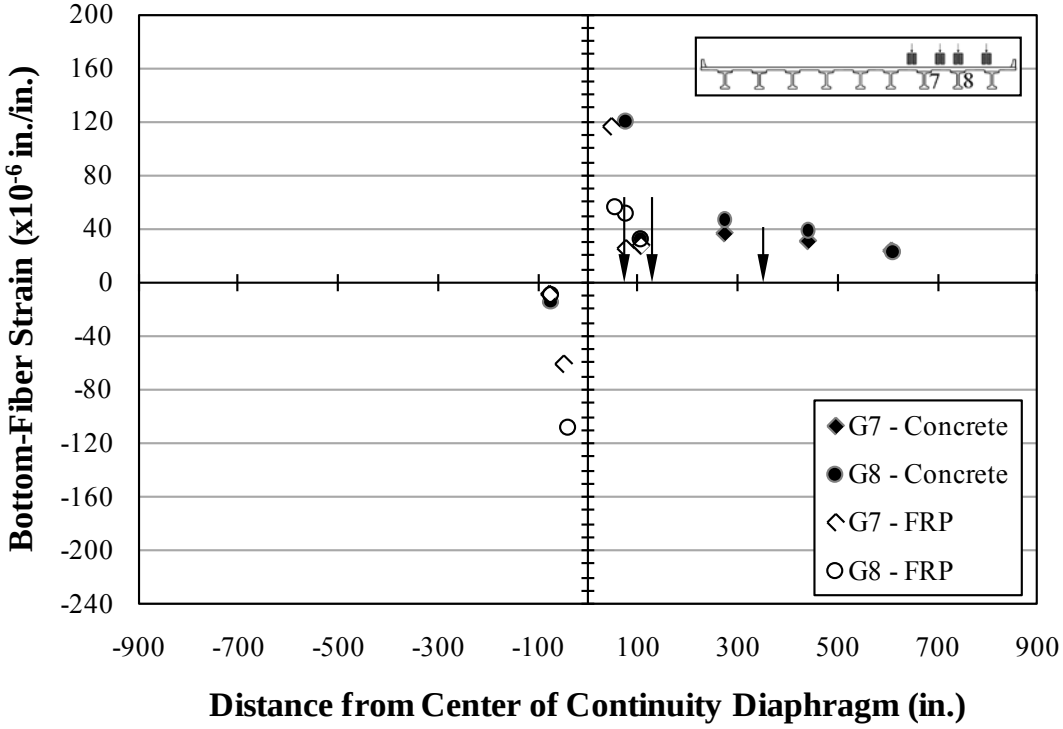

Figure B.214: Bottom-fiber strains—C7

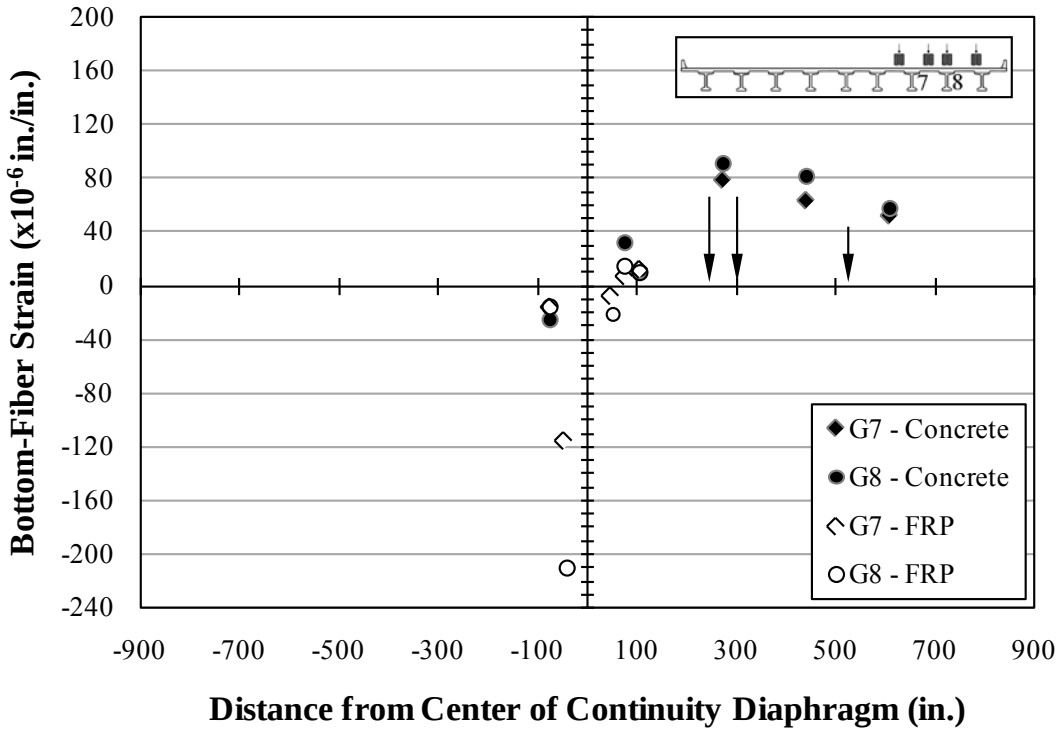

Figure B.215: Bottom-fiber strains—C8

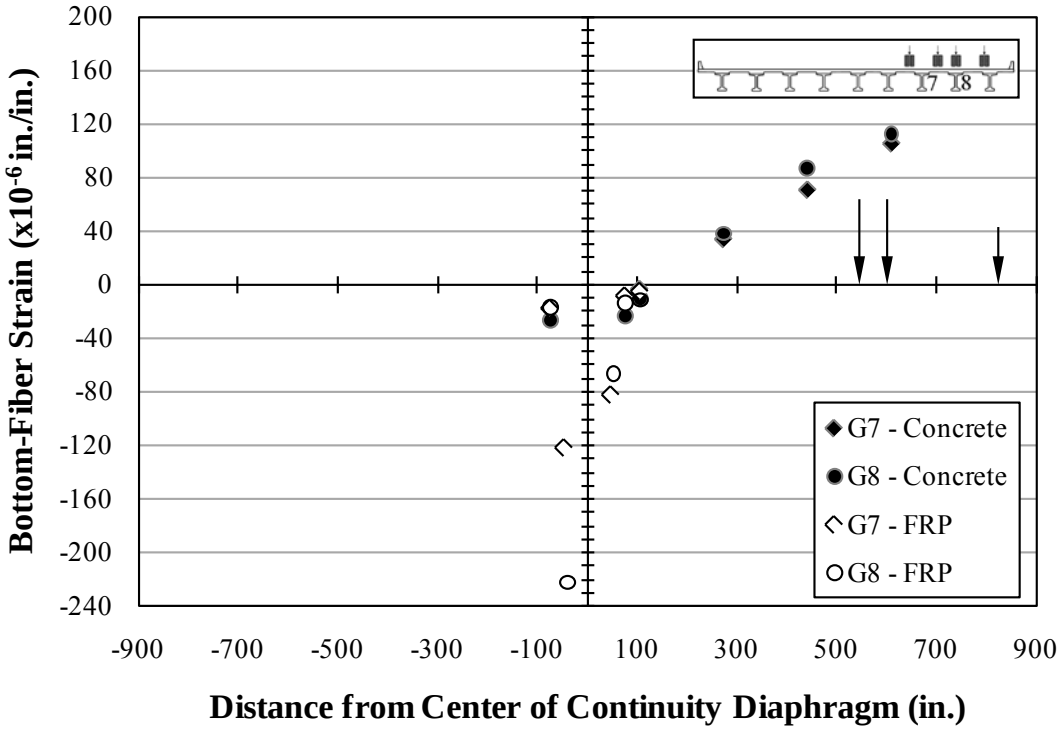

Figure B.216: Bottom-fiber strains—C9

B.2.4.1 Bottom-Fiber Strains—Girder 7

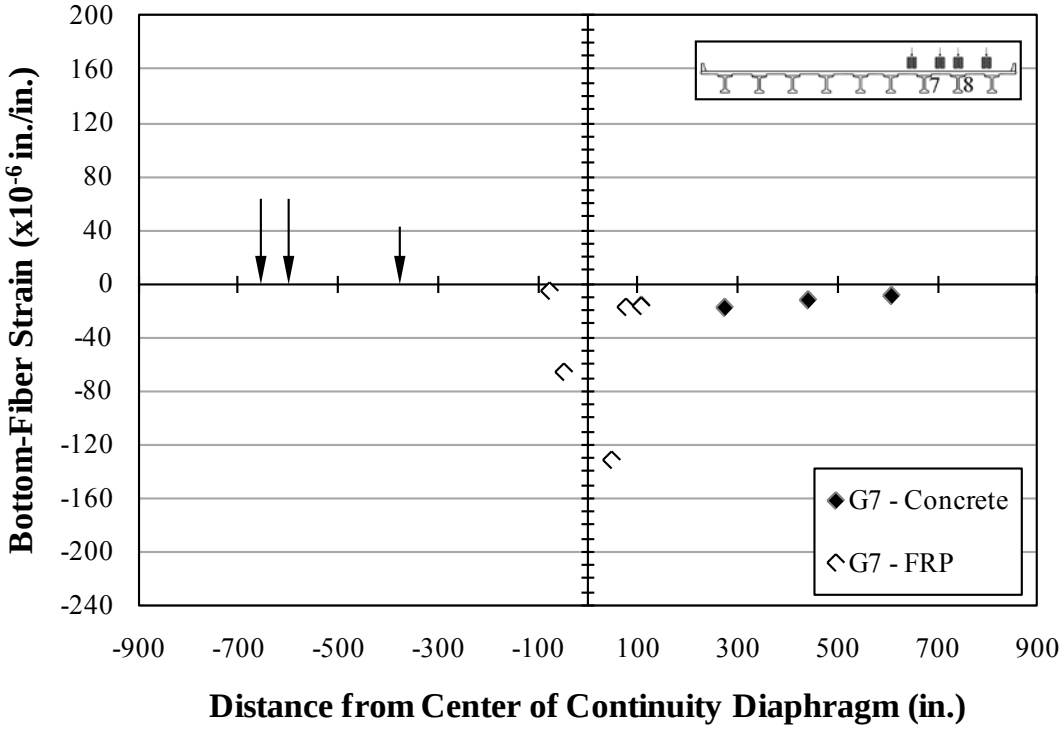

Figure B.217: Bottom-fiber strains—Girder 7—C1

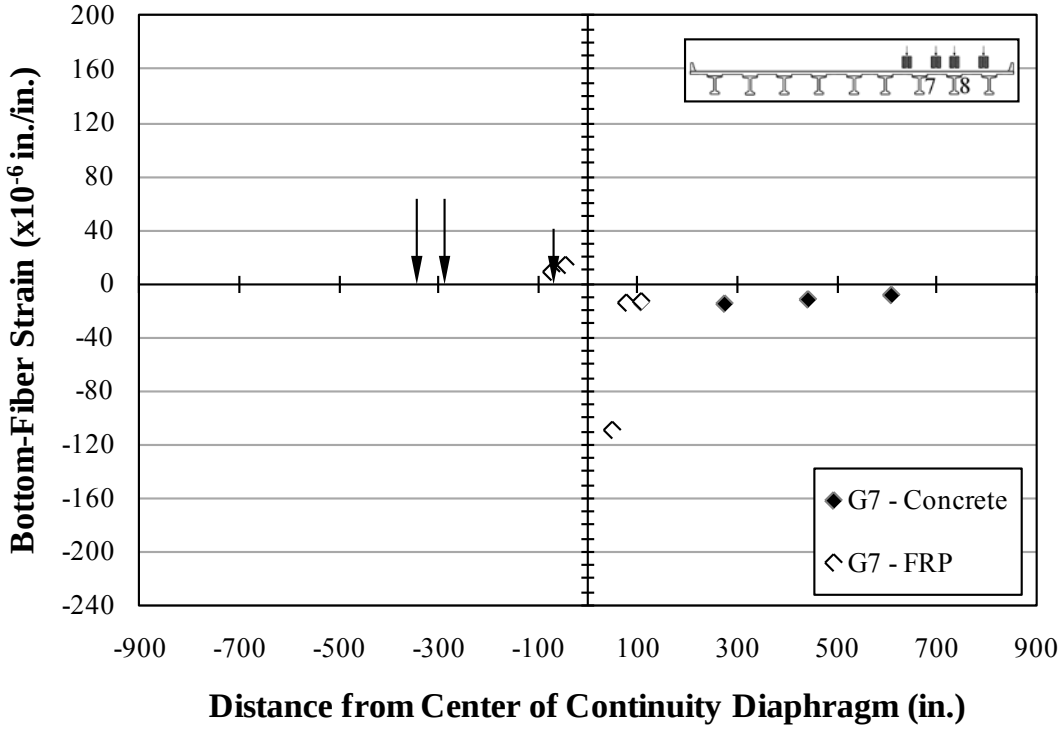

Figure B.218: Bottom-fiber strains—Girder 7—C2

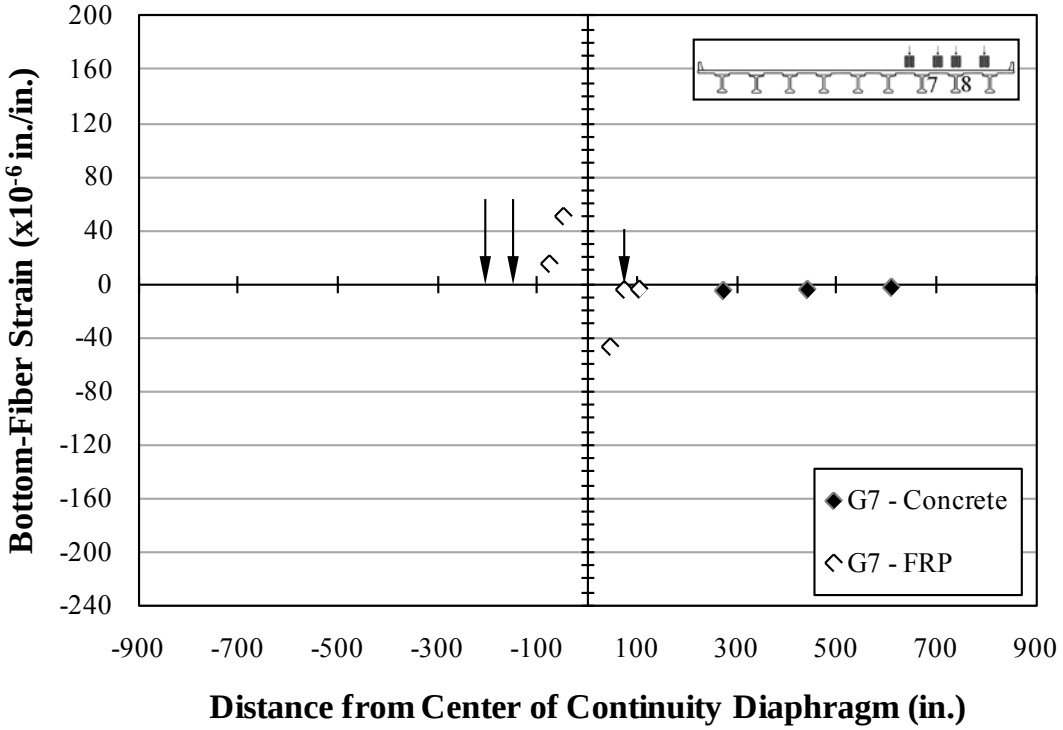

Figure B.219: Bottom-fiber strains—Girder 7—C3

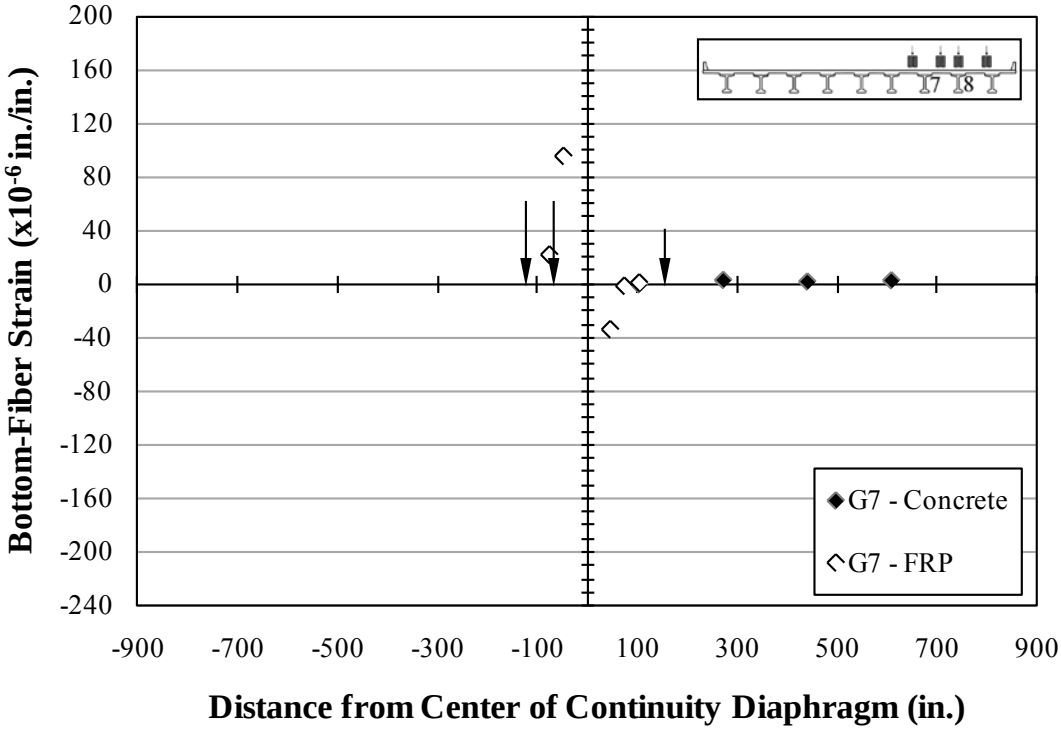

Figure B.220: Bottom-fiber strains—Girder 7—C4

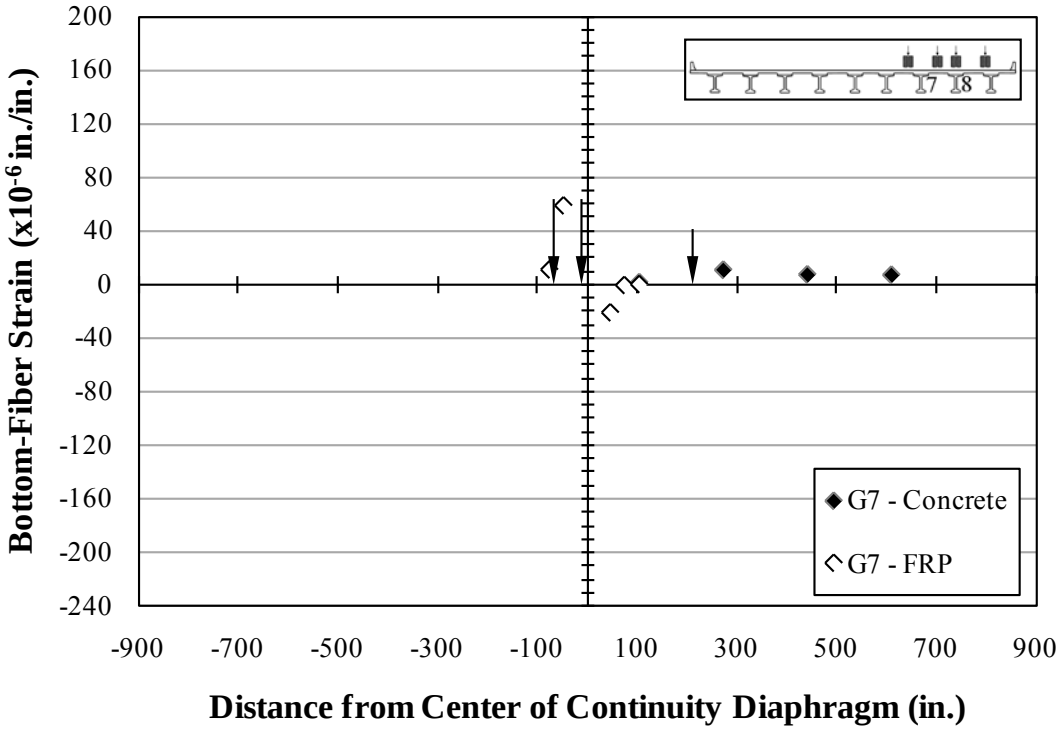

Figure B.221: Bottom-fiber strains—Girder 7—C5

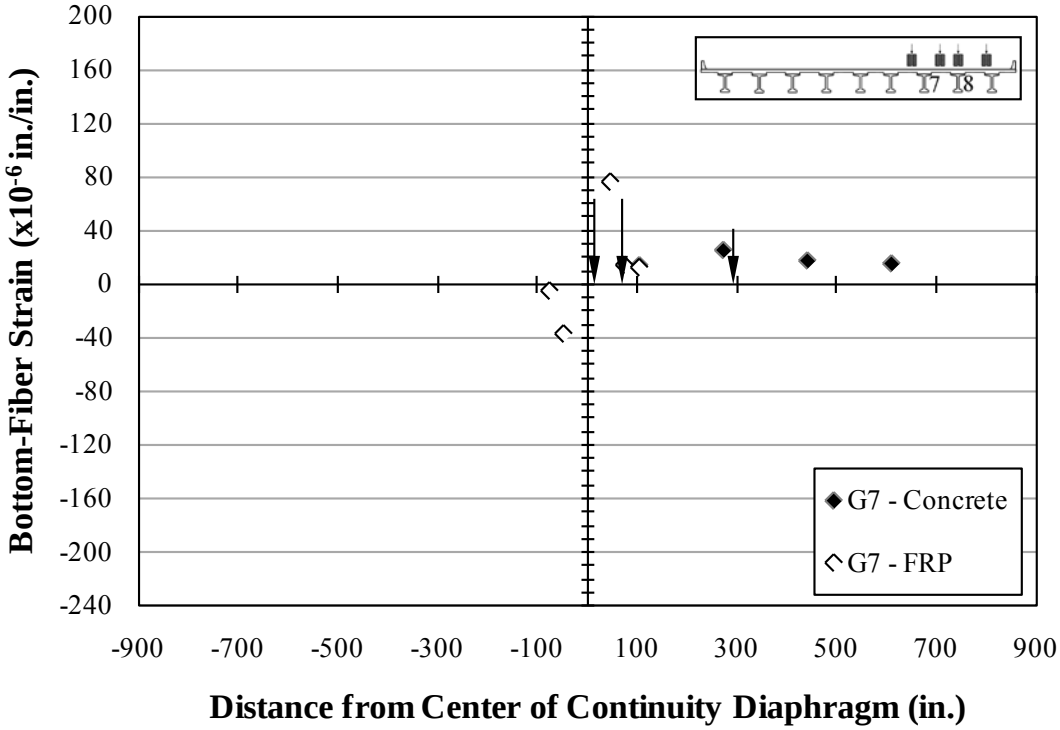

Figure B.222: Bottom-fiber strains—Girder 7—C6

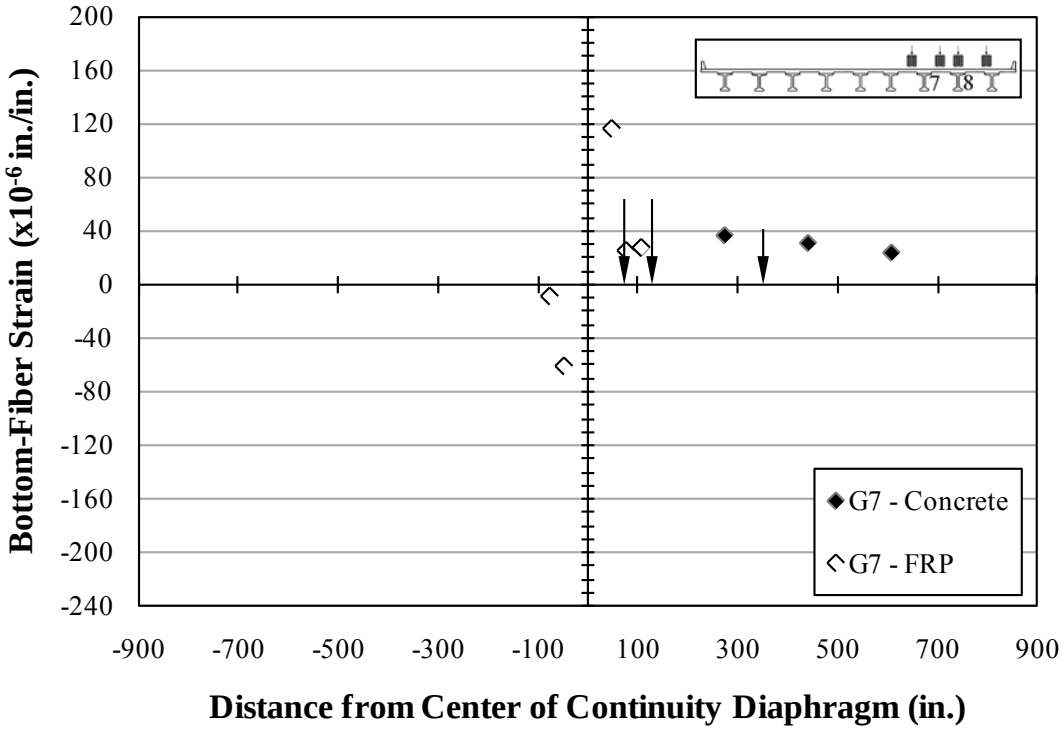

Figure B.223: Bottom-fiber strains—Girder 7—C7

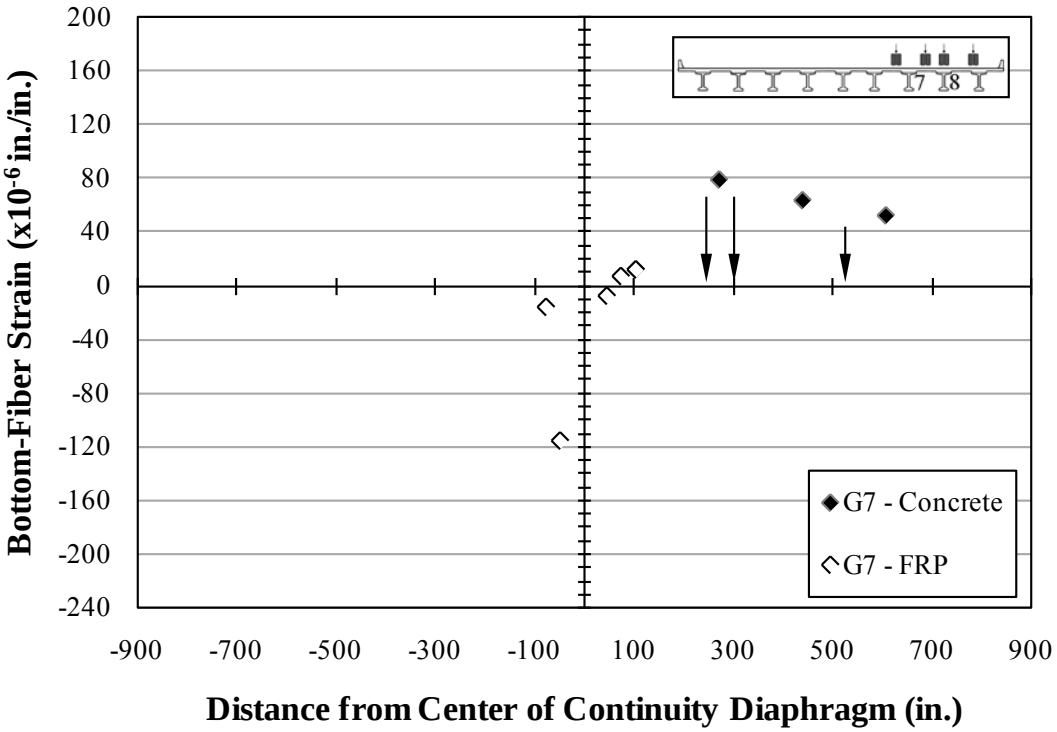

Figure B.224: Bottom-fiber strains—Girder 7—C8

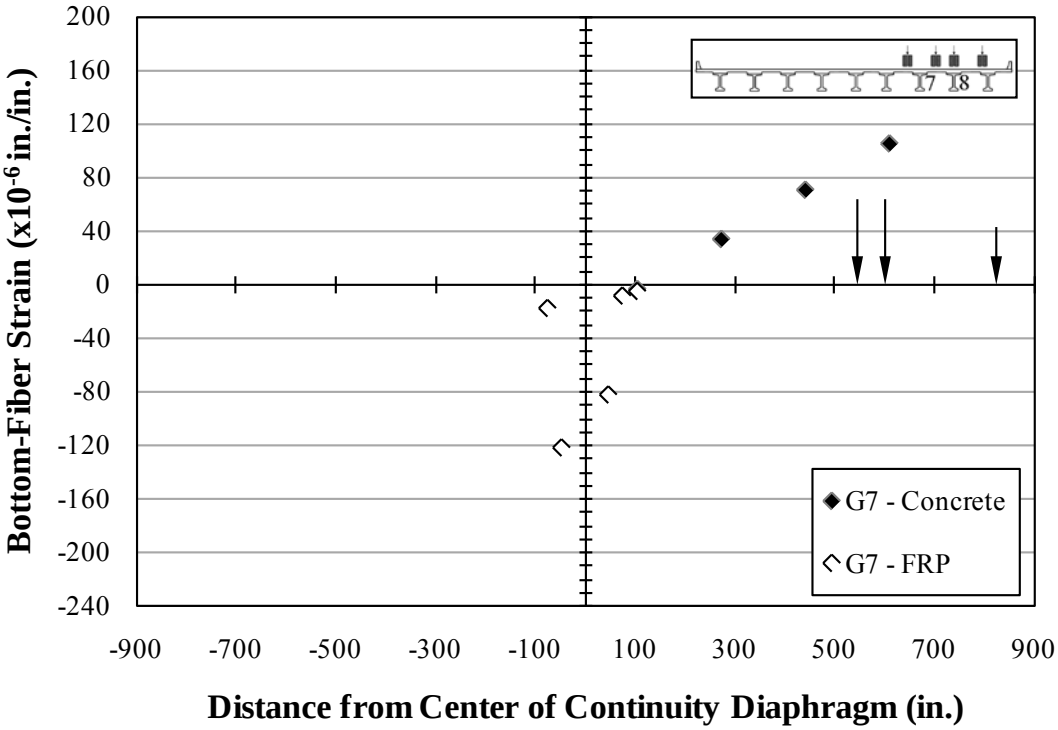

Figure B.225: Bottom-fiber strains—Girder 7—C9

B.2.4.2 Bottom-Fiber Strains—Girder 8

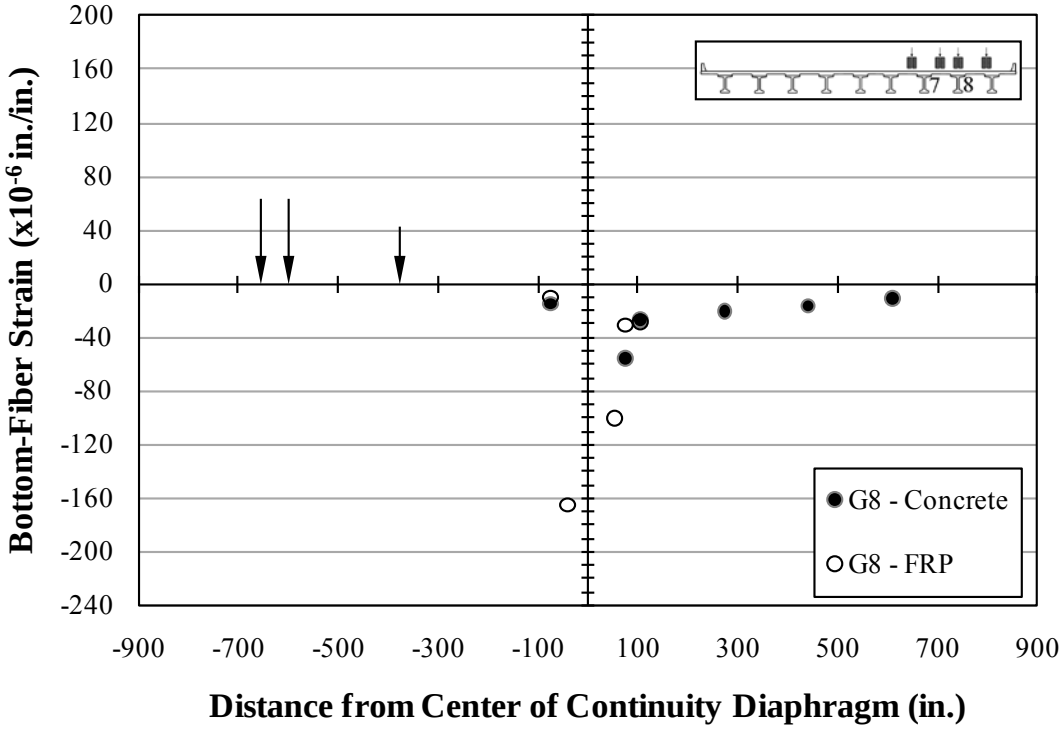

Figure B.226: Bottom-fiber strains—Girder 8—C1

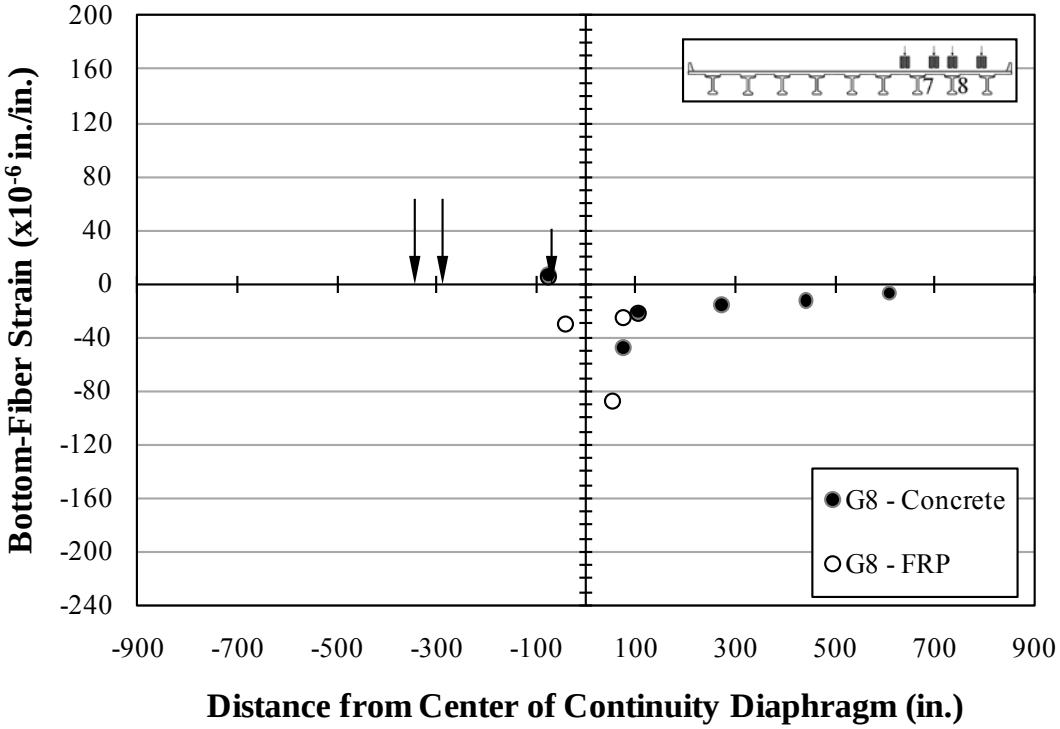

Figure B.227: Bottom-fiber strains—Girder 8—C2

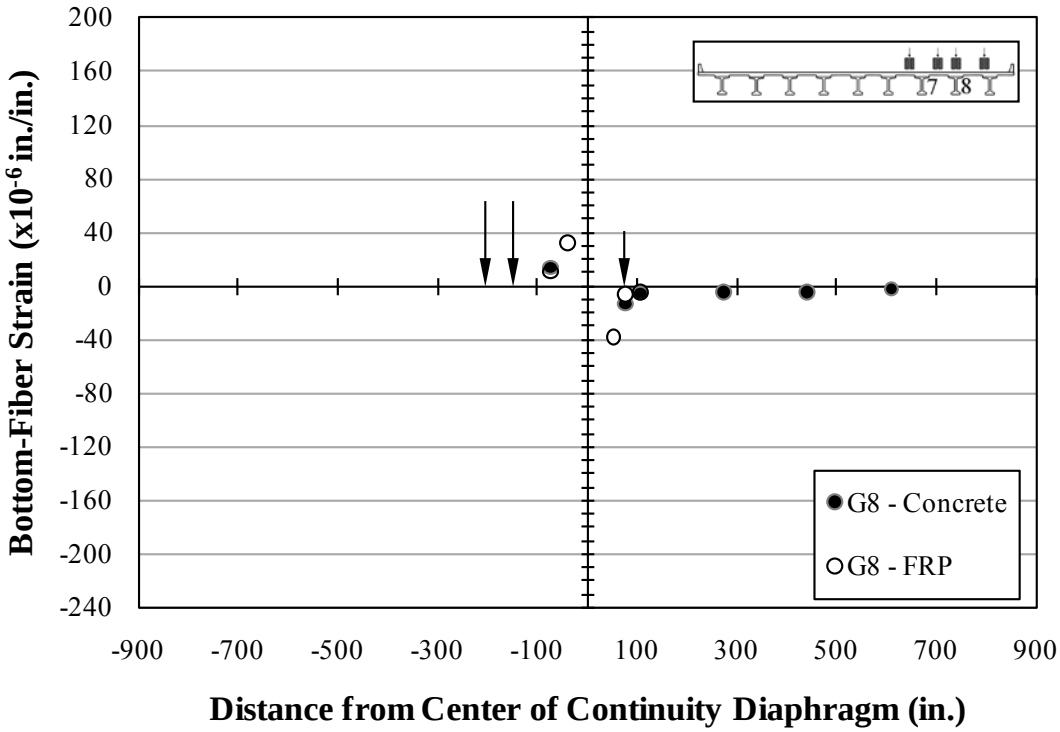

Figure B.228: Bottom-fiber strains—Girder 8—C3

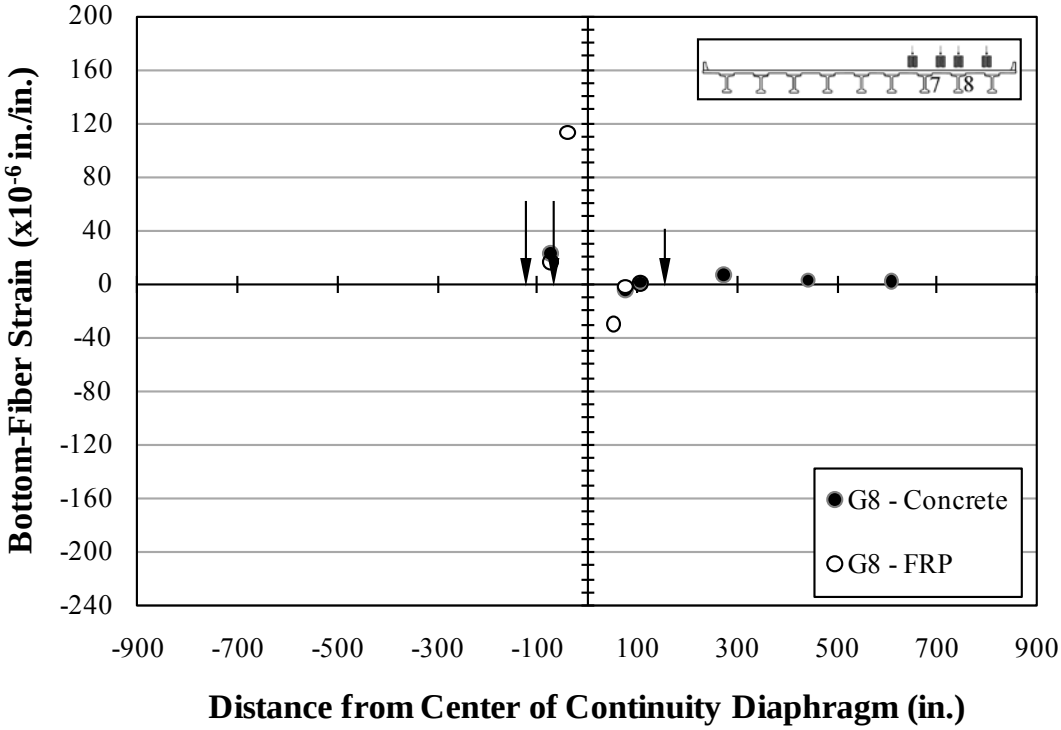

Figure B.229: Bottom-fiber strains—Girder 8—C4

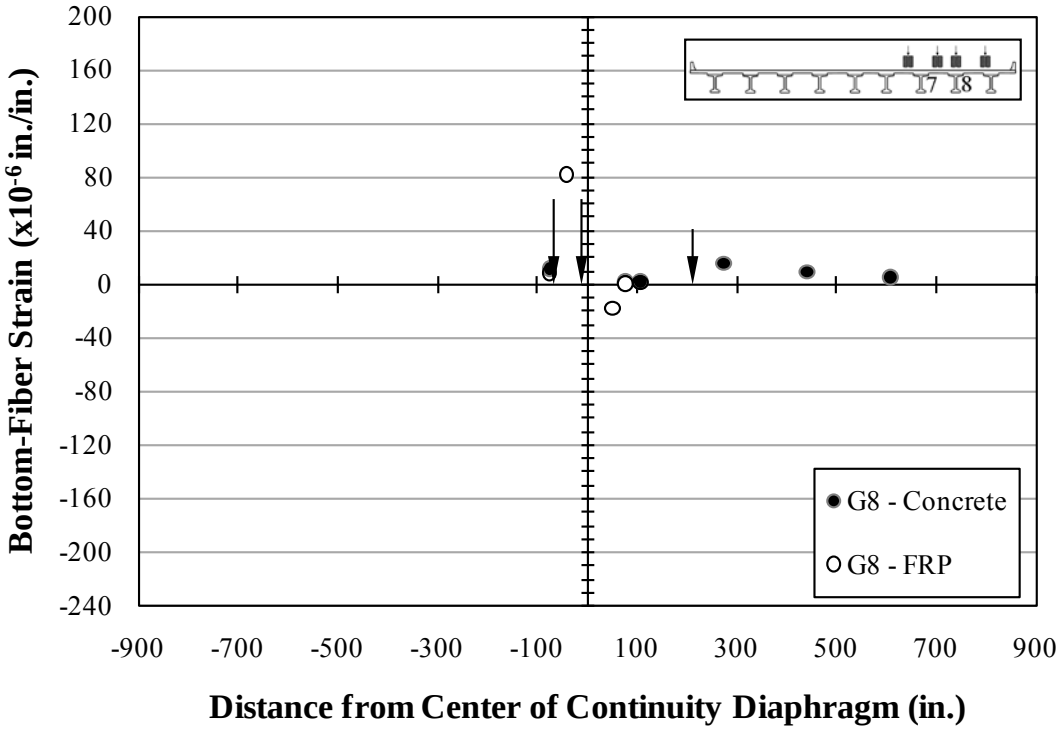

Figure B.230: Bottom-fiber strains—Girder 8—C5

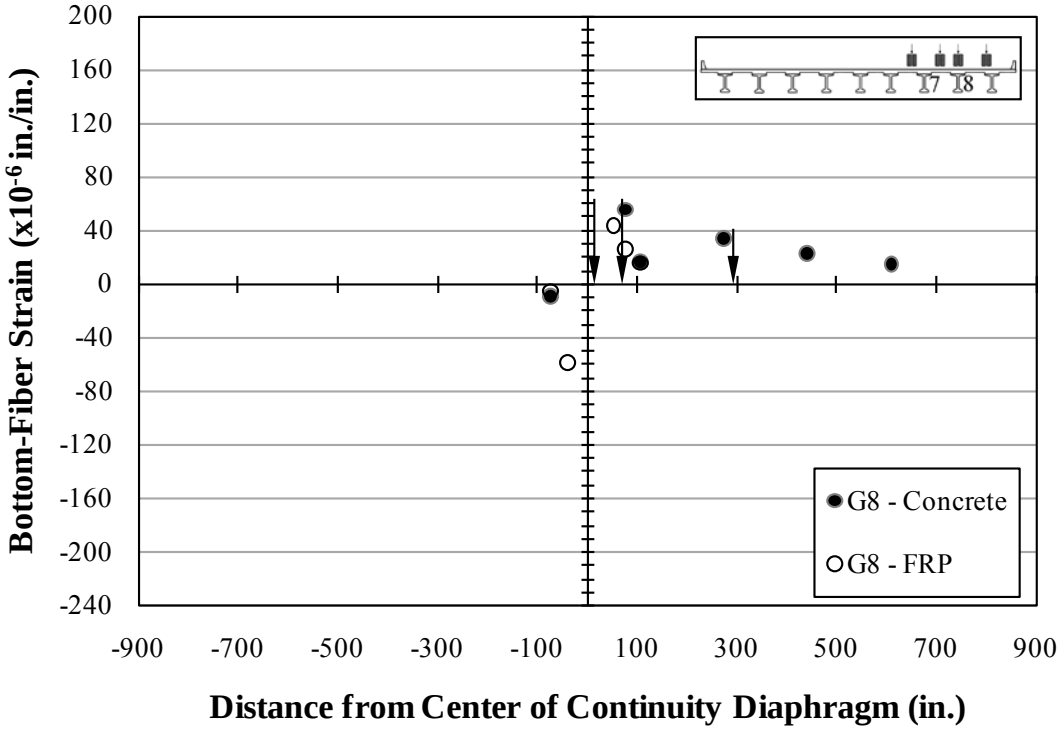

Figure B.231: Bottom-fiber strains—Girder 8—C6

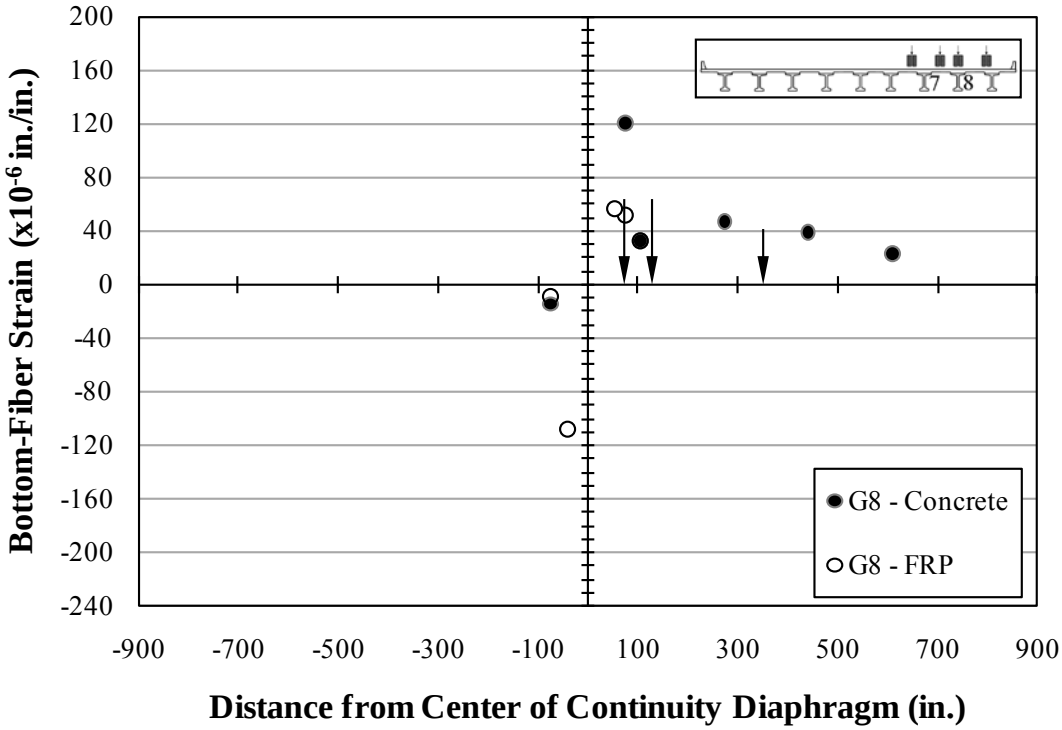

Figure B.232: Bottom-fiber strains—Girder 8—C7

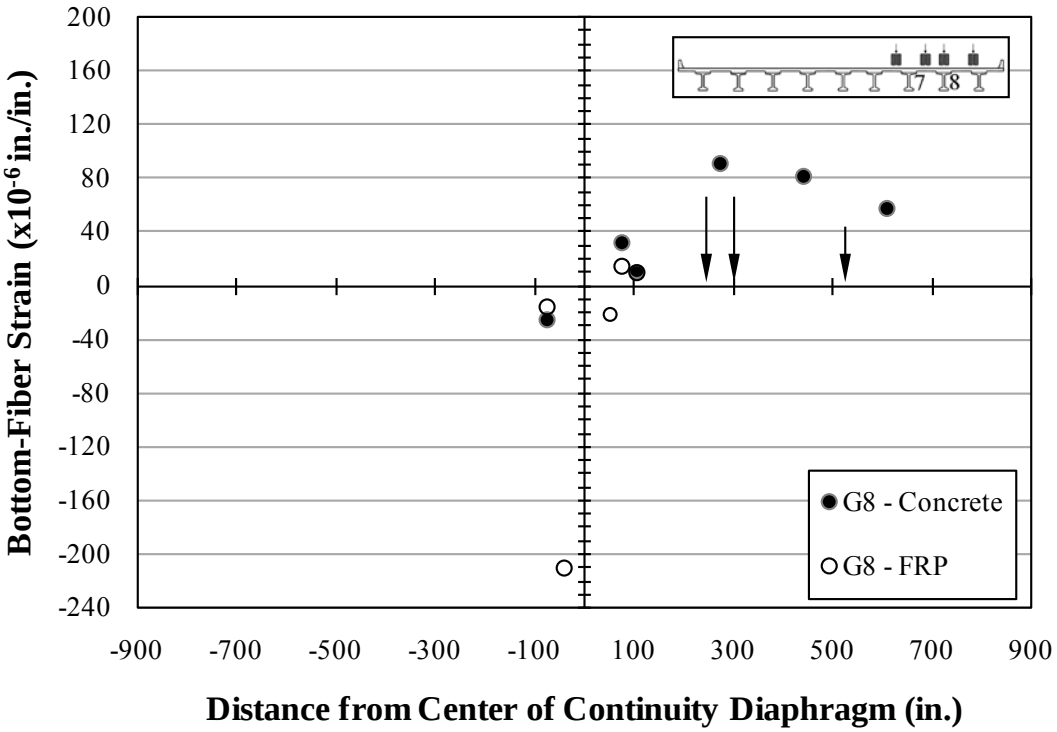

Figure B.233: Bottom-fiber strains—Girder 8—C8

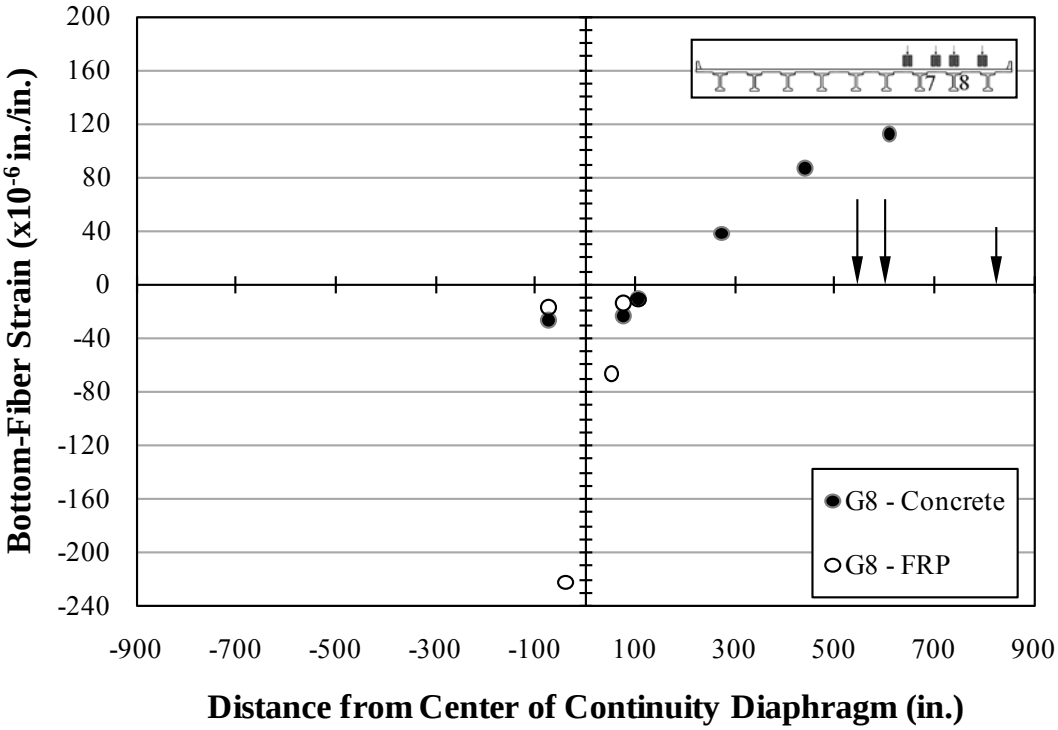

Figure B.234: Bottom-fiber strains—Girder 8—C9

Appendix C

MULTIPOSITION LOAD TEST—MEASUREMENTS

C.1 LANE A

The following tables represent measurements from the multiposition load test due to traversing Lane A

Table C.1: Lane A—crack-opening displacements

Girder	Gage	Height from bottom of girder (in.)	Distance from center of continuity diaphragm (in.) – Span 10 + Span 11	Crack-Opening Displacement (mm) – closing + opening								
				A1	A2	A3	A4	A5	A6	A7	A8	A9
7	CO7_10	13.5	-50	-0.008	0.010	0.016	0.024	0.014	-0.005	-0.008	-0.015	-0.016
	CO7_11	13.5	48	-0.027	-0.023	-0.005	-0.003	-0.003	0.022	0.041	0.012	-0.014
8	CO8_10	13.5	-40	-0.011	-0.009	-0.006	-0.004	-0.002	-0.004	-0.005	-0.008	-0.009
	CO8_11	13.5	56	-0.013	-0.011	-0.004	-0.002	-0.001	0.010	0.018	0.005	-0.005

Table C.2: Lane A—deflections

Girder	Gage	Height from bottom of girder (in.)	Distance from center of continuity diaphragm (in.) – Span 10 + Span 11	Deflection (in.) – downward + upward								
				A1	A2	A3	A4	A5	A6	A7	A8	A9
7	D7_10_A	n/a	-608	-0.32	-0.20	-0.11	-0.06	-0.02	0.01	0.02	0.04	0.04
	D7_10_B	n/a	-308	-0.22	-0.18	-0.11	-0.07	-0.03	0.00	0.01	0.03	0.04
	D7_11_C	n/a	158	0.02	0.01	0.00	-0.02	-0.03	-0.05	-0.08	-0.12	-0.12
	D7_11_D	n/a	308	0.04	0.03	0.00	-0.02	-0.04	-0.07	-0.11	-0.20	-0.22
	D7_11_E	n/a	458	0.05	0.03	0.01	-0.02	0.03	-0.08	-0.12	-0.22	-0.29
	D7_11_F	n/a	608	0.05	0.03	0.01	-0.01	-0.03	-0.07	-0.11	-0.22	-0.33
8	D8_10_A	n/a	-608	-0.26	-0.16	-0.09	-0.05	-0.02	0.01	0.02	0.04	0.04
	D8_10_B	n/a	-308	-0.17	-0.13	-0.08	-0.05	-0.02	0.00	0.01	0.03	0.03
	D8_11_C	n/a	158	0.02	0.01	0.00	-0.01	-0.02	-0.04	-0.06	-0.09	-0.09
	D8_11_D	n/a	308	0.04	0.03	0.00	-0.01	-0.03	-0.06	-0.08	-0.15	-0.17
	D8_11_E	n/a	458	0.04	0.03	0.01	-0.01	-0.03	-0.06	-0.09	-0.18	-0.23
	D8_11_F	n/a	608	0.04	0.03	0.01	-0.01	-0.02	-0.06	-0.09	-0.17	-0.25

Table C.3: Lane A—cross-section strains—Girder 7—Span 10

Section	Gage	Height from bottom of girder (in.)	Distance from center of continuity diaphragm (in.) – Span 10 + Span 11	Strain ($x10^{-6}$in./in.) – compressive + tensile								
				A1	A2	A3	A4	A5	A6	A7	A8	A9
Girder 7 Cross Section 1	S7_10_1V	28.5	-75	-6	2	3	5	3	-2	-3	-6	-6
	S7_10_1W	13.5	-75	-7	4	7	10	4	-4	-6	-11	-12
	S7_10_1X	13.5	-75	-6	5	8	11	5	-4	-6	-11	-12
	S7_10_1Y	3.0	-75	-11	7	14	18	8	-6	-9	-19	-20
	F7_10_1M	0.0	-74	-9	11	16	23	13	-6	-9	-18	-19
Girder 7 Cross Section 2	S7_10_2V	28.5	-13	2	3	3	3	3	1	-1	-4	-5
	S7_10_2W	13.5	-13	0	-1	-1	-3	-1	1	0	-4	-4
	S7_10_2X	13.5	-13	6	4	3	0	2	2	1	-1	-2
	S7_10_2Y	3.0	-13	-157	-135	-91	-49	-27	-46	-64	-127	-131
	F7_10_2Z	3.0	-14	-39	-27	-16	-7	-3	-12	-17	-29	-27

Table C.4: Lane A—cross-section strains—Girder 7—Span 11

Section	Gage	Height from bottom of girder (in.)	Distance from center of continuity diaphragm (in.) – Span 10 + Span 11	Strain ($x10^{-6}$in./in.) – compressive + tensile								
				A1	A2	A3	A4	A5	A6	A7	A8	A9
Girder 7 Cross Section 3	S7_11_3V	28.5	13	-7	-4	-3	-1	0	1	-2	-2	-2
	S7_11_3W	13.5	13	-17	-10	0	4	7	12	9	2	-2
	S7_11_3X	13.5	13	-8	-2	1	4	7	6	2	4	4
	S7_11_3Y	3.0	13	-11	-8	-5	-7	-2	-3	-6	-15	-17
	S7_11_3Z	3.0	13	-10	-8	-6	-5	-4	-6	-9	-13	-11
Girder 7 Cross Section 4	S7_11_4V	28.5	75	-2	-1	0	-2	-2	-2	-5	-8	-6
	S7_11_4W	13.5	75	-10	-7	-3	-1	-1	4	5	-3	-8
	S7_11_4X	13.5	75	-11	-8	-2	-1	-1	5	6	-2	-8
	S7_11_4Y	3.0	75	-17	-13	-2	0	1	13	22	6	-8
	F7_11_4M	0.0	74	-21	-16	-3	0	1	17	28	8	9

Table C.5: Lane A—cross-section strains—Girder 8—Span 10

Section	Gage	Height from bottom of girder (in.)	Distance from center of continuity diaphragm (in.) – Span 10 + Span 11	Strain ($x10^{-6}$in./in.) – compressive + tensile								
				A1	A2	A3	A4	A5	A6	A7	A8	A9
Girder 8 Cross Section 1	S8_10_1V	28.5	-75	-5	-2	-1	0	0	-3	-3	-5	-6
	S8_10_1W	13.5	-75	-7	1	3	5	2	-4	-6	-11	-12
	S8_10_1X	13.5	-75	-9	1	3	7	4	-4	-7	-12	-12
	F8_10_1Y	3.0	-74	-5	1	2	3	1	-3	-4	-8	-8
	S8_10_1M	0.0	-75	-11	4	7	13	7	-6	-9	-16	-17
	F8_10_1M	0.0	-74	-4	5	6	10	5	-4	-6	-11	-11
Girder 8 Cross Section 2	S8_10_2V	28.5	-13	0	1	1	1	2	0	-1	-3	-4
	S8_10_2W	13.5	-13	2	4	3	3	2	-1	-2	-7	-9
	S8_10_2X	13.5	-13	4	6	5	3	4	1	-2	-6	-8
	F8_10_2Y	3.0	-14	-32	-21	-14	-10	-7	-14	-18	-28	-30
	F8_10_2Z	3.0	-14	-28	-19	-11	-5	-2	-4	-8	-13	-13

Table C.6: Lane A—cross-section strains—Girder 8—Span 11

Section	Gage	Height from bottom of girder (in.)	Distance from center of continuity diaphragm (in.) – Span 10 + Span 11	Strain ($x10^{-6}$in./in.) – compressive + tensile								
				A1	A2	A3	A4	A5	A6	A7	A8	A9
Girder 8 Cross Section 3	S8_11_3V	28.5	13	-42	-35	-26	-22	-17	-13	-17	-26	-32
	S8_11_3W	13.5	13	-18	-10	-5	-1	1	0	-3	-6	-7
	S8_11_3X	13.5	13	-31	-21	-5	-2	2	15	17	-1	-14
	F8_11_3Y	3.0	14	-33	-25	-15	-11	-7	-2	-5	-15	-22
	F8_11_3Z	3.0	14	-28	-22	-17	-15	-12	-12	-22	-48	-49
Girder 8 Cross Section 4	S8_11_4V	28.5	75	-4	-2	-2	-4	-4	-5	-12	-16	-12
	S8_11_4W	13.5	75	-11	-8	-4	-3	-2	0	-2	-8	-12
	S8_11_4X	13.5	75	-9	-16	-2	-3	-1	3	2	-2	-5
	F8_11_4Y	3.0	74	-11	-8	-3	-1	0	4	6	1	-5
	S8_11_4M	0.0	75	-39	-32	-11	-4	-1	27	58	26	-7
	F8_11_4M	0.0	74	-23	-18	-6	-1	0	14	25	9	-6

Table C.7: Lane A—bottom-fiber strains—Girder 7

Span	Gage	Height from bottom of girder (in.)	Distance from center of continuity diaphragm (in.) – Span 10 + Span 11	Strain ($x10^{-6}$in./in.) – compressive + tensile								
				A1	A2	A3	A4	A5	A6	A7	A8	A9
10	F7_10_1M	0	-74	-9	11	16	23	13	-6	-9	-18	-19
	F7_10_CK	0	-47	-87	21	58	108	73	-33	-60	-125	-132
11	F7_11_CK	0	47	-148	-119	-36	-25	-13	90	128	-8	-93
	F7_11_4M	0	74	-21	-16	-3	0	1	17	28	8	-9
	F7_11_5M	0	104	-20	-15	-3	3	3	17	32	14	-5
	S7_11_5M	0	105	-18	-15	-3	2	3	15	29	13	-5
	S7_11_6M	0	273	-19	-15	-6	4	12	30	42	84	35
	S7_11_7M	0	441	-14	-11	-3	4	9	22	36	69	75
	S7_11_8M	0	609	-8	-6	-3	1	4	10	16	40	75

Table C.8: Lane A—bottom-fiber strains—Girder 8

Span	Gage	Height from bottom of girder (in.)	Distance from center of continuity diaphragm (in.) – Span 10 + Span 11	Strain ($x10^{-6}$in./in.) – compressive + tensile								
				A1	A2	A3	A4	A5	A6	A7	A8	A9
10	S8_10_1M	0	-75	-11	4	7	13	7	-6	-9	-16	-17
	F8_10_1M	0	-74	-4	5	6	10	5	-4	-6	-11	-11
	F8_10_CK	0	-41	-104	-17	8	53	41	-42	-71	-126	-139
11	F8_11_CK	0	52	-65	-51	-21	-17	-10	21	27	-18	-44
	F8_11_4M	0	74	-23	-18	-6	-1	0	14	25	9	-6
	S8_11_4M	0	75	-39	-32	-11	-4	-1	27	58	26	-7
	F8_11_5M	0	104	-20	-14	-3	1	2	11	22	9	-4
	S8_11_5M	0	105	-18	-14	-4	1	1	10	20	7	-5
	S8_11_6M	0	273	-15	-11	-4	3	9	21	28	56	26
	S8_11_7M	0	441	-11	-8	-3	2	6	17	27	54	61
	S8_11_8M	0	609	-8	-6	-3	1	4	10	16	40	75

Table C.9: Lane A—FRP strains—Girder 7

Span	Gage	Height from bottom of girder (in.)	Distance from center of continuity diaphragm (in.) – Span 10 + Span 11	Strain ($x10^{-6}$in./in.) – compressive + tensile								
				A1	A2	A3	A4	A5	A6	A7	A8	A9
10	F7_10_1M	0	-74	-9	11	16	23	13	-6	-9	-18	-19
	F7_10_CK	0	-47	-87	21	58	108	73	-33	-60	-125	-132
	F7_10_2Z	3	-13	-39	-27	-16	-7	-3	-12	-17	-29	-27
11	F7_11_CK	0	47	-148	-119	-36	-25	-13	90	128	-8	-93
	F7_11_4M	0	74	-21	-16	-3	0	1	17	28	8	-9
	F7_11_5M	0	104	-20	-15	-3	3	3	17	32	14	-5

Table C.10: Lane A—FRP strains—Girder 8

Span	Gage	Height from bottom of girder (in.)	Distance from center of continuity diaphragm (in.) – Span 10 + Span 11	Strain ($x10^{-6}$in./in.) – compressive + tensile								
				A1	A2	A3	A4	A5	A6	A7	A8	A9
10	F8_10_1Y	3	-74	-5	1	2	3	1	-3	-4	-8	-8
	F8_10_1M	0	-74	-4	5	6	10	5	-4	-6	-11	-11
	F8_10_CK	0	-41	-104	-17	8	53	41	-42	-71	-126	-139
	F8_10_2Y	3	-14	-32	-21	-14	-10	-7	-14	-18	-28	-30
	F8_10_2Z	3	-14	-28	-19	-11	-5	-2	-4	-8	-13	-13
11	F8_11_3Y	3	14	-33	-25	-15	-11	-7	-2	-5	-15	-22
	F8_11_3Z	3	14	-28	-22	-17	-15	-12	-12	-22	-48	-49
	F8_11_CK	0	52	-65	-51	-21	-17	-10	21	27	-18	-44
	F8_11_4Y	3	74	-11	-8	-3	-1	0	4	6	1	-5
	F8_11_4M	0	74	-23	-18	-6	-1	0	14	25	9	-6
	F8_11_5M	0	104	-20	-14	-3	1	2	11	22	9	-4

C.2 LANE C

The following tables represent measurements from the multiposition load test due to traversing Lane C.

Table C.11: Lane C—crack-opening displacements

Girder	Gage	Height from bottom of girder (in.)	Distance from center of continuity diaphragm (in.) – Span 10 + Span 11	Crack-Opening Displacement (mm) – closing + opening								
				C1	C2	C3	C4	C5	C6	C7	C8	C9
7	CO7_10	13.5	-50	-0.003	0.010	0.016	0.022	0.011	-0.006	-0.009	-0.015	-0.017
	CO7_11	13.5	48	-0.025	-0.022	-0.008	-0.006	-0.004	0.020	0.039	0.015	-0.008
8	CO8_10	13.5	-40	-0.016	-0.013	-0.008	-0.005	-0.002	-0.005	-0.008	-0.015	-0.015
	CO8_11	13.5	56	-0.020	-0.018	-0.007	-0.004	-0.002	0.017	0.032	0.011	-0.007

Table C.12: Lane C—deflections

Girder	Gage	Height from bottom of girder (in.)	Distance from center of continuity diaphragm (in.) – Span 10 + Span 11	Deflection (in.) – downward + upward								
				C1	C2	C3	C4	C5	C6	C7	C8	C9
7	D7_10_A	n/a	-608	-0.29	-0.18	-0.10	-0.05	-0.02	0.01	0.02	0.03	0.04
	D7_10_B	n/a	-308	-0.20	-0.17	-0.10	-0.06	-0.03	0.00	0.01	0.03	0.03
	D7_11_C	n/a	158	0.02	0.01	0.00	-0.02	-0.02	-0.05	-0.07	-0.11	-0.11
	D7_11_D	n/a	308	0.04	0.03	0.00	-0.02	-0.03	-0.07	-0.10	-0.19	-0.21
	D7_11_E	n/a	458	0.04	0.03	0.00	-0.02	-0.03	-0.07	-0.11	-0.21	-0.27
	D7_11_F	n/a	608	0.04	0.03	0.00	-0.02	-0.03	-0.07	-0.11	-0.22	-0.31
8	D8_10_A	n/a	-608	-0.35	-0.21	-0.12	-0.06	-0.02	0.01	0.02	0.04	0.05
	D8_10_B	n/a	-308	-0.22	-0.18	-0.11	-0.06	-0.03	0.01	0.02	0.04	0.04
	D8_11_C	n/a	158	0.03	0.02	0.00	-0.02	-0.03	-0.05	-0.08	-0.13	-0.13
	D8_11_D	n/a	308	0.04	0.03	0.00	-0.02	-0.04	-0.08	-0.12	-0.22	-0.24
	D8_11_E	n/a	458	0.05	0.03	0.01	-0.02	-0.04	-0.09	-0.13	-0.26	-0.33
	D8_11_F	n/a	608	0.05	0.04	0.01	-0.02	-0.03	-0.08	-0.12	-0.25	-0.35

Table C.13: Lane C—cross-section strains—Girder 7—Span 10

Section	Gage	Height from bottom of girder (in.)	Distance from center of continuity diaphragm (in.) – Span 10 + Span 11	Strain ($x10^{-6}$in./in.) – compressive + tensile								
				C1	C2	C3	C4	C5	C6	C7	C8	C9
Girder 7 Cross Section 1	S7_10_1V	28.5	-75	-4	1	2	4	2	-4	-3	-5	-6
	S7_10_1W	13.5	-75	-5	4	8	9	4	-4	-5	-10	-11
	S7_10_1X	13.5	-75	-5	3	7	9	4	-4	-5	-9	-10
	S7_10_1Y	3.0	-75	-8	7	15	18	7	-6	-9	-17	-18
	F7_10_1M	0.0	-74	-6	9	15	22	11	-5	-8	-16	-17
Girder 7 Cross Section 2	S7_10_2V	28.5	-13	2	3	2	2	2	1	-1	-3	-4
	S7_10_2W	13.5	-13	2	2	1	-1	-1	1	0	-3	-4
	S7_10_2X	13.5	-13	4	2	1	-1	1	2	1	-1	-2
	S7_10_2Y	3.0	-13	-154	-135	-87	-45	-24	-37	-47	-99	-105
	F7_10_2Z	3.0	-14	-18	-9	-6	-2	0	-10	-16	-28	-27

Table C.14: Lane C—cross-section strains—Girder 7—Span 11

Section	Gage	Height from bottom of girder (in.)	Distance from center of continuity diaphragm (in.) – Span 10 + Span 11	Strain ($x10^{-6}$in./in.) – compressive + tensile								
				C1	C2	C3	C4	C5	C6	C7	C8	C9
Girder 7 Cross Section 3	S7_11_3V	28.5	13	-7	-5	-3	-2	0	0	-3	-3	-2
	S7_11_3W	13.5	13	-14	-8	-1	2	6	9	7	1	-2
	S7_11_3X	13.5	13	-7	-3	-1	2	6	4	0	2	3
	S7_11_3Y	3.0	13	-11	-9	-6	-5	-6	-6	-9	-17	-20
	S7_11_3Z	3.0	13	-11	-9	-6	-5	-3	-3	-5	-6	-7
Girder 7 Cross Section 4	S7_11_4V	28.5	75	-2	-2	0	-1	-1	0	-3	-5	-4
	S7_11_4W	13.5	75	-9	-7	-2	-2	-1	4	6	-1	-6
	S7_11_4X	13.5	75	-9	-7	-3	-3	-2	3	4	-3	-8
	S7_11_4Y	3.0	75	-15	-12	-3	0	1	13	23	8	-6
	F7_11_4M	0.0	74	-18	-14	-4	-2	-1	14	25	7	-8

Table C.15: Lane C—cross-section strains—Girder 8—Span 10

Section	Gage	Height from bottom of girder (in.)	Distance from center of continuity diaphragm (in.) – Span 10 + Span 11	Strain ($x10^{-6}$in./in.) – compressive + tensile								
				C1	C2	C3	C4	C5	C6	C7	C8	C9
Girder 8 Cross Section 1	S8_10_1V	28.5	-75	-10	-3	0	3	1	-4	-5	-9	-10
	S8_10_1W	13.5	-75	-13	1	7	10	4	-6	-10	-18	-19
	S8_10_1X	13.5	-75	-14	0	6	11	5	-6	-10	-18	-19
	F8_10_1Y	3.0	-74	-9	2	8	10	5	-4	-7	-13	-14
	S8_10_1M	0.0	-75	-15	7	14	23	11	-9	-14	-25	-27
	F8_10_1M	0.0	-74	-10	5	10	16	9	-5	-9	-16	-17
Girder 8 Cross Section 2	S8_10_2V	28.5	-13	0	2	2	3	3	0	-2	-5	-6
	S8_10_2W	13.5	-13	1	5	5	5	4	-1	-4	-12	-15
	S8_10_2X	13.5	-13	4	6	6	4	6	2	-2	-10	-12
	F8_10_2Y	3.0	-14	-74	-51	-30	-19	-10	-19	-26	-47	-46
	F8_10_2Z	3.0	-14	-26	-18	-10	-4	0	-5	-12	-23	-23

Table C.16: Lane C—cross-section strains—Girder 8—Span 11

Section	Gage	Height from bottom of girder (in.)	Distance from center of continuity diaphragm (in.) – Span 10 + Span 11	Strain ($x10^{-6}$in./in.) – compressive + tensile								
				C1	C2	C3	C4	C5	C6	C7	C8	C9
Girder 8 Cross Section 3	S8_11_3V	28.5	13	-65	-57	-43	-36	-27	-17	-25	-42	-51
	S8_11_3W	13.5	13	-27	-18	-9	-3	2	1	-7	-15	-16
	S8_11_3X	13.5	13	-54	-40	-9	-3	5	25	28	-2	-22
	F8_11_3Y	3.0	14	-45	-38	-23	-17	-11	-5	-14	-45	-54
	F8_11_3Z	3.0	14	-44	-37	-25	-22	-15	-11	-25	-53	-53
Girder 8 Cross Section 4	S8_11_4V	28.5	75	-6	-5	-3	-6	-5	-6	-17	-23	-16
	S8_11_4W	13.5	75	-17	-13	-5	-4	-2	3	2	-11	-16
	S8_11_4X	13.5	75	-12	-9	-3	-4	-2	1	-2	-11	-14
	F8_11_4Y	3.0	74	-16	-12	-3	-1	0	10	17	0	-10
	S8_11_4M	0.0	75	-56	-48	-13	-4	2	56	121	32	-23
	F8_11_4M	0.0	74	-31	-25	-6	-2	1	26	52	14	-13

Table C.17: Lane C—bottom-fiber strains—Girder 7

Span	Gage	Height from bottom of girder (in.)	Distance from center of continuity diaphragm (in.) – Span 10 + Span 11	Strain ($x10^{-6}$in./in.) – compressive + tensile								
				C1	C2	C3	C4	C5	C6	C7	C8	C9
10	F7_10_1M	0	-74	-6	9	15	22	11	-5	-8	-16	-17
	F7_10_CK	0	-47	-67	14	51	95	59	-37	-60	-115	-122
11	F7_11_CK	0	47	-132	-110	-46	-34	-21	76	116	-8	-82
	F7_11_4M	0	74	-18	-14	-4	-2	-1	14	25	7	-8
	F7_11_5M	0	104	-17	-13	-4	1	0	12	28	12	-4
	S7_11_5M	0	105	-16	-13	-4	0	1	14	27	12	-4
	S7_11_6M	0	273	-18	-14	-5	3	10	25	37	79	34
	S7_11_7M	0	441	-12	-11	-4	2	7	14	31	63	71
	S7_11_8M	0	609	-9	-8	-2	3	7	15	24	52	105

Table C.18: Lane C—bottom-fiber strains—Girder 8

Span	Gage	Height from bottom of girder (in.)	Distance from center of continuity diaphragm (in.) – Span 10 + Span 11	Strain ($x10^{-6}$in./in.) – compressive + tensile								
				C1	C2	C3	C4	C5	C6	C7	C8	C9
10	S8_10_1M	0	-75	-15	7	14	23	11	-9	-14	-25	-27
	F8_10_1M	0	-74	-10	5	10	16	9	-5	-9	-16	-17
	F8_10_CK	0	-41	-165	-30	32	113	82	-58	-108	-211	-222
11	F8_11_CK	0	52	-100	-87	-38	-30	-18	44	56	-21	-67
	F8_11_4M	0	74	-31	-25	-6	-2	1	26	52	14	-13
	S8_11_4M	0	75	-56	-48	-13	-4	2	56	121	32	-23
	F8_11_5M	0	104	-29	-22	-4	1	1	16	32	10	-12
	S8_11_5M	0	105	-26	-21	-5	1	2	17	32	10	-11
	S8_11_6M	0	273	-20	-16	-4	7	16	34	46	91	38
	S8_11_7M	0	441	-16	-13	-4	3	9	23	39	82	87
	S8_11_8M	0	609	-10	-7	-2	2	6	14	24	58	113

Table C.19: Lane C—FRP strains—Girder 7

Span	Gage	Height from bottom of girder (in.)	Distance from center of continuity diaphragm (in.) – Span 10 + Span 11	Strain ($x10^{-6}$in./in.) – compressive + tensile								
				C1	C2	C3	C4	C5	C6	C7	C8	C9
10	F7_10_1M	0	-74	-6	9	15	22	11	-5	-8	-16	-17
	F7_10_CK	0	-47	-67	14	51	95	59	-37	-60	-115	-122
	F7_10_2Z	3	-14	-18	-9	-6	-2	0	-10	-16	-28	-27
11	F7_11_CK	0	47	-132	-110	-46	-34	-21	76	116	-8	-82
	F7_11_4M	0	74	-18	-14	-4	-2	-1	14	25	7	-8
	F7_11_5M	0	104	-17	-13	-4	1	0	12	28	12	-4

Table C.20: Lane C—FRP strains—Girder 8

Span	Gage	Height from bottom of girder (in.)	Distance from center of continuity diaphragm (in.) – Span 10 + Span 11	Strain ($x10^{-6}$in./in.) – compressive + tensile								
				C1	C2	C3	C4	C5	C6	C7	C8	C9
10	F8_10_1Y	3	-74	-9	2	8	10	5	-4	-7	-13	-14
	F8_10_1M	0	-74	-10	5	10	16	9	-5	-9	-16	-17
	F8_10_CK	0	-41	-165	-30	32	113	82	-58	-108	-211	-222
	F8_10_2Y	3	-14	-74	-51	-30	-19	-10	-19	-26	-47	-46
	F8_10_2Z	3	-14	-26	-18	-10	-4	0	-5	-12	-23	-23
11	F8_11_3Y	3	14	-45	-38	-23	-17	-11	-5	-14	-45	-54
	F8_11_3Z	3	14	-44	-37	-25	-22	-15	-11	-25	-53	-53
	F8_11_CK	0	52	-100	-87	-38	-30	-18	44	56	-21	-67
	F8_11_4Y	3	74	-16	-12	-3	-1	0	10	17	0	-10
	F8_11_4M	0	74	-31	-25	-6	-2	1	26	52	14	-13
	F8_11_5M	0	104	-29	-22	-4	1	1	16	32	10	-12

Appendix D

BRIDGE MONITORING—GRAPHICAL RESULTS

D.1 CRACK-OPENING DISPLACEMENTS

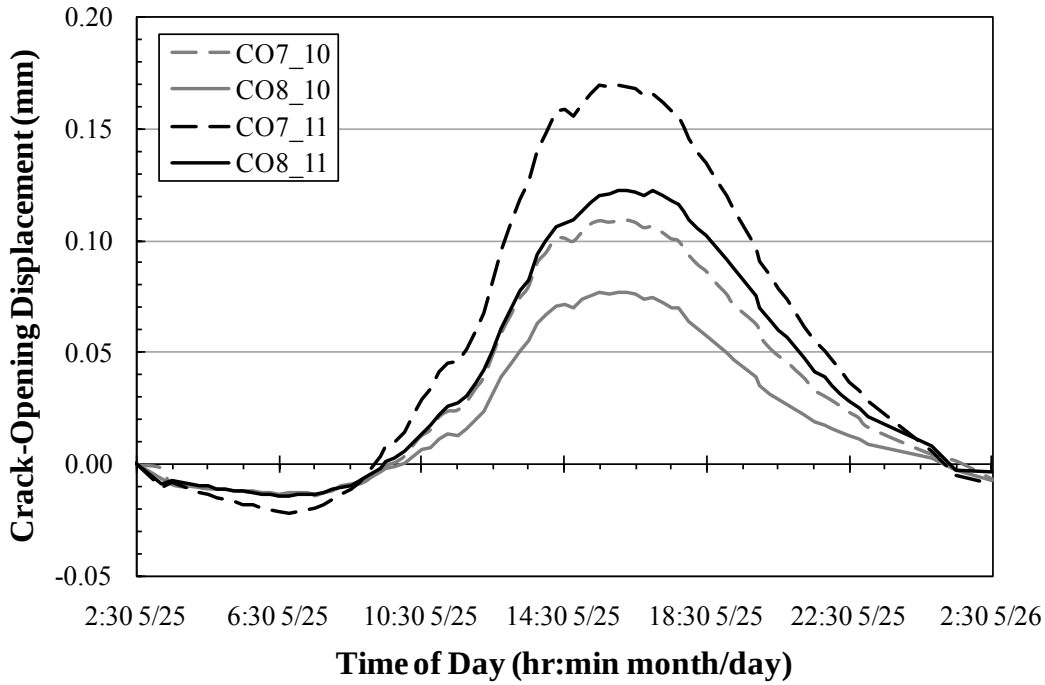

Figure D.1: Crack-opening displacements—24 hrs

D.2 DEFLECTIONS

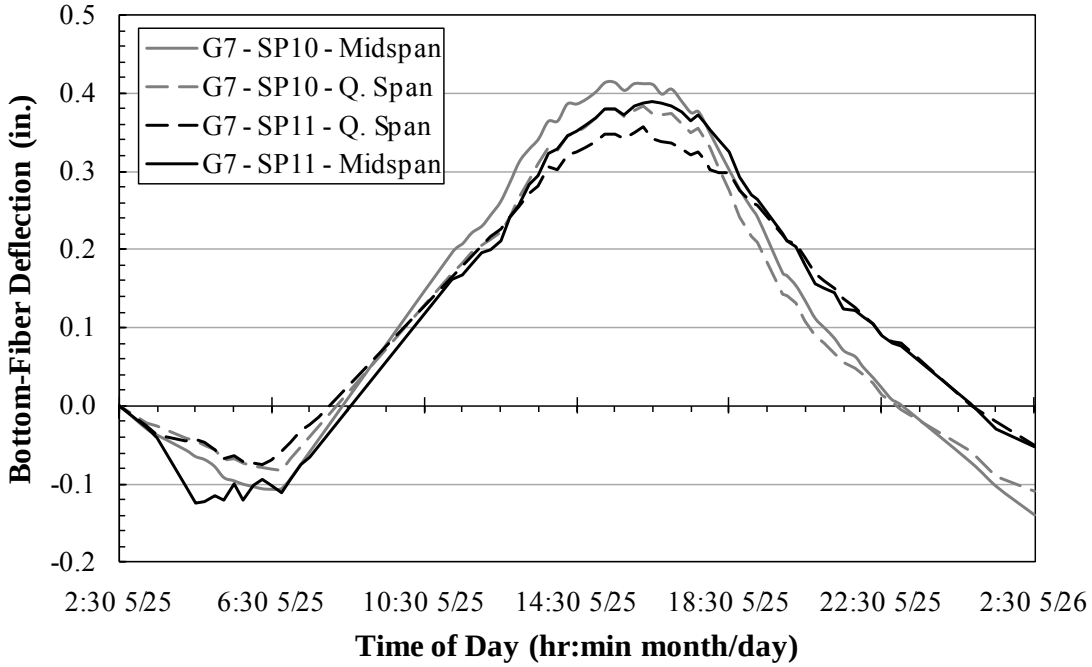

Figure D.2: Deflections—24 hrs—Girder 7

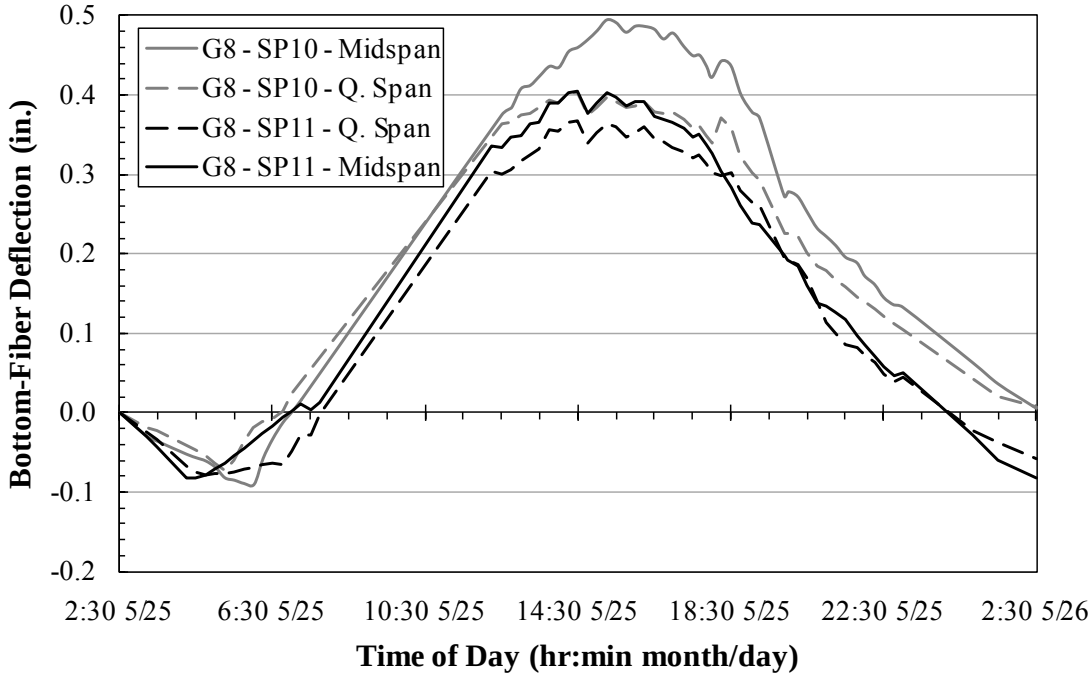

Figure D.3: Deflections—24 hrs—Girder 8

D.3 BOTTOM-FIBER STRAINS

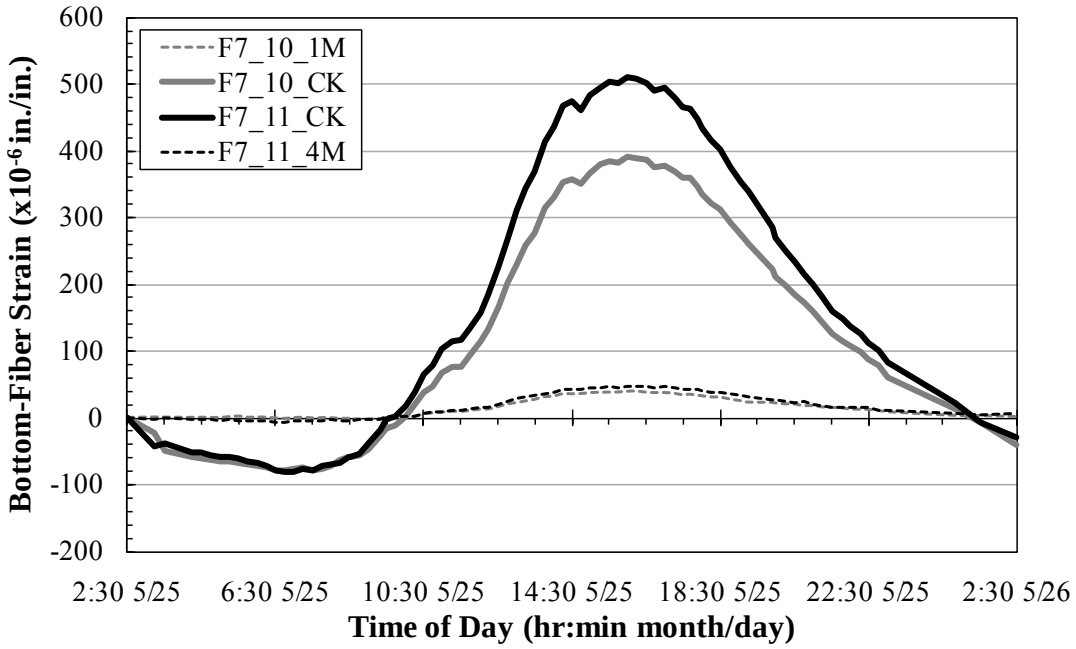

Figure D.4: Bottom-fiber strains—24 hrs—Girder 7—within 80 in. from diaphragm

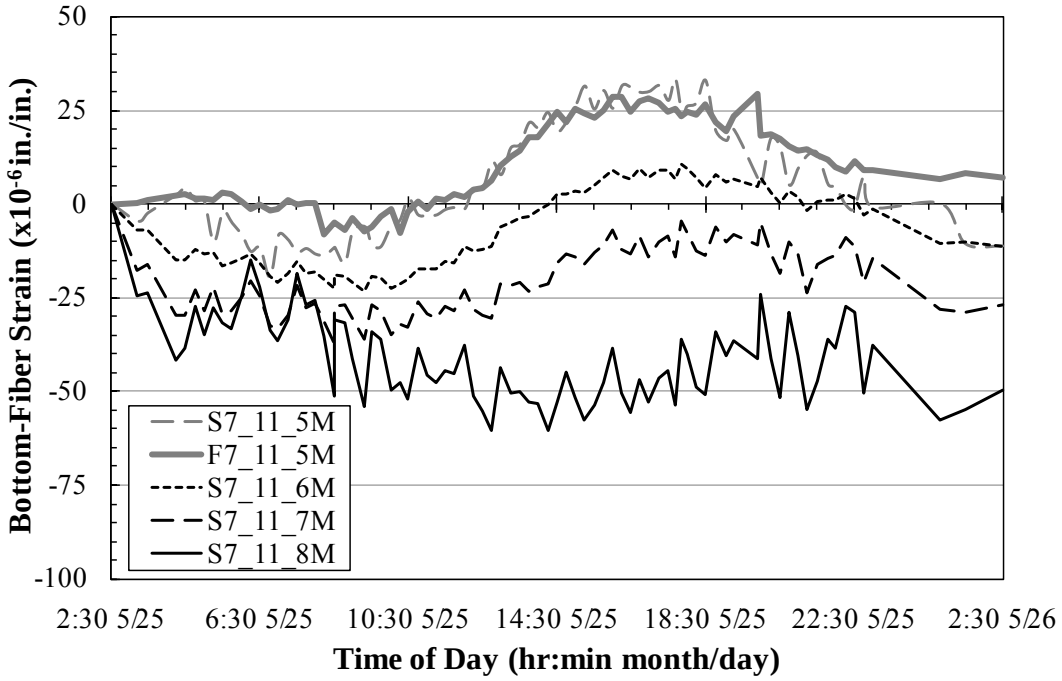

Figure D.5: Bottom-fiber strains—24 hrs—Girder 7—beyond 80 in. from diaphragm

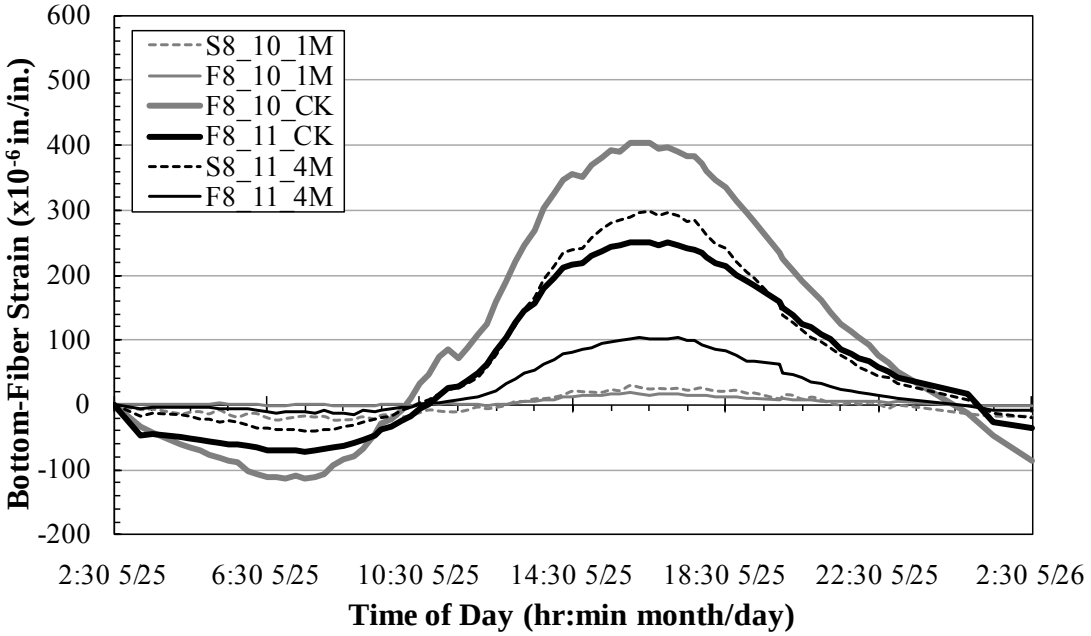

Figure D.6: Bottom-fiber strains—24 hrs—Girder 8—within 80 in. from diaphragm

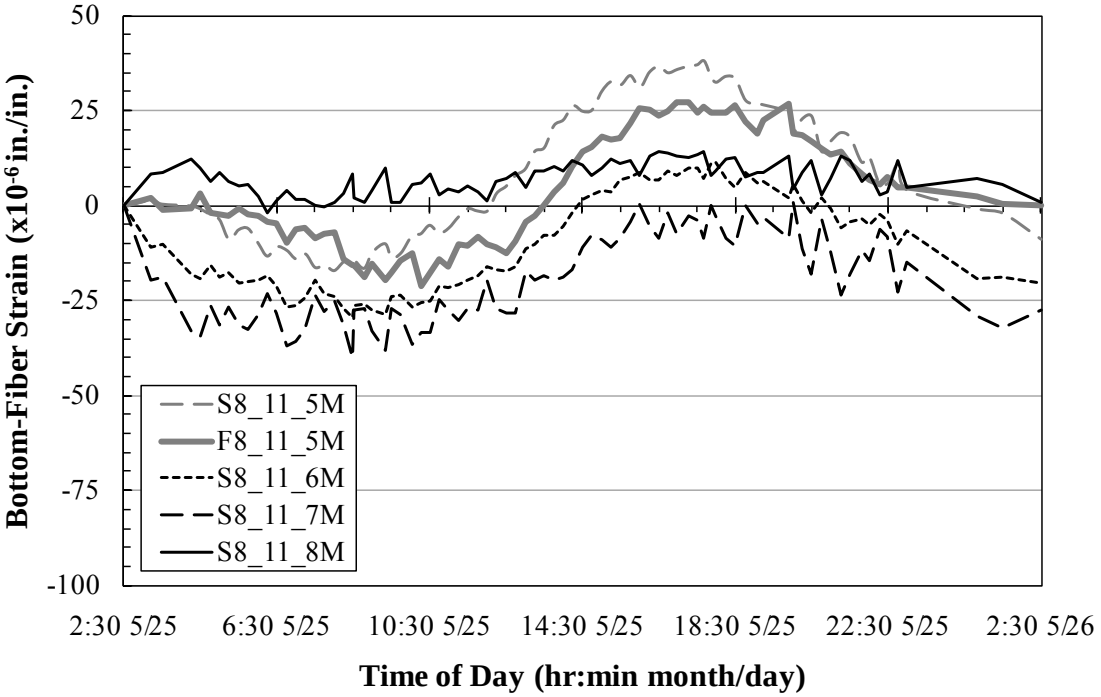

Figure D.7: Bottom-fiber strains—24 hrs—Girder 8—beyond 80 in. from diaphragm

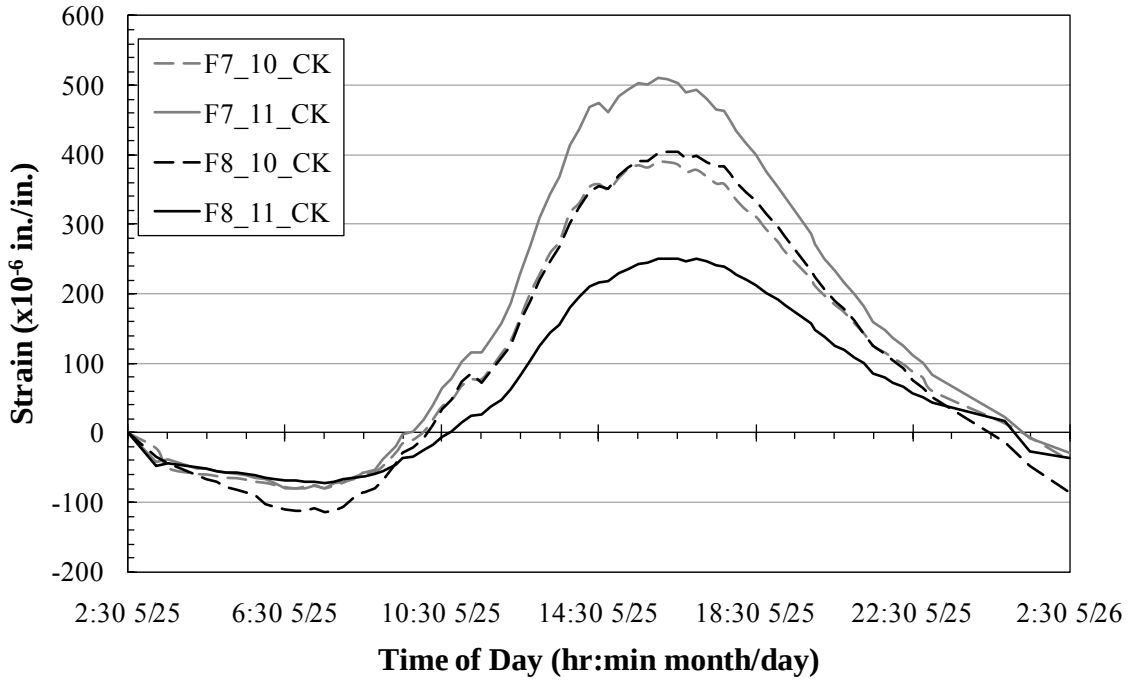

Figure D.8: Bottom-fiber strains—24 hrs—FRP near crack locations

D.4 BOTTOM-FIBER STRAINS AND CRACK-OPENING DISPLACEMENTS

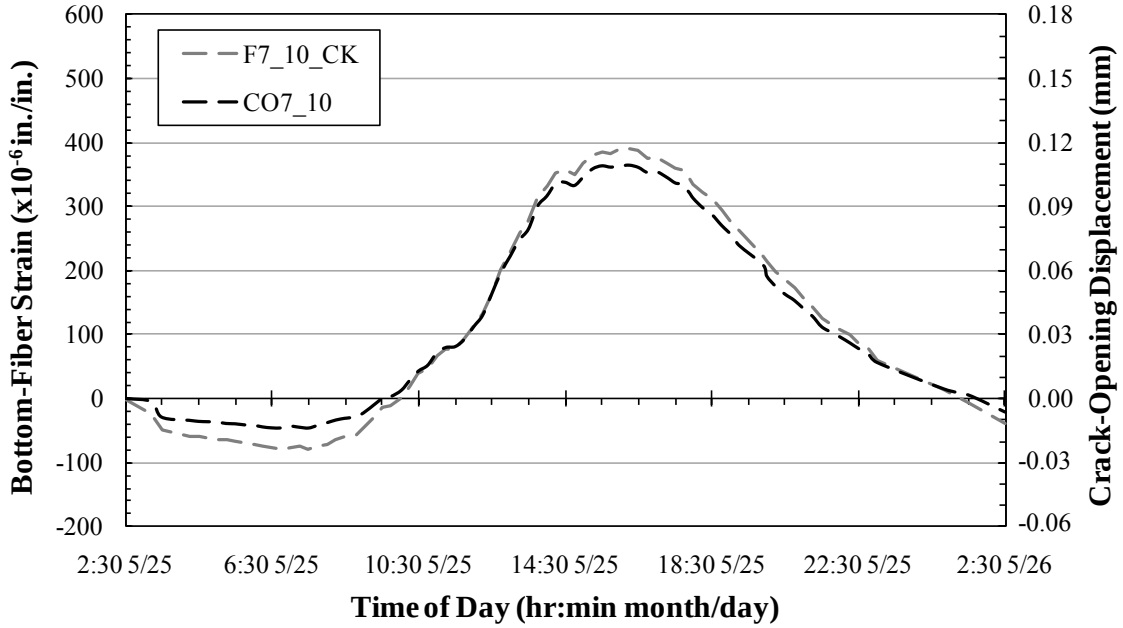

Figure D.9: Bottom-fiber strain and COD—24 hrs—Girder 7—Span 10

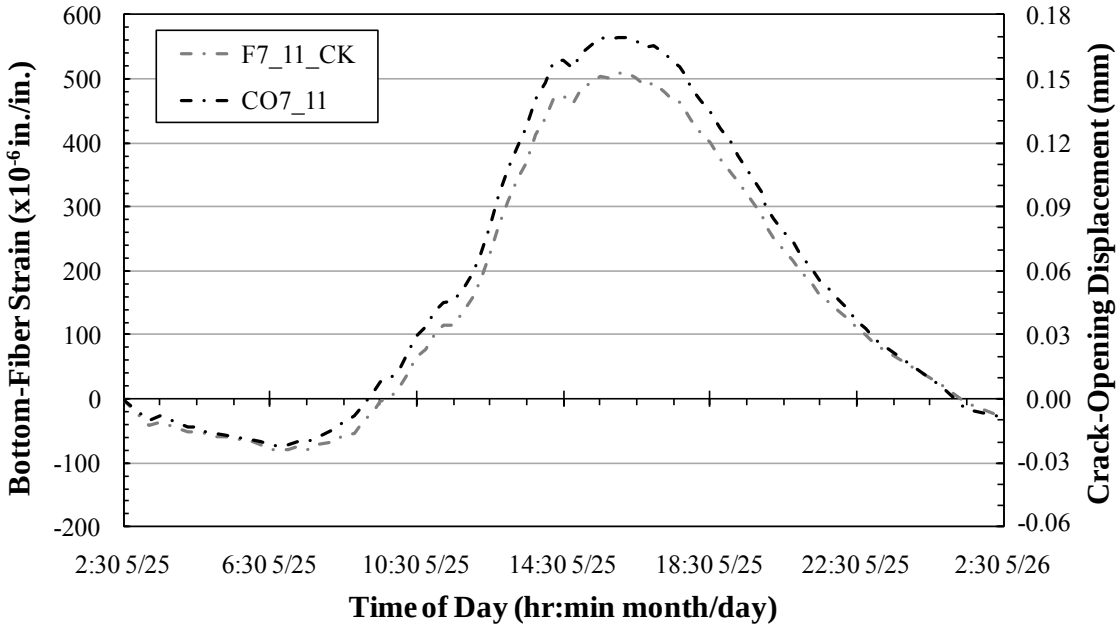

Figure D.10: Bottom-fiber strain and COD—24 hrs—Girder 7—Span 11

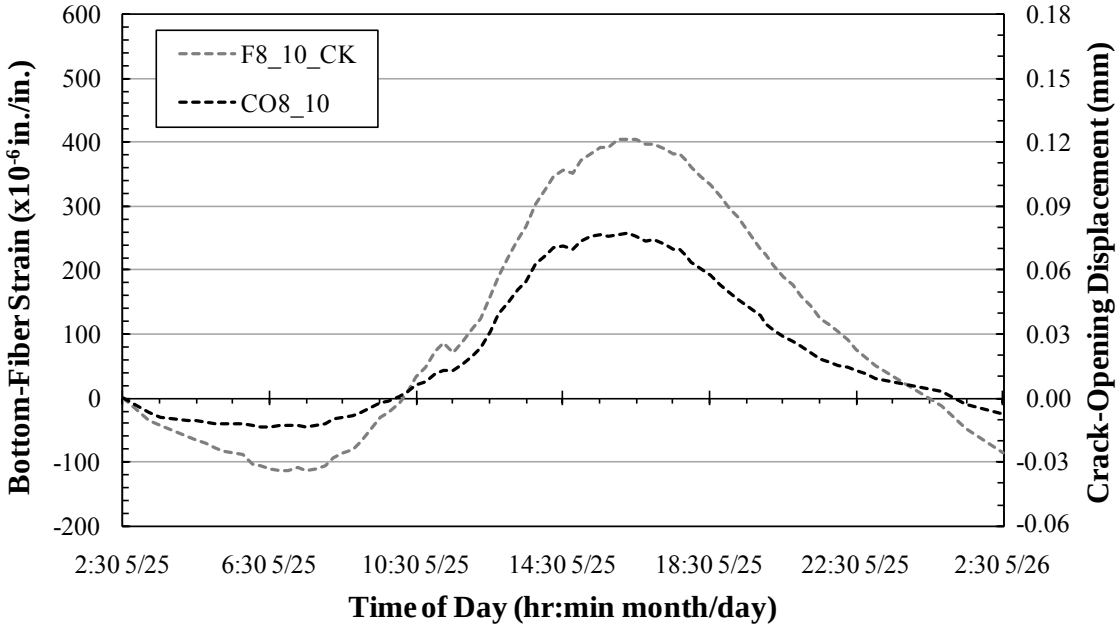

Figure D.11: Bottom-fiber strain and COD—24 hrs—Girder 8—Span 10

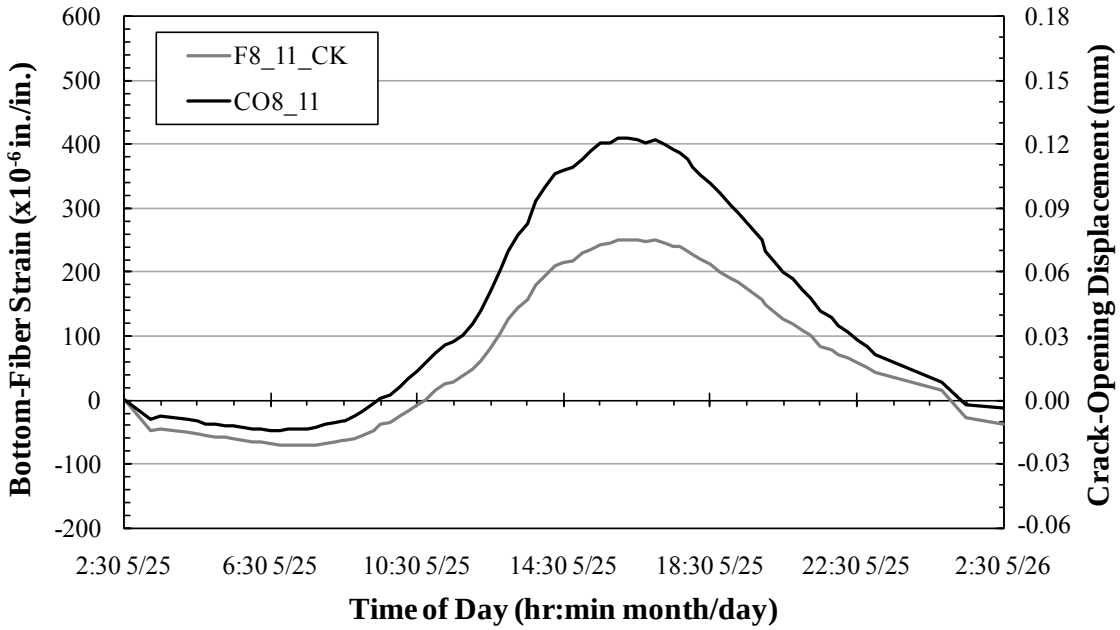

Figure D.12: Bottom-fiber strain and COD—24 hrs—Girder 8—Span 11

Appendix E

BRIDGE MONITORING MEASUREMENTS

E.1 CRACK-OPENING DISPLACEMENTS

Table E.1: Bridge monitoring—crack-opening displacements

		Girder 7		Girder 8	
		CO7_10	CO7_11	CO8_10	CO8_11
Ht. from girder base (in.)		13.5	13.5	13.5	13.5
Dist. from center of cont. dia. (in.)		-50	48	-40	56
Units		mm			
Date	**Time**				
5/25/2010	2:30	0.000	0.000	0.000	0.000
	3:30	-0.009	-0.008	-0.009	-0.007
	4:30	-0.011	-0.013	-0.011	-0.010
	5:30	-0.012	-0.018	-0.012	-0.012
	6:30	-0.014	-0.022	-0.014	-0.014
	7:30	-0.014	-0.020	-0.013	-0.013
	8:30	-0.009	-0.011	-0.009	-0.009
	9:30	0.000	0.008	-0.002	0.001
	10:30	0.013	0.029	0.006	0.014
	11:30	0.024	0.046	0.013	0.027
	12:30	0.049	0.082	0.031	0.051
	13:30	0.079	0.127	0.055	0.083
	14:30	0.101	0.159	0.072	0.108
	15:30	0.109	0.169	0.077	0.120
	16:30	0.108	0.168	0.076	0.122
	17:30	0.101	0.158	0.070	0.118
	18:30	0.086	0.134	0.058	0.102
	19:15	0.071	0.114	0.047	0.088
	20:30	0.049	0.078	0.029	0.060
	21:30	0.033	0.055	0.019	0.041
	22:30	0.023	0.037	0.013	0.028
	23:00	0.017	0.028	0.009	0.021
5/26/2010	0:50	0.004	0.006	0.003	0.008
	1:30	0.002	-0.005	-0.003	-0.002
	2:30	-0.006	-0.009	-0.007	-0.004

E.2 DEFLECTIONS

Table E.2: Bridge monitoring—deflections—Girder 7

		Span 10		Span 11			
		D7_10_A	D7_10_B	D7_11_C	D7_11_D	D7_11_E	D7_11_F
Ht. from girder base (in.)		n/a	n/a	n/a	n/a	n/a	n/a
Dist. from center of cont. dia. (in.)		-608	-308	158	308	458	608
Units		in.					
Date	**Time**						
5/25/2010	2:30	0.00	0.00	0.00	0.00	0.00	0.00
	3:30	-0.04	-0.03	-0.03	-0.04	-0.04	-0.04
	4:30	-0.07	-0.04	0.00	-0.04	-0.04	-0.13
	5:30	-0.10	-0.07	-0.01	-0.06	-0.06	-0.10
	6:30	-0.11	-0.08	-0.01	-0.07	-0.09	-0.10
	7:30	0.00	0.00	0.00	-0.02	0.00	-0.07
	8:30	0.00	0.00	0.00	0.00	0.00	0.00
	9:30	0.00	0.00	0.00	0.00	0.00	0.00
	10:30	0.00	0.00	0.00	0.00	0.00	0.00
	11:30	0.21	0.18	0.17	0.00	0.17	0.17
	12:30	0.26	0.22	0.19	0.23	0.21	0.21
	13:30	0.34	0.31	0.23	0.28	0.28	0.29
	14:30	0.39	0.35	0.27	0.32	0.34	0.35
	15:30	0.41	0.38	0.29	0.35	0.36	0.38
	16:30	0.41	0.37	0.28	0.34	0.38	0.39
	17:30	0.37	0.35	0.26	0.32	0.35	0.37
	18:30	0.30	0.28	0.23	0.30	0.30	0.32
	19:15	0.24	0.21	0.19	0.26	0.24	0.26
	20:30	0.13	0.11	0.13	0.19	0.16	0.18
	21:30	0.07	0.06	0.09	0.14	0.10	0.12
	22:30	0.02	0.01	0.06	0.09	0.06	0.09
	23:00	0.00	0.00	0.05	0.08	0.04	0.08
5/26/2010	0:50	-0.07	-0.06	-0.02	0.00	-0.05	0.00
	1:30	-0.10	-0.09	-0.04	-0.02	-0.07	-0.03
	2:30	-0.14	-0.11	-0.06	-0.05	-0.10	-0.05

Table E.3: Bridge monitoring—deflections—Girder 8

		Span 10		Span 11			
		D8_10_A	D8_10_B	D8_11_C	D8_11_D	D8_11_E	D8_11_F
Ht. from girder base (in.)		n/a	n/a	n/a	n/a	n/a	n/a
Dist. from center of cont. dia. (in.)		-608	-308	158	308	458	608
Units		in.					
Date	**Time**						
5/25/2010	2:30	0.00	0.00	0.00	0.00	0.00	0.00
	3:30	-0.04	-0.02	-0.03	-0.03	-0.03	-0.04
	4:30	-0.06	-0.05	-0.03	-0.08	-0.04	-0.08
	5:30	-0.08	-0.06	-0.05	-0.07	-0.02	-0.05
	6:30	-0.03	-0.01	-0.06	-0.06	0.00	-0.02
	7:30	0.00	0.00	-0.03	-0.03	0.02	0.00
	8:30	0.00	0.00	0.00	0.00	0.00	0.00
	9:30	0.00	0.00	0.00	0.00	0.00	0.00
	10:30	0.00	0.00	0.00	0.00	0.00	0.00
	11:30	0.00	0.00	0.00	0.00	0.00	0.00
	12:30	0.37	0.36	0.17	0.30	0.32	0.33
	13:30	0.42	0.38	0.20	0.33	0.36	0.37
	14:30	0.46	0.40	0.22	0.37	0.39	0.40
	15:30	0.49	0.39	0.22	0.36	0.39	0.40
	16:30	0.48	0.38	0.22	0.34	0.36	0.37
	17:30	0.45	0.36	0.20	0.32	0.34	0.35
	18:30	0.44	0.36	0.18	0.30	0.28	0.28
	19:15	0.37	0.29	0.16	0.26	0.23	0.24
	20:30	0.25	0.20	0.10	0.17	0.17	0.16
	21:30	0.20	0.16	0.06	0.09	0.11	0.12
	22:30	0.14	0.12	0.03	0.05	0.07	0.06
	23:00	0.13	0.10	0.03	0.04	0.06	0.05
5/26/2010	0:50	0.06	0.04	-0.04	-0.02	-0.03	-0.03
	1:30	0.04	0.02	-0.06	-0.04	-0.05	-0.06
	2:30	0.01	0.01	-0.08	-0.06	-0.08	-0.08

E.3 CROSS-SECTION STRAINS

Table E.4: Bridge monitoring—strains—Girder 7—Section 1

		S7_10_1V	S7_10_1W	S7_10_1X	S7_10_1Y	F7_10_1M
Ht. from girder base (in.)		28.5	13.5	13.5	3.0	0.0
Dist. from center of cont. dia. (in.)		-75	-75	-75	-75	-74
Units		$x10^{-6}$ in/in				
Date	**Time**					
5/25/2010	2:30	0	0	0	0	0
	3:30	-1	0	0	-3	0
	4:30	-5	-3	-1	-1	0
	5:30	-8	-6	-2	-4	2
	6:30	-10	-9	-4	-9	-1
	7:30	-10	-9	-4	-9	-1
	8:30	-6	-7	-3	-9	-1
	9:30	0	-3	0	-5	0
	10:30	4	0	4	2	5
	11:30	6	3	6	4	9
	12:30	11	9	10	15	16
	13:30	17	17	17	27	27
	14:30	24	25	23	39	35
	15:30	24	26	25	41	38
	16:30	24	26	26	40	38
	17:30	23	24	24	36	34
	18:30	20	20	21	30	30
	19:15	17	16	18	24	23
	20:30	14	11	14	18	20
	21:30	10	7	12	11	15
	22:30	6	4	10	7	12
	23:00	4	2	7	6	9
5/26/2010	0:50	-2	-4	0	-1	3
	1:30	-3	-4	0	-3	3
	2:30	-5	-6	-1	-3	1

Table E.5: Bridge monitoring—strains—Girder 7—Section 2

		S7_10_2V	S7_10_2W	S7_10_2X	S7_10_2Y	F7_10_2Z
Ht. from girder base (in.)		28.5	13.5	13.5	3.0	3.0
Dist. from center of cont. dia. (in.)		-13	-13	-13	-13	-14
Units		$x10^{-6}$ in/in				
Date	**Time**					
5/25/2010	2:30	0	0	0	0	0
	3:30	-1	-1	0	-67	-4
	4:30	-3	-2	5	-79	-5
	5:30	-4	8	8	-90	-6
	6:30	-7	5	13	-109	-7
	7:30	-7	5	16	-111	-7
	8:30	-6	6	16	-90	-3
	9:30	-5	7	17	5	6
	10:30	-4	9	16	135	15
	11:30	-4	9	15	201	20
	12:30	-2	10	12	425	33
	13:30	0	11	11	743	55
	14:30	3	13	11	963	72
	15:30	3	12	10	1039	77
	16:30	3	12	10	1038	76
	17:30	3	12	12	940	68
	18:30	2	12	15	768	57
	19:15	1	11	17	611	46
	20:30	1	12	19	376	32
	21:30	0	10	19	254	24
	22:30	-1	9	20	169	19
	23:00	-1	9	21	126	14
5/26/2010	0:50	-6	4	21	19	6
	1:30	-6	5	20	-29	4
	2:30	-7	4	21	-75	0

Table E.6: Bridge monitoring—strains—Girder 7—Section 3

		S7_11_3V	S7_11_3W	S7_11_3X	S7_11_3Y	S7_11_3Z
Ht. from girder base (in.)		28.5	13.5	13.5	3.0	3.0
Dist. from center of cont. dia. (in.)		13	13	13	13	13
Units		$x10^{-6}$ in/in				
Date	**Time**					
5/25/2010	2:30	0	0	0	0	0
	3:30	-2	-6	0	-15	2
	4:30	1	-6	1	-49	4
	5:30	0	-6	1	-70	4
	6:30	-2	-8	2	-91	1
	7:30	-3	-8	1	5761	1
	8:30	-4	-7	1	5296	4
	9:30	-1	-3	-2	4918	4
	10:30	9	3	0	4489	12
	11:30	8	3	-3	3784	12
	12:30	14	7	-7	3110	21
	13:30	27	13	-11	2500	30
	14:30	39	20	-9	2175	35
	15:30	38	19	-14	2037	31
	16:30	36	17	-17	1955	29
	17:30	35	17	-13	1795	29
	18:30	35	16	-8	1738	31
	19:15	28	14	-4	1701	29
	20:30	21	10	-3	1631	18
	21:30	13	6	-5	1584	12
	22:30	10	3	-2	1559	8
	23:00	9	3	-1	1549	7
5/26/2010	0:50	2	-2	-6	1492	-3
	1:30	5	-4	3	1478	5
	2:30	1	-8	-2	1428	3

Table E.7: Bridge monitoring—strains—Girder 7—Section 4

		S7_11_4V	S7_11_4W	S7_11_4X	S7_11_4Y	F7_11_4M
Ht. from girder base (in.)		28.5	13.5	13.5	3.0	0.0
Dist. from center of cont. dia. (in.)		75	75	75	75	74
Units		$x10^{-6}$ in/in				
Date	**Time**					
5/25/2010	2:30	0	0	0	0	0
	3:30	-1	0	0	1	0
	4:30	-3	-3	-1	-3	-2
	5:30	-5	-3	-1	-4	-4
	6:30	-7	-4	-4	-6	-6
	7:30	-7	-5	-5	-7	-4
	8:30	-4	-2	-4	-4	-4
	9:30	-1	0	-1	1	1
	10:30	3	5	5	7	6
	11:30	5	8	6	11	11
	12:30	12	16	13	24	21
	13:30	19	25	21	36	34
	14:30	25	35	31	50	44
	15:30	25	36	29	50	46
	16:30	24	35	31	48	46
	17:30	22	34	29	46	43
	18:30	17	29	28	40	38
	19:15	15	27	24	36	32
	20:30	9	20	17	25	23
	21:30	5	16	12	19	16
	22:30	3	12	9	16	15
	23:00	2	9	7	13	12
5/26/2010	0:50	-4	0	-2	3	6
	1:30	-3	1	-1	7	4
	2:30	-6	-1	-4	4	6

Table E.8: Bridge monitoring—strains—Girder 8—Section 1

		S8_10_1V	S8_10_1W	S8_10_1X	F8_10_1Y	S8_10_1M	F8_10_1M
Ht. from girder base (in.)		28.5	13.5	13.5	3.0	0.0	0.0
Dist. from center of cont. dia. (in.)		-75	-75	-75	-74	-75	-74
Units		$x10^{-6}$ in/in					
Date	**Time**						
5/25/2010	2:30	0	0	0	0	0	0
	3:30	-2	-5	0	0	-7	1
	4:30	-5	-1	-3	0	-11	1
	5:30	-3	-5	-6	0	-15	0
	6:30	-6	-10	-9	-1	-20	-1
	7:30	-5	-12	-9	2	-17	0
	8:30	0	-10	-6	0	-23	0
	9:30	6	-4	0	1	-16	0
	10:30	13	2	5	3	-12	0
	11:30	19	6	9	4	-11	1
	12:30	26	14	16	7	-4	0
	13:30	36	24	25	11	9	7
	14:30	43	32	34	15	22	13
	15:30	44	33	35	14	24	16
	16:30	44	32	35	13	25	15
	17:30	44	32	35	12	23	15
	18:30	40	29	31	11	21	13
	19:15	37	26	28	9	19	10
	20:30	30	20	21	6	9	8
	21:30	24	13	15	3	0	5
	22:30	20	10	12	5	1	6
	23:00	17	8	9	4	0	5
5/26/2010	0:50	9	0	1	3	-14	-1
	1:30	8	1	2	4	-18	-1
	2:30	5	-2	-1	4	-18	-1

Table E.9: Bridge monitoring—strains—Girder 8—Section 2

		S8_10_2V	S8_10_2W	S8_10_2X	F8_10_2Y	F8_10_2Z
Ht. from girder base (in.)		28.5	13.5	13.5	3.0	3.0
Dist. from center of cont. dia. (in.)		-13	-13	-13	-14	-14
Units		$x10^{-6}$ in/in				
Date	**Time**					
5/25/2010	2:30	0	0	0	0	0
	3:30	-2	-2	1	-11	1
	4:30	-3	-4	0	9	-1
	5:30	-5	-3	0	23	-1
	6:30	-5	-5	-1	43	-2
	7:30	-4	-5	-1	42	-2
	8:30	-3	-4	0	52	0
	9:30	-1	-3	-1	69	3
	10:30	1	-4	-1	84	2
	11:30	2	-5	-1	90	4
	12:30	5	-4	-2	125	9
	13:30	8	-4	-5	167	16
	14:30	11	-1	-5	202	23
	15:30	10	-2	-5	210	23
	16:30	10	-1	-5	208	23
	17:30	10	0	-4	195	21
	18:30	10	-1	-3	170	18
	19:15	9	-1	-2	147	14
	20:30	7	4	0	110	9
	21:30	5	3	0	90	6
	22:30	4	2	0	80	6
	23:00	4	1	0	75	5
5/26/2010	0:50	0	-2	-1	58	4
	1:30	0	-5	-1	57	3
	2:30	-1	-5	1	51	3

Table E.10: Bridge monitoring—strains—Girder 8—Section 3

		S8_11_3V	S8_11_3W	S8_11_3X	F8_11_3Y	F8_11_3Z
Ht. from girder base (in.)		28.5	13.5	13.5	3.0	3.0
Dist. from center of cont. dia. (in.)		13	13	13	14	14
Units		$x10^{-6}$ in/in				
Date	**Time**					
5/25/2010	2:30	0	0	0	0	0
	3:30	-21	-1	-11	-11	-13
	4:30	-29	-5	-15	-18	-14
	5:30	-40	-6	-17	-22	-16
	6:30	-50	-8	-20	-26	-21
	7:30	-52	-7	-21	-28	-21
	8:30	-33	-4	-20	-18	-11
	9:30	5	-3	-16	-5	-8
	10:30	60	0	-9	10	5
	11:30	101	2	-2	25	20
	12:30	196	5	13	57	53
	13:30	318	4	37	94	97
	14:30	405	-2	69	119	130
	15:30	430	0	84	125	140
	16:30	429	2	85	126	142
	17:30	409	7	83	118	132
	18:30	365	8	72	101	112
	19:15	320	9	65	87	91
	20:30	228	7	46	57	58
	21:30	167	4	34	36	35
	22:30	126	1	28	22	20
	23:00	109	-2	24	15	12
5/26/2010	0:50	75	-7	15	-1	3
	1:30	-3	-7	-9	-9	-11
	2:30	-29	-10	-19	-16	-12

Table E.11: Bridge monitoring—strains—Girder 8—Section 4

		S8_11_4V	S8_11_4W	S8_11_4X	F8_11_4Y	S8_11_4M	F8_11_4M
Ht. from girder base (in.)		28.5	13.5	13.5	3.0	0.0	0.0
Dist. from center of cont. dia. (in.)		75	75	75	74	75	74
Units		$x10^{-6}$ in/in					
Date	**Time**						
5/25/2010	2:30	0	0	0	0	0	0
	3:30	-2	-1	-1	-4	-12	-4
	4:30	-3	-2	0	-5	-18	-3
	5:30	-4	-1	-1	-7	-25	-5
	6:30	-6	-2	-3	-10	-36	-9
	7:30	-6	-3	-4	-11	-39	-11
	8:30	-3	-1	-4	-10	-32	-12
	9:30	-1	3	-1	-7	-19	-9
	10:30	3	9	6	-2	4	2
	11:30	2	11	5	1	26	7
	12:30	5	16	9	9	77	23
	13:30	9	24	17	22	165	54
	14:30	11	29	23	32	239	82
	15:30	8	28	24	37	279	97
	16:30	7	30	22	38	297	101
	17:30	6	28	23	37	284	98
	18:30	8	27	22	31	241	84
	19:15	5	22	18	25	195	68
	20:30	5	18	11	14	116	41
	21:30	1	12	7	6	76	25
	22:30	-1	9	4	1	45	14
	23:00	0	7	4	0	33	10
5/26/2010	0:50	-2	-1	-2	-4	7	-1
	1:30	-2	-1	0	-7	-13	-7
	2:30	-5	-4	-2	-9	-20	-8

E.4 BOTTOM-FIBER STRAINS

Table E.12: Bridge monitoring—bottom-fiber strains—Girder 7

		Span 10		Span 11	
		F7_10_1M	F7_10_CK	F7_11_CK	F7_11_4M
Ht. from girder base (in.)		0	0	0	0
Dist. from center of cont. dia. (in.)		-74	-47	47	74
Units		$x10^{-6}$ in/in			
Date	**Time**				
5/25/2010	2:30	0	0	0	0
	3:30	0	-50	-37	0
	4:30	0	-60	-51	-2
	5:30	2	-67	-62	-4
	6:30	-1	-78	-79	-6
	7:30	-1	-79	-79	-4
	8:30	-1	-59	-58	-4
	9:30	0	-15	-3	1
	10:30	5	38	65	6
	11:30	9	77	116	11
	12:30	16	167	228	21
	13:30	27	277	368	34
	14:30	35	358	475	44
	15:30	38	385	504	46
	16:30	38	387	502	46
	17:30	34	359	466	43
	18:30	30	312	401	38
	19:15	23	261	340	32
	20:30	20	185	233	23
	21:30	15	125	160	16
	22:30	12	88	112	15
	23:00	9	61	84	12
5/26/2010	0:50	3	14	23	6
	1:30	3	-6	-7	4
	2:30	1	-39	-28	6

Table E.12 cont.: Bridge monitoring—bottom-fiber strains—Girder 7

		Span 11				
		S7_11_5M	F7_11_5M	S7_11_6M	S7_11_7M	S7_11_8M
Ht. from girder base (in.)		0	0	0	0	0
Dist. from center of cont. dia. (in.)		105	104	273	441	609
Units		$x10^{-6}$ in/in				
Date	**Time**					
5/25/2010	2:30	0	0	0	0	0
	3:30	-2	1	-7	-16	-24
	4:30	4	3	-15	-30	-38
	5:30	-2	3	-16	-29	-32
	6:30	-12	0	-16	-24	-22
	7:30	-13	0	-15	-22	-19
	8:30	-12	-5	-23	-37	-51
	9:30	-11	-6	-19	-27	-34
	10:30	1	-2	-20	-33	-52
	11:30	-2	1	-15	-27	-45
	12:30	4	4	-12	-29	-55
	13:30	16	14	-4	-21	-50
	14:30	19	25	2	-16	-53
	15:30	25	23	5	-13	-54
	16:30	31	25	7	-14	-56
	17:30	27	25	9	-8	-45
	18:30	33	27	4	-14	-51
	19:15	20	23	6	-8	-37
	20:30	15	17	0	-19	-52
	21:30	14	13	0	-16	-47
	22:30	-1	11	1	-11	-29
	23:00	-1	9	-1	-15	-38
5/26/2010	0:50	0	7	-10	-28	-58
	1:30	-11	8	-10	-29	-55
	2:30	-11	7	-11	-27	-50

Table E.13: Bridge monitoring—bottom-fiber strains—Girder 8

		Span 10			Span 11		
		S8_10_1M	F8_10_1M	F8_10_CK	F8_11_CK	S8_11_4M	F8_11_4M
Ht. from girder base (in.)		0	0	0	0	0	0
Dist. from center of cont. dia. (in.)		-75	-74	-41	52	75	74
Units		$x10^{-6}$ in/in					
Date	**Time**						
5/25/2010	2:30	0	0	0	0	0	0
	3:30	-7	1	-43	-45	-12	-4
	4:30	-11	1	-66	-52	-18	-3
	5:30	-15	0	-86	-60	-25	-5
	6:30	-20	-1	-111	-69	-36	-9
	7:30	-17	0	-114	-71	-39	-11
	8:30	-23	0	-85	-62	-32	-12
	9:30	-16	0	-29	-37	-19	-9
	10:30	-12	0	34	-6	4	2
	11:30	-11	1	72	27	26	7
	12:30	-4	0	159	82	77	23
	13:30	9	7	268	156	165	54
	14:30	22	13	355	215	239	82
	15:30	24	16	391	244	279	97
	16:30	25	15	404	251	297	101
	17:30	23	15	383	241	284	98
	18:30	21	13	334	213	241	84
	19:15	19	10	283	185	195	68
	20:30	9	8	190	126	116	41
	21:30	0	5	124	85	76	25
	22:30	1	6	76	57	45	14
	23:00	0	5	50	43	33	10
5/26/2010	0:50	-14	-1	-13	16	7	-1
	1:30	-18	-1	-47	-27	-13	-7
	2:30	-18	-1	-86	-36	-20	-8

Table E.13 cont.: Bridge monitoring—bottom-fiber strains—Girder 8

		Span 11				
		S8_11_5M	F8_11_5M	S8_11_6M	S8_11_7M	S8_11_8M
Ht. from girder base (in.)		0	0	0	0	0
Dist. from center of cont. dia. (in.)		105	104	273	441	609
Units		$x10^{-6}$ in/in				
Date	**Time**					
5/25/2010	2:30	0	0	0	0	0
	3:30	0	-1	-10	-19	9
	4:30	-1	3	-19	-35	10
	5:30	-6	-1	-20	-31	5
	6:30	-11	-5	-21	-28	1
	7:30	-16	-8	-20	-23	0
	8:30	-14	-16	-29	-40	8
	9:30	-14	-18	-24	-27	1
	10:30	-5	-17	-25	-33	8
	11:30	-1	-10	-20	-27	5
	12:30	5	-12	-17	-28	7
	13:30	15	0	-8	-19	9
	14:30	25	14	1	-11	11
	15:30	32	18	7	-9	11
	16:30	37	24	7	-9	14
	17:30	37	25	10	-4	13
	18:30	33	27	5	-11	13
	19:15	26	22	6	-3	9
	20:30	23	17	-2	-18	12
	21:30	18	11	-4	-18	12
	22:30	6	8	-4	-8	4
	23:00	4	5	-7	-15	5
5/26/2010	0:50	-1	2	-19	-29	7
	1:30	-2	1	-19	-32	6
	2:30	-9	0	-21	-28	1

E.5 FRP STRAINS

Table E.14: Bridge monitoring—FRP strains—Girder 7

		Span 10			Span 11		
		F7_10_1M	F7_10_CK	F7_10_2Z	F7_11_CK	F7_11_4M	F7_11_5M
Ht. from girder base (in.)		0	0	3	0	0	0
Dist. from center of cont. dia. (in.)		-74	-47	-14	47	74	104
Units		$x10^{-6}$ in/in					
Date	**Time**						
5/25/2010	2:30	0	0	0	0	0	0
	3:30	0	-50	-4	-37	0	1
	4:30	0	-60	-5	-51	-2	3
	5:30	2	-67	-6	-62	-4	3
	6:30	-1	-78	-7	-79	-6	0
	7:30	-1	-79	-7	-79	-4	0
	8:30	-1	-59	-3	-58	-4	-5
	9:30	0	-15	6	-3	1	-6
	10:30	5	38	15	65	6	-2
	11:30	9	77	20	116	11	1
	12:30	16	167	33	228	21	4
	13:30	27	277	55	368	34	14
	14:30	35	358	72	475	44	25
	15:30	38	385	77	504	46	23
	16:30	38	387	76	502	46	25
	17:30	34	359	68	466	43	25
	18:30	30	312	57	401	38	27
	19:15	23	261	46	340	32	23
	20:30	20	185	32	233	23	17
	21:30	15	125	24	160	16	13
	22:30	12	88	19	112	15	11
	23:00	9	61	14	84	12	9
5/26/2010	0:50	3	14	6	23	6	7
	1:30	3	-6	4	-7	4	8
	2:30	1	-39	0	-28	6	7

Table E.15: Bridge monitoring—FRP strains—Girder 8

		Span 10				
		F8_10_1Y	F8_10_1M	F8_10_CK	F8_10_2Y	F8_10_2Z
Ht. from girder base (in.)		3	0	0	3	3
Dist. from center of cont. dia. (in.)		-74	-74	-41	-14	-14
Units		$x10^{-6}$ in/in				
Date	**Time**					
5/25/2010	2:30	0	0	0	0	0
	3:30	0	1	-43	-11	1
	4:30	0	1	-66	9	-1
	5:30	0	0	-86	23	-1
	6:30	-1	-1	-111	43	-2
	7:30	2	0	-114	42	-2
	8:30	0	0	-85	52	0
	9:30	1	0	-29	69	3
	10:30	3	0	34	84	2
	11:30	4	1	72	90	4
	12:30	7	0	159	125	9
	13:30	11	7	268	167	16
	14:30	15	13	355	202	23
	15:30	14	16	391	210	23
	16:30	13	15	404	208	23
	17:30	12	15	383	195	21
	18:30	11	13	334	170	18
	19:15	9	10	283	147	14
	20:30	6	8	190	110	9
	21:30	3	5	124	90	6
	22:30	5	6	76	80	6
	23:00	4	5	50	75	5
5/26/2010	0:50	3	-1	-13	58	4
	1:30	4	-1	-47	57	3
	2:30	4	-1	-86	51	3

Table E.15 cont.: Bridge monitoring—FRP strains—Girder 8

		Span 11					
		F8_11_3Y	F8_11_3Z	F8_11_CK	F8_11_4Y	F8_11_4M	F8_11_5M
Ht. from girder base (in.)		3	3	0	3	0	0
Dist. from center of cont. dia. (in.)		14	14	52	74	74	104
Units		$x10^{-6}$ in/in					
Date	**Time**						
5/25/2010	2:30	0	0	0	0	0	0
	3:30	-11	-13	-45	-4	-4	-1
	4:30	-18	-14	-52	-5	-3	3
	5:30	-22	-16	-60	-7	-5	-1
	6:30	-26	-21	-69	-10	-9	-5
	7:30	-28	-21	-71	-11	-11	-8
	8:30	-18	-11	-62	-10	-12	-16
	9:30	-5	-8	-37	-7	-9	-18
	10:30	10	5	-6	-2	2	-17
	11:30	25	20	27	1	7	-10
	12:30	57	53	82	9	23	-12
	13:30	94	97	156	22	54	0
	14:30	119	130	215	32	82	14
	15:30	125	140	244	37	97	18
	16:30	126	142	251	38	101	24
	17:30	118	132	241	37	98	25
	18:30	101	112	213	31	84	27
	19:15	87	91	185	25	68	22
	20:30	57	58	126	14	41	17
	21:30	36	35	85	6	25	11
	22:30	22	20	57	1	14	8
	23:00	15	12	43	0	10	5
5/26/2010	0:50	-1	3	16	-4	-1	2
	1:30	-9	-11	-27	-7	-7	1
	2:30	-16	-12	-36	-9	-8	0

Appendix F

BRIDGE MONITORING—MEASUREMENT ADJUSTMENTS

F.1 INCONSISTENT MEASUREMENTS

Sensors were balanced at the beginning of bridge monitoring. During the duration of the bridge monitoring test, some of the instruments provided inconsistent measurements at different points in time that may have had an effect on the remaining measurements. These inconsistent measurements could be a result of electrical noise/interference or physical effects at the sensor location. The sensors that were the most inconsistent were the deflectometers. The bottom-fiber strain gage near the crack location of Girder 8 in Span 10 also measured inconsistencies. During the analysis of bridge monitoring measurements, efforts were made to decrease the effects associated with inconsistent sensor behavior.

F.2 DEFLECTOMETER BEHAVIOR

The deflectometers seemed to be sensitive to temporary direct sunlight on the aluminum bar during the sunrise hours. An example of this type of sensitivity is evident during the morning hours plotted in Figure F.1. Unexpected physical movement of a deflectometer could also have an effect relative to the original baseline and cause a permanent data shift. Electrical noise or interference could have also caused a momentary or permanent movement relative to the original baseline. Instruments not returning to a similar measurement at the end of the test, in relation to either the initial measurement of that sensor or the concluding measurements of other comparable sensors, were the primary reason for deciding to adjust certain results. An example of this type of offset can be readily observed in the response of Sensor D7_10_B in the early afternoon in Figure F.1. Measurements that seemed to be inconsistent with the expected result were inspected and adjustments were proposed and implemented when deemed appropriate.

F.3 DEFLECTION ADJUSTMENTS

Deflection measurements considered to be affected by deflectometers exposed to direct sunlight were disregarded. When plotting the deflection results, a straight line was used to connect measurements on either side of a discarded time interval during the sunrise period when this was a particular problem.

Results that seemed to be inconsistent compared to adjacent time intervals were disregarded and replaced with an estimated value based on the following procedure.
The estimated adjusted value was created by projecting a change in value over time from the prior measurement. This projected change in value over time was based on the average of two slopes bounding the time intervals to be replaced. All time intervals following the last adjusted

result maintain their original relative change in value between time intervals. Measurements following the last adjusted measurement are shifted by the same magnitude.

F.4 GRAPHICAL PRESENTATIONS OF DEFLECTION ADJUSTMENTS

The graphical presentations within this section, Figures F.1–F.28, have been provided to illustrate the deflection adjustments that were made during the analysis of bridge monitoring measurements.

F.4.1 Original Deflections—Girders 7 and 8

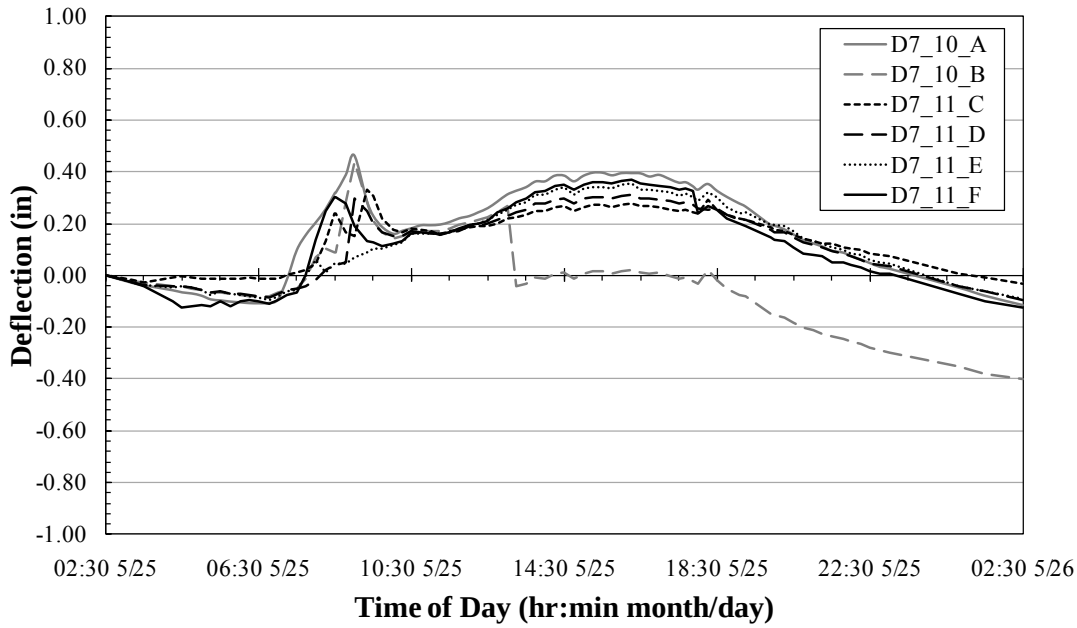

Figure F.1: Original deflection results—Girder 7

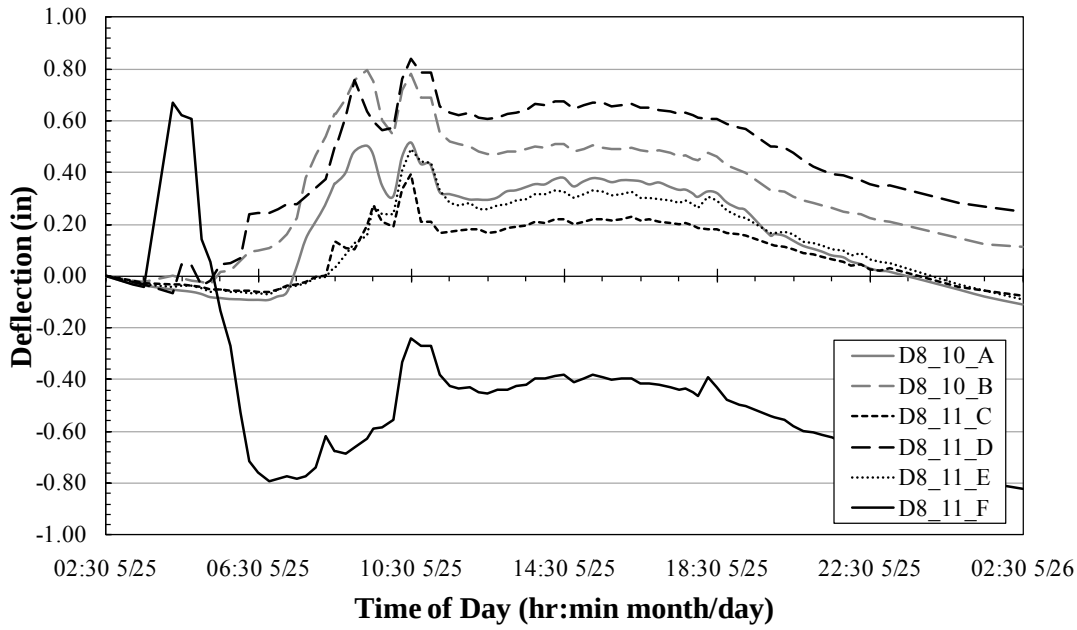

Figure F.2: Original deflection results—Girder 8

F.4.2 Adjusted Deflections of Girder 7 in Span 10

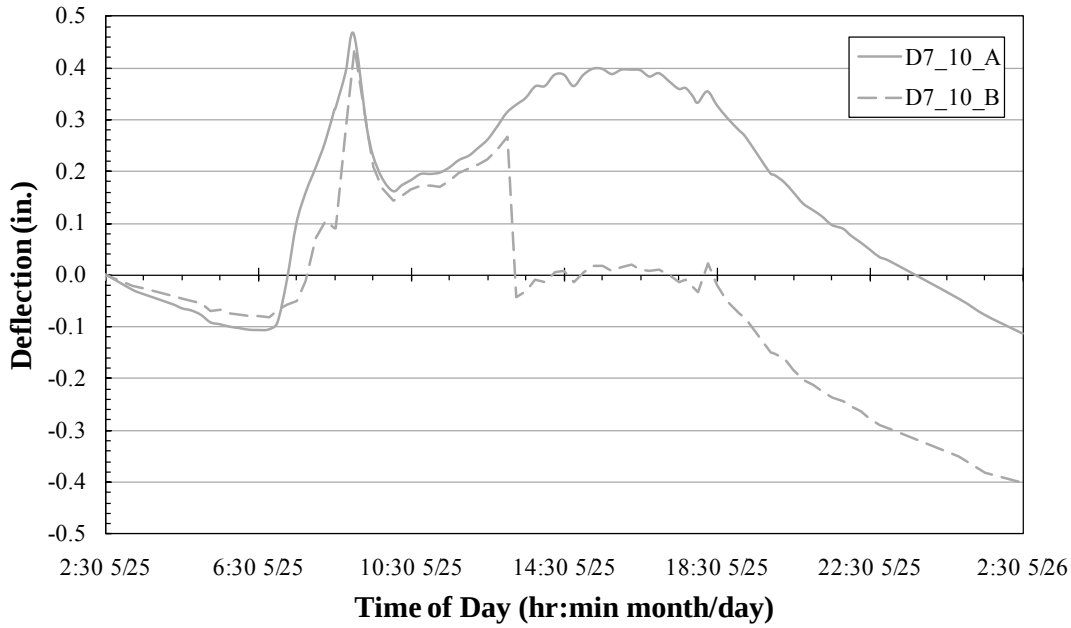

Figure F.3: Original deflection results—Girder 7—Span 10

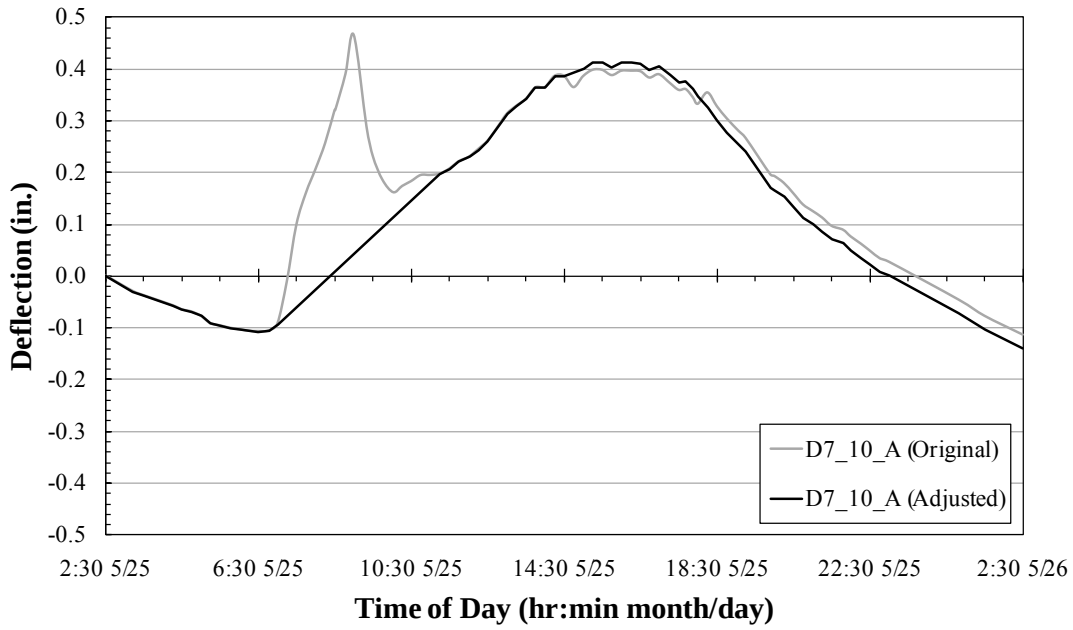

Figure F.4: Adjusted deflection results—D7_10_A

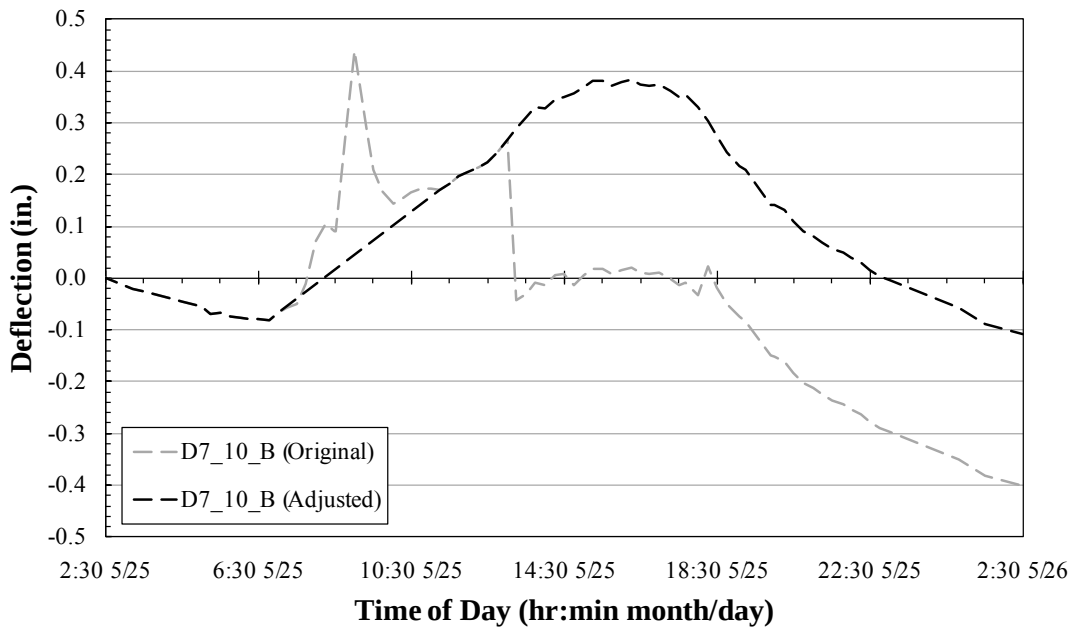

Figure F.5: Adjusted deflection results—D7_10_B

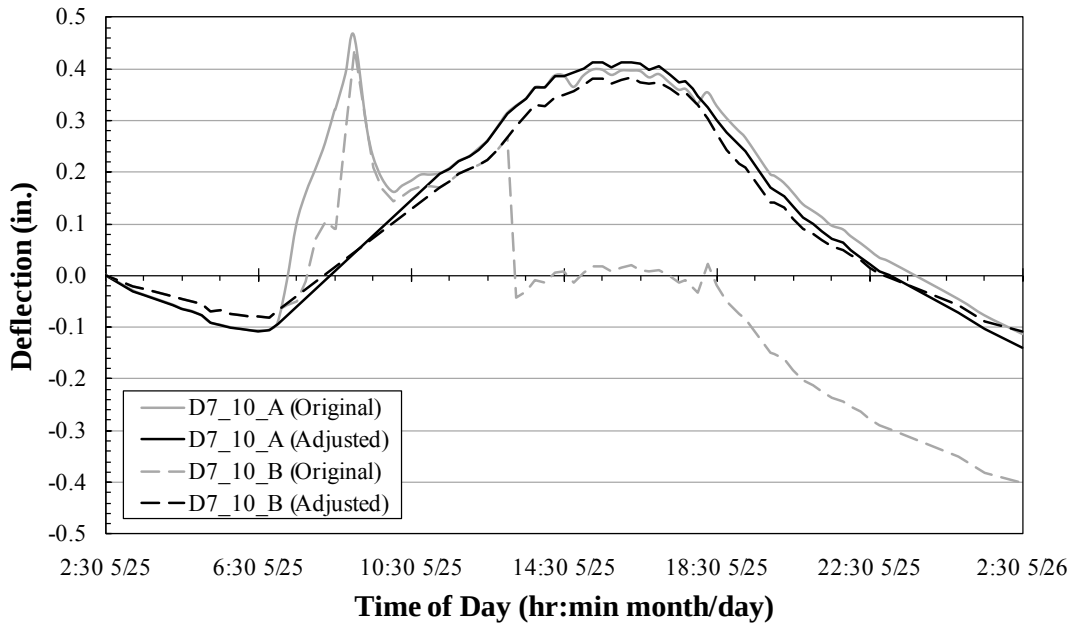

Figure F.6: Adjusted deflection results—Girder 7—Span 10

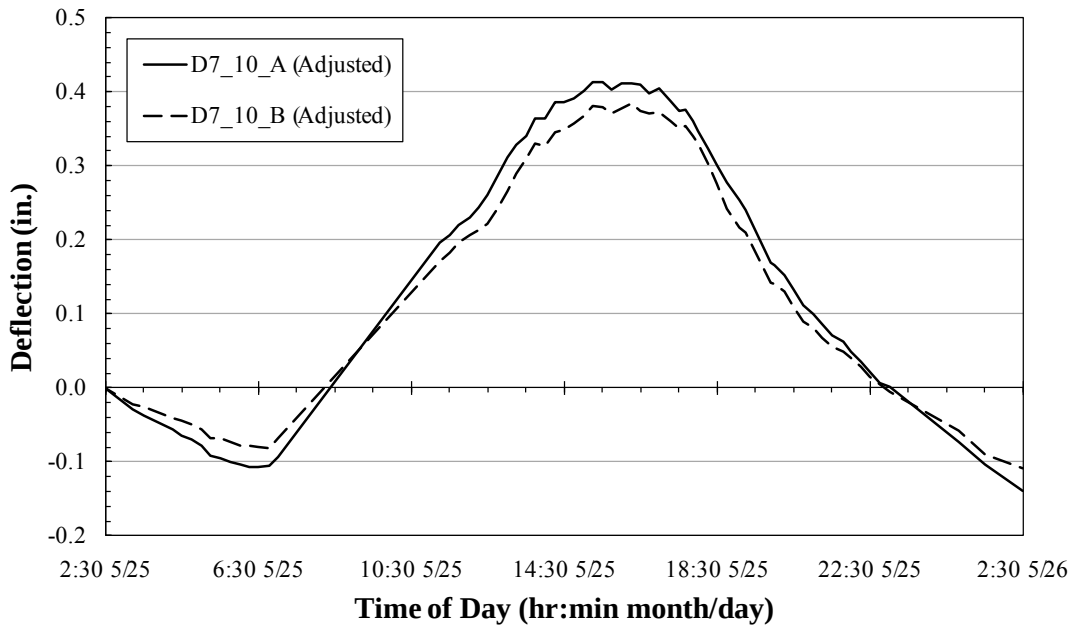

Figure F.7: Final deflection results—Girder 7—Span 10

F.4.3 Adjusted Deflections of Girder 7 in Span 11

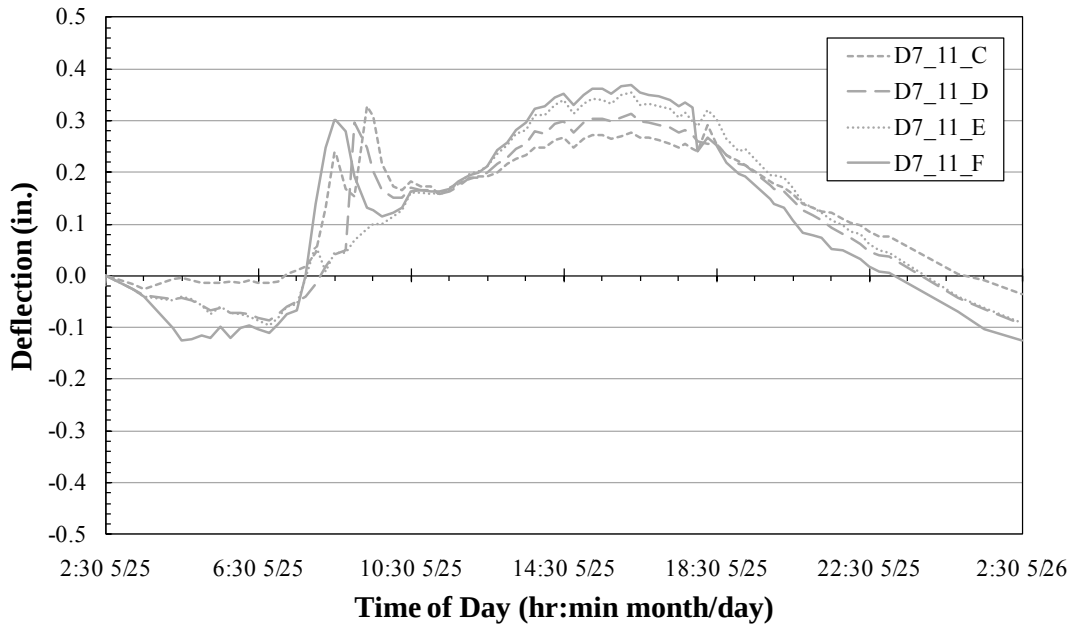

Figure F.8: Original deflection results—Girder 7—Span 11

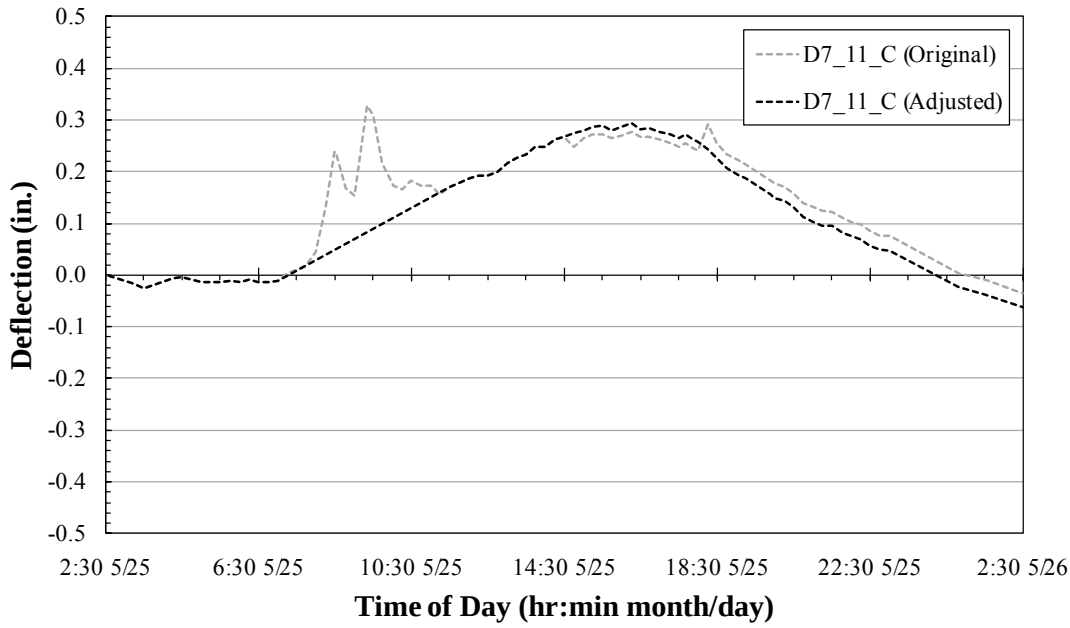

Figure F.9: Adjusted deflection results—D7_11_C

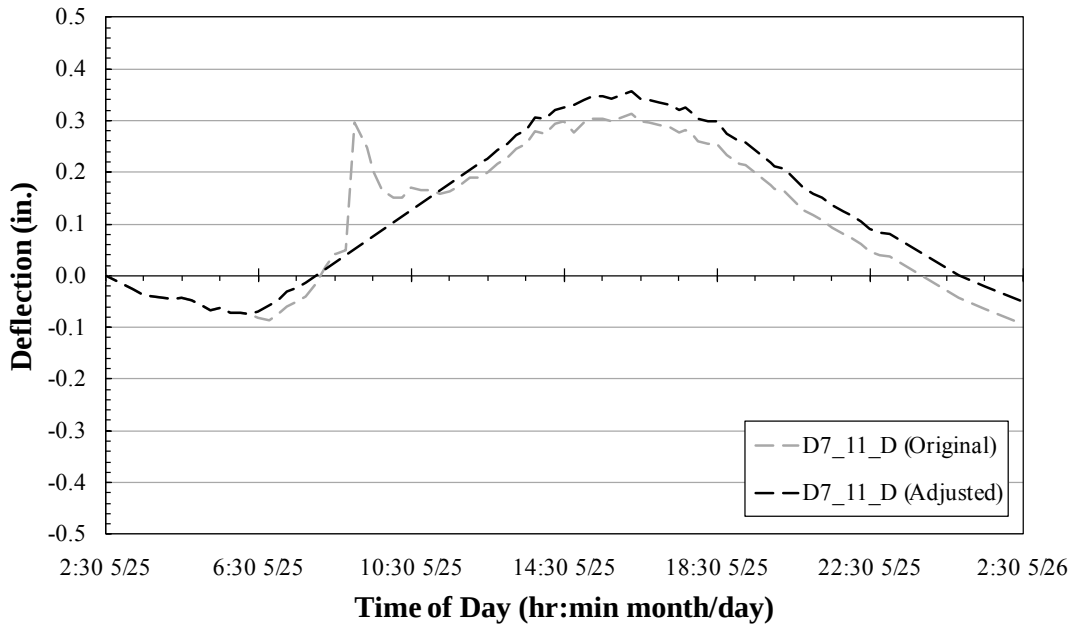

Figure F.10: Adjusted deflection results—D7_11_D

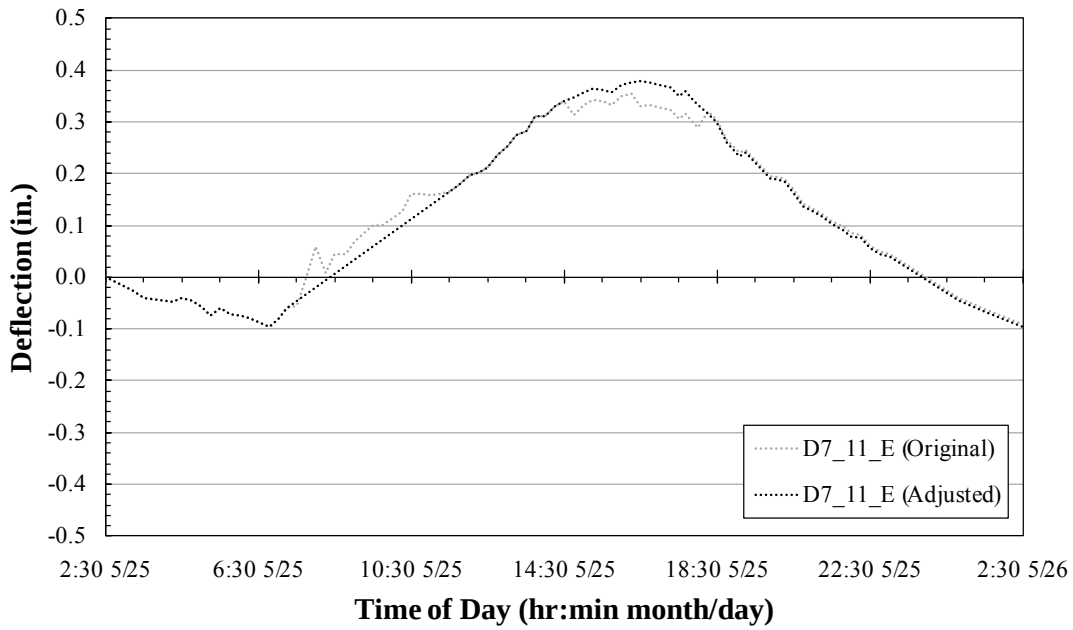

Figure F.11: Adjusted deflection results—D7_11_E

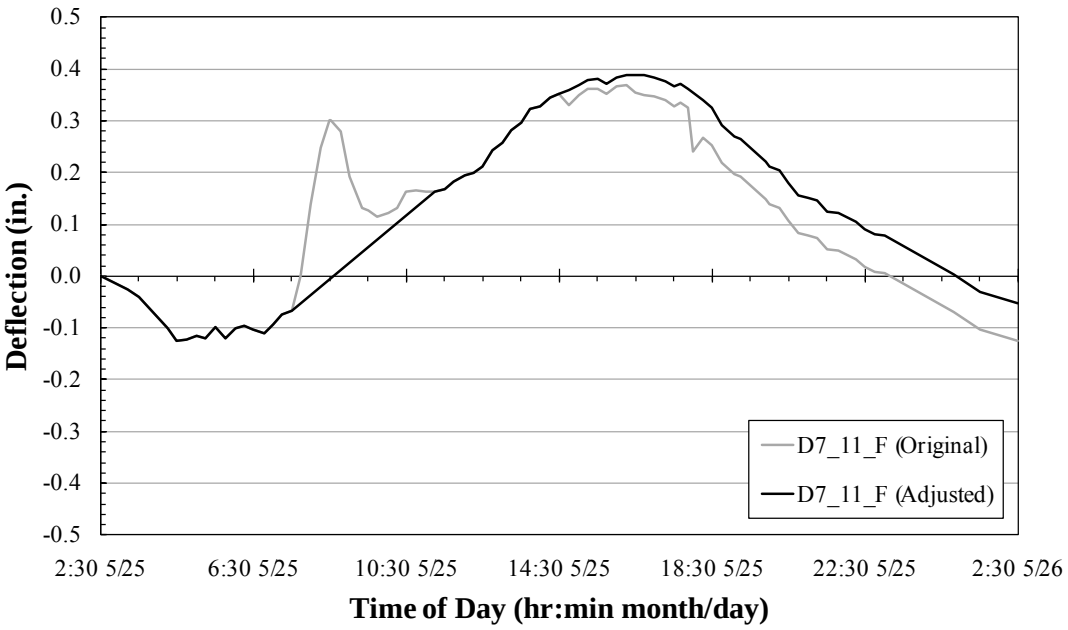

Figure F.12: Adjusted deflection results—D7_11_F

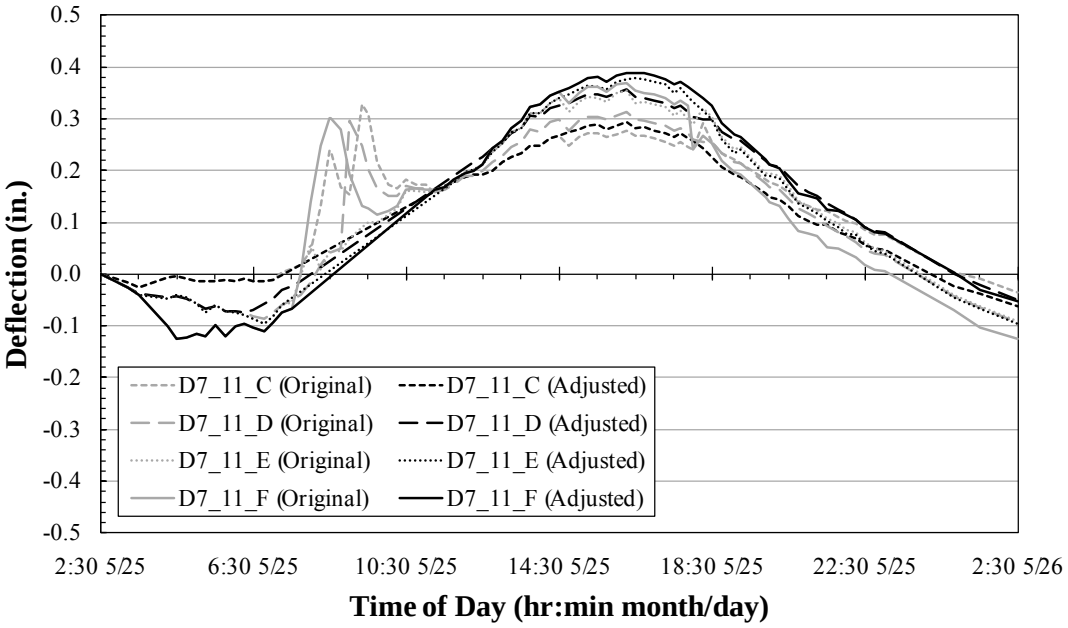

Figure F.13: Adjusted deflection results—Girder 7—Span 11

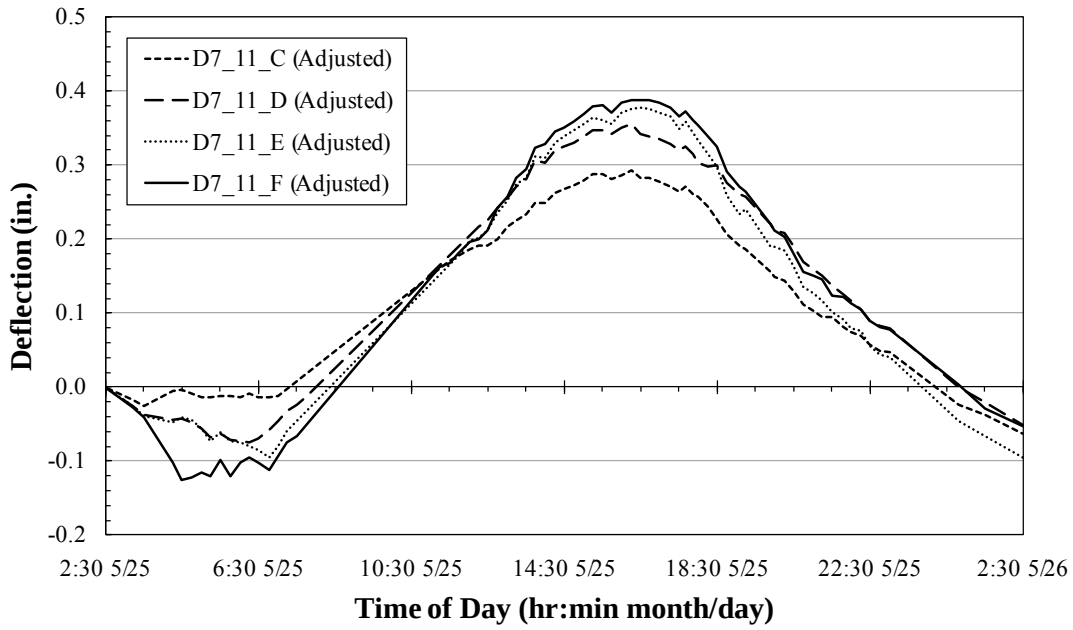

Figure F.14: Final deflection results—Girder 7—Span 11

F.4.4 Adjusted Deflections of Girder 8 in Span 10

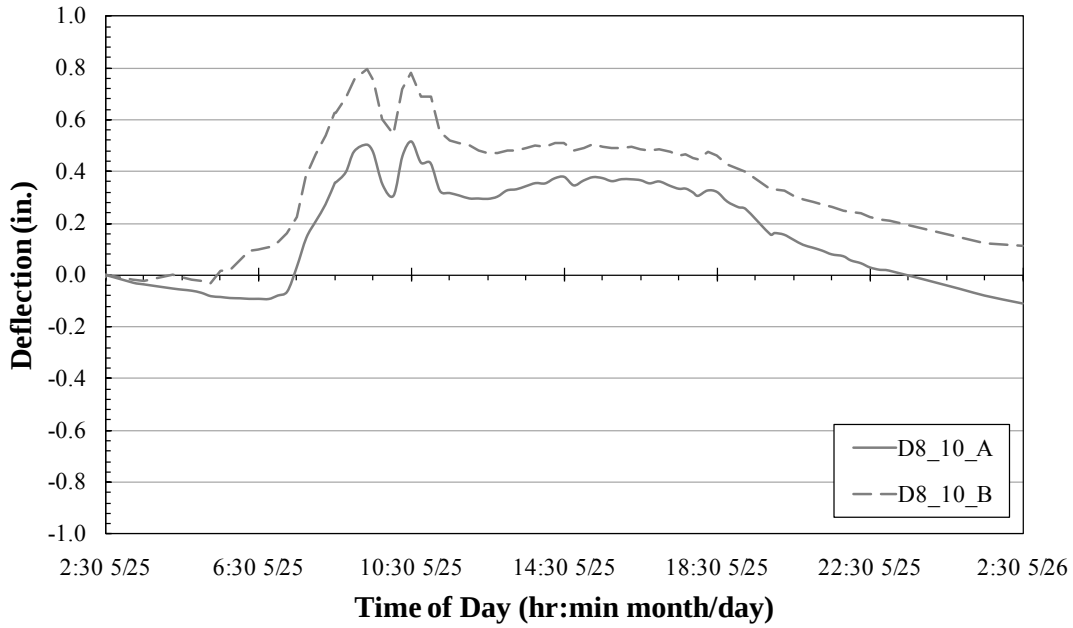

Figure F.15: Original deflection results—Girder 8—Span 10

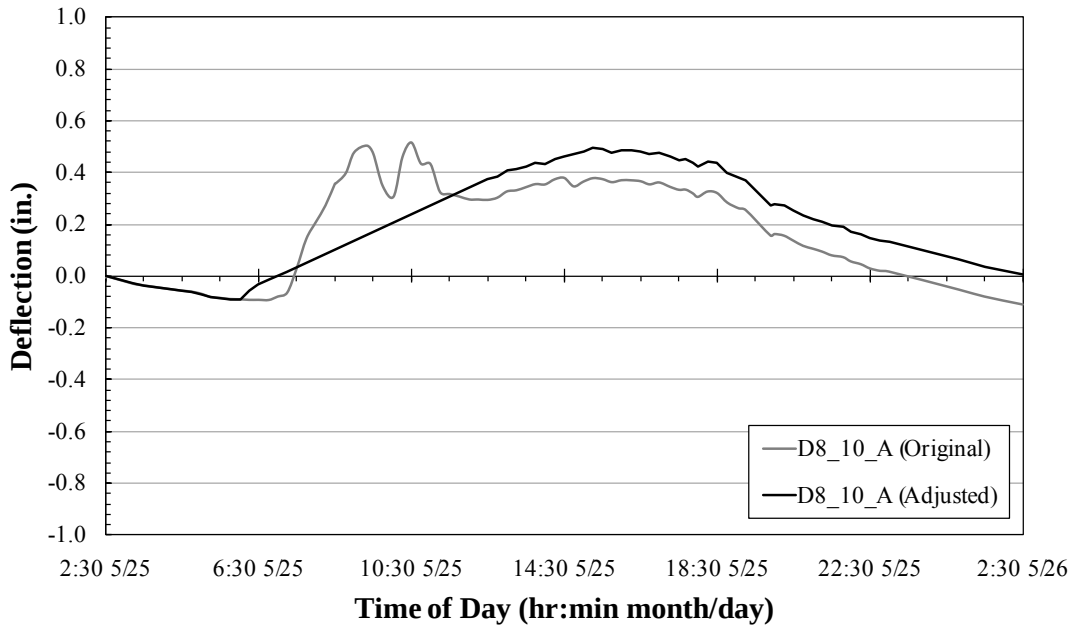

Figure F.16: Adjusted deflection results—D8_10_A

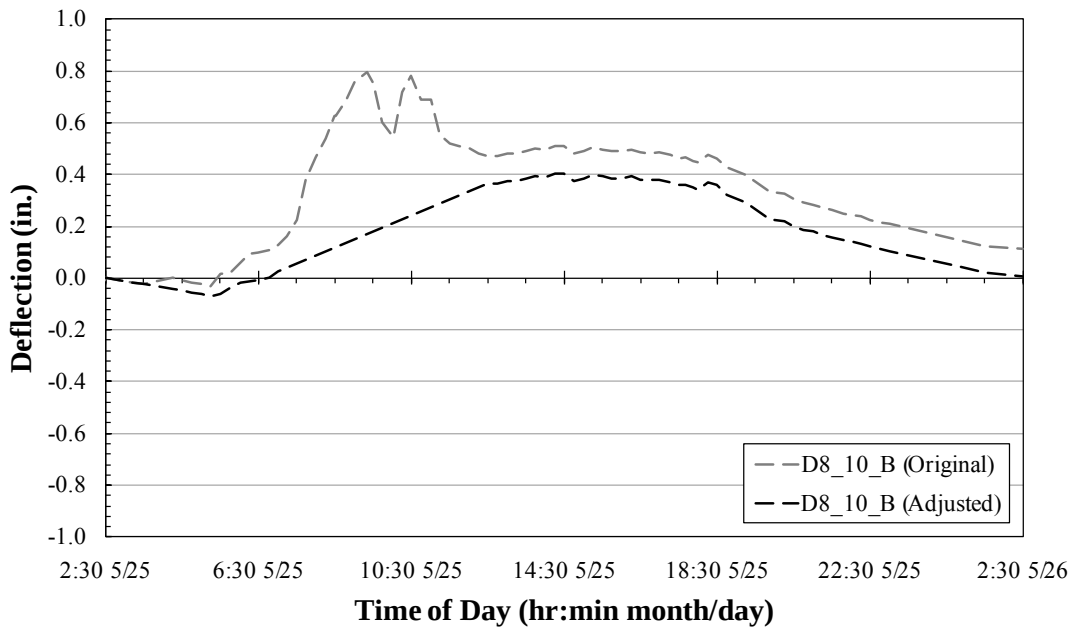

Figure F.17: Adjusted deflection results—D8_10_B

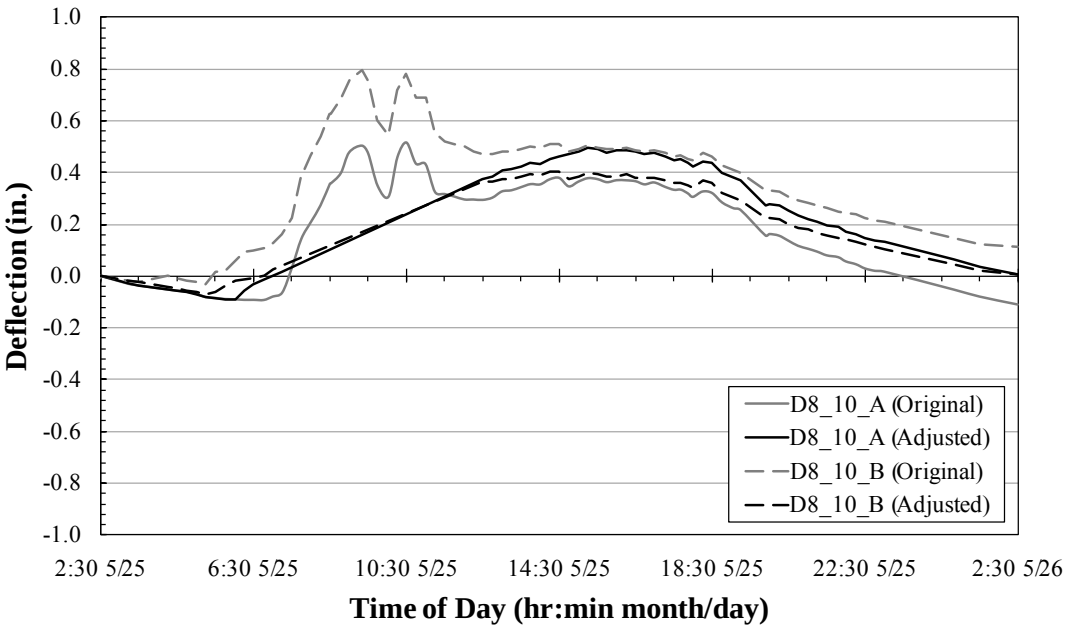

Figure F.18: Adjusted deflection results—Girder 8—Span 10

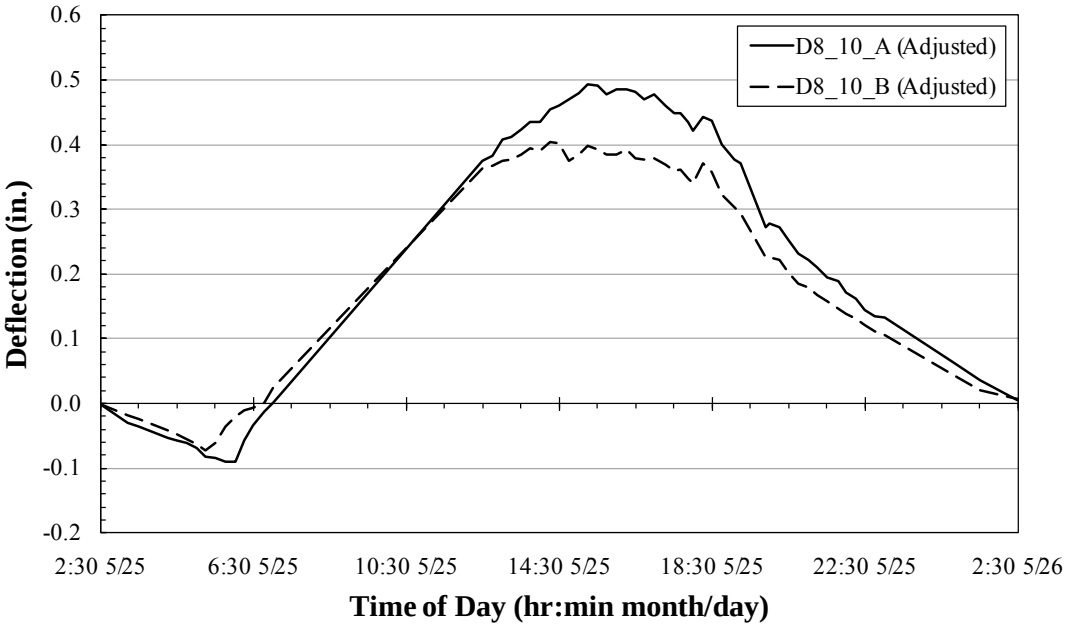

Figure F.19: Final deflection results—Girder 8—Span 10

F.4.5 Adjusted Deflections of Girder 8 in Span 11

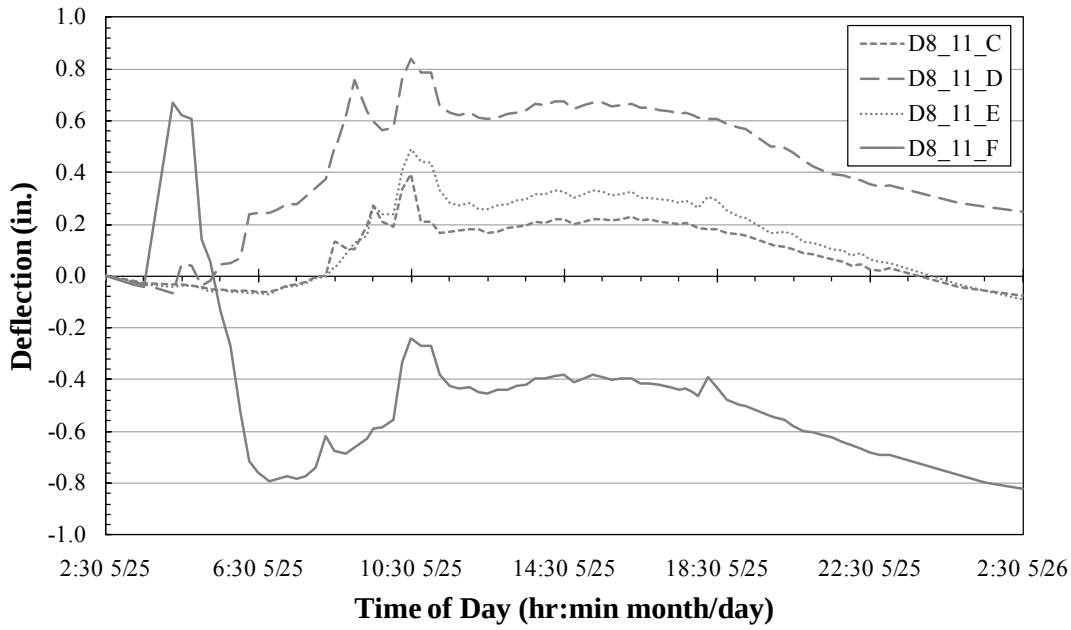

Figure F.20: Original deflection results—Girder 8—Span 11

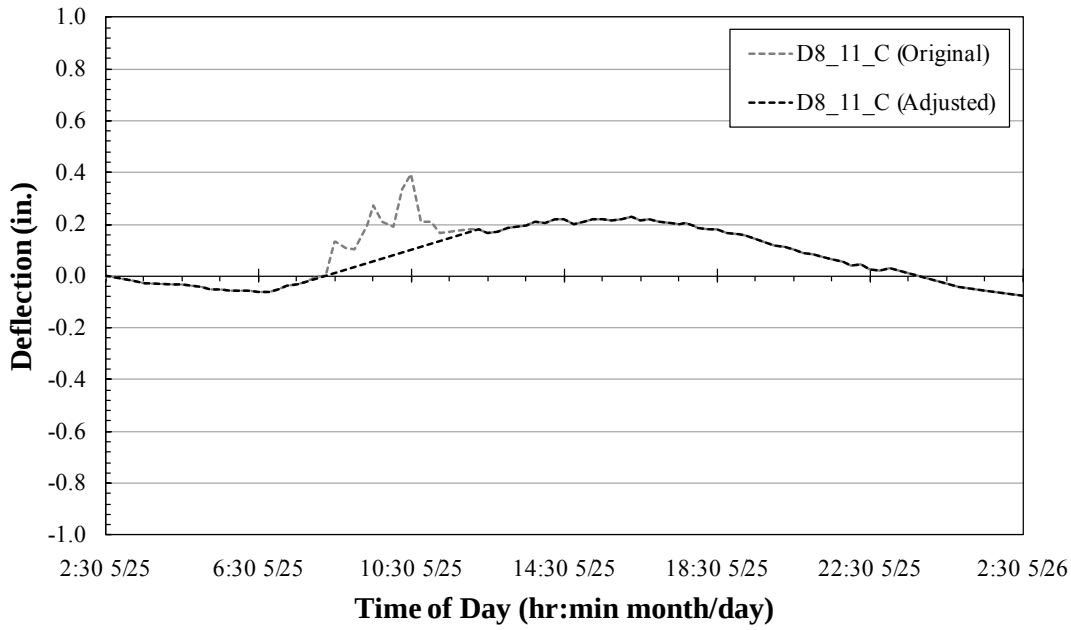

Figure F.21: Adjusted deflection results—D8_11_C

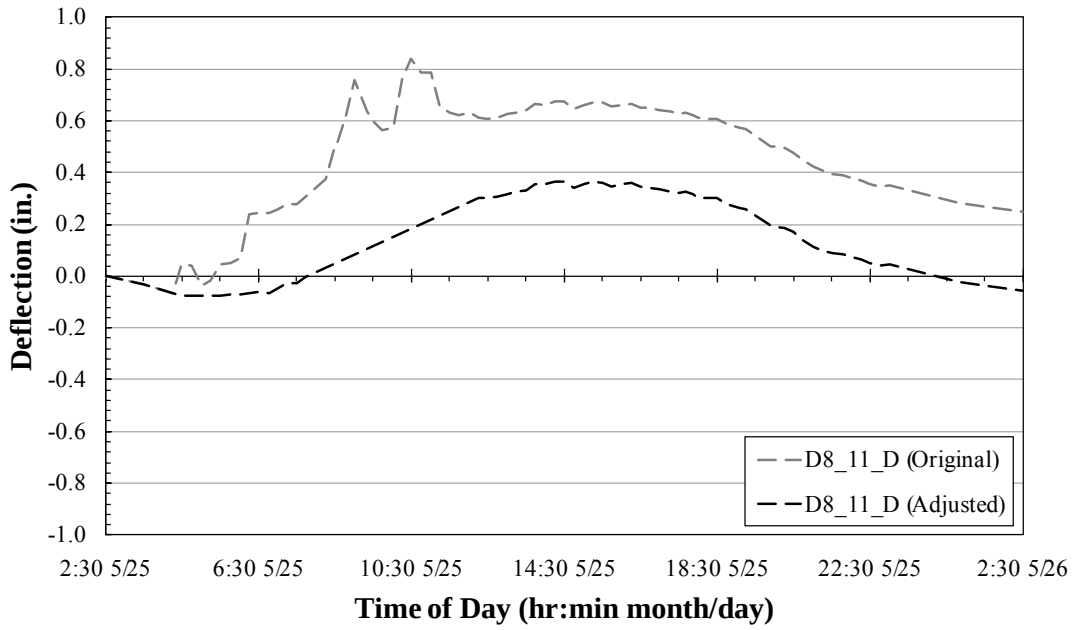

Figure F.22: Adjusted deflection results—D8_11_D

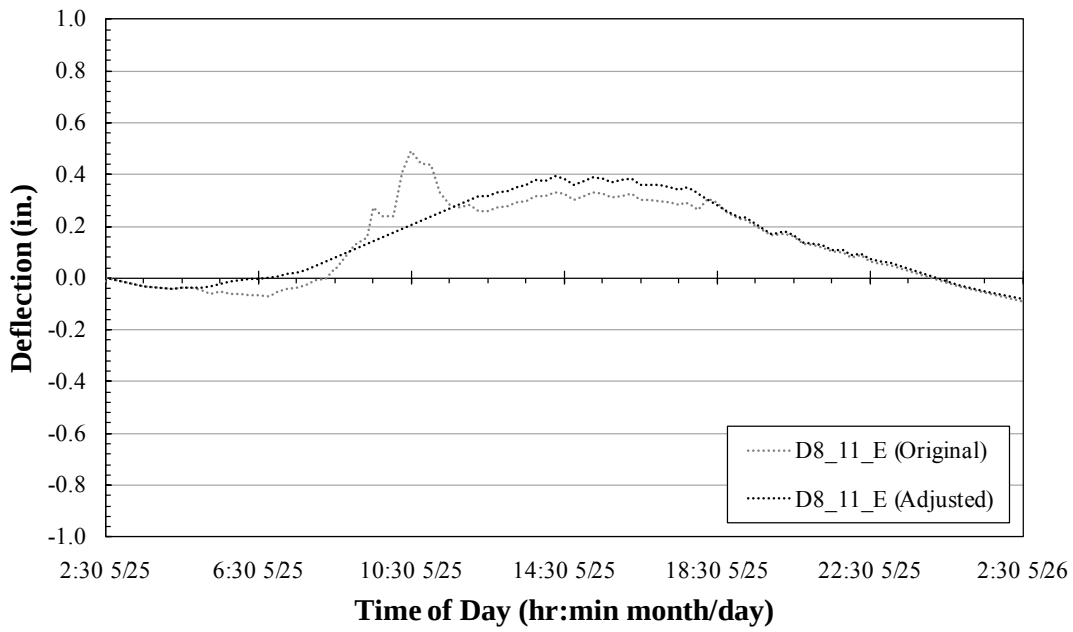

Figure F.23: Adjusted deflection results—D8_11_E

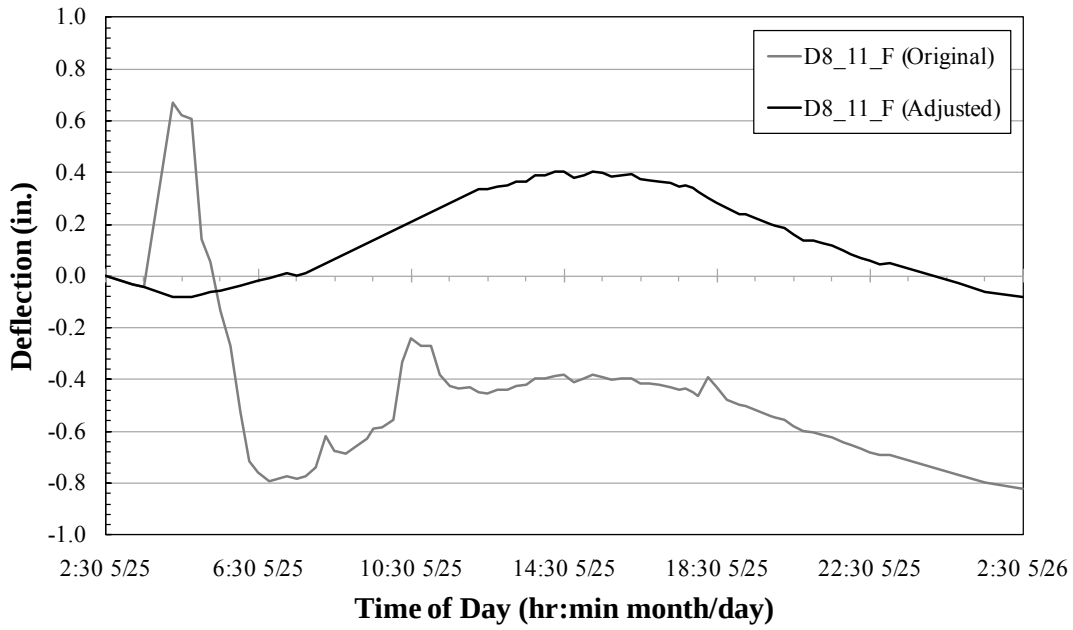

Figure F.24: Adjusted deflection results—D8_11_F

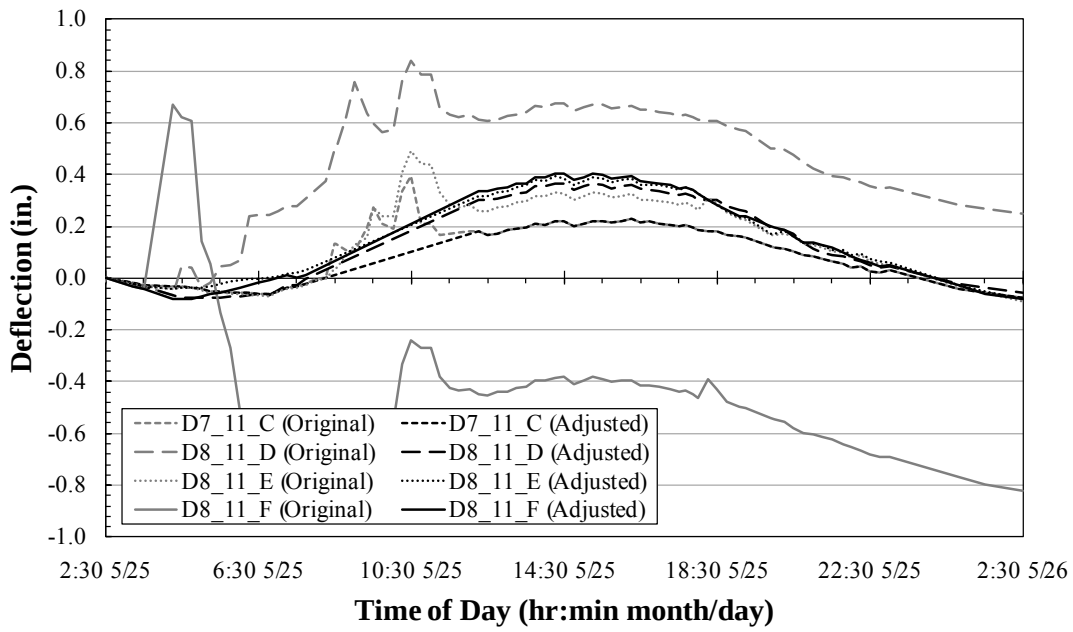

Figure F.25: Adjusted deflection results—Girder 8—Span 11

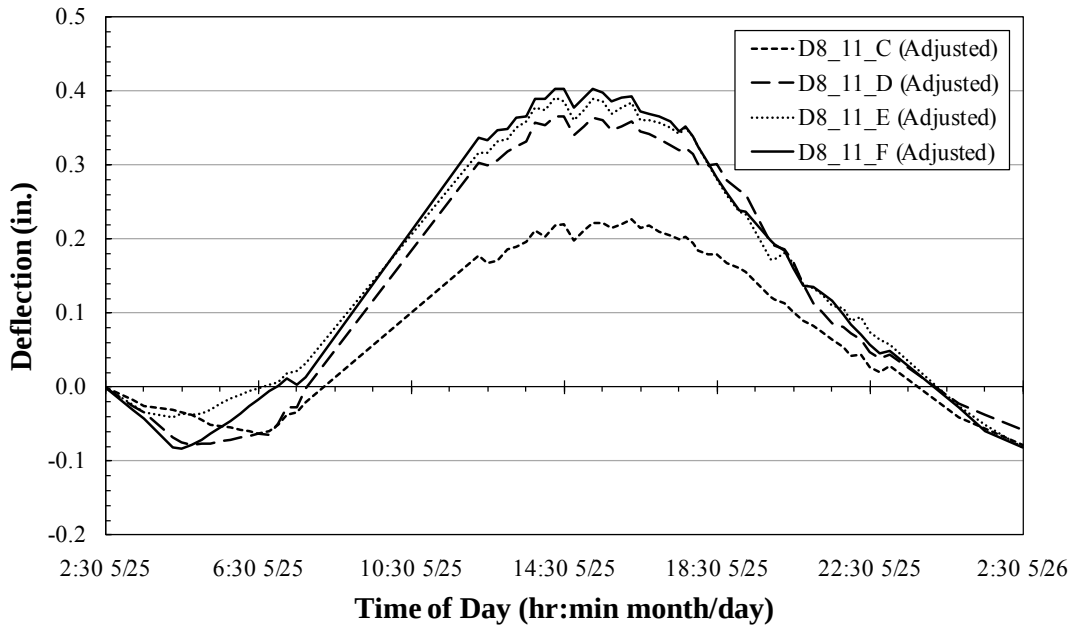

Figure F.26: Final deflection results—Girder 8—Span 11

F.4.6 Final Adjusted Deflections—Girders 7 and 8

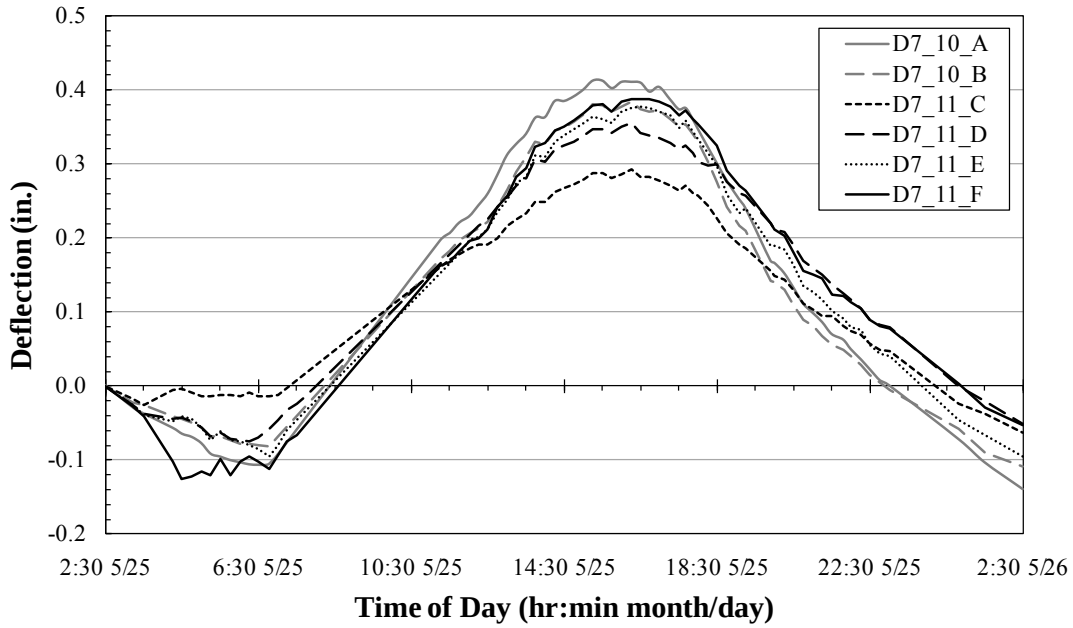

Figure F.27: Final deflection results—Girder 7

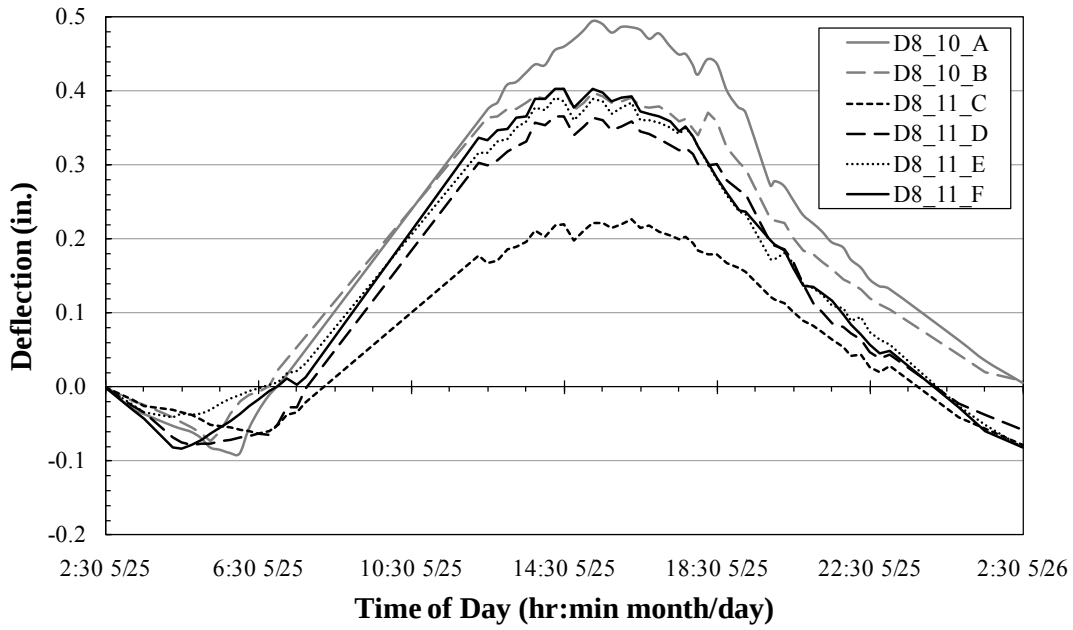

Figure F.28: Final deflection results—Girder 8

F.5 STRAIN MEASUREMENT ADJUSTMENTS

Some of the strain gages also contained inconsistent results. Strain gages that displayed data shifts similar to deflectometer data shifts were also investigated. For the bottom-fiber strain gage sensors, only the measurements on the FRP at the crack location of Girder 8 in Span 10 were adjusted. Some measurements during the early morning hours (3:30 a.m. through 5:30 a.m.) were disregarded and estimated using the same method for estimating deflection measurements that were inconsistent compared to adjacent measurements. The original FRP strains measured near the crack locations are presented in Figure F.29. The adjusted FRP strains measured near the crack location of Girder 8 in Span 10 are presented with the other crack location FRP strains in Figure F.30.

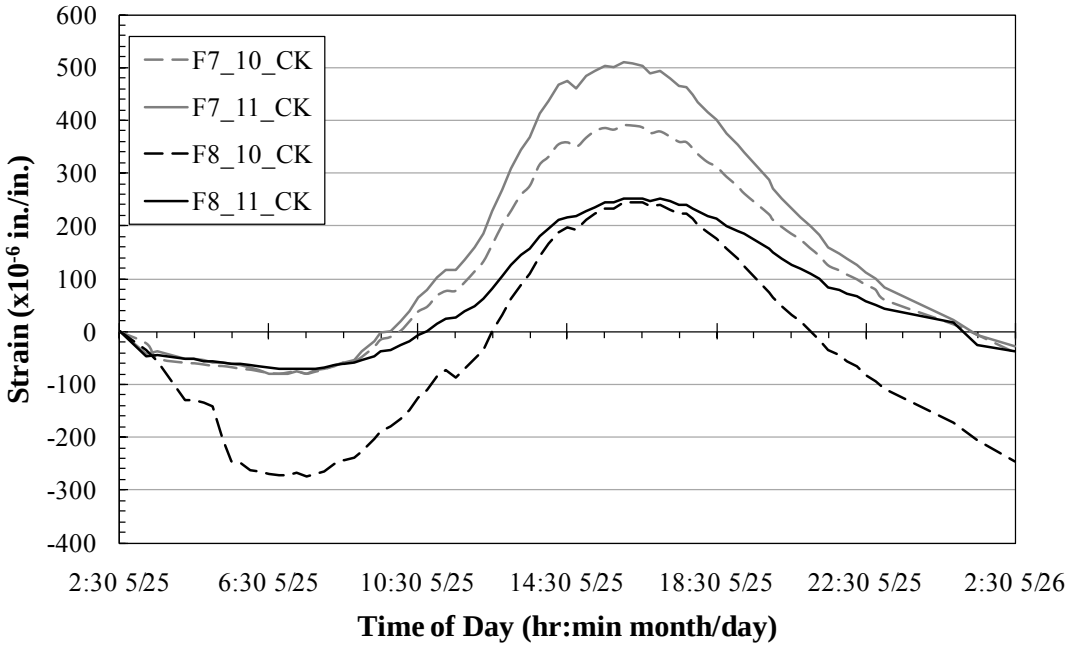

Figure F.29: Crack location FRP strain measurements—original F8_10_CK

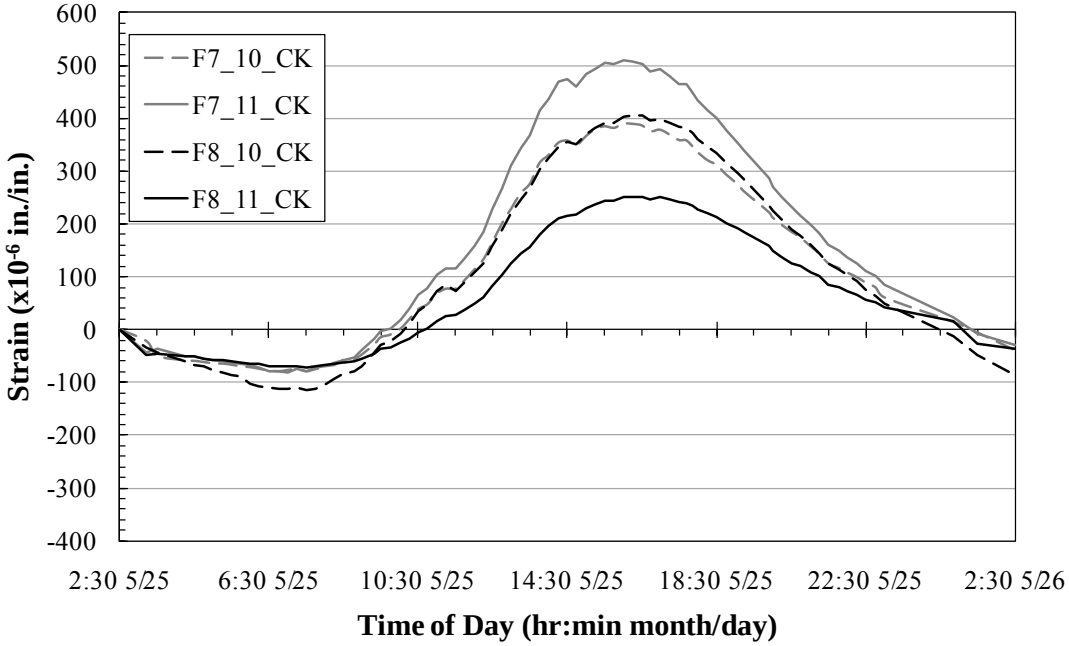

Figure F.30: Crack location FRP strain measurements—adjusted F8_10_CK

Appendix G

SUPERPOSITION—GRAPHICAL RESULTS

G.1 CRACK-OPENING DISPLACEMENTS

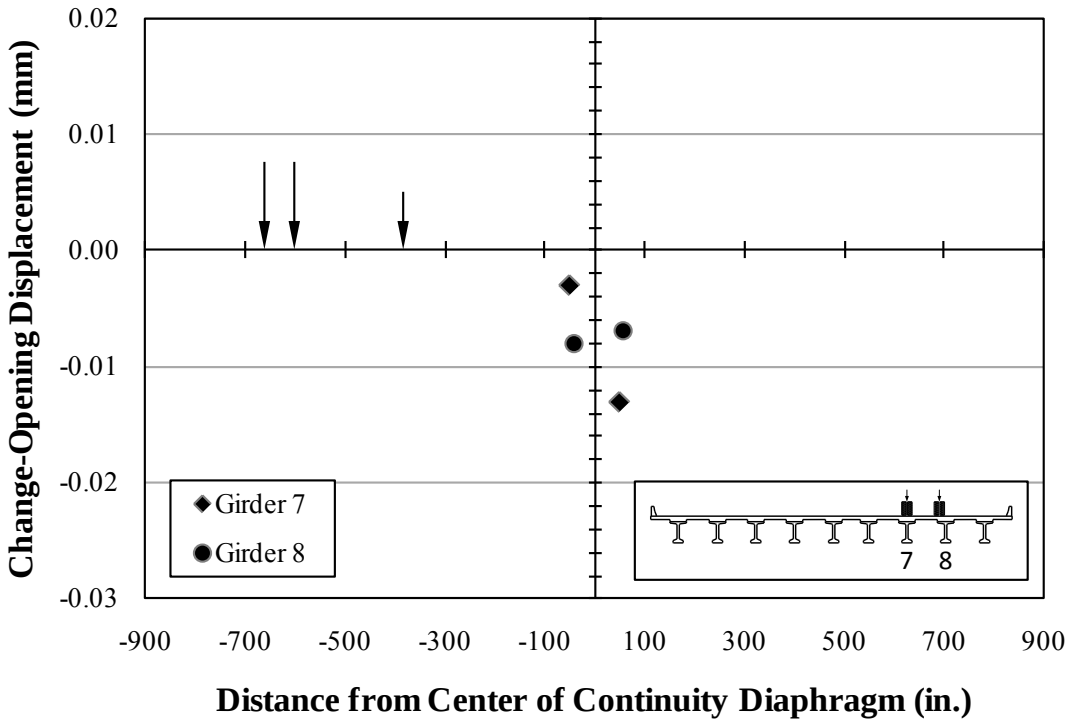

Figure G.1: Crack-opening displacements—A1 (east)

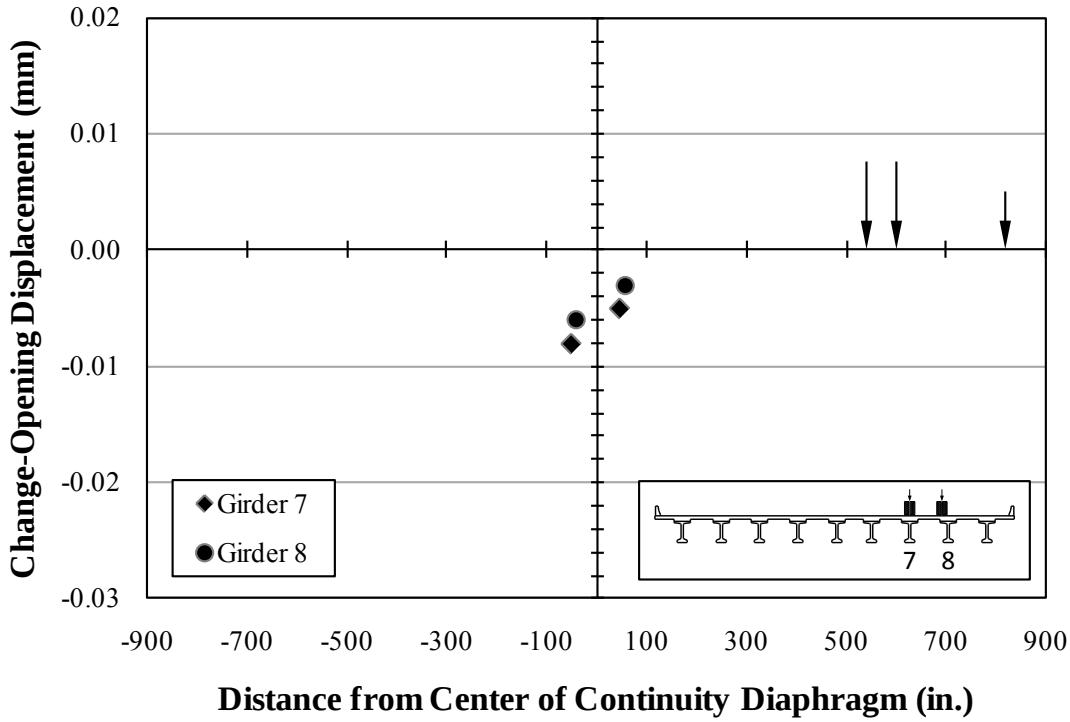

Figure G.2: Crack-opening displacements—A9 (east)

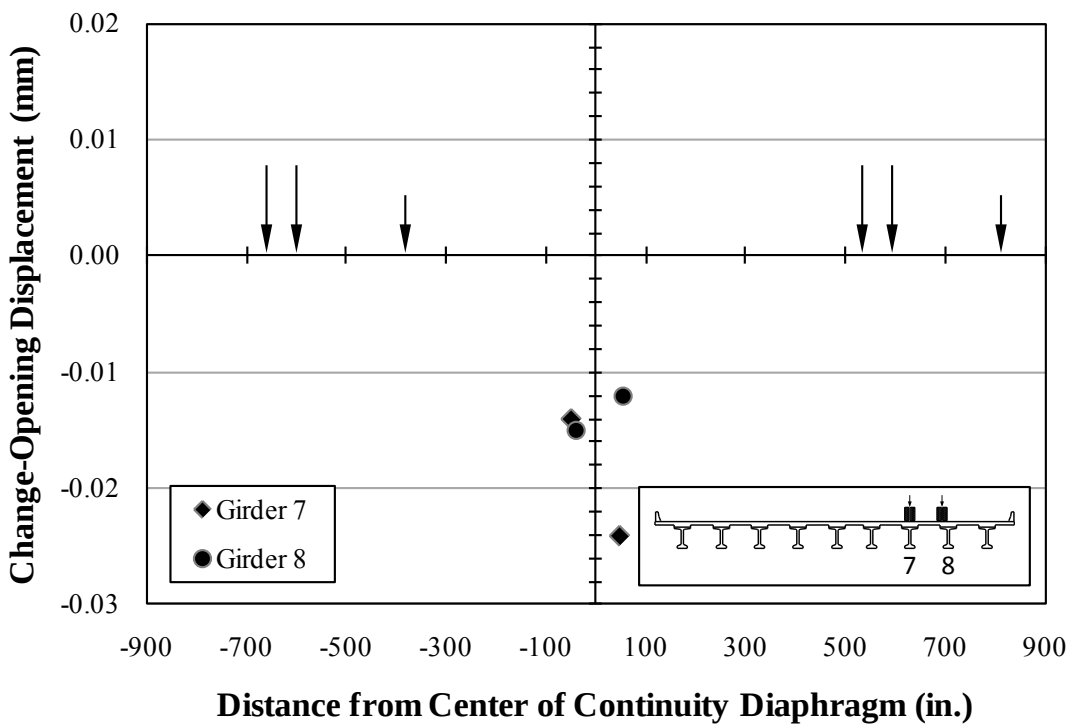

Figure G.3: Crack-opening displacements—A1 (east) + A9 (east)

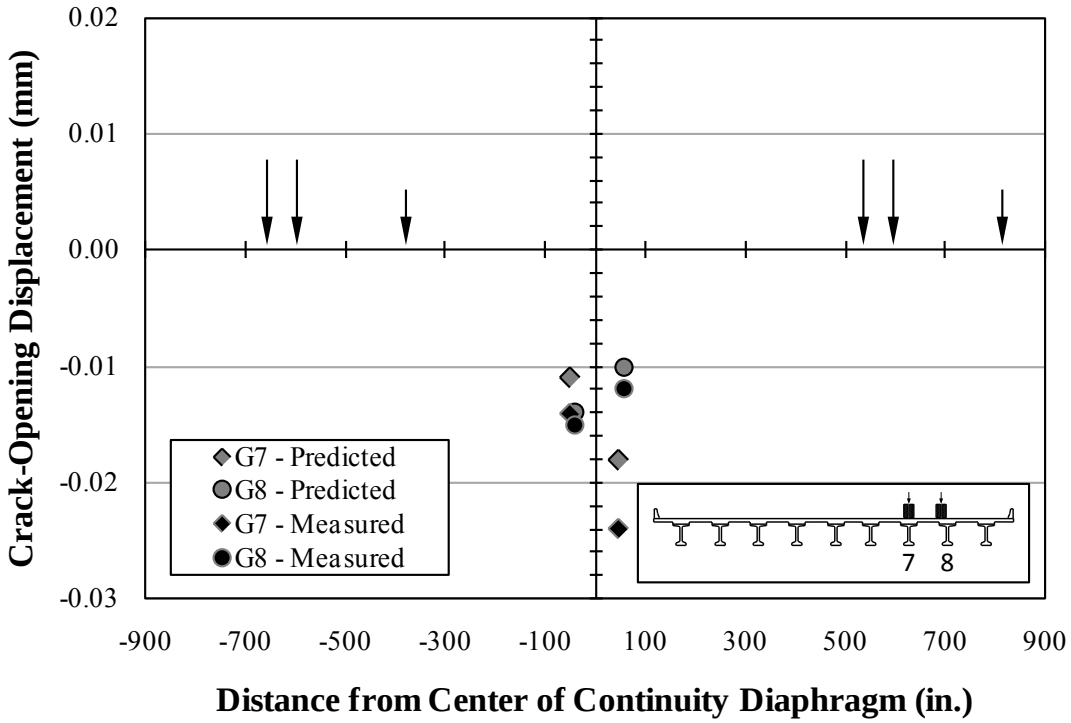

Figure G.4: Crack-opening displacements—superposition—actual and predicted

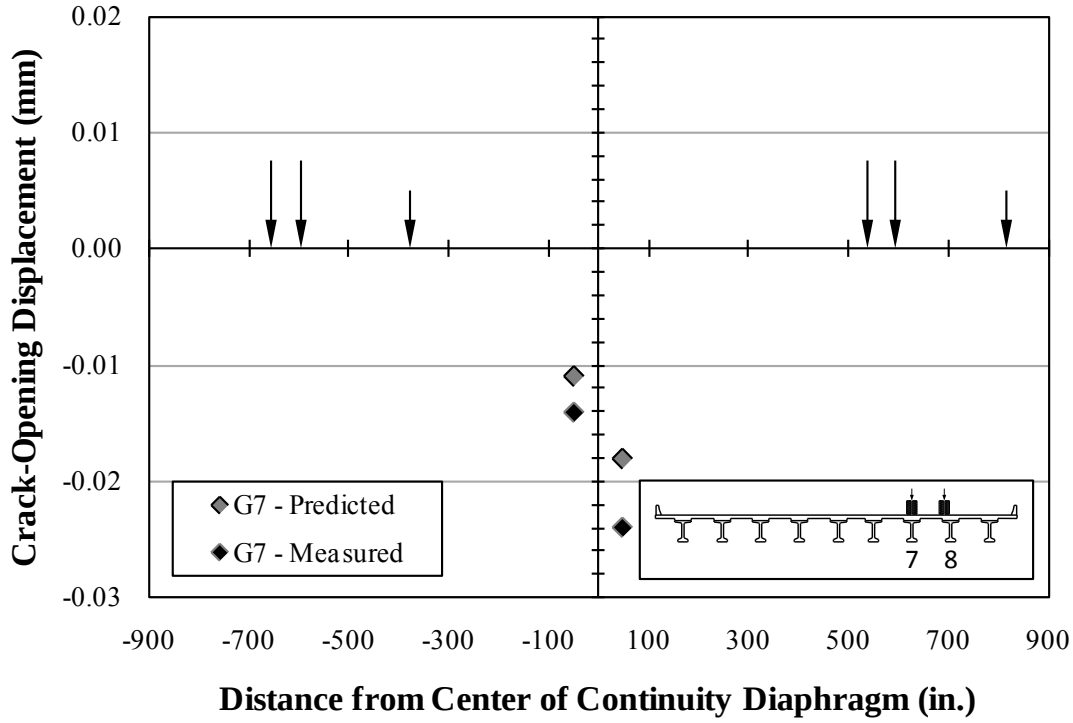

Figure G.5: COD—superposition—actual and predicted—Girder 7

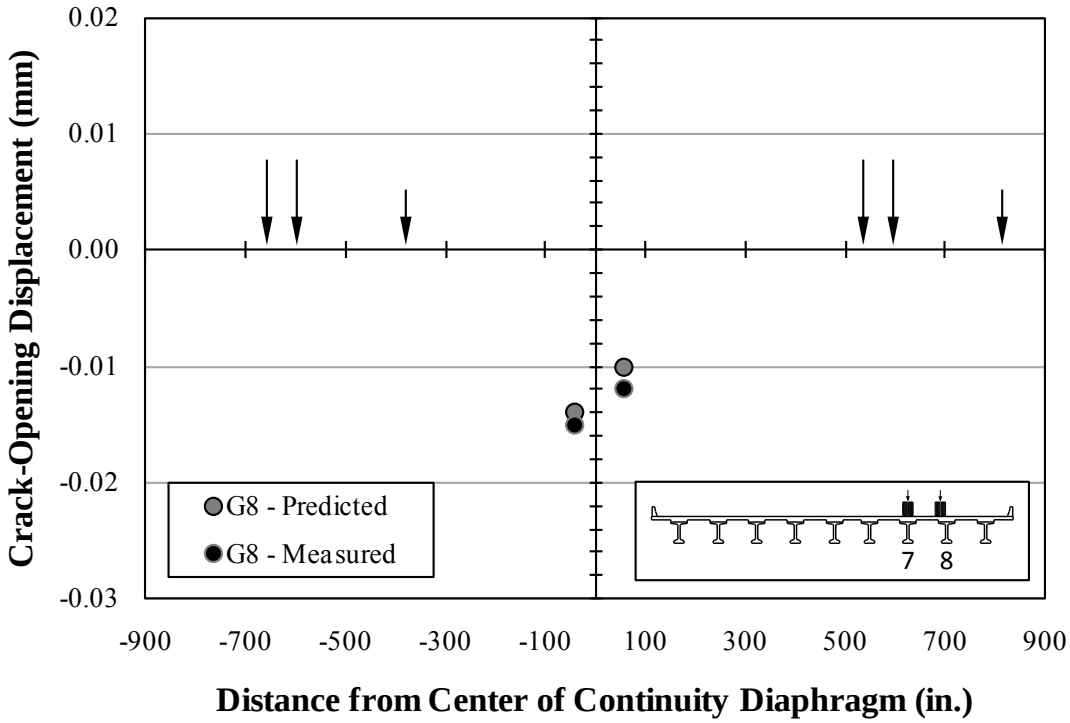

Figure G.6: COD—superposition—actual and predicted—Girder 8

G.2 DEFLECTIONS

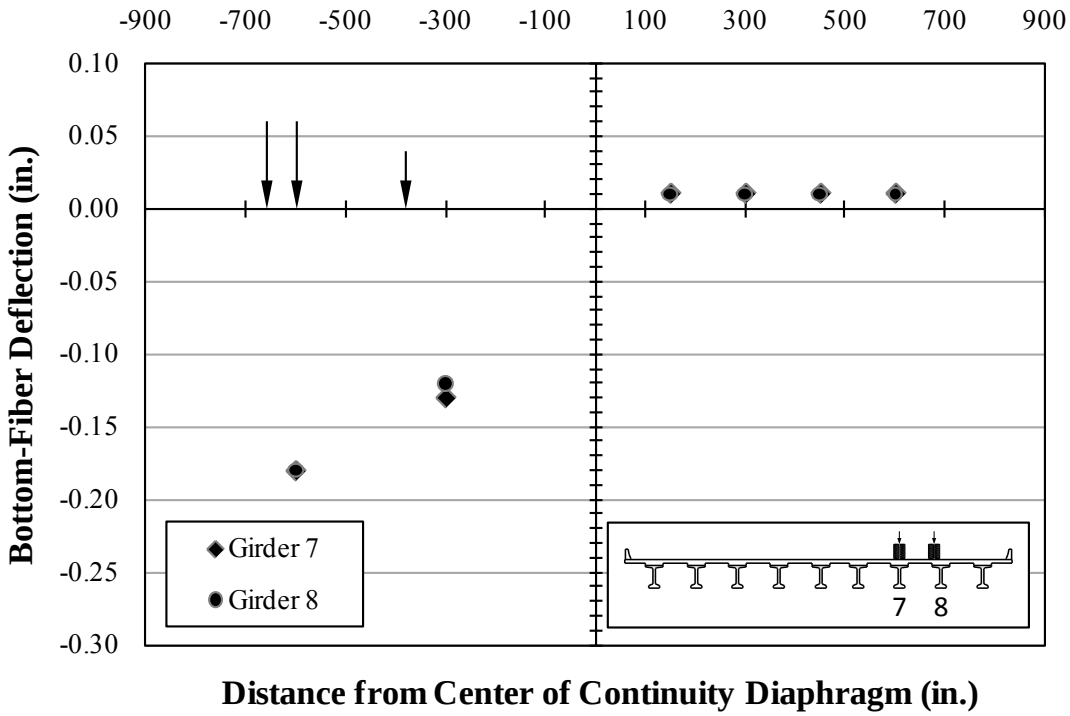

Figure G.7: Deflections—A1 (east)

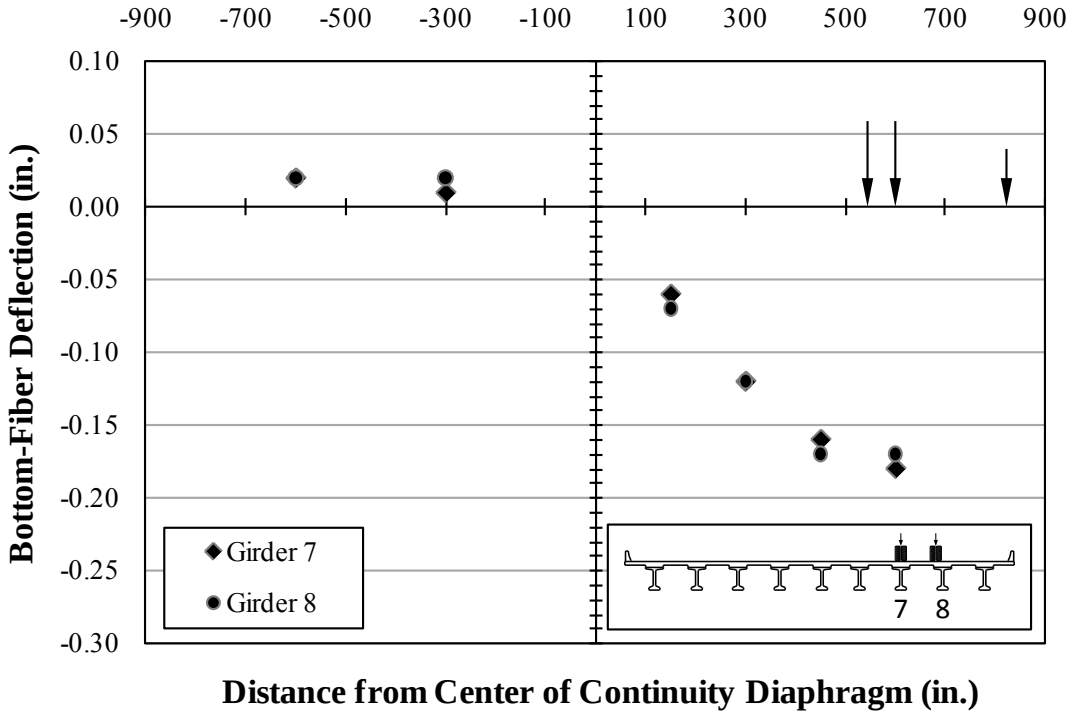

Figure G.8: Deflections—A9 (east)

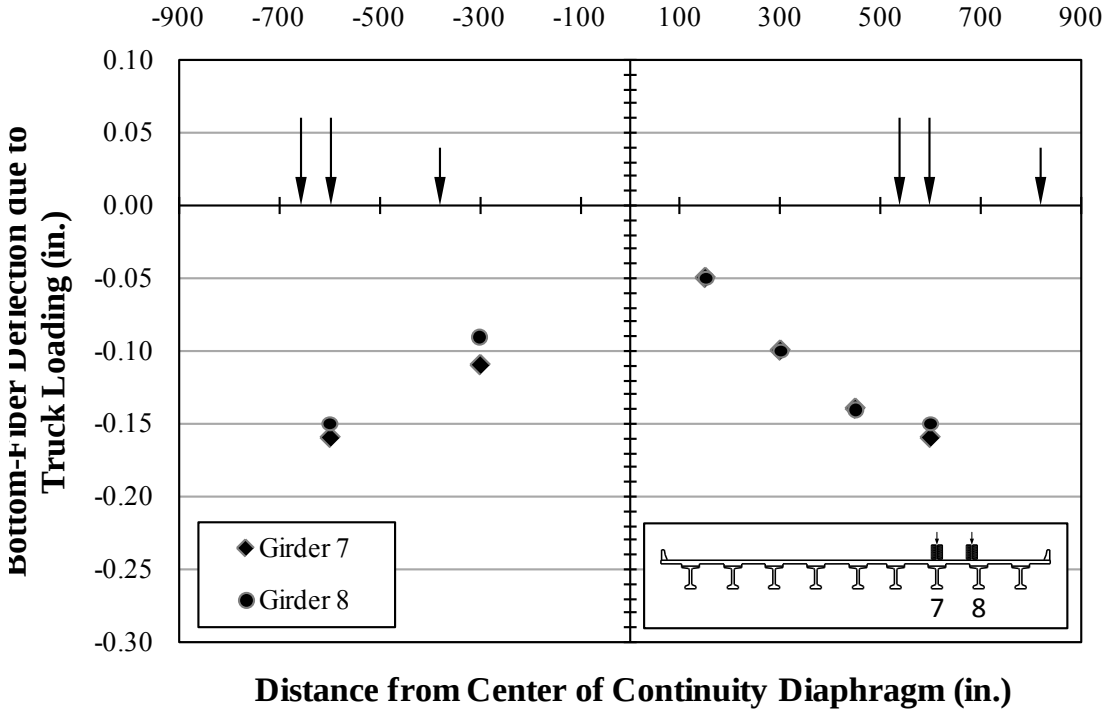

Figure G.9: Deflections—A1 (east) + A9 (east)

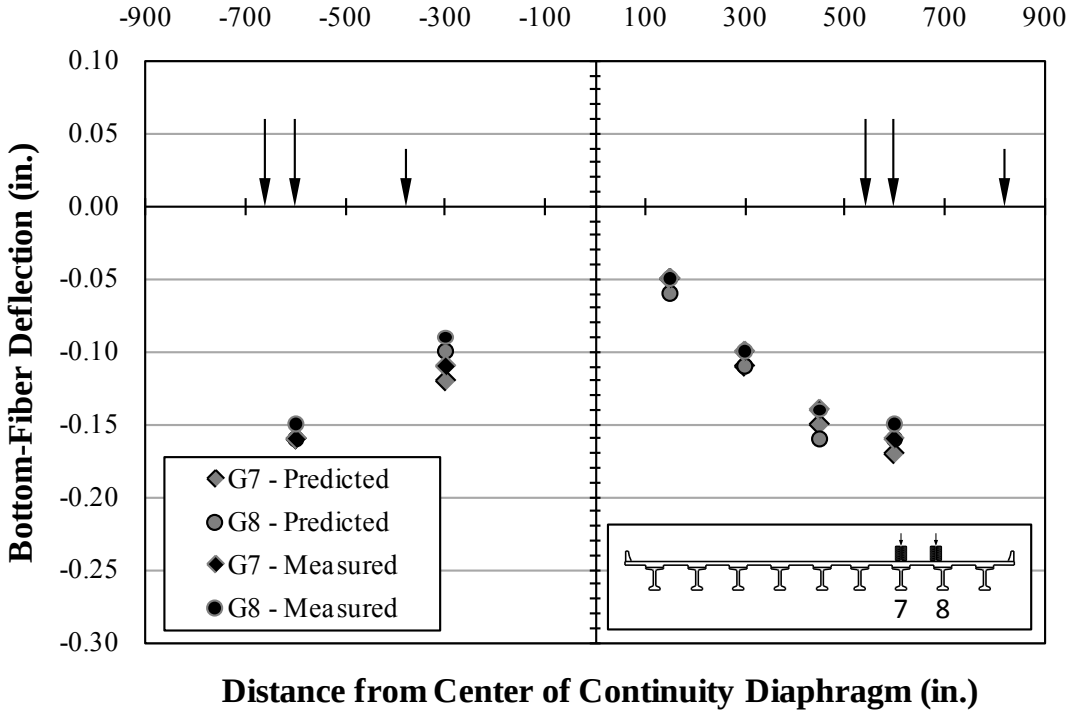

Figure G.10: Deflections—superposition—actual and predicted

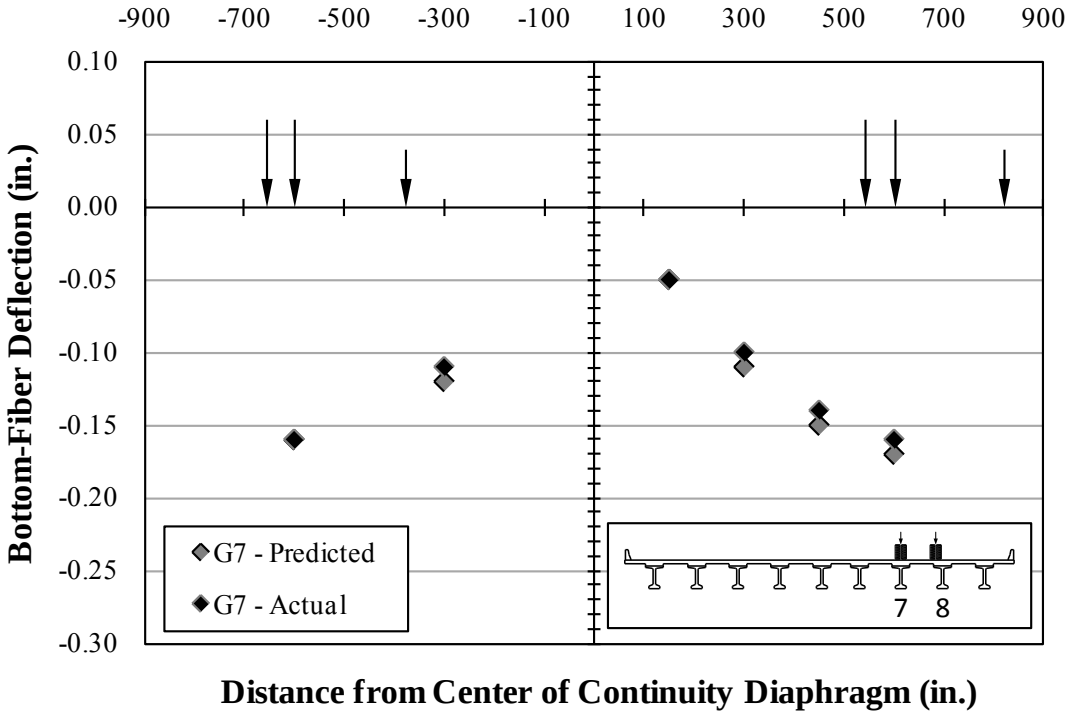

Figure G.11: Deflections—superposition—actual and predicted—Girder 7

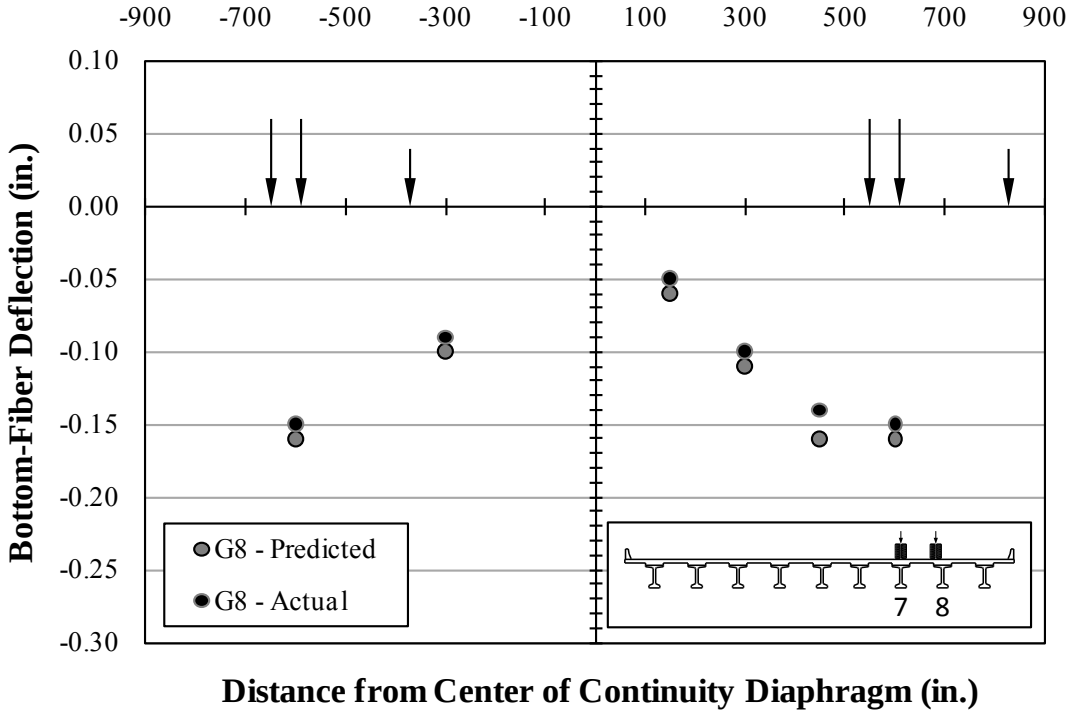

Figure G.12: Deflections—superposition—actual and predicted—Girder 8

G.3 BOTTOM-FIBER STRAINS

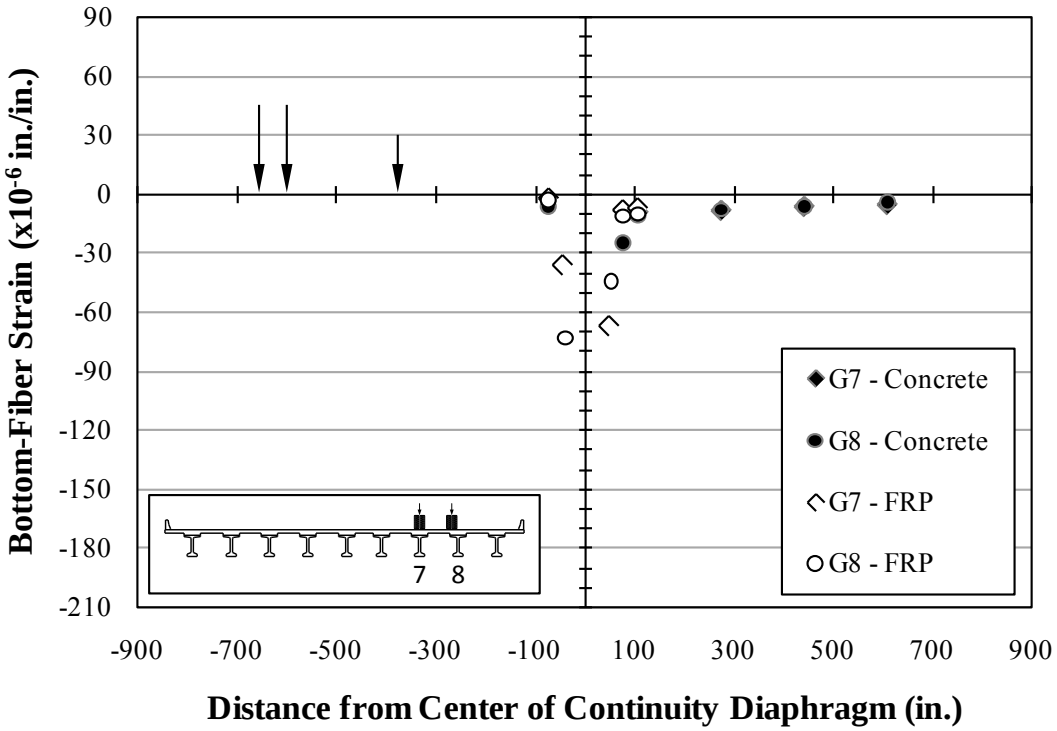

Figure G.13: Bottom-fiber strains—A1 (east)

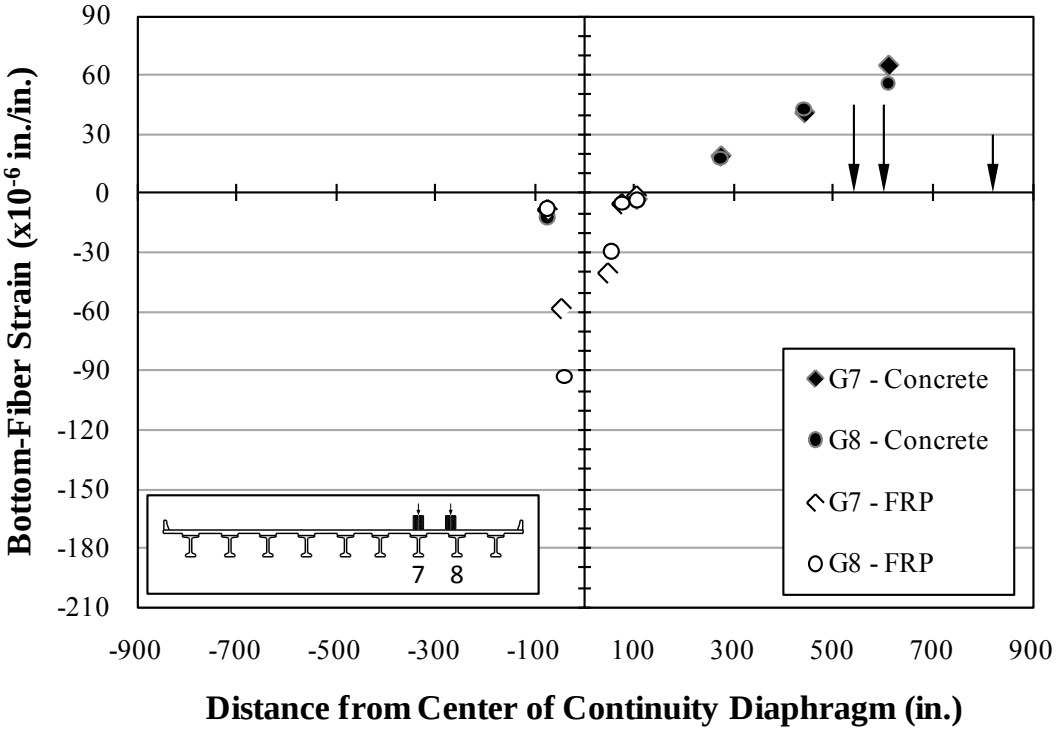

Figure G.14: Bottom-fiber strains—A9 (east)

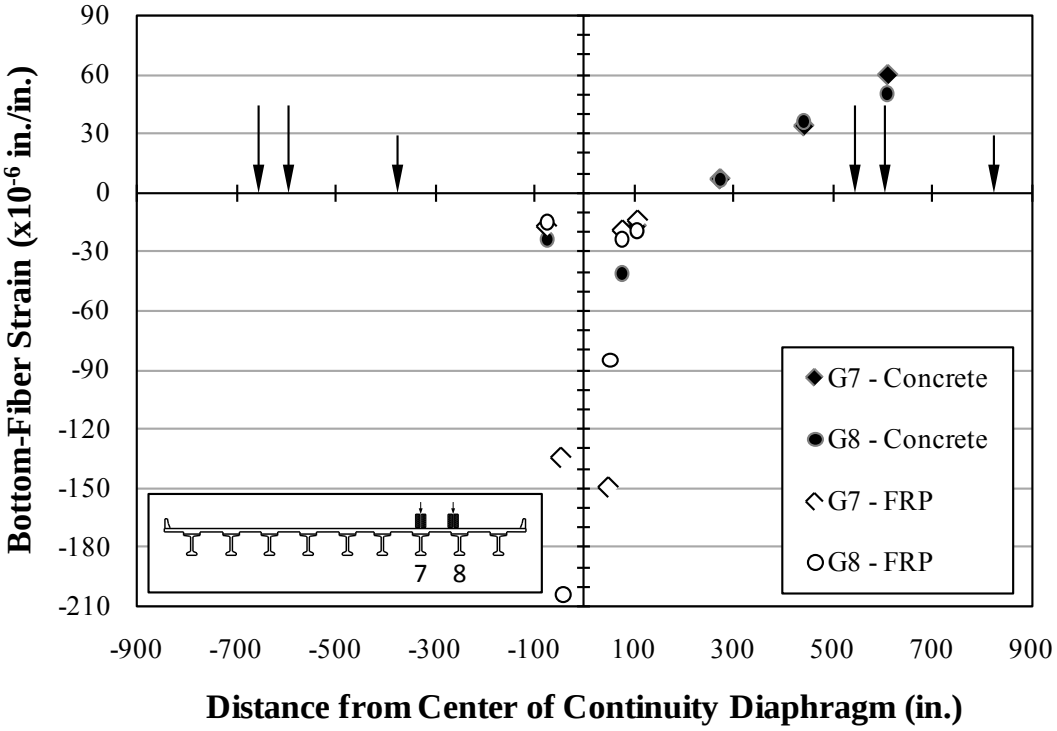

Figure G.15: Bottom-fiber strains—A1 (east) + A9 (east)

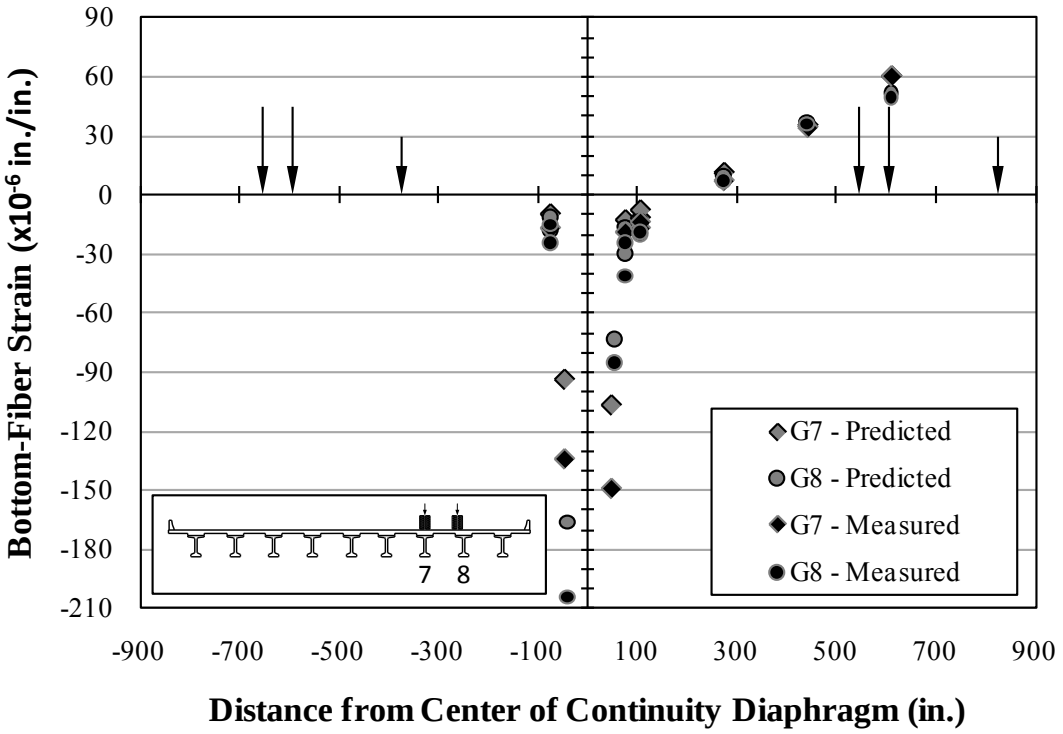

Figure G.16: Bottom-fiber strains—superposition—actual and predicted

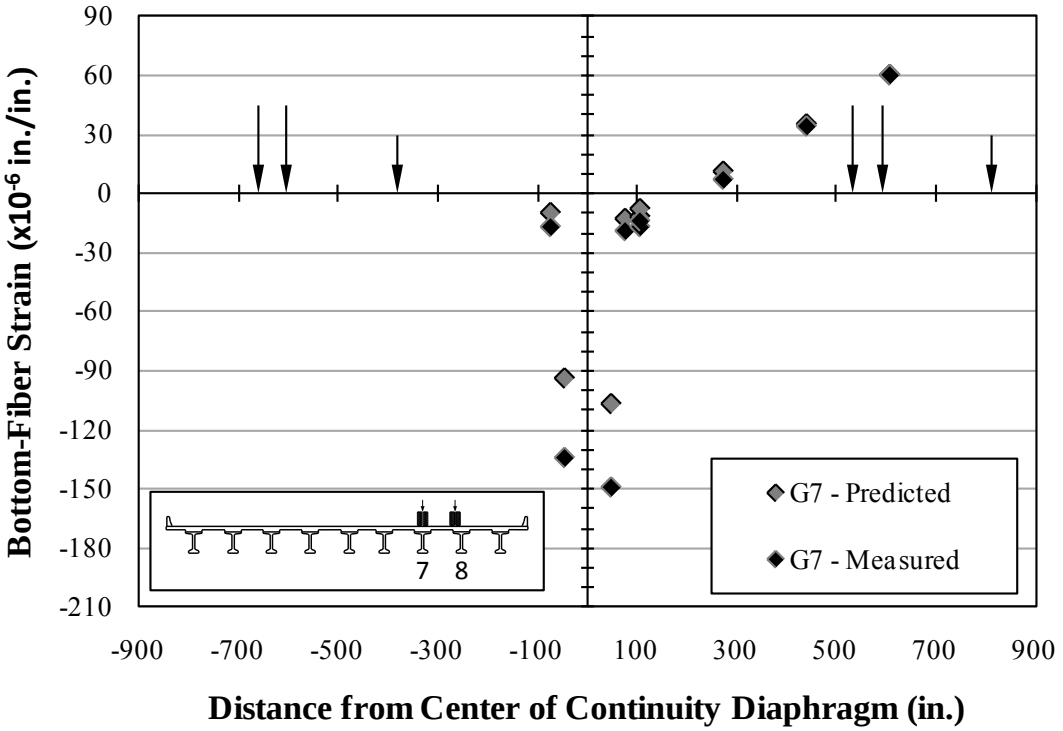

Figure G.17: Bottom-fiber strains—superposition—actual and predicted—Girder 7

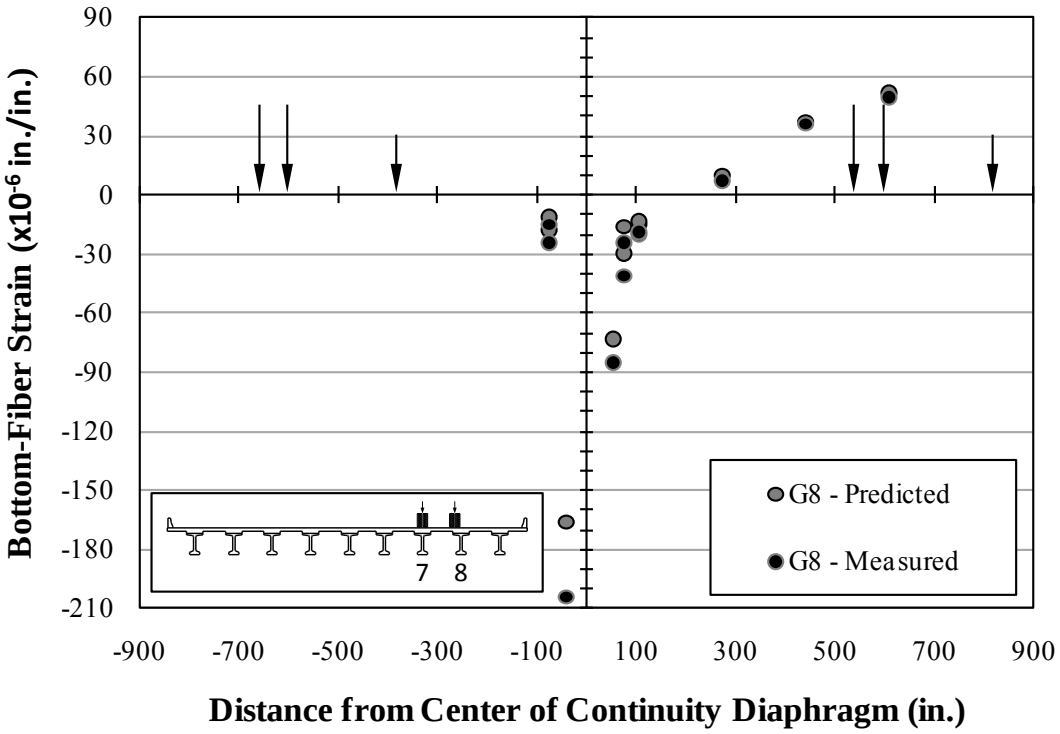

Figure G.18: Bottom-fiber strains—superposition—actual and predicted—Girder 8

Appendix H

SUPERPOSITION—MEASUREMENTS

Table H.1: Superposition—crack-opening displacements

Girder	Gage	Height from bottom of girder (in.)	Distance from center of continuity diaphragm (in.) – Span 10 + Span 11	Crack-Opening Displacement (mm) – closing + opening					
				Load Position		Superposition		Difference (Pred.–Meas.)	
				A1	A9	Predicted (A1+A9)	Measured (A1 and A9)	mm	%
7	CO7_10	13.5	-50	-0.003	-0.008	-0.011	-0.014	0.003	21
	CO7_11	13.5	48	-0.013	-0.005	-0.018	-0.024	0.006	25
8	CO8_10	13.5	-40	-0.008	-0.006	-0.014	-0.015	0.001	7
	CO8_11	13.5	56	-0.007	-0.003	-0.010	-0.012	0.002	17

Note: Percent difference is reported as a percentage of the measured superposition

Table H.2: Superposition—deflections

Girder	Gage	Height from bottom of girder (in.)	Distance from center of continuity diaphragm (in.) – Span 10 + Span 11	Deflection (in.) – downward + upward					
				Load Position		Superposition		Difference (Pred.–Meas.)	
				A1	A9	Predicted (A1+A9)	Measured (A1 and A9)	in.	%
7	D7_10_A	n/a	-608	-0.18	0.02	-0.16	-0.16	0.00	0
	D7_10_B		-308	-0.13	0.01	-0.12	-0.11	-0.01	-9
	D7_11_C		158	0.01	-0.06	-0.05	-0.05	0.00	0
	D7_11_D		308	0.01	-0.12	-0.11	-0.10	-0.01	-10
	D7_11_E		458	0.01	-0.16	-0.15	-0.14	-0.01	-7
	D7_11_F		608	0.01	-0.18	-0.17	-0.16	-0.01	-6
8	D8_10_A	n/a	-608	-0.18	0.02	-0.16	-0.15	-0.01	-7
	D8_10_B		-308	-0.12	0.02	-0.10	-0.09	-0.01	-10
	D8_11_C		158	0.01	-0.07	-0.06	-0.05	-0.01	-20
	D8_11_D		308	0.01	-0.12	-0.11	-0.10	-0.01	-10
	D8_11_E		458	0.01	-0.17	-0.16	-0.14	-0.02	-14
	D8_11_F		608	0.01	-0.17	-0.16	-0.15	-0.01	-7

Note: Percent difference is reported as a percentage of the measured superposition

Table H.3: Superposition—bottom-fiber strains—Girder 7

Span	Gage	Height from bottom of girder (in.)	Distance from center of continuity diaphragm (in.) – Span 10 + Span 11	Strain ($x10^{-6}$ in/in) – compressive + tensile					
				Load Position		Superposition		Difference (Pred.–Meas.)	
				A1	A9	Predicted (A1+A9)	Measured (A1 and A9)	$x10^{-6}$ in./in.	%
10	F7_10_1M	0	-74	-2	-8	-10	-17	7	41
	F7_10_CK		-47	-36	-58	-94	-134	40	30
11	F7_11_CK	0	47	-67	-40	-107	-149	42	28
	F7_11_4M		74	-8	-5	-13	-19	6	32
	F7_11_5M		104	-7	-1	-8	-14	6	40
	S7_11_5M		105	-9	-3	-12	-17	5	29
	S7_11_6M		273	-8	19	11	7	4	60
	S7_11_7M		441	-6	41	35	34	1	3
	S7_11_8M		609	-5	65	60	60	0	0

Note: Percent difference is reported as a percentage of the measured superposition

Table H.4: Superposition—bottom-fiber strains—Girder 8

Span	Gage	Height from bottom of girder (in.)	Distance from center of continuity diaphragm (in.) – Span 10 + Span 11	Strain ($x10^{-6}$ in/in) – compressive + tensile					
				Load Position		Superposition		Difference (Pred.–Meas.)	
				A1	A9	Predicted (A1+A9)	Measured (A1 and A9)	$x10^{-6}$ in./in.	%
10	S8_10_1M	0	-75	-6	-12	-18	-24	6	25
	F8_10_1M		-74	-3	-8	-11	-15	4	27
	F8_10_CK		-41	-73	-93	-166	-204	38	19
11	F8_11_CK	0	52	-44	-29	-73	-85	12	14
	F8_11_4M		74	-11	-5	-16	-24	8	33
	S8_11_4M		75	-25	-5	-30	-41	11	27
	F8_11_5M		104	-10	-3	-13	-19	6	32
	S8_11_5M		105	-11	-4	-15	-20	5	25
	S8_11_6M		273	-8	18	10	7	3	40
	S8_11_7M		441	-6	43	37	36	1	3
	S8_11_8M		609	-4	56	52	50	2	4

Note: Percent difference is reported as a percentage of the measured superposition

Appendix I

AE STATIC POSITIONS—GRAPHICAL RESULTS

I.1 CRACK-OPENING DISPLACEMENTS

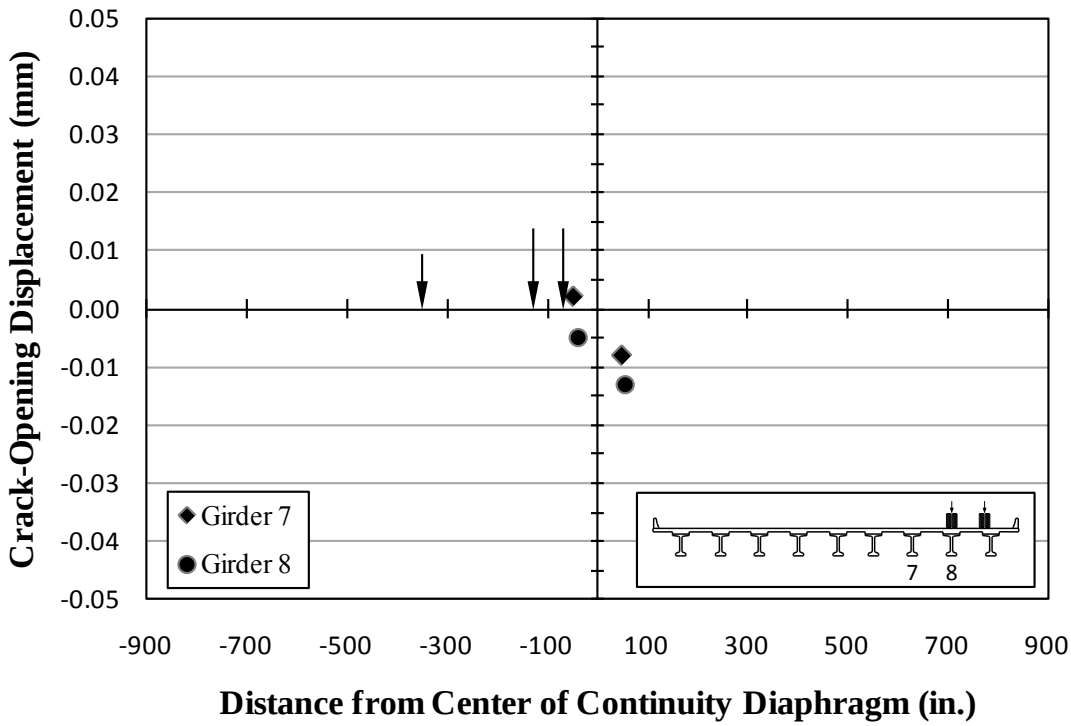

Figure I.1: Crack-opening displacements—LC 6.5—AE Span 10 (east)

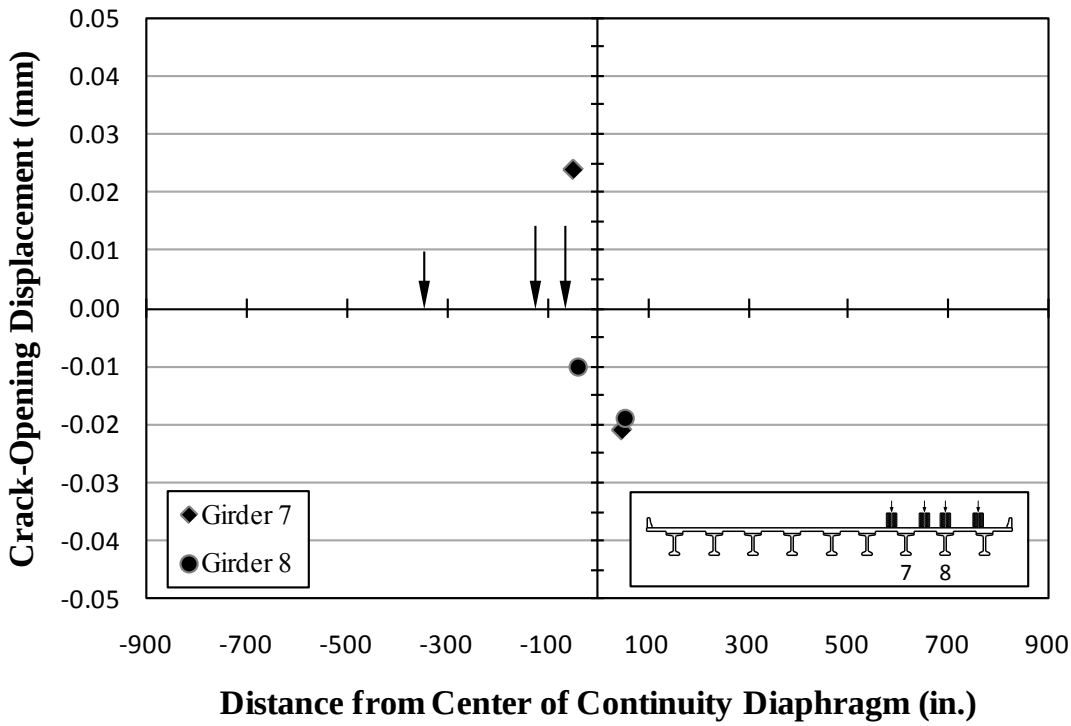

Figure I.2: Crack-opening displacements—LC 6.5—AE Span 10 (both)

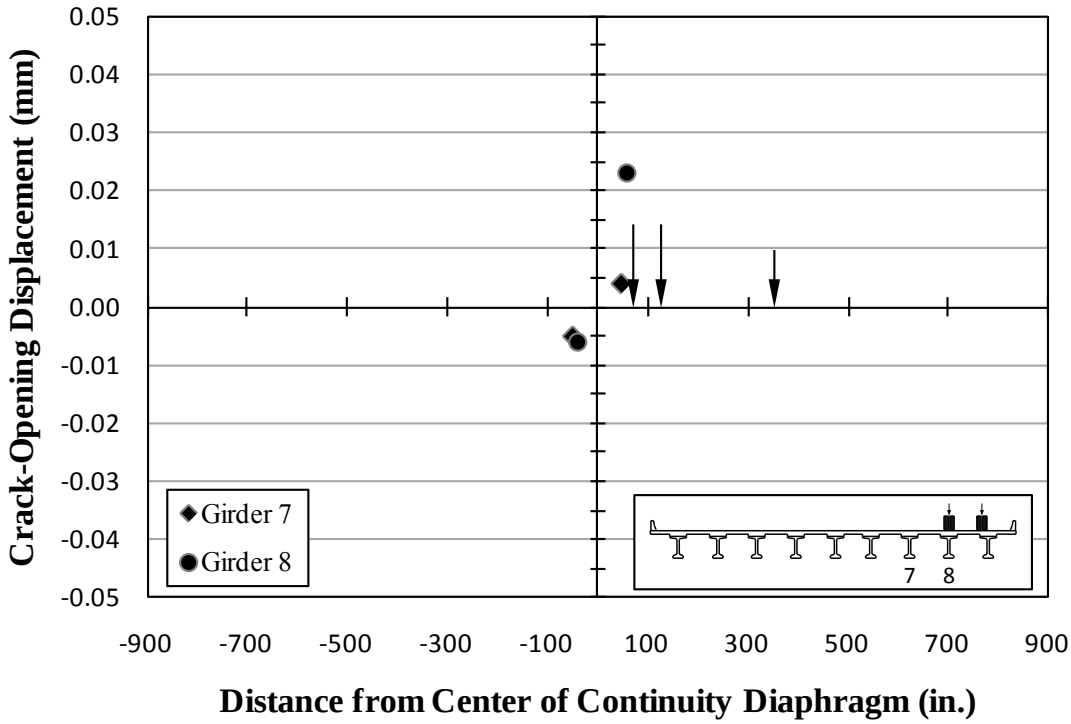

Figure I.3: Crack-opening displacements—LC 6.5—AE Span 11 (east)

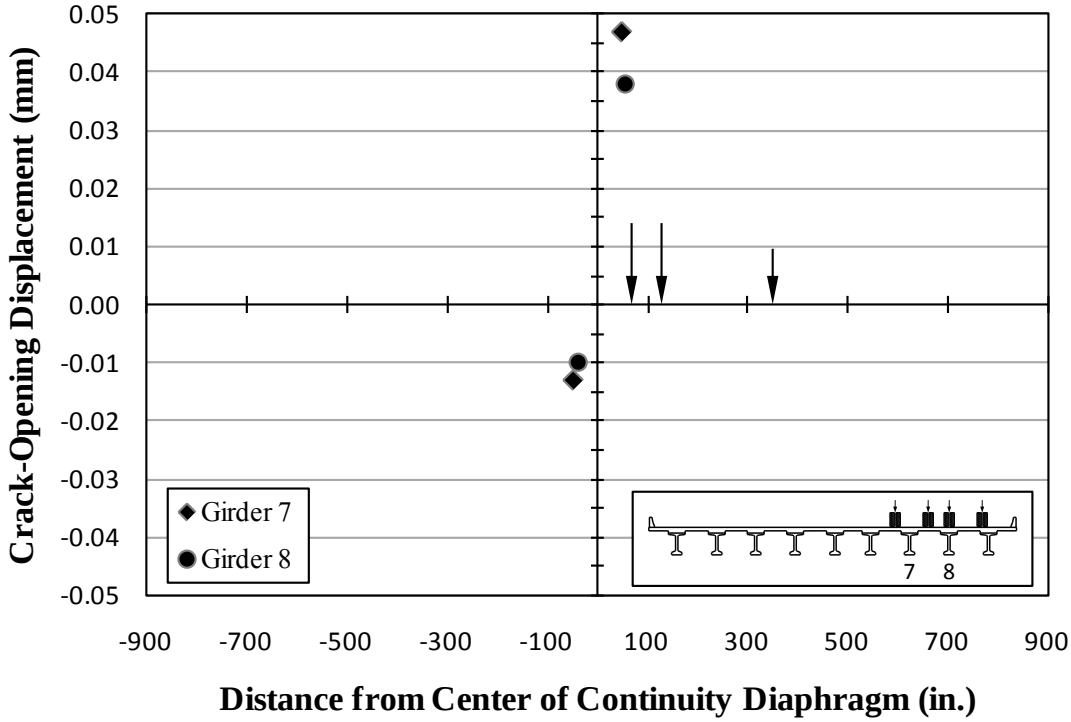

Figure I.4: Crack-opening displacements—LC 6.5—AE Span 11 (both)

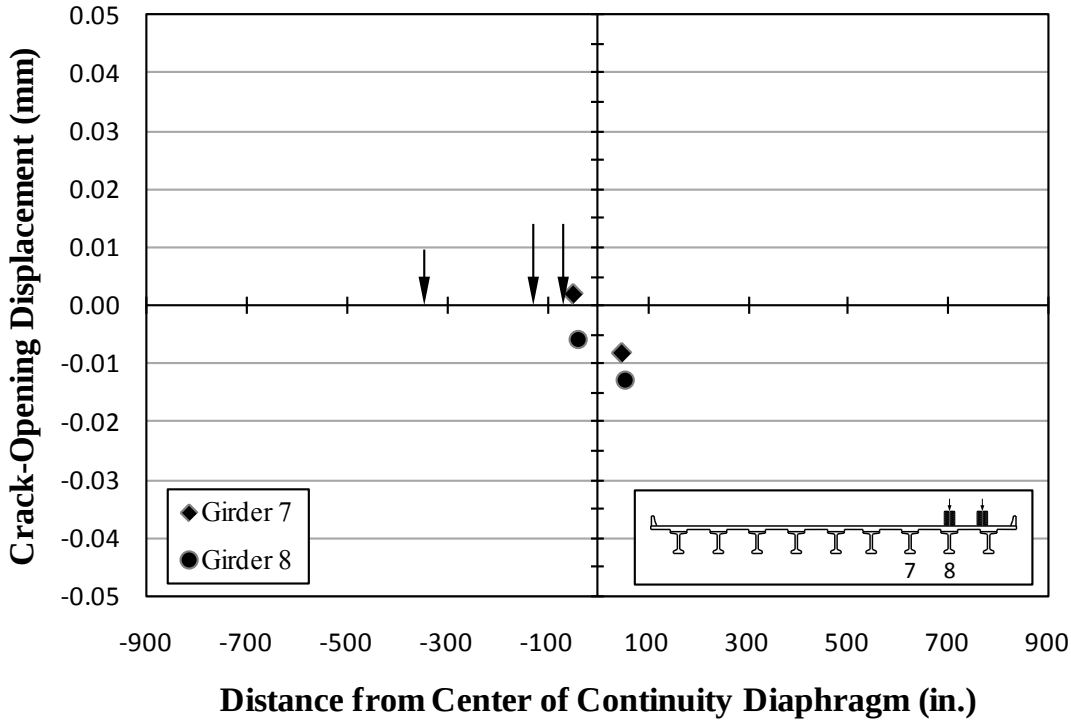

Figure I.5: Crack-opening displacements—LC 6—AE Span 10 (east)

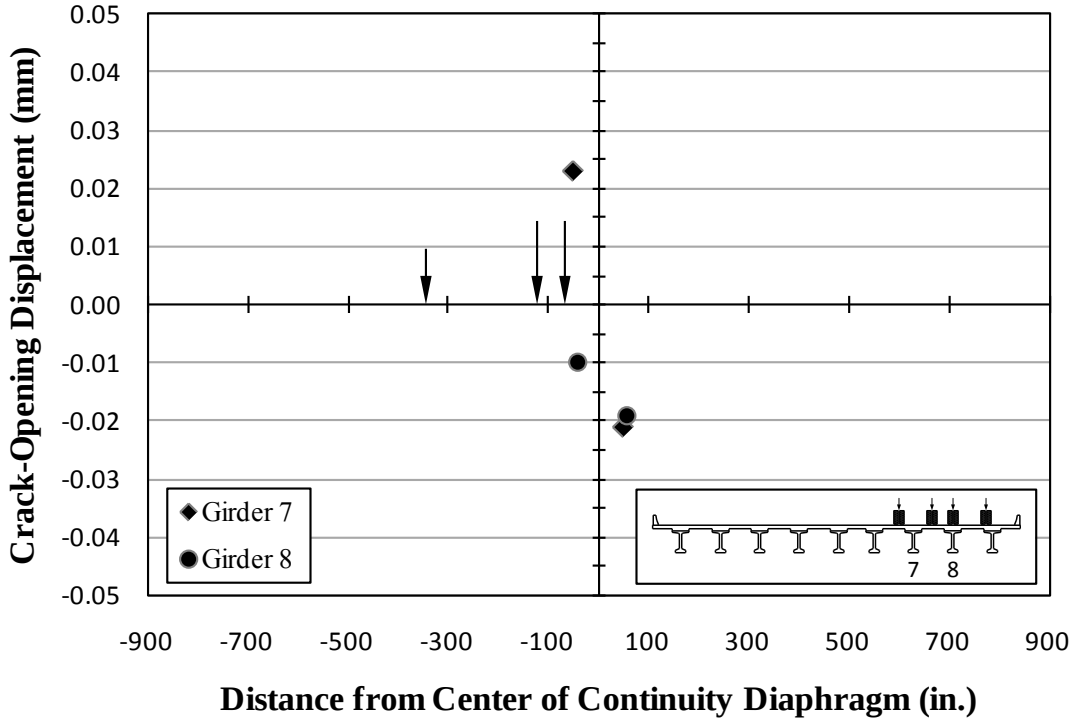

Figure I.6: Crack-opening displacements—LC 6—AE Span 10 (both)

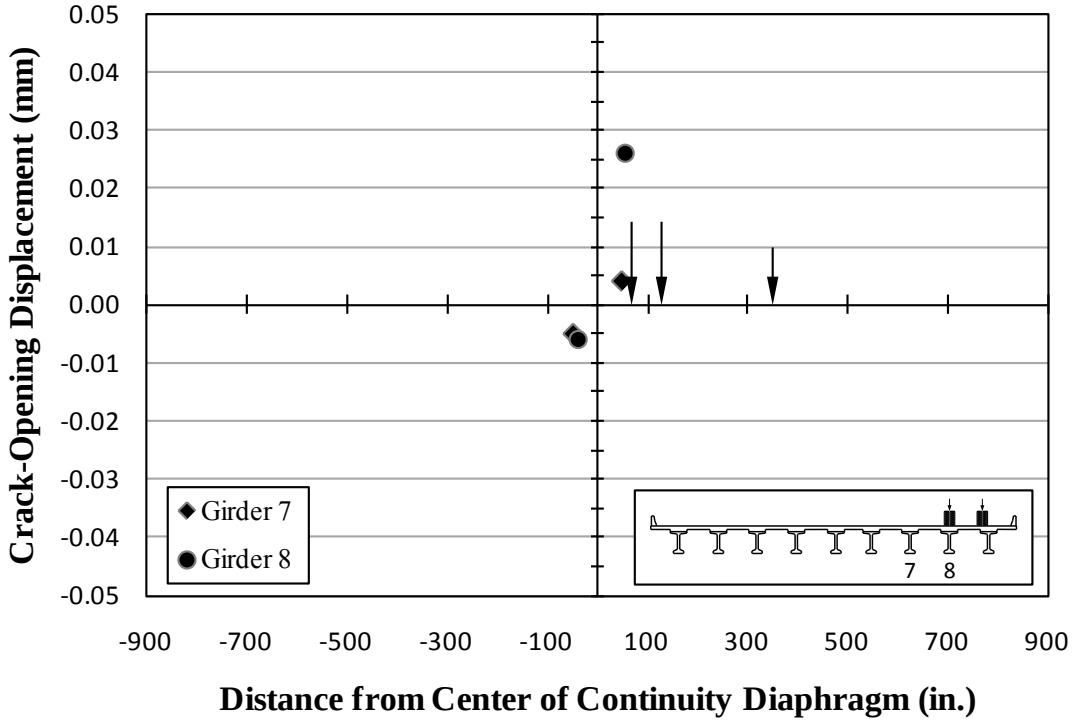

Figure I.7: Crack-opening displacements—LC 6—AE Span 11 (east)

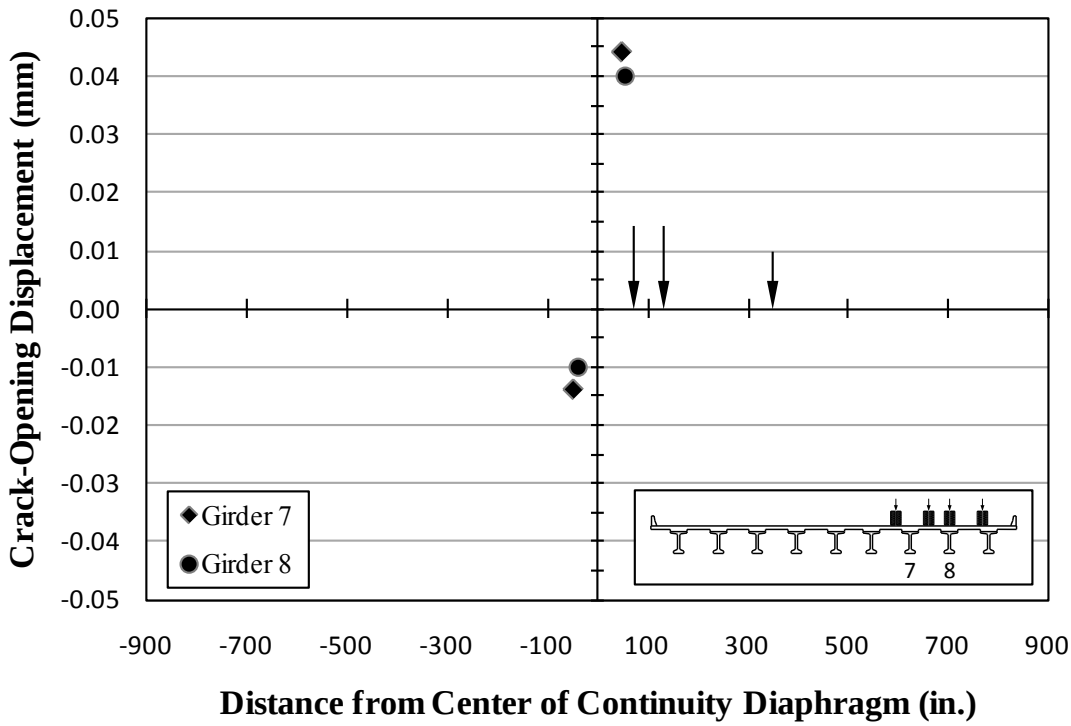

Figure I.8: Crack-opening displacements—LC 6—AE Span 11 (both)

I.2 DEFLECTIONS

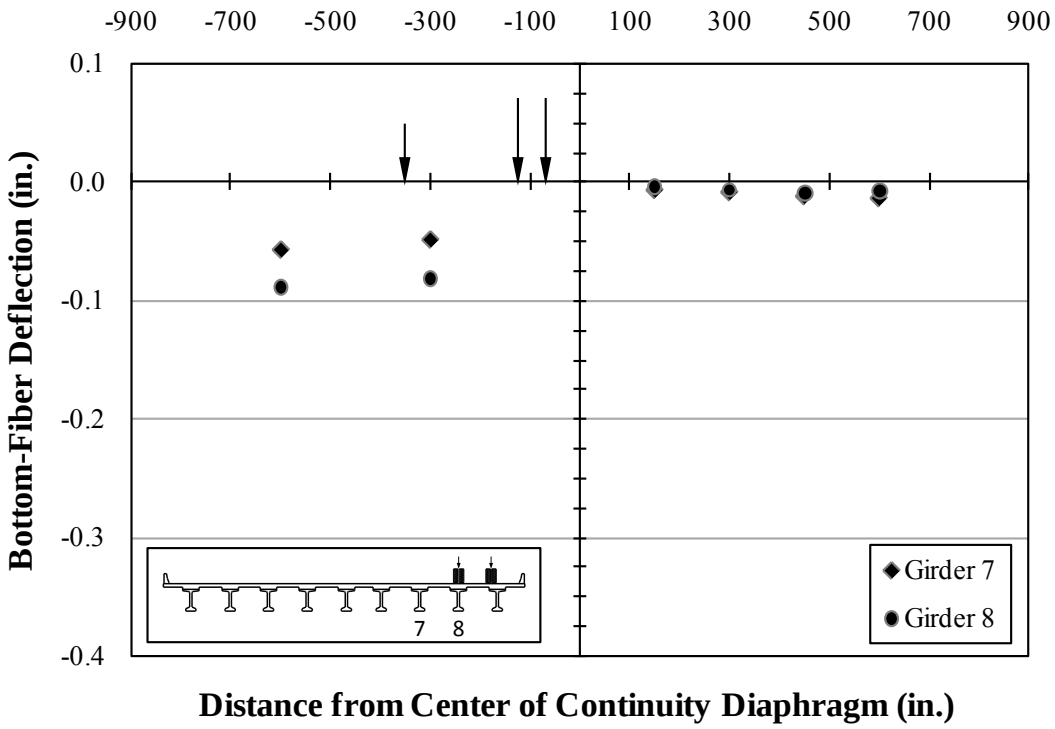

Figure I.9: Deflections—LC 6.5—AE Span 10 (east)

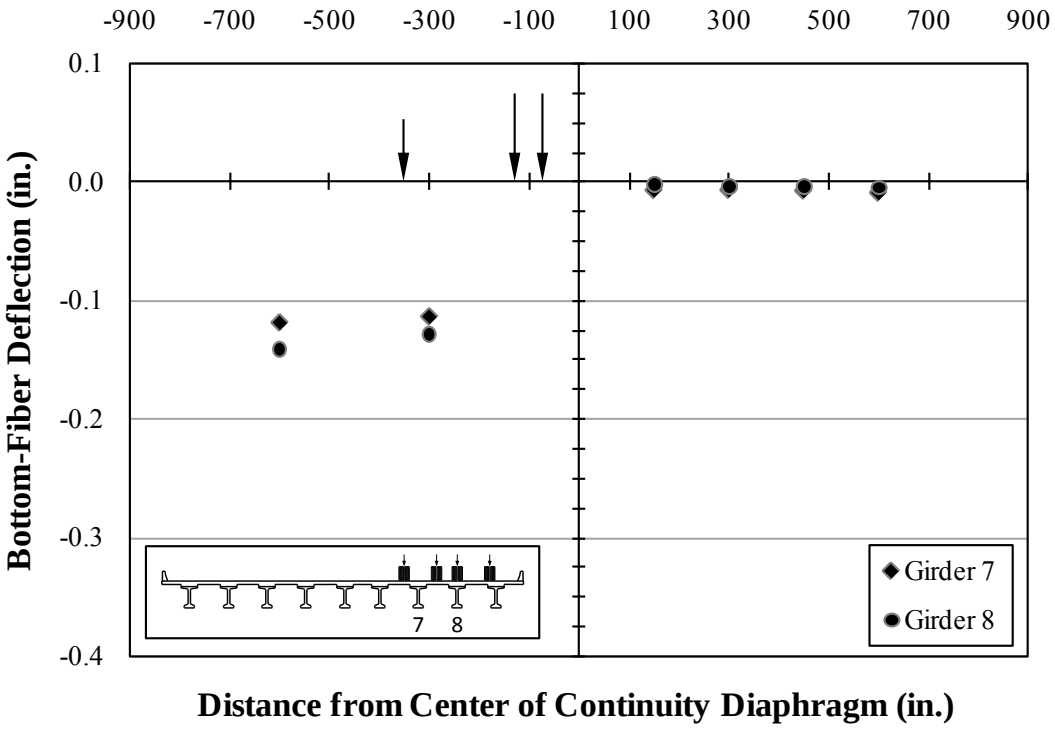

Figure I.10: Deflections—LC 6.5—AE Span 10 (both)

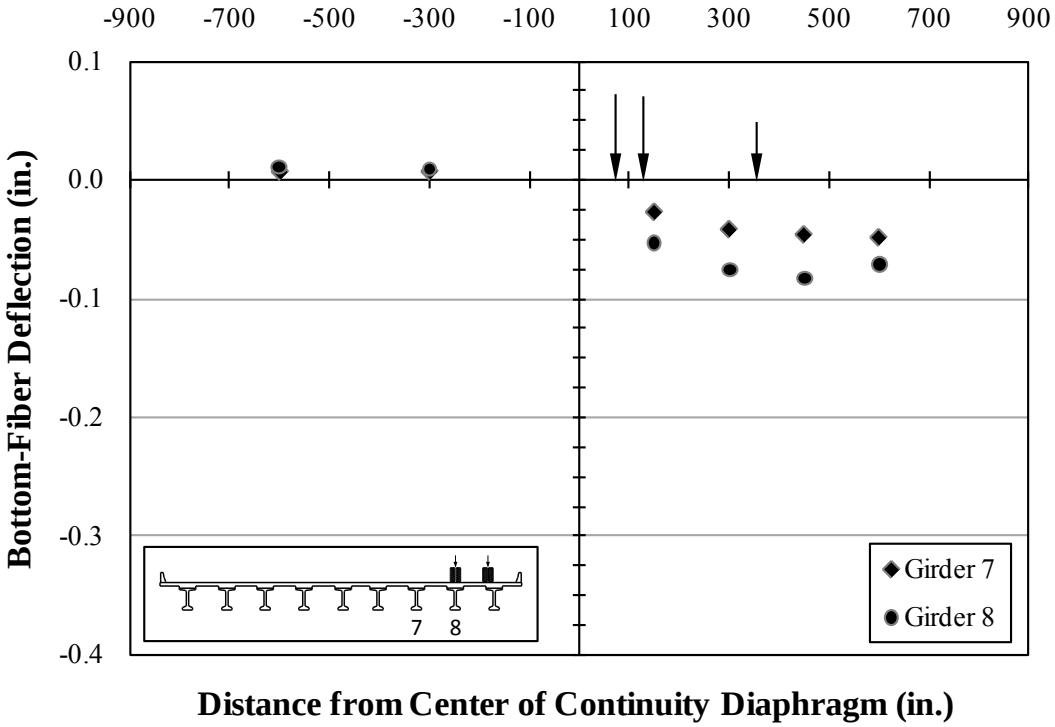

Figure I.11: Deflections—LC 6.5—AE Span 11 (east)

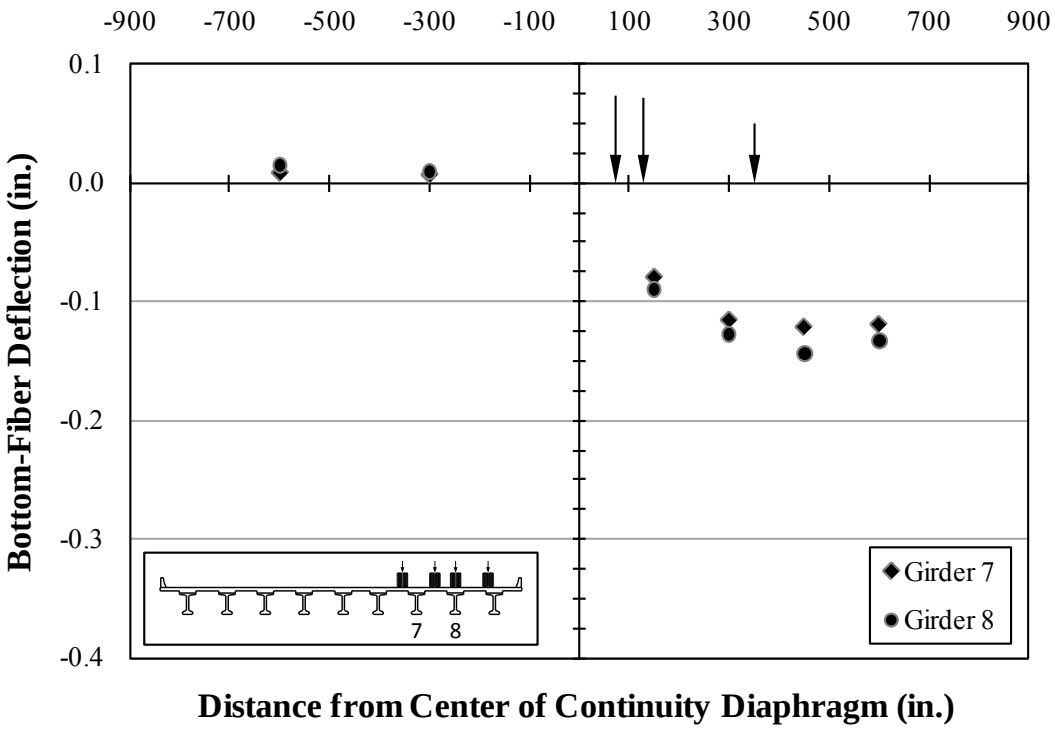

Figure I.12: Deflections—LC 6.5—AE Span 11 (both)

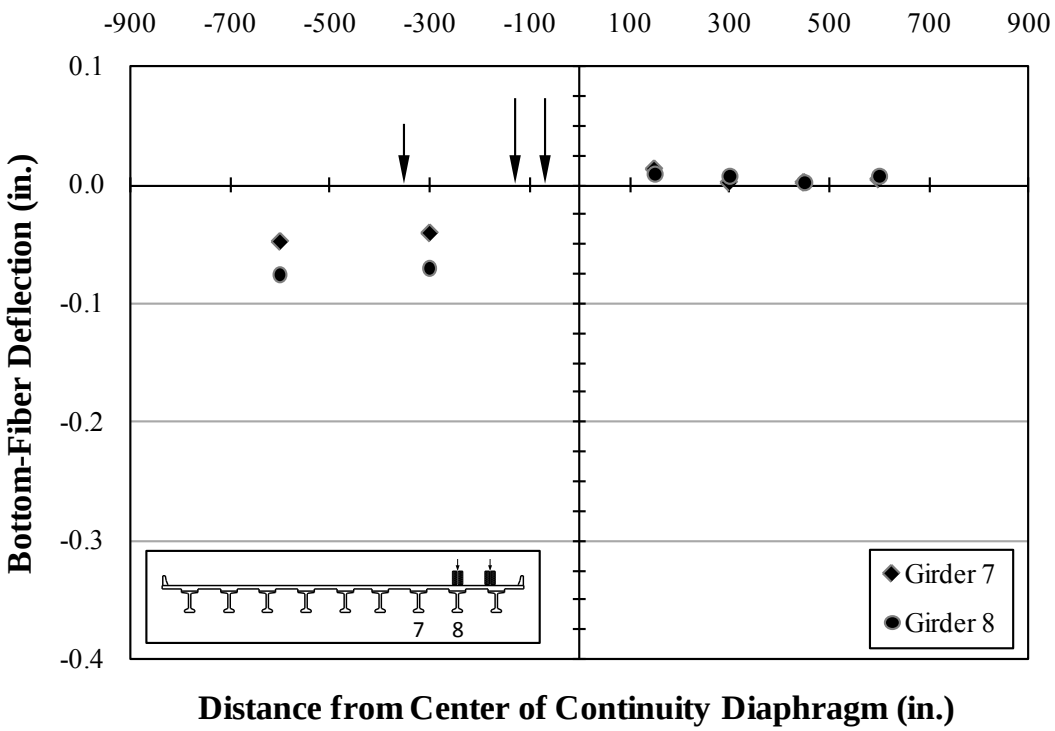

Figure I.13: Deflections—LC 6—AE Span 10 (east)

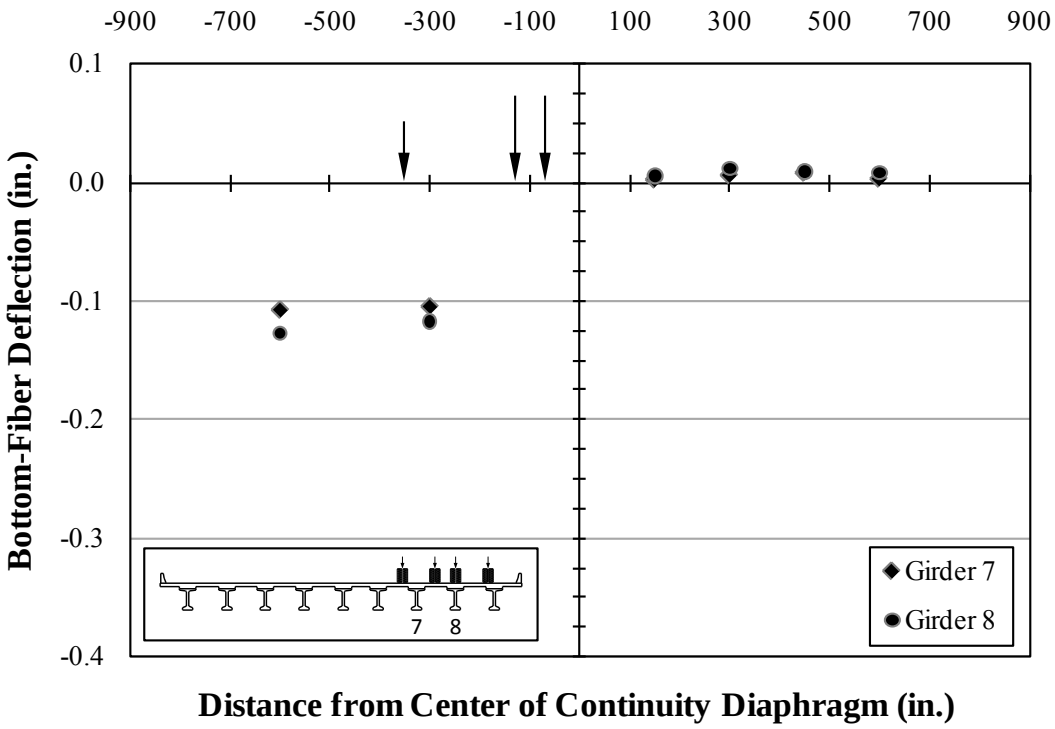

Figure I.14: Deflections—LC 6—AE Span 10 (both)

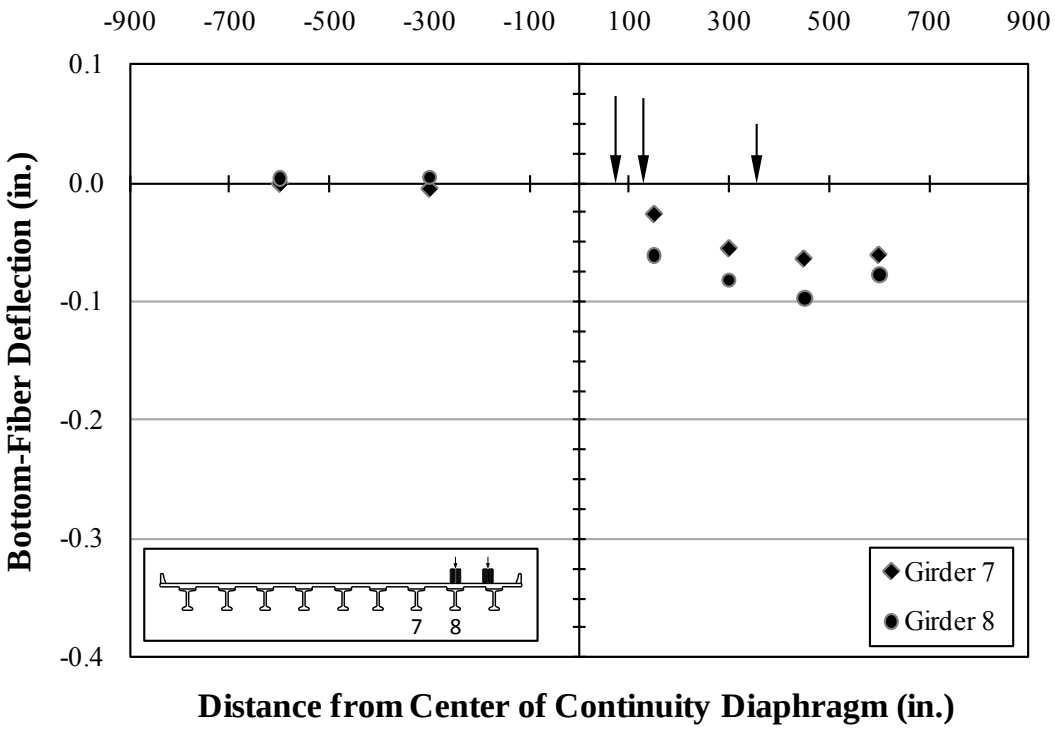

Figure I.15: Deflections—LC 6—AE Span 11 (east)

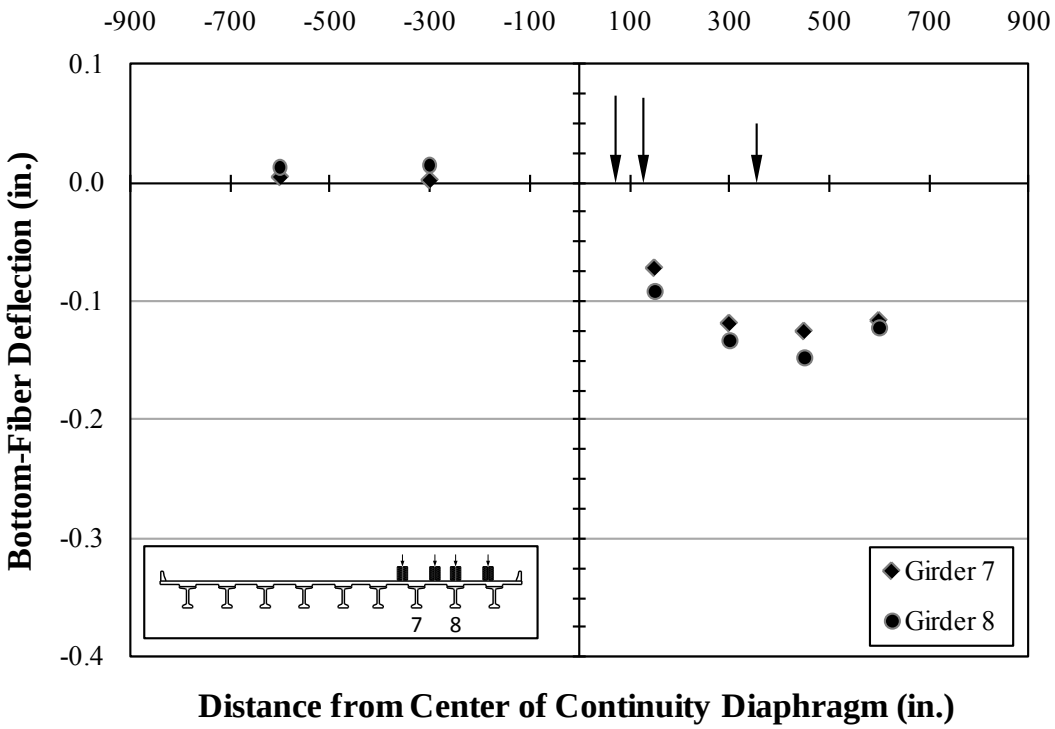

Figure I.16: Deflections—LC 6—AE Span 11 (both)

I.3 BOTTOM-FIBER STRAINS

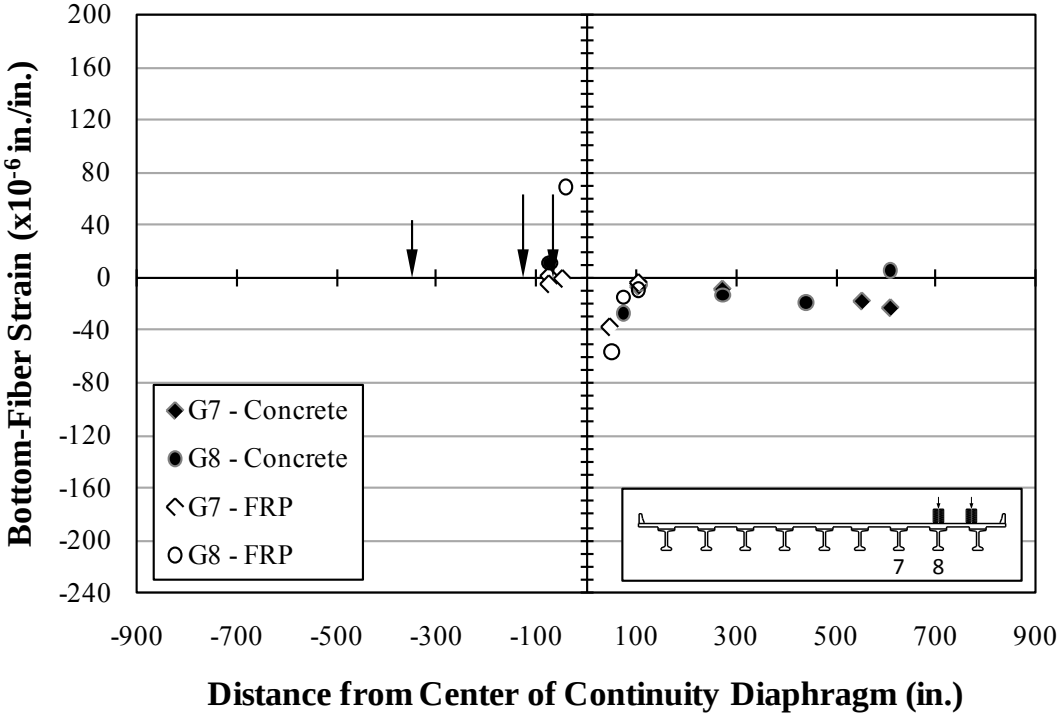

Figure I.17: Bottom-fiber strains—LC 6.5—AE Span 10 (east)

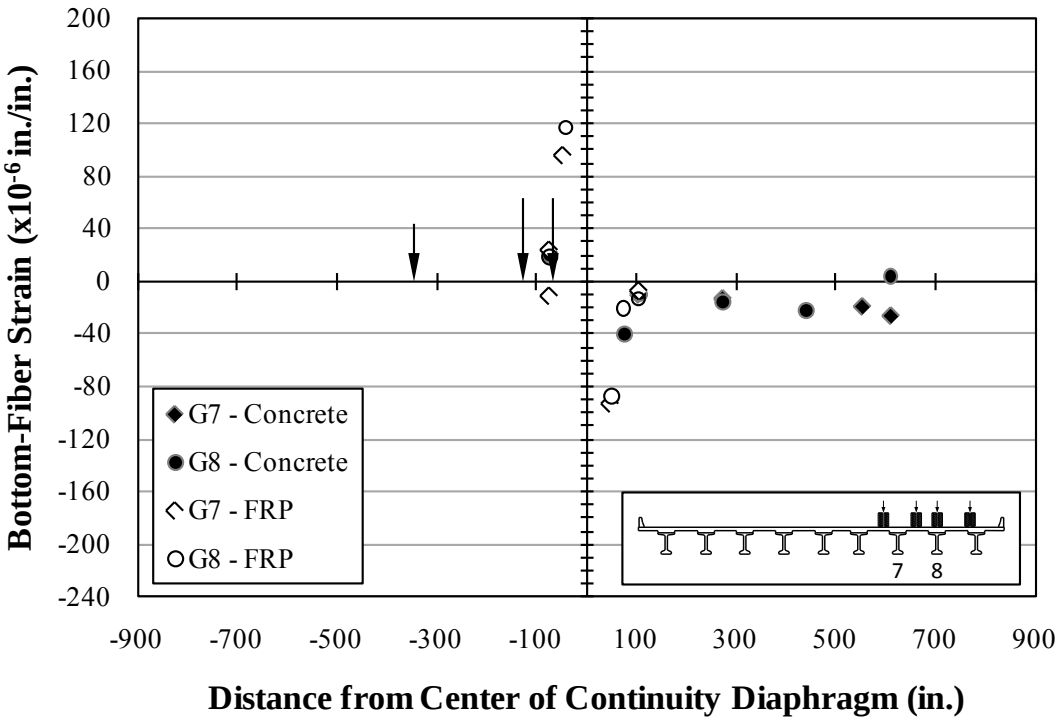

Figure I.18: Bottom-fiber strains—LC 6.5—AE Span 10 (both)

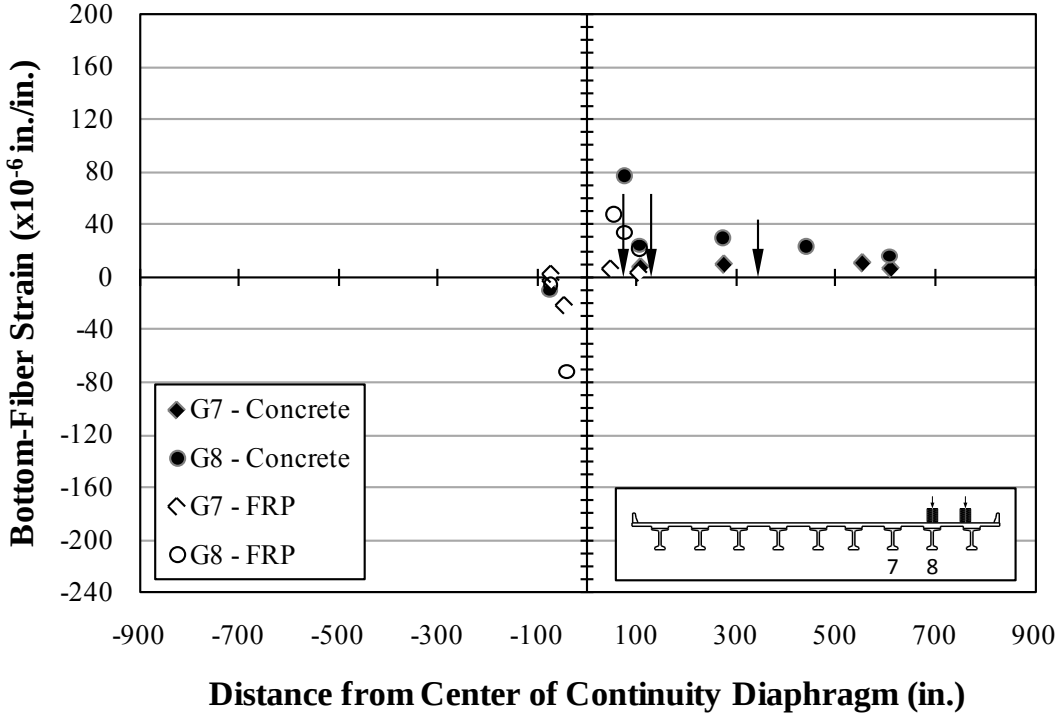

Figure I.19: Bottom-fiber strains—LC 6.5—AE Span 11 (east)

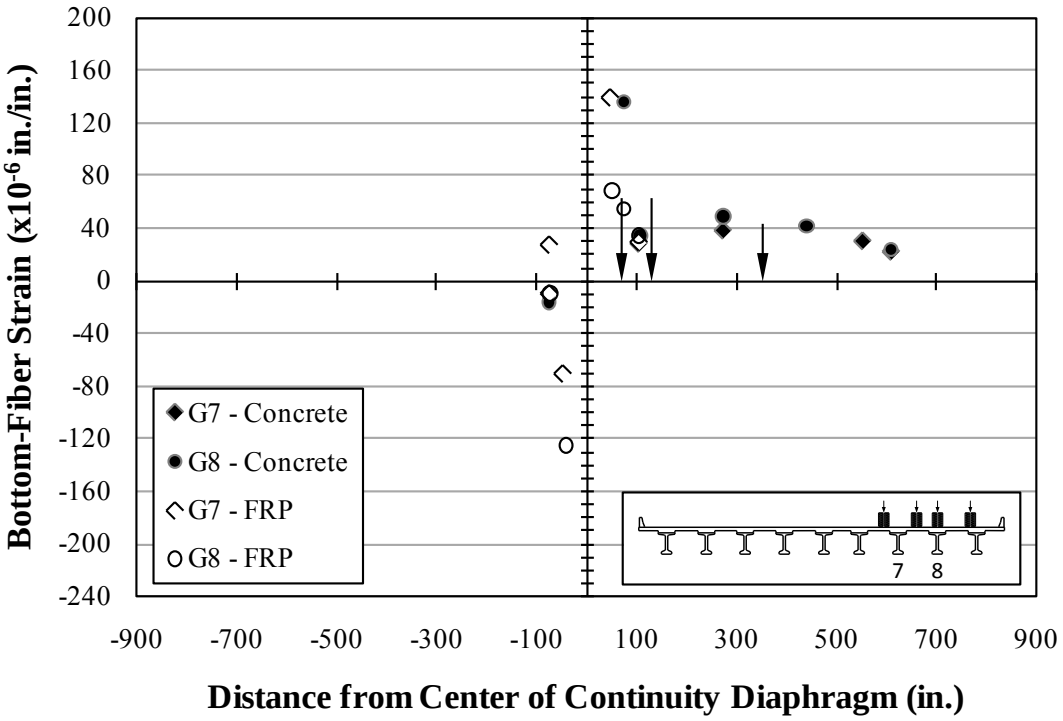

Figure I.20: Bottom-fiber strains—LC 6.5—AE Span 11 (both)

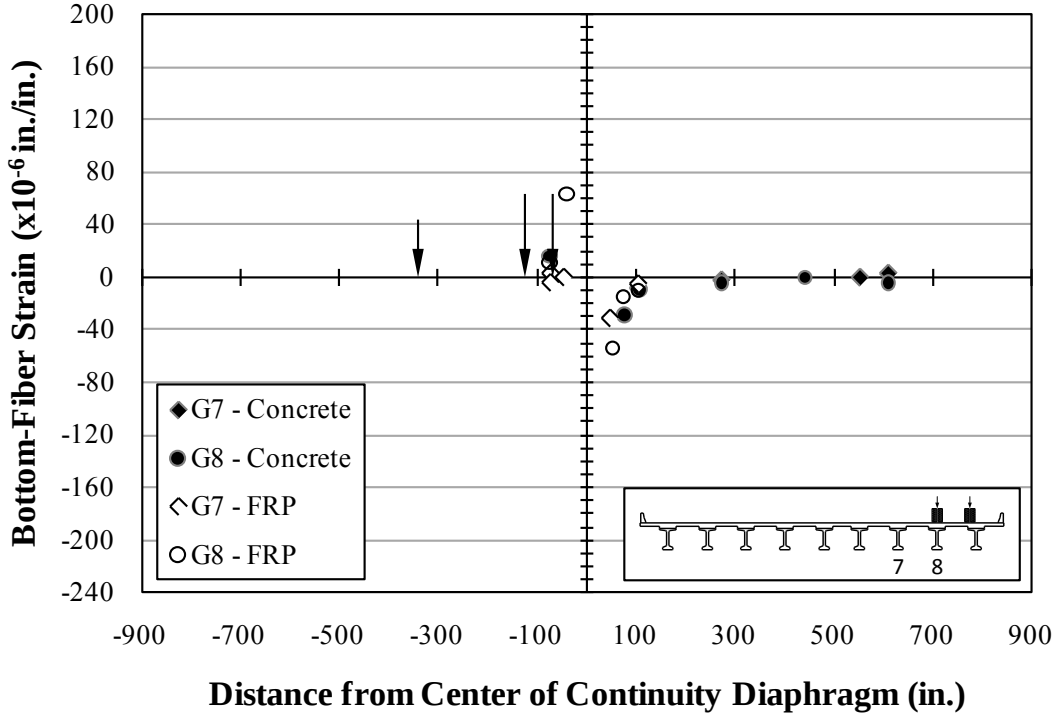

Figure I.21: Bottom-fiber strains—LC 6—AE Span 10 (east)

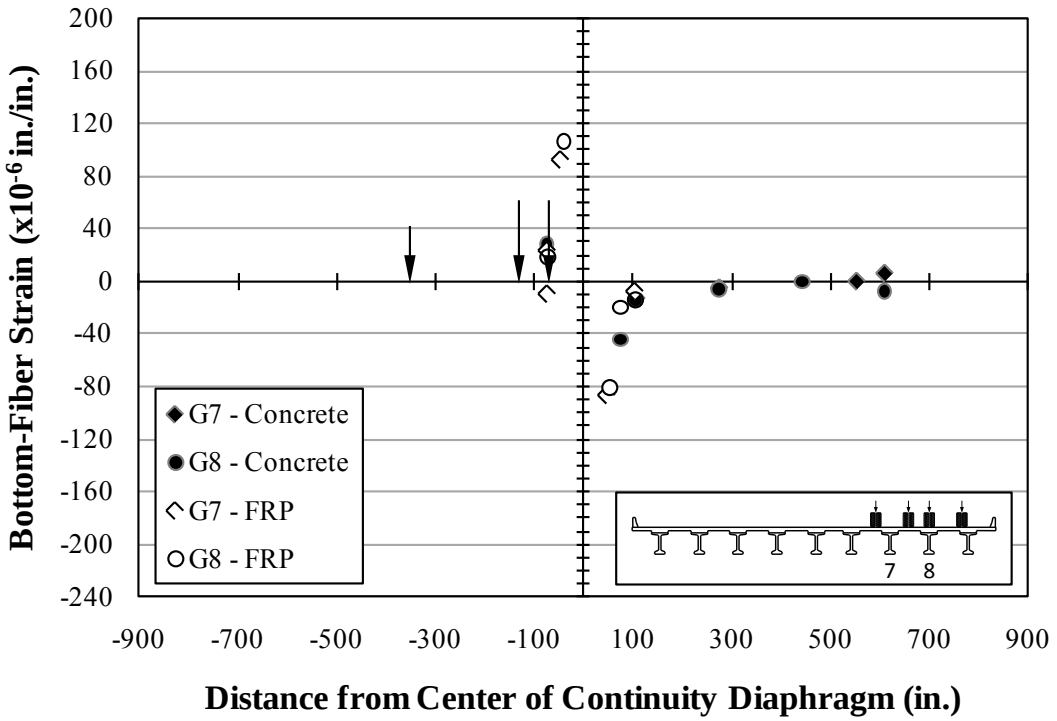

Figure I.22: Bottom-fiber strains—LC 6—AE Span 10 (both)

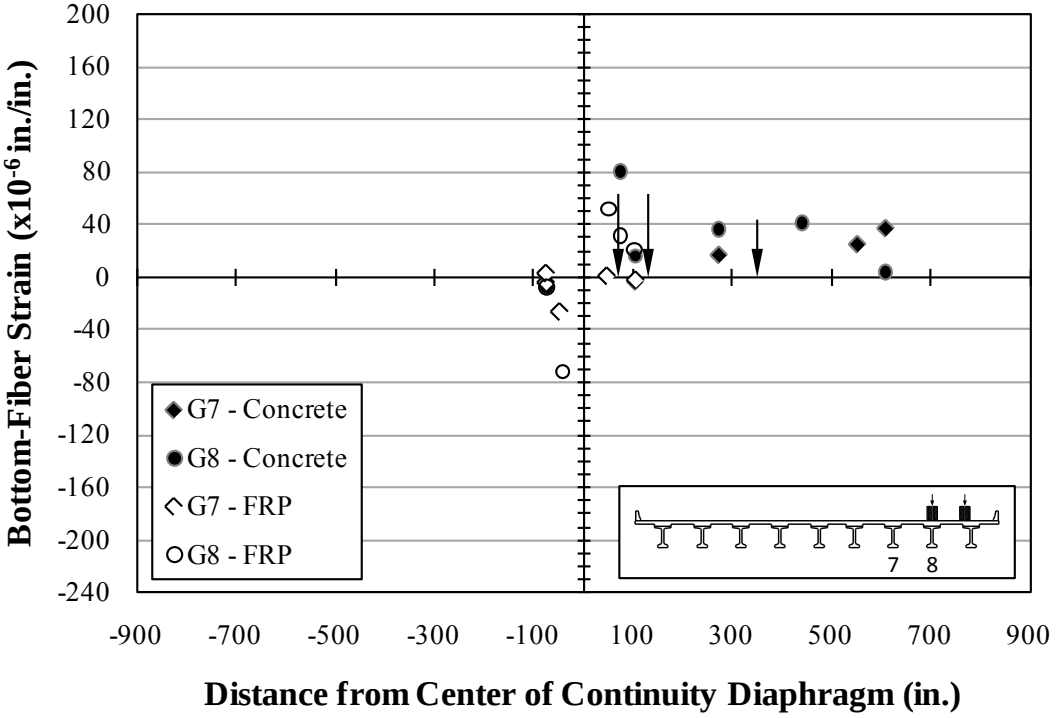

Figure I.23: Bottom-fiber strains—LC 6—AE Span 11 (east)

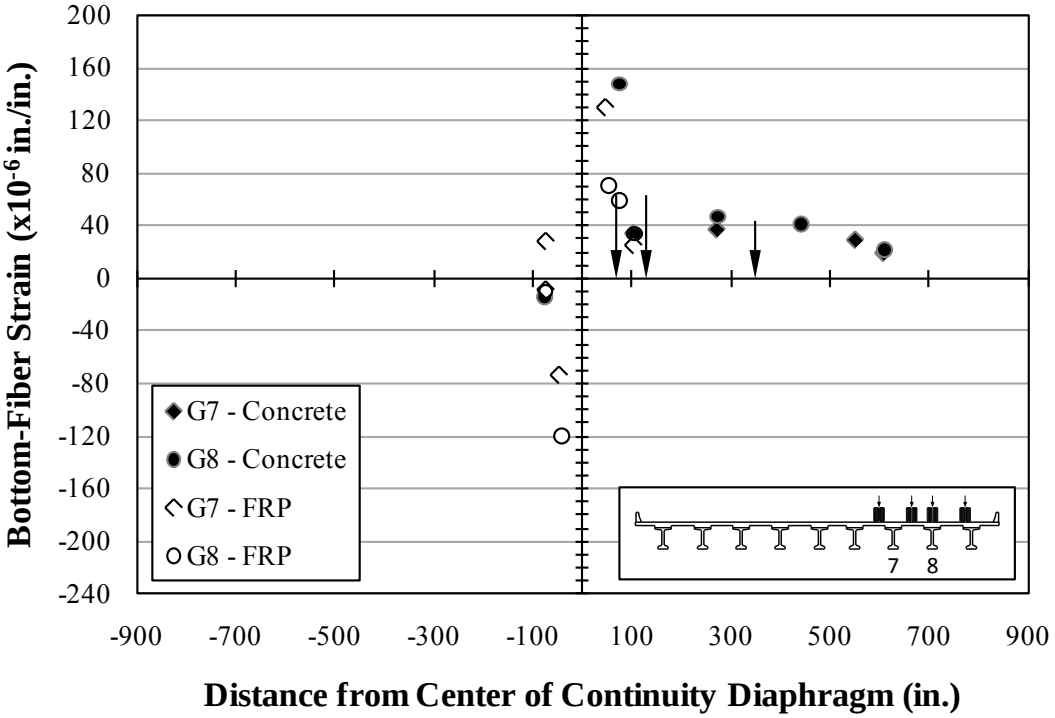

Figure I.24: Bottom-fiber strains—LC 6—AE Span 11 (both)

I.3.1 Bottom-Fiber Strains—Girder 7

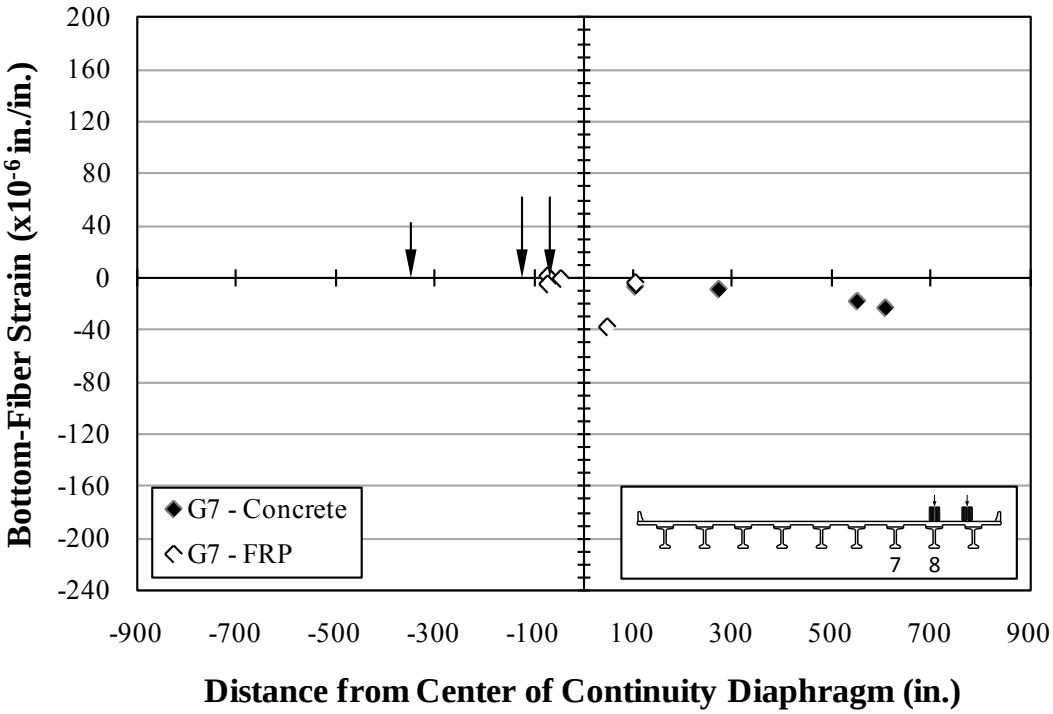

Figure I.25: Bottom-fiber strains—Girder 7—LC 6.5—AE Span 10 (east)

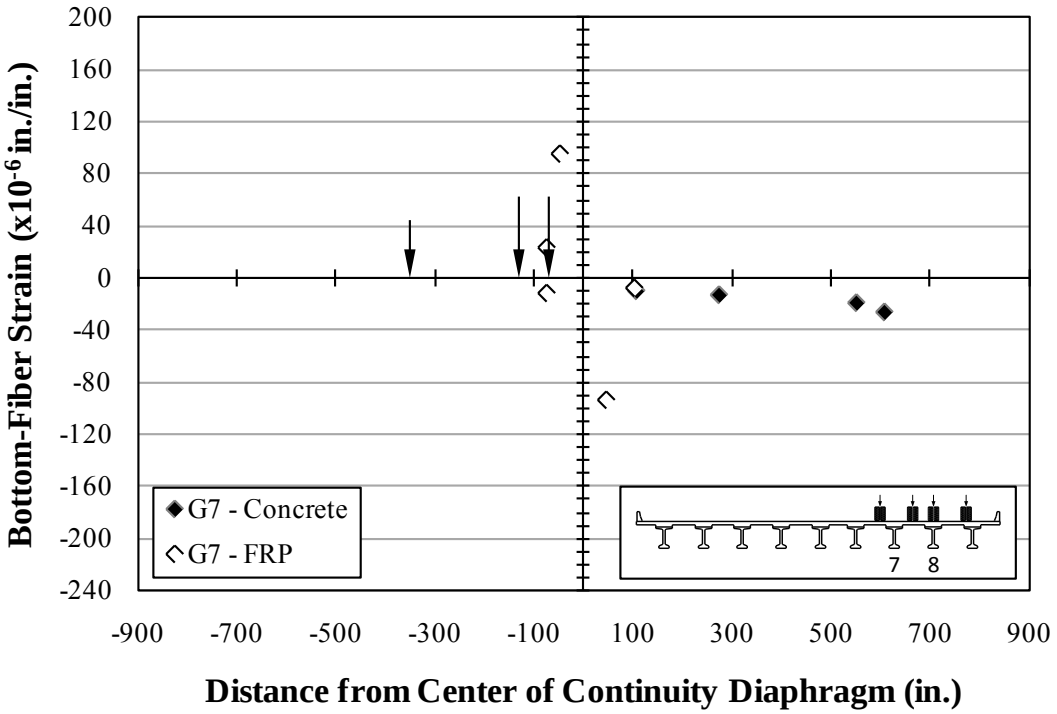

Figure I.26: Bottom-fiber strains—Girder 7—LC 6.5—AE Span 10 (both)

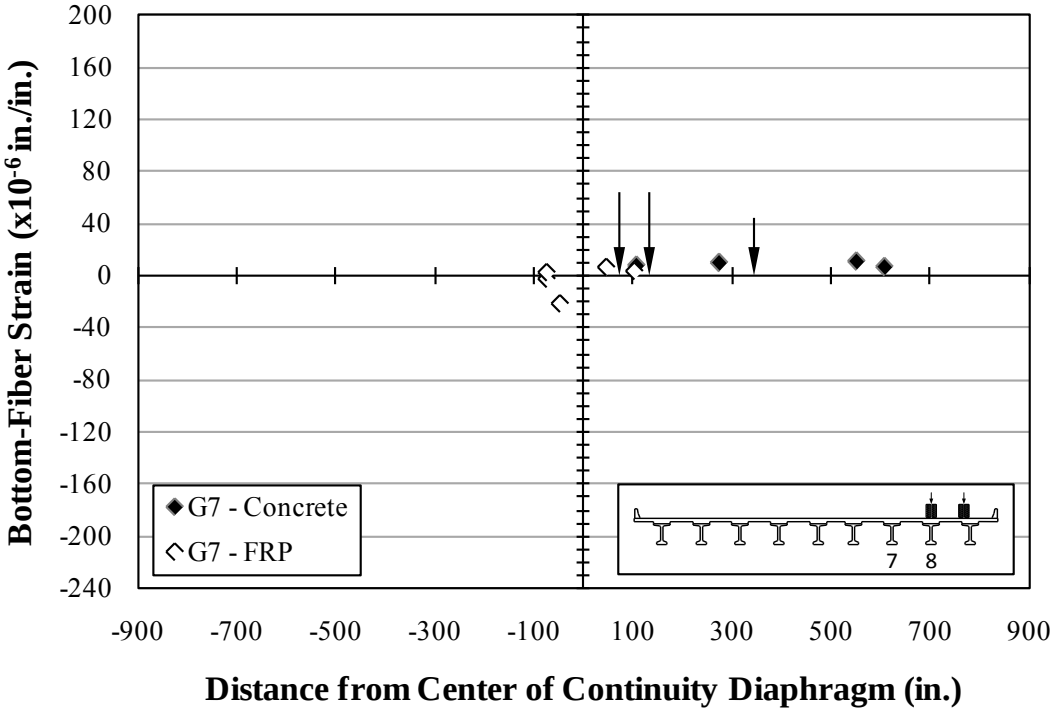

Figure I.27: Bottom-fiber strains—Girder 7—LC 6.5—AE Span 11 (east)

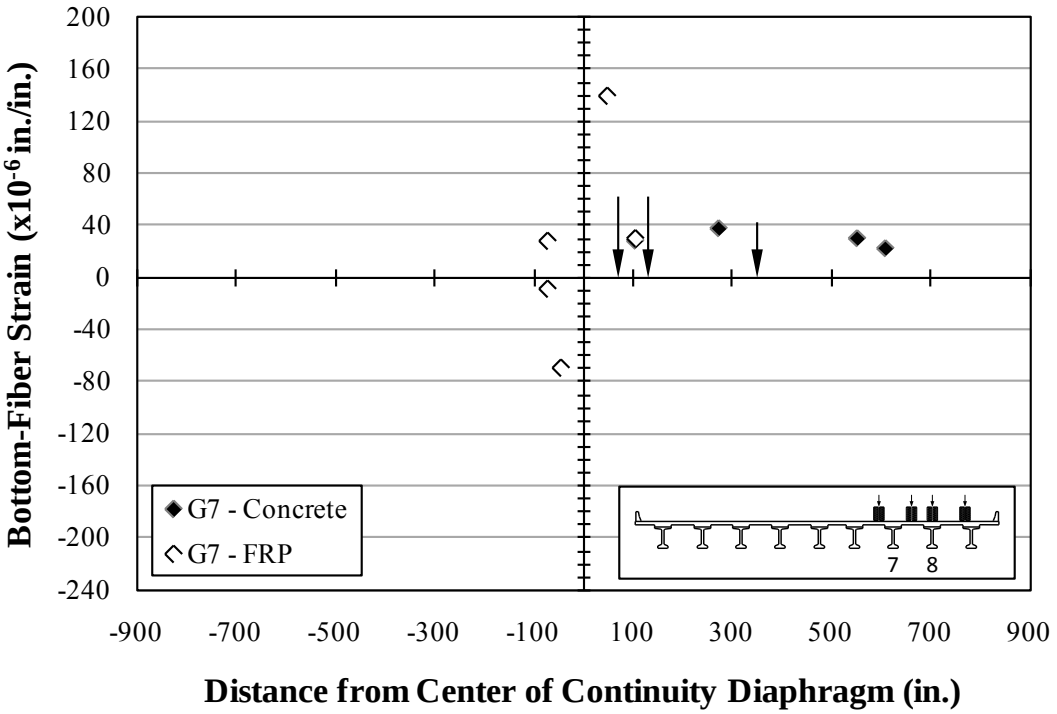

Figure I.28: Bottom-fiber strains—Girder 7—LC 6.5—AE Span 11 (both)

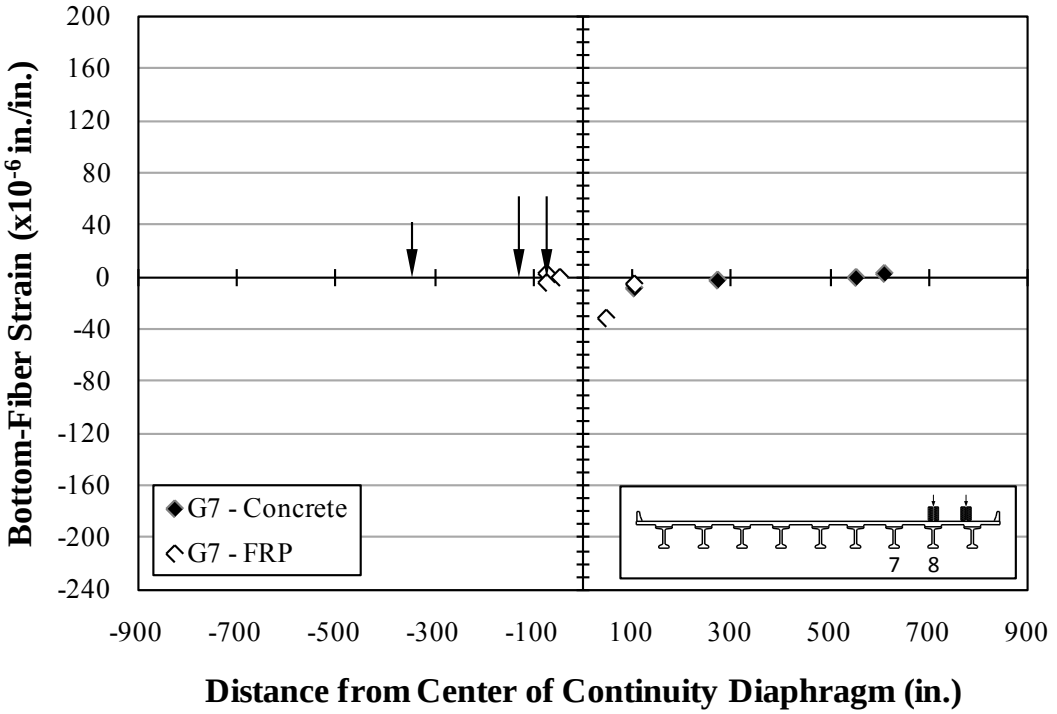

Figure I.29: Bottom-fiber strains—Girder 7—LC 6—AE Span 10 (east)

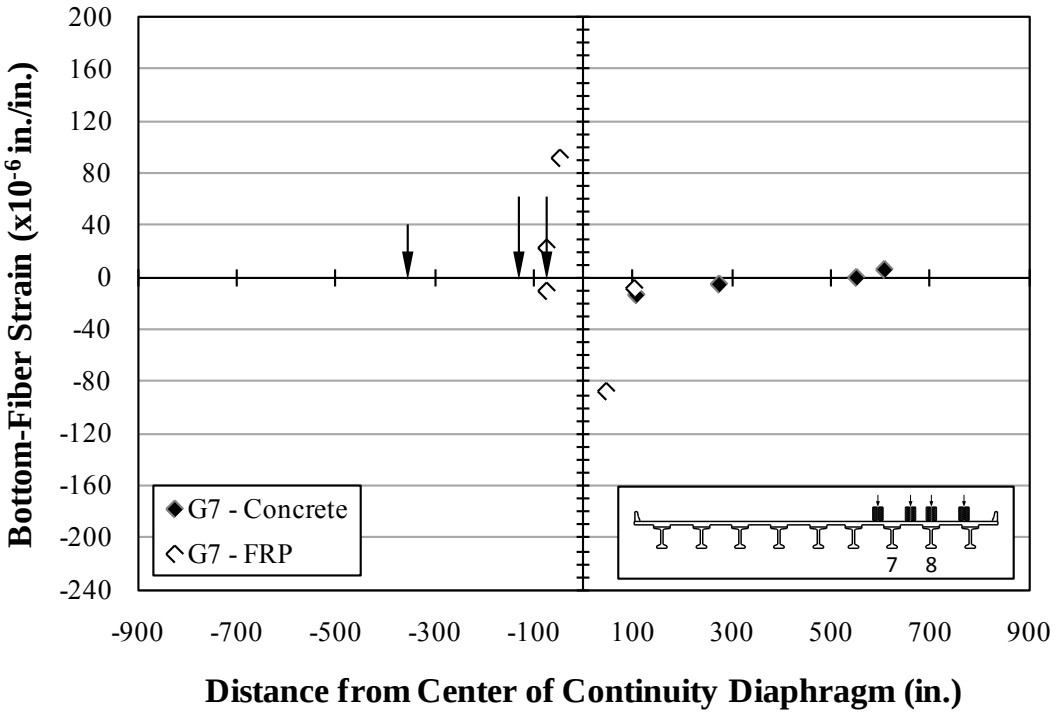

Figure I.30: Bottom-fiber strains—Girder 7—LC 6—AE Span 10 (both)

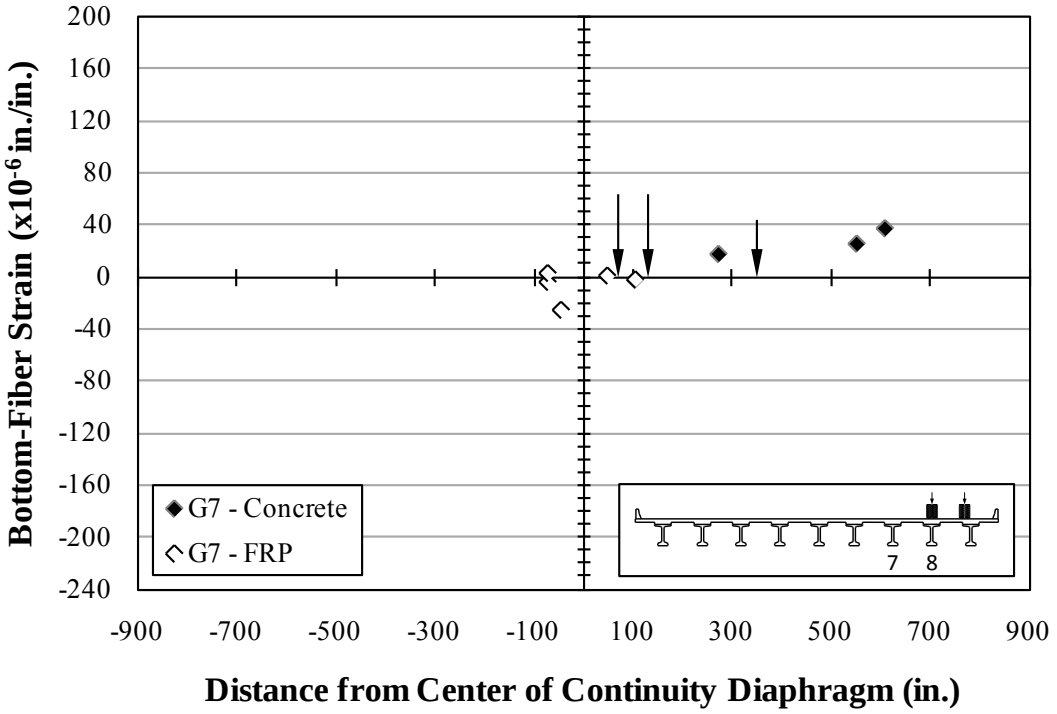

Figure I.31: Bottom-fiber strains—Girder 7—LC 6—AE Span 11 (east)

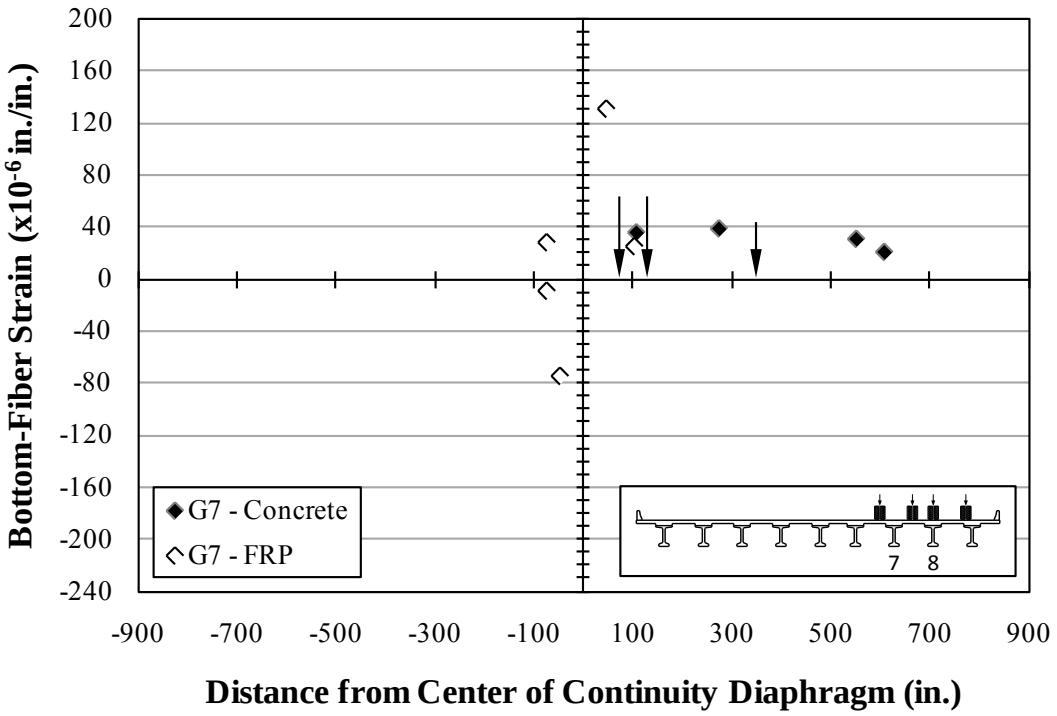

Figure I.32: Bottom-fiber strains—Girder 7—LC 6—AE Span 11 (both)

I.3.2 Bottom-Fiber Strains—Girder 8

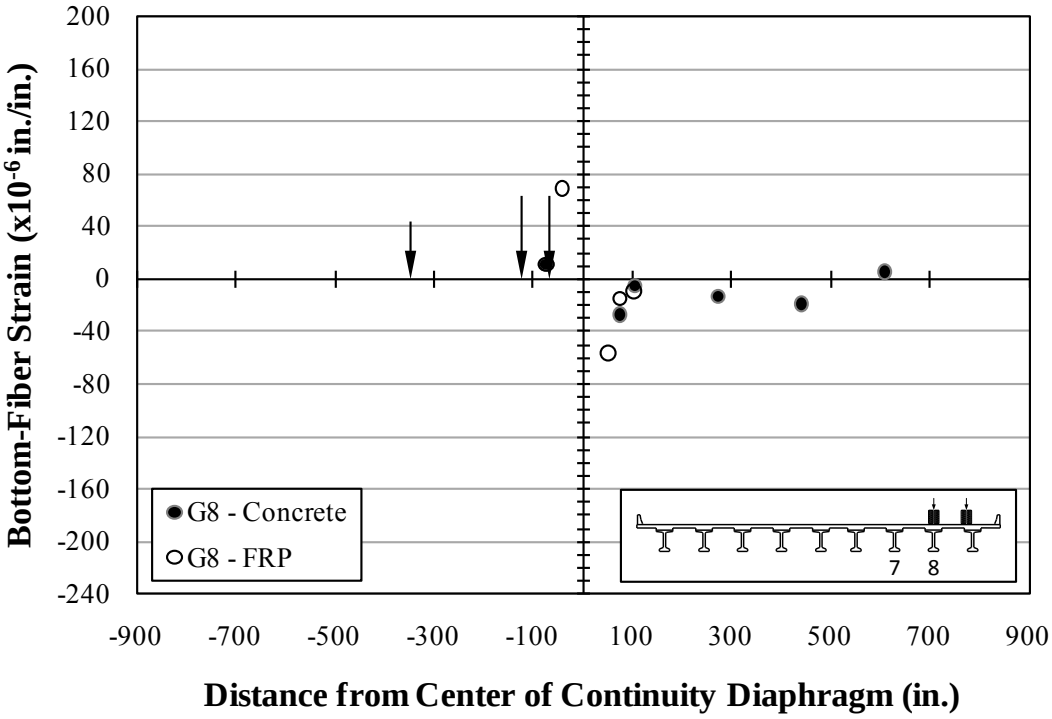

Figure I.33: Bottom-fiber strains—Girder 8—LC 6.5—AE Span 10 (east)

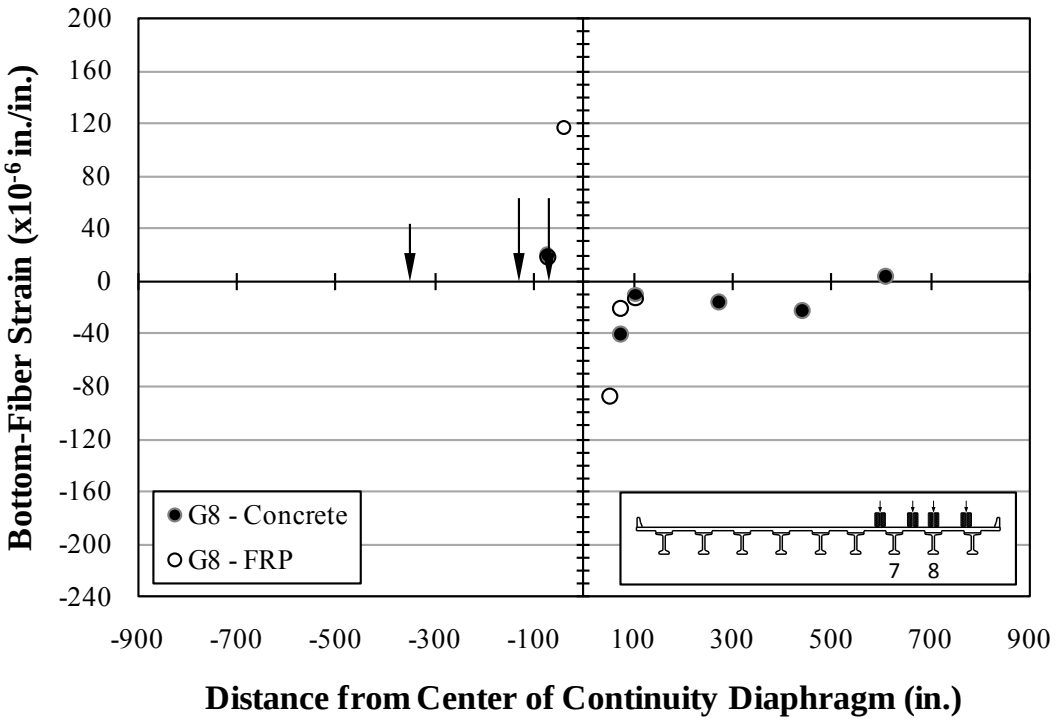

Figure I.34: Bottom-fiber strains—Girder 8—LC 6.5—AE Span 10 (both)

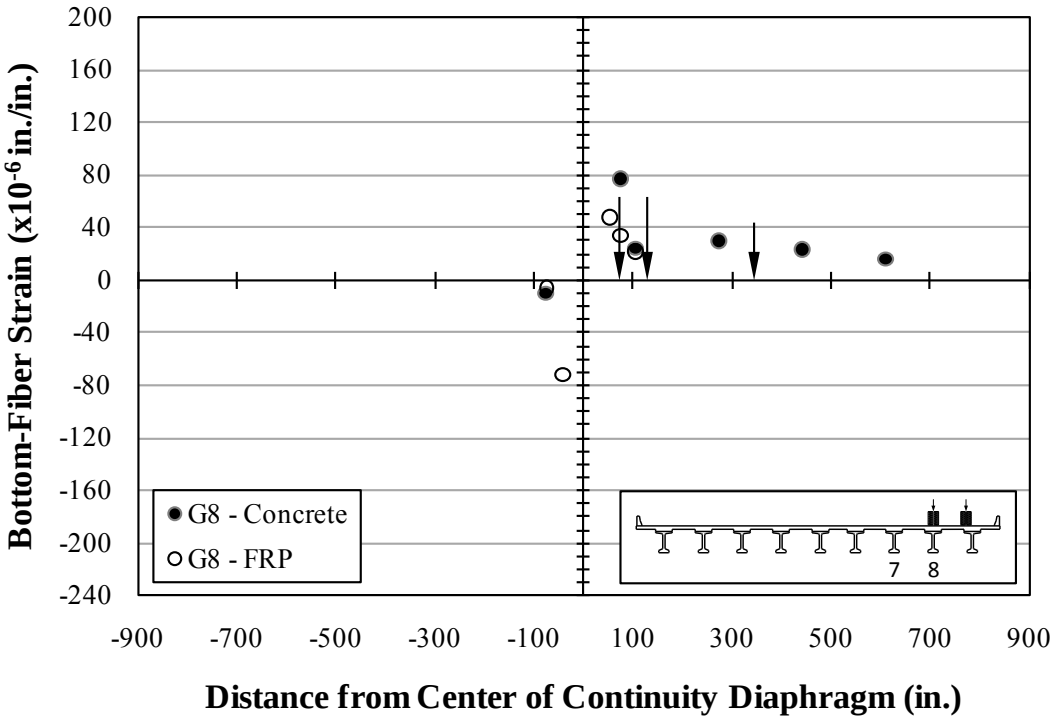

Figure I.35: Bottom-fiber strains—Girder 8—LC 6.5—AE Span 11 (east)

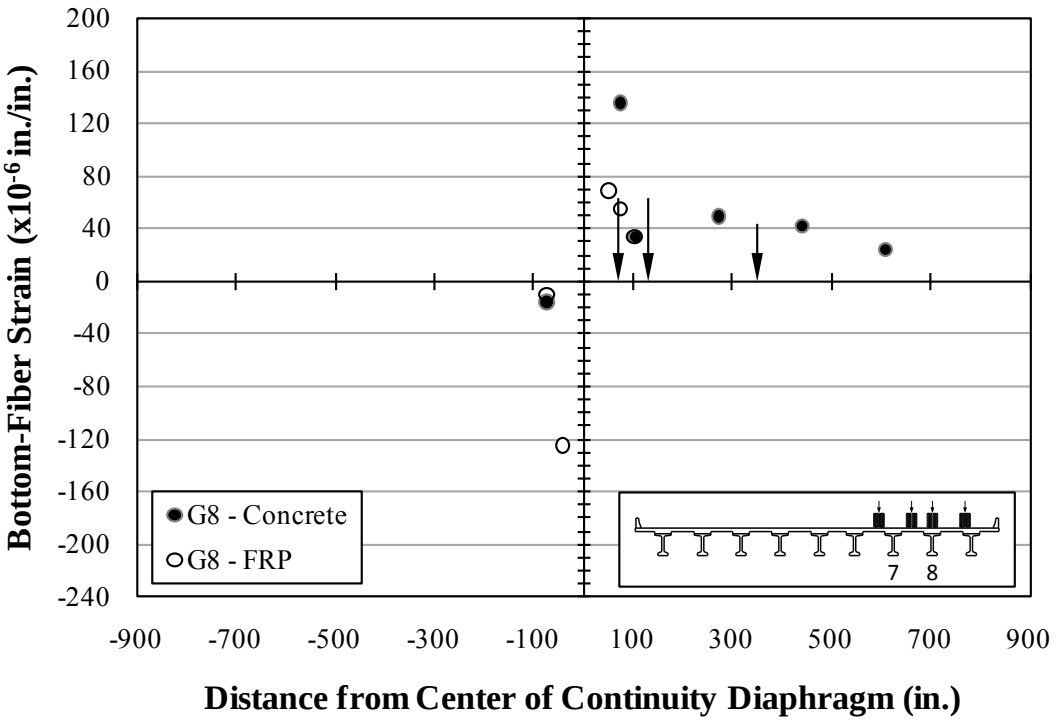

Figure I.36: Bottom-fiber strains—Girder 8—LC 6.5—AE Span 11 (both)

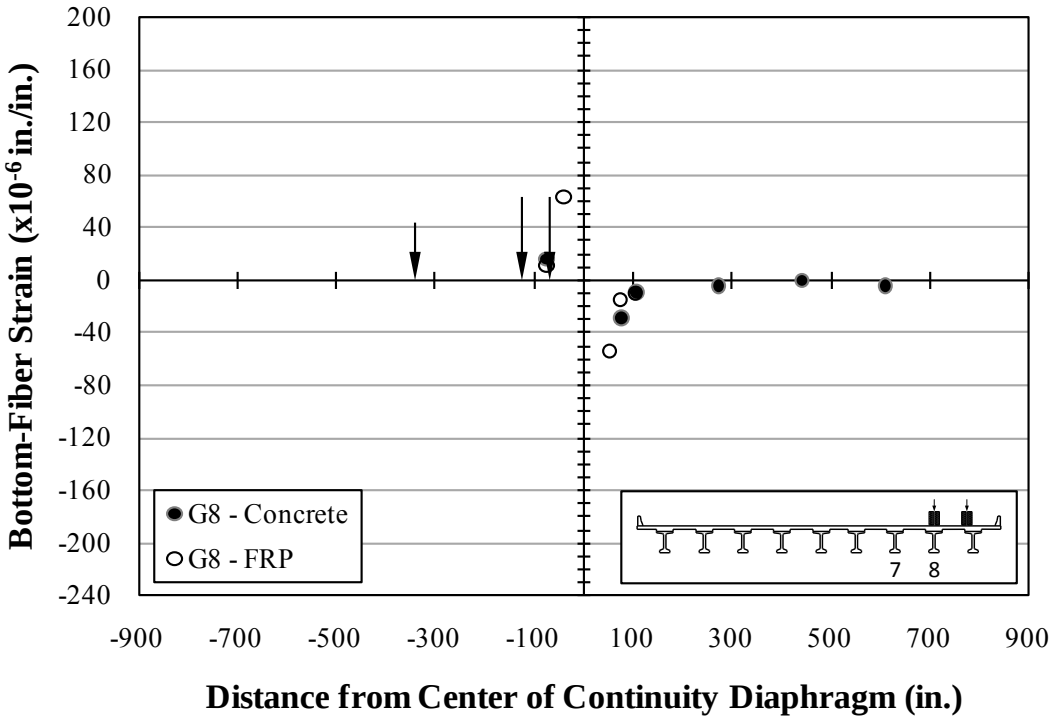

Figure I.37: Bottom-fiber strains—Girder 8—LC 6—AE Span 10 (east)

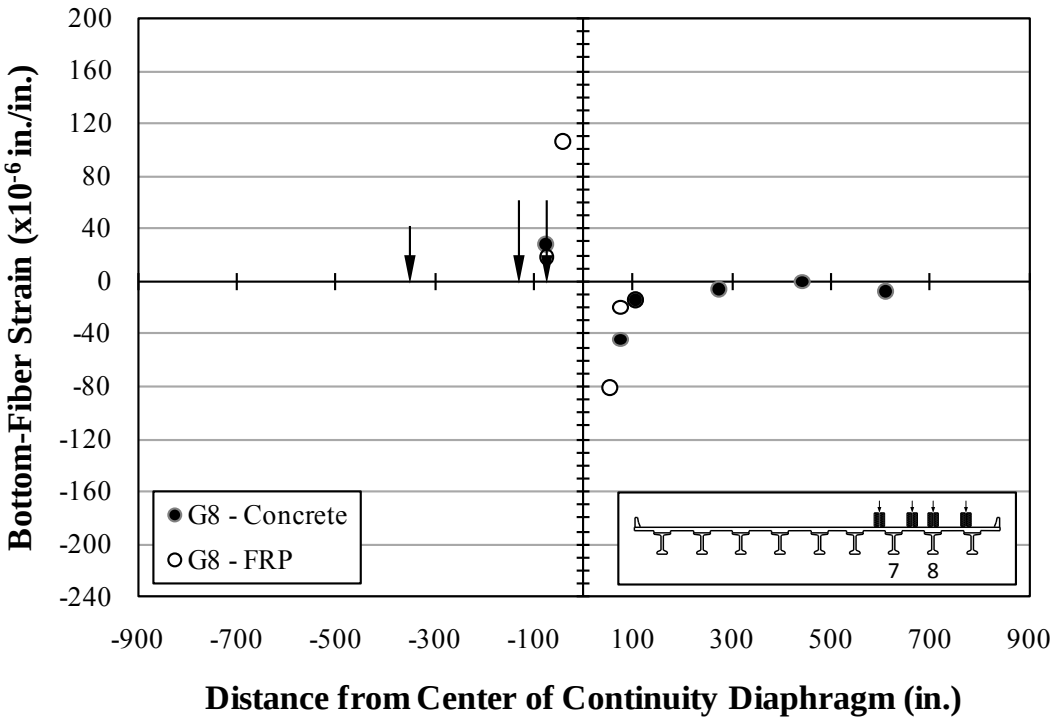

Figure I.38: Bottom-fiber strains—Girder 8—LC 6—AE Span 10 (both)

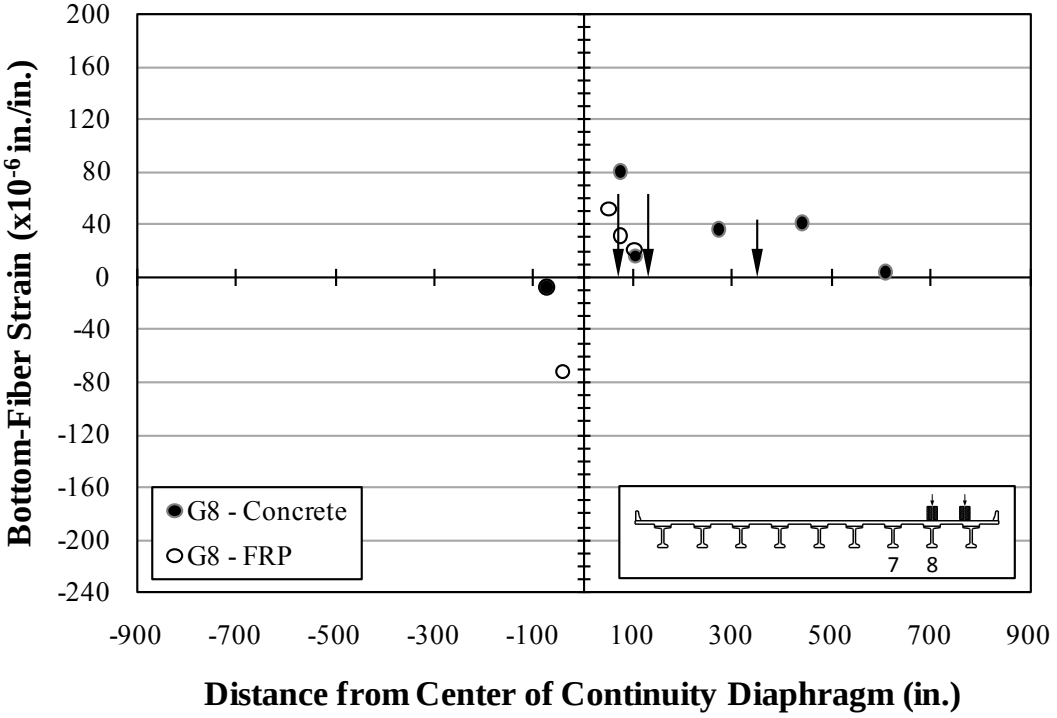

Figure I.39: Bottom-fiber strains—Girder 8—LC 6—AE Span 11 (east)

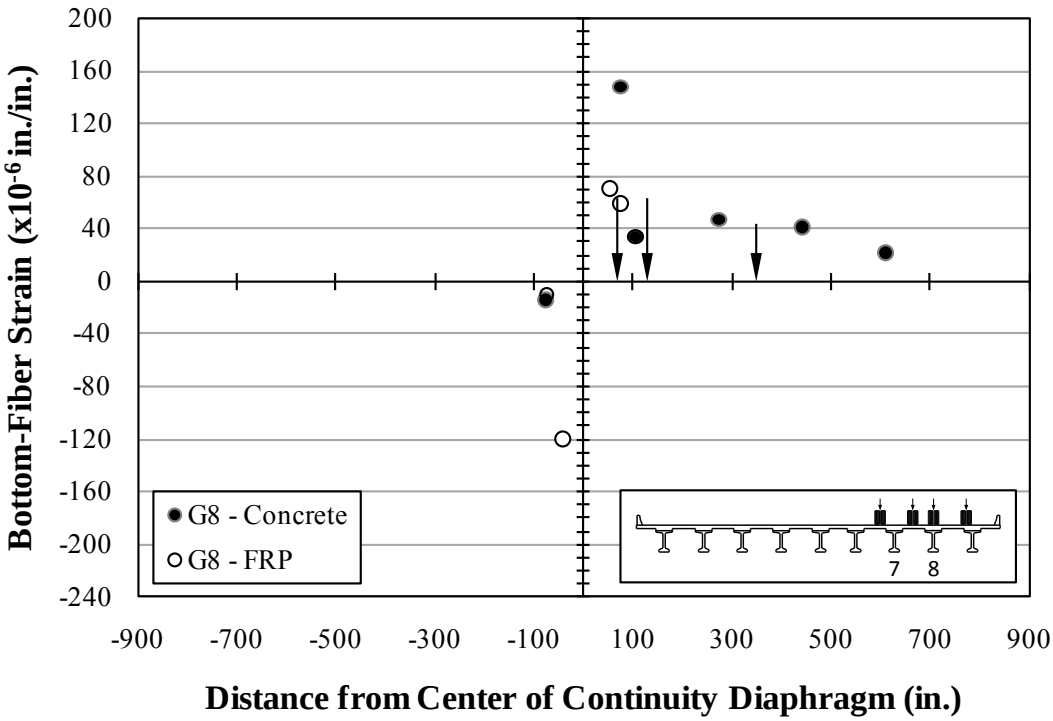

Figure I.40: Bottom-fiber strains—Girder 8—LC 6—AE Span 11 (both)

Appendix J

AE STATIC POSITIONS—MEASUREMENTS

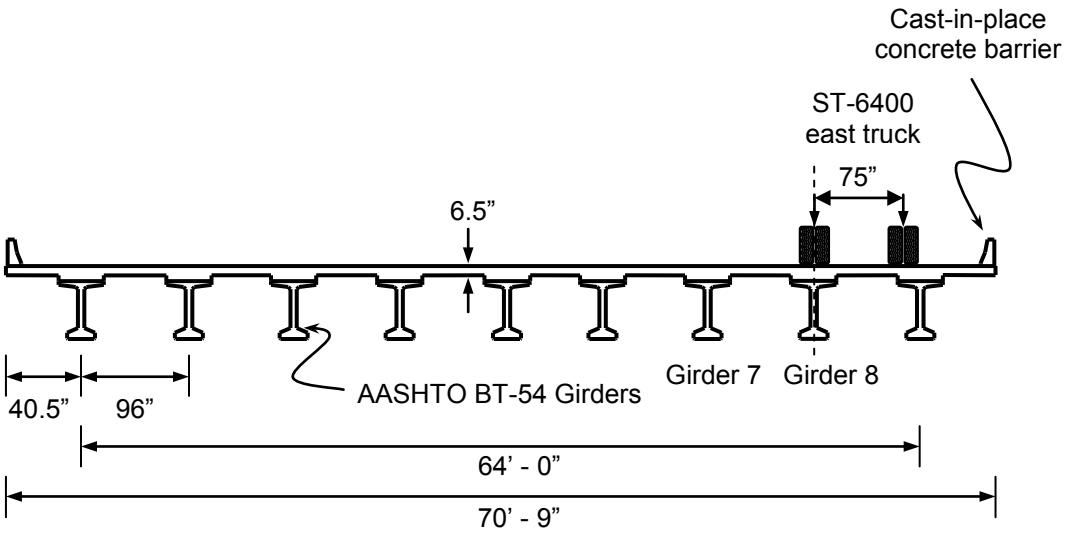

Figure J.1: Transverse load position—AE testing—Lane C—east truck

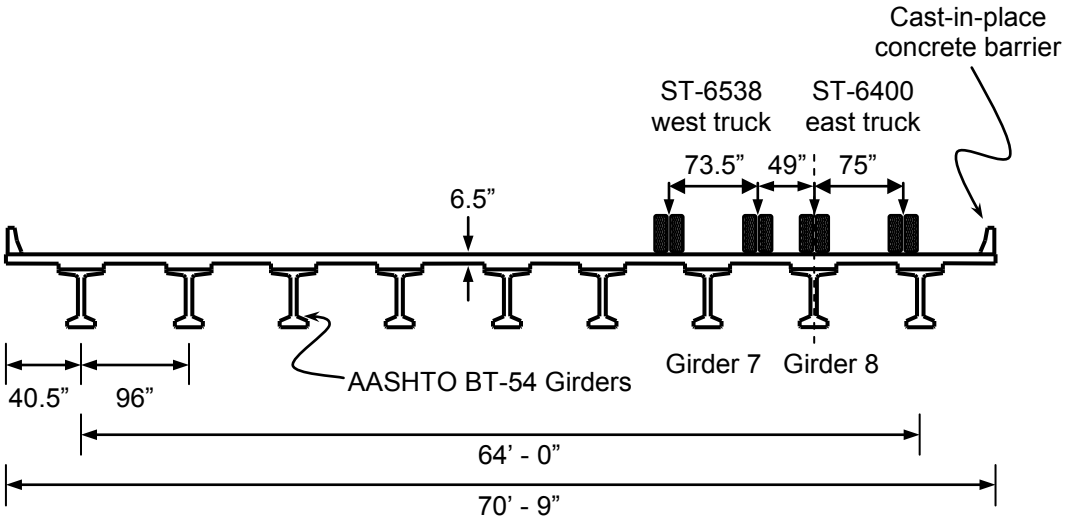

Figure J.2: Transverse load position—AE testing—Lane C—both trucks

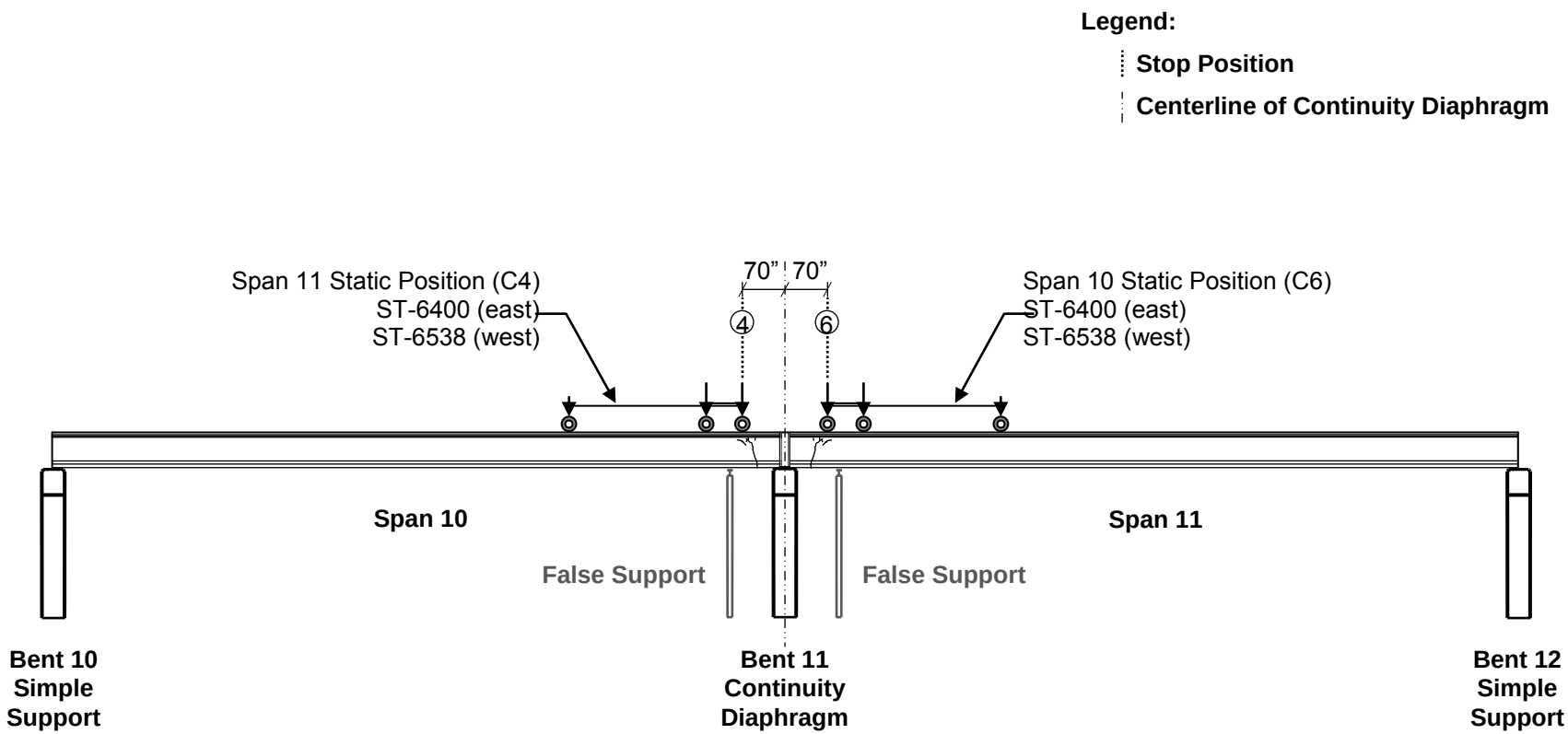

Figure J.3: Longitudinal stop positions—AE testing—Spans 10 and 11

Table J.1: AE static positions—crack-opening displacements

Girder	Gage	Height from bottom of girder (in.)	Distance from center of continuity diaphragm (in.) – Span 10 + Span 11	Crack-Opening Displacement (mm) – closing + opening							
				AE—Night 1 (LC-6.5)				AE—Night 2 (LC-6)			
				Span 10 Loading		Span 11 Loading		Span 10 Loading		Span 11 Loading	
				East Truck	Both Truck	East Truck	Both Truck	East Truck	Both Truck	East Truck	Both Truck
7	CO7_10	13.5	-50	0.002	0.024	-0.005	-0.013	0.002	0.023	-0.005	-0.014
	CO7_11	13.5	48	-0.008	-0.021	0.004	0.047	-0.008	-0.021	0.004	0.044
8	CO8_10	13.5	-40	-0.005	-0.010	-0.006	-0.010	-0.006	-0.010	-0.006	-0.010
	CO8_11	13.5	56	-0.013	-0.019	0.023	0.038	-0.013	-0.019	0.026	0.040

Table J.2: AE static positions—deflections

Girder	Gage	Height from bottom of girder (in.)	Distance from center of continuity diaphragm (in.) – Span 10 + Span 11	Deflection (in.) – downward + upward							
				AE—Night 1 (LC-6.5)				AE—Night 2 (LC-6)			
				Span 10		Span 11		Span 10		Span 11	
				East Truck	Both Truck	East Truck	Both Truck	East Truck	Both Truck	East Truck	Both Truck
7	D7_10_A	n/a	-608	-0.06	-0.12	0.01	0.01	-0.05	-0.11	0.00	0.01
	D7_10_B		-308	-0.05	-0.11	0.01	0.01	-0.04	-0.10	0.00	0.00
	D7_11_C		158	-0.01	-0.01	-0.03	-0.08	0.01	0.00	-0.03	-0.07
	D7_11_D		308	-0.01	-0.01	-0.04	-0.12	0.00	0.01	-0.05	-0.12
	D7_11_E		458	-0.01	-0.01	-0.05	-0.12	0.00	0.01	-0.06	-0.12
	D7_11_F		608	-0.01	-0.01	-0.05	-0.12	0.00	0.00	-0.06	-0.12
8	D8_10_A	n/a	-608	-0.09	-0.14	0.01	0.01	-0.08	-0.13	0.00	0.01
	D8_10_B		-308	-0.08	-0.13	0.01	0.01	-0.07	-0.12	0.00	0.01
	D8_11_C		158	0.00	0.00	-0.05	-0.09	0.01	0.01	-0.06	-0.09
	D8_11_D		308	-0.01	0.00	-0.08	-0.13	0.01	0.01	-0.08	-0.13
	D8_11_E		458	-0.01	0.00	-0.08	-0.14	0.00	0.01	-0.10	-0.15
	D8_11_F		608	-0.01	0.00	-0.07	-0.13	0.01	0.01	-0.08	-0.12

Table J.3: AE static positions—cross-section strains—Girder 7—Span 10

Cross Section	Gage	Height from bottom of girder (in.)	Distance from center of continuity diaphragm (in.) – Span 10 + Span 11	Strain ($x10^{-6}$ in/in) – compressive + tensile							
				AE—Night 1 (LC-6.5)				AE—Night 2 (LC-6)			
				Span 10		Span 11		Span 10		Span 11	
				East Truck	Both Truck	East Truck	Both Truck	East Truck	Both Truck	East Truck	Both Truck
Girder 7 Cross Section 1	S7_10_1V	28.5	-75	0	5	-1	-3	0	5	-2	-3
	S7_10_1W	13.5	-75	2	12	-2	-5	2	11	-3	-6
	S7_10_1X	13.5	-75	0	10	-1	-4	1	11	-2	-5
	S7_10_1Y	3.0	-75	0	21	-4	-10	2	22	-4	-8
	F7_10_1M	0.0	-74	1	24	-3	-9	3	23	-4	-9
Girder 7 Cross Section 2	S7_10_2V	28.5	-13	0	3	0	1	2	3	-1	-1
	S7_10_2W	13.5	-13	0	-1	1	3	8	4	-1	2
	S7_10_2X	13.5	-13	-1	-1	0	2	1	5	0	1
	S7_10_2Y	3.0	-13	-47	-108	-12	-63	-51	-107	-23	-69
	F7_10_2Z	3.0	-14	0	-4	-4	-21	1	-3	-5	-20

Table J.4: AE static positions—cross-section strains—Girder 7—Span 11

Cross Section	Gage	Height from bottom of girder (in.)	Distance from center of continuity diaphragm (in.) – Span 10 + Span 11	Strain ($x10^{-6}$ in./in.) – compressive + tensile							
				AE—Night 1 (LC-6.5)				AE—Night 2 (LC-6)			
				Span 10		Span 11		Span 10		Span 11	
				East Truck	Both Truck	East Truck	Both Truck	East Truck	Both Truck	East Truck	Both Truck
Girder 7 Cross Section 3	S7_11_3V	28.5	13	-4	-3	0	-5	-2	-1	-7	-7
	S7_11_3W	13.5	13	-3	-3	1	5	-4	-4	-2	3
	S7_11_3X	13.5	13	1	3	-2	-4	2	5	-6	-7
	S7_11_3Y	3.0	13	-2	-4	-3	-7	0	-5	-10	-10
	S7_11_3Z	3.0	13	-2	-3	2	-6	3	-1	-6	-7
Girder 7 Cross Section 4	S7_11_4V	28.5	75	0	0	-1	-3	1	1	-1	-4
	S7_11_4W	13.5	75	0	-2	1	7	0	-3	0	6
	S7_11_4X	13.5	75	-2	-4	-1	5	-1	-3	-3	4
	S7_11_4Y	3.0	75	-1	-5	4	26	0	-5	3	23
	F7_11_4M	0.0	74	-5	-11	2	28	-4	-10	3	28

Table J.5: AE static positions—cross-section strains—Girder 8—Span 10

Cross Section	Gage	Height from bottom of girder (in.)	Distance from center of continuity diaphragm (in.) – Span 10 + Span 11	Strain ($x10^{-6}$ in./in.) – compressive + tensile							
				AE—Night 1 (LC-6.5)				AE—Night 2 (LC-6)			
				Span 10		Span 11		Span 10		Span 11	
				East Truck	Both Truck	East Truck	Both Truck	East Truck	Both Truck	East Truck	Both Truck
Girder 8 Cross Section 1	S8_10_1V	28.5	-75	3	3	-4	-6	3	3	-5	-7
	S8_10_1W	13.5	-75	10	13	-6	-12	10	13	-8	-11
	S8_10_1X	13.5	-75	8	14	-6	-11	7	13	-7	-12
	F8_10_1Y	3.0	-74	10	11	-5	-8	11	12	-5	-7
	S8_10_1M	0.0	-75	11	20	-10	-16	16	28	-7	-14
	F8_10_1M	0.0	-74	11	19	-6	-10	11	19	-7	-10
Girder 8 Cross Section 2	S8_10_2V	28.5	-13	2	3	-1	-2	3	5	-2	-2
	S8_10_2W	13.5	-13	6	6	0	-1	5	7	-2	-1
	S8_10_2X	13.5	-13	5	7	0	0	5	7	0	0
	F8_10_2Y	3.0	-14	-16	-24	-14	-26	-17	-25	-16	-26
	F8_10_2Z	3.0	-14	0	-5	-6	-14	1	-4	-4	-12

Table J.6: AE static positions—cross-section strains—Girder 8—Span 11

Cross Section	Gage	Height from bottom of girder (in.)	Distance from center of continuity diaphragm (in.) – Span 10 + Span 11	Strain ($x10^{-6}$ in/in) – compressive + tensile							
				AE—Night 1 (LC-6.5)				AE—Night 2 (LC-6)			
				Span 10		Span 11		Span 10		Span 11	
				East Truck	Both Truck	East Truck	Both Truck	East Truck	Both Truck	East Truck	Both Truck
Girder 8 Cross Section 3	S8_11_3V	28.5	13	-76	-107	-23	-28	-71	-100	-24	-27
	S8_11_3W	13.5	13	-1	-2	-4	-6	-2	-3	-6	-6
	S8_11_3X	13.5	13	-8	-14	8	10	-5	-9	7	10
	F8_11_3Y	3.0	14	-13	-27	-11	-15	-15	-27	-10	-16
	F8_11_3Z	3.0	14	-19	-33	-3	-20	-15	-29	0	-16
Girder 8 Cross Section 4	S8_11_4V	28.5	75	-2	-3	-10	-19	-2	-1	-11	-19
	S8_11_4W	13.5	75	-5	-8	4	3	-4	-6	2	1
	S8_11_4X	13.5	75	-5	-7	-2	-3	-2	-3	-6	-1
	F8_11_4Y	3.0	74	-6	-8	15	16	-6	-8	13	16
	S8_11_4M	0.0	75	-27	-40	77	136	-29	-44	80	148
	F8_11_4M	0.0	74	-15	-21	34	55	-15	-20	31	59

Table J.7: AE static positions—bottom-fiber strains—Girder 7

Span	Gage	Height from bottom of girder (in.)	Distance from center of continuity diaphragm (in.) – Span 10 + Span 11	Strain ($x10^{-6}$ in/in) – compressive + tensile							
				AE—Night 1 (LC-6.5)				AE—Night 2 (LC-6)			
				Span 10		Span 11		Span 10		Span 11	
				East Truck	Both Truck	East Truck	Both Truck	East Truck	Both Truck	East Truck	Both Truck
10	F7_10_1M	0	-74	1	24	-3	-9	3	23	-4	-9
	F7_10_CK		-47	-1	96	-22	-70	0	92	-26	-74
11	F7_11_CK	0	47	-37	-93	6	140	-31	-87	1	130
	F7_11_4M		74	-5	-11	2	28	-4	-10	3	28
	F7_11_5M		104	-4	-7	3	30	-5	-8	-2	25
	S7_11_5M		105	-7	-10	8	28	-8	-13	-3	35
	S7_11_6M		273	-9	-13	10	38	-2	-5	17	38
	S7_11_7M		441	-18	-19	11	30	0	0	25	30
	S7_11_8M		609	-23	-26	7	22	3	6	37	20

Table J.8: AE static positions—bottom-fiber strains—Girder 8

Span	Gage	Height from bottom of girder (in.)	Distance from center of continuity diaphragm (in.) – Span 10 + Span 11	Strain ($x10^{-6}$ in/in) – compressive + tensile							
				AE—Night 1 (LC-6.5)				AE—Night 2 (LC-6)			
				Span 10		Span 11		Span 10		Span 11	
				East Truck	Both Truck	East Truck	Both Truck	East Truck	Both Truck	East Truck	Both Truck
10	S8_10_1M	0	-75	11	20	-10	-16	16	28	-7	-14
	F8_10_1M		-74	11	19	-6	-10	11	19	-7	-10
	F8_10_CK		-41	69	117	-72	-125	63	106	-72	-120
11	F8_11_CK	0	52	-56	-87	48	69	-54	-81	52	71
	F8_11_4M		74	-15	-21	34	55	-15	-20	31	59
	S8_11_4M		75	-27	-40	77	136	-29	-44	80	148
	F8_11_5M		104	-9	-13	22	34	-10	-14	21	34
	S8_11_5M		105	-5	-10	24	34	-9	-14	16	34
	S8_11_6M		273	-13	-16	30	49	-4	-6	36	47
	S8_11_7M		441	-19	-22	23	42	0	0	41	41
	S8_11_8M		609	5	4	16	24	-4	-7	4	22

Table J.9: AE static positions—FRP strains—Girder 7

Span	Gage	Height from bottom of girder (in.)	Distance from center of continuity diaphragm (in.) – Span 10 + Span 11	Strain ($x10^{-6}$ in/in) – compressive + tensile							
				AE—Night 1 (LC-6.5)				AE—Night 2 (LC-6)			
				Span 10		Span 11		Span 10		Span 11	
				East Truck	Both Truck	East Truck	Both Truck	East Truck	Both Truck	East Truck	Both Truck
10	F7_10_1M	0	-74	1	24	-3	-9	3	23	-4	-9
	F7_10_CK	0	-47	-1	96	-22	-70	0	92	-26	-74
	F7_10_2Z	3	-13	0	-4	-4	-21	1	-3	-5	-20
11	F7_11_CK	0	47	-37	-93	6	140	-31	-87	1	130
	F7_11_4M	0	74	-5	-11	2	28	-4	-10	3	28
	F7_11_5M	0	104	-4	-7	3	30	-5	-8	-2	25

Table J.10: AE static positions—FRP strains—Girder 8

Span	Gage	Height from bottom of girder (in.)	Distance from center of continuity diaphragm (in.) – Span 10 + Span 11	Strain ($x10^{-6}$ in/in) – compressive + tensile							
				AE—Night 1 (LC-6.5)				AE—Night 2 (LC-6)			
				Span 10		Span 11		Span 10		Span 11	
				East Truck	Both Truck	East Truck	Both Truck	East Truck	Both Truck	East Truck	Both Truck
10	F8_10_1Y	3	-74	10	11	-5	-8	11	12	-5	-7
	F8_10_1M	0	-74	11	19	-6	-10	11	19	-7	-10
	F8_10_CK	0	-41	69	117	-72	-125	63	106	-72	-120
	F8_10_2Y	3	-14	-16	-24	-14	-26	-17	-25	-16	-26
	F8_10_2Z	3	-14	0	-5	-6	-14	1	-4	-4	-12
11	F8_11_3Y	3	14	-13	-27	-11	-15	-15	-27	-10	-16
	F8_11_3Z	3	14	-19	-33	-3	-20	-15	-29	0	-16
	F8_11_CK	0	52	-56	-87	48	69	-54	-81	52	71
	F8_11_4Y	3	74	-6	-8	15	16	-6	-8	13	16
	F8_11_4M	0	74	-15	-21	34	55	-15	-20	31	59
	F8_11_5M	0	104	-9	-13	22	34	-10	-14	21	34

Appendix K

FALSE SUPPORT BEARING PAD EFFECTS DURING LOAD TESTING

K.1 INSTALLATION OF FALSE SUPPORTS WITH BEARING PADS

In response to the severity of cracking observed at the continuous ends of prestressed concrete girders of I-565, ALDOT installed steel frame false supports under spans containing damaged girders, as shown in Figure K.1. False supports were installed within ten feet of the bents, allowing the cracked regions of damaged girders to be contained between false supports and the nearest bent.

Figure K.1: Steel frame false supports

The false supports were installed to leave a gap of at least one inch between the top of false supports and the bottom of girders before adding bearing pads. Elastomeric bearing pads were

then installed under each girder, attaching them to the tops of the false supports, as shown in Figure K.2

Figure K.2: Bearing pad between false support and exterior girder

A small gap between the bearing pad and girder bottom remained after false support installation. Bearing pads were installed to prevent catastrophic collapse in case of further deterioration of the bridge girders, but it was undesirable for bearing pads to remain in contact with bridge girders during load testing. An installed bearing pad with space remaining between the pad and girder is shown in Figure K.3. A bearing pad that is in contact with a girder and likely transferring loads through the false support is shown in Figure K.4.

Figure K.3: Bearing pad location *with* space between the bearing pad and girder

Figure K.4: Bearing pad location *without* space between the bearing pad and girder

K.2 PRE-REPAIR BEARING PAD CONDITIONS

During initial test preparation, it was observed that some of the gaps between bearing pads and false supports had closed, and bearing pads were in contact with instrumented girders, as shown in Figure K.5. The closure of gaps between girders and false support bearing pads was likely due to downward creep deformations of the girders or settlement of the bridge structure.

Figure K.5: Bearing pad in contact with girder during pre-repair testing

An attempt was made to remove the bearing pads; however, initial removal attempts were unsuccessful. A surface-mounted strain gage was attached to one column of the false supports to determine if the false supports were supporting normal traffic loads due to the bearing pads being in direct contact with the girders. Due to the measurement of small compressive strains, it was determined that the bearing pads were transmitting some load through the false supports during normal traffic conditions (Fason 2009).

For research purposes, it was desirable to test the bridge without additional load-bearing supports. The removal of bearing pads was scheduled to take place on the day of the pre-repair testing; however, the overcast weather conditions on that day were not conducive to the upward movement expected of the girders during the warmest time of the day in late spring. Under the overcast weather conditions, the gap between the bearing pads and the girders was so small—in some cases non-existent—that the complete removal of all bearing pads prior to the scheduled pre-repair tests was not possible using the available equipment and methods. After realizing that

complete removal of all bearing pads would not be possible before conducting pre-repair load tests, holes were drilled in the bearing pads to alleviate pressure and reduce the effective stiffness of the pads (Fason 2009).

Fason (2009) reported that, prior to the pre-repair tests, one bearing pad was completely removed (Girder 8 of Span 10), one half of another bearing pad was removed (east half of Girder 7 of Span 10), and holes were drilled in the remaining bearing pads to reduce their effective stiffness (west half of Girder 7 of Span 10, Girder 7 of Span 11, and Girder 8 of Span 11).

The pre-repair tests were conducted without complete removal of all bearing pads. Following the pre-repair tests, it was suggested that the presence of the bearing pads could have had an effect on the measured bridge behavior (Fason 2009).

K.3 BEARING PAD REMOVAL DURING FRP INSTALLATION

The installation of the FRP reinforcement required that all bearing pads be removed. These bearing pads inhibited FRP installation to the bottom of the girder at false-support locations. The bearing pads under Span 11 were, in general, more difficult to remove than the bearing pads under Span 10. Initially, the contractor attempted to remove each bearing pad by punching it out of place using a chisel and hammer. When a bearing pad was under enough pressure to prevent removal, the contractor then used a reciprocating saw on the pad in an attempt to alleviate some of that pressure, as shown in Figure K.6.

Figure K.6: Use of reciprocating saw during bearing pad removal

In some cases, saw cutting alone was not effective at alleviating enough pressure for successful bearing pad removal. In these cases, a propane torch was used to soften the rubber, as shown in Figure K.7, which then allowed for a more effective sawing process.

Figure K.7: Use of propane torch during bearing pad removal

After successful pressure alleviation, the bearing pad was removed using the initial chisel-and-hammer removal method, as shown in Figure K.8. An example of a bearing pad that required forceful removal is shown in Figure K.9. Bearing pads were *not* replaced following the installation of the FRP reinforcement.

Figure K.8: Successful removal of bearing pad

Figure K.9: Bearing pad after forceful removal

K.4 POST-REPAIR BEARING PAD CONDITIONS

The post-repair tests were conducted *without* the presence of any bearing pads. Fason (2009) indicated that direct relationships between structural behavior measured and observed during pre-repair and post-repair load testing may be affected by the variation of support conditions.

K.5 ANALYSIS OF NUMERICAL RESULTS

The measurements of the pre- and post-repair tests were compared to better determine the effects related to the presence of the bearing pads. These comparisons include: deflections, crack opening displacements, and surface strains measured during multiposition load testing as well as deflections measured during superposition testing.

K.5.1 Deflections—Multiposition Load Testing

Truck positions resulting in maximum downward deflections measured during pre- and post-repair multiposition load testing have been analyzed to assess whether the bearing pads had an effect on the pre-repair support conditions and general pre-repair bridge behavior. Pre- and post-repair deflections measured in response to four midspan truck positions (A1, C1, A9, and C9) are shown in Figures K.10–K.13. The arrows in the figures represent the position of the wheel loads on the bridge. For each midspan truck position, the midspan and quarterspan deflection measurements—and the differences between pre- and post-repair testing—are presented in Tables K.1–K.4. For each midspan truck position, the table of measurements follows the figure that illustrates the measured deflections.

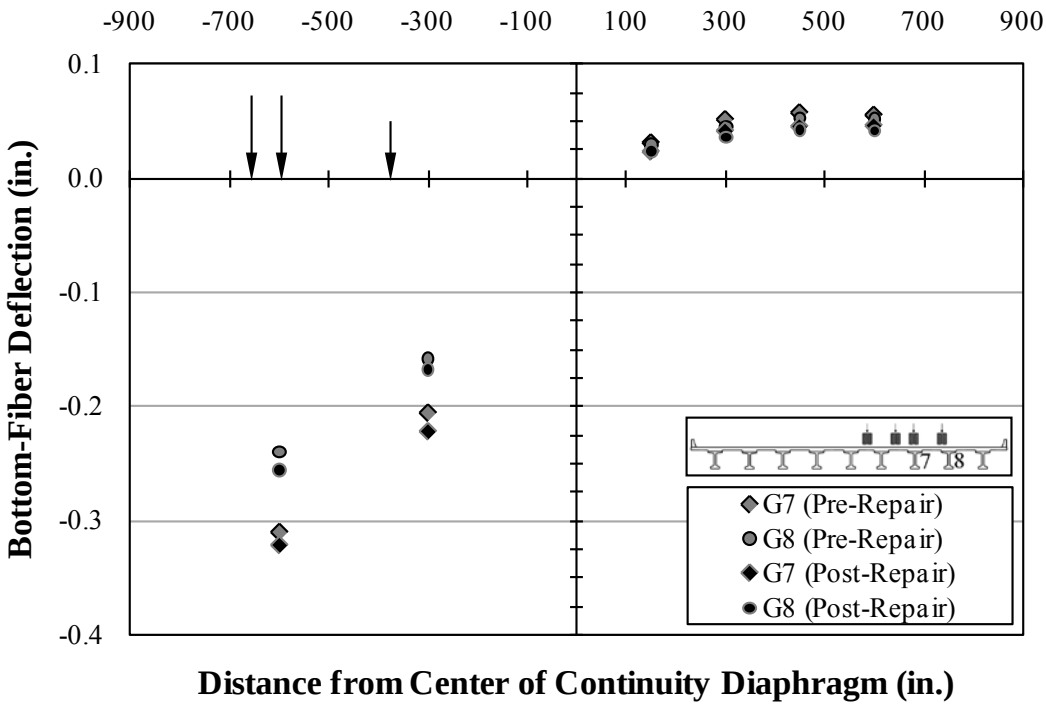

Figure K.10: Deflections—A1

Table K.1: Deflections—A1

Span	Girder	Location (span)	Post-Repair (in.)	Pre-Repair (in.)	Diff. (in.)	Percent Diff. (%)
10	7	mid	-0.32	-0.31	-0.01	3
		quarter	-0.22	-0.20	-0.02	10
	8	mid	-0.26	-0.24	-0.02	8
		quarter	-0.17	-0.16	-0.01	6
11	7	quarter	0.04	0.05	-0.01	20
		mid	0.05	0.06	-0.01	20
	8	quarter	0.04	0.05	-0.01	20
		mid	0.04	0.05	-0.01	20

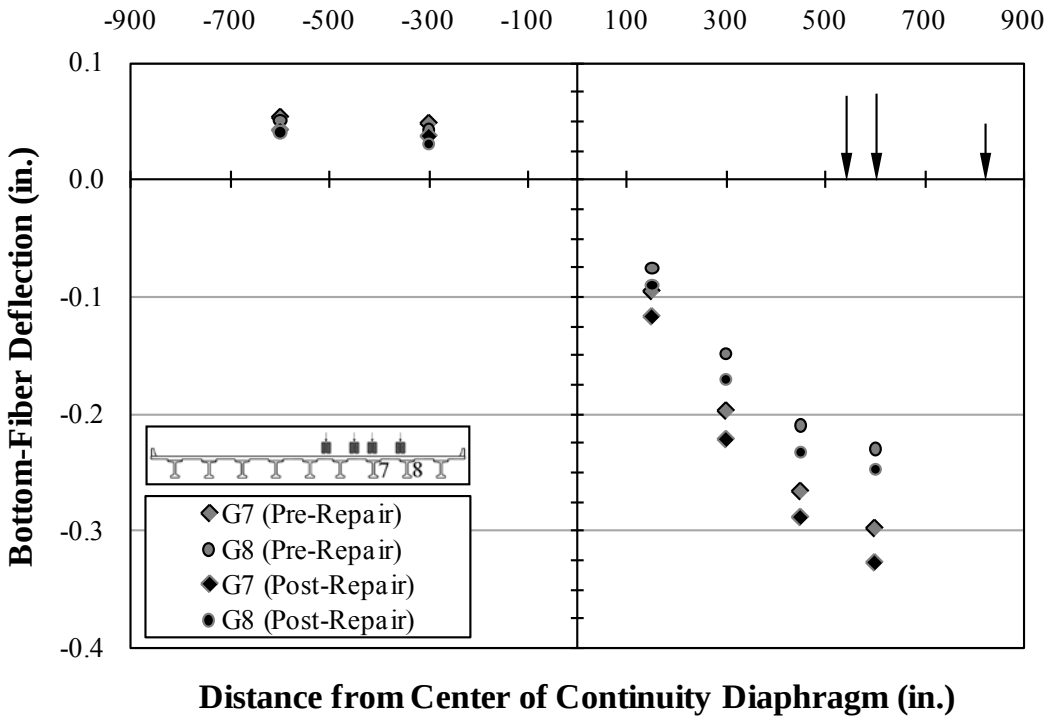

Figure K.11: Deflections—A9

Table K.2: Deflections—A9

Span	Girder	Location (span)	Post-Repair (in.)	Pre-Repair (in.)	Diff. (in.)	Percent Diff. (%)
10	7	mid	0.04	0.05	-0.01	20
		quarter	0.04	0.05	-0.01	20
	8	mid	0.04	0.05	-0.01	20
		quarter	0.03	0.04	-0.01	30
11	7	quarter	-0.22	-0.20	-0.02	10
		mid	-0.33	-0.30	-0.03	10
	8	quarter	-0.17	-0.15	-0.02	13
		mid	-0.25	-0.23	-0.02	8

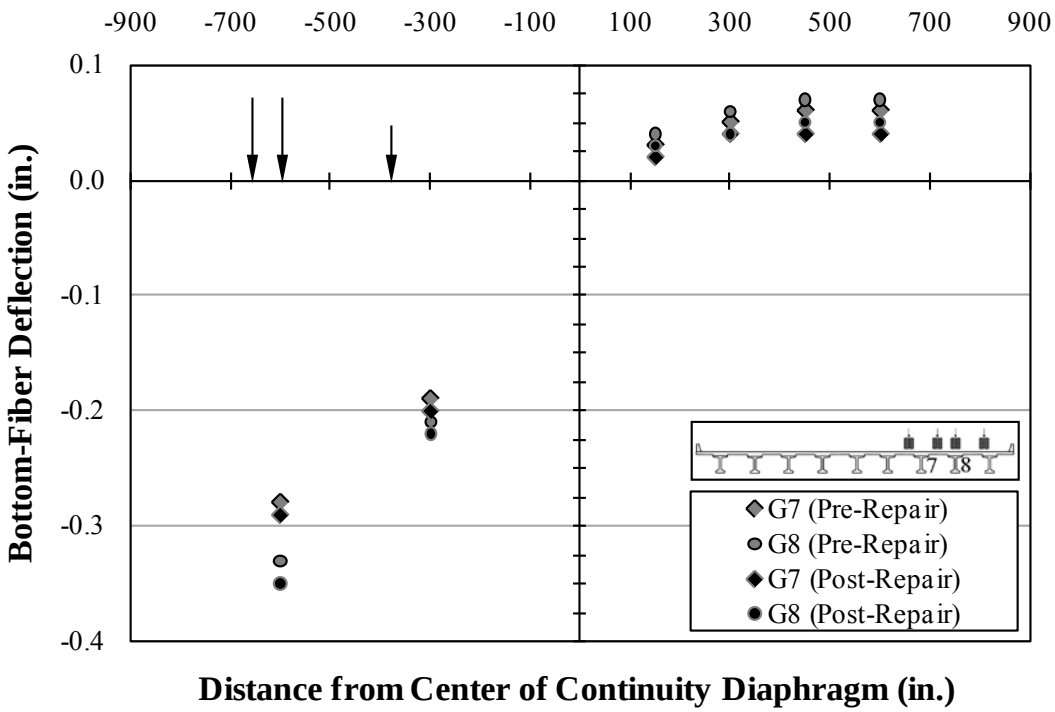

Figure K.12: Deflections—C1

Table K.3: Deflections—C1

Span	Girder	Location (span)	Post-Repair (in.)	Pre-Repair (in.)	Diff. (in.)	Percent Diff. (%)
10	7	mid	-0.29	-0.28	-0.01	4
		quarter	-0.20	-0.19	-0.01	5
	8	mid	-0.35	-0.33	-0.02	6
		quarter	-0.22	-0.21	-0.01	5
11	7	quarter	0.04	0.05	-0.01	20
		mid	0.04	0.06	-0.02	40
	8	quarter	0.04	0.06	-0.02	40
		mid	0.05	0.07	-0.02	30

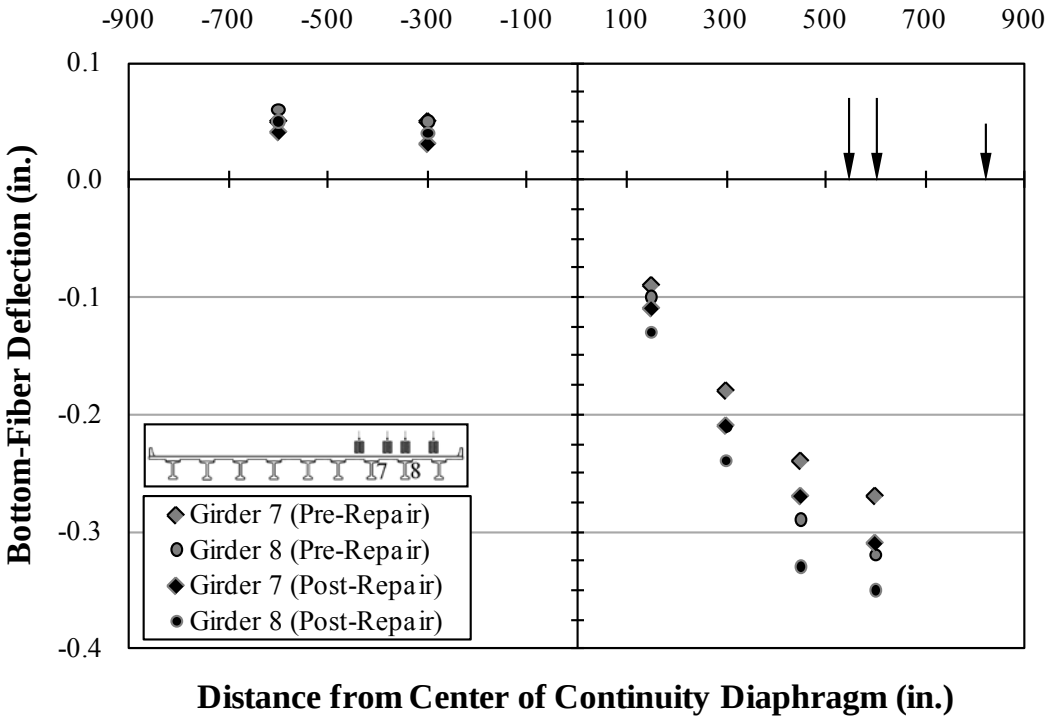

Figure K.13: Deflections—C9

Table K.4: Deflections—C9

Span	Girder	Location (span)	Post-Repair (in.)	Pre-Repair (in.)	Diff. (in.)	Percent Diff. (%)
10	7	mid	0.04	0.05	-0.01	20
		quarter	0.03	0.05	-0.02	50
	8	mid	0.05	0.06	-0.01	20
		quarter	0.04	0.05	-0.01	20
11	7	quarter	-0.21	-0.18	-0.03	15
		mid	-0.31	-0.27	-0.04	14
	8	quarter	-0.24	-0.21	-0.03	13
		mid	-0.35	-0.32	-0.03	9

During the post-repair load tests, the measured downward deflections of the loaded span were increased while the upward deflections of the unloaded span were decreased when compared to pre-repair measurements. This behavior could be attributed to the false support of the loaded span acting as an active load-bearing support during the pre-repair test but not during the post-repair test. If the false supports were acting as load-bearing supports, the loaded span would have a shorter effective span length. The post-repair downward deflections of the loaded span could have been larger due to an increased effective span length causing a decrease in apparent stiffness when compared to the pre-repair test conditions.

The post-repair upward deflections of the non-loaded span could have been smaller due to the bent becoming the only active support during post-repair testing. If the false support acted as an active support during pre-repair testing, that support could have shifted the inflection point further from the main support, which could result in greater upward deflections being measured in the non-loaded span, when compared to the post-repair conditions that had just one true support condition at the bent.

K.5.2 Crack-Opening Displacements—Multiposition Load Testing

Truck positions that resulted in crack openings during pre- and post-repair multiposition load testing were analyzed to assess bearing pad effects on pre-repair damaged region behavior. Truck position locations are described in Section 4.4 of this report. During both pre- and post-repair testing, Stop Position 4 had the greatest effect on the Span 10 crack openings, and Stop Position 7 had the greatest effect on the Span 11 crack openings. The pre- and post-repair crack-opening displacements measured for Stop Positions A4, A7, C4, and C7 are presented in Figures K.14–K.17 and Table K.5. The arrows in the figures represent the position of the wheel loads on the bridge.

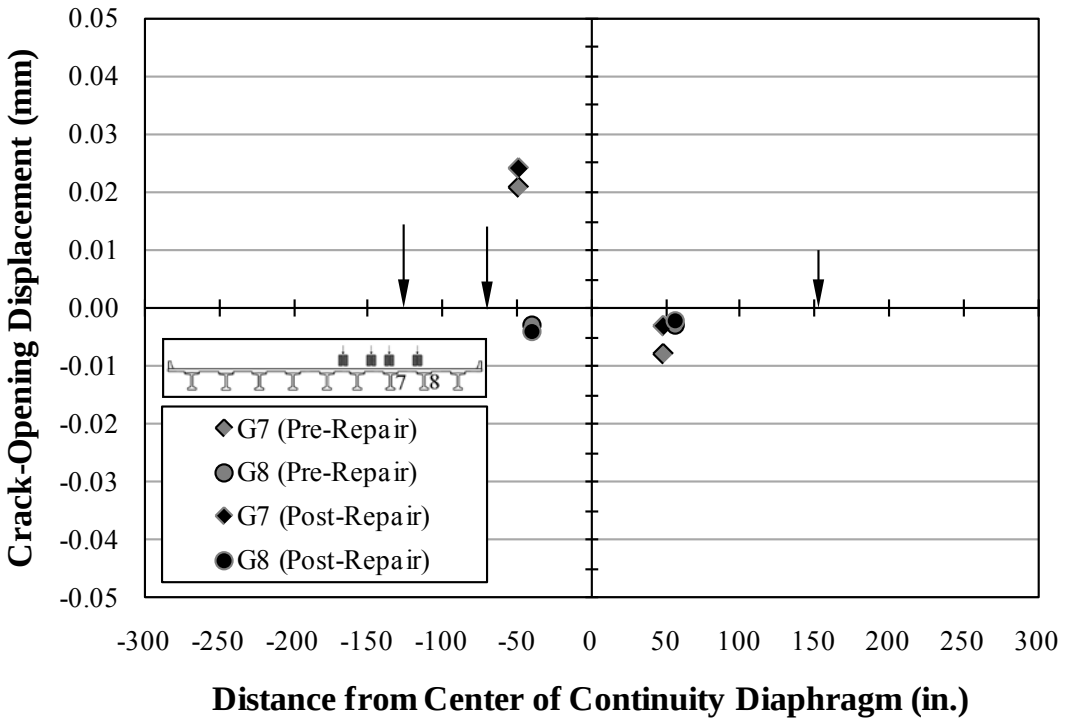

Figure K.14: Crack-opening displacements—pre- and post-repair—A4

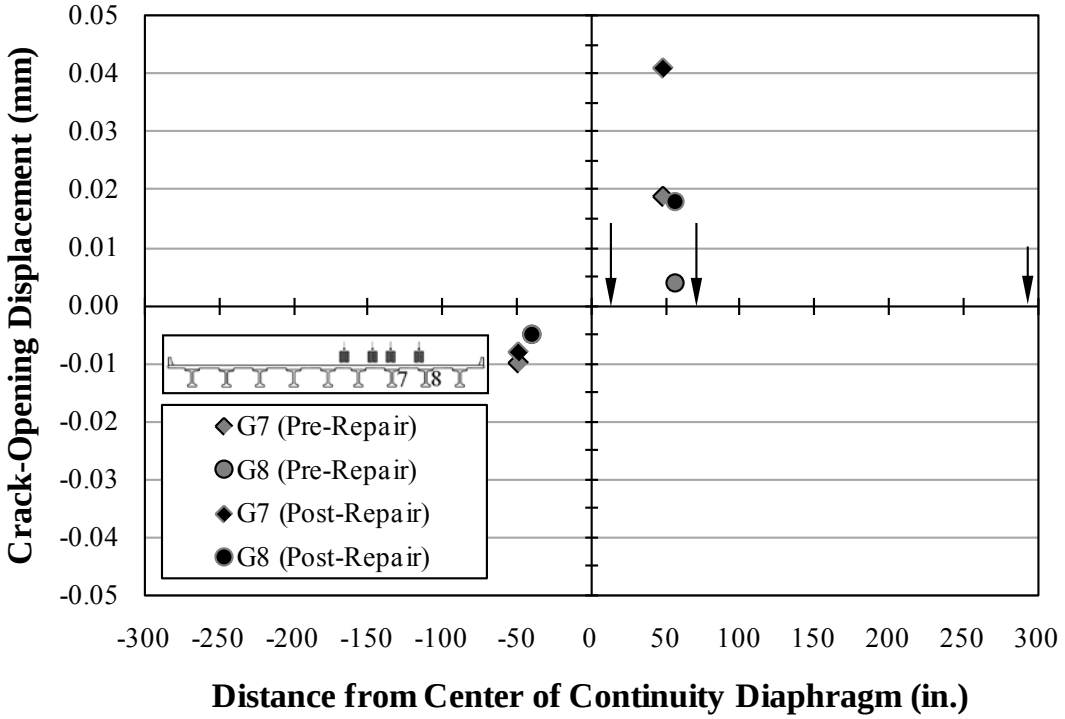

Figure K.15: Crack-opening displacements—pre- and post-repair—A7

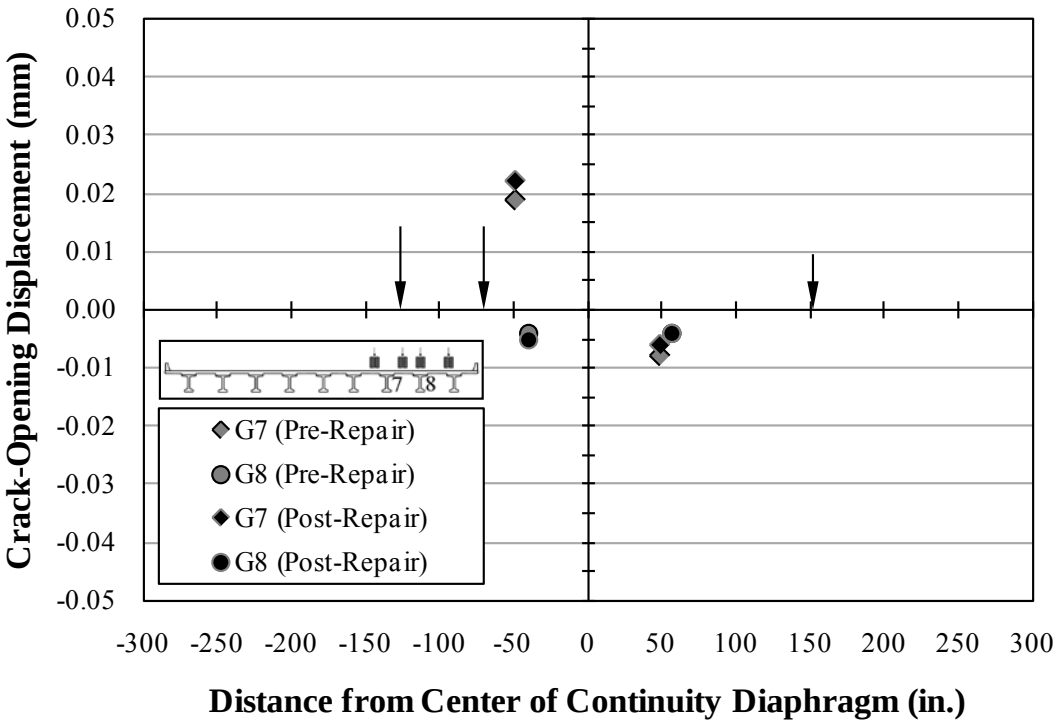

Figure K.16: Crack-opening displacements—pre- and post-repair—C4

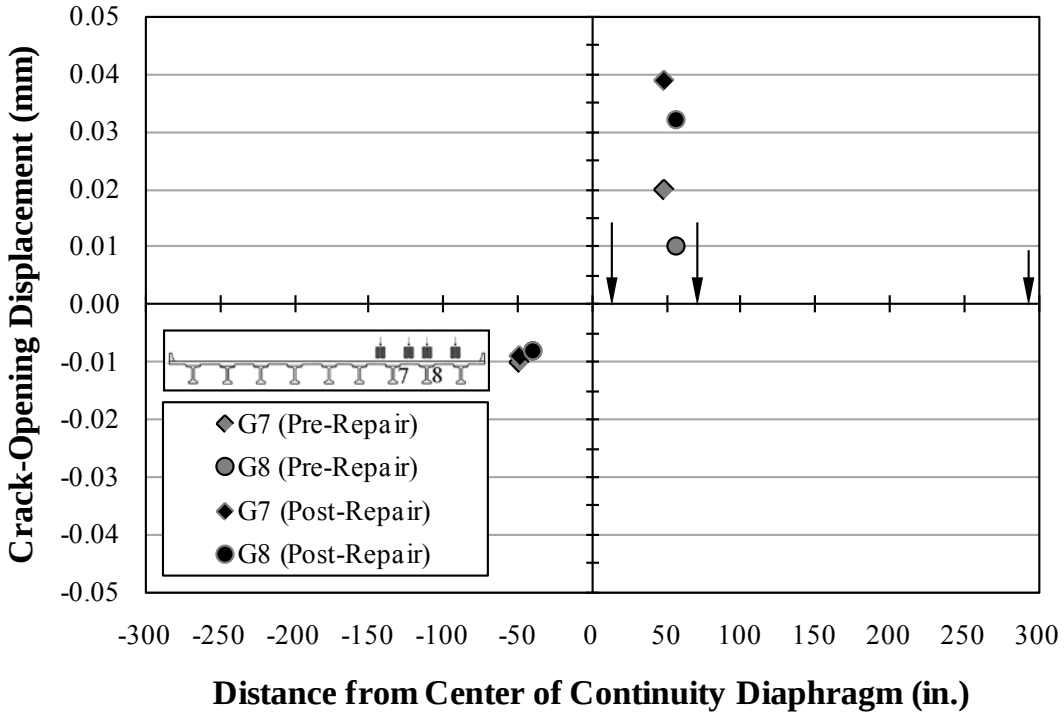

Figure K.17: Crack-opening displacements—pre- and post-repair—C7

Table K.5: Bearing pad effects—crack-opening displacements

Girder	Span	*Pre-* or Post-Repair	Crack-Opening Displacement (mm) – closing + opening			
			A4	A7	C4	C7
7	10	*Pre-*	0.021	-0.010	0.019	-0.010
		Post-	0.024	-0.008	0.022	-0.009
	11	*Pre-*	-0.008	**0.019**	-0.008	**0.020**
		Post-	-0.003	**0.041**	-0.006	**0.039**
8	10	*Pre-*	-0.003	-0.005	-0.004	-0.008
		Post-	-0.004	-0.005	-0.005	-0.008
	11	*Pre-*	-0.003	**0.004**	-0.004	**0.010**
		Post-	-0.002	**0.018**	-0.004	**0.032**

Notes: Measurements presented in **bold** represent the crack openings with the greatest difference between pre- and post-repair testing
1 in. = 25.4 mm

The crack-opening displacements measured in Span 10 were similar for both pre- and post-repair testing, but the crack-opening displacements measured in Span 11 in response to the Stop Position 7 load condition of the post-repair test increased in comparison to the crack-opening displacements measured in response to the same load condition during pre-repair testing. This behavior corresponds with the Span 10 bearing pads being partially removed prior to pre-repair testing, and the Span 11 bearing pads being under enough pressure to prevent any removal prior to pre-repair testing. It is apparent that girder contact with the false support bearing pads under Span 11 resulted in additional support conditions that affected pre-repair measurements.

K.5.3 Surface Strains

Truck positions that resulted in tension strains measured within damaged regions during pre- and post-repair multiposition load testing were analyzed to assess bearing pad effects on pre-repair damaged region behavior. During both pre- and post-repair testing, Stop Position 4 had the greatest effect on the Span 10 damaged region tension strains, and Stop Position 7 had the greatest effect on the Span 11 damaged region tension strains. The cross-section locations that contain the most sensors near the false support locations are Section 1 in Span 10 and Section 4

in Span 11. Stop Positions A4, A7, C4, and C7 of pre- and post-repair testing have been analyzed to assess the bearing pad effects exhibited by bottom-fiber strains as well as strain profiles at Sections 1 and 4.

It should be noted that some of the concrete strain gages from the pre-repair tests that were covered during the FRP repair had become defective and were discontinued for the post-repair tests. At the locations of discontinued sensors, strain gages were installed on the surface of the FRP reinforcement. The comparison of pre-repair concrete strains and post-repair FRP strains may not be appropriate for analyzing bearing pad effects.

The bottom-fiber strains measured in response to truck position A4 are shown in Figure K.18. The strains measured within the Section 1 cross section of Girders 7 and 8 in response to truck position A4 are shown in Figures K.19 and K.20 respectively.

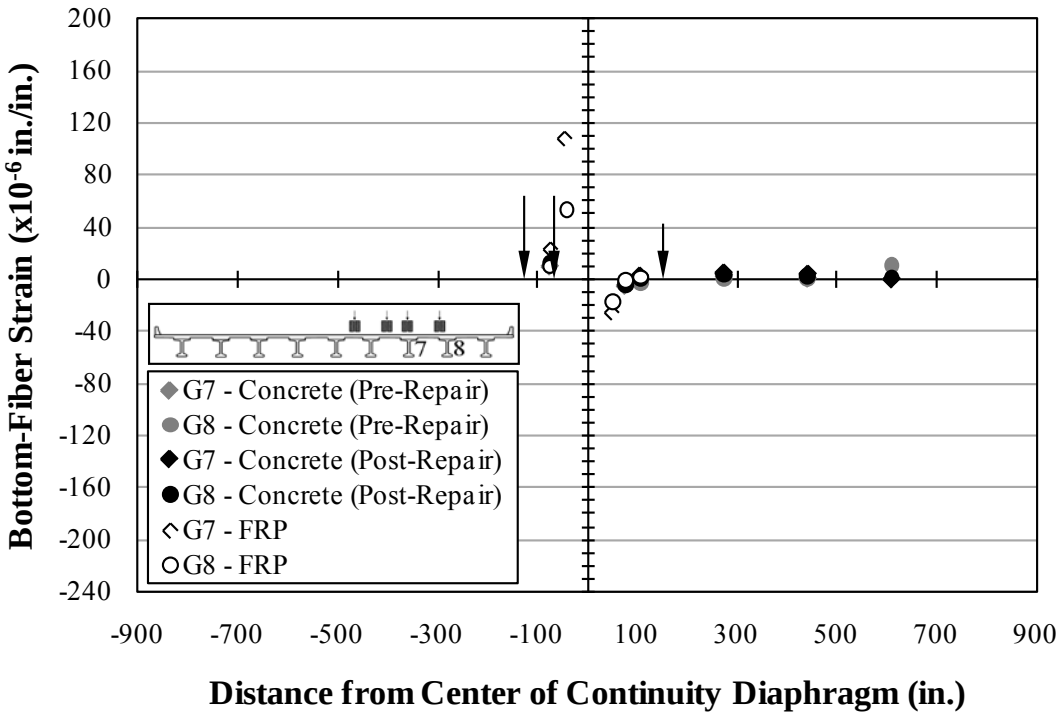

Figure K.18: Bottom-fiber strain—A4

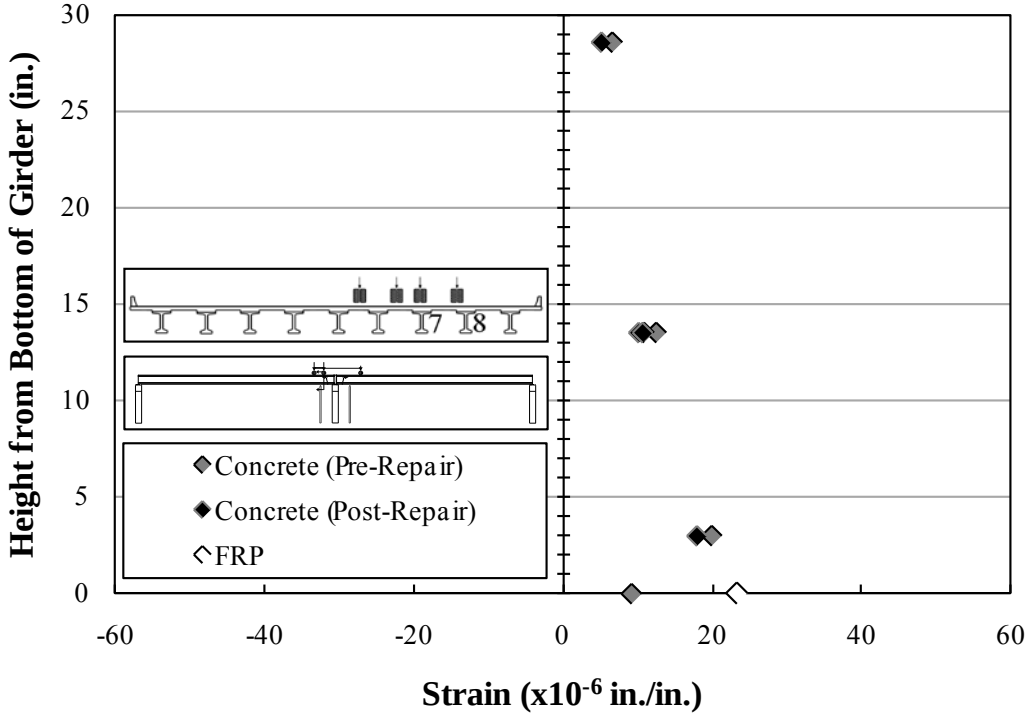

Figure K.19: Strain profile—Girder 7—Section 1—A4

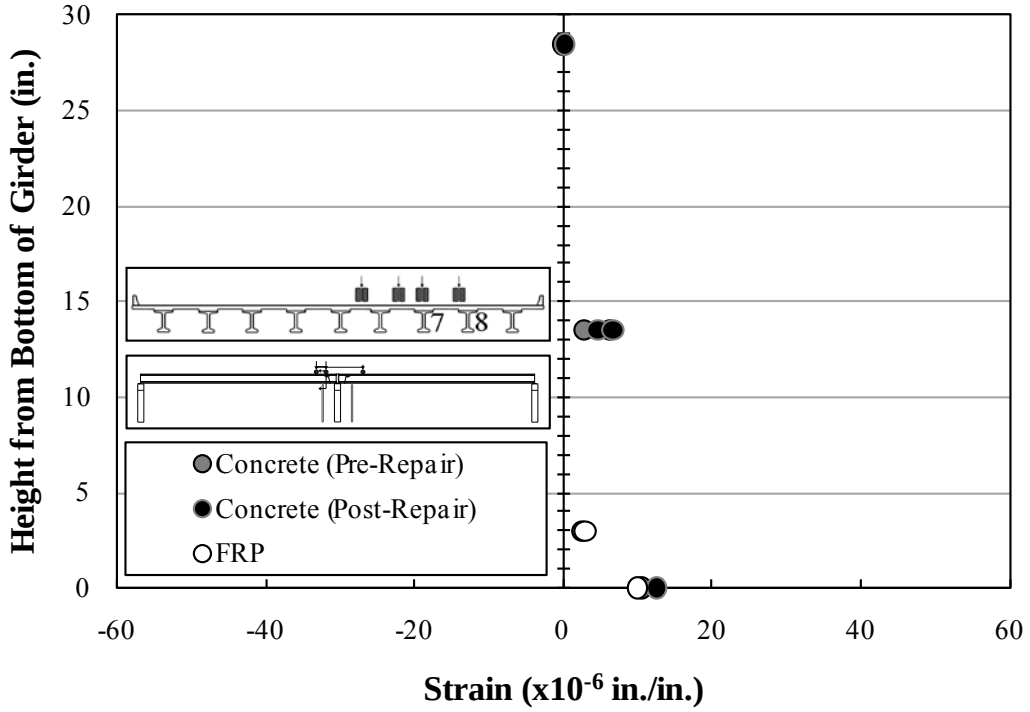

Figure K.20: Strain profile—Girder 8—Section 1—A4

The bottom-fiber strains measured in response to truck position C4 are shown in Figure K.21. The strains measured within the Section 1 cross section of Girders 7 and 8 in response to truck position C4 are shown in Figures K.22 and K.23 respectively.

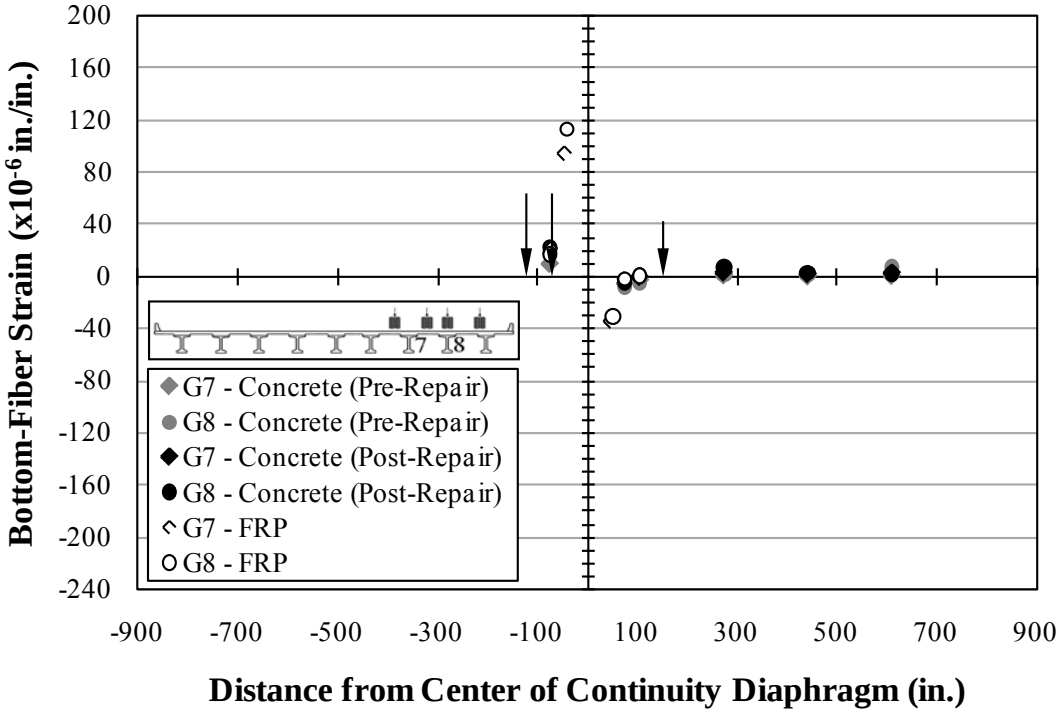

Figure K.21: Bottom-fiber strain—C4

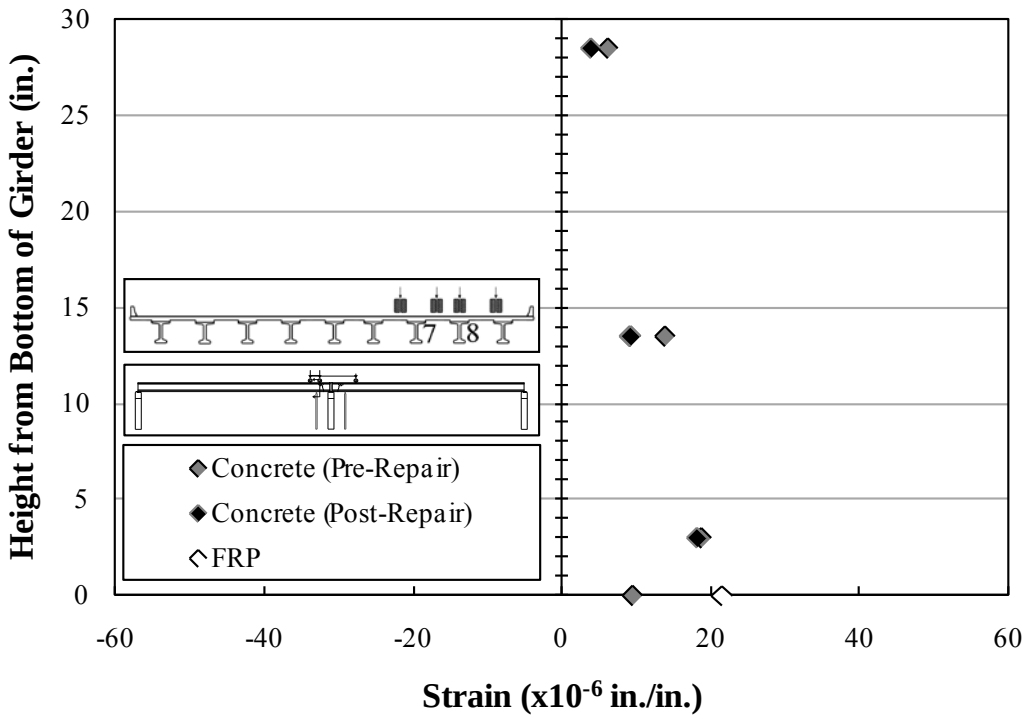

Figure K.22: Strain profile—Girder 7—Section 1—C4

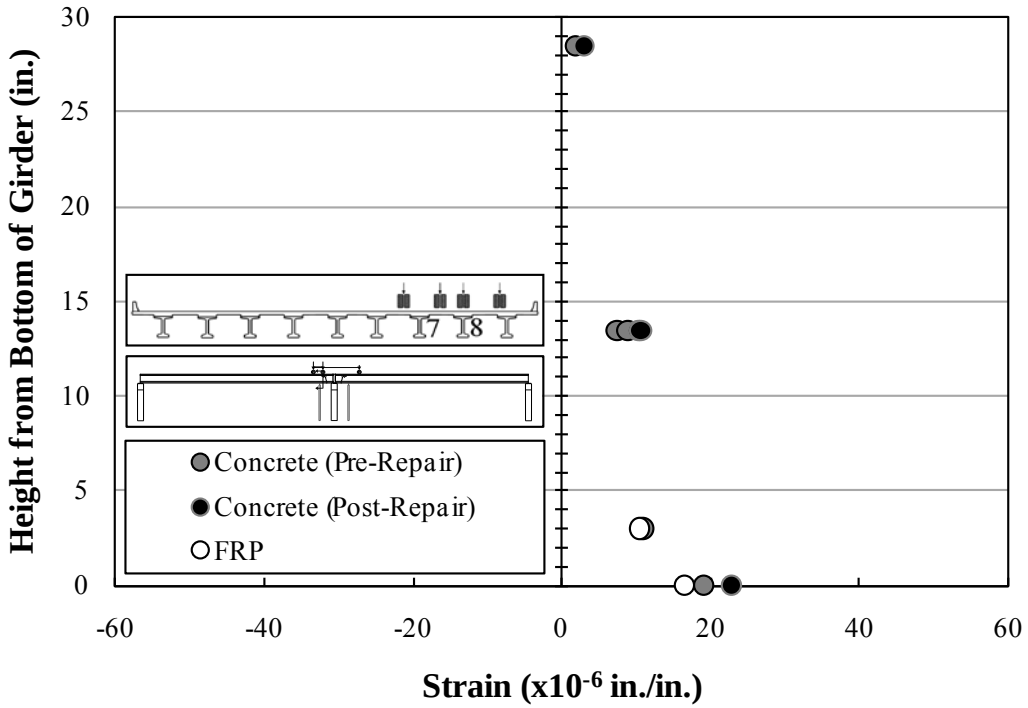

Figure K.23: Strain profile—Girder 8—Section 1—C4

The bottom-fiber strains measured in response to truck position A7 are shown in Figure K.24. The strains measured within the Section 4 cross section of Girders 7 and 8 in response to truck position A7 are shown in Figures K.25 and K.26 respectively.

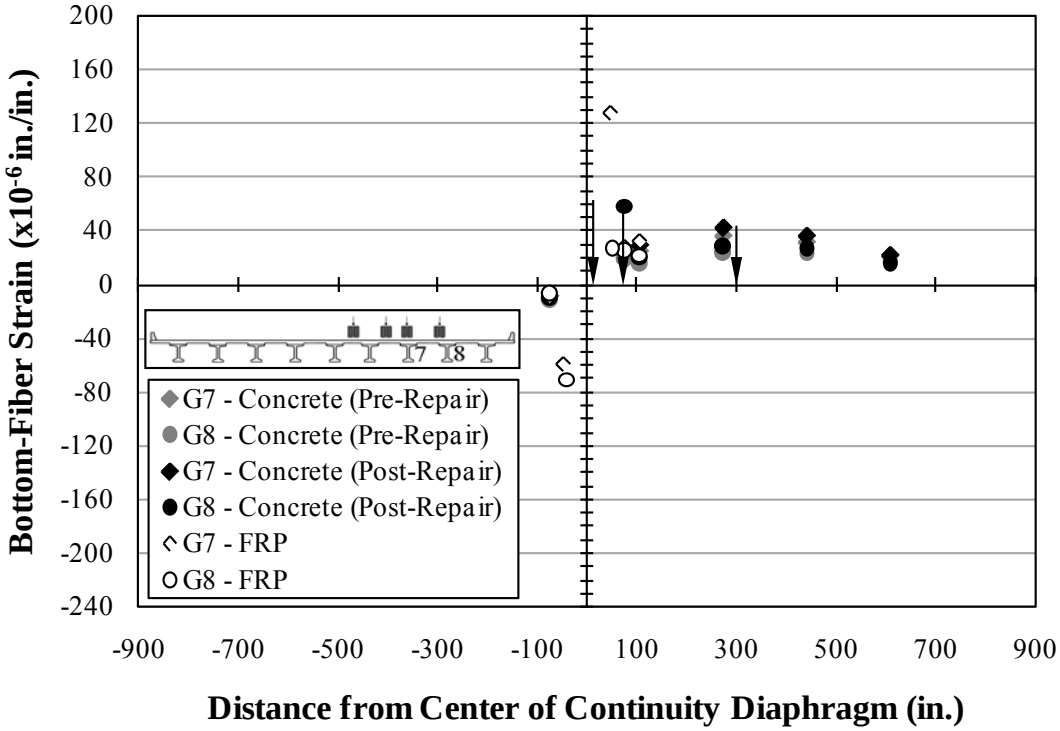

Figure K.24: Bottom-fiber strain—A7

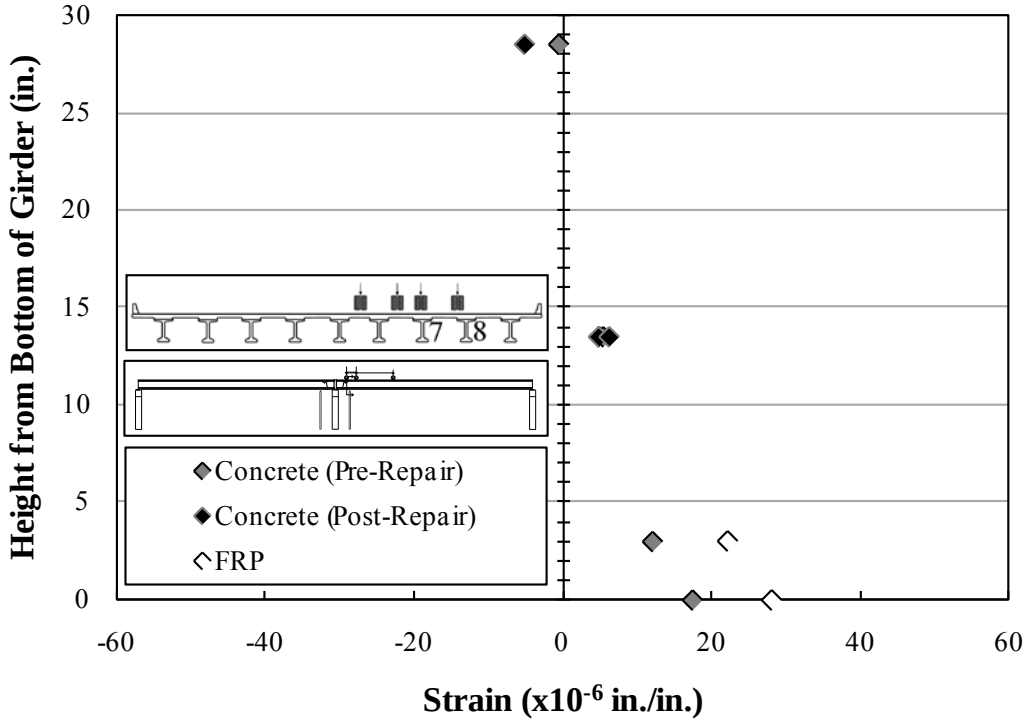

Figure K.25: Strain profile—Girder 7—Section 4—A7

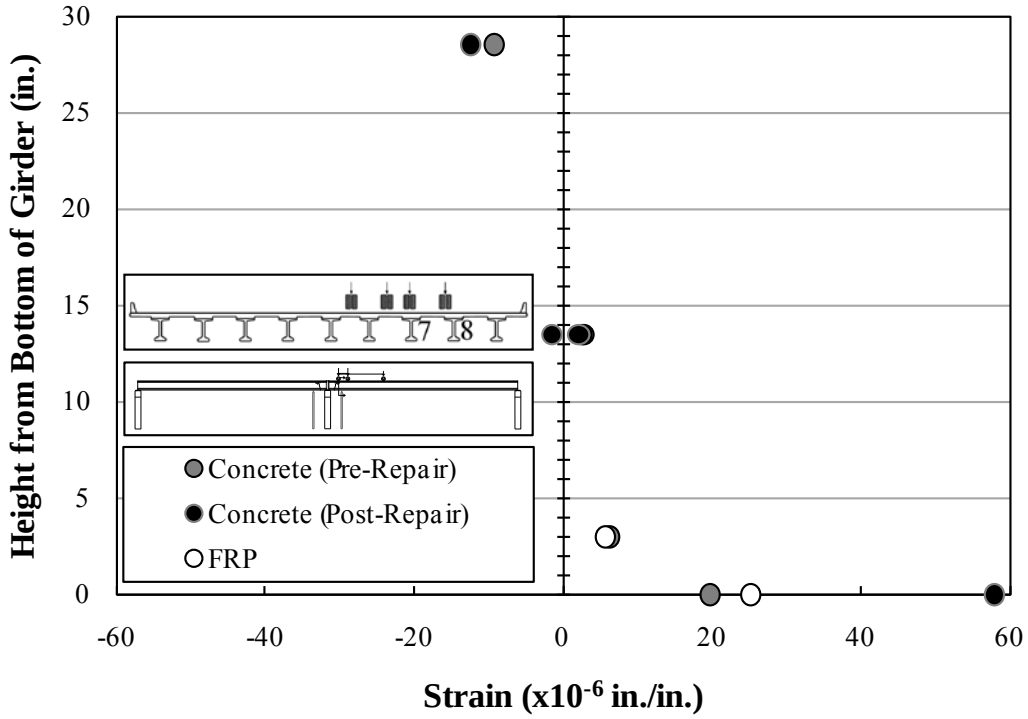

Figure K.26: Strain profile—Girder 8—Section 4—A7

The bottom-fiber strains measured in response to truck position C7 are shown in Figure K.27. The strains measured within the Section 4 cross section of Girders 7 and 8 in response to truck position C7 are shown in Figures K.28 and K.29 respectively.

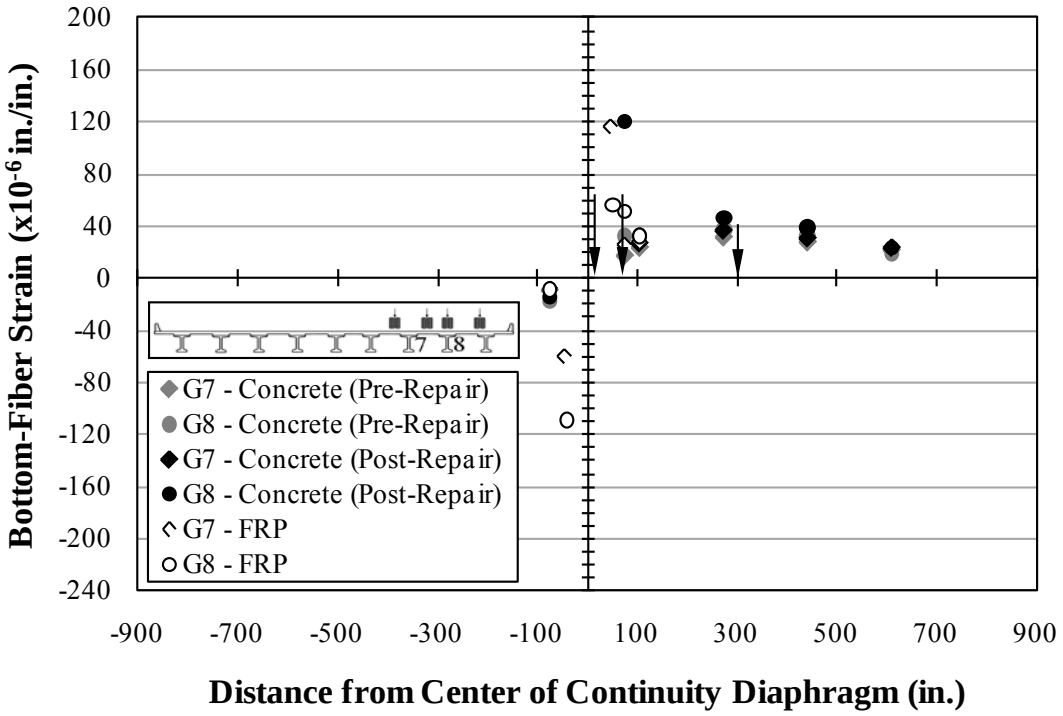

Figure K.27: Bottom-fiber strain—C7

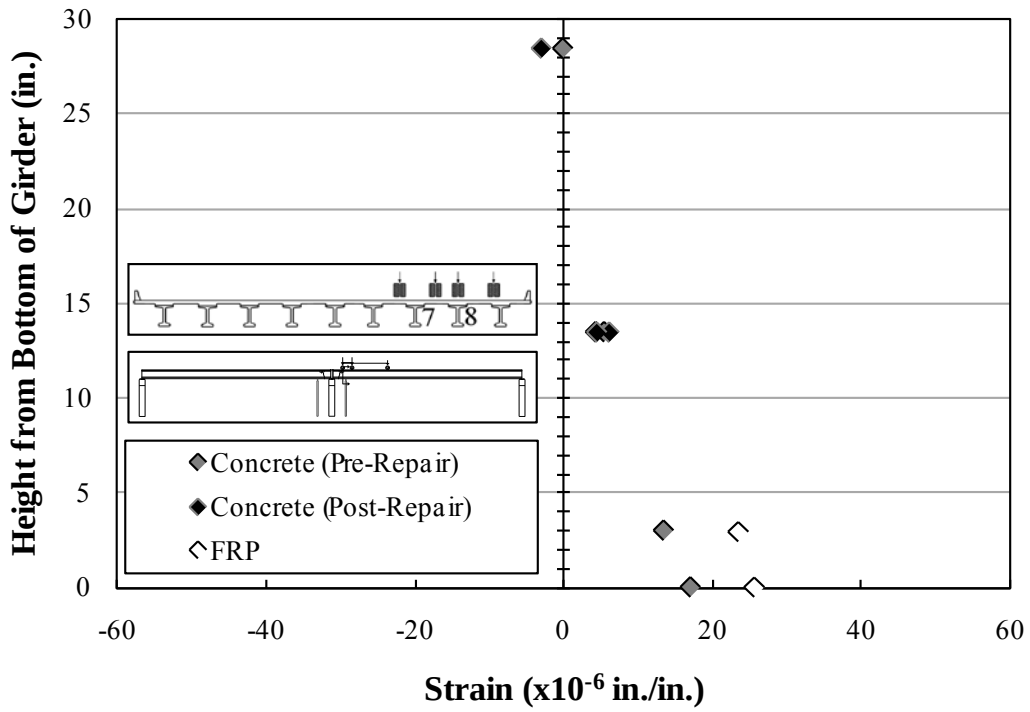

Figure K.28: Strain profile—Girder 7—Section 4—C7

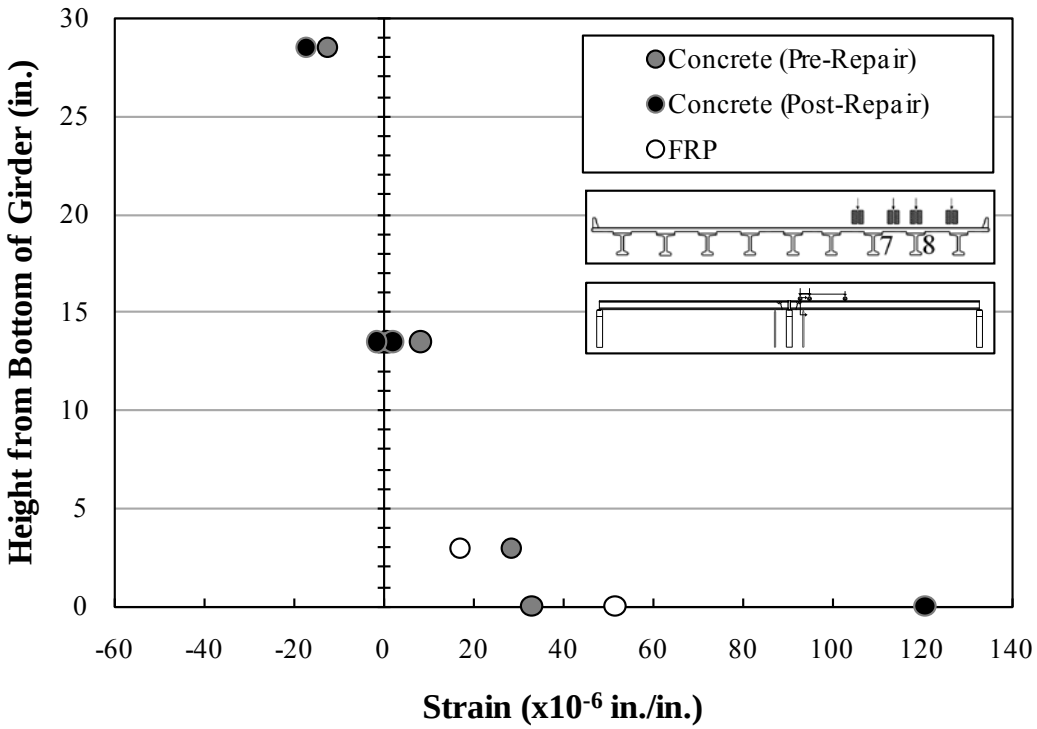

Figure K.29: Strain profile—Girder 8—Section 4—C7

When comparing the pre- and post-repair test measurements, sensors located near the bottom of Section 4 cross sections experienced a greater increased tension demand during post-repair testing in response to truck positions A7 and C7 (Span 11—load scenarios) than the sensors located near the bottom of Section 1 cross sections experienced in response to truck positions A4 and C4 (Span 10—load scenarios).

K.5.4 Superposition Deflections

Pre-and post-repair superposition deflection measurements have also been analyzed to assess whether the bearing pads had an effect on pre-repair bridge behavior. Measured superposition deflections (A1 and A9) are shown in Figure K.30 and Table K.6. Predicted superposition deflections (A1 + A9) are shown in Figure K.31 and Table K.7

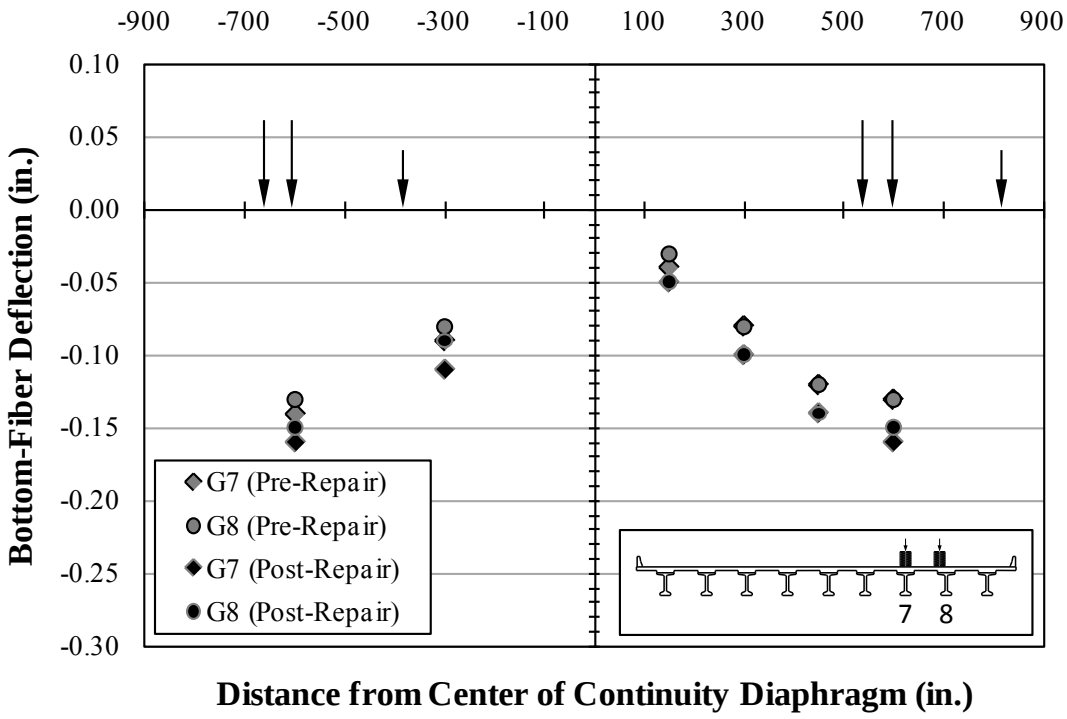

Figure K.30: Deflections—superposition—A1 and A9

Table K.6: Deflections—superposition—A1 and A9

Span	Girder	Location *from Bent 11*	Post-Repair (in.)	Pre-Repair (in.)	Diff. (in.)	Percent Diff. (%)
10	7	midspan	-0.16	-0.14	-0.02	13
		quarterspan	-0.11	-0.09	-0.02	20
	8	midspan	-0.15	-0.13	-0.02	14
		quarterspan	-0.09	-0.08	-0.01	10
11	7	quarterspan	-0.10	-0.08	-0.02	22
		midspan	-0.16	-0.13	-0.03	21
	8	quarterspan	-0.10	-0.08	-0.02	22
		midspan	-0.15	-0.13	-0.02	14

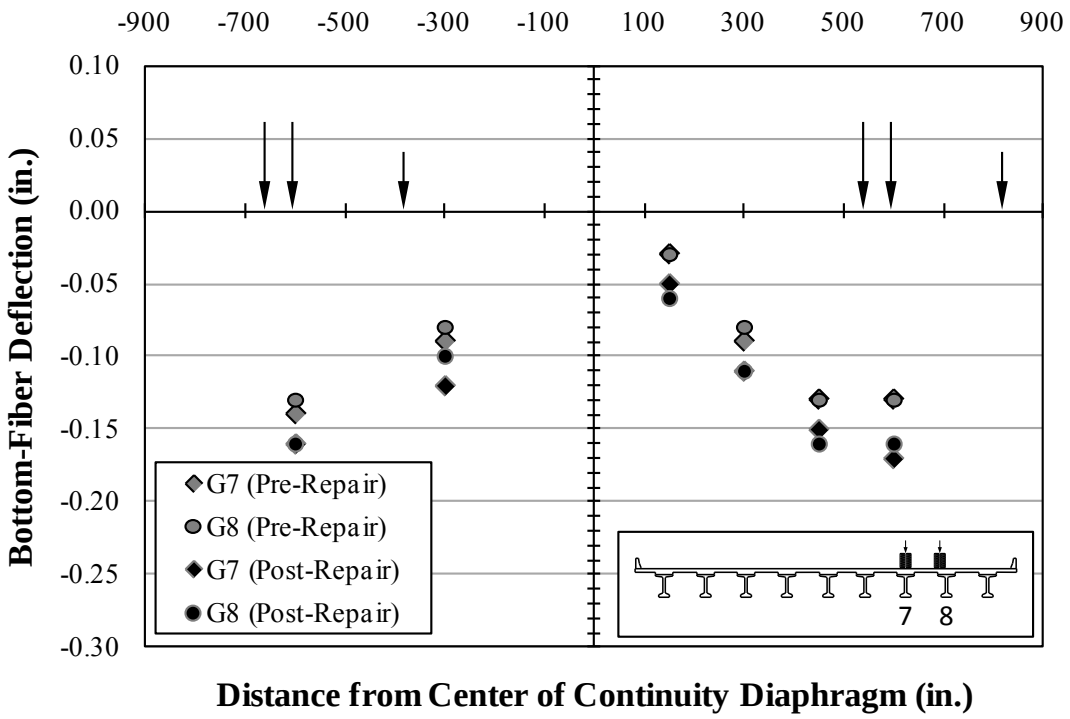

Figure K.31: Deflections—superposition—A1 + A9

Table K.7: Deflections—superposition—A1 + A9

Span	Girder	Location *from Bent 11*	Post-Repair (in.)	Pre-Repair (in.)	Diff. (in.)	Percent Diff. (%)
10	7	midspan	-0.16	-0.14	-0.02	13
		quarterspan	-0.12	-0.09	-0.03	30
	8	midspan	-0.16	-0.13	-0.03	21
		quarterspan	-0.10	-0.08	-0.02	20
11	7	quarterspan	-0.11	-0.09	-0.02	20
		midspan	-0.17	-0.13	-0.04	27
	8	quarterspan	-0.11	-0.08	-0.03	30
		midspan	-0.16	-0.13	-0.03	21

Greater downward deflections were measured for all of the post-repair measured superposition deflections compared to the pre-repair measurements. These greater deflections support the conclusion that a decrease in apparent stiffness was observed during the post-repair tests. The measured superposition deflections of Span 11 were observed to result in greater differences between pre- and post-repair measurements compared to Span 10 deflections. This behavior further supports the conclusion that the bearing pad conditions of Span 11 had a greater effect on pre-repair bridge behavior than the bearing pad conditions of Span 10.

K.6 BEARING PAD EFFECTS

The bearing pads that remained in place during the pre-repair tests appear to have increased the apparent stiffness of the bridge structure during pre-repair testing. Span 10 bearing pads were removed with some success prior to pre-repair testing, but Span 11 bearing pads were not removed and only had holes drilled into them to reduce effective stiffness. All bearing pads were removed during the FRP reinforcement installation process and were not replaced prior to post-repair testing.

During comparison of pre- and post-repair measurements, the Span 10 truck positions were observed to result in more similar pre- and post-repair measurements than the Span 11 truck positions. Increased deflections, crack opening displacements, and bottom-fiber tensile strains indicate a decrease in apparent stiffness between conducting pre-repair and post-repair testing. For these reasons, direct comparisons of pre-repair and post-repair behavior are not useful to accurately gauge the effectiveness of the FRP repair.

Appendix L

DATA ACQUISITION CHANNEL LAYOUT

Table L.1: Data acquisition channels—crack-opening displacement gages

MEGADAC Information			Sensor Description and Location				
Channel	**Tag**	**Units**	**Type**	**Span**	**Girder**	**Location ID**	**COD ID**
70	CO7_10	mm	COD	10	7	NA	C
68	CO8_10				8	NA	A
71	CO7_11			11	7	NA	D
69	CO8_11				8	NA	B

Notes: AD-1 808FB-1 card used with gain of 100 for all Channels (64-71)
Card set for full-bridge measurements for Channels 68-71

Table L.2: Data acquisition channels—deflectometers

MEGADAC Information			Sensor Description and Location				
Channel	**Tag**	**Units**	**Type**	**Span**	**Girder**	**Location ID**	**DEFL ID**
65	D7_10_A	in.	deflectometer	10	7	A	J
64	D7_10_B					B	I
67	D8_10_A				8	A	L
66	D8_10_B					B	K
0	D7_11_C			11	7	C	A
1	D7_11_D					D	B
2	D7_11_E					E	C
3	D7_11_F					F	D
4	D8_11_C				8	C	E
5	D8_11_D					D	F
6	D8_11_E					E	G
7	D8_11_F					F	H

Notes: AD-1 808FB-1 card used with gain of 100 for all Channels (64–71)
Card set for quarter-bridge measurements for Channels 64–67
AD808QB card used with gain of 100 for all Channels (0–7)

Table L.3: Data acquisition channels—strain gages—Span 10

MEGADAC Information			Sensor Description and Location				
Channel	**Tag**	**Units**	**Type**	**Span**	**Girder**	**Cross Section**	**Location ID**
18	S7_10_1V	$x10^{-6}$ in./in.	concrete	10	7	1	V
17	S7_10_1W		concrete				W
14	S7_10_1X		concrete				X
16	S7_10_1Y		concrete				Y
12	S7_10_2V		concrete			2	V
11	S7_10_2W		concrete				W
8	S7_10_2X		concrete				X
10	S7_10_2Y		concrete				Y
9	F7_10_2Z		FRP				Z
30	S8_10_1V		concrete		8	1	V
29	S8_10_1W		concrete				W
26	S8_10_1X		concrete				X
28	S8_10_1Y		concrete				Y
24	S8_10_2V		concrete			2	V
23	S8_10_2W		concrete				W
20	S8_10_2X		concrete				X
22	F8_10_2Y		FRP				Y
21	F8_10_2Z		FRP				Z
15	F7_10_1M		FRP		7	1	M
27	S8_10_1M		concrete		8	1	M
31	F8_10_1M		FRP				M
13	F7_10_CK		FRP–CK		7	Crack	CK
19	F8_10_CK		FRP–CK		8	Crack	CK

Notes: Three AD808QB cards used with gain of 100 for all Channels 8–15, 16–23, and 24–31

Table L.4: Data acquisition channels—strain gages—Span 11

MEGADAC Information			Sensor Description and Location				
Channel	Tag	Units	Type	Span	Girder	Cross Section	Location ID
36	S7_11_3V	$x10^{-6}$ in./in.	concrete	11	7	3	V
35	S7_11_3W		concrete				W
32	S7_11_3X		concrete				X
34	S7_11_3Y		concrete				Y
33	S7_11_3Z		concrete				Z
42	S7_11_4V		concrete			4	V
41	S7_11_4W		concrete				W
38	S7_11_4X		concrete				X
40	S7_11_4Y		concrete				Y
48	S8_11_3V		concrete		8	3	V
47	S8_11_3W		concrete				W
44	S8_11_3X		concrete				X
46	F8_11_3Y		FRP				Y
45	S8_11_3Z		concrete				Z
54	S8_11_4V		concrete			4	V
53	S8_11_4W		concrete				W
50	S8_11_4X		concrete				X
52	F8_11_4Y		FRP				Y
25	F7_11_4M		FRP		7	4	M
56	S7_11_5M		concrete			5	M
39	F7_11_5M		FRP				M
57	S7_11_6M		concrete			6	M
58	S7_11_7M		concrete			7	M
59	S7_11_8M		concrete			8	M
51	S8_11_4M		concrete		8	4	M
49	F8_11_4M		FRP				M
60	S8_11_5M		concrete			5	M
55	F8_11_5M		FRP				M
61	S8_11_6M		concrete			6	M
62	S8_11_7M		concrete			7	M
63	S8_11_8M		concrete			8	M
37	F7_11_CK		FRP–CK		7	Crack	CK
43	F8_11_CK		FRP–CK		8	Crack	CK

Notes: Two AD884D cards used with gain of 500 for Channels 32–39 and 48–55
Two AD885D cards used with gain of 500 for Channels 40–47 and 56–63

Appendix M

STRAIN GAGE INSTALLATION PROCEDURE—FRP REINFORCEMENT

Strain Gage Installation Procedure—FRP Reinforcement Composite Material

Prepare FRP Surface

1. Mark area for gage.
2. Spray gaging area with degreaser.
3. Brush area with wire brush.
4. Smooth area with grinder if needed to remove irregularities, paint, or epoxy.
5. Continue to smooth with 220 grit sandpaper.
6. Blow loose dust from surface with compressed air.
7. Rinse area with isopropyl alcohol.
8. Sand lightly with 320 grit sandpaper.
9. Blow loose dust from surface with compressed air.
10. Rinse area with isopropyl alcohol.
11. Blot area with gauze sponges.
12. Rinse area thoroughly with clean water.
13. Blot area with gauze sponges.
14. Blow loose gauze from surface with compressed air.
15. Dry surface thoroughly (warming surface with heat gun may help).

Apply 100% solids epoxy

16. Place equal portions of PC-7 A and B on a flat surface using separate tools.
17. Mix PC-7 A and B together with putty knife.
18. Apply epoxy to gaging area, work into voids, and smooth with putty knife.
19. Allow epoxy to cure.
20. Sand surface initially with 220 grit sandpaper.
21. Blow loose particles from surface with compressed air.
22. Sand smooth with 320 grit sandpaper.
23. Blow loose particles from surface with compressed air.
24. Draw layout lines for gage location.

Apply Gage to Surface

1. Apply M-Prep A Conditioner with cotton.
2. Apply M-Prep 5A Neutralizer with cotton.
3. Dry surface thoroughly (warming surface with heat gun may help).
4. Carefully mount strain gage to glass plate with Cellophane Tape.
5. Remove the tape and gage from glass plate by lifting from gage side of tape
6. Tape gage at the desired location on FRP surface.
7. Peel tape and gage back to expose back of gage until clear of desired location by ½ in.
8. Apply 200 Catalyst-C to gage with a single stroke, allow to dry 1 minute
9. Apply M-Bond 200 just behind desired gage location
10. Apply gage to FRP surface, using thumb to spread M-Bond 200 the length of the gage.
11. Apply pressure for at least 1 minute
12. Wait at least 2 minutes to remove tape.
13. After at least 1 hour, apply M-Coat B Nitrile Rubber Coating and allow to dry.
14. Apply Mastic Tape.
15. Attach wire ends to mounted terminal strips.

Figure M.1: Strain gage installation—applying degreaser to gage location

Figure M.2: Strain gage installation—removal of surface irregularities

Figure M.3: Strain gage installation—initial surface cleaning

Figure M.4: Strain gage installation—clean surface prepared for solid epoxy

Figure M.5: Strain gage installation—application of solid epoxy

Figure M.6: Strain gage installation—epoxy surface

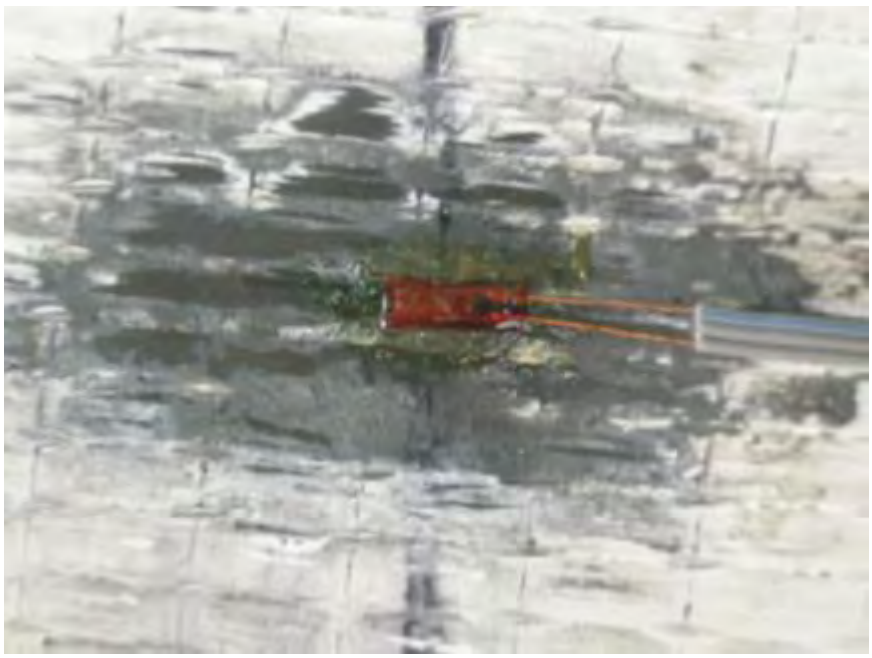

Figure M.7: Strain gage installation—rubber coating for moisture protection

Figure M.8: Strain gage installation—mastic tape for mechanical protection

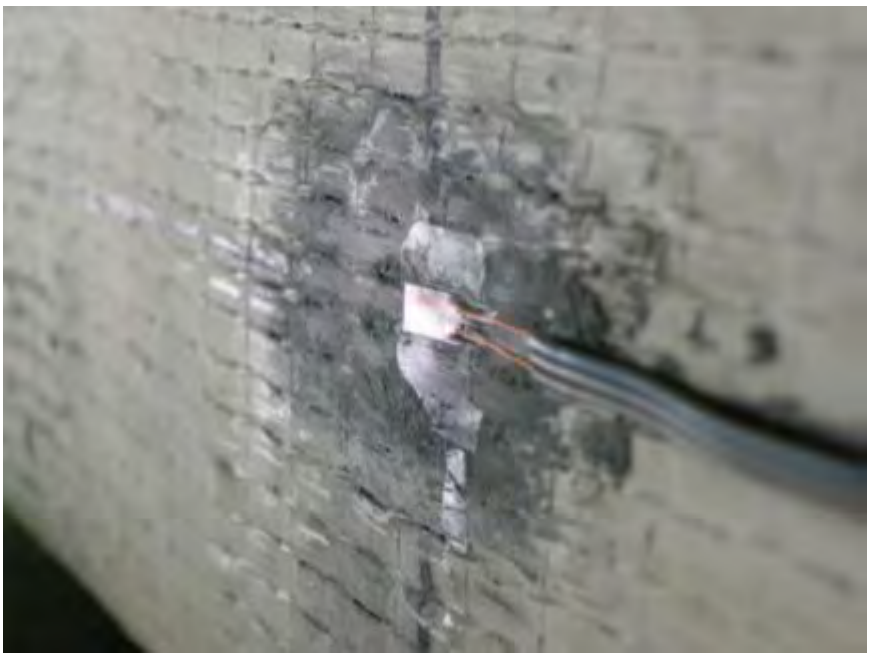

Figure M.9: Strain gage installation—gage application with thin epoxy

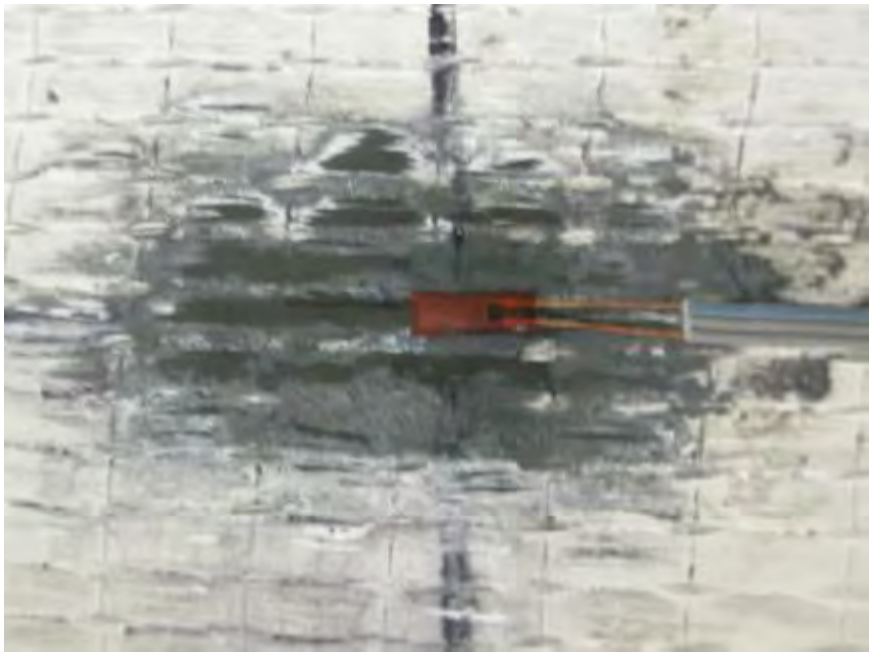

Figure M.10: Strain gage installation—gage applied to FRP reinforcement

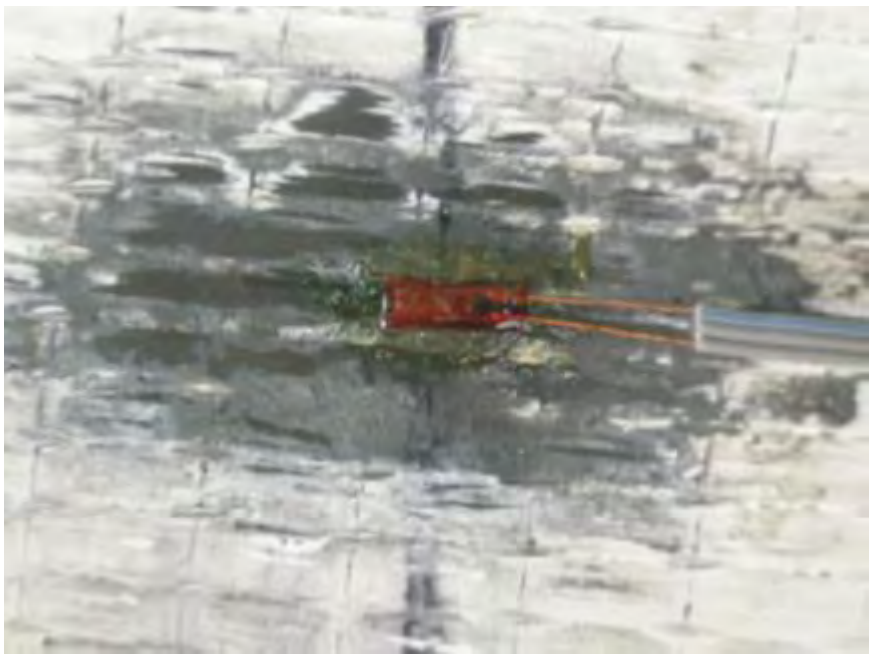

Figure M.11: Strain gage installation—rubber coating for moisture protection

Figure M.12: Strain gage installation—mastic tape for mechanical protection

Appendix N

FRP REINFORCEMENT DESIGN EXAMPLE

N.1 INTRODUCTION

An FRP reinforcement design example is presented in this appendix based on the material and dimensional properties of Northbound Spans 10 and 11 of I-565 and the FRP reinforcement system proposed for girder repair.

N.2 PRODUCT SELECTION

The Auburn University Highway Research Center (AUHRC) selected the Tyfo SCH-41 FRP laminate material (Fyfe 2010) as the reinforcement product for the proposed repair of Spans 10 and 11 on I-565 in Huntsville, Alabama. Material properties for this design are based on properties documented by the manufacturer, but samples should be prepared by the contractor responsible for the installation of the proposed reinforcement system for further testing to verify documented product performance.

N.3 STRENGTH-LIMIT-STATE DESIGN

After selecting an FRP reinforcement material, a reinforcement system can be designed to satisfy strength limit states with that material.

Strength-limit-state capacities and demands are determined in accordance with the American Association of State Highway and Transportation Officials *LRFD Bridge Design Specification* (AASHTO 2010), referred to as AASHTO LRFD within this report.

Limiting behavior expected of FRP reinforcement is determined in accordance with provisions presented by the American Concrete Institute (ACI) Committee 440.2R-08 *Guide for the Design and Construction of Externally Bonded FRP Systems for Strengthening Concrete Structures* (ACI Committee 440 2008), referred to as ACI 440.2R-08 within this report.

N.3.1 Critical Cross-Section Locations

Critical cross sections are specified at locations of reinforcement transition. The cross-section locations that have been determined to be the most critical within the girders of Northbound Spans 10 and 11 of I-565 are presented in Table N.1 and Figure N.1.

Table N.1: Critical cross-section locations

Location Reference	Critical Section	
	Interior Face of Bearing Pad (A-A)	Termination of Continuity Reinforcement (B-B)
from Girder End	6.5 in.	38 in.
from Diaphragm Centerline	14.5 in.	46 in.

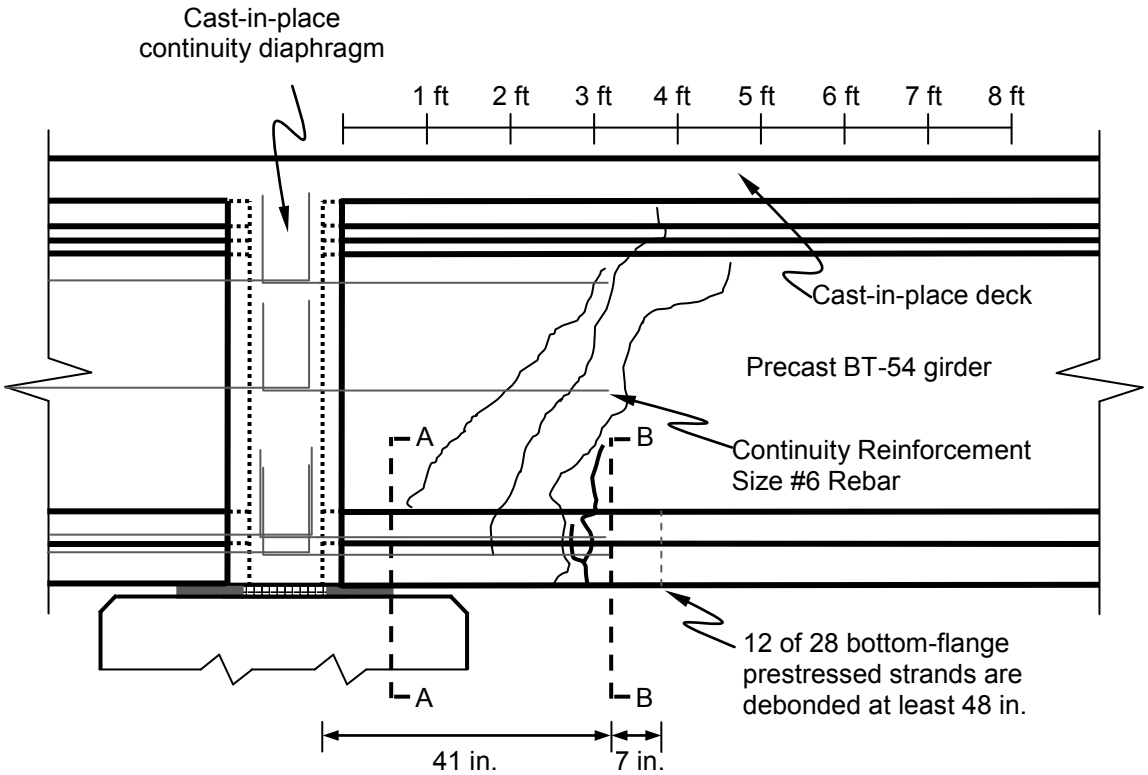

Figure N.1: Cracked girder with continuity reinforcement details (Barnes et al. 2006)

Analysis of test measurements, crack patterns, and documented reinforcement details provided evidence supporting the identification of two critical cross sections. The cross sections determined to be critical for the design of an FRP reinforcement system—similar to the FRP reinforcement system discussed in this report—include the cross section at the interior face of the bearing pad and the cross section at the termination of the mild steel continuity reinforcement.

Shear cracks within the web were observed near the interior face of the bearing pad, and flexural cracking was observed near the termination of the continuity reinforcement, as shown in Figure N.1. These critical cross sections have also been noted for a girder with an overlaying illustration of an example FRP reinforcement system with unknown number of layers and length of FRP reinforcement, as shown in Figure N.2.

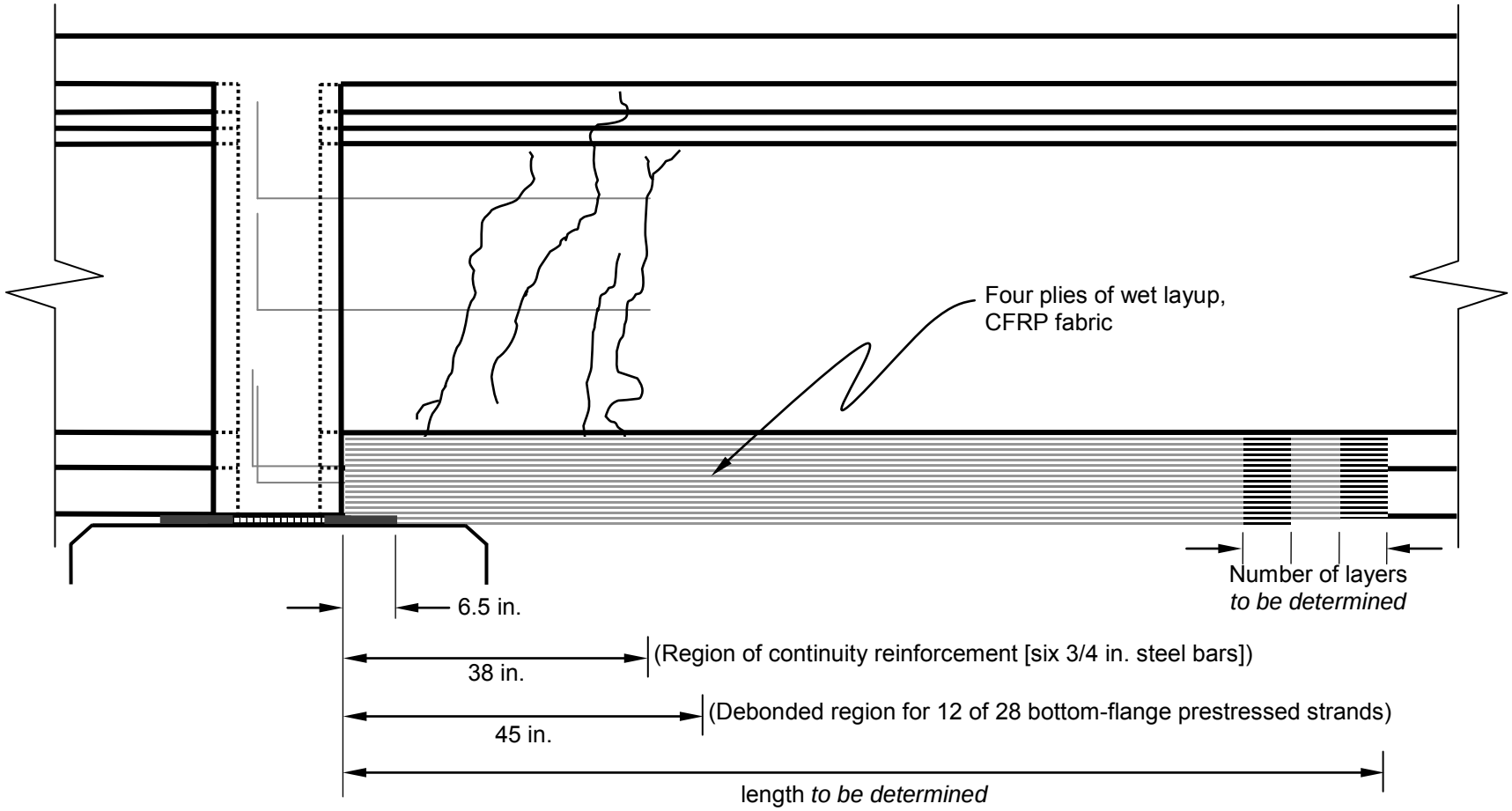

Figure N.2: Longitudinal configuration profile for FRP (adapted from Barnes et al. 2006)

The end regions of continuous sheets of reinforcement must be cut appropriately to account for support conditions. At the interior face of the bearing pad, FRP reinforcement cannot be installed along the bottom face of the girder, as shown in Figure N.3. At the termination of the continuity reinforcement, the FRP reinforcement can be installed to wrap around the entire perimeter of the tension flange, as shown in Figure N.4.

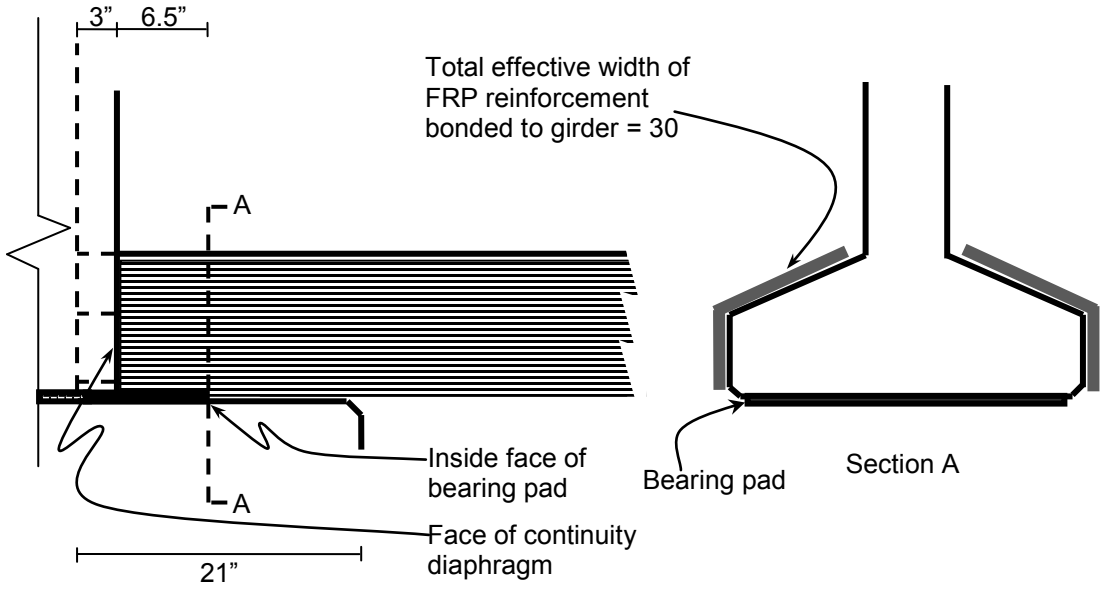

Figure N.3: Cross-sectional configuration of FRP—near diaphragm (Swenson 2003)

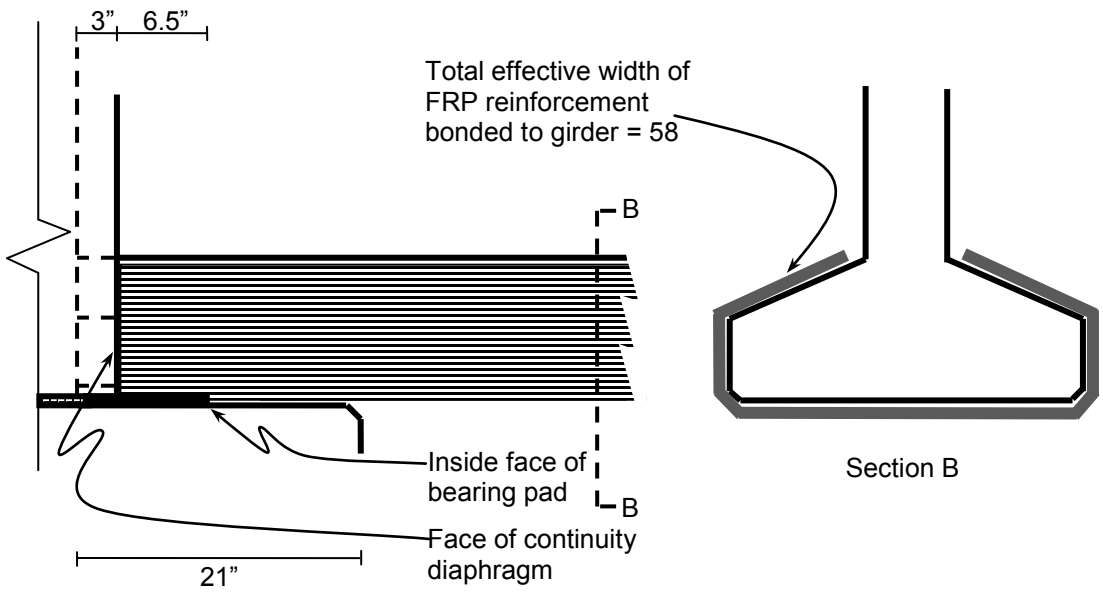

Figure N.4: Cross-sectional configuration of FRP—typical (Swenson 2003)

The cross section at the interior face of the bearing pad at the continuity diaphragm is located roughly 6.5 in. from the face of the diaphragm. This location is considered critical because it is a support condition and the bearing pad obstructs the ability to install FRP reinforcement around the entire tension flange, which also represents a reinforcement transition location. This is also the point of maximum shear force influence on the bottom flange of the girder.

FRP reinforcement installed between the interior face of the bearing pad and the face of the continuity diaphragm must be modified to allow the maximum possible amount of FRP reinforcement to extend to the face of the diaphragm. The interference from the girder bearing results in a decrease in the width of FRP that can be considered longitudinal reinforcement.

At the interior face of the bearing pad, it is appropriate to assume that the mild steel continuity reinforcement is effective longitudinal reinforcement for tension resistance as long as it is adequately developed on each side of the section. Due to cracked (or potentially cracked) conditions beyond the interior face of the bearing pad, it is also conservative and appropriate to assume that prestressed strands do not provide concrete precompression (for concrete shear resistance) or act as effective longitudinal reinforcement between the face of the diaphragm and the interior face of the bearing pad.

The cross section at the termination of the mild steel continuity reinforcement is located 38 in. from the face of the diaphragm. This location is considered critical because it represents the initiation of a region without longitudinal steel reinforcement that can safely be considered effective for tension resistance in response to shear or positive bending moment demands. Even if cracking is only present between this location and the face of the diaphragm, the short distance

between the cracks and this section makes it appropriate to assume that the prestressed strands do not provide precompression or act as effective longitudinal reinforcement at this cross-section location also. In this example girder, the FRP is the only bonded reinforcement that can be considered effective at this cross section.

N.3.2 Critical Load Conditions

The critical load conditions are those that result in maximum factored shear demand at the critical locations. The maximum shear demands (V_u) and the corresponding positive bending moment demands (M_u) for both critical locations are presented in Table N.2.

Table N.2: Critical load conditions

Load Effect	Critical Section	
	Interior Face of Bearing Pad (A-A)	Termination of Continuity Reinforcement (B-B)
V_u	242 kips	231 kips
M_u	1500 kip-in.	6000 kip-in.

The factored shear and moment demands were determined from graphical presentations of shear and moment demand presented by Swenson (2003). The factored shear demand diagram is presented in Figure N.5, and the factored moment demand diagram is presented in Figure N.6.

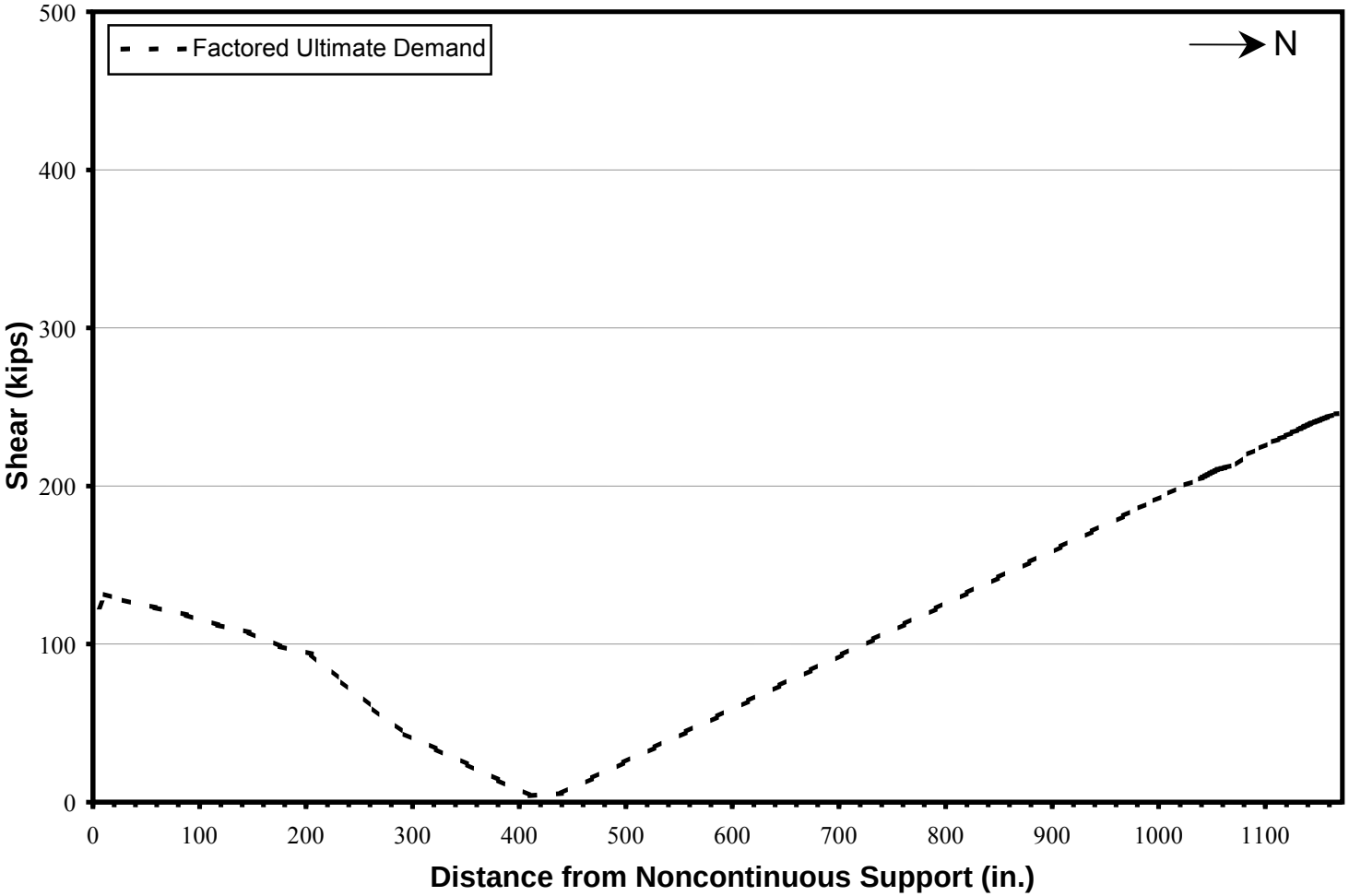

Figure N.5: Factored shear demand—simply supported (Swenson 2003)

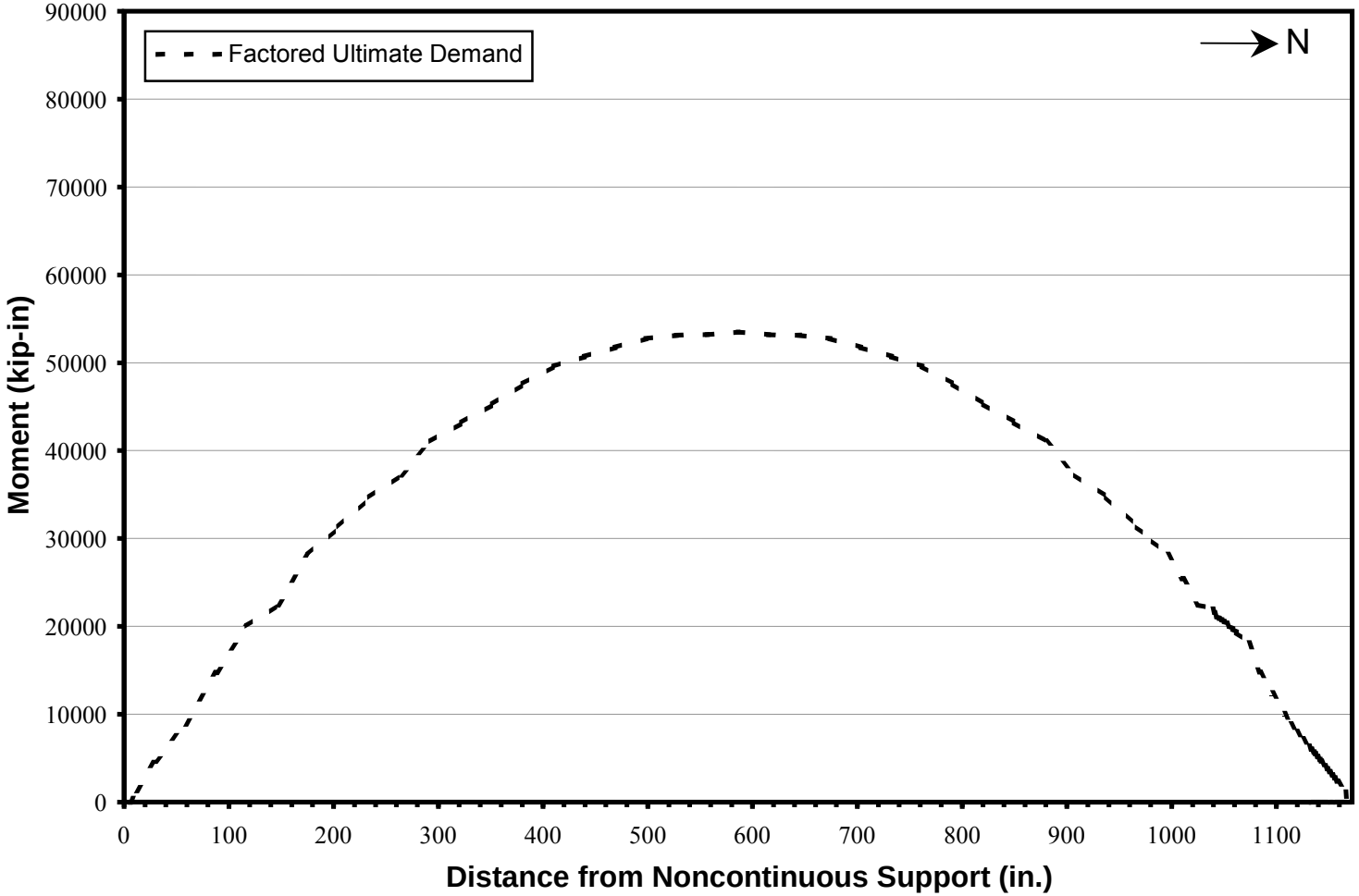

Figure N.6: Factored moment demand—simply supported (Swenson 2003)

The shear and moment demand diagrams present maximum shear and moment demands that consist of factored lane and truck live load effects (including impact forces, which could have been disregarded as previously recommended) and factored dead load effects. It has been recommended that the moment demand correspond with the load condition resulting in maximum shear demand; however, these moment demands represent maximum moment demands, which are of greater magnitude than those expected in response to the load conditions resulting in maximum shear demand at the critical cross-section locations. It is recommended that these demands be determined using bridge rating analysis software. Spans should be modeled as *simply supported* during analysis. All demands associated with simply supported behavior assumption should be satisfied along the *entire length* of the girder. This includes shear and bending moment demands at midspan.

N.3.3 Material Properties

Relevant material properties for the girder concrete, deck concrete, steel reinforcement, and FRP reinforcement are summarized in Table N.3. These properties include concrete design strength (f'_c), longitudinal steel reinforcement modulus of elasticity (E_s) and yield stress (f_y), FRP reinforcement modulus of elasticity (E_f) and nominal thickness ($t_{f,n}$), and an initial lower bound estimate of effective debonding strain ($\varepsilon_{fe,min}$).

Table N.3: Material properties

Material Property	Value
f'_c girder	6 ksi
f'_c deck	4 ksi
E_s	29000 ksi
f_y longitudinal steel	60 ksi
f_y vertical steel	60 ksi
E_f	11900 ksi
$t_{f,n}$	0.04 in.
$\varepsilon_{fe,min}$	0.003 in./in.

The concrete and steel material properties of original design and construction have been documented by ALDOT (1988). The FRP material properties have been documented for the for the Tyfo SCH-41 FRP-epoxy laminate reinforcement product (Fyfe 2011). The minimum effective debonding strain ($\varepsilon_{fe,min}$) is not a documented material property of the Tyfo SCH-41 product, but is an appropriate approximate value for initial design of a carbon FRP wet-layup reinforcement system that should not debond prior to yielding of longitudinal steel reinforcement.

N.3.4 Dimensional Properties

Relevant dimensional properties for the typical BT-54 cross-section constructed to behave compositely with the bridge deck are presented in Table N.4. These properties include the effective width of the compression zone (b), width of the girder web (b_v), and height of the girder-deck composite cross section.

Table N.4: Cross section dimensional properties

Dimensional Property	Value
b	91 in.
b_v	6 in.
h	64 in.

The typical BT-54 cross section constructed to behave compositely with the bridge deck is shown in Figure N.7.

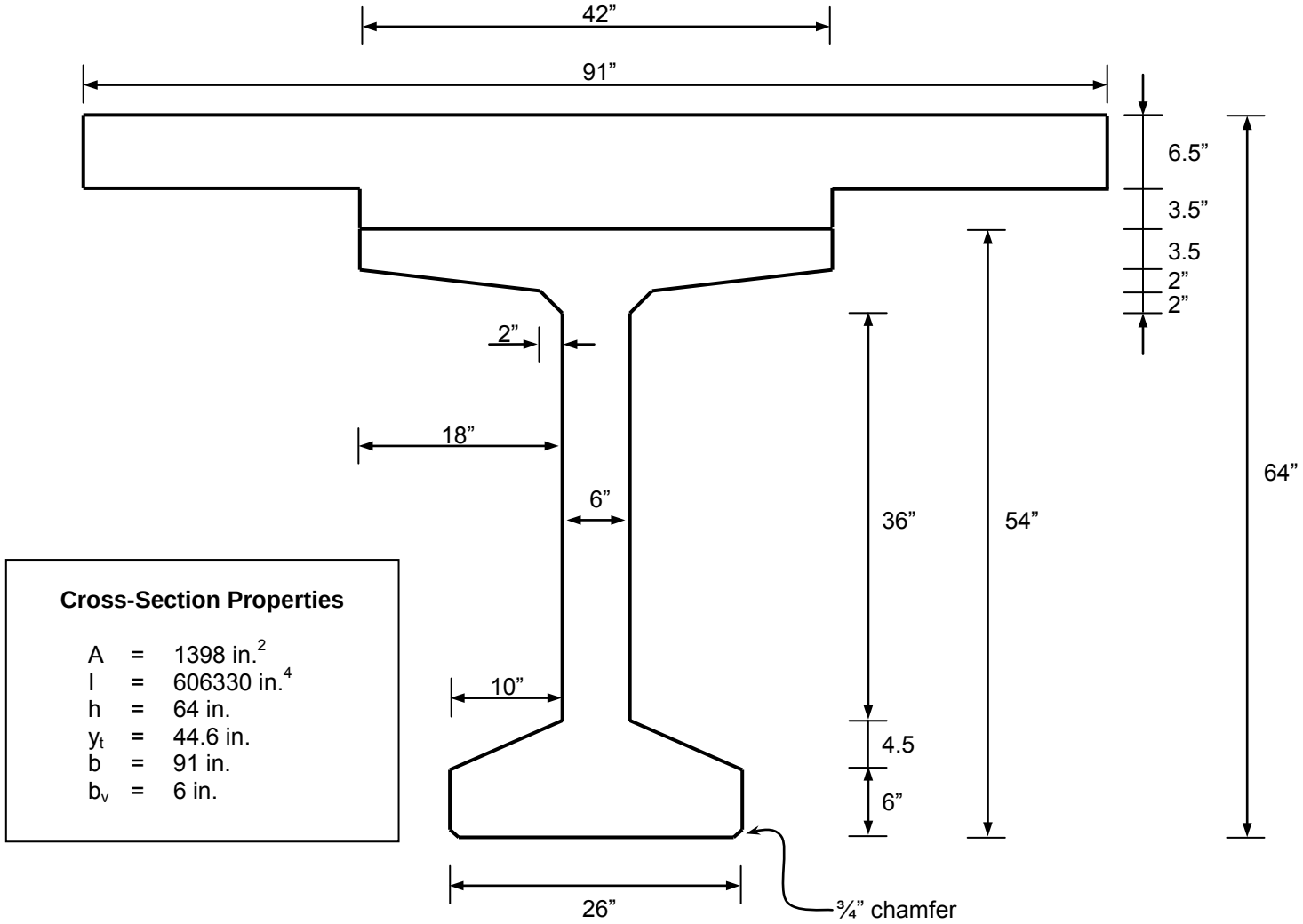

Figure N.7: Typical girder-deck composite cross section

The cross section dimensions have been documented by ALDOT (1988). The build-up depth between the deck and girder was documented as varying along the girder length. The maximum build-up depth of 3.5 in. has been assumed for the end region composite cross-sections. The effective compression zone width (b) of 91 in. has been determined in accordance with Article 4.6.2.6 of AASHTO LRFD.

Dimensional properties for the reinforcement associated with the two critical cross-section locations are presented in Table N.5. Reinforcement details and figures are presented following the table.

Table N.5: Reinforcement dimensional properties

Dimensional Property	Critical Section	
	Interior Face of Bearing Pad (A-A)	Termination of Continuity Reinforcement (B-B)
A_s	2.64 in.^{2}	0 in.^{2}
y_s	4.17 in.	—
d_s	59.8 in.	—
b_f	30 in.	58 in.
y_f	6.5 in.	3.4 in.
d_f	57.5 in.	60.6 in.
L_b	6.5 in.	38 in.
A_v	0.62 in.^{2}	0.62 in.^{2}
s	3.5 in.	6 in.

The mild steel continuity reinforcement details from original design and construction have been documented by ALDOT (1988). The continuity reinforcement configuration is shown in Figure N.8. The continuity reinforcement of the tension flange is considered to be effective reinforcement for tension capacity. The area (A_s) of reinforcement located in the tension flange is

equal to 2.64 in.^{2}, and the centroid (y_s) of this reinforcement is located 4.17 in. from the bottom of the girder, which equates to a reinforcement depth (d_s) of 59.8 in.

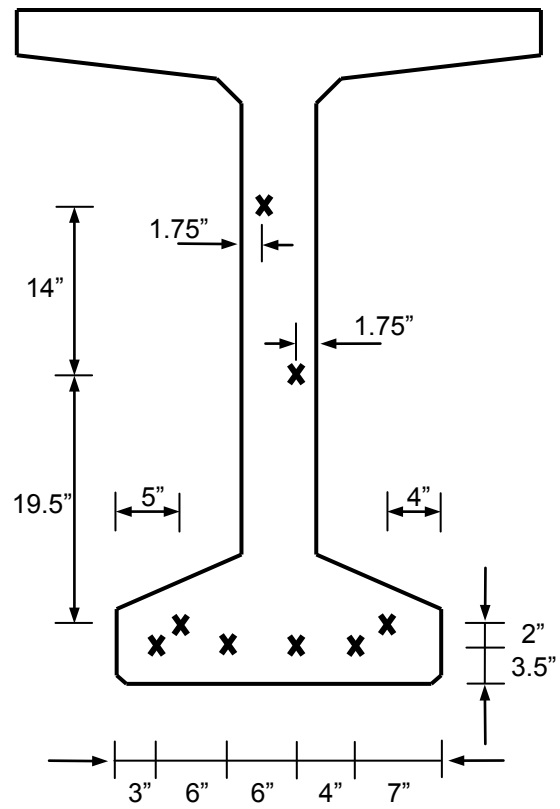

✘ Mild Steel Bent Bar (3/4” diameter)

Figure N.8: Continuity reinforcement—typical BT-54 cross section (ALDOT 1988; Swenson 2003)

The effective widths of FRP reinforcement (b_f) are representative of the repair system designed for Northbound Spans 10 and 11 of I-565 (Swenson 2003). The FRP reinforcement configurations are different for the two critical locations, as shown in Figures N.9 and N.10.

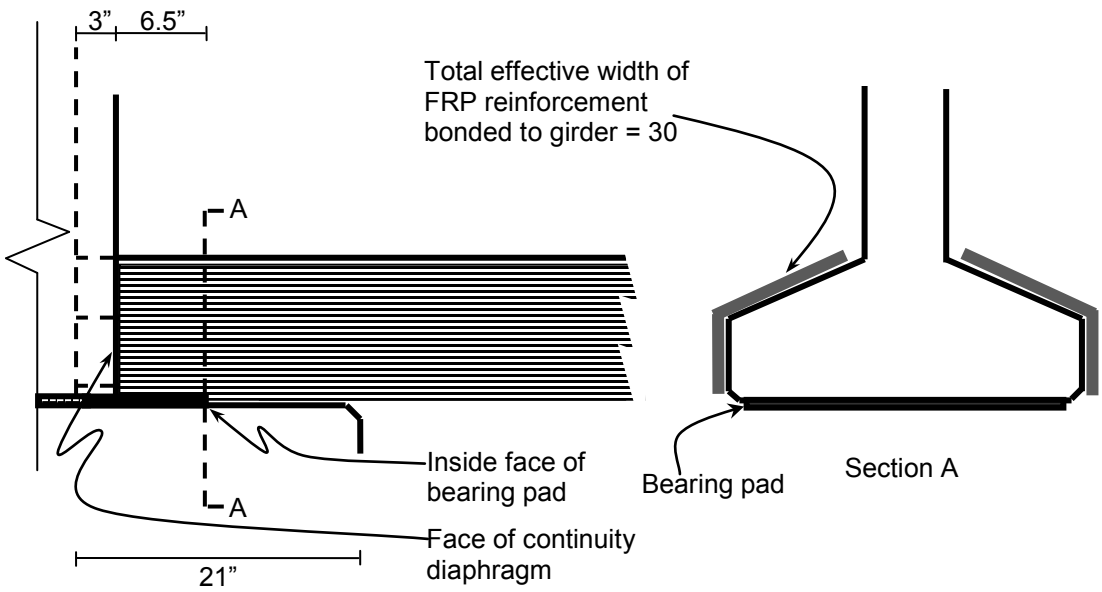

Figure N.9: Cross-sectional configuration of FRP—near diaphragm (Swenson 2003)

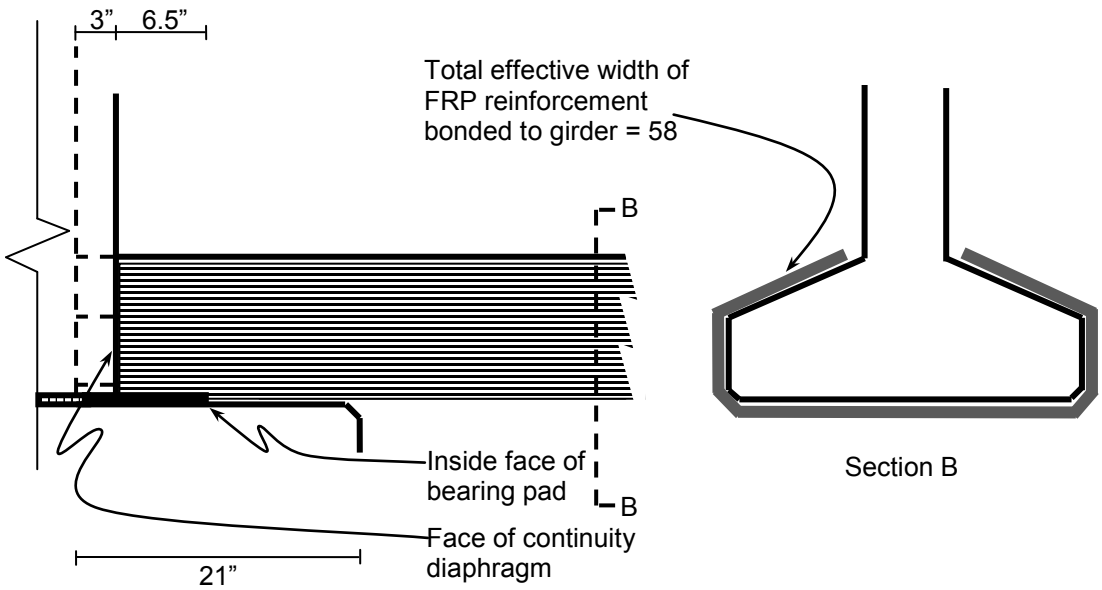

Figure N.10: Cross-sectional configuration of FRP—typical (Swenson 2003)

The FRP reinforcement configuration at the interior face of the bearing pad has an available effective width (b_f) of 30 in., and the typical configuration that wraps the perimeter of the tension flange has an effective width of 58 in. The centroid of FRP reinforcement (y_f) at the interior face of the bearing pad is roughly 6.5 in. from the bottom face of the girder, which equates to a reinforcement depth (d_f) of 57.5 in. The bonded length (L_b) from the FRP termination at the

face of the continuity diaphragm to the face of the bearing pad is roughly 6.5 in. The centroid of the typical FRP reinforcement configuration is roughly 3.4 in. from the bottom face of the girder, which equates to depth of 60.6 in. The bonded length from the diaphragm is roughly 38 in.

The vertical reinforcement details vary along the length of the girder, and have been documented by ALDOT (1988). The typical end region vertical reinforcement details are shown in Figure N.11.

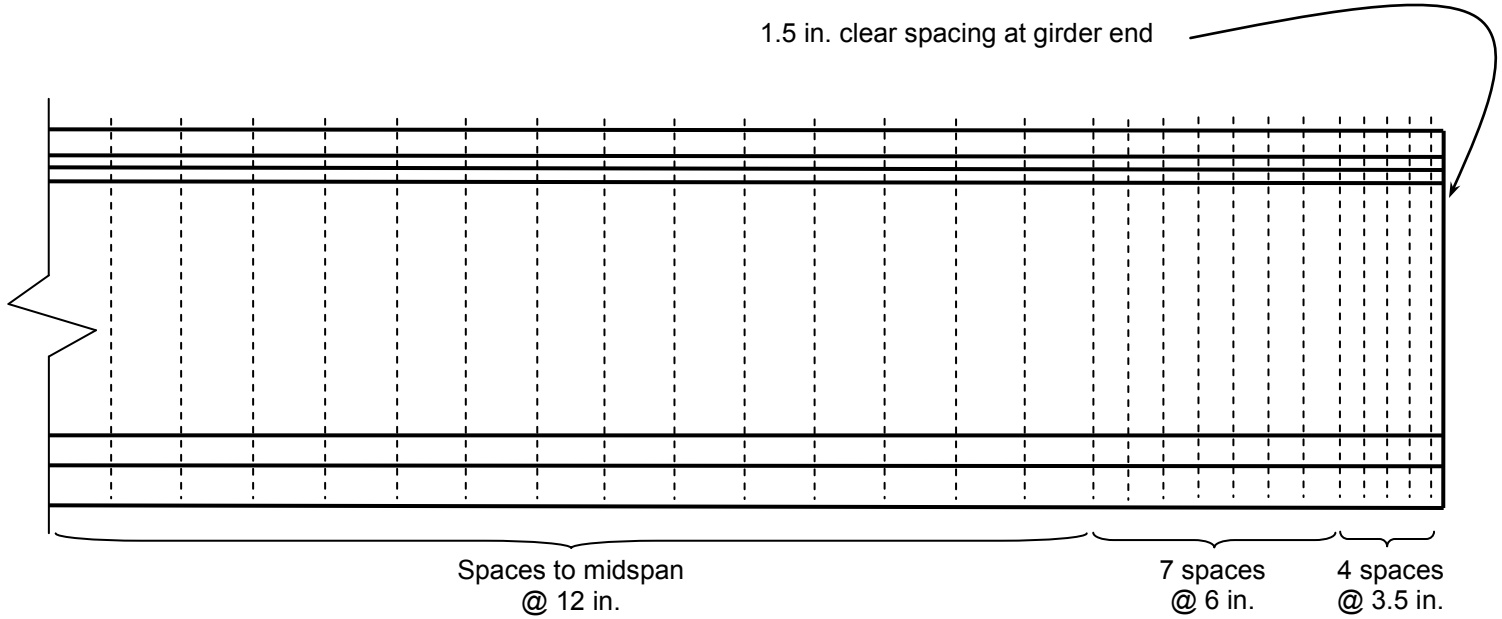

-- All stirrups within 24 ft of midspan are #4 bars (MK-452) @ 12 in. spacing.
All other stirrups are #5 bars (MK-553), spaced as shown above.

Figure N.11: Vertical shear reinforcement—location and spacing (ALDOT 1988; Swenson 2003)

The area (A_v) of vertical reinforcement within a representative cross section is equal to the area of two 5/8 in. diameter bars (0.62 in.^{2}). The stirrup spacing (s) for the region encompassing the interior face of the bearing pad is equal to 3.5 in. on center. The stirrup spacing for the region encompassing the termination of the continuity reinforcement is equal to 6 in. on center.

N.3.5 Initial Estimate of Required FRP Layers

An initial estimate of required FRP layers (n) is determined in accordance with the simplified procedure presented in Section 6.4.6 of this report. The terms associated with determining the area of FRP reinforcement required are shown in Table N.5, which include factored shear demand (V_u), resistance factor (ϕ), assumed crack inclination angle (θ), cross-sectional area of steel reinforcement (A_s), yield stress of longitudinal steel reinforcement (f_y), and an effective debonding stress ($f_{fe,min}$) based on the initial lower bound estimate of effective debonding strain ($\varepsilon_{fe,min}$). Formulas used to determine the required area of FRP reinforcement are shown following the table.

Table N.6: Initial estimate for minimum area of FRP required

Term	Units	Critical Section	
		Interior Face of Bearing Pad (A-A)	Termination of Continuity Reinforcement (B-B)
V_u	kips	242	231
ϕ	—	0.9	0.9
θ	degrees	45	45
$T_{n,req}$	kips	269	257
A_s	in.^{2}	2.64	0
f_y	ksi	60	—
$f_{fe,min}$	ksi	35.7	35.7
$A_{f,req}$	in.^{2}	3.10	7.20

$$T_{n,req} = \frac{V_u \cot(\theta)}{\phi}$$ **Eq. N.1**

$$A_{f,req} = \frac{\left(T_{n,req} - A_s f_y\right)}{f_{fe,min}}$$ **Eq. N.2**

The layers of FRP reinforcement required are determined based on the effective width (b_f) of the FRP composite at the critical cross-section locations and the manufacturer documented nominal thickness ($t_{f,n}$) per layer of installed FRP reinforcement. The terms associated with determining the layers of FRP reinforcement required are shown in Table N.7, which include FRP reinforcement width (b_f), nominal per layer thickness ($t_{f,n}$) required area ($A_{f,req}$) and required thickness ($t_{f,req}$). Formulas used to determine the required layers of FRP reinforcement are shown following the table.

Table N.7: Initial estimate for minimum layers of FRP required

Term	Units	Critical Section	
		Interior Face of Bearing Pad (A-A)	Termination of Continuity Reinforcement (B-B)
$A_{f,req}$	in.^{2}	3.10	7.20
b_f	in.	30	58
$t_{f,req}$	in.	0.10	0.12
$t_{f,n}$	in.	0.04	0.04
n required	layers	2.5	3.0
n whole number	layers	3	3

$$t_{f,req} = \frac{A_{f,req}}{b_f} \quad \textbf{Eq. N.3}$$

$$n_{req} = \frac{t_{f,req}}{t_{f,n}} \quad \textbf{Eq. N.4}$$

The 3 layers of FRP required at the critical location corresponding with the termination of continuity reinforcement controls the initial estimate of layers required.

N.3.6 Shear Strength Check—Three Layers

The nominal shear strength (V_n) of the proposed three-layer system must be checked in accordance with procedures presented in Section 6.4.7 of this report. First the effective debonding strain (ε_{fe}) of the FRP system must be checked to determine if the net tension strain (ε_s) in response to ultimate strength demands is satisfied. Once the net tension strain is satisfied, then the vertical shear strength must be checked to determine if the factored vertical shear demand (V_u) is satisfied.

N.3.6.1 Limiting Effective FRP Debonding Strain—Three Layers

The effective FRP debonding strain (ε_{fe}) is the strain limit at which a debonding failure may occur. It is likely that this strain limit is the controlling failure mode for this repair system. The terms associated with determining the limiting effective FRP strain are shown in Table N.8, which include FRP modulus of elasticity (E_f), nominal thickness per layer of reinforcement ($t_{f,n}$), girder concrete design strength (f'_c), FRP bonded length (L_b), FRP development length (L_{df}), bonded length reduction factor (β_L), and general FRP debonding strain (ε_{fd}). Formulas used to determine the effective FRP strain are shown following the table.

Table N.8: Effective FRP debonding strain—three layers

Term	Units	Critical Section	
		Interior Face of Bearing Pad (A-A)	Termination of Continuity Reinforcement (B-B)
n	layers	3	3
$t_{f,n}$	in	0.04	0.04
E_f	psi	11.9×10^6	11.9×10^6
f'_c	psi	6000	6000
L_b	in.	6.5	38
L_{df}	in.	7.74	7.74
β_L	–	0.97	1
ε_{fd}	in./in.	0.0054	0.0054
ε_{fe}	in./in.	0.0040	0.0040

$$L_{df} = 0.057\sqrt{\frac{nE_f t_f}{\sqrt{f'_c}}} \text{ in.} \quad (\text{in.} - \text{lb units}) \qquad \textbf{Eq. N.5}$$

$$\beta_L = \sin\left(\frac{\pi L_b}{2L_{df}}\right) \qquad \textbf{Eq. N.6}$$

$$\varepsilon_{fd} = 0.083\sqrt{\frac{f'_c}{nE_f t_f}} \text{ in.} \quad (\text{in.} - \text{lb units}) \qquad \textbf{Eq. N.7}$$

$$\varepsilon_{fe} = \varepsilon_{fd}\beta_L \leq 0.004 \text{ in./in.} \quad (\text{in.} - \text{lb units}) \qquad \textbf{Eq. N.8}$$

These formulas are presented as conversions from SI units, and the terms that control the effective debonding strain must maintain in.–lb units rather than in.–kip units to satisfy this

conversion. The maximum effective debonding strain permitted during design is 0.004 in./in. (0.4%). This limit controls the effective debonding strain for three layers of Tyfo SCH-41 installed on 6 ksi concrete at both critical locations.

N.3.6.2 Effective Shear Depth—Three Layers

The magnitude of the net tension strain in the tension flange response to shear demand is dependent upon the effective shear depth (d_v) of the cross section. This effective shear depth is controlled by the area of FRP reinforcement and the limiting effective stress. The terms associated with determining the effective shear depth are shown in Table N.9, which include cross sectional nominal bending moment strength (M_n), effective depth (d_e), and cross section height (h). Formulas used to determine the effective shear depth are shown following the table.

Table N.9: Effective shear depth—three layers

Term	Units	Critical Section	
		Interior Face of Bearing Pad (A-A)	**Termination of Continuity Reinforcement (B-B)**
M_n	kip-in.	19200	19900
$d_{v,1}$	in.	**58.1**	**60.1**
d_e	in.	58.6	60.6
$d_{v,2}$	in.	52.8	54.5
h	in.	64	64
$d_{v,3}$	in.	46.1	46.1
d_v	in.	58.1	60.1

Note: **Bold** values represent maximum effective shear depth that controls design

$$M_n = A_s f_y \left(d_s - \frac{a}{2}\right) + A_f \varepsilon_{fe} E_f d_f - \frac{a}{2} + 0.85 f'_c$$ **Eq. N.9**

$$a = \frac{A_s f_y + A_f \varepsilon_{fe} E_f}{0.85 f'_c b}$$ **Eq. N.10**

$$d_s = h - y_s$$ **Eq. N.11**

$$d_f = h - y_f$$ **Eq. N.12**

$$d_{v,1} \geq \frac{M_n}{A_s f_y + A_f f_{fe}}$$ **Eq. N.13**

$$d_{v,2} \geq 0.9 d_e$$ **Eq. N.14**

$$d_e = \frac{A_s f_y d_s + A_f f_{fe} d_f}{A_s f_y + A_f f_{fe}}$$ **Eq. N.15**

$$d_{v,3} \geq 0.72h$$ **Eq. N.16**

The maximum effective shear depth controls design. However, the larger of the two values that do not require the calculation of the nominal bending moment capacity can be used for simplicity if desired.

N.3.6.3 Net Longitudinal Tensile Strain—Initial Estimate

The net longitudinal tensile strain (ε_s) is the tensile strain expected in the tension reinforcement in response to ultimate strength shear demand. The terms associated with determining the net longitudinal tensile strain are shown in Table N.10, which include factored shear (V_u) and bending moment (M_u) demands, effective shear depth (d_v), longitudinal steel reinforcement modulus of elasticity (E_s) and cross sectional area (A_s), and FRP reinforcement modulus of elasticity (E_f) and cross sectional area (A_f). The formula used to determine the net longitudinal tensile strain is shown following the table.

Table N.10: Net longitudinal tensile strain—three layers

Term	Units	Critical Section	
		Interior Face of Bearing Pad (A-A)	Termination of Continuity Reinforcement (B-B)
M_u	kip-in	1500	6000
V_u	kips	242	231
d_v	in.	58.1	60.1
$V_u d_v$	kip-in.	**14100**	**13900**
E_s	ksi	29000	29000
A_s	in.^{2}	2.64	0
E_f	ksi	11900	11900
A_f	in.^{2}	3.60	6.96
ε_s	in./in.	0.0041	0.0056

Note: **Bold** values represent maximum value of either M_u or $V_u d_v$

$$\varepsilon_s = \frac{\frac{M_u}{d_v} + V_u}{E_s A_s + E_f A_f} \qquad \textbf{Eq. N.17}$$

The moment demand of this formula may not be taken to be less than the product of the shear demand multiplied by a distance equal to the effective shear depth, as shown in Equation N.18. The shear demand controls for this proposed repair system, as shown in Table N.10.

$$M_u \geq V_u d_v \qquad \textbf{Eq. N.18}$$

This net tensile strain must be less than the limiting effective debonding strain to proceed with design. If the net tensile strain exceeds the limiting effective debonding strain due to inadequate development length, but is less than the effective debonding strain permitted with

adequate development length, supplemental anchorage solutions can be used to decrease the required development length. If supplemental anchorage is required, proposed anchorage solutions should be tested to verify desired performance. Supplemental anchorage may be provided to decrease the required development length, but additional anchorage cannot be considered to increase the limiting effective debonding strain.

If the net tensile strain exceeds the limiting effective debonding strain at a critical location with adequate development length, then additional layers of FRP reinforcement are required. Increasing the amount of tension reinforcement will decrease the corresponding net tensile strain. A reiteration of the design checks are then required.

N.3.6.4 Layers Required to Satisfy Tensile Strain Demand

The tensile strain demand of the proposed three-layer repair system exceeds the limiting effective debonding strain at both critical locations, which is controlled by the maximum appropriate effective debonding strain limit of 0.004 in./in. Additional layers of FRP reinforcement are therefore required to decrease the net tensile strain demand. The amount of reinforcement required to satisfy the net tensile demand can be determined. The terms associated with determining the layers of FRP reinforcement required to satisfy the net longitudinal tensile strain demand are shown in Table N.11. The formula used to determine the required layers of FRP reinforcement is shown following the table.

Table N.11: Layers required satisfying net longitudinal tensile strain

Term	Units	Critical Section	
		Interior Face of Bearing Pad (A-A)	Termination of Continuity Reinforcement (B-B)
n	layers	3	3
ε_s	kip-in	0.0041	0.0056
ε_{fe}	kips	0.0040	0.0040
n required	layers	3.11	4.18
n whole number	layers	4	5

$$n = \frac{\frac{M_u}{d_v} + V_u - E_s A_s \varepsilon_{fe}}{E_f w_f t_{fn} \varepsilon_{fe}} \qquad \textbf{Eq. N.19}$$

The moment requirement presented in Equation N.19 still applies. The 5 layers of FRP required at the critical location corresponding with the termination of continuity reinforcement controls the layers of reinforcement required along the girder end region.

N.3.7 Shear Strength—Five Layers

The shear strength of the proposed five-layer system must be checked. Although the five-layer system was determined by satisfying the effective debonding strain limit of the three-layer system, the effective debonding strain of the five-layer system must still be checked to confirm that the net tension strain in response to strength-limit-state demands is satisfied. If the net tension strain is satisfied, then the vertical shear strength must be checked to determine if the factored vertical shear demand is satisfied.

N.3.7.1 Effective FRP Strain—Five Layers

The FRP debonding strain decreases as the number of FRP layers increases. The terms associated with determining the limiting effective FRP strain for the five-layer system are shown in Table N.12. Formulas used to determine the effective FRP strain have been previously presented following Table N.8.

Table N.12: Effective FRP debonding strain—five layers

Term	Units	Critical Section	
		Interior Face of Bearing Pad (A-A)	Termination of Continuity Reinforcement (B-B)
n	layers	5	5
$t_{f,n}$	in.	0.04	0.04
E_f	psi	11.9×10^6	11.9×10^6
f'_c	psi	6000	6000
L_b	in.	6.5	38
L_{df}	in.	9.99	9.99
β_L	–	0.85	1
ε_{df}	in./in.	0.0042	0.0042
ε_{fe}	in./in.	0.0036	0.0040

Due to the limited bonded length between the interior face of the bearing pad and the face of the diaphragm, the effective debonding strain at the interior face of the bearing pad is less than the maximum limit of 0.004 in./in. that controlled the effective debonding strain at the same location for the three-layer system.

N.3.7.2 Effective Shear Depth—Five Layers

The effective shear depth is also affected by the change in area of FRP reinforcement. The terms associated with determining the effective shear depth for the five-layer system are shown in Table N.13. Formulas used to determine the effective shear depth have been previously presented following Table N.9.

Table N.13: Effective shear depth—five layers

Term	Units	Critical Section	
		Interior Face of Bearing Pad (A-A)	Termination of Continuity Reinforcement (B-B)
M_n	kip-in.	20400	33000
$d_{v,1}$	in.	**57.7**	**59.7**
d_e	in.	58.4	60.6
$d_{v,2}$	in.	52.6	54.5
h	in.	64	64
$d_{v,3}$	in.	46.1	46.1
d_v	in.	57.7	59.7

Note: **Bold** values represent maximum effective shear depth that controls design

The shear depths at two critical locations are similar for the three- and five-layer systems, but the increased area of reinforcement for the five-layer system did result in a slightly decreased effective shear depth for both locations.

N.3.7.3 Net Longitudinal Tensile Strain—Five Layers

Although the limiting effective debonding strain decreases with additional layers of FRP reinforcement, the additional area of reinforcement also decreases the net longitudinal strain demand in response to ultimate strength demands. The terms associated with determining the

net longitudinal tensile strain are shown in Table N.14. The formula used to determine the net longitudinal tensile strain has been previously presented following Table N.10.

Table N.14: Net longitudinal tensile strain—five layers

Term	Units	Critical Section	
		Interior Face of Bearing Pad (A-A)	Termination of Continuity Reinforcement (B-B)
M_u	kip-in	1500	6000
V_u	kips	242	231
d_v	in.	57.7	59.7
$V_u d_v$	kip-in.	**14000**	**13800**
E_s	ksi	29000	29000
A_s	in.^{2}	2.64	0
E_f	ksi	11900	11900
A_f	in.^{2}	6	11.6
ε_s	in./in.	0.0033	0.0033

Note: **Bold** values represent maximum value of either M_u or $V_u d_v$

At the termination of the continuity reinforcement, the net longitudinal strain demand has decreased from 0.0056 in./in. with three layers to 0.0033 in./in. with five layers, which satisfies the limiting effective debonding strain at the termination of the continuity reinforcement that is still controlled by the maximum limit of 0.0040 in./in.

At the interior face of the bearing pad, the net longitudinal strain demand has decreased from 0.0041 in./in. with three layers of reinforcement to 0.0033 in./in. with five layers of reinforcement. Due to the relatively short bond length between the face of the face of the diaphragm and the critical location, the debonding strain at the interior face of the bearing pad required a reduction to 85 percent of the full value. This reduced the effective debonding strain from 0.0042 in./in. to 0.0036 in./in. at this location. Even though the effective debonding strain is

reduced, the net longitudinal strain demand is still satisfied with five layers of FRP reinforcement at the interior face of the bearing pad.

The net longitudinal strain demand is satisfied by the effective debonding strain capacity at both critical cross-section locations.

N.3.7.4 Vertical Shear Strength—Five Layers

After confirming that the net longitudinal strain in response to shear demand does not exceed the effective debonding strain, the vertical shear strength corresponding to that net longitudinal strain can be determined. The concrete and vertical reinforcement both provide vertical shear strength that is affected by the net longitudinal strain.

N.3.7.4.1 Concrete Shear Strength

The terms associated with determining the vertical shear strength (V_c) provided by the concrete are shown in Table N.15, which include net tension strain (ε_s), girder web concrete design strength (f'_c) and width (b_v), effective shear depth (d_v), and concrete shear capacity factor (β). Formulas used to determine the vertical shear strength provided by the concrete are shown following the table.

Table N.15: Vertical shear strength—concrete—five layers

Term	Units	Critical Section	
		Interior Face of Bearing Pad (A-A)	Termination of Continuity Reinforcement (B-B)
ε_s	in./in.	0.0033	0.0033
β	–	1.39	1.37
f'_c	ksi	6	6
b_v	in.	6	6
d_v	in.	58	59.7
V_c	kips	37	38

$$\beta = \frac{4.8}{1 + 750\varepsilon_s}$$ **Eq. N.20**

$$V_c = 0.0316\beta\sqrt{f'_c}b_v d_v$$ **Eq. N.21**

N.3.7.4.2 Vertical Reinforcement Shear Strength

The terms associated with determining the vertical shear strength (V_s) provided by the vertical reinforcement are shown in Table N.16, which includes net tension strain (ε_s), vertical steel reinforcement area (A_v) spacing (s) and yield strength (f_y), effective shear depth (d_v), and angle of crack inclination (θ). Formulas used to determine the vertical shear strength provided by the vertical reinforcement are shown following the table.

Table N.16: Vertical shear strength—vertical reinforcement—five layers

Term	Units	Critical Section	
		Interior Face of Bearing Pad (A-A)	Termination of Continuity Reinforcement (B-B)
ε_s	in./in.	0.0033	0.0033
θ	degrees	40.4	40.7
A_v	in.^{2}	0.62	0.62
f_y	ksi	60	60
s	in.	3.5	6.0
d_v	in.	58	59.7
V_s	kips	723	430

$$\theta = 29 + 3500\varepsilon_s \qquad \textbf{Eq. N.22}$$

$$V_s = \frac{A_v f_y d_v \cot(\theta)}{s} \qquad \textbf{Eq. N.23}$$

N.3.7.4.3 Nominal Vertical Shear Strength

The terms associated with determining the nominal vertical shear strength (V_n) are shown in Table N.17. Formulas used to determine the nominal vertical shear strength are shown following the table.

Table N.17: Nominal shear strength—five layers

Term	Units	Critical Section	
		Interior Face of Bearing Pad (A-A)	Termination of Continuity Reinforcement (B-B)
V_c	kips	37	38
V_s	kips	723	430
V_n	kips	760	**468**
f'_c	ksi	6	6
b_v	in.	6	6
d_v	in.	58	59.7
$V_{n,max}$	kips	522	537
V_n	kips	**522**	468

Note: **Bold** values represent the limiting value of either V_n or $V_{n,max}$

$$V_n = V_c + V_s \quad \textbf{Eq. N.24}$$

$$V_{n,max} = 0.25f'_c b_v d_v \quad \textbf{Eq. N.25}$$

The nominal shear strength at the interior face of the bearing pad is controlled by the limiting nominal vertical shear strength. The nominal shear strength at the termination of the continuity reinforcement is controlled by the increased vertical reinforcement spacing that decreases the vertical shear strength provided by the vertical reinforcement.

N.3.7.4.4 Vertical Shear Strength Verification—Five layers

The shear strength provided at both critical cross-section locations must satisfy the shear demand (V_u) at those locations. A reduction factor is applied to the nominal shear strength in accordance with AASHTO LRFD. This reduced shear strength must satisfy the factored shear demand. The reduced shear strengths and factored shear demands for both critical cross-section locations have been presented in Table N.18.

Table N.18: Vertical shear strength verification—five layers

Term	Units	Critical Section	
		Interior Face of Bearing Pad (A-A)	Termination of Continuity Reinforcement (B-B)
V_n	kips	522	468
ϕ	—	0.9	0.9
ϕV_n	kips	470	421
V_u	kips	242	231

The vertical shear strength provided with the five-layer system satisfies the vertical shear demand at both critical cross-section locations. If the vertical shear demands had not been satisfied, additional longitudinal FRP reinforcement would likely not improve the situation. Adding longitudinal FRP would increase the components of V_n only slightly. If the vertical shear demands are not satisfied by a proposed longitudinal reinforcement system, supplemental vertical reinforcement must be provided. The performance of any proposed supplemental vertical reinforcement solutions should be verified before installation.

N.3.7.5 Longitudinal Tension Strength Provided—Five Layers

The longitudinal reinforcement must also provide longitudinal tensile strength to satisfy longitudinal tension demand in response to combined shear and moment effects in the girder end region. The terms associated with determining the longitudinal tensile strength provided ($T_{n,prov}$) are shown in Table N.19. The formula used to determine the longitudinal tensile strength is shown following the table.

Table N.19: Longitudinal tension strength—five layers

Term	Units	Critical Section	
		Interior Face of Bearing Pad (A-A)	Termination of Continuity Reinforcement (B-B)
A_s	in.^{2}	2.64	0
f_y	ksi	60	—
n	layers	5	5
A_f	in.^{2}	6	11.6
f_{fe}	ksi	32.3	47.6
$T_{n,prov}$	kips	352	552

$$T_{n,prov} = A_s f_y + A_f f_{fe}$$ **Eq. N.26**

N.3.7.6 Longitudinal Tension Strength Required—Five Layers

The terms associated with determining the longitudinal tensile strength required ($T_{n,req}$) are shown in Table N.20. The formula used to determine the longitudinal tensile demand is shown following the table.

Table N.20: Longitudinal tension demand—five layers

Term	Units	Critical Section	
		Interior Face of Bearing Pad (A-A)	Termination of Continuity Reinforcement (B-B)
ϕ_f	–	0.9	0.9
M_u	kip-in.	1500	6000
d_v	in.	58	59.7
ϕ_v	–	0.9	0.9
V_u	kips	242	231
V_s	kips	723	430
V_u/ϕ_v	kips/in.	269	257
θ	degrees	40.4	40.7
$T_{n,req}$	kips	186	261

$$T_{n,req} = \left[\frac{M_u}{d_v \phi_f}\right] + \left[\frac{V_u}{\phi_v} - 0.5V_s\right]\cot(\theta) \qquad \textbf{Eq. N.27}$$

N.3.7.7 Longitudinal Tension Strength Verification—Five Layers

Reduction factors are applied to the factored longitudinal tension demand formula to amplify the longitudinal tension demand, as shown in Equation N.27. Thus, the nominal longitudinal tension strength does not require reduction to safely satisfy factored demand. The nominal longitudinal tension strengths and factored longitudinal tension demands from Tables N.19 and N.20 are presented in Table N.21 for comparison.

Table N.21: Longitudinal tension strength verification—five layers

Term	Units	Critical Section	
		Interior Face of Bearing Pad (A-A)	Termination of Continuity Reinforcement (B-B)
$T_{n,prov}$	kips	352	552
$T_{n,req}$	kips	186	261

N.3.7.8 Strength and Demand Comparisons—Five Layers

The reinforcement system should allow the critical cross-section locations of the structure to satisfy moment, shear, and longitudinal tension demands in response to the load condition resulting in the maximum ultimate strength shear demands at that location. The reinforcement system must also satisfy the shear demand without the resulting net longitudinal tension strain exceeding the effective debonding strain limit of the reinforcement system. The strengths and demands relevant to the proposed five-layer FRP reinforcement system are presented in Table N.22 for comparison.

Table N.22: Comparisons of strength and demand—five layers

Term	Units	Critical Section	
		Interior Face of Bearing Pad (A-A)	Termination of Continuity Reinforcement (B-B)
n	layers	5	5
ϕM_n	kip-in.	18400	29700
M_u	kip-in.	1500	6000
ε_{fe}	in./in.	0.036	0.040
ε_s	in./in.	0.033	0.033
ϕV_n	kips	470	421
V_u	kips	242	231
$T_{n,prov}$	kips	352	552
$T_{n,req}$	kips	186	261

Note: All of the demands are shown to be satisfied.

N.4 EXTENT OF FRP INSTALLATION

The length of FRP reinforcement to be installed is dependent upon the development of the prestressed strands after consideration of the cracking damage, as discussed in Section 6.5 of this report. It is recommended to extend the FRP reinforcement along the girder for a distance long enough to allow for full development of stresses in the prestressed strands.

It was previously assumed that the prestressed strands are not safely considered to be effective between the face of the end of the girder and the end of the initial region of debonded strands. Thus, the FRP reinforcement should be extended for a distance of at least one development length (ℓ_d) of the prestressed strands from the end of the initial region of debonded strands. The development length can be estimated using the approximation presented as Equation 6.32 in Section 6.5 of this report, as shown below.

$$\ell_d = 180 d_b \qquad \textbf{Eq. N.28}$$

$$d_b = 0.51 \text{ in.}$$

$$\ell_d = 92 \text{ in.}$$

The end of the initial region of debonded strands is located 45 in. from the face of the diaphragm, as shown in Figure N.2. The first (longest) layer of FRP reinforcement installed should extend from the face of the diaphragm to a distance of 137 in. from the face of the diaphragm.

Each subsequently installed layer should extend a distance 6 in. less than its respective underlying layer, as discussed in Section 6.5. Thus, the final (shortest) layer of FRP reinforcement should extend to a distance of 113 in. from the face of the diaphragm. These recommended lengths of FRP reinforcement for the five-layer FRP repair are shown in Figure N.12.

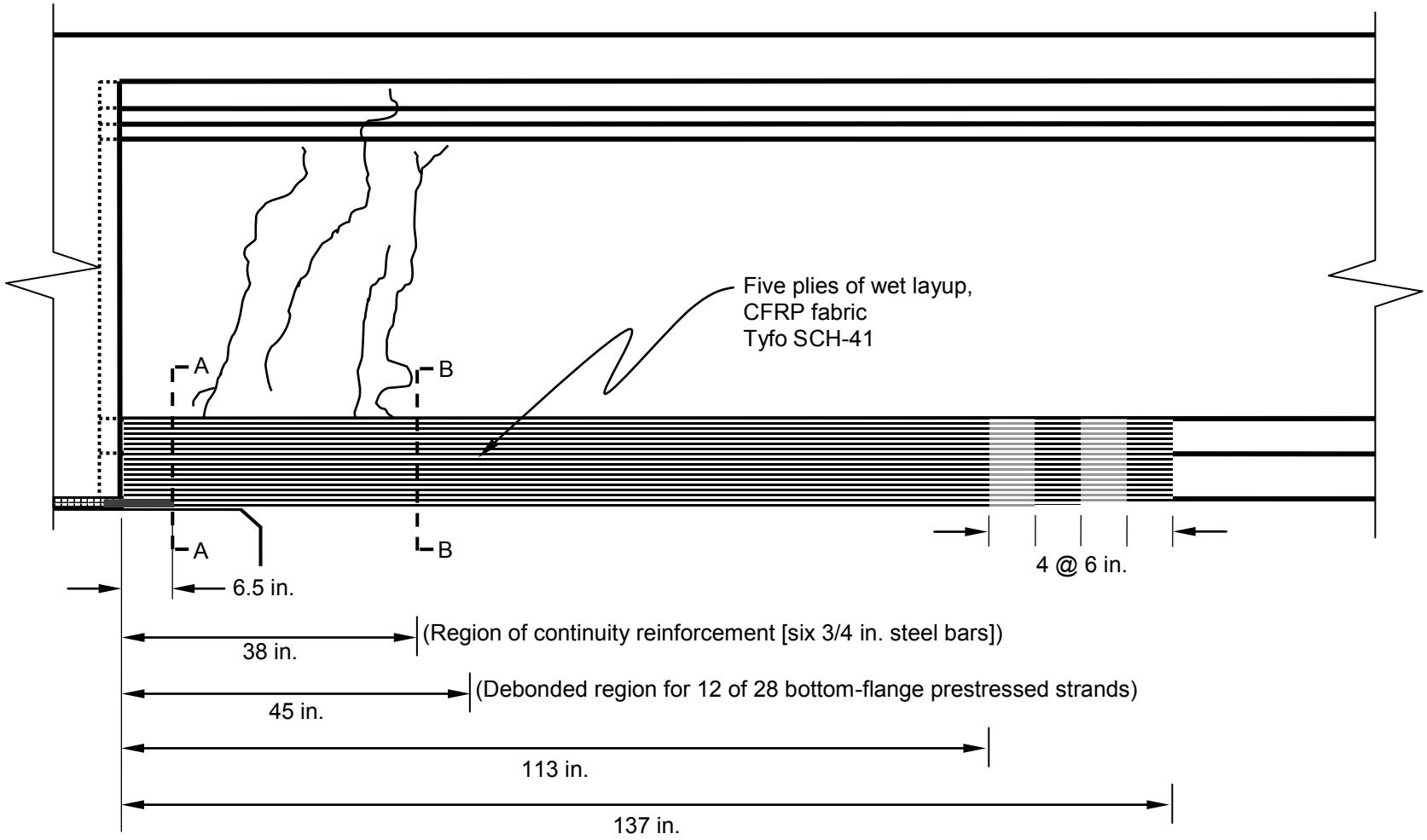

Figure N.12: Longitudinal configuration profile for five-layer FRP reinforcement system

N.5 ANCHORAGE

The limiting effective debonding strain at the interior face of the bearing has been reduced to reflect the bonded length available from the termination of reinforcement at the face of the diaphragm, as shown in Table N.12. The reduced effective debonding strain at this location still satisfies the net tension strain demand, as shown in Table N.22. Thus, the proposed five-layer FRP reinforcement system does not require additional anchorage at the termination of reinforcement at the face of the diaphragm. Supplemental anchorage may still be provided to decrease the required development length, but a proposed method for providing additional anchorage must be tested before implementation.

N.6 SERVICE-LIMIT-STATE VERIFICATION

It is appropriate to assume that the bridge structure will maintain partial continuity in response to service loads, as discussed in Section 6.7 of this report. The assumption of simply supported bridge behavior during strength-limit-state design results in FRP requirements that conservatively satisfy service-limit-state demands for a bridge structure that maintains partial continuity.

The stress-induced strain resulting from expected diurnal temperature variation must be checked with respect to the effective debonding strain of the FRP system. The formula for the maximum stress-induced strain expected in response to ambient temperatures is presented as Equation 6.33 in Section 6.7 of this report. This equation is also presented below with the values for the concrete coefficient of thermal expansion and the maximum expected change in temperature gradient that are presented in Section 5.4.2.2.2 of this report.

$$\varepsilon_{fe} > \frac{3}{2}[\alpha_T \delta(\Delta T_h)] \qquad \textbf{Eq. N.29}$$

$$\alpha_T = 6 \text{ x } 10^{-6} \text{ (in./in.)/°F}$$

$$\delta(\Delta T_h) = 60 \text{ °F}$$

$$\frac{3}{2}[\alpha_T \delta(\Delta T_h)] = 0.0005 \text{ in./in.}$$

$$\varepsilon_{fe} = 0.0036 \text{ in./in.}$$

A temperature gradient of 60 °F was selected to exceed measured temperature gradients as well as temperature gradients recommended by AASHTO for design. The effective debonding strain

limit far exceeds the expected stress-induced FRP strain in response to restrained ambient temperature changes.

N.7 DESIGN SUMMARY

The Tyfo SCH-41 FRP reinforcement product was selected for the proposed repair solution. Five layers of this FRP reinforcement are required to satisfy ultimate strength demands. All first installed (longest) layer must extend a distance of at least 137 in. from the face of the diaphragm to allow for full development of stresses in prestressed strands. It has been determined that supplemental anchorage is not necessary at the termination of FRP reinforcement at the face of the diaphragm, but additional anchorage may be provided to further decrease the risk of debonding failure, if an appropriate anchorage method has been verified. Also, the minimum effective debonding strain of this five-layer system is shown to adequately satisfy the maximum strain demand expected in response to ambient thermal conditions.

N.8 INSTALLATION RECOMMENDATIONS

Installation of the proposed five-layer FRP reinforcement system must adhere to the guidelines presented in Section 6.9 of this report. These guidelines refer to standard procedures for surface preparation and FRP reinforcement installation. Appropriate installation procedures are required for the effects assumed of the designed FRP reinforcement system to remain valid.

N.9 COMPARISON OF DESIGN RECOMMENDATION AND PREVIOUSLY INSTALLED FRP

An FRP reinforcement system was designed by Auburn University researchers (Swenson 2003) for the repair of Northbound Spans 10 and 11 of I-565 in Huntsville, Alabama—the same spans considered for the design example in this appendix. The repair was designed to resist tension forces that were predicted with strut-and-tie models. The reinforcement system was also designed in accordance with the effective debonding strain (ε_{fe}) specifications of ACI 440.2R-02, which have since been updated in ACI 440.2R-08 to reflect the findings of more recent research. The FRP reinforcement system was installed in December 2007.

The installed FRP reinforcement consists of 4 layers of FRP, with the longest layer extending 130 in. from the face of the continuity diaphragm. The FRP reinforcement design presented in this appendix—for the repair of the same girders using the same FRP reinforcement product—recommends an FRP reinforcement system consisting of 5 layers of FRP, with the longest layer extending 137 in. from the face of the continuity diaphragm.

The updated limiting effective debonding strain ($\varepsilon_{fe} \leq 0.004$ in./in.) of ACI 440.2R-08 is the primary reason for recommending 5 layers of reinforcement instead of the previously

recommended 4 layers. The longer recommended length of FRP reinforcement is due in part to the recommendation that the FRP be extended one prestressed strand development length (ℓ_d) beyond the primary region of debonded strands *as well as* beyond the previously recommended (Swenson 2003) assumed location of primary cracking. The updated design also recommends a simplified and appropriately conservative formula for the approximation of prestressed strand development length beginning at or beyond damaged regions within a girder.

Although the FRP reinforcement systems that were installed on Spans 10 and 11 in December 2007 do not satisfy the updated design recommendation, installation of an additional layer of reinforcement may not be absolutely necessary. The limiting effective debonding strain ($\varepsilon_{fe} \leq 0.004$ in./in.) controls the recommendation of 5 layers of reinforcement instead of 4 layers. The current installation of 4 layers satisfies strength requirements at the interior face of the bearing pad, but the net tension strain at the termination of the continuity reinforcement in response to factored AASHTO LRFD strength-limit-state shear demand is calculated to be 0.00418 in./in., which exceeds the limiting effective debonding strain of 0.004 in./in. by less than 5 percent. At sections like this one that are near a simple support—where there is minimal positive bending moment—the net tension strain determined in accordance with AASHTO LRFD specifications is a linear function of the factored shear demand. Therefore, the net tension strain exceeding the limiting effective debonding strain by 0.00018 in./in. represents a strength deficiency of less than 5 percent in response to factored shear demand at the termination of the continuity reinforcement.

The length of FRP reinforcement has been conservatively estimated by the design recommendation presented by Swenson (2003) and the slightly modified design recommendation presented in this report. It is appropriate to assume that the prestressed strands have slipped, but it is conservative to assume that this slip has resulted in the complete loss of effective prestress forces between the cracked section and the end of the girder. The simplified and appropriately conservative method for determining the required length of FRP reinforcement in accordance with the design procedure of this report is recommended for the design of FRP reinforcement systems for a general range of bridges that have experienced or are susceptible to the type of damage exhibited in the I-565 structures. Based on the cracking observed thus far in the life of this particular structure, it is appropriate to assume that the lengths of FRP reinforcement currently installed on the girders of Northbound Spans 10 and 11 are acceptable.

The installed 4 layers of reinforcement nearly satisfy the requirements of the updated design recommendations of this report. The small computed strength deficiency is based on full strength-limit-state AASHTO LRFD design loads for new construction in conjunction with the conservative limiting effective debonding strain of the FRP reinforcement. The length of FRP reinforcement currently installed allows for adequate development of prestressed strands beyond the primary crack locations in these particular spans. It is unknown if an additionally installed fifth

layer of reinforcement would perform as expected when bonded to previously installed FRP reinforcement that has been fully cured. Surface preparation procedures required for proper installation of additional FRP reinforcement may also be detrimental to the integrity of the existing FRP reinforcement. Whether or not the computed strength discrepancy justifies the cost, effort, and uncertainty associated with installation of an additional layer of FRP in Spans 10 and 11 is a decision best left to the discretion of ALDOT after consideration of these factors in light of the department's established maintenance philosophy. On the other hand, FRP reinforcement configurations for new repairs should be designed to satisfy the design recommendations proposed within this report.

N.10 VARYING MODULUS OF ELASTICITY FOR FRP REINFORCEMENT

The design effective debonding strain in areas of short bonded lengths is very dependent upon the modulus of elasticity (E_f) of the FRP reinforcement product. For design purposes, it is recommended to assume the design modulus of elasticity of the FRP reinforcement product reported by the manufacturer; however testing of representative samples may indicate that the installed product exhibits more tensile stiffness than originally assumed during design.

An increased modulus of elasticity may affect the effective debonding strain for locations with limited bonded length. Increasing the modulus of elasticity decreases the reinforcement debonding strain and increases the required development length. Both of these factors independently decrease the limiting effective debonding strain of the reinforcement system.

To better understand the ramifications of this issue, laboratory testing is recommended to assess the effective debonding strain for FRP reinforcement products with varying modulus of elasticity values determined in accordance with procedures (ASTM D3039 2008) recommended for testing representative samples of installed FRP reinforcement systems.